

**Construction Engineering
Research Laboratory**

ERDC/CERL MP-03-2



**US Army Corps
of Engineers®**

Engineer Research and
Development Center

Nonlinear Seismic Response of Asymmetric Structures

Jon F. Sfura

July 2003

20040329 007

Nonlinear Seismic Response of Asymmetric Structures

Jon F. Sfura

*Construction Engineering Research Laboratory
PO Box 9005
Champaign, IL 61826-9005*

Final Report

Approved for public release; distribution is unlimited.

Prepared for U.S. Army Corps of Engineers
 Washington, DC 20314-1000

Under Work Unit EJ0

NONLINEAR SEISMIC RESPONSE OF ASYMMETRIC STRUCTURES

Jon Fredric Sfura, Ph.D.

Department of Civil Engineering

University of Illinois at Urbana-Champaign, 2003

Douglas A. Foutch, Advisor

The purpose of this study was to investigate the nonlinear, inelastic response of one-story, symmetric- and asymmetric-plan structures to uniaxial and biaxial lateral earthquake ground motions. The investigation is a combined experimental and analytical program. Through the study, the lateral-torsional response of the system was studied for a range of system parameters with the goals of examining the adequacy of current building code torsional design assumptions and the ability of analytical software to predict inelastic response.

The experimental part of the investigation involved subjecting a single-story steel moment-frame to a series of uniaxial and biaxial earthquake ground motions on the U.S. Army CERL shaketable. The structure used in this study was a rigid diaphragm, approximately eight feet on a side, supported by four steel pipe columns, five feet in length. Sixteen steel masses were attached to the structure in various configurations in order to provide dead load and mass asymmetry. In addition, different types of pipe columns and steel strap braces were used to create eight different configurations of mass, strength, and stiffness eccentricity.

The analytical part of the investigation involved the nonlinear finite element programs Abaqus and Drain-3DX to analyze the response of the model during the earthquake simulations. Analytical models were created using the experimentally measured dynamic properties of the test structure and material properties of the steel columns. The elastic and inelastic response of the structure during each configuration was then predicted using both Abaqus and Drain-3DX. Subsequently, analytical models were created based on typical design assumptions, without the benefit of experimentally measured structural properties. The inelastic response of the structure was then predicted using Drain-3DX.

Implications of the experimental results on the adequacy of seismic design provisions are discussed. In addition, the ability of analytical software to predict inelastic torsional response is discussed for both a model tuned to the measured dynamic properties of the actual structure and a model based on common modeling assumptions. Further, the effects on prediction accuracy of different analytical modeling parameters and assumptions is discussed

TABLE OF CONTENTS

Chapter

1.	INTRODUCTION	1
1.1	OBJECTIVE	1
1.2	BACKGROUND	1
1.3	EXPERIMENTAL PROGRAM	8
1.4	SCOPE OF STUDY	10
1.5	REPORT REFERENCES	11
2.	EXPERIMENTAL PROGRAM	12
2.1	DESIGN OF THE MODEL STRUCTURE	12
2.2	SELECTION OF INPUT MOTIONS	17
2.3	EXPERIMENTAL SETUP	19
2.4	TEST SEQUENCE	20
2.5	TESTING PROCEDURE	22
3.	EXPERIMENTAL AND ANALYTICAL RESPONSE OVERVIEW	59
3.1	ACCELERATION	59
3.2	DISPLACEMENT	60
3.3	SHAKETABLE MOTION CONTROL ISSUES	61
3.4	BASE SHEAR AND TORSIONAL MOMENT	64
3.5	OVERTURNING MOMENT	68
3.6	COLUMN END BENDING MOMENT AND SHEAR	69
3.7	DYNAMIC CHARACTERIZATION OF THE MODEL	73
3.8	COLUMN STRAINS	74
3.9	DIAPHRAGM RIGIDITY	77
3.10	FINITE ELEMENT MODEL	80
3.11	FINITE ELEMENT ANALYSES	90
4.	EXPERIMENTAL AND ANALYTICAL RESPONSE OF TEST CONFIGURATION 1	129
4.1	OBSERVED STRUCTURAL RESPONSE	130
4.2	OBSERVED RESPONSE DISCUSSION	131
4.3	DYNAMIC CHARACTERIZATIONS OF THE MODEL	135
4.4	OBSERVED CONDITION OF THE STRUCTURE	136
4.5	FINITE ELEMENT ANALYSIS	136
4.6	SUMMARY AND CONCLUSIONS	141

5.	EXPERIMENTAL AND ANALYTICAL RESPONSE OF TEST CONFIGURATION 2	188
	5.1 OBSERVED STRUCTURAL RESPONSE	189
	5.2 OBSERVED RESPONSE DISCUSSION	189
	5.3 DYNAMIC CHARACTERIZATIONS OF THE MODEL	194
	5.4 OBSERVED CONDITION OF THE STRUCTURE	194
	5.5 FINITE ELEMENT ANALYSIS	195
	5.6 SUMMARY AND CONCLUSIONS	199
6.	EXPERIMENTAL AND ANALYTICAL RESPONSE OF TEST CONFIGURATION 4	257
	6.1 OBSERVED STRUCTURAL RESPONSE	258
	6.2 OBSERVED RESPONSE DISCUSSION	258
	6.3 DYNAMIC CHARACTERIZATIONS OF THE MODEL	264
	6.4 OBSERVED CONDITION OF THE STRUCTURE	265
	6.5 FINITE ELEMENT ANALYSIS	265
	6.6 SUMMARY AND CONCLUSIONS	269
7.	EXPERIMENTAL AND ANALYTICAL RESPONSE OF TEST CONFIGURATION 3	324
	7.1 OBSERVED STRUCTURAL RESPONSE	325
	7.2 OBSERVED RESPONSE DISCUSSION	325
	7.3 DYNAMIC CHARACTERIZATIONS OF THE MODEL	329
	7.4 OBSERVED CONDITION OF THE STRUCTURE	329
	7.5 FINITE ELEMENT ANALYSIS	330
	7.6 SUMMARY AND CONCLUSIONS	332
8.	EXPERIMENTAL AND ANALYTICAL RESPONSE OF TEST CONFIGURATION 8	376
	8.1 OBSERVED STRUCTURAL RESPONSE	377
	8.2 OBSERVED RESPONSE DISCUSSION	377
	8.3 DYNAMIC CHARACTERIZATIONS OF THE MODEL	379
	8.4 OBSERVED CONDITION OF THE STRUCTURE	379
	8.5 FINITE ELEMENT ANALYSIS	380
	8.6 SUMMARY AND CONCLUSIONS	382
9.	EXPERIMENTAL AND ANALYTICAL RESPONSE OF TEST CONFIGURATION 5	416
	9.1 OBSERVED STRUCTURAL RESPONSE	417
	9.2 OBSERVED RESPONSE DISCUSSION	417
	9.3 DYNAMIC CHARACTERIZATIONS OF THE MODEL	421

9.4	OBSERVED CONDITION OF THE STRUCTURE	422
9.5	FINITE ELEMENT ANALYSIS	423
9.6	SUMMARY AND CONCLUSIONS	426
10.	EXPERIMENTAL AND ANALYTICAL RESPONSE OF TEST CONFIGURATION 6	481
10.1	OBSERVED STRUCTURAL RESPONSE	482
10.2	OBSERVED RESPONSE DISCUSSION	483
10.3	DYNAMIC CHARACTERIZATIONS OF THE MODEL	487
10.4	OBSERVED CONDITION OF THE STRUCTURE	488
10.5	FINITE ELEMENT ANALYSIS	488
10.6	SUMMARY AND CONCLUSIONS	491
11.	EXPERIMENTAL AND ANALYTICAL RESPONSE OF TEST CONFIGURATION 7	546
11.1	OBSERVED STRUCTURAL RESPONSE	547
11.2	OBSERVED RESPONSE DISCUSSION	547
11.3	DYNAMIC CHARACTERIZATIONS OF THE MODEL	549
11.4	OBSERVED CONDITION OF THE STRUCTURE	550
11.5	FINITE ELEMENT ANALYSIS	550
11.6	SUMMARY AND CONCLUSIONS	553
12.	APPLICABILITY OF ANALYTICAL RESULTS	592
13.	SUMMARY AND CONCLUSIONS	606
13.1	OBJECTIVE AND SCOPE	606
13.2	EXPERIMENTAL PROGRAM	606
13.3	PRIMARY OBSERVATIONS FROM THE EXPERIMENTAL PROGRAM	608
13.4	PRIMARY OBSERVATIONS FROM THE ANALYTICAL PROGRAM	618
13.5	CONCLUSIONS	623
	LIST OF REFERENCES	629

Appendix

A.	SHAKING TABLE CHARACTERISTICS, INSTRUMENTATION, AND DATA DESCRIPTIONS	636
A.1	CERL SHAKETABLE	636
A.2	INSTRUMENTATION	637

LIST OF TABLES

<u>Number</u>		
1.1	Test Configuration Summary	11
2.1	Test Configuration Summary	24
2.2	List of Earthquake Simulations Performed	25
3.1	Test Configuration Summary	91
3.2.a	Maximum Table Accelerations and Diaphragm Acceleration and Angular Acceleration Response	92
3.2.b	Maximum Table Accelerations and Diaphragm Acceleration and Angular Acceleration Response	93
3.3.a	Maximum Diaphragm Relative Displacement and Rotation Response	94
3.3.b	Maximum Diaphragm Relative Displacement and Rotation Response	95
3.4.a	Maximum Base Shear and Torsional Moment	96
3.4.b	Maximum Base Shear and Torsional Moment	97
3.5	Test Structure Dynamic Properties	98
3.6	Abaqus Finite Element Model Dynamic Properties	99
3.7	Drain-3DX Finite Element Model Dynamic Properties	100
4.1	Test Structure Dynamic Properties - Test Configuration 1	145
4.2	Earthquake Simulations and Dynamic Characterization Tests - Test Configuration 1	146
4.3	Maximum Diaphragm Relative Displacement and Rotation – Test Configuration 1	147
4.4	Maximum Diaphragm Acceleration and Angular Acceleration Response - Test Configuration 1	148
4.5	Maximum Base Shear, Torsional Moment, and Overturning Moment - Test Configuration 1	149
4.6	Maximum Column End Moments - Test Configuration 1	150
4.7	Maximum Column End Shears - Test Configuration 1	151
4.8	Abaqus Stress-Strain Best-Fit Material Model - Test Configuration 1	152
4.9	Drain-3DX Stress-Strain Best-Fit Material Model - Test Configuration 1	152
4.10	Analytical vs. Experimental Displacement and Rotation Response Comparison - Test Configuration 1	153
5.1	Test Structure Dynamic Properties - Test Configuration 2	205
5.2	Earthquake Simulations and Dynamic Characterization Tests - Test Configuration 2	206

5.3	Maximum Diaphragm Relative Displacement and Rotation - Test Configuration 2	207
5.4	Maximum Diaphragm Acceleration and Angular Acceleration Response - Test Configuration 2	208
5.5	Maximum Base Shear, Torsional Moment, and Overturning Moment - Test Configuration 2	209
5.6	Maximum Column End Moments - Test Configuration 2	210
5.7	Maximum Column End Shears - Test Configuration 2	211
5.8	Abaqus Stress-Strain Best-Fit Material Model - Test Configuration 2	212
5.9	Drain-3DX Stress-Strain Best-Fit Material Model - Test Configuration 2	212
5.10	Analytical vs. Experimental Displacement and Rotation Response Comparison - Test Configuration 2	213
6.1	Test Structure Dynamic Properties - Test Configuration 4	274
6.2	Earthquake Simulations and Dynamic Characterization Tests - Test Configuration 4	275
6.3	Maximum Diaphragm Relative Displacement and Rotation - Test Configuration 4	276
6.4	Maximum Diaphragm Acceleration and Angular Acceleration Response - Test Configuration 4	277
6.5	Maximum Base Shear, Torsional Moment, and Overturning Moment - Test Configuration 4	278
6.6	Maximum Column End Moments - Test Configuration 4	279
6.7	Maximum Column End Shears - Test Configuration 4	280
6.8	Abaqus Stress-Strain Best-Fit Material Model - Test Configuration 4	281
6.9	Drain-3DX Stress-Strain Best-Fit Material Model - Test Configuration 4	281
6.10	Analytical vs. Experimental Displacement and Rotation Response Comparison - Test Configuration 4	282
7.1	Test Structure Dynamic Properties - Test Configuration 3	336
7.2	Earthquake Simulations and Dynamic Characterization Tests - Test Configuration 3	337
7.3	Maximum Diaphragm Relative Displacement and Rotation - Test Configuration 3	338
7.4	Maximum Diaphragm Acceleration and Angular Acceleration Response - Test Configuration 3	339
7.5	Maximum Base Shear, Torsional Moment, and Overturning Moment - Test Configuration 3	340
7.6	Maximum Column End Moments - Test Configuration 3	341
7.7	Maximum Column End Shears - Test Configuration 3	342
7.8	Abaqus Stress-Strain Best-Fit Material Model - Test Configuration 3	343
7.9	Drain-3DX Stress-Strain Best-Fit Material Model - Test Configuration 3	343

7.10	Analytical vs. Experimental Displacement and Rotation Response Comparison - Test Configuration 3	344
8.1	Test Structure Dynamic Properties - Test Configuration 8	386
8.2	Earthquake Simulations and Dynamic Characterization Tests - Test Configuration 8	387
8.3	Maximum Diaphragm Relative Displacement and Rotation - Test Configuration 8	388
8.4	Maximum Diaphragm Acceleration and Angular Acceleration Response - Test Configuration 8	389
8.5	Maximum Base Shear, Torsional Moment, and Overturning Moment - Test Configuration 8	390
8.6	Maximum Column End Moments - Test Configuration 8	391
8.7	Maximum Column End Shears - Test Configuration 8	392
8.8	Abaqus Stress-Strain Best-Fit Material Model - Test Configuration 8	393
8.9	Drain-3DX Stress-Strain Best-Fit Material Model - Test Configuration 8	393
8.10	Analytical vs. Experimental Displacement and Rotation Response Comparison - Test Configuration 8	394
9.1	Test Structure Dynamic Properties - Test Configuration 5	432
9.2	Earthquake Simulations and Dynamic Characterization Tests - Test Configuration 5	433
9.3	Maximum Diaphragm Relative Displacement and Rotation - Test Configuration 5	434
9.4	Maximum Diaphragm Acceleration and Angular Acceleration Response - Test Configuration 5	435
9.5	Maximum Base Shear, Torsional Moment, and Overturning Moment - Test Configuration 5	436
9.6	Maximum Column End Moments - Test Configuration 5	437
9.7	Maximum Column End Shears - Test Configuration 5	438
9.8	Abaqus Stress-Strain Best-Fit Material Model – 5” Standard Columns – Test Configuration 5	439
9.9	Abaqus Stress-Strain Best-Fit Material Model – 4” Double Extra-Strong Columns – Test Configuration 5	440
9.10	Drain-3DX Stress-Strain Best-Fit Material Model – 5” Standard Columns – Test Configuration 5	441
9.11	Drain-3DX Stress-Strain Best-Fit Material Model – 4” Double Extra-Strong Columns – Test Configuration 5	441
9.12	Analytical vs. Experimental Displacement and Rotation Response Comparison - Test Configuration 5	442
10.1	Test Structure Dynamic Properties - Test Configuration 6	497

10.2	Earthquake Simulations and Dynamic Characterization Tests - Test Configuration 6	498
10.3	Maximum Diaphragm Relative Displacement and Rotation - Test Configuration 6	499
10.4	Maximum Diaphragm Acceleration and Angular Acceleration Response - Test Configuration 6	500
10.5	Maximum Base Shear, Torsional Moment, and Overturning Moment - Test Configuration 6	501
10.6	Maximum Column End Moments - Test Configuration 6	502
10.7	Maximum Column End Shears - Test Configuration 6	503
10.8	Abaqus Stress-Strain Best-Fit Material Model - 4" Extra-Strong Columns Test Configuration 6	504
10.9	Abaqus Stress-Strain Best-Fit Material Model - Diagonal Braces Test Configuration 6	505
10.10	Drain-3DX Stress-Strain Best-Fit Material Model – 4" Extra-Strong Columns – Test Configuration 6	506
10.11	Drain-3DX Stress-Strain Best-Fit Material Model – Diagonal Braces Test Configuration 6	506
10.12	Analytical vs. Experimental Displacement and Rotation Response Comparison - Test Configuration 6	507
11.1	Test Structure Dynamic Properties - Test Configuration 7	556
11.2	Earthquake Simulations and Dynamic Characterization Tests - Test Configuration 7	557
11.3	Maximum Diaphragm Relative Displacement and Rotation - Test Configuration 7	558
11.4	Maximum Diaphragm Acceleration and Angular Acceleration Response - Test Configuration 7	559
11.5	Maximum Base Shear, Torsional Moment, and Overturning Moment - Test Configuration 7	560
11.6	Maximum Column End Moments - Test Configuration 7	561
11.7	Maximum Column End Shears - Test Configuration 7	562
11.8	Abaqus Stress-Strain Best-Fit Material Model - 5" Standard Columns Test Configuration 7	563
11.9	Abaqus Stress-Strain Best-Fit Material Model - 4" Double Extra-Strong Columns – Test Configuration 7	564
11.10	Abaqus Stress-Strain Best-Fit Material Model - Diagonal Braces Test Configuration 7	565
11.11	Drain-3DX Stress-Strain Best-Fit Material Model – 5" Standard Columns Test Configuration 7	566
11.12	Drain-3DX Stress-Strain Best-Fit Material Model – 4" Double Extra-Strong Columns – Test Configuration 7	566
11.13	Drain-3DX Stress-Strain Best-Fit Material Model – Diagonal Braces Test Configuration 7	566

11.14	Analytical vs. Experimental Displacement and Rotation Response Comparison - Test Configuration 7	567
12.1	Modal Frequencies – Test Structure and Case 1 & 2 Analytical Models	599
12.2	Analytical vs. Experimental Displacement and Rotation Response Comparison – Elastic Simulations – Analytical Models with Design Assumptions	600
12.3	Analytical vs. Experimental Displacement and Rotation Response Comparison – Inelastic Simulations – Non-Rigid Link Models Case 1 and Case 2 – Experimental Material Model	601
12.4	Analytical vs. Experimental Displacement and Rotation Response Comparison – Inelastic Simulations – Elastic-Plastic with Hardening and Elastic-Perfectly Plastic Material Models – Non-Rigid Link Model Case 2 ...	602
13.1	Analytical vs. Experimental Displacement and Rotation Response Comparison – Elastic Simulations	626
13.2.a	Analytical vs. Experimental Displacement and Rotation Response Comparison – Inelastic Simulations	627
13.2.b	Analytical vs. Experimental Displacement and Rotation Response Comparison – Inelastic Simulations	628
A.1	TESS Performance Parameters	643
A.2.a	Instrumentation List for Model	644
A.2.b	Instrumentation List for Model	645
A.2.c	Instrumentation List for Model	646
A.2.d	Instrumentation List for Model	647

LIST OF FIGURES

Number

2.1	Perspective View of Model Structure	26
2.2	Elevation View of East Side of Structure	27
2.3	Elevation View of South Side of Structure	28
2.4	Plan View of Diaphragm	29
2.5	Diaphragm Elevation C-C	30
2.6	Elevation View of Slab Detail	31
2.7	Diaphragm Elevation A-A	32
2.8	Diaphragm Section D-D	32
2.9	Diaphragm Elevation B-B	33
2.10	Diaphragm Beam Flange Detail 1	34
2.11	Diaphragm Beam Flange Detail 2	34
2.12	Pipe Column Assembly	35
2.13	Column Top End Plate Detail	36
2.14	Column Bottom End Plate Detail	36
2.15	1-1/8" Diameter A490 Bolt	37
2.16	Octagonal Steel Mass	38
2.17	Square Steel Mass	39
2.18	Diaphragm Elevation C-C	40
2.19	Elevation View of Structure with Concentric Lateral Bracing	41
2.20	Plan View of Bottom Gusset Plate	42
2.21	Elevation View of Bottom Gusset Plate	42
2.22	Plan View of Top Gusset Plate	43
2.23	Elevation View of Top Gusset Plate	43
2.24	Original Imperial Valley Input Motions – X-Axis – No Filtering – Scaled to Shaketable Displacement Limits	44
2.25	Original Imperial Valley Input Motions – Y-Axis – No Filtering – Scaled to Shaketable Displacement Limits	45
2.26	Modified Imperial Valley Input Motions – X-Axis – High-Pass Filtered at ½ Hz – Scaled to Shaketable Displacement Limits	46
2.27	Modified Imperial Valley Input Motions – Y-Axis – High-Pass Filtered at ½ Hz – Scaled to Shaketable Displacement Limits	47
2.28	Modified Imperial Valley Input Motions – X-Axis – High-Pass Filtered at 1 Hz – Scaled to Shaketable Displacement Limits	48
2.29	Elastic Response Spectra – Unfiltered Imperial Valley Ground Motions	49
2.30	Elastic Response Spectra – Test Configuration 2 Filtered Imperial Valley Ground Motions	50
2.31	Perspective View of Test Configuration Model 1	51

2.32	Perspective View of Test Configuration Model 2	52
2.33	Perspective View of Test Configuration Model 3	53
2.34	Perspective View of Test Configuration Model 4	54
2.35	Perspective View of Test Configuration Model 5	55
2.36	Perspective View of Test Configuration Model 6	56
2.37	Perspective View of Test Configuration Model 7	57
2.38	Perspective View of Test Configuration Model 8	58
3.1	Diaphragm Acceleration Transducers	101
3.2	Diaphragm Displacement Transducers	102
3.3	Shaketable Accelerations vs. Time – EQ 02 – 25% Y-Axis Imperial Valley – Symmetric Mass	103
3.4	Shaketable Accelerations vs. Time – EQ 03 – 25% Biaxial Imperial Valley – Symmetric Mass	104
3.5	Shaketable Accelerations vs. Time – EQ 07 – 100% Y-Axis Imperial Valley – Symmetric Mass	105
3.6	Shaketable Accelerations vs. Time – EQ 15 – 100% Biaxial Imperial Valley – Symmetric Mass	106
3.7	Shaketable Accelerations vs. Time – EQ 23 – 100% Biaxial Imperial Valley – 1/4 Asymmetric Mass	107
3.8	Fourier Transforms – Y-Axis Shaketable Response During X-Axis Uniaxial Simulations	108
3.9	Shaketable Acceleration vs. Time – 100% Biaxial Imperial Valley – Symmetric Mass – 1/2 Asymmetric Mass – 1/4 Asymmetric Mass	109
3.10	Typical White Noise Transfer Functions – Symmetric Mass	110
3.11	Typical White Noise Transfer Functions – 1/2 Asymmetric Mass	111
3.12	Typical White Noise Transfer Functions – 1/4 Asymmetric Mass	112
3.13	Typical Sine Decay Time Histories – Symmetric Mass	113
3.14	Typical Sine Decay Time Histories – 1/2 Asymmetric Mass	114
3.15	Typical Sine Decay Time Histories – 1/4 Asymmetric Mass	115
3.16	Typical Sine Sweep Transfer Functions – Symmetric Mass	116
3.17	Typical Sine Sweep Transfer Functions – 1/2 Asymmetric Mass	117
3.18	Typical Sine Sweep Transfer Functions – 1/4 Asymmetric Mass	118
3.19	Angular Acceleration vs. Time – EQ 29 – 150% Biaxial Imperial Valley – 1/2 Asymmetric Mass	119
3.20	Test Structure Diaphragm Original Composite Section and Transformed Section	120
3.21	Typical Abaqus Test Structure Finite Element Model	121
3.22	Typical Drain-3DX Test Structure Finite Element Model	122
3.23	Abaqus Pipe Section Integration Points	123
3.24	Drain-3DX Nonlinear Fiber Locations Relative to Pipe Column Cross-Section	123

3.25	Schematic Illustration of Hardening Models	124
3.26	Combined Isotropic/Kinematic Hardening Material Model	125
3.27	Perfect Plasticity Material Model	125
3.28	Isotropic Hardening Material Model	126
3.29	Kinematic Hardening Material Model	126
3.30	One-Dimensional Representation of the Nonlinear Isotropic/Kinematic Hardening Model	127
3.31	Cyclic Hardening Behavior of A 36 Steel	128
4.1	Perspective View of Test Configuration Model 1	154
4.2	Acceleration and Displacement vs. Time – EQ 01	155
4.3	Force vs. Displacement and Torsional Moment vs. Rotation – EQ 01	156
4.4	Acceleration and Displacement vs. Time – EQ 02	157
4.5	Force vs. Displacement and Torsional Moment vs. Rotation - EQ 02	158
4.6	Acceleration and Displacement vs. Time – EQ 03	159
4.7	Force vs. Displacement and Torsional Moment vs. Rotation - EQ 03	160
4.8	Acceleration and Displacement vs. Time – EQ 07	161
4.9	Force vs. Displacement and Torsional Moment vs. Rotation – EQ 07	162
4.10	Force-Deformation Response – Test Configuration 1	163
4.11	Torsional Moment-Rotation Response – Test Configuration 1	164
4.12	Elastic Response Spectra – EQ 01 – 25% X-Axis Imperial Valley Ground Motion	165
4.13	Elastic Response Spectra – EQ 02 – 25% Y-Axis Imperial Valley Ground Motion	166
4.14	Elastic Response Spectra – EQ 03 – 25% Biaxial Imperial Valley Ground Motion	167
4.15	Elastic Response Spectra – EQ 07 – 100% Y-Axis Imperial Valley Ground Motion	168
4.16	Test Structure Prior to Earthquake Simulations	169
4.17	Test Structure Prior to Earthquake Simulations	169
4.18	Test Structure After Earthquake Simulations	170
4.19	Test Structure After Earthquake Simulations	170
4.20	Test Structure Northeast Column After Earthquake Simulations	171
4.21	Fracture at Column and Column Base Plate	172
4.22	Abaqus Stress vs. Strain Finite Element Material Model Definition – Test Configuration 1	173
4.23	Drain-3DX Stress vs. Strain Finite Element Material Model Definition – Test Configuration 1	174
4.24	Abaqus Finite Element Model for Test Configuration 1	175
4.25	Drain-3DX Finite Element Model for Test Configuration 1	176
4.26	Abaqus Analytical Displacement vs. Time – EQ 01 – 25% X-Axis Imperial Valley	177

4.27	Drain-3DX Analytical Displacement vs. Time – EQ 01 – 25% X-Axis Imperial Valley	178
4.28	Abaqus Analytical Displacement vs. Time – EQ 02 – 25% Y-Axis Imperial Valley	179
4.29	Drain-3DX Analytical Displacement vs. Time – EQ 02 – 25% Y-Axis Imperial Valley	180
4.30	Abaqus Analytical Displacement vs. Time – EQ 03 – 25% Biaxial Imperial Valley	181
4.31	Drain-3DX Analytical Displacement vs. Time – EQ 03 – 25% Biaxial Imperial Valley	182
4.32	Abaqus Analytical Displacement vs. Time – EQ 07 – 100% Y-Axis Imperial Valley – Combined Material Hardening	183
4.33	Drain-3DX Analytical Displacement vs. Time – EQ 07 – 100% Y-Axis Imperial Valley	184
4.34	Abaqus Analytical Displacement vs. Time – EQ 07 – 100% Y-Axis Imperial Valley – Perfect Plasticity	185
4.35	Abaqus Analytical Displacement vs. Time – EQ 07 – 100% Y-Axis Imperial Valley – Isotropic Material Hardening	186
4.36	Abaqus Analytical Displacement vs. Time – EQ 07 – 100% Y-Axis Imperial Valley – Kinematic Material Hardening	187
5.1	Perspective View of Test Configuration Model 2	214
5.2	Acceleration and Displacement vs. Time – EQ 12	215
5.3	Force vs. Displacement and Torsional Moment vs. Rotation – EQ 12	216
5.4	Acceleration and Displacement vs. Time – EQ 13	217
5.5	Force vs. Displacement and Torsional Moment vs. Rotation - EQ 13	218
5.6	Acceleration and Displacement vs. Time – EQ 14	219
5.7	Force vs. Displacement and Torsional Moment vs. Rotation - EQ 14	220
5.8	Acceleration and Displacement vs. Time – EQ 15	221
5.9	Force vs. Displacement and Torsional Moment vs. Rotation - EQ 15	222
5.10	Acceleration and Displacement vs. Time – EQ 16	223
5.11	Force vs. Displacement and Torsional Moment vs. Rotation - EQ 16	224
5.12	Force-Deformation Response – Test Configuration 2	225
5.13	Torsional Moment-Rotation Response – Test Configuration 2	226
5.14	Maximum Force vs. Displacement and Maximum Torsional Moment vs. Rotation – Test Configuration 2 – 10% - 150% Biaxial Imperial Valley	227
5.15	Elastic Response Spectra – EQ 12 – 25% X-Axis Imperial Valley Ground Motion	228
5.16	Elastic Response Spectra – EQ 13 – 25% Y-Axis Imperial Valley Ground Motion	229
5.17	Elastic Response Spectra – EQ 14 – 25% Biaxial Imperial Valley Ground Motion	230

5.18	Elastic Response Spectra – EQ 15 – 100% Biaxial Imperial Valley Ground Motion	231
5.19	Test Structure Prior to Earthquake Simulations	232
5.20	Test Structure After Earthquake Simulations	233
5.21	Test Structure After Earthquake Simulations	234
5.22	Test Structure Northeast Column After Earthquake Simulations	235
5.23	Fracture at Column and Column Base Plate	236
5.24	Abaqus Stress vs. Strain Finite Element Material Model Definition – Test Configuration 2	236
5.25	Drain-3DX Stress vs. Strain Finite Element Material Model Definition – Test Configuration 2	237
5.26	Abaqus Finite Element Model for Test Configuration 2	238
5.27	Drain-3DX Finite Element Model for Test Configuration 2	239
5.28	Abaqus Analytical Displacement vs. Time – EQ 12	240
5.29	Drain-3DX Analytical Displacement vs. Time – EQ 12	241
5.30	Abaqus Analytical Displacement vs. Time – EQ 13	242
5.31	Drain-3DX Analytical Displacement vs. Time – EQ 13	243
5.32	Abaqus Analytical Displacement vs. Time – EQ 14	244
5.33	Drain-3DX Analytical Displacement vs. Time – EQ 14	245
5.34	Abaqus Analytical Displacement vs. Time – EQ 15 – 100% Biaxial Imperial Valley – Combined Material Hardening	246
5.35	Abaqus Analytical Rotation vs. Time – EQ 15 – 100% Biaxial Imperial Valley – Combined Material Hardening	247
5.36	Drain-3DX Analytical Displacement vs. Time – EQ 15 – 100% Biaxial Imperial Valley	248
5.37	Drain-3DX Analytical Rotation vs. Time – EQ 15 – 100% Biaxial Imperial Valley	249
5.38	Abaqus Analytical Displacement vs. Time – EQ 16 – 150% Biaxial Imperial Valley – Combined Material Hardening	250
5.39	Abaqus Analytical Rotation vs. Time – EQ 16 – 150% Biaxial Imperial Valley – Combined Material Hardening	251
5.40	Drain-3DX Analytical Displacement vs. Time – EQ 16 – 150% Biaxial Imperial Valley	252
5.41	Drain-3DX Analytical Rotation vs. Time – EQ 16 – 150% Biaxial Imperial Valley	253
5.42	Abaqus Analytical Displacement vs. Time – EQ 16 – 150% Biaxial Imperial Valley – Perfect Plasticity	254
5.43	Abaqus Analytical Displacement vs. Time – EQ 16 – 150% Biaxial Imperial Valley – Isotropic Material Hardening	255
5.44	Abaqus Analytical Displacement vs. Time – EQ 16 – 150% Biaxial Imperial Valley – Kinematic Material Hardening	256
6.1	Perspective View of Test Configuration Model 4	283

6.2	Acceleration and Displacement vs. Time – EQ 25	284
6.3	Force vs. Displacement and Torsional Moment vs. Rotation – EQ 25	285
6.4	Acceleration and Displacement vs. Time – EQ 26	286
6.5	Force vs. Displacement and Torsional Moment vs. Rotation - EQ 26	287
6.6	Acceleration and Displacement vs. Time – EQ 27	288
6.7	Force vs. Displacement and Torsional Moment vs. Rotation - EQ 27	289
6.8	Acceleration and Displacement vs. Time – EQ 28	290
6.9	Force vs. Displacement and Torsional Moment vs. Rotation - EQ 28	291
6.10	Acceleration and Displacement vs. Time – EQ 29	292
6.11	Force vs. Displacement and Torsional Moment vs. Rotation - EQ 29	293
6.12	Force-Deformation Response – Test Configuration 4	294
6.13	Torsional Moment-Rotation Response – Test Configuration 4	295
6.14	Maximum Force vs. Displacement and Maximum Torsional Moment vs. Rotation – Test Configuration 4 – 10% - 150% Biaxial Imperial Valley	296
6.15	Elastic Response Spectra – EQ 25 – 10% X-Axis Imperial Valley Ground Motion	297
6.16	Elastic Response Spectra – EQ 26 – 10% Y-Axis Imperial Valley Ground Motion	298
6.17	Elastic Response Spectra – EQ 27 – 10% Biaxial Imperial Valley Ground Motion	299
6.18	Elastic Response Spectra – EQ 28 – 100% Biaxial Imperial Valley Ground Motion	300
6.19	Test Structure Prior to Earthquake Simulations	301
6.20	Test Structure Prior to Earthquake Simulations	301
6.21	Test Structure After Earthquake Simulations	302
6.22	Test Structure After Earthquake Simulations	302
6.23	Test Structure Southeast Column After Earthquake Simulations	303
6.24	Abaqus Stress vs. Strain Finite Element Material Model Definition – Test Configuration 4	304
6.25	Drain-3DX Stress vs. Strain Finite Element Material Model Definition – Test Configuration 4	305
6.26	Abaqus Finite Element Model for Test Configuration 4	306
6.27	Drain-3DX Finite Element Model for Test Configuration 4	307
6.28	Abaqus Analytical Displacement vs. Time – EQ 27 – 10% Biaxial Imperial Valley	308
6.29	Abaqus Analytical Rotation vs. Time – EQ 27 – 10% Biaxial Imperial Valley	309
6.30	Drain-3DX Analytical Displacement vs. Time – EQ 27 – 10% Biaxial Imperial Valley	310
6.31	Drain-3DX Analytical Rotation vs. Time – EQ 27 – 10% Biaxial Imperial Valley	311
6.32	Abaqus Analytical Displacement vs. Time – EQ 28 – 100% Biaxial Imperial Valley – Combined Material Hardening	312

6.33	Abaqus Analytical Rotation vs. Time – EQ 28 – 100% Biaxial Imperial Valley – Combined Material Hardening	313
6.34	Drain-3DX Analytical Displacement vs. Time – EQ 28 – 100% Biaxial Imperial Valley	314
6.35	Drain-3DX Analytical Rotation vs. Time – EQ 28 – 100% Biaxial Imperial Valley	315
6.36	Abaqus Analytical Displacement vs. Time – EQ 29 – 150% Biaxial Imperial Valley – Combined Material Hardening	316
6.37	Abaqus Analytical Rotation vs. Time – EQ 29 – 150% Biaxial Imperial Valley – Combined Material Hardening	317
6.38	Drain-3DX Analytical Displacement vs. Time – EQ 29 – 150% Biaxial Imperial Valley	318
6.39	Drain-3DX Analytical Rotation vs. Time – EQ 29 – 150% Biaxial Imperial Valley	319
6.40	Abaqus Analytical Displacement vs. Time – EQ 28 – 100% Biaxial Imperial Valley – Isotropic Material Hardening	320
6.41	Abaqus Analytical Rotation vs. Time – EQ 28 – 100% Biaxial Imperial Valley – Isotropic Material Hardening	321
6.42	Abaqus Analytical Displacement vs. Time – EQ 29 – 150% Biaxial Imperial Valley – Isotropic Material Hardening	322
6.43	Abaqus Analytical Rotation vs. Time – EQ 29 – 150% Biaxial Imperial Valley – Isotropic Material Hardening	323
7.1	Perspective View of Test Configuration Model 3	345
7.2	Acceleration and Displacement vs. Time – EQ 18	346
7.3	Force vs. Displacement and Torsional Moment vs. Rotation – EQ 18	347
7.4	Acceleration and Displacement vs. Time – EQ 19	348
7.5	Force vs. Displacement and Torsional Moment vs. Rotation - EQ 19	349
7.6	Acceleration and Displacement vs. Time – EQ 22	350
7.7	Force vs. Displacement and Torsional Moment vs. Rotation - EQ 22	351
7.8	Acceleration and Displacement vs. Time – EQ 23	352
7.9	Force vs. Displacement and Torsional Moment vs. Rotation - EQ 23	353
7.10	Force-Deformation Response – Test Configuration 3	354
7.11	Torsional Moment-Rotation Response – Test Configuration 3	355
7.12	Elastic Response Spectra – EQ 18 – 10% X-Axis Imperial Valley Ground Motion	356
7.13	Elastic Response Spectra – EQ 19 – 10% Y-Axis Imperial Valley Ground Motion	357
7.14	Elastic Response Spectra – EQ 22 – 10% Biaxial Imperial Valley Ground Motion	358
7.15	Elastic Response Spectra – EQ 23 – 100% Biaxial Imperial Valley Ground Motion	359
7.16	Test Structure Prior to Earthquake Simulations	360

7.17	Test Structure Prior to Earthquake Simulations	361
7.18	Test Structure After Earthquake Simulations	362
7.19	Test Structure Southeast Column After Earthquake Simulations	363
7.20	Abaqus Stress vs. Strain Finite Element Material Model Definition – Test Configuration 3	364
7.21	Drain-3DX Stress vs. Strain Finite Element Material Model Definition – Test Configuration 3	365
7.22	Abaqus Finite Element Model for Test Configuration 3	366
7.23	Drain-3DX Finite Element Model for Test Configuration 3	367
7.24	Abaqus Analytical Displacement vs. Time – EQ 22 – 10% Biaxial Imperial Valley	368
7.25	Abaqus Analytical Rotation vs. Time – EQ 22 – 10% Biaxial Imperial Valley	369
7.26	Drain-3DX Analytical Displacement vs. Time – EQ 22 – 10% Biaxial Imperial Valley	370
7.27	Drain-3DX Analytical Rotation vs. Time – EQ 22 – 10% Biaxial Imperial Valley	371
7.28	Abaqus Analytical Displacement vs. Time – EQ 23 – 100% Biaxial Imperial Valley	372
7.29	Abaqus Analytical Rotation vs. Time – EQ 23 – 100% Biaxial Imperial Valley	373
7.30	Drain-3DX Analytical Displacement vs. Time – EQ 23 – 100% Biaxial Imperial Valley	374
7.31	Drain-3DX Analytical Rotation vs. Time – EQ 23 – 100% Biaxial Imperial Valley	375
8.1	Perspective View of Test Configuration Model 8	395
8.2	Acceleration and Displacement vs. Time – EQ 45	396
8.3	Force vs. Displacement and Torsional Moment vs. Rotation – EQ 45	397
8.4	Acceleration and Displacement vs. Time – EQ 46	398
8.5	Force vs. Displacement and Torsional Moment vs. Rotation - EQ 46	399
8.6	Force-Deformation Response – Test Configuration 8	400
8.7	Torsional Moment-Rotation Response – Test Configuration 8	401
8.8	Elastic Response Spectra – EQ 45 – 100% Biaxial Imperial Valley Ground Motion	402
8.9	Analytical Displacement vs. Time – EQ 23 vs. EQ 45 – 100% Biaxial Imperial Valley	403
8.10	Abaqus Stress vs. Strain Finite Element Material Model Definition – Test Configuration 8	404
8.11	Drain-3DX Stress vs. Strain Finite Element Material Model Definition – Test Configuration 8	405
8.12	Abaqus Finite Element Model for Test Configuration 8	406
8.13	Drain-3DX Finite Element Model for Test Configuration 8	407

8.14	Abaqus Analytical Displacement vs. Time – EQ 45 – 100% Biaxial Imperial Valley	408
8.15	Abaqus Analytical Rotation vs. Time – EQ 45 – 100% Biaxial Imperial Valley	409
8.16	Drain-3DX Analytical Displacement vs. Time – EQ 45 – 100% Biaxial Imperial Valley	410
8.17	Drain-3DX Analytical Rotation vs. Time – EQ 45 – 100% Biaxial Imperial Valley	411
8.18	Abaqus Analytical Displacement vs. Time – EQ 46 – 135% Biaxial Imperial Valley	412
8.19	Abaqus Analytical Rotation vs. Time – EQ 46 – 135% Biaxial Imperial Valley	413
8.20	Drain-3DX Analytical Displacement vs. Time – EQ 46 – 135% Biaxial Imperial Valley	414
8.21	Drain-3DX Analytical Rotation vs. Time – EQ 46 – 135% Biaxial Imperial Valley	415
9.1	Perspective View of Test Configuration Model 5	443
9.2	Acceleration and Displacement vs. Time – EQ 30	444
9.3	Force vs. Displacement and Torsional Moment vs. Rotation – EQ 30	445
9.4	Acceleration and Displacement vs. Time – EQ 31	446
9.5	Force vs. Displacement and Torsional Moment vs. Rotation - EQ 31	447
9.6	Acceleration and Displacement vs. Time – EQ 32	448
9.7	Force vs. Displacement and Torsional Moment vs. Rotation - EQ 32	449
9.8	Acceleration and Displacement vs. Time – EQ 34	450
9.9	Force vs. Displacement and Torsional Moment vs. Rotation - EQ 34	451
9.10	Acceleration and Displacement vs. Time – EQ 35	452
9.11	Force vs. Displacement and Torsional Moment vs. Rotation - EQ 35	453
9.12	Force-Deformation Response – Test Configuration 5	454
9.13	Torsional Moment-Rotation Response – Test Configuration 5	455
9.14	Maximum Force vs. Displacement and Maximum Torsional Moment vs. Rotation – Test Configuration 5 – 10% - 150% Biaxial Imperial Valley	456
9.15	Elastic Response Spectra – EQ 30 – 10% X-Axis Imperial Valley Ground Motion	457
9.16	Elastic Response Spectra – EQ 31 – 10% Y-Axis Imperial Valley Ground Motion	458
9.17	Elastic Response Spectra – EQ 32 – 10% Biaxial Imperial Valley Ground Motion	459
9.18	Elastic Response Spectra – EQ 34 – 100% Biaxial Imperial Valley Ground Motion	460
9.19	Test Structure Prior To Earthquake Simulations	461
9.20	Test Structure Prior To Earthquake Simulations	461
9.21	Test Structure Prior To Earthquake Simulations	462

9.22	Abaqus Stress vs. Strain Finite Element Material Model Definition – 5” Standard Columns – Test Configuration 5	463
9.23	Abaqus Stress vs. Strain Finite Element Material Model Definition – 4” Double Extra-Strong Columns – Test Configuration 5	464
9.24	Drain-3DX Stress vs. Strain Finite Element Material Model Definition – 5” Standard Columns – Test Configuration 5	465
9.25	Drain-3DX Stress vs. Strain Finite Element Material Model Definition – 4” Double Extra-Strong Columns – Test Configuration 5	466
9.26	Abaqus Finite Element Model for Test Configuration 5	467
9.27	Drain-3DX Finite Element Model for Test Configuration 5	468
9.28	Abaqus Displacement vs. Time – EQ 32 – 10% Biaxial Imperial Valley	469
9.29	Abaqus Rotation vs. Time – EQ 32 – 10% Biaxial Imperial Valley	470
9.30	Drain-3DX Displacement vs. Time – EQ 32 – 10% Biaxial Imperial Valley ...	471
9.31	Drain-3DX Rotation vs. Time – EQ 32 – 10% Biaxial Imperial Valley	472
9.32	Abaqus Displacement vs. Time – EQ 34 – 100% Biaxial Imperial Valley	473
9.33	Abaqus Rotation vs. Time – EQ 34 – 100% Biaxial Imperial Valley	474
9.34	Drain-3DX Displacement vs. Time – EQ 34 – 100% Biaxial Imperial Valley	475
9.35	Drain-3DX Rotation vs. Time – EQ 34 – 100% Biaxial Imperial Valley	476
9.36	Abaqus Displacement vs. Time – EQ 35 – 150% Biaxial Imperial Valley	477
9.37	Abaqus Rotation vs. Time – EQ 35 – 150% Biaxial Imperial Valley	478
9.38	Drain-3DX Displacement vs. Time – EQ 35 – 150% Biaxial Imperial Valley	479
9.39	Drain-3DX Rotation vs. Time – EQ 35 – 150% Biaxial Imperial Valley	480
10.1	Perspective View of Test Configuration Model 6	508
10.2	Acceleration and Displacement vs. Time – EQ 37	509
10.3	Force vs. Displacement and Torsional Moment vs. Rotation – EQ 37	510
10.4	Acceleration and Displacement vs. Time – EQ 38	511
10.5	Force vs. Displacement and Torsional Moment vs. Rotation - EQ 38	512
10.6	Acceleration and Displacement vs. Time – EQ 36	513
10.7	Force vs. Displacement and Torsional Moment vs. Rotation - EQ 36	514
10.8	Acceleration and Displacement vs. Time – EQ 39	515
10.9	Force vs. Displacement and Torsional Moment vs. Rotation - EQ 39	516
10.10	Acceleration and Displacement vs. Time – EQ 40	517
10.11	Force vs. Displacement and Torsional Moment vs. Rotation - EQ 40	518
10.12	Force-Deformation Response – Test Configuration 6	519
10.13	Torsional Moment-Rotation Response – Test Configuration 6	520
10.14	Elastic Response Spectra – EQ 37 – 10% X-Axis Imperial Valley Ground Motion	521
10.15	Elastic Response Spectra – EQ 38 – 10% Y-Axis Imperial Valley Ground Motion	522

10.16	Elastic Response Spectra – EQ 36 – 10% Biaxial Imperial Valley Ground Motion	523
10.17	Elastic Response Spectra – EQ 39 – 100% Biaxial Imperial Valley Ground Motion	524
10.18	Test Structure Prior To Earthquake Simulations	525
10.19	Test Structure After Earthquake Simulations	525
10.20	Test Structure After Earthquake Simulations	526
10.21	Test Structure After Earthquake Simulations	526
10.22	Test Structure Southeast Column After Earthquake Simulation	527
10.23	Abaqus Stress vs. Strain Analytical Material Model Definition – 4" Extra-Strong Columns – Test Configuration 6	528
10.24	Abaqus Stress vs. Strain Analytical Material Model Definition – Diagonal Bracing – Test Configuration 6	529
10.25	Drain-3DX Stress vs. Strain Analytical Material Model Definition – 4" Extra-Strong Columns – Test Configuration 6	530
10.26	Drain-3DX Stress vs. Strain Analytical Material Model Definition – Diagonal Bracing – Test Configuration 6	531
10.27	Abaqus Finite Element Model for Test Configuration 6	532
10.28	Drain-3DX Finite Element Model for Test Configuration 6	533
10.29	Abaqus Analytical Displacement vs. Time – EQ 36 – 10% Biaxial Imperial Valley	534
10.30	Abaqus Analytical Rotation vs. Time – EQ 36 – 10% Biaxial Imperial Valley	535
10.31	Drain-3DX Analytical Displacement vs. Time – EQ 36 – 10% Biaxial Imperial Valley	536
10.32	Drain-3DX Analytical Rotation vs. Time – EQ 36 – 10% Biaxial Imperial Valley	537
10.33	Abaqus Analytical Displacement vs. Time – EQ 39 – 100% Biaxial Imperial Valley	538
10.34	Abaqus Analytical Rotation vs. Time – EQ 39 – 100% Biaxial Imperial Valley	539
10.35	Drain-3DX Analytical Displacement vs. Time – EQ 39 – 100% Biaxial Imperial Valley	540
10.36	Drain-3DX Analytical Rotation vs. Time – EQ 39 – 100% Biaxial Imperial Valley	541
10.37	Abaqus Analytical Displacement vs. Time – EQ 40 – 100% X-Axis 90% Y-Axis Imperial Valley	542
10.38	Abaqus Analytical Rotation vs. Time – EQ 40 – 100% X-Axis 90% Y-Axis Imperial Valley	543
10.39	Drain-3DX Analytical Displacement vs. Time – EQ 40 – 100% X-Axis 90% Y-Axis Imperial Valley	544
10.40	Abaqus Analytical Rotation vs. Time – EQ 40 – 100% X-Axis 90% Y-Axis Imperial Valley	545

11.1	Perspective View of Test Configuration Model 7	568
11.2	Acceleration and Displacement vs. Time – EQ 41	569
11.3	Force vs. Displacement and Torsional Moment vs. Rotation – EQ 41	570
11.4	Acceleration and Displacement vs. Time – EQ 42	571
11.5	Force vs. Displacement and Torsional Moment vs. Rotation – EQ 42	572
11.6	Force-Deformation Response – Test Configuration 7	573
11.7	Torsional Moment-Rotation Response – Test Configuration 7	574
11.8	Elastic Response Spectra – EQ 41 – 100% X-Axis 75% Y-Axis Imperial Valley Ground Motion	575
11.9	Abaqus Stress vs. Strain Finite Element Material Model Definition – 5” Standard Columns – Test Configuration 7	576
11.10	Abaqus Stress vs. Strain Finite Element Material Model Definition – 4” Double Extra-Strong Columns – Test Configuration 7	577
11.11	Abaqus Stress vs. Strain Analytical Material Model Definition – Diagonal Bracing – Test Configuration 7	578
11.12	Drain-3DX Stress vs. Strain Finite Element Material Model Definition – 5” Standard Columns – Test Configuration 7	579
11.13	Drain-3DX Stress vs. Strain Finite Element Material Model Definition – 4” Double Extra-Strong Columns – Test Configuration 7	580
11.14	Drain-3DX Stress vs. Strain Analytical Material Model Definition – Diagonal Bracing – Test Configuration 7	581
11.15	Abaqus Finite Element Model for Test Configuration 7	582
11.16	Drain-3DX Finite Element Model for Test Configuration 7	583
11.17	Abaqus Analytical Displacement vs. Time – EQ 41 – 100% X-Axis 75% Y-Axis Imperial Valley	584
11.18	Abaqus Analytical Rotation vs. Time – EQ 41 – 100% X-Axis 75% Y-Axis Imperial Valley	585
11.19	Drain-3DX Analytical Displacement vs. Time – EQ 41 – 100% X-Axis 75% Y-Axis Imperial Valley	586
11.20	Drain-3DX Analytical Rotation vs. Time – EQ 41 – 100% X-Axis 75% Y-Axis Imperial Valley	587
11.21	Abaqus Analytical Displacement vs. Time – EQ 42 – 100% X-Axis 85% Y-Axis Imperial Valley	588
11.22	Abaqus Analytical Rotation vs. Time – EQ 42 – 100% X-Axis 85% Y-Axis Imperial Valley	589
11.23	Drain-3DX Analytical Displacement vs. Time – EQ 42 – 100% X-Axis 85% Y-Axis Imperial Valley	590
11.24	Drain-3DX Analytical Rotation vs. Time – EQ 42 – 100% X-Axis 85% Y-Axis Imperial Valley	591
12.1	Material Models – 4” Extra-Strong Columns – Test Configurations 1 – 4	603
12.2	Material Models – 4” Extra-Strong Columns – Test Configuration 8	603
12.3	Material Models – 5” Standard Columns – Test Configurations 5 & 7	604

12.4	Material Models – 4" Double Extra-Strong Columns – Test Configurations 5 & 7	604
12.5	Material Models – 4" Extra-Strong Columns – Test Configuration 6	605
12.6	Models – Diagonal Concentric Bracing – Test Configurations 5 & 7	605
A.1	Plan View of USACERL Shake Table	648
A.2	Shaketable Acceleration Transducers	649
A.3	Diaphragm Acceleration Transducers	649
A.4	Shaketable Displacement Transducers	650
A.5	Diaphragm Displacement Transducers	651
A.6	Mass Stack Acceleration Transducers	652
A.7	Elevation View of Column Base Plate LVDT Transducer	653
A.8	Plan View of Column Base Plate LVDT Transducer	653
A.9	Column Strain Gage Locations	654
A.10	Diagonal Brace Strain Gage Locations	655
A.11	Block Diagram Showing Shake Table Controls and Data Acquisition Systems	656

PREFACE

This study was conducted and documented in partial fulfillment of requirements for the degree of Doctor of Philosophy in Civil Engineering from the University of Illinois at Urbana-Champaign (UIUC). The work was supported by Headquarters, U.S. Army Corps of Engineers under Project 4A161102AT23, "Basic Research/Military Construction"; Work Unit EJ0, "Nonlinear Torsional Building Response."

This work was performed under the auspices of the Materials and Structures Branch (CF-M) of the Facilities Division (CF), Construction Engineering Research Laboratory (CERL). The CERL work unit Principal Investigator was Dr. John R. Hayes, Jr., and the author's Academic Advisor at UIUC was Dr. Douglas A. Foutch, Department of Civil and Environmental Engineering. Martin J. Savoie is Chief, CEERD-CF-M, and L. Michael Golish is Chief, CEERD-CF. The Technical Director of the Facilities Acquisition and Revitalization business area is Dr. Paul A. Howdyshell, CEERD-CV-ZT. The Director of CERL is Dr. Alan W. Moore.

CERL is an element of the U.S. Army Engineer Research and Development Center (ERDC), U.S. Army Corps of Engineers. The Commander and Executive Director of ERDC is COL James R. Rowan, EN, and the Director is Dr. James R. Houston.

CHAPTER 1

INTRODUCTION

1.1 OBJECTIVE

The purpose of this research project is to investigate the nonlinear, inelastic response of one-story, symmetric- and asymmetric-plan systems to biaxial lateral earthquake ground motions. This combined experimental-analytical investigation seeks to characterize the lateral-torsional response of the system for a range of system parameters.

1.2 BACKGROUND

The complete inelastic response of structures is of great interest because collapse is prevented during earthquakes primarily by the dissipation of energy that occurs after yielding. The current strategy employed in designing structures to withstand large seismic ground motions is one in which the structure is sacrificed to the benefit of its occupants; the preservation of human life is the primary goal. As long as the structure doesn't collapse, it has not failed, and this is achieved by dissipating the energy imparted to the structure by the ground through the inelastic, hysteretic behavior of the structure. In structures with low damping, this hysteretic behavior is the primary mechanism of energy dissipation. Thus, understanding the seismic behavior of structures in the inelastic region is the first step in an effective design.

One mechanism that is of particular interest in seismic behavior of structures is torsion. Torsion is the twisting of the structure. When it is coupled with the lateral response, the forces and displacements of the various resisting elements are different from those experienced when the structure responds only in the planar directions. Torsion is the result when the mass distribution and stiffness distribution of a structure are not symmetric with respect to both planar axes of motion. Due to architectural constraints, buildings are typically designed with the aforementioned asymmetries. However, even when they are designed to be symmetric, in actuality asymmetries are present as a result of the imprecise nature of construction, the variability of the objects and people occupying the structure, etc. Thus, lateral-torsional coupling, to

some degree, is a mechanism always present in the seismic response of a structure. Therefore, to generate a complete understanding of the response of structures during earthquakes, the inelastic lateral-torsional behavior must be characterized.

Initially, the elastic seismic response of structures was studied [5, 12, 18, 19, 43, 50, 51, 52, 53], and a complete picture of this behavior now exists. The elastic torsional response depends on four system parameters: the uncoupled vibration period $T = 2\pi/\omega$, the eccentricity between the center of stiffness and the center of mass e_s , or the normalized stiffness eccentricity e_s/r ; the uncoupled torsional to lateral vibration frequency ratio Ω ; and the damping ratio ξ . However, the elastic torsional response does not depend independently on the number, location, and stiffness of the individual resisting elements. The effect of the lateral-torsional coupling is such that the dynamic shear force, in the direction of motion, is reduced due to the coupling as compared to the response of the uncoupled, or symmetric system. Also, the lateral-torsional coupling produces a dynamic amplification of the story torque about the center of resistance. The torsional coupling effect depends on the uncoupled torsional to lateral frequency ratio. The reduction in the base shear force due to dynamic torsional coupling is more pronounced if the eccentricity is large and if the uncoupled torsional to lateral frequency ratio is close to unity. The dynamic amplification of the torque is more pronounced if the uncoupled torsional to lateral frequency ratio is close to unity and the eccentricity is small.

Based on the studies of the elastic response of structures, code provisions have been evaluated [5, 14, 26, 44, 70, 71, 81, 83], and in many cases, suggestions for modifications have been made. In one study, Chopra and Goel [14] found that although symmetric-plan systems designed with $R = 1$ are expected to remain elastic in response, similarly designed asymmetric-plan systems may deform into the inelastic range, and that the ductility demands for the asymmetric system are generally greater than for the symmetric system as well. DeStefano and Rutenberg [26] also found, when evaluating the *UBC Torsional Provisions*, that systems designed with a strength level corresponding to the serviceability limit state may sustain relatively large inelastic excursions. In another study, Rutenberg and Pekau [70] found that static code provisions underestimate the response of members on the rigid side of the center of stiffness at low frequency ratios, as well as of torque resisting members when Ω is near unity and the eccentricity is small. They also found that the provisions overestimate the response of members on the flexible side at low frequency ratios and when the eccentricity is large.

The design eccentricity is one aspect of code provisions that has been the subject of many investigations. Some codes amplify the static eccentricity to account for the dynamic amplification of the story torque,

while other codes do not. In addition, the accidental eccentricity is also the subject of discussion. In all codes, the accidental eccentricity is defined as some fraction of the width of the structure, but that fraction differs with the various code provisions. Some codes allow reduction of the stiff-side element strength to take advantage of the torsional behavior, while others do not. The primary problem here is that design codes are attempting to account for inelastic behavior of structures through an elastic design model.

However, the elastic response represents an incomplete picture of the overall seismic structural response. As time passed and analysis tools advanced, the focus of study shifted to the inelastic seismic response of structures. A great deal of research has been done in this area, and with good reason: building codes specify a design for current structures which will produce inelastic behavior at the ultimate limit state. However, the inelastic response is not only a function of the four elastic system parameters (uncoupled lateral vibration period, uncoupled torsional to lateral vibration frequency ratio, eccentricity between the center of stiffness and the center of mass, and the damping ratio), but is also a function of the distribution of mass, stiffness, and strength in plan. This has made the task of studying the inelastic behavior of structures and especially accounting for that behavior in design codes much more difficult.

For elastic structural response, only the distance between the center of stiffness and center of mass is important. A mass-eccentric model and a stiffness-eccentric model will behave in a similar manner as long as the eccentricities are the same. For inelastic response, however, the absolute locations of the mass center and stiffness center are important, not just their relative positions to one another. Thus, a mass-eccentric model and a stiffness-eccentric model will not behave in a similar manner even though the eccentricities are the same. Tso and Ying [78] investigated the effect of strength distribution on the ductility demand of both the flexible-side and stiff-side elements in eccentric, inelastic systems. The researchers studied both stiffness-eccentric systems (SES) and mass-eccentric system (MES), and found that it was necessary to develop separate guidelines for each of these types of systems. When the system was excited into the inelastic region, the flexible-side elements experienced large additional ductility demand for the SES, while the stiff-side elements experienced large additional ductility demand for the MES. In both the SES and MES, the flexible-side element experienced significant additional displacement. Goel and Chopra [36] conclude that for a system with equal strength and stiffness eccentricities, mass-eccentric and stiffness-eccentric systems may be used interchangeably to estimate the deformations at the center of stiffness, but not for predicting the maximum ductility demand. For systems with no strength eccentricity, the mass-eccentric and stiffness-eccentric systems respond very differently.

In addition, for structures behaving elastically, the strength distribution is not an independent factor in the response, because in the elastic region, the strength is proportional to the stiffness. However, the strength eccentricity is an independent factor in the inelastic region of behavior. Goel and Chopra [36] found that strength-symmetric systems and systems with strength eccentricity much smaller than stiffness eccentricity generally experience smaller effects of torsional coupling than do systems with equal strength and stiffness eccentricities. Ferhi and Truman [30, 31] found that systems with normalized strength eccentricity (NP) in the vicinity of the normalized stiffness eccentricity (NR) undergo controlled inelastic rotations and lateral displacements, while systems with NP larger than NR undergo excessive inelastic rotations but small lateral displacements, and systems with NP smaller than NR undergo small inelastic rotations. Sadek and Tso [72] proposed that the strength eccentricity should be favored over the stiffness eccentricity as the parameter of interest in the inelastic response region. They found that the intensity of inelastic torsional response and stiffness eccentricity become less well correlated, while the strength eccentricity does a better job of correlating the peak response parameters of interest.

As the dissipation of energy is of paramount importance in the ultimate limit state of structures, characterizing the total cyclic energy dissipation capacity has received recent attention. Bruneau and Wang [3] suggest using a relative energy method to evaluate the hysteretic energy as it is found to provide a good indicator of the nonlinear inelastic seismic structural performance. Goel [38] uses various energy quantities, such as total energy input and total hysteretic energy, to investigate the inelastic responses of code-designed, asymmetric-plan systems with large eccentricities in both directions and subjected to biaxial input motion.

As is evident from the brief review of inelastic behavior, not only are the number of parameters which affect response greater than for elastic response, but in many cases, the variation of effects which the different parameters produce are dependent on each other in a complex manner. For example, Bozorgnia and Tso [2] found that the effect of asymmetry on the element ductility demand and on the edge displacement is greatest for stiff systems with yield strength greatly reduced from the elastic strength demand. As noted above, Tso and Ying [78] found that in studying the effect of strength distribution, guidelines that apply to stiffness eccentric systems lead to poor response performance when they are applied to mass eccentric systems, and vice versa.

Many problems have arisen in attempting to produce research results that are applicable in a general sense to inelastic response. Most studies have utilized models that are basically uniaxial in nature, with asymmetry in only one planar direction and subjected to uniaxial input motions. Obviously, this is a

simplification, as real structures will nearly always be subjected to components of motion to some degree from both planar directions. However, this approach is taken in order to more easily understand the effects of various factors on the inelastic response and to reduce the computational effort, but at the expense of more realistic modeling of the structure.

Some researchers have noted that most actual structures have resisting elements which are perpendicular to the studied direction of motion, and that these resisting elements would not provide lateral resistance, they would provide torsional resistance. Consequently, many studies have been based on models with perpendicular resisting elements while subjected to uniaxial ground motions [14, 15, 25, 34, 35, 36, 37, 38, 49, 71, 80, 84, 85, 86]. One notable response characteristic that these studies have uncovered is that as structures move further into the inelastic region of response, the torsional response becomes less important. This response characteristic is not at all surprising based on the model chosen, due to the fact that as the structure deforms inelastically, the lateral stiffness becomes very small at times, while the perpendicular resisting elements will generally, for this model, remain elastic. Thus, the torsional-to-lateral stiffness will become infinitely large at times, preventing the structure from responding torsionally.

However, one must examine the validity of this type of model, because in a real earthquake with biaxial input motions, the perpendicular resisting elements will be subjected to lateral motions as well, possibly causing them to deform inelastically. Chandler et. al. [7] found that evidence from past earthquakes supports this observation. This type of behavior is not taken into account in the aforementioned model. Based on this argument, other researchers have chosen to return to a purely uniaxial research model, with no perpendicular resisting elements. Proponents of using perpendicular resisting elements have argued that the lateral ground motion that affects the perpendicular elements is generally much smaller, and thus will not cause inelastic deformation. Correnza and Hutchinson [16] found that uni-directional analyses on a model with transverse resisting elements give satisfactory estimates of the inelastic responses of systems designed in accordance with a range of code static torsional provisions.

It seems clear that each of these model configurations are limiting cases to the actual structure behavior, with the absence of the perpendicular resisting element being the more conservative case. Chandler, et. al. [7] found that a uniaxial approach neglecting transverse elements and loading, has been found to give accurate and reasonably conservative estimates of the critical flexible-edge deformation, but may underestimate the stiff-edge element ductility demand by a factor of two or more in the short-period range. Correnza and Hutchinson [16] found that systems considering only the lateral load-resisting elements and the corresponding earthquake ground motion input, may significantly overestimate the

response of the flexible-edge element in short-period systems, but are only slightly conservative for the design of such elements in medium- and long-period systems. Thus, although uniaxial models do provide useful insight into the inelastic behavior of structures, it is clear that a model subjected to biaxial input motions is necessary to gain an accurate picture of true inelastic response and to validate any simplifications made in the analysis models chosen.

A greater number of recent studies have been based on inelastic models subjected to biaxial ground motions [7, 16, 20, 28, 33, 42, 67, 68]. Riddell and Santa-Maria [68] used a model with force-resisting elements in both planar directions and subjected to both uniaxial and biaxial ground motions. Based on a series of 15 two-component earthquake records, they found that the effect of biaxial ground motions on the deformations of the flexible-side element was significant for short period, acceleration-sensitive systems. Further, they found that the deformations increase as the eccentricity and the intensity of the second ground motion component increase, and as the yield strength and lateral period decrease. Another study by Ghersi and Rossi [33], using 30 pairs of artificially generated accelerograms, showed that the inelastic response of asymmetric systems is not affected significantly by the presence of both ground motion components. And a study by De Stefano et. al. [28] on the performance of one-way asymmetric systems designed according to the Uniform Building Code and subjected to biaxial ground motions indicated that the peak ductility demands on elements aligned along the asymmetric system direction were very close to, and sometimes lower than, those for the corresponding symmetric system. On the other hand, the elements aligned along the symmetric direction experience significantly larger ductility demand than those for the corresponding symmetric system.

This interaction of parameters and their effects on the structural response has made the task of developing code guidelines particularly difficult. The design codes are basically trying to account for the complex inelastic response, which is a function of many parameters, using only an effective eccentricity measurement. Many researchers have studied the adequacy of torsional provisions or the performance of code-designed structures [5, 7, 8, 9, 10, 14, 17, 20, 21, 22, 26, 28, 29, 34, 41, 44, 48, 54, 58, 62, 65, 69, 70, 74, 75, 80, 81, 82, 83, 84, 85, 86]. The studies that have been performed to investigate the adequacy of code provisions have used various response quantities, typically some measure of ductility demand or maximum displacement, or some measure of torsion. Some studies attempt to correlate these quantities for both the flexible- and stiff-side elements, and some only choose one, typically the flexible-side element. Additionally, the accidental eccentricity provision has been the subject of much study as well [14, 21, 22, 56], including: its effect on torsional response; whether the scaling factor should be

modified; how to account for accidental torsion; whether accidental eccentricity should be included in research model formulations, and if so, how.

In essence, engineering is nothing more than applied science. As science is concerned with the behavior of the world around us, principles and theories are only useful in as far as they accurately describe or predict that behavior. Thus, it is of paramount importance to verify, through experimental tests, that what we believe should happen actually does happen. For the purposes of testing the response of structures to seismic loading, we need to employ some type of device to produce a cyclic response in our structure of choice. The device can be as simple as a single hydraulic piston which cyclically loads a frame at some point, or as complex as a triaxial shaketable which can comprehensively simulate ground motions input to a model structure. Any type of test has some value in the results produced, but at the same time, it is highly desirable to conduct a test that most accurately simulates the behavior of the real world. This is particularly true when we are investigating the inelastic torsional behavior of structures under seismic loading, which is complex and influenced by many variables.

Few shaketable tests have focused solely on the problem of inelastic torsion, although other aspects of seismic response have been studied. Chen and Wu [13] investigated the inelastic behavior of a 1/4-scale steel frame structure subjected to shaketable input motions. However, the main thrust of the study was the effectiveness of the mass-tuned dampers on reducing the overall seismic response of the structure under strong ground motions. Nader and Astaneh-Asl [59] performed shaketable tests on a one-story, one-bay steel structure. However, the primary objective of this study was to look at the beam-column connections, which could be changed from flexible to semi-rigid to rigid. Thewalt and Mahin [73] used shaketable tests to help develop a pseudodynamic test method for three-dimensional testing of structures under multiple components of base excitation.

This study aims to first and foremost begin to fill part of the void in the realm of the experimental, shaketable investigation of the inelastic torsional response of structures. The parameters of the research study are in great part influenced by some of the issues discussed above. Specifically, the planar distributions of mass, strength, and stiffness are each potentially independent factors in the seismic torsional response. Thus, this research study will utilize a model that contains any or all of the three types of eccentricity. Additionally, any type of uniaxial test can only provide a limited picture of the total inelastic torsional behavior; thus, this study will utilize a model with strength, stiffness, and mass eccentricities in both planar directions and subjected to input motions in both planar directions. Until this time, the facilities have not been present in this country to conduct complete three-dimensional

earthquake simulations on a structure. Now, this is no longer true; thanks to the recent retrofit, the Tri-axial Earthquake and Shock Simulator (TESS) located at the Construction Engineering Research Laboratory (CERL) in Champaign, Illinois has full triaxial motion capability. An experimental study of this nature is a natural and necessary companion to the analytical work that has been done thus far in the seismic behavior of structures. However, due to the complexity of inelastic torsional response and the many factors that are influential, this study, which employs a limited sampling of representative structural configurations, is only a first step.

1.3 EXPERIMENTAL PROGRAM

Since this is one of the first experimental studies of this kind, a simple one-story system is appropriate to lay the groundwork for further experimental studies of more complex structures.

(A) MODEL STRUCTURE

The structure used in this study consists of a diaphragm, approximately eight feet on a side, supported by four circular steel pipe columns, five feet in length. Eight octagonal and eight rectangular steel masses are available to be attached to the slab in various configurations in order to provide additional dead load and mass asymmetry. The diaphragm has various construction details which were necessary for the assembly of the various elements into a cohesive whole. The diaphragm was designed to be used throughout the entire sequence of tests, while the columns, having plastically deformed, were replaced after each model configuration sequence was complete. Circular pipe columns were chosen because of their complete plan symmetry and their reduced sensitivity to torsional buckling and, thus, greater stability. The focus of this study is the lateral-torsional behavior of the system as a whole, not the local behavior of the columns. Non-circular columns would only add unnecessary complexity to the analysis of the system.

(B) TESTING PROCEDURES

Eight different model configurations are studied. The configurations consist of different combinations of varying parameters: one-quarter asymmetric mass, one-half asymmetric mass, symmetric mass, asymmetric and symmetric column strength, and concentric lateral bracing. The mass asymmetries are

achieved simply by placing the masses all on one-quarter or one-half of the diaphragm. In both the asymmetrical and symmetrical cases, half of the masses were attached above and half below the diaphragm to keep the vertical mass center reasonably near the center of the diaphragm. The strength asymmetry in the structure is achieved by pairing two sets of columns which have similar stiffness but different yield strengths. The stiffness asymmetry is achieved through the use of asymmetrical lateral bracing. The inclusion of each of these different types of asymmetry will allow the scope of the results to be more general.

The test sequence for each model configuration was essentially the same. Preliminary tests were performed before any earthquake simulations in order to determine the natural frequencies and damping characteristics of the structure. First, the structure was subjected to white noise base motions. Transfer functions of the acceleration response of the structure were used to determine the natural frequencies. Second, the structure was excited sinusoidally at its measured natural frequency. The input motion was then discontinued, and the motion of the structure was allowed to decay to rest. Analysis of this response using the so-called logarithmic decrement of damping was performed to determine the equivalent viscous-damping ratio. Third, the structure was subjected to sinusoidal motions ranging in frequency from 1-20 Hertz. The response of the structure to the sine sweep tests was used to confirm the natural frequencies of the structure. Each of the aforementioned tests were performed once in each planar axis, and once in the yaw-axis, for a total of nine preliminary tests for each model configuration.

Following the preliminary tests, the structure was subjected to earthquake simulations. The 230 [X] and 140 [Y] degree acceleration components from the 1979 Imperial Valley earthquake recorded at Bonds Corner were chosen as the base earthquake motions based on the large response spectrum magnitudes near the natural frequency of the structure. The goal in choosing the motions was to achieve a ductility in the response of the structure in the neighborhood of four to five. To this end, the motions were modified using a combination of scaling and filtering, and then checked in finite element simulations, in order to produce the desired ductility while not violating the performance limits of the shaketable. This procedure produced a set of reference ground motion accelerograms to be used on the structure.

The structure was first subjected to low-level earthquake tests. The low-level tests were performed using first the X-Axis input motion, then the Y-Axis input motion, followed by both axes simultaneously. Next, the structure was subjected to the full-scale accelerograms. Typically, the shaketable displacement limits were such that the earthquake accelerograms could be scaled up by 50% in order to perform a subsequent simulation. When possible, this was done, followed by white noise tests to analyze any

changes in the natural frequency of the structure. This general sequence of preliminary tests and earthquake simulations was followed for each of the eight different model configurations.

1.4 SCOPE OF STUDY

Chapter 2 provides an overview of the design of the model structure, and the overall layout of all aspects of the experimental stage of this study. The design of the model structure is described, along with the details of each of the components used in the model. The selection of the input ground motions to be used during the earthquake simulations are discussed, along with the modifications made to the original ground motions to best adapt them to the features and limitations of the test apparatus and test model. The experimental setup is presented, including the placement of the model structure on the shake table and the instrumentation used during the simulations. The test sequence is outlined, focusing on the eight different test configurations, and their characteristics, used during the study. The specifics of the testing procedure are presented, including the general sequence of earthquake simulations performed for each test configuration, and the dynamic characterization tests performed before the simulations.

Chapter 3 provides descriptions of the experimental test program and the finite element modeling procedures. This chapter first summarizes response data of the test structure during the earthquake simulations and the dynamic characterization tests. Summaries of test model accelerations, displacements, torsional moments, overturning moments, column end moments, and base shears are provided. The general methodologies used in the computation and analysis of the response quantities mentioned above that are common to all of the test configurations are discussed in this chapter. Regarding the analysis of the structure, a general presentation is made of the nonlinear finite element analyses performed during this study, along with the basic model used in the analyses and any other features common throughout the analyses of the different test configurations.

Chapters 4 – 11 provide summaries of the experimental test data for each test configuration, along with the specific finite element modeling of each configuration. Each chapter is focused on one of the eight test configurations, providing a detailed description of the specific physical properties and characteristics of the model for the particular configuration, along with the resulting dynamic properties. In addition, the specific sequence of test simulations are presented and discussed, including any simulations that were not appropriate to present in this report. The observed response of the structure in each simulation are presented and discussed, along with any physical observations made during the testing. Nonlinear finite

element analyses are employed in an effort to compare the actual experimental response with analytical response predictions. Finally, preliminary summaries and conclusions specific to each test configuration are presented. A list of each of the test configurations, along with their general structural characteristics and the specific chapter in which they are presented, is shown below.

Chapter	Test Configuration	Mass Distribution	Strength Distribution	Stiffness Distribution
4	1	Symmetric	Symmetric	Symmetric
5	2	Symmetric	Symmetric	Symmetric
6	4	$\frac{1}{2}$ Asymmetric	Symmetric	Symmetric
7	3	$\frac{1}{4}$ Asymmetric	Symmetric	Symmetric
8	8	$\frac{1}{4}$ Asymmetric	Symmetric	Symmetric
9	5	$\frac{1}{2}$ Asymmetric	Asymmetric	Symmetric
10	6	$\frac{1}{2}$ Asymmetric	Symmetric	Asymmetric
11	7	$\frac{1}{2}$ Asymmetric	Asymmetric	Asymmetric

Table 1.1 Test Configuration Summary

Chapters 12 and 13 provide a summary of this study, conclusions drawn from the experimental results and corresponding analytical results along with interpretations of all of the test configurations. Recommendations for future research and design were also given.

1.5 REPORT REFERENCES

References used in this report are listed in the List of References, which is placed after Chapter 13. References are listed alphabetically and numbered. In the body of each chapter and appendix, reference numbers are provided.

CHAPTER 2

EXPERIMENTAL PROGRAM

This chapter provides an overview of the design of the model structure, the selection and modification of the input ground motions, experimental setup and instrumentation, the sequence of tests of the different model configurations, the earthquake simulations, the dynamic characterization tests performed with the simulations, and data recorded. Additional details may be found in Appendix A. Section 2.1 describes the design of the model structure, along with the details of each of the components used in the model. Section 2.2 describes the selection of the input ground motions to be used during the earthquake simulations. Also described are the modifications made to the original ground motions to best adapt them to the features and limitations of the test apparatus and test model. Section 2.3 briefly describes the experimental setup, including the placement of the model structure on the shake table, and the instrumentation used during the simulations. More detailed information on the instrumentation setup can be found in Appendix A. Section 2.4 outlines the test sequence, focusing on the eight different test configurations, and their characteristics, used during the study. Section 2.5 briefly describes the testing procedure, including the general sequence of earthquake simulations performed for each test configuration, and the dynamic characterization tests performed before the simulations.

2.1 DESIGN OF THE MODEL STRUCTURE

The primary purpose of this experiment was to test a general theoretical concept, not the behavior of any one particular structure. Because it was not intended to replicate and model an actual structure, it was possible to design the test model to match the specifications of the CERL shaking table, to accommodate the use of existing equipment, and to best allow the observation of the theoretical phenomena of interest.

Since this is one of the first experimental studies of this kind, a simple one-story system is appropriate to lay the groundwork for further experimental studies of more complex structures.

Figure 2.1 provides a perspective view of the model structure. Many of the details of the structure have been omitted from Figure 2.1, as its purpose is only to provide a general picture of the model. The structure consists of a very stiff diaphragm, approximately eight feet on a side, supported by four pipe-columns five feet in length. Large steel masses are attached to the top and bottom of the diaphragm to provide dead load and mass asymmetry. The positions of the masses are based on the degree, if any, of mass eccentricity desired. The masses are held in place by a number of DYWIDAG bars, which run through holes in the masses and the diaphragm; "nuts" thread onto the top and bottom of these threaded rods to secure the masses. In this study, the columns are expected to undergo significant damage, and they are the only part of the model structure that is designed to undergo damage. The diaphragm is designed for use throughout the entire sequence of tests, while the columns, having plastically deformed, will be replaced after each model configuration sequence is complete. Circular pipe columns were chosen because of their complete plan symmetry and their reduced sensitivity to torsional buckling and greater stability. The focus of this study is the lateral-torsional behavior of the system as a whole, not the local behavior of the columns; non-circular columns under biaxial bending would only add unnecessary complexity to the analysis of the system. Two elevation views of the model structure are shown in Figures 2.2 and 2.3, looking at the east side and south side of the model, respectively. In these elevation views, as in the perspective view in Figure 2.1, the masses are located on the east half of the diaphragm.

The diaphragm, as seen in a plan view in Figure 2.4, is composed of four W12x65 beams on the perimeter, with reinforced concrete used to fill the void in the center. All structural steel in the diaphragm has a yield strength of 50 ksi, and the concrete has a compressive strength of 4000 psi. The center-to-center spacing of the columns is 96.5 inches, which requires two of the W12x65 beams to have a length of 108.5 inches and the other two beams to have a length of 84.5 inches.

Elevation C-C in Figure 2.4 is shown in Figure 2.5. As seen in Figure 2.5, the concrete infill is not of constant thickness, but is predominantly 8 inches thick, with the infill becoming thicker near the beams. The concrete is reinforced, top and bottom, by fourteen equally spaced No. 5 bars, each way. Also, 36 hollow steel tubes, with an outer diameter of 2 inches, a thickness of 7/32 inches, and a height of 8 inches, are spaced at 12-1/6 inches center-to-center in the concrete infill, as can be seen in both Figure 2.4 and Figure 2.5. These steel tubes are the pass-through points of the previously mentioned Dywidag bars.

Elevation A-A in Figure 2.4 is shown in Figure 2.7. From Figures 2.7, 2.8, and 2.9, the details of the diaphragm corners can be seen. At each corner, eight steel tubes, each with an outer diameter of 2-1/4 inches and a thickness of ½ inch, are welded in place between the flanges of the W12x65 beams. Bolts will pass through a hole in the top flange, one of the steel tubes, a hole in the bottom flange, and then a hole in the column top plate to attach the diaphragm to the columns. The tubes support the flanges in bearing the loads from the column bolts. In addition, the details of the steel tubes can be seen in Figures 2.5 and 2.6. Also welded in place between the flanges of the beams are 3/8-inch stiffener plates. These plates are welded perpendicular to the webs of the longer W12x65 beams, thereby appearing to extend the webs of the shorter beams. This provides symmetry at the corners, as can best be seen in Figure 2.8.

Beam flange details 1 and 2 from Figure 2.4 are shown in Figures 2.10 and 2.11, respectively. Figure 2.10 provides a view of the holes in the top flange at one of the diaphragm corners, which are also the previously discussed pass-through points of the bolts that secure the columns to the diaphragm. At the midpoint of each beam, large eye bolts were attached to the diaphragm to provide lifting points for the overhead crane. Figure 2.11 shows the pass-through points for these eye bolts. At each of these four locations, a hole was cut in the top and bottom flanges of the beams and a steel tube was welded in place between the flanges, in a similar fashion to the previously discussed column bolt pass-through points at the diaphragm corners.

Figures 2.12 - 2.14 show the column assemblies that are bolted to each of the four corners of the diaphragm. Each column assembly consists of a 60 inch steel pipe with a top end plate and a bottom end plate welded to the pipe. In total, three different types of steel pipe are used: 4-inch extra-strong, 5-inch standard, and 4-inch double extra-strong. The exact configurations during which each of these types is used will be discussed later in this chapter. Although three different types of pipe are used, the cross-sectional properties are the only parameters that change. In each case, the pipes are 60 inches in length, and have the exact same types of end plates attached to the top and bottom.

The top and bottom end plate details are shown in Figures 2.13 and 2.14. In each case, the plates are 2 inches thick. The pattern and spacing of the holes in the top end plate are designed to match the pattern and spacing of the bolt holes at each corner of the diaphragm. In the same manner, the pattern and spacing of the holes in the bottom end plate are designed to match the pattern and spacing of the threaded bolt holes in the surface of the shake table. In each case, the overall

dimensions of the end plates followed from the bolt hole locations. The end plates are welded to each pipe column with a complete joint penetration weld, and reinforced with a fillet weld. In order to remove any residual stresses in the pipe, and also to proof test the strength of the welds, a tension test was performed on each column assembly. Each assembly was loaded through the end plates past the average yield stress of the pipe column. For the 4" Extra-Strong columns used in Test Configurations 1-4, the yield load was approximately 150 kips. For the 5" Standard columns used in Test Configurations 5 and 7, the yield load was approximately 210 kips. For the 4" Extra-Strong columns used in Test Configuration 6, the yield load was approximately 340 kips. For the 4" Double Extra-Strong columns used in Test Configurations 5 and 7, the yield load was approximately 340 kips. Due to time constraints, the 4" Extra-Strong columns used in Test Configuration 8 were not proof tested.

Each column assembly was secured to the diaphragm via the top end plate with eight A490 bolts, 1-1/8 inches in diameter, as seen in Figure 2.15. The bolts were passed down through a hole in the top flange, through one of the steel tubes welded in between the flanges, through a hole in the bottom flange, and then through the column top end plate. A nut was attached to the bolt below the column top end plate. Each column assembly was secured to the shake table via the bottom end plate with four bolts, 1-9/16 inches in diameter. The shake table surface has a pattern of holes regularly spaced at 12-1/16 inches, and tapped into the surface 6 inches deep. Shake table mounting bolts, which are 1-1/4 x 7 high-strength steel studs threaded over the entire length, are screwed down into the appropriate shake table holes, and then pass up through one of the holes in the column bottom end plate. A washer and nut were placed on the bolt above the column bottom end plate. Each of the nuts was tightened with a minimum torque of approximately 600 ft*lbs.

In order to allow for different test configurations with differing degrees of mass eccentricity, large removable steel masses were utilized on the experimental model. Two different types of masses were used, as seen in Figures 2.16 and 2.17. The octagonal masses had been used previously in shake table testing at CERL. Thus only the square masses were manufactured new for this study. Eight 1500 pound masses of each type were used in each test. The diaphragm and masses were designed such that the masses could be placed both above and below the diaphragm in order to keep the vertical center of mass roughly at the mid-height of the diaphragm, regardless of how the masses were arranged. The octagonal masses, having larger plan dimensions, were located on the top of the diaphragm, and the square masses were designed to fit when attached to the bottom of the diaphragm. The masses and their placements are shown in Figure 2.18, which

is again Elevation C-C from Figure 2.4. Because the octagonal masses were already available to use, their hole pattern dictated the hole pattern and spacing in the square masses and in the diaphragm concrete infill.

Securing the masses in place on and under the diaphragm were Dywidag Threadbars. These bars are essentially 1-1/4 inch diameter rebar, with an ultimate stress of 150 ksi. The Threadbars are designed for prestressing, and have “a continuous rolled-in pattern of thread-like deformations” along their entire length. Three different lengths, 50 inches, 64 inches, and 100 inches, were used in the various test configurations, depending on the number of masses in each stack. Nine bars were used for each stack. On each end of the Dywidag bars, a nut and a washer plate were used to secure the bar. Before the nuts were tightened, each bar was pulled using a compact hydraulic jack to approximately one-half of the ultimate load. The nuts were then tightened by hand, and the bars were released from the jack, thereby leaving each bar stressed.

Test Configurations 6 and 7 utilized asymmetric concentric lateral bracing to produce a stiffness asymmetry as shown in Figure 2.19. Test Configuration 6 featured 1-3/8" x 1/4" steel strap braces on the north side, and 1-7/8 x 1/4" steel strap braces on the south side of the model. Test Configuration 7 featured 1-1/4" x 1/4" strap braces on the north side, and 1-3/4" x 1/4" strap braces on the south side of the structure. All braces were 65" in length. The straps were welded both to attachment plates secured to the model structure (Figures 2.22 and 2.23) to and attachment plates secured to the shake table surface (Figures 2.20 and 2.21). The braces were designed to provide strength and stiffness only while in tension.

With the exception of the octagonal masses, each of the experimental test components was fabricated by a local machine shop and delivered to the testing facility at CERL. The column assemblies were delivered having already been proof tested, and the diaphragm was delivered as one complete unit. Assembly of the entire structure, including securing the columns to the shake table surface and to the diaphragm, and securing the masses to the diaphragm, was performed by in-house personnel.

2.2 SELECTION OF INPUT MOTIONS

The 1971 San Fernando - Pacoima Dam [Pacoima] 164- and 254-degree components and the 1979 Imperial Valley - Bonds Corner [Imperial Valley] 230- and 140-degree components were initially chosen as the two candidates to be used throughout the testing as the input ground motions. They were chosen on the basis of their response spectrum near the period of the model. Other motions considered were from the Taft, Castaic, Northridge, El Centro, and San Fernando earthquakes. Also, two simulated earthquakes were considered. Both the Pacoima and Imperial Valley motions had spectral accelerations which were relatively large in magnitude compared with the other earthquake motions considered, and were also relatively constant in the period range of the structure.

Both motions were altered based on simulations using Abaqus, a nonlinear finite-element analysis program, as described below. Two criteria, after the initial selection of the Pacoima and Imperial Valley motions, were used to determine the suitability of the input motions. First, the shake table has displacement limits of ± 2.375 inches and ± 6.0 inches in the X [north - south] and Y [east - west] directions, respectively. Thus, the input motions must be scaled accordingly so as not to exceed these limits. Second, it was desired that the structure reach a ductility of 4 – 5, during the strongest tests. Thus, the input motions needed to be scaled accordingly to produce the desired response. The first condition is a function of the maximum input record displacements, while the second condition is primarily a function of the maximum input record accelerations.

Initially, the motions were simply scaled such that the input displacements did not exceed the shake table displacement limits. In order to determine the model response, nonlinear finite element simulations were performed using Abaqus. Three structure models were created. The first had the masses symmetrically distributed on the top of the structure. The second had the masses placed only on one-half of the structure. The third had the masses placed only on one-quarter of the structure. These three models were representative of the three structure configurations planned for the first four tests. The model was first analyzed using a pushover analysis to determine the yield displacement of the structure. It was found to be approximately $\frac{1}{2}$ -inch. Each of the three models was then subjected to the original scaled motions. It was found that the scaling factor required, approximately 0.4, reduced the input accelerations to such a degree that the desired ductility in the model was not being achieved. Thus, the next option considered was filtering the input motions.

The input motions were first subjected to a high-pass filter at 1/3 Hz, meaning that all motion information at frequencies greater than 1/3 Hz was retained, while all information at frequencies below 1/3 Hz was discarded. This had the effect of reducing the maximum displacements while not affecting the maximum accelerations. The acceleration records do lose some information in the filtering process, but the information lost is small in magnitude, and therefore the maximum accelerations of the record are unchanged. With regard to displacements, the opposite is true. The larger magnitude displacements arise from the low-frequency waves. Filtering out the low-frequency information will greatly reduce the maximum displacements in the record. Thus, a high-pass frequency filter will reduce the maximum displacements without reducing the maximum accelerations. This is exactly what is needed, as it will allow the filtered records to be scaled up with respect to the unfiltered records, thereby increasing the maximum accelerations imposed on the structure, while not exceeding the shake table displacement limits.

The input motions filtered at 1/3 Hz were then again scaled to fall within the maximum shake table displacement limits. It was found through the Abaqus simulations that the model displacement ductility response was approximately 3 when these motions were used. With a larger ductility response desired, the input motions were then high-pass filtered at 1/2 Hz and scaled according to the shake table limits. The resulting model ductility response was approximately 4 - 5 according to the Abaqus simulations. Thus, the input motions subjected to a high-pass filter at 1/2 Hz produced the desired ductility, and were therefore used as the initial input motion set.

Another factor came into play which influenced the choice of the Imperial Valley records as the primary motion. The shake table Y-Axis, which has a larger displacement capability than the X-Axis, has a smaller acceleration capability than the X-Axis. Thus, it would be desirable to have a set of input motions which were a good fit to these displacement capabilities. The Imperial Valley record had a larger peak acceleration along the 230 degree axis than the 140 degree axis, but had a larger peak displacement along the 140 degree axis. The Pacoima record had its largest peak acceleration and displacement along the same axis.

The Imperial Valley input motions high-pass filtered at 1/2 Hz were used as the reference ground motions in Test Configuration 1. After reviewing the model response, it was determined that the X-Axis input motion needed to be scaled up further. Thus, the X-Axis motion was high-pass

filtered at 1 Hz, and then scaled according to the shake table displacement limits. The Y-Axis motion was not modified any further. Beginning with Test Configuration 2, the reference ground motions used were Imperial Valley with frequency information less than $\frac{1}{2}$ Hz filtered out in the Y-Axis, and less than 1 Hz filtered out in the X-Axis.

The goal in choosing the motions was to achieve ductility in the response of the structure in the neighborhood of four to five. To this end, the motions were modified using a combination of scaling and filtering and then checked in finite element simulations using Abaqus, in order to produce the desired ductility and not exceed the displacement limits of the shake table. This procedure produced a set of reference ground motion accelerograms to be used on the structure. Figures 2.24 and 2.25 show the original X-Axis and Y-Axis Imperial Valley input motions, before any filtering was performed, and scaled according to the shake table limits. Figures 2.26 and 2.27 show the X-Axis and Y-Axis Imperial Valley input motions high-pass filtered at $\frac{1}{2}$ Hz, and scaled according to the shake table limits. These motions were used in Test Configuration 1. Figure 2.28 shows the X-Axis Imperial Valley input motion high-pass filtered at 1 Hz, and scaled according to the shake table limits. Beginning with Test Configuration 2, the motions shown in Figures 2.27 and 2.28 were used as the reference ground motions. Figures 2.29 and 2.30 show the response spectra for the original unfiltered motions and for the Test Configuration 2 ground motions, respectively.

2.3 EXPERIMENTAL SETUP

The first step in preparing the model structure for experimental tests was to place the column assemblies on the shake table, and secure them to the table with the shake table mounting bolts, such that the column bottom plates experience the same motion as the shake table itself. The diaphragm was then moved into position and secured to the tops of the columns. Next, the masses were attached to the diaphragm in the appropriate locations. All nut-bolt assemblies were then retightened once the entire model was setup on the shake table.

The overhead crane in the shake table bay was used to move all of the model structure components into position. During the tests, the overhead crane remained very loosely connected to the diaphragm to prevent the model from damaging the shake table in the event the model structure collapsed.

Test structure instrumentation was installed on the model structure to record absolute accelerations of the shake table and diaphragm, absolute displacements of the shake table and diaphragm, and strains in the columns and diagonal braces. Details of the data acquisition system and test instrumentation are provided in Appendix A. Table A.1 lists all data acquisition channels and in which test configuration each was used. Figures A.2 – A.10 show the locations of all transducers.

2.4 TEST SEQUENCE

Eight different model configurations were studied as shown in Table 2.1. Perspective views of a simplified model structure in each of the eight different configurations are shown in Figures 2.31–2.38. The configurations consist of different combinations of varying parameters: one-quarter asymmetric mass, one-half asymmetric mass, symmetric mass, asymmetric and symmetric column strength, and concentric lateral bracing, which also provides stiffness asymmetry. The inclusion of each of these different types of asymmetry will allow the scope of the results to be more general in nature.

The one-half mass asymmetry is achieved by placing the masses in two stacks on one-half of the diaphragm, as shown in Figure 2.34. Similarly, the one-quarter mass asymmetry is achieved by placing the masses on one-quarter of the diaphragm in one stack, as shown in Figure 2.33. In the case of the one-half mass asymmetric system, the center of mass moves approximately 15.3 inches from the geometric center of the diaphragm in the direction of the mass stack. In that the span of the diaphragm, column center to column center, is 96.5 inches, the eccentricity generated is approximately 16% of the plan dimension along one axis. In the case of the one-quarter mass asymmetric system, the center of mass moves approximately 15.3 inches from the geometric center along both lateral axes, creating an eccentricity of approximately 16% along both the north-south, or X, axis and the east-west, or Y, axis. In both the mass-asymmetrical and mass-symmetrical cases, half of the masses are attached above and half below the diaphragm to keep the vertical mass center reasonably near the center of the diaphragm. Regardless of the mass distribution, all 16 masses, 8 above and 8 below the diaphragm, were used for each test configuration.

Test Configurations 1 and 2 featured a symmetric mass distribution and four 4" Extra-Strong columns as shown in Figures 2.31 and 2.32. In Test Configuration 1, the model structure was subjected to full-scale earthquake input motions along the east-west [Y] axis only. The objective of this was to provide a simpler input and structural response, in an effort to check the behavior of the shake table, model structure, and all instrumentation under full-scale input. Following Test Configuration 1, all subsequent test configurations utilized full-scale input motions along both horizontal axes. Test Configuration 3, as shown in Figure 2.33, featured a one-quarter asymmetric mass distribution, with the masses in the northeast diaphragm corner, and four 4" Extra-Strong columns. Test Configuration 4 featured a one-half asymmetric mass distribution, with the masses on the east side of the diaphragm, and four 4" Extra-Strong columns as shown in Figure 2.34.

Test Configuration 5, as shown in Figure 2.35, featured a one-half asymmetric mass distribution, with the masses on the north side of the diaphragm. Test Configuration 5 also featured a strength asymmetry achieved by placing two 5" Standard pipe-columns on the north side of the model structure and two 4" Double Extra-Strong pipe-columns on the south side of the structure. The 5" Standard pipe and 4" Double Extra-Strong pipe have similar moments of inertia, 15.2 in^4 and 15.3 in^4 , respectively, and thus have similar elastic stiffness. On the other hand, the 5" Standard pipe has a yield moment of 363.5 kip-inches and an axial yield load of 215 kips, while the 4" Double Extra-Strong pipe has a yield moment of 438.7 kip-inches and an axial yield load of 356.4 kips, creating the strength asymmetry

Test Configurations 6 and 7, as shown in Figures 2.36 and 2.37, both featured a one-half asymmetric mass distribution, with the masses on the south side of the diaphragm. Four 4" Extra-Strong columns were used for Test Configuration 6. Test Configuration 7 features a strength asymmetry with two 5" Standard pipe-columns on the west side and two 4" Double Extra-Strong pipe-columns on the east side of the structure. Both test configurations also possessed a stiffness asymmetry, achieved through the use of asymmetrical concentric lateral bracing consisting of slender steel straps. The straps were welded both to attachment plates secured to the model structure and attachment plates secured to the shake table surface. Test Configuration 6 featured 1-3/8" x 1/4" strap braces on the north side, and 1-7/8 x 1/4" strap braces on the south side of the model. Test Configuration 7 featured 1-1/4" x 1/4" strap braces on the north side, and 1-3/4" x 1/4" strap braces on the south side of the structure. The braces were designed to provide strength and stiffness only while in tension.

Test Configuration 8, as shown in Figure 2.38, was identical to Test Configuration 3 and thus featured a one-quarter asymmetric mass distribution, with the masses in the northeast diaphragm corner, and four 4" Extra-Strong columns.

2.5 TESTING PROCEDURE

Prior to performing any shake table simulations using the earthquake input motions, a series of tests were performed to characterize the model structure, including the determination of its natural frequencies and damping characteristics. First, the structure was subjected to white noise base motions. Transfer functions of the acceleration response of the structure were used to determine the natural frequencies. Second, the structure was excited sinusoidally at its measured natural frequency. The input motion was then suddenly discontinued, and the motion of the structure was allowed to decay to rest. Analysis of this response using the so-called logarithmic decrement of damping was performed to determine the equivalent viscous-damping ratio. Third, the structure was subjected to sinusoidal motions ranging in frequency from 1-20 Hertz. The response of the structure to the sine sweep tests was used to confirm the natural frequencies of the structure. Each of the aforementioned tests were performed once in each planar axis, and once in the yaw-axis, for a minimum total of nine preliminary tests for each model configuration.

Following the characterization tests, the structure was subjected to the earthquake simulations. The 230 [X] and 140 [Y] degree acceleration components from the 1979 Imperial Valley earthquake recorded at Bonds Corner, as discussed previously, were chosen as the base earthquake motions. The structure was first subjected to low-level earthquake tests, typically with input motions of 10-25% of the reference input record. The low-level tests were performed using first the X-Axis input motion, then the Y-Axis input motion, followed by both axes simultaneously. Next, the structure was subjected to the full-scale reference accelerograms. If possible, the full-scale reference accelerograms were scaled up to the extent allowed by the shake table displacement limits in order to perform a subsequent simulation. No vertical motions were used as input in this study. Following each earthquake simulation, the characterization tests were again performed to assess any changes to the properties of the model structure. Also, following each full-scale earthquake simulation, visual inspection of the model structure was conducted. This general sequence of preliminary characterization tests and earthquake simulations was

followed for each of the eight different model configurations. The specific sequence of the earthquake simulations performed on the model structure is presented in Table 2.2.

Test Configuration	Figure	Input Motion	Mass Distribution	Stiffness Distribution	Strength Distribution	Notes
1	2.31	Uniaxial	Symmetric	Symmetric	Symmetric	4 - 4" Extra-Strong Columns
2	2.32	Biaxial	Symmetric	Symmetric	Symmetric	4 - 4" Extra-Strong Columns
3	2.33	Biaxial	1/4 Asymmetric	Symmetric	Symmetric	4 - 4" Extra-Strong Columns
4	2.34	Biaxial	1/2 Asymmetric [X]	Symmetric	Symmetric	4 - 4" Extra-Strong Columns
5	2.35	Biaxial	1/2 Asymmetric [Y]	Symmetric	Symmetric [X] Asymmetric [Y]	2 - 5" Standard Columns 2 - 4" Double Extra-Strong Columns
6	2.36	Biaxial	1/2 Asymmetric [Y]	Symmetric [X] Asymmetric [Y]	Symmetric [X] Asymmetric [Y]	4 - 4" Extra-Strong Columns Asymmetric Lateral Bracing [Y]
7	2.37	Biaxial	1/2 Asymmetric [Y]	Symmetric [X] Asymmetric [Y]	Asymmetric [X] Asymmetric [Y]	2 - 5" Standard Columns 2 - 4" Double-Extra Strong Columns Asymmetric Lateral Bracing [Y]
8	2.38	Biaxial	1/4 Asymmetric	Symmetric	Symmetric	4 - 4" Extra-Strong Columns

Table 2.1 Test Configuration Summary

Test Configuration	Earthquake Simulation Test No.	Input Motions	PGA _X (g)	PGA _Y (g)
1	1	25% X-Axis	0.238	N/A
	2	25% Y-Axis	N/A	0.162
	3	25% Biaxial	0.232	0.160
	4	25% X-Axis Pacoima	0.209	N/A
	5	25% Y-Axis Pacoima	N/A	0.236
	6	25% Biaxial Pacoima	0.211	0.240
	7	100% Y-Axis	N/A	0.678
	8	200% Y-Axis	N/A	1.625
	9	100% Y-Axis	N/A	0.682
	10	150% Y-Axis	N/A	1.104
	11	150% Y-Axis	N/A	1.123
2	12	25% X-Axis	0.250	N/A
	13	25% Y-Axis	N/A	0.168
	14	25% Biaxial	0.248	0.170
	15	100% Biaxial	1.080	0.699
	16	150% Biaxial	1.582	1.141
	17	150% Biaxial	1.586	1.123
3	18	10% X-Axis	0.102	N/A
	19	10% Y-Axis	N/A	0.064
	20	10% Biaxial	0.098	0.061
	21	10% Biaxial	0.096	0.062
	22	10% Biaxial	0.109	0.066
	23	100% Biaxial	1.299	0.797
	24	150% Biaxial	1.916	1.137
4	25	10% X-Axis	0.105	N/A
	26	10% Y-Axis	N/A	0.070
	27	10% Biaxial	0.102	0.062
	28	100% Biaxial	1.115	0.711
	29	150% Biaxial	1.629	1.121
5	30	10% X-Axis	0.102	N/A
	31	10% Y-Axis	N/A	0.064
	32	10% Biaxial	0.100	0.059
	33	100% Biaxial	1.084	0.664
	34	100% Biaxial	1.086	0.658
	35	150% Biaxial	1.637	1.045
6	36	10% Biaxial	0.117	0.191
	37	10% X-Axis	0.119	N/A
	38	10% Y-Axis	N/A	0.189
	39	100% Biaxial	0.846	1.926
	40	100% X-Axis 90% Y-Axis	1.318	1.951
7	41	100% X-Axis 75% Y-Axis	1.367	1.582
	42	100% X-Axis 85% Y-Axis	1.357	1.881
	43	100% Biaxial	1.354	1.986
	44	100% X-Axis 90% Y-Axis	1.367	1.861
8	45	100% Biaxial	1.187	0.699
	46	135% Biaxial	1.559	0.990

Table 2.2 List of Earthquake Simulations Performed

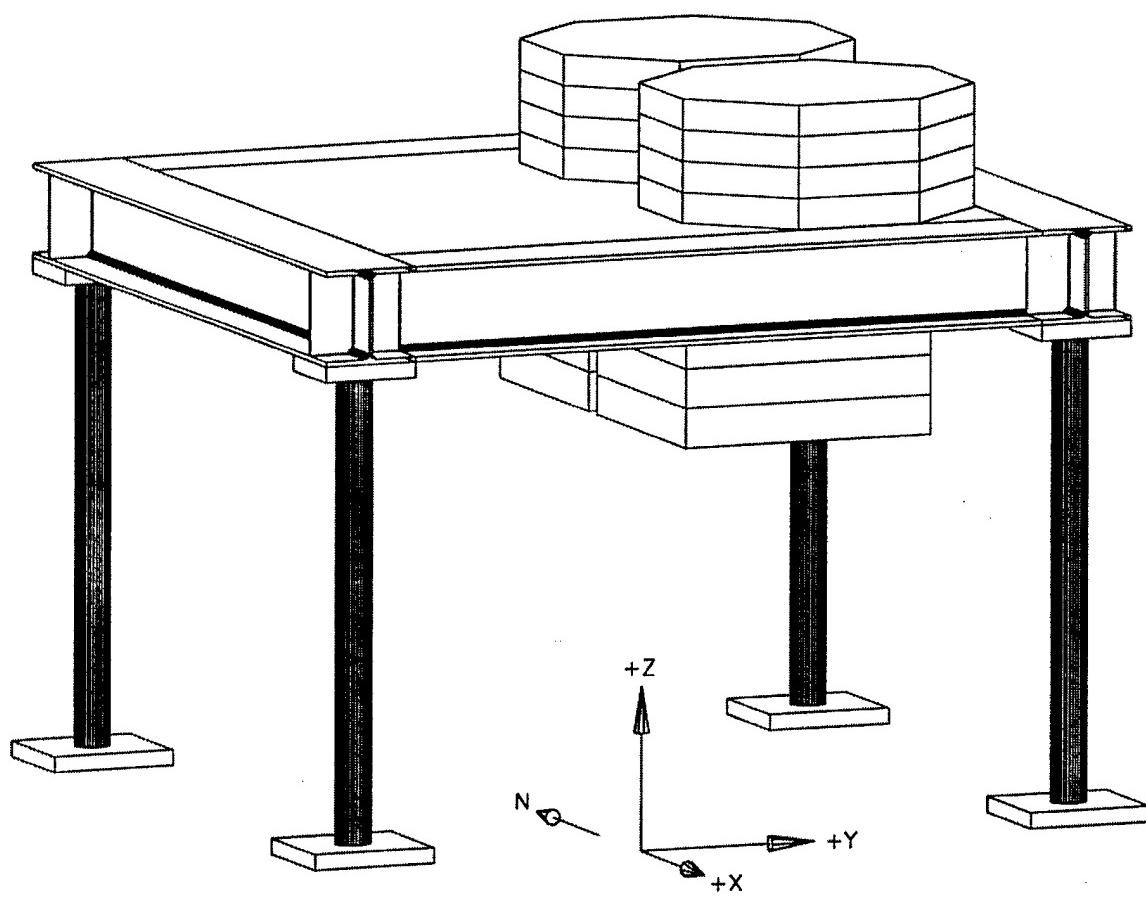


Figure 2.1 Perspective View of Model Structure

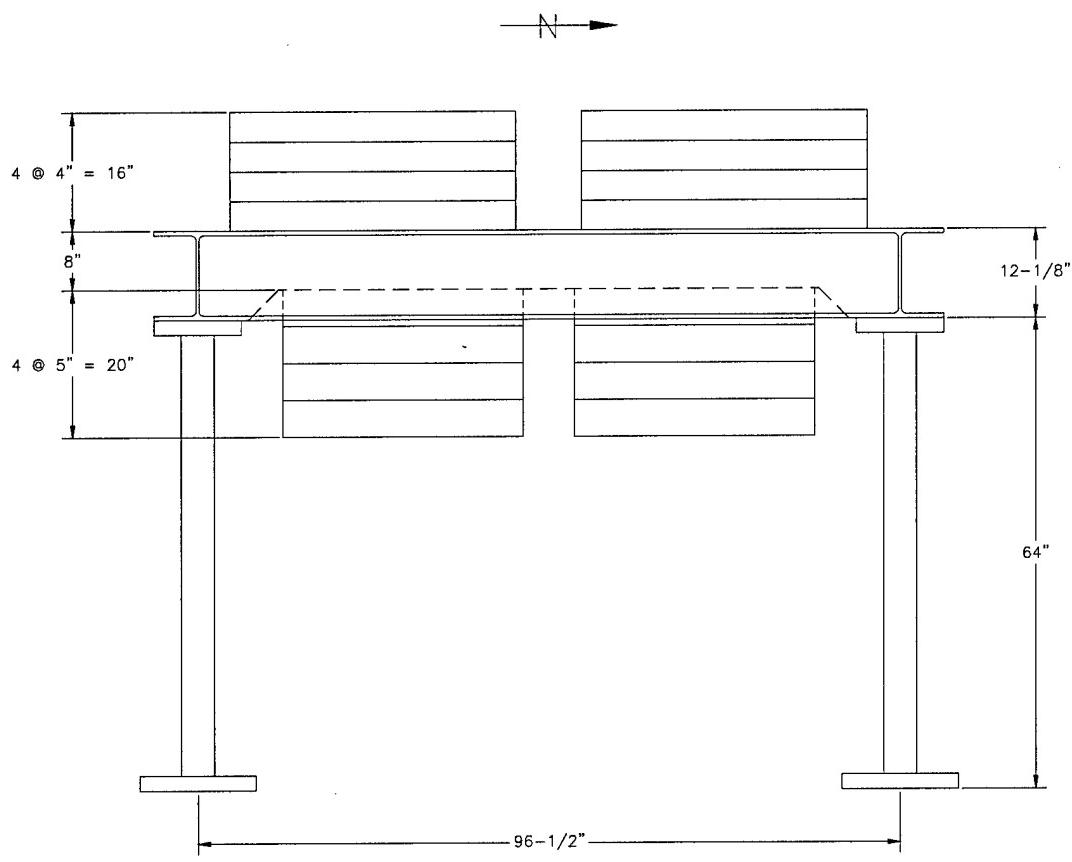


Figure 2.2 Elevation View of East Side of Structure

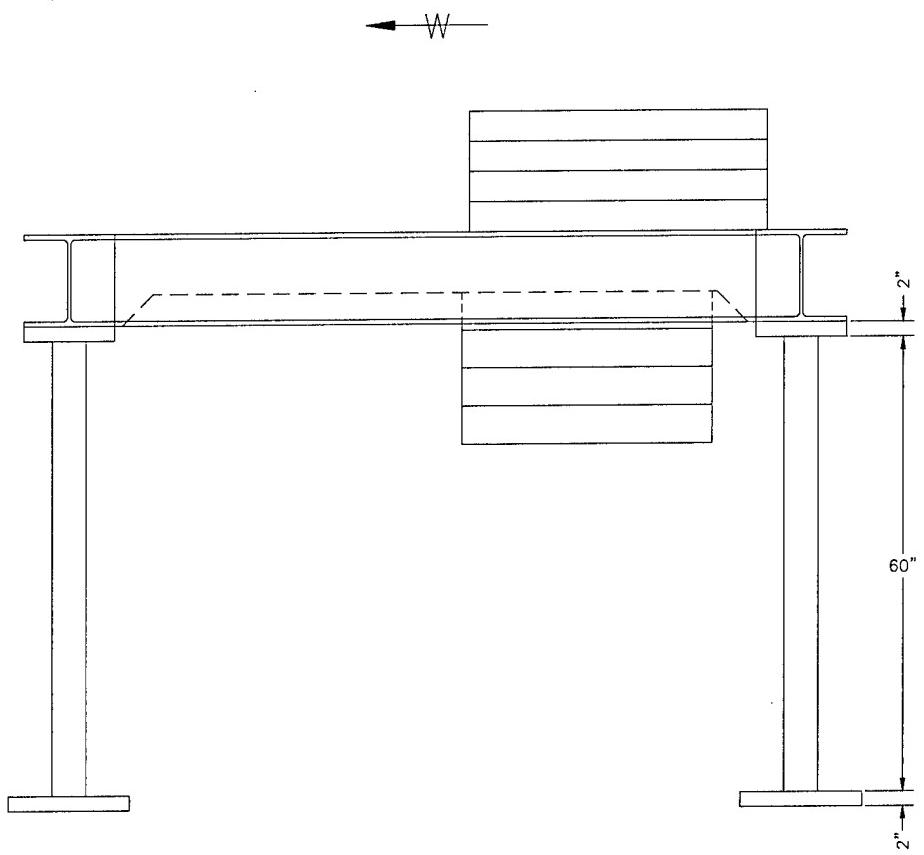


Figure 2.3 Elevation View of South Side of Structure

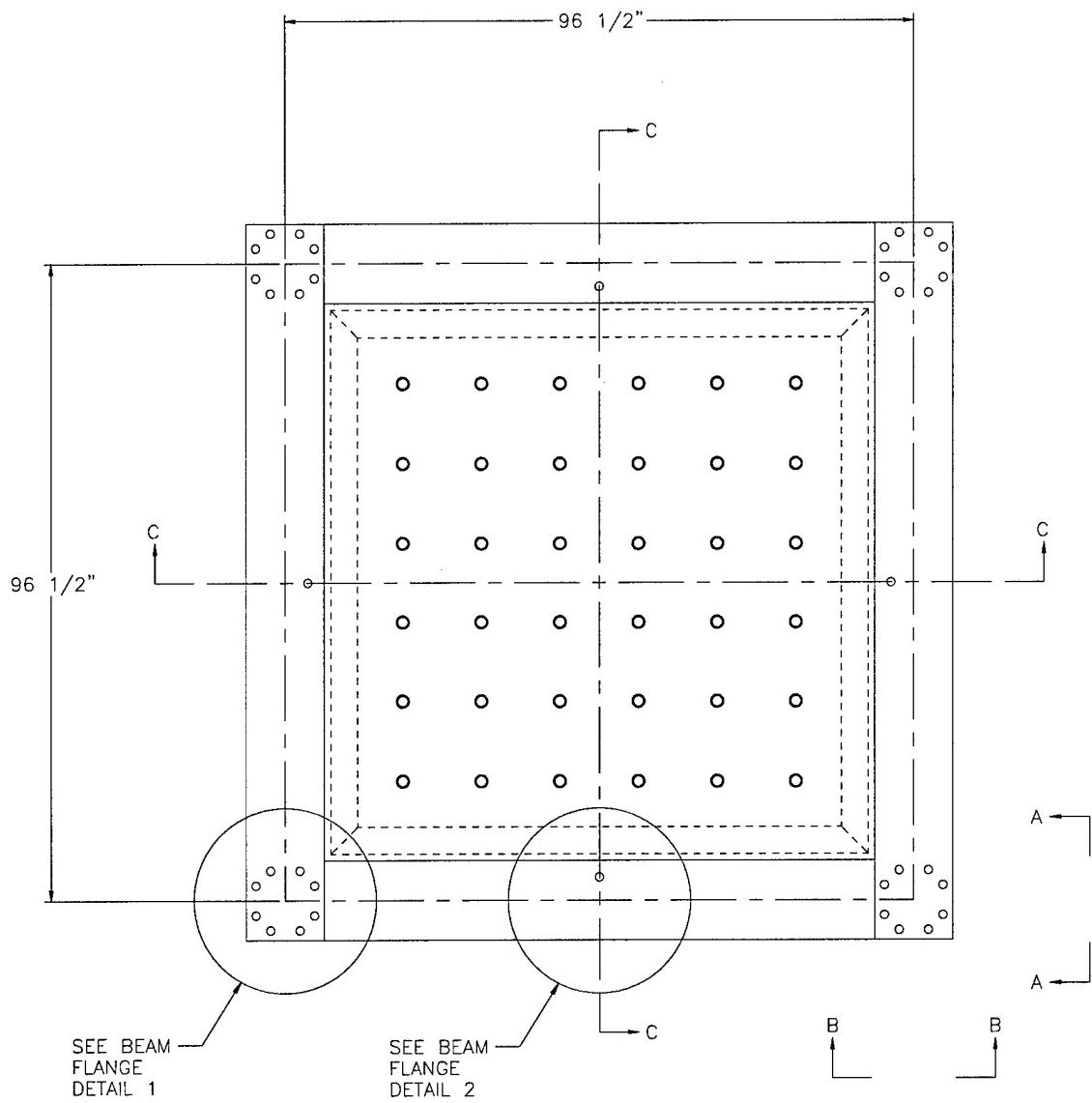


Figure 2.4 Plan View of Diaphragm

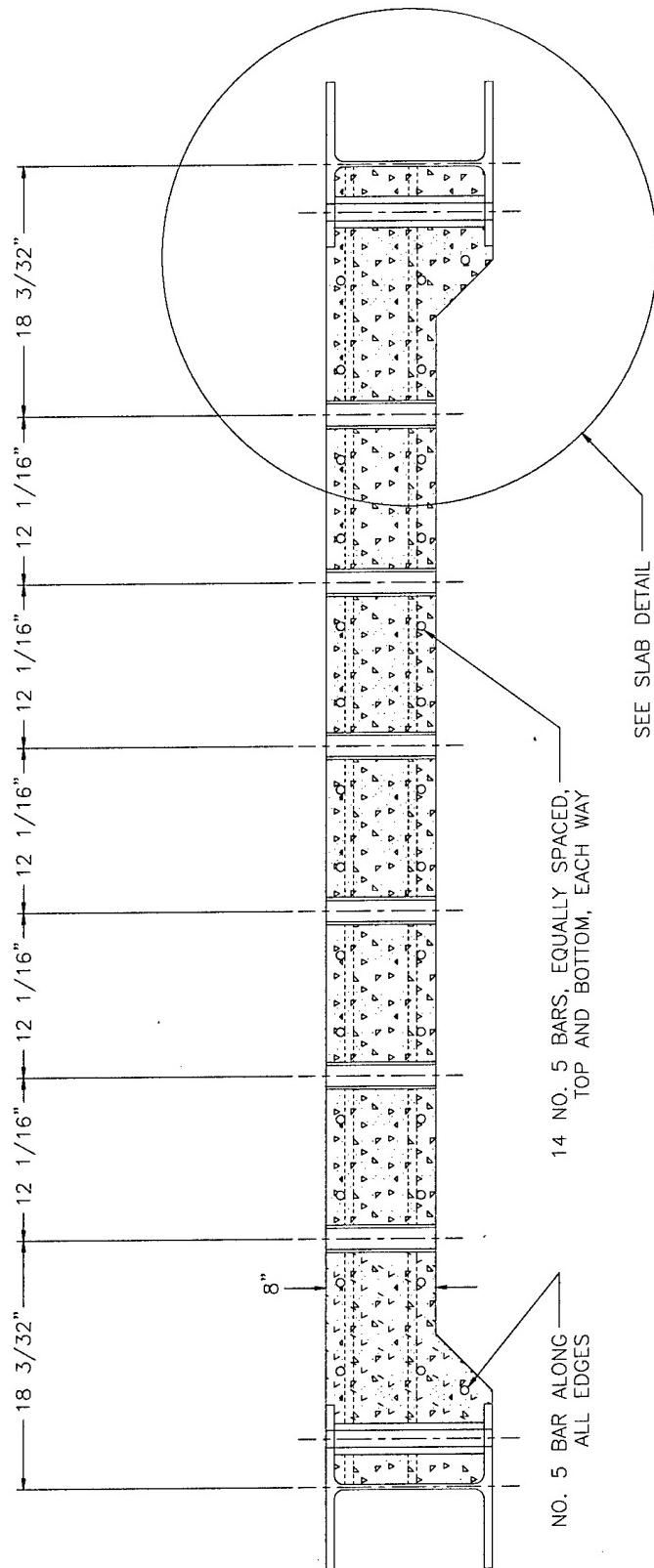


Figure 2.5 Diaphragm Elevation C-C

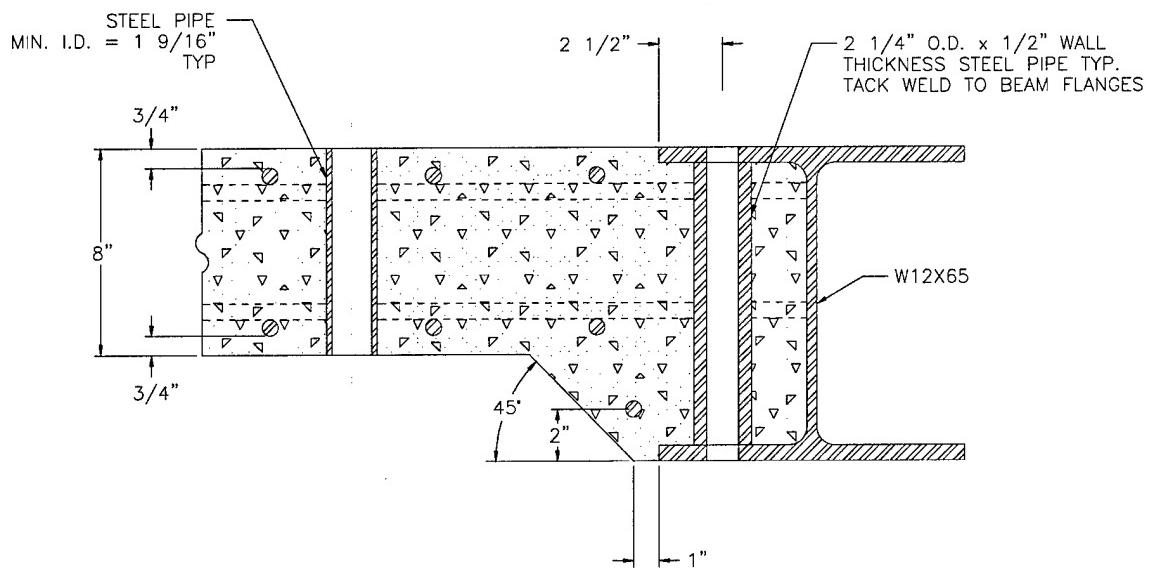


Figure 2.6 Elevation View of Slab Detail

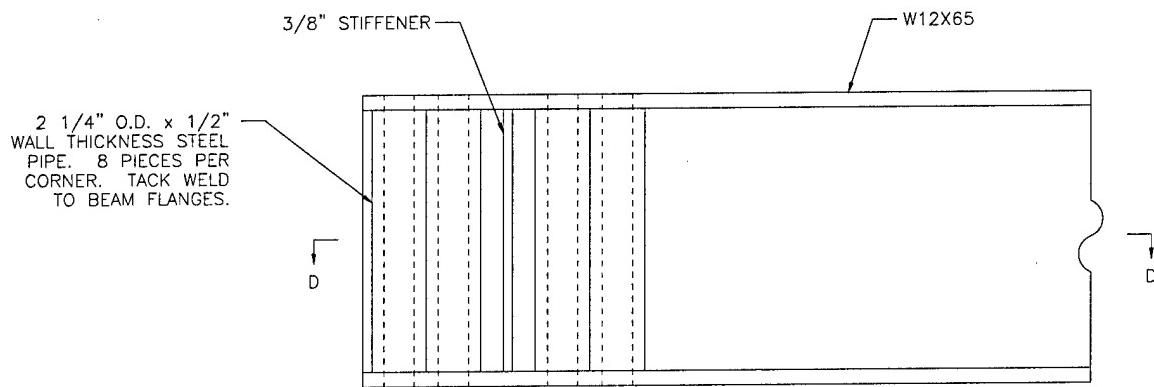


Figure 2.7 Diaphragm Elevation A-A

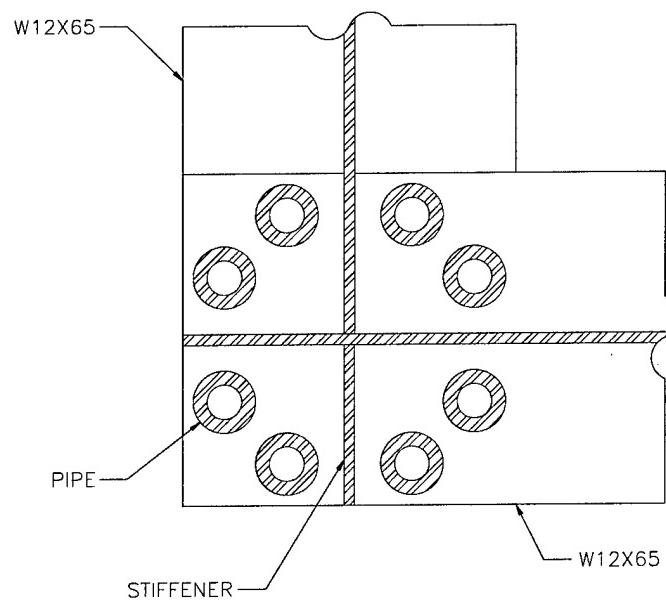


Figure 2.8 Diaphragm Section D-D

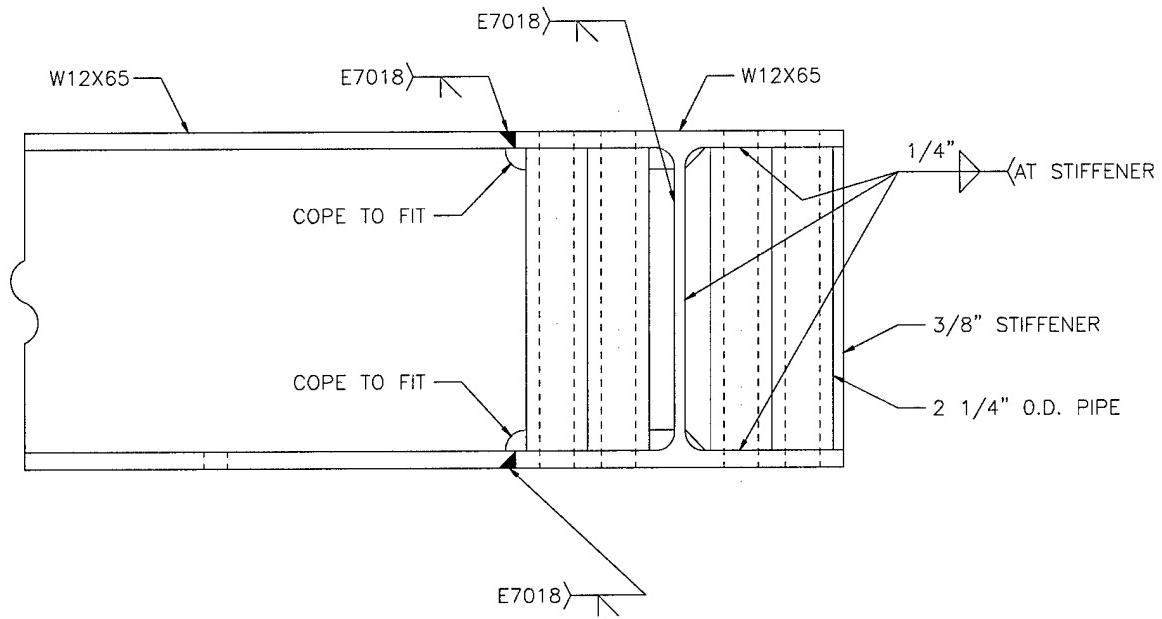


Figure 2.9 Diaphragm Elevation B-B

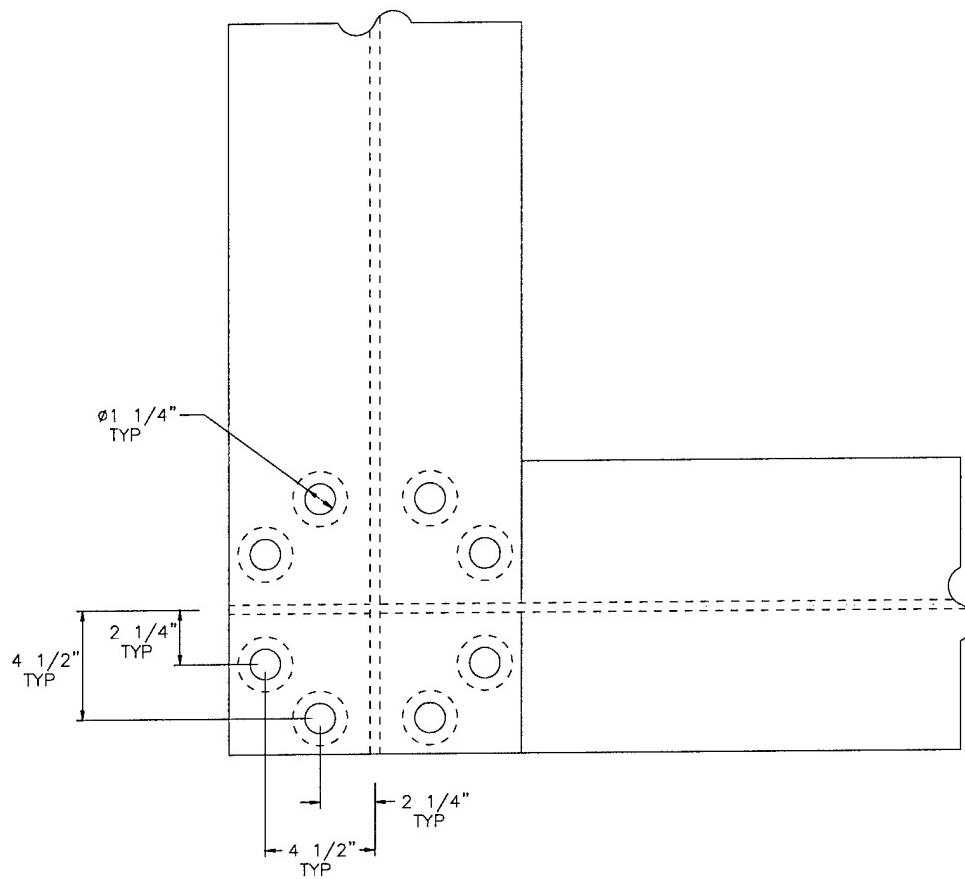


Figure 2.10 Diaphragm Beam Flange Detail 1

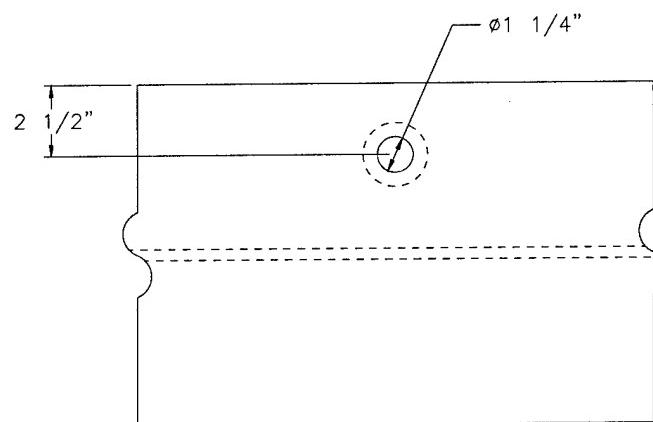


Figure 2.11 Diaphragm Beam Flange Detail 2

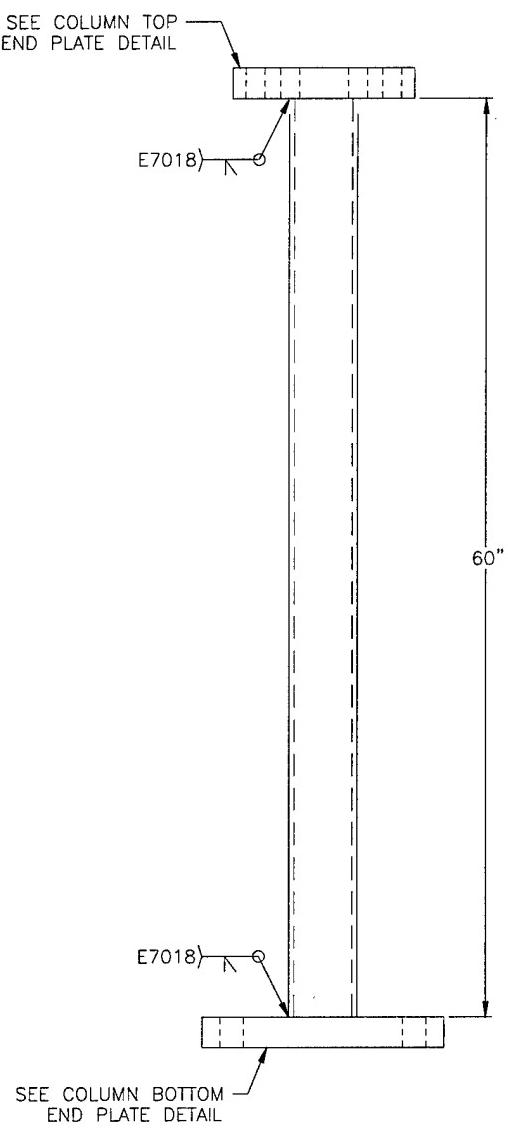


Figure 2.12 Pipe Column Assembly

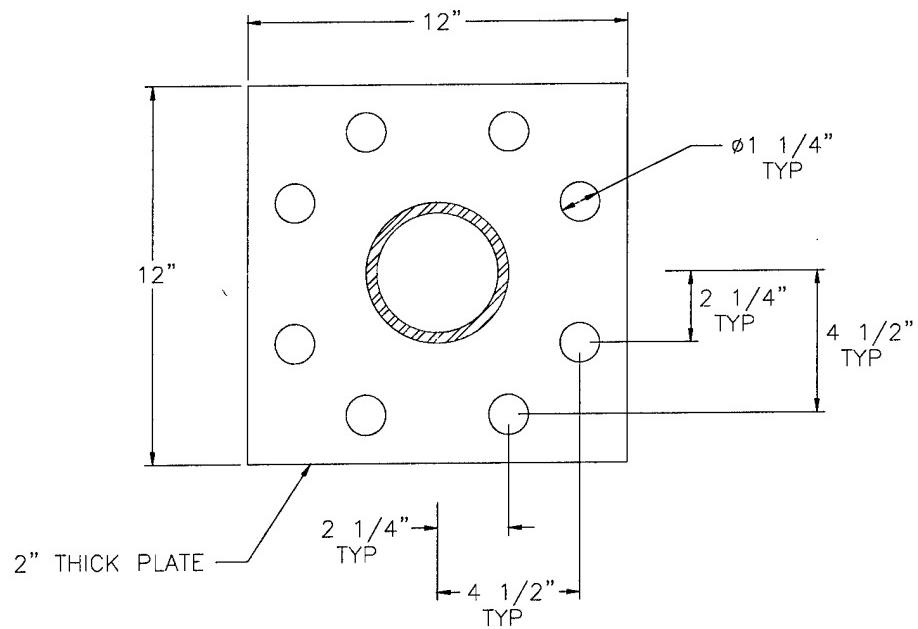


Figure 2.13 Column Top End Plate Detail

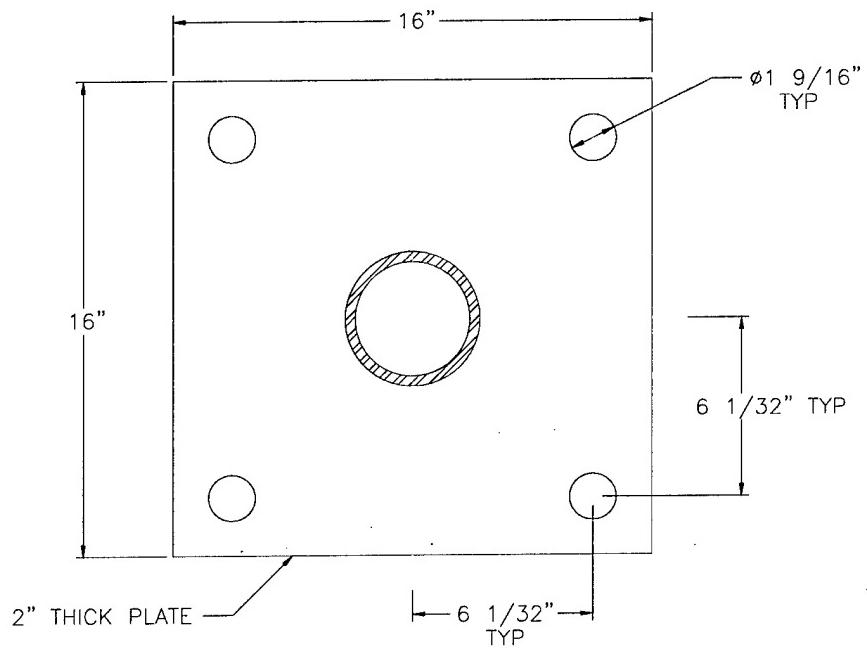


Figure 2.14 Column Bottom End Plate Detail

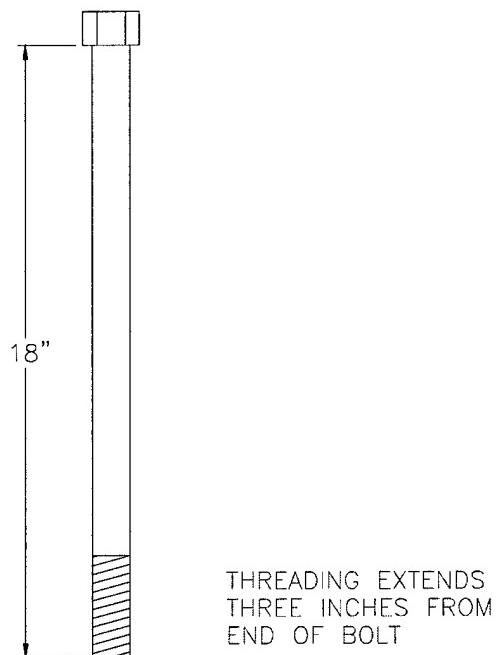


Figure 2.15 1-1/8" Diameter A490 Bolt

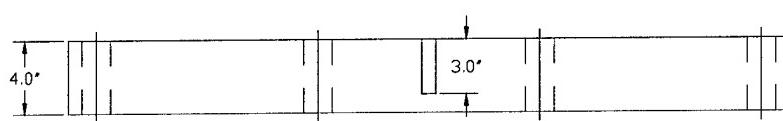
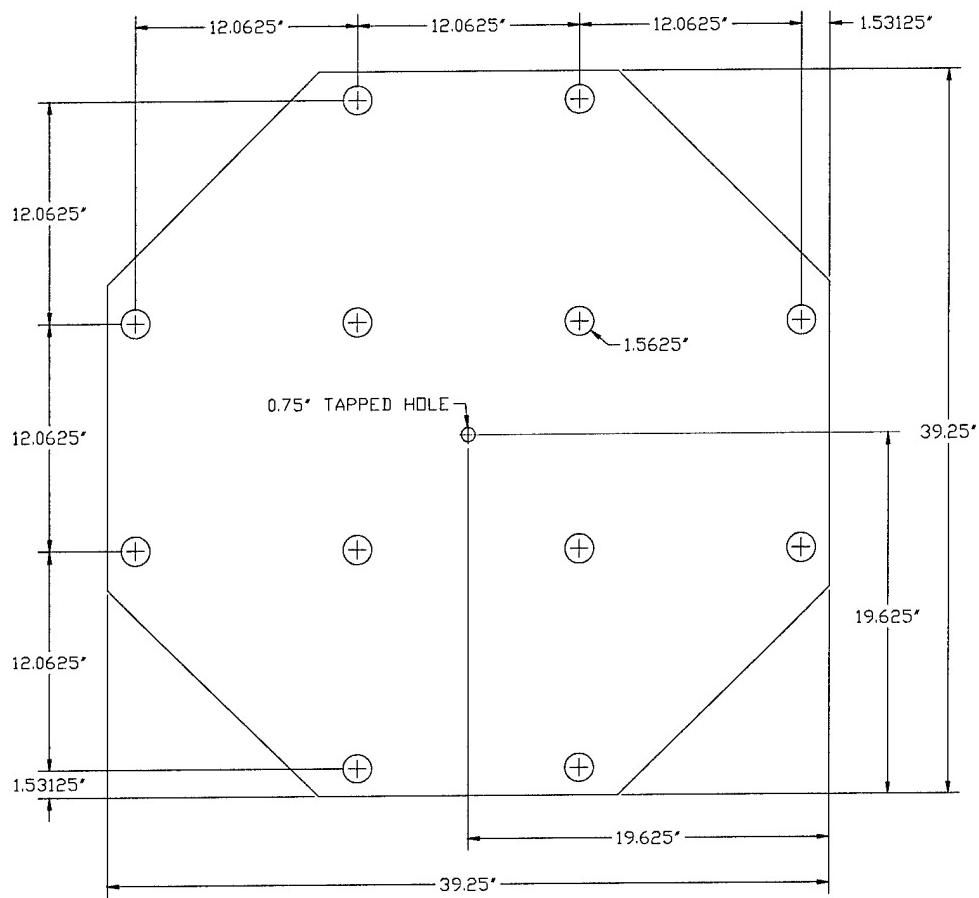


Figure 2.16 Octagonal Steel Mass

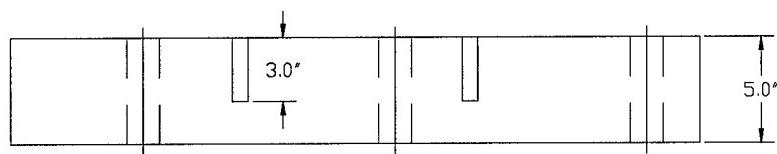
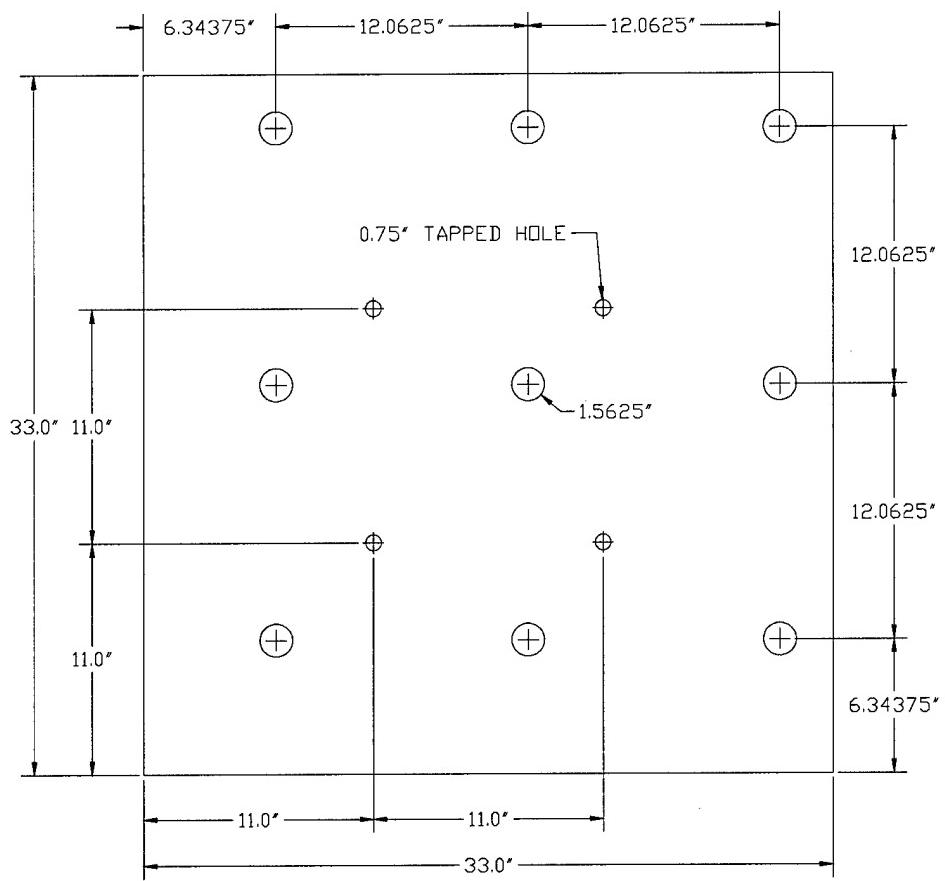


Figure 2.17 Square Steel Mass

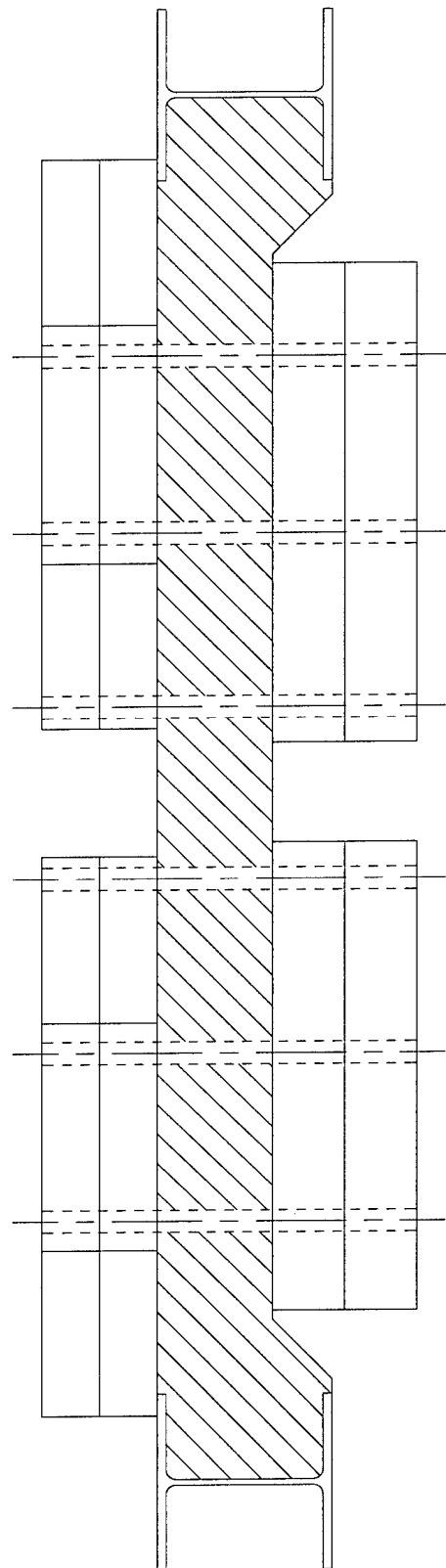


Figure 2.18 Diaphragm Elevation C-C

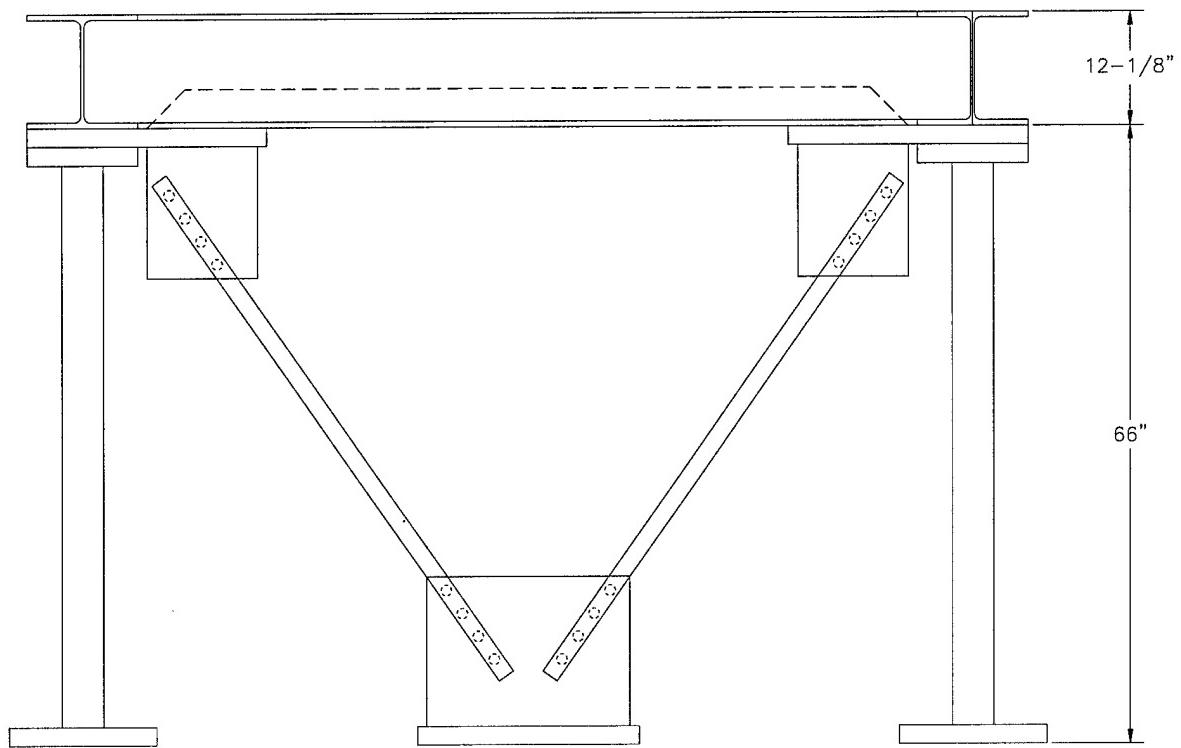


Figure 2.19 Elevation View of Structure with Concentric Lateral Bracing

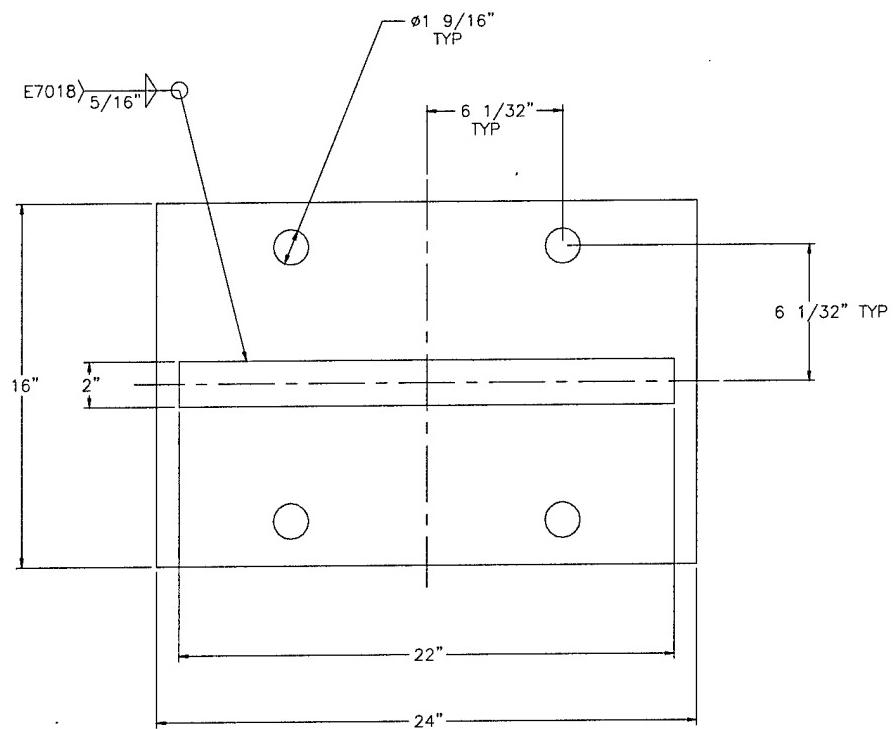


Figure 2.20 Plan View of Bottom Gusset Plate

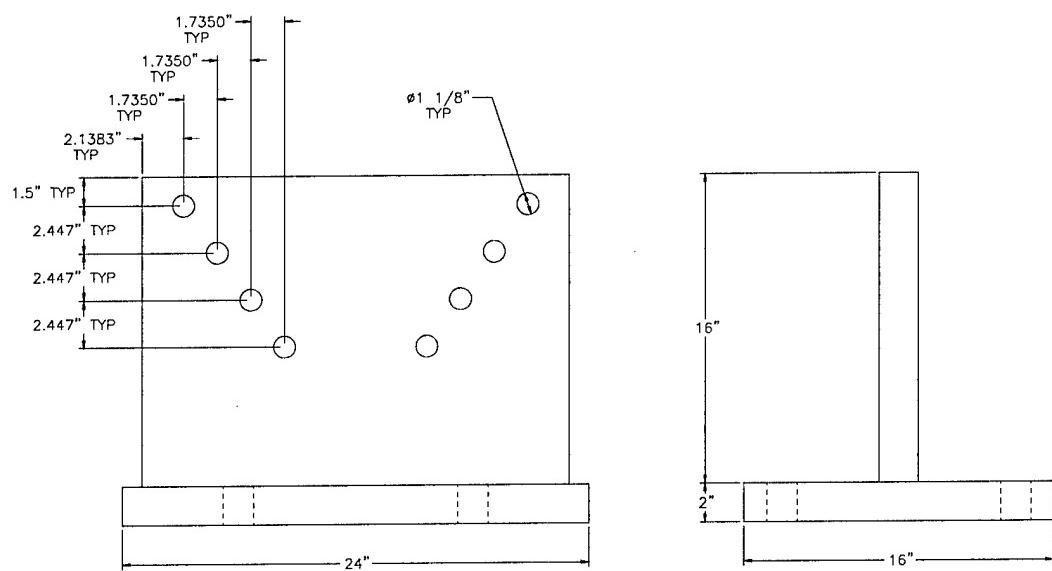


Figure 2.21 Elevation View of Bottom Gusset Plate

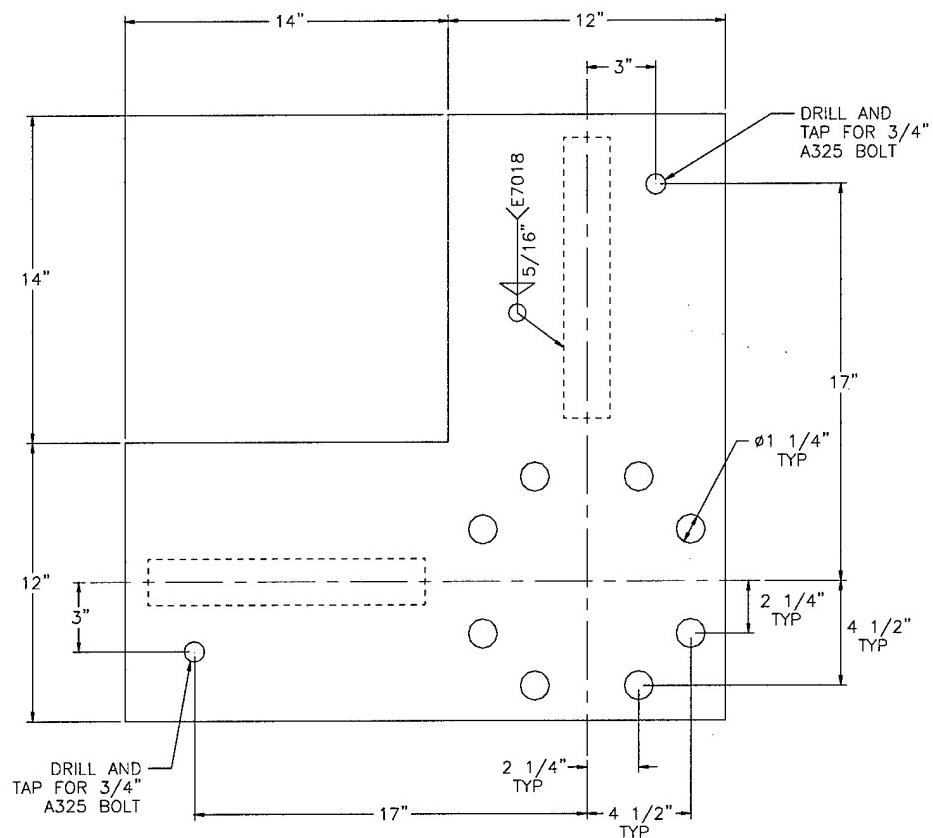


Figure 2.22 Plan View of Top Gusset Plate

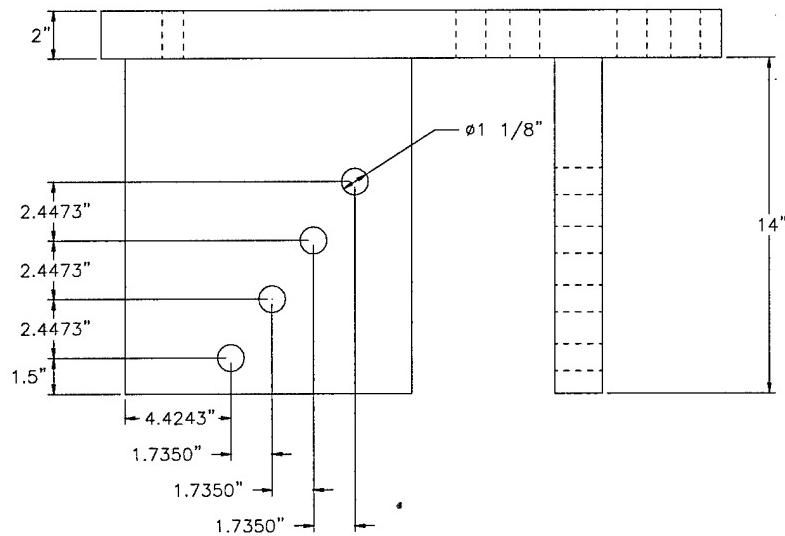


Figure 2.23 Elevation View of Top Gusset Plate

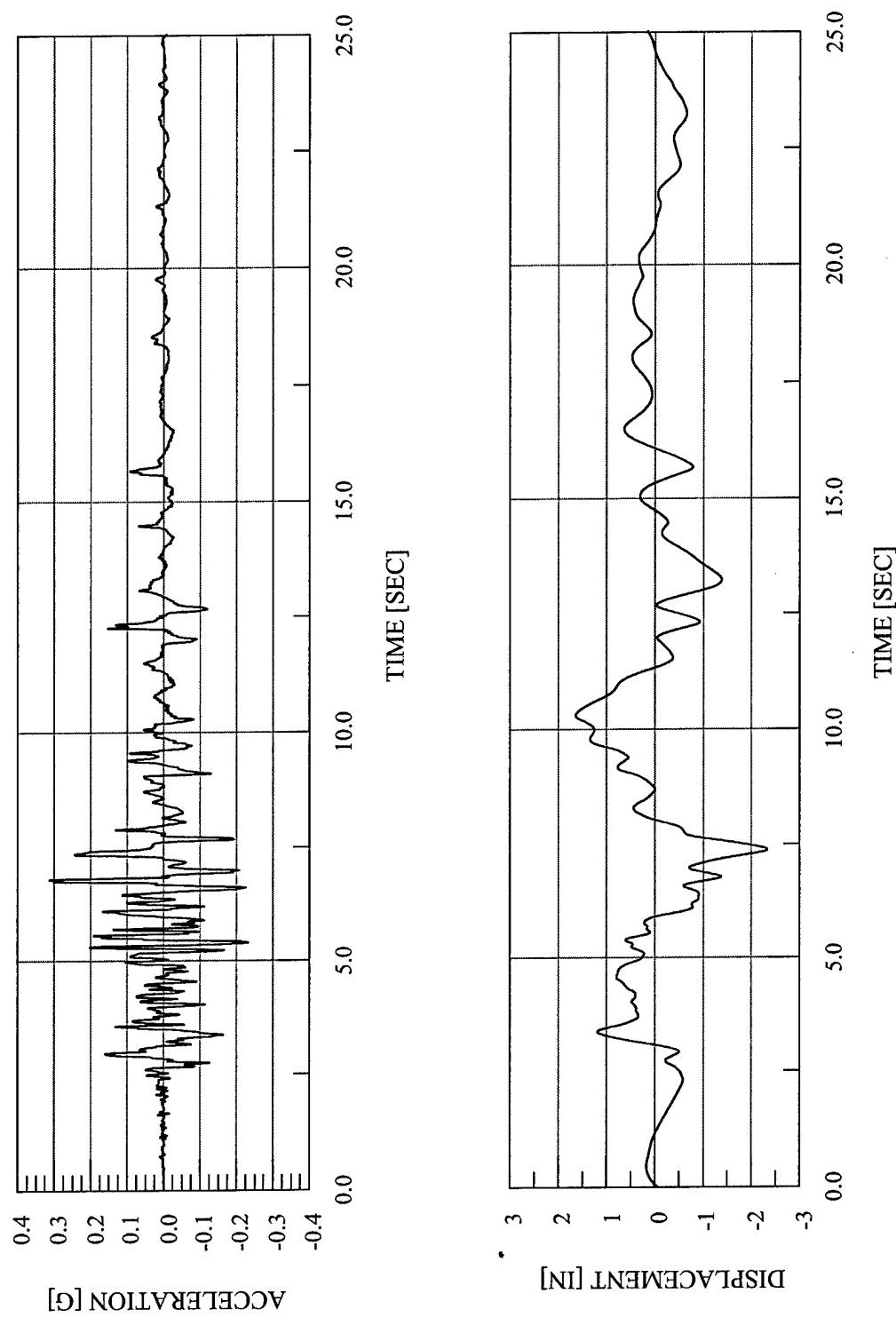


Figure 2.24 Original Imperial Valley Input Motions – X-Axis – No Filtering – Scaled to Shaketable Displacement Limits

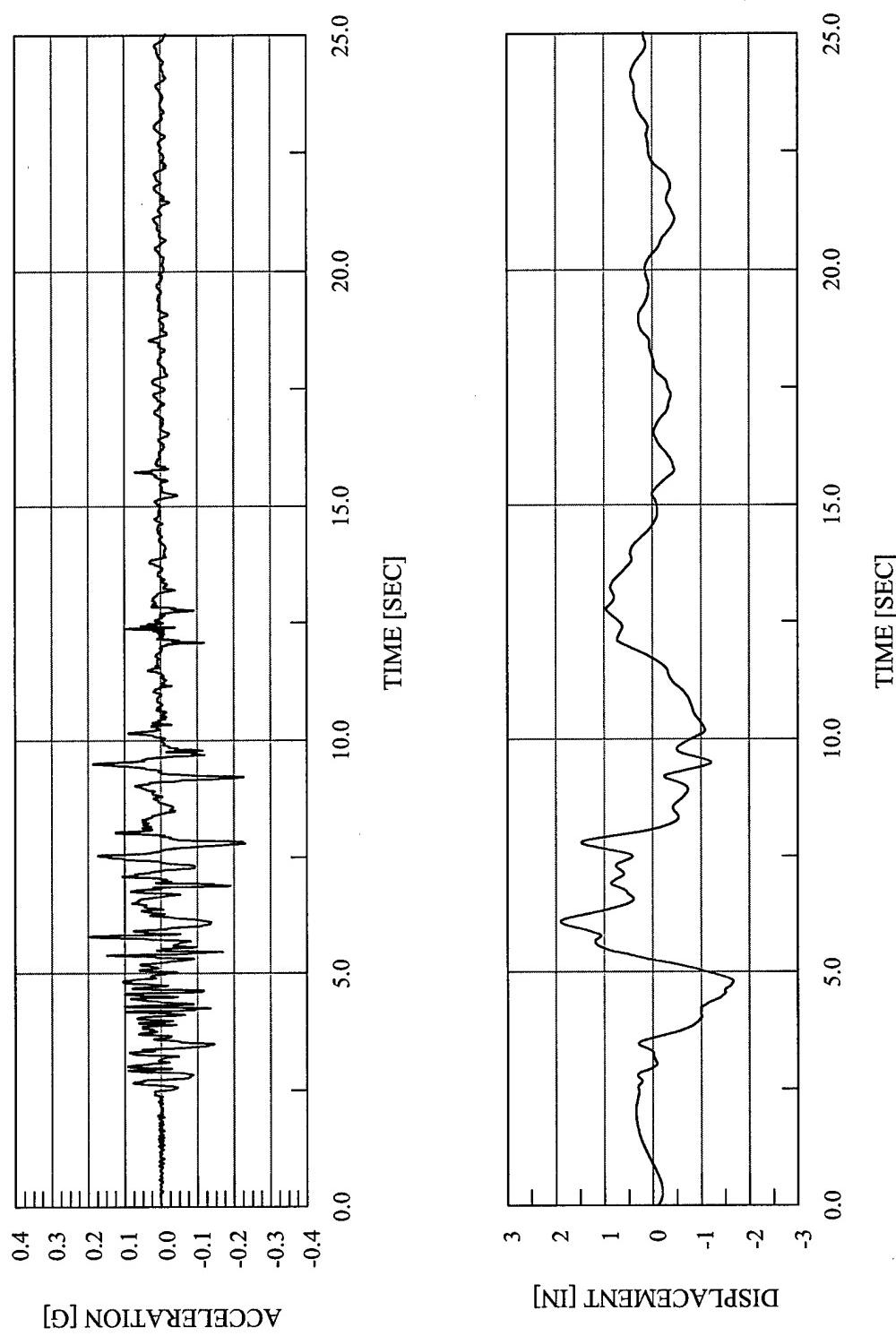


Figure 2.25 Original Imperial Valley Input Motions – Y-Axis – No Filtering – Scaled to Shaketable Displacement Limits

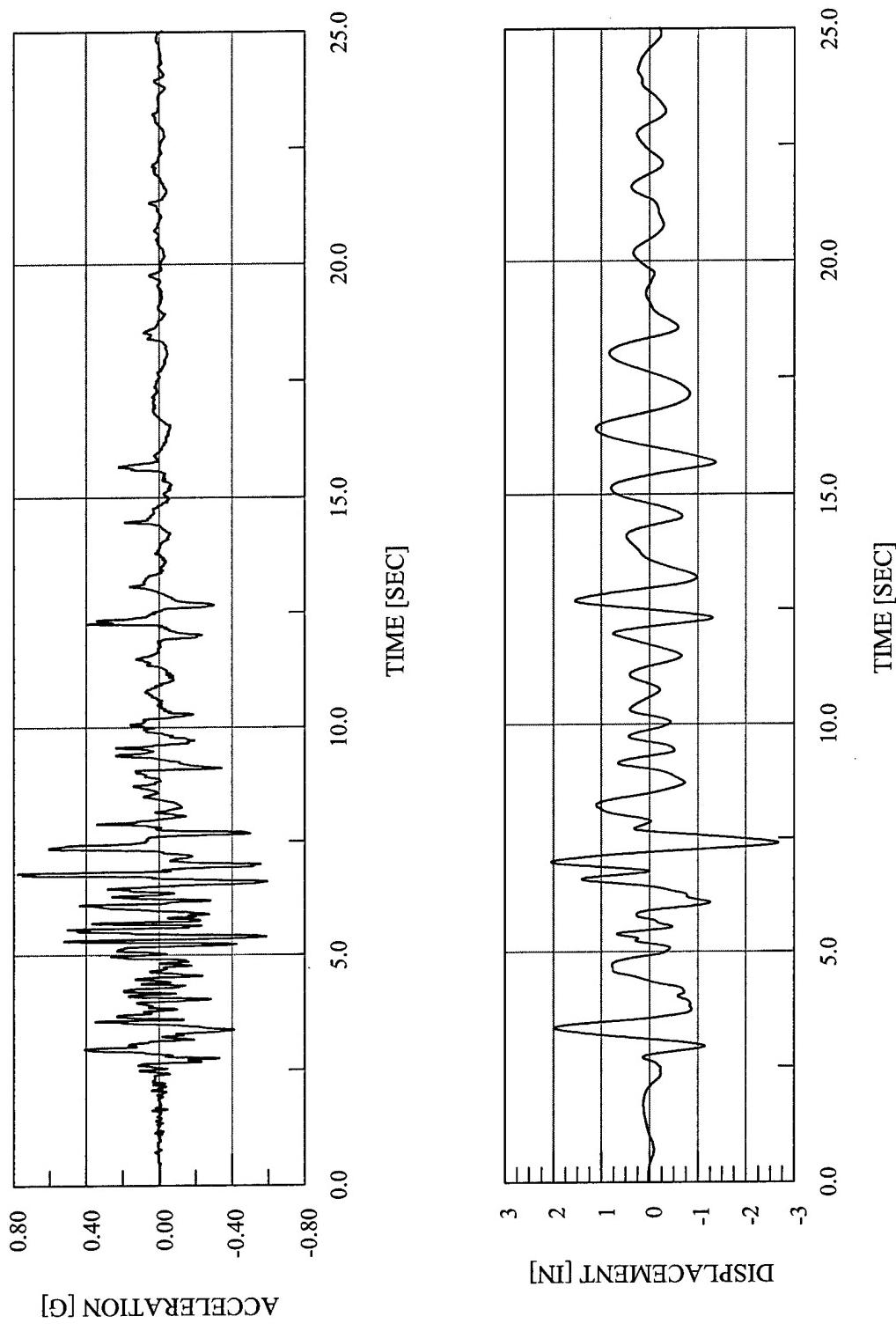


Figure 2.26 Modified Imperial Valley Input Motions – X-Axis – High-Pass Filtered at 1/2 Hz – Scaled to Shaketable Displacement Limits

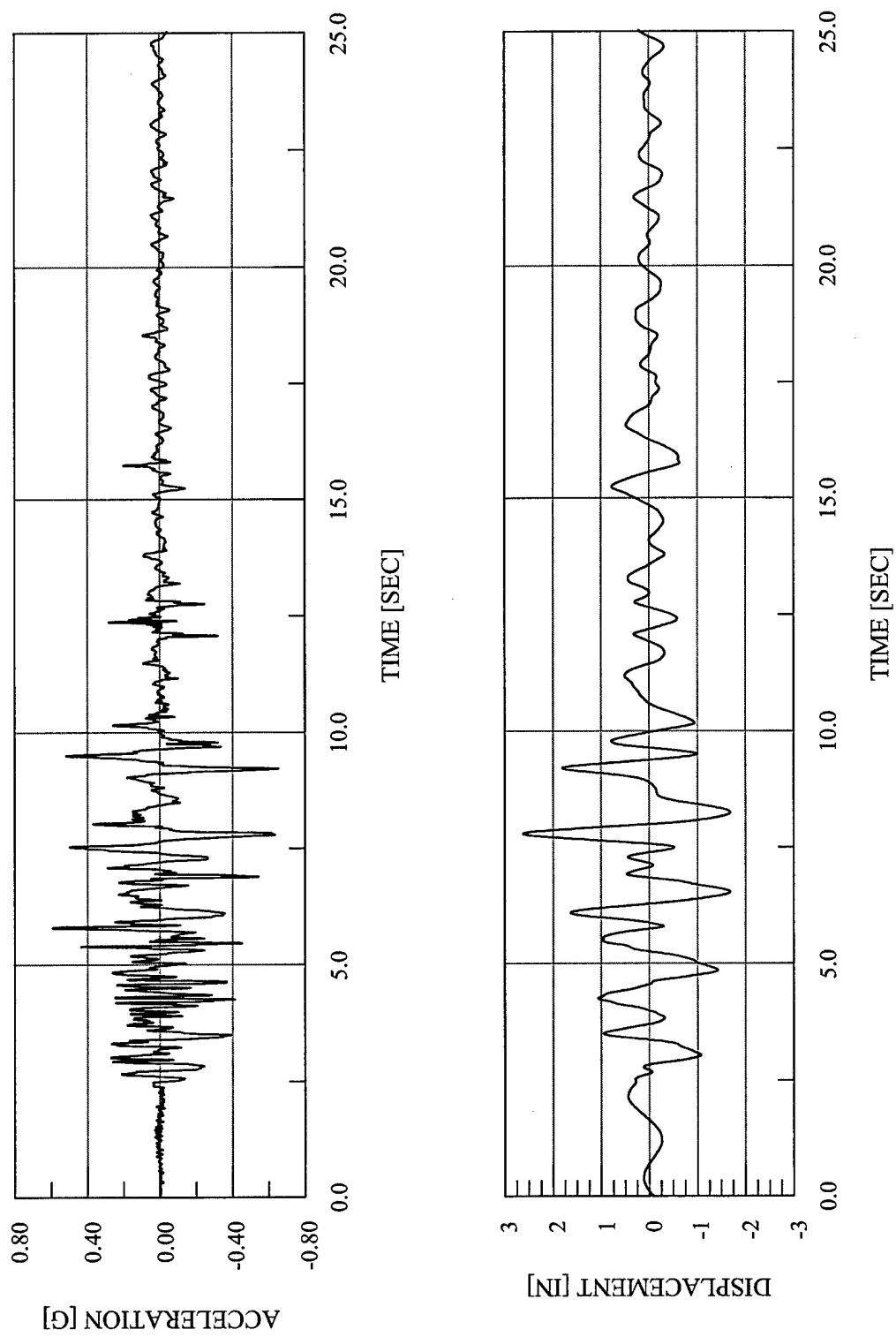


Figure 2.27 Modified Imperial Valley Input Motions – Y-Axis – High-Pass Filtered at 1/2 Hz – Scaled to Shaketable Displacement Limits

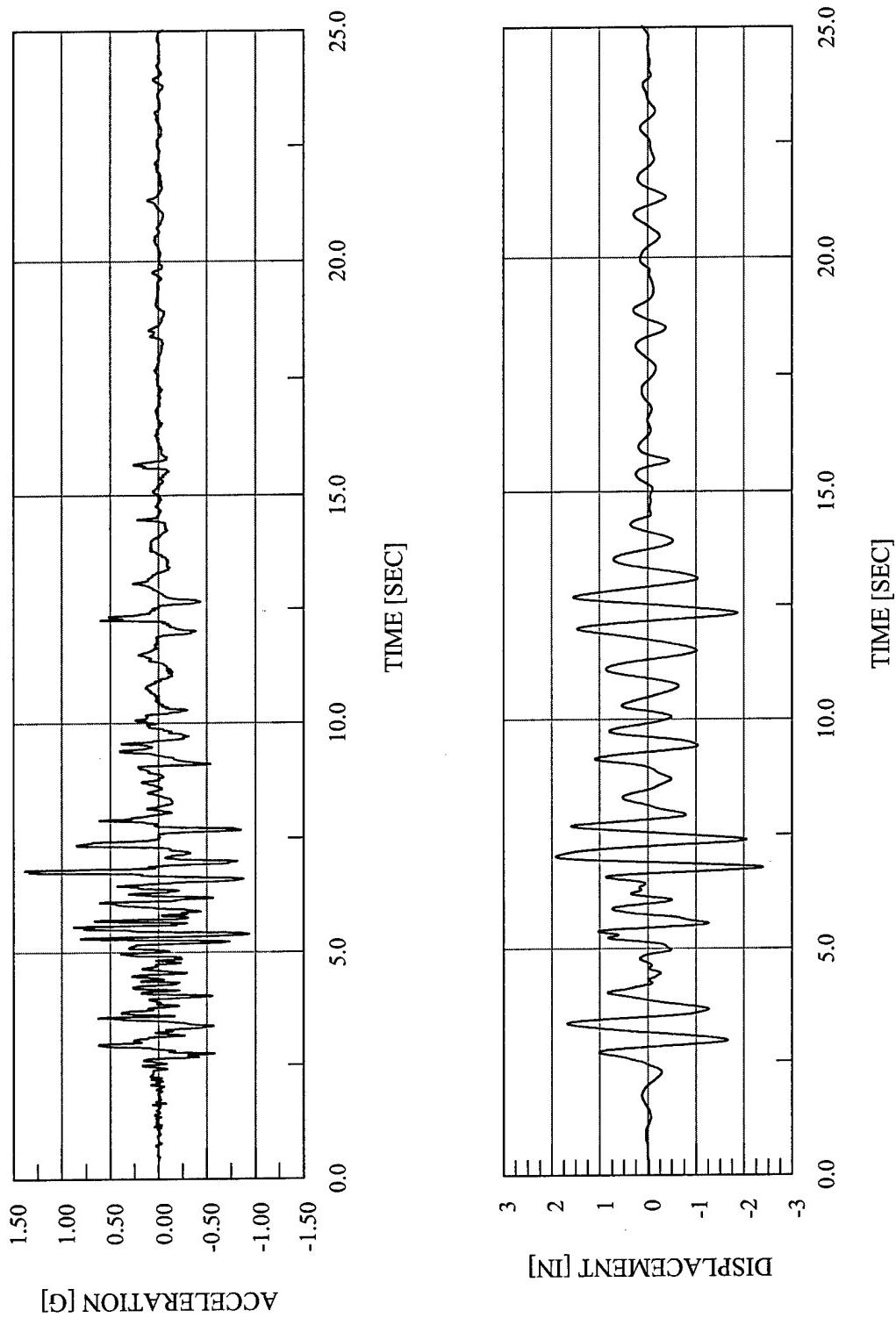


Figure 2.28 Modified Imperial Valley Input Motions – X-Axis – High-Pass Filtered at 1 Hz – Scaled to Shaketable Displacement Limits

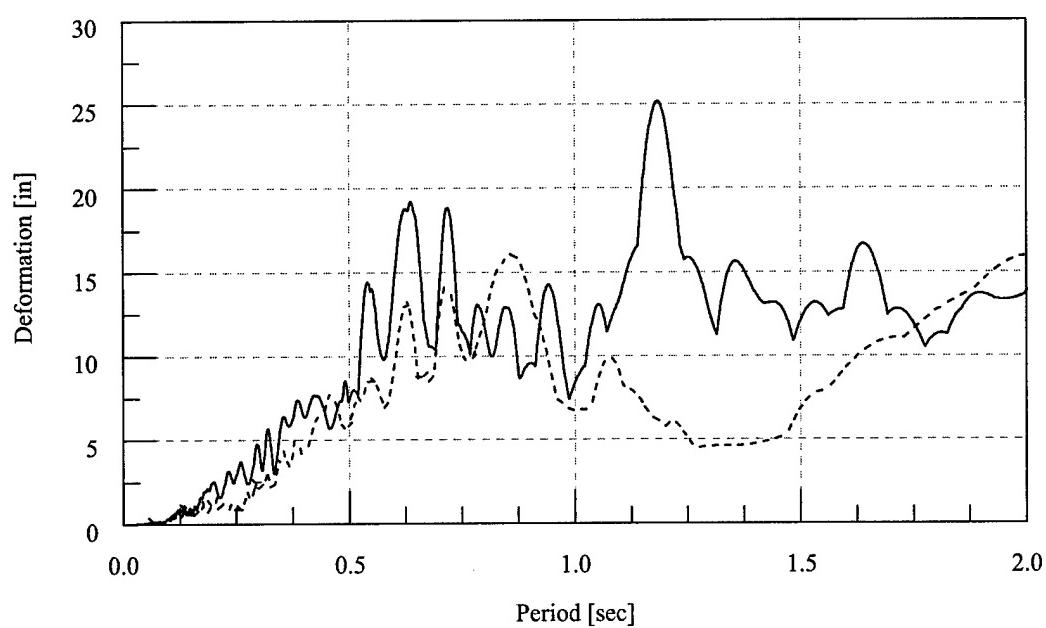
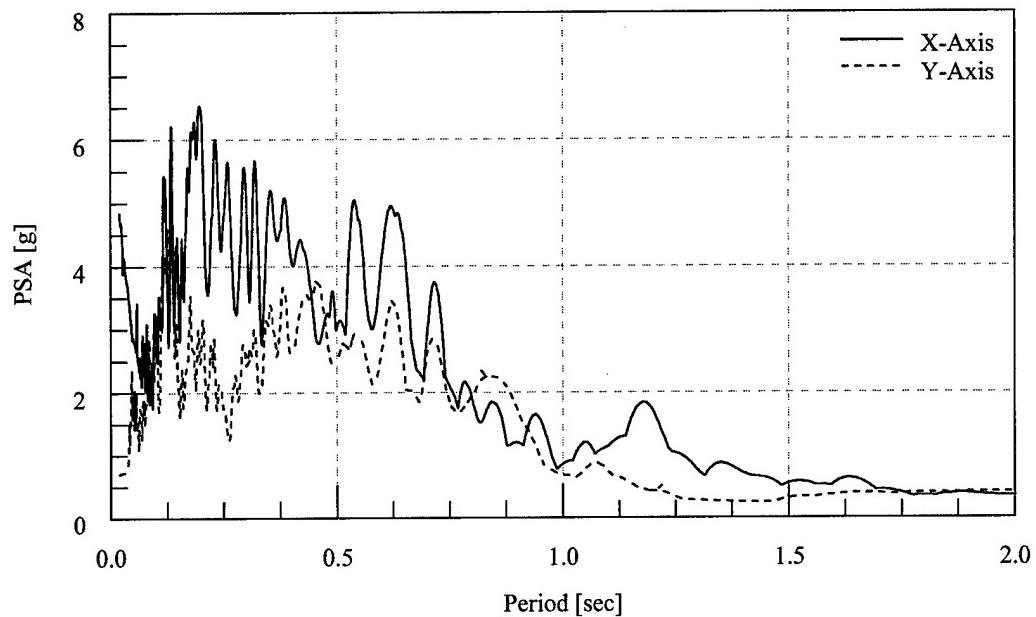


Figure 2.29 Elastic Response Spectra – Unfiltered Imperial Valley Ground Motions

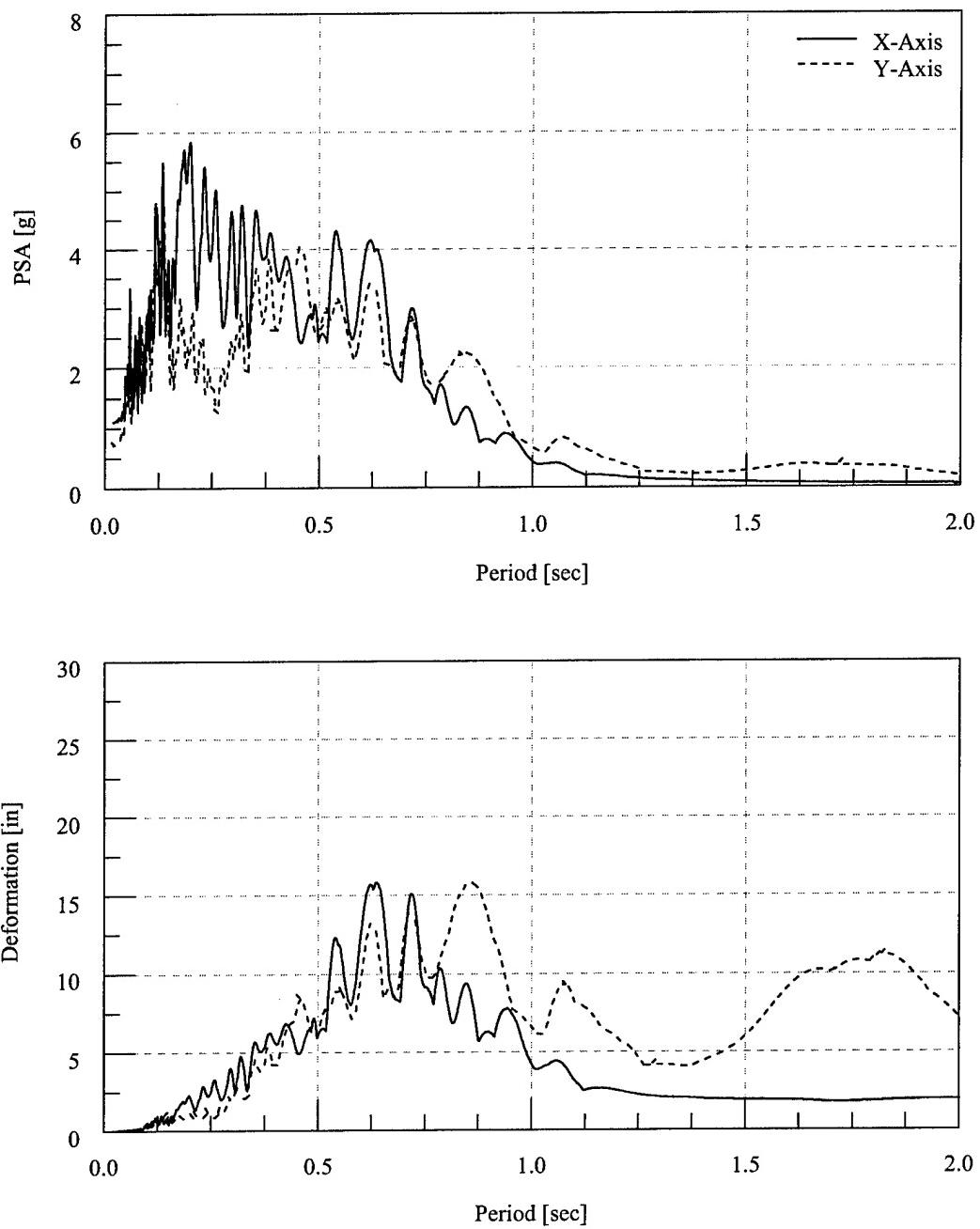


Figure 2.30 Elastic Response Spectra – Filtered Imperial Valley Ground Motion

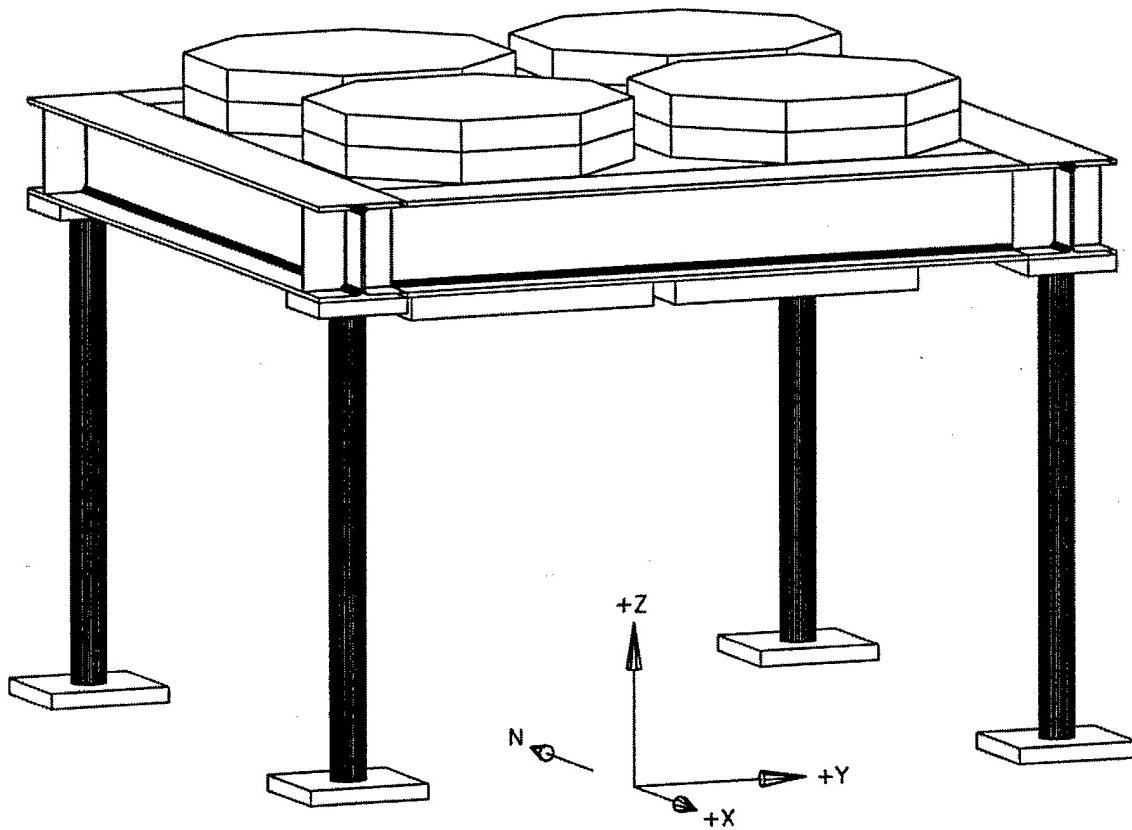


Figure 2.31 Perspective View of Test Configuration Model 1
4 - 4" Extra-Strong Columns

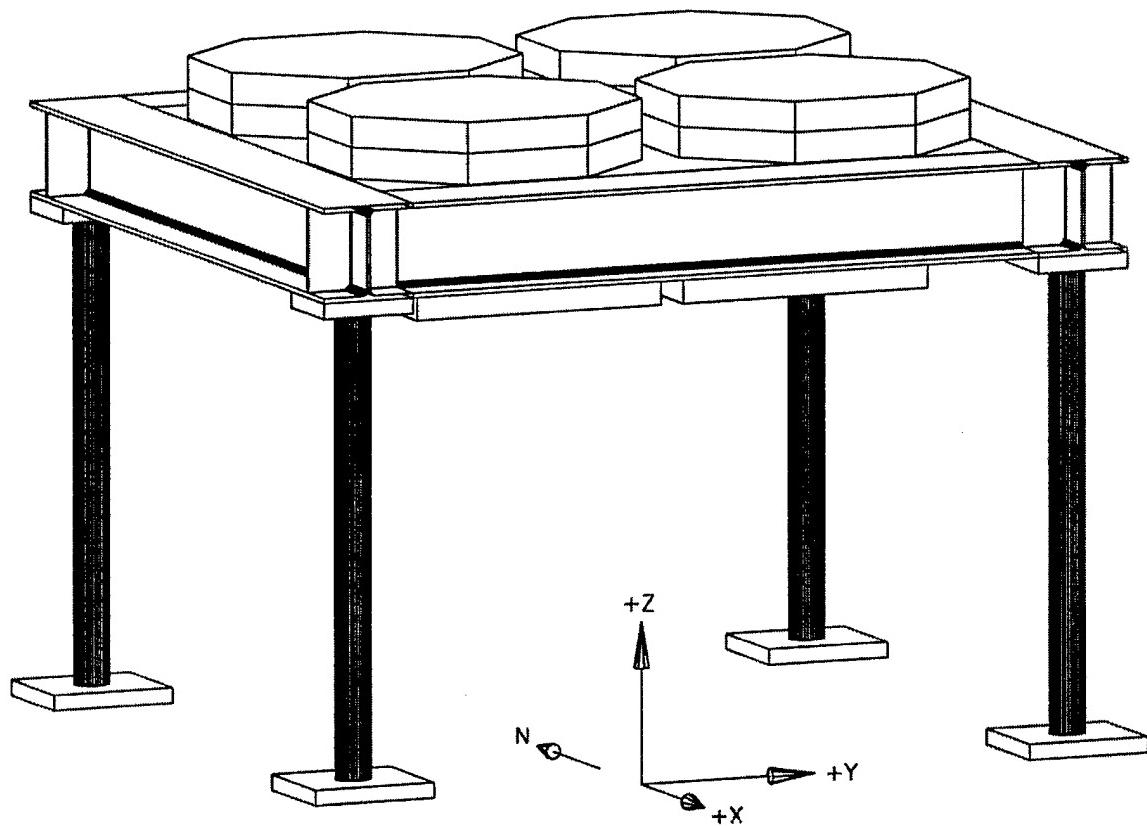


Figure 2.32 Perspective View of Test Configuration Model 2
4 – 4" Extra-Strong Columns

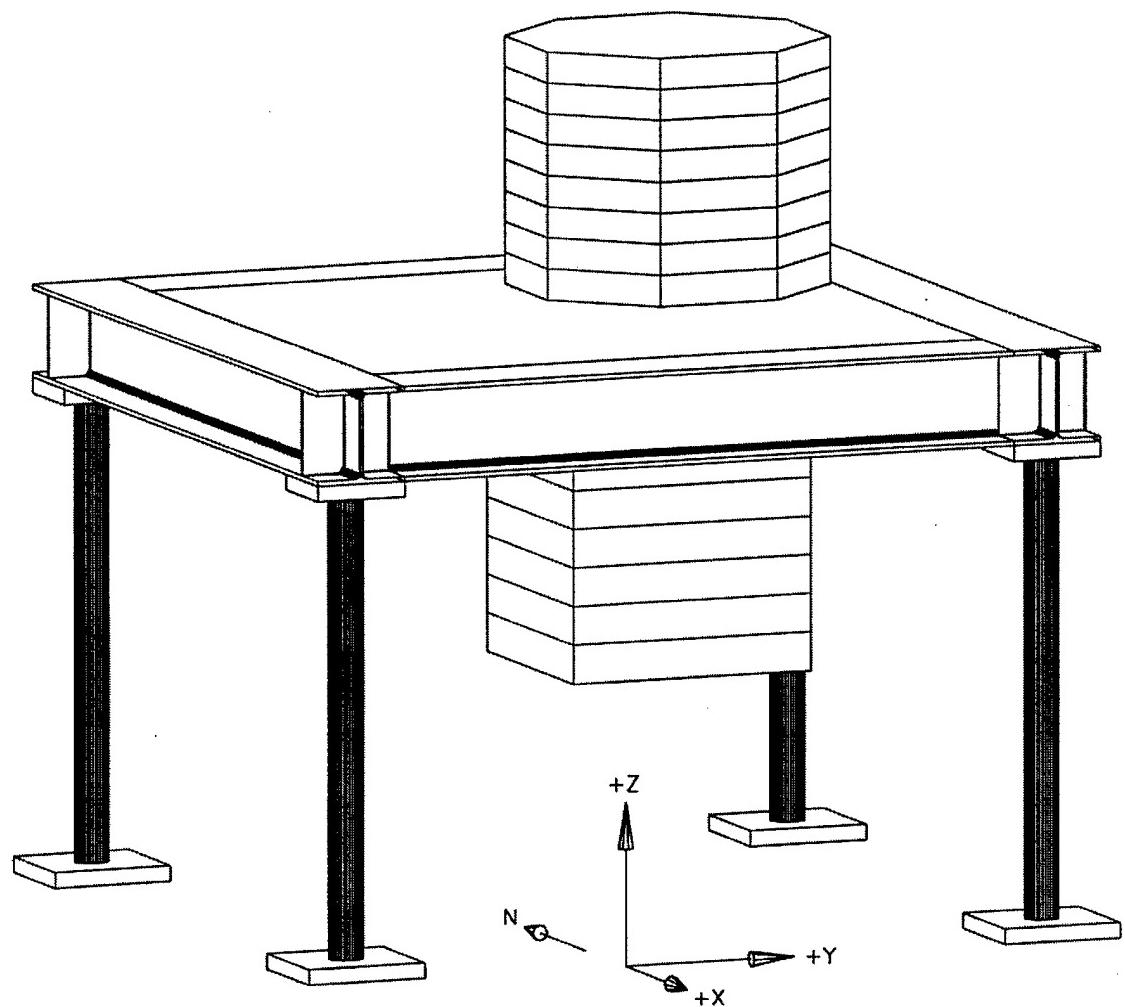


Figure 2.33 Perspective View of Test Configuration Model 3
4 - 4" Extra-Strong Columns

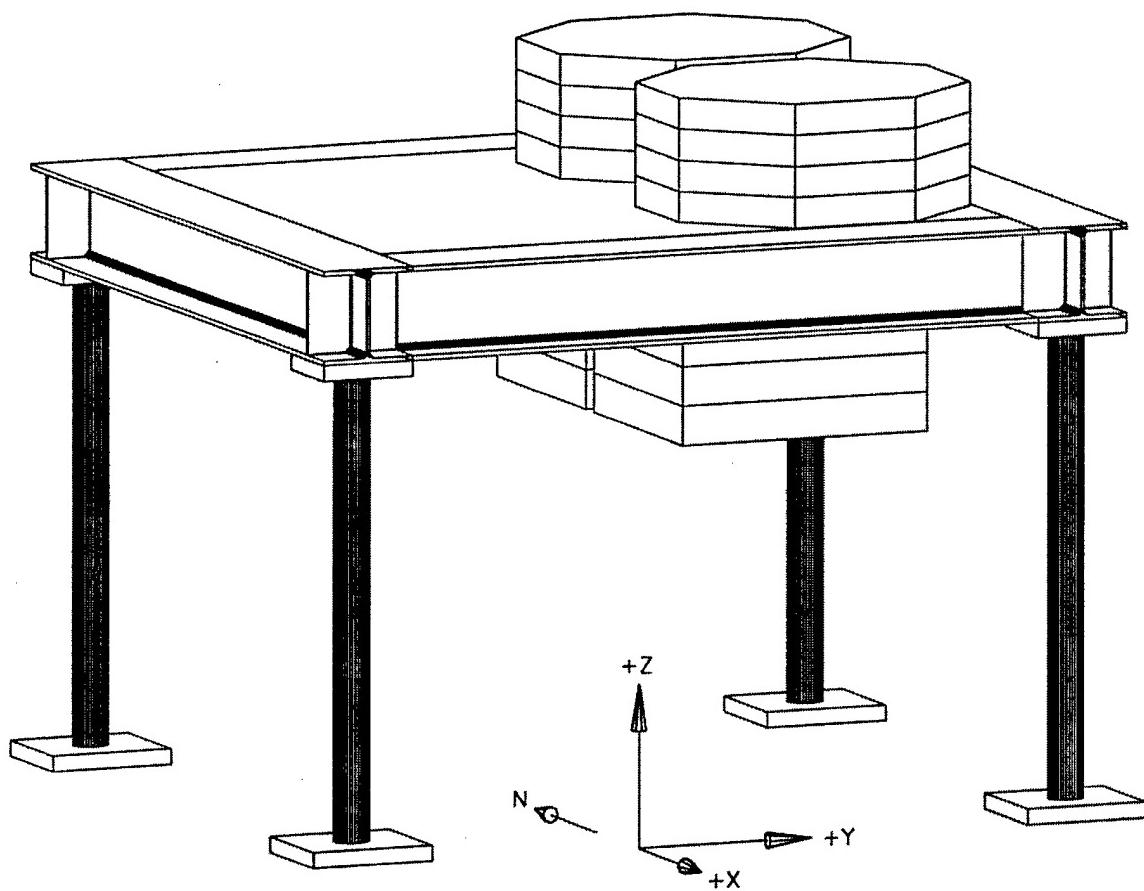


Figure 2.34 Perspective View of Test Configuration Model 4
4 - 4" Extra-Strong Columns

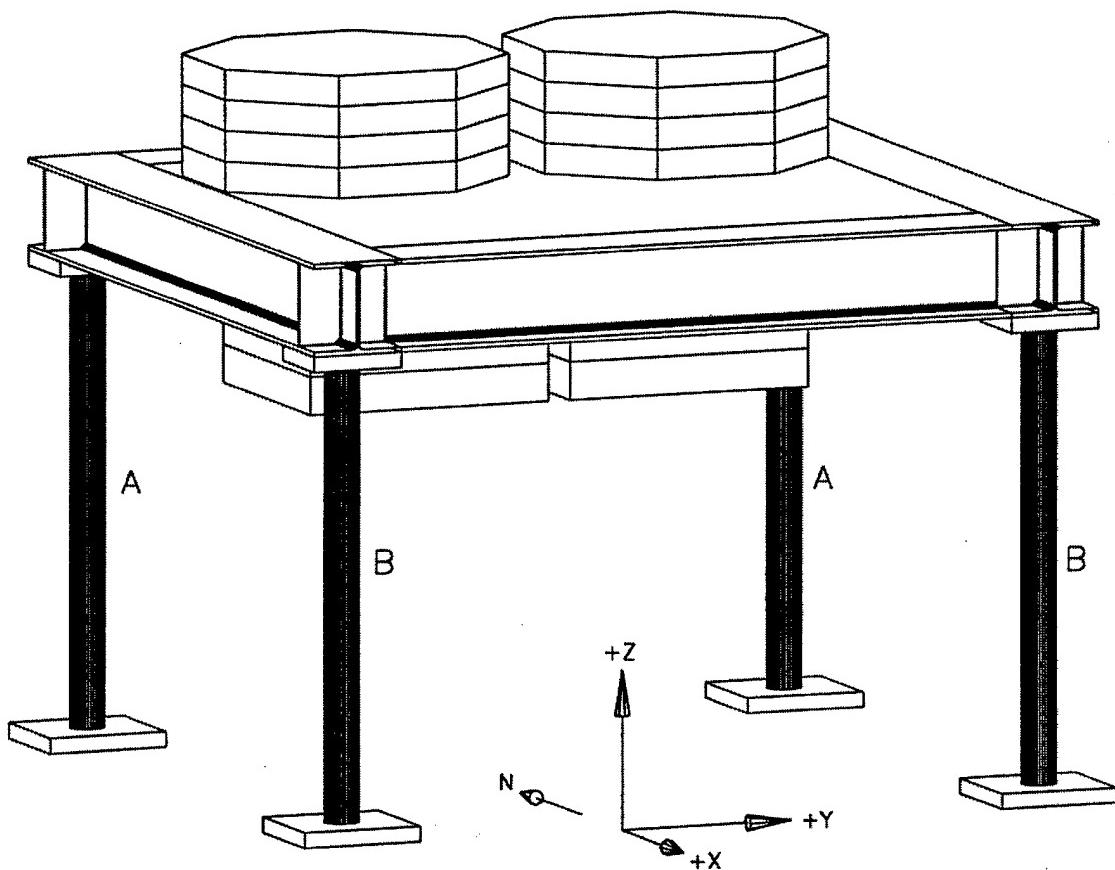


Figure 2.35 Perspective View of Test Configuration Model 5
[A] 2 – 5" Standard Columns and [B] 2 – 4" Double Extra-Strong Columns

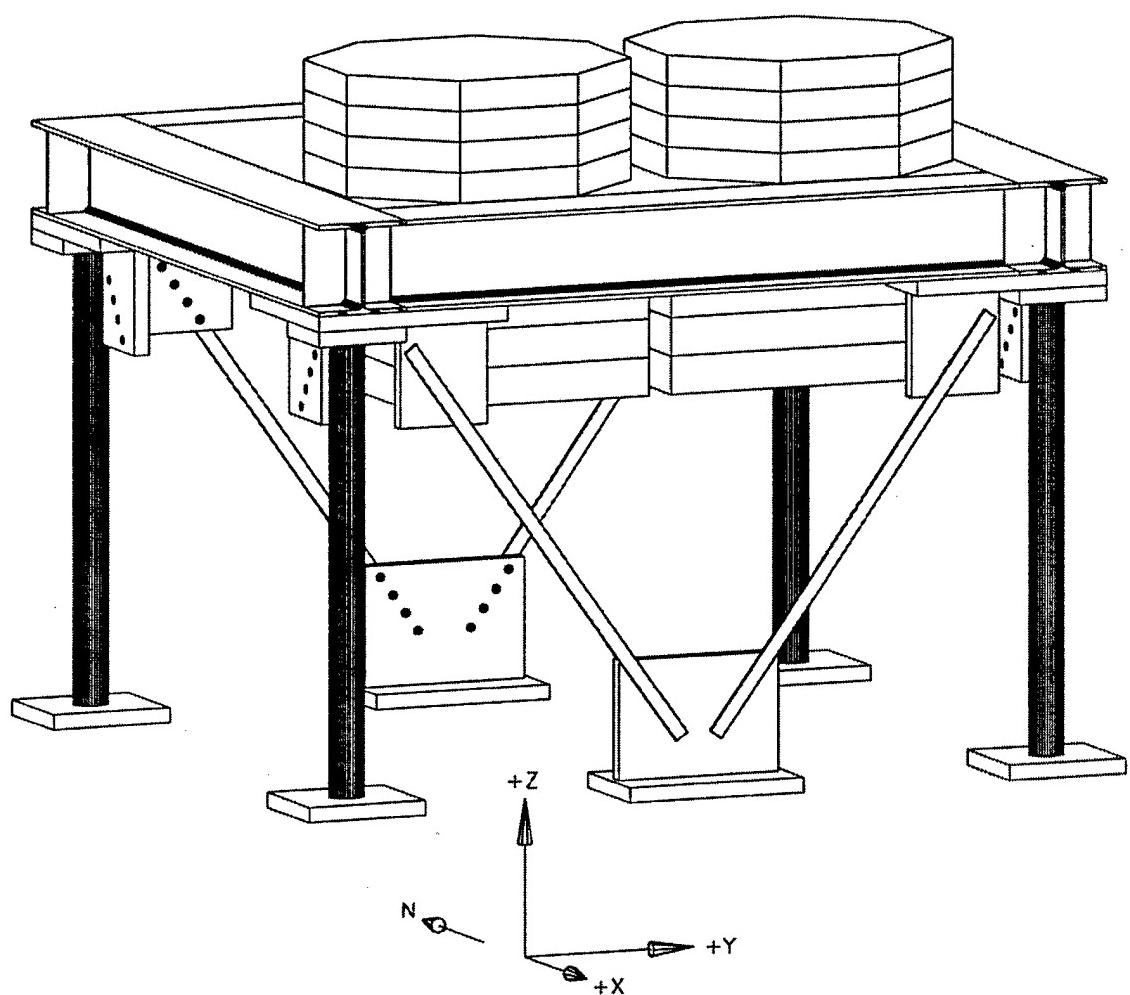


Figure 2.36 Perspective View of Test Configuration Model 6
4 – 4" Extra-Strong Columns

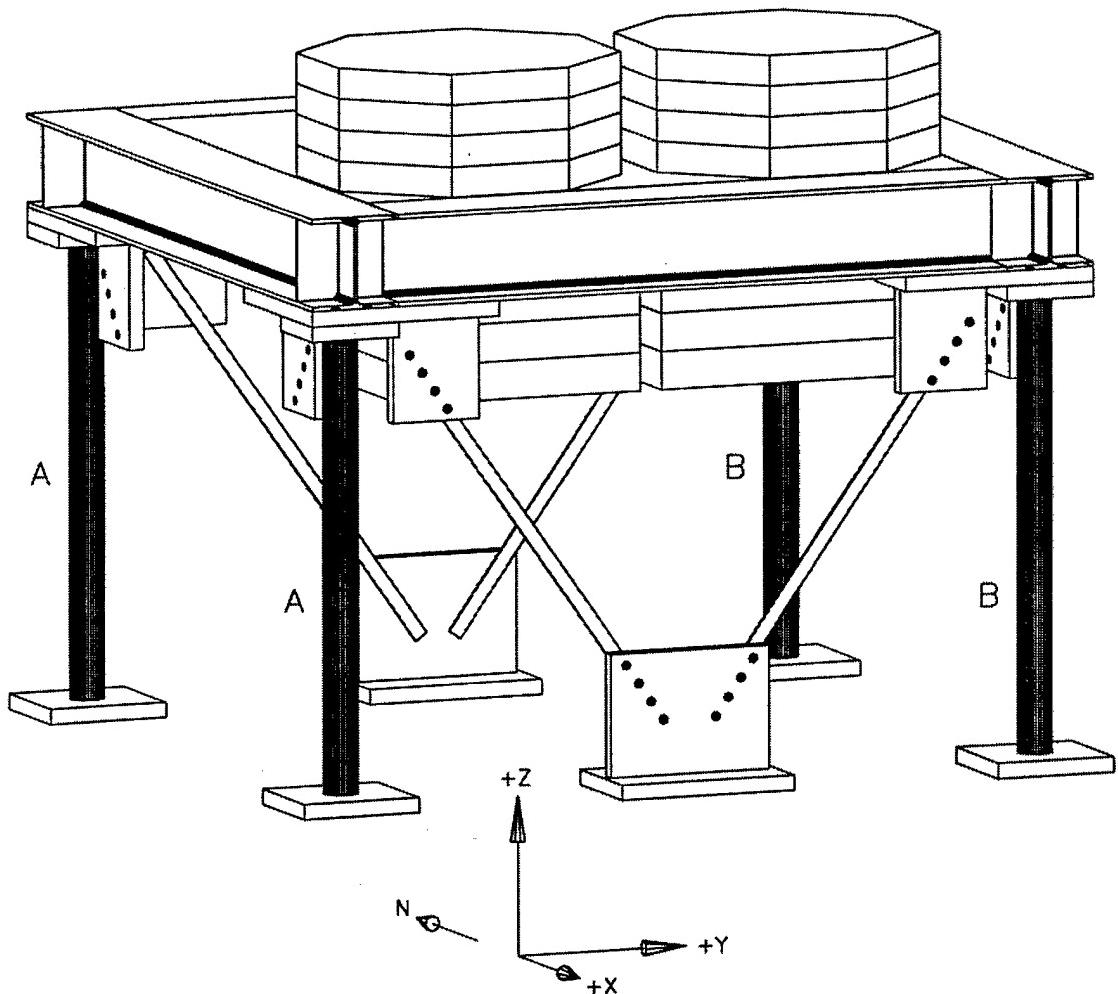


Figure 2.37 Perspective View of Test Configuration Model 7
[A] 2 – 5" Standard Columns and [B] 2 – 4" Double Extra-Strong Columns

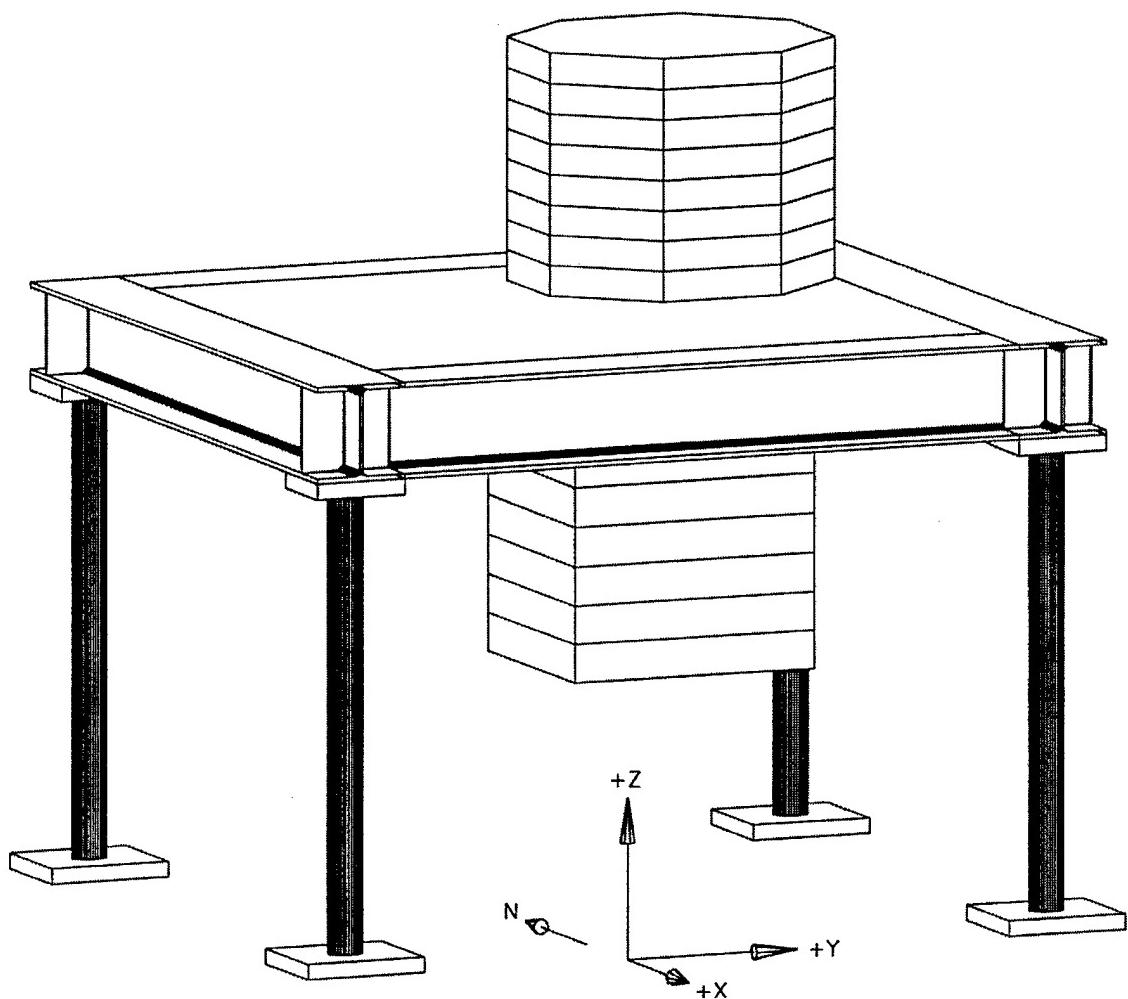


Figure 2.38 Perspective View of Test Configuration Model 8
4 - 4" Extra-Strong Columns

CHAPTER 3

EXPERIMENTAL AND ANALYTICAL RESPONSE OVERVIEW

This chapter provides descriptions of the experimental test program and the finite element modeling procedures. This chapter first summarizes response data of the test structure during the earthquake simulations and the dynamic characterization tests. Summaries of test model accelerations, displacements, torsional moments, overturning moments, column end moments, and base shears are provided. A summary of the test configurations used in this study is provided in Table 3.1. The general methodologies used in the computation and analysis of the response quantities mentioned above that are common to all of the test configurations are discussed in this chapter. Specific test data, observations, and finite element analyses for each of the earthquake simulations performed for each test configuration are presented in subsequent chapters.

3.1 ACCELERATION

The acceleration motion of the diaphragm was recorded using 7 accelerometers in both the X (north-south) and Y (east-west) directions, for a total of 14 accelerometers as shown in Figure 3.1. Diaphragm acceleration test data are reported with the sign convention of positive X-Axis acceleration directed south and positive Y-Axis acceleration directed east.

Angular accelerations were computed by first subtracting the acceleration on one diaphragm edge from the acceleration on the opposite edge, and next dividing by the distance between them. Only two accelerometers were needed to compute a value for the angular acceleration. However, the angular acceleration for the diaphragm was computed using multiple pairs of accelerometers, in anticipation of the possibility of a bad data channel. An average value was then computed using all of the angular acceleration records that seemed reasonable. Angular acceleration data are reported with the sign convention of positive z-axis directed up, away from the shaketable. By the right-hand rule convention, this corresponds to a counter-clockwise angular acceleration if viewing the diaphragm from above.

The acceleration motion of the shaketable was recorded using 2 accelerometers in both the X (north-south) and Y (east-west) directions, and 4 accelerometers in the Z direction (up), for a total of 8 accelerometers mounted on the table surface. In addition, the shaketable itself has 3 internal accelerometers, recording motion in the X, Y, and Z directions. Shaketable acceleration test data are reported with the sign convention of positive X-Axis acceleration directed south, and positive Y-Axis acceleration directed east.

The rigidity of the diaphragm allows the planar motion of the diaphragm to be described by three degrees-of-freedom. The three acceleration components needed to describe the diaphragm motion are therefore the X-Axis and Y-Axis acceleration response histories, and the angular acceleration response history about the Z-Axis. Table 3.2 lists the maximum recorded diaphragm accelerations and their corresponding PGA for each of the earthquake simulations discussed in subsequent chapters. The omission of any earthquake simulations, which were performed but are not listed in Tables 3.2 - 3.4, will be discussed in the appropriate chapter.

3.2 DISPLACEMENT

The displacement motion of the diaphragm was recorded using 3 displacement gages in both the X (north-south) and Y (east-west) directions, for a total of 6 displacement gages, measured with respect to a fixed reference point, as shown in Figure 3.2. Diaphragm relative displacements were computed by subtracting the measured diaphragm displacement from the measured shaketable displacement. Both measurements are made with respect to a fixed reference point. Diaphragm displacement test data are reported with the sign convention of positive X-Axis displacement directed south, and positive Y-Axis displacement directed east.

Diaphragm rotations were computed by first subtracting the displacement on one diaphragm edge from the displacement on the opposite edge, and then dividing by the distance between them. Only two displacement gages were needed to compute a value for the rotation. However, the diaphragm rotation was computed using a pair of displacement gages in the X direction and a pair of gages in the Y direction, in anticipation of the possibility of a bad data channel. An average value was then computed using both records if both seemed reasonable. If only one appeared

reasonable, then it was chosen as the representative rotation record. Rotation data are reported with the sign convention of positive Z-Axis directed up, away from the shaketable.

The displacement motion of the shaketable was recorded using three displacement gages in both the X (north-south) and Y (east-west) directions, for a total of six displacement gages connected to the table surface, measured with respect to a fixed reference point. In addition, the shaketable itself has three internal displacement gages, recording motion in the X, Y, and Z directions.

Shaketable displacement test data are reported with the sign convention of positive X-Axis displacement directed south, and positive Y-Axis displacement directed east. The three displacement components needed to describe the diaphragm motion are the X-Axis and Y-Axis relative displacements of the geometric diaphragm center, and the rotation about the Z-Axis.

Table 3.3 lists the maximum recorded diaphragm displacements and their corresponding PGA for each of the earthquake simulations discussed in subsequent chapters.

3.3 SHAKETABLE MOTION CONTROL ISSUES

The issue of the motion control of the shaketable, which potentially can impact the response of the structure during the earthquake simulations, is discussed here. As this experimental study was the first to make use of the shaketable following the upgrade, which added the capability of motion in the east-west lateral direction, the control of the table motion was now more complex and not thoroughly tested. In each of the test configurations, both uniaxial and biaxial tests were performed. It was during the uniaxial tests that a motion control problem initially became apparent. In examining recorded data of the shaketable motion, it was discovered that in each uniaxial simulation the motion of the shaketable in the perpendicular direction was nonzero.

Figures 3.3 – 3.7 show recorded shaketable accelerations for five simulations: EQ 2 [25% Y-Axis, Symmetric Mass], EQ 3 [25% Biaxial, Symmetric Mass], EQ 7 [100% Y-Axis, Symmetric Mass], EQ 15 [100% Biaxial, Symmetric Mass], and EQ 23 [100% Biaxial, ¼ Asymmetric Mass]. In these figures, Yaw represents rotational shaketable motion about the Z-Axis, Pitch represents rotational shaketable motion about the X-Axis and Roll represents rotational shaketable motion about the Y-Axis. As seen in the figures, although the recorded off-axis motions were not large, it was still important to ascertain what effects, if any, these motions would have on the response of the structure and also to discover the cause of these motions.

Shown below is peak shaketable acceleration and angular acceleration values for the aforementioned five simulations.

Earthquake Test No.	Table Acceleration [g]		Table Angular Acceleration [10^{-3} g/in]		
	X-Axis	Y-Axis	Yaw	Pitch	Roll
2	0.006	0.162	0.29	0.11	0.02
3	0.232	0.160	0.45	0.12	0.17
7	0.014	0.678	0.64	0.27	0.07
15	1.080	0.699	0.76	0.25	0.38
23	1.299	0.797	1.65	0.26	0.38

The initial investigation revealed that when the uniaxial tests were performed, the table control software and hydraulics in the direction perpendicular to the motion were not turned on. This allowed the shaketable to resonate with the response of the test structure during the simulations, as seen in Figure 3.8, and the lack of motion control in the perpendicular direction was allowing the table to move in the perpendicular direction. This behavior can be seen in Figures 3.3 and 3.5. It was believed that during the biaxial tests, in which both the X-Axis and Y-Axis actuators were being driven, that no table control problem would be present. However, as seen in Figures 3.4, 3.6 and 3.7, there are Yaw, Pitch, and Roll accelerations present during biaxial simulations.

Subsequent to the completion of the tests described in this report, CERL retained engineers from MTS Corporation to perform a system trouble-shooting visit. During this visit, several problems that were associated with errors made during the triaxial upgrade project were found. These problems led to several actuator interaction control conflicts that created undesired motions of the shaketable during use, particularly with respect to Yaw rotations. Specifically, one of the X-Axis actuators was being fed a signal 180 degrees out of phase with the actual input signal. Thus, even during biaxial simulations, a shaketable control problem was present. MTS engineers corrected these problems during the visit.

Subsequent to the correction of the table Yaw problems, CERL and MTS engineers determined that some rocking (Roll and Pitch rotations) of the shaketable is likely to occur when heavy specimens are tested on the shaketable, particularly when the specimens have high centers of

gravity with respect to the shaketable platform. Such rocking motion is associated with the overturning moments that result from the motions of such specimens and the inherent stiffness of the oil columns that are associated with the system actuators. These rocking motions are evident in both uniaxial and biaxial simulations, as seen in Figures 3.3 – 3.7. For the specimens reported on here, it was not felt that the rocking phenomenon would have been consequential. In addition, finite element analyses were performed which incorporated the Yaw rotational motion of the shaketable as input ground motion in addition to the X-Axis and Y-Axis translational motion. It was found that the Yaw motion of the shaketable resulted in no discernable effect on the translational or rotational response of the structure.

For both the uniaxial and biaxial simulations, the interaction between the structure and the table demonstrated a noticeable effect on the motion of the shaketable in the X and Y directions even when the table was being actively driven in those directions. When simulations were performed with each test configuration, a reference set of ground motions were input into the table control system. For the first four test configurations, the exact same reference ground motions were used. However, the actual recorded table motion was slightly different for each configuration. Figure 3.9 shows the 100% Imperial Valley simulation table acceleration time histories for the symmetric mass configuration, $\frac{1}{2}$ asymmetric mass configuration, and $\frac{1}{4}$ asymmetric mass configuration. As shown, the wave shapes of the table motions match well, but differ slightly at the larger peaks. For the symmetric mass configuration, the peak table accelerations are 1.080g in the X direction and 0.699g in the Y direction. For the $\frac{1}{2}$ asymmetric mass configuration, the peak table accelerations are 1.115g in the X direction and 0.711g in the Y direction. For the $\frac{1}{4}$ asymmetric mass configuration, the peak table accelerations are 1.299g in the X direction and 0.797g in the Y direction. Thus, it is apparent that as the degree of asymmetry increases, and thus the degree of torsional response increases, the interaction between the structure and the table increases.

Although the table motions are in fact slightly different for simulations which are intended to be the same, it is the recorded table motions that are taken in this analysis as “ground motions”, not the set of motions input into the table control system. Another point of note is that the moniker “100% Imperial Valley” does refer to the set of motions input into the table control system. Thus, as seen in Figure 3.9, the ground motions for a 100% Imperial Valley simulation with a symmetric mass configuration are not identical to the ground motions for a simulation with a $\frac{1}{4}$ asymmetric mass configuration, but are still a very good indicator of the relative magnitude of the

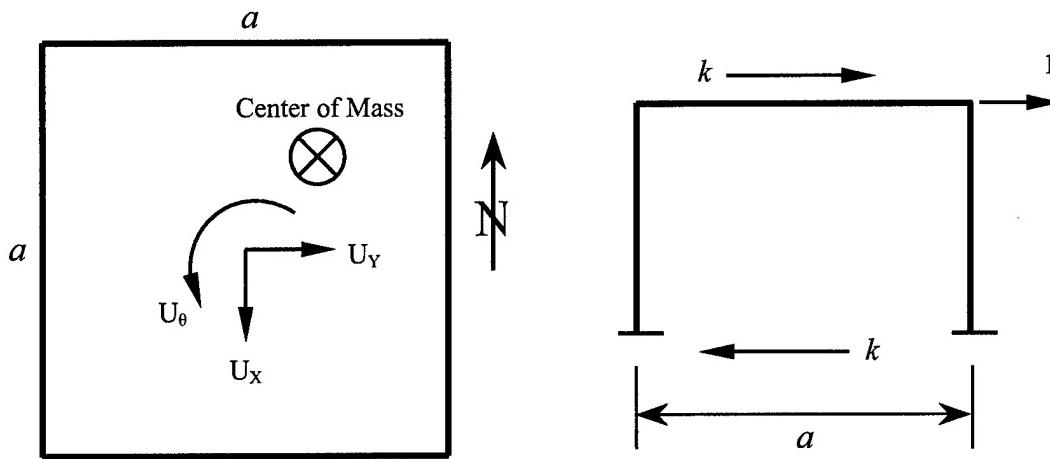
ground motions. Due to the effects of the interaction between the shaketable and the test structure, it will be important to consider characteristics of the ground motions, such as the Peak Ground Acceleration (PGA) and the Pseudo-Spectral Acceleration (PSA), when comparing response characteristics of the structure during different simulations. This will be true even when comparing two simulations in the same test configuration, such as when comparing 10% X-Axis and 10% Biaxial simulations to check the linearity of the response.

3.4 BASE SHEAR AND TORSIONAL MOMENT

As discussed previously, three degrees-of-freedom are sufficient to describe the planar motion of the diaphragm. The inertial forces of interest with respect to the structure will therefore be those corresponding to the three degrees-of-freedom of the diaphragm, the inertial force in the X direction, in the Y direction, and the inertial moment about the Z-Axis. These quantities are also referred to as the base shear in the X and Y directions and the base torsional moment. These quantities will be derived in this section as functions of recorded diaphragm acceleration data.

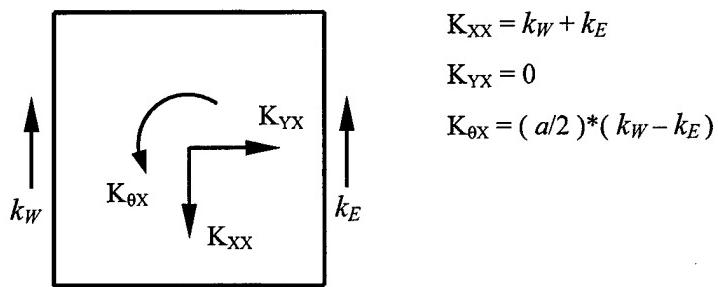
Because the motion of the diaphragm is referenced with respect to the geometric center of the diaphragm, and the center of mass is not coincident with this point, the inertial forces in the X and Y directions and the inertial moment are coupled. Thus, the inertial forces cannot be calculated as simply the product of the diaphragm acceleration, in the respective direction, and the diaphragm mass. Nor can the inertial moment be calculated as simply the product of the diaphragm angular acceleration and the rotational mass moment of inertia of the diaphragm.

For this system the diaphragm positive degrees of freedom are shown below. The global degrees of freedom are located at the geometric center of the diaphragm. In all but two of the test configurations, the center of stiffness is also located at the geometric center of the diaphragm. However, in the two configurations with concentric lateral bracing , there does exist a stiffness eccentricity along with a mass eccentricity. Thus, the equations of motion are derived here for the most general configuration in this study. In the following derivation, the stiffness of a lateral frame is taken as k and the span of a frame is taken as a . Because each of the frames can potentially possess a different stiffness, the frame stiffnesses will be designated as k_N , k_S , k_E , and k_W , respectively representing the stiffness of the *North* frame, the *South* frame, the *East* frame, and the *West* frame.

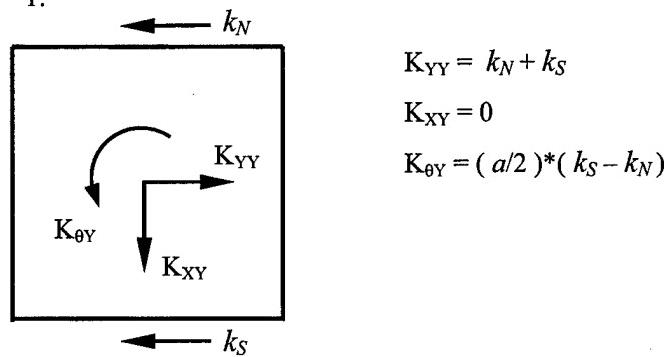


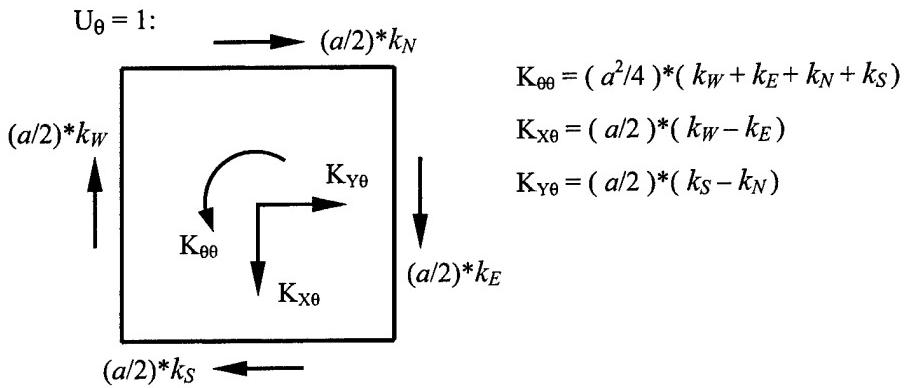
As seen in the following illustrations, the model is subjected to a unit displacement in each degree of freedom, with the bending stiffness of the diaphragm much greater than the bending stiffness of each column.

$$U_x = 1:$$



$$U_y = 1:$$

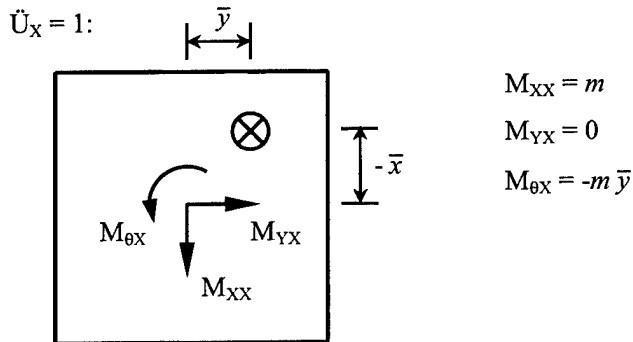




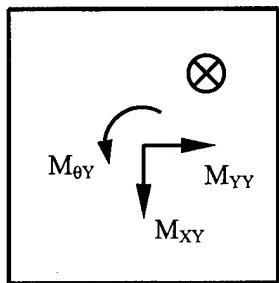
Thus, the stiffness matrix is $\mathbf{K} =$

$$\begin{bmatrix} k_W + k_E & 0 & \frac{a}{2}(k_W - k_E) \\ 0 & k_S + k_N & \frac{a}{2}(k_S - k_N) \\ \frac{a}{2}(k_W - k_E) & \frac{a}{2}(k_S - k_N) & \frac{a^2}{4}(k_W + k_E + k_S + k_N) \end{bmatrix} [3.1]$$

As seen below, the model is next subjected to a unit acceleration in each degree of freedom. Note that the inertia forces that result from the unit acceleration act at the center of mass, while the unit accelerations act at the geometric center of the model.

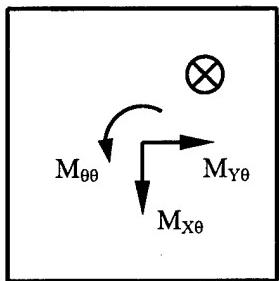


$\ddot{U}_Y = 1$:



$$\begin{aligned}M_{YY} &= m \\M_{XY} &= 0 \\M_{\theta Y} &= m \bar{x}\end{aligned}$$

$\ddot{U}_{\theta} = 1$:



$$\begin{aligned}M_{\theta\theta} &= \bar{I}_0 + m\bar{y}^2 + m\bar{x}^2 = I_0 \\M_{X\theta} &= -m\bar{y} \\M_{Y\theta} &= m\bar{x}\end{aligned}$$

where:

\bar{I}_0 = the moment of inertia with respect to the mass center

I_0 = the moment of inertia with respect to the geometric center

The resulting mass matrix is $\mathbf{M} = \begin{bmatrix} m & 0 & -m\bar{y} \\ 0 & m & m\bar{x} \\ -m\bar{y} & m\bar{x} & I_0 \end{bmatrix}$ [3.2]

Thus, the governing equations of motion are:

$$\begin{bmatrix} m & 0 & -m\bar{y} \\ 0 & m & m\bar{x} \\ -m\bar{y} & m\bar{x} & I_0 \end{bmatrix} \begin{Bmatrix} \ddot{u}_x \\ \ddot{u}_y \\ \ddot{u}_\theta \end{Bmatrix} + \begin{bmatrix} k_w + k_E & 0 & \frac{a}{2}(k_w - k_E) \\ 0 & k_s + k_N & \frac{a}{2}(k_s - k_N) \\ \frac{a}{2}(k_w - k_E) & \frac{a}{2}(k_s - k_N) & \frac{a^2}{4}(k_w + k_E + k_s + k_N) \end{bmatrix} \begin{Bmatrix} u_x \\ u_y \\ u_\theta \end{Bmatrix} = - \begin{Bmatrix} m\ddot{u}_{gx}(t) \\ m\ddot{u}_{gy}(t) \\ m\bar{x}\ddot{u}_{gy}(t) - m\bar{y}\ddot{u}_{gx}(t) \end{Bmatrix} \quad [3.3]$$

Which lead to the following equations for the inertial forces and moment:

$$F_x = -m(\ddot{u}_x - \bar{y}\ddot{\theta}) \quad [3.4]$$

$$F_y = -m(\ddot{u}_y + \bar{x}\ddot{\theta}) \quad [3.5]$$

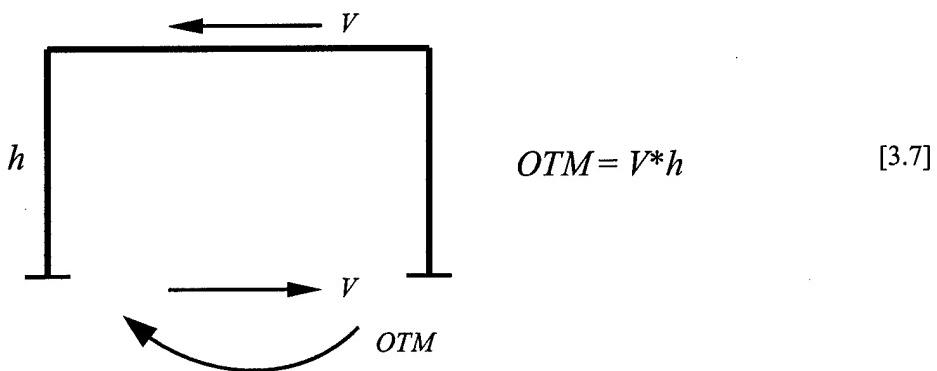
$$M = -\left(m\bar{x}\ddot{u}_y - m\bar{y}\ddot{u}_x + I_O\ddot{\theta}\right) \quad [3.6]$$

Because the model structure used in this study is one story only, the base shear of the system in each direction is equal to the respective inertial force of the diaphragm in each direction. Also, the inertial moment will be described here as the torsional moment. Table 3.4 lists the maximum base shears and torsional moments and their corresponding PGA for each of the earthquake simulations discussed in the subsequent chapters.

3.5 OVERTURNING MOMENT

Overturning moments for the structure in both the X and Y directions were calculated as the product of the inertial forces in each direction and the distance from the table to the vertical center of mass of the diaphragm assembly, as shown below. The vertical location of the diaphragm assembly center of mass for each test configuration is shown in Table 3.5. What is

here termed the overturning moment in the X direction is the product of the base shear, or inertial force, along the X-Axis and the height of the diaphragm mass center. If the base shear is positive, then the overturning moment is taken as positive as well. In actuality, what is referred to as an overturning moment in the X direction is a moment about the Y-Axis, and vice versa for an overturning moment in the Y direction.



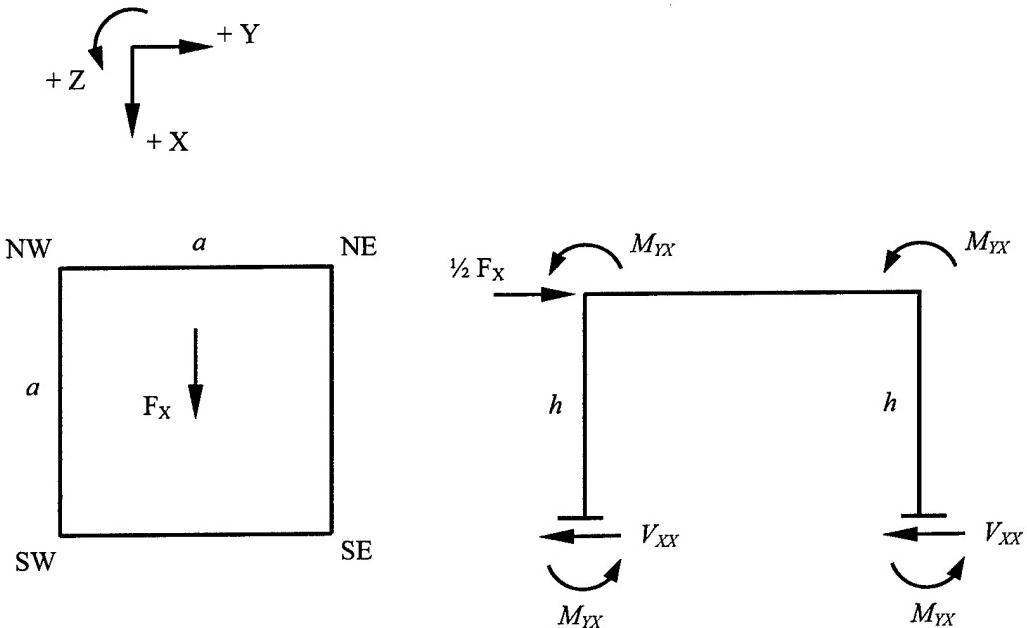
3.6 COLUMN END BENDING MOMENT AND SHEAR

The base shear in either the X direction or Y direction that was discussed above is produced by the inertial forces, or equivalent static forces, in the diaphragm. The inertial forces are transmitted through the columns to the base, and thus the sum of the shear forces at the base of each column must be equal to the total base shear force. The inertial forces and moment acting on the diaphragm not only produce shear forces in the columns, but bending moments as well. Both the column shear forces and bending moments will be dependent on the inertial forces in both the X and Y directions, and the inertial moment. Because forces are applied to the columns only at the top and bottom, the shear distribution will be constant, and the bending moment distribution will be linear along the height of each column. Thus, knowing the shear and moments at the column ends is sufficient to describe the internal force distribution in each of the columns. The column end bending moments and shears were computed using the inertial forces in the X and Y directions, and the inertial moment, as described below. An inertial force in the X direction, or a diaphragm translation in the X direction will produce a column end bending

moment about the Y-Axis and a column end shear in the X direction. Further, a positive column end shear is taken as that shear produced by a diaphragm translation in the positive X direction, or south. A positive column end bending moment is taken as a bending moment about the positive Y-Axis. This convention can also be extended to the column end moments and shears produced by inertial forces in the Y direction and about the Z-Axis.

For the derivation of the column moments and shears, M_{ij} = the moment about the i-Axis due to F_j , and V_{ij} = the shear in the i direction due to F_j , where F_j is the inertial force in the j direction. Also, the bending stiffness of the beam (or diaphragm) is assumed to be infinitely large compared with the bending stiffness of the columns. Also note that although the height to the center-of-mass of the diaphragm in the test structure and finite element model is always greater than 60 inches, in computing the column moments $h = 60$ inches, which is the height of each column. The following derivation is based on the structure having no stiffness eccentricity. Thus, the equations that result are valid for Test Configurations 1-5 and 8. Deriving the equations for the column end moments and shears for Test Configurations 6 and 7, which have a stiffness eccentricity due to the concentric lateral bracing, is discussed at the end of this derivation.

First, the model, with side length = a , is given an inertial force in the positive X direction:



Thus, for each column:

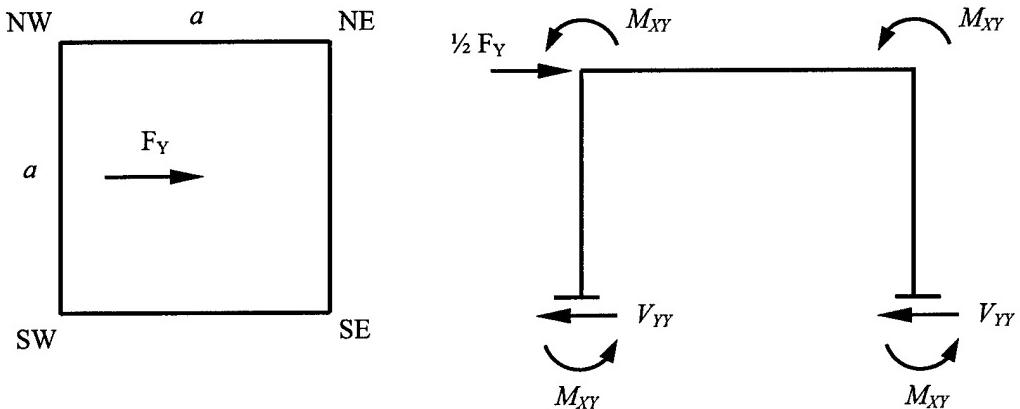
$$V_{XX} = 1/4 F_X \quad [3.8]$$

$$V_{YX} = 0 \quad [3.9]$$

$$M_{YX} = 1/2 V_{XX} * h = -1/8 F_X * h \quad [3.10]$$

$$M_{XX} = 0 \quad [3.11]$$

Next the model is given an inertial force in the positive Y direction:



Thus, for all four columns:

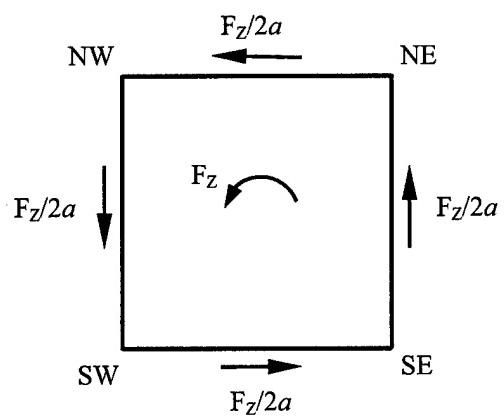
$$V_{YY} = 1/4 F_Y \quad [3.12]$$

$$V_{XY} = 0 \quad [3.13]$$

$$M_{XY} = 1/2 V_{YY} * h = 1/8 F_Y * h \quad [3.14]$$

$$M_{YY} = 0 \quad [3.15]$$

Next the model, with side length = a , is given an inertial moment in the positive Z direction:



Thus, from the diagram at left, a positive moment in the Z direction produces positive column end shears in the X direction and negative column end moments about the Y-Axis for the NW and SW columns. At the same time, a positive moment in the Z direction produces negative column end shears in the X direction and positive column end moments about the Y-Axis for the NE and SE columns. This is similarly true in the Y direction.

Southeast [SE] Column:

$$V_{XZ} = -1/4 F_Z/a \quad [3.16]$$

$$M_{XZ} = 1/8 F_Z h/a \quad [3.18]$$

$$V_{YZ} = 1/4 F_Z/a \quad [3.17]$$

$$M_{YZ} = 1/8 F_Z h/a \quad [3.19]$$

Southwest [SW] Column:

$$V_{XZ} = 1/4 F_Z/a \quad [3.20]$$

$$M_{XZ} = 1/8 F_Z h/a \quad [3.22]$$

$$V_{YZ} = 1/4 F_Z/a \quad [3.21]$$

$$M_{YZ} = -1/8 F_Z h/a \quad [3.23]$$

Northwest [NW] Column:

$$V_{XZ} = 1/4 F_Z/a \quad [3.24]$$

$$M_{XZ} = -1/8 F_Z h/a \quad [3.26]$$

$$V_{YZ} = -1/4 F_Z/a \quad [3.25]$$

$$M_{YZ} = -1/8 F_Z h/a \quad [3.27]$$

Northeast [NE] Column:

$$V_{XZ} = -1/4 F_Z/a \quad [3.28]$$

$$M_{XZ} = -1/8 F_Z h/a \quad [3.30]$$

$$V_{YZ} = -1/4 F_Z/a \quad [3.29]$$

$$M_{YZ} = 1/8 F_Z h/a \quad [3.31]$$

Thus, column end bending moments and shears for each column in the most general loading case are:

Southeast [SE] Column:

$$V_X = 1/4 F_X - 1/4 F_Z/a \quad [3.32]$$

$$M_X = 1/8 F_Y h + 1/8 F_Z h/a \quad [3.34]$$

$$V_Y = 1/4 F_Y + 1/4 F_Z/a \quad [3.33]$$

$$M_Y = -1/8 F_X h + 1/8 F_Z h/a \quad [3.35]$$

Southwest [SW] Column:

$$V_X = 1/4 F_X + 1/4 F_Z/a \quad [3.36]$$

$$M_X = 1/8 F_Y h + 1/8 F_Z h/a \quad [3.38]$$

$$V_Y = 1/4 F_Y + 1/4 F_Z/a \quad [3.37]$$

$$M_Y = -1/8 F_X h - 1/8 F_Z h/a \quad [3.39]$$

Northwest [NW] Column:

$$V_X = 1/4 F_X + 1/4 F_Z/a \quad [3.40]$$

$$M_X = 1/8 F_Y h - 1/8 F_Z h/a \quad [3.42]$$

$$V_Y = 1/4 F_Y - 1/4 F_Z/a \quad [3.41]$$

$$M_Y = -1/8 F_X h - 1/8 F_Z h/a \quad [3.43]$$

Northeast [NE] Column:

$$V_X = 1/4 F_X - 1/4 F_Z/a \quad [3.44]$$

$$M_X = 1/8 F_Y h - 1/8 F_Z h/a \quad [3.46]$$

$$V_Y = 1/4 F_Y - 1/4 F_Z/a \quad [3.45]$$

$$M_Y = -1/8 F_X h + 1/8 F_Z h/a \quad [3.47]$$

As mentioned previously, these equations for column end moments and shears are valid for configurations with no stiffness eccentricity. In Test Configurations 6 and 7, the structure does possess a stiffness eccentricity in the Y direction, resulting in an additional torsional moment equal to $F_Y * e_Y$. Thus, the total torsional moment which must be distributed to the lateral frames is $M_{TOTAL} = F_Z - F_Y * e_Y$. In addition, because the stiffnesses of the *North* frame and *South* frame are different from the *East* and *West* frames, M_{TOTAL} must be distributed to each frame according to their relative stiffnesses. Further, it must be determined in the North frame and South frame what proportion of the frame base shear is resisted by the diagonal bracing and what proportion by the columns, according to their relative stiffnesses. Once the lateral forces are determined for each frame, and the proportion resisted by the diagonal bracing is determined, the computation of the column end moments and shears follows from the previous derivation.

3.7 DYNAMIC CHARACTERIZATIONS OF THE MODEL

Prior to performing any shaketable simulations using the earthquake input motions, a series of tests was performed to characterize the model structure, including the determination of the modal frequencies and damping characteristics of the structure. First, the structure was subjected to white noise base motions over a frequency range of 1 to 50 Hertz. Transfer functions of the acceleration response of the structure were used to determine the modal frequencies. A transfer function is a frequency domain function, which presents the ratio of the structural response to the input motion at each frequency. Typical transfer functions produced from the white noise tests are shown in Figures 3.10 – 3.12, for a symmetric mass configuration, a $\frac{1}{2}$ asymmetric mass configuration, and a $\frac{1}{4}$ asymmetric mass configuration, respectively. Each of the transfer functions shown has been normalized to a maximum value of one.

Second, the structure was excited sinusoidally at each modal frequency determined from the white noise tests. The input motion was then discontinued, and the motion of the structure was allowed to decay to rest. Analysis of this response using the so-called logarithmic decrement of damping was performed to determine the equivalent viscous damping ratio. Typical sine decay time histories are shown in Figures 3.13 – 3.15, for a symmetric mass configuration, a $\frac{1}{2}$ asymmetric mass configuration, and a $\frac{1}{4}$ asymmetric mass configuration, respectively. The beating that can be seen in a number of the sine decay time histories is typical of real systems with closely spaced modes, indicating that there is not a completely pure response at a single

frequency. In order to isolate the response due to the fundamental frequency before performing the logarithmic decrement of damping, a band-pass filter was applied around the appropriate modal frequency.

Third, the structure was subjected to sinusoidal motions ranging in frequency from 1 to 20 Hertz. The response of the structure to the sine sweep tests was used to confirm the natural frequencies of the structure. Typical sine sweep response functions are shown in Figures 3.16 – 3.18, for a symmetric mass configuration, a $\frac{1}{2}$ asymmetric mass configuration, and a $\frac{1}{4}$ asymmetric mass configuration, respectively. Each of the aforementioned tests was performed once in each planar axis, and once in the yaw-axis, for a minimum total of nine preliminary tests for each model configuration. In addition, white noise tests were often performed immediately after any earthquake simulation exhibiting inelastic behavior. The purpose of these additional characterization tests was to monitor any changes in the dynamic properties of the model as a result of the inelastic behavior. Both the modal frequencies and damping ratios for each of the test configurations are shown in Table 3.5. As can be seen in Table 3.5, even when the structure is ostensibly symmetric, the measured dynamic properties in the X and Y directions may be noticeably different. In addition to the possibility of the aforementioned table control problems being a factor in these differences, inexactitudes of the experimental structure are possible contributors, such as orientation of the structure on the shaketable and the mass and stiffness symmetry.

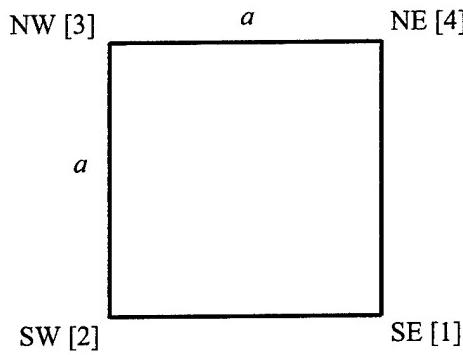
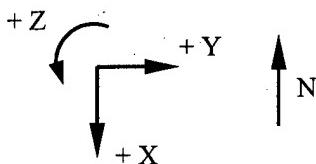
3.8 COLUMN STRAINS

For each pipe column, as shown in Figure A.9, four gages were equally spaced about the perimeter at each end, for a total of eight gages. In placing the four gages around the pipe perimeter, two were lined up along the north-south axis, and two along the east-west axis, in order to measure each of the two bending moment components in the pipe at the location of the strain gages. Computing the column end bending moments based on strain data provides an independent check of the column end shear and moment values found using the equivalent force method. Strain gage data were also used to determine the degree of inelastic behavior in the columns, which was useful in developing the material models used in the finite element analyses.

The list of strain gages, including their designation and location, can be found in Table A.1. The designation for each strain gage consisted of a sequence of four letters and numbers. For example, one such designation was *SIBE*. The first letter, *S*, in the gage name designated *strain*. The number, *I*, designated the column number, where *1* designates the *southeast* column, *2* designates the *southwest* column, *3* designates the *northwest* column, and *4* designates the *northeast* column. The third character, *B*, designates whether the strain gage was located at the *top* or the *bottom* of the column. The *top* of the column is designated by *T*, while the *bottom* is designated by *B*. The fourth character, *E*, designates on which side of the column the strain gage was located. The *E* designated the gage was on the *east* side of the column, while *W* designated the *west* side, *N* designated the north side, and *S* designated the *south* side.

In order to facilitate the computation of the bending moments from the strain measurements, strain gages should be placed at locations that do not experience plastic strain. The closer the gages are to the ends of the pipe, the larger the measured strains will be. Because the shear is constant throughout the column, knowing the elastic moments at two locations allows for the projection of the column-end moments. If the columns do not remain elastic at the strain gage locations, the yield stress is dependent on the load history of the material and is difficult to find. Yielding in the vicinity of the strain gages thus puts computing column end moments out of reach. In the low-level tests, the measured strains were typically below yield, allowing the computation of the column end bending moments. However, in the simulations when the structure experienced inelastic deformations, the measured strains were often larger than yield.

The column end moments were computed using the column strains based on the following derivation. The southeast column, Column 1, will be taken as a typical column.



As discussed previously, a positive column end bending moment is defined as a moment about a positive coordinate axis.

Thus, for Column 1, a positive bending moment about the Y-Axis would produce:

$$SITN > SITS, \text{ and}$$

$$SIBS > SIBN$$

Also, a positive bending moment about the X-Axis would produce:

$$SITE > SITW, \text{ and}$$

$$SIBW > SIBE$$

Any strain distribution at a cross section is composed of strains due to bending moments and strains due to axial forces. As an example, at the top of Column 1 in the X direction:

$$\text{Strain due to axial load} = \epsilon_A = \frac{1}{2} [SITS + SITN] \quad [3.48]$$

$$\text{Strain due to bending moment} = \epsilon_B = \frac{1}{2} [SITN - SITS] \quad [3.49]$$

For elastic behavior:

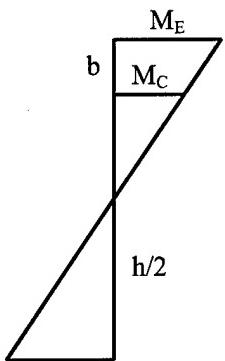
$$\text{Axial Force} = P = A\sigma_A = AE\epsilon_A = \frac{1}{2} AE [SITS + SITN] \quad [3.50]$$

$$\text{Bending Moment} = BM = S\sigma_B = SE\epsilon_B = \frac{1}{2} SE [SITN - SITS] \quad [3.51]$$

Where S = Section Modulus, and

E = Elastic Modulus

The bending moments computed above using strain gage data are the bending moments at a cross section some distance b from the end of the column.



For a cross section located a distance = b away from the column end, on a column of height = h :

$$\frac{M_C}{M_E} = \frac{h/2 - b}{h/2} \text{ and thus} \quad [3.52]$$

$$M_E = \frac{M_C h}{h - 2b} \quad [3.53]$$

Thus, for Column 1:

$$M_x^{\text{TOP}} = \frac{h}{h - 2b} SE \frac{1}{2} [SITN - SITS] \quad [3.54]$$

$$M_x^{\text{BOT}} = \frac{h}{h - 2b} SE \frac{1}{2} [SIBS - SIBN] \quad [3.55]$$

$$M_y^{\text{TOP}} = \frac{h}{h - 2b} SE \frac{1}{2} [SITE - SITW] \quad [3.56]$$

$$M_y^{\text{BOT}} = \frac{h}{h - 2b} SE \frac{1}{2} [SIBW - SIBE] \quad [3.57]$$

The column end moments at the top and bottom of each column in each direction should be equal, providing a check on the computation. The column end moments of the other three columns are computed in an analogous manner using the appropriate columns strains.

3.9 DIAPHRAGM RIGIDITY

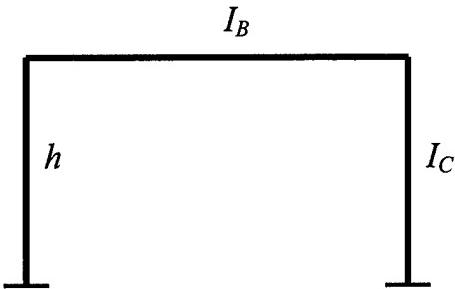
The diaphragm in the test structure was designed to behave as a rigid body and to experience no permanent damage. If the diaphragm did in fact behave as a rigid body, the planar motion of the diaphragm could be completely described by three degrees-of-freedom. The three motion components needed to describe the diaphragm motion are translation along the X-Axis and Y-Axis, and rotation about the Z-Axis. This would simplify the presentation of response data, and also allow the diaphragm in the finite element model to be modeled as a rigid plate. Also, in addition to the in-plane rigidity, it is important to look at the stiffness of the diaphragm in bending

about the X-Axis and Y-Axis. If the bending stiffness of the diaphragm is large enough compared to the bending stiffness of the columns, then the diaphragm can be modeled as rigid in bending in the finite element analysis as well.

If a body is rigid, then as it rotates, the angular acceleration is the same everywhere on the body. If the body is not rigid, then the angular acceleration may depend on the location on the body. Thus, the rigidity of the diaphragm can be verified by investigating its angular acceleration properties. As discussed above, the angular acceleration of the diaphragm was computed by first subtracting the acceleration on one diaphragm edge from the acceleration on the opposite edge, and next dividing by the distance between them. Figure 3.1 shows the number and orientation of the accelerometers placed on the test structure diaphragm. One angular acceleration computation can be made with records from only two accelerometers. Figure 3.19 shows six angular acceleration records each computed from an independent set of accelerometers for the earthquake simulation EQ 29, with 150% Biaxial Imperial Valley Ground Motions and a ½ Asymmetric Mass Distribution. This test was chosen for three reasons: first, the test used large-scale ground motions, which produced a large angular acceleration response; second, the test featured a mass-asymmetry which would again amplify the angular acceleration response; third, the test was performed during Test Configuration 4, and thus the test structure diaphragm would have potentially lost some of its rigidity during the previous earthquake simulations. With reference to Figure 3.19, angular acceleration time history AA1X was computed with accelerometers AS5X and AS7X; AA2X was computed with AS4X and AS8X; AA3X was computed with AS3X and AS1X; AA1Y was computed with AS3Y and AS5Y; AA2Y was computed with AS2Y and AS6Y; and AA3Y was computed with AS1Y and AS7Y. Also shown in Figure 3.19 is the average angular acceleration time history computed by averaging the previous six time histories. As shown by the six independent angular acceleration time histories, it is evident that the test structure diaphragm is in fact behaving as a rigid body in the plane of the body.

Also of interest is the bending stiffness of the test structure diaphragm. The primary contributors to the bending stiffness are the W12x65 beams which are located on the perimeter of the diaphragm, and possess an $I_{xx} = 533 \text{ in}^4$. However, the reinforced concrete infill contributes to the bending stiffness as well. Thus, each of the perimeter W12x65 beams acts as a composite beam. To simplify this analysis, the rebar in the concrete infill will be ignored. Figure 3.20 shows the original composite section and the transformed section. The width of the contributing concrete section was found to be 12.0625 inches from the center of the beam web using the 1994

AISC LRFD Design Code Section I on Composite Beams. Adding the stiffness contribution of the concrete, which has the properties of $f'_c = 4$ ksi and $w_c = 145$ pcf, the composite beam possesses an $I_{xx} = 663.11$ in 4 . The impact of the beam bending stiffness is shown using the following simple one-story planar frame.



For this frame, the lateral stiffness K is defined as follows:

$$K = \frac{24EI_c}{h^3} \frac{12\rho + 1}{12\rho + 4} \quad [3.58]$$

$$\text{where } \rho = \frac{I_B}{4I_C} \quad [3.59]$$

If $I_B = 0$ then $\rho = 0$, and $K = 6EI_c/h^3$, which is the limiting case for column stiffness dominating beam stiffness. If $I_B = \infty$, then $\rho = \infty$, and $K = 24EI_c/h^3$, which is the limiting case for the beam being infinitely stiff, or rigid. In the case of the test structure and the composite beam discussed above, $I_B = 663.11$ in 4 and $I_C = 9.61$ in 4 , assuming the use of 4-Inch Extra-Strong Columns.

These values produce a $\rho = 17.25$, which leads to a $K = 23.66EI_c/h^3$ or $K = (0.986)*24EI_c/h^3$.

Thus, the frame stiffness for this test structure is very close to the idealization of infinite beam stiffness. The rigidity of the test structure diaphragm is therefore also very close to the rigid idealization, and will be approximated as rigid in bending. Further checks of this assumption using the finite element analysis indicated no change in model response by using the rigid idealization.

3.10 FINITE ELEMENT MODEL

In modeling the behavior of the test structure, two Nonlinear Finite Element Analysis programs were employed: Abaqus and Drain-3DX. Two different programs were used in order to first provide an initial check on the reasonableness of the analysis computations, and second, to compare and contrast the different features and limitations of each program and their potential impact on the analysis solutions. Enough similarities exist between the two analysis programs that they will be discussed together in this section, with any significant differences noted.

Abaqus is a very versatile commercial analysis program developed and supported by Abaqus, Inc., formerly known as Hibbit, Karlsson & Sorenson, Inc., while Drain-3DX is a simpler program developed at the University of California at Berkeley.

During the earthquake simulations employing the larger scale input motions, the structural response exhibits both geometric and material nonlinearities. Both Abaqus and Drain-3DX can model both of these situations. Both programs feature elements of “distributed plasticity” type, which allows the very useful ability to designate the elastic-plastic behavior for any element through the input of stress-strain data. The element then accounts for the spread of inelastic behavior both over the cross sections and along the member length. Thus, the locations of plastic hinges, which are used in a “lumped plasticity” model, do not have to be found and added to the model before running the analysis.

The finite element model employed with both Abaqus and Drain-3DX to simulate the response of the test structure during the earthquake simulations consists of three primary parts: the columns, the diaphragm, and the masses. Each of these parts is discussed below in more detail, and can be seen in Figures 3.21 and 3.22. Figure 3.21 shows a typical Abaqus model, while Figure 3.22 shows a typical Drain-3DX model. The primary difference between the two basic models is that rigid beam and rigid plate elements are used to model the diaphragm in Abaqus, while they are not used in Drain-3DX.

(A) COLUMNS

The columns in the finite element model are composed of beam elements and extend from the ground to the center of mass of the diaphragm assembly. As the location of the center of mass

differs depending on the configuration of the masses, the column lengths in each finite element model can be different, as can be seen in Table 3.6 for the Abaqus models and in Table 3.7 for the Drain-3DX models. The total column length consists of two parts. The first part, which will be called the Pipe Column, extends up from the ground 60 inches. The second part, which will be called the Non-Rigid Link, extends from the top of the Pipe Column to the center of mass of the diaphragm assembly.

The Pipe Column part of the finite element model column models the actual 60-inch columns present in the test structure. In the test structure, the columns are the only parts of the model which undergo plastic deformations, and thus their behavior and response is responsible for the overall response and motion of the model. Therefore, in order to most accurately simulate the test structure response, only the 60-inch Pipe Column part of the total column will be allowed to undergo plastic deformations in the finite element model. Each Pipe Column is modeled with a pipe, or hollow circular, cross-section. The Pipe Column part consists of 20 elements, and the cross-sectional and material properties of each Pipe Column in the finite element model match the cross-sectional and material properties of the actual columns in the respective test structure configurations. Because each Pipe Column can potentially deform inelastically, stress-strain material behavior past the yield point is specified for each column. The specific stress-strain behavior model used in each test configuration is presented in the respective chapter.

The Non-Rigid Link parts of the finite element model columns connect the tops of the Pipe Column part to the diaphragm assembly. Because the Pipe Column part is limited to 60 inches, the presence of the Non-Rigid Link allows the diaphragm in the finite element model to be located at the same height as the diaphragm assembly center-of-mass in each test structure. The other benefit of the Non-Rigid Links is that the stiffness of the model can be adjusted such that the modal frequencies of the finite element model match those of the test structure. Both the elastic modulus and the cross-sectional properties of the Non-Rigid Links are adjusted as seen in Tables 3.6 and 3.7. This can be achieved while keeping the finite element diaphragm at the test structure diaphragm assembly center-of-mass height, and keeping the material properties of the Pipe Columns matched to those of the test structure. As an example of the need for the non-rigid links, if the diaphragm were located at a height of 60 inches, which is the top of the columns, the modal frequencies in the X and Y directions for Test Configuration 1 would be 4.09 Hz. In addition, if the columns were extended to the height of the center of mass of the diaphragm, 68.798 inches, the modal frequencies in the X and Y directions for Test Configuration 1 would be

3.33 Hz. The actual measured modal frequencies of the test structure are 3.57 in the X direction and 3.45 in the Y direction for this configuration, as shown in Table 3.5, and are not equal to either of the theoretical frequencies calculated above. The first example, in which the diaphragm was located at the tops of the columns, resulted in a model that was too stiff. The second example, in which the columns were extended to the center of mass of the diaphragm, resulted in a model that was too flexible. By giving the Non-Rigid Links a larger stiffness than the columns, the overall stiffness of the model could be increased from the second example to match the measured stiffness. Thus, the use of the Non-Rigid Links, while adding more complexity to the finite-element model, allows more control in calibrating the modal frequencies.

The Non-Rigid Link is modeled using a rectangular section, which allows the stiffness of the model in each planar direction to be different. This is again helpful, as the first modal frequencies in each of the two planar directions were different in each test configuration. As seen in Tables 3.6 and 3.7, the length of the Non-Rigid Link is different in the different test configurations, depending on the mass distribution. Also, the Non-Rigid Link is restricted to elastic behavior. In the actual test structure, inelastic deformation takes place in the pipe columns only. Thus, it is desired to restrict any inelastic deformation in the finite-element model to the Pipe Column part of the finite element model. Following from the restriction to elastic behavior, one element is sufficient to accurately model each Non-Rigid Link.

(1) ABAQUS

Abaqus contains a pipe section in its cross-section library to define the cross-sectional properties of beam elements, which was utilized here. The Abaqus pipe section, along with the integration points, is shown in Figure 3.23. The pipe section requires the input of the outside radius and wall thickness of the pipe. Timoshenko 2-node linear beam elements were used in modeling the 4 columns, including both the Pipe Column and Non-Rigid Link of each column. The Timoshenko element allows for transverse shear deformation, and is generally an accurate model for non-slender beams. The columns used in the test structure have slenderness ratios (length to cross-sectional dimension) of between 13.3 and 10.8. Typically, Euler-Bernoulli beam elements, which neglect transverse shear flexibility, are used to model members with slenderness ratios larger than 15. Thus, the Timoshenko element, which in Abaqus is formulated to be efficient for thin members as well as thick members, is used. The 2-node linear element features one integration point at the midpoint of each element. Modeling the pipe columns with shell

elements was also a possibility. Preliminary analyses suggested that using shell elements generally resulted in better predictions of rotational response, but slightly less accurate predictions of displacement response. Two other factors influenced the choice of beam elements to model the columns. First, Drain-3DX does not offer shell elements, and thus a comparison of the relative accuracy of each analysis program could likely be influenced by the differences in the elements used modeling the columns. Second, in analyses used to model actual structures beam elements would most likely be the element chosen, which gives a better indicator of the performance of this element.

(2) DRAIN-3DX

An inelastic fiber beam-column element (Type 15) was used in modeling the Pipe Column part of the 4 columns in Drain-3DX. Each cross-section is either elastic or is divided into a number of fibers, which can have nonlinear stress-strain behavior. If the elements were nonlinear, each was divided into 5 segments, and then each segment was divided into a number of fibers. The behavior is monitored at the center cross-section in each segment. In defining the columns when the nonlinear fibers were utilized, the number, location and area of each fiber were required. For these analyses, 12 fibers were used, arrayed in a circular pattern along the midline of the pipe column cross-section, as seen in Figure 3.24. For the low-level tests, when the elements are specified to be elastic, Drain-3DX requires the input of the cross-sectional area, both cross-sectional moments of inertia, and the polar moment of inertia. Transverse shear deformation is accounted for in this element. An elastic beam-column element (Type 17) was used in modeling the Non-Rigid Link part of the 4 columns in the Drain-3DX models. The cross-sectional area, both cross-sectional moments of inertia, and the polar moment of inertia are required to define the element.

(B) DIAPHRAGM

The diaphragm in the test structure was designed to behave as a rigid body and to experience no permanent damage. Therefore, although it was expected that the diaphragm could be modeled as a rigid plate in the finite element analysis, verifying this assumption was necessary. Both the in-plane and bending rigidity of the diaphragm in the test structure were studied, and were shown previously in this chapter to be valid modeling assumptions. Thus, the diaphragm in the finite

element model was designed as a rigid body as well. This was achieved by two different methods in the two analysis programs.

(1) ABAQUS

The diaphragm in the Abaqus finite element model consists of two types of elements, which work together to produce a rigid plate. The diaphragm surface is composed of 16 rigid 4-node bilinear quadrilateral elements. Around the perimeter of the diaphragm are 16 rigid 2-node beam elements. The presence of the rigid beam elements is necessitated by the lack of bending rigidity of the quadrilateral elements about the X- and Y-Axis. The rigid quadrilateral elements and the rigid beam elements are combined to form a rigid body, which then all share a common rigid body reference node. The rigid body reference node is located at the geometric center of the diaphragm.

(2) DRAIN-3DX

The diaphragm in the Drain-3DX model is composed of the same elastic beam-column element (Type 17) used to model the Non-Rigid Links. Forty elements were used to create a grid connecting the 25 diaphragm nodes, as seen in Figure 3.22. The elements were specified to have a large bending stiffness and to be massless. In order to ensure that the diaphragm moved in a rigid manner, the rotation of each diaphragm node was slaved to a reference node. This reference node is located at the geometric center of the diaphragm.

(C) MASS

In choosing the method of mass distribution, a number of criteria were important. First, the vertical mass distribution of the test structure needed to be modeled correctly. In determining the center of mass of the test structure diaphragm assembly, both the masses located above and below the diaphragm and the column top plates were included in the computation. Thus, for purposes of the Abaqus finite element modeling, all components of the test structure other than the 60-inch pipe columns were lumped together and termed the diaphragm assembly. The total mass of the test structure diaphragm assembly was distributed in the plane of the rigid diaphragm plate. The mass and center of mass of this diaphragm assembly was computed, and the diaphragm rigid plate in the finite element model was located at the same height as the test structure diaphragm

assembly. The only other component of the test structure for which mass was accounted were the 60-inch pipe columns. In the Abaqus finite element model of the structure, the Pipe Columns were given the appropriate mass density of steel, thereby modeling the true mass distribution of the 60-inch pipe columns. With Drain-3DX, the mass must be lumped at the nodes. Thus, the only difference with Drain-3DX is that the mass of the columns is also incorporated into the masses placed in the diaphragm. This has the effect of placing the diaphragm at a slightly reduced height in the Drain-3DX model as compared to the Abaqus model. In both the Abaqus and Drain-3DX models, mass placement thus matched the true vertical mass distribution of the test structure.

Second, the horizontal mass distribution of the test structure needed to be modeled correctly. In determining the distribution of the diaphragm assembly total mass within the plane of the rigid diaphragm, three test structure properties were considered: the rotational moment of inertia of the diaphragm assembly, the mass center of the diaphragm assembly in its plane, and the total mass of the diaphragm assembly. The rotational moment of inertia was calibrated using the torsional modal frequency of the test structure. The method used to model these three properties was to place nodal masses at eight nodes in the plane of the rigid diaphragm as shown in Figures 3.21 and 3.22. One mass was placed at each of the four exterior corners of the diaphragm, and one mass was placed at each of the four interior nodes. In each test configuration, the corner masses each had the same magnitude, while the interior masses did not necessarily have the same magnitude. The magnitudes of each of the diaphragm masses for each test configuration are listed in Tables 3.6 and 3.7, and are also covered in the following chapters. As a result of this nodal mass distribution in the finite element model, 25 nodes were required to compose the rigid diaphragm. Thus the model contained the four interior nodes plus the center node.

Since nodal masses were used to model the entire mass of the diaphragm assembly, all of the elements in the Abaqus finite element model, with the exception of the 60-inch Pipe Columns, were massless. In the Drain-3DX model, all elements were massless, including the columns. Thus, the rigid plate elements and the rigid beam elements used in the rigid diaphragm, and the linear beam elements used to model the Non-Rigid Links were all defined with a very small mass density.

(D) MATERIAL DEFINITION

(1) ABAQUS

The rigid quadrilateral elements and the rigid beam elements used to model the diaphragm are massless in the finite element model, as discussed above, and as such require no material definition. The Non-Rigid Links are massless as well, but do require other material property definitions. The Non-Rigid Links require an elastic modulus definition, but no post-yield stress-strain behavior definition as they are limited to elastic behavior. The elastic modulus of the Non-Rigid Links was adjusted, as were the planar dimensions of the Links, such that the modal frequencies of the finite element model match the measured modal frequencies of the test structure. Thus, both the elastic modulus and planar dimensions of the Non-Rigid Links were potentially different in each of the test configurations.

The Pipe Columns required the most detailed material definition. They are not massless, and thus require a mass density definition. The material damping is also defined for the Pipe Columns, as the damping here is a material property and not a modal property of the structure, as discussed below. The most important material definition for the Pipe Columns for this study is the stress-strain behavior of the steel. The elastic modulus of the pipe columns was defined as 29000 ksi for all of the test configurations. Since the columns in the test structure experience significant excursions past yield, the post-yield stress-strain behavior is very important to the test structure response. In order to model this post-yield behavior, tension tests were performed to failure on coupon samples taken from the columns. The stress-strain behavior of these material samples was the basis for the finite element material models in each test configuration. Specific tension test data of the coupons applicable to each test configuration, and the resulting finite element material model definition, are presented in their respective chapters. Cyclic tests on the column coupons were not performed, but as the columns in the test structure undergo a moderate number of post-yield loading cycles, material hardening can significantly affect structural response.

Abaqus provides a number of material hardening models, but the model which is most appropriate for this study is the nonlinear combined isotropic/kinematic hardening model. This model is based on the work of Lemaitre and Chaboche [54].

The basic idea behind isotropic hardening is that the yield surface changes size uniformly in all directions such that the yield stress increases or decreases in all stress directions as plastic

straining occurs. This is illustrated schematically in Figure 3.25. The isotropic hardening component of the material model defines the evolution of the size of the elastic range as a function of the plastic strain. The method used to define the isotropic hardening characteristics for this study was by defining the yield stress as a tabular function of plastic strain. The yield stress at a given state was then interpolated from the table of data.

Isotropic hardening has been used extensively in plasticity theory, and this phenomenon has been observed experimentally. While this model alone gives accurate results for monotonic loading, it does not correctly model the Bauschinger effect, which is characterized by a reduced yield stress upon post-yield load reversal. This effect could potentially be significant in the response of the test structure as it undergoes numerous post-yield loading cycles. With kinematic hardening, the yield surface shifts in stress space so that straining in one direction reduces the yield stress in the opposite direction as illustrated in Figure 3.25. The different hardening models are also illustrated in Figures 3.26 – 3.29 through cyclic load-displacement plots. The combined isotropic/kinematic hardening model is shown in Figure 3.26, the perfect plasticity model is shown in Figure 3.27, the isotropic hardening model is shown in Figure 3.28 and the kinematic hardening model is shown in Figure 3.29.

The use of the kinematic hardening model along with the isotropic hardening model does take the Bauschinger effect into consideration. The kinematic hardening component of the material model defines the evolution of the translation of the yield surface in stress space. This is done with the following equation, that is used to define α , the backstress. The backstress at any plastic strain is the difference between the total stress and the yield stress as defined by the isotropic hardening component, which is illustrated in Figure 3.30.

$$\dot{\alpha} = C \frac{1}{\sigma^0} (\sigma - \alpha) \dot{\varepsilon}^{pl} - \gamma \alpha \dot{\varepsilon}^{pl} \quad [3.60]$$

In this equation, σ^0 is the size of the elastic range, ε^{pl} is the equivalent plastic strain, and C and γ are material parameters which must be calibrated from test data. In this case, test data used to calibrate the model are stress-strain data obtained from the column coupon tests. Backstress data are computed at each level of plastic strain as the difference between the total stress, taken from the coupon tests, and the yield stress, as defined by isotropic hardening tabular data. Isotropic hardening data are computed as a percentage of the total hardening. The parameters C and γ are

then determined by Abaqus based on backstress data. The isotropic hardening model in Abaqus does allow one to account for cyclic hardening as well, through the definition of the elastic range as a function of the number of load reversals. However, experimental cyclic material tests were not performed and thus, no set of data are available to calibrate the model for cyclic hardening as a function of load reversals. The cyclic hardening behavior of A36 steel under symmetric strain-control, as studied in Reference 64, is shown in Figure 3.31. This data plot illustrates that a large number of load reversals is necessary to significantly impact the stress-strain behavior of A36 steel. The number of plastic load reversals during each experimental simulation in this study is not very large, approximately 10-15, thus the lack of cyclic hardening data as a function of load cycle should not significantly impact the ability to model the experimental simulations.

(2) DRAIN-3DX

In the Drain-3DX model, the Non-Rigid Link elements and the diaphragm elements are both linear beam-column elements. They require the cross-sectional area, both cross-sectional moments of inertia, the polar moment of inertia, and the shear and elastic moduli to be defined. The elastic modulus of the Non-Rigid Links was adjusted, as were the planar dimensions of the Links, such that the modal frequencies of the finite element model match the measured modal frequencies of the test structure. Thus, both the elastic modulus and planar dimensions of the Non-Rigid Links were potentially different in each of the test configurations.

As with the Abaqus model, the Pipe Columns require the most detailed material definition. For the low-level earthquake simulations, when the Pipe Column elements are defined as elastic, the input data requirements are similar to the Non-Rigid Link and diaphragm elements. The cross-sectional area, both cross-sectional moments of inertia, the polar moment of inertia, and the shear and elastic moduli must be defined. The elastic modulus of the pipe columns was defined as 29000 ksi for all of the test configurations. When the nonlinear fiber elements are used to define the columns, the material input is similar to the Abaqus material definition. Although Drain-3DX does not feature the diverse set of material hardening models that Abaqus does, it does allow a set of five stress-strain points to be defined. This gives Drain-3DX the ability to model isotropic hardening, which was discussed previously. Specific tension test data of the coupons applicable to each test configuration, and the resulting finite element material model definition, are presented in their respective chapters.

(E) OTHER MODELING ISSUES

Three other issues common to finite element models in each test configuration are the structural damping of the model, the fixity of the column bases, and the input ground motions. First, with regard to the structural damping, two limitations in Abaqus impact this study. The first limitation is the inability to define modal damping for the model when using the direct-integration dynamic analysis in Abaqus. Damping must be defined as a material property, and the damping definition available is stiffness proportional Rayleigh damping. Thus, the measured damping characteristics of the overall test structure cannot be directly defined in Abaqus. The solution used was to adjust the stiffness proportional damping of the finite element model such that the response of the model matched the test structure response at low ground motion input levels. The second limitation was that since the damping was a material property, it was impossible to define a different level of damping for the X and Y directions. Drain-3DX presented similar limitations. A viscous damping matrix that is proportional to the element stiffnesses and nodal masses can be specified for the structure. Although the stiffnesses are different for the X and Y directions, they are not dissimilar enough to produce the different damping ratios needed for some configurations. As can be seen in Table 3.5, the measured level of damping for the test structure in the X and Y directions were often different, many times differing by a factor of two or more. Thus, it was often necessary to choose a level of damping that split the difference, or minimized the error in each direction. The amount of damping present in the test structure, as is typical of steel structures, is relatively small. For the low level tests, it does have a significant impact on the model response, but for the large-scale tests, the inherent structural damping is greatly overshadowed by the energy dissipation due to nonlinear behavior.

In the test structure, the pipe columns were welded to the column bottom plates, which were then bolted to the shaketable, as described in Chapter 2. This design of the test structure was meant to produce a constraint of complete fixity at the base of each column. Thus, in the finite element model, the bottom node of each column was completely constrained.

Two ground motions were input to the finite element model, those along the X- and the Y-Axis. The motions used in the Abaqus analyses were the shaketable displacement records along the X- and the Y-Axis recorded during each test. Abaqus allows the definition of non-zero displacement, velocity, or acceleration time histories for any node. Thus, the node located at the bottom of each of the four columns was provided with the recorded shaketable displacement

records as displacement time histories in both the X and Y directions. The motions used in the Drain-3DX analyses were the shaketable acceleration records along the X- and Y-Axis recorded during each test. Drain-3DX requires acceleration records to be used as ground motion inputs if the base nodes are completely fixed, which is the case here.

3.11 FINITE ELEMENT ANALYSES

Due to its rigidity, the planar motion of the diaphragm can be completely characterized by three degrees-of-freedom, two translational components along the X- and Y-Axis and one rotational component about the Z-Axis. Because of this, the relative displacement of the diaphragm along the X- and Y-Axis and the rotation of the diaphragm about the Z-Axis were chosen as the response quantities used to compare the accuracy of the finite element simulations. Utilizing the respective acceleration response histories would have been a valid choice as well, but displacements were chosen as they have a more intuitive quality than accelerations. Thus, the relative displacements along the X- and Y-Axis and the rotation about the Z-Axis, for both the test structure and the finite element model, are shown in the following chapters for various levels of ground motion input as a means of comparison between the finite element analysis and the test structure response.

Chapter	Test Configuration	Mass Distribution	Strength Distribution	Stiffness Distribution
4	1	Symmetric	Symmetric	Symmetric
5	2	Symmetric	Symmetric	Symmetric
6	4	$\frac{1}{2}$ Asymmetric	Symmetric	Symmetric
7	3	$\frac{1}{4}$ Asymmetric	Symmetric	Symmetric
8	8	$\frac{1}{4}$ Asymmetric	Symmetric	Symmetric
9	5	$\frac{1}{2}$ Asymmetric	Asymmetric	Symmetric
10	6	$\frac{1}{2}$ Asymmetric	Symmetric	Asymmetric
11	7	$\frac{1}{2}$ Asymmetric	Asymmetric	Asymmetric

Table 3.1 Test Configuration Summary

Test Configuration	Earthquake Test No.	Input Motions	PGA [g]			Diaphragm Acceleration Δa_{dipl} [10^3 in/in]			Diaphragm Angular Acceleration $\Delta \alpha_{dipl}$ [10^3 rad/in]
			X-Axis	Y-Axis	Z-Axis	X-Axis	Y-Axis	Z-Axis	
1	1	25% X-Axis	0.238	N/A	0.678	0.095		0.72	
	2	25% Y-Axis	N/A	0.162	0.055	0.475		0.75	
	3	25% Biaxial	0.232	0.160	0.623	0.491		1.11	
	7	100% Y-Axis	N/A	0.678	0.064	0.941		1.87	
	12	25% X-Axis	0.250	N/A	0.658	0.075		0.54	
	13	25% Y-Axis	N/A	0.168	0.030	0.425		1.01	
	14	25% Biaxial	0.248	0.170	0.631	0.438		1.13	
2	15	100% Biaxial	1.080	0.699	1.055	0.910		2.61	
	16	150% Biaxial	1.582	1.141	1.184	1.101		2.68	
	18	10% X-Axis	0.102	N/A	0.240	0.175		1.701	
	19	10% Y-Axis	N/A	0.064	0.057	0.122		1.250	
	22	10% Biaxial	0.109	0.066	0.223	0.209		2.136	
3	23	100% Biaxial	1.299	0.797	1.146	0.938		14.819	

Table 3.2.a Maximum Table Accelerations and Diaphragm Acceleration and Angular Acceleration Response

Test Configuration	Earthquake Test No.	Input Motions	PGA [g]			Diaphragm Acceleration [in/s ²]			Diaphragm Angular Acceleration [rad/s ²]
			X-Axis	Y-Axis	Z-Axis	X-Axis	Y-Axis	Z-Axis	
4	25	10% X-Axis	0.105	N/A	0.360	0.076			2.18
	26	10% Y-Axis	N/A	0.070	0.019	0.205			0.25
	27	10% Biaxial	0.102	0.062	0.349	0.266			1.99
	28	100% Biaxial	1.115	0.711	1.041	0.957			10.88
	29	150% Biaxial	1.629	1.121	1.156	1.153			16.01
5	30	10% X-Axis	0.102	N/A	0.403	0.047			0.94
	31	10% Y-Axis	N/A	0.064	0.011	0.107			0.82
	32	10% Biaxial	0.100	0.059	0.404	0.136			1.28
	34	100% Biaxial	1.086	0.658	1.706	0.856			9.87
	35	150% Biaxial	1.637	1.045	1.682	1.364			17.10
6	36	10% Biaxial	0.117	0.191	0.263	0.398			3.54
	37	10% X-Axis	0.119	N/A	0.270	0.016			0.85
	38	10% Y-Axis	N/A	0.189	0.028	0.388			3.43
	39	100% Biaxial	0.846	1.926	1.065	1.980			32.06
	40	100% X-Axis 90% Y-Axis	1.318	1.951	1.263	1.973			30.00
7	41	100% X-Axis 75% Y-Axis	1.367	1.582	1.667	1.909			20.08
	42	100% X-Axis 85% Y-Axis	1.357	1.881	1.633	2.214			25.08
8	43	100% Biaxial	1.354	1.986	1.636	2.302			26.66
	45	100% Biaxial	1.187	0.699	0.942	0.803			12.215
	46	135% Biaxial	1.559	0.990	0.978	0.915			12.761

Table 3.2.b Maximum Table Accelerations and Diaphragm Acceleration and Angular Acceleration Response

Test Configuration	Earthquake Test No.	Input Motions	PGA [g]			Relative Displacement [in]	Rotation [10^{-3} rad]
			X-Axis	Y-Axis	Z-Axis		
1	1	25% X-Axis	0.238	N/A	0.535	0.087	0.29
	2	25% Y-Axis	N/A	0.162	0.041	0.377	0.40
	3	25% Biaxial	0.232	0.160	0.488	0.414	0.79
	7	100% Y-Axis	N/A	0.678	0.054	1.216	0.85
2	12	25% X-Axis	0.250	N/A	0.511	0.050	0.33
	13	25% Y-Axis	N/A	0.168	0.022	0.350	0.41
	14	25% Biaxial	0.248	0.170	0.501	0.356	0.78
	15	100% Biaxial	1.080	0.699	2.828	1.294	2.85
3	16	150% Biaxial	1.582	1.141	5.409	4.343	5.35
	18	10% X-Axis	0.102	N/A	0.175	0.112	0.845
	19	10% Y-Axis	N/A	0.064	0.039	0.123	0.845
	22	10% Biaxial	0.109	0.066	0.163	0.160	0.967
	23	100% Biaxial	1.299	0.797	3.154	1.197	21.938

Table 3.3.a Maximum Diaphragm Relative Displacement and Rotation Response

Test Configuration	Earthquake Test No.	Input Motions	PGA [g]			Relative Displacement mm^{-1}	Rotation $[10^{-3} \text{ rad}]$
			X-Axis	Y-Axis	Z-Axis		
4	25	10% X-Axis	0.105	N/A	0.360	0.076	2.18
	26	10% Y-Axis	N/A	0.070	0.019	0.205	0.25
	27	10% Biaxial	0.102	0.062	0.349	0.266	1.99
	28	100% Biaxial	1.115	0.711	1.041	0.957	10.88
5	29	150% Biaxial	1.629	1.121	1.156	1.153	16.01
	30	10% X-Axis	0.102	N/A	0.211	0.027	0.363
	31	10% Y-Axis	N/A	0.064	0.025	0.058	0.606
	32	10% Biaxial	0.100	0.059	0.214	0.063	0.606
6	34	100% Biaxial	1.086	0.658	1.313	0.458	8.394
	35	150% Biaxial	1.637	1.045	2.805	1.221	13.816
	36	10% Biaxial	0.117	0.191	0.186	0.056	0.677
	37	10% X-Axis	0.119	N/A	0.192	0.015	0.342
7	38	10% Y-Axis	N/A	0.189	0.019	0.053	0.618
	39	100% Biaxial	0.846	1.926	1.537	1.966	18.49
	40	100% X-Axis 90% Y-Axis	1.318	1.951	3.903	3.150	27.80
	41	100% X-Axis 75% Y-Axis	1.367	1.582	2.172	1.008	11.52
8	42	100% X-Axis 85% Y-Axis	1.357	1.881	2.320	1.420	13.66
	43	100% Biaxial	1.354	1.986	2.444	1.774	13.75
	45	100% Biaxial	1.187	0.699	2.481	1.572	16.462
	46	135% Biaxial	1.559	0.990	3.735	3.818	23.279

Table 3.3.b Maximum Diaphragm Relative Displacement and Rotation Response

Test Configuration	Earthquake Test No.	Input Motions	PGA [g]			Base Shear [k]	Torsional Moment M_{L*inl}	<u>Base Shear</u> <u>W_{airht}</u>
			X-Axis	Y-Axis	Z-Axis			
1	1	25% X-Axis	0.238	N/A	24.53	3.45	38.30	0.68
	2	25% Y-Axis	N/A	0.162	1.97	17.18	39.93	0.05
	3	25% Biaxial	0.232	0.160	22.54	17.75	59.26	0.62
	7	100% Y-Axis	N/A	0.678	2.32	34.04	99.30	0.06
	12	25% X-Axis	0.250	N/A	23.80	2.70	28.65	0.66
	13	25% Y-Axis	N/A	0.168	1.07	15.37	54.02	0.03
	14	25% Biaxial	0.248	0.170	22.83	15.85	60.17	0.63
2	15	100% Biaxial	1.080	0.699	38.17	32.91	138.85	1.06
	16	150% Biaxial	1.582	1.141	42.84	39.84	142.78	1.18
	18	10% X-Axis	0.102	N/A	8.44	4.49	140.44	0.24
	19	10% Y-Axis	N/A	0.064	1.92	4.55	118.56	0.06
3	22	10% Biaxial	0.109	0.066	7.81	6.78	184.95	0.22
	23	100% Biaxial	1.299	0.797	36.67	31.05	960.34	1.05
								0.89

Table 3.4.a Maximum Base Shear and Torsional Moment

Test Configuration	Earthquake Test No.	Input Motions	PGA [g]			Base Shear [k]			Torsional Moment [k-in]		Base Shear Weight	
			X-Axis	Y-Axis	Z-Axis	X-Axis	Y-Axis	Z-Axis	X-Axis	Y-Axis	X-Axis	Y-Axis
4	25	10% X-Axis	0.105	N/A	12.78	2.66	272.11	0.36	0.08			
	26	10% Y-Axis	N/A	0.070	0.67	7.19	16.43	0.02	0.20			
	27	10% Biaxial	0.102	0.062	12.40	9.34	260.40	0.35	0.27			
	28	100% Biaxial	1.115	0.711	36.48	33.61	927.50	1.04	0.95			
	29	150% Biaxial	1.629	1.121	40.44	40.49	1028.23	1.15	1.15			
5	30	10% X-Axis	0.102	N/A	14.27	1.39	56.64	0.40	0.04			
	31	10% Y-Axis	N/A	0.064	0.41	3.88	92.24	0.01	0.11			
	32	10% Biaxial	0.100	0.059	14.29	4.74	113.58	0.40	0.13			
	34	100% Biaxial	1.086	0.658	60.36	31.42	732.22	1.71	0.89			
	35	150% Biaxial	1.637	1.045	59.51	47.66	1300.42	1.68	1.35			
6	36	10% Biaxial	0.117	0.191	9.74	15.29	349.15	0.26	0.41			
	37	10% X-Axis	0.119	N/A	10.02	0.60	46.14	0.27	0.02			
	38	10% Y-Axis	N/A	0.189	1.04	14.92	329.74	0.03	0.40			
	39	100% Biaxial	0.846	1.926	39.48	67.93	2117.60	1.06	1.83			
	40	100% X-Axis 90% Y-Axis	1.318	1.951	46.83	63.49	2318.05	1.26	1.71			
7	41	100% X-Axis 75% Y-Axis	1.367	1.582	61.99	75.08	1913.27	1.67	2.02			
	42	100% X-Axis 85% Y-Axis	1.357	1.881	60.75	85.29	2028.28	1.63	2.29			
	43	100% Biaxial	1.354	1.986	60.83	85.63	2244.53	1.64	2.30			
8	45	100% Biaxial	1.187	0.699	30.58	27.23	793.62	0.88	0.78			
	46	135% Biaxial	1.559	0.990	32.95	32.32	796.59	0.95	0.93			

Table 3.4.b Maximum Base Shear and Torsional Moment

Test Configuration	Mass [lb*s ² /in]	Mass Centers			Modal Frequencies [Hz]			Modal Damping [%]		
		X ₀ [in]	Y ₀ [in]	Z ₀ [in]	X	Y	θ	X	Y	θ
1	93.618	0.0	0.0	68.798	3.565	3.445	6.515	0.497	1.074	0.491
2	93.618	0.0	0.0	68.798	3.589	3.454	6.450	0.596	0.636	N/A
3	90.141	-15.201	15.201	67.479	3.546	3.283	8.287	0.525	1.290	0.580
4	91.256	0.0	15.236	68.362	3.468	3.415	7.255	0.474	0.873	0.675
5	91.572	-15.007	0.0	68.229	4.348	4.255	9.091	0.767	1.597	0.579
6	95.943	13.429	0.0	69.810	3.636	8.333	13.333	0.653	4.617	2.217
7	96.259	13.552	0.0	69.679	4.444	7.692	11.765	0.818	5.237	1.271
8	90.141	-15.201	15.201	67.479	3.704	3.333	8.696	0.389	0.654	0.671

Table 3.5 Test Structure Dynamic Properties

Test Configuration	Height of Diaphragm Assembly C-O-M [in]	Pipe Column Length [in]	Non-Rigid Link Dimensions [in]		Corner Masses [lb*s ² /in]	Interior Masses [lb*s ² /in]			
			X	Y		NW	NE	SE	SW
1	69.123	60.0	9.123	3.150	2.820	2.800	20.355	20.355	20.355
2	69.123	60.0	9.123	3.199	2.821	2.941	20.270	20.270	20.270
3	67.804	60.0	7.804	3.017	2.510	1.705	6.595	62.761	6.595
4	68.691	60.0	8.691	3.083	2.661	2.397	5.283	35.163	35.163
5	68.691	60.0	8.691	3.356	3.447	2.705	35.252	35.252	4.578
6	70.134	60.0	10.134	3.802	3.654	2.852	5.804	5.804	36.075
7	70.134	60.0	10.134	3.752	3.701	3.155	7.020	7.020	34.254
8	67.804	60.0	7.804	4.295	2.752	1.791	6.117	63.847	6.117

Table 3.6 Abaqus Finite Element Model Dynamic Properties

Test Configuration	Height of Diaphragm C-O-M [in]	Pipe Column Length [in]	Non-Rigid Link Dimensions [in]				Corner Masses [lb*s ² /in]	Interior Masses [lb*s ² /in]					
			Length [in]	Dimensions [in]		X	Y						
				N	E								
1	68.798	60.0	8.798	3.273	2.817	2.994	20.411	20.411	20.411	20.411			
2	68.798	60.0	8.798	3.347	2.816	2.994	20.411	20.411	20.411	20.411			
3	67.479	60.0	7.479	3.006	2.280	0.024	5.483	72.820	5.483	5.483			
4	68.362	60.0	8.362	2.857	2.701	1.943	3.033	38.321	38.321	3.033			
5	68.691	60.0	8.691	3.356	3.447	2.705	35.252	35.252	4.578	4.578			
6	70.134	60.0	10.134	3.802	3.654	2.852	5.804	5.804	36.075	36.075			
7	70.134	60.0	10.134	3.752	3.701	3.155	7.020	7.020	34.254	34.254			
8	67.804	60.0	7.804	4.295	2.752	1.791	6.117	63.847	6.117	6.117			

Table 3.7 Drain-3DX Finite Element Model Dynamic Properties

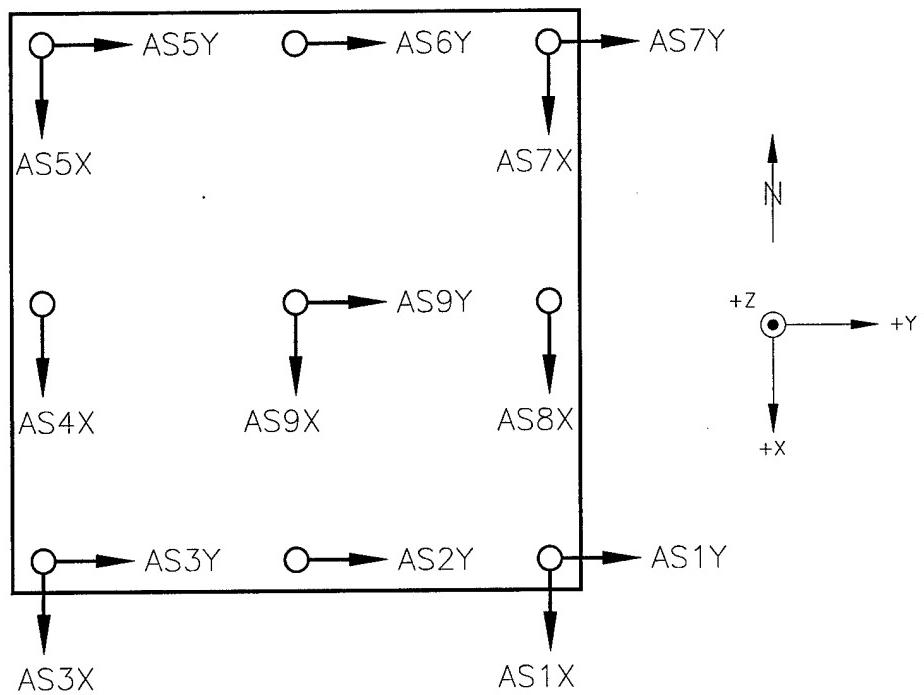


Figure 3.1 Diaphragm Acceleration Transducers

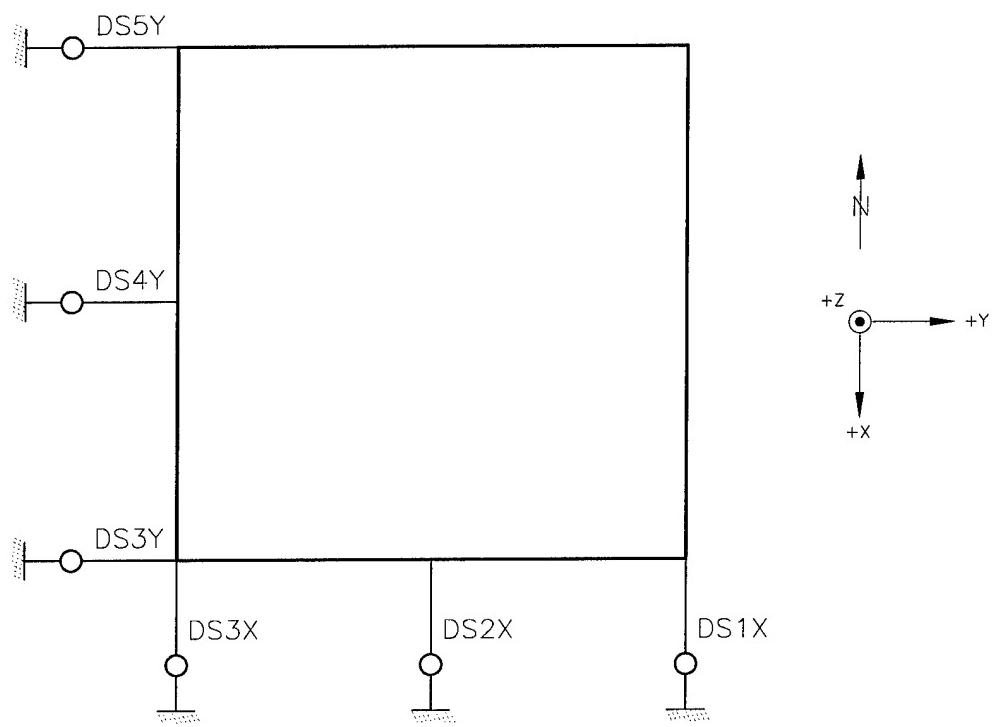


Figure 3.2 Diaphragm Displacement Transducers

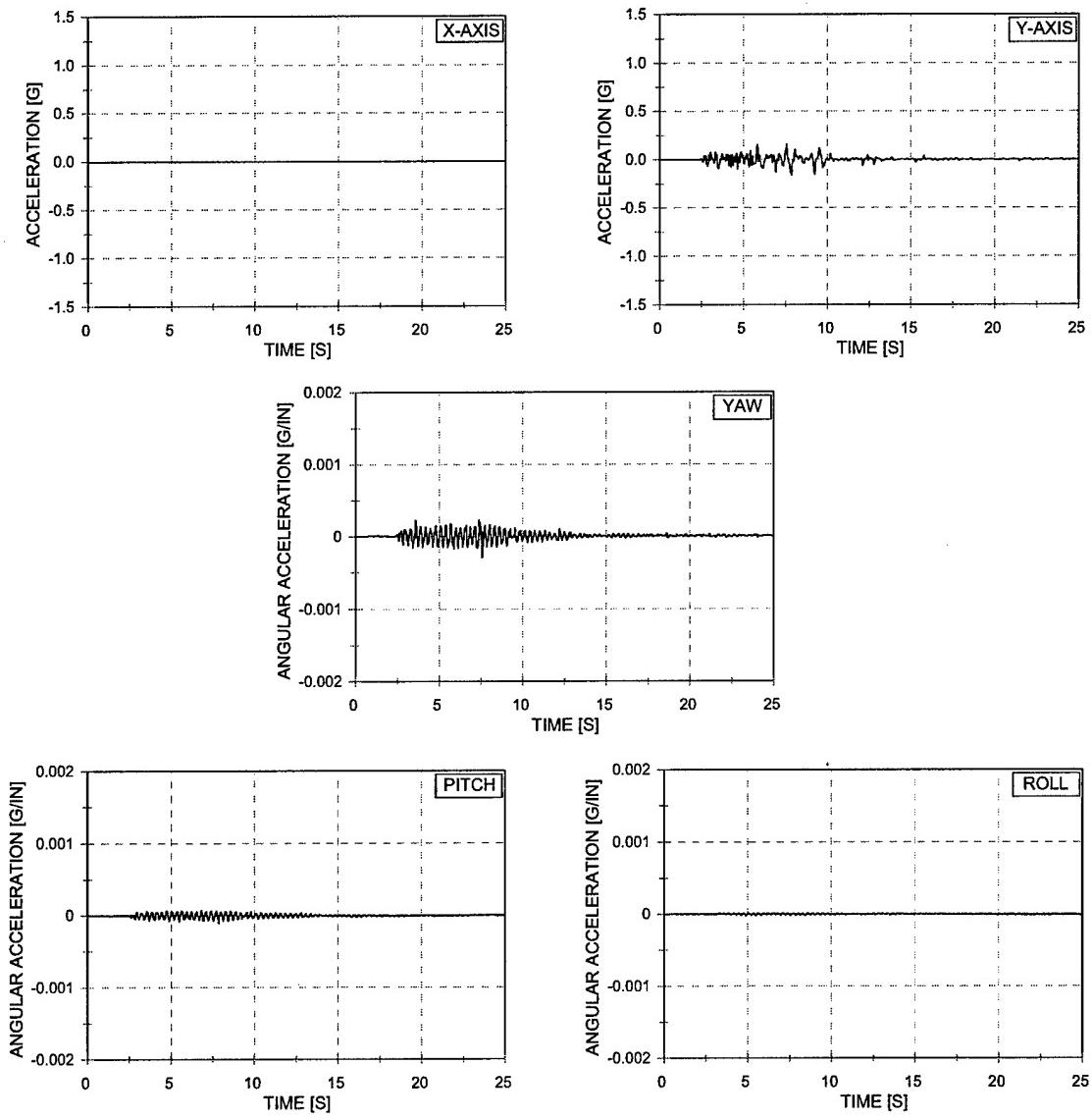


Figure 3.3 Shaketable Accelerations vs. Time – EQ 02
25% Y-Axis Imperial Valley – Symmetric Mass

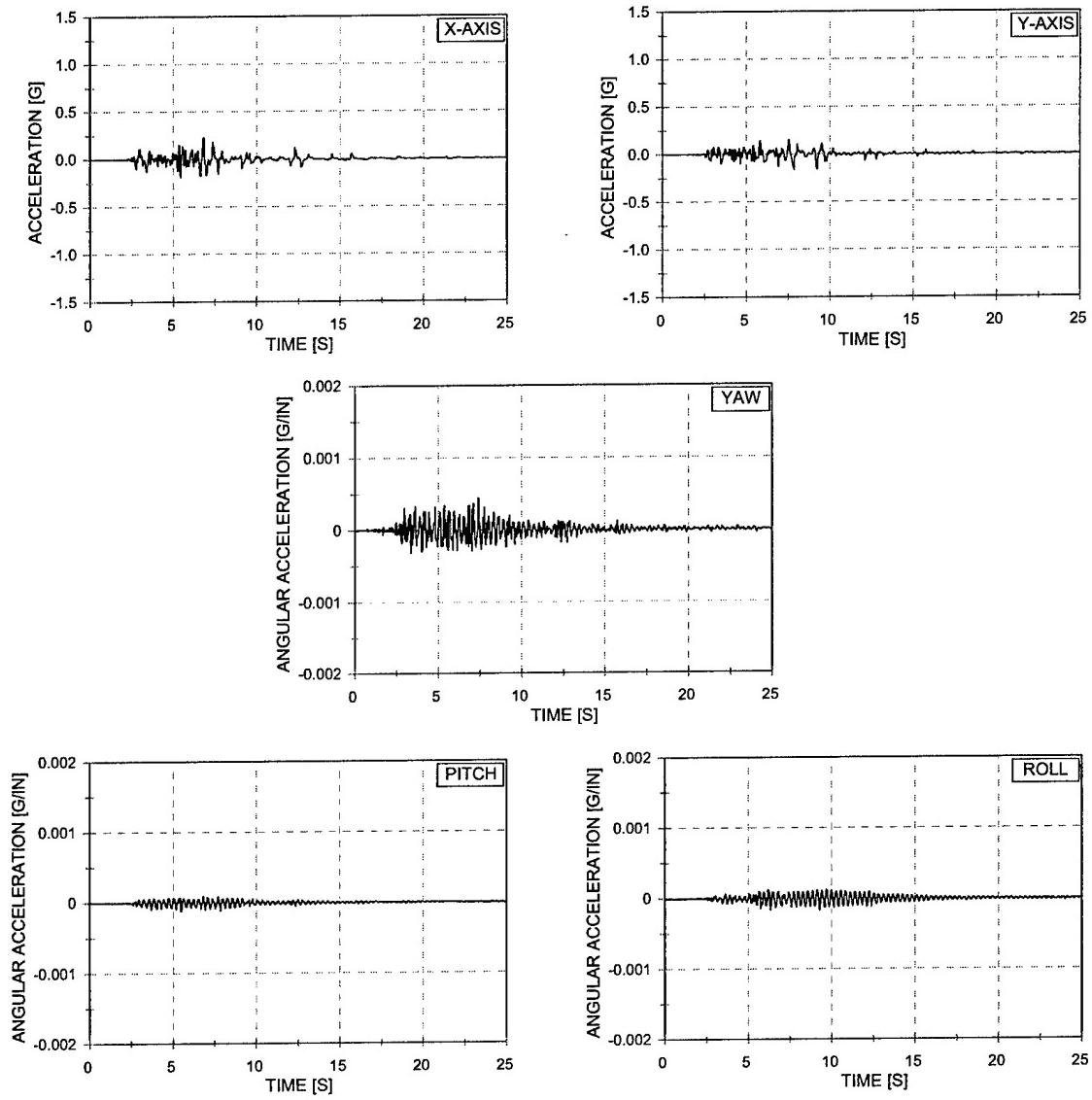


Figure 3.4 Shaketable Accelerations vs. Time – EQ 03
25% Biaxial Imperial Valley – Symmetric Mass

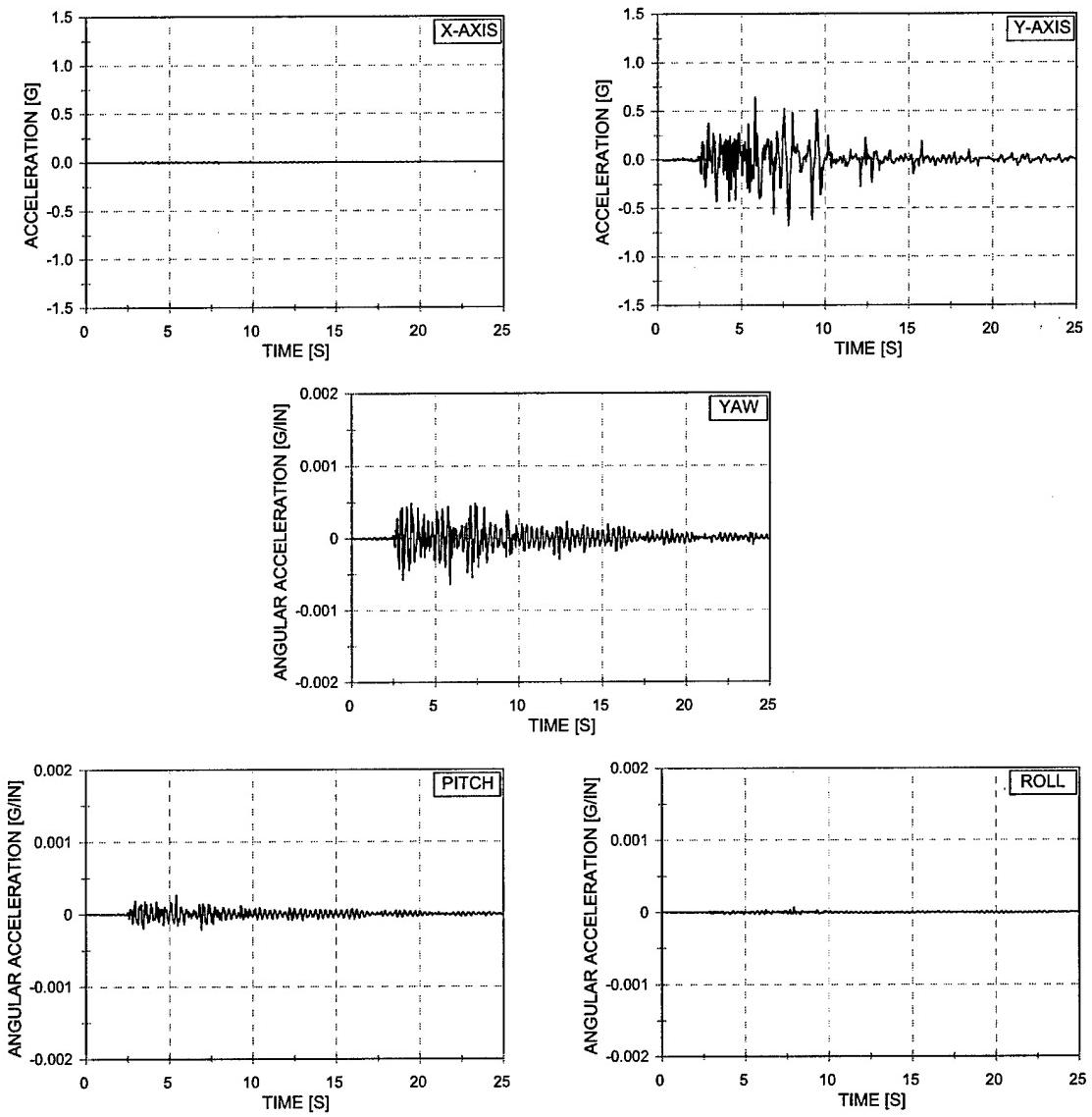


Figure 3.5 Shaketable Accelerations vs. Time – EQ 07
100% Y-Axis Imperial Valley – Symmetric Mass

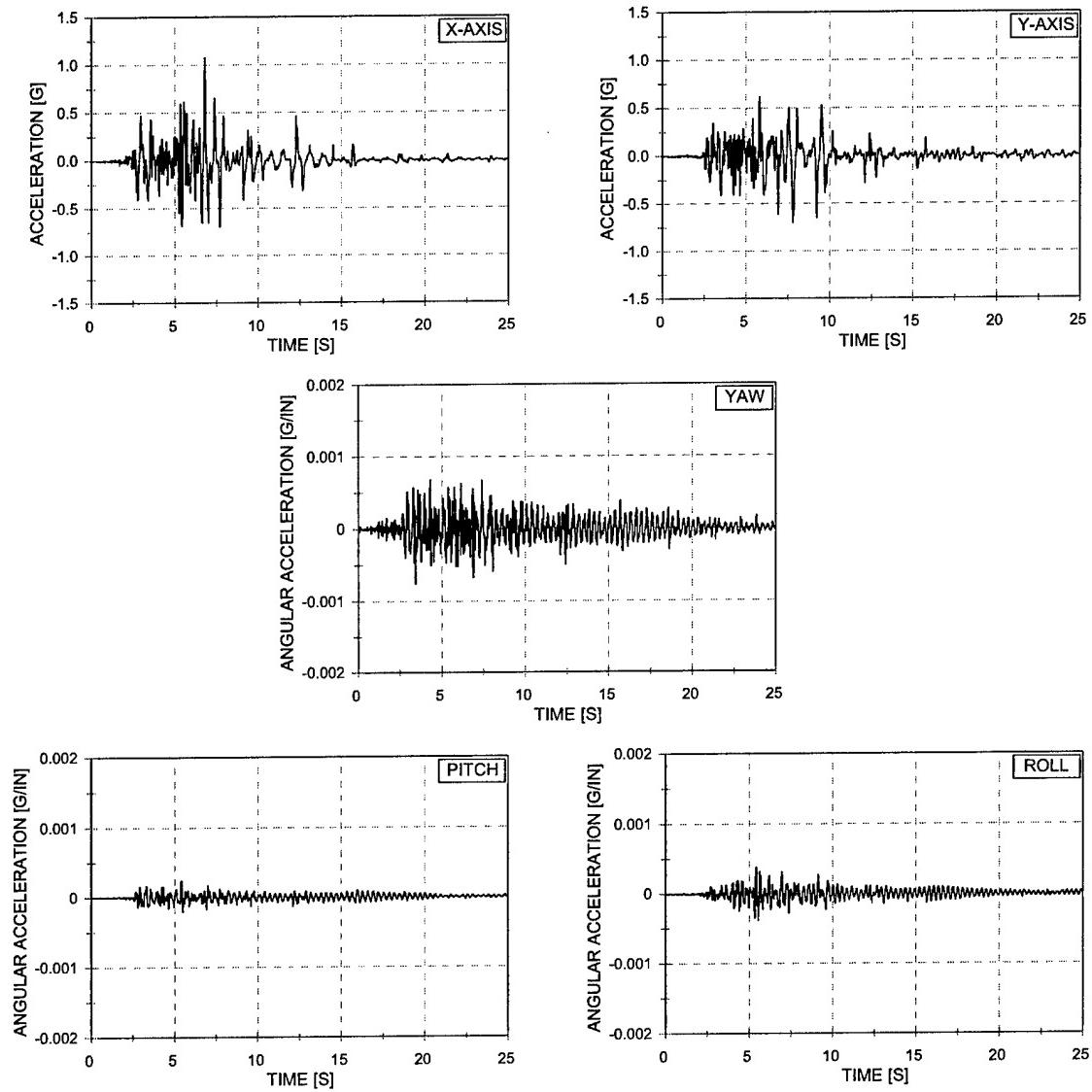


Figure 3.6 Shaketable Accelerations vs. Time – EQ 15
100% Biaxial Imperial Valley – Symmetric Mass

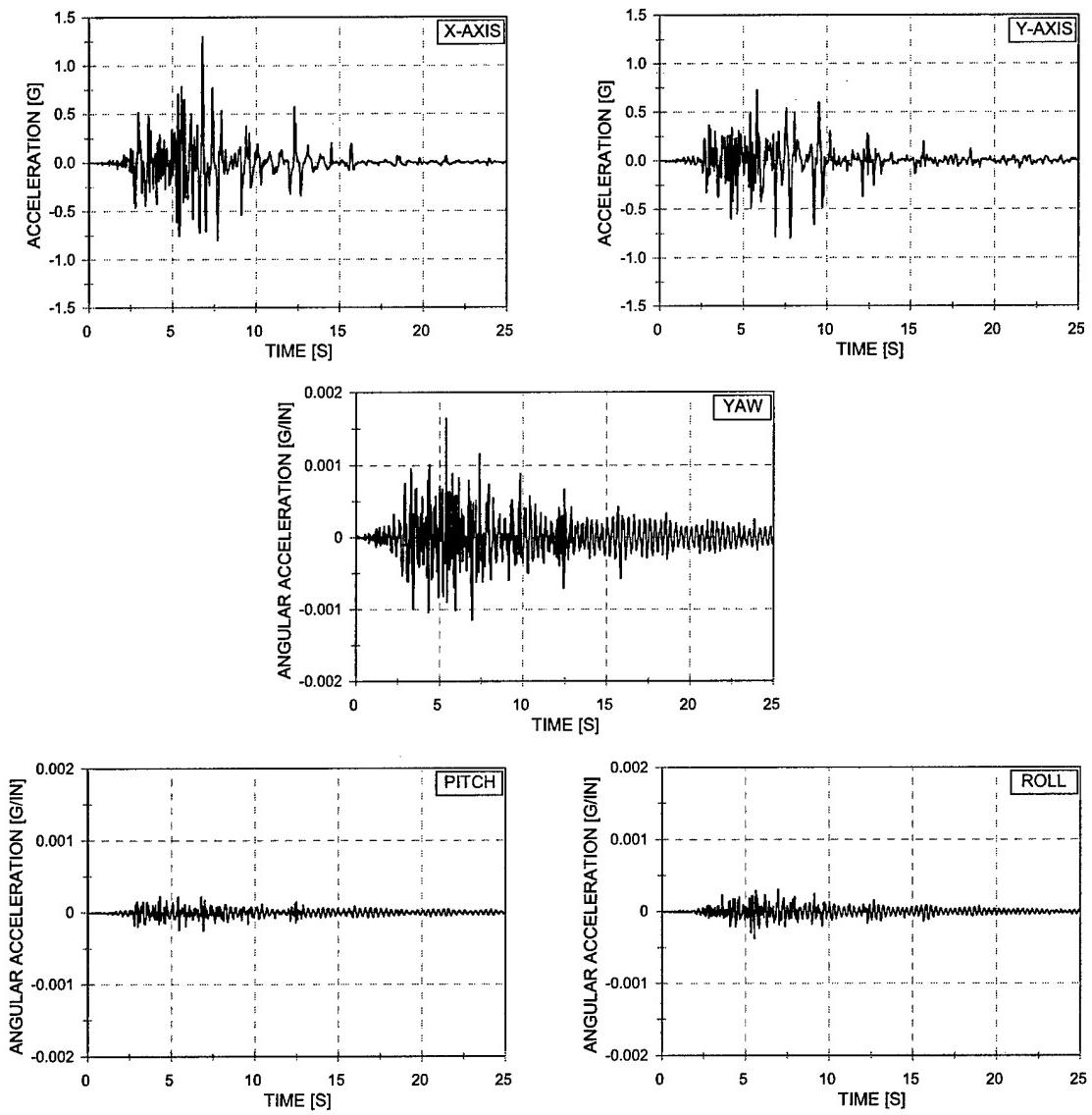


Figure 3.7 Shaketable Accelerations vs. Time – EQ 23
100% Biaxial Imperial Valley – 1/4 Asymmetric Mass

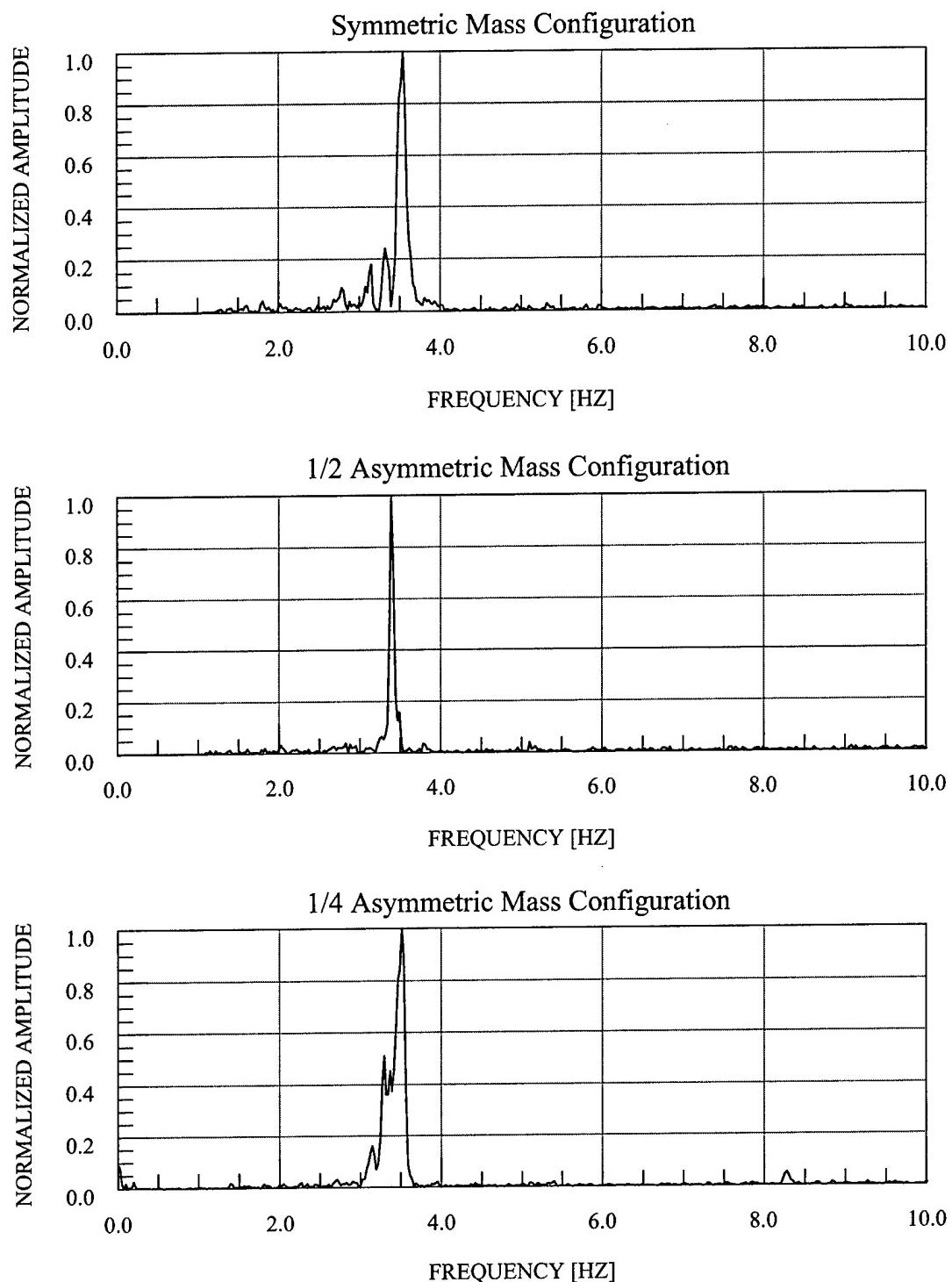


Figure 3.8 Fourier Transforms – Y-Axis Shaketable Response During X-Axis Uniaxial Simulations

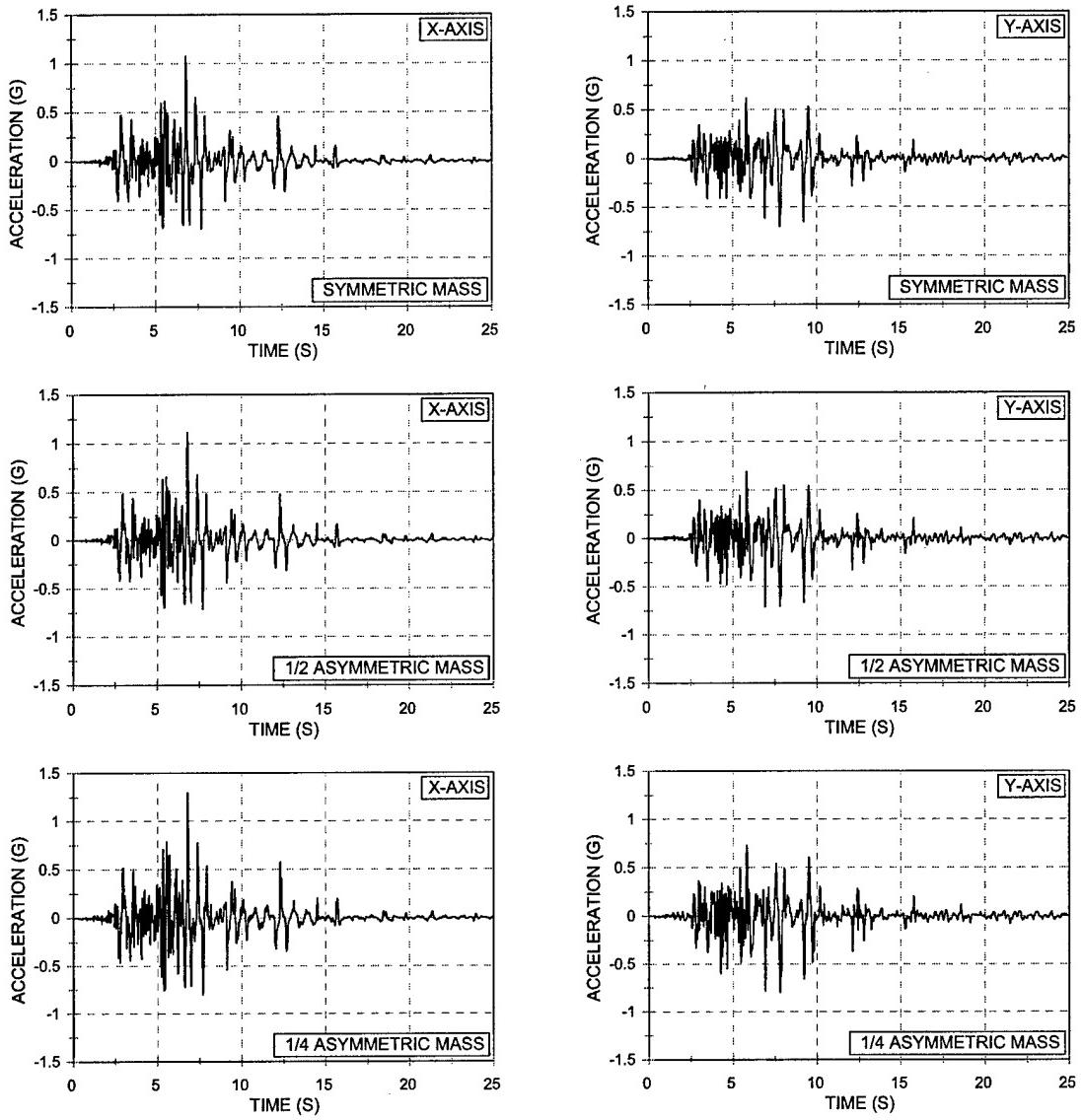


Figure 3.9 Shaketable Acceleration vs. Time – 100% Biaxial Imperial Valley
Symmetric Mass – 1/2 Asymmetric Mass – 1/4 Asymmetric Mass

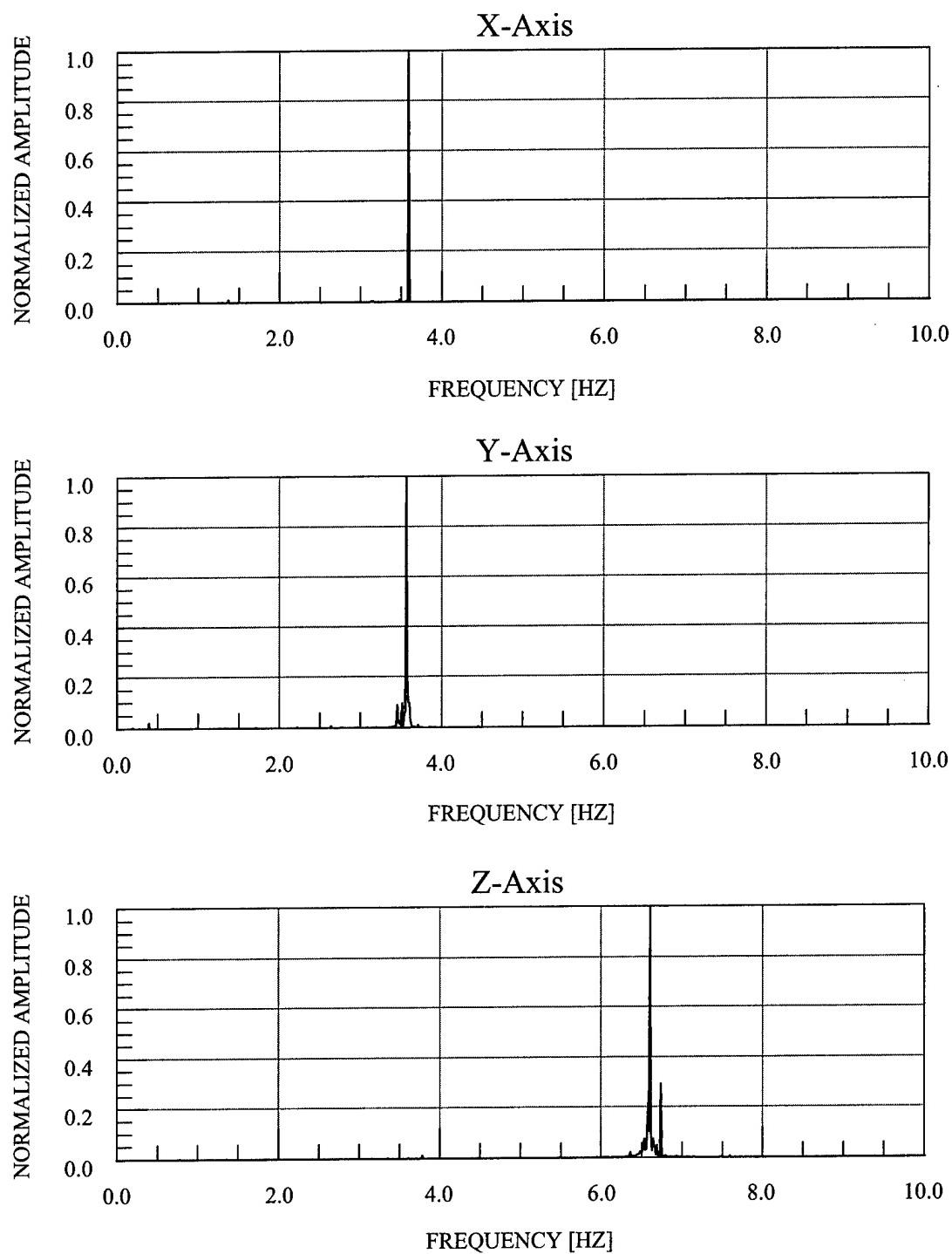


Figure 3.10 Typical White Noise Transfer Functions – Symmetric Mass

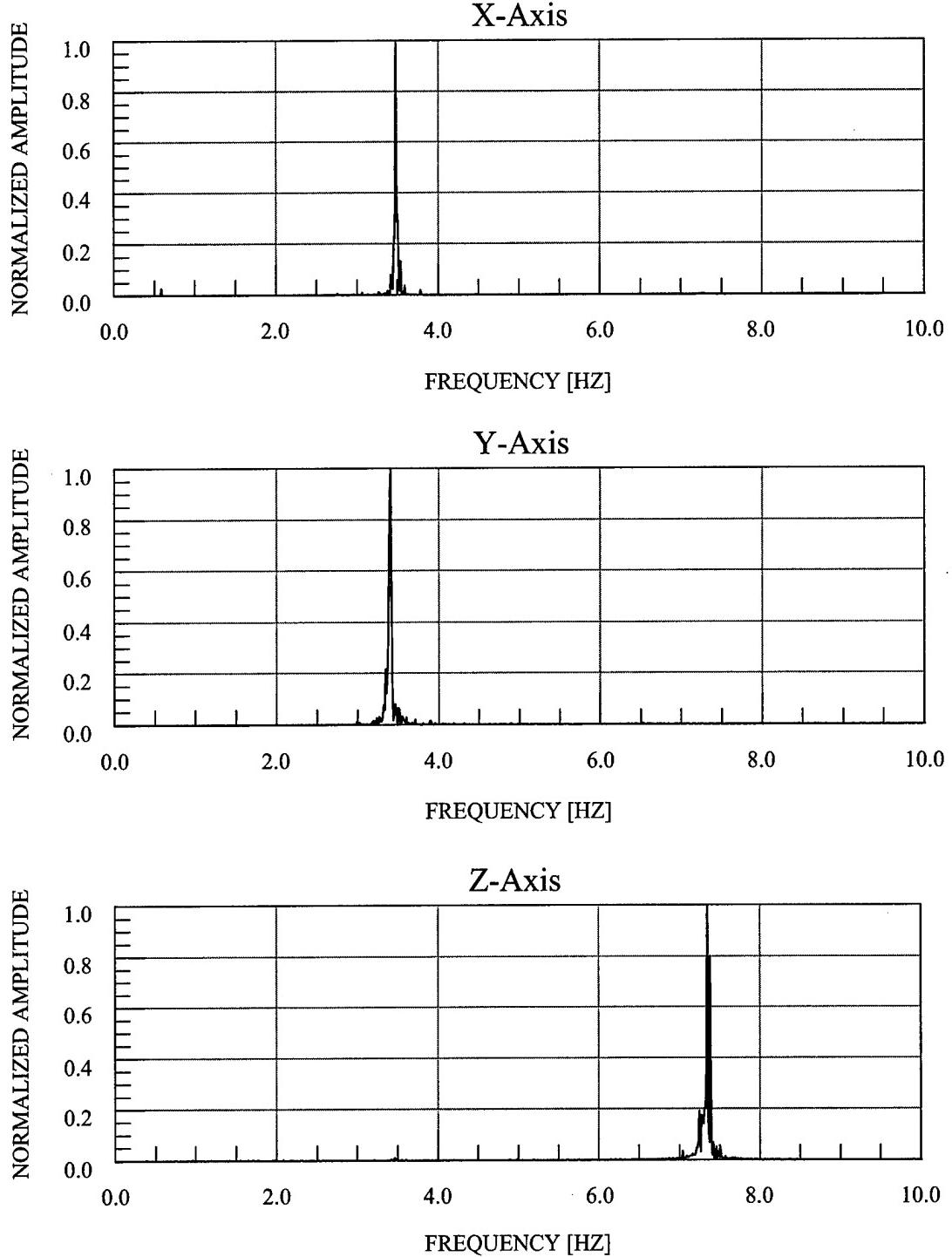


Figure 3.11 Typical White Noise Transfer Functions – 1/2 Asymmetric Mass

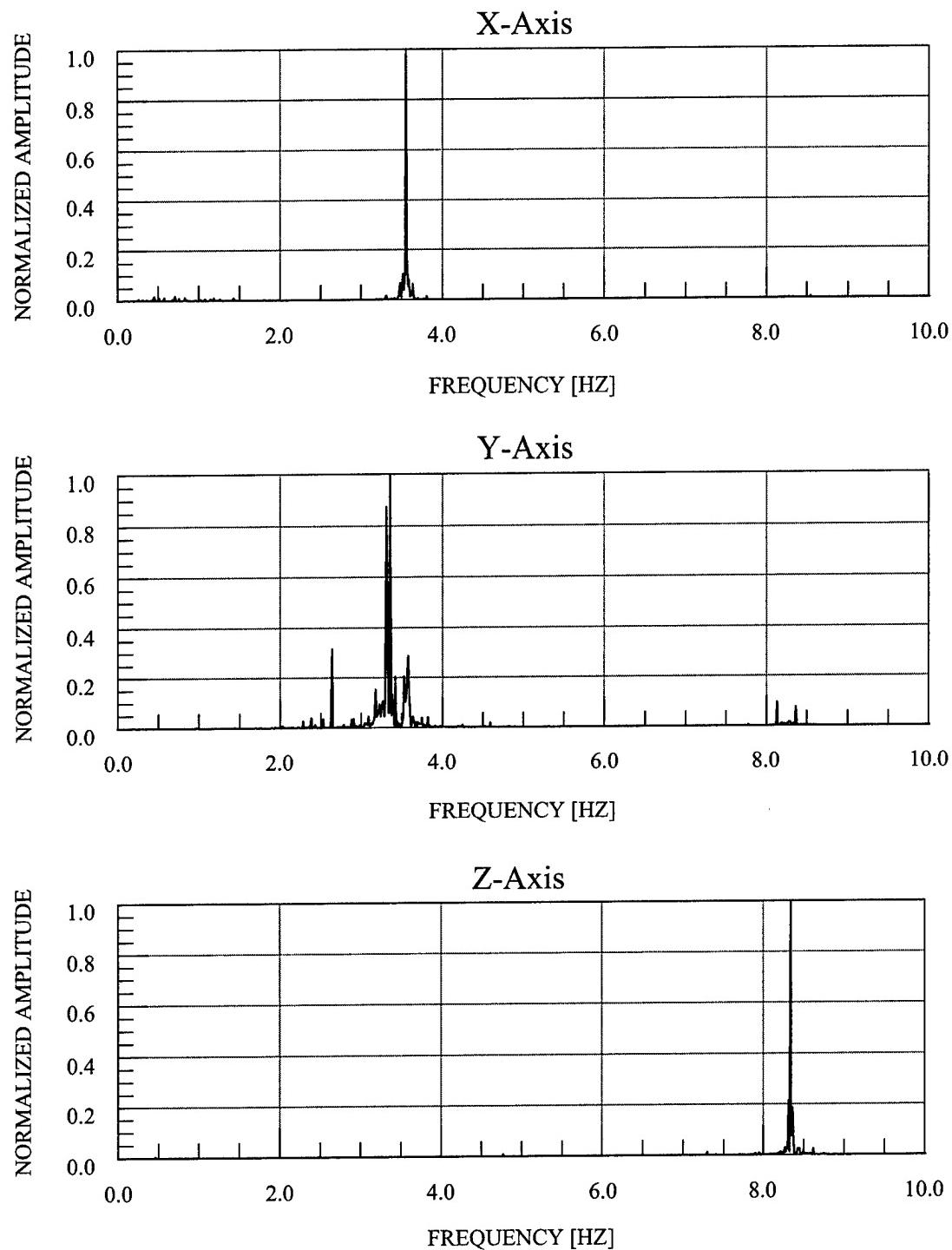


Figure 3.12 Typical White Noise Transfer Functions – 1/4 Asymmetric Mass

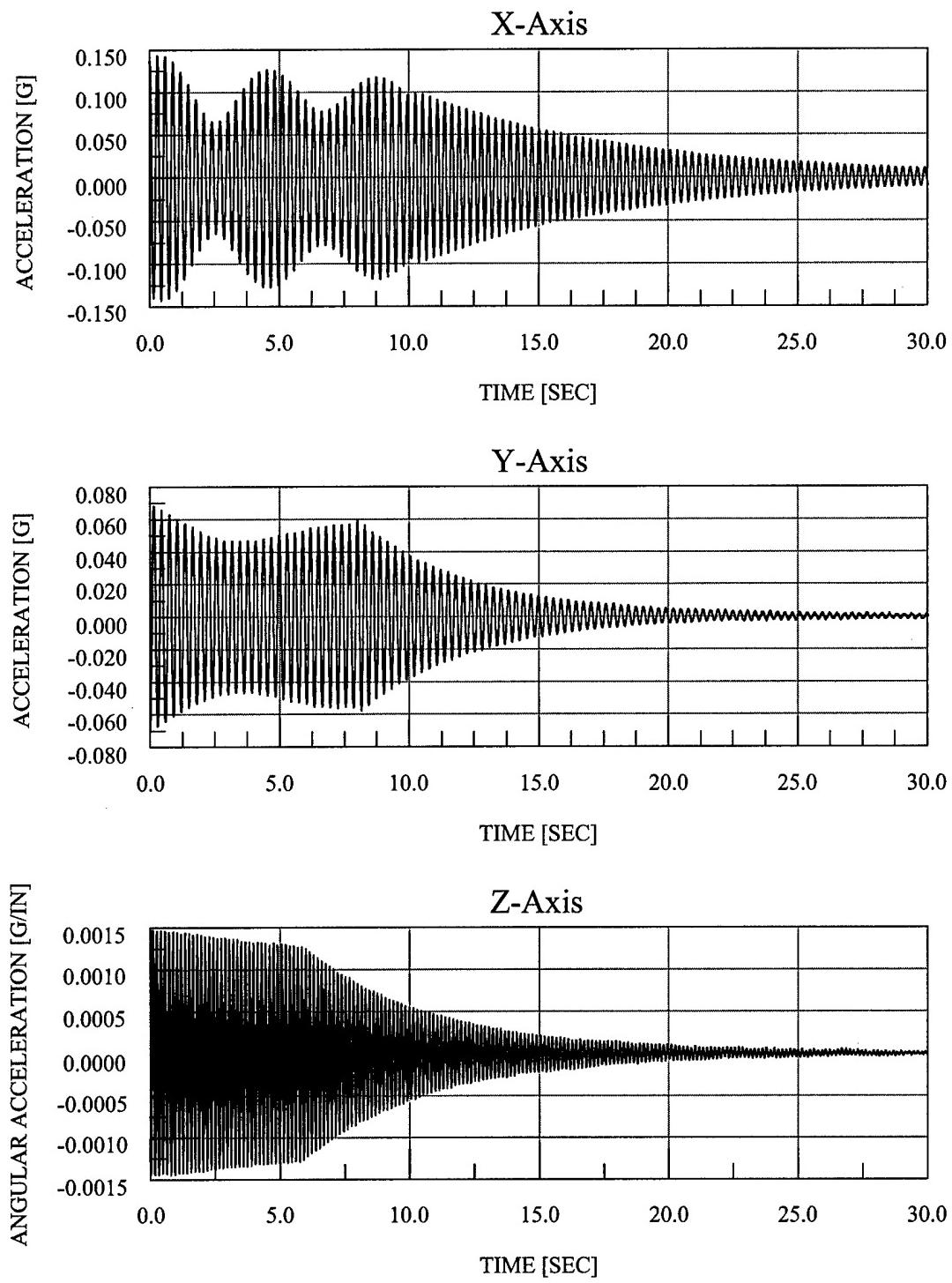


Figure 3.13 Typical Sine Decay Time Histories – Symmetric Mass

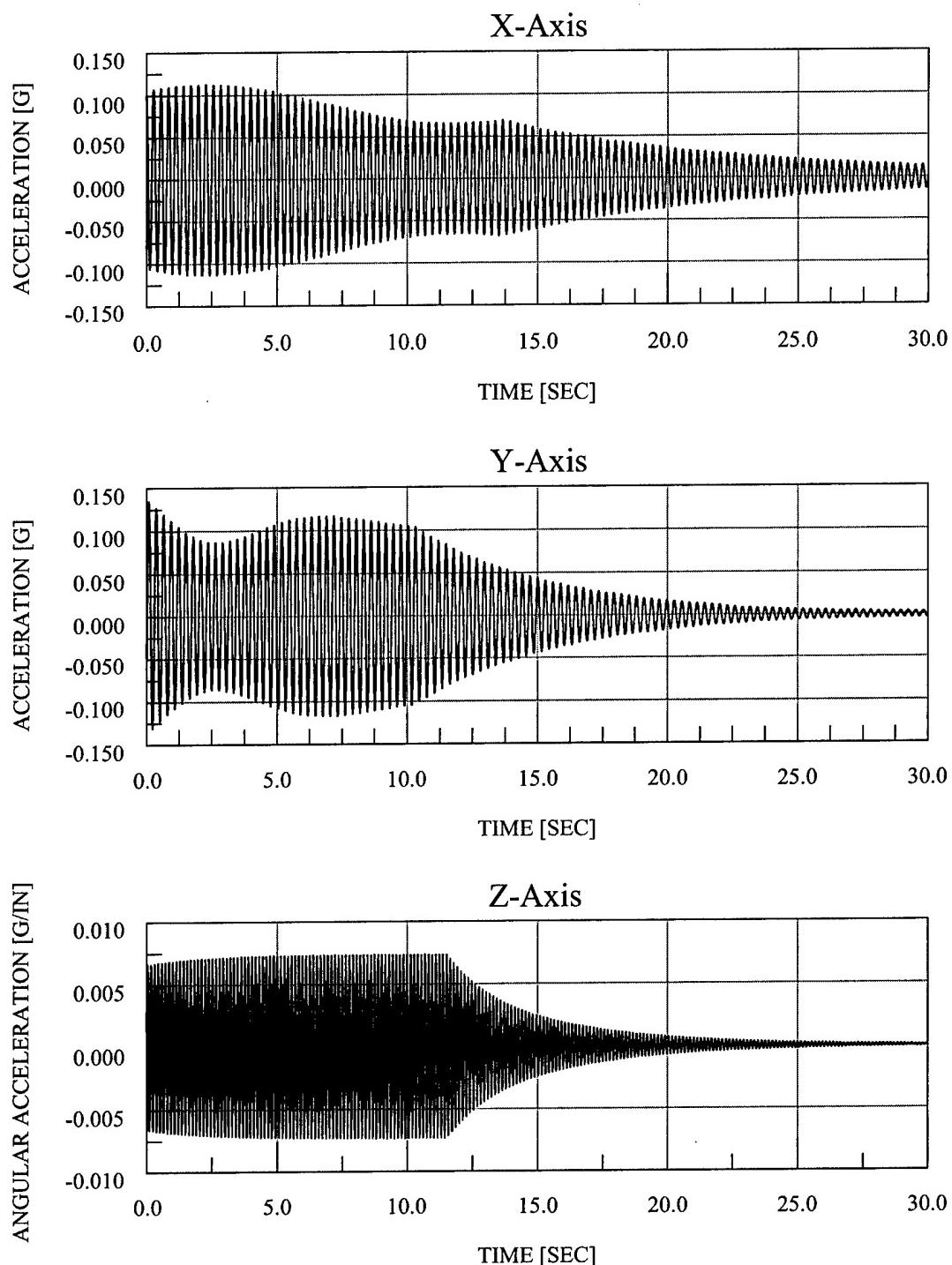


Figure 3.14 Typical Sine Decay Time Histories – 1/2 Asymmetric Mass

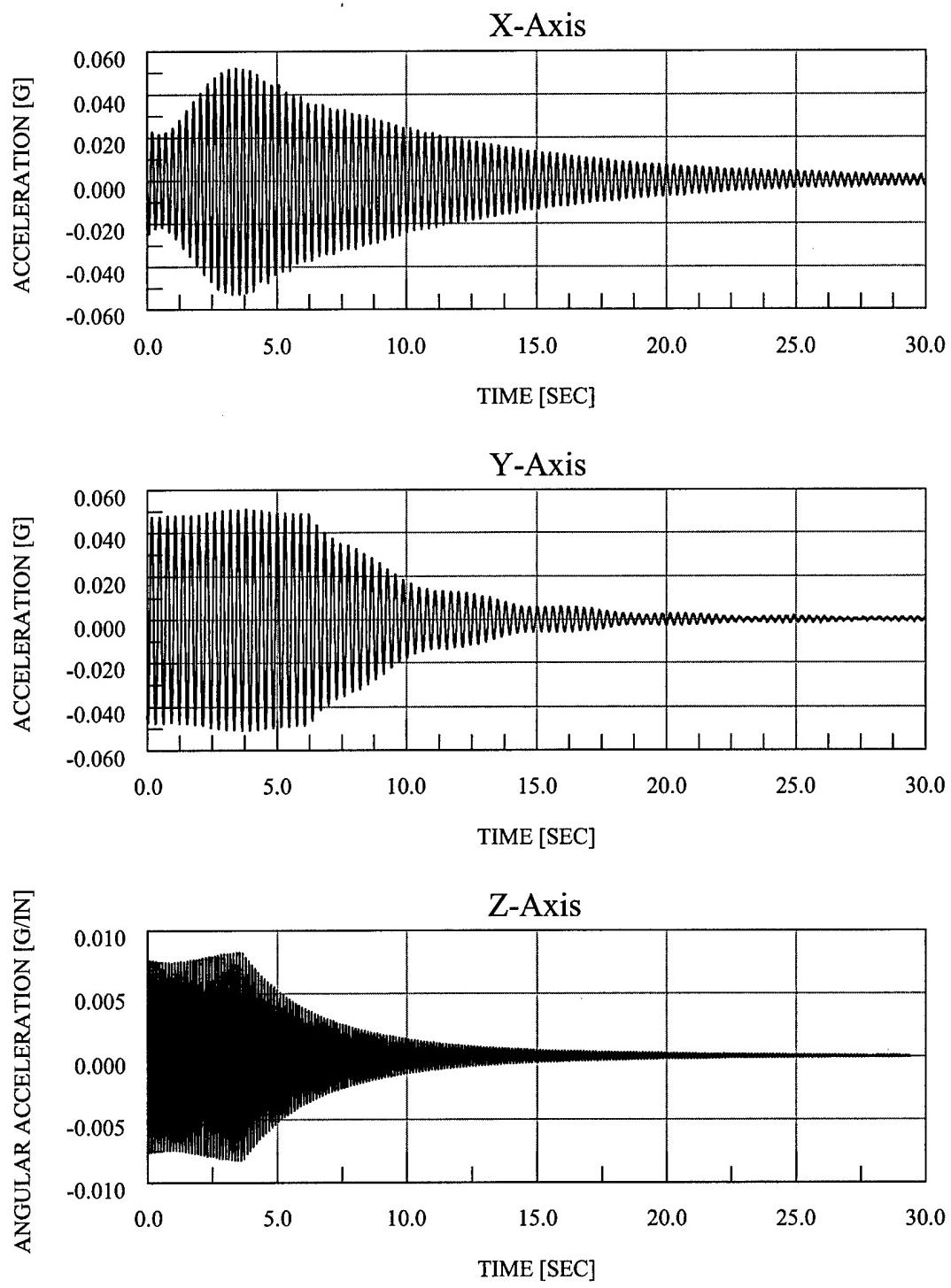


Figure 3.15 Typical Sine Decay Time Histories – 1/4 Asymmetric Mass

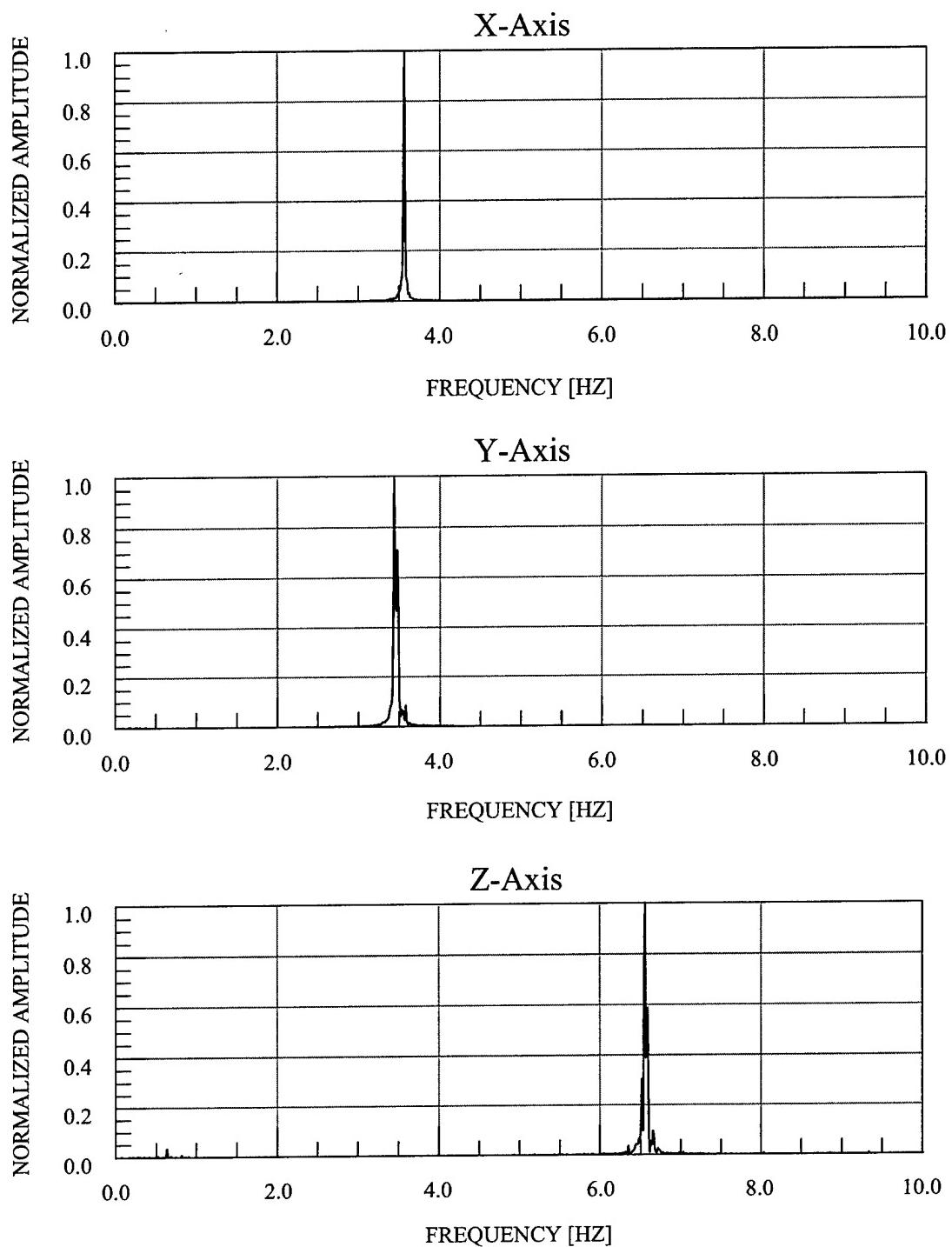


Figure 3.16 Typical Sine Sweep Transfer Functions – Symmetric Mass

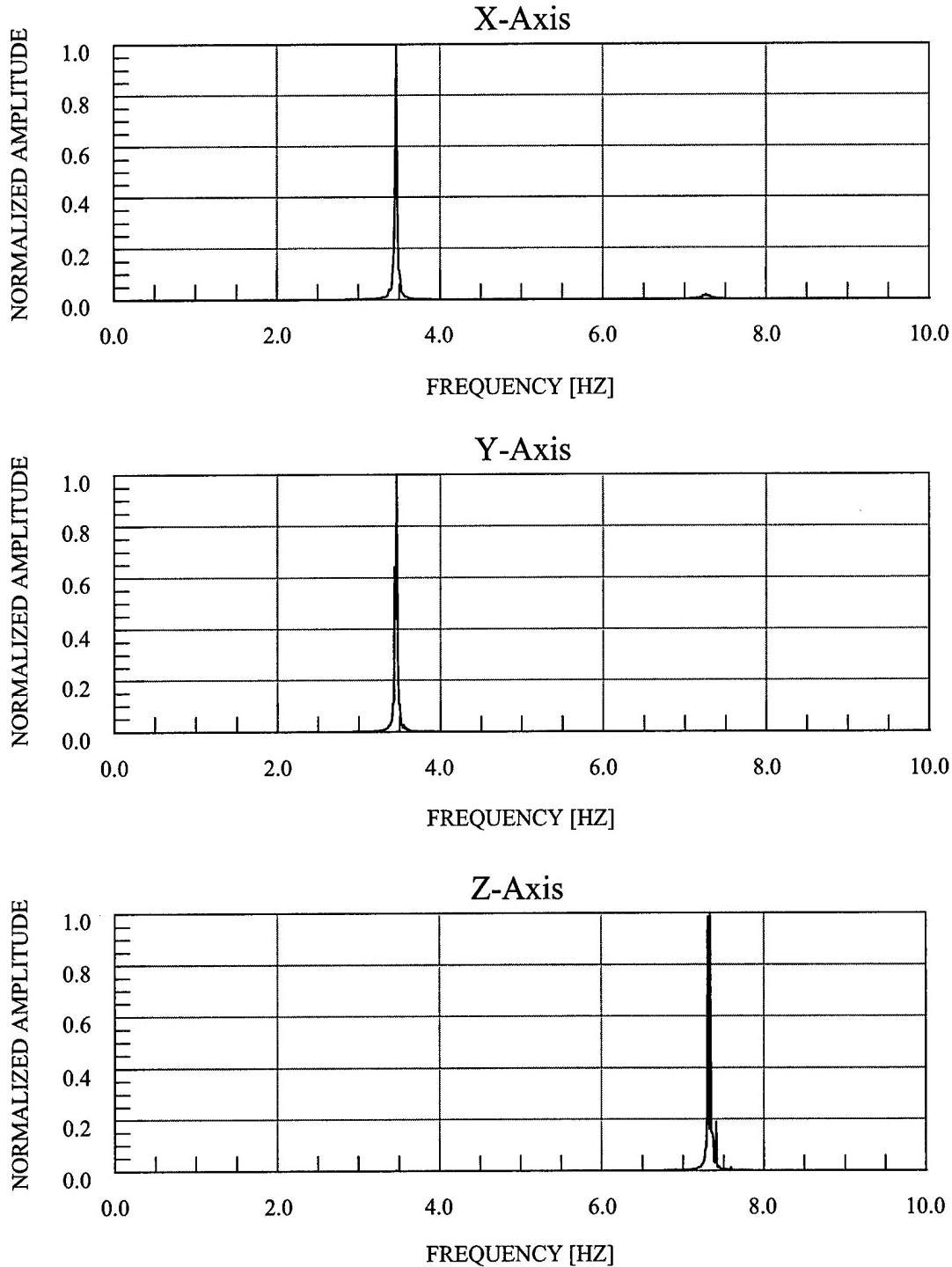


Figure 3.17 Typical Sine Sweep Transfer Functions – 1/2 Asymmetric Mass

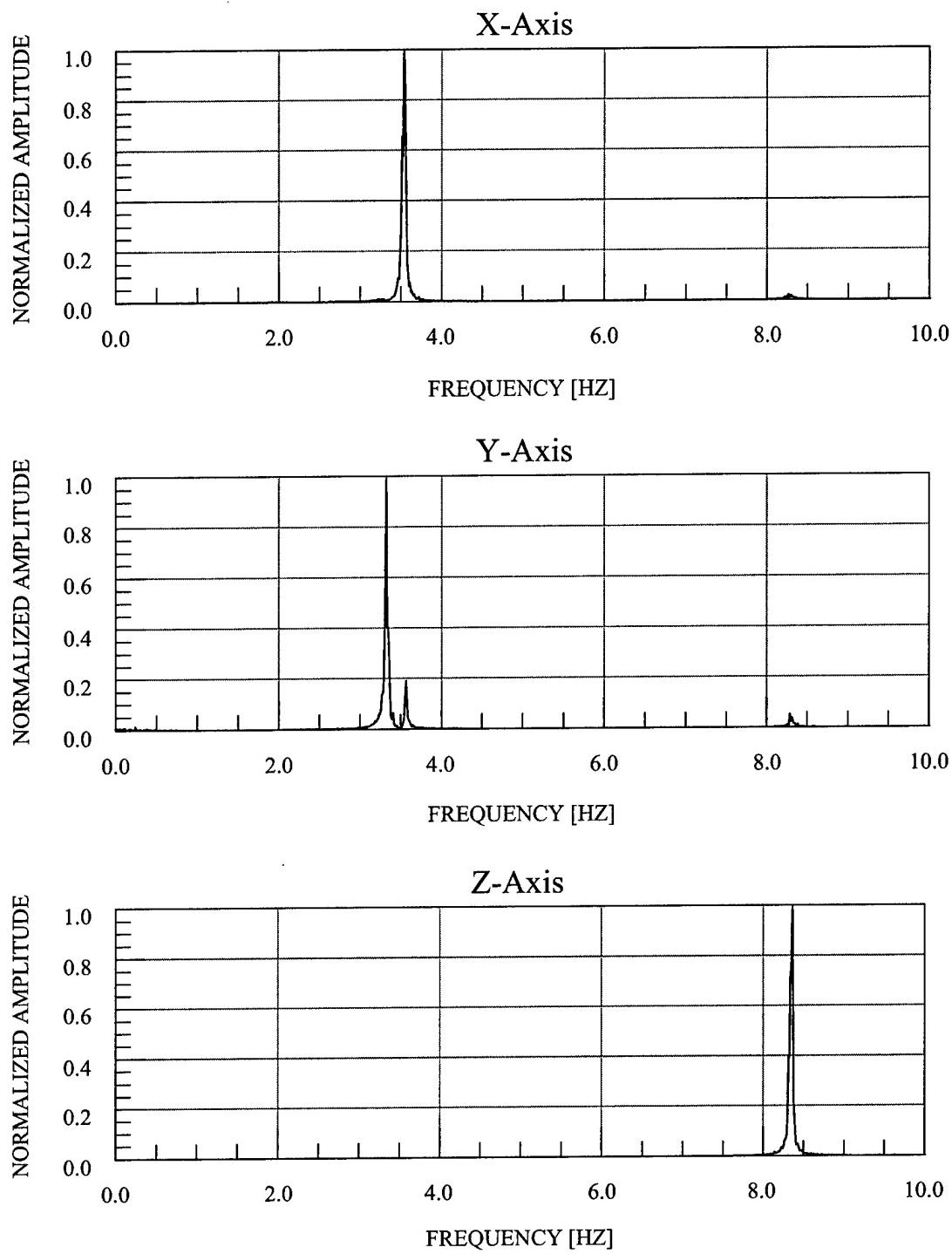


Figure 3.18 Typical Sine Sweep Transfer Functions – 1/4 Asymmetric Mass

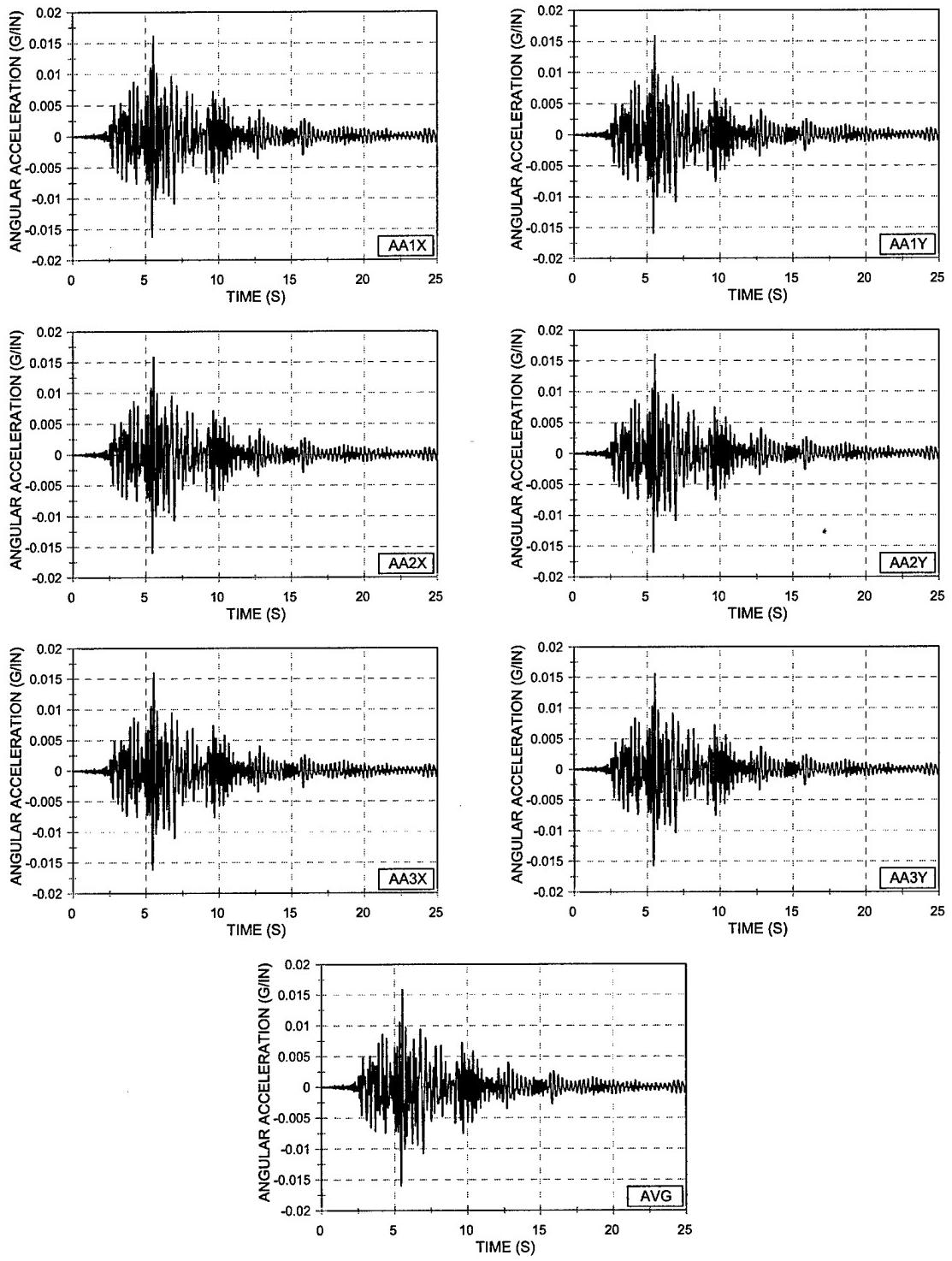
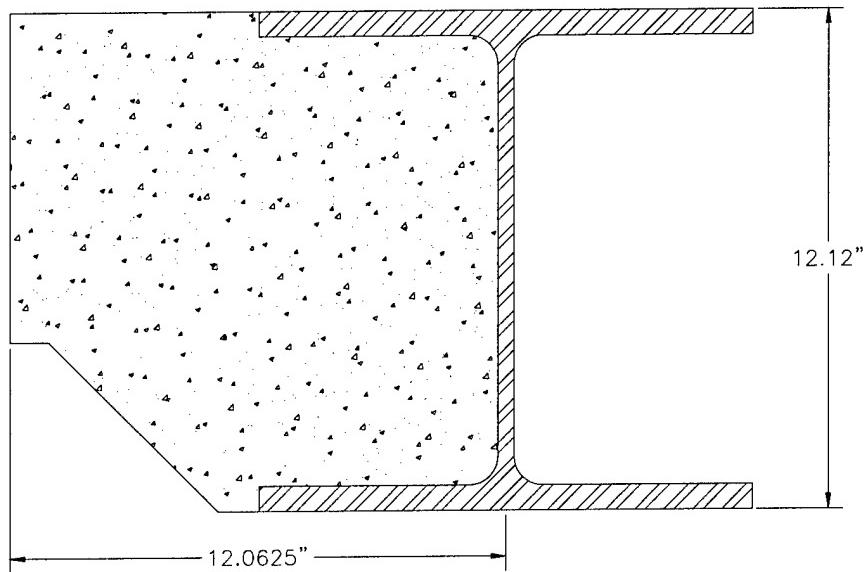
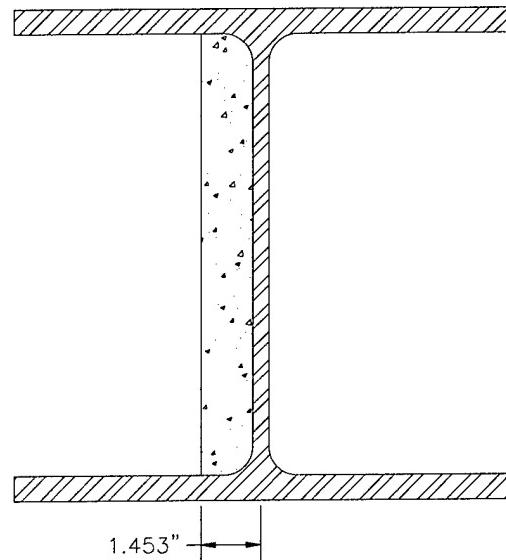


Figure 3.19 Angular Acceleration vs. Time – EQ 29
150% Biaxial Imperial Valley – 1/2 Asymmetric Mass



Original Section



Transformed Section

Figure 3.20 Test Structure Diaphragm Original Composite Section and Transformed Section

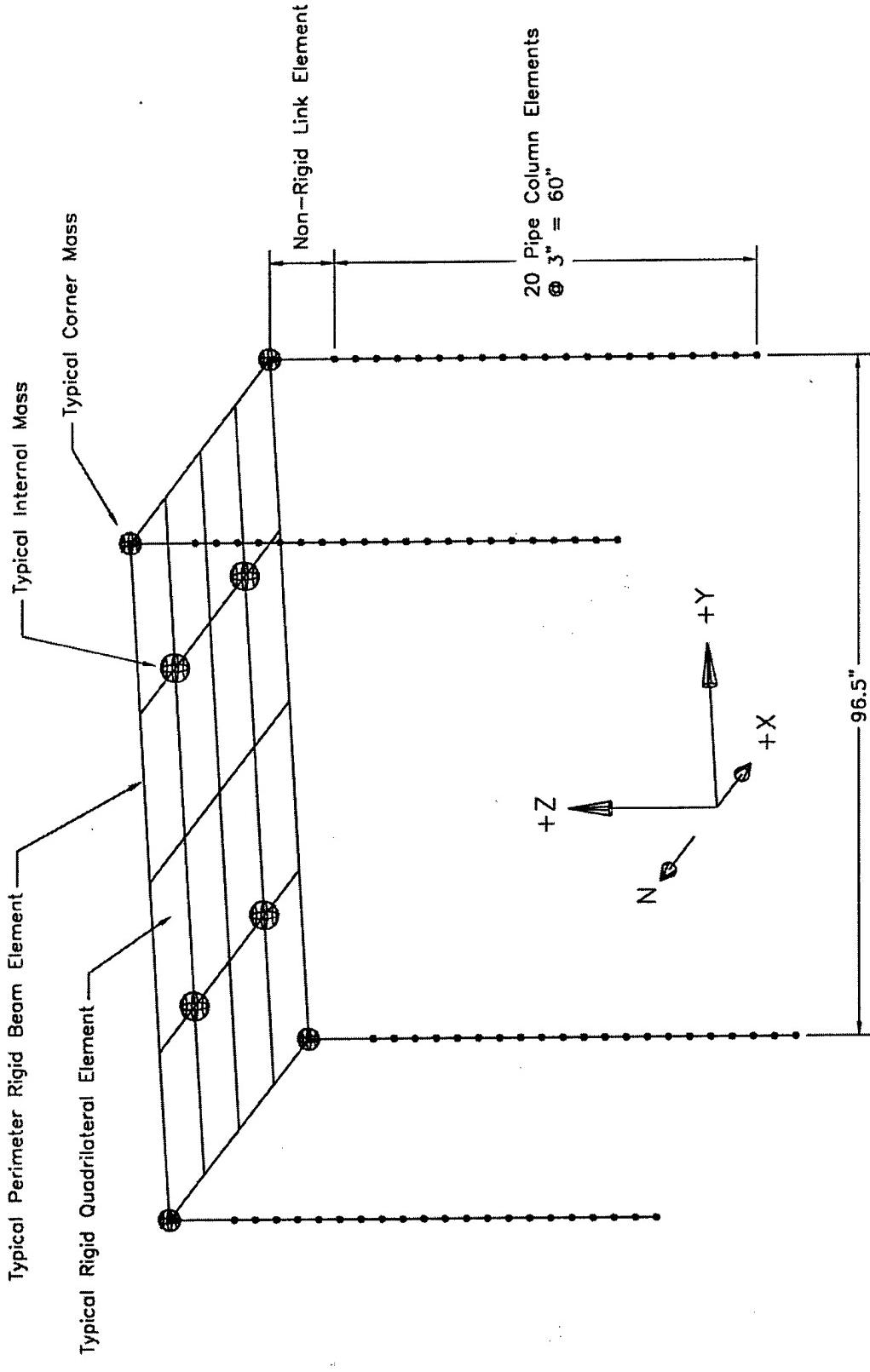


Figure 3.21 Typical Abaqus Test Structure Finite Element Model

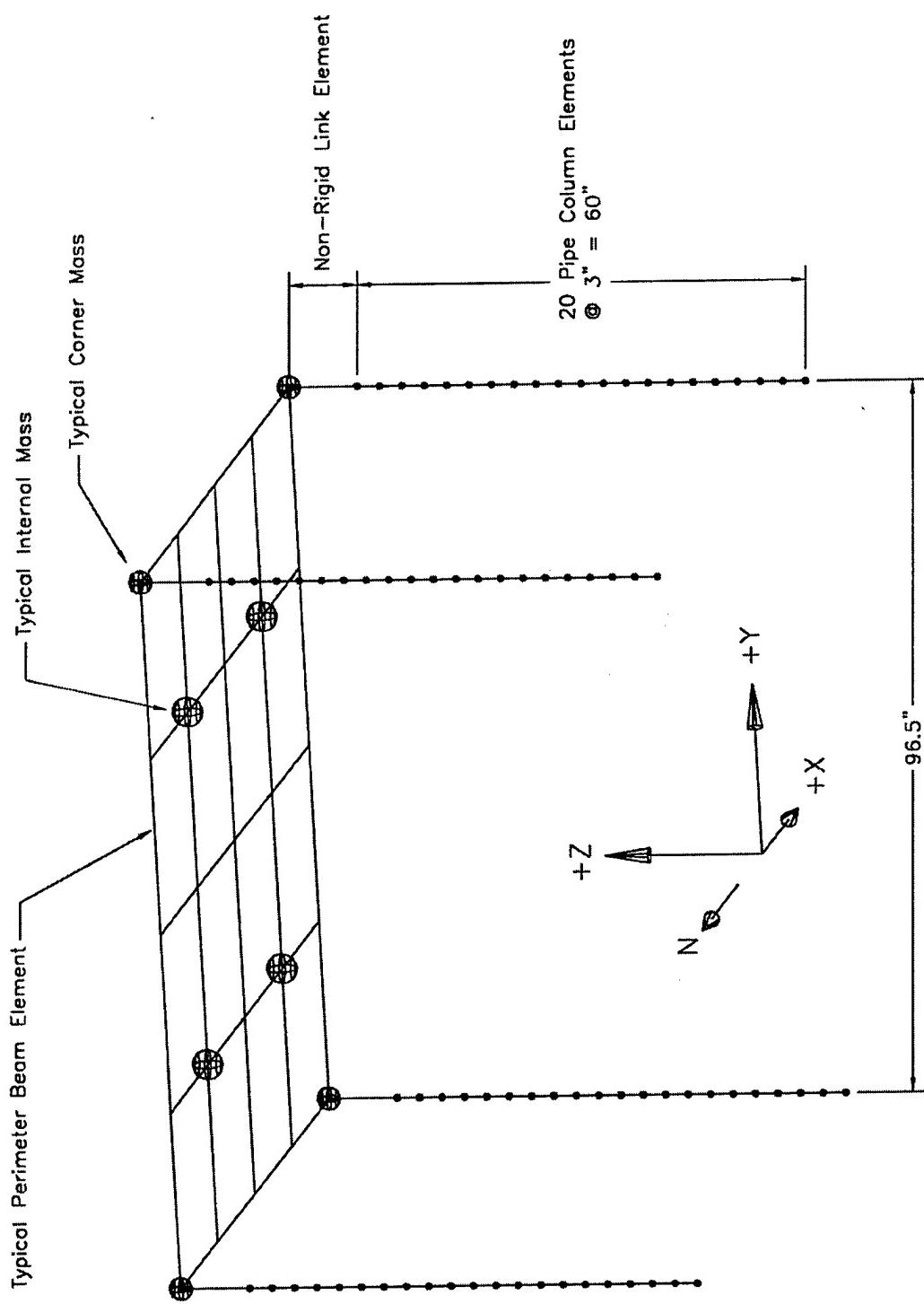


Figure 3.22 Typical Drain-3DX Test Structure Finite Element Model

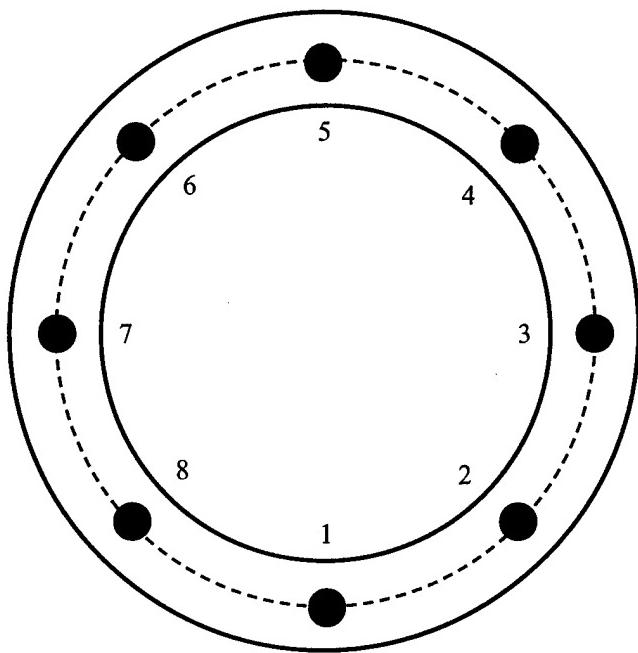


Figure 3.23 Abaqus Pipe Section Integration Points

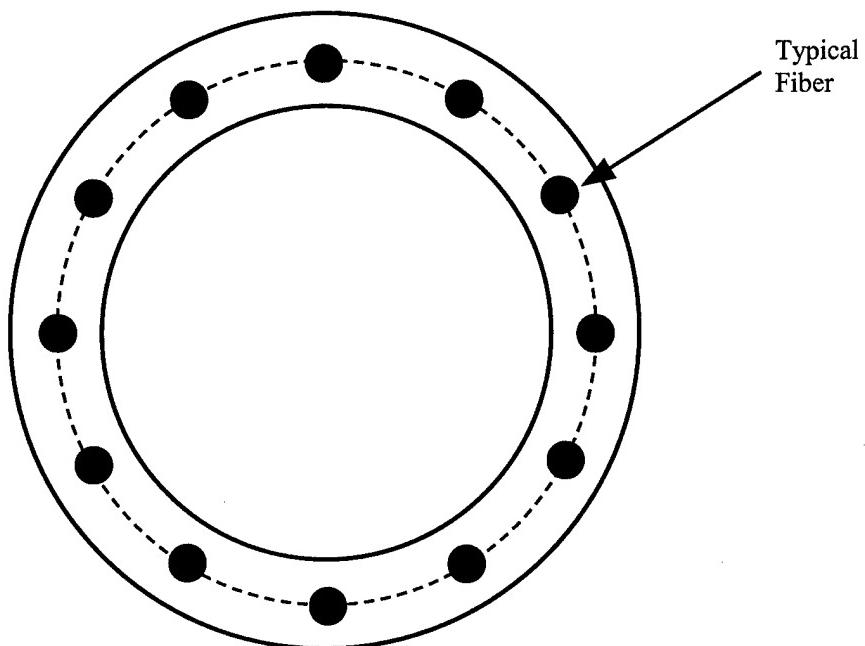


Figure 3.24 Drain-3DX Nonlinear Fiber Locations Relative to Pipe Column Cross-Section

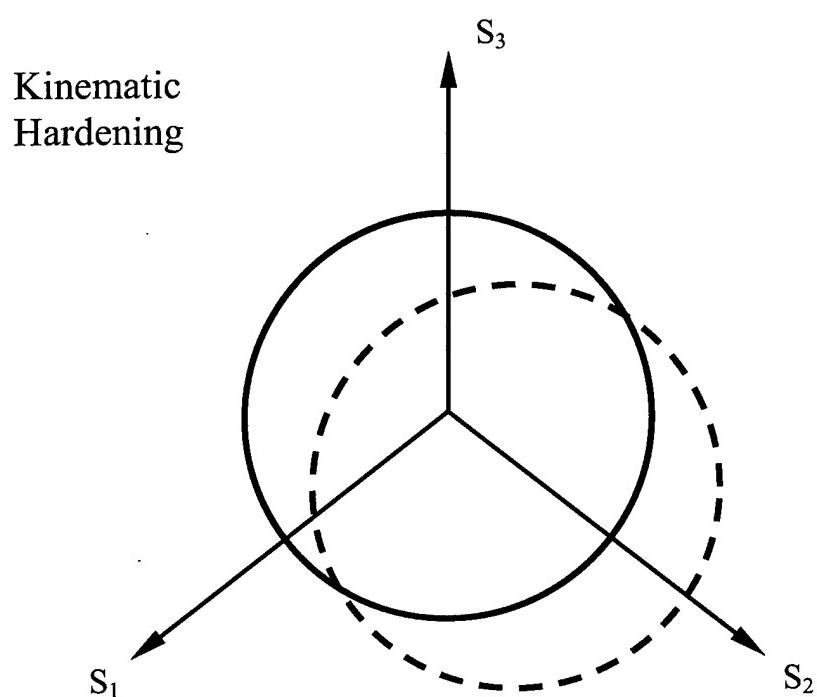
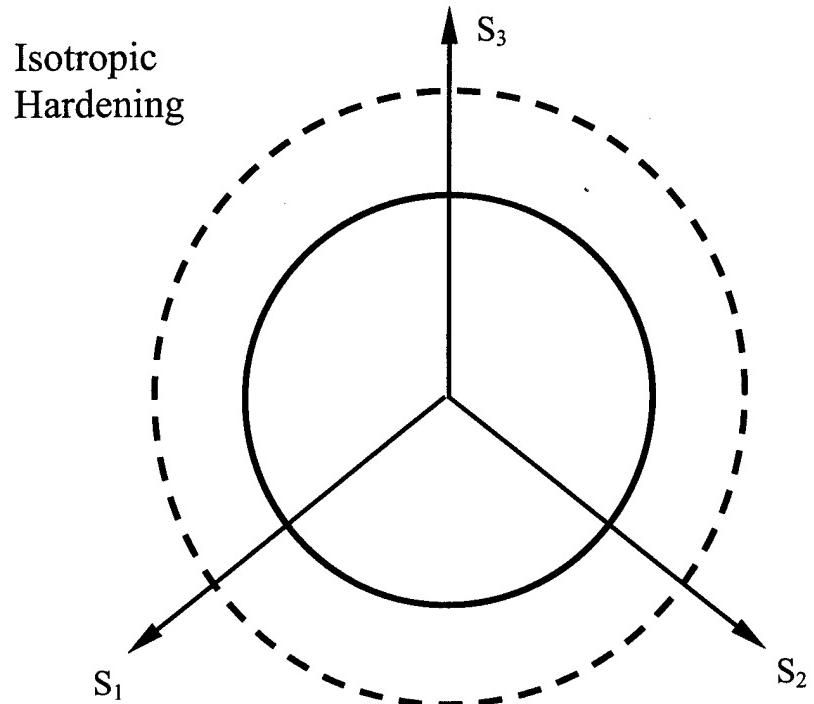


Figure 3.25 Schematic Illustration of Hardening Models

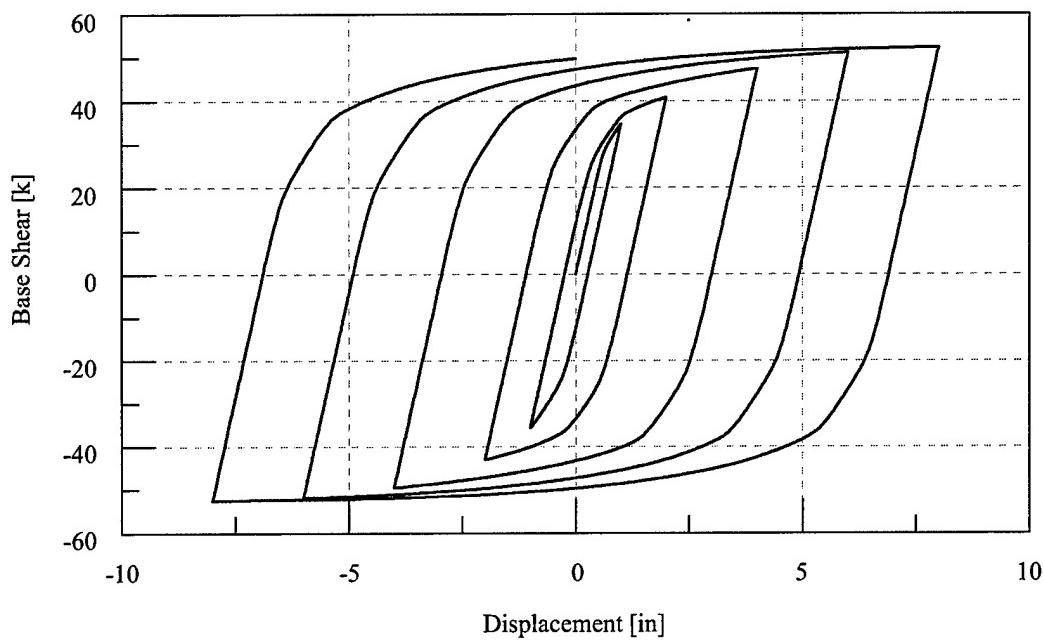


Figure 3.26 Combined Isotropic/Kinematic Hardening Material Model

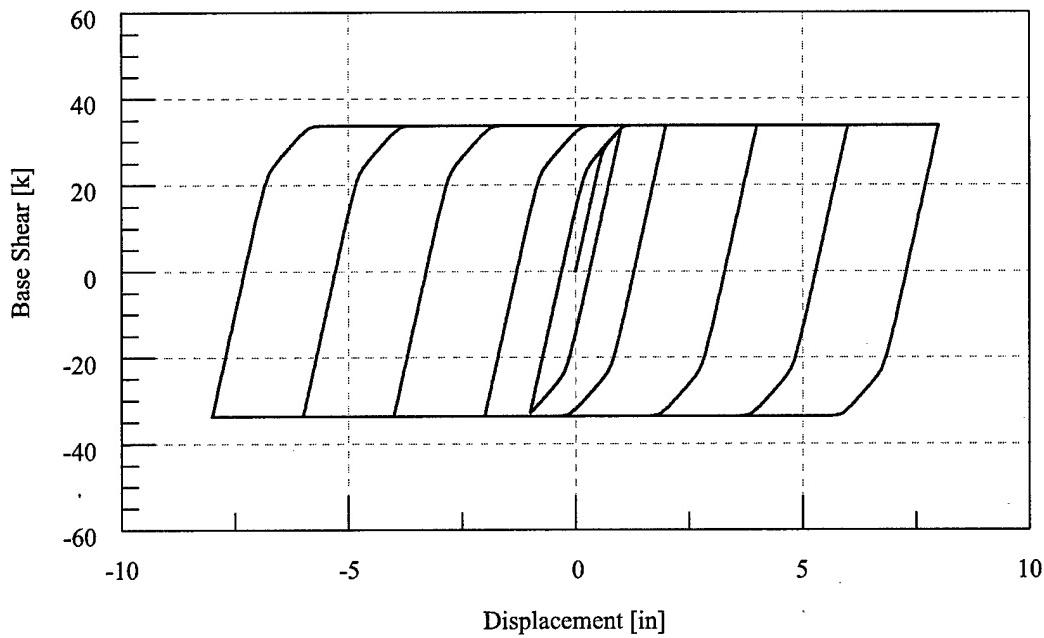


Figure 3.27 Perfect Plasticity Material Model

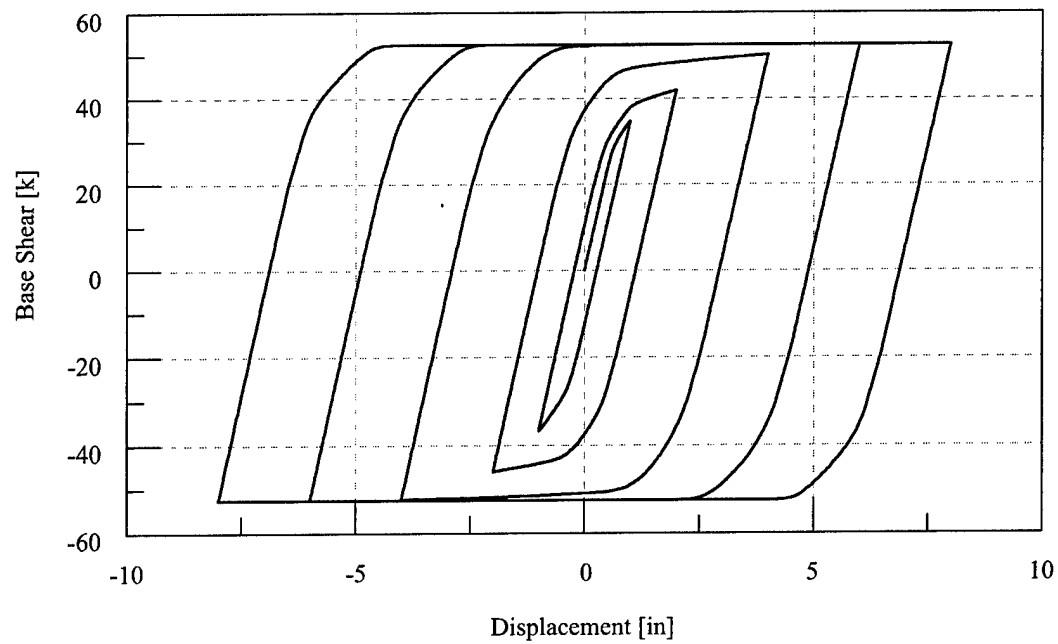


Figure 3.28 Isotropic Hardening Material Model

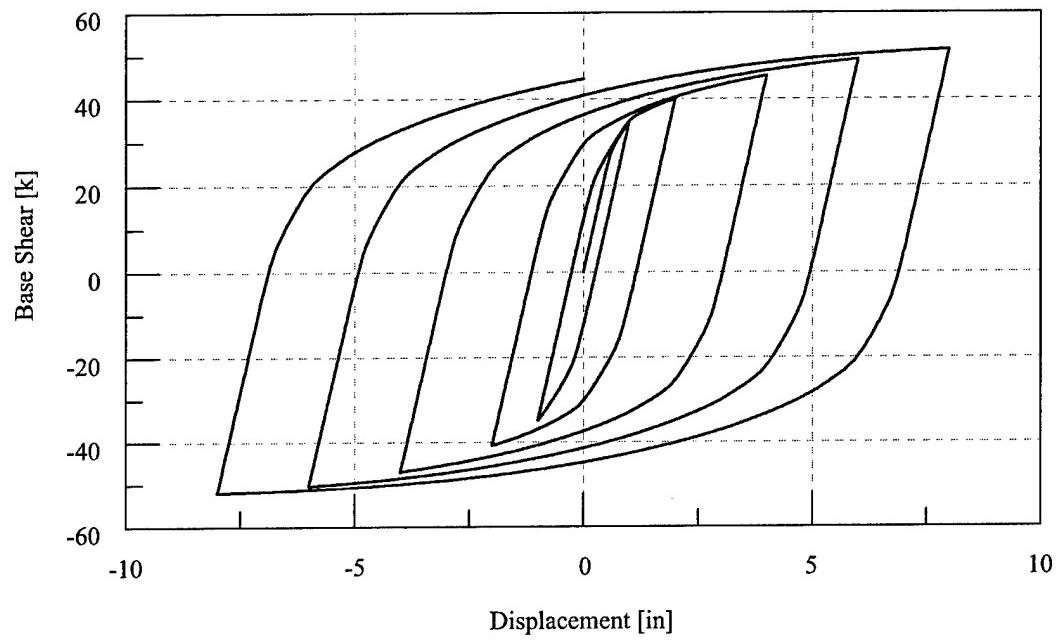


Figure 3.29 Kinematic Hardening Material Model

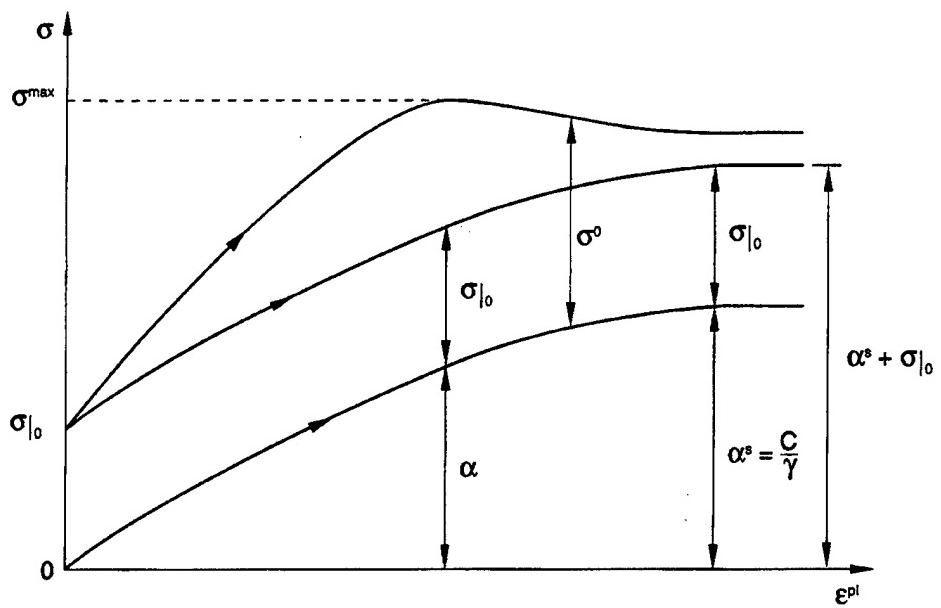


Figure 3.30 One-Dimensional Representation of the Nonlinear Isotropic/Kinematic Hardening Model

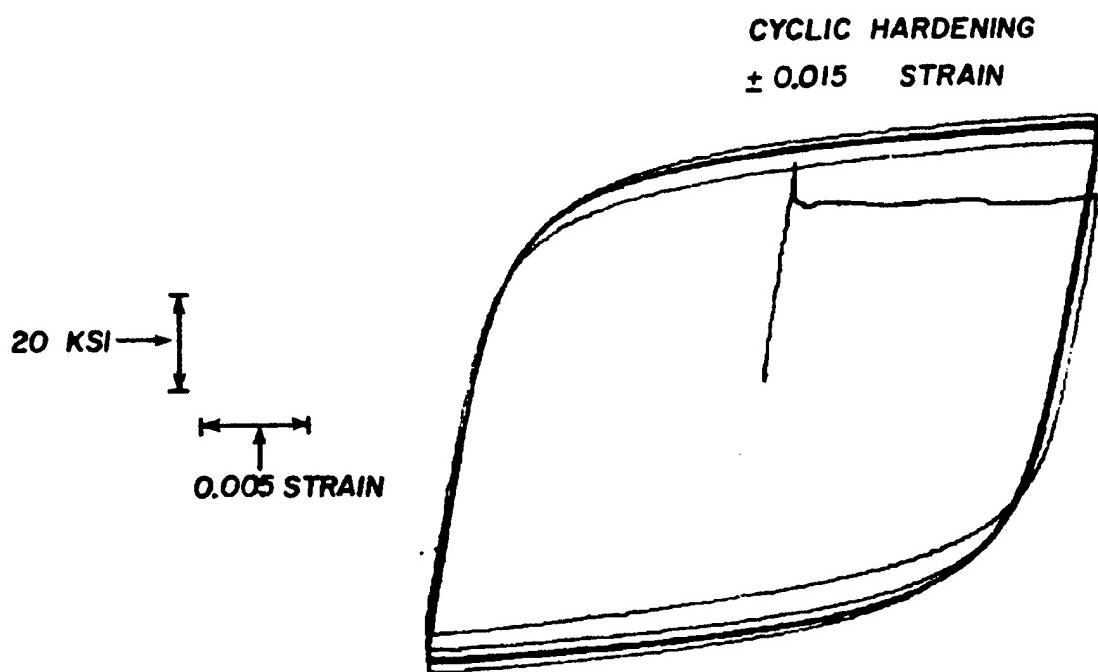


Figure 3.31 Cyclic Hardening Behavior of A 36 Steel
[Cycles 1, 2, 5, 10, 20, and 100 are plotted]

CHAPTER 4

EXPERIMENTAL AND ANALYTICAL RESPONSE OF TEST CONFIGURATION 1

This chapter provides a summary of the experimental test data and the finite element analysis results of Test Configuration 1. The first configuration, as seen in Figure 4.1, featured the masses loaded symmetrically on the diaphragm, and four 4" Extra-Strong Columns. The dynamic properties of the test structure in Test Configuration 1 are shown in Table 4.1.

Eleven earthquake simulations were performed with this test configuration, with the only difference during each simulation being the set of input ground motions. Although eleven simulations were performed, only four will be discussed here. The earthquake simulations using the Pacoima record as the input ground motion, EQ 04 – EQ 06, were performed to verify the preliminary analysis to select the reference set of input motions. The eighth earthquake simulation, EQ 08, saw a number of data channels fail, and beyond the eighth simulation the accumulated damage was significant enough to make any data analysis difficult. Thus, EQ 01 – EQ 03 and EQ 07 are the four earthquake simulations that will be discussed in this chapter. The base ground motion used in this test configuration and all subsequent test configurations was the 1979 Imperial Valley record at Bonds Corner. In addition to the earthquake simulations, characterization tests were performed to determine the dynamic properties of the model as described in Chapter 2. The complete test sequence for Test Configuration 1 is shown in Table 4.2.

The first three earthquake simulations, EQ 01 with 25% X-Axis only [$\text{PGA}_X = 0.238 \text{ g}$], EQ 02 with 25% Y-Axis only [$\text{PGA}_Y = 0.162 \text{ g}$], and EQ 03 with 25% Biaxial input motions [$\text{PGA}_X = 0.232 \text{ g}$ and $\text{PGA}_Y = 0.160 \text{ g}$], were intended to feature elastic behavior only. During this and all subsequent test configurations, the earthquake simulations utilizing only the X-Axis or the Y-Axis ground motion component may often be referred to as *uniaxial* simulations, while the simulations utilizing both X-Axis and Y-Axis ground motion components may be referred to as *biaxial* simulations. During the simulations, the structure slightly exceeded the yield displacement in the X direction during EQ 01 and EQ 03. The fourth simulation, EQ 07, using

100% Y-Axis input motions [$\text{PGA}_Y = 0.678 \text{ g}$], was the initial test with significant inelastic response for this configuration. As discussed in Chapter 3, due to the interaction between the response of the structure and the table motion, the PGAs of the 25% earthquake simulations are not exactly the same, and the PGAs of the 100% simulation are not exactly four times as large as those for the 25% simulation. This was found to be true in all subsequent test configurations, to varying degrees.

This chapter summarizes response data of the test structure during the earthquake simulations and the dynamic characterization tests. Summaries of test model accelerations, displacements, torsional moments, overturning moments, column end moments, and base shears are provided. Representative data have been selected for presentation in this chapter to describe the response of the model.

4.1 OBSERVED STRUCTURAL RESPONSE

The three acceleration components needed to describe the diaphragm motion are the X-Axis and Y-Axis accelerations, and the angular acceleration response about the Z-Axis. The three displacement components needed to describe the diaphragm motion are the X-Axis and Y-Axis relative displacements, and the rotation about the Z-Axis. The inertial forces of interest with respect to the structure will be those corresponding to the three degrees-of-freedom of the diaphragm, the inertial forces in the X and Y directions, and the inertial moment about the Z-Axis. As discussed in Chapter 3, the inertial forces are computed using Equations 3.4, 3.5, and 3.6. The aforementioned acceleration components, displacement components, and inertial forces will be the primary means of describing the structural response for this and all subsequent test configurations.

The diaphragm acceleration and displacement time history responses for the 25% X-Axis simulation are shown in Figure 4.2. The base shear vs. displacement and torque vs. rotation are shown in Figure 4.3. Similar responses for the 25% Y-Axis simulation are shown in Figures 4.4 and 4.5. Results for the 25% Biaxial simulation are shown in Figures 4.6 and 4.7. The responses for the 100% Y-Axis simulation are shown in Figures 4.8 and 4.9.

Table 4.3 lists the maximum recorded diaphragm relative displacements and their corresponding PGA for each of the four earthquake simulations performed in this test configuration. Table 4.4 lists the maximum diaphragm accelerations and their corresponding PGA for each of the four earthquake simulations. Table 4.5 lists the maximum base shears, torsional moments, and overturning moments. Table 4.6 lists the maximum column end moments in the X and Y directions for each column. Table 4.7 lists the maximum column end shears in the X and Y directions for each column. The response data listed in Tables 4.3 – 4.7 are also presented for all subsequent test configurations in each of the following chapters.

4.2 OBSERVED RESPONSE DISCUSSION

In order to better interpret the response data, finite element pushover analyses were performed to determine the lateral force-deformation and torsional moment-rotation behavior of the model structure. Figure 4.10 shows the calculated force-deformation behavior of the structure in the X and Y directions. Because the model structure has different natural frequencies in the X and Y directions, despite the symmetry of the structure, the stiffness and thus the force-deformation behavior along each axis are also different. In the X direction, the model has a yield displacement of 0.46 inches at a yield force of 21.35 kips. In the Y direction, the model has a yield displacement of 0.49 inches at a yield force of 21.35 kips. Figure 4.11 shows the calculated torsional moment-rotation behavior of the structure, or the force-deformation behavior about the Z-axis. The model has a yield rotation of 0.0065 radians at a yield moment of 1457 kip*inches. Also, elastic response spectra of the recorded table motions for EQ 01 – EQ 03 and EQ 07 are shown in Figures 4.12 – 4.15, respectively. The modal frequencies for this configuration with respect to the response spectra are indicated in Figures 4.12 – 4.15 as well.

The first earthquake simulation for this configuration, EQ 01, features 25% Imperial Valley input motion in the X-Axis only [$\text{PGA}_X = 0.238 \text{ g}$]. Time history plots of the structural response are shown in Figure 4.2. The peak displacements of the structure were 0.535 inches in the X direction, which is slightly greater than the yield displacement of 0.46 inches, and 0.087 inches in the Y direction, which is well below the yield displacement of 0.49 inches. The peak displacement predicted by static analysis for EQ 01, using the elastic response spectrum, is 0.524 inches along the X-Axis, with no displacement predicted along the Y-Axis. The peak rotation of the structure was 0.29×10^{-3} radians, also well below the yield rotation of 6.5×10^{-3} radians. The

static analysis predicts no rotation. Further, the displacement time histories indicate no residual displacement or permanent deformation. Also verifying the inelastic response in the X direction and the elastic response in the Y direction and torsionally are the peak base shears, which are 24.53 kips in the X direction, 3.45 kips in the Y direction, and 38.30 kip*inches about the vertical axis. The peak base shear in the X direction is greater than the yield shear, 21.35 kips, while the peak base shear in the Y direction is less than the yield shear of 21.35 kips. The peak moment is less than the torsional yield moment of 1457 kip*inches. Figure 4.3 shows the base shear vs. displacement plots, which are both tight and linear, apparently indicating no yielding. The appearance of elastic response in the shear vs. displacement plot for the X-Axis, despite the structure exceeding the yield displacement, arises from the very gradual reduction in stiffness of the structure after initial yield. This can be seen in the force vs. deformation plot in Figure 4.10. Also, although the input motion for EQ 01 was along the X-Axis only, Figure 4.2 shows that the structure did have a displacement response in the Y-Axis. The oscillatory nature of the response, combined with the fact that the modal frequency in the Y-Axis, 3.445 Hz, is so close to the modal frequency in the X-Axis, 3.565 Hz, leads to the conclusion that the response along the Y-Axis is a resonant vibration caused by the motion along the X-Axis. This resonant vibration is present not only in the Y-Axis diaphragm motion but also the Y-Axis table motion, in which the latter is a product of the table control problems discussed in Chapter 3. This phenomenon was observed during many of the subsequent earthquake simulations. This motion is not predicted at all by the static analysis. In EQ 01, with complete mass symmetry, a torsional effect is not expected, and it appears from the rotation time history in Figure 4.2 that the measured rotation is predominantly a combination of noise in the data acquisition system and a resonant vibration.

In EQ 02 the model is subjected to a 25% Y-Axis input motion [$\text{PGA}_Y = 0.162 \text{ g}$]. Time history plots of the structural response are shown in Figure 4.4. The peak displacements of the structure were 0.377 inches in the Y direction and 0.041 inches in the X direction, which are both below the yield displacements of 0.49 inches and 0.46 inches, respectively. The peak displacement predicted by static analysis for EQ 02 is 0.355 inches in the Y direction, with no displacements predicted along the X-Axis. The peak rotation of the structure was 0.40×10^{-3} radians, also well below the yield rotation of 6.5×10^{-3} radians. The static analysis predicts no rotation. Further, the displacement time histories indicate no permanent deformation. In EQ 02, with no eccentricity, a torsional effect is not expected, and it appears from the rotation time history in Figure 4.4 that the measured rotation is predominantly a resonant vibration response. Also, the displacement time history along the X-Axis in Figure 4.4 seems to indicate that the measured X-

Axis displacement is a resonant vibration response, as seen along the Y-Axis in EQ 01 and discussed above. Both the torsional and X-Axis motion appear to be products of the shaketable motion control problem discussed in Chapter 3. Although ground motion was input to the shaketable in the Y direction only, there is a small but nonzero table motion in the X-Axis. An FFT of the X-Axis table motion indicated that the table is vibrating at the Y-Axis modal frequency of the structure. An FFT analysis also indicated that the small but nonzero torsional motion of the shaketable is also a vibration at the Y-Axis modal frequency. The aforementioned X-Axis and torsional motion of the diaphragm are also predominantly vibratory at the same frequency as the X-Axis and torsional table motions. This general phenomenon was seen to be present throughout the study. Inexactitudes of the experimental structure are also possible contributors to this motion, such as orientation of the structure on the shaketable and the mass and stiffness symmetry. The peak base shears and peak torsional moment are 17.18 kips in the Y direction, 1.97 kips in the X direction, and 39.93 kip*inches about the vertical axis. The peak base shears are less than the yield shears, 21.35 kips in the Y and X directions, and the peak moment is less than the torsional yield moment, 1457 kip*inches. Figure 4.5 shows the base shear vs. displacement plots and torsional moment vs. rotation plot, which are tight and linear.

The third earthquake simulation for this configuration, EQ 03, features 25% Imperial Valley input motion along both the X-Axis and Y-Axis [$\text{PGA}_X = 0.232 \text{ g}$ and $\text{PGA}_Y = 0.160 \text{ g}$]. Time history plots of the structural response are shown in Figure 4.6. The peak displacements of the structure were 0.488 inches in the X direction, which is slightly greater than the yield displacement of 0.46 inches, and 0.414 inches in the Y direction, which is slightly less than the yield displacement of 0.49 inches. The peak displacements predicted by static analysis for EQ 27 are 0.485 inches along the X-Axis and 0.404 inches along the Y-Axis. The peak rotation of the structure was 0.79×10^{-3} radians, well below the yield rotation of 6.5×10^{-3} radians. No rotation is predicted by static analysis. Thus, the displacements and rotation indicate that the structural response for this simulation remained elastic torsionally and along the Y-Axis, but was slightly inelastic along the X-Axis. Further, although the structure exceeded the yield displacement along the X-Axis, the displacement time histories indicate no residual displacement or permanent deformation. As in EQ 01, this can be attributed to the very gradual decrease in the stiffness of the structure after initial yield, as seen in Figure 4.10. Bearing this out are the base shear vs. displacement plots and torsional moment vs. rotation plot in Figure 4.7, which are all tight and linear. The peak base shears are 22.54 kips in the X direction, 17.75 kips in the Y direction, and 59.26 kip*inches about the vertical axis. The peak base shear in the X direction is greater than the yield shear, 21.35

kips, while the peak base shear in the Y direction is slightly less than the yield shear. The peak moment is less than the torsional yield moment.

In EQ 07, the initial inelastic test in this configuration, the model structure is subjected to 100% Imperial Valley input motion along the Y-Axis [$\text{PGA}_Y = 0.678 \text{ g}$]. Time history plots of the structural response are shown in Figure 4.8. The peak displacements were 1.216 inches in the Y direction and 0.054 inches in the X direction. The peak rotation of the structure was 0.85×10^{-3} radians. Thus, the displacements and rotation indicate that the structural response for this simulation was inelastic in the Y direction and elastic in the X direction and torsionally, as expected. Although the structure was ostensibly symmetric, and was subjected to ground motion in the Y direction only, the structure did respond noticeably in the X direction and torsionally. As this simulation was basically a scaled-up version of EQ 02, the response observed here is caused by the same phenomenon explained previously for EQ 02. The only difference between EQ 02 and EQ 07 is that the X-Axis and torsional response are significantly larger for EQ 07, which follows from the fact that the Y-Axis ground motion is also significantly larger. The peak base shears are 34.04 kips in the Y direction, 2.32 kips in the X direction, and 99.30 kip*inches about the vertical axis. The peak base shear in the Y direction is greater than the yield shear, 21.35 kips. The base shear in the Y direction demonstrates the overstrength of the structure, as the peak shear is nearly twice the yield shear. Figure 4.9 shows the base shear vs. displacement plots and torsional moment vs. rotation plot. The Y-Axis shear vs. displacement plot is no longer tight and linear, but now is beginning to take on a fuller shape, indicating inelastic behavior. Both the X-Axis shear vs. displacement and the moment vs. rotation are tight and linear. Despite the onset of inelastic behavior in the Y direction, no residual displacement is present following EQ 07, as seen in Figure 4.8.

The acceleration response of the diaphragm divided by the peak ground acceleration (PGA) is shown in Table 4.4 as the normalized acceleration. In EQ 02, with 25% Y-Axis input motions, the normalized acceleration response of the diaphragm is 2.93 in the Y direction. The input ground motion is increased by approximately a factor of 4 in EQ 07, but the acceleration response of the diaphragm only increases by about 2 in the Y direction. This is illustrated in the normalized acceleration response of the diaphragm, which has decreased to 1.39 in the Y direction. This trend verifies the expected inelastic behavior of the structure in EQ 07. Because the base shears are roughly proportional to the diaphragm accelerations, the same trends can be observed by comparing the peak base shears to the peak ground accelerations.

The displacement response of the diaphragm divided by, or normalized by, the peak ground acceleration (PGA) is shown in Table 4.3. In EQ 02, with a 25% Y-Axis input motion, the relative displacement of the diaphragm is 2.33 in/g in the Y direction. The input ground motions are increased to 100% Biaxial in EQ 07, but the normalized displacement decreases slightly in the Y direction to 1.79 in/g. Although it is expected that the period of the structure will increase during inelastic response, the elastic deformation response spectra for EQ 07, as shown in Figure 4.14, indicates that the deformation response may increase or decrease as the period increases from the natural period of about 0.29 seconds. In this case, the normalized deformation response decreases as the period of the structure increases in moving to inelastic behavior, from EQ 02 to EQ 07. Although not predictable, this behavior is not inconsistent with the deformation response spectra for this configuration.

Due to the fact that the base shears are directly proportional to the diaphragm accelerations, and the torsional moment is directly proportional to the diaphragm angular acceleration, it is not surprising that the same trends observed through the base shears and torsional moment responses can be observed through the acceleration and angular acceleration as well. Following this trend, the overturning moments are directly proportional to the base shears. Also, the column end shears and moments are computed from only the base shears and the torsional moment. Thus, the same trends observed through the acceleration and angular acceleration responses are present in the base shear, torsional moment, overturning moment, column end shear, and column end moment responses.

4.3 DYNAMIC CHARACTERIZATIONS OF THE MODEL

Prior to performing any shaketable simulations using the earthquake input motions, white noise, sine sweep, and sine decay tests were performed, as discussed in Chapter 3. This general pattern was followed for Test Configuration 1, as can be seen in Table 4.1. As discussed previously, due to the rigidity of the diaphragm, the diaphragm motion can be represented completely with only three degrees-of-freedom. Because of this, and the fact that the test structure is single-story structure, three modal frequencies, corresponding to the first mode in each of the three degrees-of-freedom, dominate the structural response. Also, the damping ratio of the test structure for all three degrees-of-freedom is near or below one percent, which is consistent with the damping

ratios of the first three test configurations. This is not surprising, as elastic steel structures inherently possess low damping characteristics, unless some external damping device is added, which was not the case here.

4.4 OBSERVED CONDITION OF THE STRUCTURE

Following each of the major earthquake simulations, the model structure was physically inspected. Typically photographs were taken as well, predominantly after the final earthquake simulation of the test configuration. Historically, the most problematic location on the model was column-to-bottom plate welded joint on each column. These areas were inspected carefully in order to document any fracture in the weld or in the base material. For Test Configuration 1, fracture occurred during EQ 11. The northeast column fractured near its base, and the southeast column baseplate weld failed.

In observing the structure condition after EQ 07, the formation of plastic hinges near the tops and bottoms of the columns was becoming discernable. Following the completion of EQ 08, permanent plastic damage in the columns was evident, with the locations of the plastic hinges in the columns becoming very clear. The deformed shape of the columns was consistent with what would be expected for a column loaded with equal and opposite end moments and shear forces. This could also be seen through the final resting displacement of the diaphragm, being permanently offset from the original location, and with respect to the ground. Figures 4.16 and 4.17 are photographs of the test structure taken before the earthquake simulations were performed. Figures 4.18 and 4.19 are photographs of the test structure taken after one of the inelastic simulations, illustrating the inelastic behavior and permanent damage of the structure. Figure 4.20 shows the formation of plastic hinges near the top and bottom of the northeast column. Figure 4.21 shows the column fracture at the bottom of the northeast column after EQ 11.

4.5 FINITE ELEMENT ANALYSIS

In modeling the behavior of the test structure, the nonlinear finite element analysis programs Abaqus and Drain-3DX were employed. During the earthquake simulations employing the larger

scale input motions, the structural response exhibits both geometric and material nonlinearities, both of which Abaqus and Drain-3DX can model. Both programs feature elements of “distributed plasticity” type, which allows the very useful ability to designate the elastic-plastic behavior for any element through the input of stress-strain data. Thus, the locations of plastic hinges do not have to be found and added to the model before running the analysis. A more complete discussion of the applicable features of Abaqus and Drain-3DX is presented in Chapter 3. Also, some aspects of the finite element model, such as the modeling of the diaphragm as a rigid component, are common throughout each test configuration, and are discussed more completely in Chapter 3.

(A) PIPE COLUMN MATERIAL MODEL

The pipe columns used in Test Configuration 1, as well as those used in Test Configurations 2-4, were produced from the same batch of raw pipe column lengths. As a result of this four coupons were taken from the overall batch of pipe columns used in Test Configurations 1-4. The material models of the pipe columns in these four test configurations were based on the stress-strain data produced during the tension tests performed on each coupon. The material model was determined by first analyzing the elastic part, verifying the elastic modulus of the material to be roughly 29000 ksi, the typical value for structural steel. Second, the inelastic part was analyzed, resulting in a best-fit stress-strain model. Both the original stress-strain data recorded during the coupon tension tests, and the best-fit material model used in the finite element analyses are shown in Figure 4.22 for Abaqus and in Figure 4.23 for Drain-3DX. Shown in Table 4.8 are the numerical stress-strain best-fit model data for the Abaqus models. Abaqus allows the stress-strain properties to be defined for a material by specifying the elastic modulus, E, and by specifying data sets of a stress value and a plastic strain value. Shown in Table 4.9 are the stress-strain best-fit model data for the Drain-3DX models. Drain-3DX allows the stress-strain properties to be defined by specifying the elastic modulus and by specifying five data sets of a stress value and a strain value.

(B) FINITE ELEMENT MODEL

The Abaqus and Drain-3DX finite element models employed to analyze the behavior of Test Configuration 1 are shown in Figures 4.24 and 4.25, respectively. Beyond the features of the finite element model, which are common throughout each test configuration and are discussed in Chapter 3, Figure 4.24 illustrates the location and magnitudes of the nodal masses and the height of the Non-Rigid Links for the Abaqus model. The nodal masses placed at each of the four corners of the diaphragm each have a magnitude of $2.800 \text{ lb*s}^2/\text{in}$. The interior nodal masses each have a magnitude of $20.411 \text{ lb*s}^2/\text{in}$. The height of the finite element model diaphragm in this test configuration is 69.123 inches, which thus produces a length of 9.123 inches for each of the four Non-Rigid Links. Figure 4.25 illustrates the location and magnitudes of the nodal masses and the height of the Non-Rigid Links for the Drain-3DX model. The nodal masses placed at the four diaphragm corners have magnitudes of $2.994 \text{ lb*s}^2/\text{in}$. The interior nodal masses each have a magnitude of $20.411 \text{ lb*s}^2/\text{in}$. The height of the finite element model diaphragm is 68.798 inches, which results in a length of 8.798 inches for the Non-Rigid Links.

(C) OBSERVED RESPONSE

The relative displacement of the diaphragm along the X- and Y-Axis and the rotation of the diaphragm about the Z-Axis were chosen as the response quantities used to compare the accuracy of the finite element simulations. Utilizing the acceleration response histories would have been a valid choice as well; however, displacements were chosen as they have a more intuitive quality than accelerations and the damage in a building is better correlated to relative displacements.

Displacement histories for both Abaqus and Drain-3DX analyses along the X- and Y-Axis, where appropriate, are provided for the 25% X-Axis simulation [$\text{PGA}_X = 0.238 \text{ g}$] in Figures 4.26 and 4.27, are provided for the 25% Y-Axis simulation [$\text{PGA}_Y = 0.162 \text{ g}$] in Figures 4.28 and 4.29, for the 25% Biaxial simulation [$\text{PGA}_X = 0.232 \text{ g}$ and $\text{PGA}_Y = 0.160 \text{ g}$] in Figures 4.30 and 4.31, and for the 100% Y-Axis simulation [$\text{PGA}_Y = 0.678 \text{ g}$] in Figures 4.32 – 4.36. The 100% Y-Axis Abaqus simulation was performed using four different post-yield material models: perfect plasticity, isotropic hardening, kinematic hardening, and combined isotropic/kinematic hardening. Table 4.10 lists the maximum peak relative displacements in the X and Y directions and the peak rotation, and the corresponding PGAs, for the four earthquake simulations listed above.

(D) OBSERVED RESPONSE DISCUSSION

In Figures 4.26 – 4.31, the displacement response histories for the uniaxial and biaxial 25% simulations can be seen for both the test structure and the finite element model. The frequency contents of the response histories in both the Abaqus and Drain-3DX simulations match the test data very well. Also, as seen in Table 4.10, the maximum relative displacements in both directions of the finite element analysis match the test data fairly well, agreeing to within 5% in the X direction and within 15% in the Y direction for the Abaqus simulations. The Drain-3DX simulations do not match quite as well as the Abaqus simulations, but are still very close, agreeing to within 11% in the X direction and within 13% in the Y direction. More importantly, the peak displacements appear to occur in the same time region for both the finite element models and the test structure. In visually inspecting the response plots, it is apparent that the damping characteristics of both the Abaqus and Drain-3DX models do not match as well with the test structure as does the frequency content. In computing the damping ratios of the test structure using the sine decay tests, the test structure was found to have a damping ratio 0.50% in the X direction and 1.07% in the Y direction. Thus, although both damping ratios are very small, the damping in the Y direction is twice that in the X direction. In developing the finite element model, Abaqus requires damping to be specified as a material property. Thus, if damping is specified for the column material, the columns possess that damping characteristic throughout, irrespective of the direction of motion. Therefore, Abaqus does not allow the modeling of different damping ratios along the X direction and the Y direction. Drain-3DX also presents limitations on the ability to define damping. A viscous damping matrix that is proportional to the element stiffnesses and nodal masses can be specified for the structure in Drain-3DX. Although the stiffnesses are different for the X and Y directions, they are not dissimilar enough to produce the different damping ratios needed for some configurations. Because it was impossible to correctly model the actual damping ratios in the X and Y directions, a compromise was found. This resulted in a damping ratio in the X direction that was larger in the finite element models than in the test structure, and a damping ratio in the Y direction that was smaller in both models than in the test structure. The plots in Figure 4.26 of the displacement response histories clearly illustrate this modeling problem. In the X direction, the displacement response in the Abaqus model is damped to a slightly larger degree than the test structure displacement response. In the Y direction plots, the displacement response in the Abaqus model is damped to a smaller degree than the test structure displacement response. The same observations can be made in the Drain-3DX plots in Figures 4.27 and 4.29.

In Figure 4.32, the displacement response history for the Y-Axis 100% Abaqus simulation can be seen for both the test structure and the finite element model, using a combined isotropic/kinematic hardening model. This simulation is largely inelastic, achieving a peak displacement of nearly 3 times the yield displacement. The structural responses during the Abaqus simulation match the test data very well, both in frequency content and the magnitudes and locations of the maximum displacements. As seen in Table 4.10, the peak displacements differ by less than 2%. In Figure 4.33, the response for the Y-Axis 100% Drain-3DX simulation can be seen also. The hardening mechanism for the Drain-3DX model is limited to isotropic hardening. Despite this, the Drain-3DX simulation responses match the test data very well. As seen in Table 4.10, the peak displacements differ by about 4%. Although the Y-Axis response appeared to be underdamped in the 25% simulations, it does not appear to be underdamped for the 100% simulation. The damping modeling problem becomes a non-issue for the inelastic cases, as the damping behavior caused by yielding of the structure overwhelms any inherent elastic damping in the structure. It appears that using Drain-3DX and its less sophisticated hardening model does not noticeably impact the analysis results for the uniaxial simulations. The primary benefit to using Drain-3DX is that with a simpler model, the analysis is completed in a shorter period of time. For this simulation, the Drain-3DX analysis was roughly five times faster than the Abaqus analysis.

The Abaqus simulation shown in Figure 4.32 utilizes a combined nonlinear isotropic/kinematic hardening model, as described in Chapter 3. For the hardening model for this simulation, it was assumed that the isotropic part of the hardening would compose 30% of the total hardening. This figure was chosen through calibration to the response of the symmetric models studied in this and the following chapter. During this calibration, it was determined that the ratio of isotropic hardening to kinematic hardening can have a significant impact on the response characteristics of the model. The lack of cyclic tests on steel specimens from the test structure columns makes it difficult to evaluate how accurate the assumed hardening model is, although it was based on other material studies of A36 steel, as discussed in Chapter 3.

Figures 4.34 – 4.36 show the same simulation, EQ 07, performed with three other post-yield material models. The post-yield behavior in Figure 4.34 was perfect plasticity, while the simulation in Figure 4.35 utilized isotropic hardening only and the simulation in Figure 4.36 utilized kinematic hardening only. This allows the investigation of the importance of a material

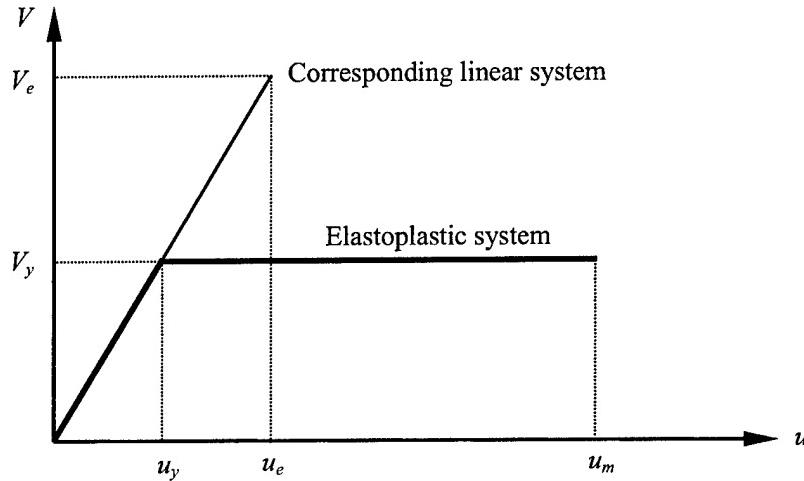
hardening model in accurately predicting structural response. As seen in these figures, although the combined hardening model predicts the closest response to the true deformation, each of the other post-yield models is fairly accurate as well. As can be seen in Appendix C, the peak recorded column strains for EQ 07 were about 0.0018 in/in, while the yield strain for the column steel was about 0.0011 in/in, as seen in Figure 4.22. Because the strain gages were placed 10 inches from the column ends for this configuration, the actual peak strains in the columns most likely exceeded the strains measured by the strain gages. However, it is still apparent that the columns strains did not extend significantly into the inelastic region. This, combined with the simulation being uniaxial, contributed significantly to the result that all four post-yield models were fairly accurate in predicting the structural response.

4.6 SUMMARY AND CONCLUSIONS

Two of the primary parameters in the seismic design of structures are the Strength Reduction Factor, or the Response Modification Coefficient R as termed in the *2000 NEHRP Recommended Provisions for Seismic Regulations*, and the Ductility Factor μ , or the Deflection Amplification Factor C_d in the *2000 NEHRP Seismic Provisions*. Structures are generally designed to respond inelastically to strong-motion earthquake shaking. However, the most common methods used for inelastic design, the Equivalent Lateral Force Procedure and the Modal Response Spectrum Analysis Procedure, are based on elastic analysis. Design base shears are reduced by the Strength Reduction Factor from the minimum strength required for the structure to remain linearly elastic during the design earthquake. The reduced base shear is then used in one of the aforementioned elastic analysis methods to determine the resulting deformation, which is then scaled up accordingly by the Ductility Demand to account for the effects on the deformation of the inelastic behavior. The Strength Reduction Factor and the Ductility Factor are coefficients that are chosen independently of any torsional irregularities or plan asymmetries, and are also independent of the presence of uniaxial or biaxial design ground motions and their magnitudes.

As the structure used in this study has not been explicitly classified according to its *Basic Seismic-Force-Resisting System*, it is not of interest to evaluate here any particular value for the Strength Reduction Factor or the Ductility Factor. Rather, it is of interest to study the ratio μ/R and whether it is influenced by different ground motions and plan asymmetries. The ratio μ/R is influenced by the fundamental period of the structure, generally decreasing with increasing

period. Although the periods of the test structure are not identical from configuration to configuration, they do not change enough to significantly impact the ratio. The aforementioned ratio, μ/R , is also equal to u_m/u_e , or the ratio of the actual peak displacement in an elastoplastic system to the peak displacement in the corresponding linear system.



With respect to the diagram above, R and μ would be defined as

$$R = \frac{V_e}{V_y} \quad \text{and} \quad \mu = \frac{u_m}{u_y}$$

where V_e is the peak value of the base shear in the corresponding linear system. But, knowing that

$$V_e = k u_e \quad \text{and} \quad V_y = k u_y$$

where k is the lateral stiffness of the system, we can also define R as

$$R = \frac{V_e}{V_y} = \frac{k u_e}{k u_y} = \frac{u_e}{u_y}$$

Using this definition of R , we can define the μ/R ratio as

$$\frac{\mu}{R} = \frac{u_m/u_y}{u_e/u_y} = \frac{u_m}{u_e}$$

For instance, the actual peak displacement would be the peak recorded displacement in EQ 07, the first inelastic simulation in this configuration. The peak displacement in the corresponding

linear system would be found by subjecting a structure to the EQ 07 ground motion, while requiring it to respond elastically. As this is impractical, the peak displacement in the corresponding linear system can instead be computed using the peak displacement in low-level, elastic earthquake simulation. In this case, the low-level simulation that would correspond to EQ 07 would be EQ 02, the 25% Y-Axis Imperial Valley simulation. The aforementioned peak displacement in the corresponding linear system, u_e , can be computed as

$$u_e = \frac{PGA_{EQ07}}{PGA_{EQ02}} u_{EQ02}$$

where $u_{max-EQ02}$ is the peak displacement in EQ 02. Incorporating this definition of u_e allows the μ/R ratio to be defined as

$$\frac{\mu}{R} = \frac{u_m}{u_e} = \frac{u_m}{\frac{PGA_{EQ07}}{PGA_{EQ02}} u_{EQ02}} = \frac{u_m / PGA_{EQ07}}{u_{max-EQ02} / PGA_{EQ02}}$$

Because u_m is the peak displacement in EQ 07, or $u_{max-EQ07}$, the μ/R ratio can be written as

$$\frac{\mu}{R} = \frac{u_m / PGA_{EQ07}}{u_{max-EQ02} / PGA_{EQ02}} = \frac{u_{max-EQ07} / PGA_{EQ07}}{u_{max-EQ02} / PGA_{EQ02}} = \frac{\text{Normalized Displacement - EQ07}}{\text{Normalized Displacement - EQ02}}$$

Thus, the μ/R ratio can be computed as the ratio of the normalized peak displacement from EQ 07, the inelastic simulation, to the normalized peak displacement from EQ 02, the low-level simulation. The resulting ratio will be referred to as the *Modified μ/R Ratio*. The *Modified μ/R Ratio* for EQ 07 is 0.77. Since there is only one inelastic simulation in this configuration, the *Modified μ/R Ratio* for EQ 07 will be compared with other *Modified μ/R Ratios* in the following chapter.

As mentioned previously, this structure has not been classified according to its seismic force resisting system, thus there is no specific target value for the *Modified μ/R Ratio*. The 2000 *NEHRP Seismic Provisions* does provide an upper and lower bound, however, for the *Modified μ/R Ratio*. The *Modified μ/R Ratio* is 0.86 for an Ordinary Moment Resisting Frame and is equal to 0.69 for a Special Moment Resisting Frame. Thus, with a *Ratio* of 0.77, the test structure falls within the expected bounds. One factor to consider when interpreting the μ/R Ratio for EQ 07 with respect to those specified in the *Seismic Provisions* is that pipe columns were used in this test structure, not the wide-flange shapes typically found in earthquake-resistant buildings. The pipe columns possess a shape factor of about 1.37, as compared to the typical shape factor for

wide-flange shapes of about 1.1. The effect of the larger shape factor is that the pipe columns possess a greater amount of reserve strength after initial yield, which also reduces the rate of stiffness degradation after yield. This would imply that the peak displacements observed during EQ 07, and consequently the μ/R Ratio, would be smaller than those expected for a structure with wide-flange shape columns. As the ductility factor increases, and hence the amount of inelastic behavior increases, the discrepancy in response due to the column shape factor increases.

The time history analyses performed for this configuration using the finite element programs Drain-3DX and Abaqus were accurate in their predictions of the structural response. With respect to the low-level linear simulations, both Drain-3DX and Abaqus predicted a peak displacement for one simulation that was slightly more than 10% different from the test data. However, each of the remaining low-level analytical simulations matched the test data very well. Both analysis programs were very accurate with regard to simulating the lone inelastic test. Also, each of the Abaqus simulations performed with different strain-hardening material models were equally accurate in matching the test data. Thus, it appears that for this uniaxial inelastic simulation, the Abaqus analysis offers no advantages over the Drain-3DX analysis to offset its significantly longer computational time. Also, it appears that the simple elastic-perfectly plastic material model is sufficient to accurately model the inelastic response of EQ 07, with a displacement ductility of about 2.5. However, if this configuration were subjected to a larger ground motion, resulting in a larger displacement ductility and a greater degree of inelastic behavior, it is possible that the material model and analysis program would be more significant in accurately modeling the experimental response.

Mass [lb*s ² /in]	Mass Centers [in]			Column Properties	
	X ₀	Y ₀	Z ₀	A [in ²]	I [in ⁴]
93.618	0.0	0.0	68.798	4.41	9.61

	Modal Frequencies [Hz]			Modal Damping [%]		
	X	Y	θ	X	Y	θ
Before EQ 01	3.565	3.445	6.515	0.497	1.074	0.491

Table 4.1 Test Structure Dynamic Properties - Test Configuration 1

Test Designation	Input Motions
WNT1	White Noise X-Axis
WNT2	White Noise Y-Axis
WNT3	White Noise Yaw-Axis
SIN1	Sine Decay X-Axis
SIN2	Sine Decay Y-Axis
SIN3	Sine Decay Yaw-Axis
EQ01	25% X-Axis Imperial Valley
EQ02	25% Y-Axis Imperial Valley
EQ03	25% Biaxial Imperial Valley
EQ04	25% X-Axis Pacoima
EQ05	25% Y-Axis Pacoima
EQ06	25% Biaxial Pacoima
SWP10	Sine Sweep X-Axis
SWP11	Sine Sweep Y-Axis
SWP12	Sine Sweep Yaw-Axis
EQ07	100% Y-Axis Imperial Valley
EQ08	200% Y-Axis Imperial Valley
EQ09	100% Y-Axis Imperial Valley
EQ10	150% Y-Axis Imperial Valley
EQ11	150% Y-Axis Imperial Valley

Table 4.2 Earthquake Simulations and Dynamic Characterization Tests - Test Configuration 1

Earthquake Test No.	Input Motions	PGA [g]			Relative Displacement [in]	Rotation [10^{-3} rad]	Normalized Displacement [in/g]	Ductility		
		X-Axis	Y-Axis	Z-Axis				X-Axis	Y-Axis	Z-Axis
1	25% X-Axis	0.238	N/A	0.515	0.076	0.23	2.16	N/A	1.12	0.16
2	25% Y-Axis	N/A	0.162	0.037	0.387	0.39	N/A	2.39	0.08	0.79
3	25% Biaxial	0.232	0.160	0.472	0.408	0.68	2.03	2.55	1.03	0.83
7	100% Y-Axis	N/A	0.678	0.058	1.215	0.85	4.14	1.79	0.13	2.48

Table 4.3 Maximum Diaphragm Relative Displacement and Rotation - Test Configuration 1

Earthquake Test No.	Input Motions	PGA [g]			Diaphragm Acceleration [g]	Diaphragm Angular Acceleration [10^{-3} g/in]	Normalized Acceleration
		X-Axis	Y-Axis	Z-Axis			
1	25% X-Axis	0.238	N/A	0.678	0.095	0.72	2.85
2	25% Y-Axis	N/A	0.162	0.055	0.475	0.75	N/A
3	25% Biaxial	0.232	0.160	0.623	0.491	1.11	2.69
7	100% Y-Axis	N/A	0.678	0.064	0.941	1.87	3.07
							1.39

Table 4.4 Maximum Diaphragm Acceleration and Angular Acceleration Response - Test Configuration 1

Earthquake Test No.	Input Motions	PGA [g]			Base Shear [k]			Torsional Moment [k*in]			Overturning Moment [k*in]		
		X-Axis	Y-Axis	Z-Axis	X-Axis	Y-Axis	Z-Axis	X-Axis	Y-Axis	Z-Axis	X-Axis	Y-Axis	
1	25% X-Axis	0.238	N/A	24.53	3.45		38.30		1695.4		238.7		
2	25% Y-Axis	N/A	0.162	1.97	17.18		39.93		136.4		1187.8		
3	25% Biaxial	0.232	0.160	22.54	17.75		59.26		1557.8		1226.8		
7	100% Y-Axis	N/A	0.678	2.32	34.04		99.30		160.3		2353.1		

Table 4.5 Maximum Base Shear, Torsional Moment, and Overturning Moment - Test Configuration 1

Earthquake Test No.	Input Motions	Column End Moments [k*in]											
		PGA [g]				SE Column				SW Column			
		X-Axis	Y-Axis	X-Axis	Y-Axis	X-Axis	Y-Axis	X-Axis	Y-Axis	NW Column	NE Column	X-Axis	Y-Axis
1	25% X-Axis	0.238	N/A	25.96	183.33	25.96	184.59	26.46	184.59	26.46	183.33		
2	25% Y-Axis	N/A	0.162	128.45	14.24	128.45	16.21	129.30	16.21	129.30	14.24		
3	25% Biaxial	0.232	0.160	131.60	168.46	131.60	169.60	134.93	169.60	134.93	168.46		
7	100% Y-Axis	N/A	0.678	256.23	19.95	256.23	25.11	256.61	25.11	256.61	19.95		

Table 4.6 Maximum Column End Moments - Test Configuration 1

Earthquake Test No.	Input Motions	PGA [g]				Column End Shears [k]					
		X-Axis		Y-Axis		SE Column		SW Column		NW Column	
		X-Axis	Y-Axis	X-Axis	Y-Axis	X-Axis	Y-Axis	X-Axis	Y-Axis	X-Axis	Y-Axis
1	25% X-Axis	0.238	N/A	6.11	0.87	6.15	0.87	6.15	0.88	6.11	0.88
2	25% Y-Axis	N/A	0.162	0.47	4.28	0.54	4.28	0.54	4.31	0.47	4.31
3	25% Biaxial	0.232	0.160	5.62	4.39	5.65	4.39	5.65	4.50	5.62	4.50
7	100% Y-Axis	N/A	0.678	0.67	8.54	0.84	8.54	0.84	8.55	0.67	8.55

Table 4.7 Maximum Column End Shears - Test Configuration 1

E [ksi] = 29000.0

Stress [ksi]	Strain [in/in]	Plastic Strain [in/in]
0.00000	0.00000	
37.50000	0.00108	0.000000
39.60000	0.00300	0.001863
40.70000	0.00500	0.003831
49.00000	0.02000	0.018593
54.00000	0.04000	0.038449
56.50000	0.06000	0.058378
57.80000	0.08000	0.078340
58.50000	0.10000	0.098320
59.00000	0.15000	0.148306
57.00000	0.20000	0.198363

Table 4.8 Abaqus Stress-Strain Best-Fit Material Model - Test Configuration 1

E [ksi] = 29000.0

Stress [ksi]	Strain [in/in]
0.00000	0.00000
37.50000	0.001293
39.60000	0.003000
49.00000	0.020000
56.50000	0.060000
58.50000	0.100000

Table 4.9 Drain-3DX Stress-Strain Best-Fit Material Model - Test Configuration 1

Earthquake Test No.	Input Motions	PGA [g]				Relative Displacement [in]			
		X-Axis	Y-Axis	Abaqus	Drain-3DX	X-Axis	Test	Abaqus	Drain-3DX
01	25% X-Axis	0.238	N/A	0.539	0.475	0.515	0.0	0.0	0.076
02	25% Y-Axis	N/A	0.162	0.0	0.0	0.037	0.430	0.368	0.387
03	25% Biaxial	0.232	0.160	0.508	0.468	0.472	0.424	0.360	0.408
07	100% Y-Axis	N/A	0.678	0.0	0.0	0.06	1.23	1.27	1.22

Table 4.10 Analytical vs. Experimental Displacement and Rotation Response Comparison - Test Configuration 1

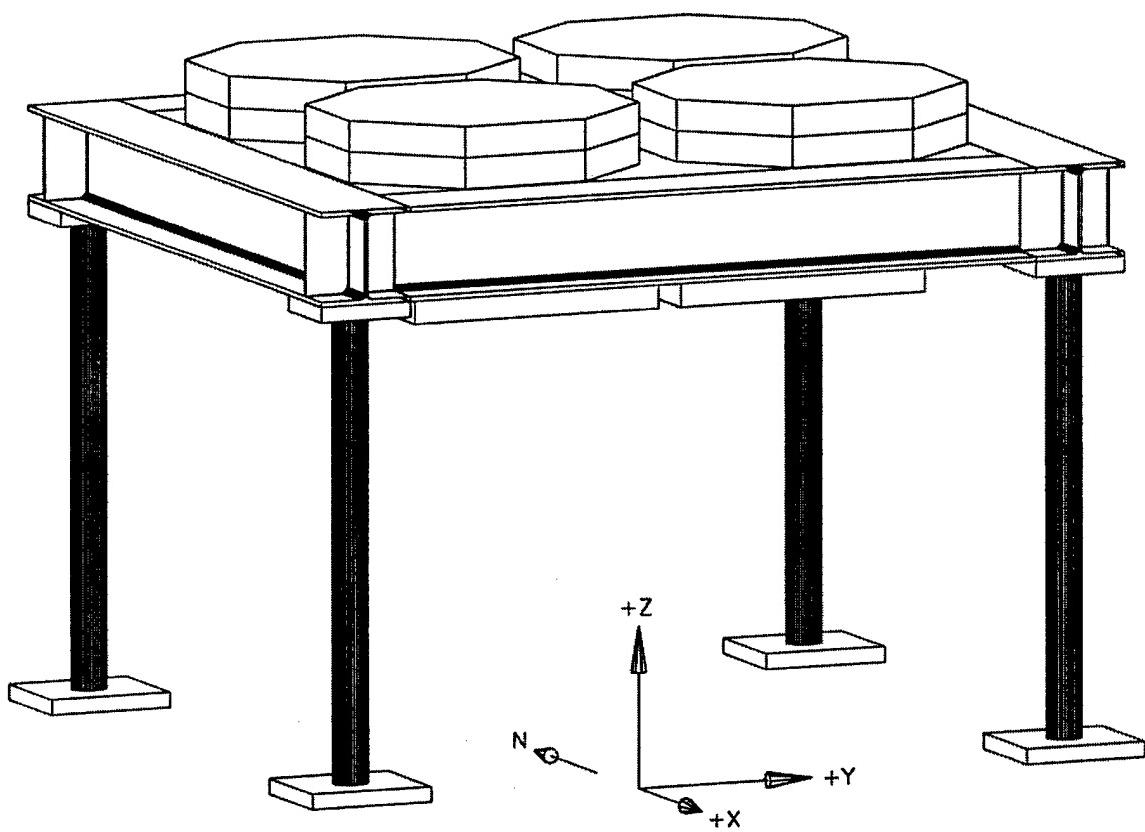


Figure 4.1 Perspective View of Test Configuration Model 1
4 - 4" Extra-Strong Columns

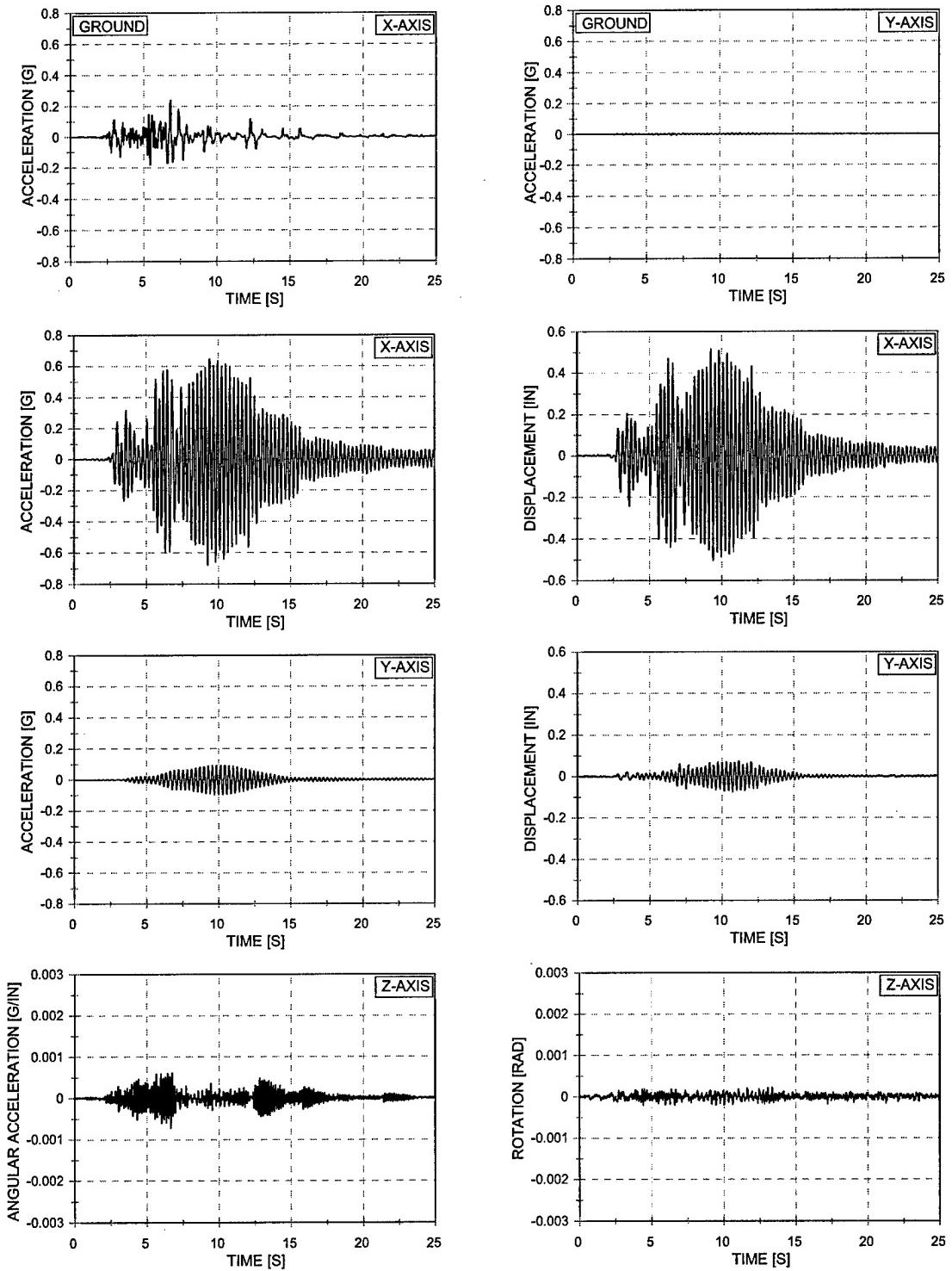


Figure 4.2 Acceleration and Displacement vs. Time – EQ 01
 25% X-Axis Imperial Valley – Symmetric Mass
 Four 4" Extra-Strong Columns

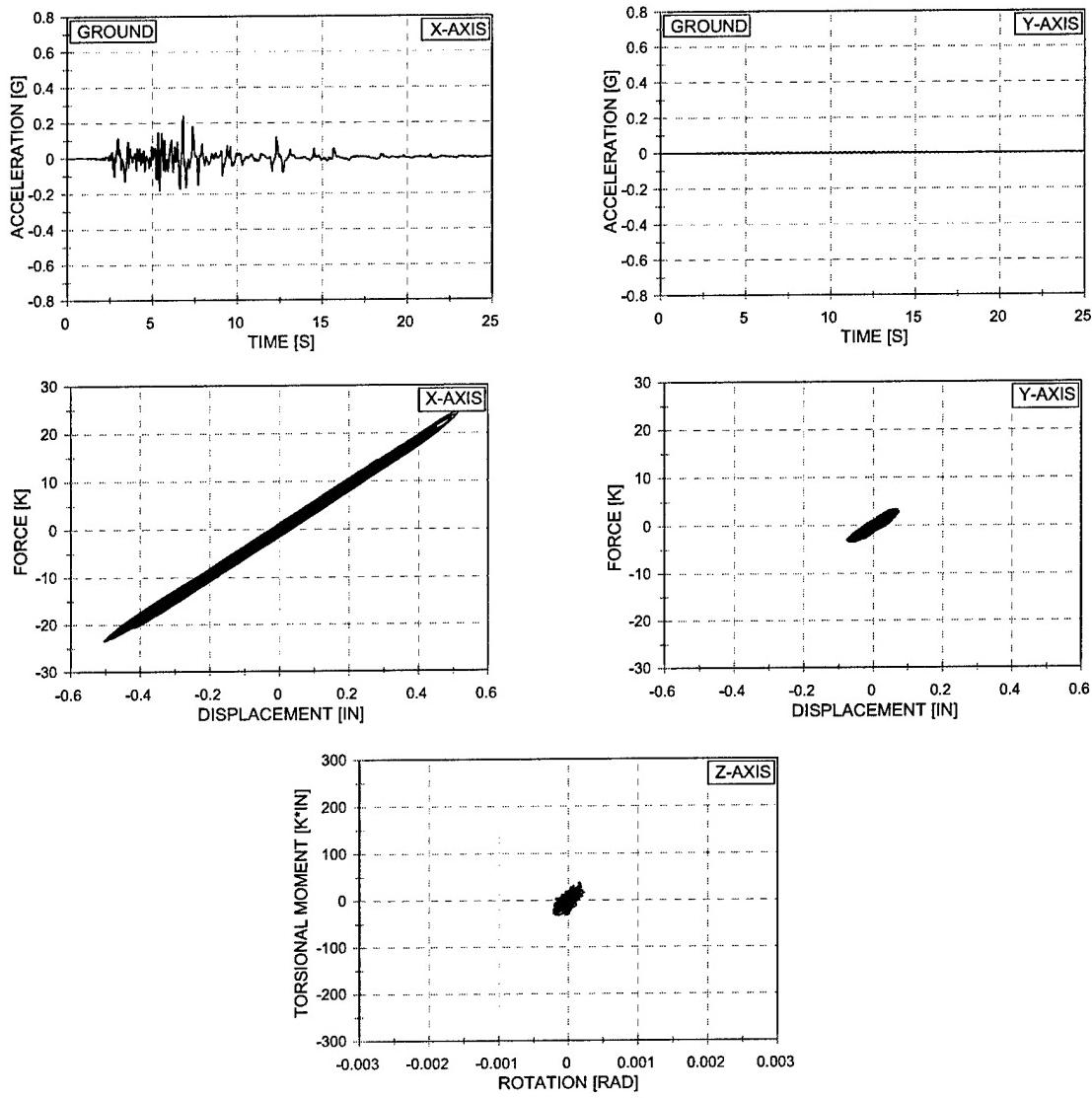


Figure 4.3 Force vs. Displacement and Torsional Moment vs. Rotation – EQ 01
 25% X-Axis Imperial Valley – Symmetric Mass
 Four 4" Extra-Strong Columns

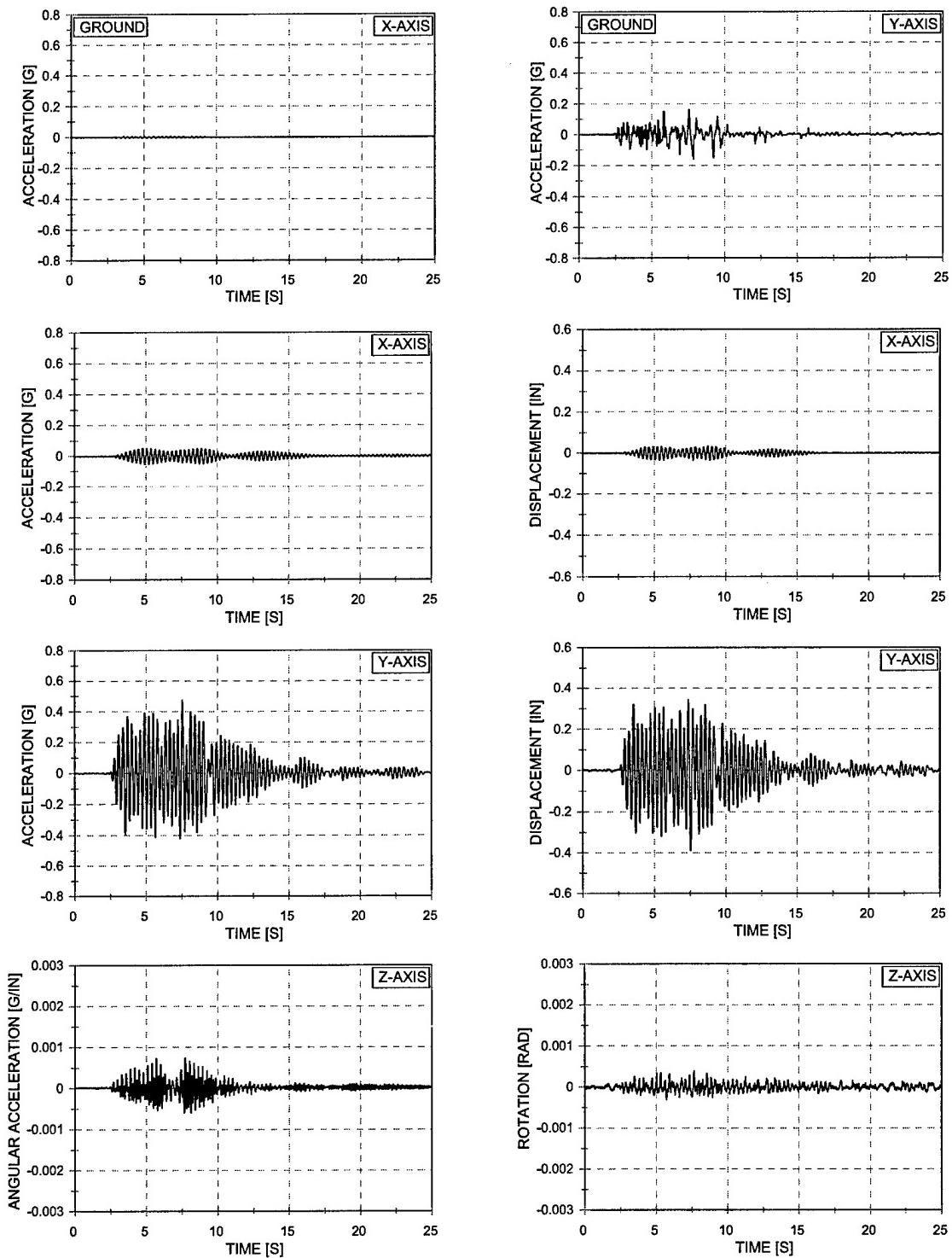


Figure 4.4 Acceleration and Displacement vs. Time – EQ 02
 25% Y-Axis Imperial Valley – Symmetric Mass
 Four 4" Extra-Strong Columns

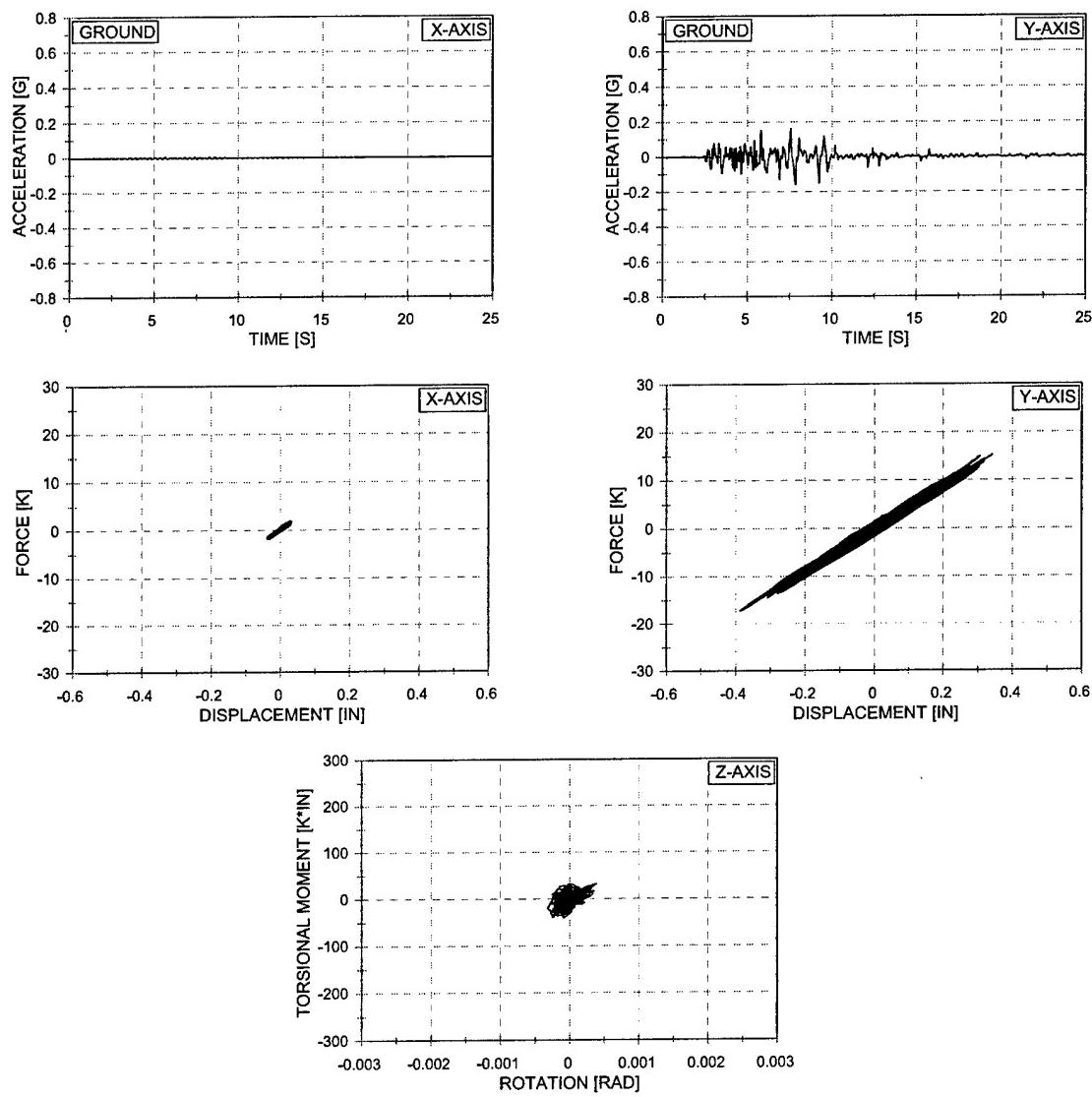


Figure 4.5 Force vs. Displacement and Torsional Moment vs. Rotation - EQ 02
25% Y-Axis Imperial Valley – Symmetric Mass
Four 4" Extra-Strong Columns

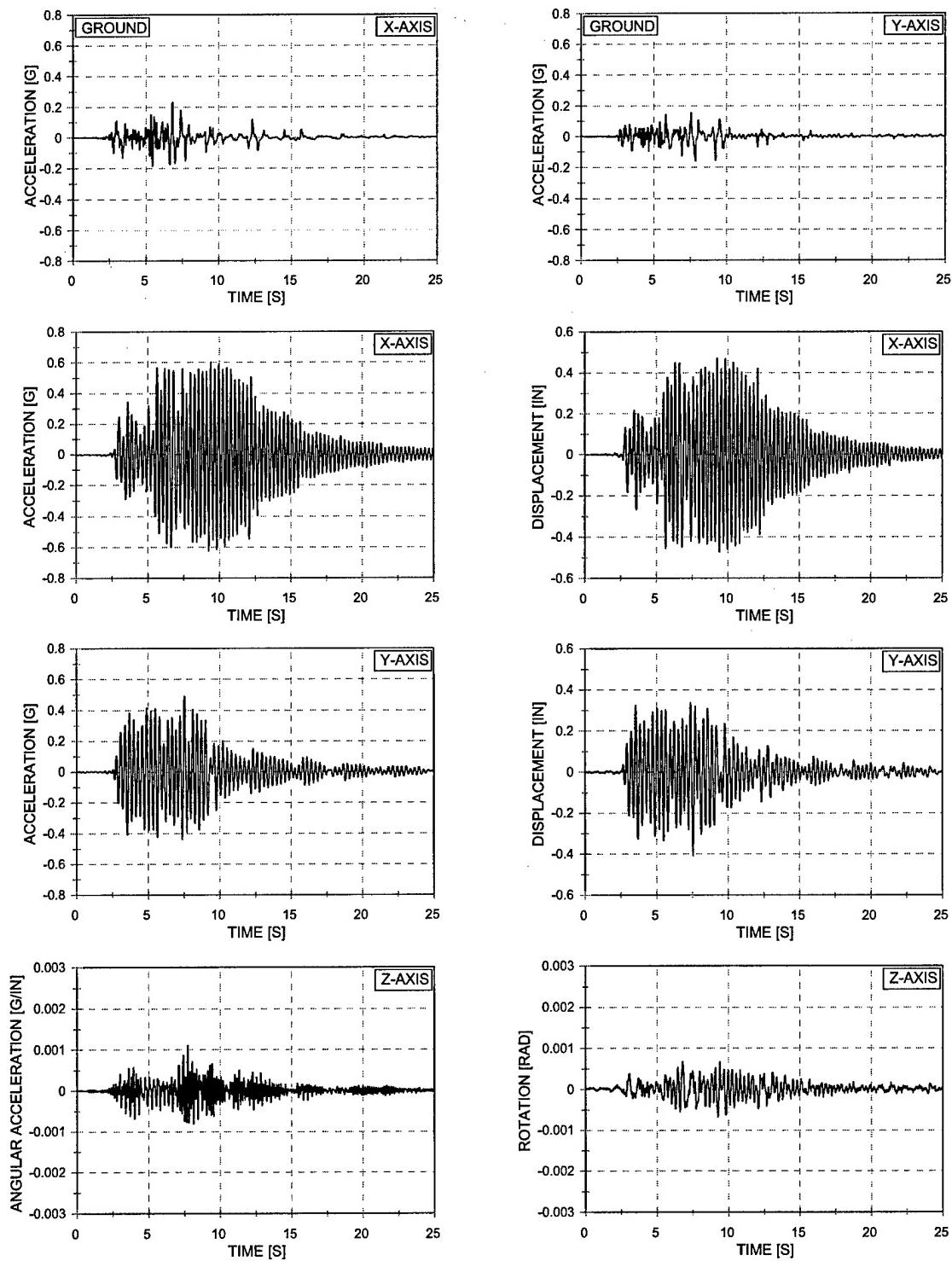


Figure 4.6 Acceleration and Displacement vs. Time – EQ 03
 25% Biaxial Imperial Valley – Symmetric Mass
 Four 4" Extra-Strong Columns

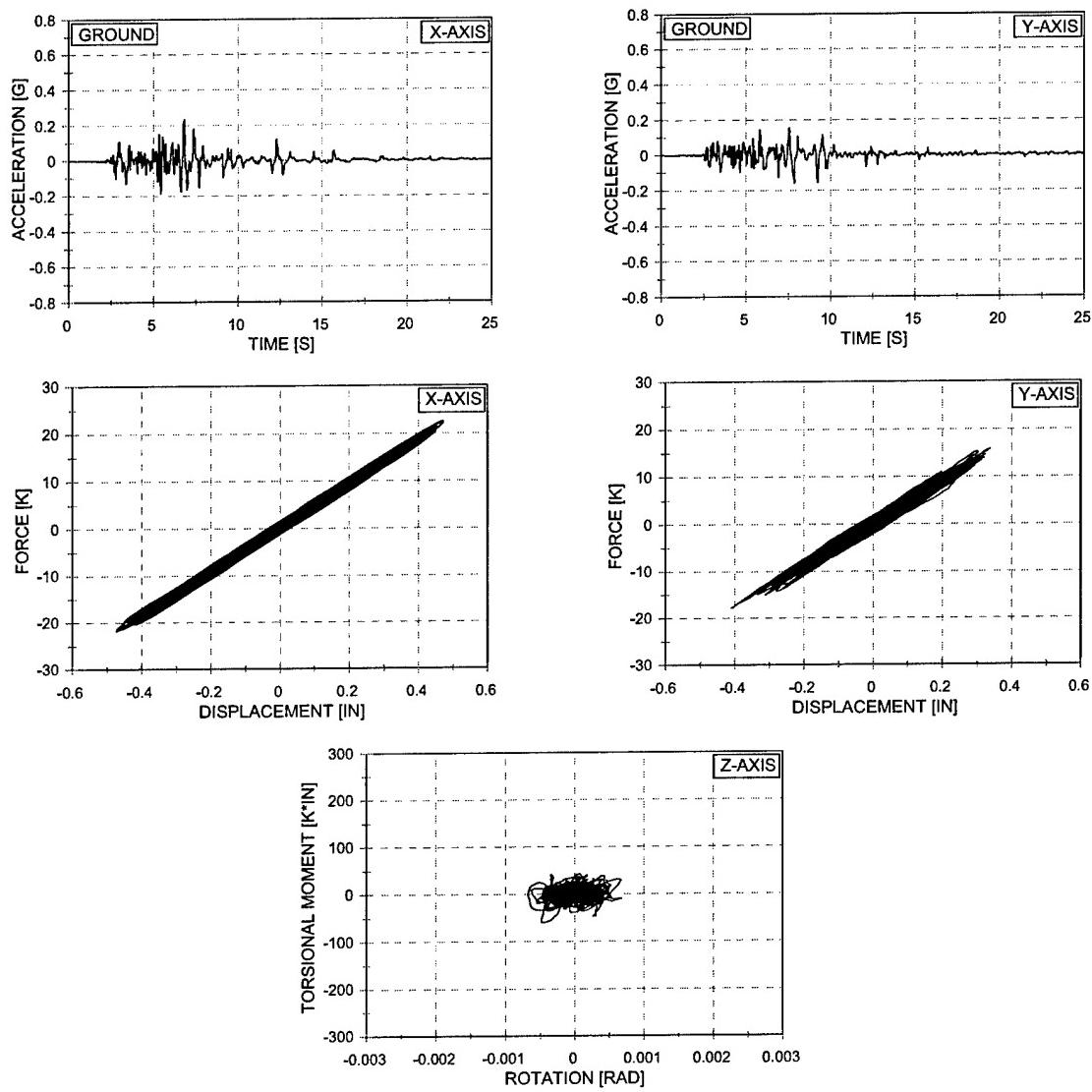


Figure 4.7 Force vs. Displacement and Torsional Moment vs. Rotation - EQ 03
 25% Biaxial Imperial Valley – Symmetric Mass
 Four 4" Extra-Strong Columns

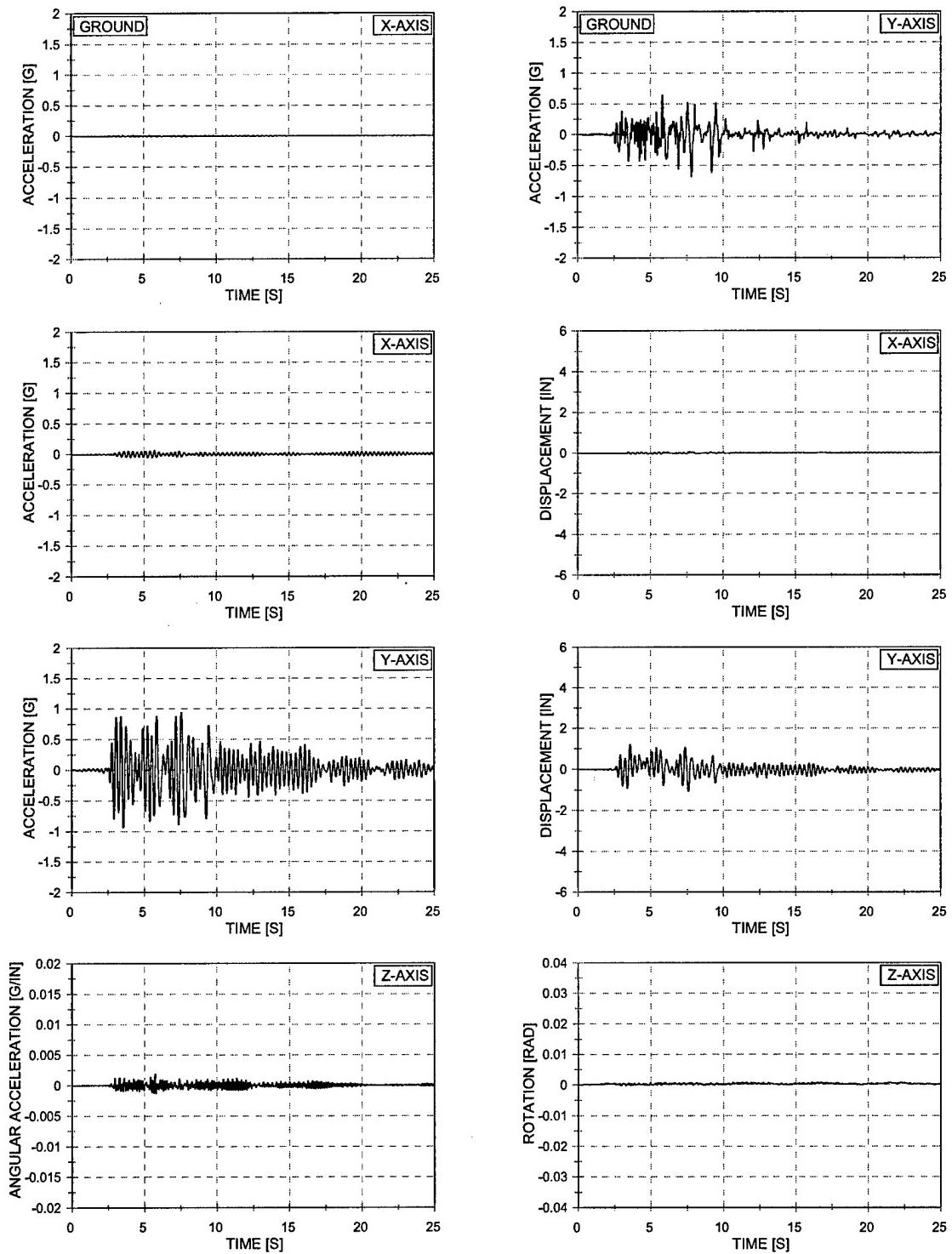


Figure 4.8 Acceleration and Displacement vs. Time – EQ 07
100% Y-Axis Imperial Valley – Symmetric Mass
Four 4" Extra-Strong Columns

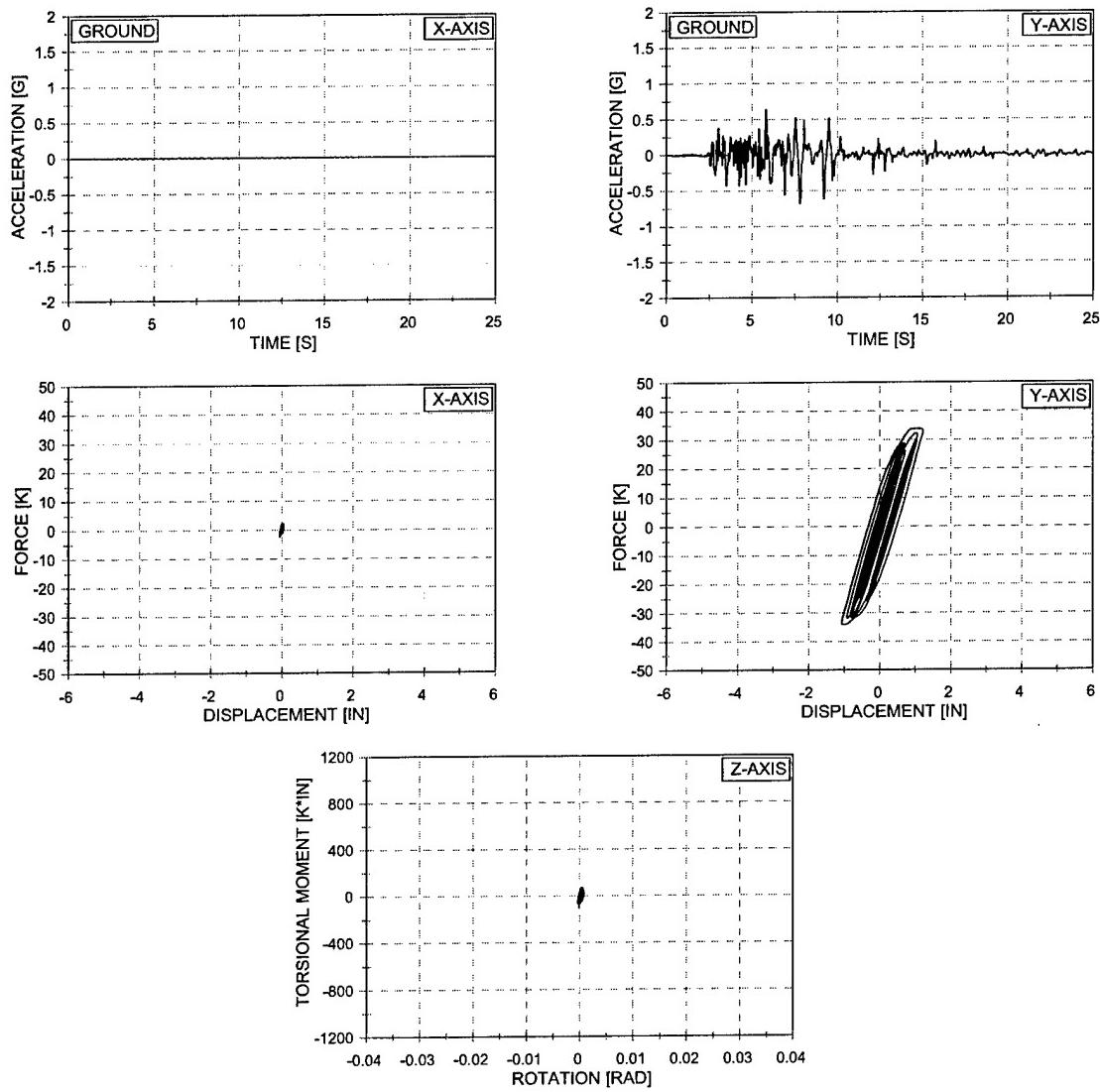


Figure 4.9 Force vs. Displacement and Torsional Moment vs. Rotation - EQ 07
 100% Y-Axis Imperial Valley – Symmetric Mass
 Four 4" Extra-Strong Columns

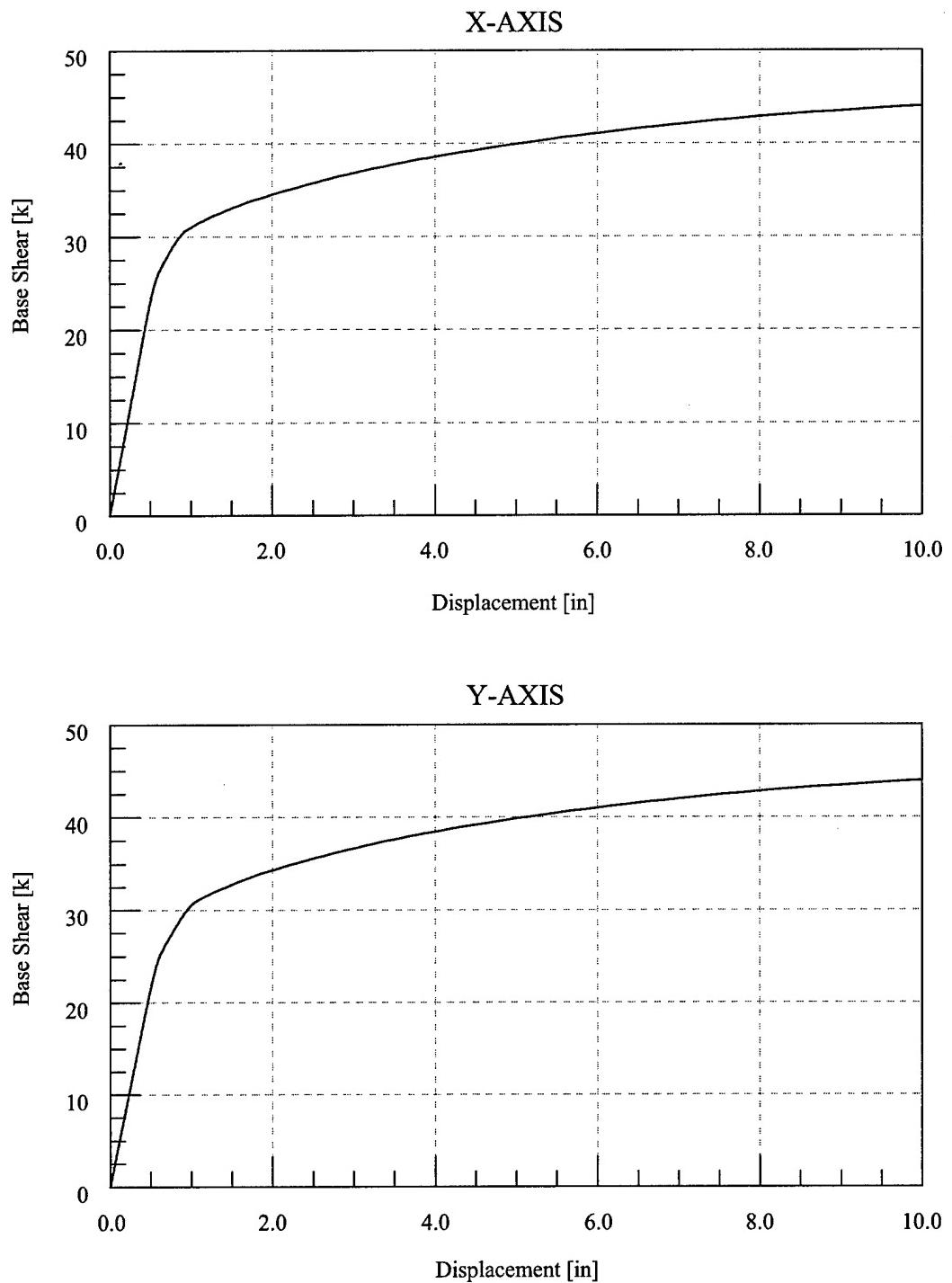


Figure 4.10 Force-Deformation Response – Test Configuration 1

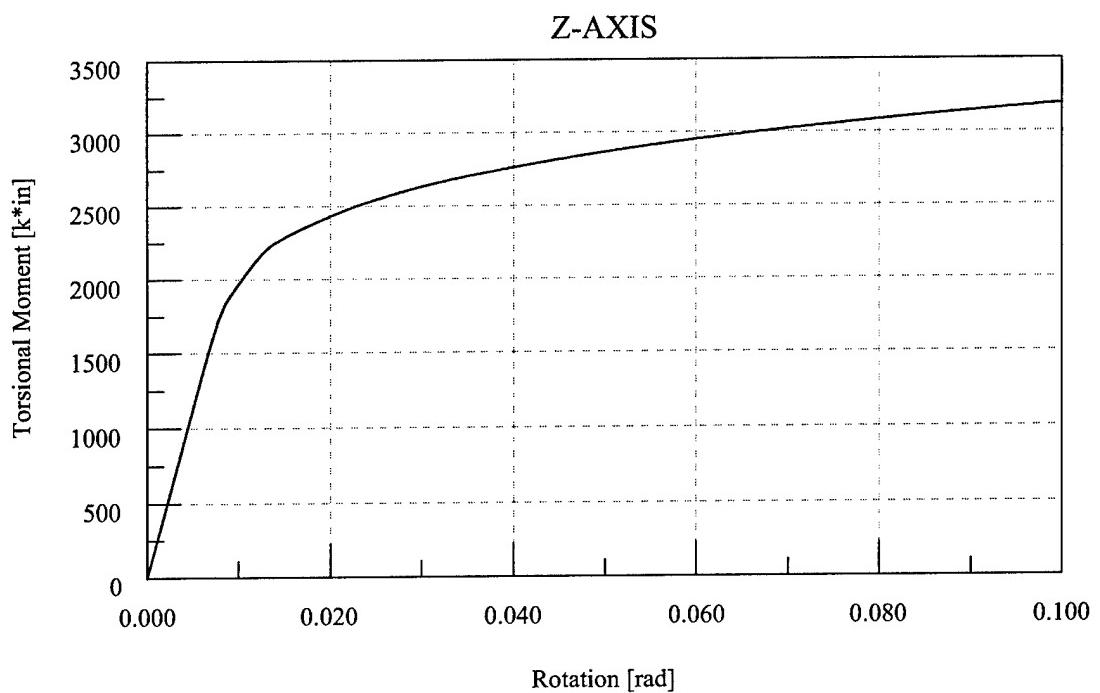


Figure 4.11 Torsional Moment-Rotation Response – Test Configuration 1

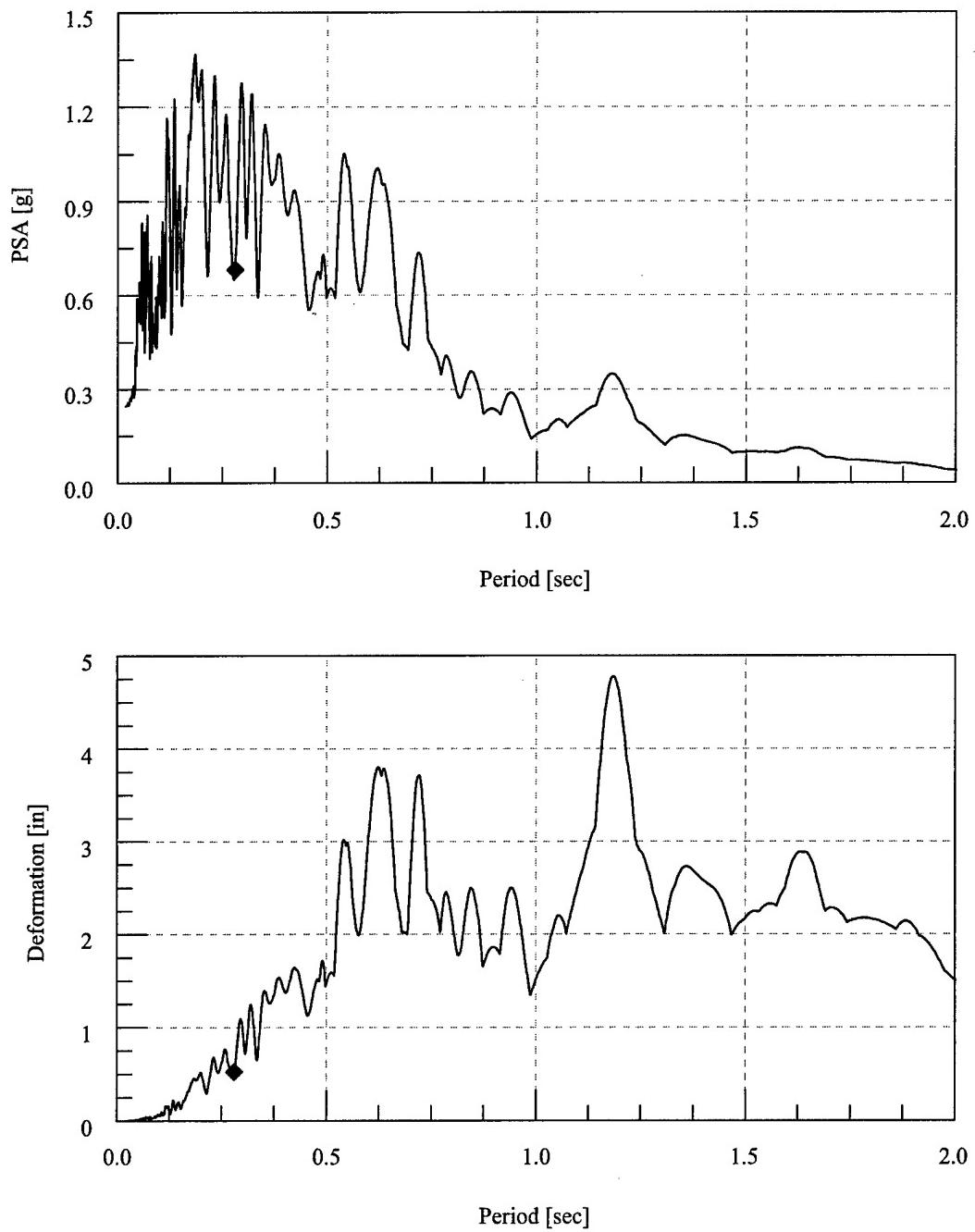


Figure 4.12 Elastic Response Spectra – EQ 01 – 25% X-Axis Imperial Valley Ground Motion

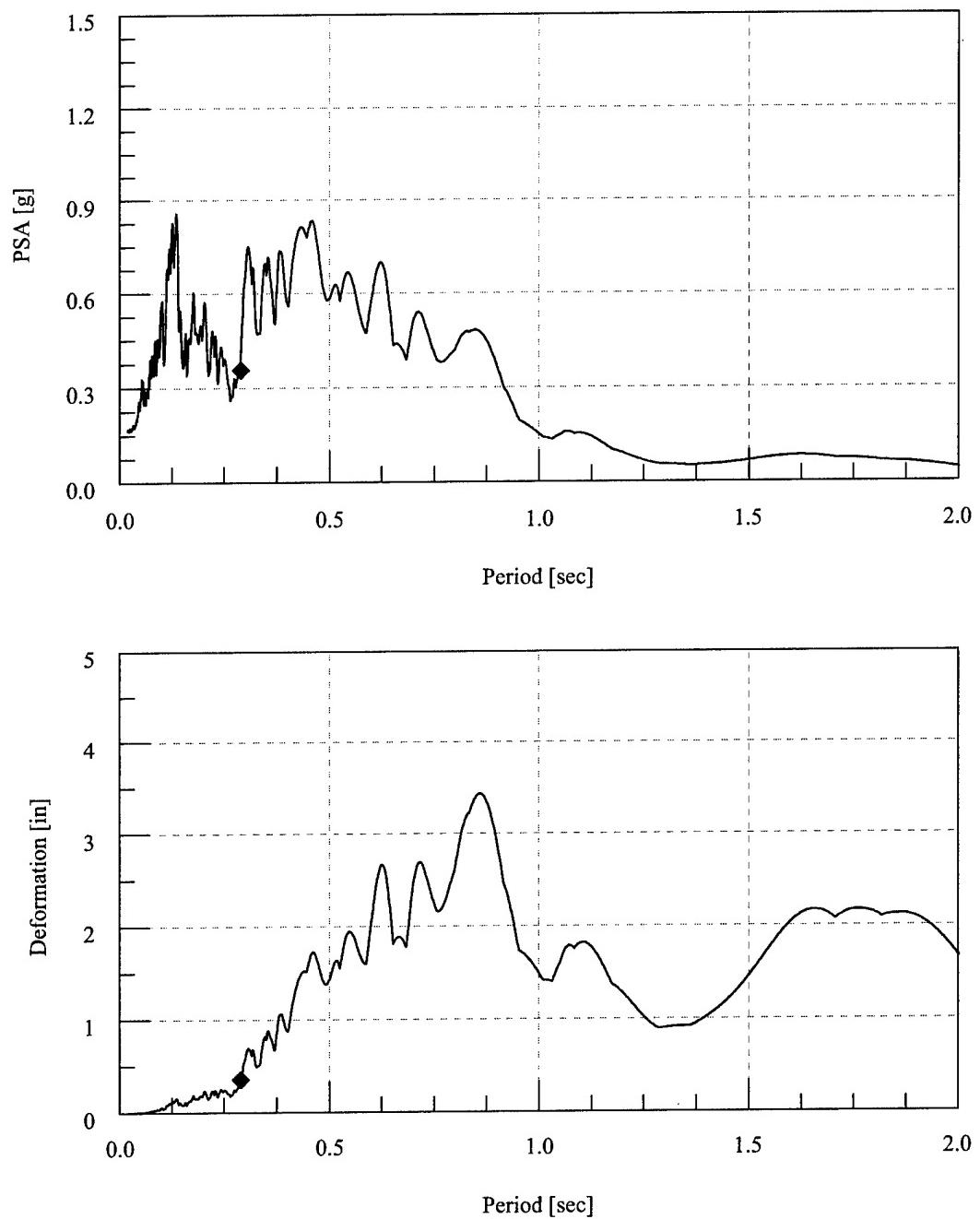


Figure 4.13 Elastic Response Spectra – EQ 02 – 25% Y-Axis Imperial Valley Ground Motion

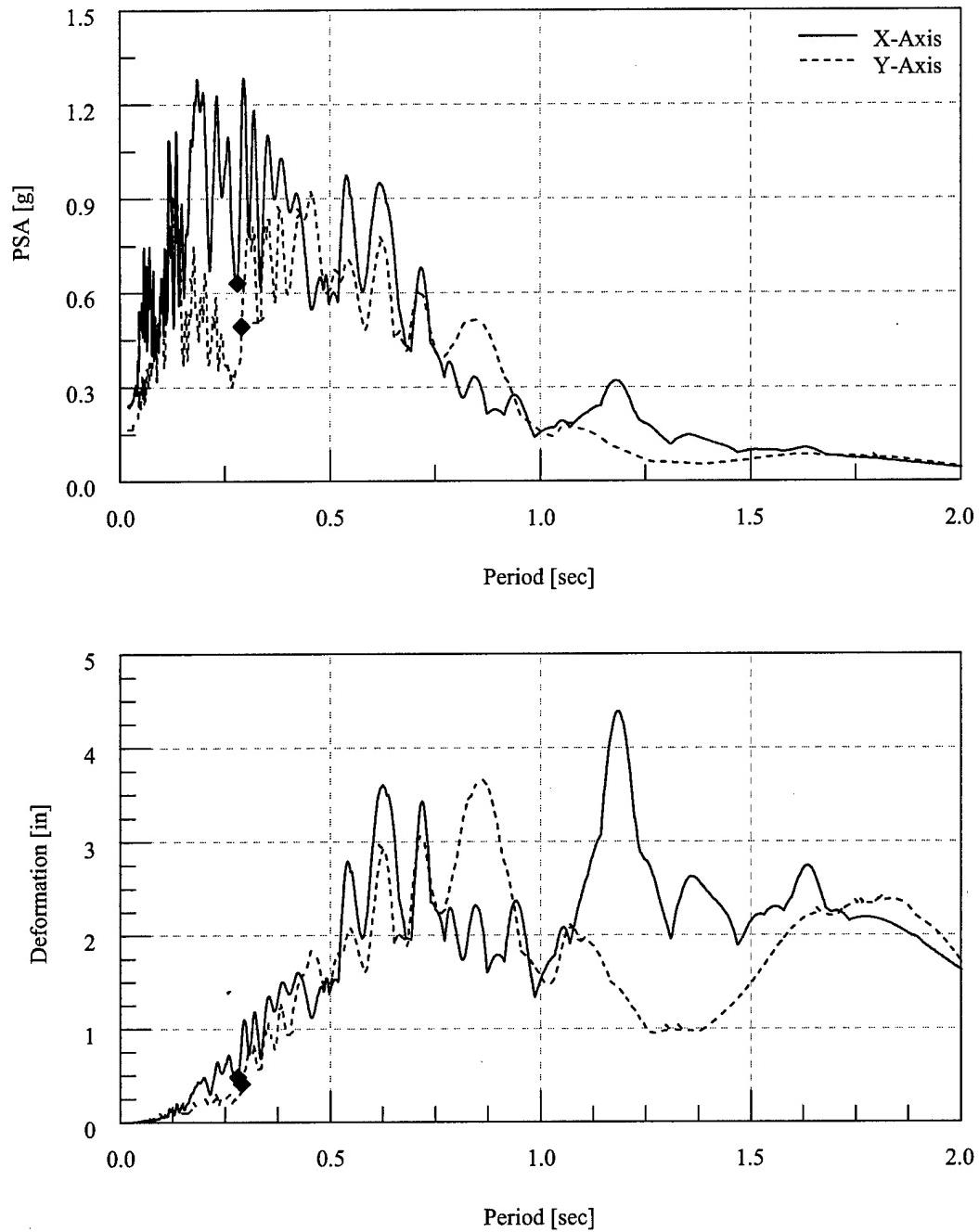


Figure 4.14 Elastic Response Spectra – EQ 03 – 25% Biaxial Imperial Valley Ground Motion

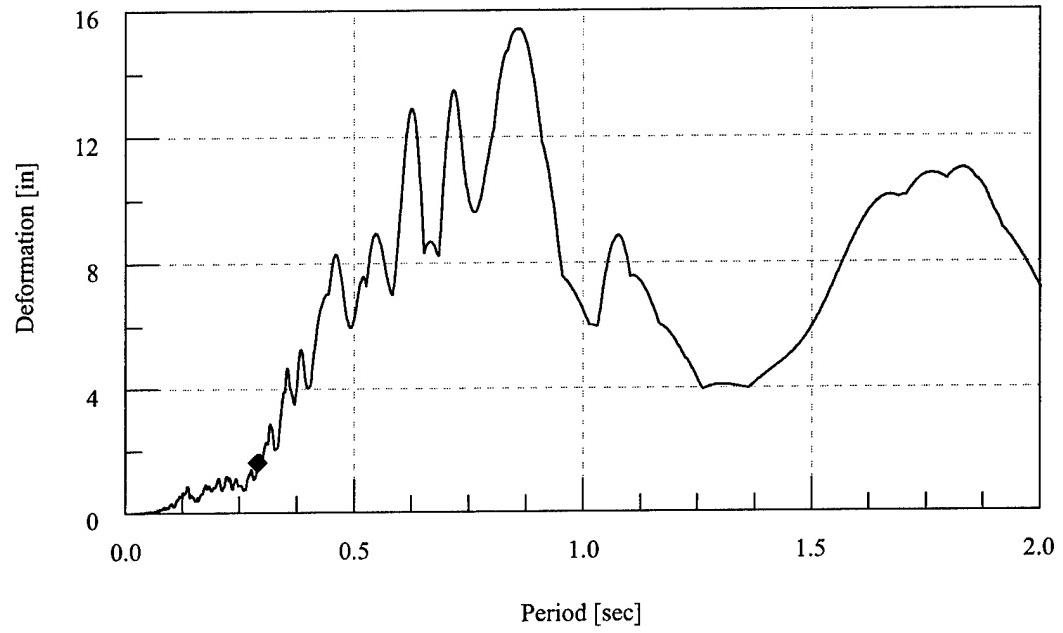
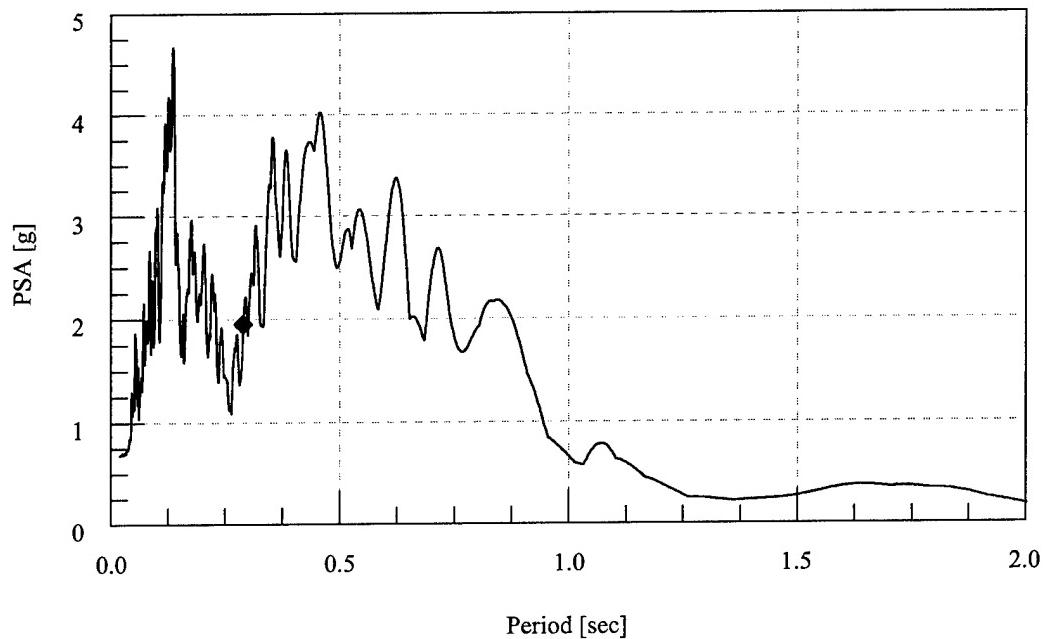


Figure 4.15 Elastic Response Spectra – EQ 07 – 100% Y-Axis Imperial Valley Ground Motion

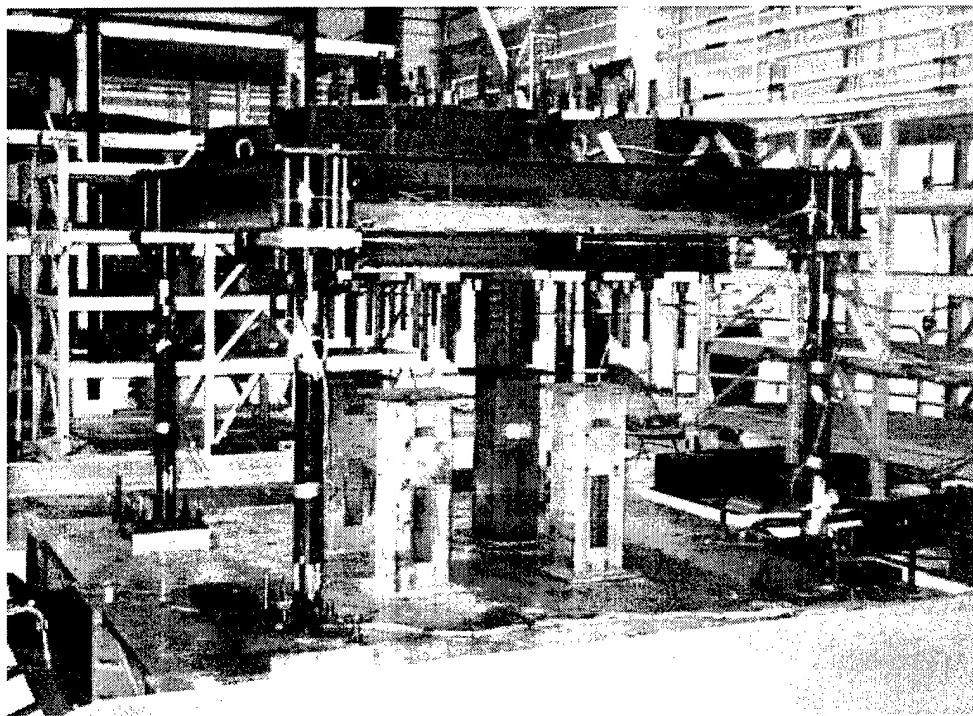


Figure 4.16 Test Structure prior to Earthquake Simulations

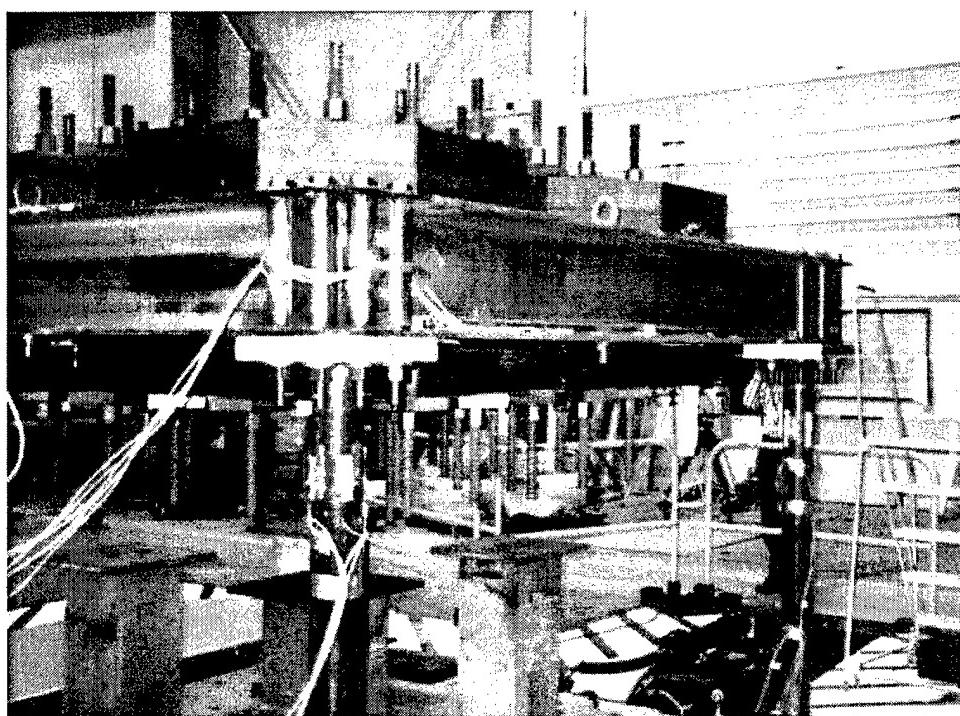


Figure 4.17 Test Structure prior to Earthquake Simulations

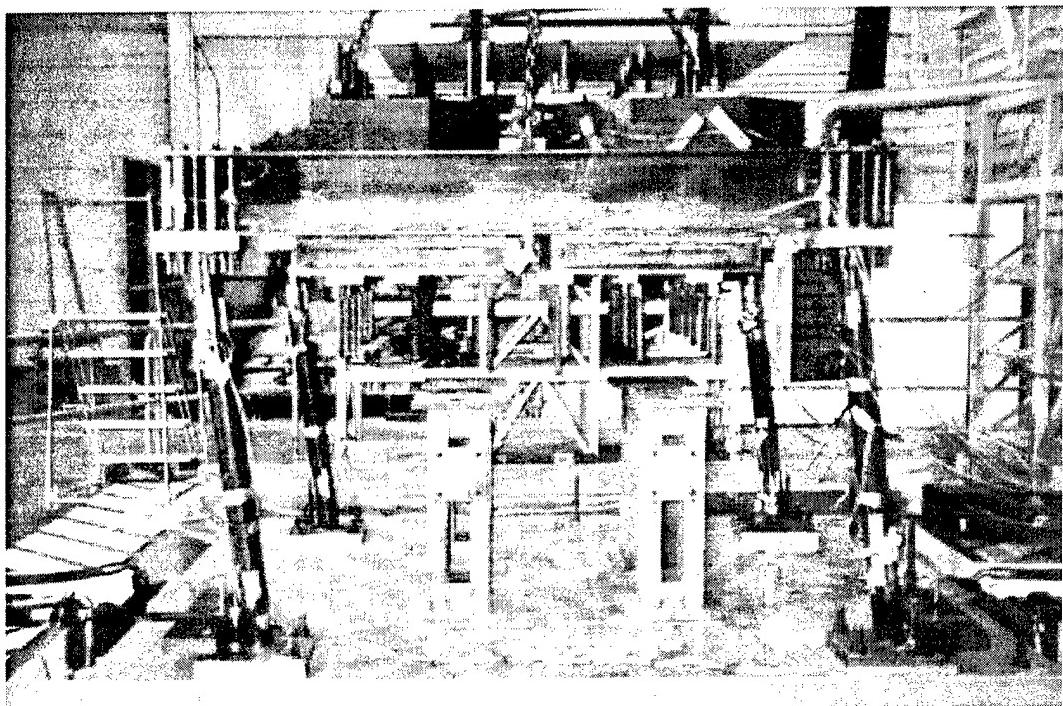


Figure 4.18 Test Structure After Earthquake Simulations

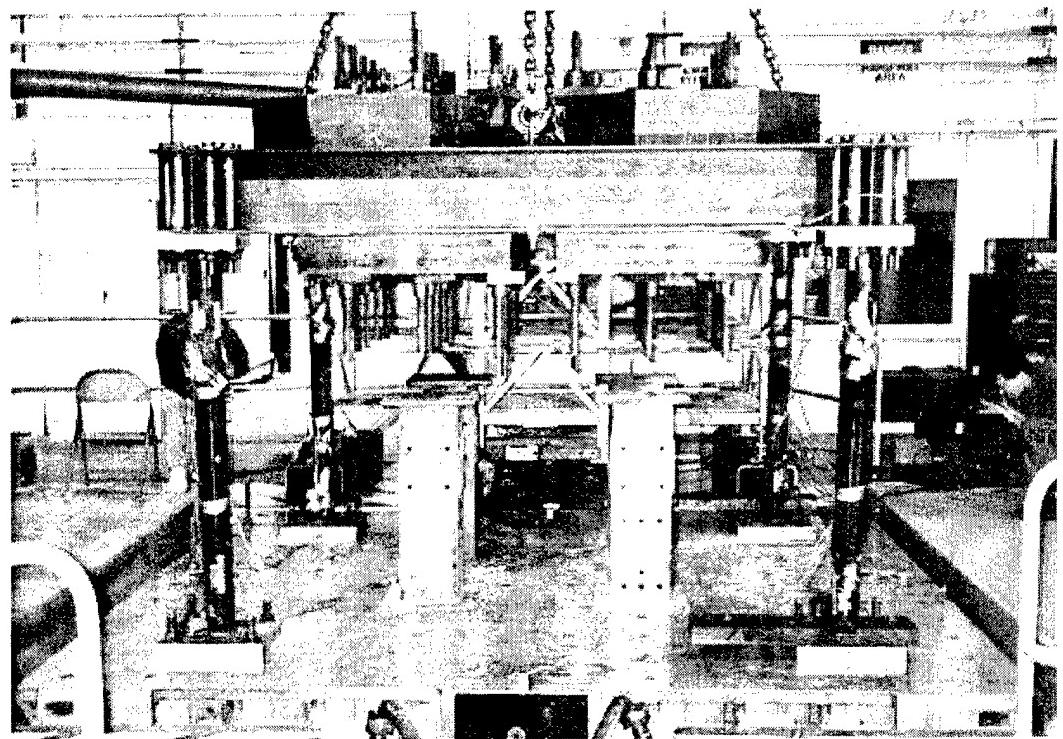


Figure 4.19 Test Structure After Earthquake Simulations

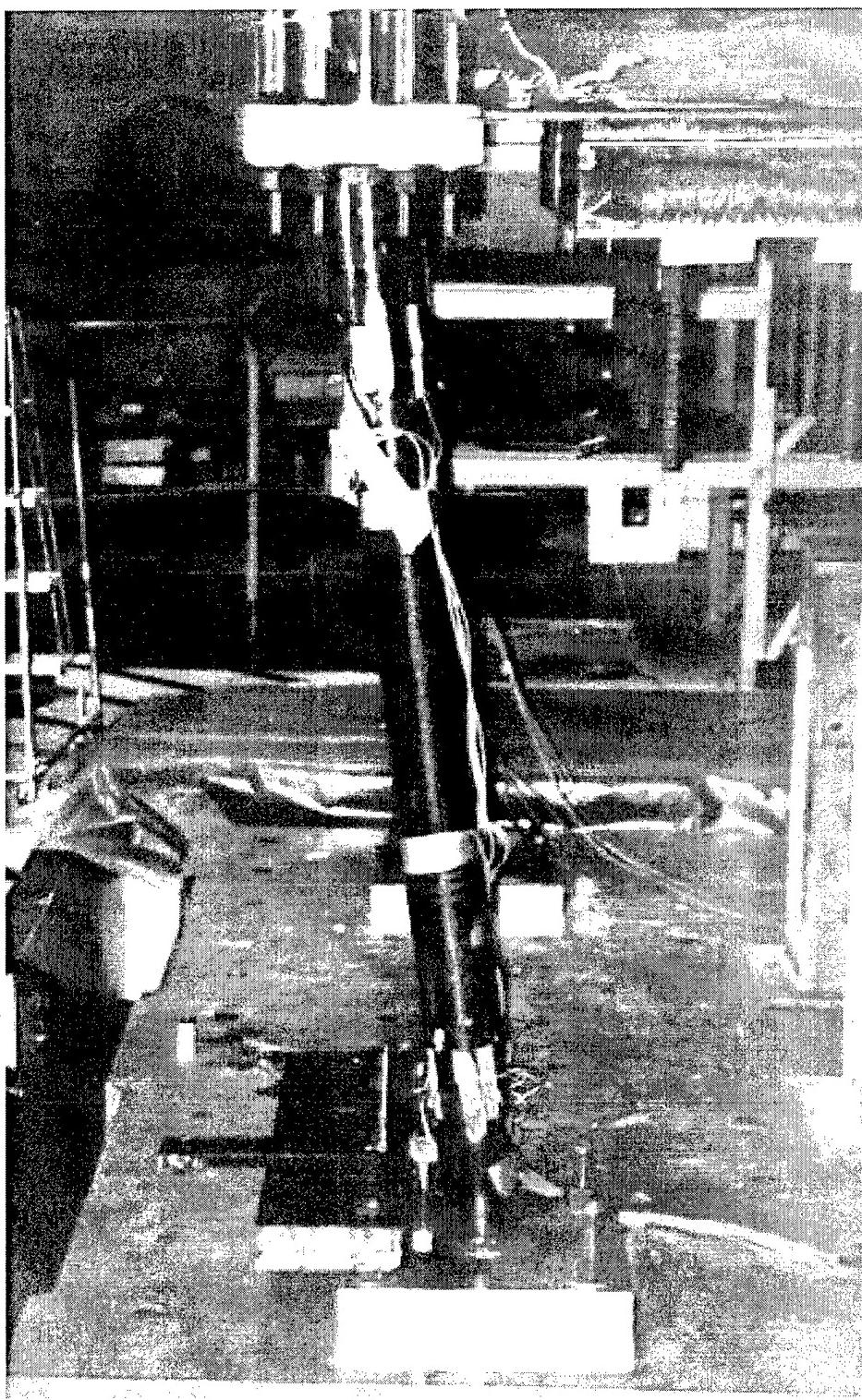


Figure 4.20 Test Structure Northeast Column After Earthquake Simulations

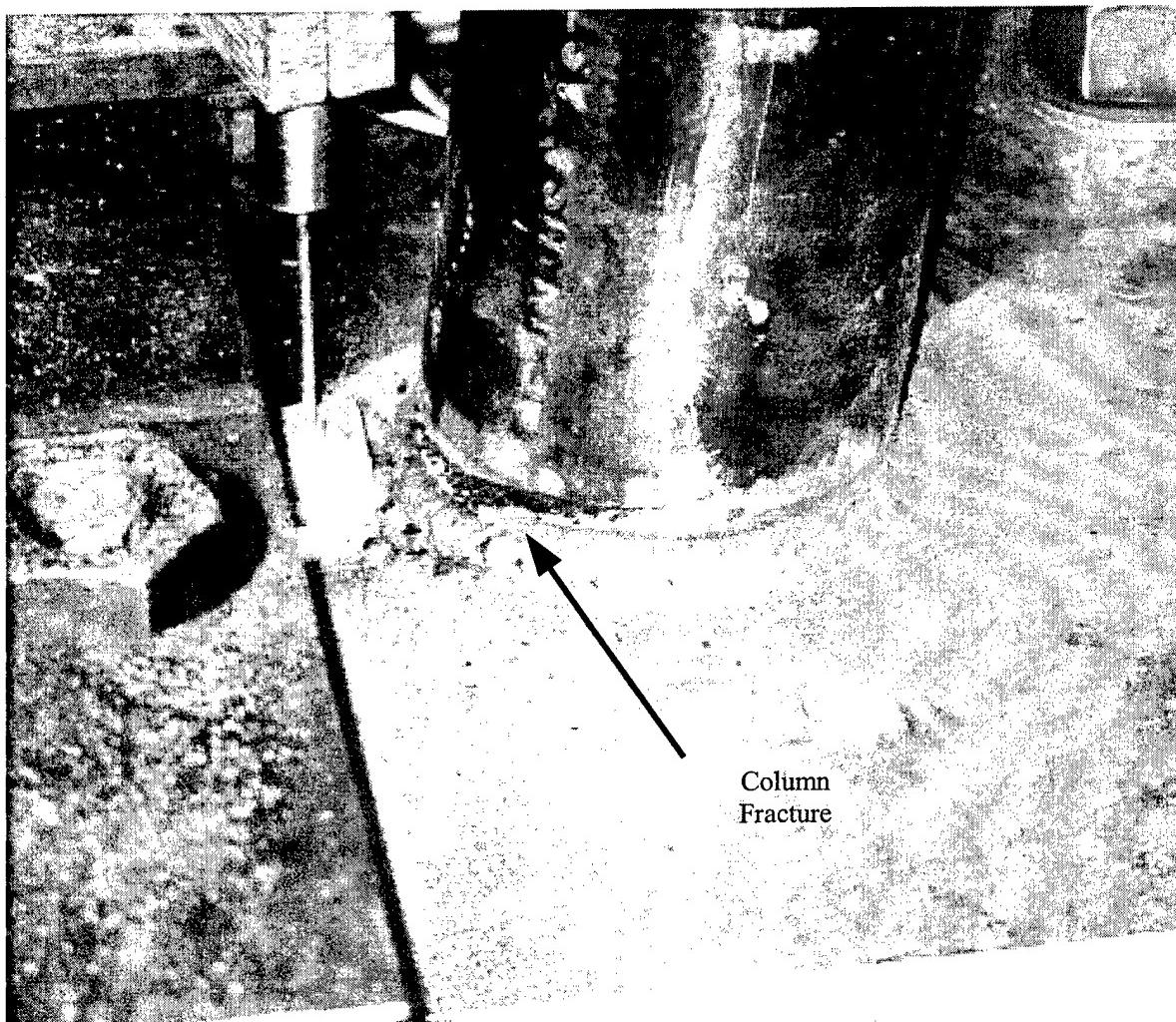


Figure 4.21 Fracture at Column and Column Base Plate

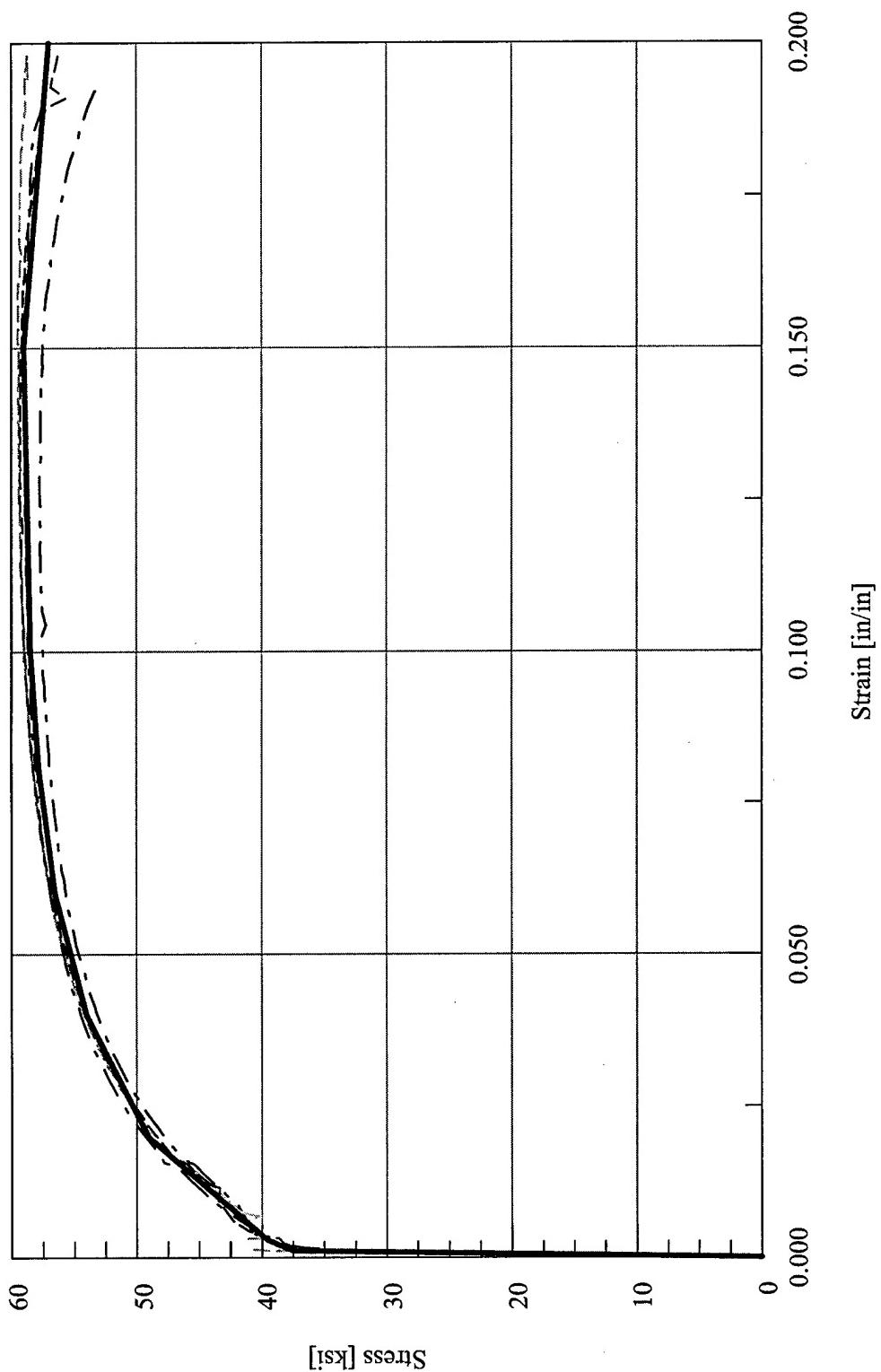


Figure 4.22 Abaqus Stress vs. Strain Finite Element Material Model Definition – Test Configuration 1

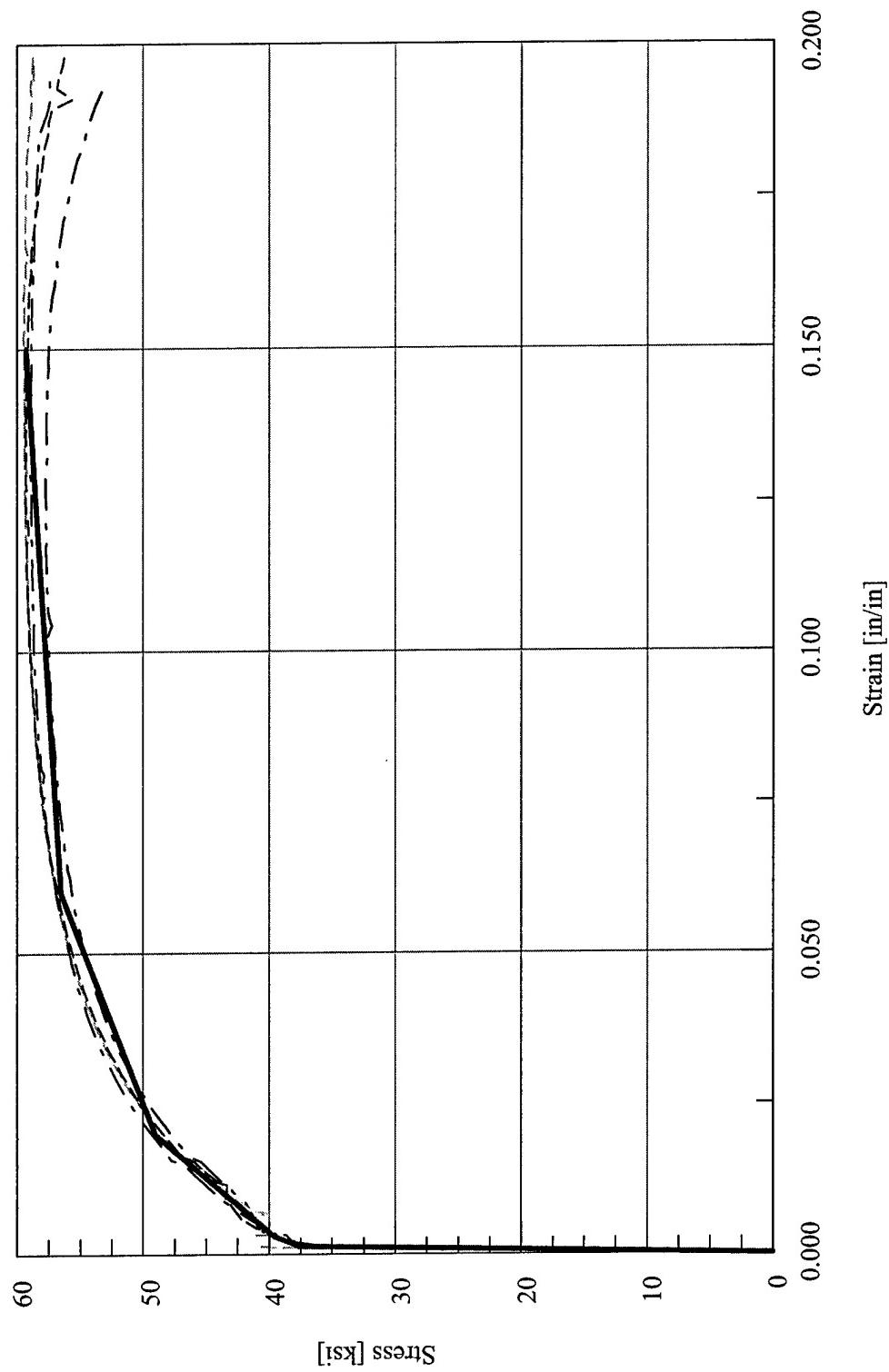


Figure 4.23 Drain-3DX Stress vs. Strain Finite Element Material Model Definition – Test Configuration 1

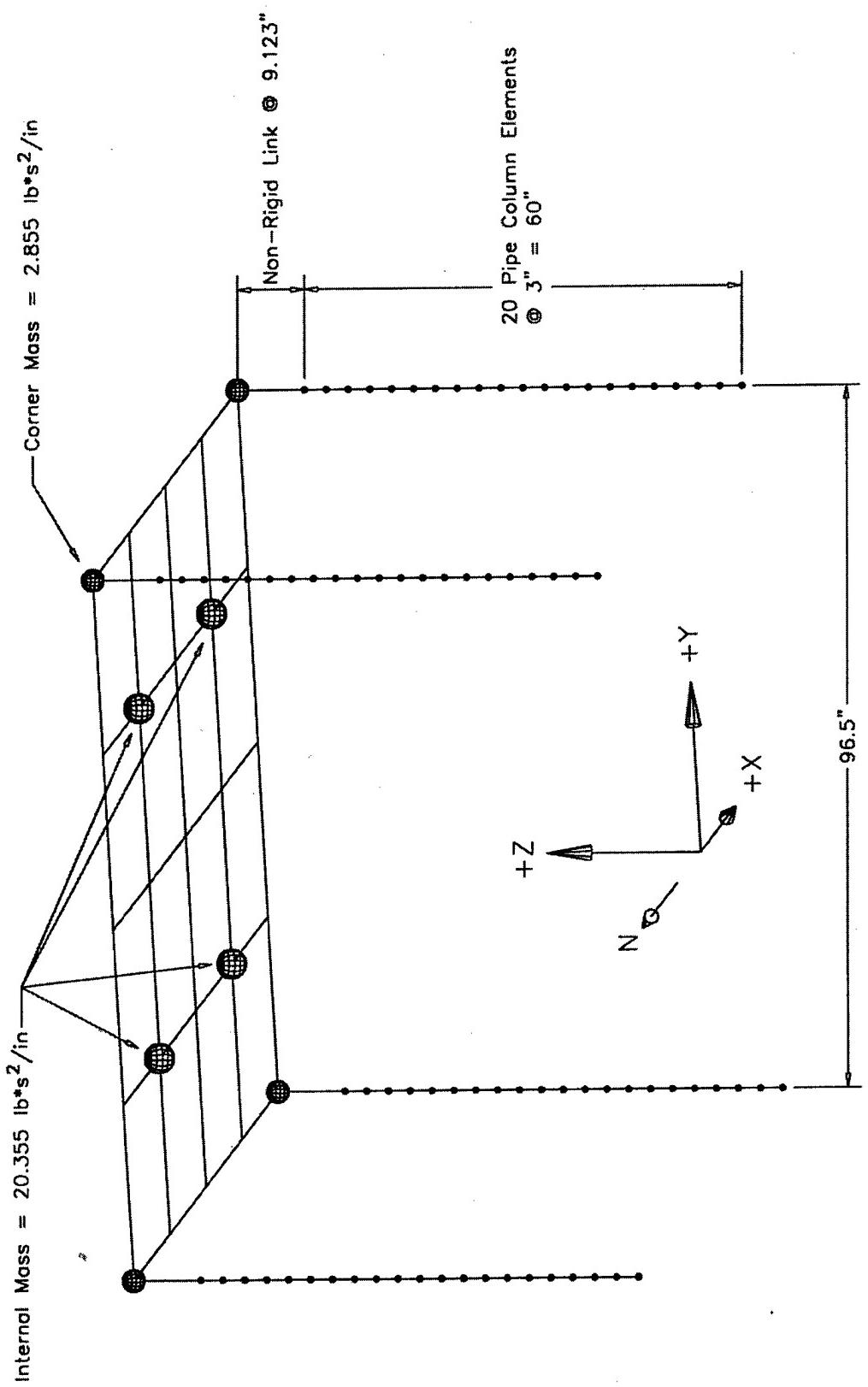


Figure 4.24 Abaqus Finite Element Model for Test Configuration 1

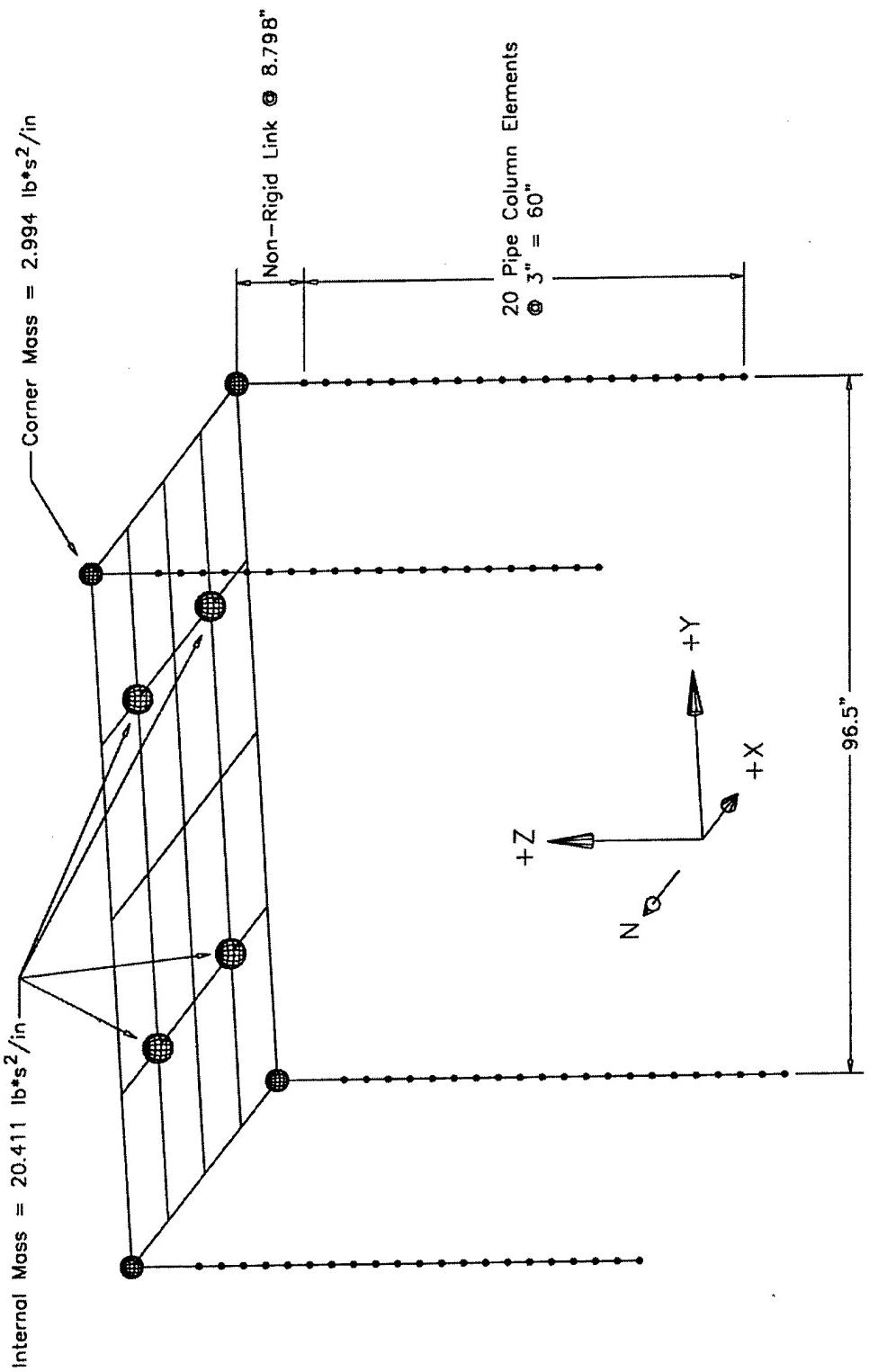


Figure 4.25 Drain-3DX Finite Element Model for Test Configuration 1

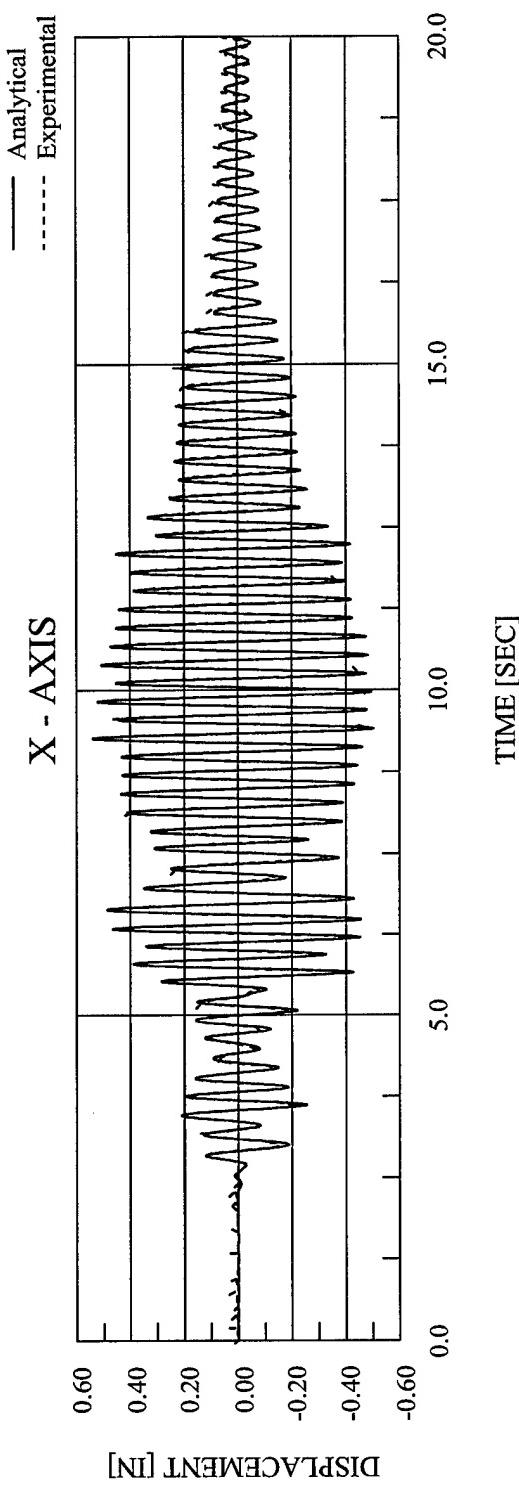


Figure 4.26 Abaqus Analytical Displacement vs. Time – EQ 01 – 25% X-Axis Imperial Valley

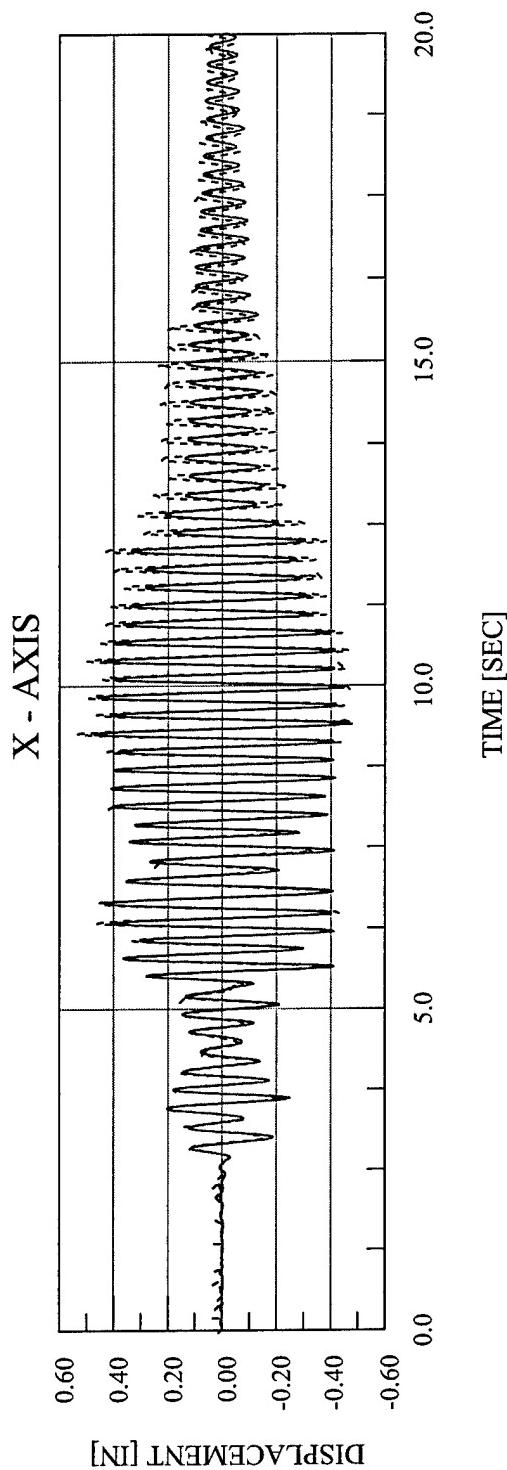


Figure 4.27 Drain-3DX Analytical Displacement vs. Time – EQ 01 – 25% X-Axis Imperial Valley

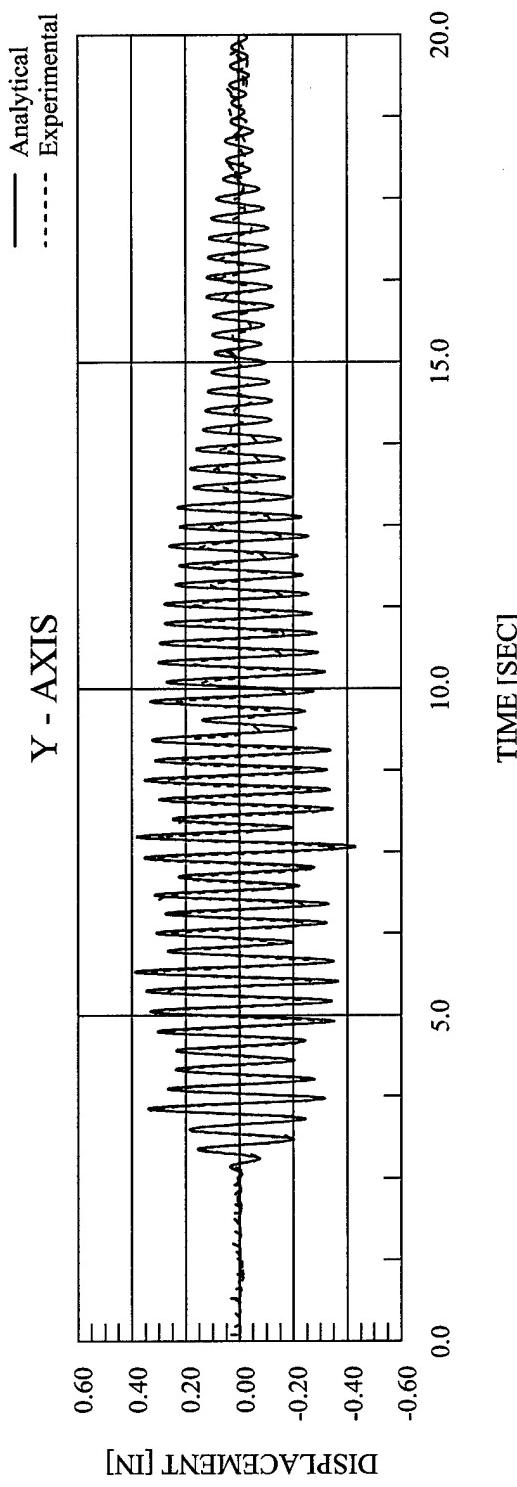


Figure 4.28 Abaqus Analytical Displacement vs. Time – EQ 02 – 25% Y-Axis Imperial Valley

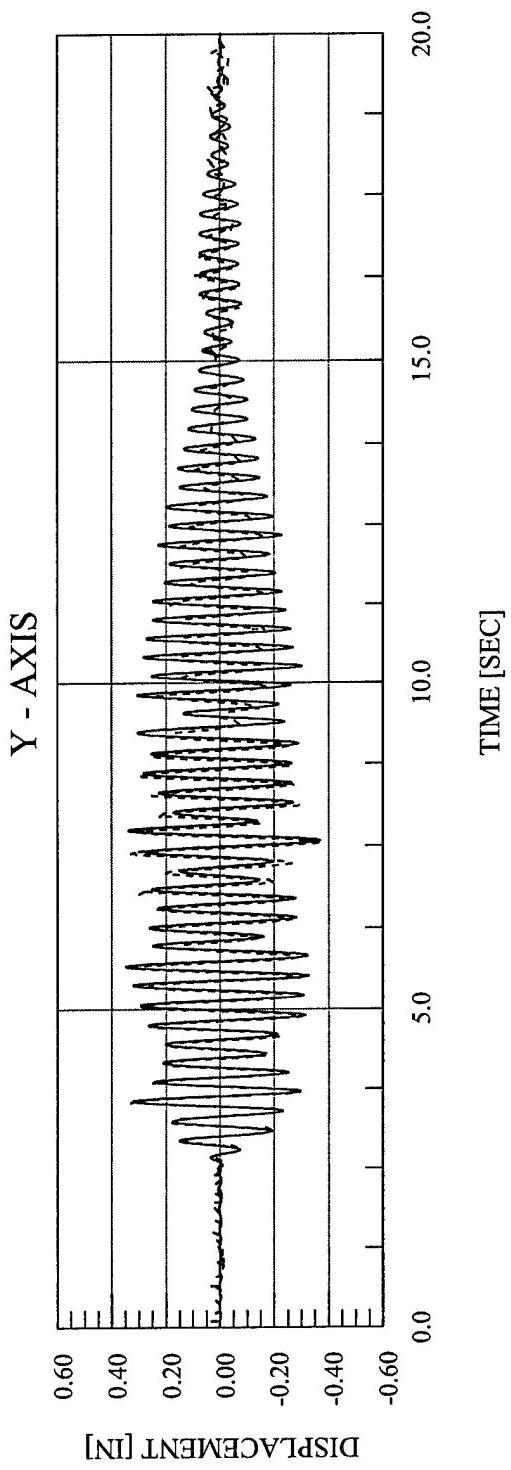


Figure 4.29 Drain-3DX Analytical Displacement vs. Time – EQ 02 – 25% Y-Axis Imperial Valley

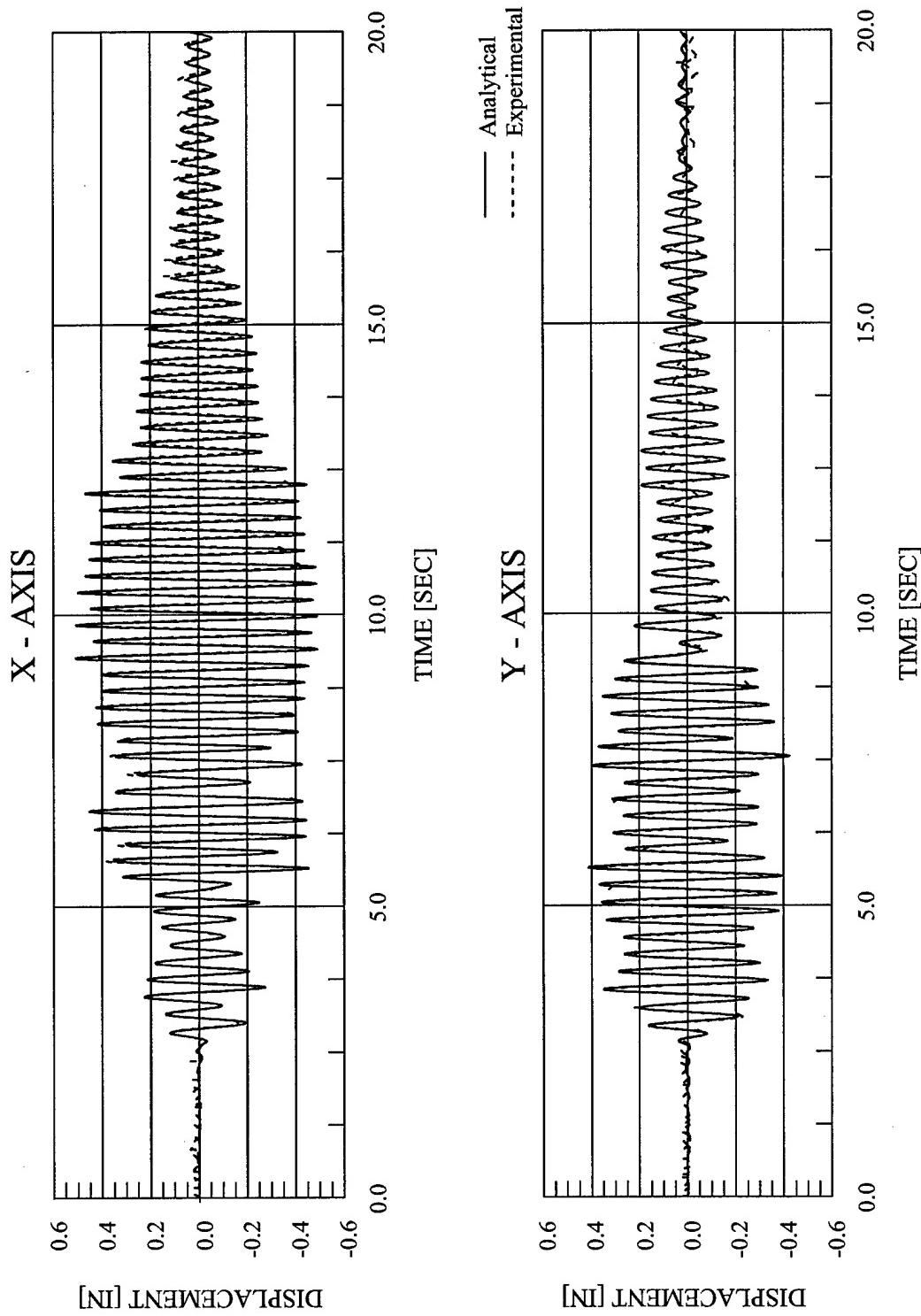


Figure 4.30 Abaqus Analytical Displacement vs. Time – EQ 03 – 25% Biaxial Imperial Valley

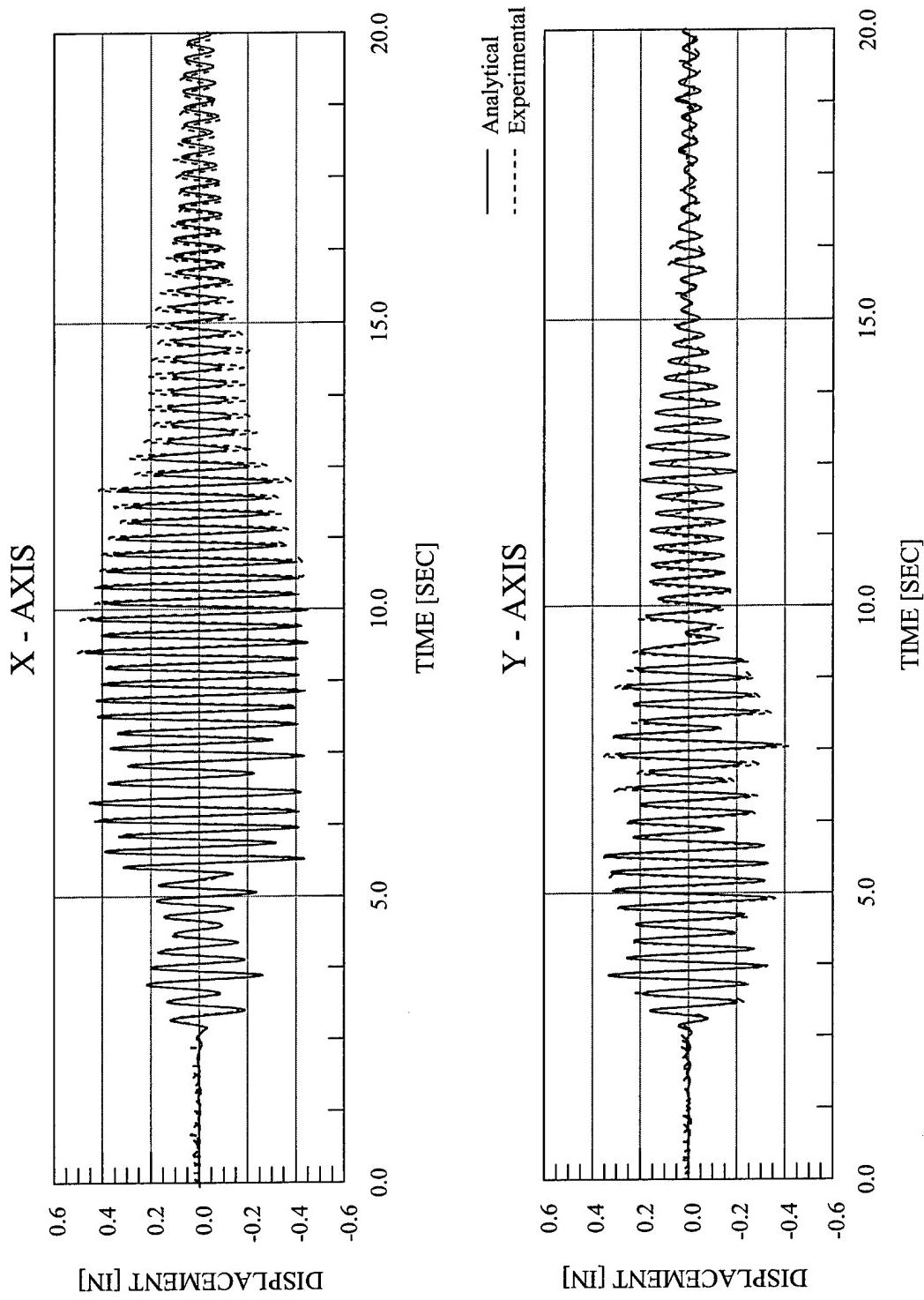


Figure 4.31 Drain-3DX Analytical Displacement vs. Time – EQ 03 – 25% Biaxial Imperial Valley

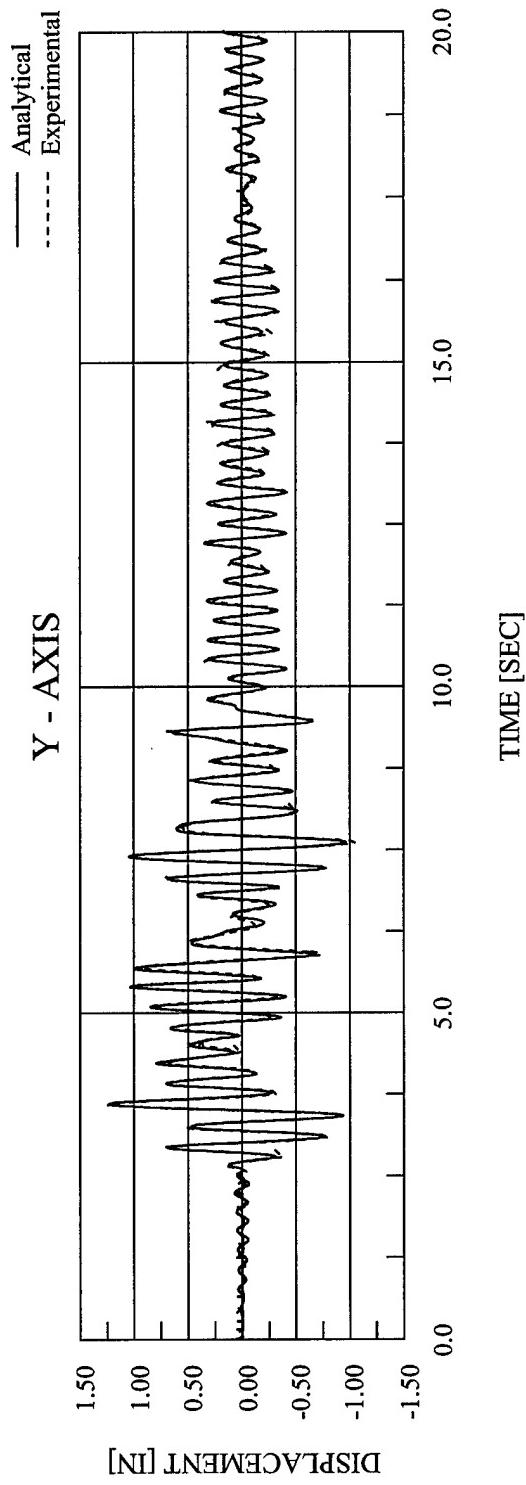


Figure 4.32 Abaqus Analytical Displacement vs. Time – EQ 07 – 100% Y-Axis Imperial Valley – Combined Material Hardening

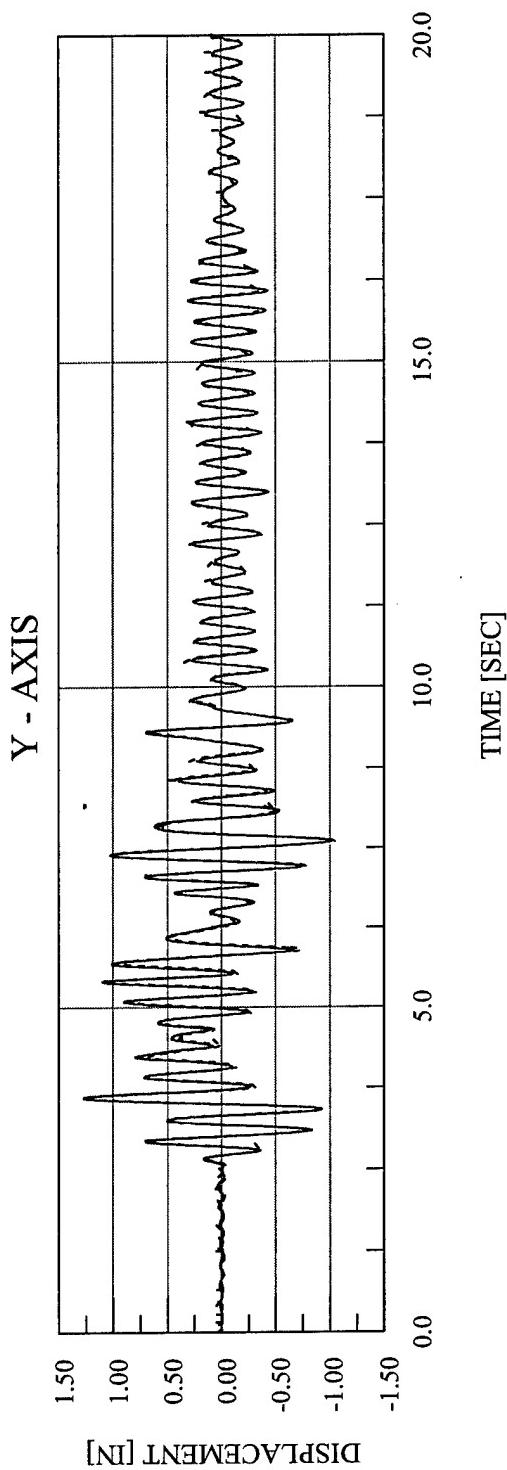


Figure 4.33 Drain-3DX Analytical Displacement vs. Time – EQ 07 – 100% Y-Axis Imperial Valley

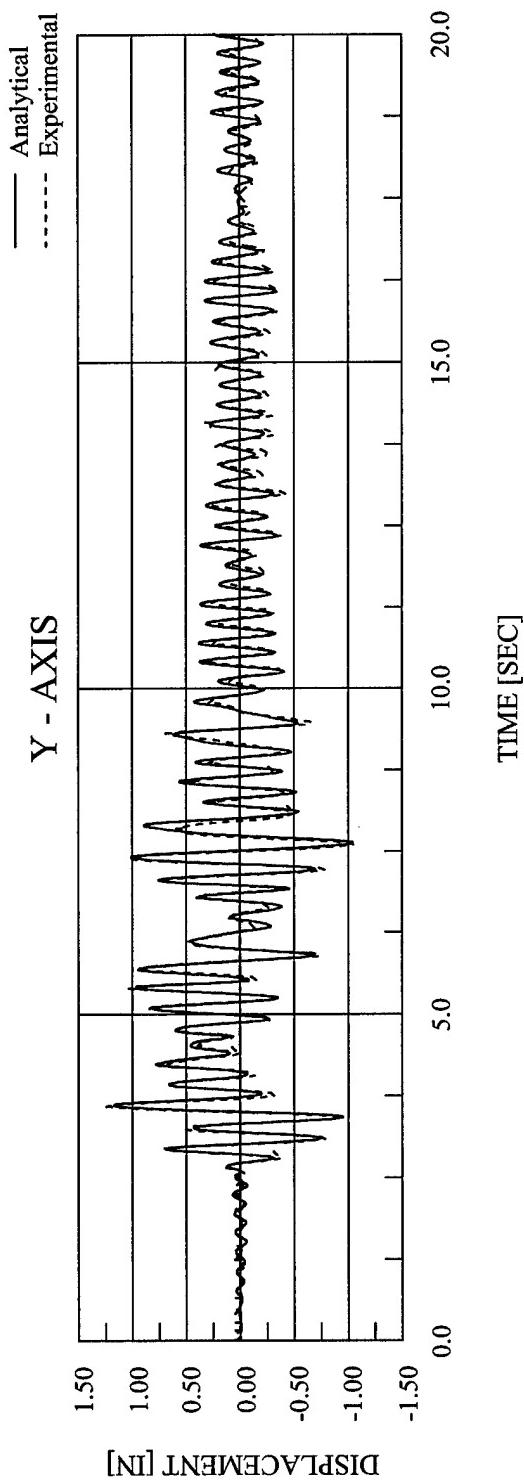


Figure 4.34 Abaqus Analytical Displacement vs. Time – EQ 07 – 100% Y-Axis Imperial Valley – Perfect Plasticity

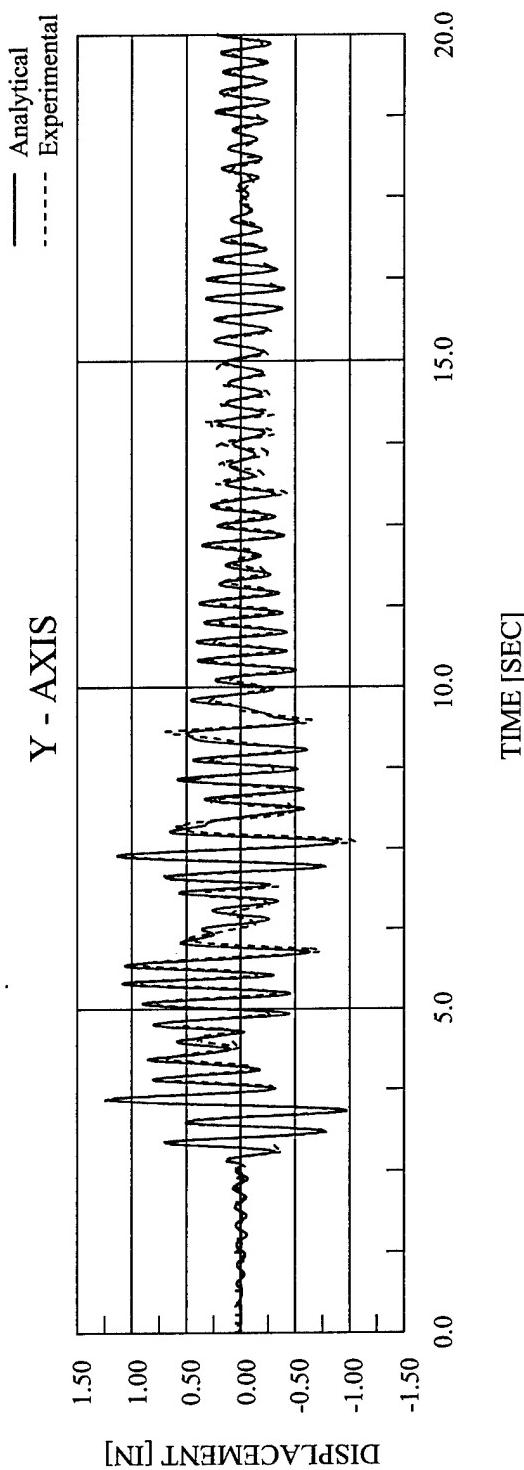


Figure 4.35 Abaqus Analytical Displacement vs. Time – EQ 07 – 100% Y-Axis Imperial Valley – Isotropic Material Hardening

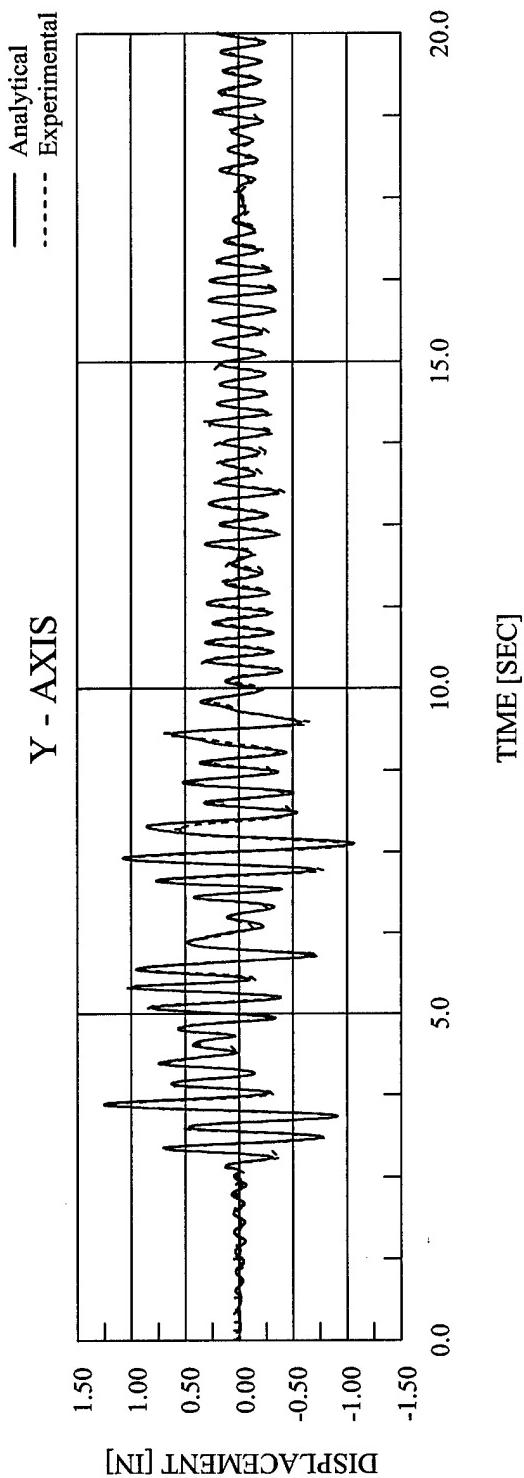


Figure 4.36 Abaqus Analytical Displacement vs. Time – EQ 07 – 100% Y-Axis Imperial Valley – Kinematic Material Hardening

CHAPTER 5

EXPERIMENTAL AND ANALYTICAL RESPONSE OF TEST CONFIGURATION 2

This chapter provides a summary of the experimental test data and the finite element analysis results of Test Configuration 2. The second configuration, as seen in Figure 5.1, featured the masses loaded symmetrically on the diaphragm, and four 4" Extra-Strong Columns. The dynamic properties of the test structure in Test Configuration 2 are shown in Table 5.1.

Six earthquake simulations were performed with this test configuration, with the only difference during each simulation being the set of input ground motions. Although six simulations were performed, only five will be discussed here. After the fifth simulation, the structure had experienced two highly inelastic tests, and the accumulated damage was significant enough to make any data analysis difficult. Thus, EQ 12 – EQ 16 are the five earthquake simulations that will be discussed in this chapter. Characterization tests also were performed to determine the dynamic properties of the model, as described in Chapter 2. The complete test sequence for Test Configuration 2 is shown in Table 5.2.

The first three earthquake simulations, EQ 12 with 25% X-Axis only [$\text{PGA}_X = 0.250 \text{ g}$], EQ 13 with 25% Y-Axis only [$\text{PGA}_Y = 0.168 \text{ g}$], and EQ 14 with 25% Biaxial input motions [$\text{PGA}_X = 0.248 \text{ g}$ and $\text{PGA}_Y = 0.170 \text{ g}$], were intended to produce elastic behavior only. During the simulations, the structure slightly exceeded the yield displacement in the X direction during EQ 12 and EQ 14. The fourth simulation, EQ 15, using 100% Biaxial input motions [$\text{PGA}_X = 1.080 \text{ g}$ and $\text{PGA}_Y = 0.699 \text{ g}$], was the initial test with significant inelastic response along both axes for this configuration. Subsequently, an additional test was performed, EQ 16, in which 150% Biaxial input motions were used [$\text{PGA}_X = 1.582 \text{ g}$ and $\text{PGA}_Y = 1.141 \text{ g}$]. This final test therefore featured not only inelastic behavior, but also pre-existing damage in the model columns.

This chapter summarizes response data of the test structure during the earthquake simulations and the dynamic characterization tests. Summaries of test model accelerations, displacements, torsional moments, overturning moments, column end moments, and base shears are provided.

5.1 OBSERVED STRUCTURAL RESPONSE

The diaphragm acceleration and displacement time history responses for the 25% X-Axis simulation are shown in Figure 5.2. The base shear vs. displacement and torque vs. rotation are shown in Figure 5.3. Similar responses for the 25% Y-Axis simulation are shown in Figures 5.4 and 5.5. Results for the 25% Biaxial simulation are shown in Figures 5.6 and 5.7. The responses for the 100% Biaxial simulation are shown in Figures 5.8 and 5.9. Results for the 150% Biaxial simulation are shown in Figures 5.10 and 5.11.

Tables 5.3 – 5.7 list the peak recorded diaphragm relative displacements and peak diaphragm accelerations, and corresponding PGA for each of the five earthquake simulations performed in this test configuration. Also listed are the maximum base shears, maximum torsional moments, maximum overturning moments, maximum column end moments for each column, and maximum column end shears for each column.

5.2 OBSERVED RESPONSE DISCUSSION

The calculated force-deformation behavior of the structure in the X and Y directions and about the Z-Axis is shown in Figures 5.12 and 5.13. Again the model structure has slightly different natural frequencies in the X and Y directions despite apparent symmetry, resulting in different force-deformation behavior along each axis. In the X direction, the model has a yield displacement of 0.45 inches at a yield force of 21.35 kips. In the Y direction, the model has a yield displacement of 0.49 inches at a yield force of 21.35 kips. The model has a yield rotation of 0.0064 radians at a yield moment of 1457 kip*inches. In Figure 5.14, the structural force-deformation behavior shown in Figures 5.12 and 5.13 is compared with the maximum force-deformation response from each of the earthquake simulations in this test configuration. Elastic response spectra of the recorded table motions for EQ 12 – EQ 15 are shown in Figures 5.15 – 5.18, respectively. The modal frequencies for this configuration with respect to the response spectra are indicated in Figures 5.15 – 5.18 as well.

The first earthquake simulation for this configuration, EQ 12, features 25% Imperial Valley input motion in the X-Axis only [PGA_X = 0.250 g]. Time history plots of the structural response are

shown in Figure 5.2. The peak displacements of the structure were 0.492 inches in the X direction, 0.050 inches in the Y direction, and 0.33×10^{-3} radians about the Z-Axis. The peak displacement predicted by static analysis, using the elastic response spectrum, is 0.484 inches along the X-Axis, with no displacement predicted along the Y-Axis or about the Z-Axis. Thus, the Y-Axis displacement and rotation indicate that the structural response for this simulation remained elastic, while the X-Axis response was slightly inelastic. The peak base shears are 23.80 kips in the X direction, 2.70 kips in the Y direction, and 28.65 kip*inches about the vertical axis. The peak base shear in the X direction is greater than the yield shear, 21.35 kips, while the peak base shear in the Y direction is less than the yield shear. The peak moment is less than the torsional yield moment, 1457 kip*inches. The base shear vs. displacement plots are both tight and linear, as shown in Figure 5.3, and the structure exhibits no permanent deformation. The apparent elastic response in the shear vs. displacement plot for the X-Axis, despite the structure exceeding the yield displacement, arises from the very gradual decrease in stiffness of the structure after initial yield, as seen in Figure 5.13. Also, although the input motion for EQ 12 was along the X-Axis only, Figure 5.2 shows that the structure did have a displacement response in the Y-Axis. Although torsional motion is not expected with complete mass symmetry, Figure 5.2 indicates that it is present. The Y-Axis and torsional motions were most likely resonance motions, a product of the shaketable control problem discussed in Chapters 3 and 4.

In EQ 13 the model is subjected to a 25% Y-Axis input motion [$\text{PGA}_Y = 0.168 \text{ g}$]. Time history plots of the structural response are shown in Figure 5.4. The peak displacements of the structure were 0.344 inches in the Y direction, 0.022 inches in the X direction and 0.41×10^{-3} radians about the Z-Axis. The peak displacement predicted by static analysis is 0.317 inches in the Y direction, with no displacements predicted along the X-Axis or about the Z-Axis. Thus, the structural response for this simulation remained elastic. In EQ 13, a torsional effect is not expected, and it appears from Figure 5.4 that the measured rotation is similar to the rotation observed in EQ 12. Also, Figure 5.4 seems to indicate that the measured X-Axis displacement is a vibratory response similar to that seen along the Y-Axis in EQ 12. The peak base shears are 15.37 kips in the Y direction are 1.07 kips in the X direction, and the peak torsional moment is 54.02 kip*inches. Figure 5.5 shows the base shear vs. displacement plots and torsional moment vs. rotation plot, which are tight and linear.

The third earthquake simulation for this configuration, EQ 14, features 25% Imperial Valley input motion along both the X-Axis and Y-Axis [$\text{PGA}_X = 0.248 \text{ g}$ and $\text{PGA}_Y = 0.170 \text{ g}$]. Time history

plots of the structural response are shown in Figure 5.6. The peak displacements of the structure were 0.480 inches in the X direction, 0.352 inches in the Y direction, and a peak rotation of 0.78×10^{-3} radians. Static analysis predicts 0.515 inches along the X-Axis, 0.333 inches along the Y-Axis, and no rotation. Thus, the displacements and rotation indicate that the structural response for this simulation remained elastic torsionally and along the Y-Axis, but was inelastic along the X-Axis. The structure underwent no permanent deformation along either axis. As for the previous test, this can be attributed to the very gradual decrease in the stiffness of the structure after initial yield, as seen in Figure 5.13. Bearing this out are the base shear vs. displacement plots and torsional moment vs. rotation plot in Figure 5.7, which are all tight and linear, apparently indicating very minor yielding. The peak base shears are 22.83 kips in the X direction, 15.85 kips in the Y direction, and 60.17 kip*inches about the vertical axis. The peak base shear in the X direction is greater than the yield shear, 21.35 kips, while the peak base shear in the Y direction is slightly less than the yield shear. The peak moment is less than the torsional yield moment, 1457 kip*inches.

As EQ 12 – 14 are very close to linearly elastic in response, the displacement response of the structure in EQ 14 should theoretically be equal to the sum of the responses from EQ 12 and EQ 13. In comparing EQ 14 with EQ 12, the addition of the 25% Y-Axis input motion results in little change in the X-Axis response of the diaphragm, as the peak displacement and base shear are 0.492 inches and 23.80 kips for EQ 12 and 0.480 inches and 22.83 kips for EQ 14. The peak displacement response is slightly smaller for EQ 14 than EQ 12, which is consistent with the fact that the PGA in the X direction is slightly smaller for EQ 14, 0.248 g, than for EQ 12, 0.250 g. In comparing EQ 14 with EQ 13, the addition of the 25% X-Axis input motion results in little change in the Y-Axis response of the diaphragm, as the peak displacement and base shear are 0.344 inches and 15.37 kips for EQ 13 and 0.352 inches and 15.85 kips for EQ 14. The peak displacement response is slightly larger for EQ 14 than EQ 13, which is consistent with the fact that the PGA in the Y direction is slightly larger for EQ 14, 0.170 g, than for EQ 13, 0.168 g. Further, when noting that the Y-Axis response in EQ 12 and the X-Axis response in EQ 13 are a free vibration resonant response, it follows that these peak responses would not be accounted for in computing the peak responses of EQ 14, as those peak responses occur during forced vibration. The rotational response in EQ 14 can also be seen in Table 5.3 to be very close to the sum of the rotational responses in EQ 12 and EQ 13. Thus, the experimental response of the structure for this test configuration conforms to the expected linear behavior very well.

In EQ 15, the first test in this configuration that features inelastic response, the model structure is subjected to 100% Imperial Valley input motion along both the X-Axis and Y-Axis [PGA_X = 1.080 g and PGA_Y = 0.699 g]. Time history plots of the structural response are shown in Figure 5.8. The peak displacements of the structure were 2.86 inches in the X direction and 1.24 inches in the Y direction, with a peak rotation of 2.85×10^{-3} radians. Thus, the structure achieved a ductility of 6.2 in the X direction and 2.6 in the Y direction for this test. Although the rotational response was less than the yield rotation, which is not surprising with mass symmetry, the response was not insignificant, as it was nearly half of the yield rotation. With no asymmetry present, the cause of the rotational response is possibly again the table control problem. Although the table was being driven along both horizontal axes, it was also moving torsionally. However, each column participates in the seismic resistance of the structure in each of the three directions of motion. As a result of the phase of each motion, the effective instantaneous stiffnesses of the columns may be different and less than their elastic stiffnesses. This will lead to torsional motion of the structure as any yielding of the columns in the X or Y directions will reduce the torsional stiffness of the structure and shift the center of rigidity causing a stiffness eccentricity. The peak base shears are 38.17 kips in the X direction and 32.91 kips in the Y direction. Thus, the base shears verify the inelastic response, but they also demonstrate the overstrength of the structure, as the peak shears are both nearly twice the yield shears. Figure 5.9 shows the base shear vs. displacement plots and torsional moment vs. rotation plot. The base shear vs. displacement plots are no longer tight and linear, but now are taking on a fuller shape.

The normalized acceleration response of the diaphragm is shown in Table 5.4. In EQ 14, with 25% Biaxial input motions, the normalized acceleration response of the diaphragm is 2.54 in the X direction and 2.58 in the Y direction. The input ground motions are increased by approximately a factor of 4 in EQ 28, but the acceleration response of the diaphragm only increases by about 1.7 in the X direction and 2.1 in the Y direction. Thus, the normalized acceleration response of the diaphragm decreases to 0.98 in the X direction and 1.30 in the Y direction. Also, although the input motions are increased by a factor of approximately 4, the angular acceleration response of the diaphragm increases from EQ 14 to EQ 15 by a little more than 2. Both of these trends verify the expected inelastic behavior of the structure in EQ 15.

The final earthquake simulation for this configuration, EQ 16, features 150% Imperial Valley input motion along both the X-Axis and Y-Axis [PGA_X = 1.582 g and PGA_Y = 1.141 g]. Time history plots of the structural response are shown in Figure 5.10. The peak displacements of the

structure were 5.41 inches in the X direction and 4.31 inches in the Y direction, with a peak rotation of 5.35×10^{-3} radians. Thus, the structure achieved a ductility of 11.9 in the X direction and 8.8 in the Y direction for this test. The peak base shears were 42.84 kips in the X direction and 39.84 kips in the Y direction. The peak torsional moment is roughly one-tenth of the yield moment, however, the peak rotation of the structure is very close to the yield rotation. This is again a result of the instantaneous stiffnesses of the columns in each direction potentially being different and less than their elastic stiffnesses, due to the phase of each of the response motions and the resulting inelastic column behavior. This response behavior can be clearly observed in Figure 5.14, which compares the actual peak force-displacement behavior of the structure throughout all of the simulations in this configuration, termed a backbone curve, to the force-deformation behavior found through pushover analyses. The backbone curves and pushover curves for the X-Axis and Y-Axis match well, while for the Z-Axis, a significant difference exists between the two. If an ostensibly symmetric structure can come close to achieving a peak rotation equal to the yield rotation, it seems reasonable that this behavior will be even more significant when analyzing an asymmetric structure, such as in subsequent test configurations.

The base shears in EQ 16 are approximately 10% larger in the X direction and 20% larger in the Y direction than those in EQ 15, despite the fact that the input motions have been increased by 50%. This is also indicative of inelastic behavior, as the base shears would be expected to increase proportionally to the input motions if the response remained elastic. With EQ 16, as shown in Figure 5.11, the base shear vs. displacement hysteresis plots exhibit a very full, smooth shape. Substantially more inelastic energy dissipation was observed for this test than for EQ 15. Contrary to EQ 12 – 14, a small amount of residual displacement is evident after EQ 15, as seen in Figure 5.8. The permanent displacement increases substantially in EQ 16, as seen in Figure 5.10.

The displacement response of the diaphragm divided by, or normalized by, the peak ground acceleration (PGA) is shown in Table 5.3. In EQ 14, with 25% Biaxial input motions, the relative displacement of the diaphragm is 1.94 in/g in the X direction, and 2.07 in/g in the Y direction. The input ground motions are increased to 100% Biaxial in EQ 15, but the normalized displacement increases slightly in the X direction to 2.65 in/g and decreases slightly in the Y direction to 1.77. Also, in moving from EQ 14 to EQ 15, the diaphragm rotation increases on a relatively proportional level with the input motion increase. In EQ 16, the input motions are increased to 150% Biaxial, and the normalized displacement response of the diaphragm is 3.42 in in the X direction and 3.78 in the Y direction. Thus, in EQ 16 the normalized displacements have

increased significantly from those in EQ 15. Also, the maximum rotation nearly doubles from EQ 15 to EQ 16, while the input motions increase by only 50%. Thus, the normalized deformation response decreases as the period of the structure increases in moving to inelastic behavior, from EQ 14 to EQ 15, and then the normalized displacements increase as the period of the structure increases further. Although not predictable, this behavior is not inconsistent with the deformation response spectra for this configuration, shown in Figure 5.18.

5.3 DYNAMIC CHARACTERIZATIONS OF THE MODEL

Prior to performing any shaketable simulations using the earthquake input motions, white noise, sine sweep, and sine decay tests were performed, as discussed in Chapter 3. This general pattern was followed for Test Configuration 2, as can be seen in Table 5.2. In addition, white noise tests were performed immediately after both earthquake simulations exhibiting inelastic behavior, EQ 16 and EQ 17.

The dynamic properties of the test structure, as measured before EQ 12 and after EQ 17, are shown in Table 5.1. Three modal frequencies, corresponding to the first mode in each of the three degrees-of-freedom, dominate the structural response. Also, the damping ratio of the test structure for all three degrees-of-freedom is below one percent, which is consistent with the damping ratios of the first test configuration. The results in Table 5.1 indicate that due to the inelastic behavior in EQ 16 and EQ 17, some permanent softening of the structure did take place. The damping also increased noticeably by the end of the final simulation. The structure experienced a significant amount of inelastic behavior during the final two simulations, which most likely began to produce micro-cracking at the column-base plate welded interface.

5.4 OBSERVED CONDITION OF THE STRUCTURE

For Test Configuration 2, fracture occurred in the column-to-plate welded joint during EQ 17. The southeast and southwest columns both fractured near the column tops, and all four columns fractured near the column bottoms. In observing the structure condition after EQ 15, the formation of plastic hinges near the tops and bottoms of the columns was becoming discernable. Following the completion of EQ 16, permanent plastic damage in the columns was evident, with

the locations of the plastic hinges in the columns becoming very clear. Figure 5.19 is a photograph of the test structure taken before the earthquake simulations were performed. Figures 5.20 and 5.21 are photographs of the test structure taken after the final earthquake simulation in this configuration, EQ 16, illustrating the inelastic behavior and permanent damage of the structure. Figure 5.22 also shows the formation of plastic hinges near the top and bottom of the northeast column. Figure 5.23 shows the column fracture at the bottom one of the columns after EQ 17.

5.5 FINITE ELEMENT ANALYSIS

In modeling the behavior of the test structure, the nonlinear finite element analysis programs Abaqus and Drain-3DX were employed. During the earthquake simulations employing the larger scale input motions, the structural response exhibits both geometric and material nonlinearities, both of which Abaqus and Drain-3DX can model. A more complete discussion of the applicable features of Abaqus and Drain-3DX is presented in Chapter 3. Also, some aspects of the finite element model, such as the modeling of the diaphragm as a rigid component, are common throughout each test configuration, and are discussed more completely in Chapter 3.

(A) PIPE COLUMN MATERIAL MODEL

The pipe columns used in Test Configuration 2, as well as those used in Test Configurations 1, 3, and 4 were produced from the same batch of raw pipe column lengths. The material models of the pipe columns in these four test configurations were based on stress-strain data produced during the tension tests performed on each coupon. Both the original stress-strain data recorded during the coupon tension tests, and the best-fit material model used in the finite element analyses are shown in Figure 5.24 for Abaqus and in Figure 5.25 for Drain-3DX. Shown in Table 5.8 are the numerical stress-strain best-fit Abaqus model data. Shown in Table 5.9 are the numerical stress-strain best-fit Drain-3DX model data.

(B) FINITE ELEMENT MODEL

The Abaqus and Drain-3DX finite element models employed to analyze the behavior of Test Configuration 2 are shown in Figures 5.26 and 5.27, respectively. Beyond the features of the finite element model, which are common throughout each test configuration and are discussed in Chapter 3, these figures illustrate the location and magnitudes of the nodal masses and the height of the Non-Rigid Links. For the Abaqus model, the nodal masses placed at each of the four corners of the diaphragm have a magnitude of $2.941 \text{ lb} \cdot \text{s}^2/\text{in}$. The interior nodal masses each have a magnitude of $20.270 \text{ lb} \cdot \text{s}^2/\text{in}$. The height of the finite element model diaphragm in this test configuration is 69.123 inches, which thus produces a length of 9.123 inches for each of the four Non-Rigid Links. Figure 5.27 illustrates the location and magnitudes of the nodal masses and the height of the Non-Rigid Links for the Drain-3DX model. The nodal masses placed at the four diaphragm corners have magnitudes of $2.994 \text{ lb} \cdot \text{s}^2/\text{in}$. The interior nodal masses each have a magnitude of $20.411 \text{ lb} \cdot \text{s}^2/\text{in}$. The height of the finite element model diaphragm is 68.798 inches, which results in a length of 8.798 inches for the Non-Rigid Links.

(C) OBSERVED RESPONSE

The relative displacement of the diaphragm along the X- and Y-Axis and the rotation of the diaphragm about the Z-Axis were chosen as the response quantities used to compare the accuracy of the finite element simulations. Displacement histories for both Abaqus and Drain-3DX analyses along the X- and Y-Axis, where appropriate, are provided for the 25% X-Axis simulation [$\text{PGA}_X = 0.250 \text{ g}$] in Figures 5.28 and 5.29, for the 25% Y-Axis simulation [$\text{PGA}_Y = 0.168 \text{ g}$] in Figures 5.30 and 5.31, and for the 25% Biaxial simulation [$\text{PGA}_X = 0.248 \text{ g}$ and $\text{PGA}_Y = 0.170 \text{ g}$] in Figures 5.32 and 5.33. Displacement histories along the X- and Y-Axis and rotation histories about the Z-Axis are provided for the 100% Biaxial simulation [$\text{PGA}_X = 1.080 \text{ g}$ and $\text{PGA}_Y = 0.699 \text{ g}$] in Figures 5.34 – 5.37, and for the 150% Biaxial simulation [$\text{PGA}_X = 1.582 \text{ g}$ and $\text{PGA}_Y = 1.141 \text{ g}$] in Figures 5.38 – 5.44. The 150% Biaxial simulation was performed using four different post-yield material models: perfect plasticity, isotropic hardening, kinematic hardening, and combined isotropic/kinematic hardening. Table 5.10 lists the maximum peak relative displacements in the X and Y directions and the peak rotation, and the corresponding PGAs, for the five earthquake simulations listed above. The 150% Biaxial simulation time histories using the perfect plasticity, isotropic hardening, and kinematic hardening models are

provided for qualitative purposes only, and as such the peak relative displacements are not provided in Table 5.10.

(D) OBSERVED RESPONSE DISCUSSION

In Figures 5.28 – 5.33, the displacement response histories for the uniaxial and biaxial 25% simulations can be seen for both the test structure and the finite element model. The frequency contents of the response histories in both the Abaqus and Drain-3DX simulations match the test data very well. As seen in Table 5.10, the maximum relative displacements in both directions of the Abaqus finite element analysis match the test data fairly well, agreeing to within about 6% in both directions. The Drain-3DX simulations also match the test data well, with differences in both directions of about 13%. As with Test Configuration 1, however, the maximum displacements do not match the test data as well as do those for the Abaqus simulations. With both the Abaqus and Drain-3DX models, the peak displacements appear to occur in the same time region for both the finite element model and the test structure. For this test configuration, the damping ratios of the test structure were 0.60% in the X direction and 0.64% in the Y direction. Thus, with the damping in this test configuration, the inability to specify the damping in each direction independently was not as significant a problem as with the previous test configuration.

In Figures 5.34 and 5.35, the displacement and rotation response histories for EQ 15 can be seen for both the test structure and the finite element model, using a combined isotropic/kinematic hardening model. This simulation is largely inelastic, achieving a peak displacement of nearly 3 times the yield displacement in the Y direction and nearly 7 times the yield displacement in the X direction. For the displacements, the frequency contents of the response histories in the Abaqus simulations match the test data fairly well. In the X direction, the magnitude of the displacement also matches very well. For the Y direction motion, the Abaqus simulations predict smaller peak displacements at a number of points in the time history. As seen in Table 5.10, the peak displacements in the X direction agree to within 7%, while the peak displacements in the Y direction agree to within only 14%. Also important, however, is the fact that the peak displacements appear to occur in the same time region for both the finite element model and the test structure. The Drain-3DX results for EQ 15 also match well. The peak displacements match to within 3% in the X direction and 13% in the Y direction, which is a better match than the Abaqus simulation. However, the Drain-3DX analysis does not predict the permanent offset that is present in the X-Axis motion at the end of the simulation. The permanent offset recorded in

the test is roughly 0.6 – 0.7 inches. Abaqus predicts this result fairly accurately, while Drain-3DX predicts a negligible final offset, if any. Also noteworthy is the rotational response, or lack thereof, during EQ 15. The recorded test rotation history is small, but non-trivial. However, neither of the finite element rotational time histories are even remotely close to the experimental result. In fact, the rotation histories from the Abaqus and Drain-3DX analyses match each other fairly well. The only point during the finite element rotation time histories when the rotation appears to be anything other than noise appears to correlate with a large excursion in the X-Axis displacement response. The rotation present during the test, when considering the finite element results, is most likely a result of the previously discussed shaketable motion control problem. Any shaketable motion other than the recorded motions in the X and Y directions is not accounted for in the finite element analyses, and therefore any actual structural response due to extraneous shaketable motion would not be present in the finite element response results.

These same trends continue in the response histories for EQ 16, the 150% simulation, shown in Figures 5.38 and 5.39, using a combined isotropic/kinematic hardening model. The peak displacements in the Y direction are actually in better agreement for EQ 16, with differences of less than 4%. Further, the peak displacements in the X direction agree to within 2%. This was true despite the fact that EQ 16 is a more difficult test for the finite element model to simulate, as there was pre-existent damage to the structure. The Drain-3DX simulations also matched well, to within 6% in the Y direction and 15% in the X direction, but again not as well as the Abaqus analyses. The first inelastic simulation, EQ 15, featured a small degree of residual displacement, especially in the X direction, indicating permanent damage to the structure. Thus, the second inelastic simulation, EQ 16, began with this permanent damage to the structure. As with EQ 15, the Drain-3DX analysis did not accurately predict the X-Axis permanent offset at the end of EQ 16. As shown in Figure 5.40, the Drain-3DX analysis predicts about one inch, while the actual offset was roughly 3 inches. In modeling an inelastic simulation, it will be shown that the material hardening model, or how the stress-strain behavior of each element changes during yielding, can significantly impact the calculated results. The changes in the stress-strain behavior are path dependent, and thus are influenced by the number and degree of inelastic excursions that each material element makes. With a second inelastic simulation following the first, the stress-strain path that each element takes becomes twice as long. Thus, any inaccuracies in the material hardening model, which will undoubtedly be present, may have twice the effect on the calculated results.

The Abaqus simulations shown in Figures 5.34 – 5.35 and 5.38 – 5.39 utilize a combined nonlinear isotropic/kinematic hardening model, as described in Chapter 3. For the hardening model for these simulations, it was assumed that the isotropic part of the hardening would compose 30% of the total hardening. This figure was chosen through calibration to the response of the symmetric models studied in this chapter and an earlier chapter. This calibration was necessary for subsequent analyses because cyclic material tests were not performed on the steel specimens from the test structure columns. It is difficult to evaluate how accurate the assumed hardening model is, although it was based to some degree on other material studies of A36 steel, as discussed in Chapter 3.

Figures 5.42 – 5.44 show the same simulation, EQ 16, performed with three other post-yield material models. The post-yield behavior in Figure 5.42 was perfect plasticity, while the simulation in Figure 5.43 utilized isotropic hardening only and the simulation in Figure 5.44 utilized kinematic hardening only. As seen in these figures, although the combined hardening model predicts the closest response to the true deformation, both the isotropic hardening and kinematic hardening models are fairly accurate as well. The perfect plasticity material model, while fairly accurate in the uniaxial case, as seen in Chapter 4, grossly overestimates the structural response in both directions. These results demonstrate that the hardening model used for finite element analyses may have a significant impact on calculated results for nonlinear dynamic problems. The peak recorded column strains for EQ 16 were about 0.01 in/in, while the yield strain for the column steel was about 0.0011 in/in, as seen in Figure 5.24. Because the strain gages were placed 10 inches from the column ends for this configuration, the actual peak strains in the columns most likely exceeded the strains measured by the strain gages. Thus, for this simulation, the column material did extend significantly into the inelastic region. As seen in Figure 5.24, at the peak strain level of approximately 0.01 in/in, hardening has increased the strength of the material by about 50% over the strength using a perfect plasticity model, which is consistent with the observations here.

5.6 SUMMARY AND CONCLUSIONS

In Chapter 4, the *Modified μ/R Ratio* was introduced. This ratio gives a measure of the amount of ductility the 2000 NEHRP Seismic Provisions expects a particular structure to experience and thus for which it must be designed. For EQ 07, a uniaxial inelastic earthquake simulation with

displacement response ductility of about 2.5, the *Modified μ/R Ratio* was 0.77. As stated in Chapter 4, this *Ratio* fell within the bounds of the μ/R *Ratio* that the 2000 NEHRP Seismic Provision provides: 0.86 for an Ordinary Moment Resisting Frame (OMRF), and 0.69 for a Special Moment Resisting Frame (SMRF). For EQ 15, an earthquake simulation of relatively equal magnitude to EQ 07 but with biaxial ground motions, the *Modified μ/R Ratios* were 1.37 in the X direction and 0.86 in the Y direction, as shown below.

Configuration	EQ	μ/R Ratio		
		X-Axis	Y-Axis	Z-Axis
Symmetric Mass 100% Uniaxial	7	N/A	0.77	N/A
Symmetric Mass 100% Biaxial	15	1.37	0.86	0.84
Symmetric Mass 150% Biaxial	16	1.77	1.83	1.08

The value for the Y direction is reasonably similar to that of EQ 07, however the value for the X direction is significantly larger, by nearly 80%, than for EQ 07. This implies that for a particular Strength Reduction Factor, the ductility that the structure will experience is significantly greater than the ductility demand required by the *Seismic Provisions*. For EQ 16, the *Modified μ/R Ratio* was 1.77 in the X direction and 1.83 in the Y direction. Thus, not only are these ratios significantly larger than those for the range between an OMRF and an SMRF, but the μ/R *Ratios* have changed from one inelastic earthquake to the next inelastic earthquake for the same test configuration. In order to be able to correctly model inelastic deformations using elastic response spectra, it is important that parameters such as the μ/R *Ratio* do not change significantly based on the amount of inelastic behavior. This is one illustration of the limits of using elastic design to predict inelastic behavior.

As mentioned above, it is important to know whether the μ/R *Ratio* changes for different earthquake configurations in actual structures because the elastic design procedure in the *Seismic Provisions* takes this ratio as a constant. In addition, a constant μ/R *Ratio* implies that the ratio of the two peak lateral displacements remains constant regardless of whether the structure responds

elastically or inelastically, and also regardless of the amount of structural asymmetry. For elastic response, the *Seismic Provisions* define the *seismic base shear*, V_e , as

$$V_{X_e} = PSA_{X_e} * W \quad \text{and} \quad V_{Y_e} = PSA_{Y_e} * W$$

where the subscript e indicates elastic response, the subscripts X and Y indicate the response direction, W is the structure weight, and PSA is the spectral acceleration. The elastic lateral deformations u_X and u_Y are defined as

$$u_{X_e} = \frac{V_{X_e}}{K_X} \quad \text{and} \quad u_{Y_e} = \frac{V_{Y_e}}{K_Y}$$

where K_X and K_Y are the structure stiffnesses in the lateral directions. The ratio of the two peak elastic lateral displacements is then defined as

$$\frac{u_{Y_e}}{u_{X_e}} = \frac{V_{Y_e}/K_Y}{V_{X_e}/K_X} = \frac{W * PSA_{Y_e}/K_Y}{W * PSA_{X_e}/K_X} = \frac{K_X}{K_Y} * \frac{PSA_{Y_e}}{PSA_{X_e}}$$

For inelastic response, the *Seismic Provisions* define the *seismic base shear*, V_i , as

$$V_{X_i} = \frac{PSA_{X_i}}{R} * W \quad \text{and} \quad V_{Y_i} = \frac{PSA_{Y_i}}{R} * W$$

The inelastic lateral deformations u_X and u_Y are defined as

$$u_{X_i} = C_d * \frac{V_{X_i}}{K_X} \quad \text{and} \quad u_{Y_i} = C_d * \frac{V_{Y_i}}{K_Y}$$

The ratio of the two peak inelastic lateral displacements is then defined as

$$\frac{u_{Y_i}}{u_{X_i}} = \frac{C_d V_{Y_i}/K_Y}{C_d V_{X_i}/K_X} = \frac{W * PSA_{Y_i}/K_Y}{W * PSA_{X_i}/K_X} = \frac{K_X}{K_Y} * \frac{PSA_{Y_i}}{PSA_{X_i}}$$

But, if $PSA_{X_i} = A * PSA_{X_e}$ and $PSA_{Y_i} = A * PSA_{Y_e}$ then

$$\frac{PSA_{Y_i}}{PSA_{X_i}} = \frac{A * PSA_{Y_e}}{A * PSA_{X_e}} = \frac{PSA_{Y_e}}{PSA_{X_e}}$$

Therefore,

$$\frac{u_{Y_e}}{u_{X_e}} = \frac{u_{Y_i}}{u_{X_i}} = \frac{u_Y}{u_X}$$

And because the *Seismic Provisions* make no modifications to these equations based on degree of eccentricity, the ratio of peak Y-Axis displacement to peak X-Axis displacement should remain constant regardless of eccentricity.

For EQ 14 in this test configuration, the u_Y/u_X ratio is equal to 0.73, as shown below. For EQ 15, the first inelastic simulation, the ratio drops significantly to 0.43, a decrease of over 40%. This result is confirmed by the fact that the displacement ductility is approximately 2.5 times larger in the X direction than in the Y direction for EQ 15. For EQ 16, the second inelastic simulation, the ratio of u_Y/u_X increases to 0.80.

Configuration	EQ	u_Y/u_X
Symmetric Mass 25% Biaxial	14	0.73
Symmetric Mass 100% Biaxial	15	0.43
Symmetric Mass 150% Biaxial	16	0.80

The displacement ductility in the X direction is now only about 35% larger than in the Y direction, which is similar to the proportion observed in EQ 14. Thus, it appears that due to the differences in the X- and Y-Axis ground motions, the structure in EQ 15 has yielded to different degrees in the two directions. In the Y direction, the structure is still in the region of the pushover curve, Figure 5.12, where the lateral stiffness has not yet decreased significantly. In the X direction, the lateral stiffness has decreased to a much greater degree, resulting in a much larger peak displacement proportionally to the Y-Axis peak displacement. In EQ 16, the stiffness appears to have decreased to a similar degree in the Y direction as in the X direction, as the structure has traveled further along the pushover curve. This phenomenon, yielding at different rates in the two lateral directions, would be expected to occur regularly in actual structures, as orthogonal ground motion components are typically different and structures lose stiffness during yielding in a very gradual manner. The result of this is that the ratio u_Y/u_X may not remain constant as the structure proceeds along its yield path, indicated by the pushover curves. But it also appears that if there is sufficient yielding in each lateral direction, the u_Y/u_X ratio during inelastic response is nearly equal to that for elastic response.

Another limitation in using elastic design occurs when rotational response is a product of inelastic behavior. As mentioned previously, when yielding occurs in one or both of the transverse directions, the torsional stiffness decreases. This has the effect of increasing the torsional response of the structure. During EQ 15 and EQ 16, the two inelastic simulations in this configuration, the structure achieved rotational ductilities of 0.44 and 0.83, despite the fact that

the structure was ostensibly symmetric. With no inherent eccentricity, the only possibility for predicting this response with the *Seismic Provisions* is through the accidental eccentricity. However, the *Provisions* predict peak rotations of 1.89×10^{-3} radians for EQ 15 and 2.83×10^{-3} radians for EQ 16. The peak rotations of the test structure were 2.85×10^{-3} radians and 5.35×10^{-3} radians for EQ 15 and EQ 16, respectively. Thus, the accidental eccentricity provision is noticeably inadequate in predicting these torsional responses. However, the additional edge displacements due to the rotational response in both EQ 15 and EQ 16 are only about 5% of the transverse peak displacements of the structure, which is a mitigating factor in assessing the adequacy of the *Provisions*.

The uniaxial inelastic earthquake simulation performed in Chapter 4, EQ 07, featured a peak ground acceleration of 0.678 g and a peak displacement of 1.216 inches along the Y-Axis, resulting in a normalized displacement of 1.79 inches/g. The first inelastic earthquake simulation in this chapter, EQ 15, featured a similar peak ground acceleration in the Y direction, but a ground motion was also present in the X direction. If a mass or stiffness asymmetry were added to the configuration, the peak displacement would likely be expected to decrease somewhat due to the presence of torsional motion. However, simply adding the X-Axis ground motion does not impact the Y-Axis peak displacement, as it is 1.294 inches in EQ 15, resulting in a normalized displacement of 1.85 inches/g as compared to 1.79 inches/g for EQ 07. This implies that without coupling of the X and Y-Axis motions due to mass or stiffness asymmetry, the X and Y-Axis responses are independent of one another for an inelastic simulation, as is obviously the case for an elastic earthquake simulation.

The time history analyses performed for this configuration using the finite element programs Drain-3DX and Abaqus were generally accurate in their predictions of the experimental response. With respect to the low-level linear simulations, Abaqus consistently predicted peak displacements more accurately than did the Drain-3DX analyses. The Abaqus analyses were off by roughly 2-7%, while the Drain-3DX analyses were typically inaccurate by about 12-13%. No consistent pattern emerged as to why some of the elastic analytical simulations were more accurate than others. The inelastic simulations proved to be similar in their results. The Abaqus analyses were slightly more accurate than those utilizing Drain-3DX. However, each predicted maximum displacements as close as 2% and as different as 15% from the test data. The Abaqus simulations did prove to be significantly better in predicting any permanent offset of the structure. Neither Abaqus nor Drain-3DX was remotely close in predicting the peak rotation,

underestimating the actual peak rotation by anywhere from a factor of 2.5 to 4. As there was no mass or stiffness asymmetry present in this structure, the rotation observed in the test structure appears to be primarily caused by the reduction in torsional stiffness, which occurs when the structure yields in one or both of the planar directions. It appears that neither finite element program models this phenomenon very well. The Abaqus simulations performed with the kinematic and isotropic hardening material models were both fairly accurate in matching the test data. However, the simulation utilizing the elastic-perfectly plastic model was not as accurate, significantly overestimating both the peak displacements and permanent offset by factors of 3-5. Thus, it appears that for this biaxial inelastic simulation, the Abaqus analysis does begin to offer advantages over the Drain-3DX analysis. Also, it is evident that the simple elastic-perfectly plastic material model is insufficient to accurately model the inelastic response of EQ 16.

Mass [lb*s ² /in]	Mass Centers [in]			Column Properties	
	X ₀	Y ₀	Z ₀	A [in ²]	I [in ⁴]
93.618	0.0	0.0	68.798	4.41	9.61

	Modal Frequencies [Hz]			Modal Damping [%]		
	X	Y	θ	X	Y	θ
Before EQ 12	3.589	3.454	6.450	0.596	0.636	N/A
After EQ 17	3.313	3.050	N/A	3.029	3.249	N/A

Table 5.1 Test Structure Dynamic Properties - Test Configuration 2

Test Designation	Input Motions
WNT4	White Noise X-Axis
WNT5	White Noise Y-Axis
WNT6	White Noise Yaw-Axis
SIN4	Sine Decay X-Axis
SIN5	Sine Decay Y-Axis
SIN6	Sine Decay Yaw-Axis
SWP4	Sine Sweep X-Axis
SWP5	Sine Sweep Y-Axis
SWP6	Sine Sweep Yaw-Axis
EQ12	25% X-Axis Imperial Valley
EQ13	25% Y-Axis Imperial Valley
EQ14	25% Biaxial Imperial Valley
EQ15	100% Biaxial Imperial Valley
WNT7	White Noise X-Axis
WNT8	White Noise Y-Axis
EQ16	150% Biaxial Imperial Valley
WNT9	White Noise X-Axis
WNT10	White Noise Y-Axis
EQ17	150% Biaxial Imperial Valley
WNT11	White Noise X-Axis
WNT12	White Noise Y-Axis

Table 5.2 Earthquake Simulations and Dynamic Characterization Tests - Test Configuration 2

Earthquake Test No.	Input Motions	PGA [g]			Relative Displacement [in]			Rotation [10^{-3} rad]			Normalized Displacement [in/g]			Ductility			
		X-Axis	Y-Axis	Z-Axis	X-Axis	Y-Axis	Z-Axis	X-Axis	Y-Axis	Z-Axis	X-Axis	Y-Axis	Z-Axis	X-Axis	Y-Axis	Z-Axis	
12	25% X-Axis	0.250	N/A	0.492	0.059	0.32	1.97	N/A	1.08	0.12	0.05						
13	25% Y-Axis	N/A	0.168	0.020	0.339	0.37	N/A	2.02	0.04	0.69	0.06						
14	25% Biaxial	0.248	0.170	0.482	0.354	0.70	1.94	2.08	1.06	0.72	0.11						
15	100% Biaxial	1.080	0.699	2.859	1.239	2.85	2.65	1.77	6.30	2.52	0.45						
16	150% Biaxial	1.582	1.141	5.407	4.314	5.35	3.42	3.78	11.91	8.77	0.84						

Table 5.3 Maximum Diaphragm Relative Displacement and Rotation - Test Configuration 2

Earthquake Test No.	Input Motions	PGA [g]			Diaphragm Acceleration [g]			Diaphragm Angular Acceleration [10^{-3} g/in]			Normalized Acceleration		
		X-Axis	Y-Axis	Z-Axis	X-Axis	Y-Axis	Z-Axis	X-Axis	Y-Axis	Z-Axis	X-Axis	Y-Axis	
12	25% X-Axis	0.250	N/A	0.658	0.075		0.54			2.63		N/A	
13	25% Y-Axis	N/A	0.168	0.030	0.425		1.01			N/A	2.53		
14	25% Biaxial	0.248	0.170	0.631	0.438		1.13			2.54	2.58		
15	100% Biaxial	1.080	0.699	1.055	0.910		2.61			0.98	1.30		
16	150% Biaxial	1.582	1.141	1.184	1.101		2.68			0.75	0.96		

Table 5.4 Maximum Diaphragm Acceleration and Angular Acceleration Response - Test Configuration 2

Earthquake Test No.	Input Motions	PGA [g]			Base Shear [k]			Torsional Moment [k*in]		Overturning Moment [k*in]
		X-Axis	Y-Axis	Z-Axis	X-Axis	Y-Axis	Z-Axis	X-Axis	Y-Axis	
12	25% X-Axis	0.250	N/A	23.80	2.70	28.65		1645.2	186.7	
13	25% Y-Axis	N/A	0.168	1.07	15.37	54.02		74.2	1062.5	
14	25% Biaxial	0.248	0.170	22.83	15.85	60.17		1578.2	1095.6	
15	100% Biaxial	1.080	0.699	38.17	32.91	138.85		2638.3	2275.1	
16	150% Biaxial	1.582	1.141	42.84	39.84	142.78		2961.3	2753.7	

Table 5.5 Maximum Base Shear, Torsional Moment, and Overturning Moment - Test Configuration 2

Earthquake Test No.	Input Motions	PGA [g]				Column End Moments [k*in]					
		X-Axis		Y-Axis		SE Column		SW Column		NW Column	
		X-Axis	Y-Axis	X-Axis	Y-Axis	X-Axis	Y-Axis	X-Axis	Y-Axis	X-Axis	Y-Axis
12	25% X-Axis	0.250	N/A	20.20	178.41	20.20	178.61	20.82	178.61	20.82	178.41
13	25% Y-Axis	N/A	0.168	117.26	8.23	117.26	9.80	113.46	9.80	113.46	8.23
14	25% Biaxial	0.248	0.170	119.89	170.86	119.89	171.61	117.85	171.61	117.85	170.86
15	100% Biaxial	1.080	0.699	247.75	284.78	247.75	287.83	245.95	287.83	245.95	284.78
16	150% Biaxial	1.582	1.141	300.46	321.57	300.46	321.05	299.34	321.05	299.34	321.57

Table 5.6 Maximum Column End Moments - Test Configuration 2

Earthquake Test No.	Input Motions	PGA [g]		Column End Shears [k]					
		X-Axis	Y-Axis	SE Column		SW Column		NW Column	NE Column
		X-Axis	Y-Axis	X-Axis	Y-Axis	X-Axis	Y-Axis	X-Axis	Y-Axis
12	25% X-Axis	0.250	N/A	5.95	0.67	5.95	0.67	5.95	0.69
13	25% Y-Axis	N/A	0.168	0.27	3.91	0.33	3.91	0.33	3.78
14	25% Biaxial	0.248	0.170	5.70	4.00	5.72	4.00	5.72	3.93
15	100% Biaxial	1.080	0.699	9.49	8.26	9.59	8.26	9.59	8.20
16	150% Biaxial	1.582	1.141	10.72	10.02	10.70	10.02	10.70	9.98

Table 5.7 Maximum Column End Shears - Test Configuration 2

E [ksi] = 29000.0

Stress [ksi]	Strain [in/in]	Plastic Strain [in/in]
0.00000	0.00000	
37.50000	0.00108	0.000000
39.60000	0.00300	0.001863
40.70000	0.00500	0.003831
49.00000	0.02000	0.018593
54.00000	0.04000	0.038449
56.50000	0.06000	0.058378
57.80000	0.08000	0.078340
58.50000	0.10000	0.098320
59.00000	0.15000	0.148306
57.00000	0.20000	0.198363

Table 5.8 Abaqus Stress-Strain Best-Fit Material Model - Test Configuration 2

E [ksi] = 29000.0

Stress [ksi]	Strain [in/in]
0.00000	0.00000
37.50000	0.001293
39.60000	0.003000
49.00000	0.020000
56.50000	0.060000
58.50000	0.100000

Table 5.9 Drain-3DX Stress-Strain Best-Fit Material Model - Test Configuration 2

Earthquake Test No.	Input Motions	PGA [g]				Relative Displacement [in]						Rotation [10^{-3} rad]		
		X-Axis		Y-Axis		X-Axis		Y-Axis		Z-Axis		Abaqus	Drain	Test
		Abaqus	Drain	Test	Abaqus	Drain	Test	Abaqus	Drain	Z-Axis	Abaqus	Drain	Test	
12	25% X-Axis	0.250	N/A	0.470	0.444	0.492	0.0	0.0	0.059	N/A	N/A	N/A	0.32	
13	25% Y-Axis	N/A	0.168	0.0	0.0	0.020	0.342	0.306	0.339	N/A	N/A	N/A	0.37	
14	25% Biaxial	0.248	0.170	0.480	0.437	0.482	0.329	0.318	0.354	N/A	N/A	N/A	0.70	
15	100% Biaxial	1.080	0.699	2.70	2.76	2.86	1.07	1.12	1.24	0.75	0.84	0.84	2.85	
16	150% Biaxial	1.582	1.141	5.53	4.61	5.41	4.14	4.63	4.31	1.28	2.14	2.14	5.35	

Table 5.10 Analytical vs. Experimental Displacement and Rotation Response Comparison - Test Configuration 2

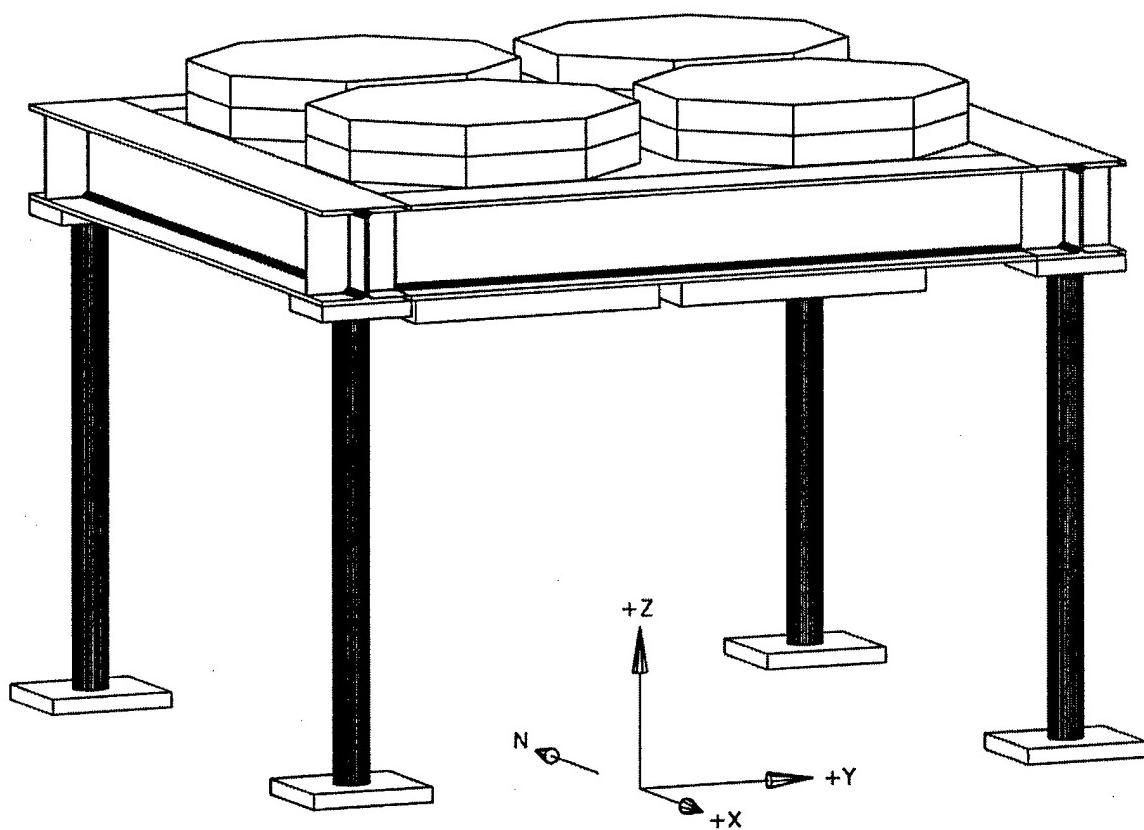


Figure 5.1 Perspective View of Test Configuration Model 2
4 - 4" Extra-Strong Columns

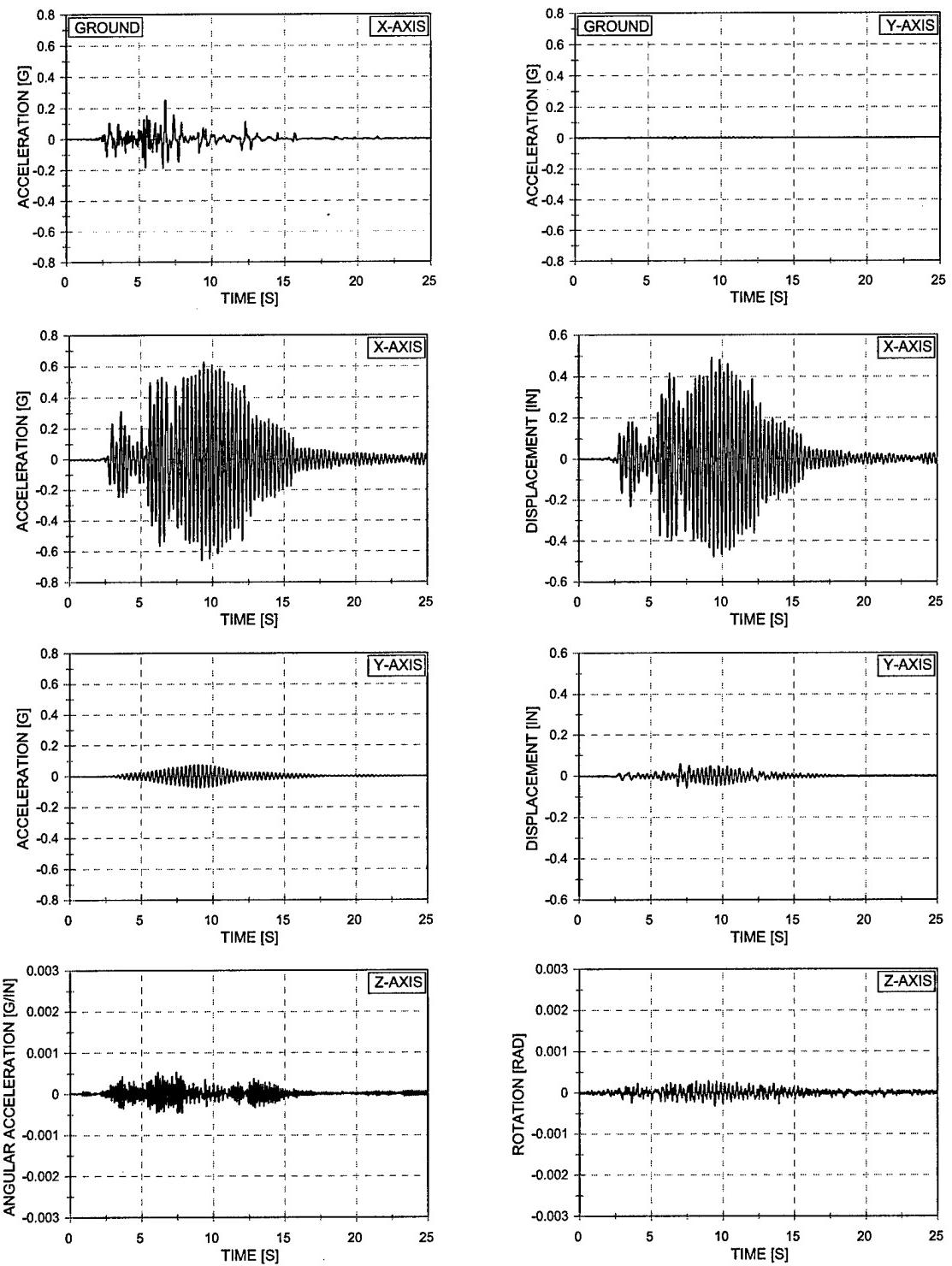


Figure 5.2 Acceleration and Displacement vs. Time – EQ 12
 25% X-Axis Imperial Valley – Symmetric Mass
 Four 4" Extra-Strong Columns

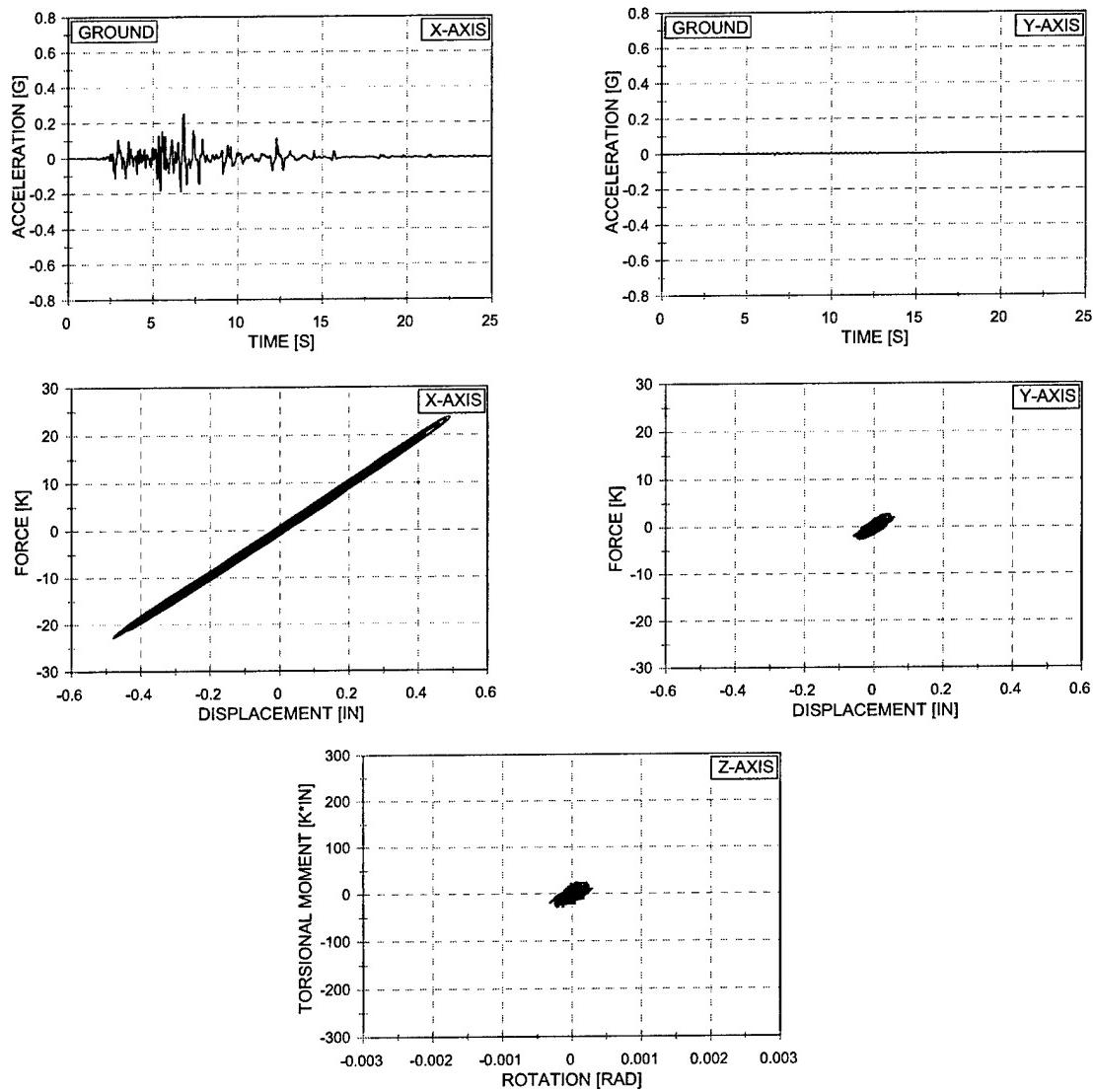


Figure 5.3 Force vs. Displacement and Torsional Moment vs. Rotation – EQ 12
 25% X-Axis Imperial Valley – Symmetric Mass
 Four 4" Extra-Strong Columns

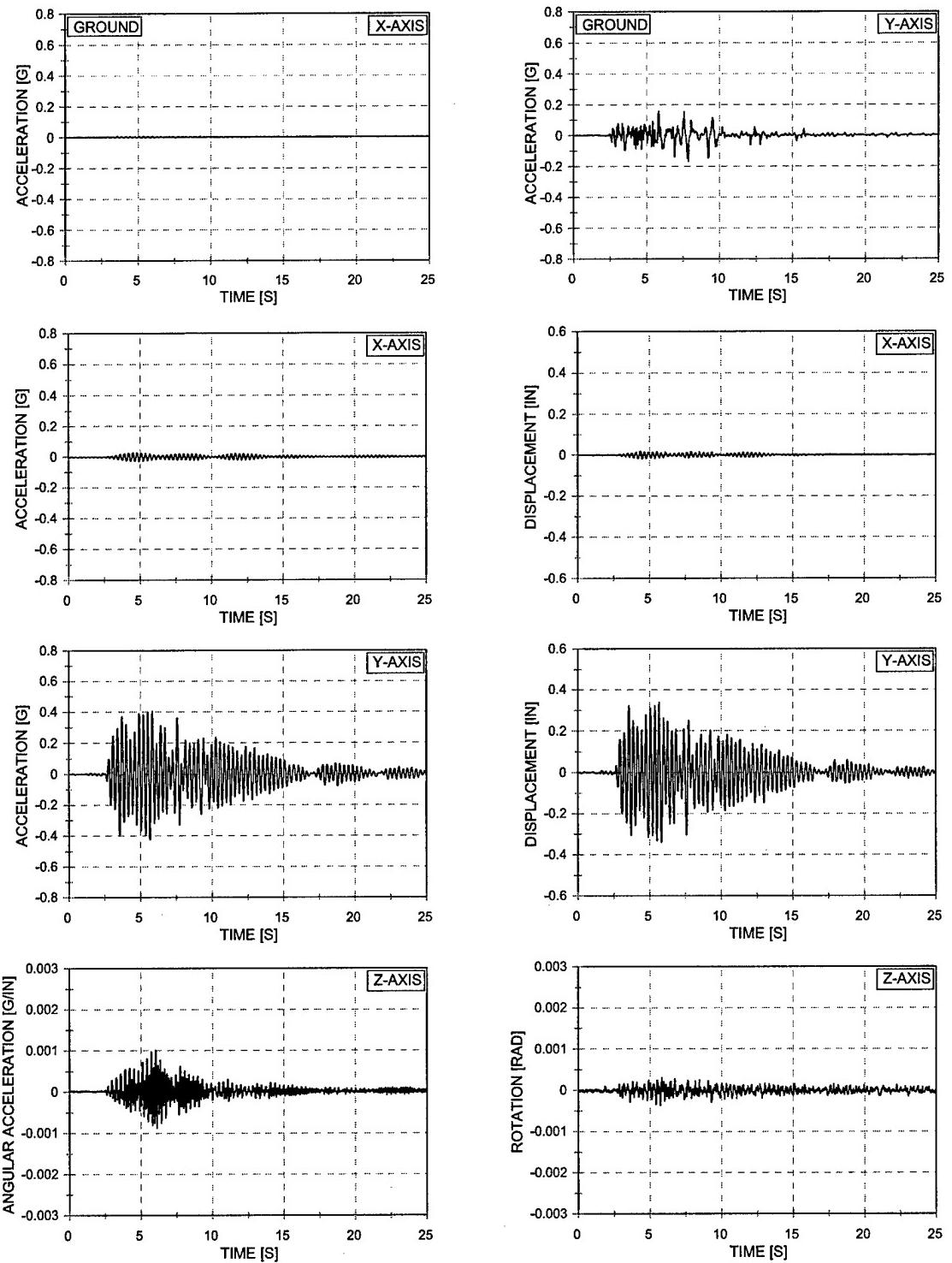


Figure 5.4 Acceleration and Displacement vs. Time – EQ 13
 25% Y-Axis Imperial Valley – Symmetric Mass
 Four 4" Extra-Strong Columns

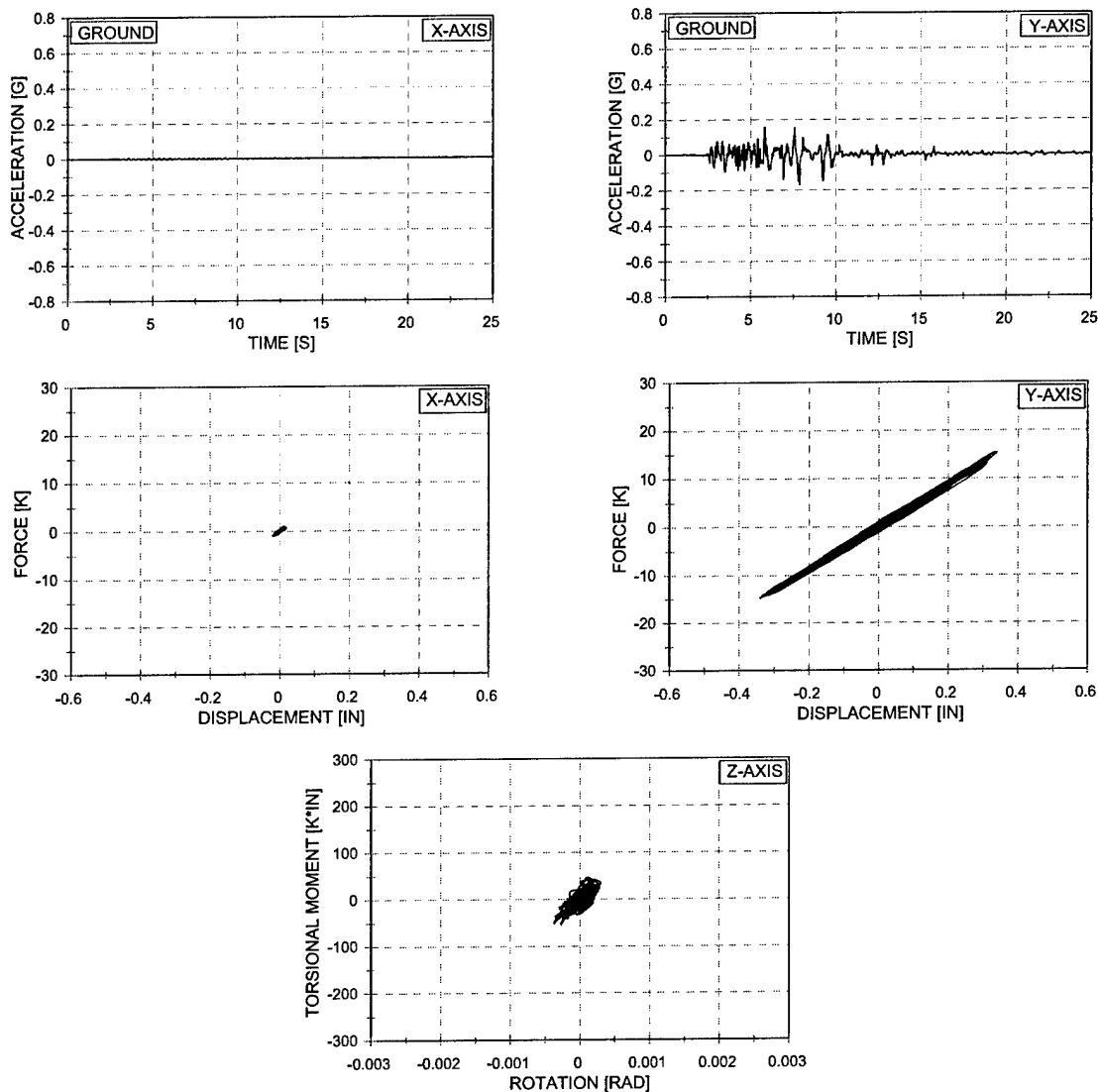


Figure 5.5 Force vs. Displacement and Torsional Moment vs. Rotation - EQ 13
 25% Y-Axis Imperial Valley – Symmetric Mass
 Four 4" Extra-Strong Columns

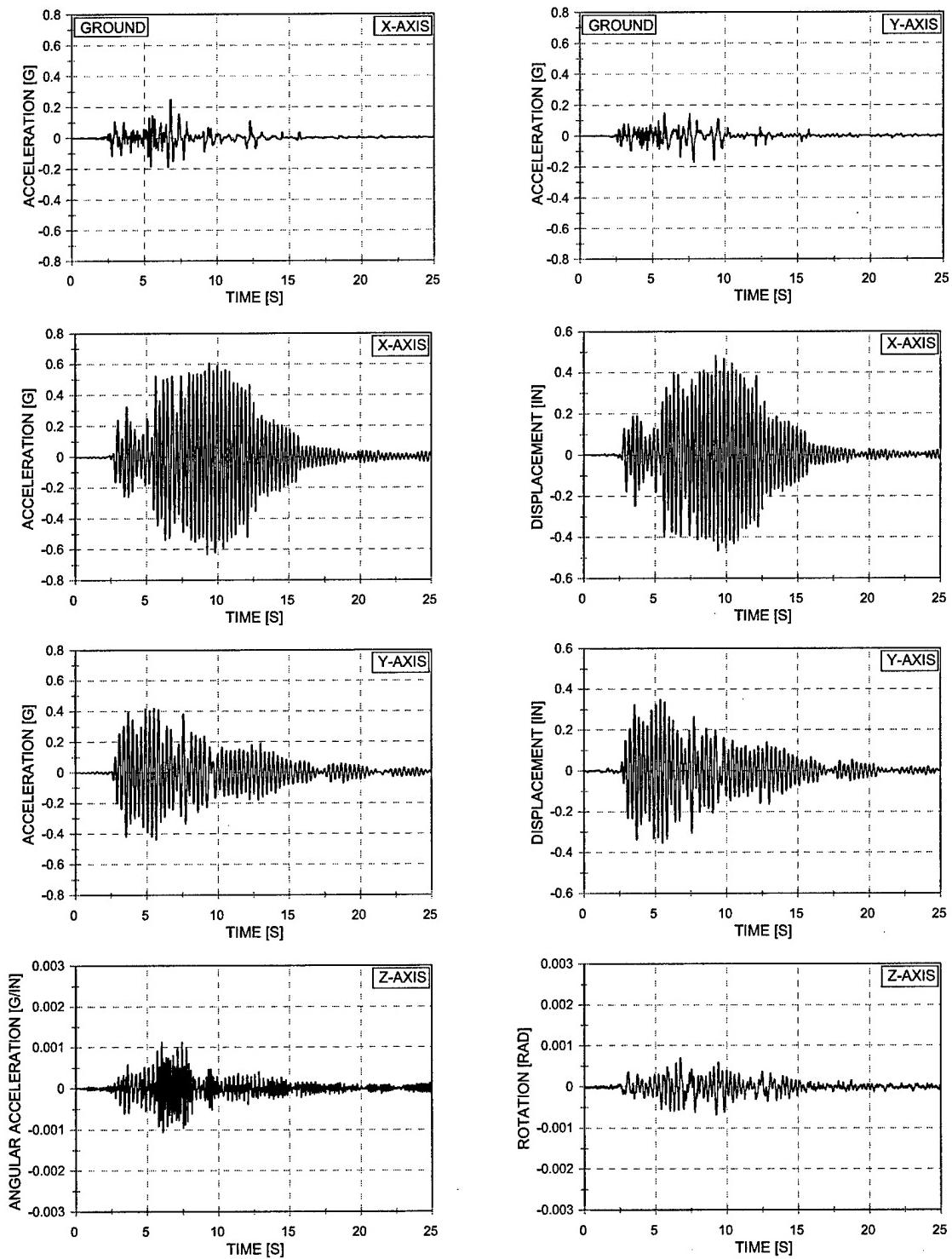


Figure 5.6 Acceleration and Displacement vs. Time – EQ 14
 25% Biaxial Imperial Valley – Symmetric Mass
 Four 4" Extra-Strong Columns

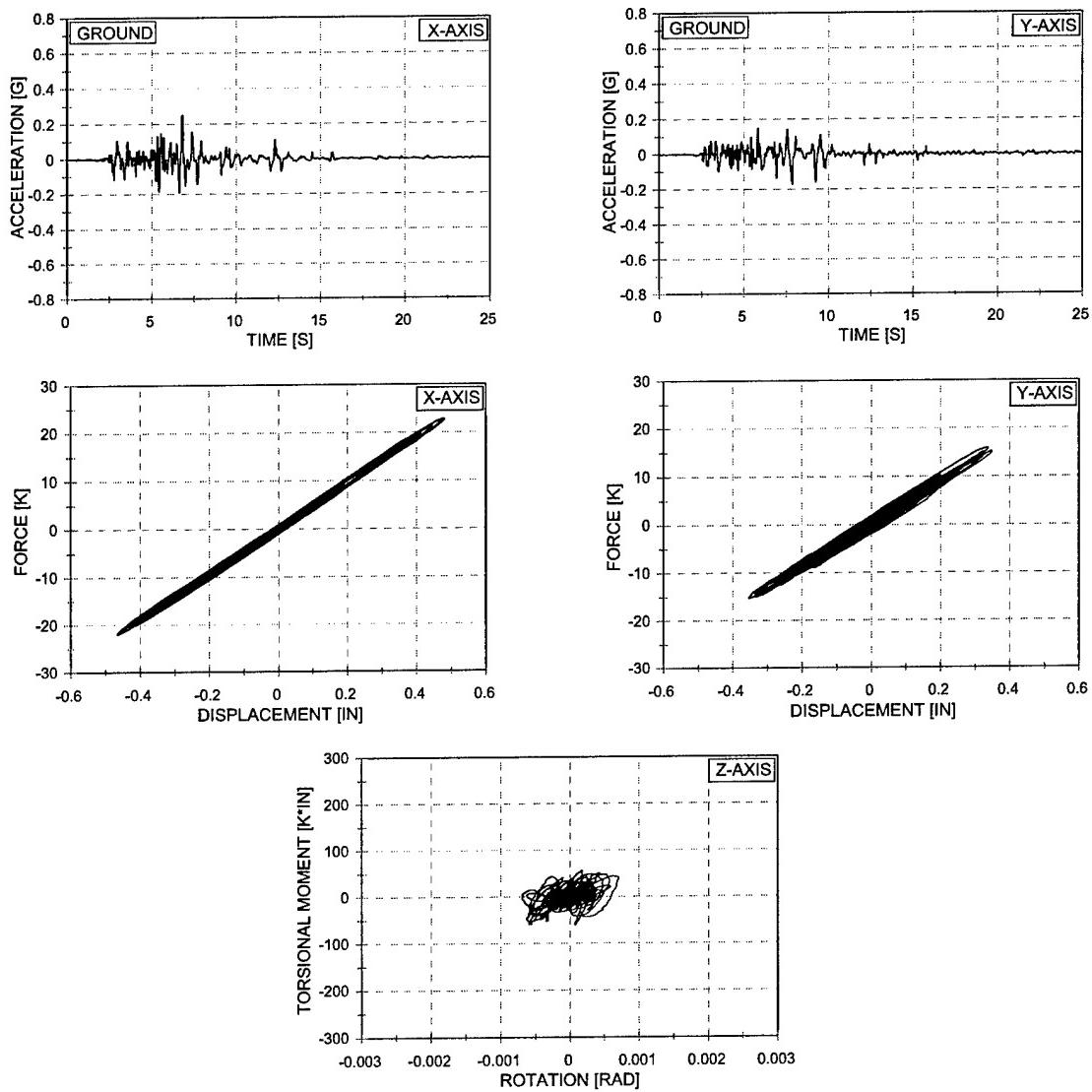


Figure 5.7 Force vs. Displacement and Torsional Moment vs. Rotation - EQ 14
 25% Biaxial Imperial Valley – Symmetric Mass
 Four 4" Extra-Strong Columns

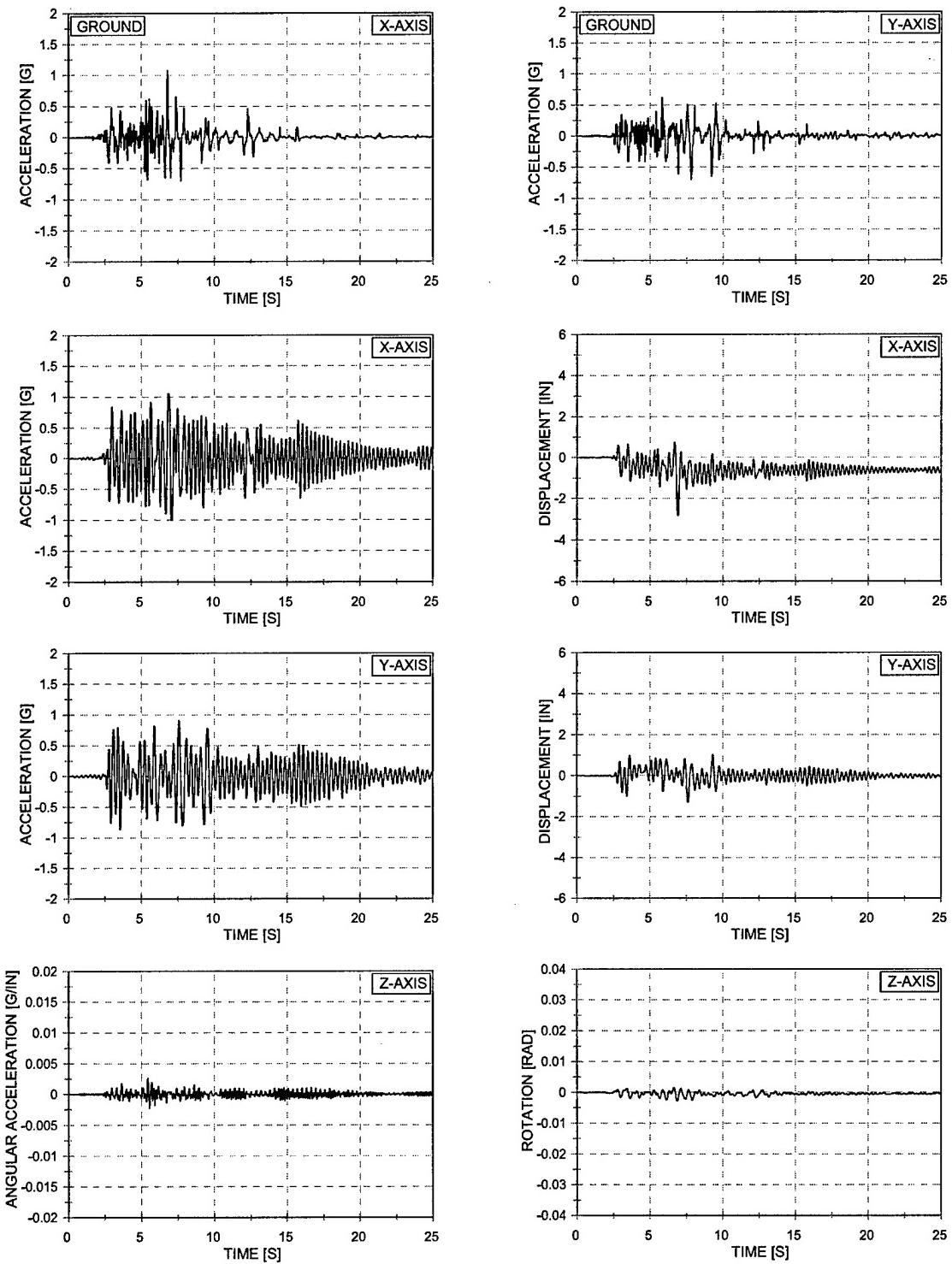


Figure 5.8 Acceleration and Displacement vs. Time – EQ 15
100% Biaxial Imperial Valley – Symmetric Mass
Four 4" Extra-Strong Columns

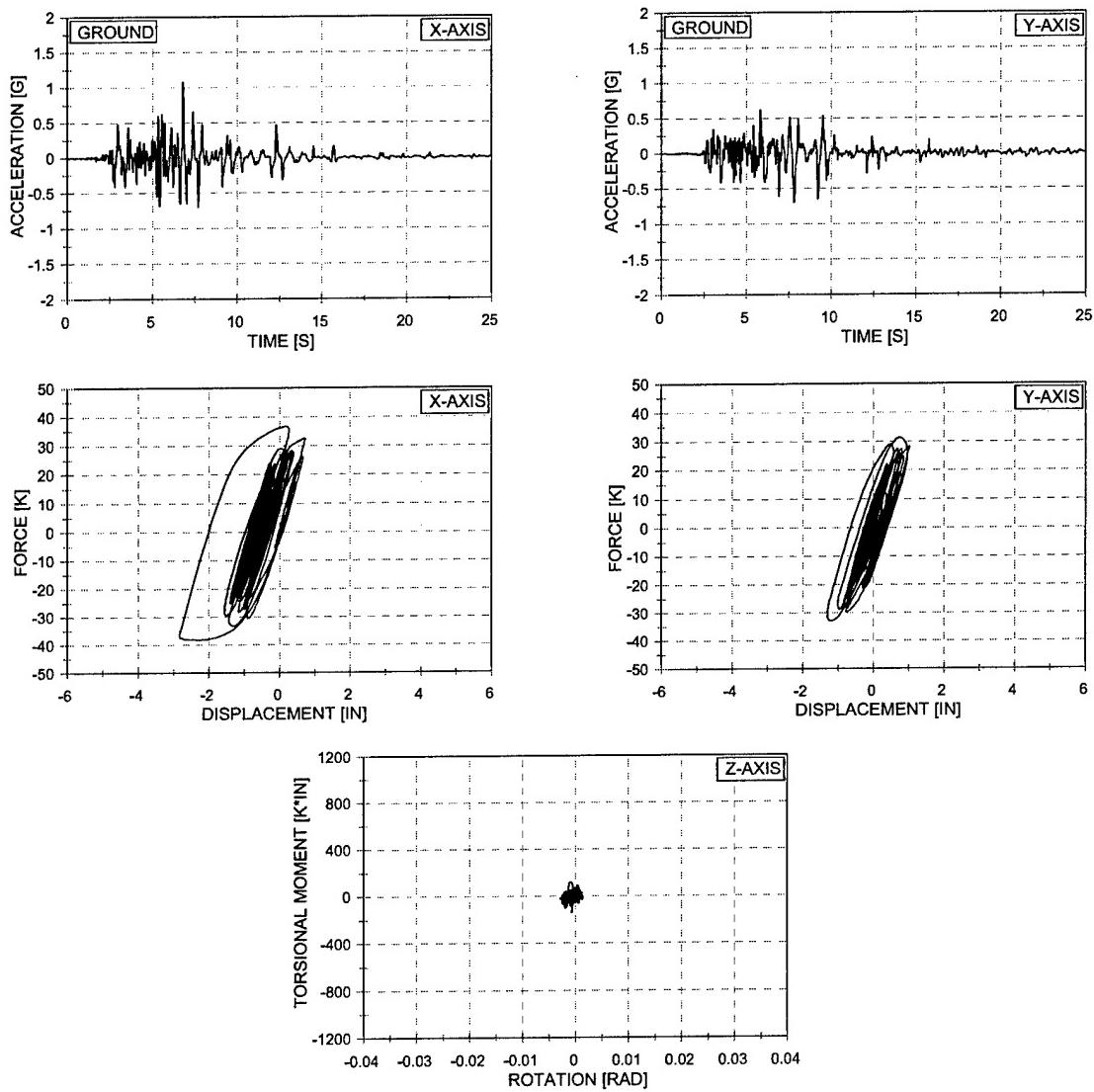


Figure 5.9 Force vs. Displacement and Torsional Moment vs. Rotation - EQ 15
 100% Biaxial Imperial Valley – Symmetric Mass
 Four 4" Extra-Strong Columns

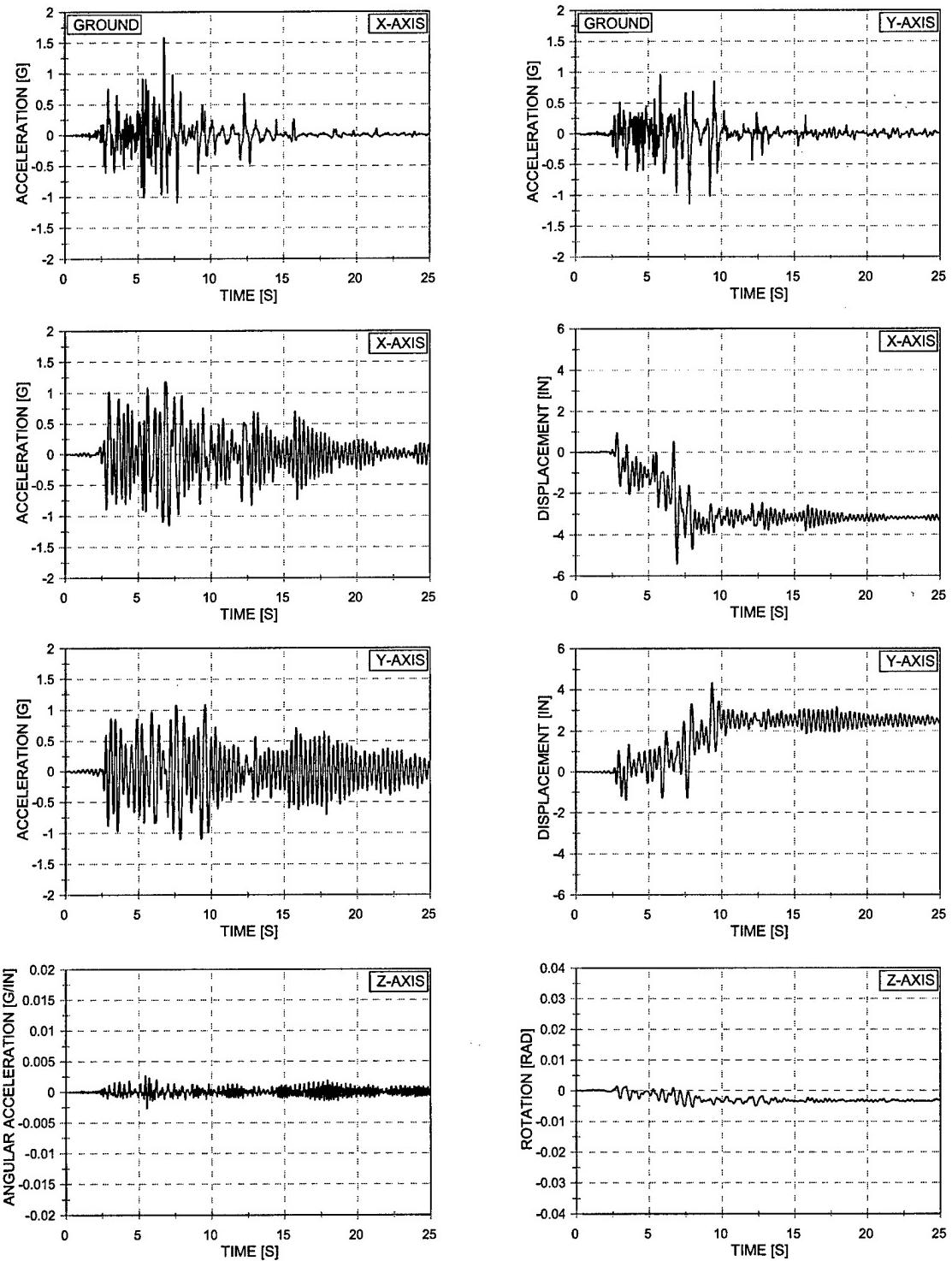


Figure 5.10 Acceleration and Displacement vs. Time – EQ 16
150% Biaxial Imperial Valley – Symmetric Mass
Four 4" Extra-Strong Columns

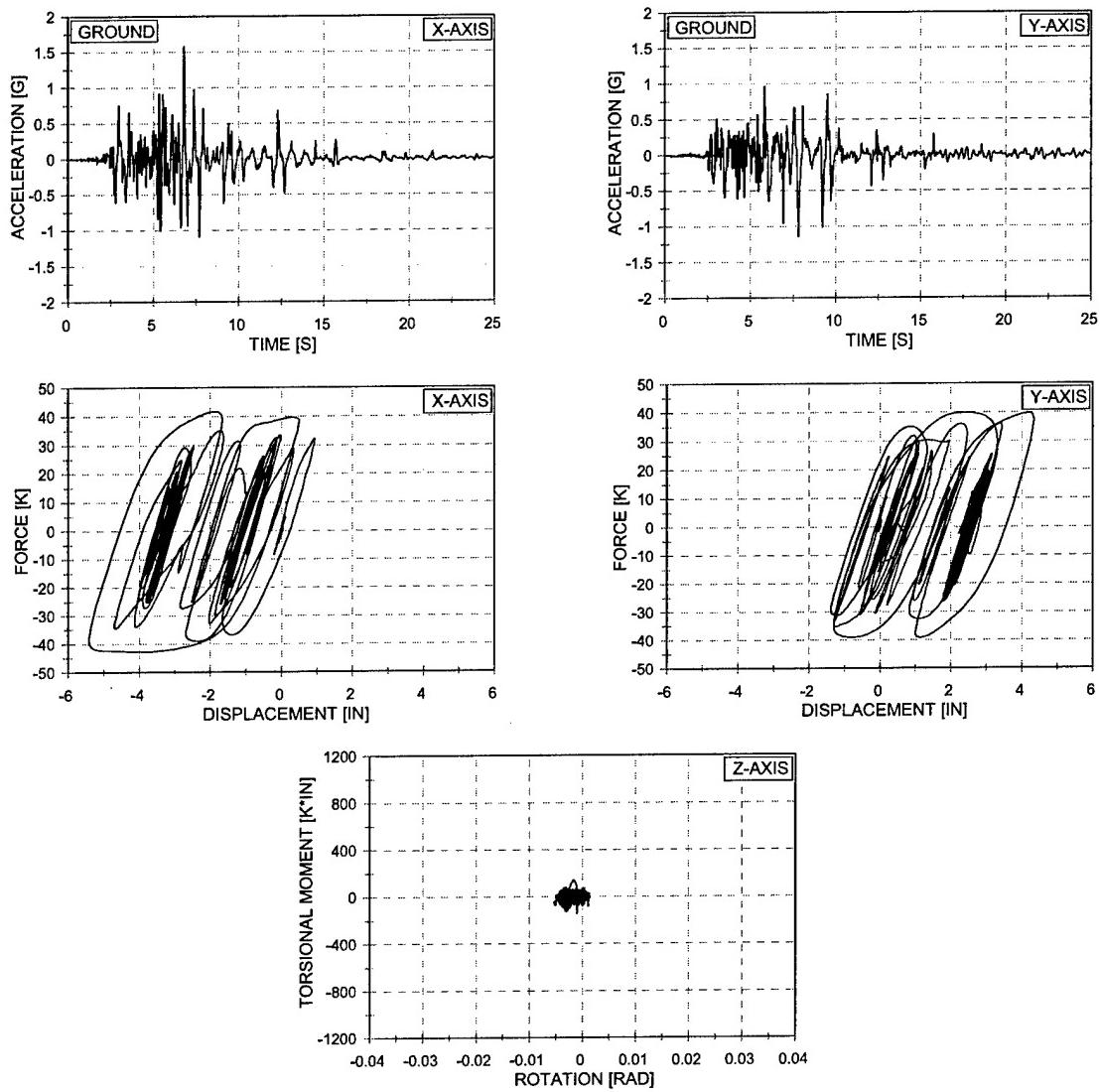


Figure 5.11 Force vs. Displacement and Torsional Moment vs. Rotation - EQ 16
 150% Biaxial Imperial Valley – Symmetric Mass
 Four 4" Extra-Strong Columns

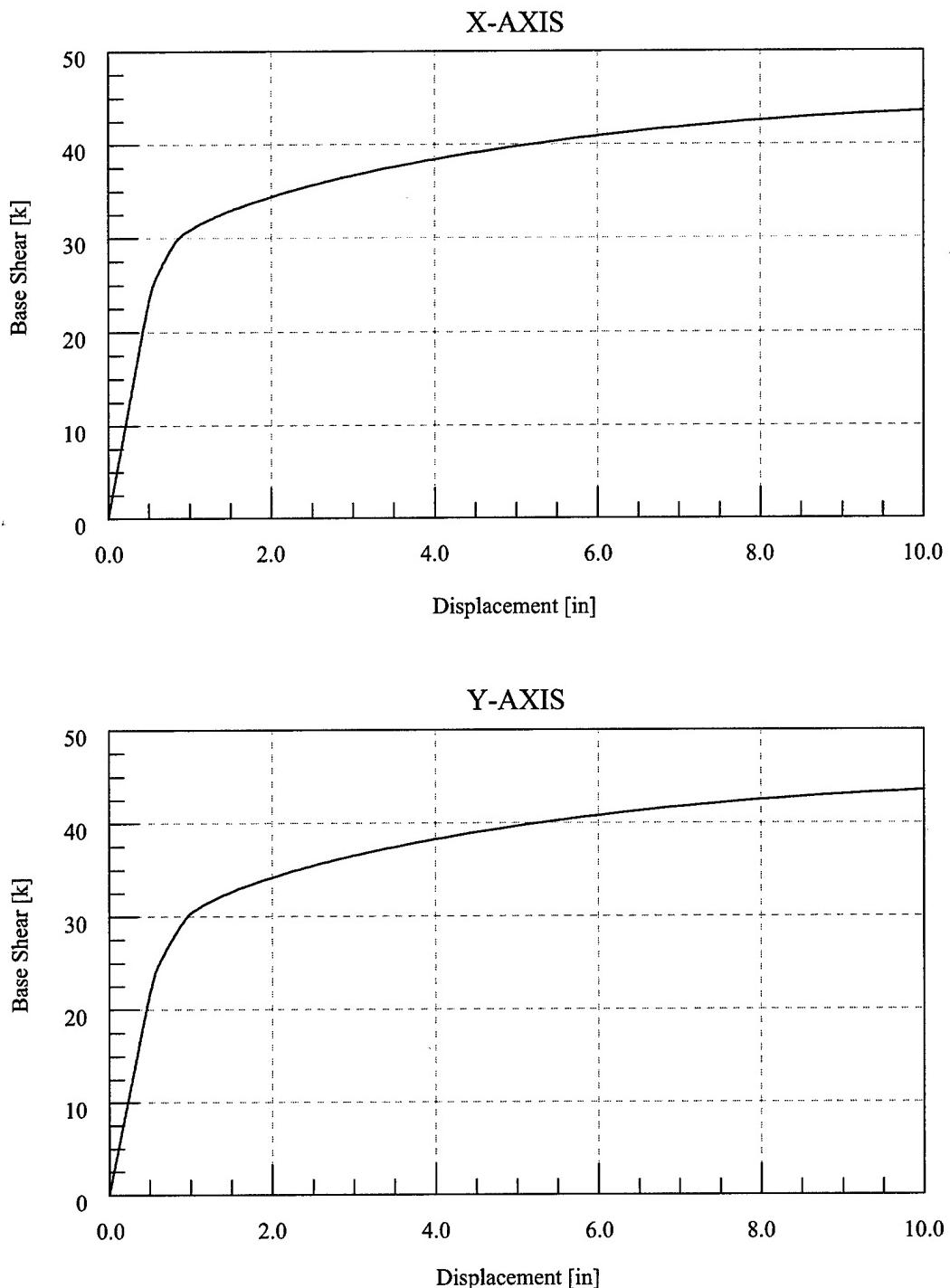


Figure 5.12 Force-Deformation Response – Test Configuration 2

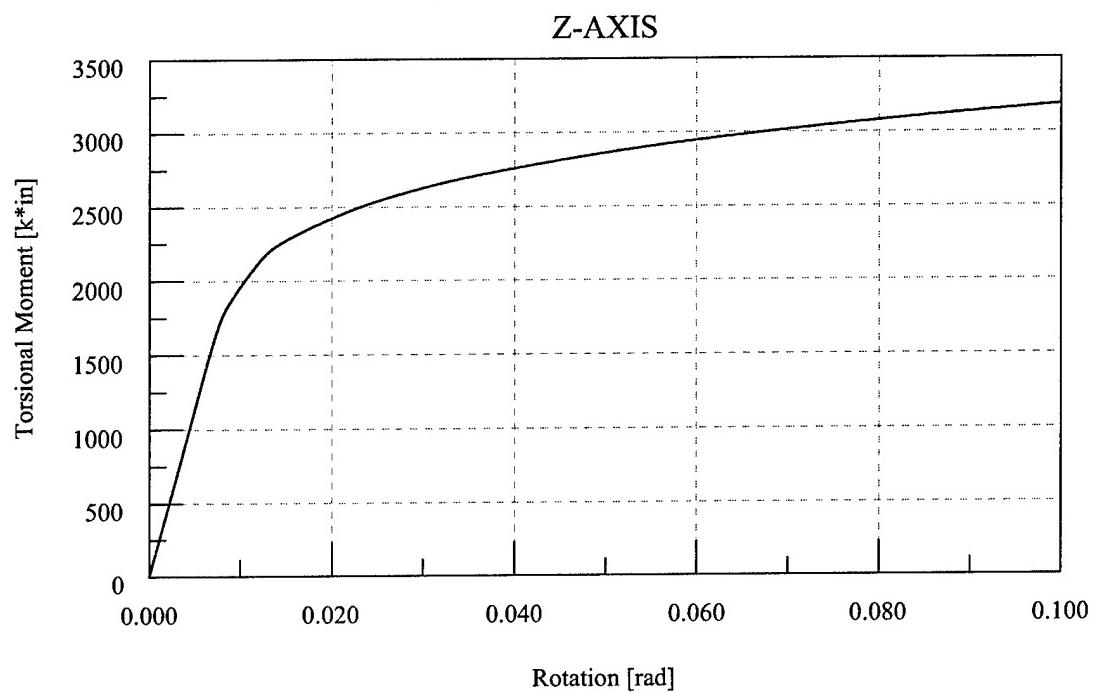


Figure 5.13 Torsional Moment-Rotation Response – Test Configuration 2

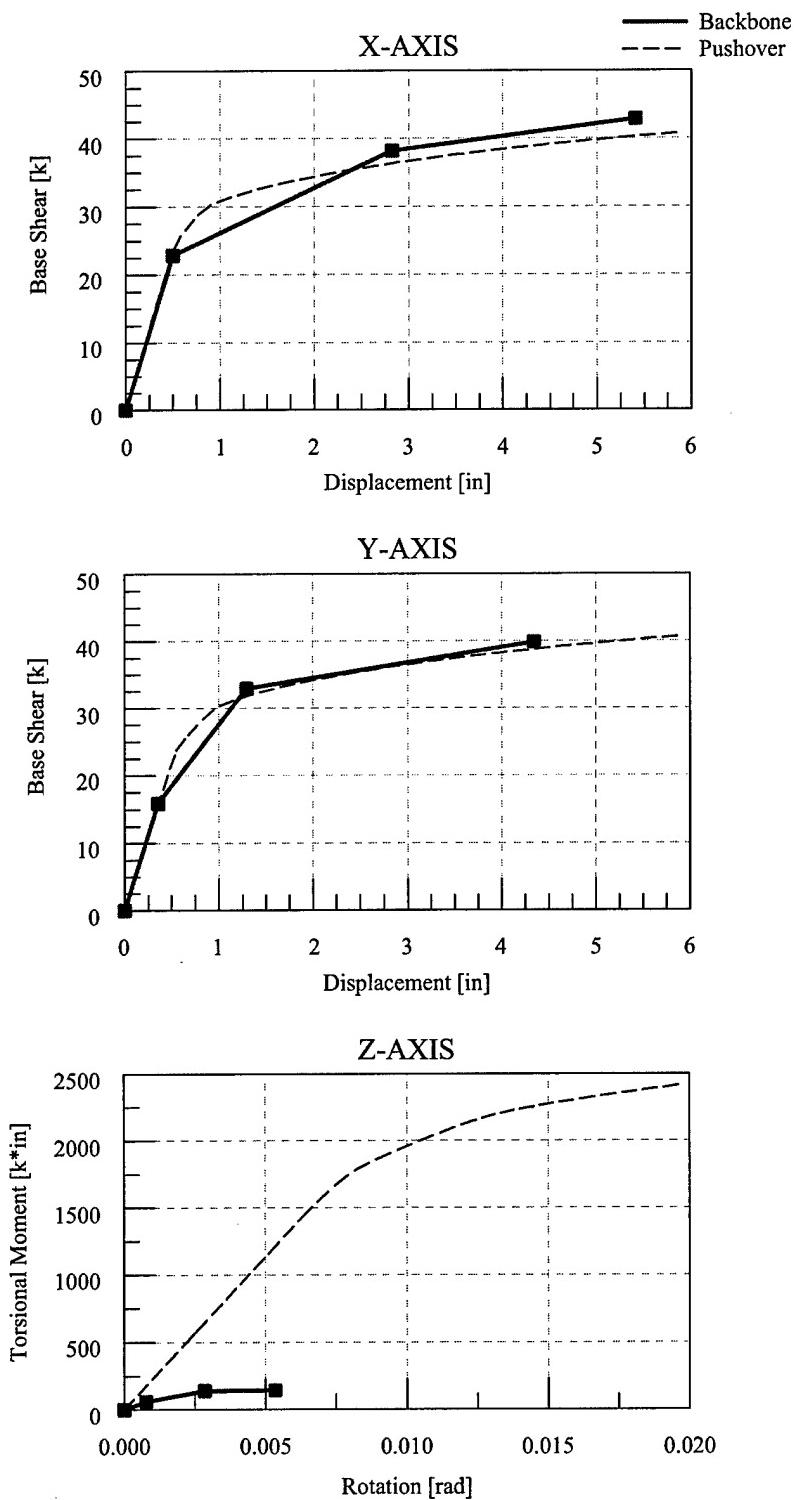


Figure 5.14 Maximum Force vs. Displacement and Maximum Torsional Moment vs. Rotation
 10% - 150% Biaxial Imperial Valley – Symmetric Mass
 Four 4" Extra-Strong Columns

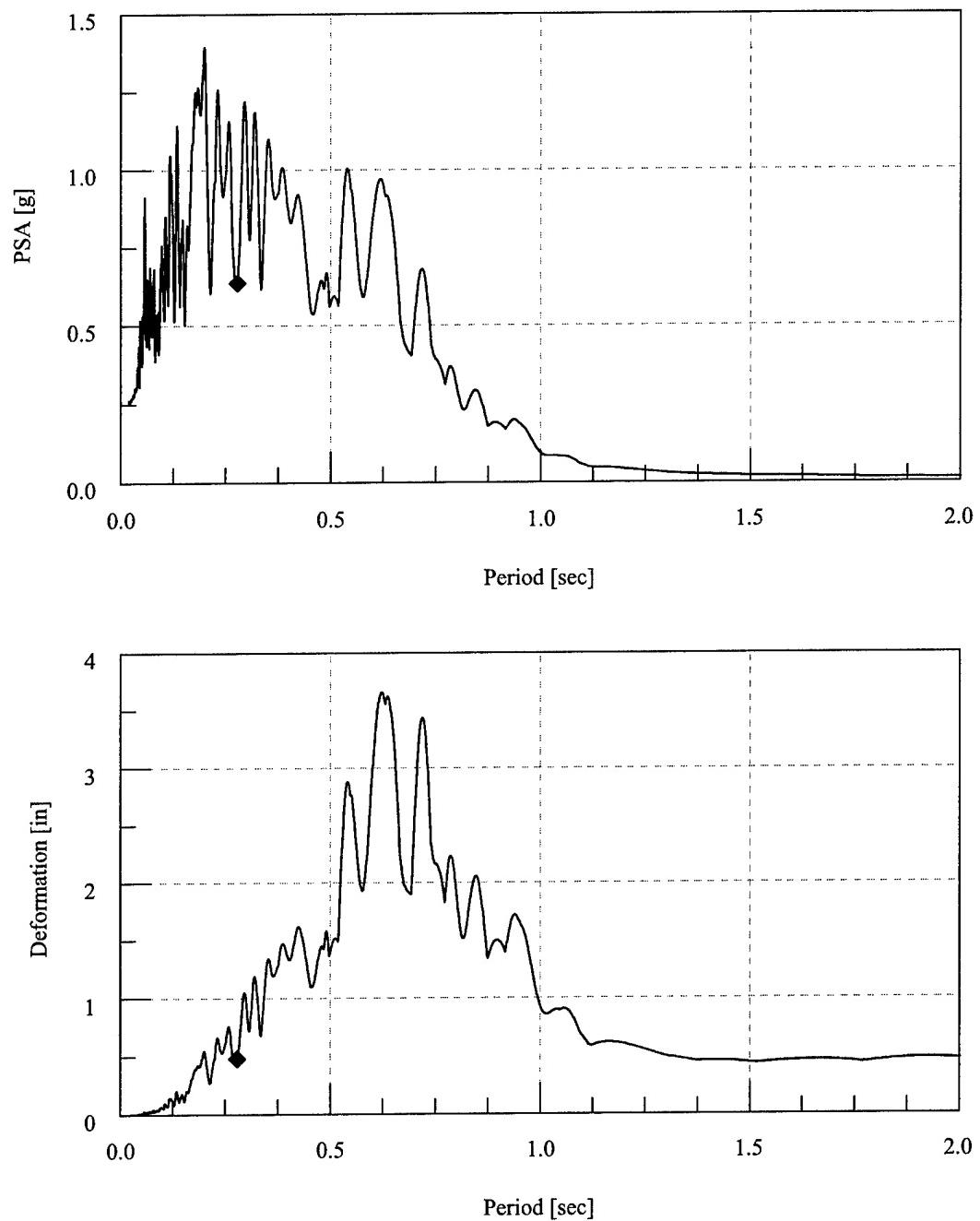


Figure 5.15 Elastic Response Spectra – EQ 12 – 25% X-Axis Imperial Valley Ground Motion

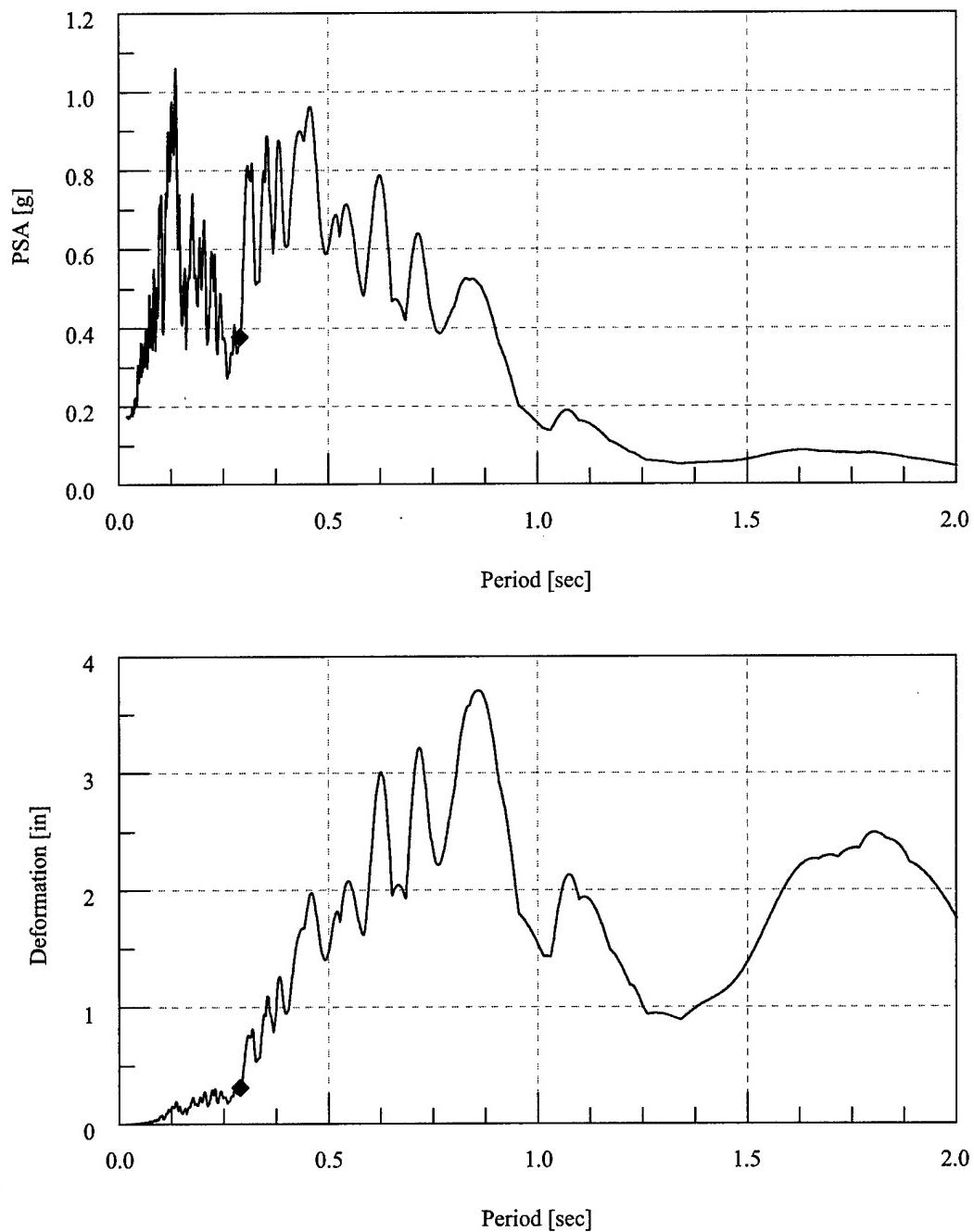


Figure 5.16 Elastic Response Spectra – EQ 13 – 25% Y-Axis Imperial Valley Ground Motion

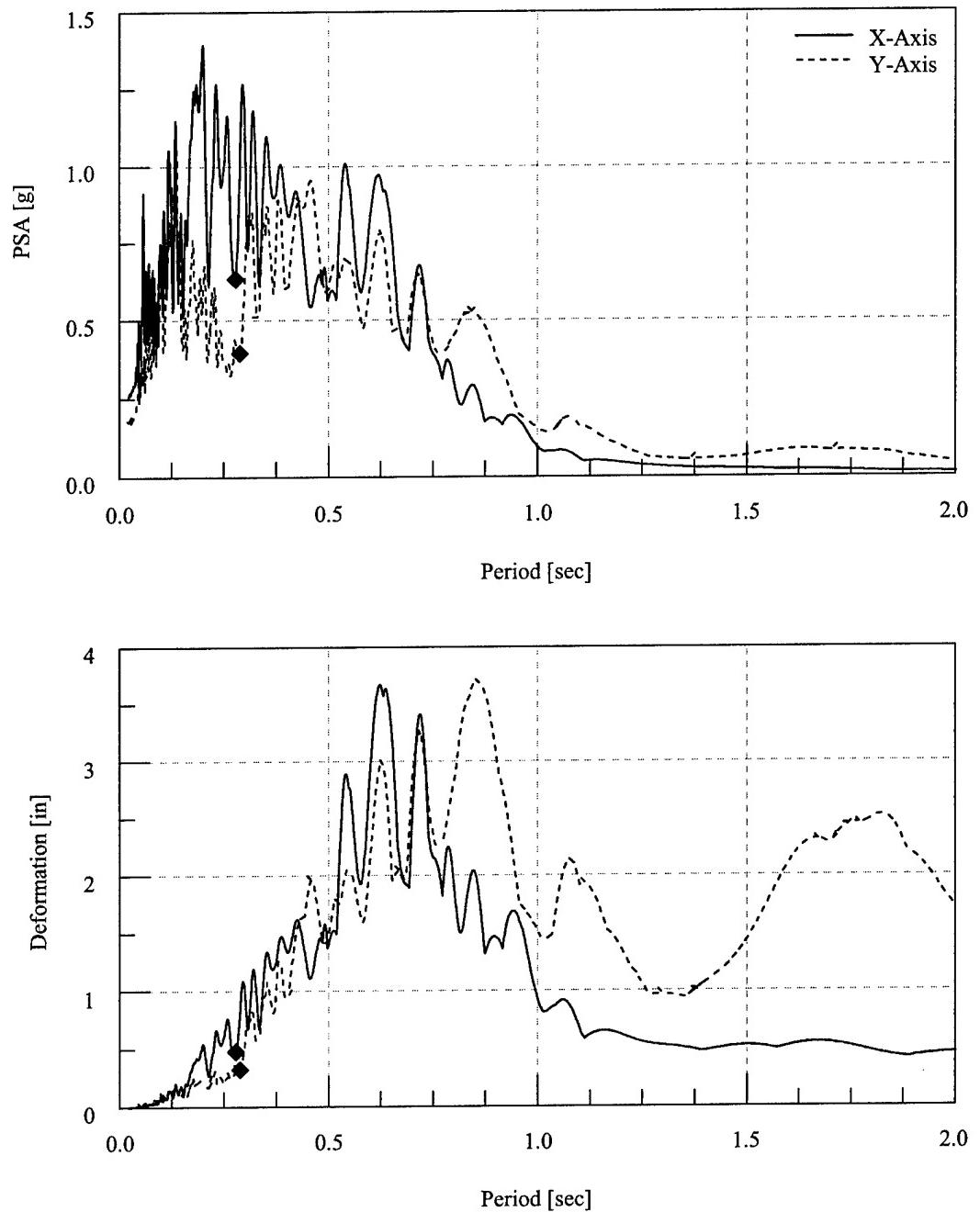


Figure 5.17 Elastic Response Spectra – EQ 14 – 25% Biaxial Imperial Valley Ground Motion

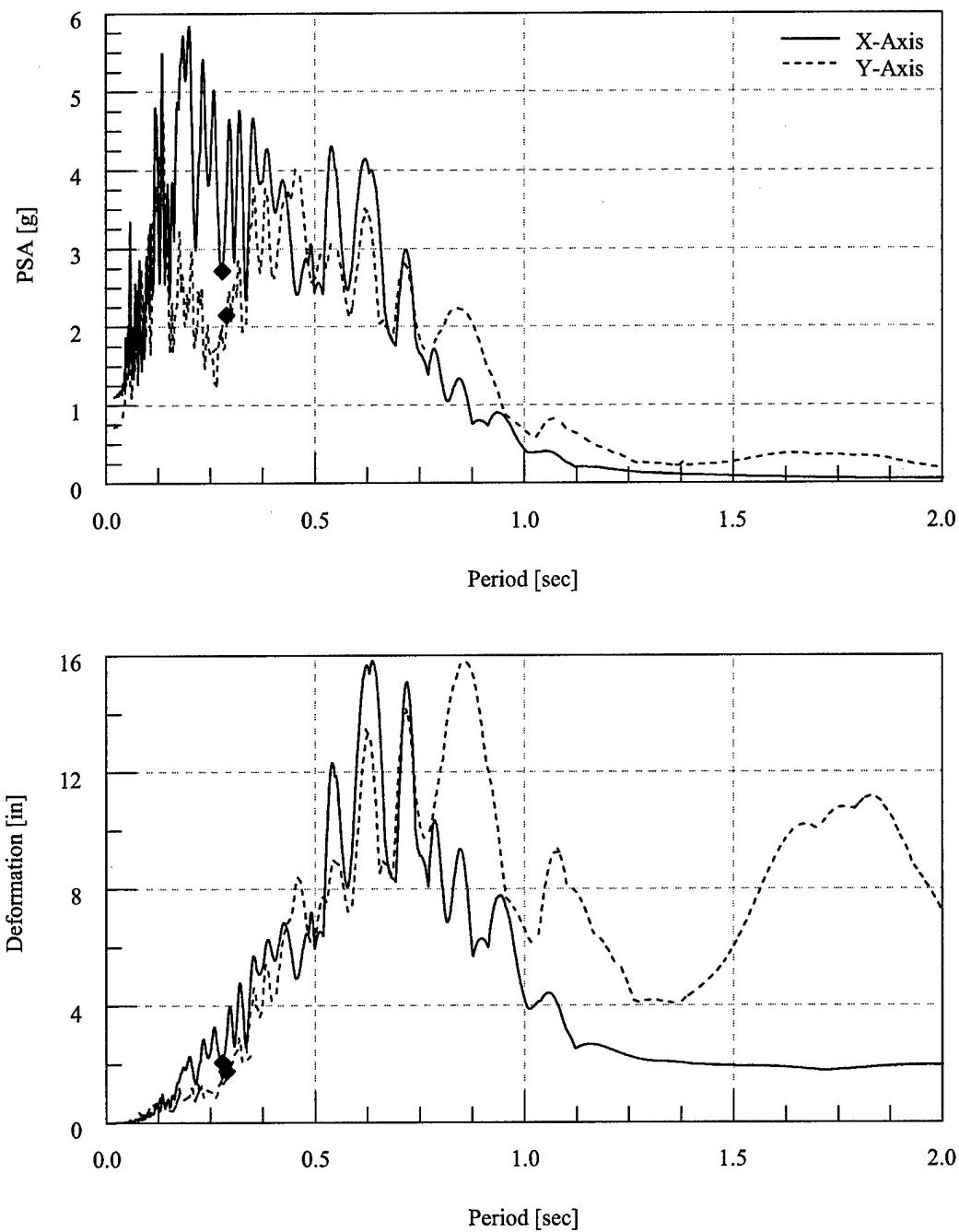


Figure 5.18 Elastic Response Spectra – EQ 15 – 100% Biaxial Imperial Valley Ground Motion

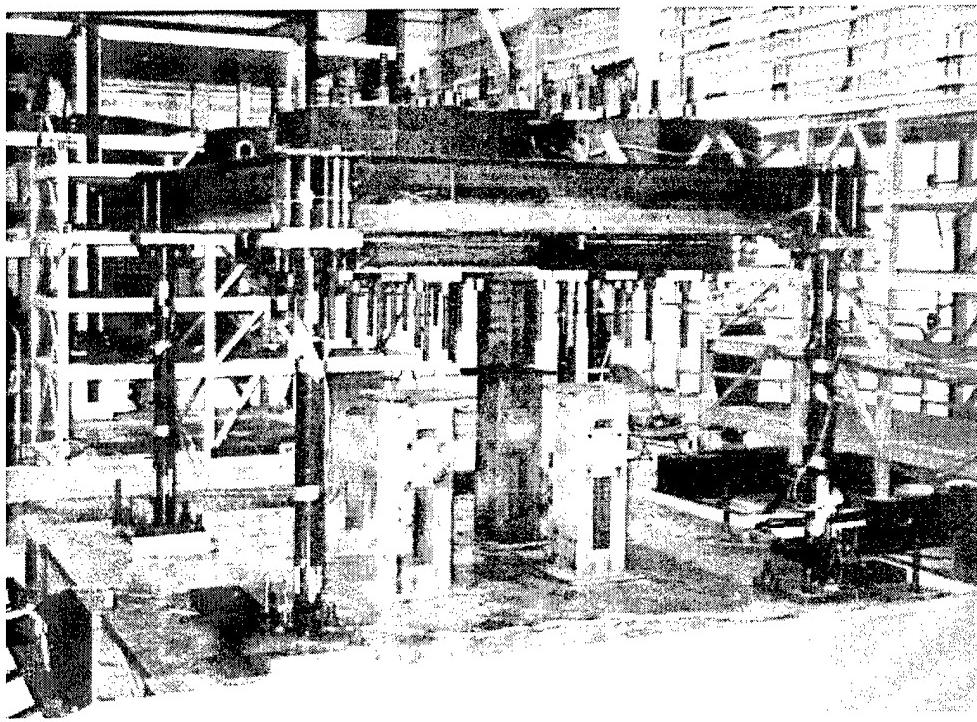


Figure 5.19 Test Structure prior to Earthquake Simulations

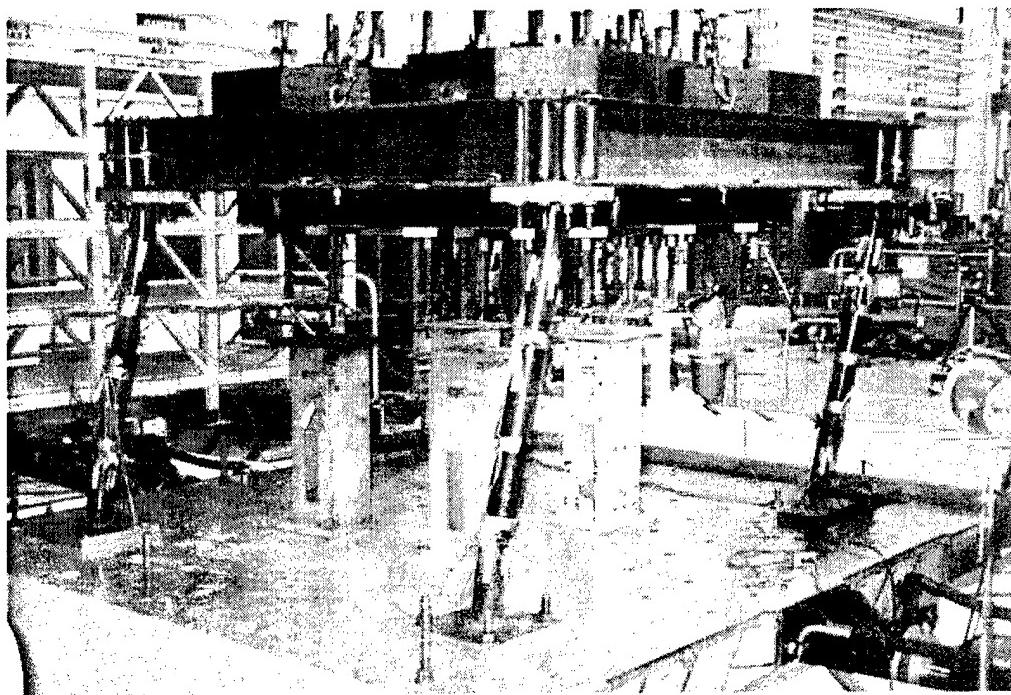


Figure 5.20 Test Structure After Earthquake Simulations

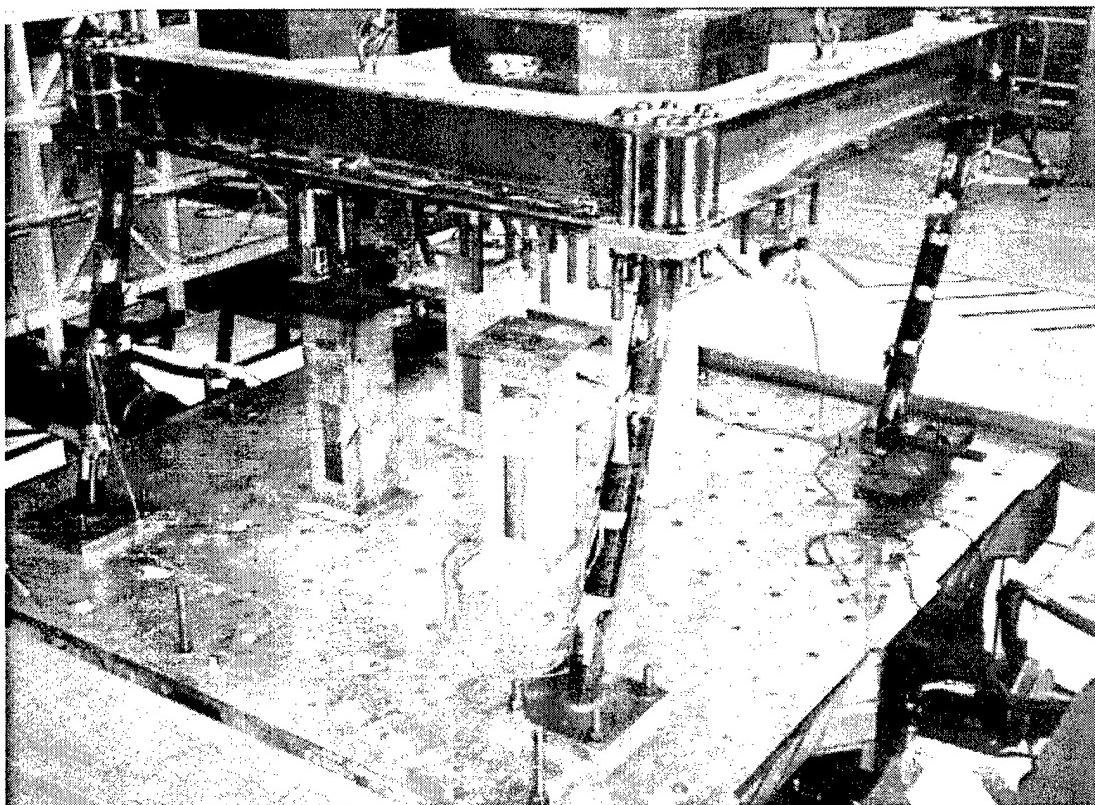


Figure 5.21 Test Structure After Earthquake Simulations

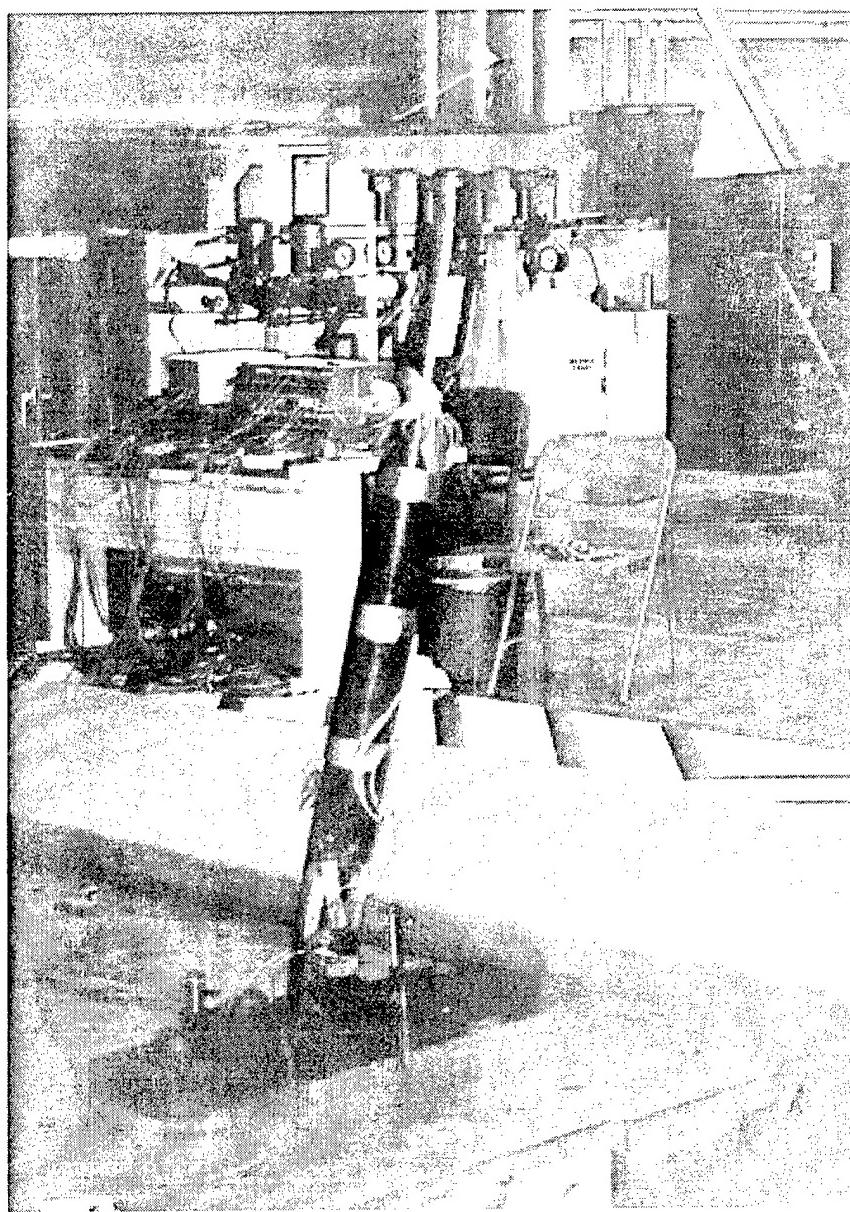


Figure 5.22 Test Structure Northeast Column After Earthquake Simulations

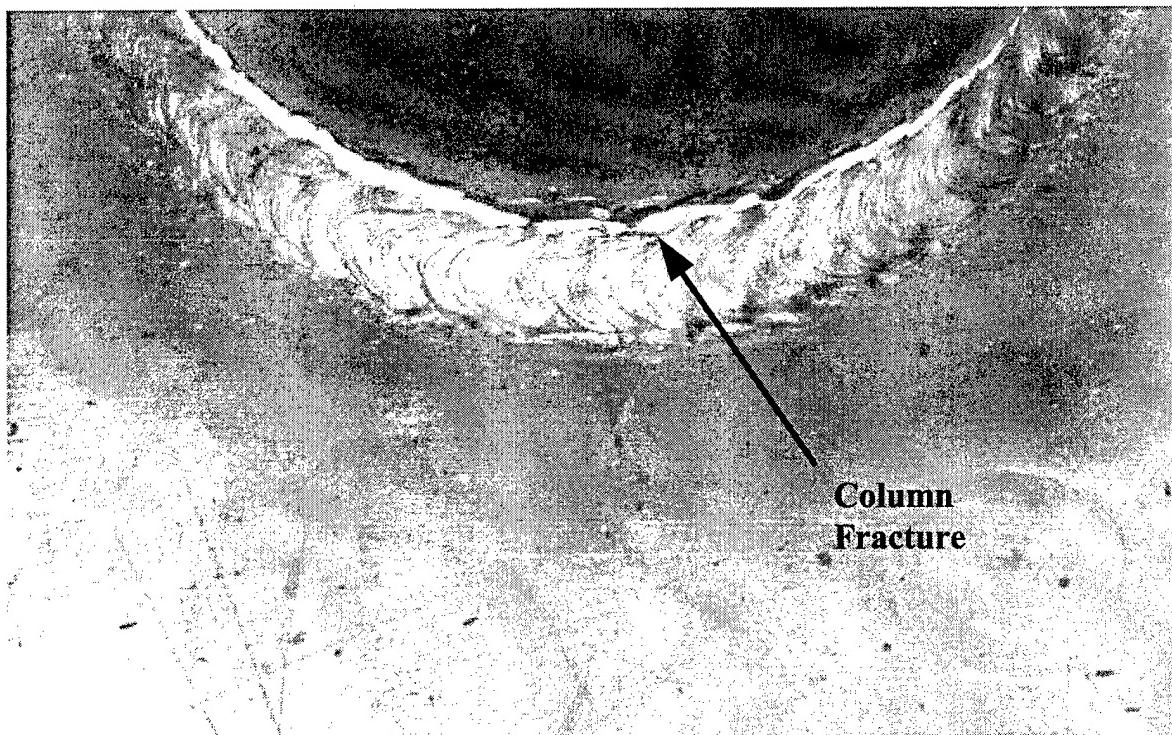


Figure 5.23 Fracture at Column and Column Base Plate

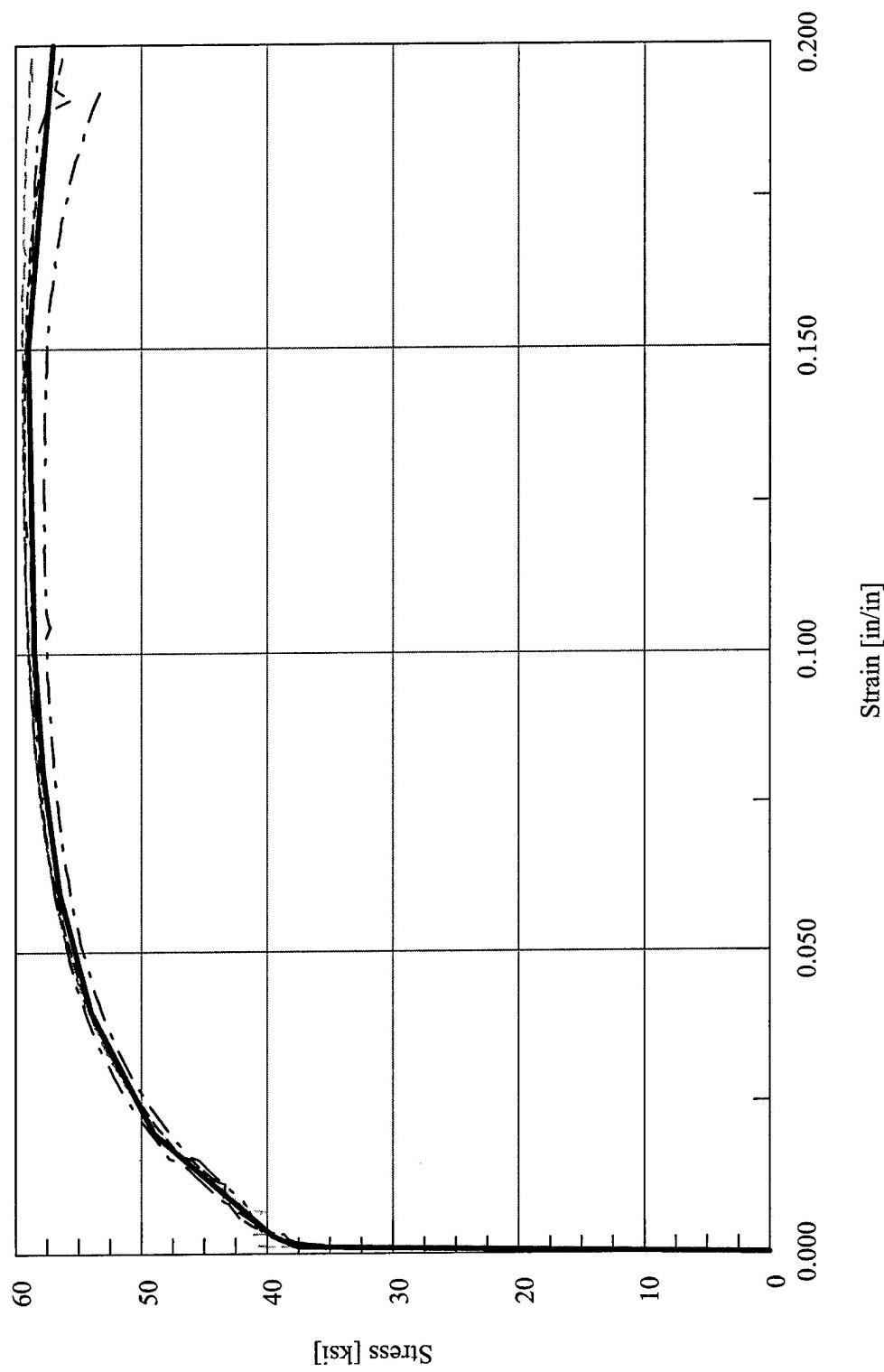


Figure 5.24 Abaqus Stress vs. Strain Finite Element Material Model Definition – Test Configuration 2

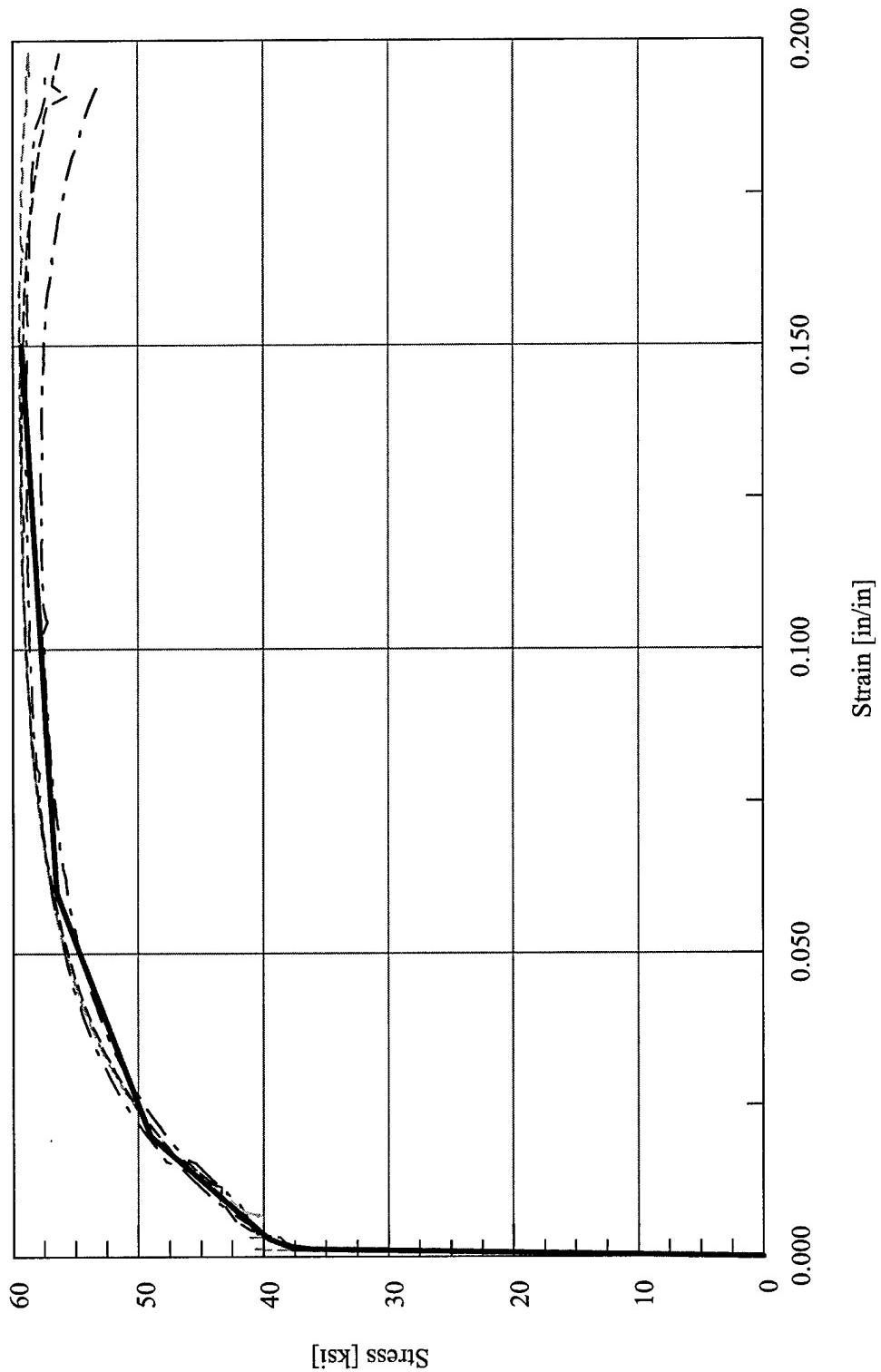


Figure 5.25 Drain-3DX Stress vs. Strain Finite Element Material Model Definition – Test Configuration 2

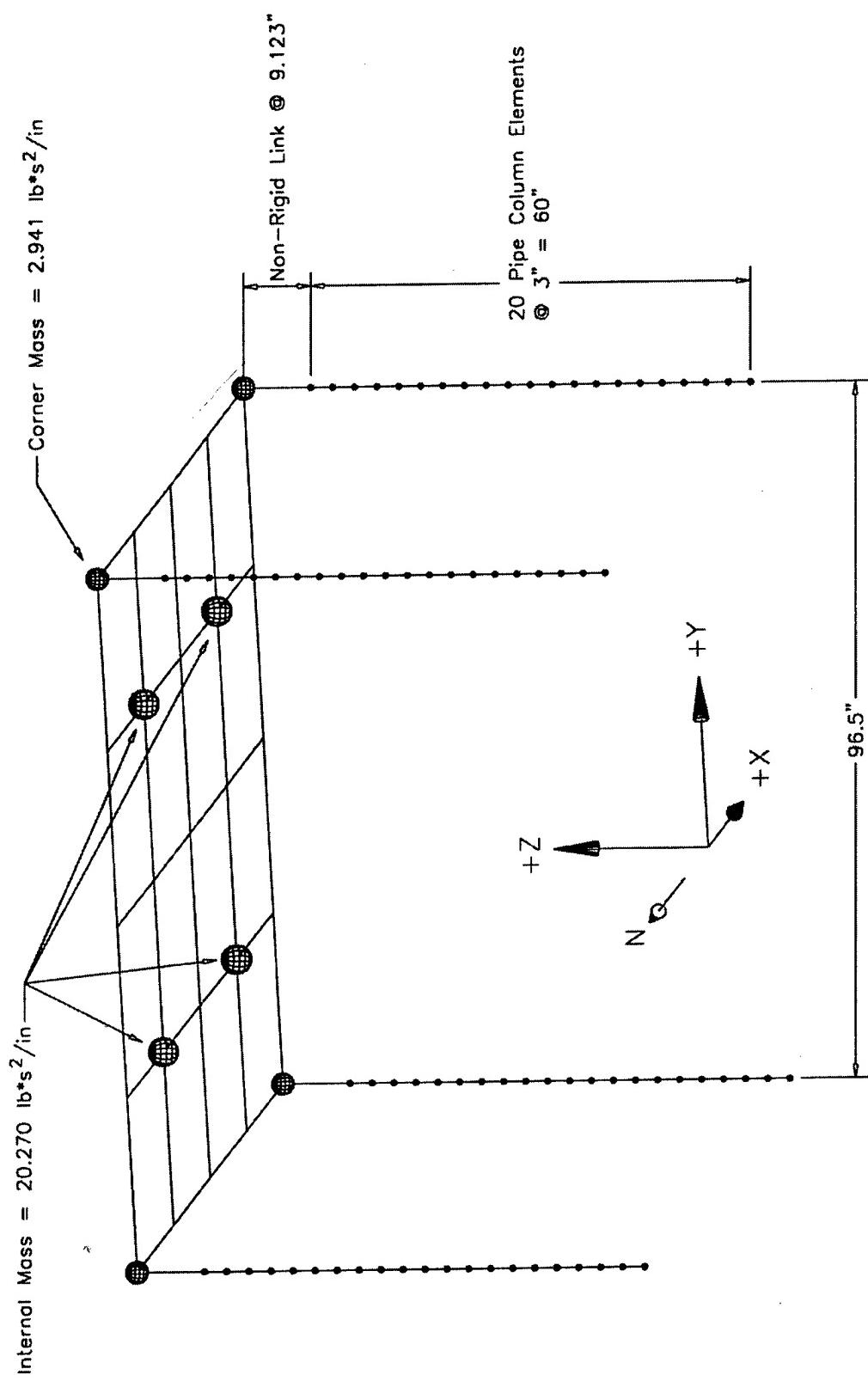


Figure 5.26 Abaqus Finite Element Model for Test Configuration 2

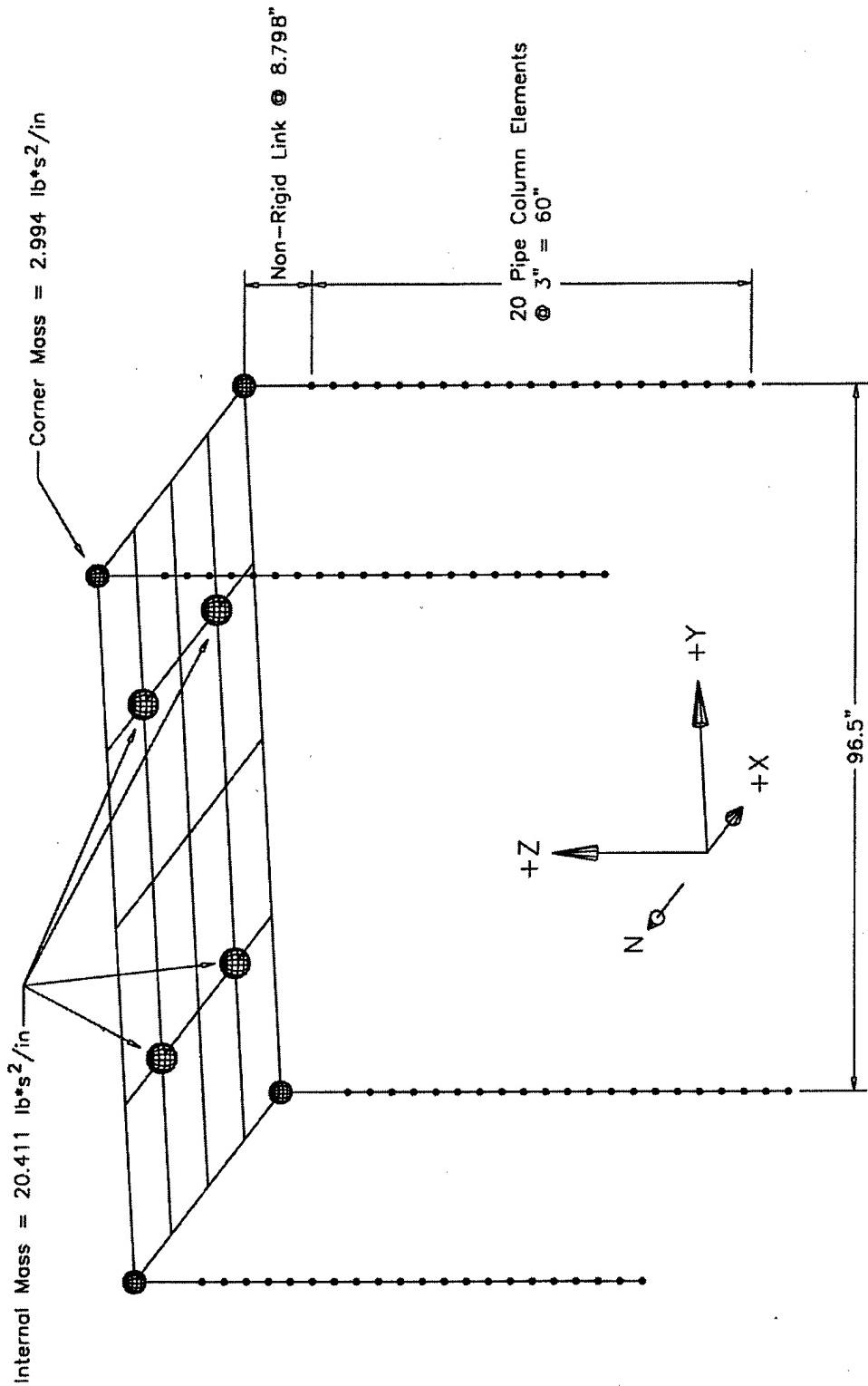


Figure 5.27 Drain-3DX Finite Element Model for Test Configuration 2

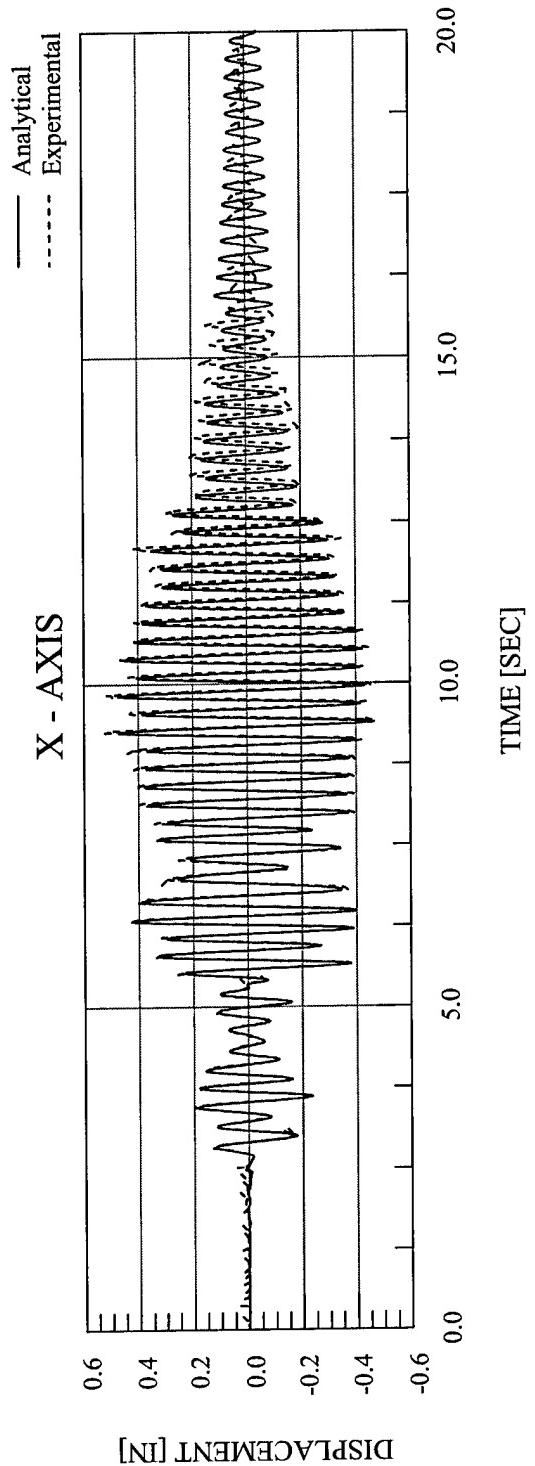


Figure 5.28 Abaqus Analytical Displacement vs. Time – EQ 12 – 25% X-Axis Imperial Valley

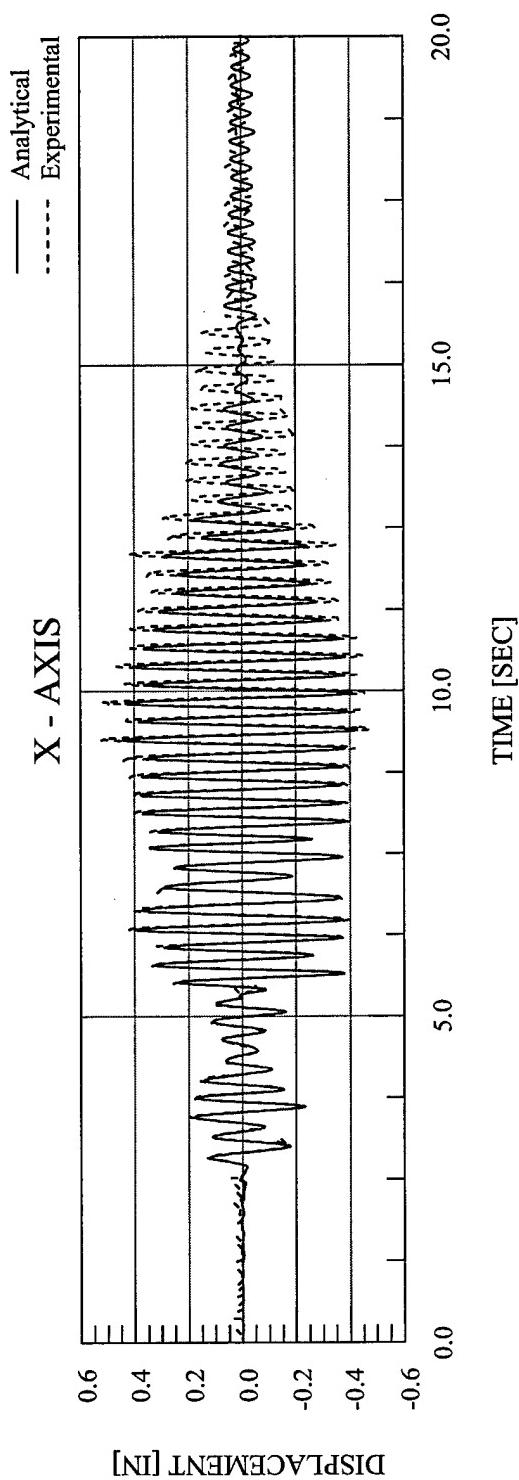


Figure 5.29 Drain-3DX Analytical Displacement vs. Time – EQ 12 – 25% X-Axis Imperial Valley

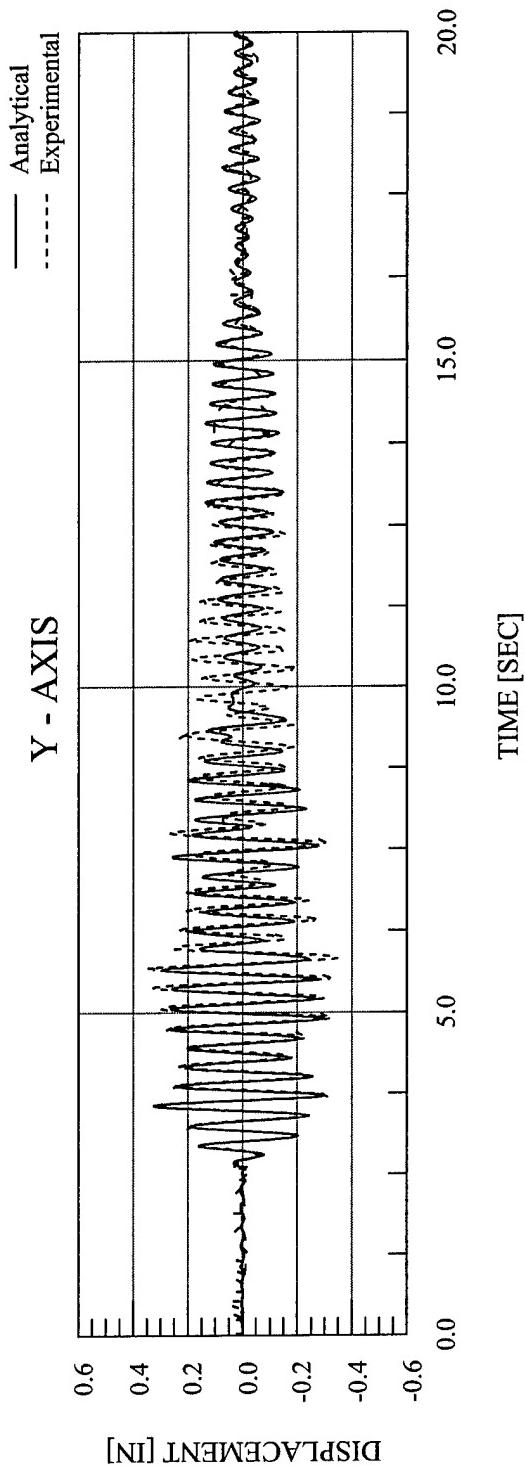


Figure 5.30 Abaqus Analytical Displacement vs. Time – EQ 13 – 25% Y-Axis Imperial Valley

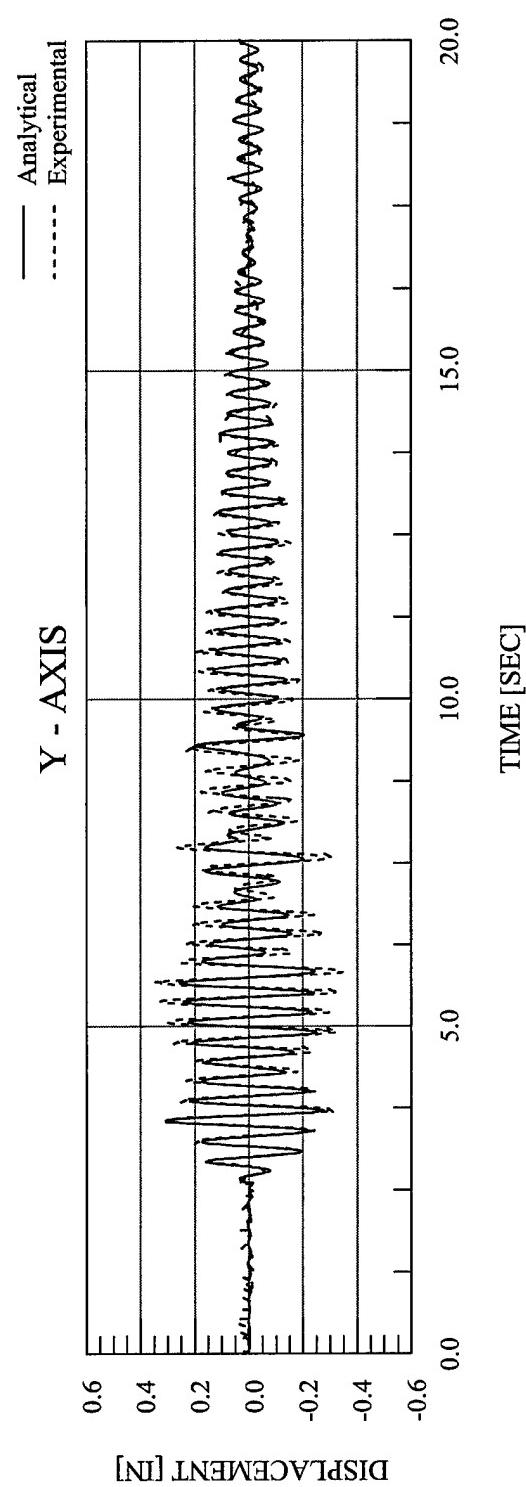


Figure 5.31 Drain-3DX Analytical Displacement vs. Time – EQ 13 – 25% Y-Axis Imperial Valley

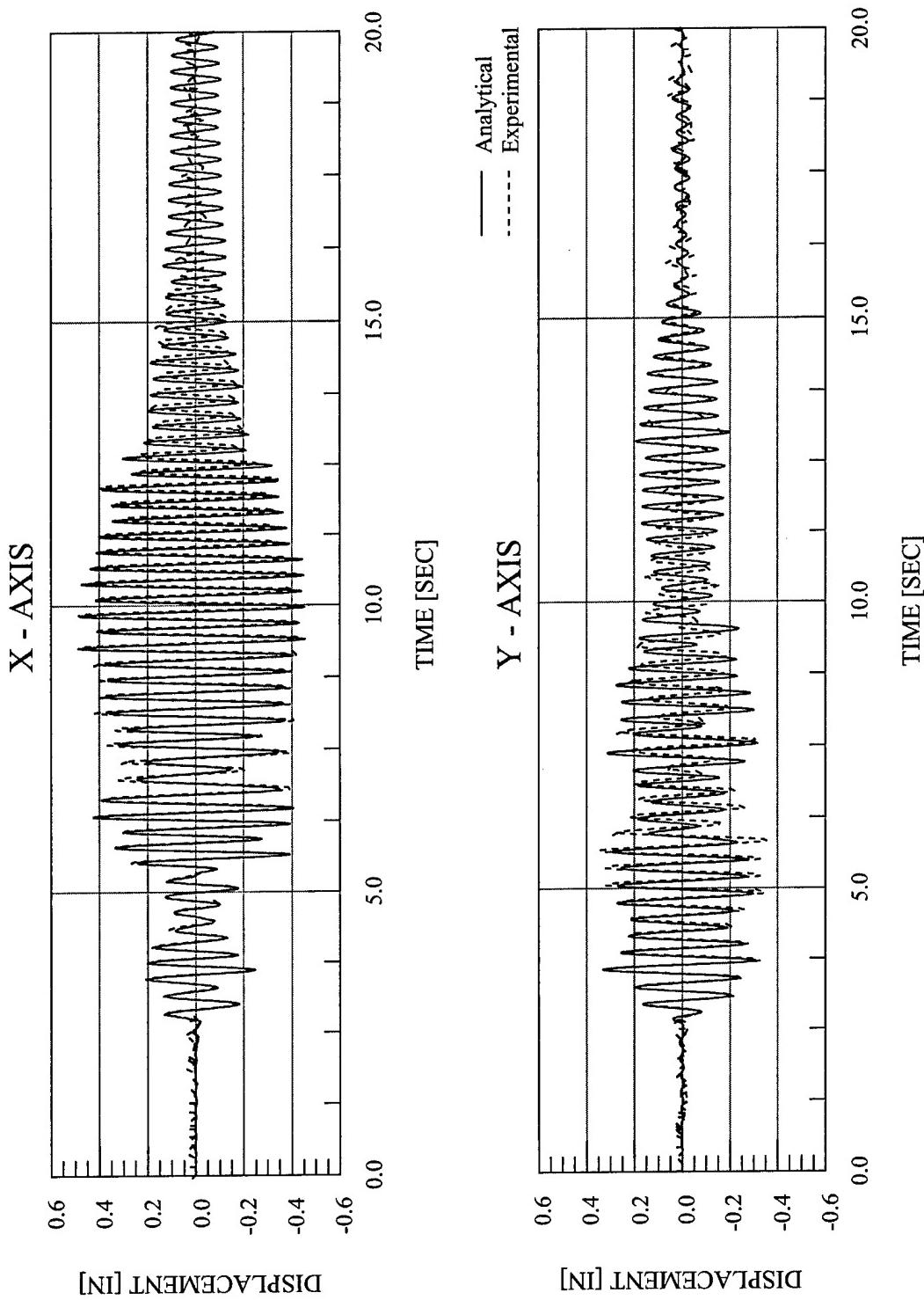


Figure 5.32 Abaqus Analytical Displacement vs. Time – EQ 14 – 25% Biaxial Imperial Valley

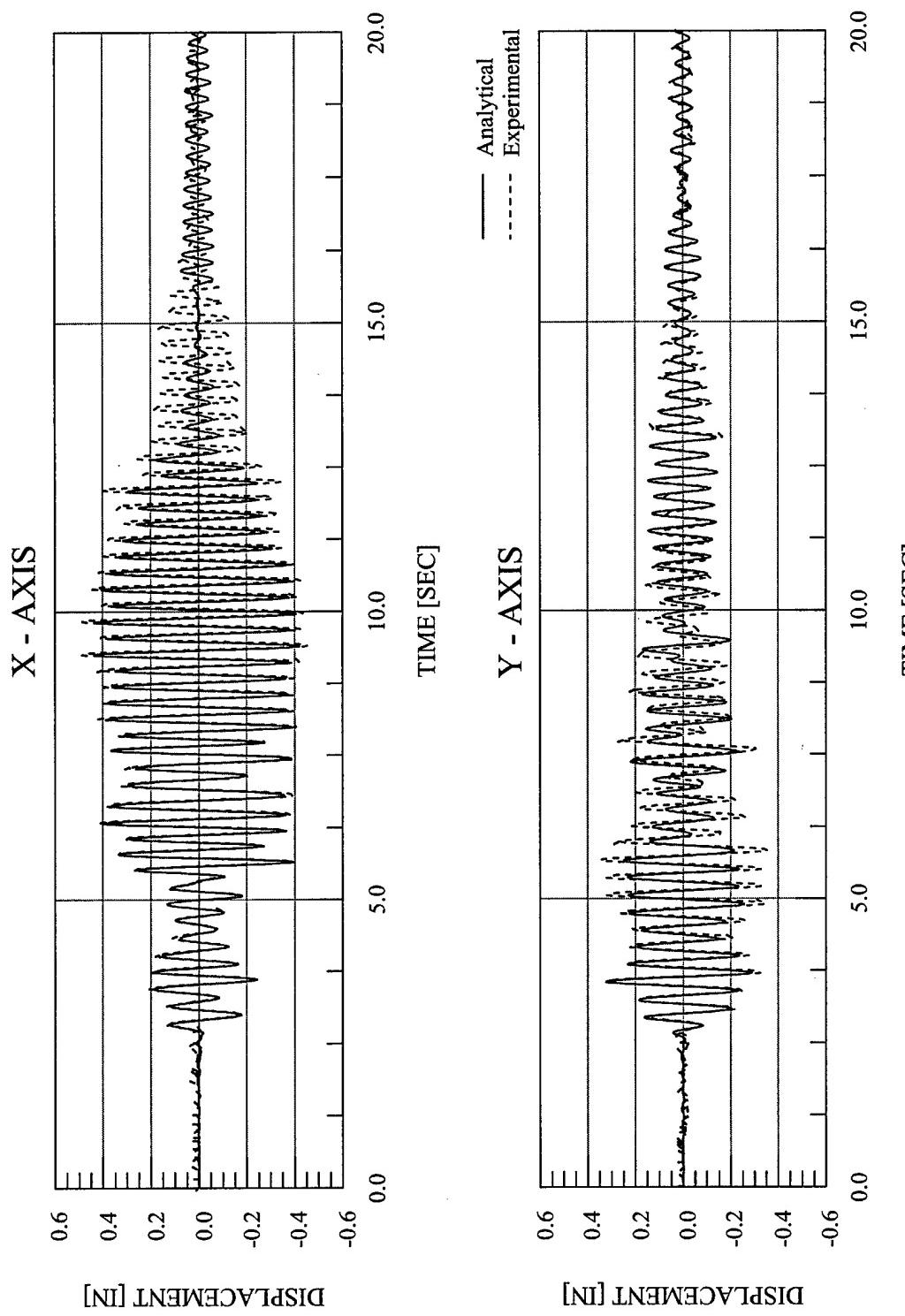


Figure 5.33 Drain-3DX Analytical Displacement vs. Time – EQ 14 – 25% Biaxial Imperial Valley

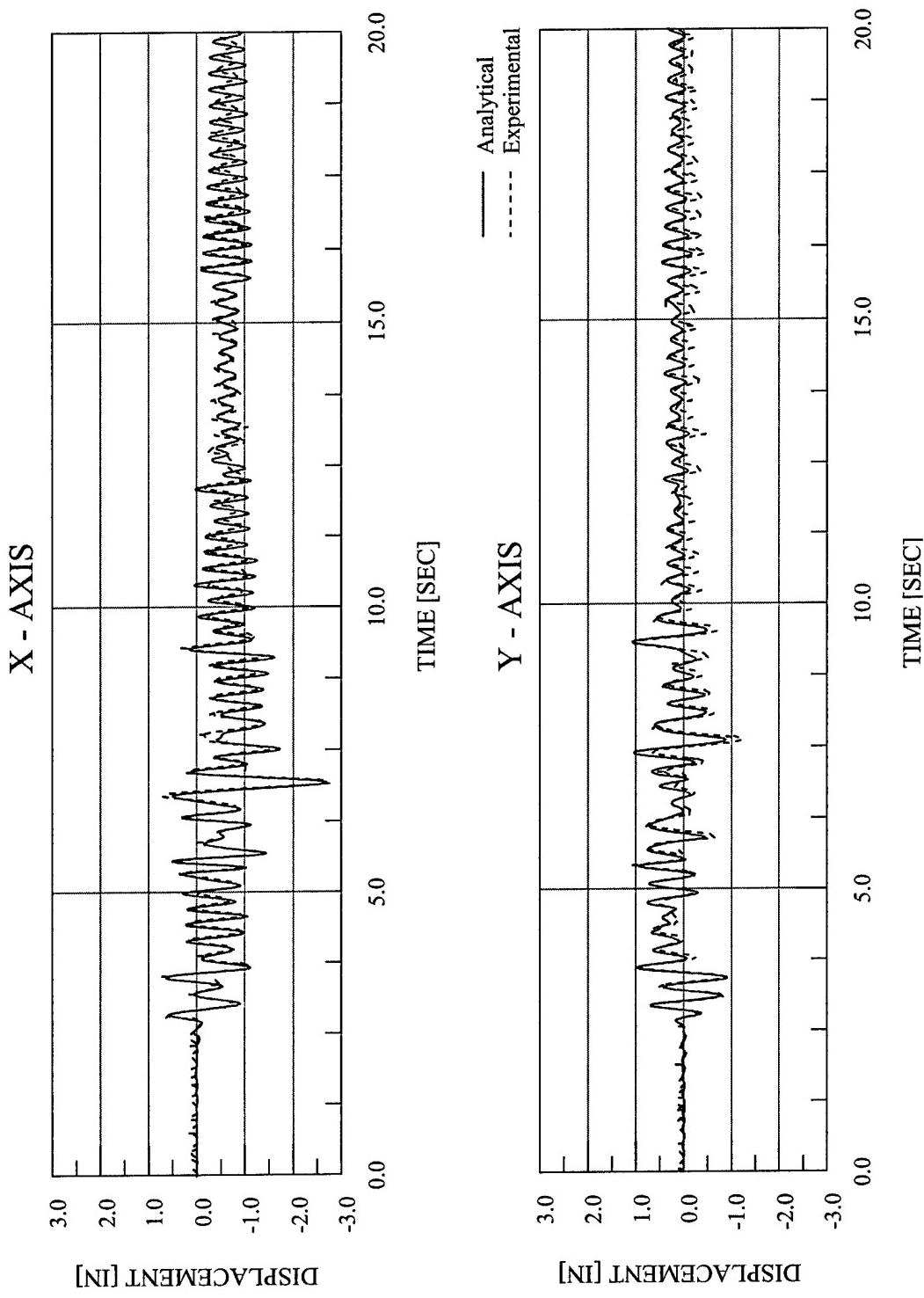


Figure 5.34 Abaqus Analytical Displacement vs. Time – EQ 15 – 100% Biaxial Impact Valley – Combined Material Hardening

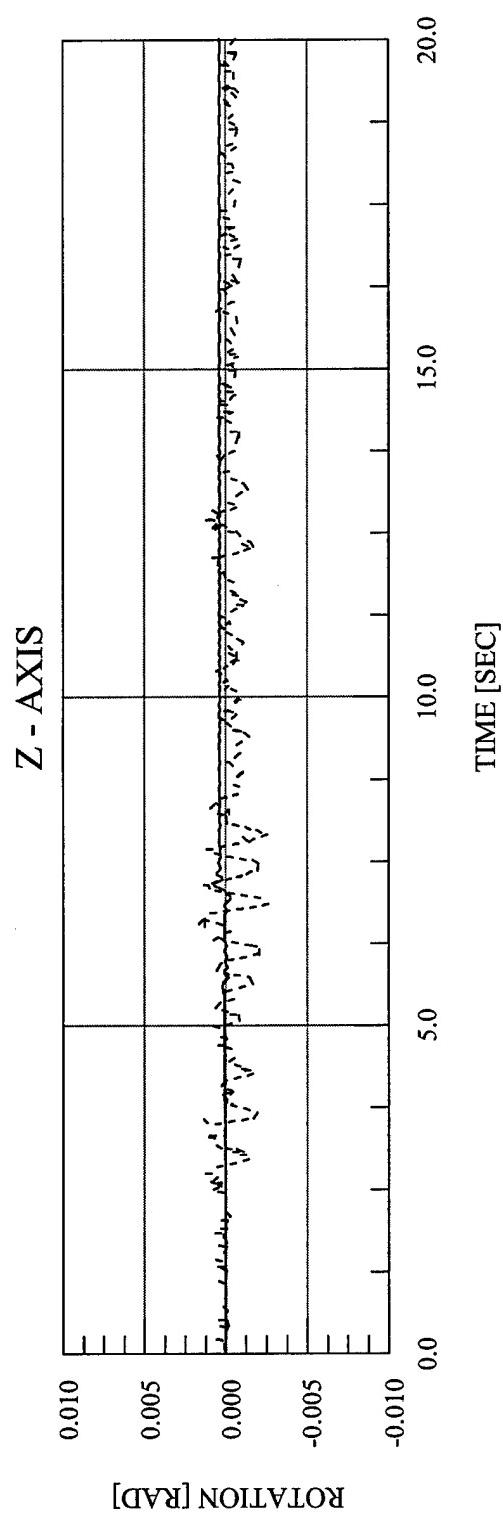


Figure 5.35 Abaqus Analytical Rotation vs. Time – EQ 15 – 100% Biaxial Imperial Valley – Combined Material Hardening

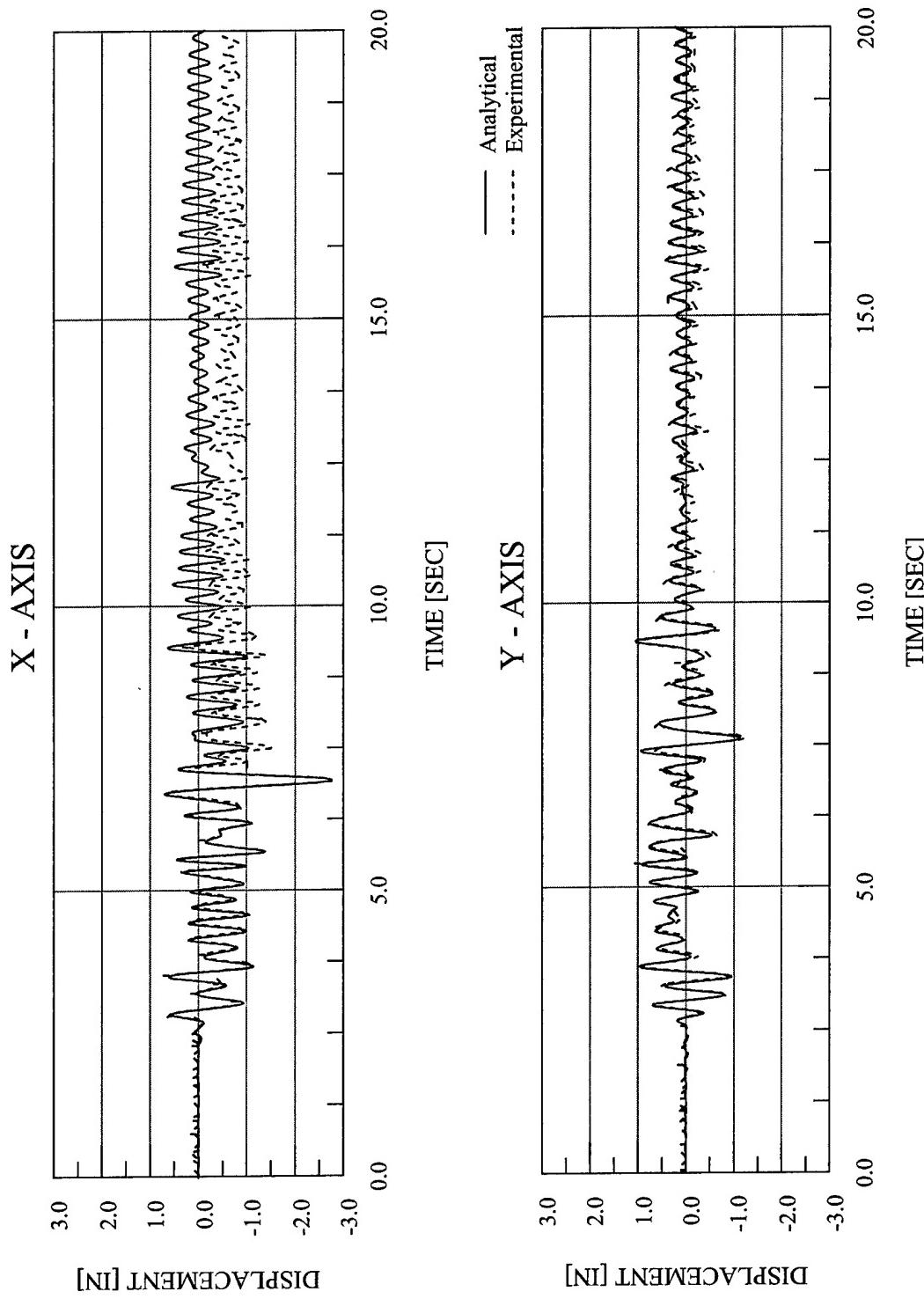


Figure 5.36 Drain-3DX Analytical Displacement vs. Time – EQ 15 – 100% Biaxial Imperial Valley

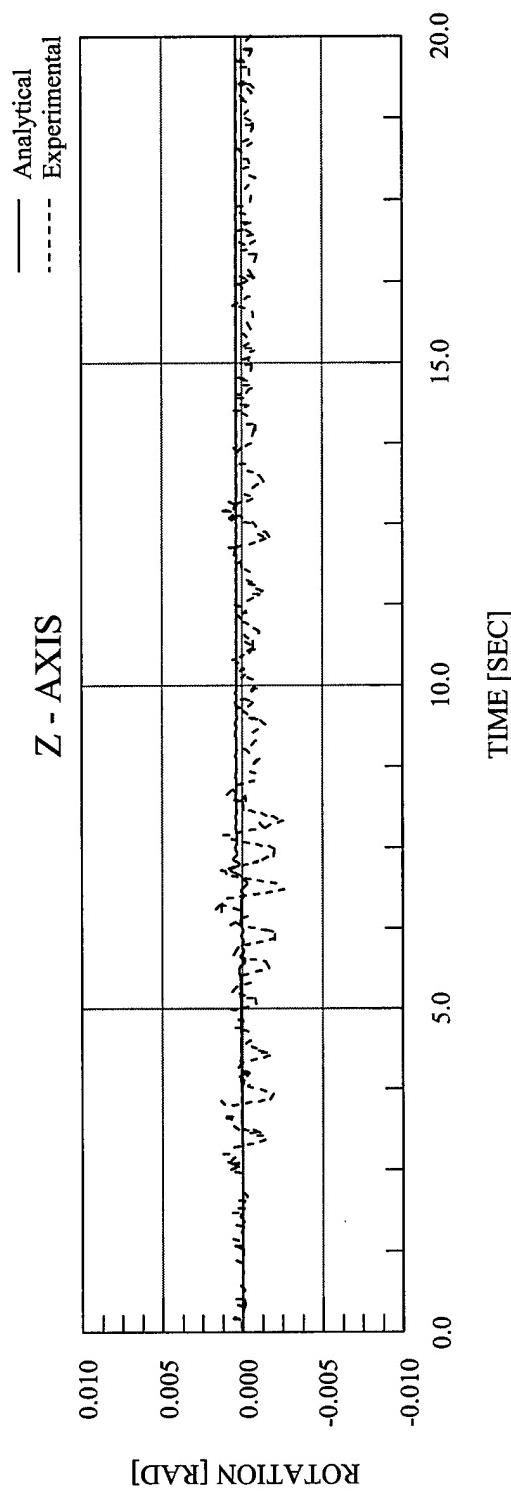


Figure 5.37 Drain-3DX Analytical Rotation vs. Time – EQ 15 – 100% Biaxial Imperial Valley

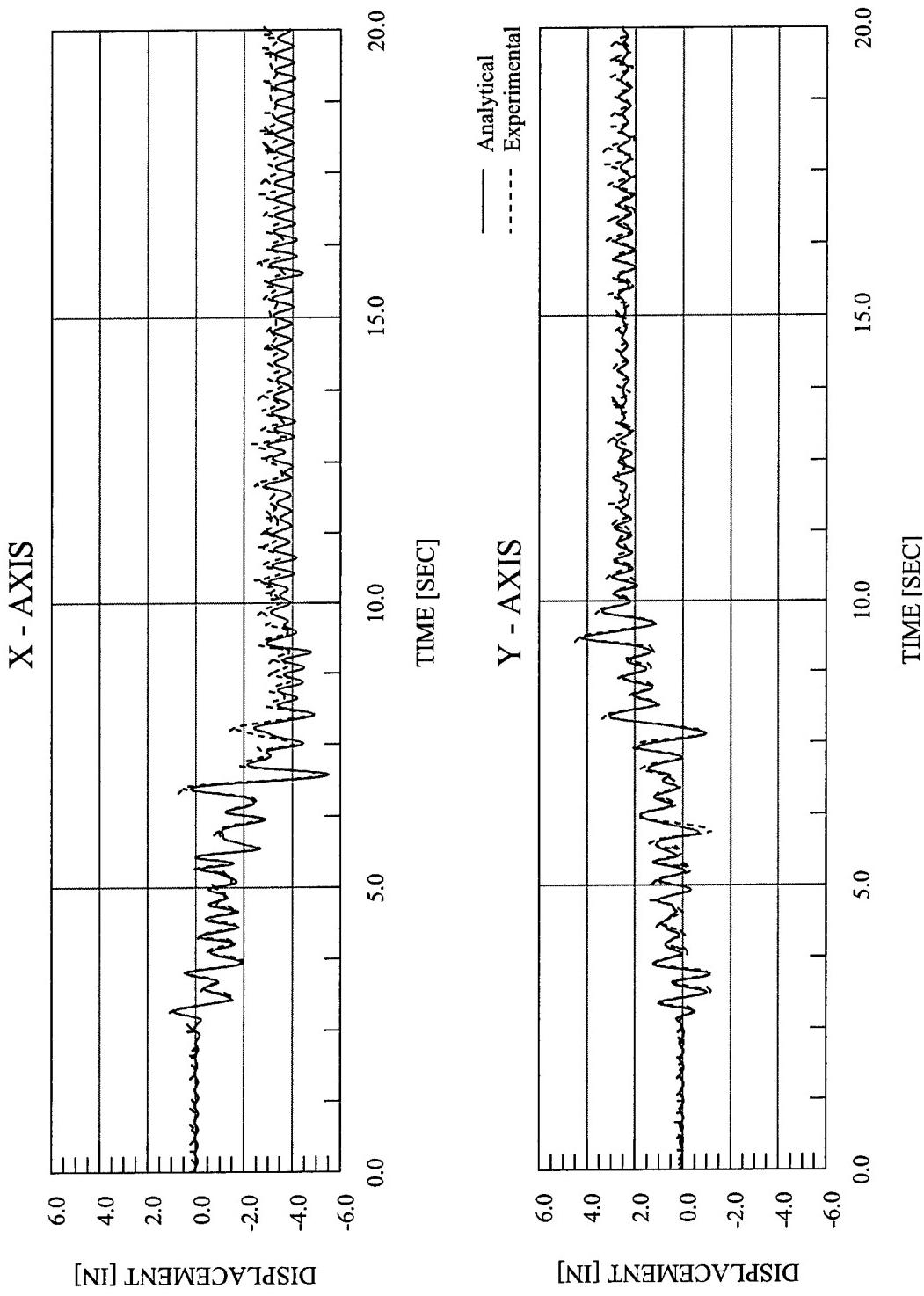


Figure 5.38 Abaqus Analytical Displacement vs. Time – EQ 16 – 150% Biaxial Imperial Valley – Combined Material Hardening

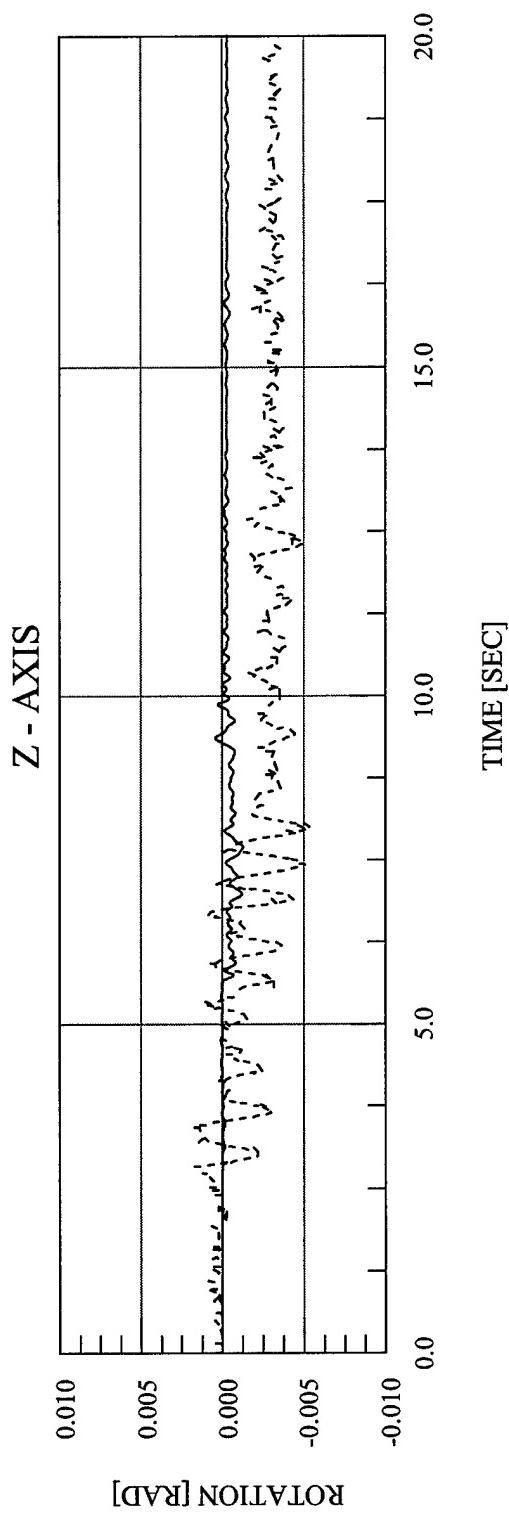


Figure 5.39 Abaqus Analytical Rotation vs. Time – EQ 16 – 150% Biaxial Imperial Valley – Combined Material Hardening

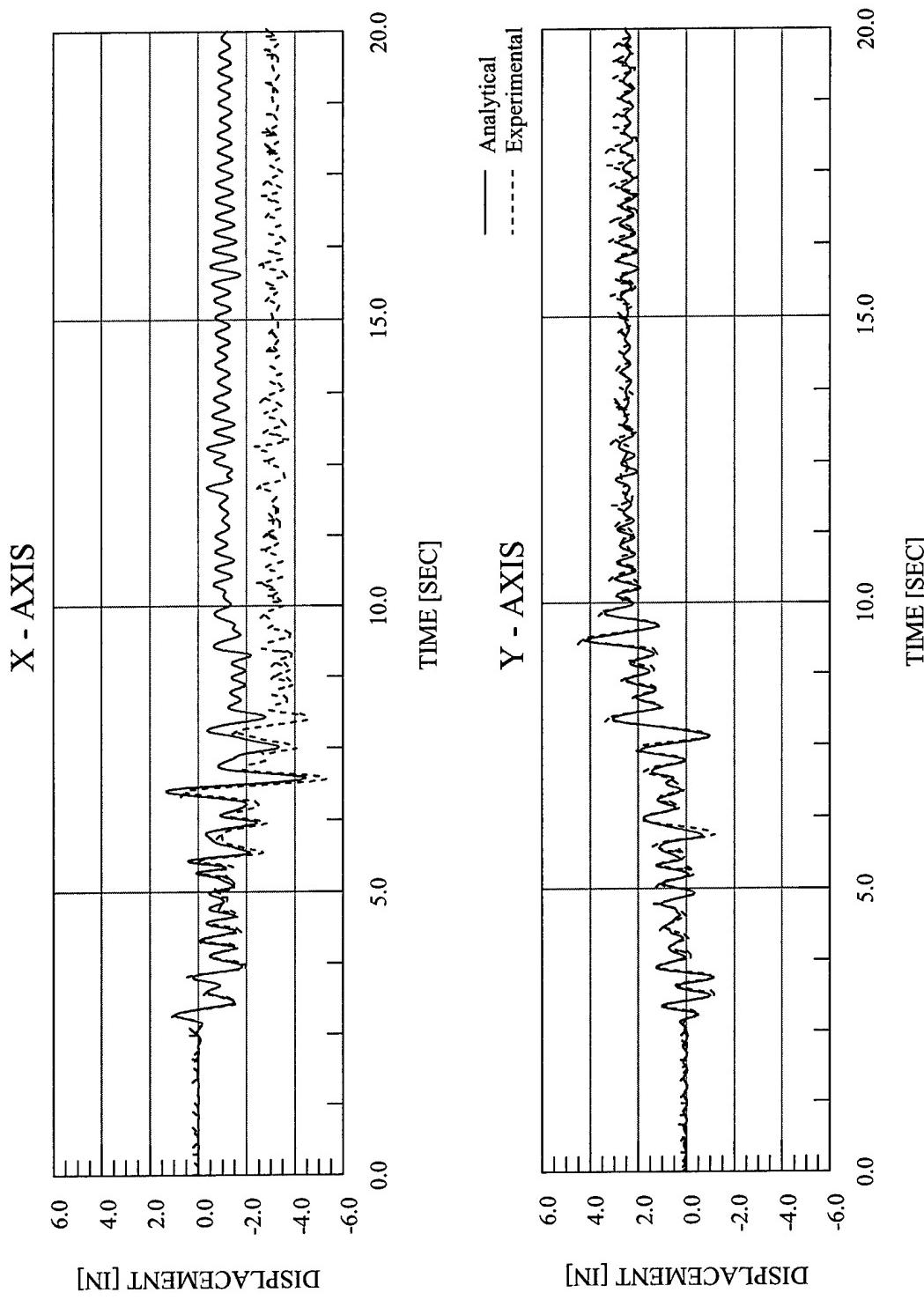


Figure 5.40 Drain-3DX Analytical Displacement vs. Time – EQ 16 – 150% Biaxial Imperial Valley

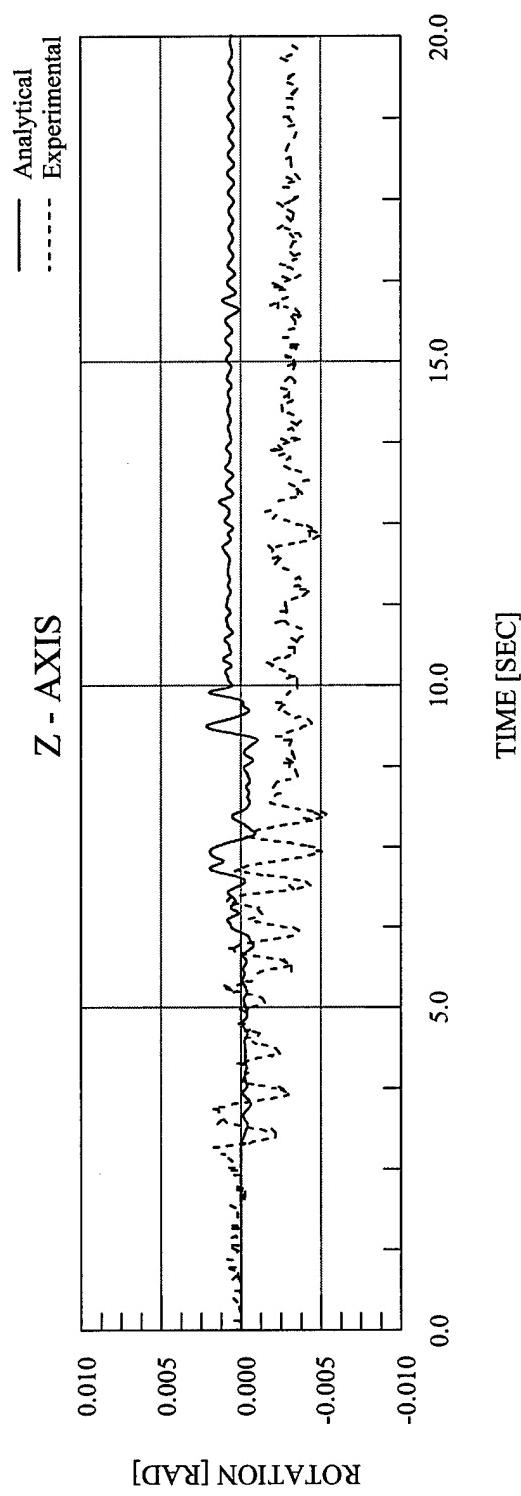


Figure 5.41 Drain-3DX Analytical Rotation vs. Time – EQ 16 – 150% Biaxial Imperial Valley

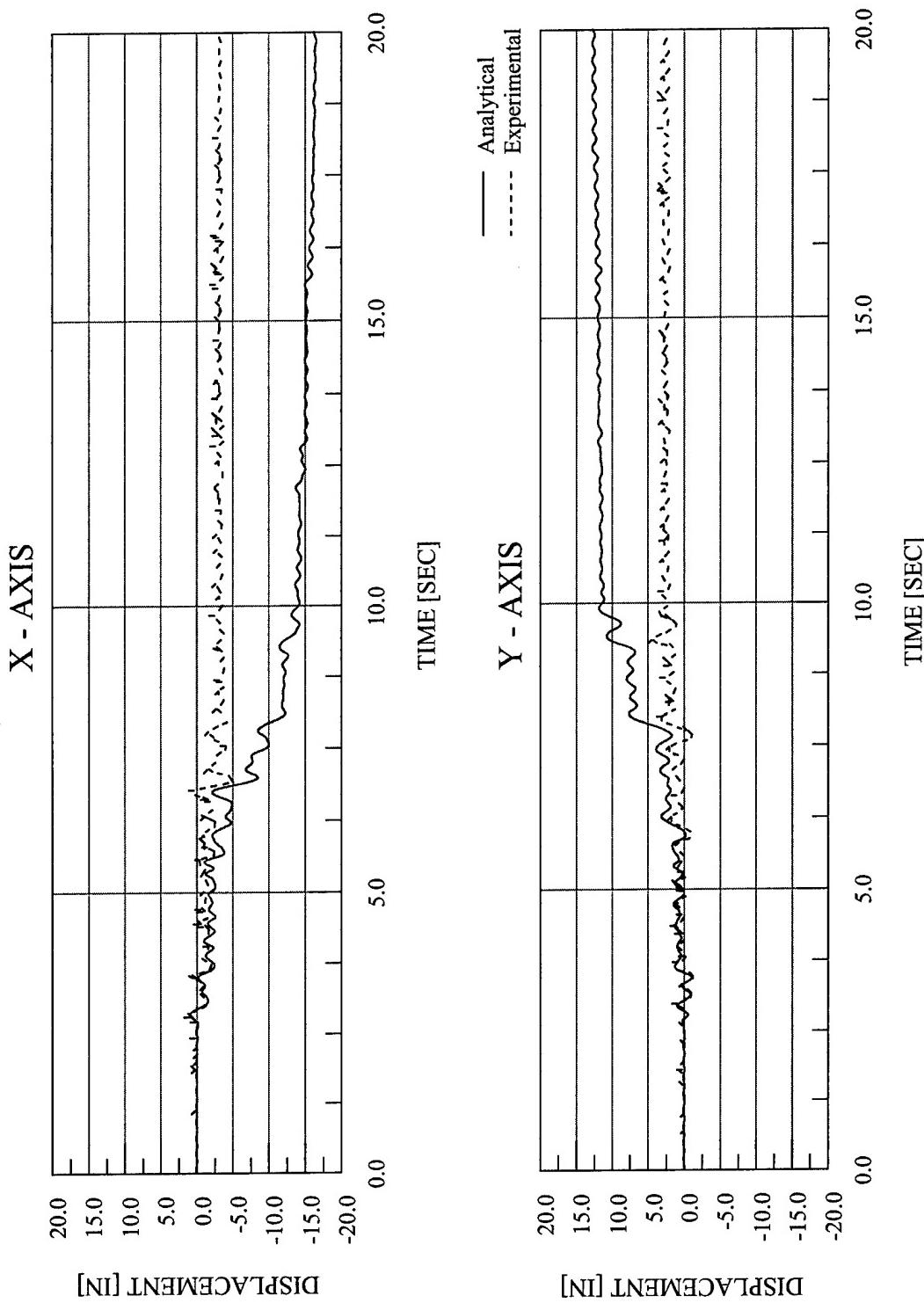


Figure 5.42 Abaqus Analytical Displacement vs. Time – EQ 16 – 150% Biaxial Imperial Valley – Perfect Plasticity

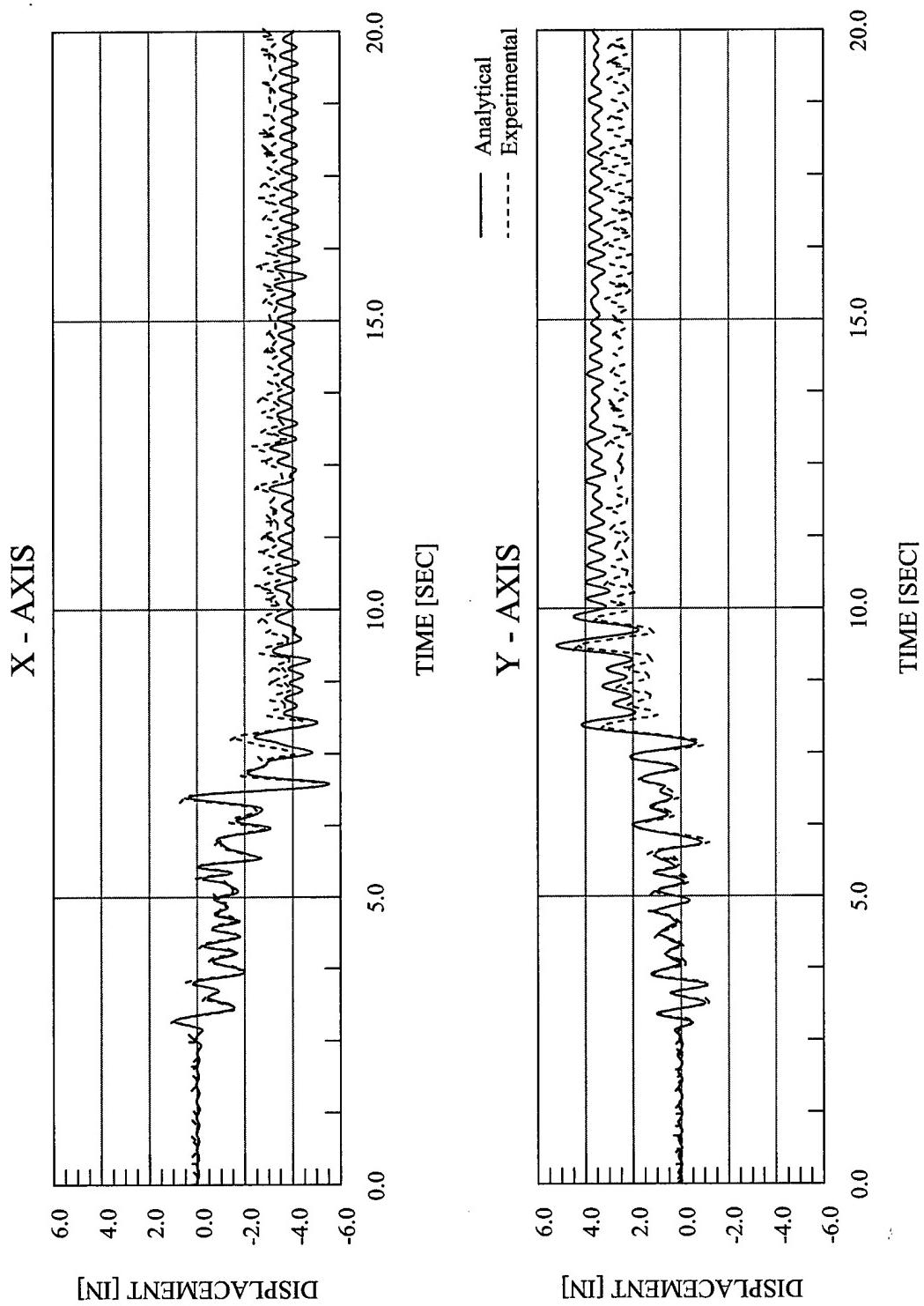


Figure 5.43 Abaqus Analytical Displacement vs. Time – EQ 16 – 150% Biaxial Imperial Valley – Isotropic Material Hardening

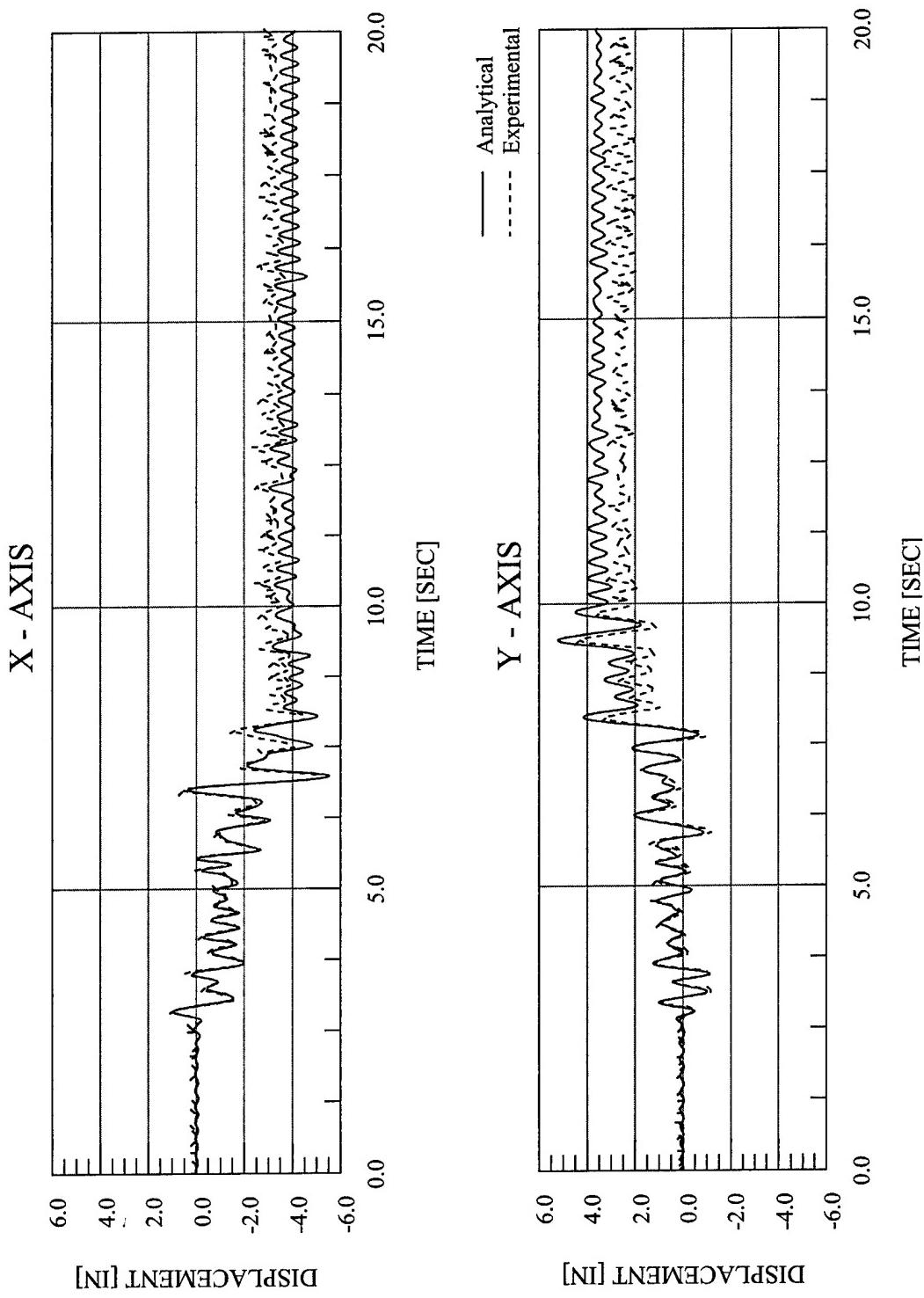


Figure 5.44 Abaqus Analytical Displacement vs. Time – EQ 16 – 150% Biaxial Imperial Valley – Kinematic Material Hardening

CHAPTER 6

EXPERIMENTAL AND ANALYTICAL RESPONSE OF TEST CONFIGURATION 4

This chapter provides a summary of the experimental test data and the finite element analysis results of Test Configuration 4. The fourth configuration, as seen in Figure 6.1, featured all of the masses loaded on the east side of the diaphragm, resulting in a $\frac{1}{2}$ mass asymmetry, and four 4" Extra-Strong Columns. The dynamic properties of the test structure in Test Configuration 4 are shown in Table 6.1.

Five earthquake simulations were performed with this test configuration: 10% X-Axis only [$\text{PGA}_X = 0.105 \text{ g}$], 10% Y-Axis only [$\text{PGA}_Y = 0.070 \text{ g}$], 10% Biaxial [$\text{PGA}_X = 0.102 \text{ g}$ and $\text{PGA}_Y = 0.062 \text{ g}$], 100% Biaxial [$\text{PGA}_X = 1.115 \text{ g}$ and $\text{PGA}_Y = 0.711 \text{ g}$], and 150% Biaxial [$\text{PGA}_X = 1.629 \text{ g}$ and $\text{PGA}_Y = 1.121 \text{ g}$]. Characterization tests were also performed to determine the dynamic properties of the model. The complete test sequence for Test Configuration 4 is shown in Table 6.2.

The first three earthquake simulations, using 10% X-Axis only, 10% Y-Axis only, and 10% Biaxial input motions, featured elastic behavior only. The fourth simulation, using 100% Biaxial input motions, was the initial inelastic test for this configuration. Subsequently, an additional test was performed in which 150% Biaxial input motions were used and featured pre-existing damage in the model columns.

This chapter summarizes response data of this test configuration during the earthquake simulations and the dynamic characterization tests. Summaries of test model accelerations, displacements, torsional moments, overturning moments, column end moments, and base shears are also provided.

6.1 OBSERVED STRUCTURAL RESPONSE

The diaphragm acceleration and displacement time history responses for the 10% X-Axis simulation are shown in Figure 6.2. The base shear vs. displacement and torque vs. rotation are shown in Figure 6.3. Similar responses for the 10% Y-Axis simulation are shown in Figures 6.4 and 6.5. Results for the 10% Biaxial simulation are shown in Figures 6.6 and 6.7. The responses for the 100% Biaxial simulation are shown in Figures 6.8 and 6.9. Results for the 150% Biaxial simulation are shown in Figures 6.10 and 6.11.

Tables 6.3 – 6.7 list the peak recorded diaphragm relative displacements and peak diaphragm accelerations, and corresponding PGA for each of the five earthquake simulations performed in this test configuration. Also listed are the maximum base shears, maximum torsional moments, maximum overturning moments, maximum column end moments for each column, and maximum column end shears for each column.

6.2 OBSERVED RESPONSE DISCUSSION

The calculated force-deformation behavior of the structure in the X and Y directions and about the Z-Axis are shown in Figures 6.12 and 6.13. In the X direction, the model has a yield displacement of 0.42 inches at a yield force of 19.28 kips. In the Y direction, the model has a yield displacement of 0.44 inches at a yield force of 18.35 kips. The model has a yield rotation of 0.0062 radians at a moment of 1356 kip-inches. In Figure 6.14, the structural force-deformation behavior shown in Figures 6.12 and 6.13 is compared with the maximum force-deformation response from each of the earthquake simulations in this test configuration. Elastic response spectra of the recorded table motions for EQ 25 – EQ 28 are shown in Figures 6.15 – 6.18, respectively. The modal frequencies for this configuration with respect to the response spectra are indicated in Figures 6.15 – 6.18 as well.

The first earthquake simulation for this configuration, EQ 25, features 10% Imperial Valley input motion in the X-Axis only [$\text{PGA}_X = 0.105 \text{ g}$]. Time history plots of the structural response are shown in Figure 6.2. The peak displacements of the structure were 0.273 inches along the X-Axis, 0.079 inches along the Y-Axis, and 1.45×10^{-3} radians about the Z-Axis. The peak

displacement predicted by static analysis is 0.291 inches along the X-Axis and 0.97×10^{-3} radians about the Z-Axis, with no displacement predicted along the Y-Axis. The peak base shears are 12.78 kips in the X direction and 2.66 kips in the Y direction, and peak torsional moment is 272.11 kip-inches. Figure 6.3 shows the base shear vs. displacement plots and torsional moment vs. rotation plot, which are all tight and linear, indicating no yielding. As the mass eccentricity in this configuration is along the Y-Axis, torsional moments and rotations are expected with input motion along the X-Axis. However, Figure 6.2 shows that the structure did have a very small response in the Y direction. This motion is most likely a resonance motion, which is a product of the shaketable control problem discussed in Chapters 3 and 4.

In EQ 26 the model is subjected to a 10% Y-Axis input motion [$\text{PGA}_Y = 0.070$ g] and response plots are shown in Figure 6.4. The peak displacements were 0.182 inches in the Y direction and 0.027 inches in the X direction, and the peak rotation was 0.36×10^{-3} radians. The peak displacements predicted by static analysis are 0.202 inches in the Y direction, with no displacements predicted along the X-Axis or torsionally. Further, the displacement time histories indicate no residual displacement or permanent deformation. In EQ 26, with no eccentricity, a torsional effect is not expected. The acceleration response in the X direction and the angular acceleration response both appear to indicate resonant responses due to the table control problems. The responses are very small, however. The displacement responses seen in Figure 6.4 appear to be largely noise, as the responses are on the same order of magnitude as the precision of the data acquisition system. Although the resonant motions are present in this simulation, they are not as pronounced as in EQ 25. This observation suggests that the torsional motion present in EQ 25 may facilitate the resonant motion. Figure 6.5 shows the base shear vs. displacement plots and torsional moment vs. rotation plot. The shear vs. displacement plot for the Y direction is tight and linear.

The third earthquake simulation for this configuration, EQ 27, features 10% Imperial Valley input motion along both the X-Axis and Y-Axis [$\text{PGA}_X = 0.102$ g and $\text{PGA}_Y = 0.062$ g], with structural response plots shown in Figure 6.6. The peak displacements of the structure were 0.270 inches in the X direction, 0.231 inches in the Y direction, and 1.56×10^{-3} radians in the Z direction. Static analysis predicted the peak displacements to be 0.293 inches along the X-Axis, 0.251 inches along the Y-Axis, and 0.97×10^{-3} radians about the Z-Axis. Further, the displacement time histories indicate no residual displacement or permanent deformation. Thus, both displacements and rotation indicate that the structural response for this simulation remained elastic, as expected.

The peak base shears and peak torsional moment are 12.40 kips in the X direction, 9.34 kips in the Y direction, and 260.40 kip-inches about the vertical axis. Figure 6.7 shows the base shear vs. displacement plots and torsional moment vs. rotation plot, which are all tight and linear.

Thus, for this test configuration, the static analysis is consistently conservative in predicting the elastic peak displacements by about 10%. However, the static analysis is consistently unconservative in predicting the elastic peak rotations, by approximately 50%. Note that the structural response does not qualify the model as torsionally irregular in any of the elastic simulations.

In comparing EQ 27 with EQ 25, the addition of the 10% Y-Axis input motion results in little change in the X-Axis response of the diaphragm, as the peak displacement and base shear are 0.273 inches and 12.78 kips for EQ 25 and 0.270 inches and 12.40 kips for EQ 27. Because this configuration has an eccentricity in the Y direction only, the addition of an input motion and thus response in the Y direction will not add to the torsional effect. This is verified by the fact that the torsional moment is virtually unchanged between EQ 25 and EQ 27. In light of the fact that the recorded table motions are not always identical to the ground motions input into the table control system, as discussed in Chapter 3, it is also of interest to compare the recorded peak ground accelerations (PGA) and resulting pseudo-spectral displacements (PSD), which give a measurement of the displacement response as a function of the ground motion and period of the structure, of any two simulations. As shown in Table 6.3, EQ 25 has a PGA of 0.105 g while EQ 27 has a PGA of 0.102 g. In addition, in referencing Figures 6.15 and 6.17, EQ 25 has a PSD of 0.304 inches while EQ 27 has a PSD of 0.294 inches. Thus, the fact that the PSD and PGA of EQ 27 are slightly less, but very close, to those of EQ 25, validates the small decrease in the recorded displacement response from EQ 25 to EQ 27. In a linear elastic system, the displacement response in EQ 27 should be the equal to the sum of the responses in EQ 25 and EQ 26. This comparison can be made if the ground motions for all three simulations were the same. The ground motions characteristics are similar enough for EQ 25 and EQ 27 in the X direction to make the comparison. As observed previously, it appears that the displacement response in the X direction for EQ 27 is roughly equal to that for EQ 25, meaning that, for a linear elastic system, EQ 26 should not produce any response in the X direction. A non-trivial displacement response was observed, however for EQ 26. This response was previously observed to be a resonant vibration response due to the shaketable motion control problem, as discussed in Chapter 3. However, EQ 27 featured a biaxial ground motion, thus no control problem was present, and the

observed resonant response in EQ 26 would not be present in EQ 27. The same argument holds in comparing the torsional response in EQ 25 to that in EQ 27.

In comparing EQ 27 to EQ 26, the addition of the 10% X-Axis input motion does result in a change in the Y-Axis response, as well as the X-Axis response. The peak displacement in the Y-Axis increases substantially from 0.182 inches in EQ 26 to 0.231 inches in EQ 27. The peak ground acceleration actually decreases from 0.070 g for EQ 26 to 0.062 g for EQ 27, which doesn't appear to support the observed results. However, the pseudo-spectral displacement for EQ 26 is 0.201 inches, as compared to 0.249 inches for EQ 27. Thus, although the PGA decreases from EQ 26 to EQ 27, changes in the frequency content of the ground motion result in an increase in the PSD from EQ 26 to EQ 27. In fact, the increase in the PSD is roughly 25%, which is about the same increase in the recorded displacement response from EQ 26 to EQ 27. Since any change in displacement response in the Y direction from EQ 26 to EQ 27 can be accounted for by the change in the character of the ground motion, it appears that the Y-Axis response observed in EQ 25 is not present in EQ 27. As was discussed in the previous paragraph, the Y-Axis response in EQ 25 was previously observed to be a resonant response due to the table control problem. However, EQ 27 featured a biaxial ground motion, thus no control problem was present, and the observed resonant response in EQ 25 would not be present in EQ 27. Thus, the expected response of a system responding linearly is observed.

In EQ 28, the first test in this configuration that features inelastic response, the model structure was subjected to 100% Imperial Valley input motion along both the X-Axis and Y-Axis [PGA_X = 1.115 g and PGA_Y = 0.711 g] and structural response plots are shown in Figure 6.8. The peak displacements of the structure were 2.59 inches in the X direction and 1.44 inches in the Y direction, which are both larger than the yield displacements. The peak rotation of the structure was, at 18.26×10^{-3} radians, larger than the yield rotation. The peak base shears, which are 36.48 kips in the X direction and 33.61 kips in the Y direction, verify the inelastic response but they also demonstrate the overstrength of the structure, as the peak shears are both nearly twice the yield shears. Figure 6.9 shows the base shear vs. displacement plots and torsional moment vs. rotation plot, which are no longer tight and linear but now are taking on a fuller shape, indicating inelastic behavior. Both the X-Axis shear vs. displacement loop and the moment vs. rotation loop exhibit a very large inelastic excursion.

The acceleration response of the diaphragm divided by the peak ground acceleration (PGA) is shown in Table 6.4 as the normalized acceleration. In EQ 27, with 10% Biaxial input motions, the normalized acceleration response of the diaphragm is 3.42 in the X direction and 4.29 in the Y direction. The input ground motions are increased by approximately a factor of 10 in EQ 28, but the acceleration response of the diaphragm only increases by about 3 in the X direction and 3.6 in the Y direction. This is illustrated in the normalized acceleration response of the diaphragm, which is 0.93 in the X direction and 1.35 in the Y direction. Also, although the input motions are increased by a factor of approximately 10, the angular acceleration response of the diaphragm increases from EQ 27 to EQ 28 by only a factor of about 5. Both of these trends verify the expected inelastic behavior of the structure in EQ 28. Because the base shears are roughly proportional to the diaphragm accelerations, the same trends can be observed by comparing the peak base shears to the peak ground accelerations.

It is interesting to note that although the test structure experiences a rotational ductility of nearly 3 for this simulation, the peak torsional moment is 927.5 kip-inches. The yield moment, as seen in Figure 6.14, is 1356 kip-inches for this model configuration. Thus, the peak torsional moment experienced by the structure is approximately two-thirds of the yield moment, but the structure has a rotational ductility greater than one. The simultaneous lateral motion of the structure interacts with the torsional motion by producing a large amount of column yielding that would be present even without the torsion, allowing the structure to experience much larger rotations than it would when subjected to torsion alone. Each of the four columns provides strength and stiffness in both the X and Y directions. The stiffness of the model in the X and Y directions working together produces the torsional stiffness of the structure. When one of the columns yields, it loses stiffness in both directions and consequently loses stiffness torsionally as well.

The final earthquake simulation for this configuration, EQ 29, features 150% Imperial Valley input motion along both the X-Axis and Y-Axis [PGA_X = 1.629 g and PGA_Y = 1.121 g]. EQ 29 is the only simulation in this configuration that begins with pre-existent damage and yielding. From Table 6.1, which shows the modal frequencies and damping ratios before EQ 25 and following EQ 29, it can be seen that the modal frequencies of the structure do not change in any meaningful way during this configuration. Thus, the pre-existent damage from EQ 28 appears to have no effect on the stiffness of the structure. Table 6.1 also shows that the damping ratios did change noticeably during this configuration, which implies that the damping ratios of the structure following EQ 28 might also have changed from the beginning of the configuration. The

damping ratios are still small, however, in comparison to the damping effect produced by the hysteretic behavior during the inelastic simulation EQ 29.

Time history plots of the structural response are shown in Figure 6.10. The peak displacements of the structure were 4.84 inches in the X direction and 4.48 inches in the Y direction, and 34.58×10^{-3} radians in the Z direction. The peak base shears were 40.44 kips in the X direction and 40.49 kips in the Y direction. The base shears in EQ 29 are approximately 10% larger than those in EQ 28, despite the fact that the input motions have been increased by 50%. With EQ 29, as shown in Figure 6.11, the base shear vs. displacement hysteresis loops exhibit a very full, smooth shape, indicating a large degree of inelastic behavior, as is expected. Substantially more inelastic energy dissipation was observed for this test than for EQ 28. The torsional moment vs. rotation loop has become more full as compared with EQ 28, but the shape is somewhat erratic as compared with the base shear vs. displacement loops. Contrary to EQ 25 – 27, a small amount of residual displacement is evident after EQ 28, as seen in Figure 6.8. The permanent displacement increases substantially in EQ 29, as seen in Figure 6.10.

The displacement response of the diaphragm normalized by the peak ground acceleration (PGA) is shown in Table 6.3. In EQ 27, with 10% Biaxial input motions, the relative displacement of the diaphragm is 2.65 in/g in the X direction, and 3.73 in/g in the Y direction. The input ground motions are increased to 100% Biaxial in EQ 28, but the normalized displacement decreases slightly in the X direction to 2.32 in/g and decreases more noticeably in the Y direction to 2.03. Also, in moving from EQ 27 to EQ28, the diaphragm rotation increases on a relatively proportional level with the input motion increase. In EQ 29, the input motions are increased to 150% Biaxial, and the normalized displacement response of the diaphragm is 2.97 in/g in the X direction and 3.99 in/g in the Y direction. Thus, in EQ 29 the ground motion was increased by 50% and the base shear increased by about 10% from those in EQ 28, while the displacement response nearly doubled in the X direction and more than tripled in the Y direction. Also, the maximum rotation nearly doubles from EQ 28 to EQ 29, while the input motions increase by only 50%. Although it is expected that the effective period of the structure will increase during inelastic response, the elastic displacement response spectra for EQ 28, as shown in Figure 6.16, indicates that the displacement response may increase or decrease as the period increases from the natural period of about 0.29 seconds, depending on the actual change in the effective period of the structure. The displacement response spectrum gives the peak displacement response as a function of the period of the structure. During the parts of the response when yielding is

occurring, the period of the structure increases in a complex, non-predictable manner, which makes it impossible to accurately predict the peak response using the response spectra. Thus, the normalized displacement response decreases as the period of the structure increases in moving to inelastic behavior, from EQ 27 to EQ 28, and then the normalized displacements increase as the period of the structure increases further. Although not predictable, this behavior is not inconsistent with the displacement response spectra for this configuration.

Another indicator of the softening of the structure is the ratio of the torsional displacement to the base shear. As yielding occurs, we expect to see displacements increase to a greater degree than the inertial forces. This is verified by the fact that the torsional displacement to base shear ratio is approximately 3.5 times larger for EQ 28 than for EQ 27. Further, for EQ 29 the ratio is more than 5 times larger than for EQ 27.

As the inelastic behavior of a structure is typically predicted based on an elastic analysis in design, it is important to know whether the ratio of peak torsional to translational displacement can be extended from elastic to inelastic response. The ratio of the peak torsional displacement to the translational displacement for the 10% Biaxial test is 1.27, using the X-Axis displacement. For the 100 % Biaxial test, the torsional to translational displacement ratio is 1.34, and for the 150 % simulation, the ratio is 1.33. Thus, the difference between the elastic and inelastic response is approximately 5%. For this configuration, the translational displacement used in these ratios was along the X-Axis as the mass eccentricity was along the Y-Axis.

6.3 DYNAMIC CHARACTERIZATIONS OF THE MODEL

Prior to performing any shaketable simulations using the earthquake input motions, white noise, sine sweep, and sine decay tests were performed, as discussed in Chapter 3. This general pattern was followed for Test Configuration 4, as can be seen in Table 6.2. In addition, white noise tests were performed immediately after both earthquake simulations exhibiting inelastic behavior, EQ 28 and EQ 29.

The dynamic properties of the test structure, as measured before EQ 25 and after EQ 29, are shown in Table 6.1. The results in Table 6.1 indicate that despite the inelastic behavior in EQ 28 and EQ 29, no meaningful permanent softening of the structure took place. The damping, on the

other hand, did increase noticeably by the end of the final simulation. The structure experienced a significant amount of inelastic behavior during the final two simulations, which most likely began to produce micro-cracking at the column-base plate welded interface.

6.4 OBSERVED CONDITION OF THE STRUCTURE

In inspecting the model structure for fracture in the weld or in the base material, none was found for Test Configuration 4. In observing the structure condition after EQ 28, the formation of plastic hinges near the tops and bottoms of the columns was becoming discernable. Following the completion of EQ 29, permanent plastic damage in the columns was evident, with the locations of the plastic hinges in the columns becoming very clear. Figures 6.19 and 6.20 are photographs of the test structure taken before the earthquake simulations were performed. Figures 6.21 and 6.22 are photographs of the test structure taken after the final earthquake simulation in this configuration, EQ 29, illustrating the inelastic behavior and permanent damage of the structure. Figure 6.23 also shows the formation of plastic hinges near the top and bottom of the column.

6.5 FINITE ELEMENT ANALYSIS

During the earthquake simulations employing the larger scale input motions, the structural response exhibits both geometric and material nonlinearities, both of which Abaqus and Drain-3DX can model. A more complete discussion of the applicable features of Abaqus and Drain-3DX is presented in Chapter 3, in addition to some aspects of the finite element model that are common throughout each test configuration.

(A) PIPE COLUMN MATERIAL MODEL

The pipe columns used in Test Configuration 4, as well as those used in Test Configurations 1-3, were produced from the same batch of raw pipe column lengths. The material models of the pipe columns in these four test configurations were based on the stress-strain data produced during each coupon tension test. Figures 6.24 and 6.25 show both the original stress-strain data recorded

during the coupon tension tests and the best-fit material model used in the Abaqus and Drain-3DX finite element analyses, respectively. Shown in Table 6.8 are the numerical stress-strain best-fit Abaqus model data. Shown in Table 6.9 are the numerical stress-strain best-fit Drain-3DX model data.

(B) FINITE ELEMENT MODEL

The Abaqus and Drain-3DX finite element models employed to analyze the behavior of Test Configuration 4 are shown in Figures 6.26 and 6.27, respectively. Beyond the features of the finite element model, which are common throughout each test configuration and are discussed in Chapter 3, these figures illustrate the location and magnitudes of the nodal masses and the height of the Non-Rigid Links. For the Abaqus model, the nodal masses placed at each of the four corners of the diaphragm have a magnitude of $1.706 \text{ lb} \cdot \text{s}^2/\text{in}$. Two of the interior masses, the northeast and southeast interior masses, each have a magnitude of $35.163 \text{ lb} \cdot \text{s}^2/\text{in}$. The other two interior masses, located on the west side of the diaphragm, have magnitudes of $5.283 \text{ lb} \cdot \text{s}^2/\text{in}$. The height of the finite element model diaphragm in this test configuration is 67.804 inches, which thus produces a length of 7.804 inches for each of the four Non-Rigid Links. The nodal masses placed at the four diaphragm corners have magnitudes of $1.943 \text{ lb} \cdot \text{s}^2/\text{in}$. The southeast and northeast interior masses have magnitudes of $38.321 \text{ lb} \cdot \text{s}^2/\text{in}$, while the southwest and northwest masses have magnitudes of $3.033 \text{ lb} \cdot \text{s}^2/\text{in}$. The height of the finite element model diaphragm is 68.362 inches, which results in a length of 8.362 inches for the Non-Rigid Links.

(C) OBSERVED RESPONSE

Displacement histories for both Abaqus and Drain-3DX analyses along the X- and Y-Axis and rotation histories about the Z-Axis are provided for the 10% Biaxial simulation [$\text{PGA}_X = 0.102 \text{ g}$ and $\text{PGA}_Y = 0.062 \text{ g}$] in Figures 6.28 – 6.31, the 100% Biaxial simulation [$\text{PGA}_X = 1.115 \text{ g}$ and $\text{PGA}_Y = 0.711 \text{ g}$] in Figures 6.32 – 6.35, and the 150% Biaxial simulation [$\text{PGA}_X = 1.629 \text{ g}$ and $\text{PGA}_Y = 1.121 \text{ g}$] in Figures 6.36 – 6.39. Shown in Figures 6.40 – 6.43 are displacement histories for the 100% and 150% Biaxial simulations utilizing an Abaqus finite element model with an isotropic material model. Table 6.10 lists the maximum peak relative displacements in the X and

Y directions and the peak rotation, and the corresponding PGAs, for the three earthquake simulations listed above.

(D) OBSERVED RESPONSE DISCUSSION

In Figures 6.28 – 6.31, the displacement and rotation response histories for EQ 27 [$\text{PGA}_X = 0.102 \text{ g}$ and $\text{PGA}_Y = 0.062 \text{ g}$] can be seen for both the test structure and the finite element model. For both displacements and the rotation, the frequency contents of the response histories in the Abaqus and Drain-3DX simulations match the test data very well. As seen in Table 6.10, the maximum relative displacements in both directions of the Abaqus finite element model match the test data fairly well, agreeing to within 10% in the X direction and within 5% in the Y direction. The Drain-3DX simulations also match the test data well, with differences about 4% in the X direction and 13% in the Y direction. With both the Abaqus and Drain-3DX models, the peak displacements appear to occur in the same time region for both the finite element model and the test structure. The peak rotation in the Abaqus model agrees to within 14% with the test data, while the Drain-3DX results only agree to within 23%.

In visually inspecting the response plots, it is apparent that the damping characteristics of the Abaqus and Drain-3DX models do not match as well with the test structure as does the frequency content. In computing the damping ratios of the test structure using the sine decay tests, the test structure was found to have a damping ratio 0.47% in the X direction and 0.87% in the Y direction. Thus, although both damping ratios are very small, the damping in the Y direction is nearly twice that in the X direction. As discussed in Chapter 4, both Abaqus and Drain-3DX present limitations on the ability to independently define the damping ratio in the X and Y directions. In developing the model for this simulation, a compromise was found, resulting in a damping ratio in the X direction that was larger in the finite element models than in the test structure, and a damping ratio in the Y direction that was smaller than in the test structure. Figure 6.15, the elastic response spectra in the X direction shows response spectra for 0.4%, 0.8%, 1.2%, and 1.6% damping, which is roughly the range of damping ratios which were observed for all of the model structures without bracing. This figure serves as an illustration of the sensitivity in acceleration and displacement response of the structure to the amount of damping. At 0.288 seconds, the period of the structure in the X direction, PSA, from 0.375 g to 0.302 g, and PSD, from 0.304 inches to 0.245 inches, vary by nearly 20% over the range of damping from 0.4% to 1.6%. The plots in Figure 6.28 and 6.30 of the displacement response histories clearly illustrate

this modeling problem. In the X direction, the displacement response in the Abaqus model is clearly damped to a larger degree than the test structure displacement response. And, in the Y direction plots, the displacement response in the Abaqus model is damped to a smaller degree than the test structure displacement response.

In Figures 6.32 – 6.35, the displacement and rotation response histories for EQ 28 [$\text{PGA}_X = 1.115 \text{ g}$ and $\text{PGA}_Y = 0.711 \text{ g}$] can be seen for both the test structure and the finite element model. For both displacements and the rotation, the frequency contents of the response histories in the Abaqus and Drain-3DX simulations match the test data fairly well. In the X direction, the magnitude of the displacement also matches very well. For both the Y direction motion and the rotation, the Abaqus simulations predict smaller peak displacements at a number of points in the time history and a lesser degree of permanent deformation. For this simulation, it appears that the Drain-3DX model does a slightly better job of matching the response history than the Abaqus model. As seen in Table 6.10, the peak displacements in the X direction agree to within 3% for the Abaqus model, while the peak displacements in the Y direction agree to within only 20%. The Abaqus rotation differs from the test data by nearly 30%. The Drain-3DX model predicts the maximum displacements in the X and Y directions to within 2% and 6% of the actual response. Despite the rotation typically being the most difficult to predict, in this simulation the Drain-3DX model agrees to within 1% of the actual peak rotation. These same trends continue in the response histories for EQ 29 [$\text{PGA}_X = 1.629 \text{ g}$ and $\text{PGA}_Y = 1.121 \text{ g}$], the 150% simulation, shown in Figures 6.36 – 6.39. The peak displacement in the Y direction and the peak rotations are actually in better agreement for EQ 29 with the Abaqus model, with differences of only 10% and 24%, respectively, while the X direction displacement matches to within 1%. This despite the fact that EQ 29 is a more difficult test for the finite element model to simulate. The peak displacements in the X and Y directions for the Drain-3DX model agree to within 23% and 13%, noticeably worse than for EQ 28. The peak rotation still matches the test data fairly well, to within 8%.

The Abaqus simulations shown in Figures 6.32 – 6.33 and 6.36 – 6.37 each utilize a combined nonlinear isotropic/kinematic hardening model, as described in Chapter 3. Figures 6.40 – 6.43 show the same two simulations, EQ 28 and EQ 29, performed with an isotropic hardening model only. Intuitively, it would seem that the material post-yield behavior would be very important in predicting response in a highly inelastic system. In Figure 6.42, the Y Axis response appears to bear this out, as Abaqus predicts very little permanent deformation, while the simulation utilizing

the combined hardening model is fairly accurate in predicting the true permanent deformation of more than 4 inches. However, in looking at the X Axis response, the simulation utilizing isotropic material hardening only is nearly as accurate as the simulation with a combined material hardening model. The rotational response, as seen in Figures 6.41 and 6.43, is somewhere in between, as it is not as accurate as the X-Axis response but not as inaccurate as the Y-Axis response.

For the hardening model for these simulations, it was assumed that the isotropic part of the hardening would compose 30% of the total hardening. This figure was chosen through calibration to the response of the symmetric models studied in earlier chapters. In the elastic Abaqus simulations, the inability to define damping independently in the X and Y directions resulted in the overestimation of the displacement in one direction and the underestimation in the other direction. This modeling problem became a non-issue in EQ 28 and EQ 29, as the damping behavior caused by yielding of the structure overwhelmed any inherent elastic damping in the structure.

6.6 SUMMARY AND CONCLUSIONS

In Chapters 4 and 5, the *Modified μ/R Ratio* was discussed. This ratio gives a measure of the amount of ductility the *2000 NEHRP Seismic Provisions* expects a particular structure to experience and thus for which it must be designed. In the previous two chapters, the *Modified μ/R Ratio* was computed as the normalized displacement in an inelastic test divided by the normalized displacement during an elastic test. The μ/R Ratio can also be defined as the ratio of the normalized rotation during an inelastic simulation to the normalized rotation during an elastic simulation. For EQ 28, the first inelastic simulation in this configuration, the μ/R Ratios are shown below and were 0.90 in the X direction, 0.51 in the Y direction, and 1.07 torsionally. As with EQ 15, the first inelastic simulation with complete symmetry, discussed in the previous chapter, these values are not very consistent. For EQ 15, the μ/R Ratios were 1.37 in the X direction, 0.86 in the Y direction, and 0.84 torsionally.

Configuration	EQ	μ/R Ratio		
		X-Axis	Y-Axis	Z-Axis
Symmetric Mass 100% Uniaxial	7	N/A	0.77	N/A
Symmetric Mass 100% Biaxial	15	1.37	0.86	0.84
Symmetric Mass 150% Biaxial	16	1.77	1.83	1.08
$\frac{1}{2}$ Asymmetric Mass 100% Biaxial	28	0.90	0.51	1.07
$\frac{1}{2}$ Asymmetric Mass 150% Biaxial	29	1.17	1.03	1.39

The *Seismic Provisions* provides a range of 0.86 to 0.69 for an Ordinary Moment Resisting Frame (OMRF) and a Special Moment Resisting Frame (SMRF), respectively. Thus, the μ/R Ratio appears to be more conservative for the X and Y directions but less so for the torsional motion. For EQ 29, the second inelastic simulation in this configuration, μ/R Ratios were 1.17 in the X direction, 1.03 in the Y direction, and 1.39 torsionally. For EQ 16, an earthquake simulation of relatively equal magnitude but with no eccentricity, discussed in Chapter 5, the *Modified μ/R Ratios* were 1.77 in the X direction, 1.83 in the Y direction and 1.08 torsionally. The values for this configuration again are more conservative in the X and Y directions than those for the symmetric configuration, and again the value torsionally is less conservative than for the symmetric configuration. Each of the values for EQ 29 is still greater, by at least 20%, than those prescribed by the *Seismic Provisions*, and, as in the previous test configuration, the μ/R Ratios have changed from one inelastic simulation to the next inelastic simulation. The emerging pattern with respect to the μ/R Ratio is that it is not constant for differing test configurations, earthquake magnitudes, and component directions. In addition, it appears to be consistently larger than the range of μ/R Ratios prescribed by the *2000 NEHRP Seismic Provisions*.

In Chapter 5, the ratio of the two peak lateral displacements, u_Y/u_X , was discussed. It was shown that the design assumption of a constant μ/R Ratio used in the *Seismic Provisions* implies that the u_Y/u_X ratio remains constant regardless of elastic or inelastic response, and regardless of the degree of eccentricity. In addition, these design assumptions also imply that the ratio of the peak rotation to the peak lateral displacement remains constant. Without these assumptions,

independent values of C_d , or μ , would need to be specified. For elastic response, the *Seismic Provisions* define the *seismic base shear*, V_e , and *torsional moment*, M_e , as

$$V_e = PSA_e * W \quad \text{and} \quad M_e = V_e * e$$

where e is the eccentricity of the structure. The elastic peak displacement and rotation are defined as

$$u_e = \frac{V_e}{K} \quad \text{and} \quad \theta_e = \frac{M_e}{K_\theta}$$

where K is the lateral stiffness and K_θ is the torsional stiffness. The elastic rotation can also be written as

$$\theta_e = \frac{M_e}{K_\theta} = \frac{V_e * e}{K_\theta} = \frac{K u_e * e}{K_\theta}$$

and therefore the ratio of elastic rotation to lateral displacement can be written as

$$\frac{\theta_e}{u_e} = \frac{K}{K_\theta} * e$$

For inelastic response, the *Seismic Provisions* define the *seismic base shear*, V_i , and *torsional moment*, M_i , as

$$V_i = \frac{PSA_i}{R} * W \quad \text{and} \quad M_i = V_i * e$$

The inelastic deformation and rotation are defined as

$$u_i = C_d \frac{V_i}{K} \quad \text{and} \quad \theta_i = C_d \frac{M_i}{K_\theta}$$

The inelastic rotation can also be written as

$$\theta_i = \frac{M_i}{K_\theta} = C_d \frac{V_i * e}{K_\theta} = \frac{K u_i * e}{K_\theta}$$

and therefore the ratio of inelastic rotation to inelastic lateral displacement can be written as

$$\frac{\theta_i}{u_i} = \frac{K}{K_\theta} * e$$

Thus,

$$\frac{\theta_e}{u_e} = \frac{\theta_i}{u_i}$$

If θ is multiplied by $a/2$, or the distance from the center to the outer edge of the diaphragm, the result is the portion of the edge displacement due solely to the torsion of the diaphragm, u_θ . Therefore, the above equality can be rewritten as

$$\frac{\frac{a}{2}\theta_e}{u_e} = \frac{\frac{a}{2}\theta_i}{u_i} = \frac{u_{\theta_e}}{u_e} = \frac{u_{\theta_i}}{u_i}$$

For EQ 27 in this test configuration, the u_Y/u_X ratio is 0.85, as shown below. For EQ 28, the first inelastic simulation, the ratio drops to 0.51, a decrease of over 40%. This result is similar to that observed for EQ 15 in the previous configuration. Like EQ 15, the displacement ductility in the X direction for EQ 28 is much larger than the ductility in the Y direction, by a factor of more than two.

Configuration	EQ	u_Y/u_X	u_θ/u_X
Symmetric Mass 25% Biaxial	14	0.73	N/A
Symmetric Mass 100% Biaxial	15	0.43	N/A
Symmetric Mass 150% Biaxial	16	0.80	N/A
½ Asymmetric Mass 10% Biaxial	27	0.86	0.29
½ Asymmetric Mass 100% Biaxial	28	0.51	0.35
½ Asymmetric Mass 150% Biaxial	29	0.85	0.35

For EQ 29, the second inelastic simulation, the ratio of u_Y/u_X increases to 0.85, which is identical to that observed for EQ 27. Also similar to EQ 27 is the displacement ductility in the X direction proportionally to that in the Y direction, both being about 25% larger in the X direction. Thus, it appears that the phenomenon observed in the previous configuration is present again, with the structure yielding and losing stiffness at different rates in the X and Y directions. With EQ 29, the structure has traveled further along the force-displacement curve to the point where the structure has lost roughly an equal amount of stiffness in each direction. As with the previous configuration, the u_Y/u_X ratio for the 150% Imperial Valley simulations matches very well with the u_Y/u_X ratio for the elastic simulations. However, while the structure is moving along the

yield path to get to the 150% Imperial Valley state, the lateral stiffnesses and thus the deformations can change at varying rates, causing the u_y/u_x ratio to change.

For EQ 27, the last elastic simulation, the u_θ/u_x ratio is 0.29. For EQ 28 and EQ 29, the two inelastic simulations, the u_θ/u_x ratio is about 0.35. Thus, the u_θ/u_x ratio is roughly 20% larger for the inelastic simulations than for the elastic simulations, but it is equal for the two inelastic simulations. The large “dip” in the u_y/u_x ratio for EQ 28 does not appear to be present for the u_θ/u_x ratio. In this configuration, the asymmetry is one-way only, with torsional motion primarily produced by X-Axis lateral motion. Thus the u_θ and u_x displacements are much more tightly coupled than the u_y and u_x displacements are, if they are at all. In addition, any reduction in stiffness due to yielding in the X direction will have a much more significant impact on the torsional stiffness of the structure than on the stiffness in the lateral Y direction. Thus, changes in the response in the X direction, due to both ground motions and lateral stiffness, will have a very pronounced effect on changes in the torsional response, to a much greater degree than any possible effects on the response in the Y direction. Thus, it is not surprising that the large “dip” in the u_y/u_x ratio for EQ 28 does not necessarily appear to be present in the u_θ/u_x ratio.

The time history analyses performed for this configuration using the finite element programs Drain-3DX and Abaqus were generally accurate in their predictions of the experimental response. With respect to the low-level linear simulations, Abaqus consistently predicted peak displacements more accurately than did the Drain-3DX analyses. The Abaqus analyses were off by roughly 10-20%, while the Drain-3DX analyses were typically within 10%. No consistent pattern emerged as to why some of the elastic analytical simulations were more accurate than others. The Abaqus analyses proved to be much more accurate during the inelastic simulations, on average off by only 3-4%. The Drain-3DX analyses were typically off to a much greater degree. As with the previous configuration, the Abaqus simulations proved to be significantly better in predicting any permanent offset of the structure, including any permanent rotation. However, Drain-3DX was much more accurate in predicting the peak rotation of the structure, off by at most 7% during the inelastic simulations. Abaqus predicted peak rotations which differed by 25-30% from the experimental values. Overall, Abaqus appears to do a better job with the analytical predictions, with the exception of the peak rotation, in which case Drain-3DX was very accurate.

Mass [lb*s ² /in]	Mass Centers [in]			Column Properties	
	X ₀	Y ₀	Z ₀	A [in ²]	I [in ⁴]
91.256	0.0	15.236	68.362	4.41	9.61

	Modal Frequencies [Hz]			Modal Damping [%]		
	X	Y	θ	X	Y	θ
Before EQ 25	3.468	3.415	7.255	0.474	0.873	0.675
After EQ 29	3.484	3.506	7.288	2.775	2.805	1.337

Table 6.1 Test Structure Dynamic Properties - Test Configuration 4

Test Designation	Input Motions
WNT19	White Noise X-Axis
WNT20	White Noise Y-Axis
WNT21	White Noise Yaw-Axis
SIN10	Sine Decay X-Axis
SIN11	Sine Decay Y-Axis
SIN12	Sine Decay Yaw-Axis
SWP10	Sine Sweep X-Axis
SWP11	Sine Sweep Y-Axis
SWP12	Sine Sweep Yaw-Axis
EQ25	10% X-Axis Imperial Valley
EQ26	10% Y-Axis Imperial Valley
EQ27	10% Biaxial Imperial Valley
EQ28	100% Biaxial Imperial Valley
WNT22	White Noise X-Axis
WNT23	White Noise Y-Axis
WNT24	White Noise Yaw-Axis
EQ29	150% Biaxial Imperial Valley
WNT25	White Noise X-Axis
WNT26	White Noise Y-Axis
WNT27	White Noise Yaw-Axis

Table 6.2 Earthquake Simulations and Dynamic Characterization Tests - Test Configuration 4

Earthquake Test No.	Input Motions	PGA [g]		Relative Displacement [in]		Rotation [10^{-3} rad]	Normalized Displacement [in/g]	Ductility		
		X-Axis	Y-Axis	X-Axis	Y-Axis			X-Axis	Y-Axis	Z-Axis
25	10% X-Axis	0.105	N/A	0.252	0.067	1.50	2.40	N/A	0.54	0.13
26	10% Y-Axis	N/A	0.070	0.019	0.159	0.38	N/A	2.27	0.04	0.31
27	10% Biaxial	0.102	0.063	0.256	0.219	1.55	2.51	3.48	0.55	0.42
28	100% Biaxial	1.115	0.711	2.592	1.292	18.26	2.27	1.82	5.40	2.50
29	150% Biaxial	1.629	1.121	4.777	4.078	34.58	2.93	3.64	10.21	7.89
										5.58

Table 6.3 Maximum Diaphragm Relative Displacement and Rotation - Test Configuration 4

Earthquake Test No.	Input Motions	PGA [g]			Diaphragm Acceleration [g]			Diaphragm Angular Acceleration [10^{-3} g/in]			Normalized Acceleration	
		X-Axis	Y-Axis	Z-Axis	X-Axis	Y-Axis	Z-Axis	X-Axis	Y-Axis	Z-Axis	X-Axis	Y-Axis
25	10% X-Axis	0.105	N/A	0.360	0.076	0.076	2.18				3.42	N/A
26	10% Y-Axis	N/A	0.070	0.019	0.205		0.25				N/A	2.93
27	10% Biaxial	0.102	0.062	0.349	0.266		1.99				3.42	4.29
28	100% Biaxial	1.115	0.711	1.041	0.957		10.88				0.93	1.35
29	150% Biaxial	1.629	1.121	1.156	1.153		16.01				0.71	1.03

Table 6.4 Maximum Diaphragm Acceleration and Angular Acceleration Response - Test Configuration 4

Earthquake Test No.	Input Motions	PGA [g]			Base Shear [k]	Torsional Moment [k*in]	Overturning Moment [k*in]
		X-Axis	Y-Axis	Z-Axis			
25	10% X-Axis	0.105	N/A	12.78	2.66	272.11	878.0
26	10% Y-Axis	N/A	0.070	0.67	7.19	16.43	182.4
27	10% Biaxial	0.102	0.062	12.40	9.34	260.40	852.1
28	100% Biaxial	1.115	0.711	36.48	33.61	927.50	2506.0
29	150% Biaxial	1.629	1.121	40.44	40.49	1028.23	2778.2
							2781.5

Table 6.5 Maximum Base Shear, Torsional Moment, and Overturning Moment - Test Configuration 4

Earthquake Test No.	Input Motions	PGA [g]		Column End Moments [K*in]					
		SE Column		SW Column		NW Column		NE Column	
		X-Axis	Y-Axis	X-Axis	Y-Axis	X-Axis	Y-Axis	X-Axis	Y-Axis
25	10% X-Axis	0.105	N/A	38.00	112.18	38.00	79.89	17.36	79.89
26	10% Y-Axis	N/A	0.070	54.16	5.97	54.16	4.14	53.65	4.14
27	10% Biaxial	0.102	0.062	83.90	111.88	83.90	77.34	65.52	77.34
28	100% Biaxial	1.115	0.711	261.97	323.80	261.97	230.91	261.23	230.91
29	150% Biaxial	1.629	1.121	307.75	357.01	307.75	256.40	325.34	256.40

Table 6.6 Maximum Column End Moments - Test Configuration 4

Earthquake Test No.	Input Motions	Column End Shears [k]															
		PGA [g]				SE Column				SW Column				NW Column		NE Column	
		X-Axis	Y-Axis	X-Axis	Y-Axis	X-Axis	Y-Axis	X-Axis	Y-Axis	X-Axis	Y-Axis	X-Axis	Y-Axis	X-Axis	Y-Axis		
25	10% X-Axis	0.105	N/A	3.74	1.27	2.66	1.27	2.66	0.58	3.74	0.58						
26	10% Y-Axis	N/A	0.070	0.20	1.81	0.14	1.81	0.14	1.79	0.20	1.79						
27	10% Biaxial	0.102	0.062	3.73	2.80	2.58	2.80	2.58	2.18	3.73	2.18						
28	100% Biaxial	1.115	0.711	10.79	8.73	7.70	8.73	7.70	8.71	10.79	8.71						
29	150% Biaxial	1.629	1.121	11.90	10.26	8.55	10.26	8.55	10.84	11.90	10.84						

Table 6.7 Maximum Column End Shears - Test Configuration 4

E [ksi] = 29000.0

Stress [ksi]	Strain [in/in]	Plastic Strain [in/in]
0.00000	0.00000	
37.50000	0.00108	0.000000
39.60000	0.00300	0.001863
40.70000	0.00500	0.003831
49.00000	0.02000	0.018593
54.00000	0.04000	0.038449
56.50000	0.06000	0.058378
57.80000	0.08000	0.078340
58.50000	0.10000	0.098320
59.00000	0.15000	0.148306
57.00000	0.20000	0.198363

Table 6.8 Stress-Strain Best-Fit Material Model - Test Configuration 4

E [ksi] = 29000.0

Stress [ksi]	Strain [in/in]
0.00000	0.00000
37.50000	0.001293
39.60000	0.003000
49.00000	0.020000
56.50000	0.060000
58.50000	0.100000

Table 6.9 Drain-3DX Stress-Strain Best-Fit Material Model - Test Configuration 4

Earthquake Test No.	Input Motions	PGA [g]				Relative Displacement [in]				Rotation [10^{-3} rad]		
		X-Axis	Y-Axis	Abaqus	Drain	X-Axis	Y-Axis	Abaqus	Drain	Test	Abaqus	Drain
27	10% Biaxial	0.102	0.062	0.305	0.282	0.256	0.244	0.201	0.219	1.30	1.17	1.55
28	100% Biaxial	1.115	0.711	2.53	2.54	2.53	1.18	1.36	1.29	12.94	18.31	18.26
29	150% Biaxial	1.629	1.121	4.79	3.75	4.78	4.03	5.05	4.08	24.94	30.12	34.58

Table 6.10 Analytical vs. Experimental Displacement and Rotation Response Comparison - Test Configuration 4

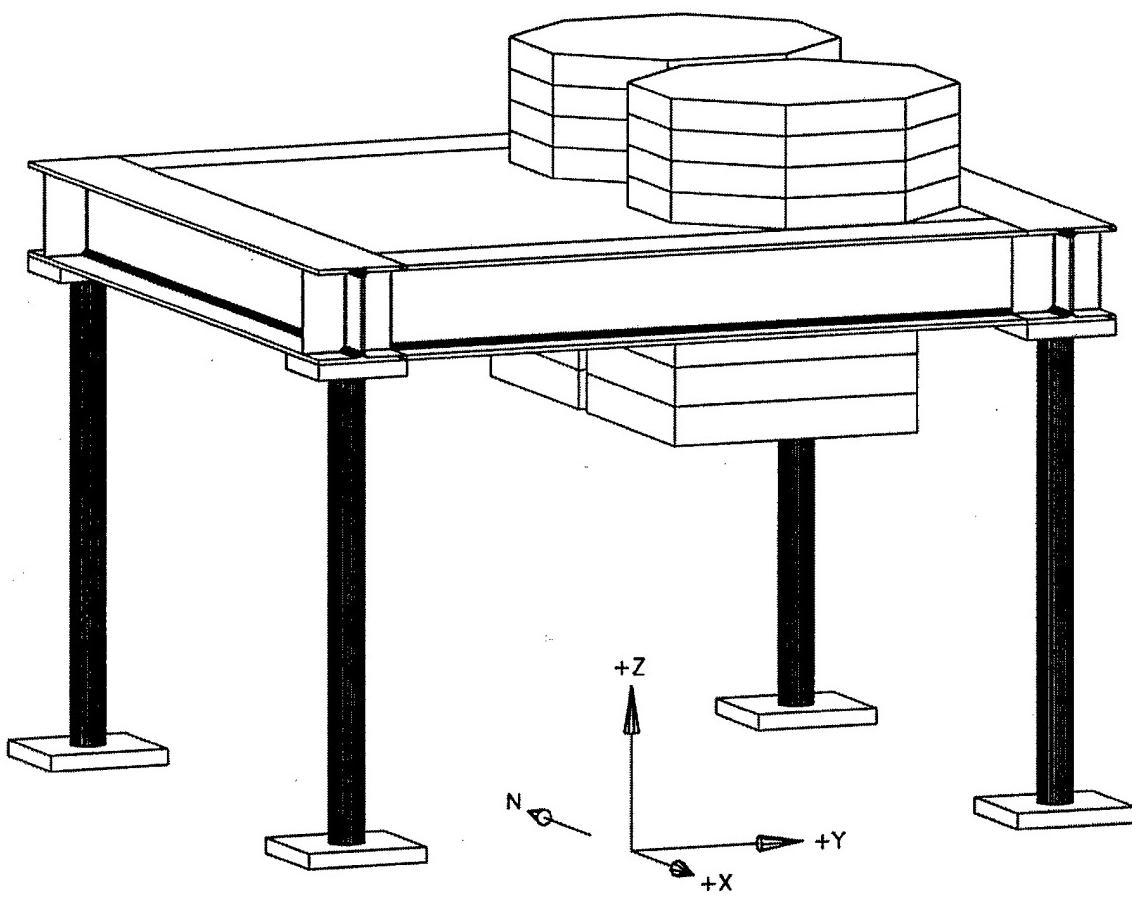


Figure 6.1 Perspective View of Test Configuration Model 4
4 – 4" Extra-Strong Columns

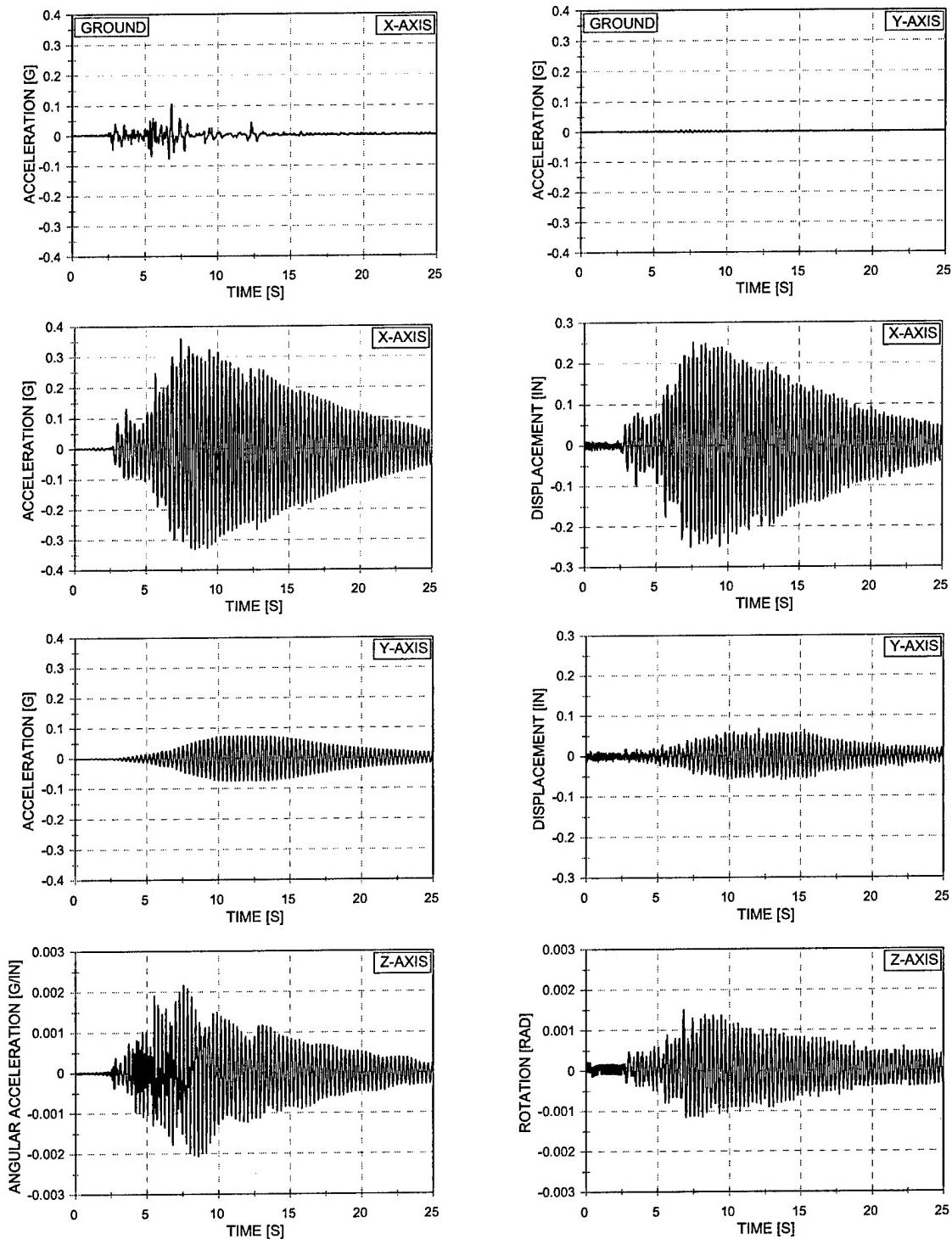


Figure 6.2 Acceleration and Displacement vs. Time – EQ 25
 10% X-Axis Imperial Valley – 1/4 Asymmetric Mass
 Four 4" Extra-Strong Columns

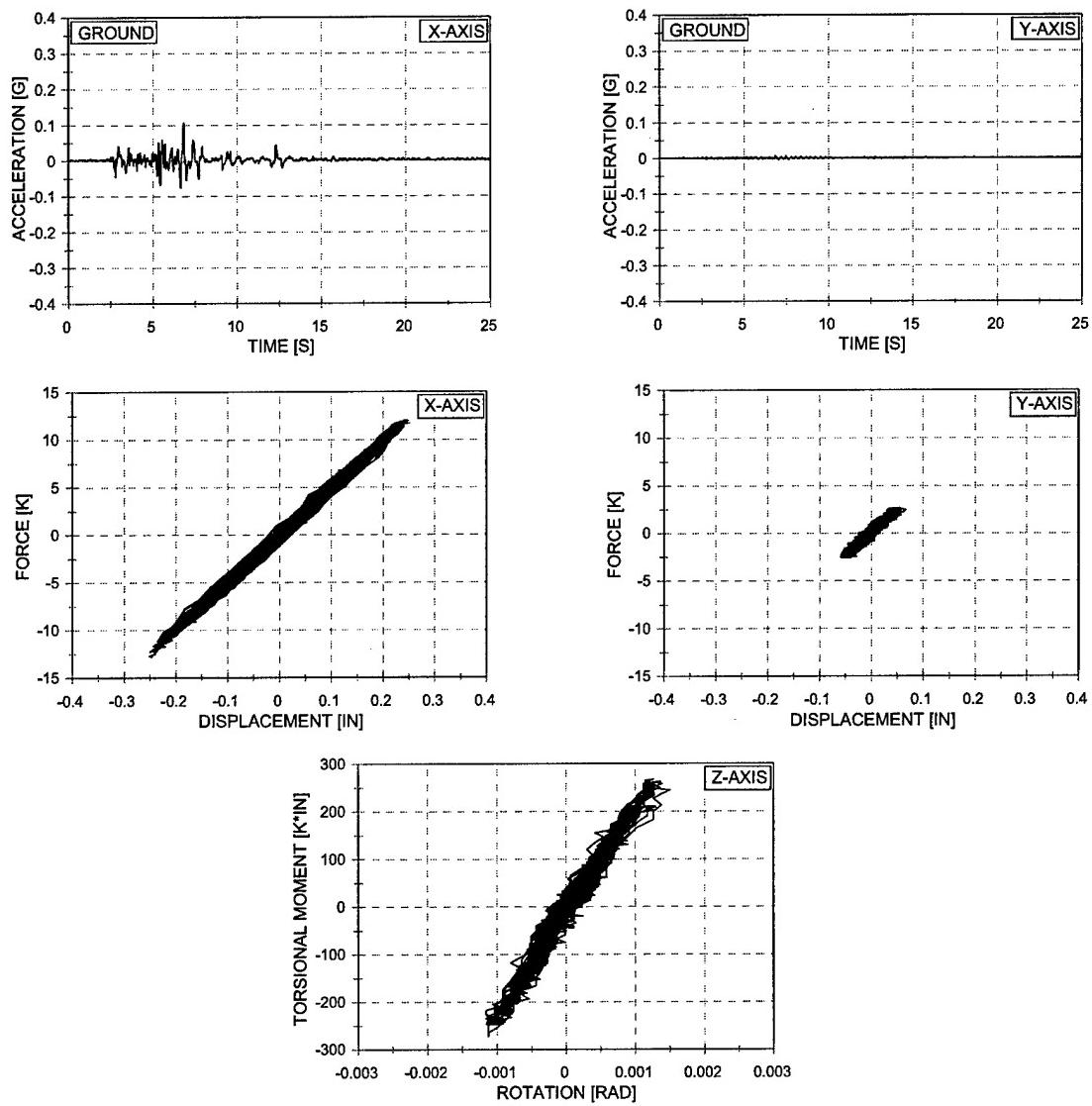


Figure 6.3 Force vs. Displacement and Torsional Moment vs. Rotation – EQ 25
 10% X-Axis Imperial Valley – 1/2 Asymmetric Mass
 Four 4" Extra-Strong Columns

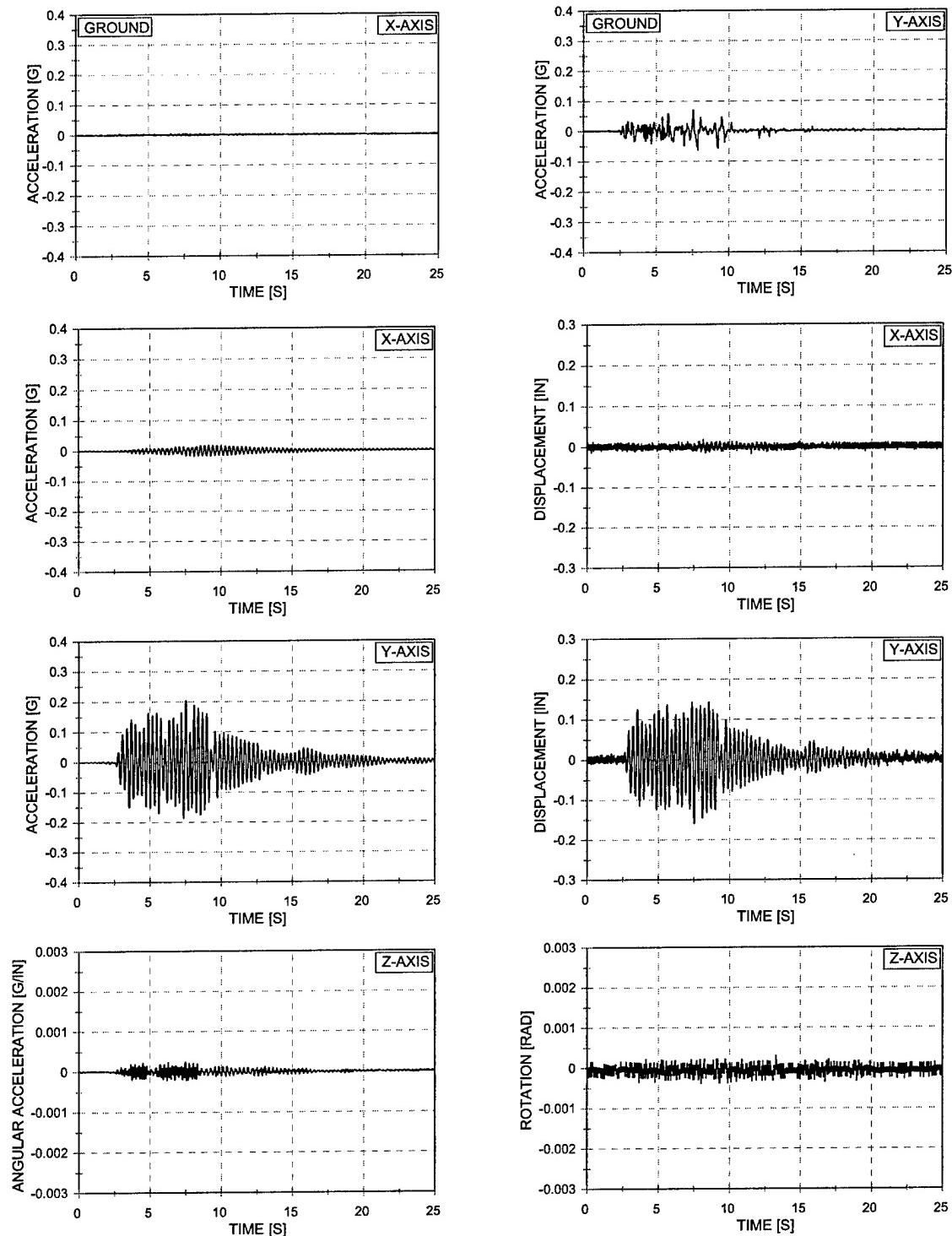


Figure 6.4 Acceleration and Displacement vs. Time – EQ 26
 10% Y-Axis Imperial Valley – 1/4 Asymmetric Mass
 Four 4" Extra-Strong Columns

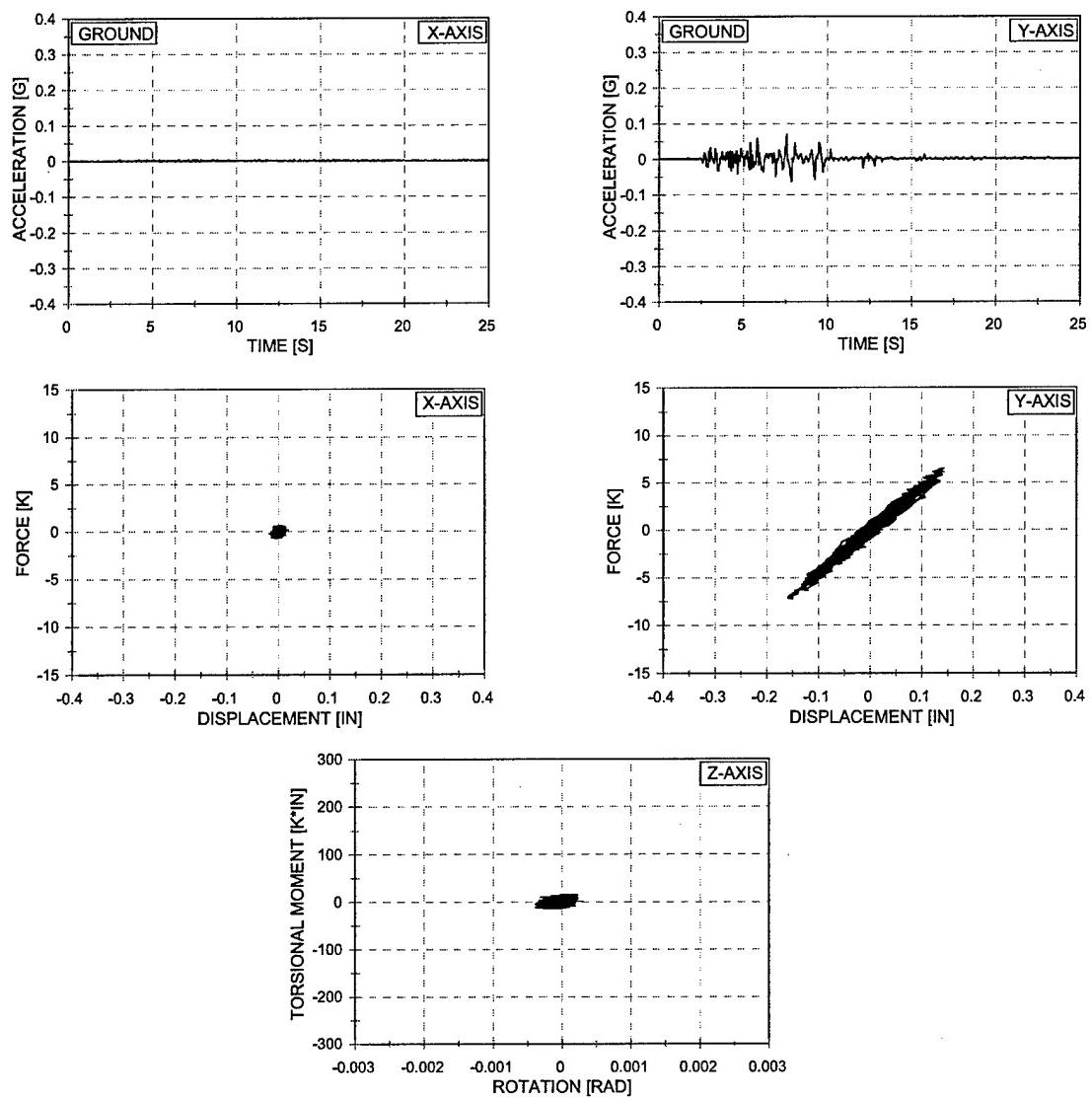


Figure 6.5 Force vs. Displacement and Torsional Moment vs. Rotation - EQ 26
 10% Y-Axis Imperial Valley – 1/2 Asymmetric Mass
 Four 4" Extra-Strong Columns

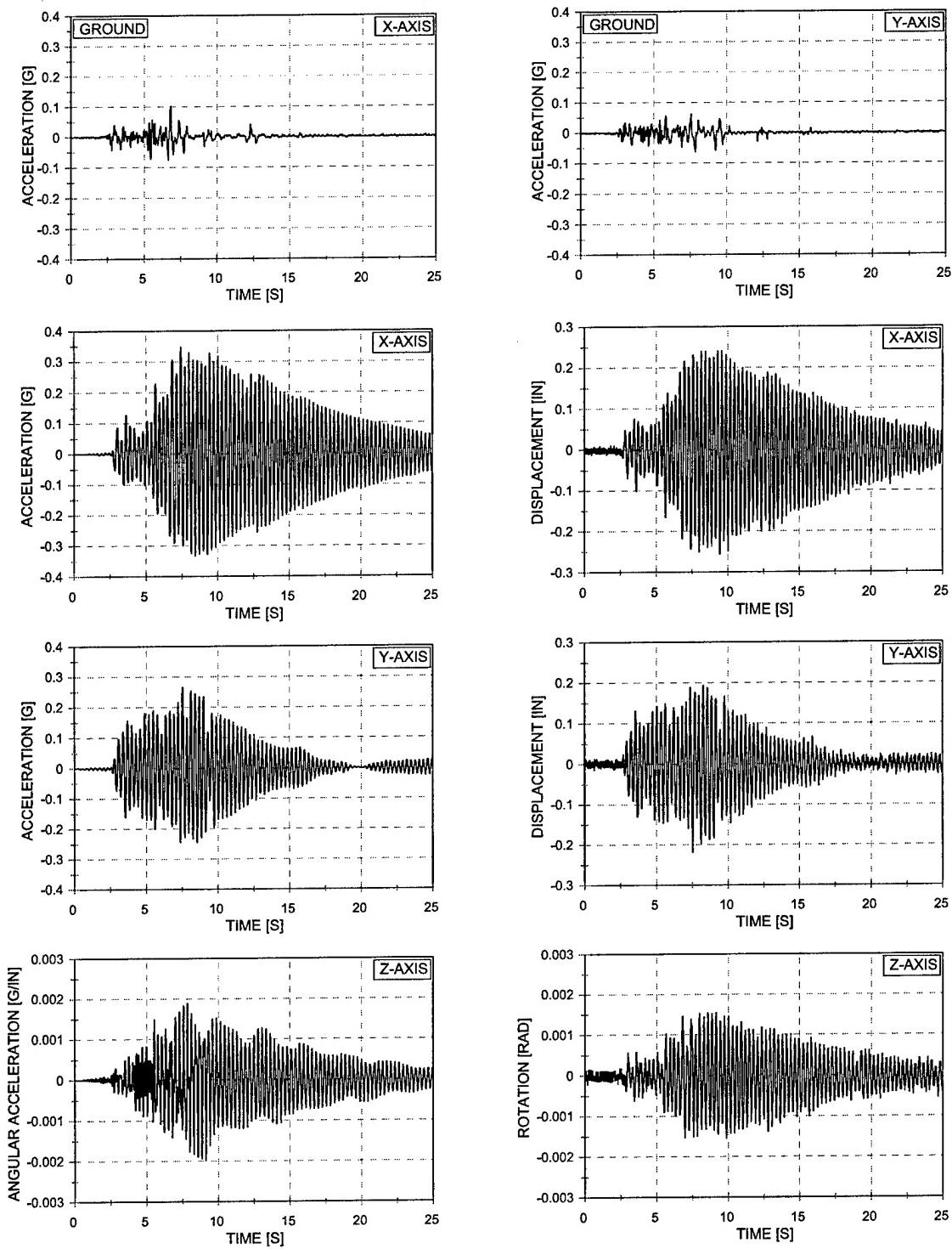


Figure 6.6 Acceleration and Displacement vs. Time – EQ 27

10% Biaxial Imperial Valley – 1/2 Asymmetric Mass

Four 4" Extra-Strong Columns

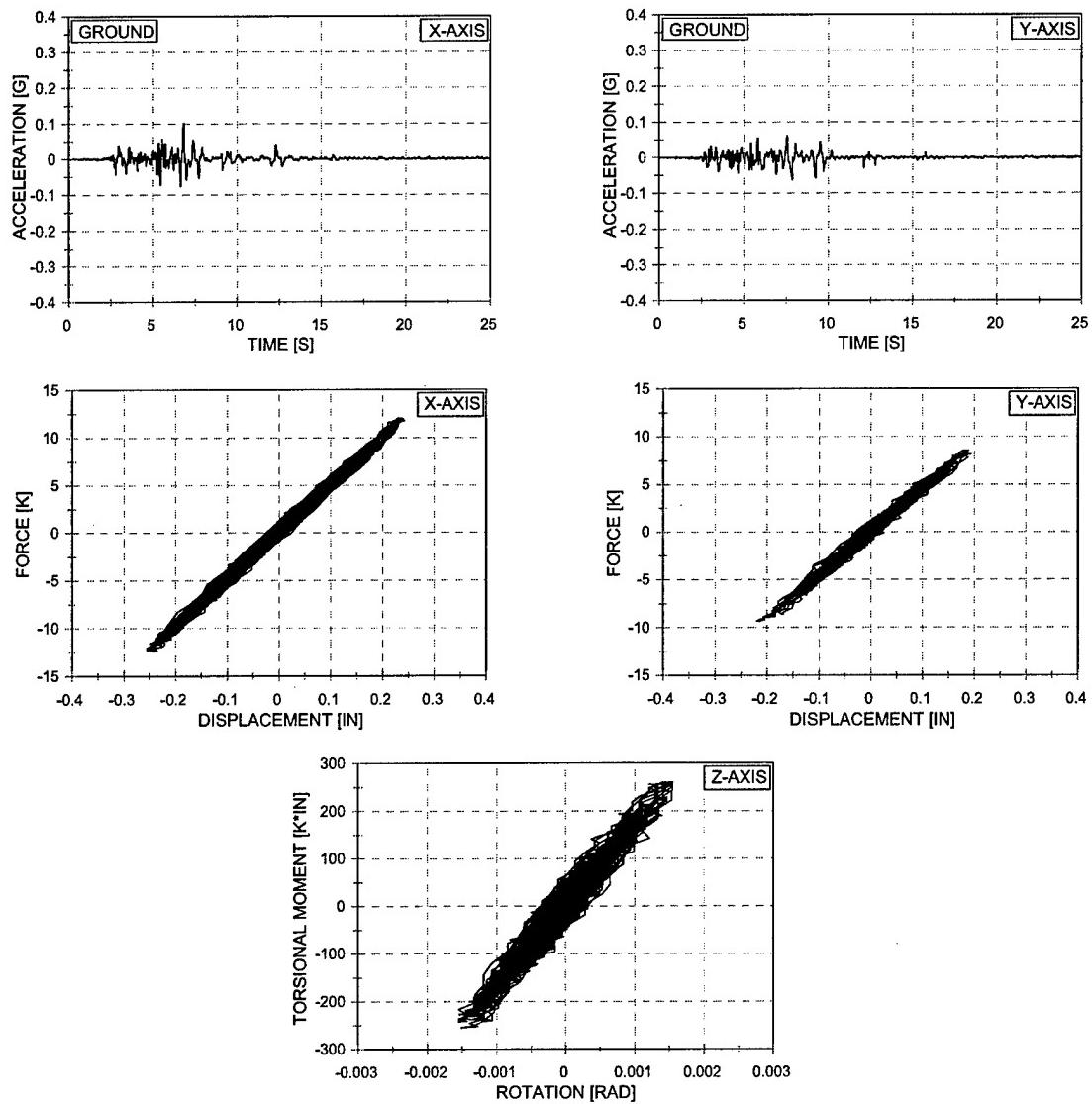


Figure 6.7 Force vs. Displacement and Torsional Moment vs. Rotation - EQ 27
 10% Biaxial Imperial Valley – 1/2 Asymmetric Mass
 Four 4" Extra-Strong Columns

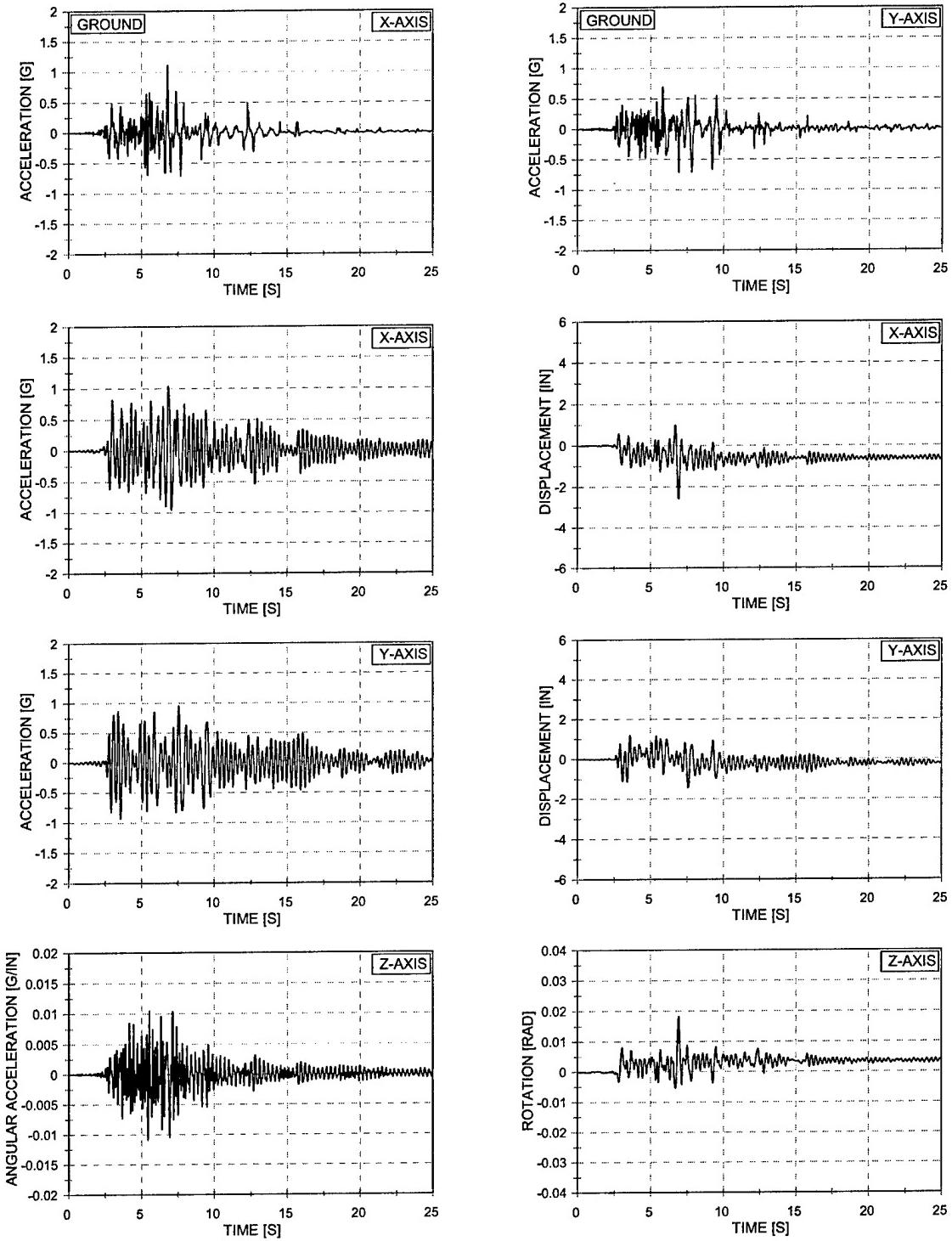


Figure 6.8 Acceleration and Displacement vs. Time – EQ 28
 100% Biaxial Imperial Valley – 1/2 Asymmetric Mass
 Four 4" Extra-Strong Columns

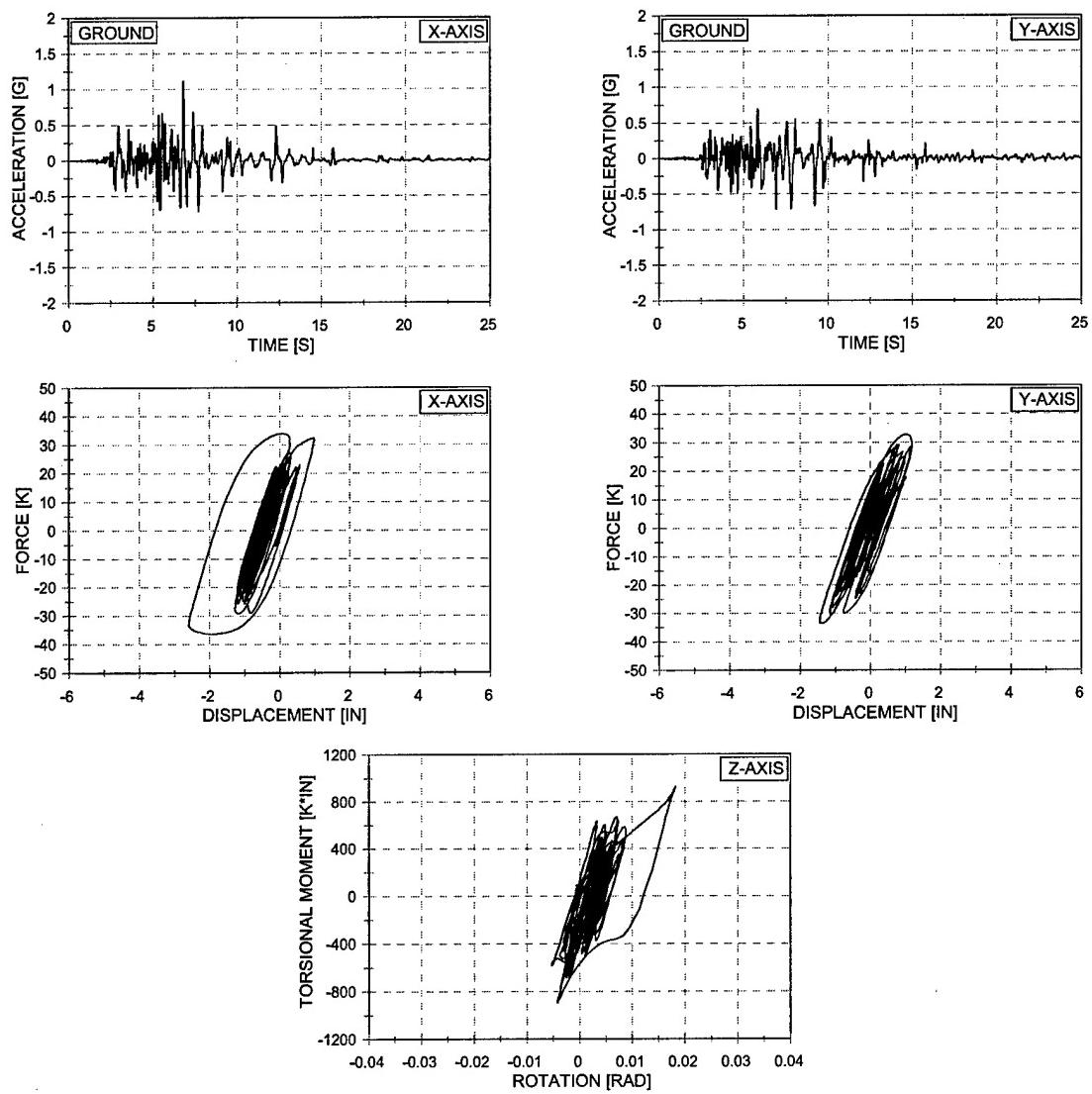


Figure 6.9 Force vs. Displacement and Torsional Moment vs. Rotation - EQ 28
 100% Biaxial Imperial Valley – 1/2 Asymmetric Mass
 Four 4" Extra-Strong Columns

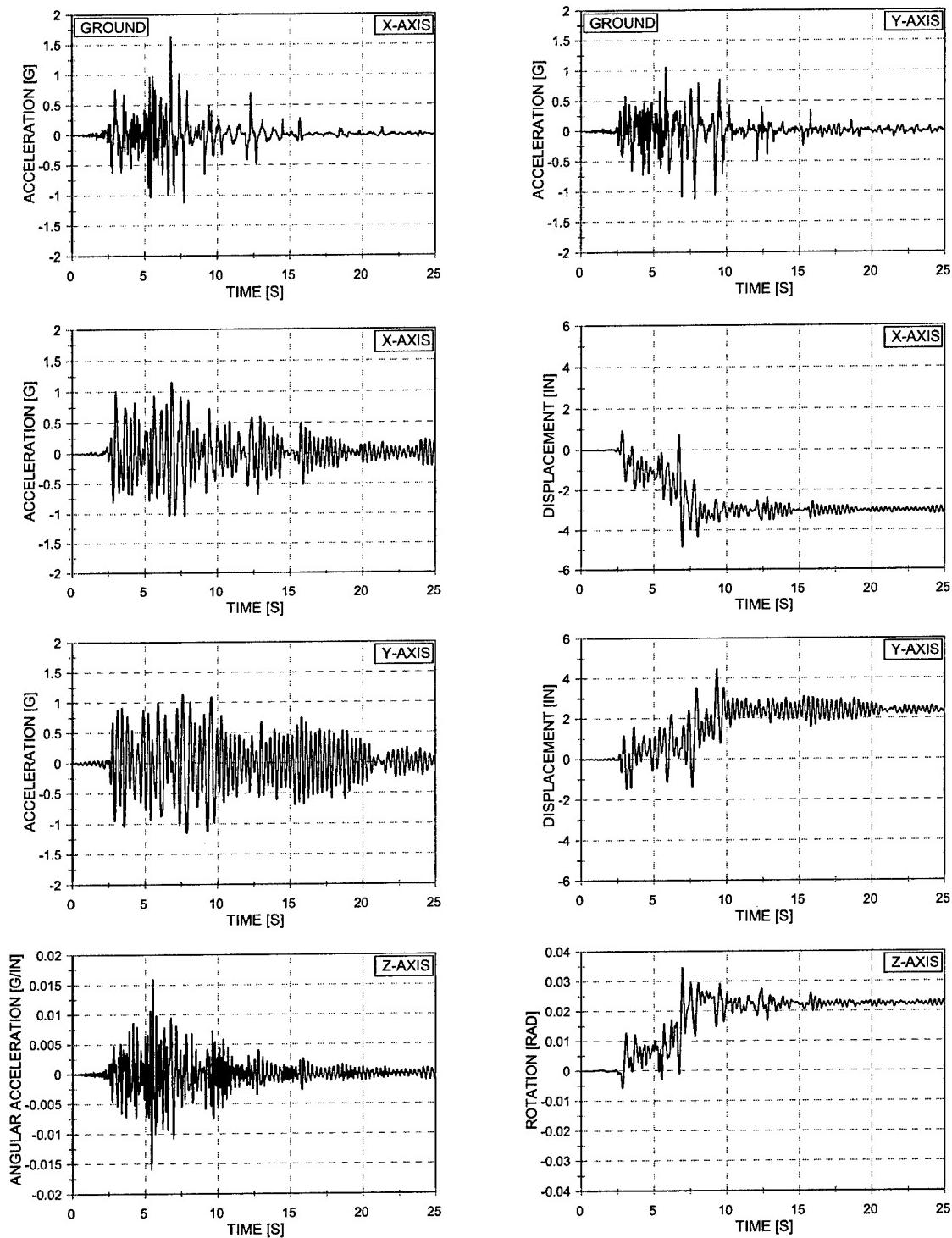


Figure 6.10 Acceleration and Displacement vs. Time – EQ 29
 150% Biaxial Imperial Valley – 1/2 Asymmetric Mass
 Four 4" Extra-Strong Columns

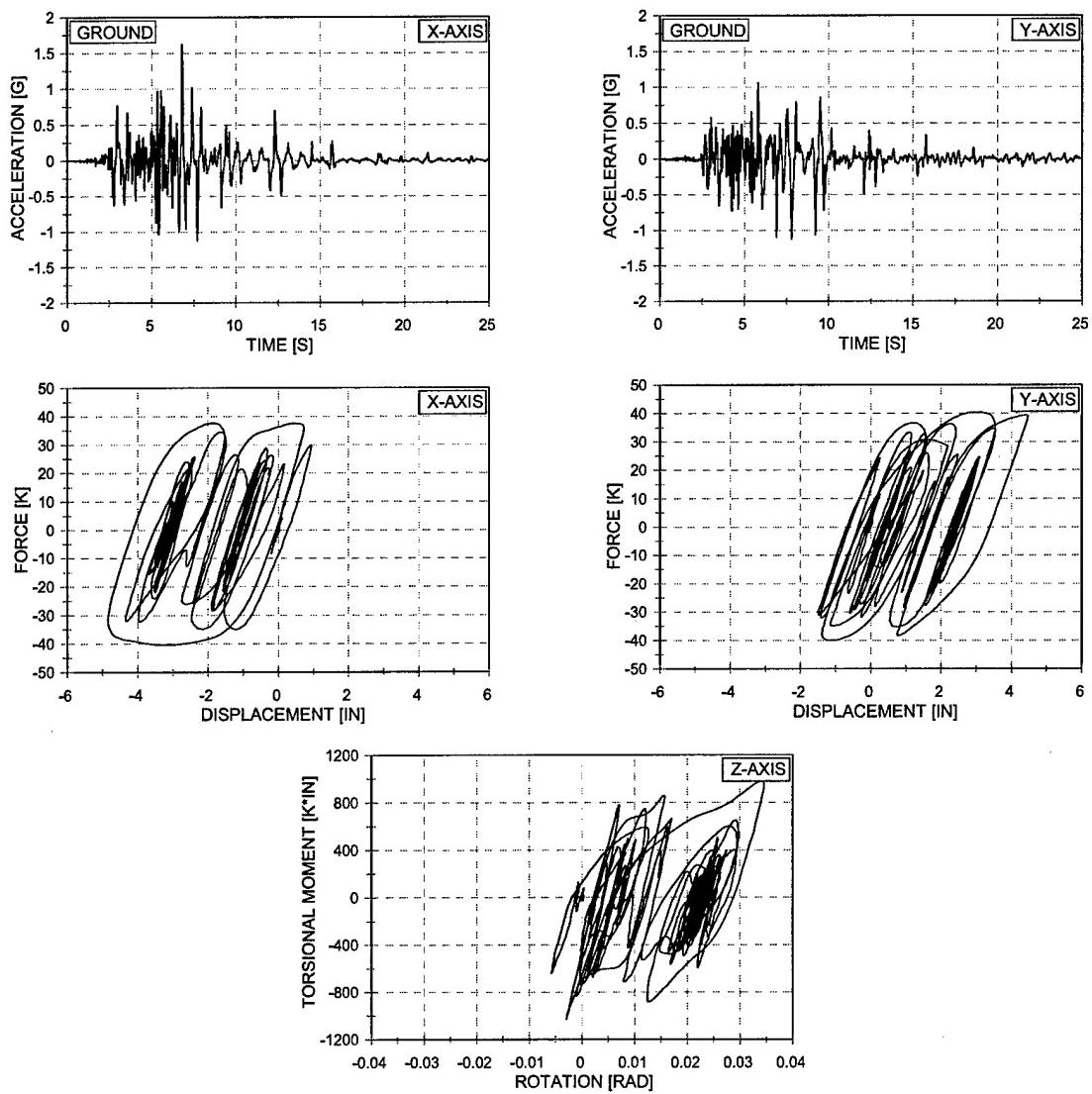


Figure 6.11 Force vs. Displacement and Torsional Moment vs. Rotation - EQ 29
 150% Biaxial Imperial Valley – 1/2 Asymmetric Mass
 Four 4" Extra-Strong Columns

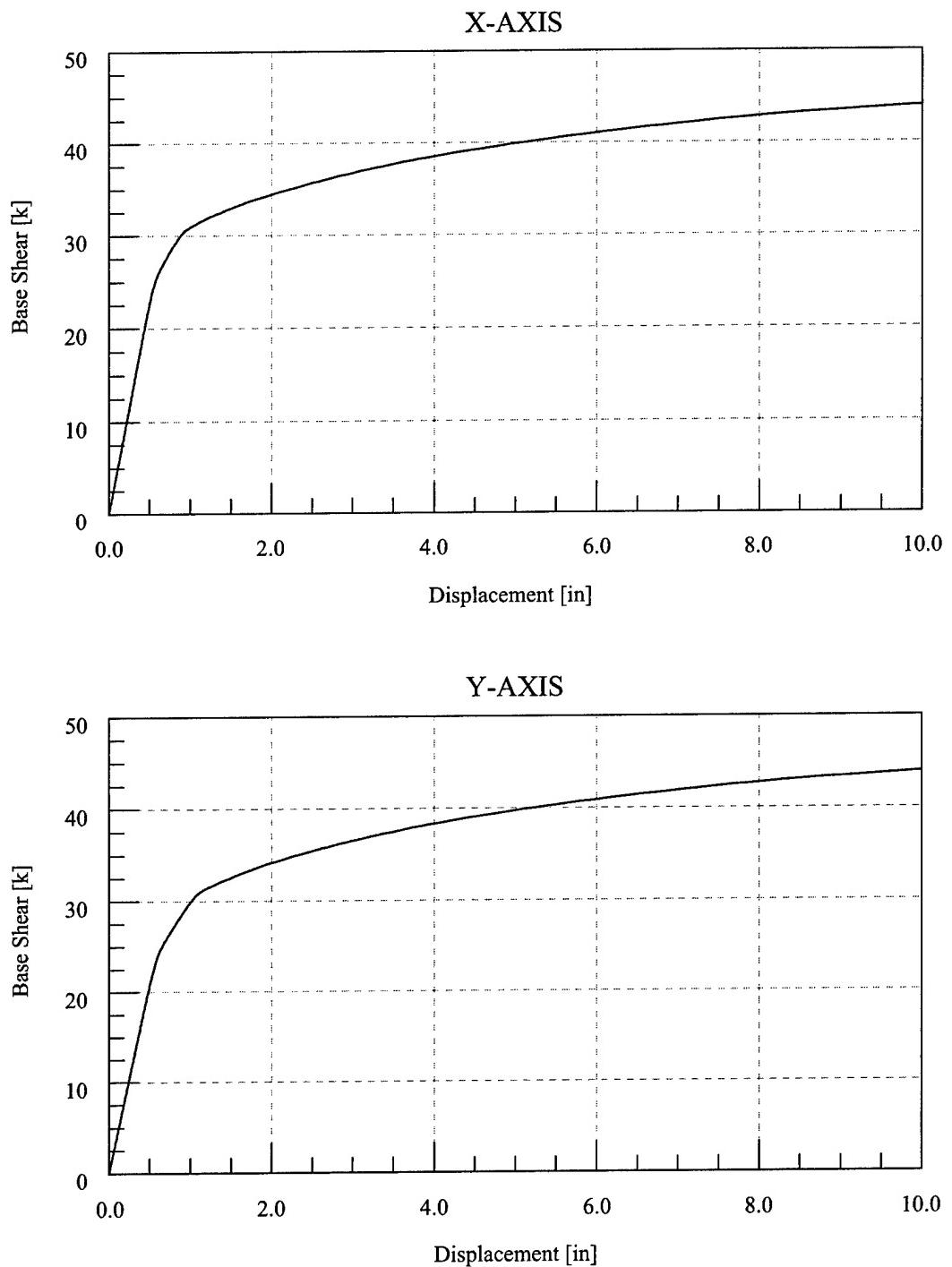


Figure 6.12 Force-Deformation Response – Test Configuration 4

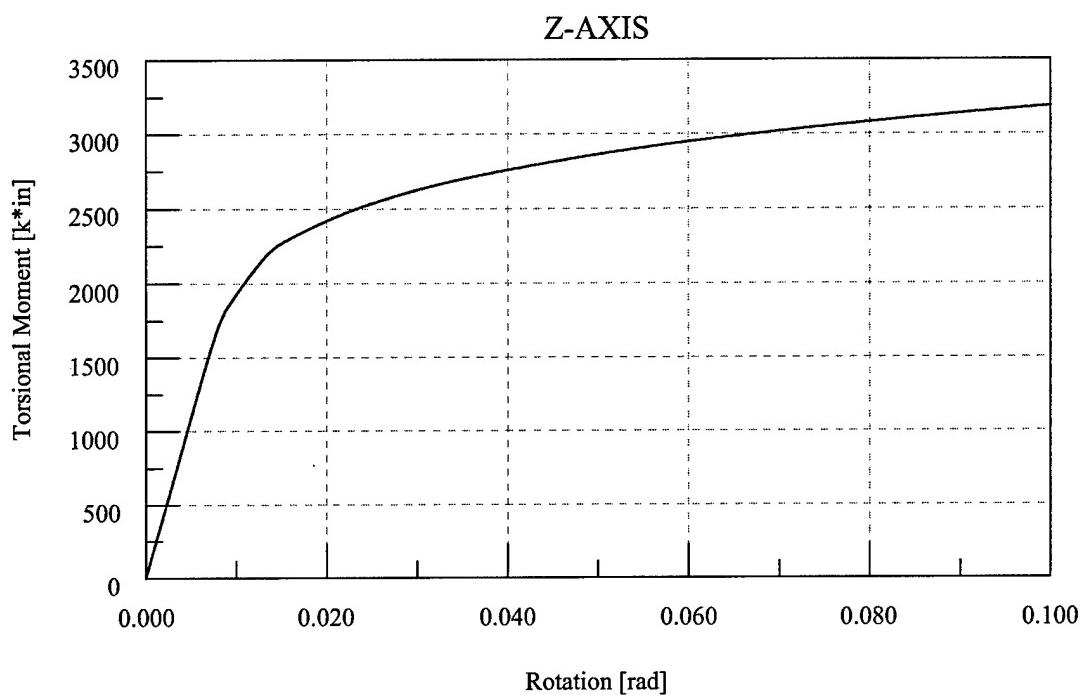


Figure 6.13 Torsional Moment-Rotation Response – Test Configuration 4

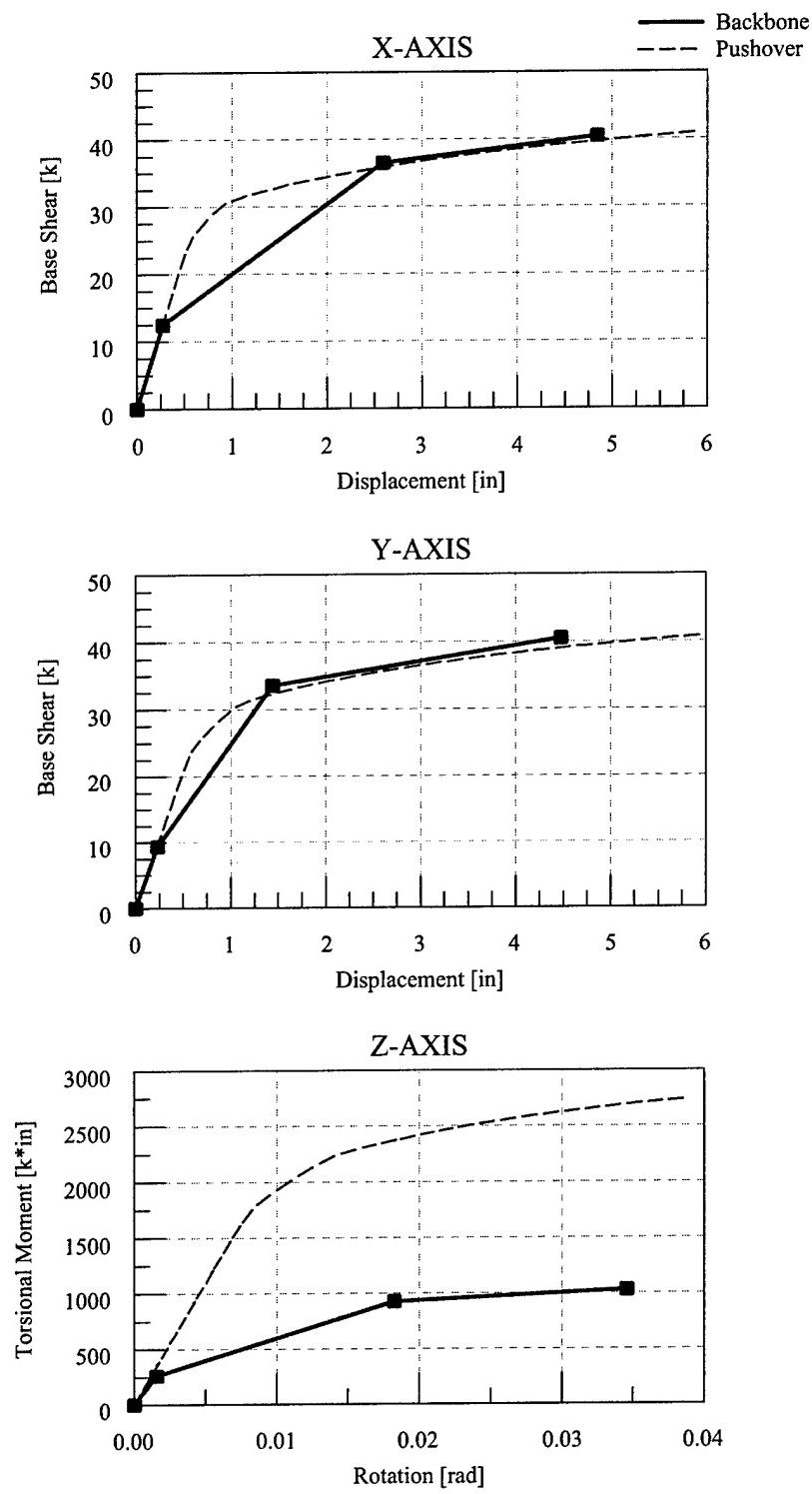


Figure 6.14 Maximum Force vs. Displacement and Maximum Torsional Moment vs. Rotation
 10% - 150% Biaxial Imperial Valley – 1/2 Asymmetric Mass
 Four 4" Extra-Strong Columns

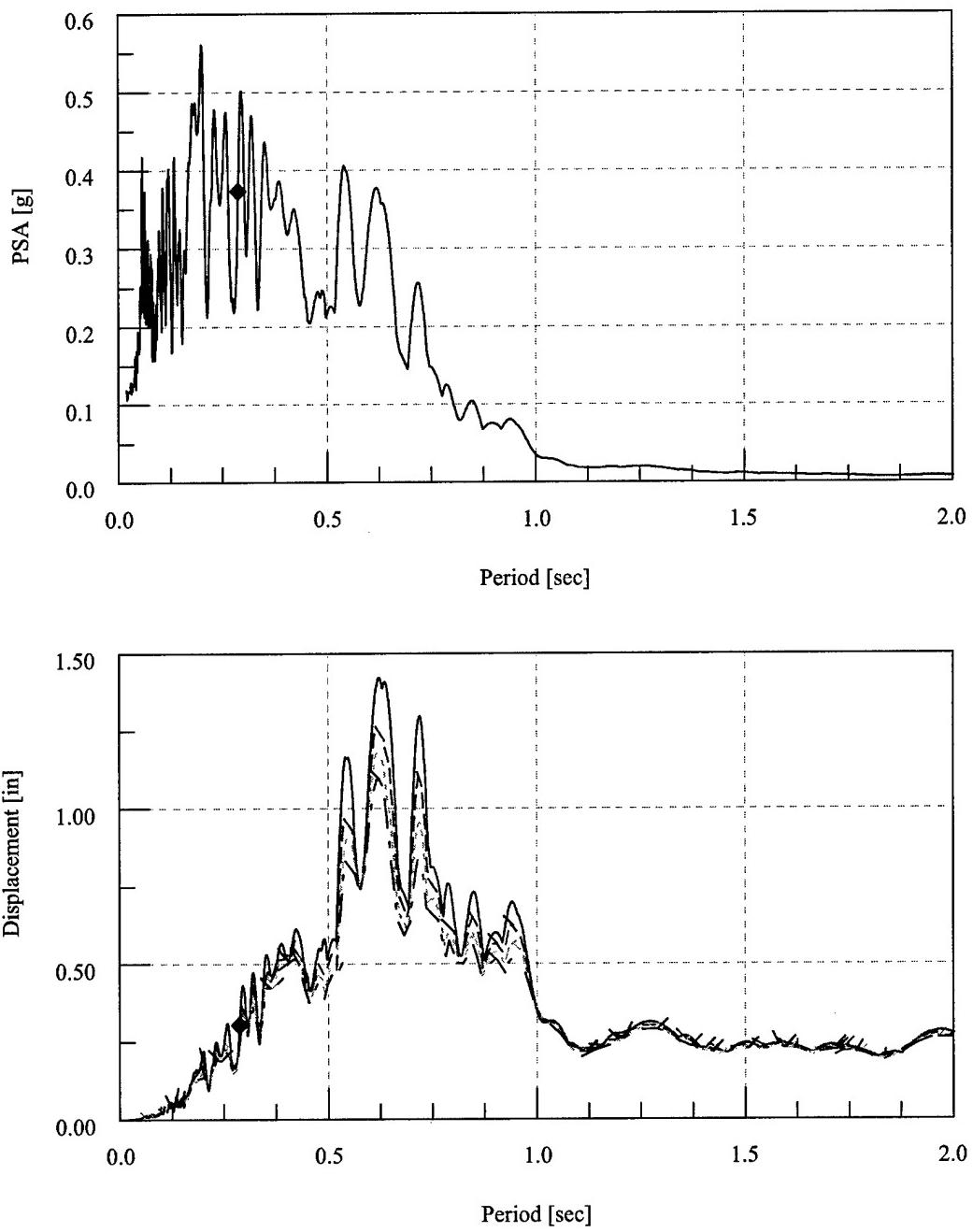


Figure 6.15 Elastic Response Spectra – EQ 25 – 10% X-Axis Imperial Valley Ground Motion

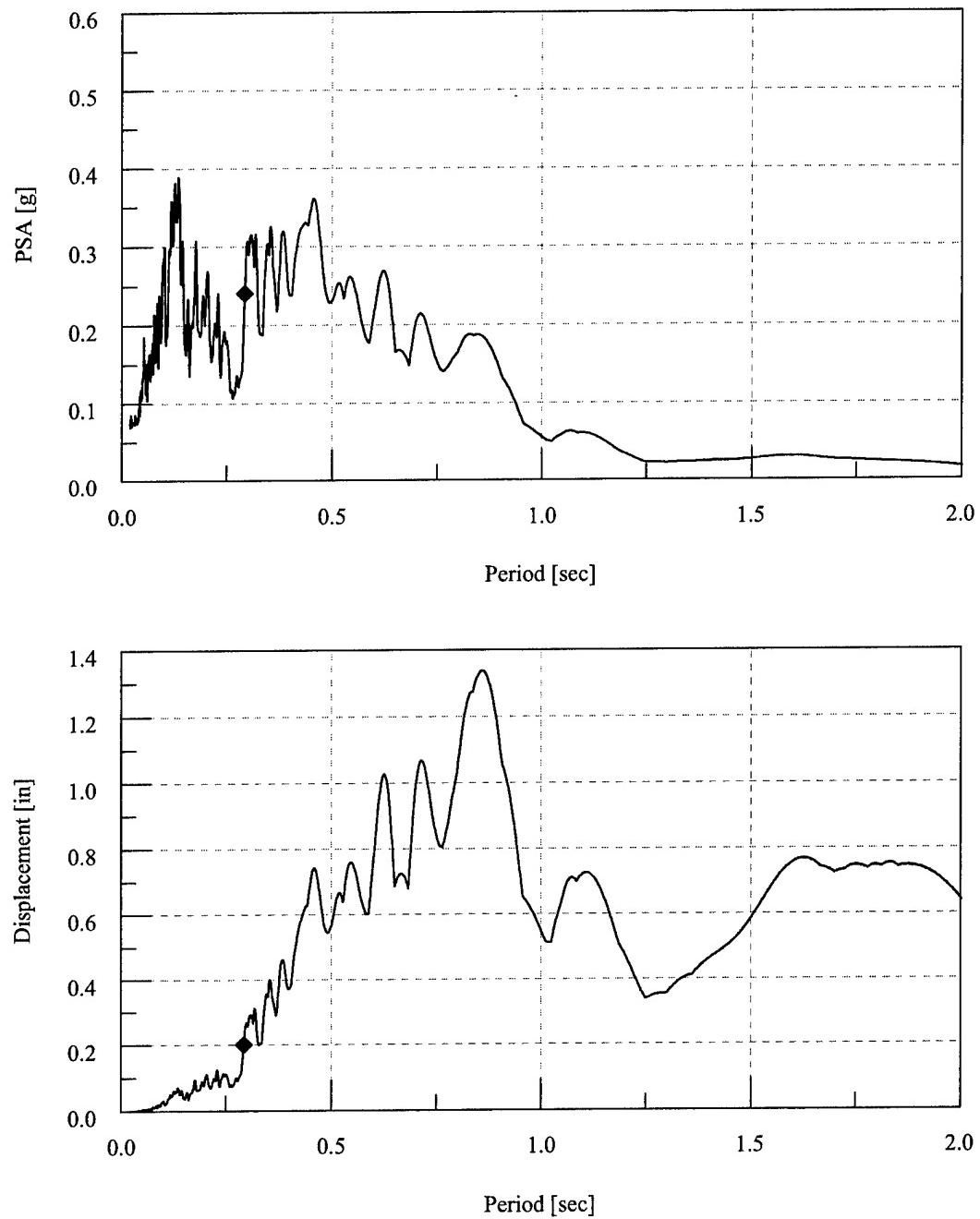


Figure 6.16 Elastic Response Spectra – EQ 26 – 10% Y-Axis Imperial Valley Ground Motion

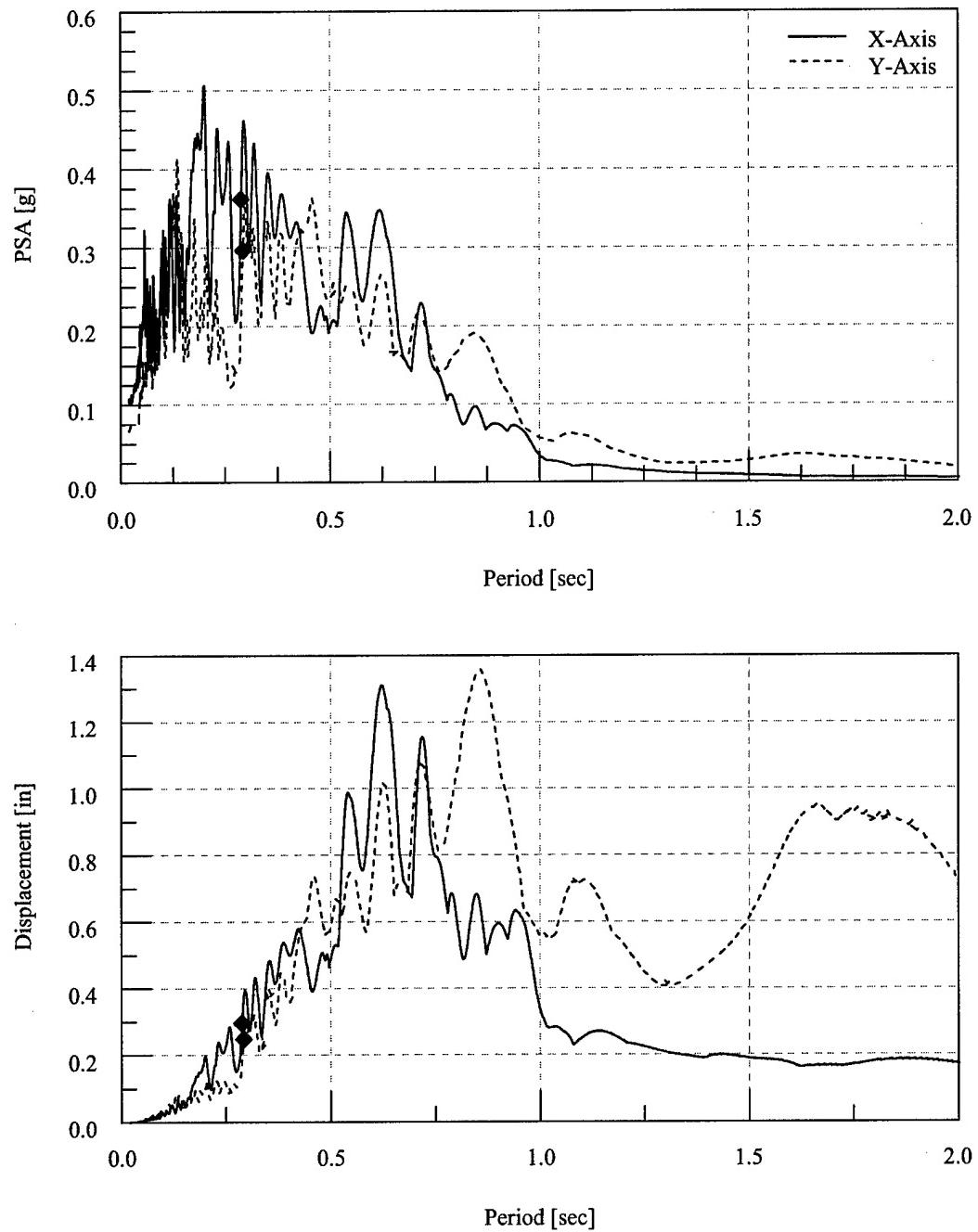


Figure 6.17 Elastic Response Spectra – EQ 27 – 10% Biaxial Imperial Valley Ground Motion

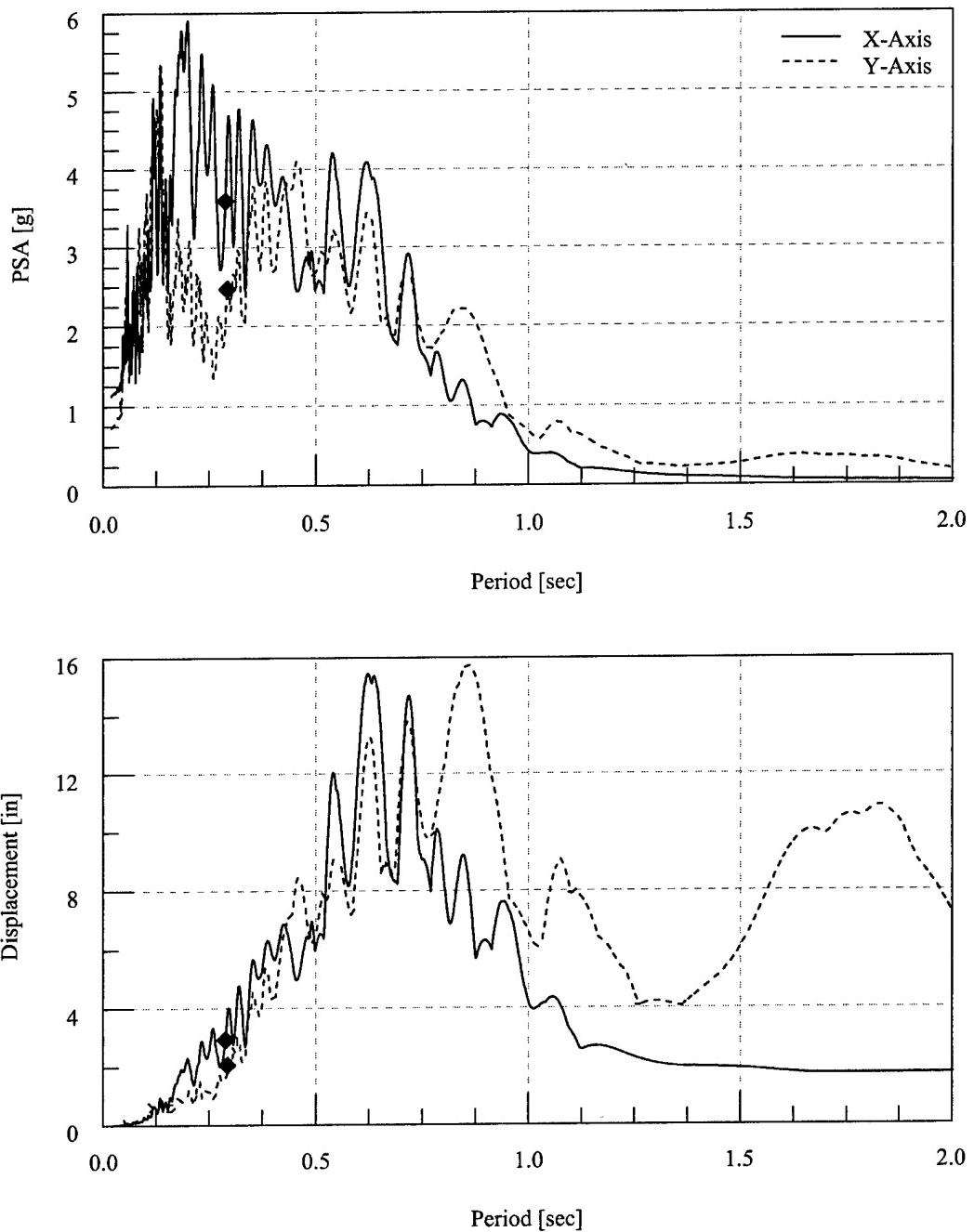


Figure 6.18 Elastic Response Spectra – EQ 28 – 100% Biaxial Imperial Valley Ground Motion

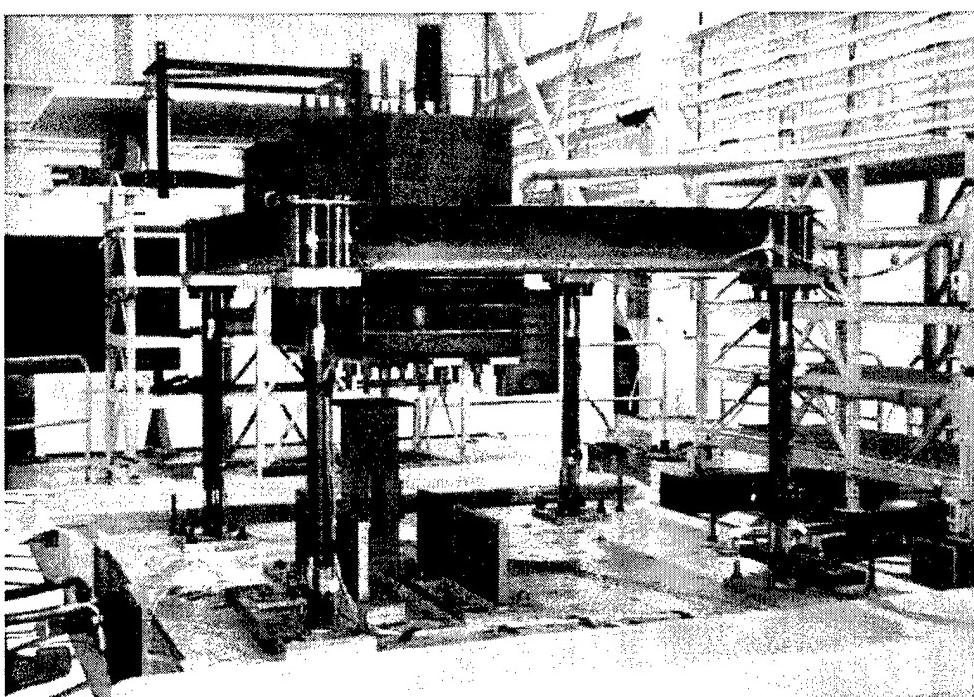


Figure 6.19 Test Structure prior to Earthquake Simulations

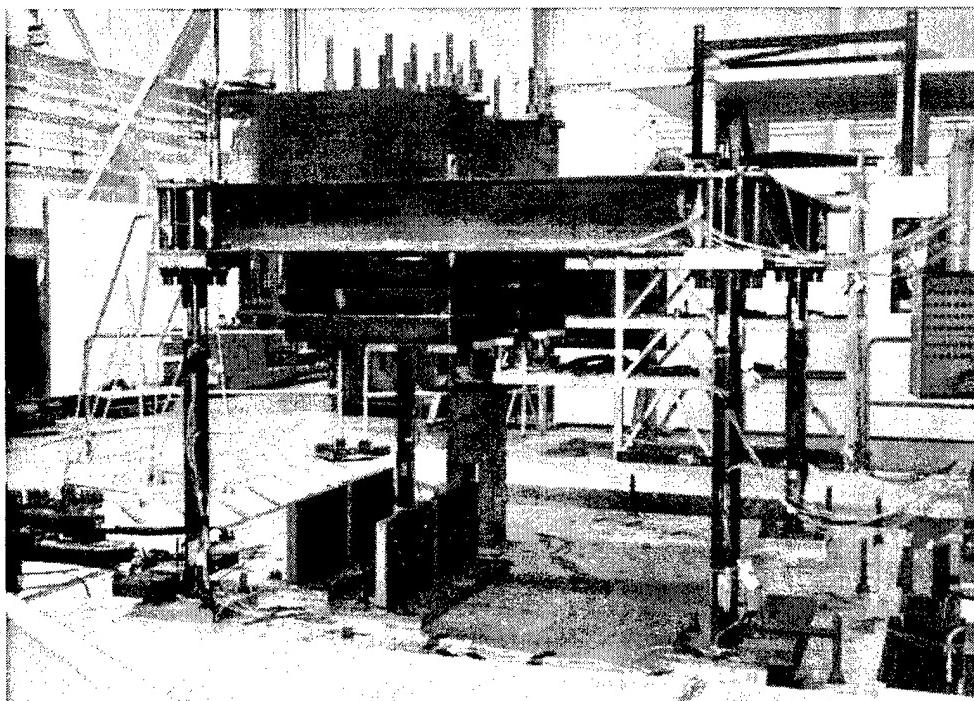


Figure 6.20 Test Structure prior to Earthquake Simulations

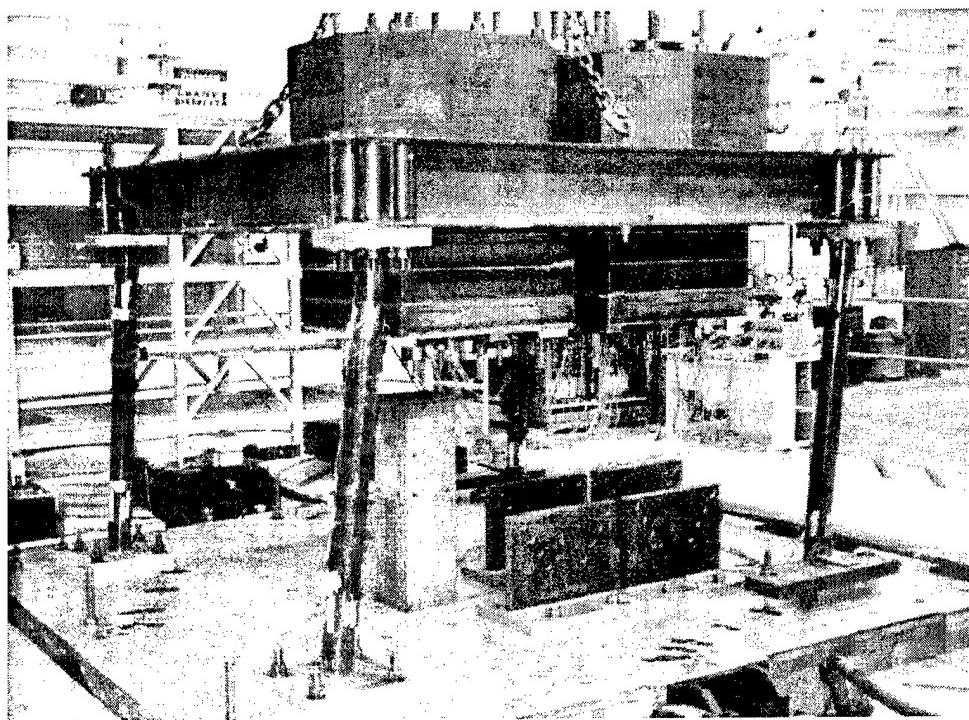


Figure 6.21 Test Structure After Earthquake Simulations

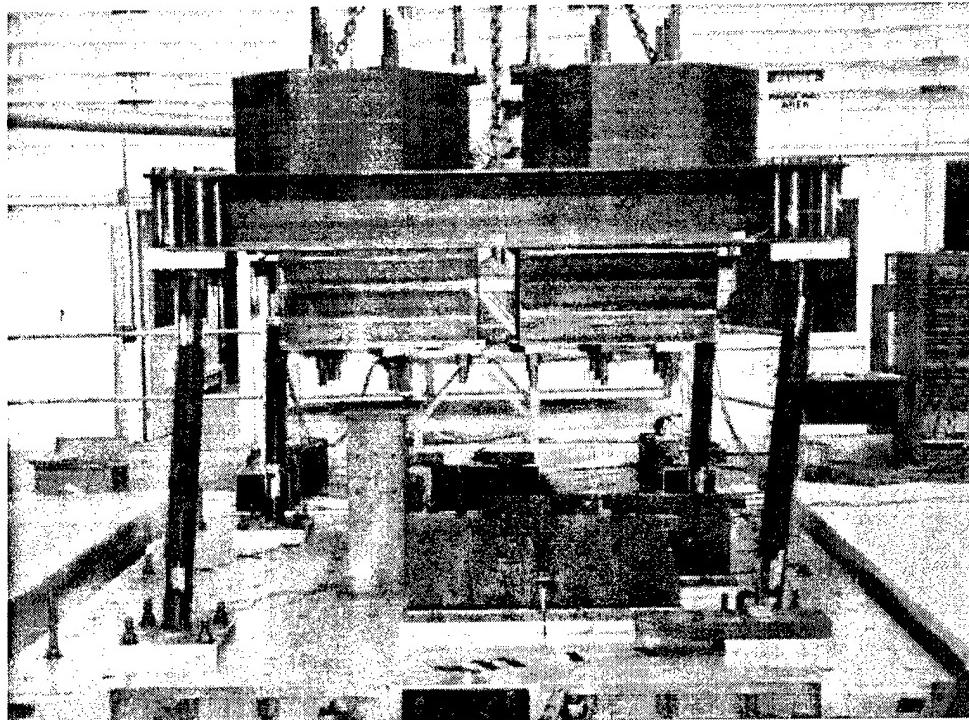


Figure 6.22 Test Structure After Earthquake Simulations

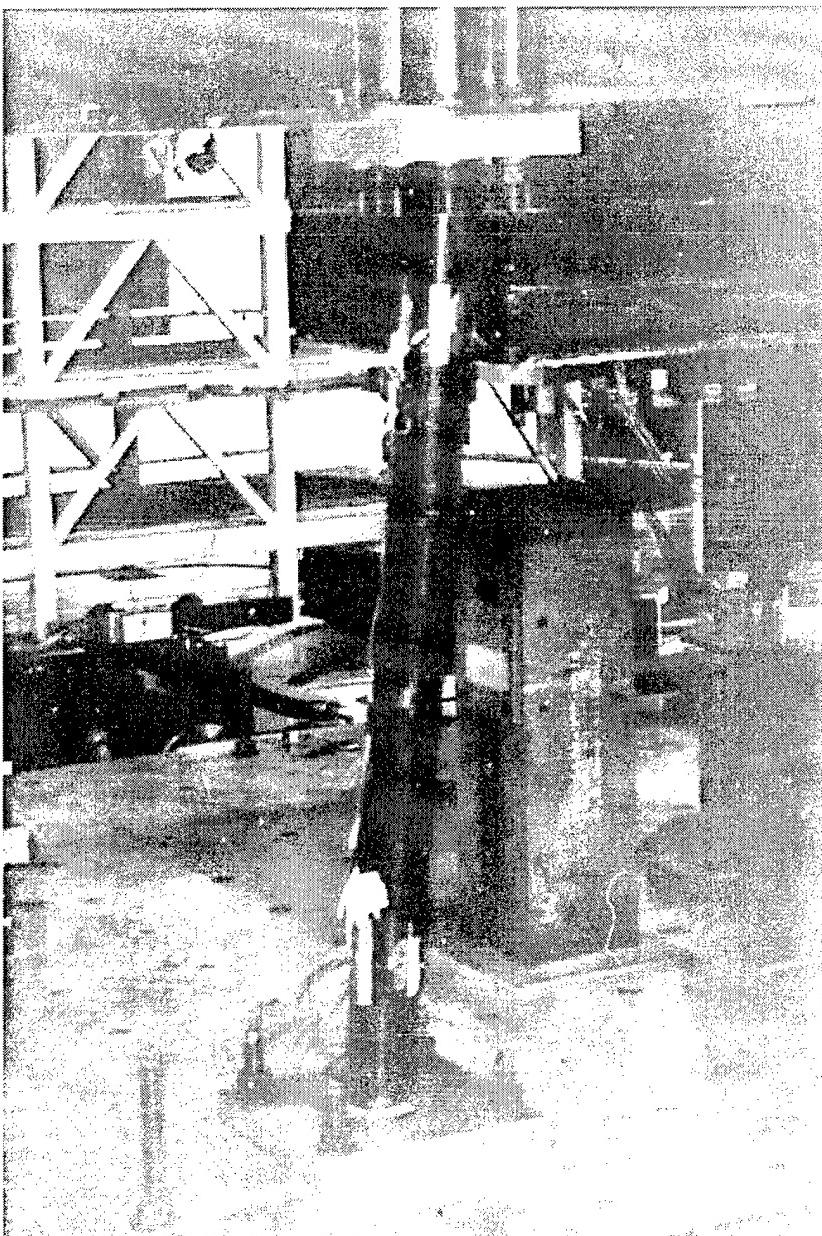


Figure 6.23 Test Structure Southeast Column After Earthquake Simulations

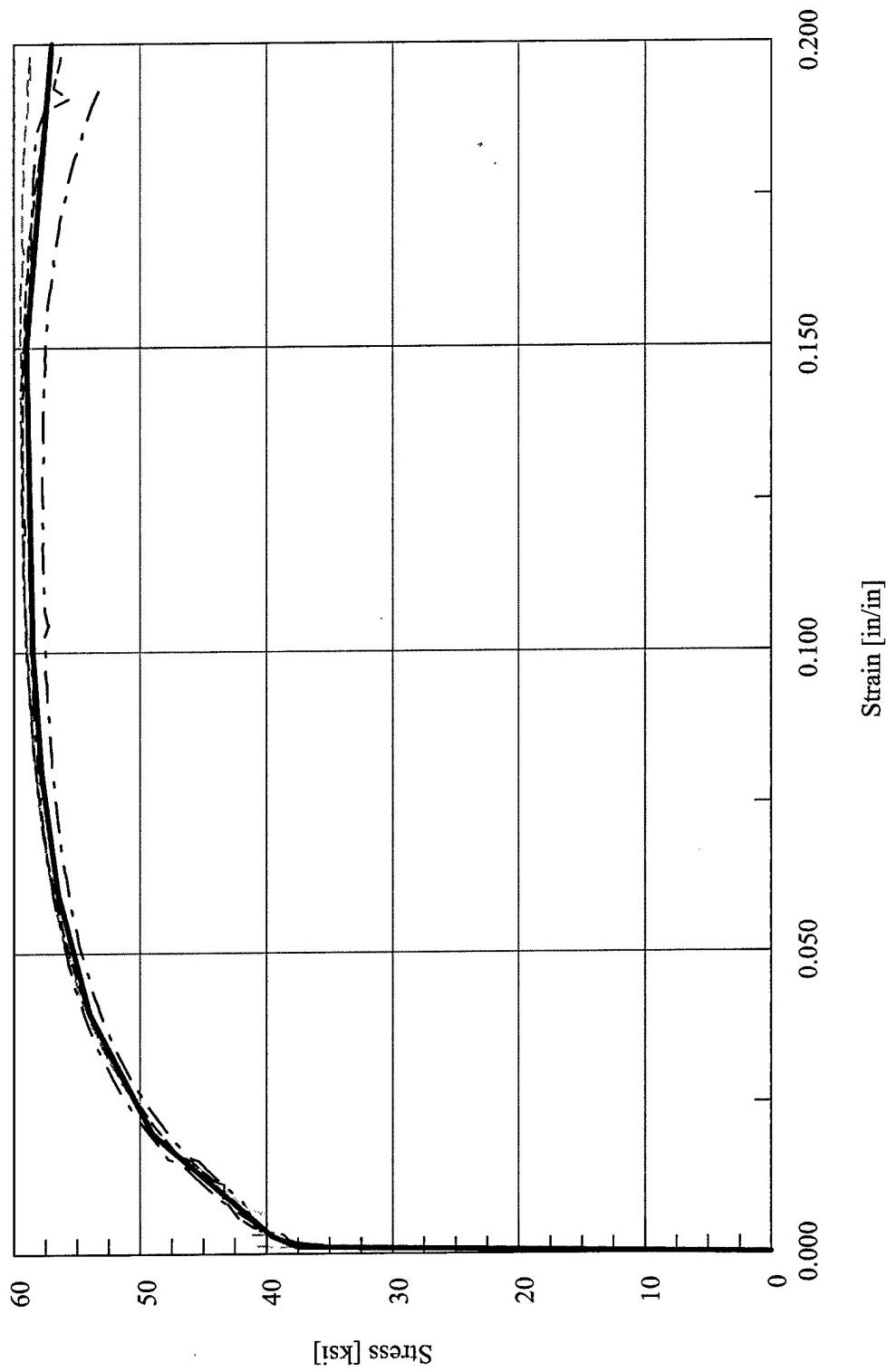


Figure 6.24 Abaqus Stress vs. Strain Finite Element Material Model Definition – Test Configuration 4

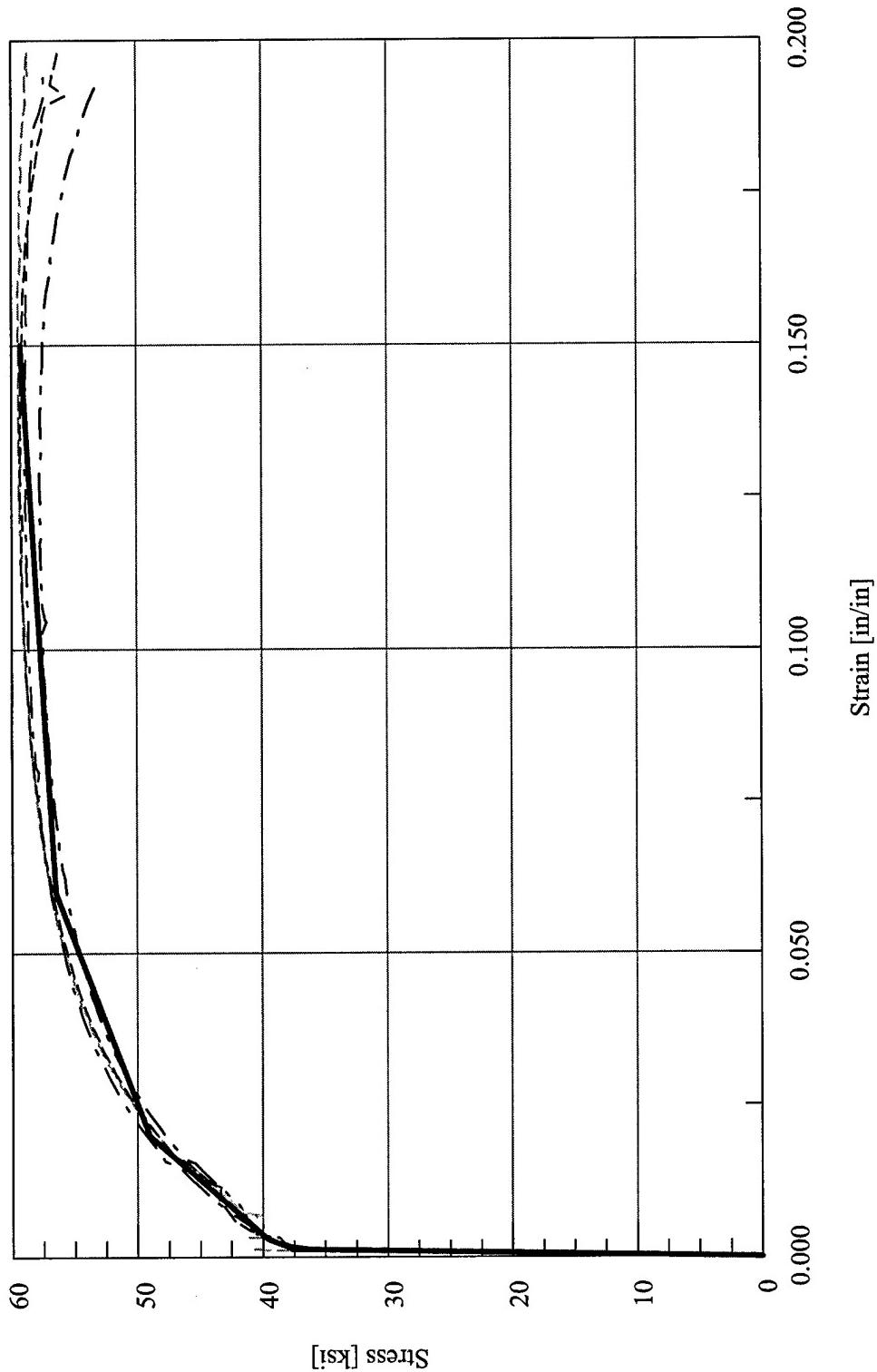


Figure 6.25 Drain-3DX Stress vs. Strain Finite Element Material Model Definition – Test Configuration 4

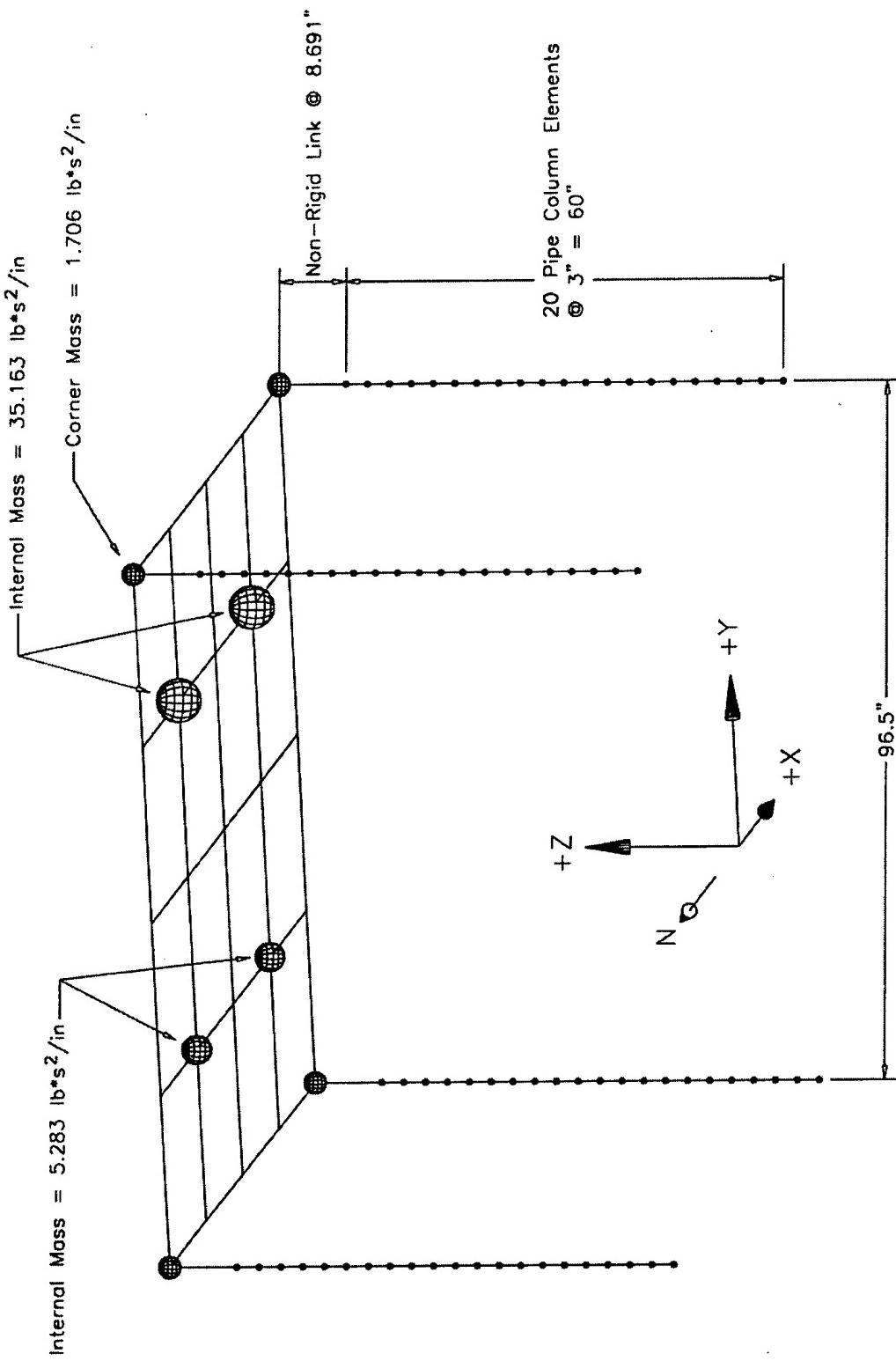


Figure 6.26 Abaqus Finite Element Model for Test Configuration 4

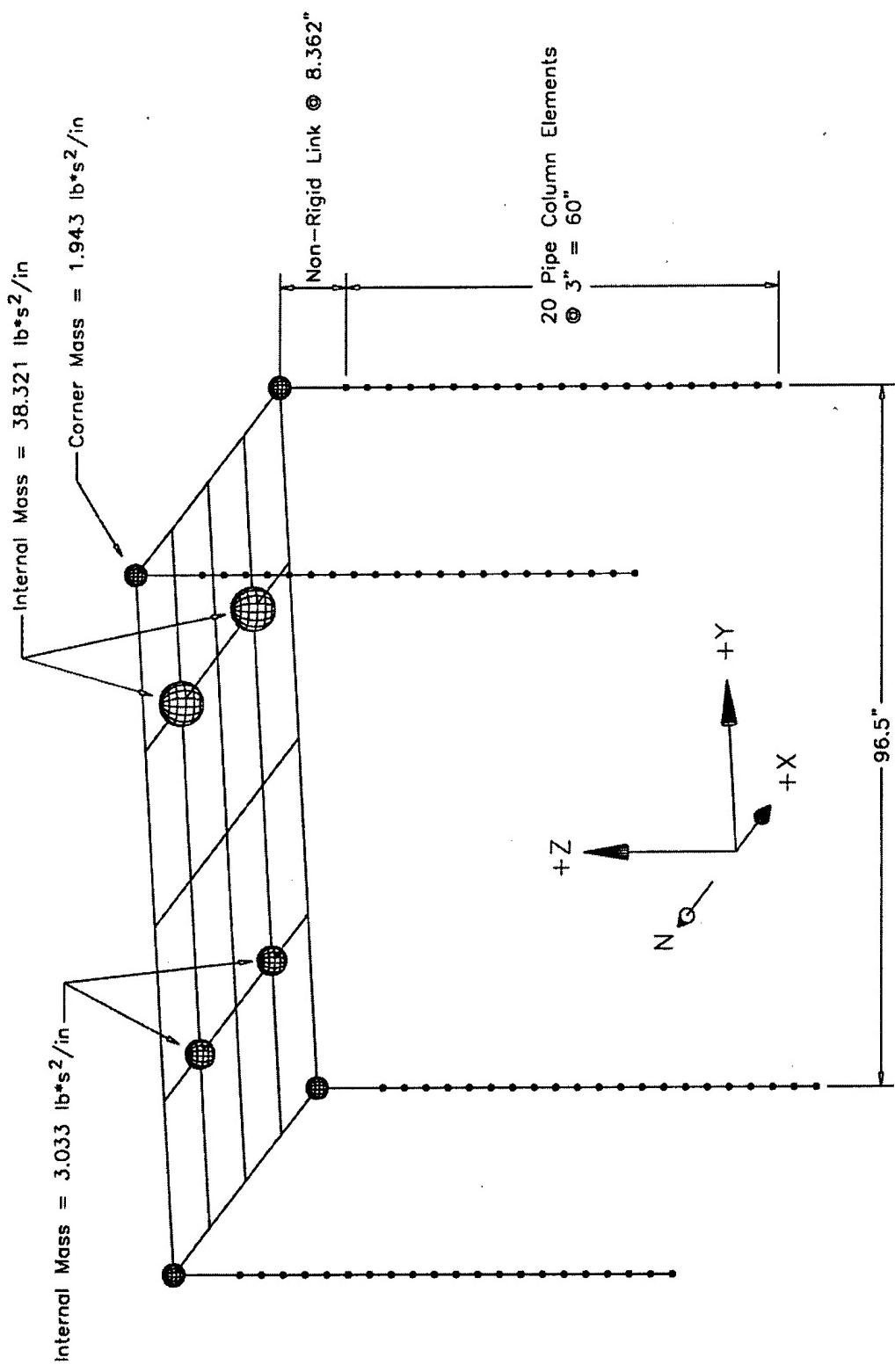


Figure 6.27 Drain-3DX Finite Element Model for Test Configuration 4

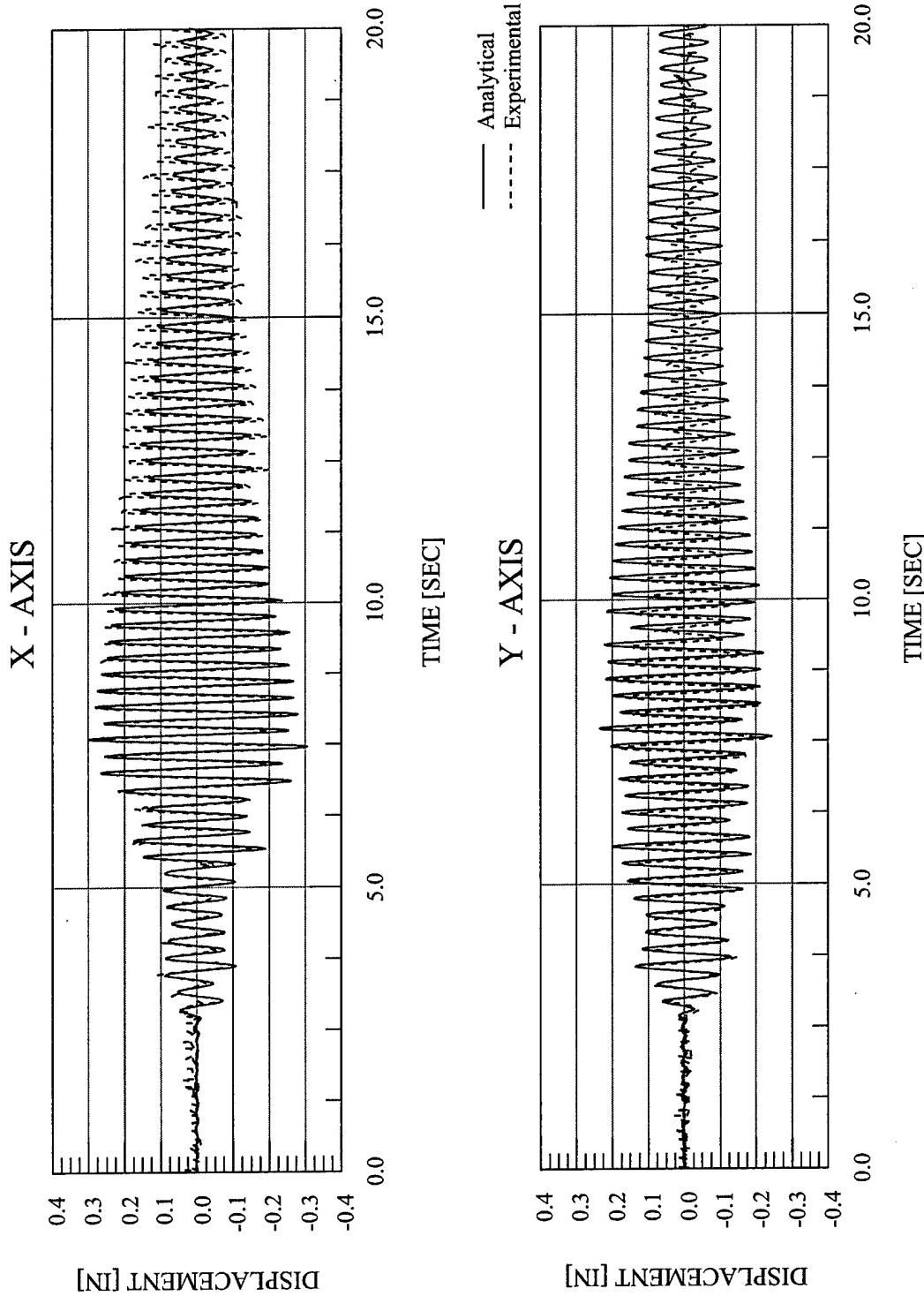


Figure 6.28 Abaqus Analytical Displacement vs. Time – EQ 27 – 10% Biaxial Impenetrable Valley

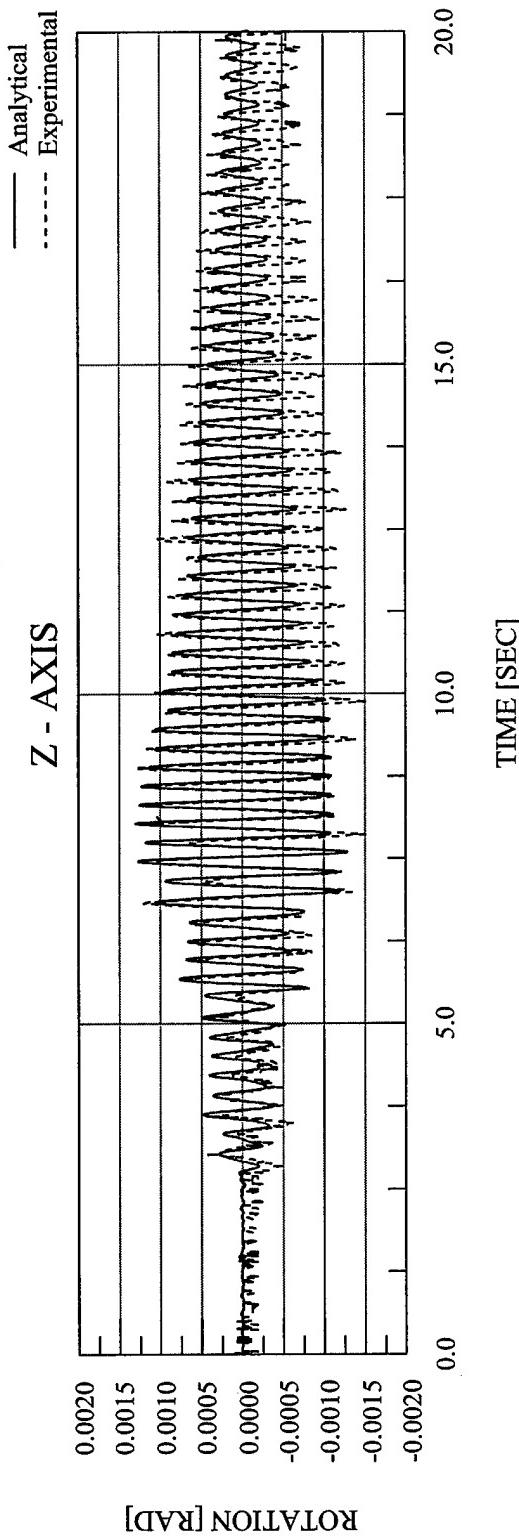


Figure 6.29 Abaqus Analytical Rotation vs. Time – EQ 27 – 10% Biaxial Imperial Valley

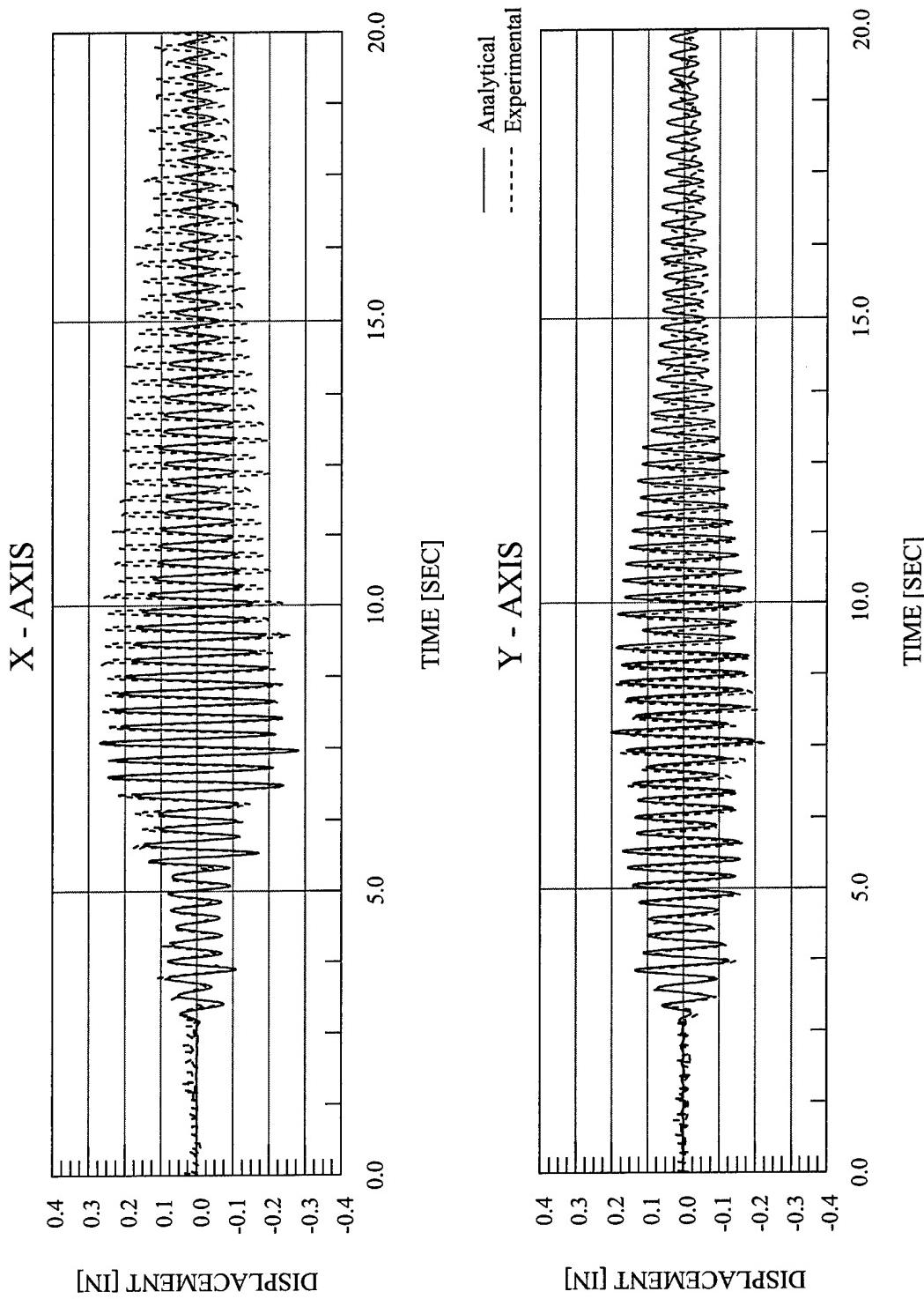


Figure 6.30 Drain-3DX Analytical Displacement vs. Time – EQ 27 – 10% Biaxial Imperial Valley

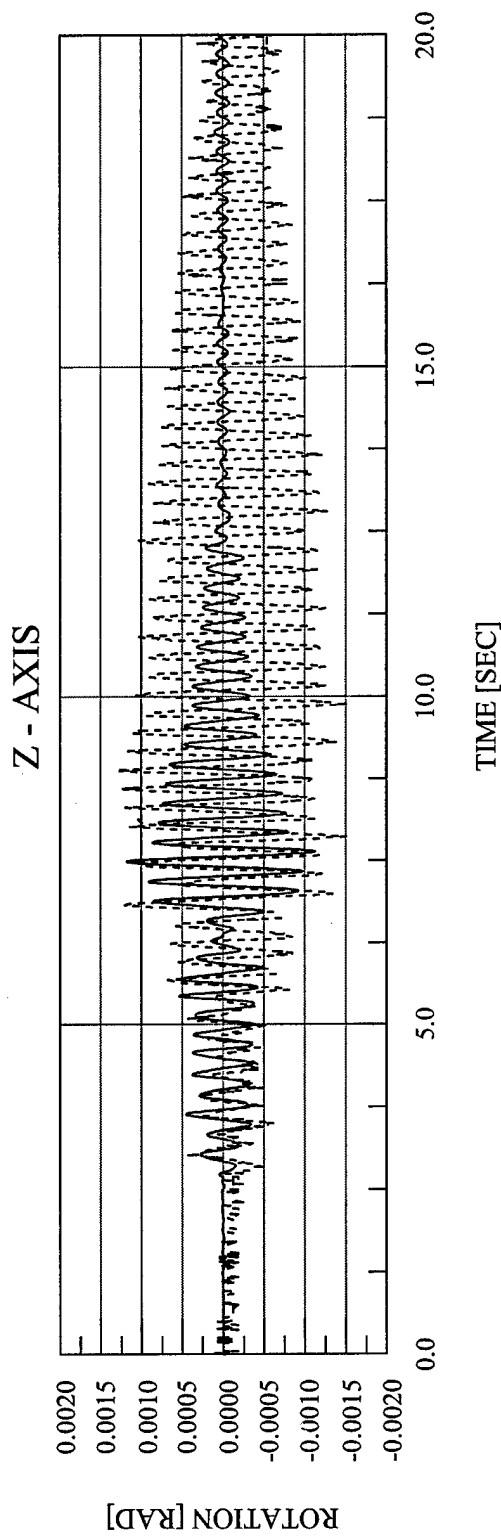


Figure 6.31 Drain-3DX Analytical Rotation vs. Time – EQ 27 – 10% Biaxial Imperial Valley

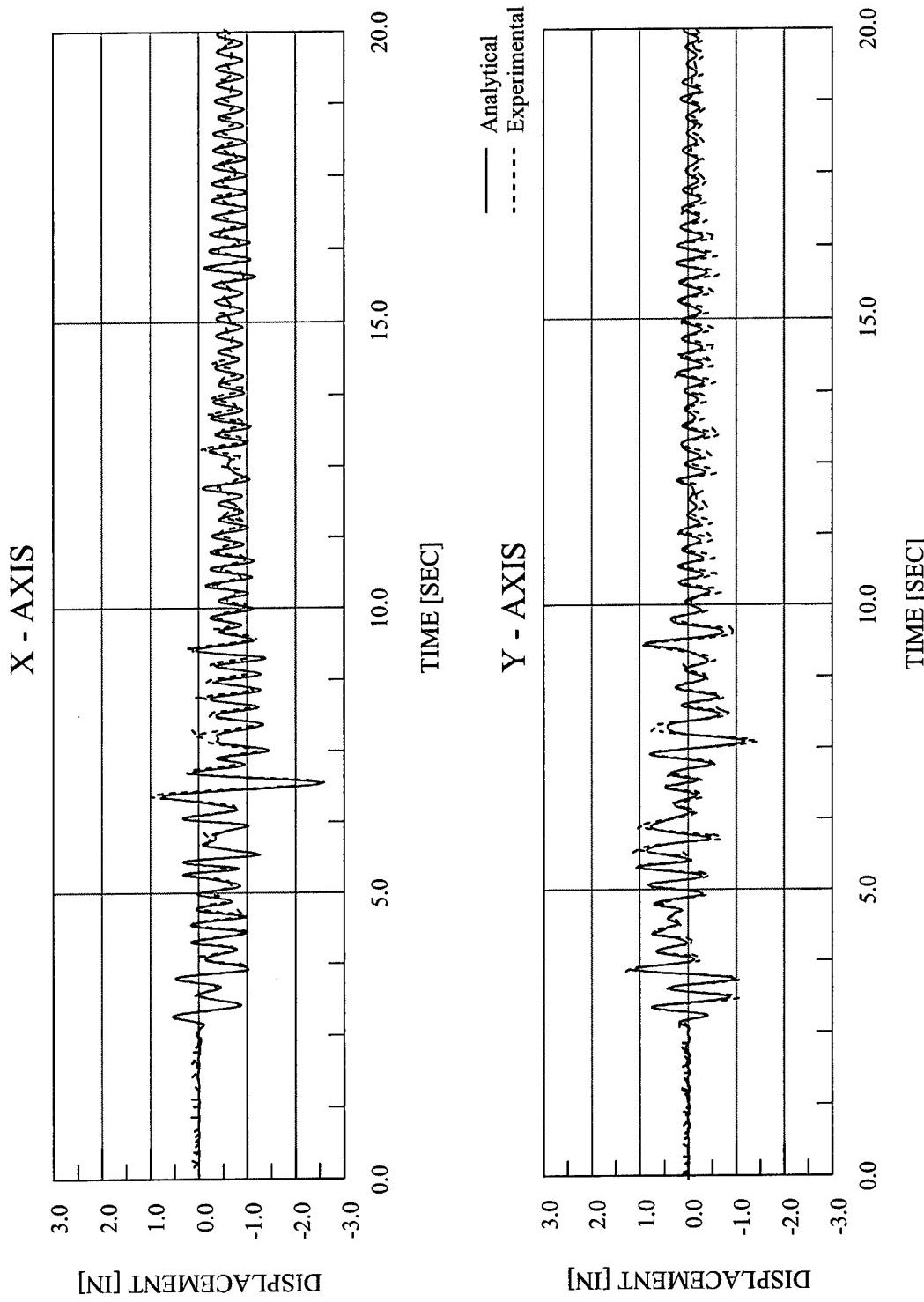


Figure 6.32 Abaqus Analytical Displacement vs. Time – EQ 28 – 100% Biaxial Imperial Valley – Combined Material Hardening

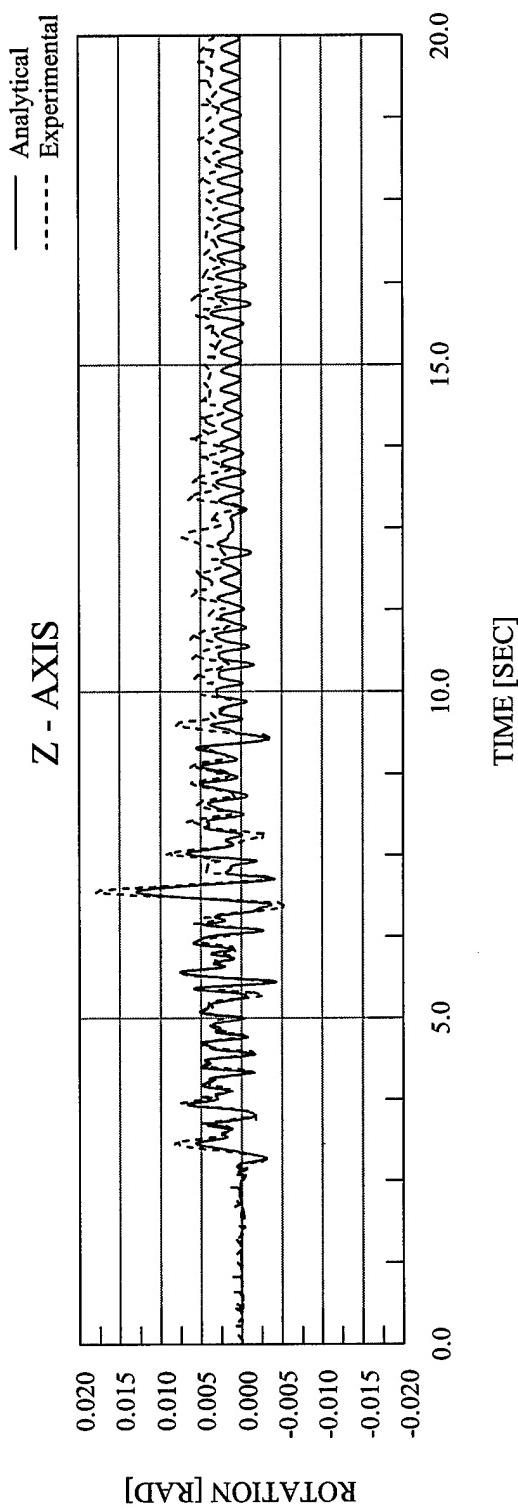


Figure 6.33 Abaqus Analytical Rotation vs. Time – EQ 28 – 100% Biaxial Imperial Valley – Combined Material Hardening

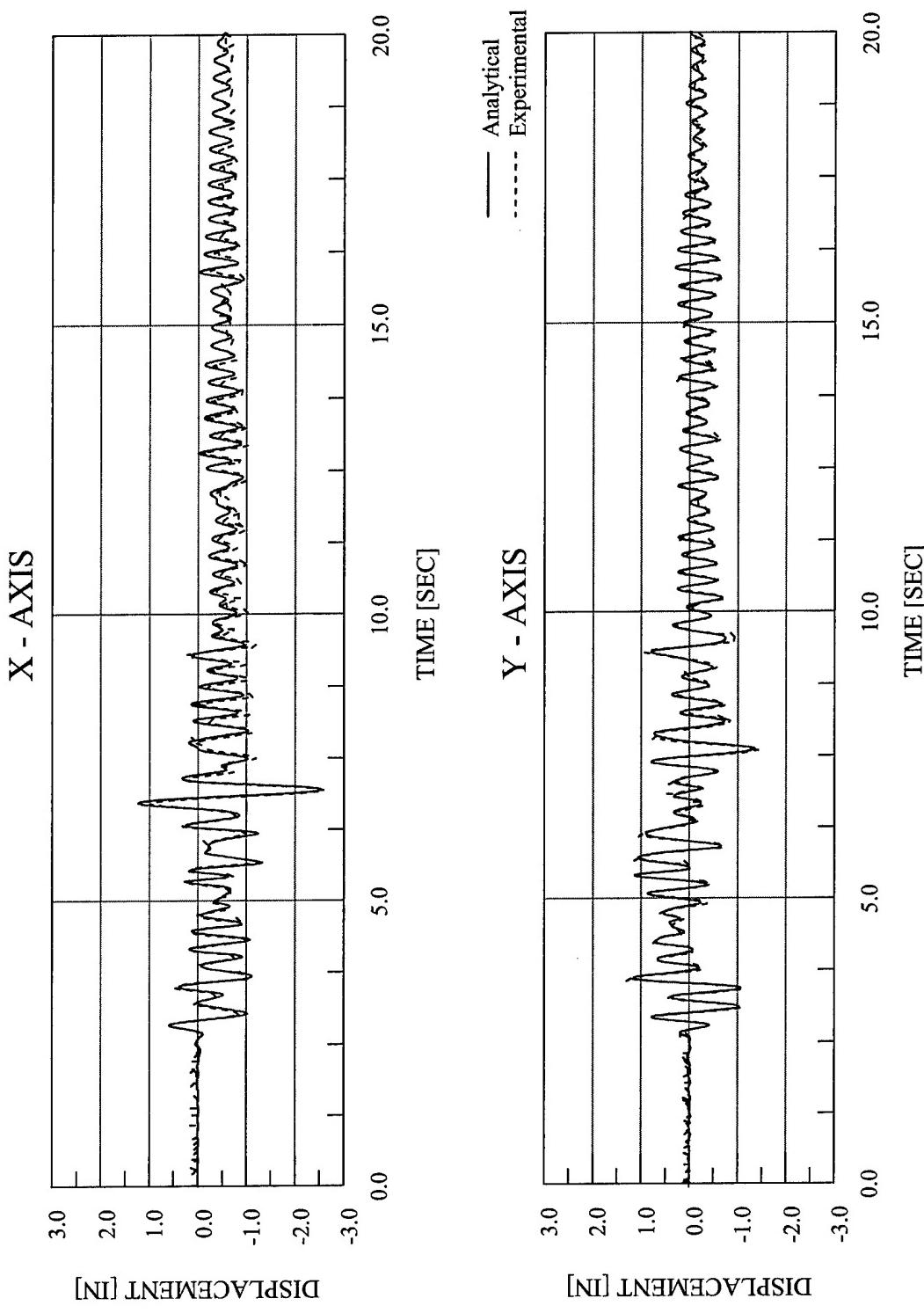


Figure 6.34 Drain-3DX Analytical Displacement vs. Time – EQ 28 – 100% Biaxial Imperial Valley

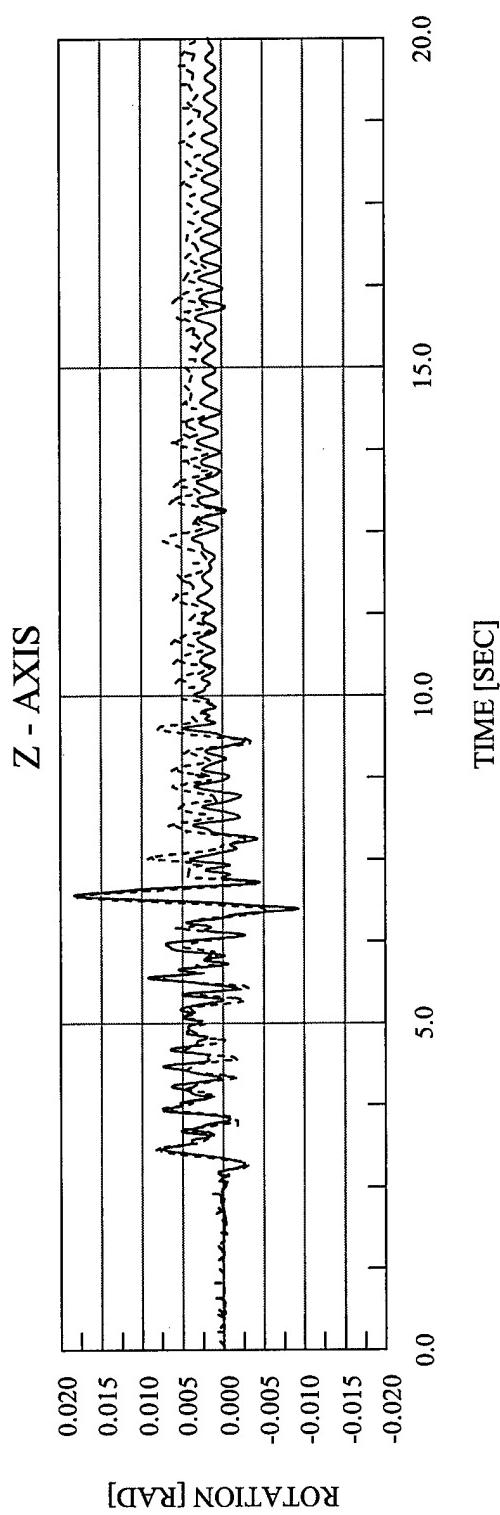


Figure 6.35 Drain-3DX Analytical Rotation vs. Time – EQ 28 – 100% Biaxial Imperial Valley

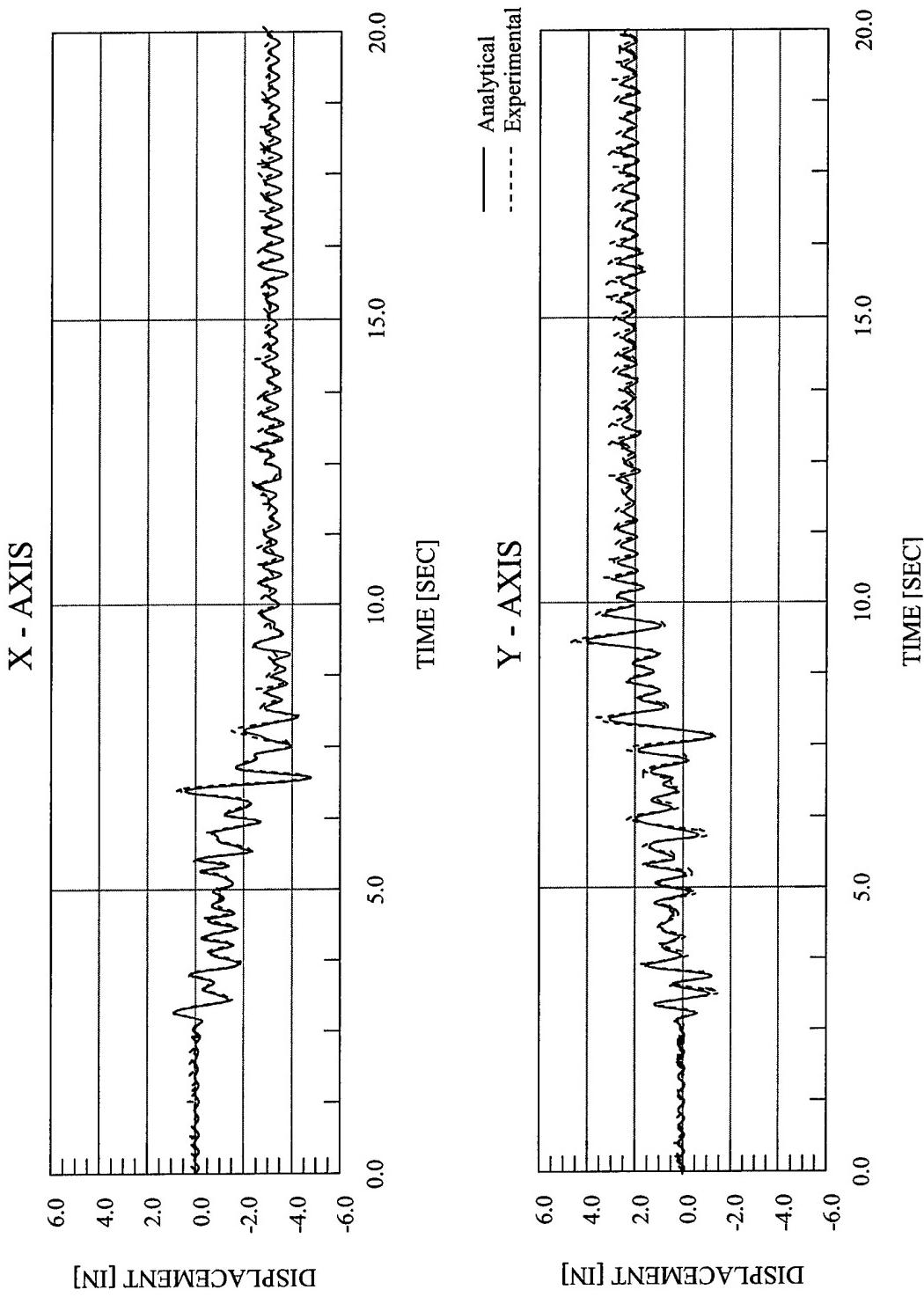


Figure 6.36 Abaqus Analytical Displacement vs. Time – EQ 29 – 150% Biaxial Imperial Valley – Combined Material Hardening

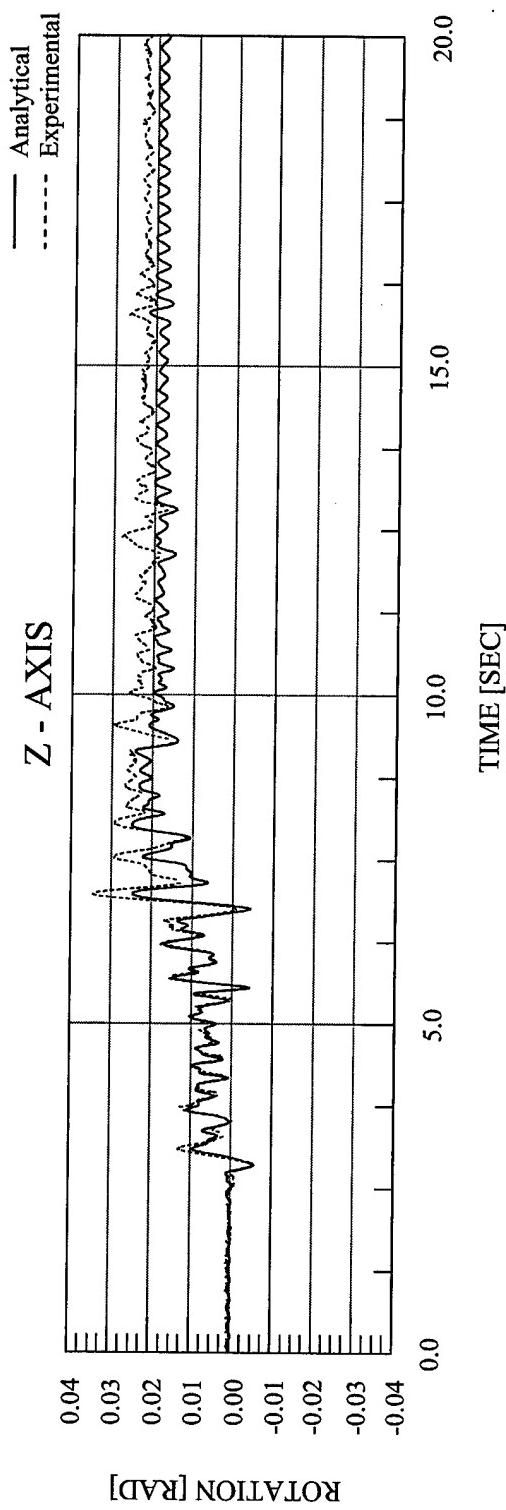


Figure 6.37 Abaqus Analytical Rotation vs. Time – EQ 29 – 150% Biaxial Imperial Valley – Combined Material Hardening

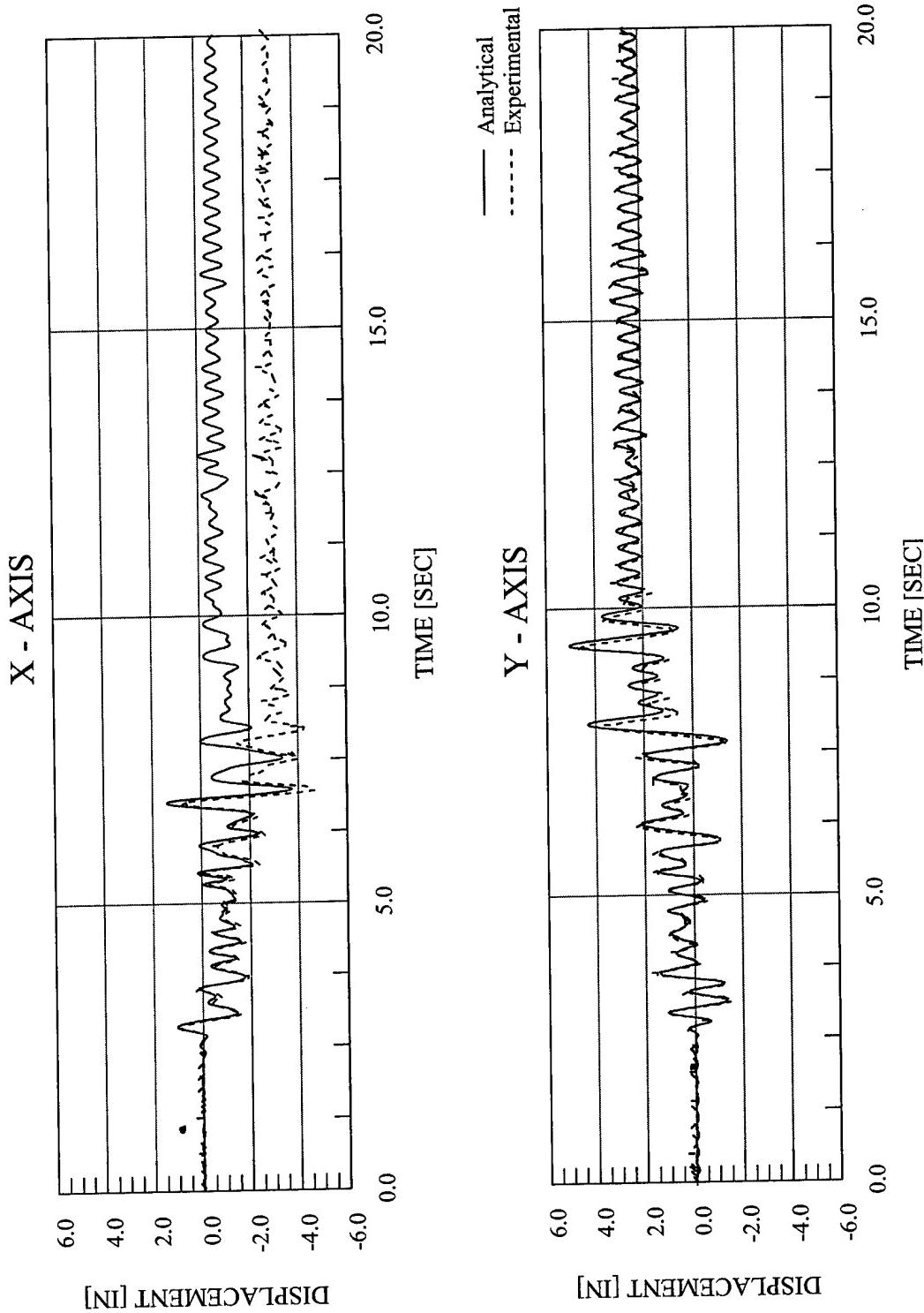


Figure 6.38 Drain-3DX Analytical Displacement vs. Time – EQ 29 – 150% Biaxial Imperial Valley

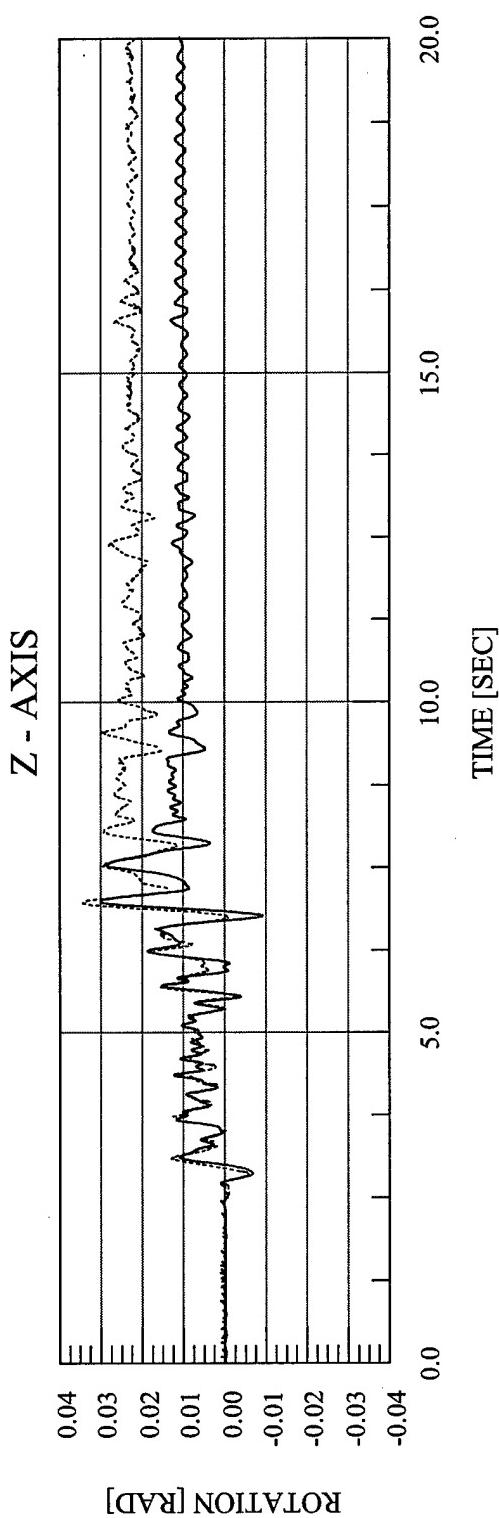


Figure 6.39 Drain-3DX Analytical Rotation vs. Time – EQ 29 – 150% Biaxial Imperial Valley

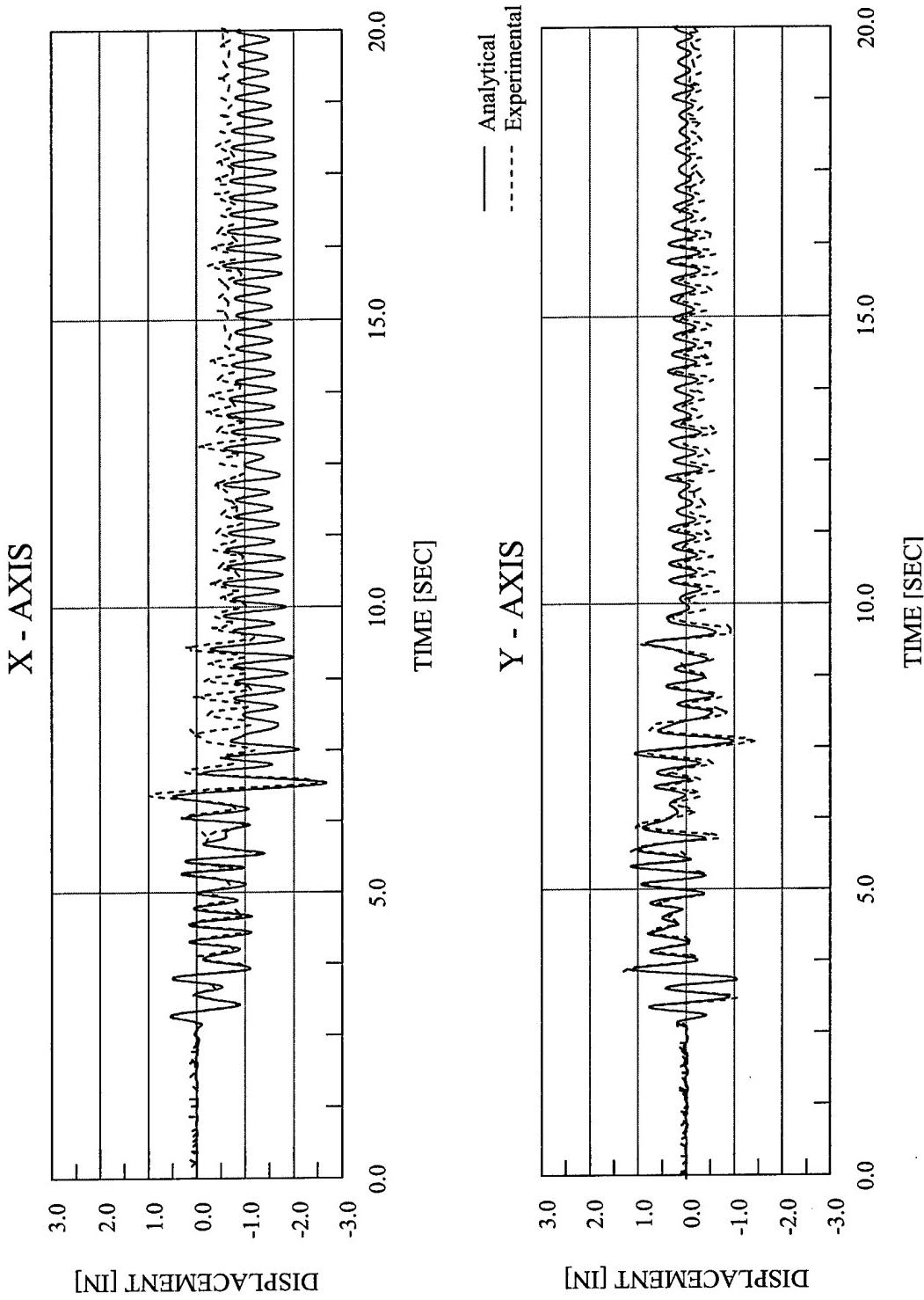


Figure 6.40 Abaqus Analytical Displacement vs. Time – EQ 28 – 100% Biaxial Imperial Valley – Isotropic Material Hardening

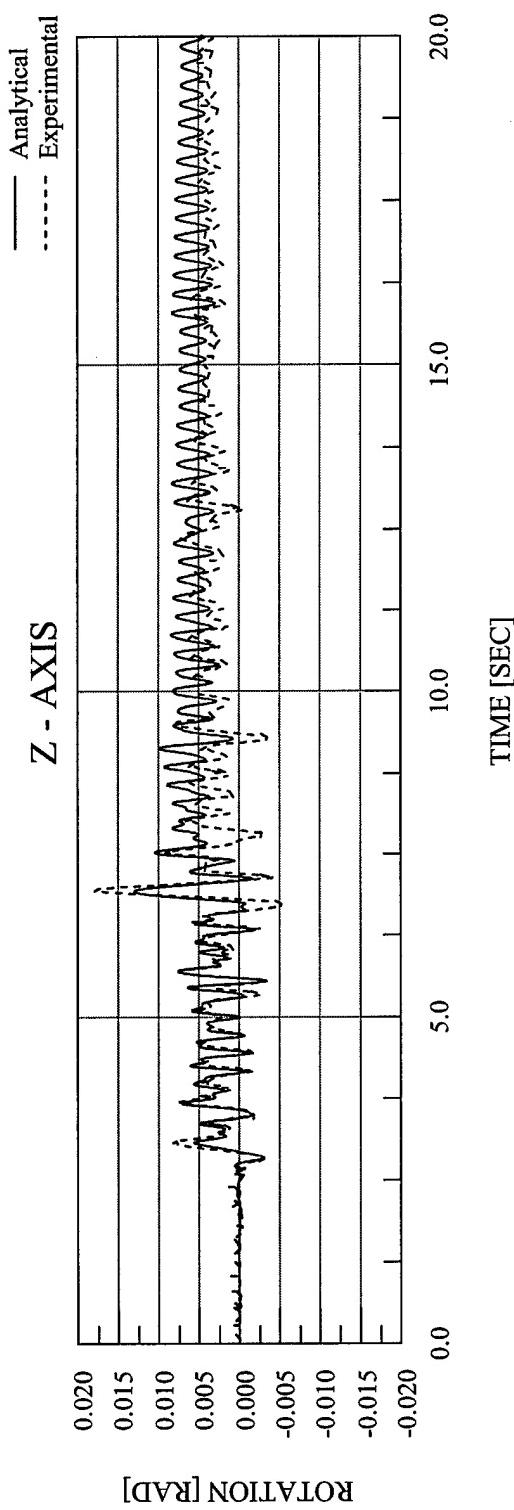


Figure 6.41 Abaqus Analytical Rotation vs. Time – EQ 28 – 100% Biaxial Imperial Valley – Isotropic Material Hardening

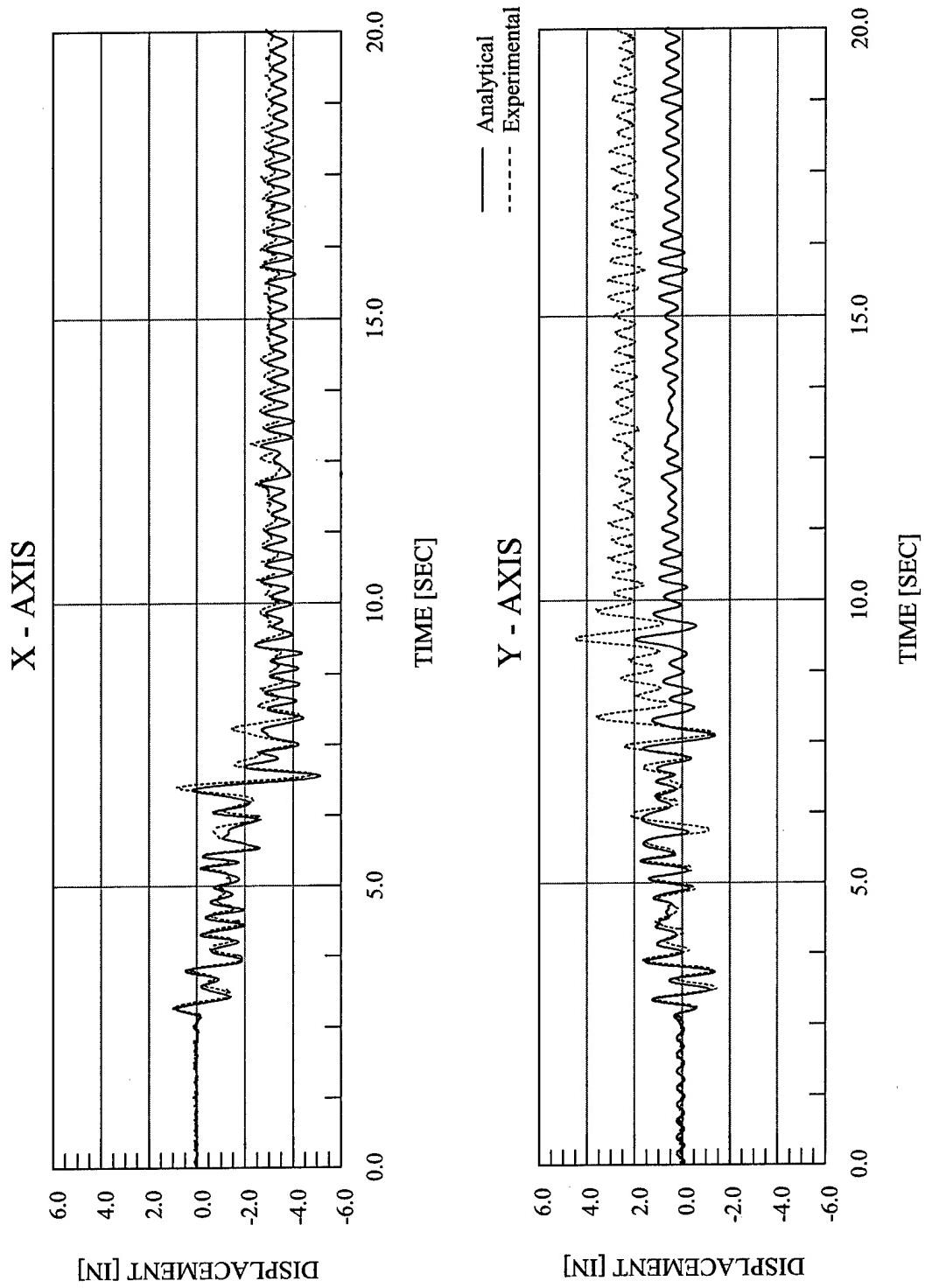


Figure 6.42 Abaqus Analytical Displacement vs. Time – EQ 29 – 150% Biaxial Imperial Valley – Isotropic Material Hardening

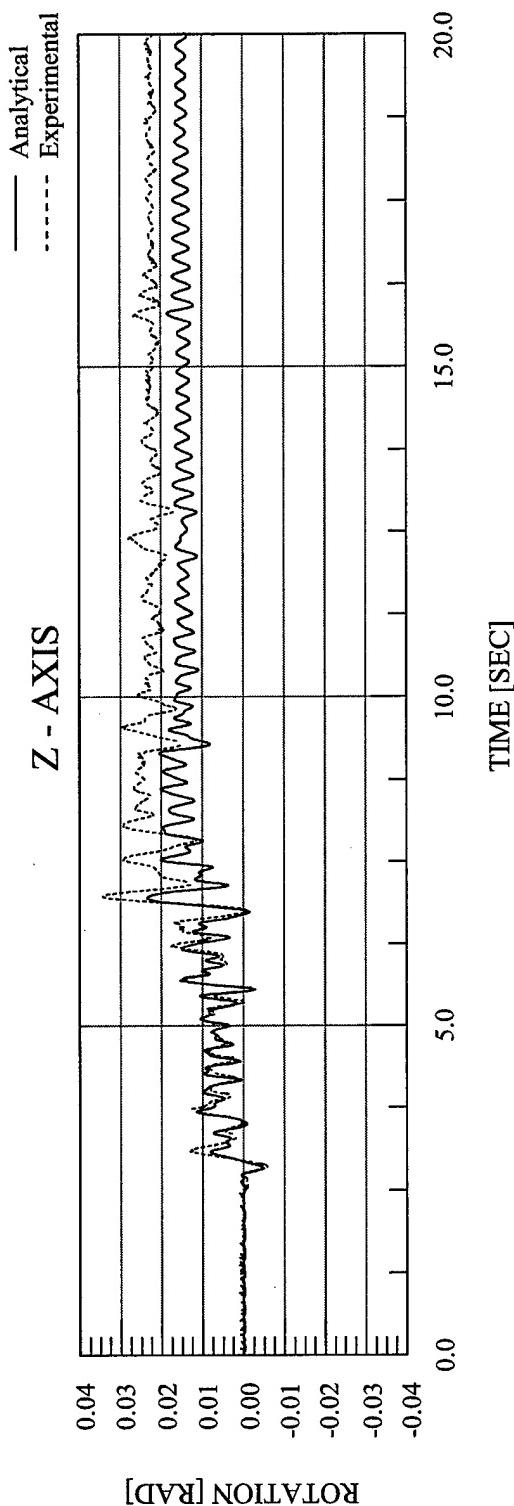


Figure 6.43 Abaqus Analytical Rotation vs. Time – EQ 29 – 150% Biaxial Imperial Valley – Isotropic Material Hardening

CHAPTER 7

EXPERIMENTAL AND ANALYTICAL RESPONSE OF TEST CONFIGURATION 3

This chapter provides a summary of the experimental test data and the finite element modeling of Test Configuration 3. The third configuration, as seen in Figure 7.1, featured all of the masses loaded on the northeast corner of the diaphragm, resulting in a $\frac{1}{4}$ mass asymmetry, and four 4" Extra-Strong Columns. The dynamic properties of the test structure in Test Configuration 3 are shown in Table 7.1.

Seven earthquake simulations were performed with this test configuration, although only four will be discussed here. During the third and fourth simulations, EQ 20 and EQ 21, instrumentation problems occurred with some of the data channels. Thus, EQ 22 was performed as a repeat of EQ 20 and EQ 21 once the problems were corrected. During the seventh and final earthquake simulation, EQ 24, the test aborted less than halfway through due to the shaketable reaching its displacement limit along the X-Axis. Thus, EQ 18 – 19 and EQ 22 – 23 are the four earthquake simulations that will be discussed in this chapter. In addition to the earthquake simulations, characterization tests were performed to determine the dynamic properties of the model. The complete test sequence for Test Configuration 3 is shown in Table 7.2.

The first three earthquake simulations, EQ 18 with 10% X-Axis only [$\text{PGA}_X = 0.102 \text{ g}$], EQ 19 with 10% Y-Axis only [$\text{PGA}_Y = 0.064 \text{ g}$], and EQ 22 with 10% Biaxial input motions [$\text{PGA}_X = 0.109 \text{ g}$ and $\text{PGA}_Y = 0.066 \text{ g}$], featured only elastic behavior. The fourth simulation, EQ 23, with 100% Biaxial input motions [$\text{PGA}_X = 1.299 \text{ g}$ and $\text{PGA}_Y = 0.797 \text{ g}$], was the initial inelastic test for this configuration.

This chapter summarizes response data of the test structure during the earthquake simulations and the dynamic characterization tests. Summaries of test model accelerations, displacements, torsional moments, overturning moments, column end moments, and base shears are provided.

7.1 OBSERVED STRUCTURAL RESPONSE

The diaphragm acceleration and displacement time history responses for the 10% X-Axis simulation are shown in Figure 7.2. The base shear vs. displacement and torque vs. rotation are shown in Figure 7.3. Similar responses for the 10% Y-Axis simulation are shown in Figures 7.4 and 7.5. Results for the 10% Biaxial simulation are shown in Figures 7.6 and 7.7. The responses for the 100% Biaxial simulation are shown in Figures 7.8 and 7.9.

Tables 7.3 – 7.7 list the peak recorded diaphragm relative displacements and peak diaphragm accelerations, and corresponding PGA for each of the four earthquake simulations discussed for this test configuration. Also listed are the maximum base shears, maximum torsional moments, maximum overturning moments, maximum column end moments for each column, and maximum column end shears for each column.

7.2 OBSERVED RESPONSE DISCUSSION

The calculated force-deformation behavior of the structure in the X and Y directions and about the Z-Axis is shown in Figures 7.10 and 7.11. In the X direction, the model has a yield displacement of 0.47 inches at a yield force of 21.35 kips. In the Y direction, the model has a yield displacement of 0.53 inches at a yield force of 21.35 kips. The model has a yield rotation of 0.0068 radians at a yield moment of 1457 kip*inches. Also, elastic response spectra of the recorded table motions for EQ 18 – 19 and EQ 22 – 23 are shown in Figures 7.12 – 7.15, respectively. The modal frequencies for this configuration with respect to the response spectra are also indicated in Figures 7.12 – 7.15.

The first earthquake simulation for this configuration, EQ 18, features 10% Imperial Valley input motion in the X-Axis only [$\text{PGA}_X = 0.102 \text{ g}$]. Time history plots of the response are shown in Figure 7.2. The peak displacements were 0.175 inches in the X direction and 0.112 inches in the Y direction, while static analysis, using the elastic response spectrum, predicts 0.210 inches along the X-Axis and no displacement along the Y-Axis. The peak rotation of the structure was 0.85×10^{-3} radians, with 0.22×10^{-3} radians predicted by static analysis. Verifying the elastic response are the peak base shears and peak torsional moment, which are 8.44 kips in the X direction, 4.49

kips in the Y direction, and 140.44 kip*inches about the vertical axis. Figure 7.3 shows the base shear vs. displacement plots and torsional moment vs. rotation plot, which are all tight and linear. As there is a mass eccentricity in this configuration along the Y-Axis, torsional moments and rotations are expected with input motion along the X-Axis. Although the input motion for EQ 25 was along the X-Axis only, Figure 7.2 shows that the structure did have a displacement response in the Y-Axis. The oscillatory nature of the response appears to indicate that this motion is a product of the shaketable control problem discussed in previous chapters. This resonance motion was also observed for Test Configuration 4, with all of the masses loaded on the east side of the diaphragm. In Test Configuration 4, with the mass eccentricity along the Y-Axis and the structure subjected to a ground motion along the X-Axis, response was observed along the Y-Axis as well as the X-Axis. The resonant response was larger for this configuration, with $\frac{1}{4}$ mass eccentricity, than for Test Configuration 4, with $\frac{1}{2}$ mass eccentricity, and very little resonant response was observed for the configurations with a symmetric mass distribution. Thus, it appears that this response along the perpendicular axis due to a single-axis ground motion depends to some extent on the degree of mass eccentricity.

In EQ 19 the model is subjected to a 10% Y-Axis input motion [$PGA_Y = 0.064 \text{ g}$]. Time history plots of the structural response are shown in Figure 7.4. The peak displacements were 0.123 inches in the Y direction, 0.039 inches in the X direction, and 0.85×10^{-3} radians about the Z-Axis. The peak displacements predicted by static analysis are 0.123 inches in the Y direction and 0.46×10^{-3} radians about the vertical axis, with no displacement predicted in the X direction. Figure 7.5 shows the base shear vs. displacement plots and torsional moment vs. rotation plot. The shear vs. displacement plots for the Y and X directions are tight and linear. The shear vs. displacement plot for the X direction, and to a lesser degree the Y direction, and the moment vs. rotation plot indicate that due to the low response level for this test, noise in the data acquisition system is present and noticeable. Figure 7.4 indicates that the resonant motion discussed above is present in this simulation as well, as the structure responds along the X-Axis when excited by a ground motion along the Y-Axis. This is not surprising as this configuration has a mass eccentricity along both axes, although the resonant response in the X direction for this simulation is not nearly as large, relative to the Y-Axis response, as the resonant response in EQ 18. The peak X-Axis displacement is roughly 30% of the peak Y-Axis displacement, while in EQ 18 the peak Y-Axis displacement is nearly 65% of the peak X-Axis displacement. As the structure possesses the same amount of mass asymmetry along each axis, the differences in the resonant

responses must result from the different characteristics of the X-Axis and Y-Axis ground motions.

In EQ 22 the model is subjected to 10% Imperial Valley input motions along both the X-Axis and Y-Axis [$\text{PGA}_X = 0.109 \text{ g}$ and $\text{PGA}_Y = 0.066 \text{ g}$]. Time history plots of the structural response are shown in Figure 7.6. The peak displacements of the structure were 0.166 inches in the X direction, 0.160 inches in the Y direction, and 0.97×10^{-3} radians torsionally. The peak displacements predicted by static analysis are 0.214 inches along the X-Axis, 0.158 inches along the Y-Axis, and 0.90×10^{-3} radians torsionally. The peak base shears and peak torsional moment are 7.81 kips in the X direction, 6.78 kips in the Y direction, and 184.95 kip*inches about the vertical axis. Figure 7.7 shows the base shear vs. displacement plots and torsional moment vs. rotation plot, which are all linear, and the displacement time histories indicate no residual displacement or permanent deformation. The moment vs. rotation plot does not appear as tight as the shear vs. displacement plots, due to noise from the data acquisition system.

In comparing EQ 22 with EQ 18, the addition of the 10% Y-Axis input motion results in little change in the X-Axis response of the diaphragm, as the peak displacement and base shear are 0.175 inches and 8.44 kips for EQ 18 and 0.166 inches and 7.81 kips for EQ 22. Because this configuration has an eccentricity in the both directions, the addition of an input motion and thus response in the Y direction should add to the torsional effect. This is verified by the fact that the torsional moment does increase between EQ 18 and EQ 22. It is also of interest to compare the recorded peak ground accelerations (PGA) and resulting pseudo-spectral displacements (PSD), which give a measurement of the displacement response as a function of the ground motion and period of the structure, of any two simulations. As shown in Table 7.3, EQ 18 has a PGA of 0.102 g while EQ 22 has a PGA of 0.109 g. In addition, in referencing Figures 7.12 and 7.14, EQ 18 has a PSD of 0.211 inches while EQ 22 has a PSD of 0.214 inches. Although the PSDs predict a small increase in the displacement response of the structure, the response appears to decrease slightly. However, considering the precision of the data, the PSDs and responses can be considered equal. In a linear elastic system, the displacement response in EQ 22 should be the equal to the sum of the responses in EQ 18 and EQ 19. This comparison can be made if the ground motions for all three simulations were the same, as they are in this configuration. In the case of both the Y-Axis response and the torsional response, the peak motions during EQ 18 and EQ 19 do not together equal the peak motion in EQ 22, which would be expected if no parts of these responses were resonant motions due to the shaketable control problem. If the Y-Axis

motion in EQ 18 were entirely a product of the resonant response of the shaketable, the peak Y-Axis displacement in EQ 19 should be nearly equal to the peak Y-Axis response in EQ 22, as has been observed in previous configurations. This observation does not hold for the Y-Axis and torsional response, however. Thus, it appears that the Y-Axis response in EQ 18 and the torsional responses in EQ 18 and EQ 19 are to some degree resonant responses, but not entirely.

In EQ 23, the first test in this configuration that features inelastic response, the model structure is subjected to 100% Imperial Valley input motion along both the X-Axis and Y-Axis [PGA_X = 1.299 g and PGA_Y = 0.797 g]. Time history plots of the response are shown in Figure 7.8. The peak displacements of the structure were 3.17 inches in the X direction and 1.18 inches in the Y direction, which are both larger than the yield displacements of 0.47 inches and 0.53 inches, respectively. The peak rotation of the structure was 21.94×10^{-3} radians, also larger than the yield rotation of 6.8×10^{-3} radians. The peak base shears, which are 36.67 kips in the X direction and 31.05 kips in the Y direction, are greater than the yield shears, 20.73 kips in the X direction and 18.32 kips in the Y direction. Thus, the base shears verify the inelastic response, but they also demonstrate the overstrength of the structure, as the peak shears are both nearly twice the yield shears. Figure 7.9 shows the base shear vs. displacement plots and torsional moment vs. rotation plot, which are no longer tight and linear but now are taking on a fuller shape, indicating inelastic behavior. Both the X-Axis shear vs. displacement loop and the moment vs. rotation loop exhibit a very large inelastic excursion. The peak torsional moment in this simulation is roughly two-thirds of the yield moment, while the rotational ductility experienced by the structure is greater than 3. As observed and discussed in the previous two configurations, this is a result of the fact that each column participates in the seismic resistance of the structure in each of the three directions of motion. As a column yields due to lateral response, the torsional stiffness of the structure consequently decreases as well, resulting in a larger torsional response. This was observed in Test Configurations 2 and 3, which featured mass symmetry and a $\frac{1}{2}$ -mass asymmetry, respectively. The peak torsional moment during EQ 28, the 100% Imperial Valley simulation in Test Configuration 3 with a $\frac{1}{2}$ -mass asymmetry, was roughly two-thirds of the yield moment, as was the case in this test configuration for EQ 23. With very similar peak torsional moments, it is not surprising that the rotational ductility experienced during EQ 23, 3.3, with $\frac{1}{4}$ -mass asymmetry, is noticeably larger than that experienced during EQ 28, 2.7, with $\frac{1}{2}$ -mass asymmetry.

The acceleration response of the diaphragm divided by the peak ground acceleration (PGA) is shown in Table 7.4 as the normalized acceleration. In EQ 22, with 10% Biaxial input motions, the normalized acceleration response of the diaphragm is 2.05 in the X direction, and 3.17 in the Y direction. The input ground motions are increased by about a factor of 10 in EQ 23, but the acceleration response of the diaphragm only increases by about 5 in the X direction and 4.5 in the Y direction, resulting in a normalized acceleration response of 0.88 in the X direction and 1.18 in the Y direction. Also, although the input motions are more than 10 times larger, the angular acceleration response of the diaphragm increases from EQ 22 to EQ 23 by only a factor of about 7. Both of these trends verify the expected inelastic behavior of the structure in EQ 23.

7.3 DYNAMIC CHARACTERIZATIONS OF THE MODEL

Prior to performing any shaketable simulations using the earthquake input motions, white noise, sine sweep, and sine decay tests were performed. This general pattern was followed for Test Configuration 3, as can be seen in Table 7.2. In addition, white noise tests were performed immediately after the earthquake simulation exhibiting inelastic behavior, EQ 23.

The dynamic properties of the test structure, as measured before EQ 18 and then after EQ 23, are shown in Table 7.1. The results in Table 7.1 indicate that despite the inelastic behavior in EQ 23, no meaningful permanent softening of the structure took place. Test Configuration 4, discussed in Chapter 6, also exhibited no permanent softening of the structure. In addition, Test Configuration 4 experienced a larger degree of inelastic behavior, being subjected to 150% Biaxial motions, while this configuration was only subjected to 100% Biaxial motions. The damping, on the other hand, did increase noticeably by the end of the final simulation. The structure experienced a significant amount of inelastic behavior during the final two simulations, which most likely began to produce micro-cracking at the column-base plate welded interface.

7.4 OBSERVED CONDITION OF THE STRUCTURE

In inspecting the model structure for fracture in the weld or in the base material, none was found for this test configuration. Figures 7.16 and 7.17 are photographs of the test structure taken before the earthquake simulations were performed. Figure 7.18 is a photograph of the test

structure taken after the final earthquake simulation in this configuration, EQ 23, illustrating the inelastic behavior and permanent damage of the structure. Figure 7.19 also shows the formation of plastic hinges near the top and bottom of the column.

7.5 FINITE ELEMENT ANALYSIS

In modeling the behavior of the test structure, the nonlinear finite element analysis programs Abaqus and Drain-3DX were employed. During the earthquake simulations employing the larger scale input motions, the structural response exhibits both geometric and material nonlinearities, both of which Abaqus and Drain-3DX can model. A more complete discussion of the applicable features of Abaqus and Drain-3DX is presented in Chapter 3. Also, some aspects of the finite element model, such as the modeling of the diaphragm as a rigid component, are common throughout each test configuration, and are discussed more completely in Chapter 3.

(A) PIPE COLUMN MATERIAL MODEL

The pipe columns used in Test Configuration 3, as well as those used in Test Configurations 1, 2, and 4 were produced from the same batch of raw pipe column lengths. The material models of the pipe columns in these four test configurations were based on stress-strain data produced during each coupon tension test. Both the original stress-strain data recorded during the coupon tension tests, and the best-fit material model used in the finite element analyses are shown in Figure 7.20 for Abaqus and in Figure 7.21 for Drain-3DX. Shown in Tables 7.8 and 7.9 are the numerical stress-strain best-fit Abaqus and Drain-3DX model data, respectively.

(B) FINITE ELEMENT MODEL

The Abaqus and Drain-3DX finite element models used for Test Configuration 3 are shown in Figures 7.22 and 7.23. Beyond the features of the finite element model common throughout each test configuration, Figure 7.22 illustrates the location and magnitudes of the nodal masses and the height of the Non-Rigid Links for the Abaqus model. The nodal masses placed at each of the four corners of the diaphragm each have a magnitude of $1.705 \text{ lb} \cdot \text{s}^2/\text{in}$. The largest interior

mass, the northeast interior mass, has a magnitude of $62.761 \text{ lb}^*\text{s}^2/\text{in}$. The other three interior masses have magnitudes of $6.595 \text{ lb}^*\text{s}^2/\text{in}$. The height of the finite element model diaphragm in this test configuration is 67.804 inches, which thus produces a length of 7.804 inches for each of the four Non-Rigid Links. Figure 7.23 illustrates the location and magnitudes of the nodal masses and the height of the Non-Rigid Links for the Drain-3DX model. The nodal masses placed at the four diaphragm corners have magnitudes of $0.024 \text{ lb}^*\text{s}^2/\text{in}$. The northeast interior mass has a magnitude of $72.820 \text{ lb}^*\text{s}^2/\text{in}$, while the remaining interior masses have magnitudes of $5.483 \text{ lb}^*\text{s}^2/\text{in}$. The height of the finite element model diaphragm is 67.479 inches, which results in a length of 7.479 inches for the Non-Rigid Links

(C) OBSERVED RESPONSE

Displacement histories along the X- and Y-Axis and rotation histories about the Z-Axis are provided for the 10% Biaxial simulation [$\text{PGA}_X = 0.109 \text{ g}$ and $\text{PGA}_Y = 0.066 \text{ g}$] in Figures 7.24 – 7.27, and the 100% Biaxial simulation [$\text{PGA}_X = 1.299 \text{ g}$ and $\text{PGA}_Y = 0.797 \text{ g}$] in Figures 7.28 – 7.31. Table 7.10 lists the maximum peak relative displacements in the X and Y directions and the peak rotation, and the corresponding PGAs, for the two earthquake simulations listed above.

(D) OBSERVED RESPONSE DISCUSSION

In Figures 7.24 – 7.27, the Abaqus and Drain-3DX displacement and rotation response histories for EQ 22 [$\text{PGA}_X = 0.109 \text{ g}$ and $\text{PGA}_Y = 0.066 \text{ g}$] can be seen for both the test structure and the finite element models. For both displacements and the rotation, the frequency contents of the response histories in the Abaqus and Drain-3DX simulations match the test data well. Also, as seen in Table 7.10, the maximum relative displacement in both directions of the Abaqus model match fairly well, agreeing to within 8% in both the X and Y directions. The Drain-3DX model is not as accurate, with differences of over 40% and 16% in the X and Y directions, respectively. For both the Abaqus and Drain-3DX models, the peak displacements appear to occur in the same time region for both the finite element model and the test structure. The peak rotation in the Abaqus model agrees to within 3% with the test data, but there are many locations during the time history where the local minimum and maximum do not match as well. The peak rotation in the Drain-3DX model agrees to within 20%. One problem with matching to the rotation data of the

test structure is that the response is low enough that noise from the data acquisition system is apparent in the data. As was observed in some of the previous configurations, the damping characteristics of the Abaqus and Drain-3DX models do not match as well with the test structure as does the frequency content. As discussed in previous chapters, the limitations of both finite element analysis models to allow the damping in each direction independently has resulted in a compromise damping ratio that attempts to minimize the lack of accuracy in each direction.

In Figures 7.28 – 7.31, the displacement and rotation response histories for EQ 23 [PGA_X = 1.299 g and PGA_Y = 0.797 g] can be seen for both the test structure and the finite element models. For both displacements and the rotation, the frequency contents of the response histories in the Abaqus and Drain-3DX simulations match the test data well. In both the X direction and Y direction, the magnitudes of the displacements also match very well. The Abaqus simulations predict smaller peak rotations at a number of points in the time history and a lesser degree of permanent deformation. As seen in Table 7.9, the Abaqus displacement in the X direction agrees to within 3%, while the peak displacement in the Y direction agrees to within 1%. The Abaqus peak rotation differs from the experimental peak rotation by approximately 30%. The Drain-3DX X-Axis peak displacement agrees to within 2%, the Y-Axis displacement agrees to within 20%, and the peak rotation to within 17%. Also important is the fact that the peak displacements appear to occur in the same time region for both the finite element models and the test structure. Although the Drain-3DX analysis predicts the peak X-Axis displacement as well as the Abaqus analysis, it does not match as well the test response after the peak displacement. Further, it predicts a permanent offset of approximately ¼-inch, while Abaqus correctly predicts the actual permanent offset of approximately 1-inch. The Drain-3DX analysis is more accurate than Abaqus in predicting the peak rotation, which is typically the most difficult response parameter to predict. However, both Abaqus and Drain-3DX are equally inaccurate in predicting the permanent rotation of the structure.

7.6 SUMMARY AND CONCLUSIONS

In the previous three chapters, the *Modified μ/R Ratio* was introduced and discussed. This ratio gives a measure of the amount of ductility the 2000 NEHRP Seismic Provisions expects a particular structure to experience and thus for which it must be designed. The *Modified μ/R Ratio* was computed as the normalized displacement in an inelastic test divided by the normalized

displacement during an elastic test and also as the ratio of the normalized rotation during an inelastic simulation to the normalized rotation during an elastic simulation. For EQ 23, the first and only inelastic simulation in this configuration, the μ/R Ratios were 1.60 in the X direction, 0.61 in the Y direction, and 1.90 torsionally. As with the values of the previous inelastic simulations, shown below, these values are not very consistent.

Configuration	EQ	μ/R Ratio		
		X-Axis	Y-Axis	Z-Axis
Symmetric Mass 100% Uniaxial	7	N/A	0.77	N/A
Symmetric Mass 100% Biaxial	15	1.37	0.86	0.84
Symmetric Mass 150% Biaxial	16	1.77	1.83	1.08
$\frac{1}{2}$ Asymmetric Mass 100% Biaxial	28	0.90	0.51	1.07
$\frac{1}{2}$ Asymmetric Mass 150% Biaxial	29	1.17	1.03	1.39
$\frac{1}{4}$ Asymmetric Mass 100% Biaxial	23	1.60	0.61	1.90

The *Seismic Provisions* provides a range of 0.86 to 0.69 for an Ordinary Moment Resisting Frame (OMRF) and a Special Moment Resisting Frame (SMRF), respectively. Thus, the μ/R Ratio appears to be more conservative for the Y direction but much less so for the X-Axis and torsional motion, which are roughly double those prescribed by the *Seismic Provisions*. In assessing the μ/R Ratio for the torsional motion, the classification of this configuration as *Torsionally Irregular* is significant. The dynamic amplification of torsion prescribed in the *Provisions* for a structure possessing a *Torsional Irregularity* or *Extreme Torsional Irregularity* could potentially mitigate the disparity between the Z-Axis μ/R Ratio for EQ 23 and those values prescribed by the *Provisions*. However, for degree of torsional irregularity present in this structural configuration, the dynamic amplification is roughly 5%, and therefore not a significant factor in the comparison. The pattern discussed in the previous chapter of the μ/R Ratio not being constant for differing test configurations, earthquake magnitudes, and component directions continues with the results from this configuration. In addition, it again appears to be generally larger than the range of μ/R Ratios prescribed by the 2000 NEHRP *Seismic Provisions*, in some cases significantly larger.

As discussed in the previous chapter, the methodology used in the *Seismic Provisions* of using an elastic analysis as the basis for determining inelastic response of structures implies that the ratio of the peak rotation to the peak lateral displacement and the ratio of the two peak lateral displacements remain constant for elastic and inelastic response. For EQ 22 in this test configuration, the u_Y/u_X ratio is 0.96, as shown below.

Configuration	EQ	u_Y/u_X	u_θ/u_X
Symmetric Mass 25% Biaxial	14	0.73	N/A
Symmetric Mass 100% Biaxial	15	0.43	N/A
Symmetric Mass 150% Biaxial	16	0.80	N/A
$\frac{1}{2}$ Asymmetric Mass 10% Biaxial	27	0.86	0.29
$\frac{1}{2}$ Asymmetric Mass 100% Biaxial	28	0.51	0.35
$\frac{1}{2}$ Asymmetric Mass 150% Biaxial	29	0.85	0.35
$\frac{1}{4}$ Asymmetric Mass 10% Biaxial	22	0.96	0.28
$\frac{1}{4}$ Asymmetric Mass 100% Biaxial	23	0.37	0.33

For EQ 23, the first inelastic simulation, the ratio drops to 0.37, a decrease of over 60%. This result is similar to that observed for EQ 15 and EQ 28, the initial inelastic simulations in the two previous configurations. As with EQ 15 and EQ 28, the X-Axis displacement ductility for EQ 23 is much larger than the Y-Axis ductility, by a factor of more than three. It again appears that due to the differences in the X- and Y-Axis ground motions, the structure in EQ 23, the initial inelastic simulation for this configuration, has yielded to a greater degree in the X direction than in the Y direction and thus has experienced a greater degree of stiffness reduction in the X direction. In the previous two configurations, it was observed that during the second, and larger, inelastic simulation the displacement ductility in the X and Y directions were proportionally similar to those observed during the elastic simulation. Unfortunately this observation cannot be confirmed for this configuration due to the lack of usable test results for the second inelastic simulation.

The trends observed for the torsional motion in the previous test configuration, with $\frac{1}{2}$ -mass asymmetry, appear to continue for this configuration, with $\frac{1}{4}$ -mass asymmetry. For EQ 22, the last elastic simulation, the u_θ/u_X ratio is 0.28. For EQ 23, the inelastic simulation, the u_θ/u_X ratio is about 0.33. Thus, the u_θ/u_X ratio is roughly 20% larger for the inelastic simulation than for the elastic simulation, which is consistent with the results observed in the previous configuration. The large “dip” in the u_Y/u_X ratio for EQ 23 does not appear to be present for the u_θ/u_X ratio. In the previous configuration, this was explained by the fact that with one-way asymmetry the torsion is produced primarily by the X-Axis lateral motion. Thus the u_θ and u_X displacements are much more tightly coupled than the u_Y and u_X displacements are. It appears that this tighter coupling is again present for this configuration, despite the presence of asymmetry along both axes. For this configuration, the X-Axis input ground motion has a peak acceleration and elastic spectral acceleration over 50% larger than for the Y-Axis. Thus, it appears that the X-Axis motion impacts the torsional displacement to a greater degree than the Y-Axis motion.

The general trends observed with the finite element analyses through the previous test configurations continue with Test Configuration 4. The time history analyses were generally accurate in their predictions of the experimental response. The peak displacements predicted by the Abaqus analysis of the elastic simulation were within 8% of the experimental data, which is relatively consistent with the accuracy of previous configurations, while the Drain-3DX predicted displacements were off by 40% and 16% in the X and Y directions. The Abaqus analysis was unusually accurate, to within 3%, in predicting the peak rotation, while the Drain-3DX analysis was within 20%. The Abaqus analysis of the inelastic simulation was equally accurate in predicting the peak displacements, to within 3% of the experimental responses. The Drain-3DX peak displacement predictions were off by up to 20%. In addition, the permanent displacement of approximately one-inch in the X direction is correctly predicted by Abaqus, while the Drain-3DX prediction is roughly $\frac{1}{4}$ -inch. The Abaqus analyses have consistently proved to be more accurate than the Drain-3DX analyses throughout the test configurations in predicting the inelastic peak displacements of the structure. In addition, Abaqus has consistently been accurate in predicting any permanent displacements, while Drain-3DX has consistently underestimated these values by a factor of 2-3. The one significant liability with the Abaqus analyses has been the prediction of the peak rotation, and that trend continues here with a difference of roughly 30%. Drain-3DX has proven to be noticeably more accurate in predicting the peak rotation, in this case with a difference of 17% from the actual response.

Mass [lb*s ² /in]	Mass Centers [in]			Column Properties	
	X ₀	Y ₀	Z ₀	A [in ²]	I [in ⁴]
90.141	-15.201	15.201	67.479	4.41	9.61

	Modal Frequencies [Hz]			Modal Damping [%]		
	X	Y	θ	X	Y	θ
Before EQ 18	3.546	3.283	8.287	0.525	1.290	0.580
After EQ 23	3.515	3.383	8.356	2.750	2.853	0.618

Table 7.1 Test Structure Dynamic Properties - Test Configuration 3

Test Designation	Input Motions
WNT13	White Noise X-Axis
WNT14	White Noise Y-Axis
WNT15	White Noise Yaw-Axis
SIN7	Sine Decay X-Axis
SIN8	Sine Decay Y-Axis
SIN9	Sine Decay Yaw-Axis
SWP7	Sine Sweep X-Axis
SWP8	Sine Sweep Y-Axis
SWP9	Sine Sweep Yaw-Axis
EQ18	10% X-Axis Imperial Valley
EQ19	10% Y-Axis Imperial Valley
EQ20	10% Biaxial Imperial Valley
EQ21	10% Biaxial Imperial Valley
EQ22	10% Biaxial Imperial Valley
EQ23	100% Biaxial Imperial Valley
WNT16	White Noise X-Axis
WNT17	White Noise Y-Axis
WNT18	White Noise Yaw-Axis
EQ24	150% Biaxial Imperial Valley

Table 7.2 Earthquake Simulations and Dynamic Characterization Tests - Test Configuration 3

Earthquake Test No.	Input Motions	PGA [g]			Relative Displacement [in]			Rotation [10^{-3} rad]	Normalized Displacement [in/g]			Ductility		
		X-Axis	Y-Axis	Z-Axis	X-Axis	Y-Axis	Z-Axis		X-Axis	Y-Axis	Z-Axis	X-Axis	Y-Axis	Z-Axis
18	10% X-Axis	0.102	N/A	0.180	0.107	0.80	1.76	N/A	0.39	0.20	0.12			
19	10% Y-Axis	N/A	0.064	0.043	0.113	0.72	N/A	1.77	0.09	0.21	0.11			
22	10% Biaxial	0.109	0.066	0.165	0.152	1.06	1.51	2.30	0.35	0.29	0.16			
23	100% Biaxial	1.299	0.797	3.171	1.177	21.94	2.44	1.48	6.80	2.22	3.23			

Table 7.3 Maximum Diaphragm Relative Displacement and Rotation - Test Configuration 3

Earthquake Test No.	Input Motions	PGA [g]			Diaphragm Acceleration [g]			Diaphragm Angular Acceleration [10^{-3} g/in]			Normalized Acceleration
		X-Axis	Y-Axis	Z-Axis	X-Axis	Y-Axis	Z-Axis	X-Axis	Y-Axis	Z-Axis	
18	10% X-Axis	0.102	N/A	0.240	0.175		1.701			2.35	N/A
19	10% Y-Axis	N/A	0.064	0.057	0.122		1.250			N/A	1.91
22	10% Biaxial	0.109	0.066	0.223	0.209		2.136			2.05	3.17
23	100% Biaxial	1.299	0.797	1.146	0.938		14.819			0.88	1.18

Table 7.4 Maximum Diaphragm Acceleration and Angular Acceleration Response - Test Configuration 3

Earthquake Test No.	Input Motions	PGA [g]			Base Shear [k]	Torsional Moment [k*in]	Overturning Moment [k*in]
		X-Axis	Y-Axis	Z-Axis			
18	10% X-Axis	0.102	N/A	8.44	4.49	140.44	572.4
19	10% Y-Axis	N/A	0.064	1.92	4.55	118.56	130.3
22	10% Biaxial	0.109	0.066	7.81	6.78	184.95	529.2
23	100% Biaxial	1.299	0.797	36.67	31.05	960.34	2486.6
							2105.5

Table 7.5 Maximum Base Shear, Torsional Moment, and Overturning Moment - Test Configuration 3

Earthquake Test No.	Input Motions	PGA [g]		Column End Moments [K*in]							
				SE Column		SW Column		NW Column		NE Column	
		X-Axis	Y-Axis	X-Axis	Y-Axis	X-Axis	Y-Axis	X-Axis	Y-Axis	X-Axis	Y-Axis
18	10% X-Axis	0.102	N/A	37.35	71.15	37.35	55.61	37.13	55.61	37.13	71.15
19	10% Y-Axis	N/A	0.064	26.39	20.94	26.39	10.32	43.11	10.32	43.11	20.94
22	10% Biaxial	0.109	0.066	50.28	68.83	50.28	49.41	54.10	49.41	54.10	68.83
23	100% Biaxial	1.299	0.797	215.63	318.20	215.63	251.17	264.02	251.17	264.02	318.20

Table 7.6 Maximum Column End Moments - Test Configuration 3

Earthquake Test No.	Input Motions	PGA [g]						Column End Shears [k]											
		X-Axis		Y-Axis		SE Column		SW Column		X-Axis		Y-Axis		NW Column		X-Axis		Y-Axis	
		X-Axis	Y-Axis	X-Axis	Y-Axis	X-Axis	Y-Axis	X-Axis	Y-Axis	X-Axis	Y-Axis	X-Axis	Y-Axis	X-Axis	Y-Axis	X-Axis	Y-Axis	X-Axis	Y-Axis
18	10% X-Axis	0.102	N/A	2.37	1.25	1.85	1.25	1.85	1.24	1.24	1.24	1.24	2.37	1.24	2.37	1.24	1.24	1.24	1.24
19	10% Y-Axis	N/A	0.064	0.70	0.88	0.34	0.88	0.34	0.34	1.44	1.44	0.70	0.70	1.44	1.44	0.70	0.70	1.44	1.44
22	10% Biaxial	0.109	0.066	2.29	1.68	1.65	1.68	1.68	1.65	1.65	1.65	1.80	1.80	2.29	1.80	2.29	1.80	2.29	1.80
23	100% Biaxial	1.299	0.797	10.61	7.19	8.37	7.19	8.37	7.19	8.37	8.37	8.80	10.61	8.80	10.61	8.80	10.61	8.80	10.61

Table 7.7 Maximum Column End Shears - Test Configuration 3

E [ksi] = 29000.0

Stress [ksi]	Strain [in/in]	Plastic Strain [in/in]
0.00000	0.00000	
37.50000	0.00108	0.000000
39.60000	0.00300	0.001863
40.70000	0.00500	0.003831
49.00000	0.02000	0.018593
54.00000	0.04000	0.038449
56.50000	0.06000	0.058378
57.80000	0.08000	0.078340
58.50000	0.10000	0.098320
59.00000	0.15000	0.148306
57.00000	0.20000	0.198363

Table 7.8 Stress-Strain Best-Fit Material Model - Test Configuration 3

E [ksi] = 29000.0

Stress [ksi]	Strain [in/in]
0.00000	0.00000
37.50000	0.001293
39.60000	0.003000
49.00000	0.020000
56.50000	0.060000
58.50000	0.100000

Table 7.9 Drain-3DX Stress-Strain Best-Fit Material Model - Test Configuration 3

Earthquake Test No.	Input Motions	Relative Displacement [in]						Rotation [10^{-3} rad]				
		PGA [g]		X-Axis		Y-Axis		Abaqus		Drain		
		X-Axis	Y-Axis	Abaqus	Drain	Test	Abaqus	Drain	Test	Abaqus	Drain	Test
22	10% Biaxial	0.109	0.066	0.179	0.230	0.165	0.174	0.186	0.152	0.94	1.17	1.06
23	100% Biaxial	1.299	0.797	3.07	3.21	3.17	1.20	1.43	1.18	14.94	18.40	21.94

Table 7.10 Analytical vs. Experimental Displacement and Rotation Response Comparison - Test Configuration 3

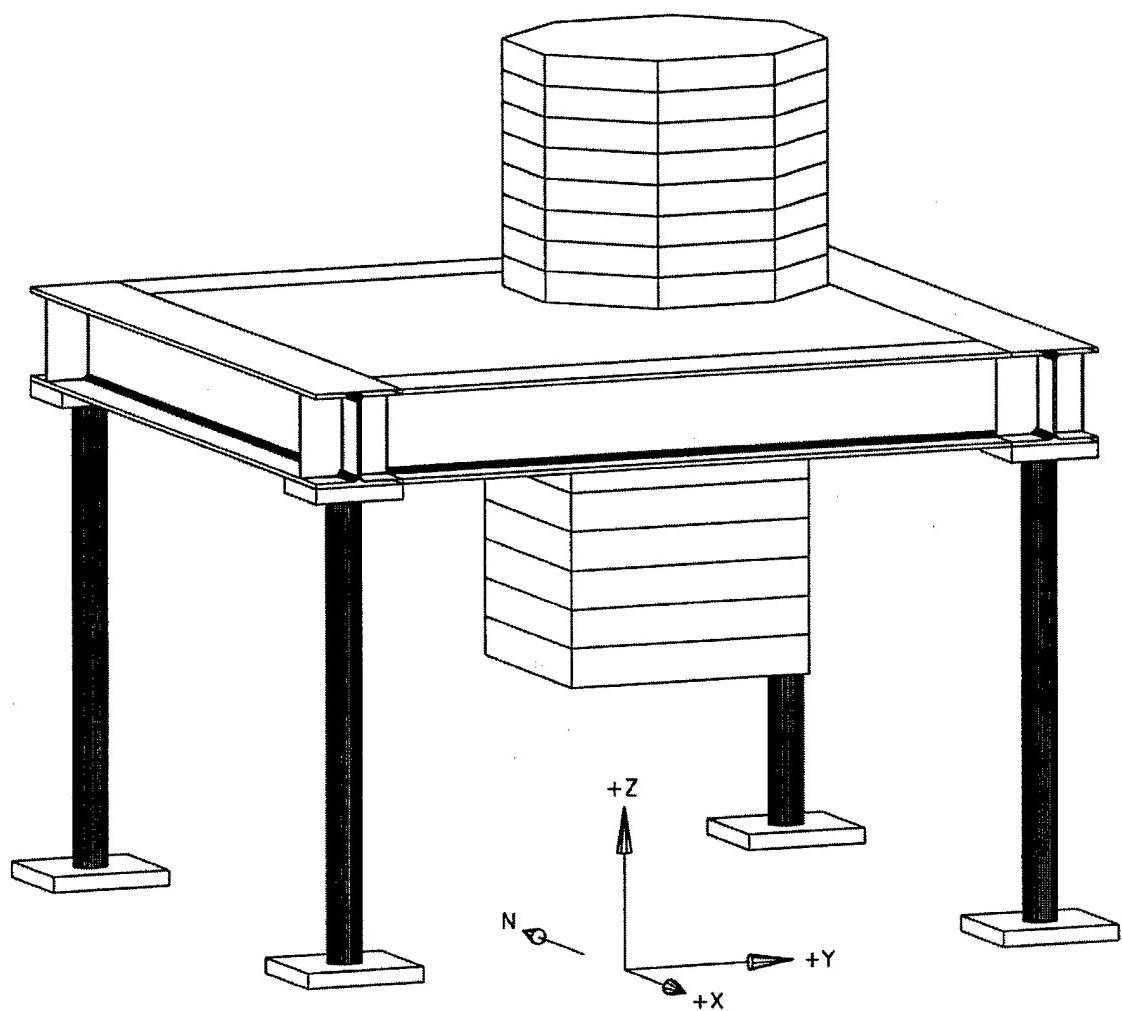


Figure 7.1 Perspective View of Test Configuration Model 3
4 - 4" Extra-Strong Columns

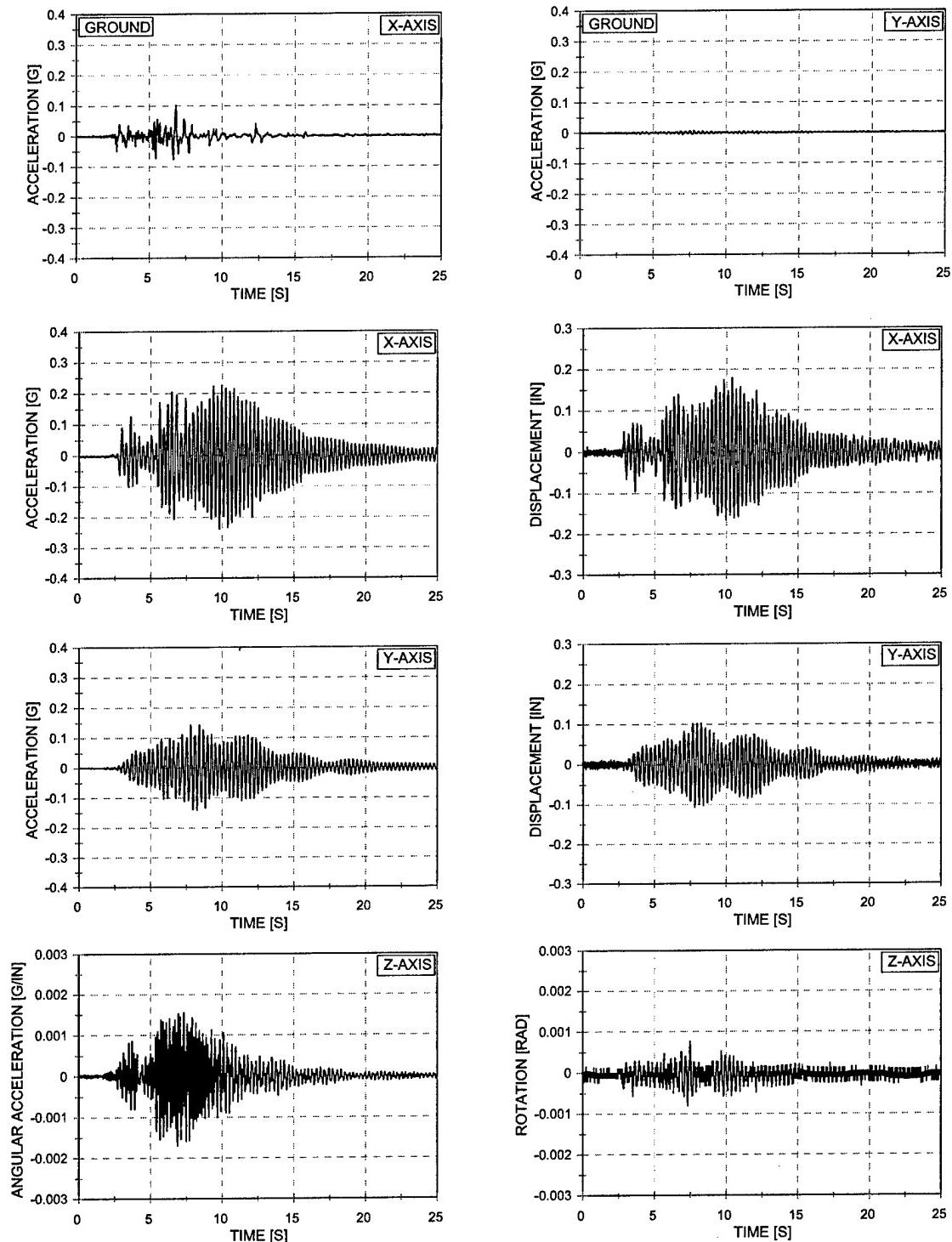


Figure 7.2. Acceleration and Displacement vs. Time – EQ 18
 10% X-Axis Imperial Valley – 1/4 Asymmetric Mass
 Four 4" Extra-Strong Columns

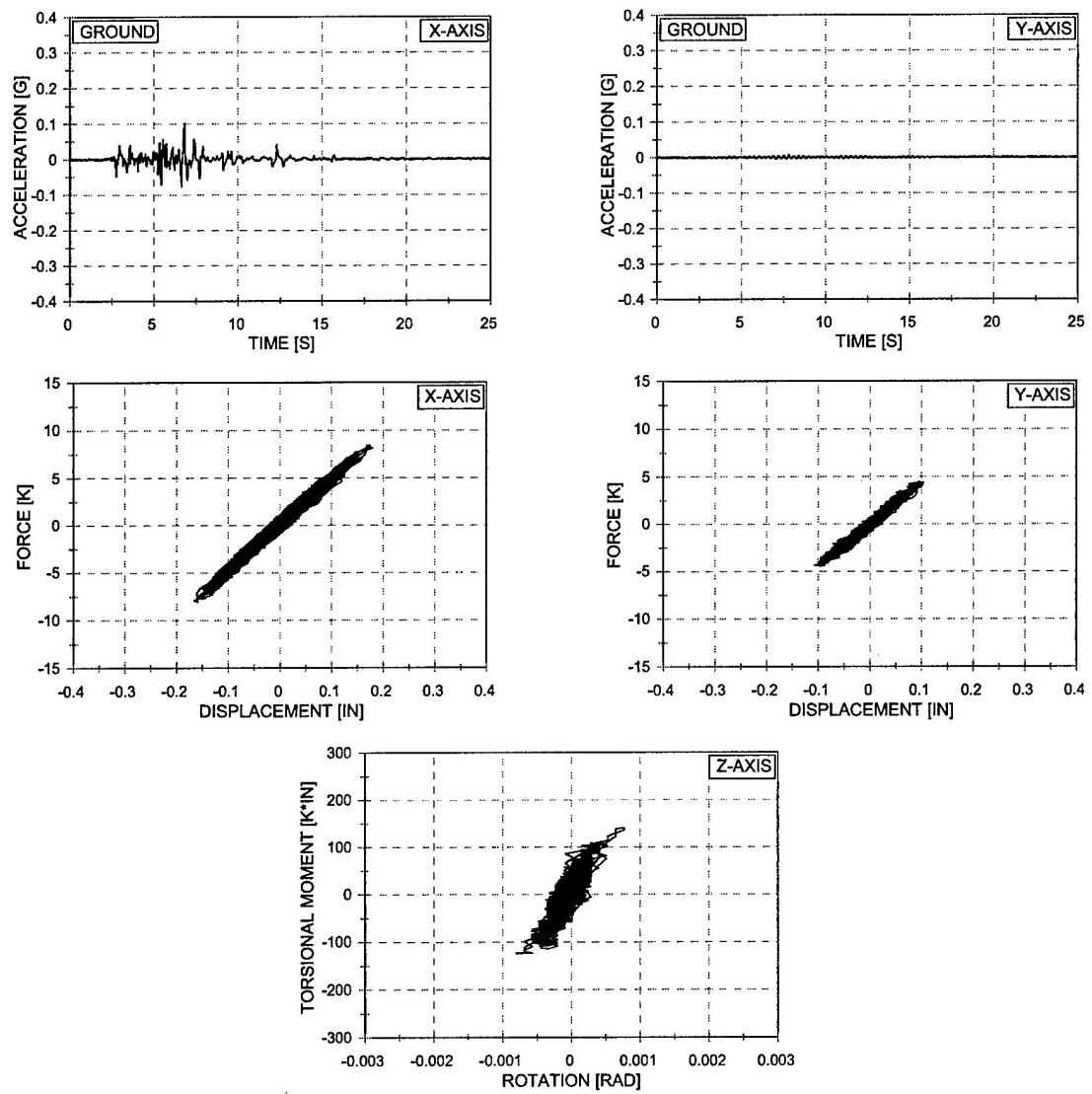


Figure 7.3. Force vs. Displacement and Torsional Moment vs. Rotation – EQ 18
 10% X-Axis Imperial Valley – 1/4 Asymmetric Mass
 Four 4" Extra-Strong Columns

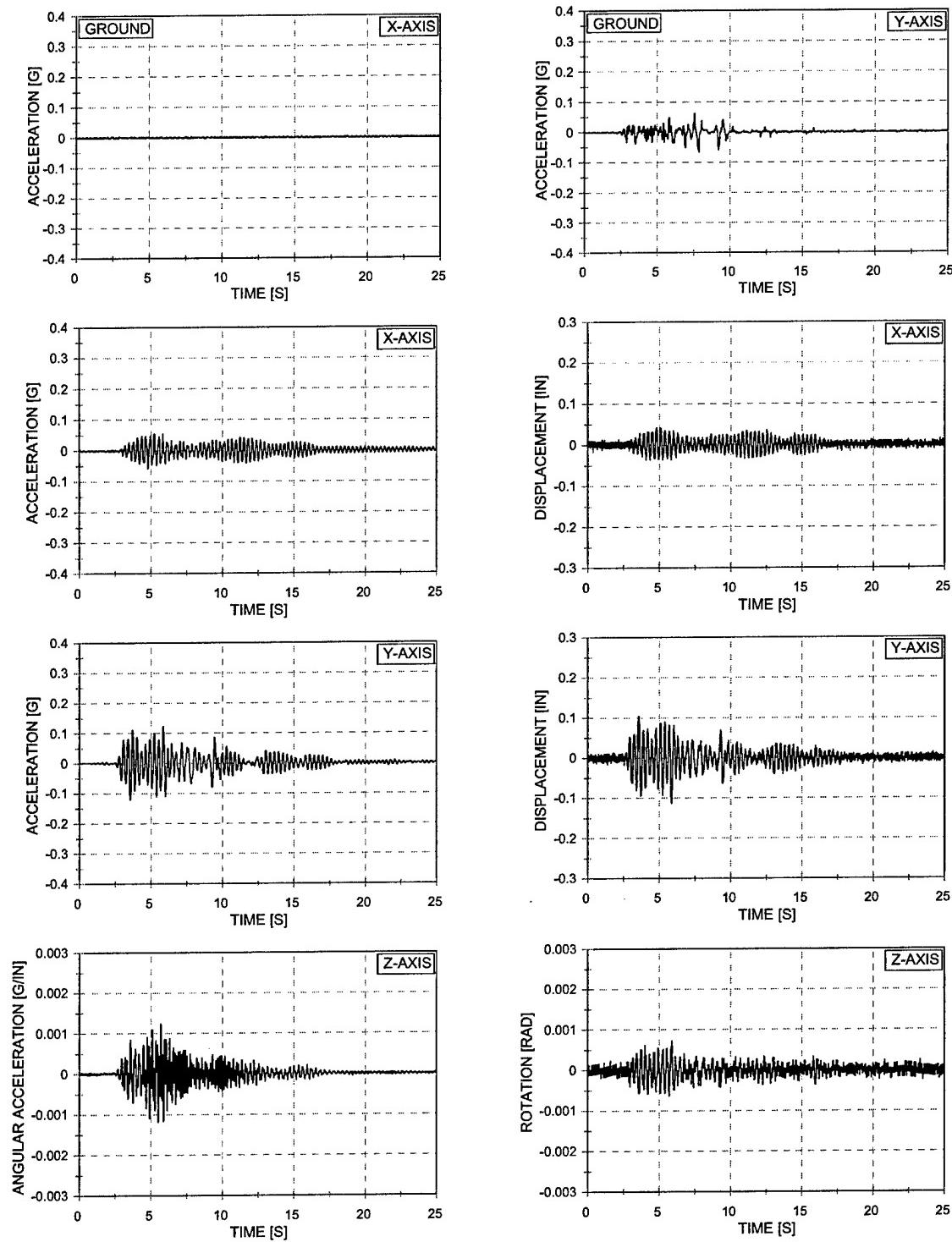


Figure 7.4. Acceleration and Displacement vs. Time – EQ 19
 10% Y-Axis Imperial Valley – 1/4 Asymmetric Mass
 Four 4" Extra-Strong Columns

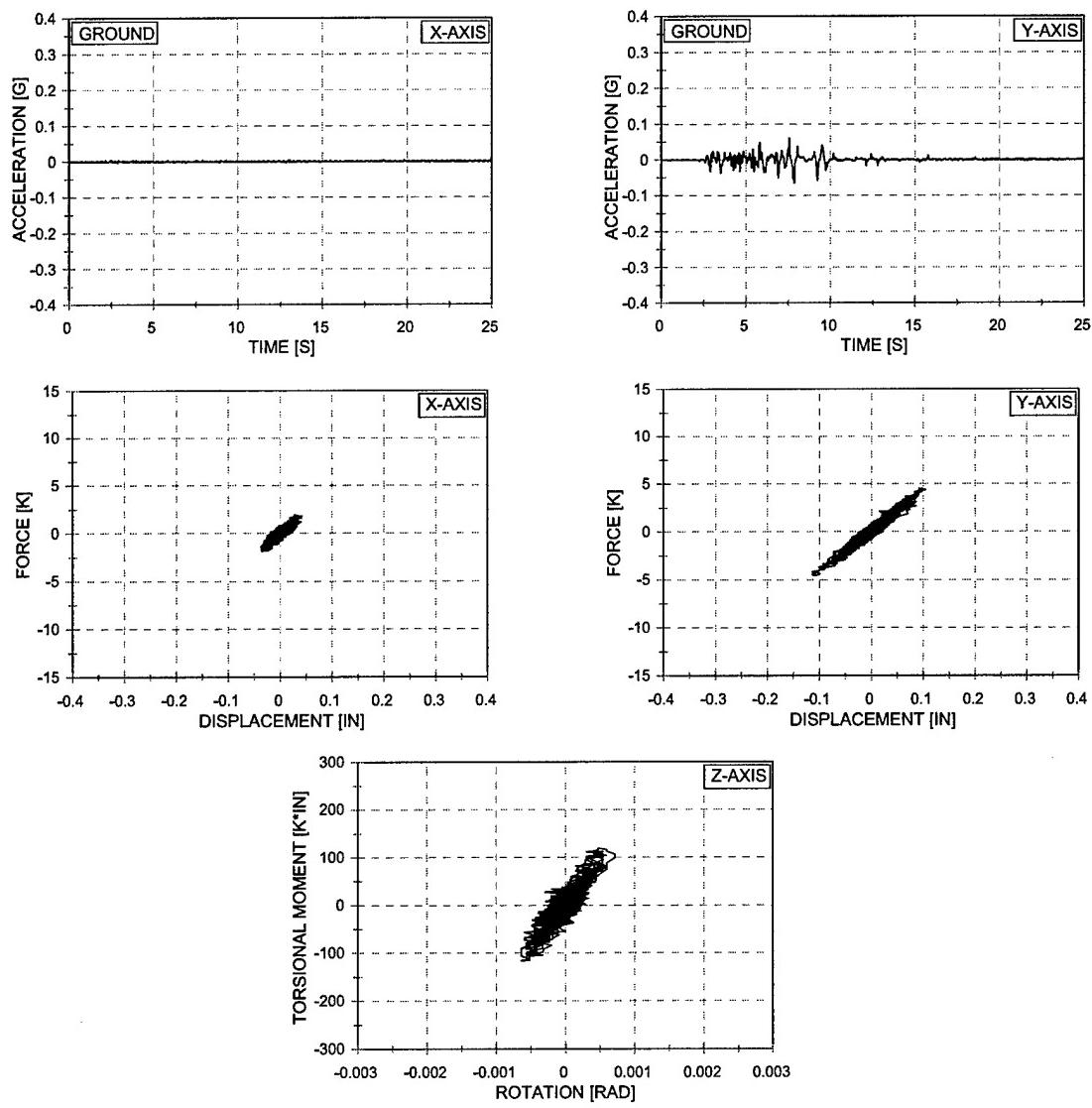


Figure 7.5. Force vs. Displacement and Torsional Moment vs. Rotation - EQ 19
 10% Y-Axis Imperial Valley – 1/4 Asymmetric Mass
 Four 4" Extra-Strong Columns

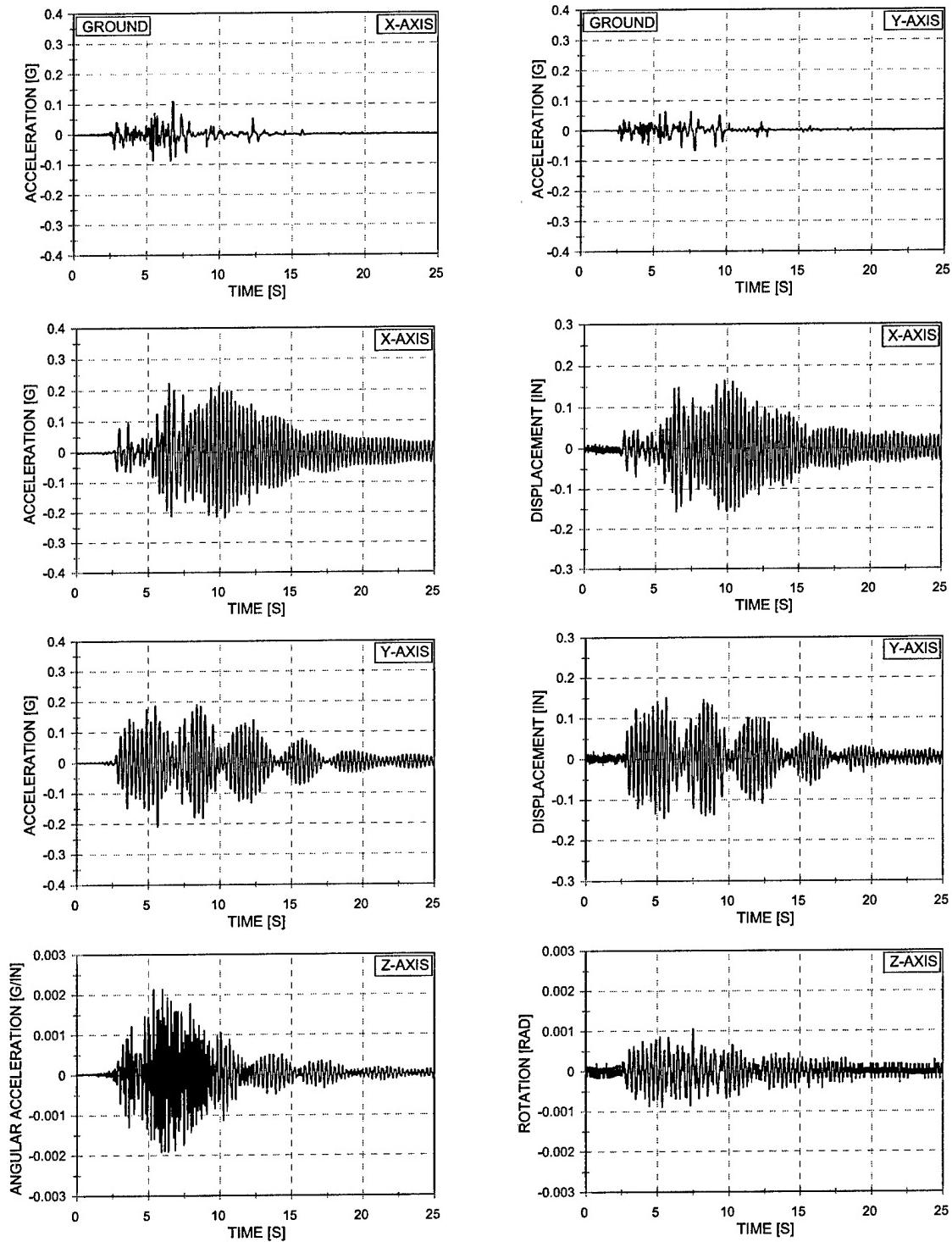


Figure 7.6. Acceleration and Displacement vs. Time – EQ 22
 10% Biaxial Imperial Valley – 1/4 Asymmetric Mass
 Four 4" Extra-Strong Columns

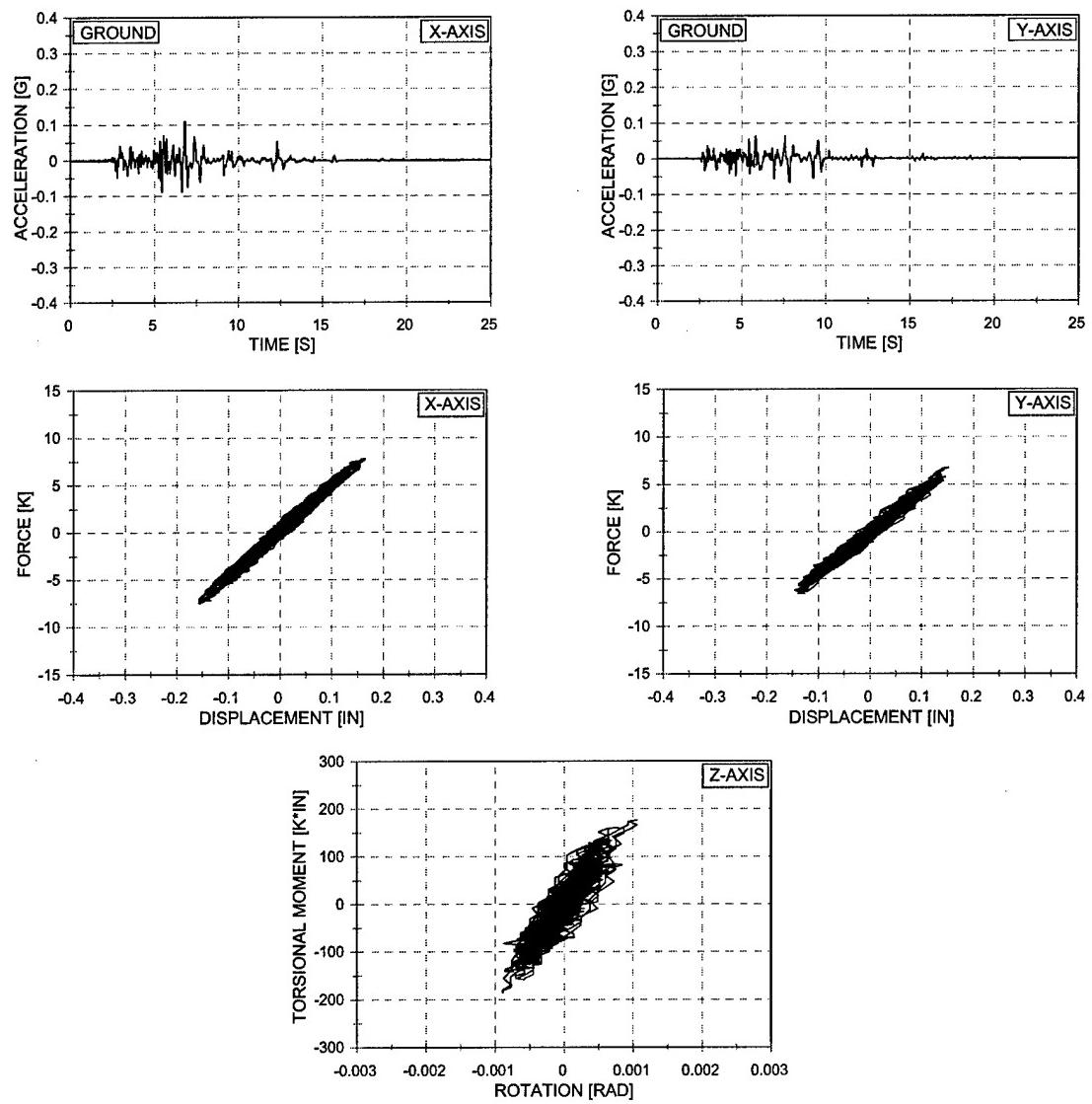


Figure 7.7. Force vs. Displacement and Torsional Moment vs. Rotation - EQ 22
 10% Biaxial Imperial Valley – 1/4 Asymmetric Mass
 Four 4" Extra-Strong Columns

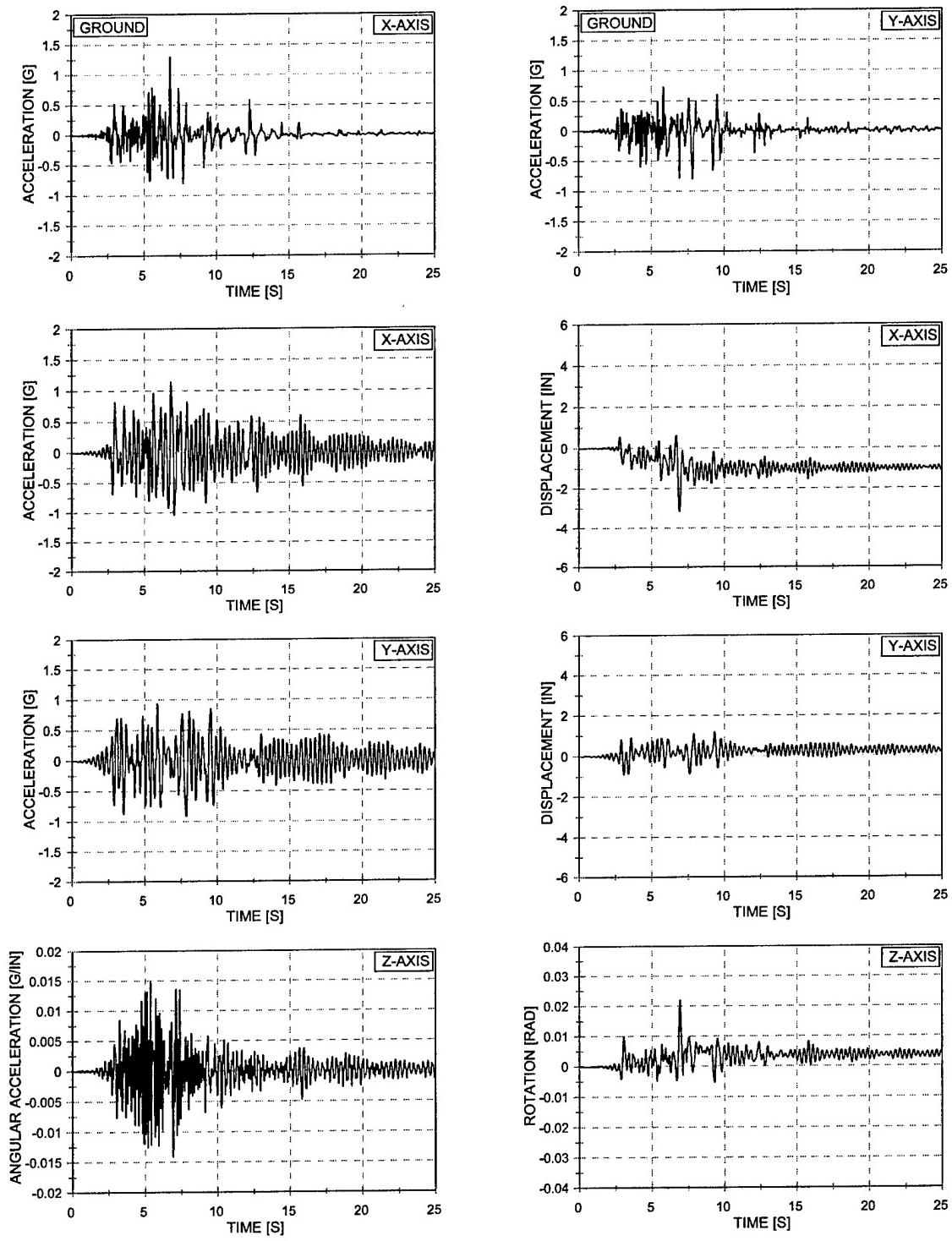


Figure 7.8. Acceleration and Displacement vs. Time – EQ 23
 100% Biaxial Imperial Valley – 1/4 Asymmetric Mass
 Four 4" Extra-Strong Columns

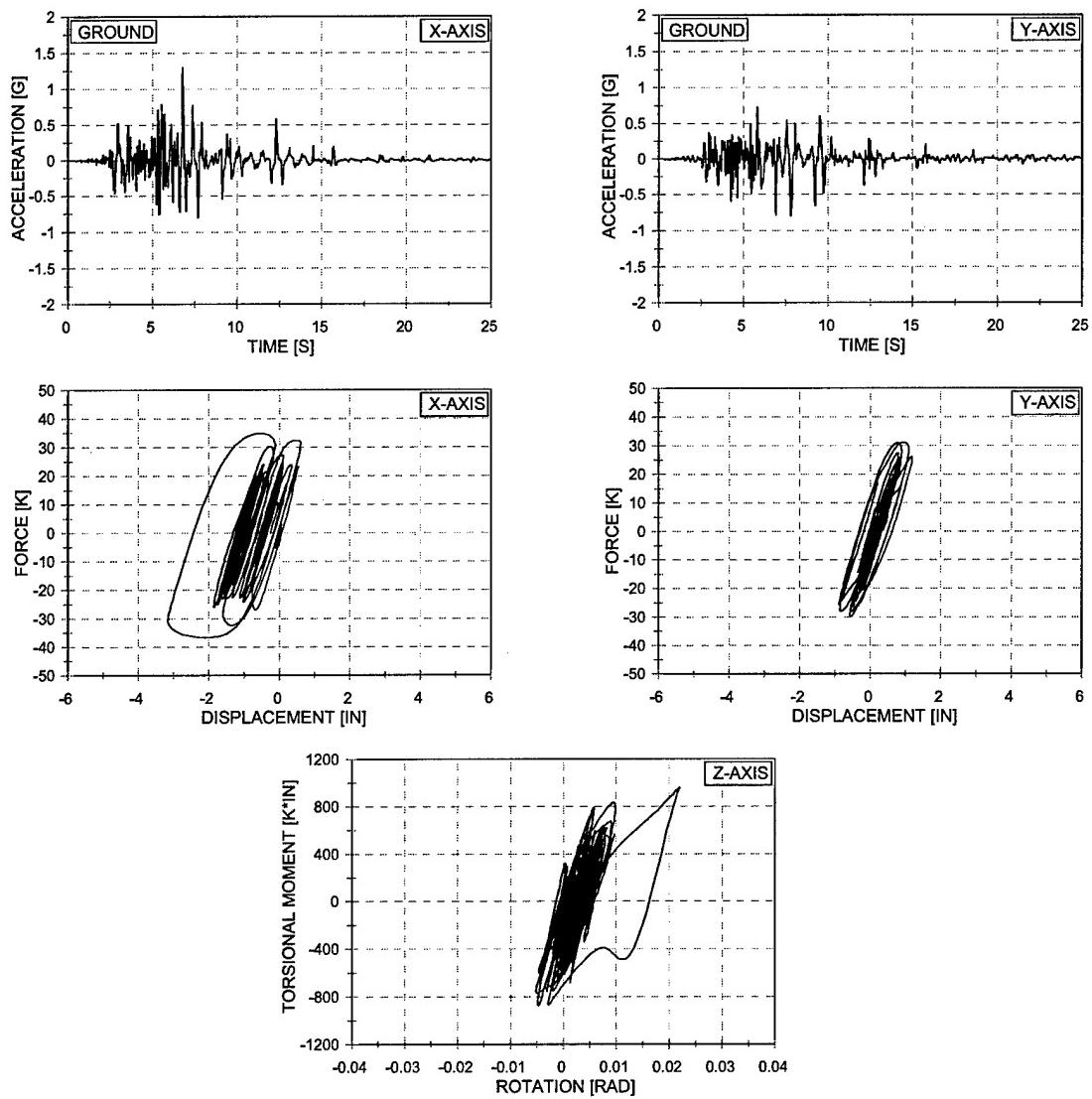


Figure 7.9. Force vs. Displacement and Torsional Moment vs. Rotation - EQ 23
 100% Biaxial Imperial Valley – 1/4 Asymmetric Mass
 Four 4" Extra-Strong Columns

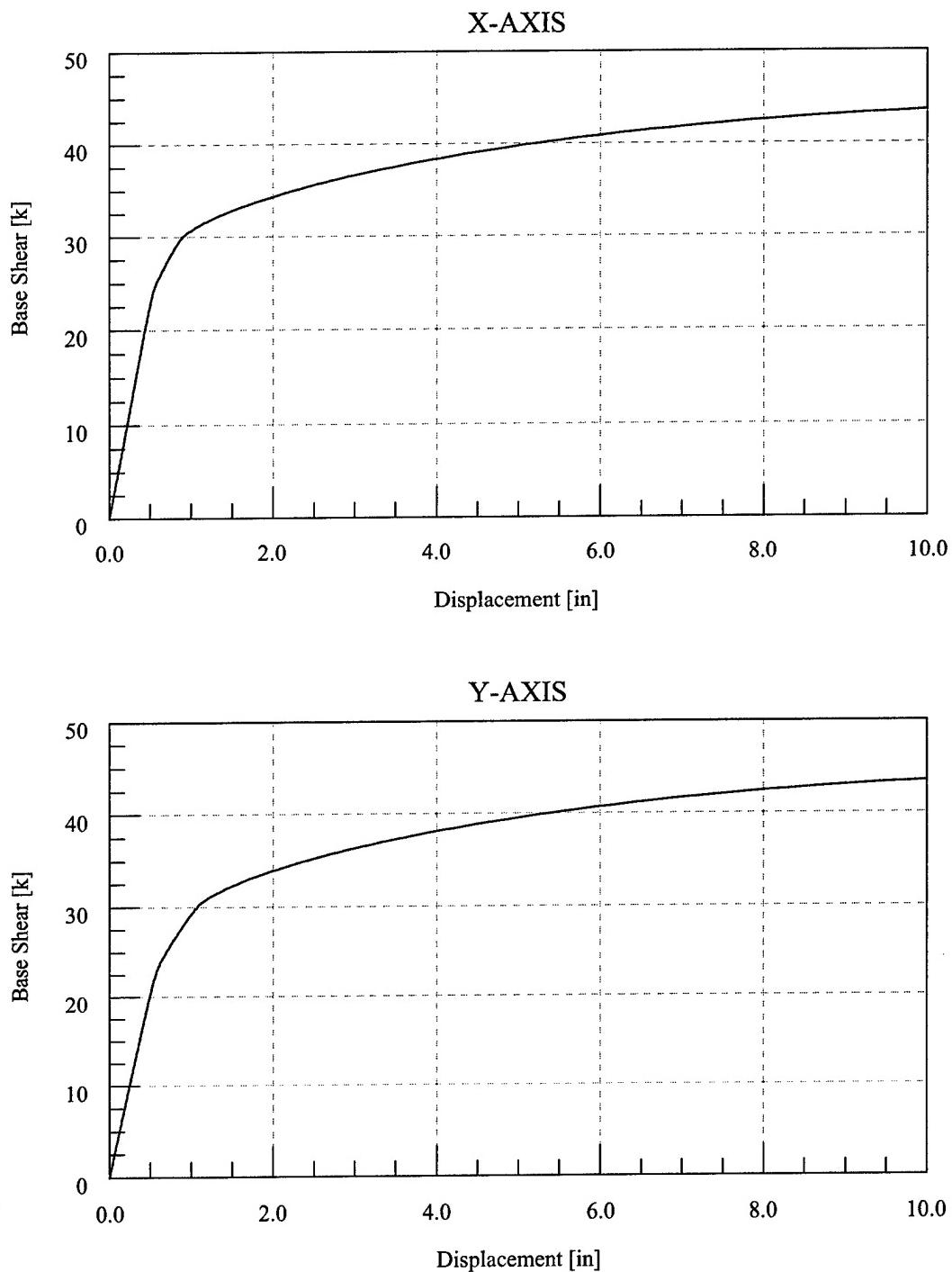


Figure 7.10 Force-Deformation Response – Test Configuration 3

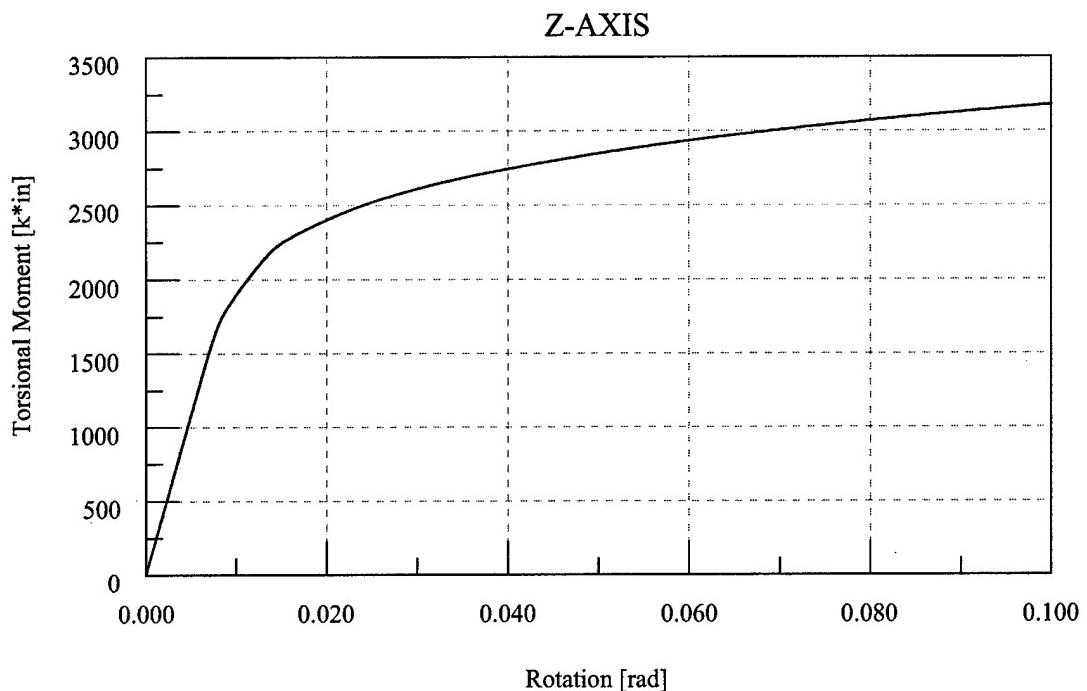


Figure 7.11 Torsional Moment-Rotation Response – Test Configuration 3

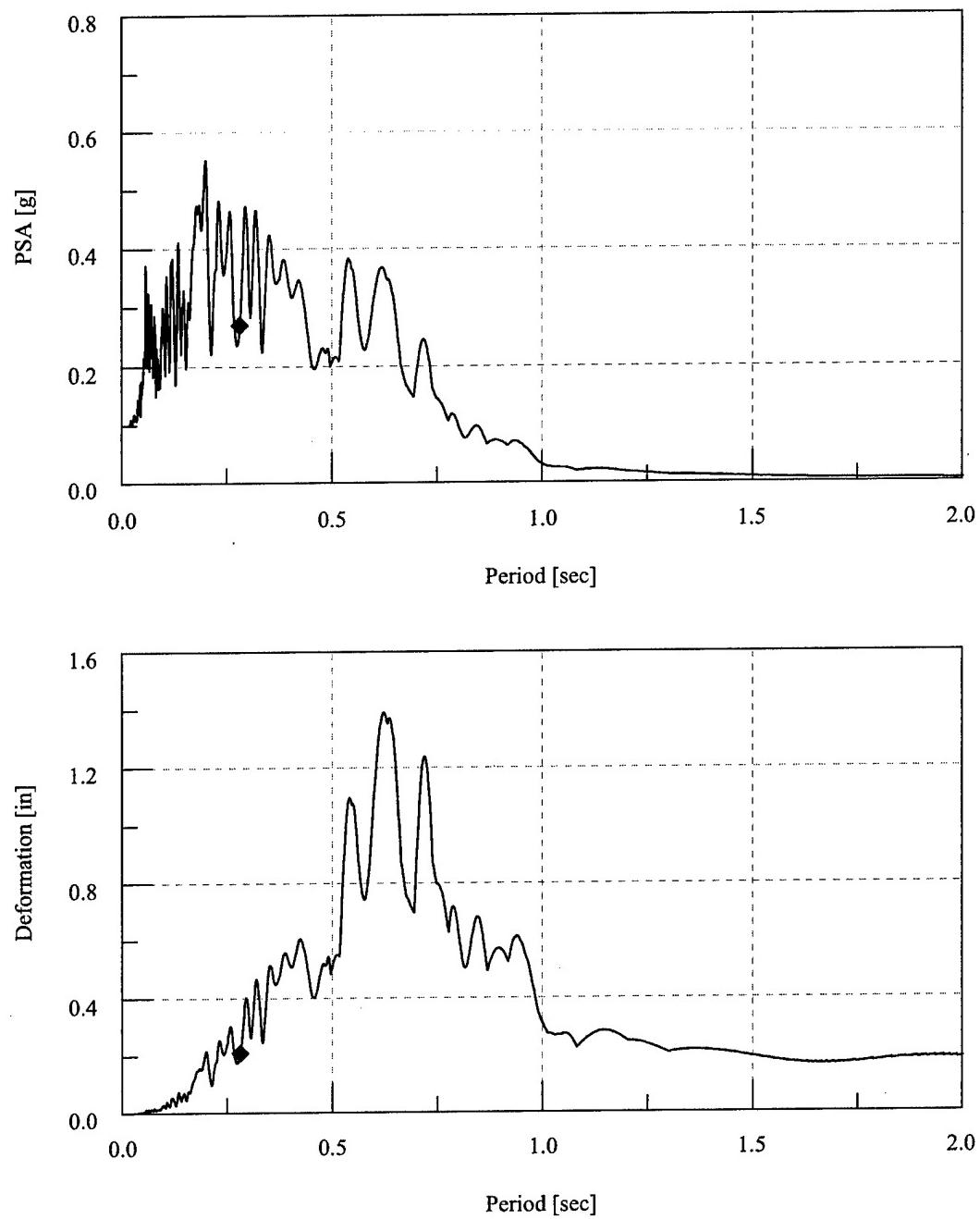


Figure 7.12 Elastic Response Spectra – EQ 18 – 10% X-Axis Imperial Valley Ground Motion

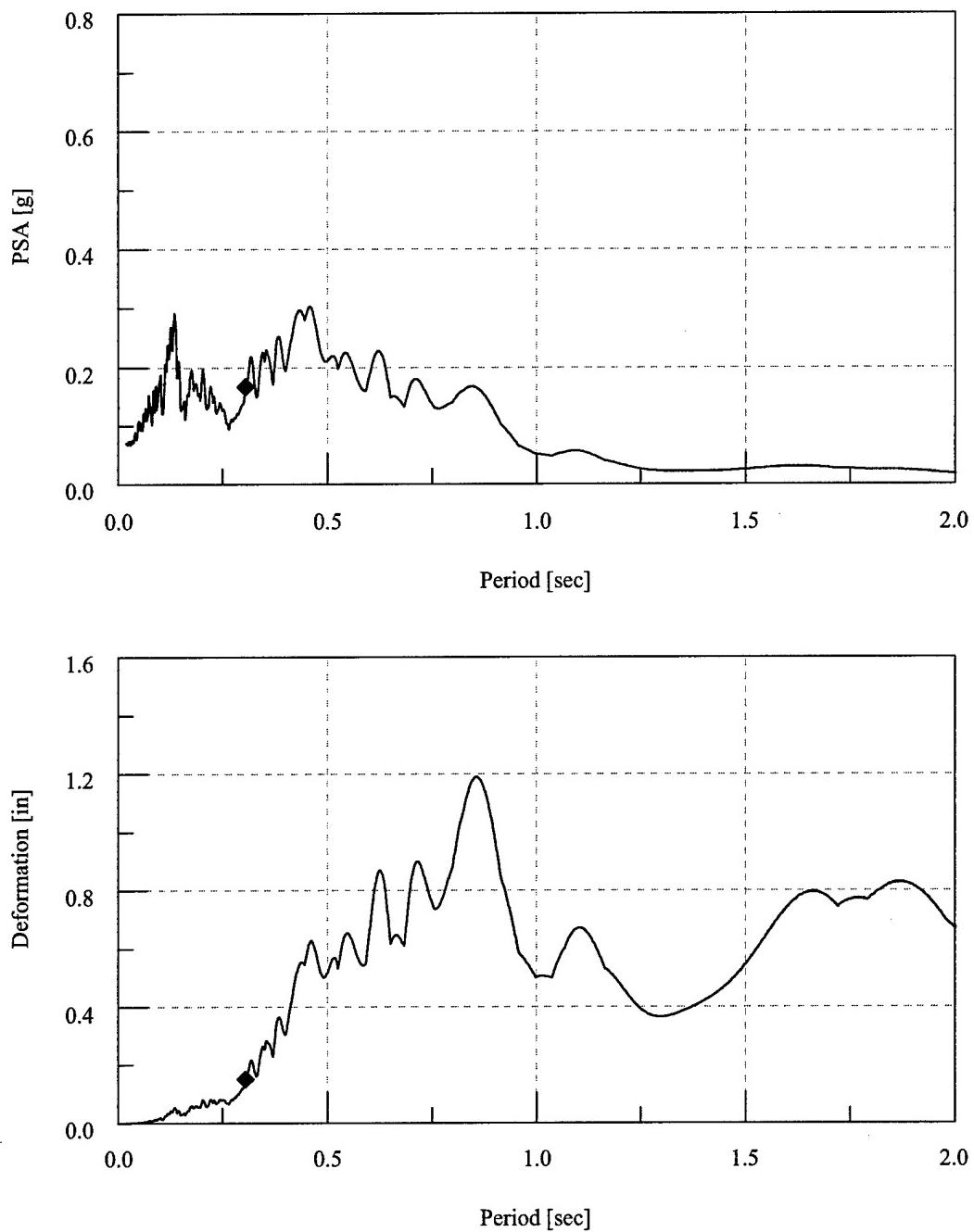


Figure 7.13 Elastic Response Spectra – EQ 19 – 10% Y-Axis Imperial Valley Ground Motion

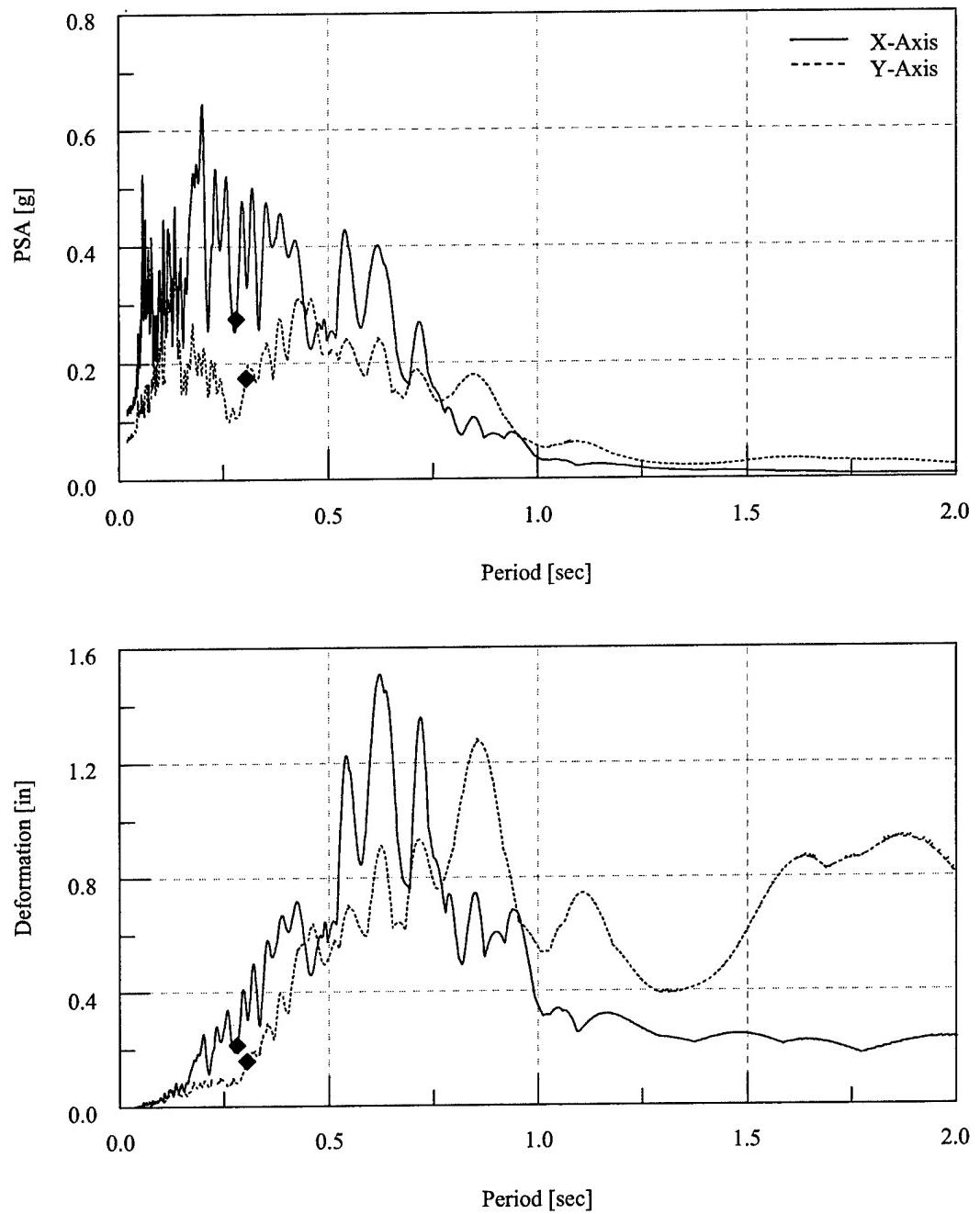


Figure 7.14 Elastic Response Spectra – EQ 22 – 10% Biaxial Imperial Valley Ground Motion

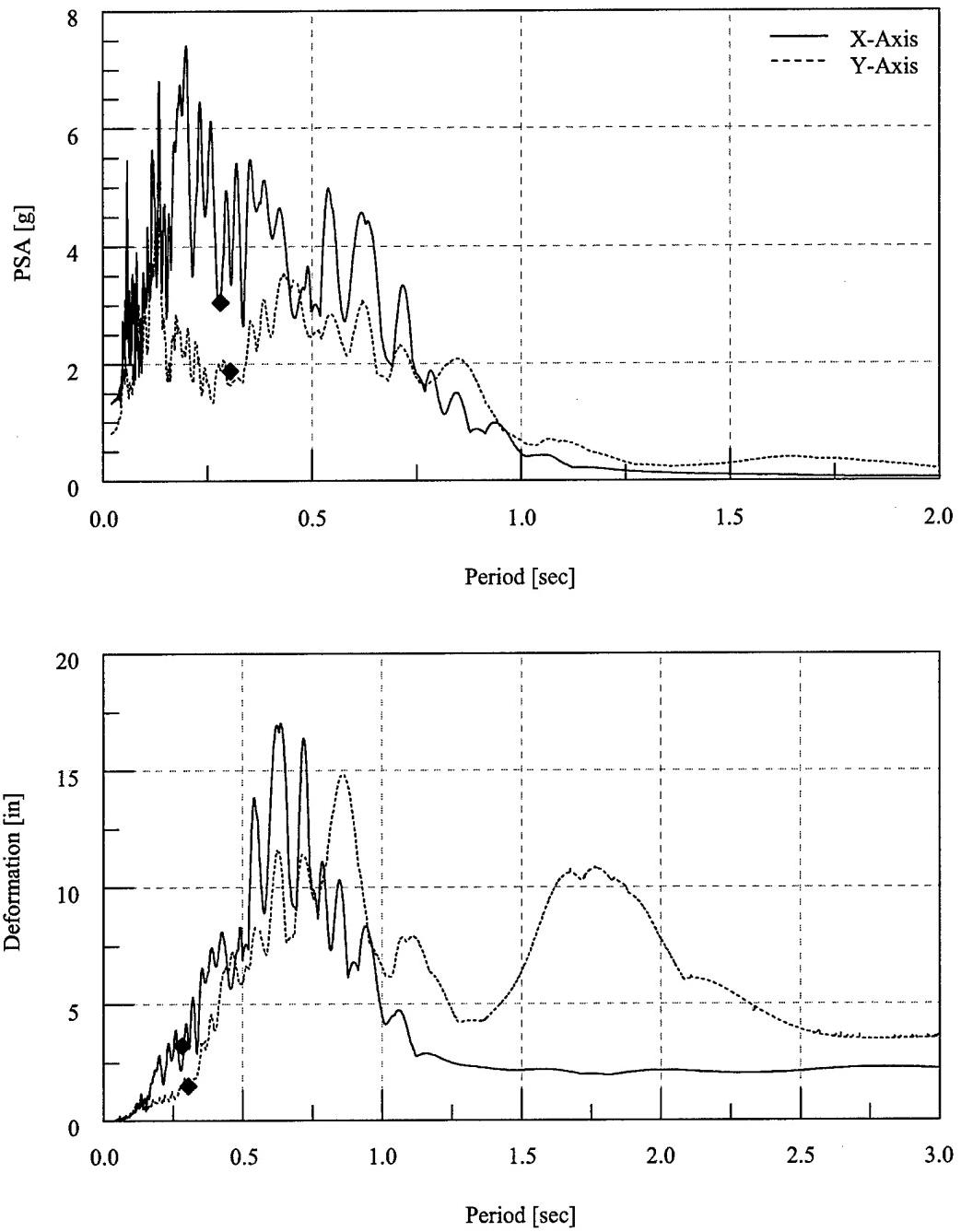


Figure 7.15 Elastic Response Spectra – EQ 23 – 100% Biaxial Imperial Valley Ground Motion

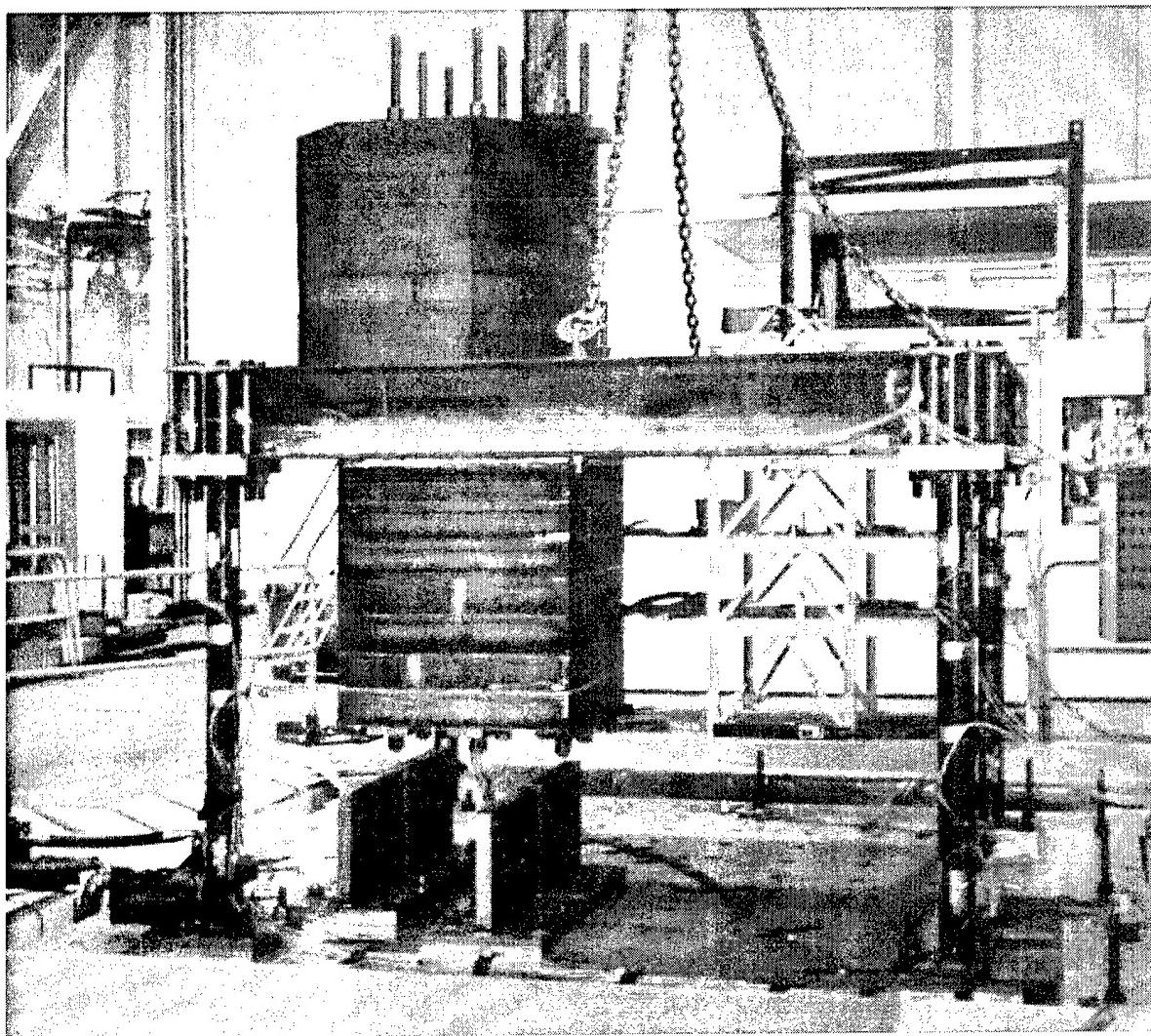


Figure 7.16 Test Structure Prior to Earthquake Simulations

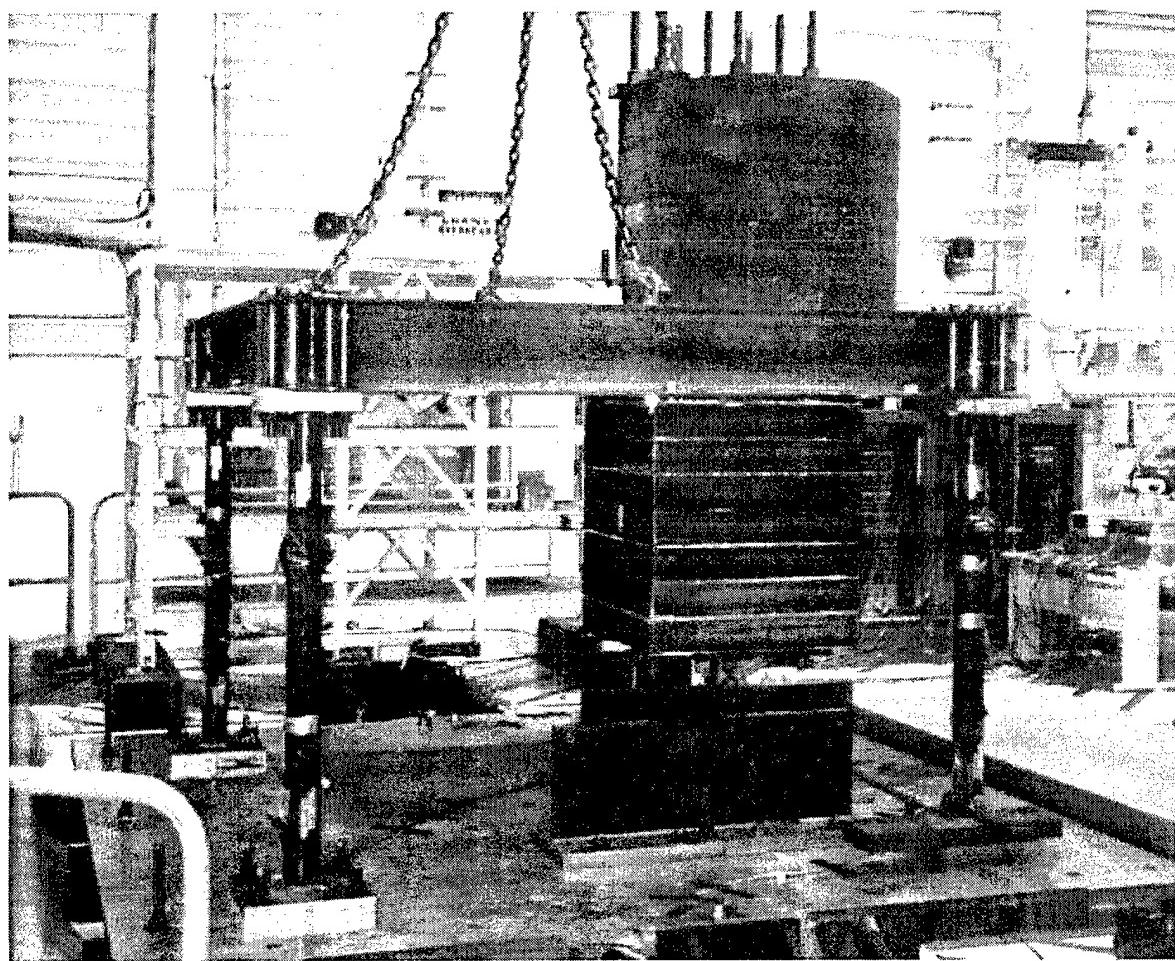


Figure 7.17 Test Structure Prior to Earthquake Simulations

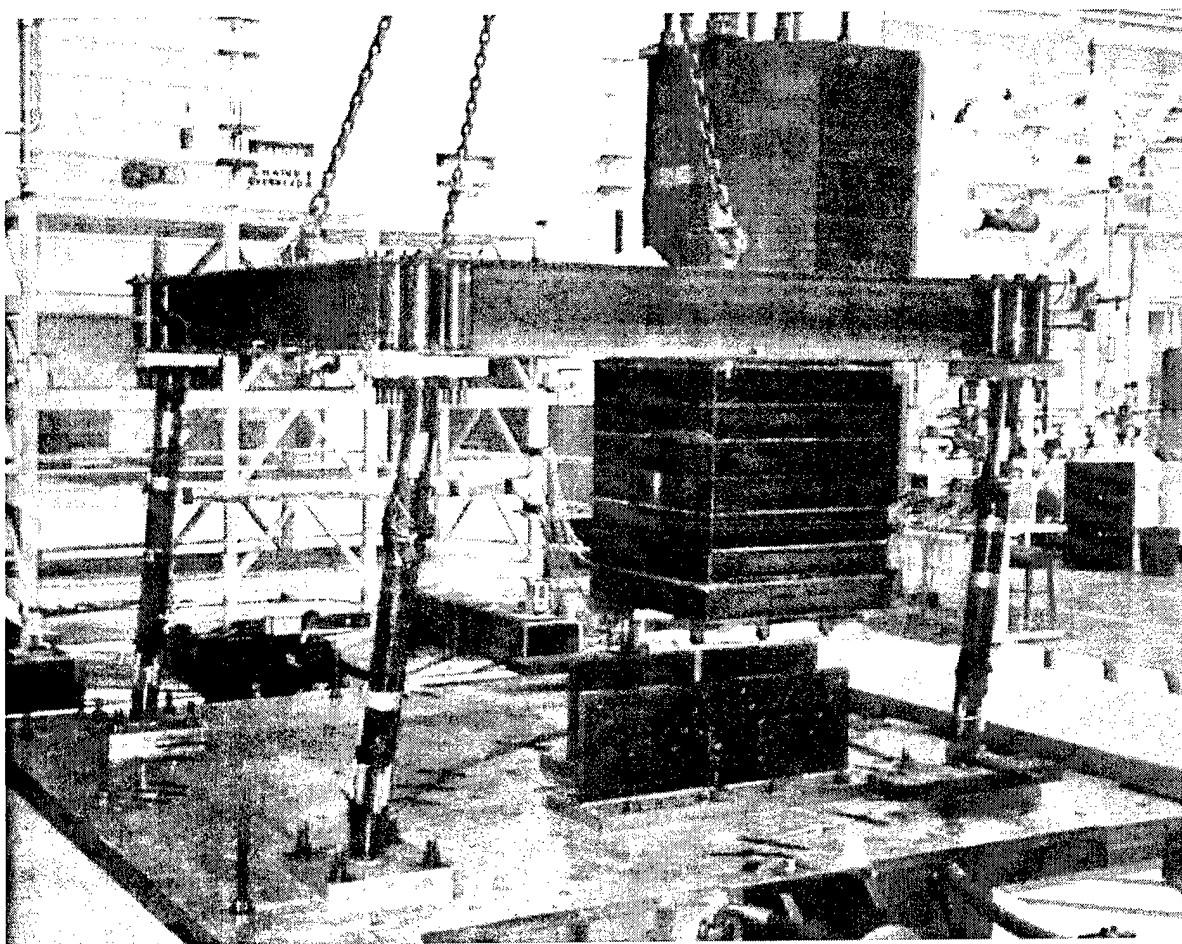


Figure 7.18 Test Structure After Earthquake Simulations

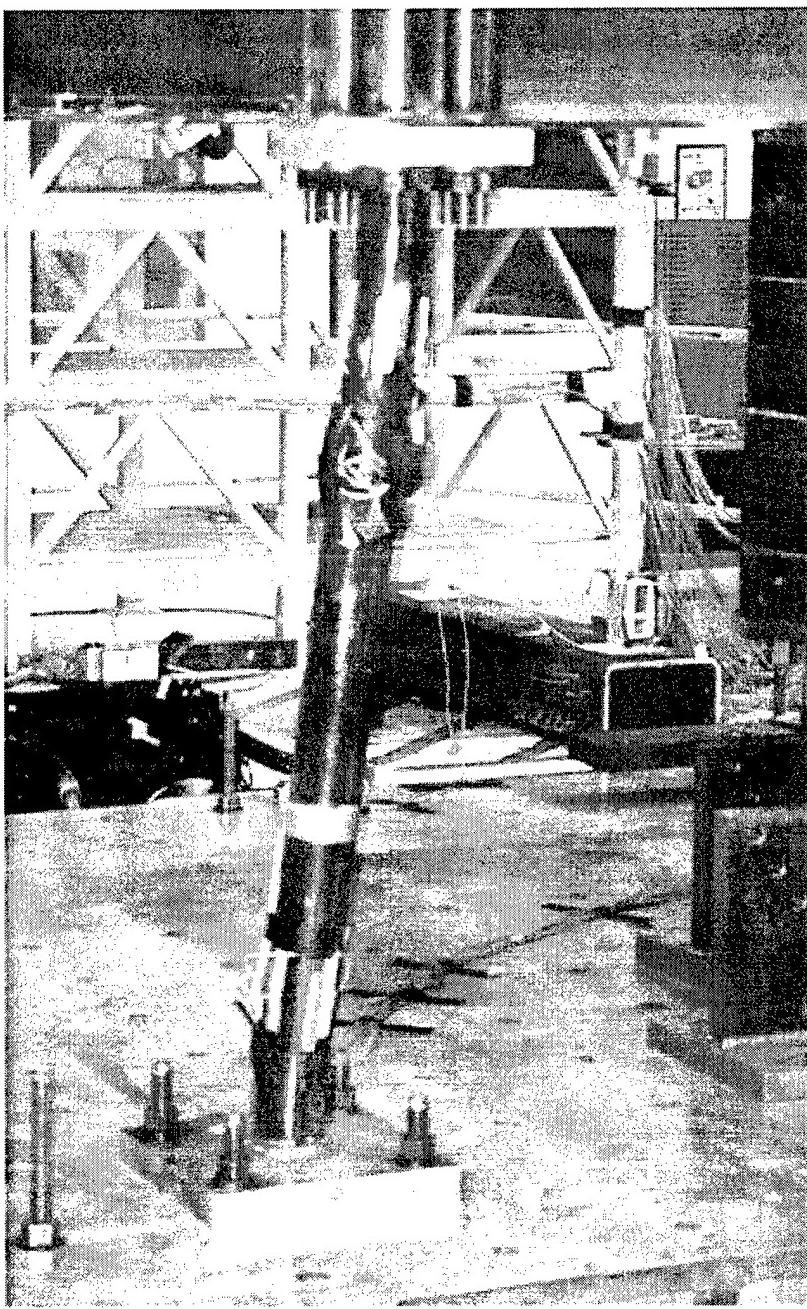


Figure 7.19 Test Structure Southeast Column After Earthquake Simulations

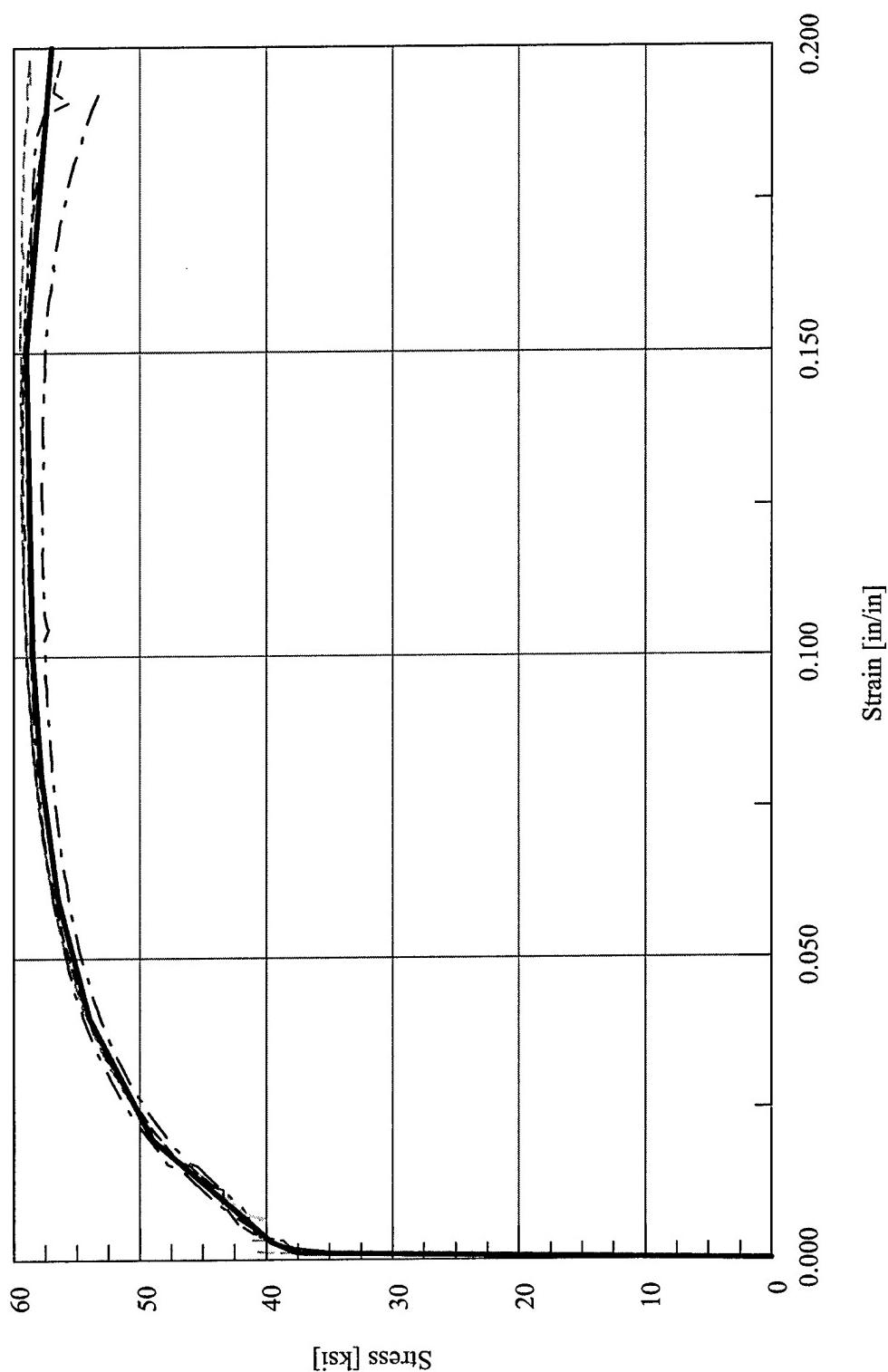


Figure 7.20 Abaqus Stress vs. Strain Finite Element Material Model Definition – Test Configuration 3

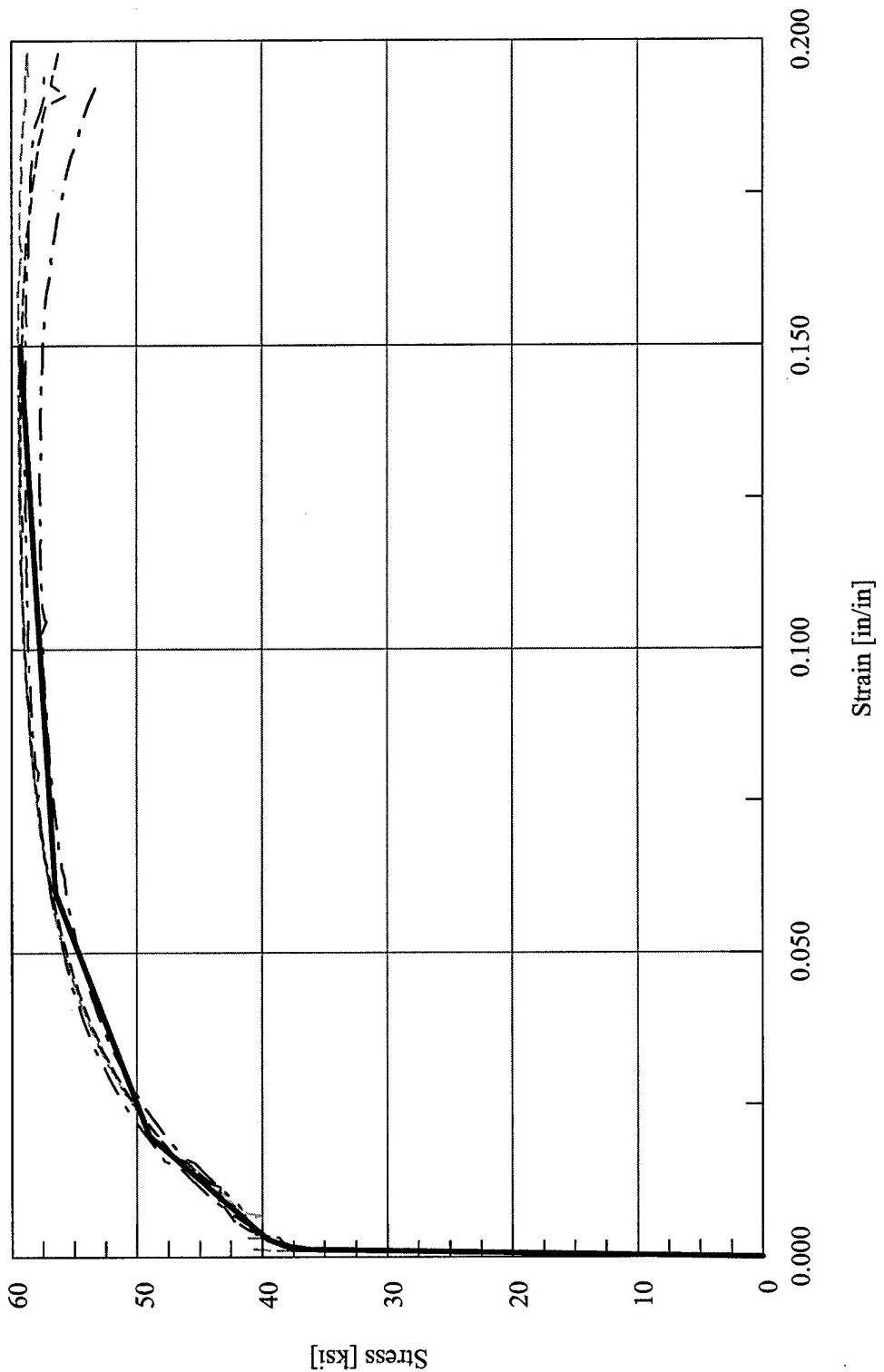


Figure 7.21 Drain-3DX Stress vs. Strain Finite Element Material Model Definition – Test Configuration 3

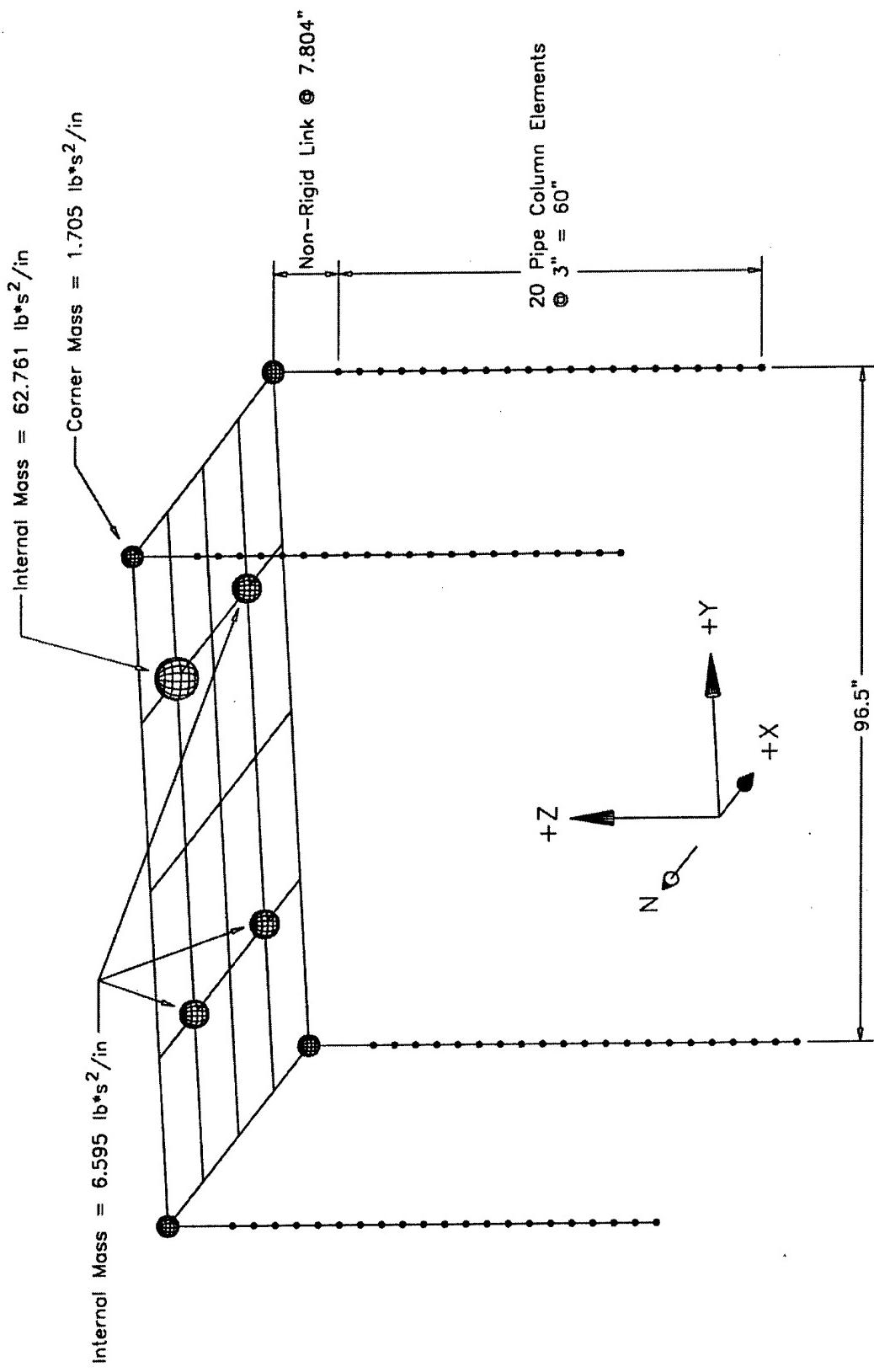


Figure 7.22 Abaqus Finite Element Model for Test Configuration 3

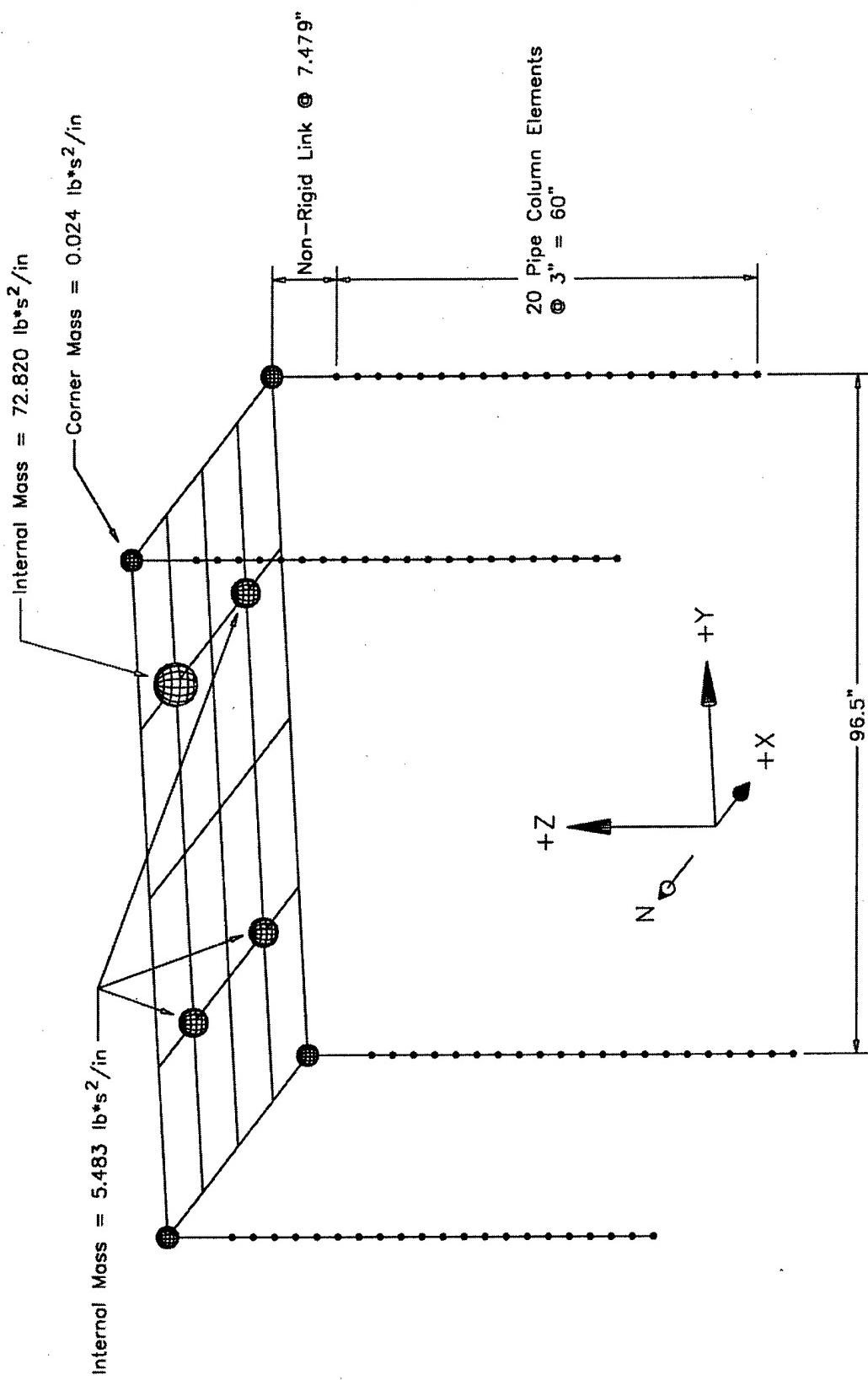


Figure 7.23 Drain-3DX Finite Element Model for Test Configuration 3

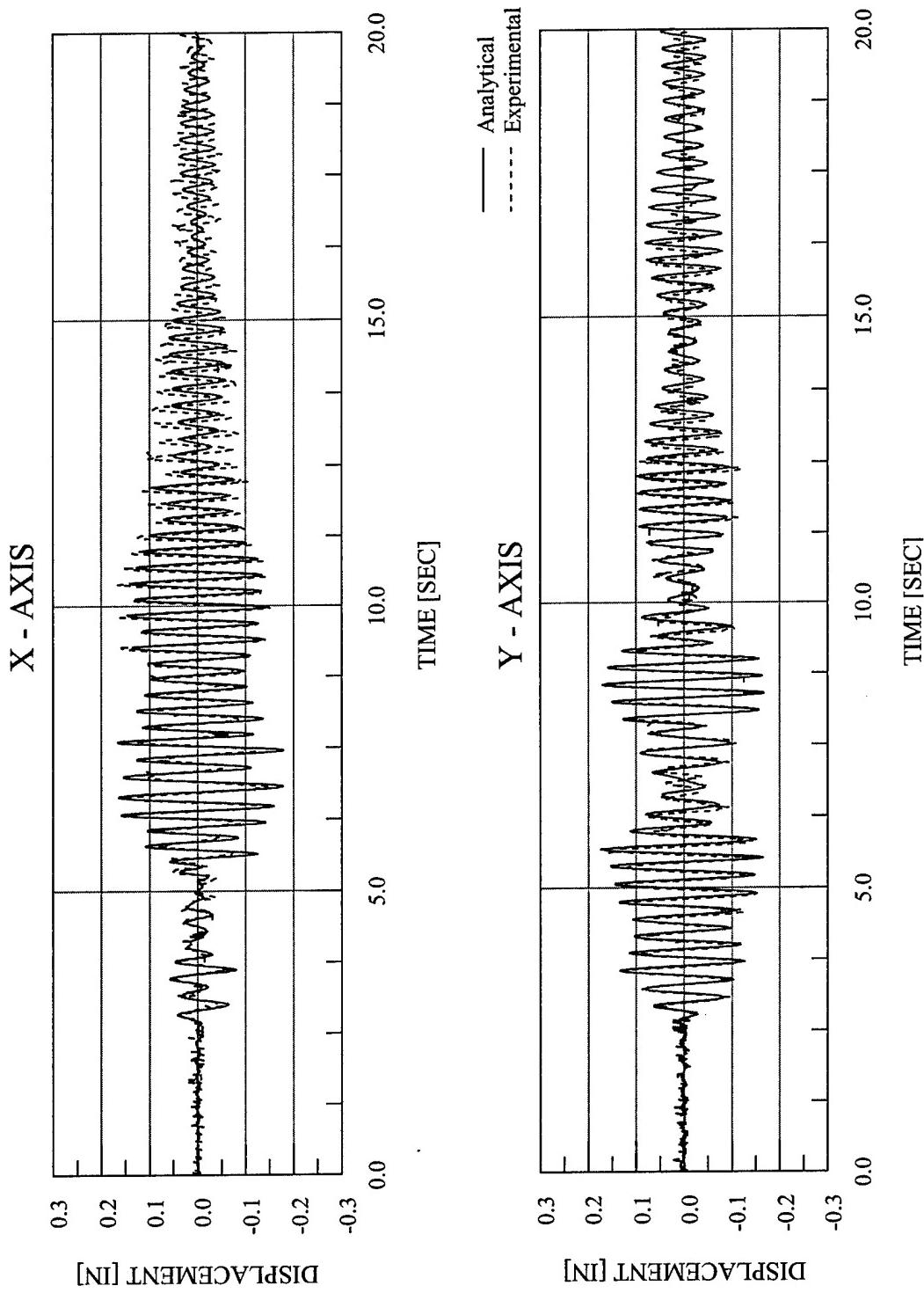


Figure 7.24 Abaqus Analytical Displacement vs. Time – EQ 22 – 10% Biaxial Imperial Valley

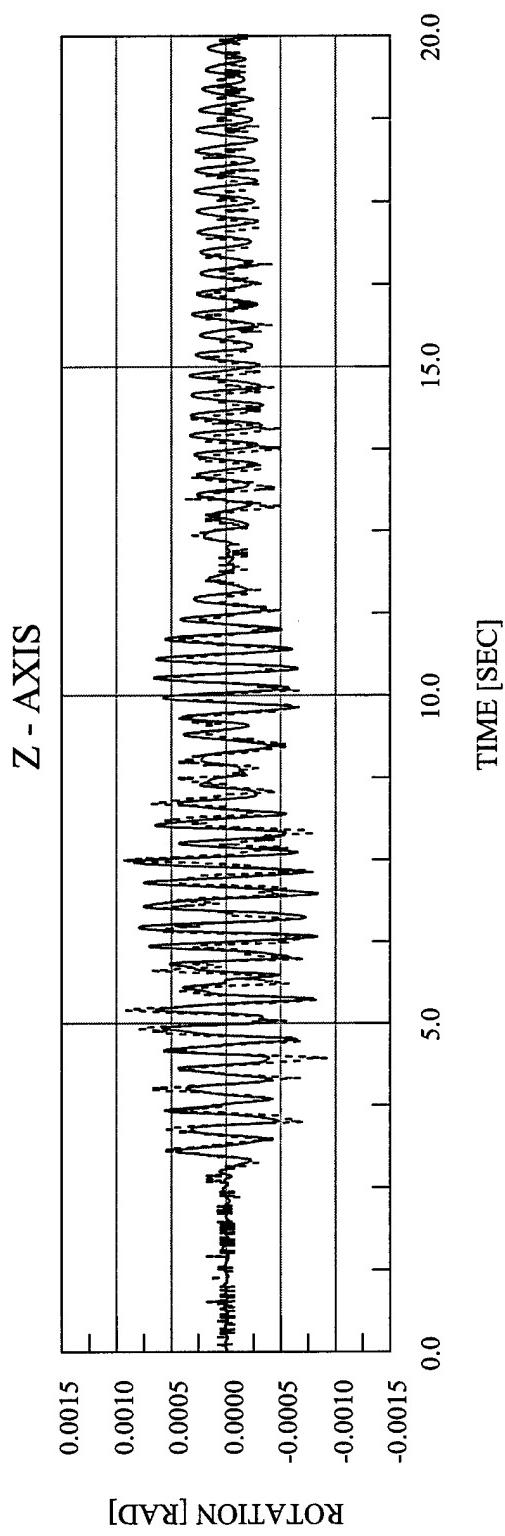


Figure 7.25 Abaqus Analytical Rotation vs. Time – EQ 22 – 10% Biaxial Imperial Valley

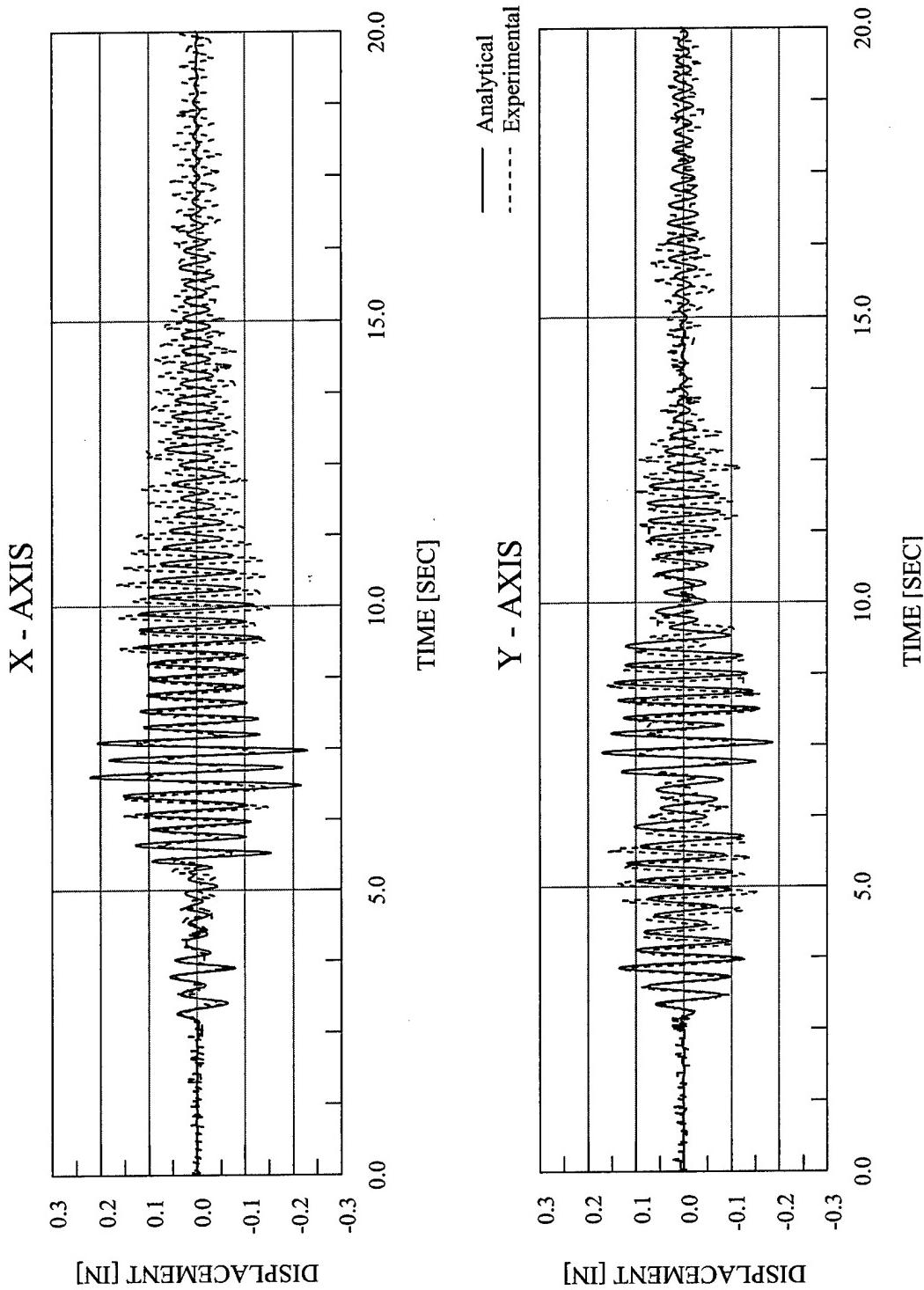


Figure 7.26 Drain-3DX Analytical Displacement vs. Time – EQ 22 – 10% Biaxial Imperial Valley

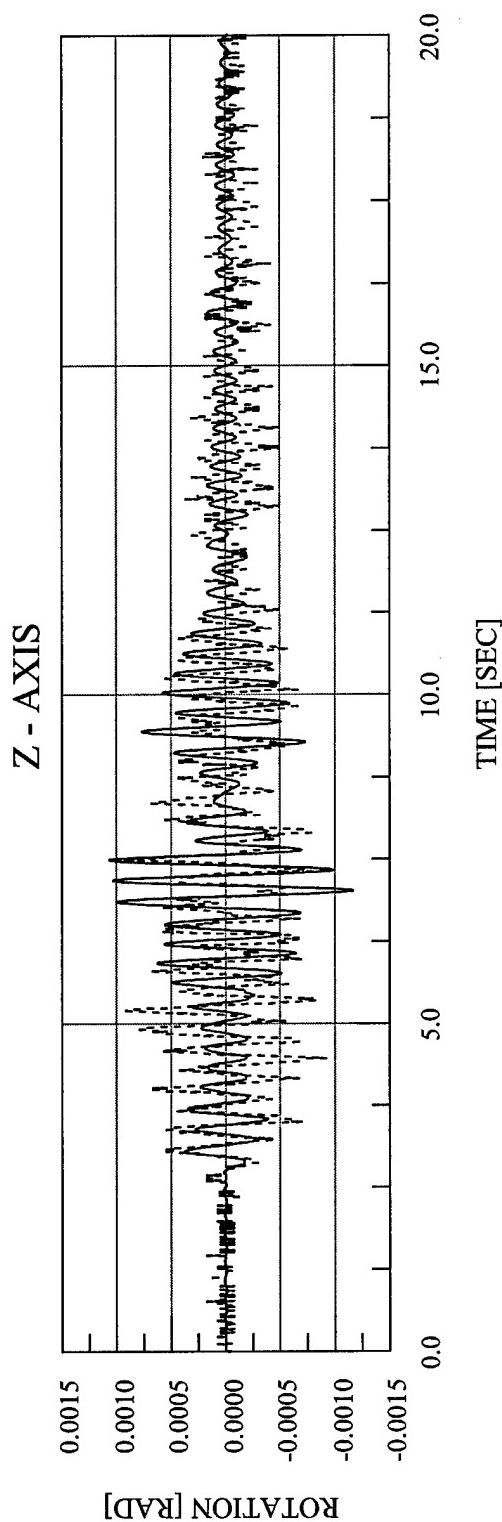


Figure 7.27 Drain-3DX Analytical Rotation vs. Time – EQ 22 – 10% Biaxial Imperial Valley

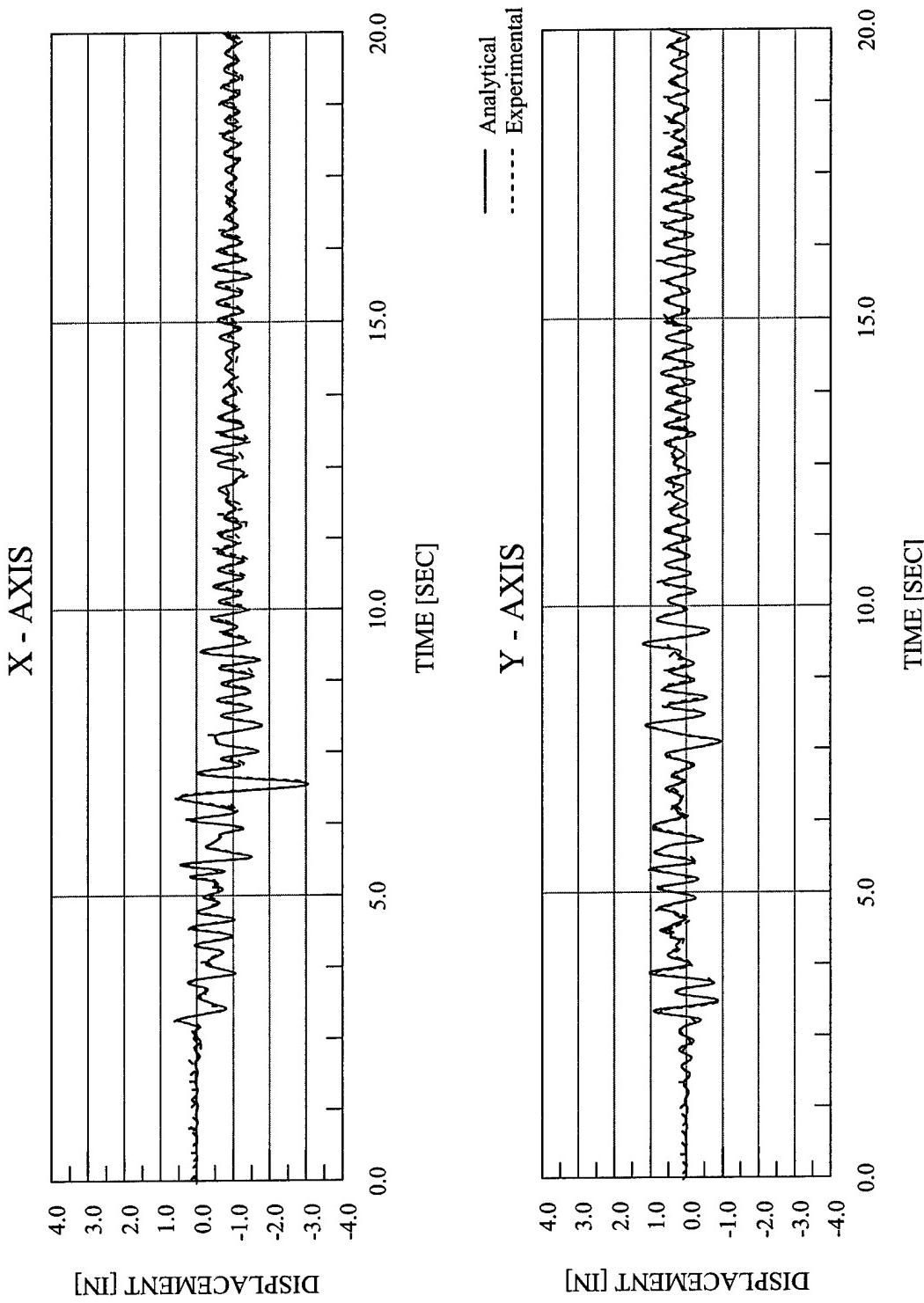


Figure 7.28 Abaqus Analytical Displacement vs. Time – EQ 23 – 100% Biaxial Imperial Valley

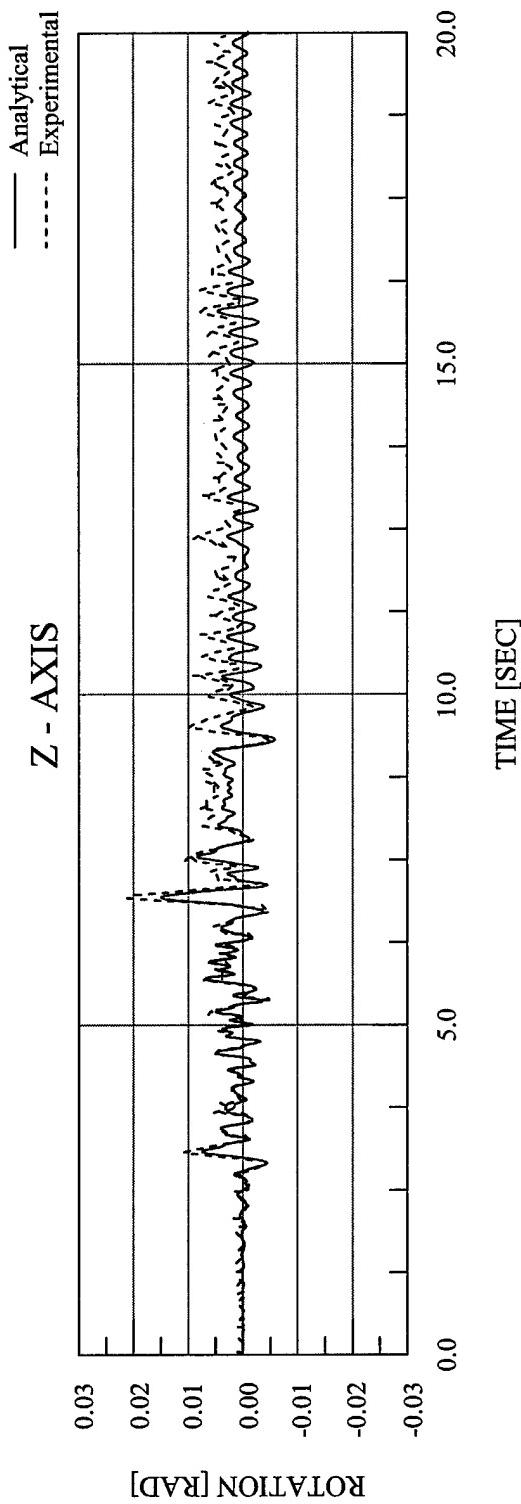


Figure 7.29 Abaqus Analytical Rotation vs. Time – EQ 23 – 100% Biaxial Imperial Valley

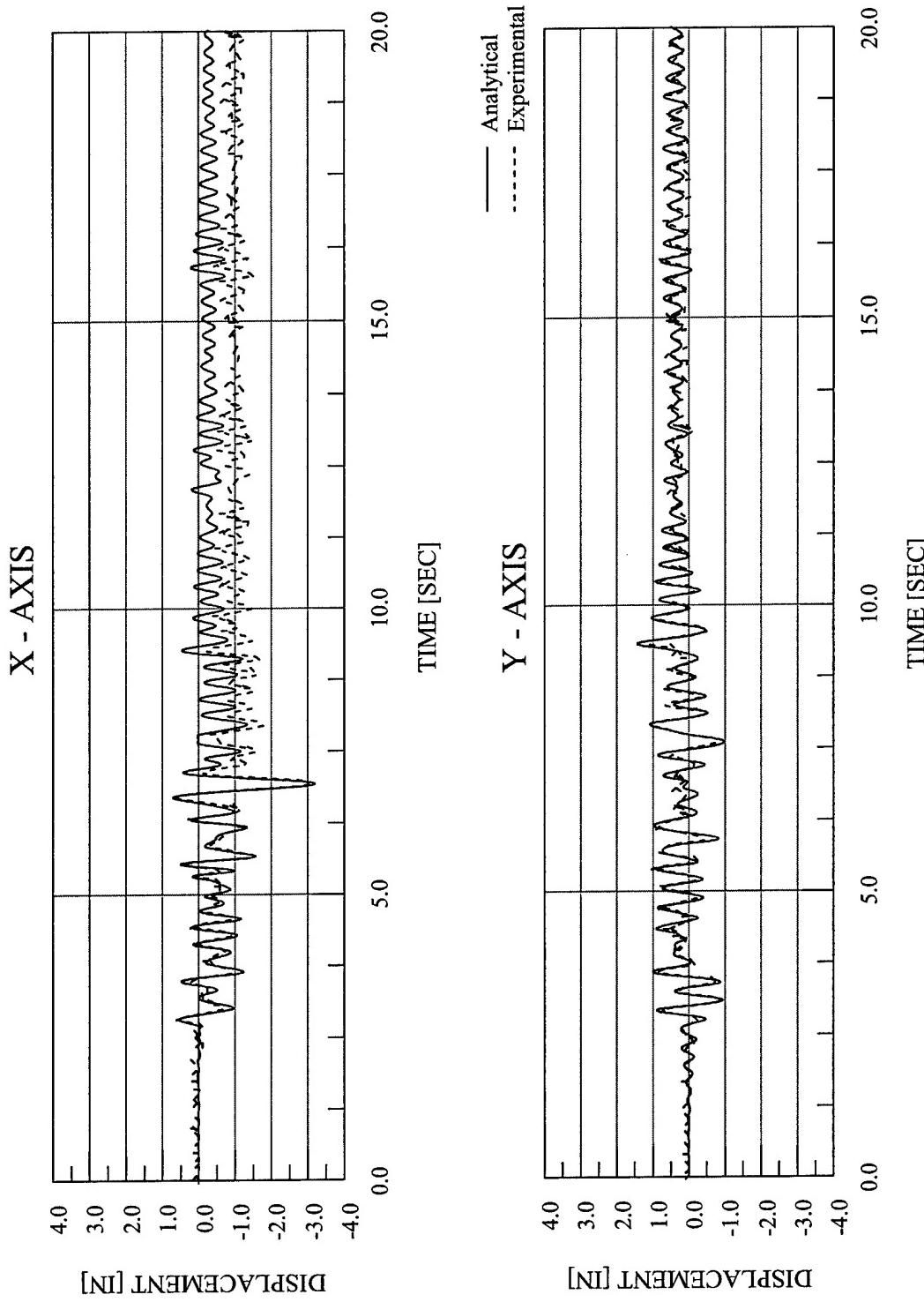


Figure 7.30 Drain-3DX Analytical Displacement vs. Time – EQ 23 – 100% Biaxial Imperial Valley

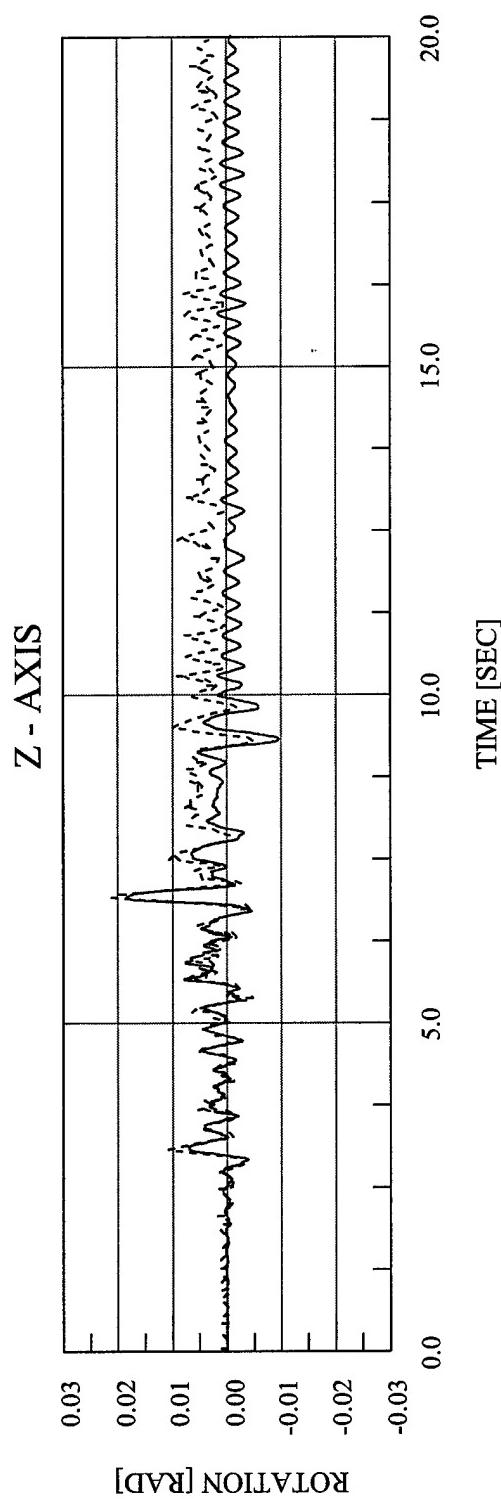


Figure 7.31 Drain-3DX Analytical Rotation vs. Time – EQ 23 – 100% Biaxial Imperial Valley

CHAPTER 8

EXPERIMENTAL AND ANALYTICAL RESPONSE OF TEST CONFIGURATION 8

This chapter provides a summary of the experimental test data and the finite element analysis results of Test Configuration 8. The eighth configuration, shown in Figure 8.1, featured all of the masses loaded on the northeast corner of the diaphragm, resulting in a $\frac{1}{4}$ mass asymmetry, and four 4" Extra-Strong Columns. This configuration is identical to Test Configuration 3, covered in Chapter 7. The dynamic properties of the test structure in Test Configuration 8 are shown in Table 8.1.

Two earthquake simulations were performed with this test configuration. Both of these simulations featured inelastic response. The first earthquake simulations, EQ 45, featured 100% Biaxial input motions [$PGA_x = 1.187$ g and $PGA_y = 0.699$ g]. The second simulation, EQ 46, featured 135% Biaxial input motions [$PGA_x = 1.559$ g and $PGA_y = 0.990$ g]. There were two reasons behind the decision to run only two simulations. First, during the simulations for Test Configuration 3, the final inelastic simulation at 150% Imperial Valley was interrupted less than halfway through, as the shaketable exceeded its displacement limits. All of the other tests for Test Configuration 3 were completed without any problems. Thus, it was desired to obtain data for a simulation using ground motions larger than 100% Imperial Valley. Second, this test configuration was used as a validation of the repeatability of the experimental simulations, as it could be compared with the test results from Test Configuration 3. It was felt that performing the first inelastic simulations would achieve this goal. The complete test sequence for Test Configuration 8 is shown in Table 8.2.

This chapter summarizes response data of the test structure during the earthquake simulations and the dynamic characterization tests. Summaries of test model accelerations, displacements, torsional moments, overturning moments, column end moments, and base shears are provided.

8.1 OBSERVED STRUCTURAL RESPONSE

The diaphragm acceleration and displacement time history responses for the 100% Biaxial simulation are shown in Figure 8.2. The base shear vs. displacement and torque vs. rotation are shown in Figure 8.3. Similar results for the 135% Biaxial simulation are shown in Figures 8.4 and 8.5.

Tables 8.3 – 8.7 list the peak recorded diaphragm relative displacements and peak diaphragm accelerations, and corresponding PGA for both of the earthquake simulations performed in this test configuration. Also listed are the maximum base shears, maximum torsional moments, maximum overturning moments, maximum column end moments for each column, and maximum column end shears for each column.

8.2 OBSERVED RESPONSE DISCUSSION

The calculated force-deformation behavior of the structure in the X and Y directions is shown in Figure 8.6 and about the Z-Axis in Figure 8.7. In the X direction, the model has a yield displacement of 0.33 inches at a yield force of 17.02 kips. In the Y direction, the model has a yield displacement of 0.41 inches at a yield force of 17.02 kips. The model has a yield rotation of 0.0051 radians at a yield moment of 1162 kip*inches. An elastic response spectra of the recorded table motions for EQ 45 is shown in Figure 8.8. In addition, the modal frequencies for this configuration with respect to the response spectra are indicated in Figure 8.8.

In EQ 45, the first test in this configuration, the model structure is subjected to 100% Imperial Valley input motion along both the X-Axis and Y-Axis [PGA_X = 1.187 g and PGA_Y = 0.699 g]. Time history plots of the structural response are shown in Figure 8.2. All of the peak displacements are greater than the yield displacements, and are 2.46 inches in the X direction, 1.57 inches in the Y direction, and 16.46×10^{-3} radians about the Z-Axis. The peak base shears are 30.58 kips in the X direction and 27.23 kips in the Y direction. Figure 8.3 shows the base shear vs. displacement plots and torsional moment vs. rotation plot, which are not tight and linear but have a somewhat full shape. Both the X-Axis shear vs. displacement loop and the moment vs. rotation loop exhibit a very large inelastic excursion.

Figure 8.9 shows a displacement response comparison between EQ 23, a simulation performed during Test Configuration 3 with 100% Imperial Valley ground motions, and EQ 45, the simulation performed during this test configuration using 100% Imperial Valley ground motions. In the X direction, the response is nearly identical, with the largest displacement excursion, occurring at approximately 7 seconds. This is slightly larger in EQ 23 than in EQ 45. In the Y direction, the response is similar for much of the response. However, a number of the largest excursions do not match well. Despite the fact that the models in the two different test configurations were assembled in the same way, the modal frequencies of the structure were different in this test configuration from those in Test Configuration 3: 3.704 Hz versus 3.546 Hz in the X direction, 3.333 Hz versus 3.283 Hz in the Y direction, and 8.696 Hz versus 8.287 Hz about the Z axis. The damping ratios were also different in the two configurations. Further, although the type of steel used in the pipe columns was specified to be the same in both test configurations, the yield stress in the column steel was smaller in this test configuration as compared to Test Configuration 3, approximately 30 ksi versus 37 ksi. Also, it is important to compare the ground motions, or recorded motions of the shaketable itself during these two simulations. As noted in Chapter 3, even two sets of “100% Imperial Valley” motions, which should ostensibly be identical, are typically not the same. In the X direction, the PGA for EQ 23 was 1.299 g and for EQ 45 was 1.187 g. In the Y direction, the PGA for EQ 23 was 0.797 g and for EQ 45 was 0.699 g. In addition, the PSD in the X direction for EQ 23 was 17.01 inches while for EQ 45 was 16.01 inches. Thus, it appears from both the PSD and PGA that the ground motions in the X direction were of slightly greater intensity during EQ 23 than for EQ 45. This is consistent with the previously mentioned observation that the peak response displacement in the X direction was slightly larger for EQ 23 than for EQ 45. In the Y direction, the PSD was 14.84 inches for EQ 23 and was 15.53 inches for EQ 45. The fact that in the Y direction the PGA was slightly larger for EQ 23 while the PSD was slightly smaller leads to no definitive comparison of the Y-Axis ground motion. This is somewhat consistent with the fact that the Y-Axis responses of the two simulations do not match nearly as well as the X-Axis responses. These differences in the dynamic properties, material properties and ground motions of the two test configurations are all potentially contributing factors in the observed differences of the dynamic response of the structure.

The second earthquake simulation for this configuration, EQ 46, features 135% Imperial Valley input motion along both the X-Axis and Y-Axis [PGA_X = 1.559 g and PGA_Y = 0.990 g]. Time

history plots of the structural response are shown in Figure 8.4. The peak displacements of the structure were 3.72 inches in the X direction, 3.87 inches in the Y direction, and 23.28×10^{-3} radians about the Z-Axis. The peak base shears are 32.95 kips in the X direction and 32.32 kips in the Y direction. The base shears in EQ 46 are approximately 10-15% larger than those in EQ 45, while the input motions have been increased by 35%. As the base shears are proportional to the acceleration response of the diaphragm, the same trends can be observed in the normalized acceleration. With EQ 46, as shown in Figure 8.5, the base shear vs. displacement hysteresis loops exhibit a very full, smooth shape, indicating a large degree of inelastic behavior. The torsional moment vs. rotation loop has become more full as compared with EQ 45, but the shape is somewhat erratic as compared with the base shear vs. displacement loops.

The test structure experiences a rotational ductility of more than 4 for this simulation, while the peak torsional moment is 796.6 kip*inches, roughly two-thirds of the yield moment. This behavior is consistent with inelastic simulations in previous configurations, and is the result of each column participating in the seismic resistance in each of the three directions of motion.

8.3 DYNAMIC CHARACTERIZATIONS OF THE MODEL

Prior to performing any shaketable simulations using the earthquake input motions, white noise, sine sweep, and sine decay tests were performed. This general pattern was followed for Test Configuration 8, as can be seen in Table 8.2. In addition, white noise tests were performed immediately after the earthquake simulation exhibiting inelastic behavior, EQ 46.

The dynamic properties of the test structure, as measured before EQ 45 and then after EQ 46, are shown in Table 8.1. The results indicate that despite the inelastic behavior in these two simulations, no meaningful permanent softening of the structure took place. Test Configuration 3, as discussed in Chapter 7, also exhibited no permanent softening of the structure.

8.4 OBSERVED CONDITION OF THE STRUCTURE

In inspecting the model structure for fracture in the weld or in the base material, none was found for this test configuration. No photographs were taken of this test configuration.

8.5 FINITE ELEMENT ANALYSIS

In modeling the behavior of the test structure, the nonlinear finite element analysis programs Abaqus and Drain-3DX were employed. During the earthquake simulations employing the larger scale input motions, the structural response exhibits both geometric and material nonlinearities, both of which Abaqus and Drain-3DX can model. A more complete discussion of the applicable features of Abaqus and Drain-3DX is presented in Chapter 3. Also, some aspects of the finite element model, such as the modeling of the diaphragm as a rigid component, are common throughout each test configuration, and are discussed more completely in Chapter 3.

(A) PIPE COLUMN MATERIAL MODEL

Two coupons were taken from the overall batch of pipe columns used in Test Configuration 8. The material models of the pipe columns used in this test configuration were based on stress-strain data produced during each coupon tension test. Both the original stress-strain data recorded during the coupon tension tests, and the best-fit material model used in the finite element analyses are shown in Figure 8.10 for Abaqus and in Figure 8.11 for Drain-3DX. Shown in Tables 8.8 and 8.9 are the numerical stress-strain best-fit Abaqus and Drain-3DX model data, respectively.

(B) FINITE ELEMENT MODEL

The Abaqus and Drain-3DX finite element models used for this configuration are shown in Figures 8.12 and 8.13, respectively. Beyond the features of the finite element model common throughout each test configuration and discussed in Chapter 3, Figure 8.12 illustrates the location and magnitudes of the nodal masses and the height of the Non-Rigid Links for the Abaqus model. The nodal masses placed at each of the four corners of the diaphragm each have a magnitude of $1.791 \text{ lb} \cdot \text{s}^2/\text{in}$. The largest interior mass, the northeast interior mass, has a magnitude of $63.847 \text{ lb} \cdot \text{s}^2/\text{in}$. The other three interior masses have magnitudes of $6.117 \text{ lb} \cdot \text{s}^2/\text{in}$. The height of the finite element model diaphragm in this test configuration is 67.804 inches, resulting in a height of 7.804 inches for each of the four Non-Rigid Links. Figure 8.13 shows the features of the Drain-3DX model, beginning with the largest interior mass having a magnitude of $64.765 \text{ lb} \cdot \text{s}^2/\text{in}$. The

remaining three interior masses have magnitudes of $5.656 \text{ lb} \cdot \text{s}^2/\text{in}$, while the corner masses have magnitudes of $1.908 \text{ lb} \cdot \text{s}^2/\text{in}$. The height of the four Non-Rigid Links is 7.479 inches.

(C) OBSERVED RESPONSE

Displacement histories along the X- and Y-Axis and rotation histories about the Z-Axis are provided for the 100% Biaxial simulation [$\text{PGA}_X = 1.187 \text{ g}$ and $\text{PGA}_Y = 0.699 \text{ g}$] in Figures 8.12 and 8.13, and the 135% Biaxial simulation [$\text{PGA}_X = 1.559 \text{ g}$ and $\text{PGA}_Y = 0.990 \text{ g}$] in Figures 8.14 and 8.15. Table 8.9 lists the maximum peak relative displacements in the X and Y directions and the peak rotation for both earthquake simulations.

(D) OBSERVED RESPONSE DISCUSSION

In Figures 8.14 – 8.17, the Abaqus and Drain-3DX displacement and rotation response histories for EQ 45, with 100% Imperial Valley ground motions, can be seen for both the test structure and the finite element model. For both displacements and the rotation, the frequency contents of the response histories in the Abaqus and Drain-3DX simulations match the test data well. In both the X direction and Y direction, the magnitudes of the displacements are overestimated by the Abaqus simulations, by approximately 12% and 20%, respectively. For the rotation, the Abaqus simulations predict smaller peak displacements at a number of points in the time history and a lesser degree of permanent deformation. The Abaqus peak rotation differs from the measured value by approximately 20%. The peak displacements in the X and Y directions predicted by the Drain-3DX simulations 5% and 30%, respectively. The Drain-3DX analysis underestimated the permanent deformation in the X direction, which is consistent with previous configuration analyses. Also consistent with previous analyses, the Drain-3DX simulation predicted the peak rotation much more accurately than the Abaqus analysis, with a difference of only 2%.

In Figures 8.18 – 8.21, the displacement and rotation response histories for EQ 46, with 135% Imperial Valley ground motions, can be seen for both the test structure and the finite element model. For both displacements and the rotation, the frequency contents of the response histories in the Abaqus and Drain-3DX simulations again match the test data well. In the X direction the displacement magnitudes are overestimated by the Abaqus simulation, while in the Y direction

the Abaqus simulation results match the test data very well. The peak displacements in the X direction agree to within 16%, while the peak displacements in the Y direction agree to within 2%. Abaqus accurately predicts the permanent deformation along the Y-Axis, while overestimating in the X direction by roughly 40%. For the rotation, the Abaqus simulations again predict smaller peak displacements at a number of points in the time history and a lesser degree of permanent deformation. The Abaqus peak rotation differs from the test data by approximately 25%. The peak displacements were underestimated by the Drain-3DX simulations, differing by roughly 30% in the X direction and 18% in the Y direction. The Drain-3DX analyses predicted virtually no permanent deformation in the X direction, while the final offset of the test structure was over 2 inches. In the Y direction, the actual offset was roughly 2.5 inches, while Drain-3DX predicted a final deformation of about 1 inch. These results are consistent with previous configurations. Again, the Drain-3DX analysis was more accurate in predicting the peak rotation, differing by only 17%.

The Abaqus simulations shown in Figures 8.12 – 8.15 each utilize the combined nonlinear isotropic/kinematic hardening model, as described in Chapter 3. For the hardening model for these simulations, it was assumed that the isotropic part of the hardening would compose 30% of the total hardening. This figure was chosen through calibration to the response of the symmetric models studied in earlier chapters. During this calibration, it was determined that the ratio of isotropic hardening to kinematic hardening also can have a large impact on the response characteristics of the model. For the configurations in previous chapters, the column material used in each test was from the same batch of pipe columns. The configuration discussed in this chapter utilized columns taken from a different batch of pipe steel. This is clear when the elastic-plastic material behavior from this configuration is compared with the column material behavior from previous configurations. The assumption is being made that the material hardening behavior for the steel used in this configuration is similar in nature to the hardening behavior of the steel used in earlier configurations when the hardening model was calibrated.

8.6 SUMMARY AND CONCLUSIONS

One of the primary goals of this test configuration was to verify the repeatability of one of the simulations. In observing the structural response in EQ 45 as compared to EQ 23, both the X- and Y-Axis response are very similar. The very small difference in X-Axis response between EQ

45 and EQ 23 is not unexpected when considering that the X-Axis PGA for EQ 23 was roughly 10% larger than for EQ 45. Although the Y-Axis responses were also similar, they possessed more deviations than the X-Axis responses. The Y-Axis PGA and PSD were not identical for EQ 23 and EQ 45, differing by as much as 15%. In addition, there were differences in the column yield strength and post-yield stress-strain behavior between EQ 23 and EQ 45, and also differences in the modal frequencies. Thus, despite the intentions of performing an identical test simulation in EQ 45 to that in EQ 23, small but noticeable discrepancies were present in the test configurations. However, these discrepancies were not significant enough to prevent validating the repeatability of an inelastic simulation.

As discussed in previous chapters, the methodology used in the *Seismic Provisions* of using an elastic analysis as the basis for determining inelastic response of structures implies that the ratio of the peak rotation to the peak lateral displacement and the ratio of the two peak lateral displacements remain constant for elastic and inelastic response. As shown below, one trend observed in the u_Y/u_X ratio is that the value drops when moving from the elastic simulation, such as EQ 14 and EQ 27, to the first inelastic simulation, EQ 15 and EQ 28.

Configuration	EQ	u_Y/u_X	u_θ/u_X
Symmetric Mass 25% Biaxial	14	0.73	N/A
Symmetric Mass 100% Biaxial	15	0.43	N/A
Symmetric Mass 150% Biaxial	16	0.80	N/A
$\frac{1}{2}$ Asymmetric Mass 10% Biaxial	27	0.86	0.29
$\frac{1}{2}$ Asymmetric Mass 100% Biaxial	28	0.51	0.35
$\frac{1}{2}$ Asymmetric Mass 150% Biaxial	29	0.85	0.35
$\frac{1}{4}$ Asymmetric Mass 10% Biaxial	22	0.96	0.28
$\frac{1}{4}$ Asymmetric Mass 100% Biaxial	23	0.37	0.33
$\frac{1}{4}$ Asymmetric Mass 100% Biaxial	45	0.64	0.32
$\frac{1}{4}$ Asymmetric Mass 135% Biaxial	46	1.04	0.30

The reason for the u_Y/u_X ratio drop is the differing degree of inelastic behavior and stiffness loss in the X and Y directions due to the differences in ground motions, as discussed previously. In moving then to the second inelastic simulation, EQ 16 and EQ 29, the u_Y/u_X ratios increase to values very near the ratios observed for the elastic simulations. As the amount of inelastic behavior increases, the degree to which stiffness is lost in the X and Y directions becomes more equal, and the displacement ductility in the X and Y directions become more proportionally similar to those observed during the elastic simulations. In analyzing the behavior of the $\frac{1}{4}$ Asymmetric Mass test configuration in the previous chapter, with EQ 22 and EQ 23, the u_Y/u_X ratio drop was observed. However, no further complete inelastic simulations were performed. Although this test configuration is not identical to Test Configuration 3, it is close enough to provide meaningful information. In comparing EQ 23 and EQ 45, both $\frac{1}{4}$ Asymmetric Mass systems with 100% Biaxial ground motions, the u_Y/u_X ratio for EQ 45 is significantly larger, 0.64 to 0.37. By extending the previous discussion of the causes of the drops and increases in the u_Y/u_X ratio, it would appear that although EQ 45 is subjected to the same set of ground motions, the system reached a greater degree of yielding than in EQ 23. This observation is supported by the fact that the yield stress of the columns used in EQ 45 was nearly 20% smaller than of those used in EQ 23. In moving to EQ 46, the second inelastic simulation, the u_Y/u_X ratio has increased to 1.04, which is slightly larger but very close to 0.96, the ratio for EQ 22, the elastic simulation. Thus, although the ground motions for this second inelastic simulation are only 135% Imperial Valley as opposed to the 150% ground motions used in EQ 16 and EQ 29, it appears that there has been a similar degree of X- and Y-Axis stiffness lost in EQ 46. Thus, EQ 46 validates the trends observed in Test Configurations 2 and 3 by combining with response data from Test Configuration 4.

The trend observed for the u_θ/u_X ratio in Test Configuration 3, with EQ 27 – 29, was a ratio of 0.29 for the elastic simulation, which then increased roughly 20% for the first inelastic simulations and then remained constant for the second. For EQ 22, the elastic simulation for Test Configuration 4, the ratio was 0.28. The u_θ/u_X ratio then increased roughly 20% for the first inelastic simulation. The values observed for EQ 45 and EQ 46 are 0.32 and 0.30, which appear to validate the trend observed in EQ 27 – 29. Although the u_θ/u_X ratios in EQ 45 and EQ 46 are not equal to each other and also are not equal to that observed for EQ 23, they are reasonably close considering the small but noticeable differences in Test Configuration 3 and Test Configuration 8. As discussed previously, the large “dip” in the u_Y/u_X ratio for EQ 23 does not appear to be present for the u_θ/u_X ratio due to the fact that the u_θ and u_X displacements are much

more tightly coupled than are the u_y and u_x displacements. For this configuration, the X-Axis input ground motion has a peak acceleration and elastic spectral acceleration over 50% larger than for the Y-Axis. Thus, it appears that the X-Axis motion impacts the torsional displacement to a greater degree than the Y-Axis motion.

The general trends observed with the finite element analyses through the previous test configurations continue with Test Configuration 8. The time history analyses were generally accurate in their response predictions, although not as accurate as with Test Configuration 3. Overall, the Abaqus analyses continued to predict the inelastic peak displacements more accurately than the Drain-3DX analyses. In addition, the Abaqus analyses continued to predict any permanent deformation much more accurately than Drain-3DX. The Drain-3DX analysis predicted virtually no permanent offset for the X-Axis response in EQ 46, while the test structure possessed a final deformation of over 2 inches. The one significant liability with the Abaqus analyses has been the prediction of the peak rotation, and that trend continues here with a difference of roughly 30%. Drain-3DX has proven to be noticeably more accurate in predicting the peak rotation, in this case with a difference of 17% from the actual response.

The Abaqus analyses have consistently proved to be more accurate than the Drain-3DX analyses throughout the test configurations in predicting the inelastic peak displacements of the structure. In addition, Abaqus has consistently been accurate in predicting any permanent displacements, while Drain-3DX has consistently underestimated these values by a factor of 2-3. The one significant liability with the Abaqus analyses has been the prediction of the peak rotation, and that trend continues here with a difference of roughly 20% and 25% in EQ 45 and EQ 46, respectively. Drain-3DX has consistently predicted the peak rotation more accurately, with differences of 2% and 17% in EQ 45 and EQ 46.

Mass [lb*s ² /in]	Mass Centers [in]			Column Properties	
	X ₀	Y ₀	Z ₀	A [in ²]	I [in ⁴]
90.141	-15.201	15.201	67.479	4.41	9.61

	Modal Frequencies [Hz]			Modal Damping [%]		
	X	Y	θ	X	Y	θ
Before EQ 45	3.704	3.333	8.696	0.389	0.654	0.671
After EQ 46	3.571	3.383	8.333	0.900	0.814	0.700

Table 8.1 Test Structure Dynamic Properties - Test Configuration 8

Test Designation	Input Motions
WNT52	White Noise X-Axis
WNT53	White Noise Y-Axis
WNT54	White Noise Yaw-Axis
SIN34	Sine Decay X-Axis
SIN35	Sine Decay Y-Axis
SIN36	Sine Decay Yaw-Axis
SWP34	Sine Sweep X-Axis
SWP35	Sine Sweep Y-Axis
SWP36	Sine Sweep Yaw-Axis
EQ45	100% Biaxial Imperial Valley
EQ46	135% Biaxial Imperial Valley
WNT55	White Noise X-Axis
WNT56	White Noise Y-Axis
WNT57	White Noise Yaw-Axis
SIN37	Sine Decay X-Axis
SIN38	Sine Decay Y-Axis
SIN39	Sine Decay Yaw-Axis

Table 8.2 Earthquake Simulations and Dynamic Characterization Tests - Test Configuration 8

Earthquake Test No.	Input Motions	PGA [g]		Relative Displacement [in]			Rotation [10^{-3} rad]	Normalized Displacement [in/g]	Ductility		
		X-Axis	Y-Axis	X-Axis	Y-Axis	Z-Axis			X-Axis	Y-Axis	Z-Axis
45	100% Biaxial	1.187	0.699	2.463	1.566	16.46	2.07	2.24	7.37	3.84	3.25
46	135% Biaxial	1.559	0.990	3.721	3.866	23.28	2.39	3.91	11.14	9.48	4.59

Table 8.3 Maximum Diaphragm Relative Displacement and Rotation - Test Configuration 8

Earthquake Test No.	Input Motions	PGA [g]			Diaphragm Acceleration [10 ⁻³ g/in]			Normalized Acceleration	
		X-Axis	Y-Axis	Z-Axis	X-Axis	Y-Axis	Z-Axis	X-Axis	Y-Axis
45	100% Biaxial	1.187	0.699	0.942	0.803	12.215		0.79	1.15
46	135% Biaxial	1.559	0.990	0.978	0.915	12.761		0.63	0.92

Table 8.4 Maximum Diaphragm Acceleration and Angular Acceleration Response - Test Configuration 8

Earthquake Test No.	Input Motions	PGA [g]			Base Shear [k]	Torsional Moment [k*in]	Overturning Moment [k*in]
		X-Axis	Y-Axis	Z-Axis			
45	100% Biaxial	1.187	0.699	30.58	27.23	793.62	2073.4
46	135% Biaxial	1.559	0.990	32.95	32.32	796.59	2234.1

Table 8.5 Maximum Base Shear, Torsional Moment, and Overturning Moment - Test Configuration 8

Earthquake Test No.	Input Motions	PGA [g]		Column End Moments [k*in]					
		SE Column		SW Column		NW Column		NE Column	
		X-Axis	Y-Axis	X-Axis	Y-Axis	X-Axis	Y-Axis	X-Axis	Y-Axis
45	100% Biaxial	1.187	0.699	185.08	259.05	185.08	208.86	249.39	208.86
46	135% Biaxial	1.559	0.990	210.15	283.72	210.15	216.63	289.89	216.63
								289.89	283.72

Table 8.6 Maximum Column End Moments - Test Configuration 8

Earthquake Test No.	Input Motions	PGA [g]				Column End Shears [k]					
		SE Column		SW Column		NW Column		NE Column			
		X-Axis	Y-Axis	X-Axis	Y-Axis	X-Axis	Y-Axis	X-Axis	Y-Axis	X-Axis	Y-Axis
45	100% Biaxial	1.187	0.699	8.63	6.17	6.96	6.17	6.96	8.31	8.63	8.31
46	135% Biaxial	1.559	0.990	9.46	7.00	7.22	7.00	7.22	9.66	9.46	9.66

Table 8.7 Maximum Column End Shears - Test Configuration 8

E [ksi] = 29000.0

Stress [ksi]	Strain [in/in]	Plastic Strain [in/in]
0.000000	0.000000	
29.900000	0.001031	0.000000
30.200000	0.001500	0.000459
30.600000	0.002000	0.000945
31.900000	0.004000	0.002900
32.600000	0.006000	0.004876
33.900000	0.008000	0.006831
35.200000	0.010000	0.008786
41.100000	0.020000	0.018583
44.800000	0.030000	0.028455
47.500000	0.040000	0.038362
49.500000	0.050000	0.048293
50.900000	0.060000	0.058245
52.890000	0.080000	0.078176
54.070000	0.100000	0.098136
55.200000	0.150000	0.148097
55.600000	0.180000	0.178083

Table 8.8 Abaqus Stress-Strain Best-Fit Material Model - Test Configuration 8

E [ksi] = 29000.0

Stress [ksi]	Strain [in/in]
0.00000	0.00000
29.90000	0.001031
31.90000	0.004000
41.10000	0.020000
49.80000	0.050000
55.20000	0.150000

Table 8.9 Drain-3DX Stress-Strain Best-Fit Material Model - Test Configuration 8

Earthquake Test No.	Input Motions	PGA [g]				Relative Displacement [in]				Rotation [10^{-3} rad]			
		X-Axis		Y-Axis		X-Axis		Y-Axis		Abaqus		Drain	
		X-Axis	Y-Axis	Abaqus	Drain	Test	Abaqus	Drain	Test	Abaqus	Drain	Test	Z-Axis
45	100% Biaxial	1.187	0.699	2.84	2.35	2.46	1.96	2.03	1.57	12.85	16.79	16.46	
46	135% Biaxial	1.559	0.990	4.47	2.60	3.72	3.74	3.25	3.87	16.93	19.33	23.28	

Table 8.10 Analytical vs. Experimental Displacement and Rotation Response Comparison - Test Configuration 8

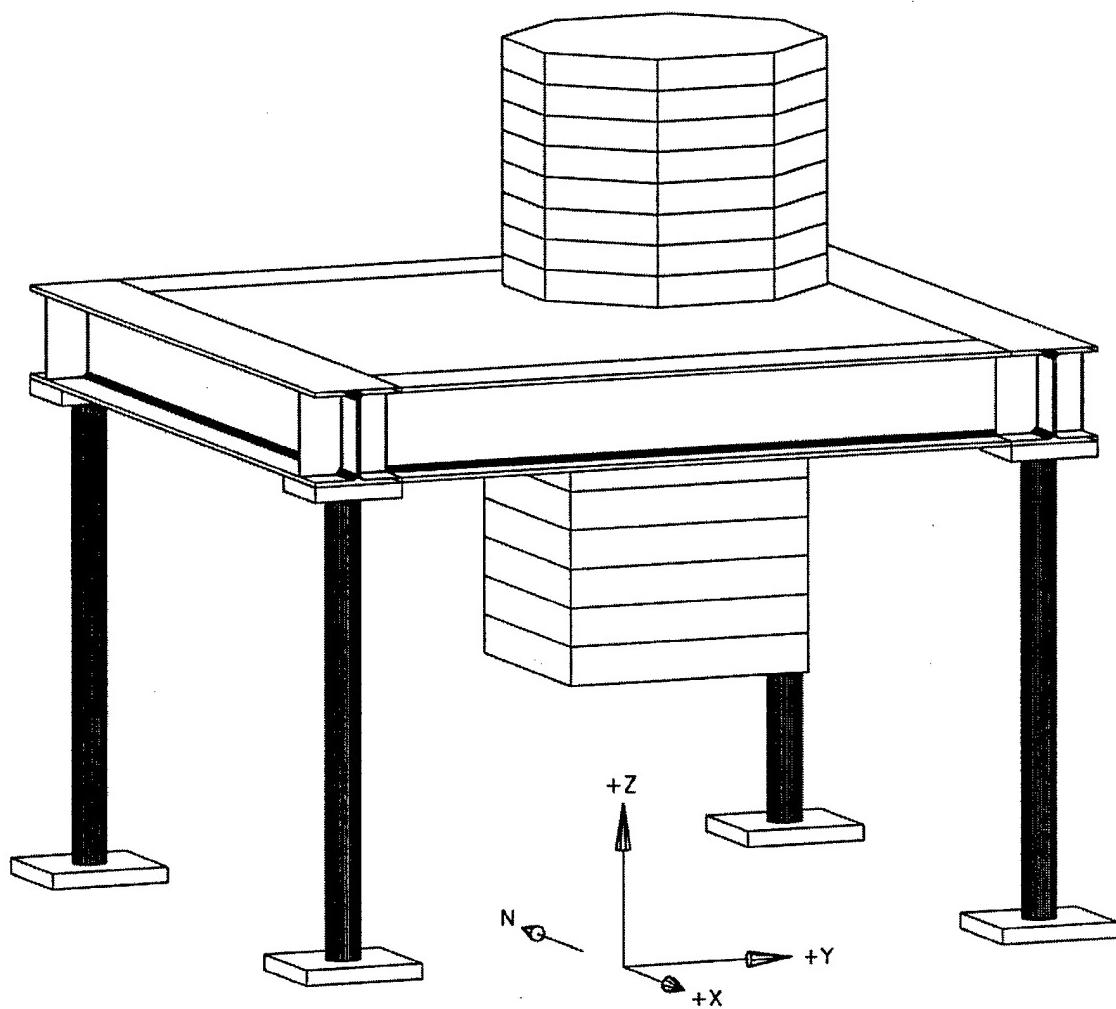


Figure 8.1 Perspective View of Test Configuration Model 8
4 - 4" Extra-Strong Columns

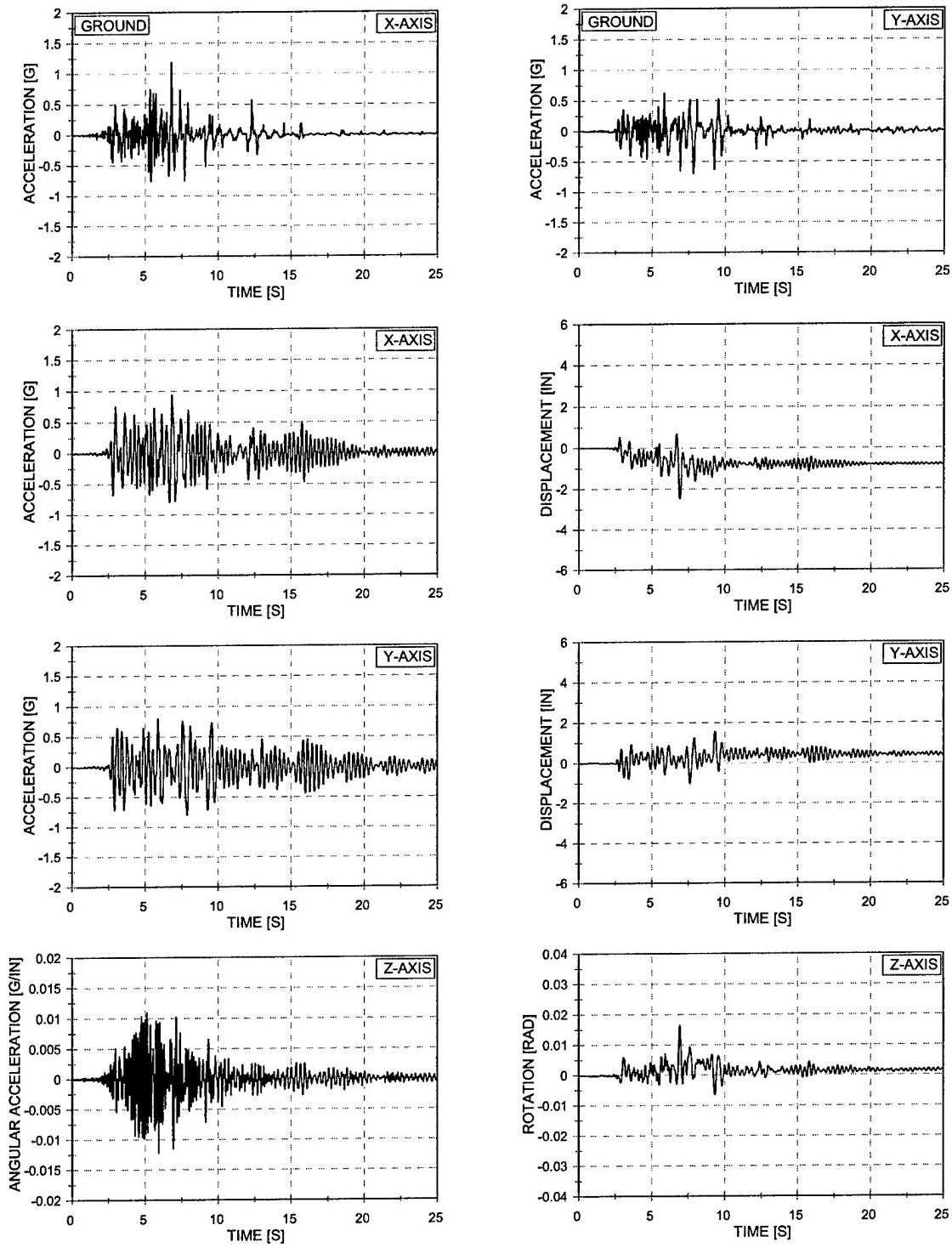


Figure 8.2 Acceleration and Displacement vs. Time – EQ 45
 100% Biaxial Imperial Valley – 1/4 Asymmetric Mass
 Four 4" Extra-Strong Columns

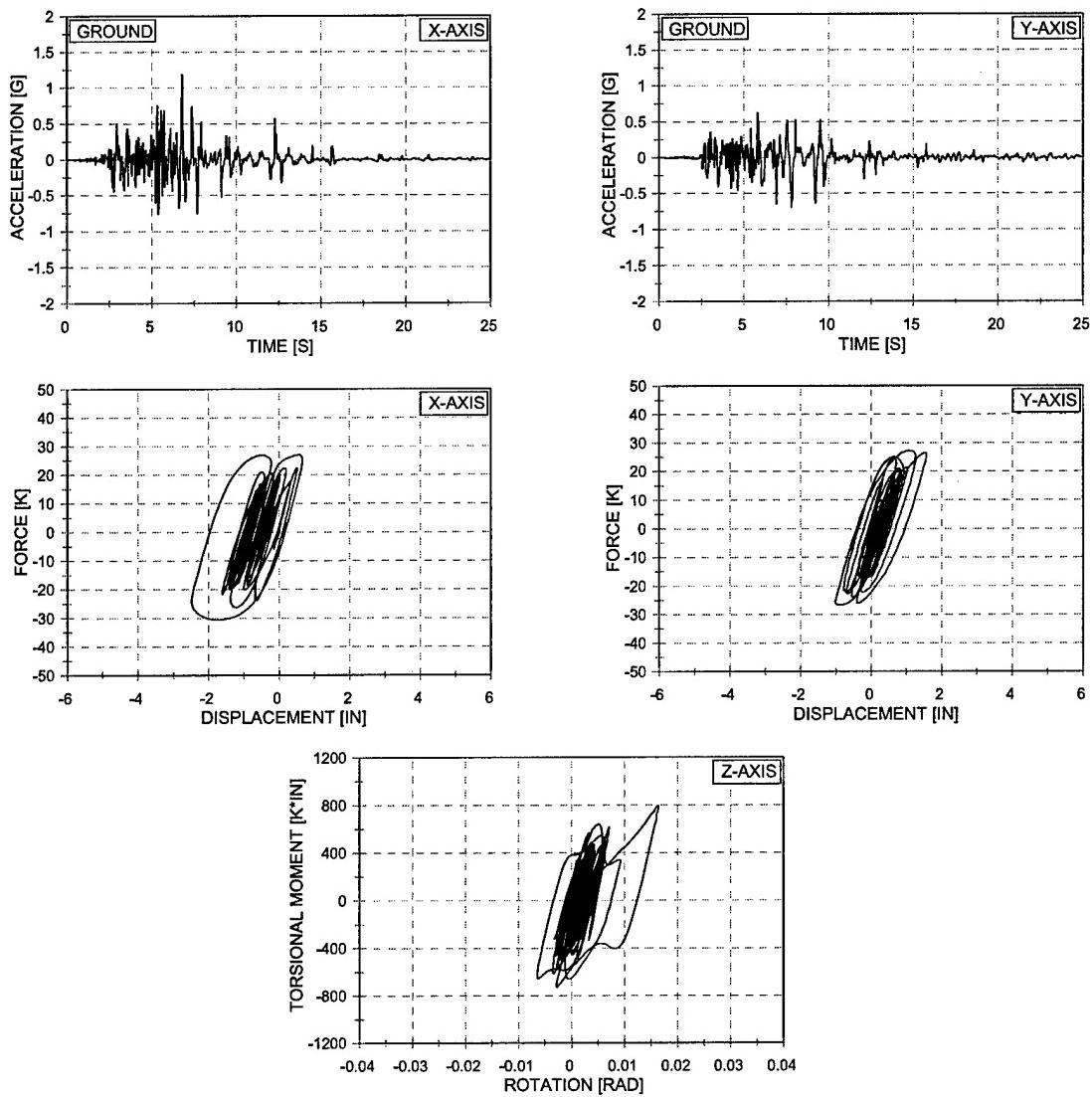


Figure 8.3 Force vs. Displacement and Torsional Moment vs. Rotation – EQ 45
 100% Biaxial Imperial Valley – 1/4 Asymmetric Mass
 Four 4" Extra-Strong Columns

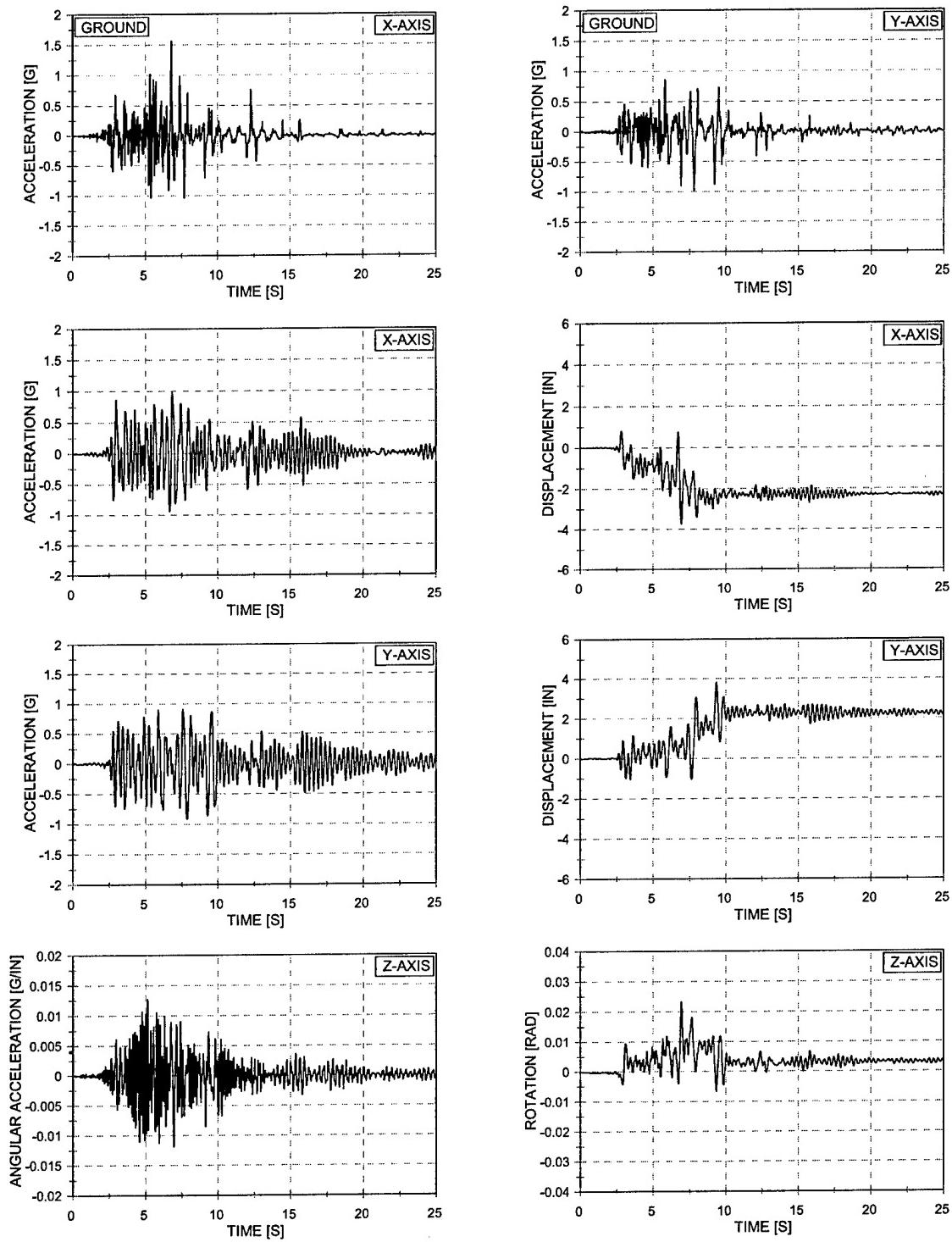


Figure 8.4 Acceleration and Displacement vs. Time – EQ 46
135% Biaxial Imperial Valley – 1/4 Asymmetric Mass
Four 4" Extra-Strong Columns

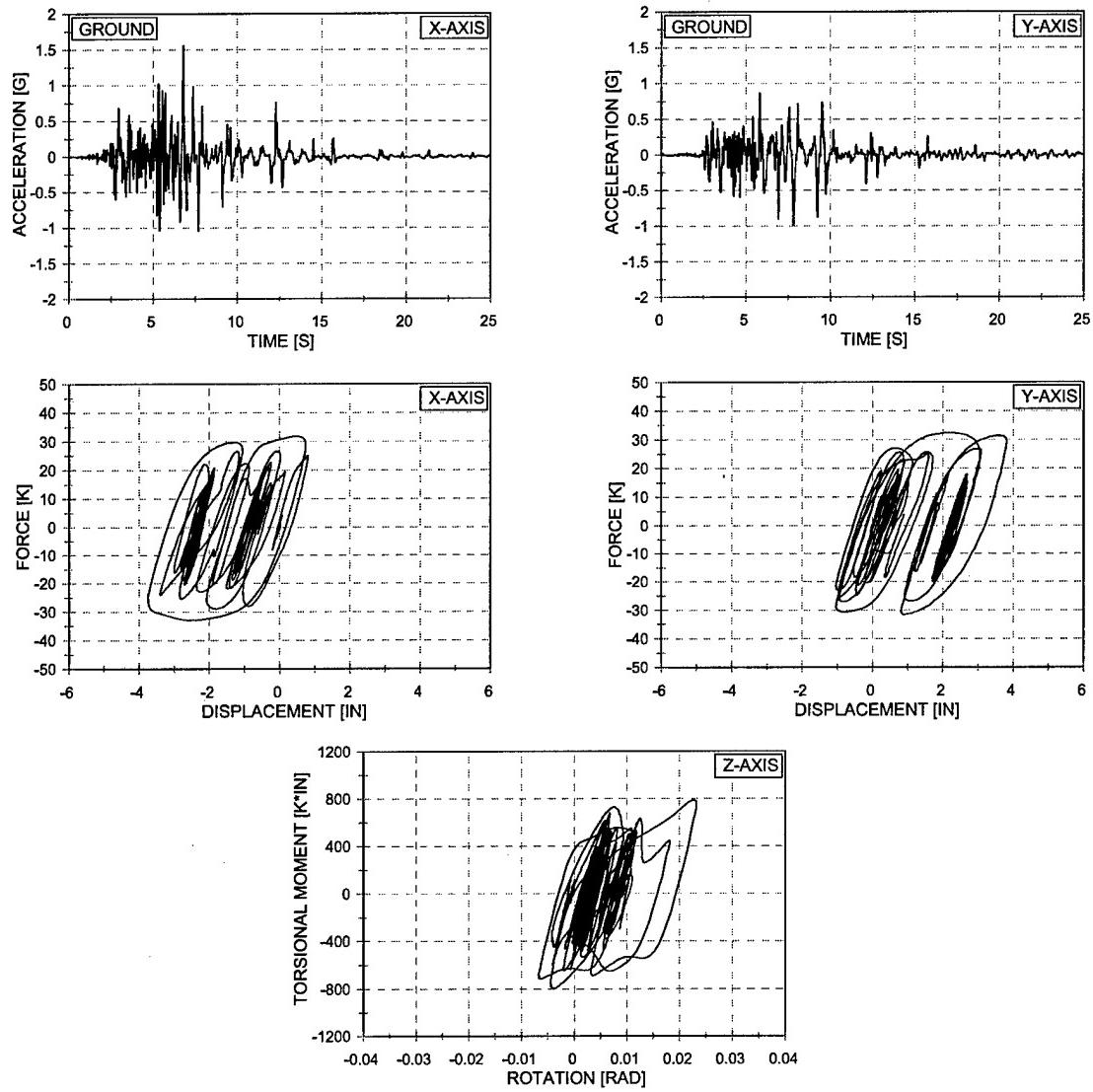


Figure 8.5 Force vs. Displacement and Torsional Moment vs. Rotation - EQ 46
 135% Biaxial Imperial Valley – 1/4 Asymmetric Mass
 Four 4" Extra-Strong Columns

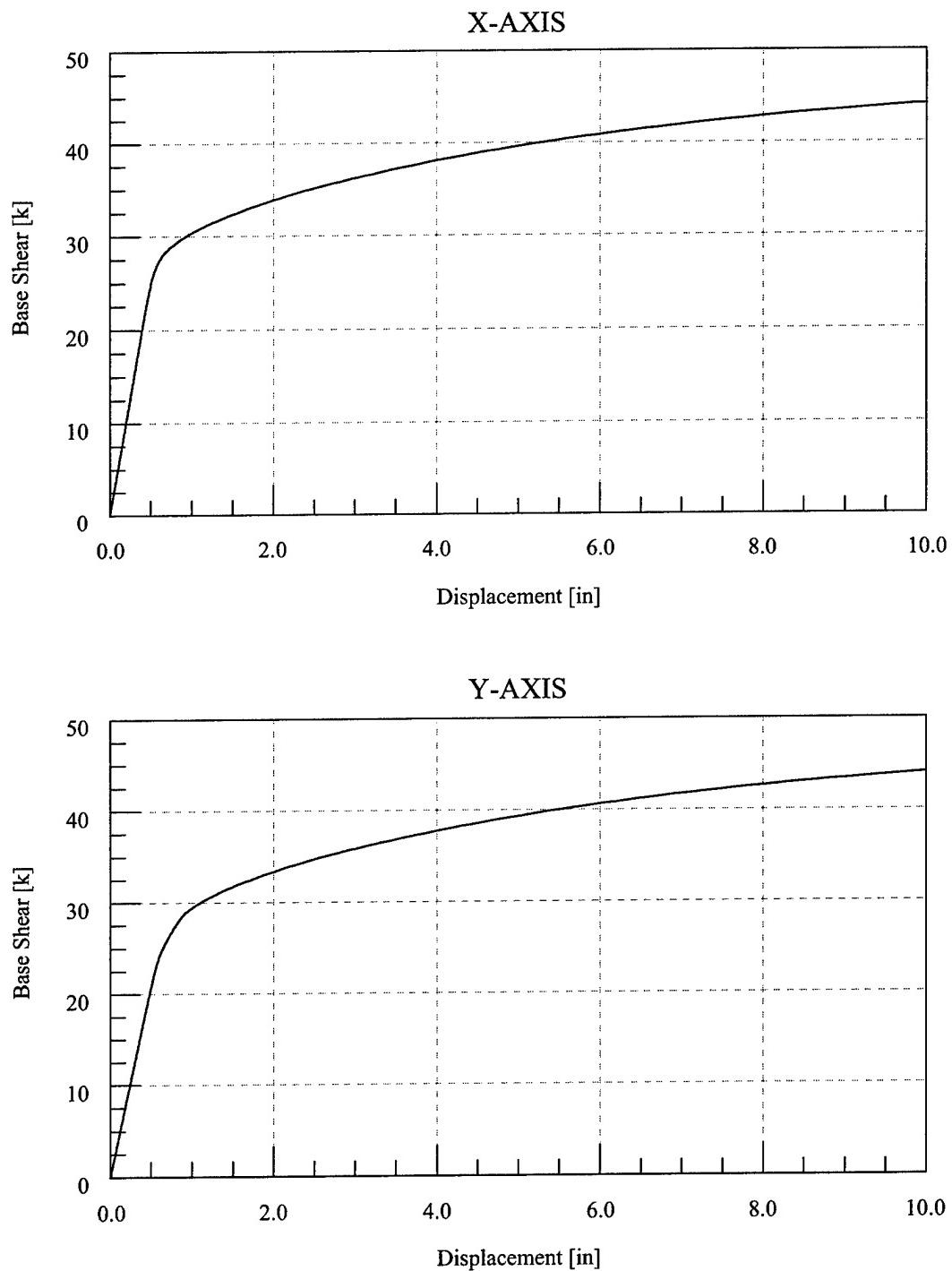


Figure 8.6 Force-Deformation Response – Test Configuration 8

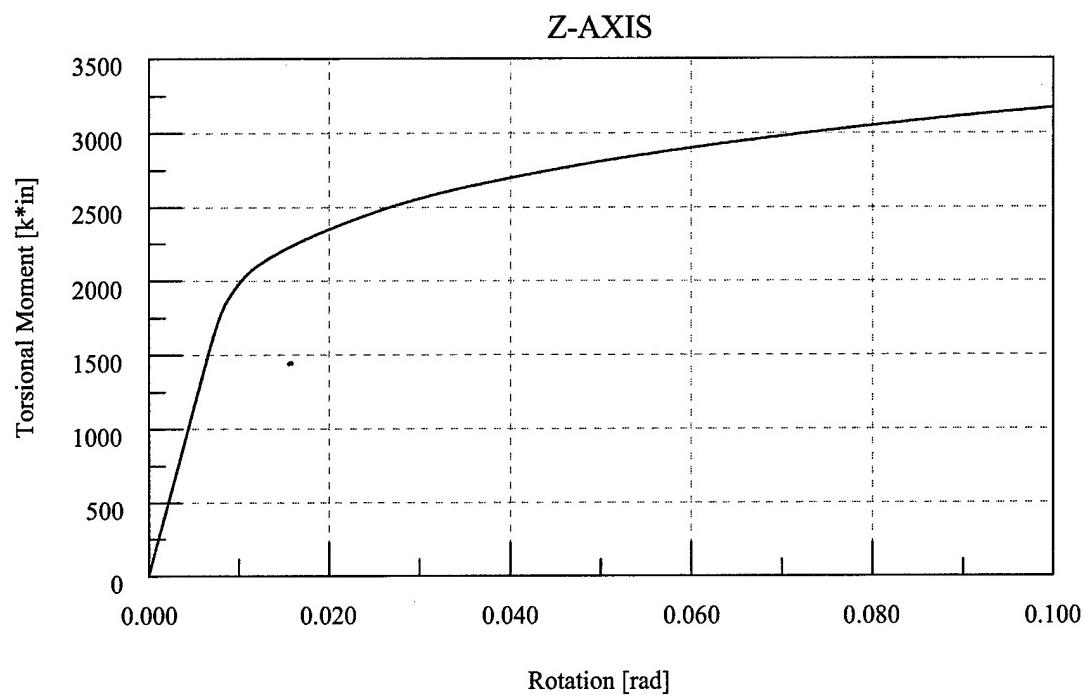


Figure 8.7 Torsional Moment-Rotation Response – Test Configuration 8

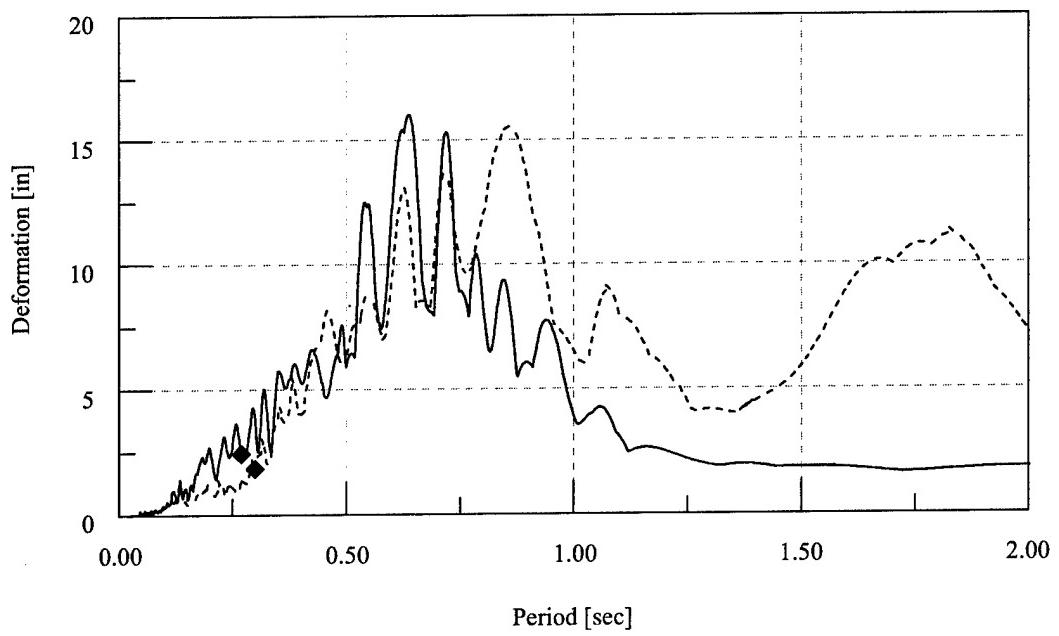
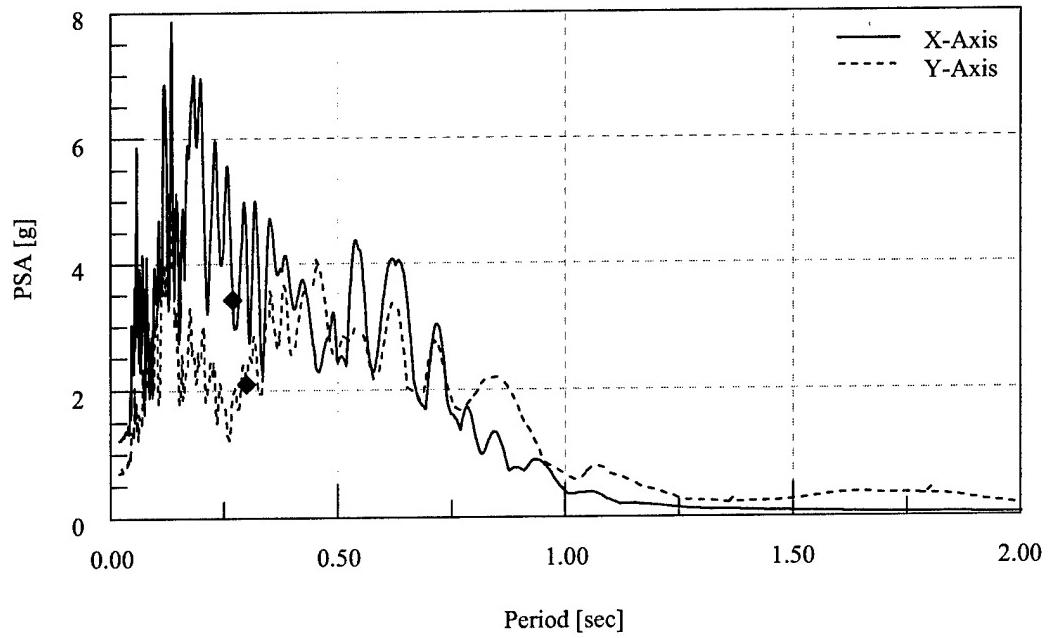


Figure 8.8 Elastic Response Spectra – EQ 45 – 100% Biaxial Imperial Valley Ground Motion

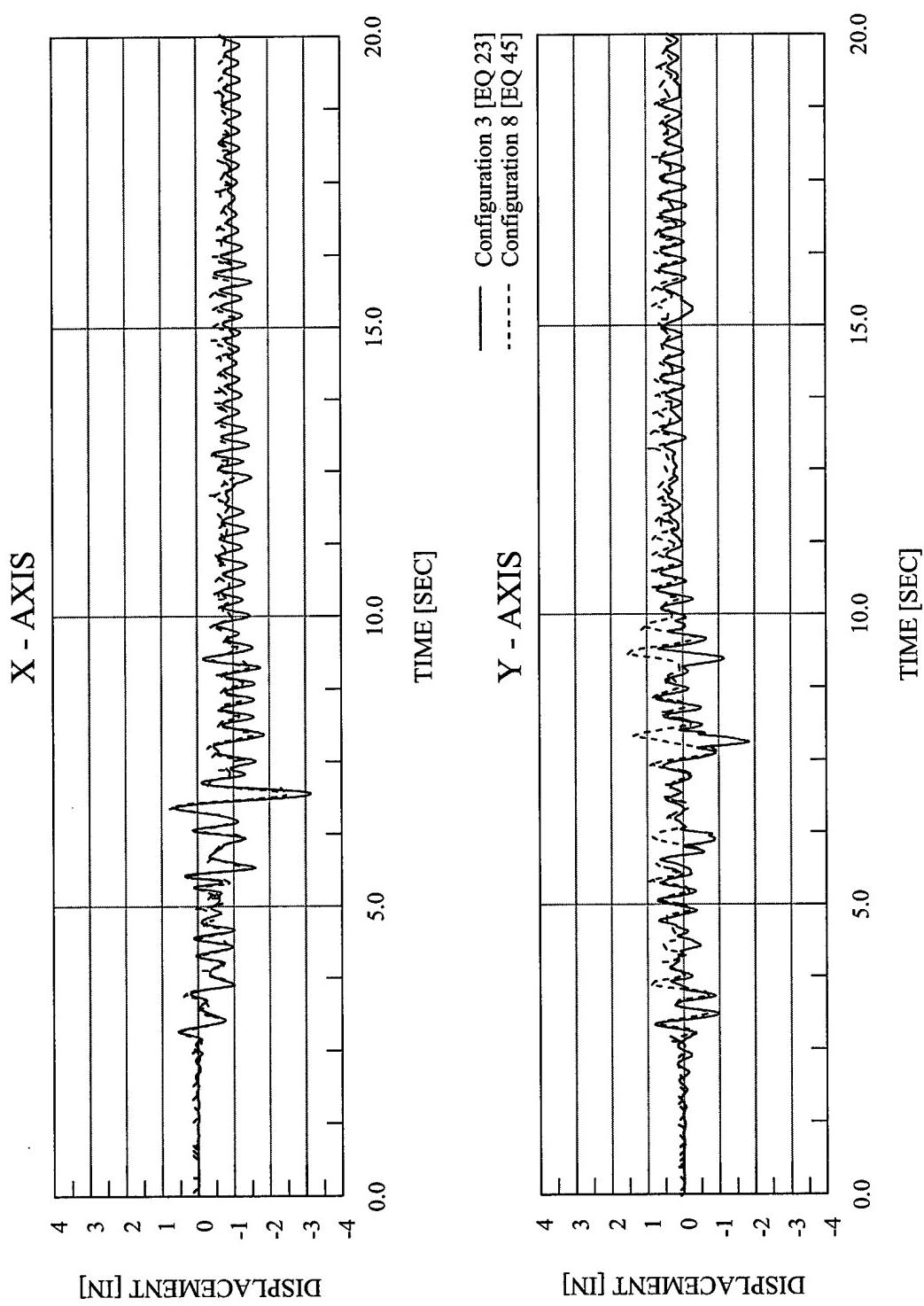


Figure 8.9 Analytical Displacement vs. Time – EQ 23 vs. EQ 45 – 100% Biaxial Imperial Valley

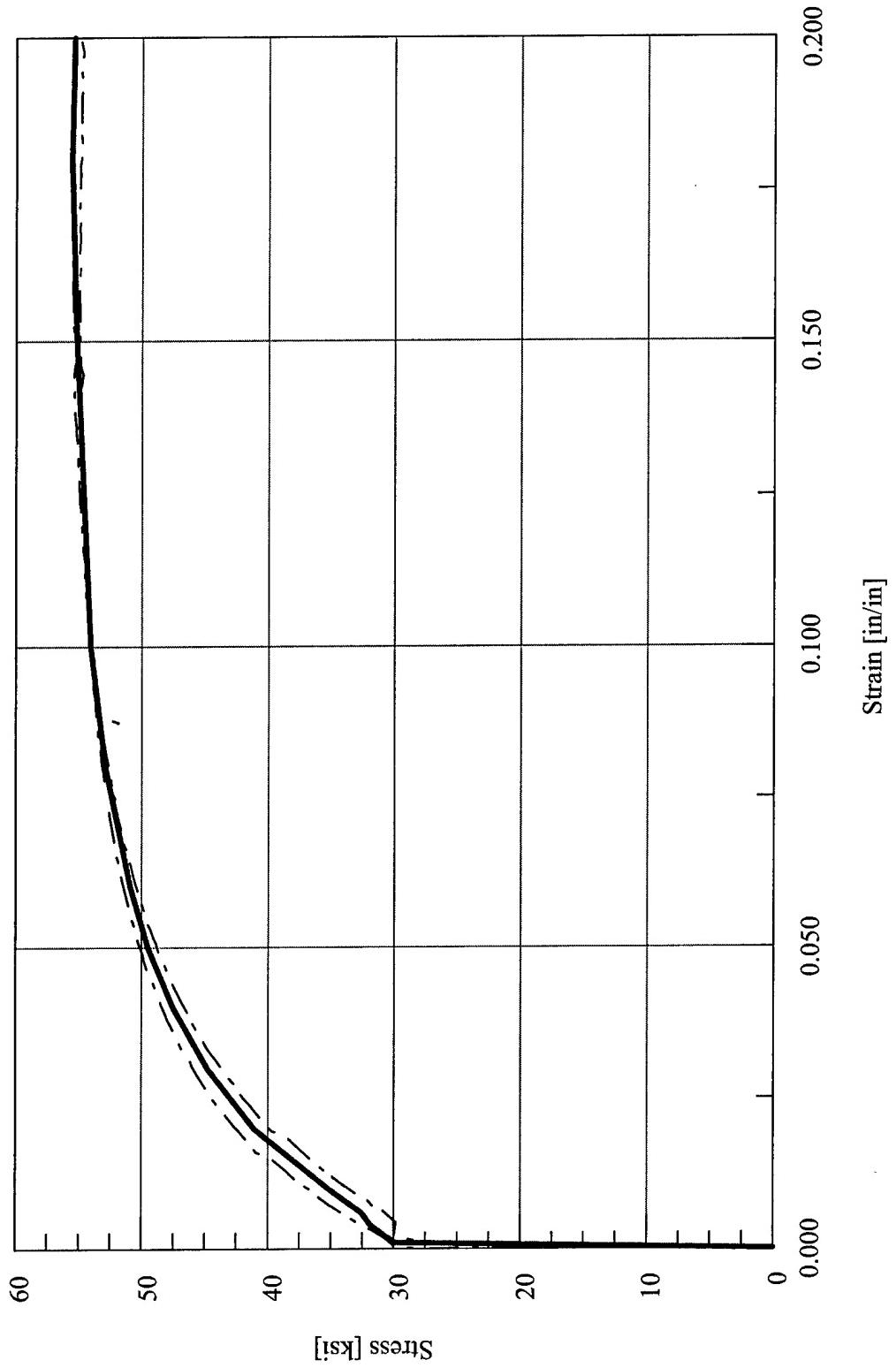


Figure 8.10 Abaqus Stress vs. Strain Finite Element Material Model Definition – Test Configuration 8

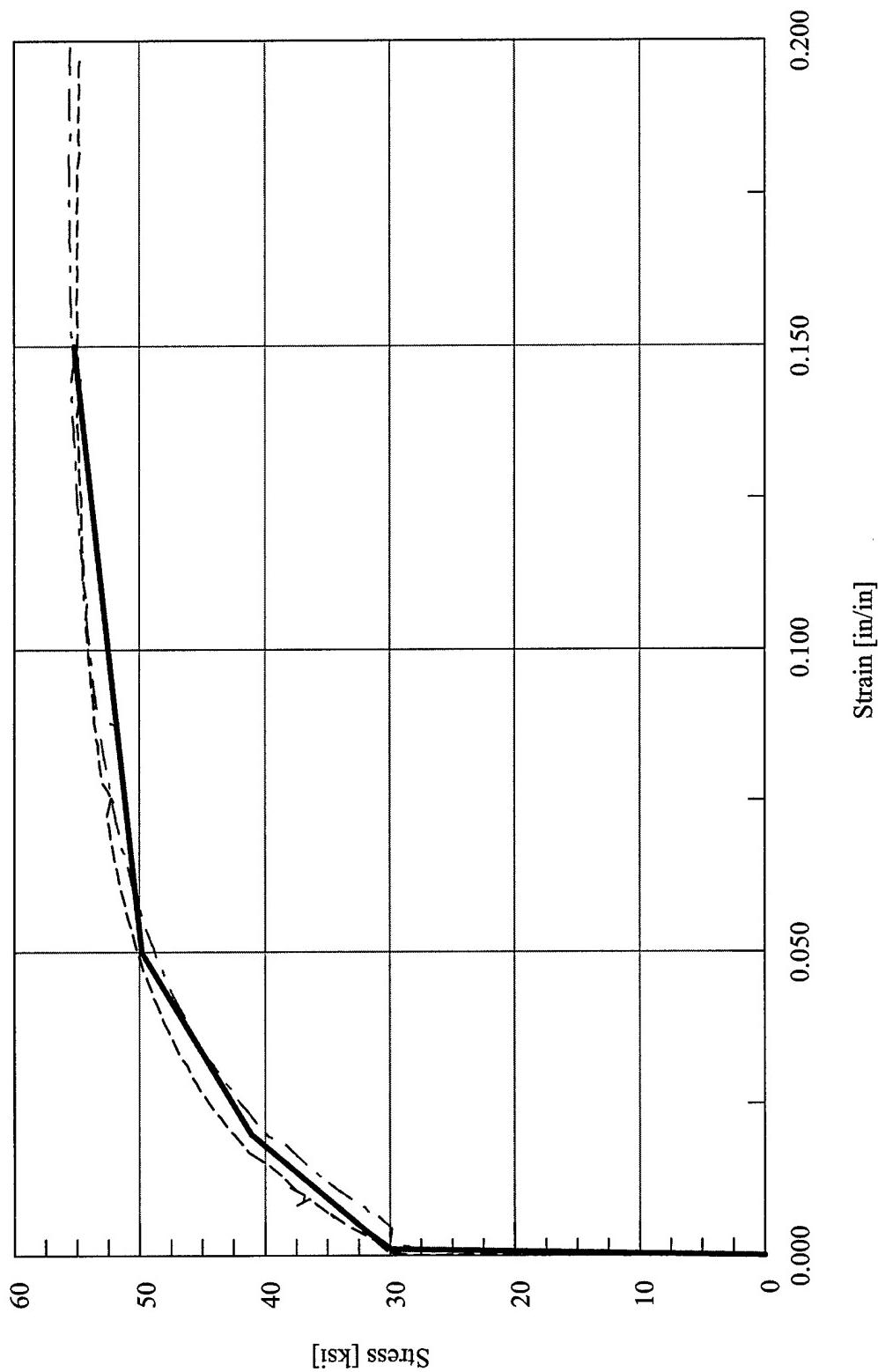


Figure 8.11 Drain-3DX Stress vs. Strain Finite Element Material Model Definition – Test Configuration 8

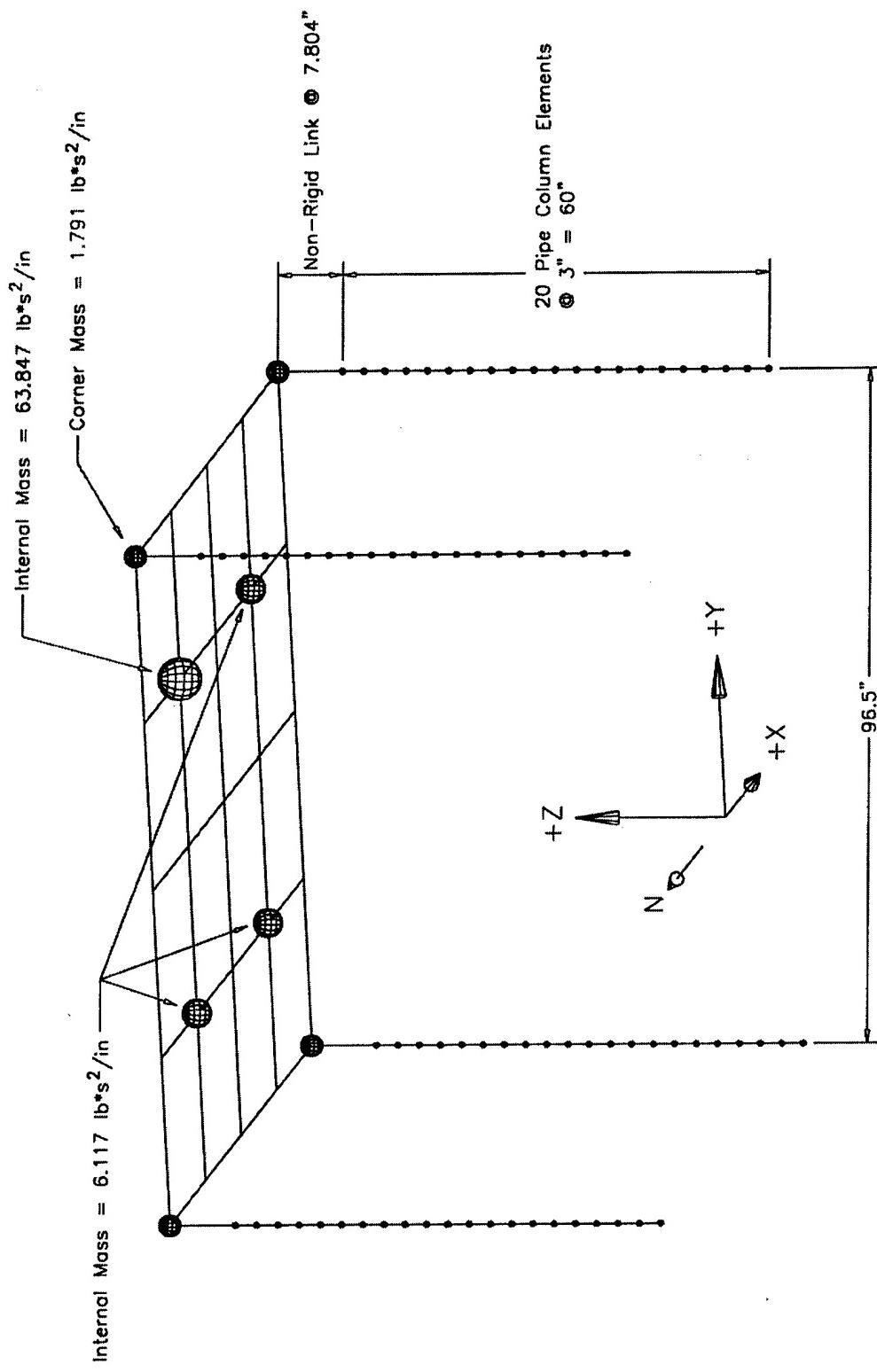


Figure 8.12 Abaqus Finite Element Model for Test Configuration 8

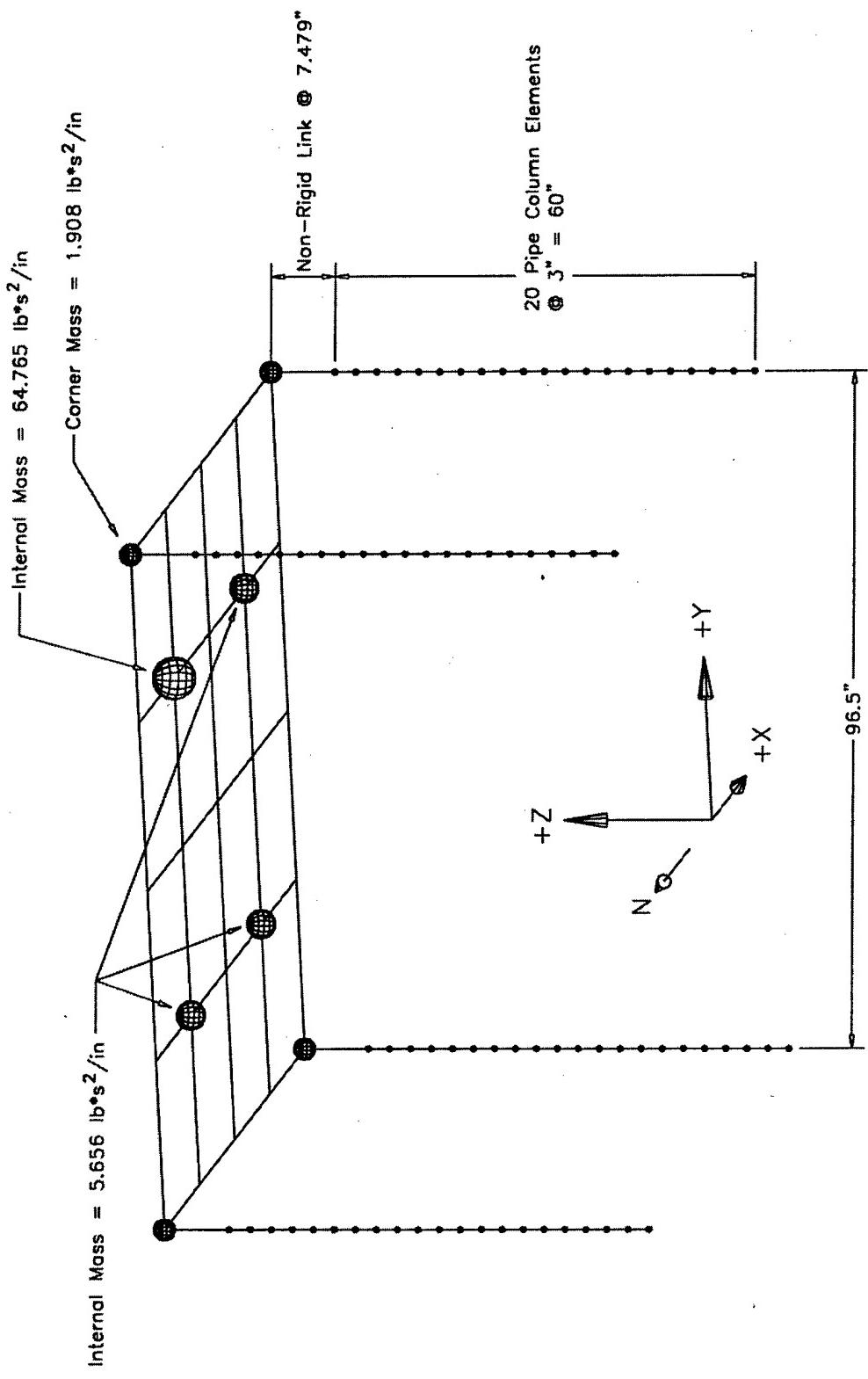


Figure 8.13 Drain-3DX Finite Element Model for Test Configuration 8

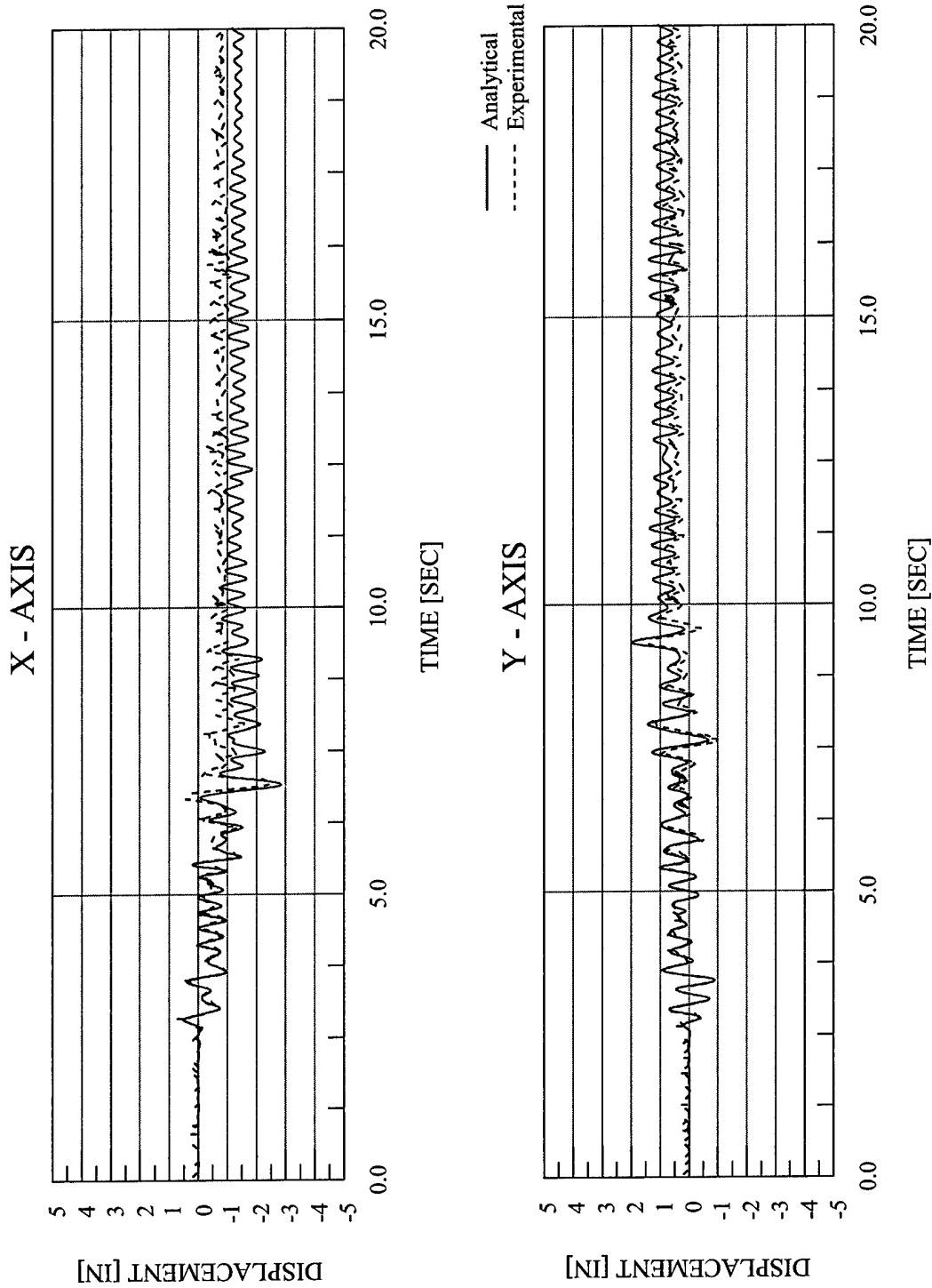


Figure 8.14 Abaqus Analytical Displacement vs. Time – EQ 45 – 100% Biaxial Imperial Valley

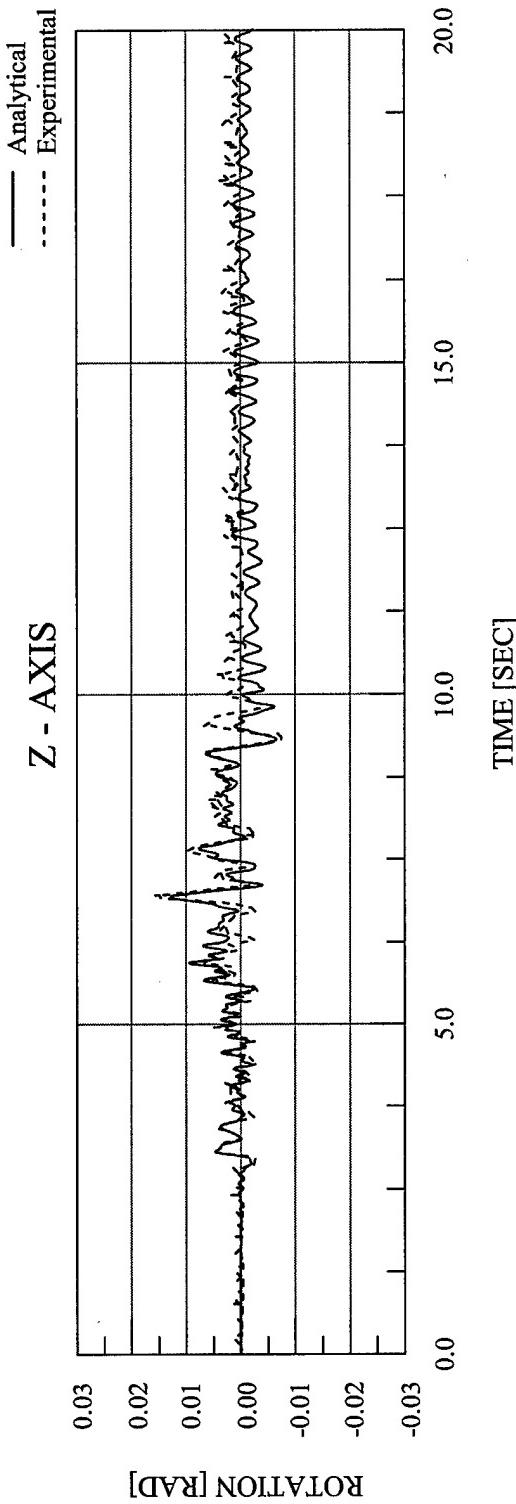


Figure 8.15 Abaqus Analytical Rotation vs. Time – EQ 45 – 100% Biaxial Imperial Valley

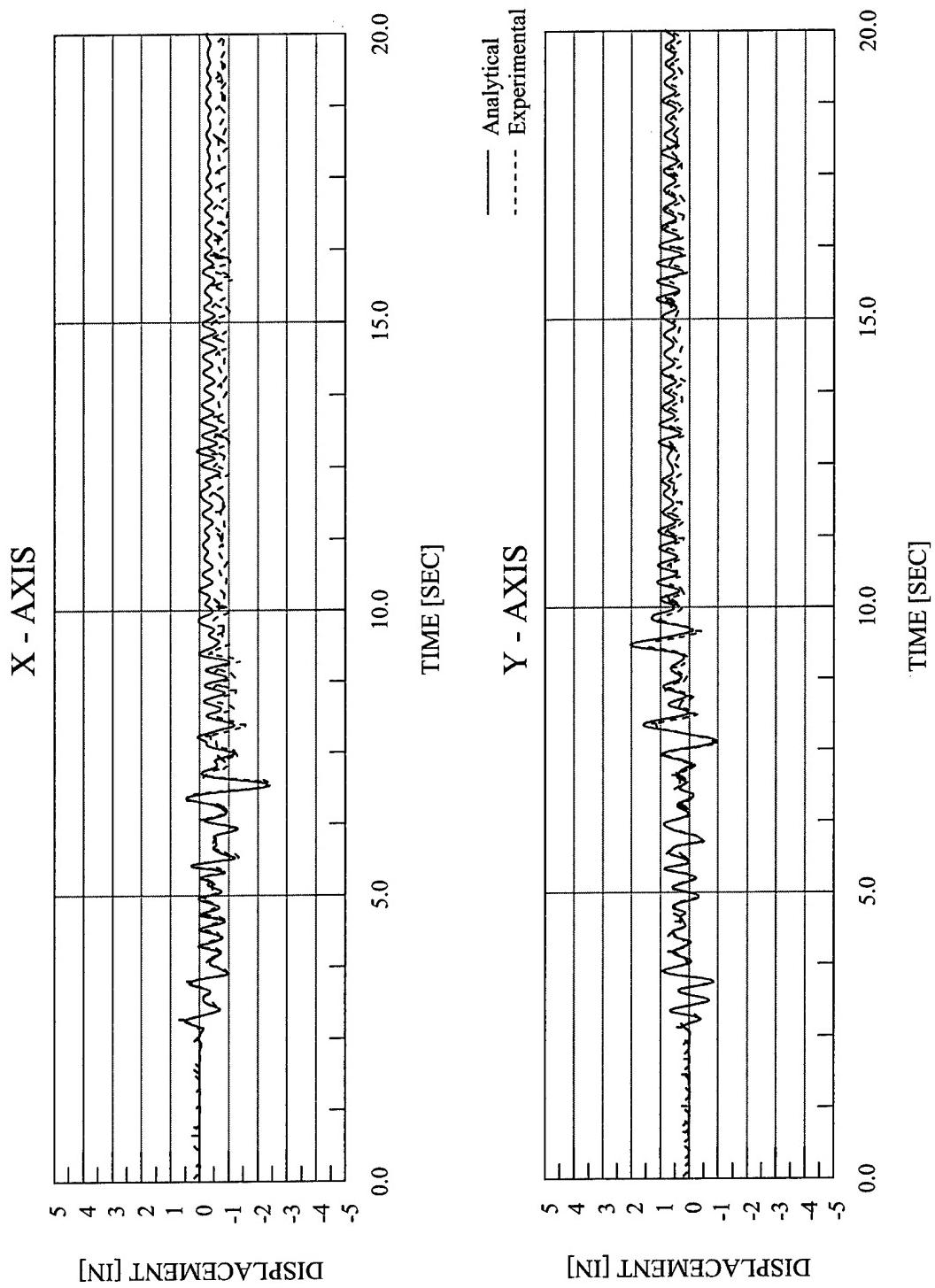


Figure 8.16 Drain-3DX Analytical Displacement vs. Time – EQ 45 – 100% Biaxial Imperial Valley

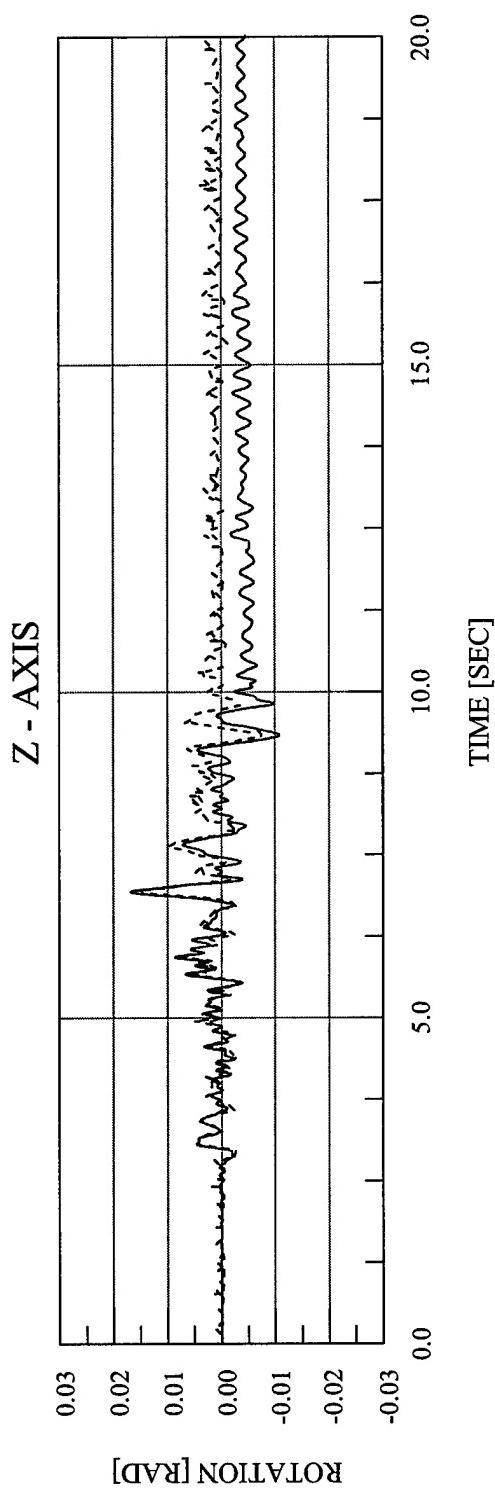


Figure 8.17 Drain-3DX Analytical Rotation vs. Time – EQ 45 – 100% Biaxial Imperial Valley

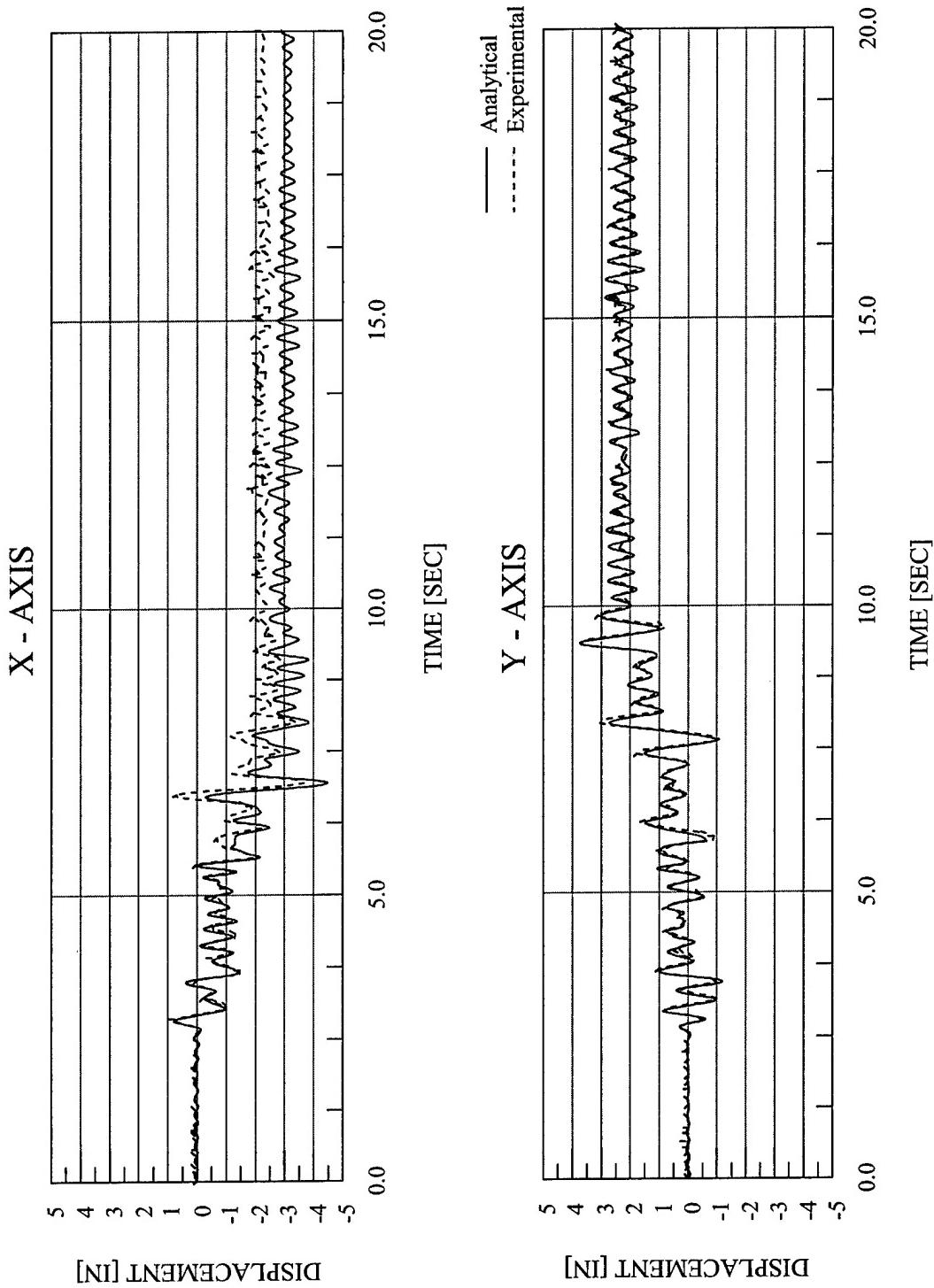


Figure 8.18 Abaqus Analytical Displacement vs. Time – EQ 46 – 135% Biaxial Imperial Valley

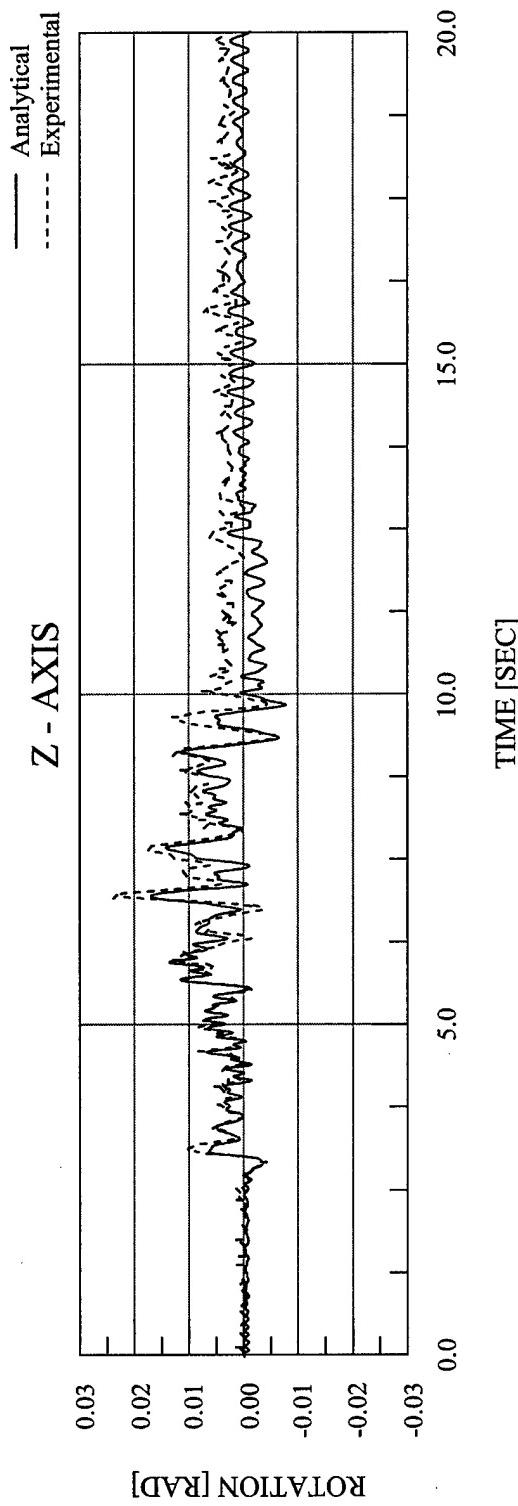


Figure 8.19 Abaqus Analytical Rotation vs. Time – EQ 46 – 135% Biaxial Imperial Valley

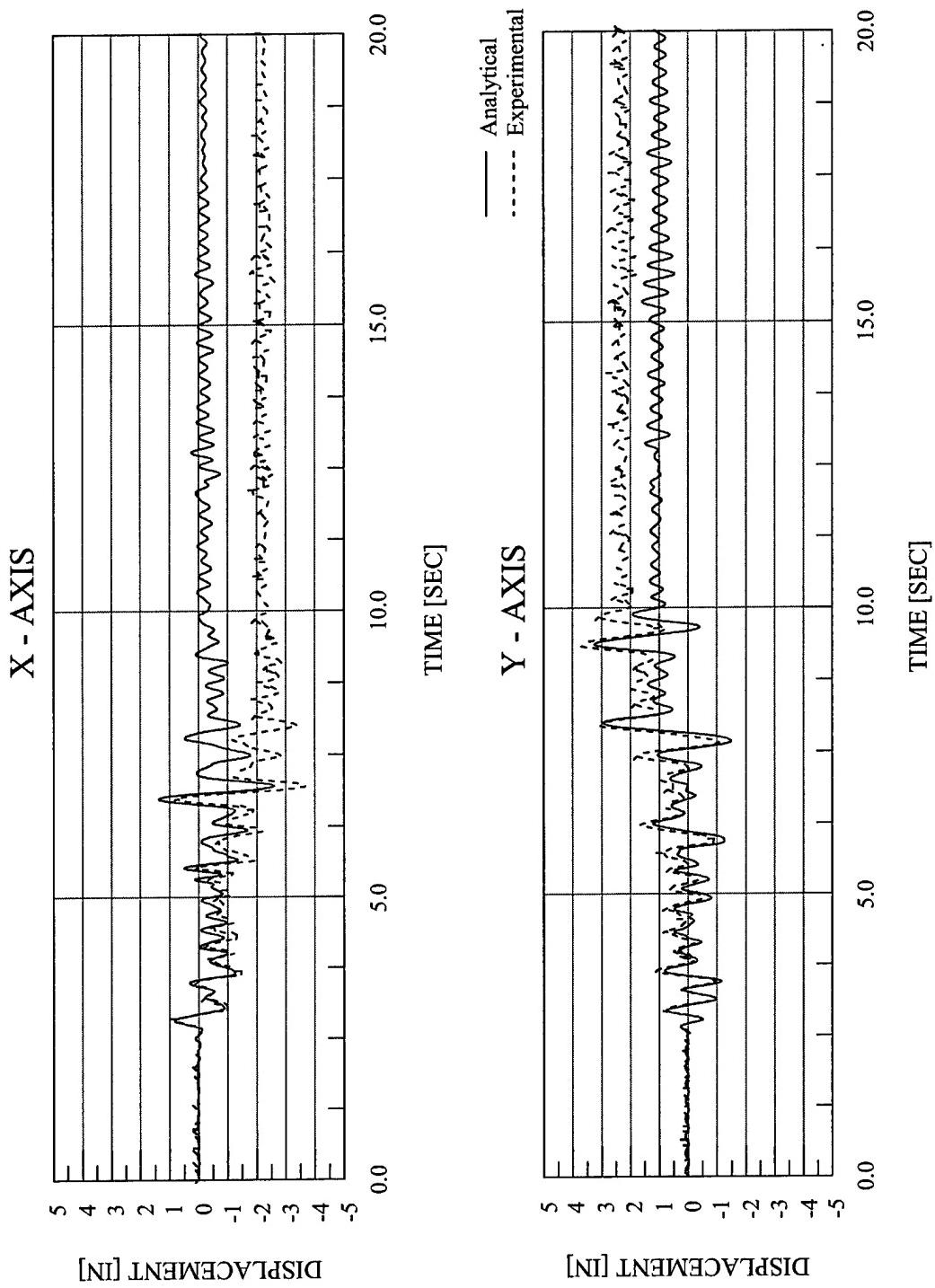


Figure 8.20 Drain-3DX Analytical Displacement vs. Time – EQ 46 – 135% Biaxial Imperial Valley

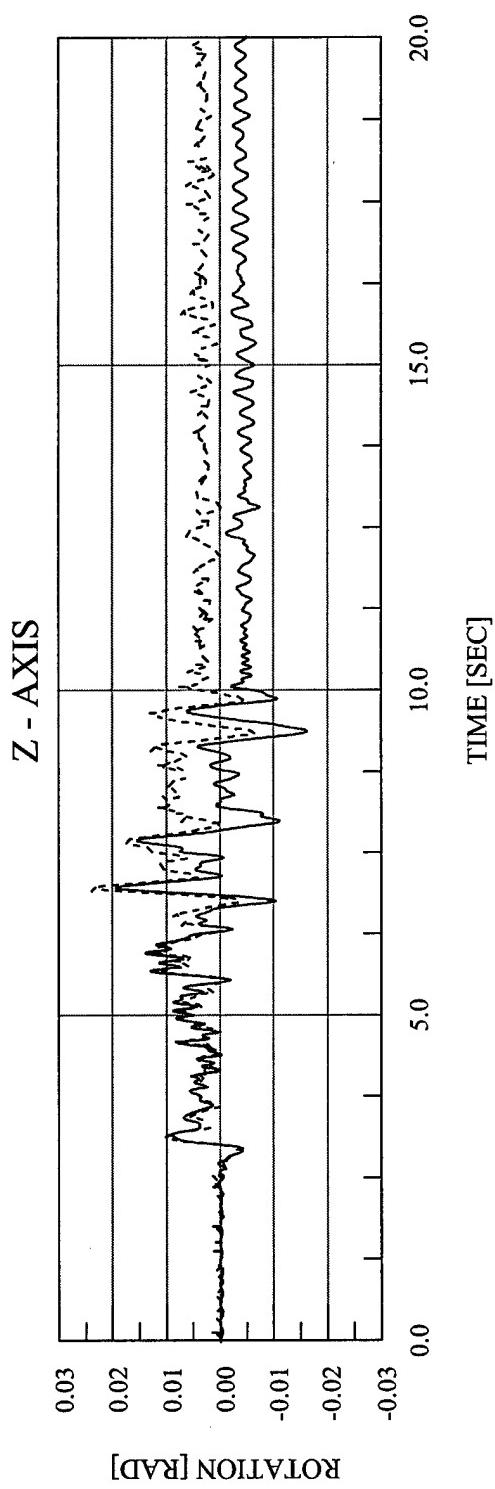


Figure 8.21 Drain-3DX Analytical Rotation vs. Time – EQ 46 – 135% Biaxial Imperial Valley

CHAPTER 9

EXPERIMENTAL AND ANALYTICAL RESPONSE OF TEST CONFIGURATION 5

This chapter provides a summary of the experimental test data and the finite element analysis results of Test Configuration 5. The fifth configuration, as seen in Figure 9.1, featured all of the masses loaded on the north side of the diaphragm, resulting in a $\frac{1}{2}$ mass asymmetry. Two 4" Double Extra-Strong Columns and two 5" Standard Columns were used. The use of these columns resulted in a strength asymmetry, as the yield bending moment and axial yield load for the 4" Double Extra-Strong Columns are both roughly 100% larger, respectively, than those of the 5" Standard Columns. No stiffness asymmetry exists, however, as both types of columns have nearly identical moments of inertia. The dynamic properties of the test structure in Test Configuration 5 are shown in Table 9.1.

Five earthquake simulations were performed with this test configuration: 10% X-Axis only [$\text{PGA}_X = 0.102 \text{ g}$], 10% Y-Axis only [$\text{PGA}_Y = 0.064 \text{ g}$], 10% Biaxial input motions [$\text{PGA}_X = 0.100 \text{ g}$ and $\text{PGA}_Y = 0.059 \text{ g}$], 100% Biaxial input motions [$\text{PGA}_X = 1.086 \text{ g}$ and $\text{PGA}_Y = 0.658 \text{ g}$], and 150% Biaxial [$\text{PGA}_X = 1.637 \text{ g}$ and $\text{PGA}_Y = 1.045 \text{ g}$]. Characterization tests were also performed to determine the dynamic properties of the model. The complete test sequence for Test Configuration 5 is shown in Table 9.2.

The first three earthquake simulations, EQ 30 with 10% X-Axis, EQ 31 with 10% Y-Axis, and EQ 32 with 10% Biaxial input motion, featured elastic behavior only. The fourth simulation, EQ 34, using 100% Biaxial input motions, was the initial inelastic test for this configuration and was followed by EQ 35, using 150% Biaxial input motions.

This chapter summarizes response data of the test structure during the earthquake simulations and the characterization tests. Summaries of test model accelerations, displacements, torsional moments, overturning moments, column end moments, and base shears are provided.

9.1 OBSERVED STRUCTURAL RESPONSE

The diaphragm acceleration and displacement time history responses for the 10% X-Axis simulation are shown in Figure 9.2. The base shear vs. displacement and torque vs. rotation are shown in Figure 9.3. Similar responses for the 10% Y-Axis simulation are shown in Figures 9.4 and 9.5. Results for the 10% Biaxial simulation are shown in Figures 9.6 and 9.7. The responses for the 100% Biaxial simulation are shown in Figures 9.8 and 9.9. Results for the 150% Biaxial simulation are shown in Figures 9.10 and 9.11.

Tables 9.3 – 9.7 list the peak recorded diaphragm relative displacements and peak diaphragm accelerations, and corresponding PGA for each of the five earthquake simulations performed in this test configuration. Also listed are the maximum base shears, maximum torsional moments, maximum overturning moments, maximum column end moments for each column, and maximum column end shears for each column.

9.2 OBSERVED RESPONSE DISCUSSION

The calculated force-deformation behavior of the structure in the X and Y directions and about the Z-Axis is shown in Figures 9.13 and 9.14. In the X direction, the model has a yield displacement of 0.53 inches at a yield force of 35.89 kips. In the Y direction, the model has a yield displacement of 0.48 inches at a yield force of 32.95 kips. The model has a yield rotation of 0.0067 radians at a yield moment of 2270 kip*inches. Elastic response spectra of the recorded table motions for EQ 30 – EQ 32 and EQ 34 are shown in Figures 9.15 – 9.18, respectively. In addition, the modal frequencies for this configuration with respect to the response spectra are indicated in Figures 9.15 – 9.18.

The first earthquake simulation for this configuration, EQ 30, features 10% Imperial Valley input motion in the X-Axis only [$\text{PGA}_X = 0.102 \text{ g}$]. Time history plots of the structural response are shown in Figure 9.2. The peak displacements of the structure were 0.211 inches in the X direction and 0.042 inches in the Y direction, with a peak rotation of 0.36×10^{-3} radians. The peak displacement predicted by static analysis is 0.202 inches along the X-Axis, with no Y-Axis displacement or rotation predicted. In EQ 30, with no eccentricity, a torsional effect is not

expected, and it appears from the rotation time history in Figure 9.2 that the measured rotation is most likely a product of the shaketable control problem discussed in Chapters 3 and 4. Further, the displacement time histories indicate no residual displacement or permanent deformation.

Also verifying the elastic response are the peak base shears and peak torsional moment, which are 14.27 kips in the X direction, 1.39 kips in the Y direction, and 56.64 kip*inches about the vertical axis. Figure 9.3 shows the base shear vs. displacement plots and torsional moment vs. rotation plot. The shear vs. displacement plot for the X direction is tight and linear.

In EQ 31 the model is subjected to a 10% Y-Axis input motion [$\text{PGA}_Y = 0.064 \text{ g}$]. Time history plots of the structural response are shown in Figure 9.4. The peak displacements of the structure were 0.058 inches in the Y direction and 0.025 inches in the X direction, with a peak rotation of 0.61×10^{-3} radians. Static analysis predicts a Y-Axis peak displacement of 0.065 inches, a peak rotation of 0.21×10^{-3} radians, and no X-Axis displacement. The peak base shears and peak torsional moment are 3.88 kips in the Y direction, 0.41 kips in the X direction, and 92.24 kip*inches about the vertical axis. Figure 9.5 shows the base shear vs. displacement plots and torsional moment vs. rotation plot, which for the Y-Axis and Z-Axis are both linear. Due to the low response levels in the Y-direction and about the Z-Axis, both hysteresis shapes are obscured by noise from the data acquisition system.

The third earthquake simulation for this configuration, EQ 32, features 10% Imperial Valley input motion along both the X-Axis and Y-Axis [$\text{PGA}_X = 0.100 \text{ g}$ and $\text{PGA}_Y = 0.059 \text{ g}$]. Time history plots of the structural response are shown in Figure 9.6. The peak displacements of the structure were 0.214 inches in the X direction and 0.063 inches in the Y direction, with a peak rotation of 0.61×10^{-3} radians. Static analysis predicts peak displacements of 0.200 inches along the X-Axis, 0.062 inches along the Y-Axis, and a peak rotation of 0.20×10^{-3} radians. The displacement time histories indicate no residual displacement or permanent deformation. The peak base shears and peak torsional moment are 14.29 kips in the X direction, 4.74 kips in the Y direction, and 113.58 kip*inches about the Z-axis. Figure 9.7 shows the base shear vs. displacement plots and torsional moment vs. rotation plot, which are all tight and linear, indicating no yielding.

Thus, for this test configuration, the static analysis was both conservative and unconservative in predicting the elastic peak displacements, differing from the measured displacements by as much as 10%. However, the static analysis is consistently unconservative in predicting the elastic peak

rotations, by as much as 200%. Note that the structural response does not qualify the model as torsionally irregular in any of the elastic simulations.

In comparing EQ 32 with EQ 31, the addition of the 10% X-Axis input motion results in little change in the Y-Axis response of the diaphragm, as the peak displacement is 0.058 inches for EQ 31 and 0.063 inches for EQ 32. Because this configuration has an eccentricity in the X direction only, the addition of an input motion and thus response in the X direction will not add to the torsional effect. This is verified by the fact that the torsional moment changes little between EQ 31 and EQ 32. In addition, the diaphragm rotation is 0.61×10^{-3} radians for both EQ 31 and EQ 32. In comparing EQ 32 to EQ 30, the addition of the 10% Y-Axis input motion causes little change in the X-Axis response, but increases the peak rotation substantially. The peak displacement in the X-Axis changes very little from EQ 30 to EQ 32, 0.211 inches to 0.214 inches. The peak rotation increases from 0.36×10^{-3} radians in EQ 30 to 0.61×10^{-3} radians. This rotation response in EQ 30 was previously observed to be a resonant vibration response due to the shake table motion control problem. However, EQ 32 featured a biaxial ground motion, thus no control problem was present, and the observed resonant response in EQ 30 would not be present in EQ 32. The same argument holds in comparing the Y-Axis response in EQ 30 to that in EQ 32. In comparing the structural response from one simulation to the next, it is also important to take note of any differences in the ground motions. The peak recorded ground accelerations (PGA) for EQ 30 – EQ 32 change very little. In the X direction, EQ 30 has a PGA of 0.102 g while EQ 32 has a PGA of 0.100 g. In the Y direction, EQ 31 has a PGA of 0.058 g while EQ 32 has a PGA of 0.059 g. Also of importance are the pseudo-spectral displacements (PSD). In the X direction, EQ 30 has a PSD of 1.241 inches while EQ 32 has a PSD of 1.245 inches. In the Y direction, EQ 31 has a PSD of 1.092 inches while EQ 32 has a PSD of 1.066 inches. In a linear elastic system, the displacement response in EQ 32 should be the equal to the sum of the responses in EQ 30 and EQ 31. This comparison can be made if the ground motions for all three simulations were the same, which appears to be the case here. In accounting for the Y-Axis and rotational response in EQ 30 as due to the table control problem, the response in EQ 32 is in fact equal to the sum of those in EQ 30 and EQ 31.

In EQ 34, the first test in this configuration that features inelastic response, the model structure is subjected to 100% Imperial Valley input motion along both the X-Axis and Y-Axis [PGA_X = 1.086 g and PGA_Y = 0.658 g]. Time history plots of the structural response are shown in Figure 9.8. The peak displacements of the structure were 1.31 inches in the X direction and 0.46 inches

in the Y direction, with a peak rotation of 8.39×10^{-3} radians. Thus, the response in the X direction exceeds the yield displacement of 0.53 inches, while the Y-Axis response is slightly less than the yield displacement of 0.47 inches. The peak base shear in the X direction of 60.36 kips is greater than the yield shear of 35.89 kips, while in the Y direction the peak base shear of 31.42 kips is nearly equal to yield shear, 32.41 kips. Despite the torsional ductility being greater than one, the peak torsional moment is approximately 1/3 of the torsional yield moment. This behavior has been observed in previous configurations as the result of the dependence of the torsional stiffness on the lateral stiffnesses of the structure, and thus the interaction of the lateral and torsional responses. Figure 9.9 shows the base shear vs. displacement plots and torsional moment vs. rotation plot, which are no longer tight and linear, but now are taking on a fuller shape. However, the shear vs. displacement plot for the Y-Axis response remains tight and linear. For this structure, the PSA in the X direction is 4.77 as compared to only 1.18 in the Y direction. This explains why the structure remains elastic in the Y direction while responding inelastically in the X direction.

The acceleration response of the diaphragm divided by the peak ground acceleration (PGA) is shown in Table 9.4 as the normalized acceleration. In EQ 32, with 10% Biaxial input motions, the normalized acceleration response of the diaphragm is 4.04 in the X direction, and 2.31 in the Y direction. The input ground motions are increased by approximately a factor of 10 in EQ 34, but the acceleration response of the diaphragm only increases by about 4 in the X direction and 6 in the Y direction. This is illustrated in the normalized acceleration response of the diaphragm, which is 1.57 in the X direction and 1.30 in the Y direction. Because the base shears are roughly proportional to the diaphragm accelerations, the same trends can be observed by comparing the peak base shears to the peak ground accelerations.

The final earthquake simulation for this configuration, EQ 35, features 150% Imperial Valley input motion along both the X-Axis and Y-Axis [PGA_X = 1.637 g and PGA_Y = 1.045 g]. Time history plots of the structural response are shown in Figure 9.10. The peak displacements of the structure were 2.81 inches in the X direction and 1.22 inches in the Y direction, with a peak rotation of 13.82×10^{-3} radians. The peak base shears are 59.51 kips in the X direction and 47.66 kips in the Y direction. The base shear in the X direction for EQ 35 actually decreased slightly from EQ 34, while the shear in the Y direction increased by approximately 50%. The increase in the Y direction shear was in proportion to the increase in the ground motions from EQ 34 to EQ 35. This indicates that the structure is responding elastically or very nearly elastically along the

Y-Axis for EQ 35. Although the yield shear in the Y direction is 32.41 kips, Figure 9.13 shows that the change in stiffness after reaching the yield shear is very small until nearly 45-50 kips. The peak base shear in the Y direction for EQ 35, at 47.66 kips, falls into this range, which explains the nearly elastic response. The peak base shear decreases slightly in EQ 35 from EQ 34, while the torsional moment nearly doubles, increasing from 732.2 kip*inches to 1300.4 kip*inches. With EQ 35, as shown in Figure 9.11, the base shear vs. displacement hysteresis loops exhibit a more full, smooth shape, indicating some degree of inelastic behavior. Although in the Y direction, the base shear is still nearly elastic, the peak displacement response is approximately 2-1/2 times the yield displacement, which explains the inelastic shape of the base shear vs. displacement loop. This behavior, in which the peak shears are elastic or nearly elastic while the ductility is much larger than one, has been observed in previous configurations for the torsional response of the structure. It was observed that the peak torsional moment was smaller than the yield moment, while the peak rotation was much greater than the yield rotation. This interaction has now produced the same effect in one of the lateral directions as well as the torsional direction, as the torsional ductility is greater than 2 while the peak torsional moment is approximately 3/5 of the yield moment. The torsional moment vs. rotation loop has become more full as compared with EQ 34, but the shape is somewhat erratic as compared with the base shear vs. displacement loops. Contrary to EQ 30 – 32, a small amount of residual displacement is evident in the X direction after EQ 34, as seen in Figure 9.8. The permanent displacement increases slightly in EQ 35 in both directions, as seen in Figure 9.10.

One indicator of the softening of the structure is the ratio of the torsional displacement to the base shear. As yielding occurs, we expect to see displacements increase to a greater degree than the inertial forces. This is verified by the fact that the torsional displacement to base shear ratio is approximately 3.5 times larger for EQ 34 than for EQ 32. Further, for EQ 35 the ratio is more than 5 times larger than for EQ 32.

9.3 DYNAMIC CHARACTERIZATIONS OF THE MODEL

Prior to performing any shake table simulations using the earthquake input motions, white noise, sine sweep, and sine decay tests were performed, as discussed in Chapter 3. This general pattern was followed for Test Configuration 5, as can be seen in Table 9.2. In addition, white noise tests

were performed immediately after the final earthquake simulation exhibiting inelastic behavior, EQ 35.

The dynamic properties of the test structure, as measured before EQ 30 and then after EQ 35, are shown in Table 9.1. The results in Table 9.1 indicate that due to the inelastic behavior during EQ 34 and EQ 35, permanent softening in the X direction did take place, with the modal frequency decreasing from 4.35 Hz to 3.85 Hz. In the Y direction, no permanent softening of the structure took place, which follows from the nearly linear behavior observed in the Y direction.

9.4 OBSERVED CONDITION OF THE STRUCTURE

Following each of the major earthquake simulations, the model structure was physically inspected. Historically, the most problematic location on the model was column-to-bottom plate welded joint on each column. For Test Configuration 5, weld fracture did become an issue.

Following EQ 32, the final elastic simulation, EQ 33 was performed using 100% Imperial Valley ground motions. This was intended to be the first inelastic simulation for Test Configuration 5. Less than five seconds into the test, a fracture occurred at the interface between the weld and pipe column at the base of one of the 4" Double Extra-Strong columns. The columns were subsequently removed and the weld was repaired before any further tests were performed.

Following the weld repair, EQ 34 was run as a repeat of EQ 33. No further weld or base material fractures were observed during the remainder of the simulations.

Due to the much greater strength of the columns as compared to the previous configurations, the peak structural displacements were much smaller for this configuration. Consequently, observing the formation of plastic hinges near the tops and bottoms of the columns was difficult. For the same reason, permanent diaphragm displacements were difficult to observe as well. In fact, for the final simulation, EQ 35 using 150% Imperial Valley ground motions, the permanent diaphragm displacements were less than $\frac{1}{2}$ -inch in the X direction and less than $\frac{1}{4}$ -inch in the Y direction. For this reason, photographs of the structure following the simulations show no apparent changes from those taken beforehand. Figures 9.19, 9.20 and 9.21 are photographs of the test structure taken before any earthquake simulations were performed.

9.5 FINITE ELEMENT ANALYSIS

In modeling the behavior of the test structure, the nonlinear finite element analysis programs Abaqus and Drain-3DX were employed. A more complete discussion of the applicable features of Abaqus and Drain-3DX is presented in Chapter 3. Also, some aspects of the finite element model, such as the modeling of the diaphragm as a rigid component, are common throughout each test configuration, and are discussed more completely in Chapter 3.

(A) PIPE COLUMN MATERIAL MODEL

The pipe columns used in Test Configuration 5, as well as those used in Test Configuration 7, were produced from the same batch of raw pipe column lengths. As a result of this, two coupons were taken from each of the two types of pipe used in Test Configurations 5 and 7, 4" Double Extra-Strong and 5" Standard. The material models of the pipe columns in these two test configurations were based on stress-strain data produced during coupon tension tests. Figures 9.22 and 9.23 show both the original stress-strain data recorded during the coupon tension tests, and the best-fit material model used in the Abaqus finite element analyses for the 5" Standard and 4" Double Extra-Strong pipe material, respectively. Figures 9.24 and 9.25 show the original material data and the best-fit material model used in the Drain-3DX finite element analyses. Shown in Tables 9.8 and 9.9 are the Abaqus numerical stress-strain best-fit model data for the 5" Standard and 4" Double Extra-Strong pipe material, respectively. Shown in Tables 9.10 and 9.11 are the Drain-3DX best-fit material model data for the two types of pipe material.

(B) FINITE ELEMENT MODEL

The Abaqus and Drain-3DX finite element models used in Test Configuration 5 are shown in Figures 9.26 and 9.27. Beyond the features of the finite element model common throughout each test configuration, these figures illustrate the location and magnitudes of the nodal masses and the height of the Non-Rigid Links. As shown in Figure 9.26, the nodal masses at each of the four diaphragm corners have a magnitude of $2.705 \text{ lb*s}^2/\text{in}$ in the Abaqus model. Two of the interior

masses, the northeast and northwest interior masses, each have a magnitude of $35.252 \text{ lb}^*\text{s}^2/\text{in}$. The other two interior masses, located on the south side of the diaphragm, have magnitudes of $4.578 \text{ lb}^*\text{s}^2/\text{in}$. The height of the Abaqus model diaphragm in this test configuration is 68.691 inches, resulting in a length of 8.691 inches for each of the four Non-Rigid Links. As shown for the Drain-3DX model in Figure 9.27, the nodal masses placed at the four diaphragm corners have magnitudes of $2.417 \text{ lb}^*\text{s}^2/\text{in}$. The interior masses on the north side of the diaphragm each have a magnitude of $35.203 \text{ lb}^*\text{s}^2/\text{in}$, while those on the south side of the diaphragm have magnitudes of $5.203 \text{ lb}^*\text{s}^2/\text{in}$.

(C) OBSERVED RESPONSE

Displacement histories along the X- and Y-Axis and about the Z-Axis are provided for the 10% Biaxial simulation [$\text{PGA}_X = 0.100 \text{ g}$ and $\text{PGA}_Y = 0.059 \text{ g}$] in Figures 9.28 – 9.31, the 100% Biaxial simulation [$\text{PGA}_X = 1.086 \text{ g}$ and $\text{PGA}_Y = 0.658 \text{ g}$] in Figures 9.32 – 9.35, and the 150% Biaxial simulation [$\text{PGA}_X = 1.637 \text{ g}$ and $\text{PGA}_Y = 1.045 \text{ g}$] in Figures 9.36 – 9.39. Table 9.12 lists the maximum peak relative displacements in the X and Y directions and the peak rotation for the three earthquake simulations listed above.

(D) OBSERVED RESPONSE DISCUSSION

In Figures 9.28 – 9.31, the Abaqus and Drain-3DX displacement and rotation response histories for EQ 32 [$\text{PGA}_X = 0.100 \text{ g}$ and $\text{PGA}_Y = 0.059 \text{ g}$] can be seen for both the test structure and the finite element models. For both displacements and the rotation, the frequency contents of the response histories in the Abaqus and Drain-3DX simulations match the test data very well. Also, as seen in Table 9.12, the peak displacements in both directions of the Abaqus results match the test data fairly well, agreeing to within 1% in the X direction and within 11% in the Y direction. The Drain-3DX model is equally accurate in the Y direction, but not so in the X direction, with a difference of nearly 30%. As discussed in previous chapters, the limitations of both finite element analysis models to allow the damping in each direction independently has resulted in a compromise damping ratio that attempts to minimize the lack of accuracy in each direction. The Drain-3DX model appears to be overdamped in the X direction, which is consistent with the fact that the actual X-Axis damping ratio is roughly half of the Y-Axis damping ratio, and is therefore

less than the “compromise” damping ratio used in the model. However, this is also true for the Abaqus model, and it accurately predicts the X-Axis response history. For both the Abaqus and Drain-3DX models, the peak displacements appear to occur in the same time region for both the finite element model and the test structure. The peak rotation in the Abaqus model does not agree well with the test data nor does the Drain-3DX model. Both predict a peak rotation less than half of the actual peak rotation. As observed in previous configurations, one problem with matching to the rotation data of the test structure is that the response is low enough that noise from the data acquisition system is apparent in the data. Despite this, it is apparent that in addition to the peak rotations not matching the actual value very well, there are many other locations in the time history where the local minima and maxima do not match well. Although the rotation has consistently been the most difficult response quantity to predict, the discrepancies in elastic simulations in previous chapters have not been as great as with this configuration.

In Figures 9.32 – 9.35, the displacement and rotation response histories for EQ 23 [$\text{PGA}_X = 1.086 \text{ g}$ and $\text{PGA}_Y = 0.658 \text{ g}$] can be seen for both the test structure and the finite element models. For both the X-Axis and Y-Axis displacements, the frequency contents of the response histories in both the Abaqus and Drain-3DX simulations match the test data well. In the X direction, the Abaqus and Drain-3DX analyses overestimate the peak displacement by 25% and 28%, respectively. In addition, most of the largest local response minima and maxima are overestimated by both analyses. In the Y direction, the Abaqus and Drain-3DX analyses overestimate the peak displacement by 17% and 22%, respectively. Both the Abaqus and Drain-3DX simulations underestimate the peak rotational response by over 100%, and are significantly inaccurate at many points along the time history. In fact, the discrepancies between the predicted rotational response and the actual response are large enough that the frequency content at times appears to be different. These same trends continue in the response histories for EQ 35 [$\text{PGA}_X = 1.637 \text{ g}$ and $\text{PGA}_Y = 1.045 \text{ g}$], the 150% simulation, shown in Figures 9.36 – 9.39. The peak rotation again is underestimated by more than 100% in the Abaqus simulation and by more than 80% in the Drain-3DX simulation. The rotation time histories do appear to match in the location of the maximum and minimum peaks. However, in general, the rotation time histories in both EQ 34 and EQ 35 do not match very well. For EQ 35, the Abaqus and Drain-3DX simulations underestimate the peak displacements in both the X and Y directions. In the X direction, the peak displacements agree to within 8% and 5%, respectively. In the Y direction, the peak displacements agree to within only 25% and 17%. There is little actual permanent displacement in the Y direction, and both analyses appear to predict it accurately. In the X direction, there is

again only a small amount of permanent offset, but the Abaqus analysis predicts a value roughly double the actual value. In general, it appears that this test configuration, with a strength asymmetry and two different column material models, is more difficult to correctly model in Abaqus. As has been shown and discussed in previous chapters, the structural response in the finite element simulations is affected by the chosen column material model. The presence of two different types of columns and thus two different material models only amplifies the difficulty in modeling the structural response, as has been shown in Figures 9.27 – 9.30.

For the hardening model for these simulations, it was assumed that the isotropic part of the hardening would compose 30% of the total hardening. This figure was chosen through calibration to the response of the symmetric models studied in Chapters 4 and 5. As with the test configuration discussed in the previous chapter, the pipe columns used in this test configuration are taken from a different batch of pipe steel than those used in the hardening model calibration test configurations. Thus, the assumption is again being made that the material hardening behavior for the steel used in this configuration is similar in nature to the hardening behavior of the steel used in earlier configurations when the hardening model was calibrated. The fact that the analytical response results do not match the experimental results as well as in previous configurations could be a result of this assumption, as it was shown that the ratio of isotropic hardening to kinematic hardening can have a large impact on the response characteristics of the model.

9.6 SUMMARY AND CONCLUSIONS

In previous chapters, the *Modified μ/R Ratio* was introduced and discussed. This ratio gives a measure of the amount of ductility the 2000 NEHRP Seismic Provisions expects a particular structure to experience and thus for which it must be designed. The *Modified μ/R Ratio* was computed as the normalized displacement in an inelastic test divided by the normalized displacement during an elastic test and also as the ratio of the normalized rotation during an inelastic simulation to the normalized rotation during an elastic simulation. For EQ 34, the first inelastic simulation in this configuration, the μ/R Ratios were 0.56 in the X direction, 0.67 in the Y direction, and 1.28 torsionally. For EQ 35, the second inelastic simulation, the μ/R Ratios were 0.80 in the X direction, 1.19 in the Y direction, and 1.39 torsionally.

Configuration	EQ	μ/R Ratio		
		X-Axis	Y-Axis	Z-Axis
Symmetric Mass 100% Uniaxial	7	N/A	0.77	N/A
Symmetric Mass 100% Biaxial	15	1.37	0.86	0.84
Symmetric Mass 150% Biaxial	16	1.77	1.83	1.08
$\frac{1}{2}$ Asymmetric Mass 100% Biaxial	28	0.90	0.51	1.07
$\frac{1}{2}$ Asymmetric Mass 150% Biaxial	29	1.17	1.03	1.39
$\frac{1}{4}$ Asymmetric Mass 100% Biaxial	23	1.60	0.61	1.90
$\frac{1}{2}$ Asymmetric Mass Strength Asymmetry 100% Biaxial	34	0.56	0.67	1.28
$\frac{1}{2}$ Asymmetric Mass Strength Asymmetry 150% Biaxial	35	0.80	1.19	1.39

The *Seismic Provisions* provides a range of 0.86 to 0.69 for an Ordinary Moment Resisting Frame (OMRF) and a Special Moment Resisting Frame (SMRF), respectively. Although the values of the μ/R Ratios continue to be inconsistent for differing test configurations, earthquake magnitudes, and component directions, they appear to generally range from near 0.69, the lower bound provided by the *Seismic Provisions*, to somewhere near twice 0.86, the upper bound. If a structure possesses a μ/R Ratio less than 0.69, it simply means that the structure was designed for larger displacements than were actually achieved. Of greater concern is a structure possessing a μ/R Ratio significantly larger than that prescribed for design by the *Seismic Provisions*. However, the expected level of overstrength structures are assumed during design to possess would be a significant mitigating factor in comparing the μ/R Ratios prescribed by the *Provisions* with those determined experimentally here.

The methodology used in the *Seismic Provisions* of using an elastic analysis as the basis for determining inelastic response of structures implies that the ratio of the peak rotation to the peak lateral displacement and the ratio of the two peak lateral displacements remain constant for elastic and inelastic response. In previous configurations, which featured four 4" Extra-Strong Columns, a general trend emerged in the u_y/u_x ratio. In comparing the initial inelastic simulations to the

elastic simulations, the u_Y/u_X ratio decreased noticeably. Due to differences in the X- and Y-Axis ground motions, primarily that the X-Axis PSA was roughly 50% greater than along the Y-Axis, the structure yielded to a greater degree in the X direction than in the Y direction in the first inelastic simulations. This resulted in a greater X-Axis stiffness loss, and a larger X-Axis displacement response proportionally to the Y-Axis response. In observing the response during the second and larger inelastic simulations, the u_Y/u_X ratios increased to roughly the same value as during the elastic tests. During the larger inelastic simulations, the structure had traveled further along the force-displacement curve to the point where it has lost roughly an equal amount of stiffness in each direction.

For EQ 32 in this test configuration, the u_Y/u_X ratio is 0.29, as shown below. This value is much smaller than the u_Y/u_X ratio for EQ 27, the elastic test for Test Configuration 4, and all other elastic tests in previous configurations. The difference between the u_Y/u_X ratios for EQ 32 and EQ 27 is a result of the spectral accelerations in the two tests. For EQ 27, the X-Axis PSA was 0.36 while the Y-Axis PSA was 0.30. For EQ 32, the X-Axis PSA was 0.39 while the Y-Axis PSA was only 0.12. With the stiffer columns used in this test configuration, the modal frequencies are noticeably larger than for previous test configurations resulting in different response characteristics. Also different from previous configurations, the u_Y/u_X ratio does not exhibit a large drop when comparing the first inelastic test to the elastic test. This decrease was previously attributed to the structure yielding significantly in the X direction, while a lesser degree of yielding occurred in the Y direction. For EQ 34, the first inelastic simulation in this configuration, the ratio increases slightly to 0.35. With the stronger and stiffer columns used in this test configuration, the X-Axis and Y-Axis pushover analysis yield forces are roughly 75% greater than in previous configurations. The effect of this is evident as the ductility experienced by the structure in the first inelastic test, EQ 34, is less than half the ductility experienced during the initial inelastic tests in previous configurations. Thus, it appears that its greater yield strength has prevented the structure from moving far enough along the force-deformation curve to create the large difference in X-Axis and Y-Axis lateral stiffness seen in previous configurations. In the second inelastic test, EQ 35 in which 150% Imperial Valley ground motions were used, the ductility experienced by the structure is roughly equal to the ductilities experienced in the initial inelastic tests in previous configurations.

Configuration	EQ	u_y/u_x	u_θ/u_x
Symmetric Mass 25% Biaxial	14	0.73	N/A
Symmetric Mass 100% Biaxial	15	0.43	N/A
Symmetric Mass 150% Biaxial	16	0.80	N/A
$\frac{1}{2}$ Asymmetric Mass 10% Biaxial	27	0.86	0.29
$\frac{1}{2}$ Asymmetric Mass 100% Biaxial	28	0.51	0.35
$\frac{1}{2}$ Asymmetric Mass 150% Biaxial	29	0.85	0.35
$\frac{1}{4}$ Asymmetric Mass 10% Biaxial	22	0.96	0.28
$\frac{1}{4}$ Asymmetric Mass 100% Biaxial	23	0.37	0.33
$\frac{1}{4}$ Asymmetric Mass 100% Biaxial	45	0.64	0.32
$\frac{1}{4}$ Asymmetric Mass 135% Biaxial	46	1.04	0.30
$\frac{1}{2}$ Asymmetric Mass Strength Asymmetry 10% Biaxial	32	0.29	0.14
$\frac{1}{2}$ Asymmetric Mass Strength Asymmetry 100% Biaxial	34	0.35	0.31
$\frac{1}{2}$ Asymmetric Mass Strength Asymmetry 150% Biaxial	35	0.44	0.24

The trend observed for the torsional motion in previous test configurations was that the u_θ/u_x ratio for the first inelastic simulation was roughly 20% larger than for the elastic test. Further, the u_θ/u_x ratio for the second inelastic test was roughly equal to that for the first inelastic test.

For EQ 32, the last elastic simulation, the u_θ/u_x ratio is 0.14. The value increases to 0.31 for EQ 34, the first inelastic test, and then decreases slightly to 0.24 for the second inelastic test. Thus, the u_θ/u_x ratio for the inelastic tests in this configuration are roughly twice as large as for the elastic test, not the 20% observed in previous configurations. The presence of the strength asymmetry in this configuration, with the two 4" Double Extra-Strong Columns having a yield

moment nearly twice as large as for the two 5" Standard Columns, is the primary source of this behavior. As the response increases to the point where yielding begins, the two 5" Standard Columns will yield before the other two columns, and to a much greater degree. In fact, it is possible that the two stronger columns may remain elastic throughout the entire response while the weaker ones yield. During the instances or periods during the simulation when one or both of the weaker columns yields, an instantaneous stiffness eccentricity appears which was not present during the elastic tests. This stiffness eccentricity may significantly increase the torsional response of the structure. Although in previous configurations it is likely that all four columns did not yield simultaneously, and therefore this phenomenon may have occurred to some degree, the presence and degree of the strength eccentricity increased the effect substantially, as demonstrated by the u_θ/u_X ratios in this configuration. This type of asymmetry may present a significant problem in design, as the stiffness eccentricity that may appear will do so only in inelastic simulations. Thus, the assumption that the u_θ/u_X ratio remains the same for elastic and inelastic response clearly does not hold for this case. The degree to which this parameter will increase for inelastic response will depend on the specific configuration and material properties of the structure.

The time history analyses performed for this configuration using Abaqus and Drain-3DX were fairly accurate in their predictions of the experimental displacement response. However, they were generally inaccurate in their predictions of the rotational response. In comparison with previous test configurations, the finite element analyses proved to be slightly less accurate in predicting displacement response and significantly less accurate in predicting rotational response. No consistent pattern emerged as to which analysis program was more accurate in this test configuration. With respect to the inelastic simulations, the Abaqus and Drain-3DX were on average inaccurate by 15-20% in predicting displacement response, in some cases overestimating and in some cases underestimating the response. In predicting the rotational response, Abaqus and Drain-3DX consistently underestimated the peak value by roughly 50%, for both the elastic and inelastic simulations. For EQ 34, the difference between the predicted and actual peak rotation is roughly 4.5×10^{-3} radians, corresponding to an edge displacement due to rotation of 0.22 inches. An edge displacement of 0.22 inches is roughly 1/6 of the peak X-Axis displacement and roughly 1/2 of the peak Y-Axis displacement. Thus, the differences between the predicted and actual rotational response are not insignificant.

In previous test configurations, the rotation has consistently been the most difficult response parameter to predict. However, even in the cases when the magnitudes of the rotational response were noticeably different between the predicted and actual responses, the frequency content of the time histories typically matched well. As observed and discussed in previous configurations, each column participates in the seismic resistance of the structure in each of the three directions of motion. As a column yields due to lateral response, the instantaneous torsional stiffness of the structure consequently changes as well, impacting the torsional response. Accurately predicting the instantaneous lateral and torsional stiffness and thus the overall response during inelastic simulations is significantly affected by the ability to accurately model the material behavior of the columns. In this configuration, two different types of columns are present, each with unique yield stress, post-yield behavior, and cross-sectional properties. Any inaccuracies in the modeling of the columns and their properties amplify the potential for difficulties in response prediction, in comparison with previous configurations having four identical columns. Thus, it is not surprising that in this configuration the Abaqus and Drain-3DX analyses were less accurate in predicting the frequency content of the rotational response, as it depends significantly on the instantaneous rotational stiffness of the structure.

Mass [lb*s ² /in]	Mass Centers [in]			5" Standard Column Properties		4" Double Extra-Strong Column Properties	
	X ₀	Y ₀	Z ₀	A [in ²]	I [in ⁴]	A [in ²]	I [in ⁴]
91.572	-15.007	0.0	68.229	4.30	15.2	8.10	15.3

	Modal Frequencies [Hz]			Modal Damping [%]		
	X	Y	θ	X	Y	θ
Before EQ 30	4.348	4.255	9.091	0.767	1.597	0.579
After EQ 35	3.846	4.255	9.091	0.664	1.597	0.579

Table 9.1 Test Structure Dynamic Properties - Test Configuration 5

Test Designation	Input Motions
WNT28	White Noise X-Axis
WNT29	White Noise Y-Axis
WNT30	White Noise Yaw-Axis
SIN13	Sine Decay X-Axis
SIN14	Sine Decay Y-Axis
SIN15	Sine Decay Yaw-Axis
SWP13	Sine Sweep X-Axis
SWP14	Sine Sweep Y-Axis
SWP15	Sine Sweep Yaw-Axis
EQ30	10% X-Axis Imperial Valley
EQ31	10% Y-Axis Imperial Valley
EQ32	10% Biaxial Imperial Valley
EQ33	100% Biaxial Imperial Valley
SIN16	Sine Decay X-Axis
SIN17	Sine Decay Y-Axis
SIN18	Sine Decay Yaw-Axis
SWP16	Sine Sweep X-Axis
SWP17	Sine Sweep Y-Axis
SWP18	Sine Sweep Yaw-Axis
EQ34	100% Biaxial Imperial Valley
EQ35	150% Biaxial Imperial Valley
WNT37	White Noise X-Axis
WNT38	White Noise Y-Axis
WNT39	White Noise Yaw-Axis
SIN19	Sine Decay X-Axis
SIN20	Sine Decay Y-Axis
SIN21	Sine Decay Yaw-Axis
SWP19	Sine Sweep X-Axis
SWP20	Sine Sweep Y-Axis
SWP21	Sine Sweep Yaw-Axis

Table 9.2 Earthquake Simulations and Dynamic Characterization Tests - Test Configuration 5

Earthquake Test No.	Input Motions	PGA [g]	Relative Displacement [in]			Rotation [10^{-3} rad]	Normalized Displacement [in/g]			Ductility		
			X-Axis	Y-Axis	Z-Axis		X-Axis	Y-Axis	Z-Axis	X-Axis	Y-Axis	Z-Axis
30	10% X-Axis	0.102	N/A	0.207	0.023	0.37	2.03	N/A	0.39	0.05	0.06	
31	10% Y-Axis	N/A	0.064	0.015	0.057	0.51	N/A	0.89	0.03	0.12	0.08	
32	10% Biaxial	0.100	0.059	0.212	0.065	0.59	2.12	1.10	0.40	0.14	0.09	
34	100% Biaxial	1.086	0.658	1.313	0.458	8.39	1.21	0.70	2.46	0.95	1.25	
35	150% Biaxial	1.637	1.045	2.805	1.221	13.82	1.71	1.17	5.26	2.54	2.06	

Table 9.3 Maximum Diaphragm Relative Displacement and Rotation - Test Configuration 5

Earthquake Test No.	Input Motions	PGA [g]			Diaphragm Acceleration [g]			Diaphragm Angular Acceleration [10^{-3} g/in]			Normalized Acceleration
		X-Axis	Y-Axis	Z-Axis	X-Axis	Y-Axis	Z-Axis	X-Axis	Y-Axis	Z-Axis	
30	10% X-Axis	0.102	N/A	0.403	0.047	0.94		3.95			N/A
31	10% Y-Axis	N/A	0.064	0.011	0.107	0.82		N/A			1.67
32	10% Biaxial	0.100	0.059	0.404	0.136	1.28		4.04			2.31
34	100% Biaxial	1.086	0.658	1.706	0.856	9.87		1.57			1.30
35	150% Biaxial	1.637	1.045	1.682	1.364	17.10		1.03			1.31

Table 9.4 Maximum Diaphragm Acceleration and Angular Acceleration Response - Test Configuration 5

Earthquake Test No.	Input Motions	PGA [g]			Base Shear [k]	Torsional Moment [k*in]	Overturning Moment [k*in]	
		X-Axis	Y-Axis	Z-Axis				
30	10% X-Axis	0.102	N/A	14.27	1.39	56.64	980.4	95.4
31	10% Y-Axis	N/A	0.064	0.41	3.88	92.24	27.9	266.7
32	10% Biaxial	0.100	0.059	14.29	4.74	113.58	981.6	325.7
34	100% Biaxial	1.086	0.658	60.36	31.42	732.22	4146.2	2158.4
35	150% Biaxial	1.637	1.045	59.51	47.66	1300.42	4088.1	3274.1

Table 9.5 Maximum Base Shear, Torsional Moment, and Overturning Moment - Test Configuration 5

Earthquake Test No.	Input Motions	PGA [g]		Column End Moments [k*in]							
				SE Column		SW Column		NW Column		NE Column	
		X-Axis	Y-Axis	X-Axis	Y-Axis	X-Axis	Y-Axis	X-Axis	Y-Axis	X-Axis	Y-Axis
30	10% X-Axis	0.102	N/A	10.68	103.76	10.68	110.34	12.83	110.34	12.83	103.76
31	10% Y-Axis	N/A	0.064	23.94	8.57	23.94	6.87	35.43	6.87	35.43	8.57
32	10% Biaxial	0.100	0.059	30.42	105.28	30.42	109.29	42.26	109.29	42.26	105.28
34	100% Biaxial	1.086	0.658	191.61	450.56	191.61	454.86	290.13	454.86	290.13	450.56
35	150% Biaxial	1.637	1.045	305.95	439.75	305.95	463.46	428.49	463.46	428.49	439.75

Table 9.6 Maximum Column End Moments - Test Configuration 5

Earthquake Test No.	Input Motions	Column End Shears [k]											
		PGA [g]				SE Column				NW Column			
		X-Axis	Y-Axis	X-Axis	Y-Axis	X-Axis	Y-Axis	X-Axis	Y-Axis	X-Axis	Y-Axis	X-Axis	Y-Axis
30	10% X-Axis	0.102	N/A	3.46	0.36	3.68	0.36	3.68	0.43	3.46	0.43		
31	10% Y-Axis	N/A	0.064	0.29	0.80	0.23	0.80	0.23	1.18	0.29	1.18		
32	10% Biaxial	0.100	0.059	3.51	1.01	3.64	1.01	3.64	1.41	3.51	1.41		
34	100% Biaxial	1.086	0.658	15.02	6.39	15.16	6.39	15.16	9.67	15.02	9.67		
35	150% Biaxial	1.637	1.045	14.66	10.20	15.45	10.20	15.45	14.28	14.66	14.28		

Table 9.7 Maximum Column End Shears - Test Configuration 5

E [ksi] = 29000.0

Stress [ksi]	Strain [in/in]	Plastic Strain [in/in]
0.000000	0.000000	
41.000000	0.001414	0.000000
44.000000	0.001600	0.000083
46.200000	0.001800	0.000207
47.820000	0.002000	0.000351
49.400000	0.002500	0.000797
50.080000	0.003000	0.001273
51.200000	0.005000	0.003234
52.800000	0.010000	0.008179
53.920000	0.015000	0.013141
55.700000	0.020000	0.018079
57.300000	0.030000	0.028024
58.600000	0.040000	0.037979
60.200000	0.060000	0.057924
61.200000	0.080000	0.077890
61.700000	0.100000	0.097872
62.100000	0.150000	0.147859
61.700000	0.200000	0.197872

Table 9.8 Abaqus Stress-Strain Best-Fit Material Model – 5" Standard Columns
Test Configuration 5

E [ksi] = 29000.0

Stress [ksi]	Strain [in/in]	Plastic Strain [in/in]
0.000000	0.000000	
42.000000	0.001448	0.000000
46.000000	0.006000	0.004414
51.000000	0.014000	0.012241
54.300000	0.020000	0.018128
59.500000	0.030000	0.027948
62.900000	0.040000	0.037831
66.100000	0.050000	0.047721
69.800000	0.070000	0.067593
71.700000	0.090000	0.087528
72.800000	0.110000	0.107490
73.400000	0.150000	0.147469
72.800000	0.200000	0.197490

Table 9.9 Abaqus Stress-Strain Best-Fit Material Model – 4" Double Extra-Strong Columns
Test Configuration 5

E [ksi] = 29000.0

Stress [ksi]	Strain [in/in]
0.00000	0.00000
48.00000	0.001666
51.20000	0.005000
57.30000	0.030000
61.20000	0.080000
62.10000	0.150000

Table 9.10 Drain-3DX Stress-Strain Best-Fit Material Model – 5" Standard Columns
Test Configuration 5

E [ksi] = 29000.0

Stress [ksi]	Strain [in/in]
0.00000	0.00000
42.00000	0.001448
46.00000	0.006000
59.50000	0.030000
69.80000	0.070000
73.40000	0.150000

Table 9.11 Drain-3DX Stress-Strain Best-Fit Material Model – 4" Double Extra-Strong Columns
Test Configuration 5

Earthquake Test No.	Input Motions	Relative Displacement [in]						Rotation [10^{-3} rad]				
		PGA [g]		X-Axis		Y-Axis		Abaqus	Drain	Test	Abaqus	Drain
X-Axis	Y-Axis	Abaqus	Drain	Test	Abaqus	Drain	Test	Abaqus	Drain	Test	Z-Axis	
32	10% Biaxial	0.100	0.059	0.213	0.152	0.212	0.056	0.057	0.065	0.230	0.234	0.588
34	100% Biaxial	1.086	0.658	1.65	1.68	1.31	0.54	0.56	0.46	3.60	4.12	8.39
35	150% Biaxial	1.637	1.045	2.59	2.68	2.81	0.91	1.02	1.22	6.28	7.56	13.82

Table 9.12 Analytical vs. Experimental Displacement and Rotation Response Comparison - Test Configuration 5

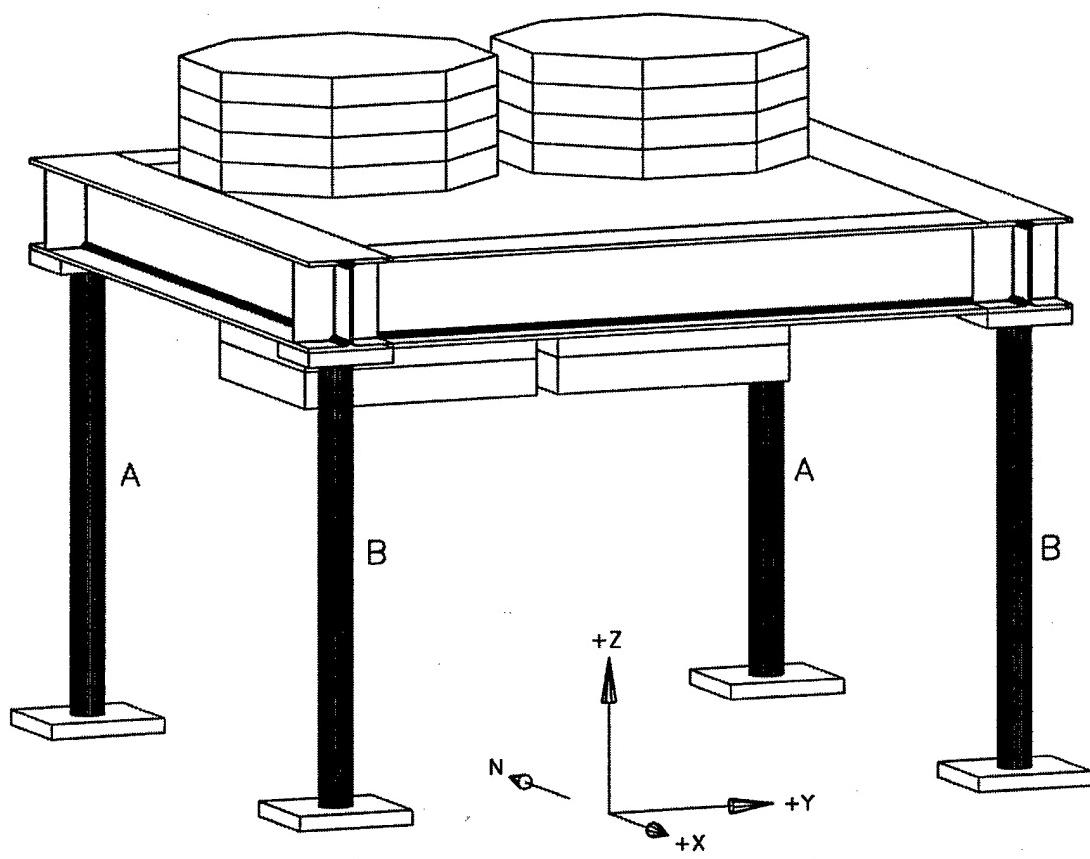


Figure 9.1 Perspective View of Test Configuration Model 5
[A] 2 - 5" Standard Columns and [B] 2 - 4" Double Extra-Strong Columns

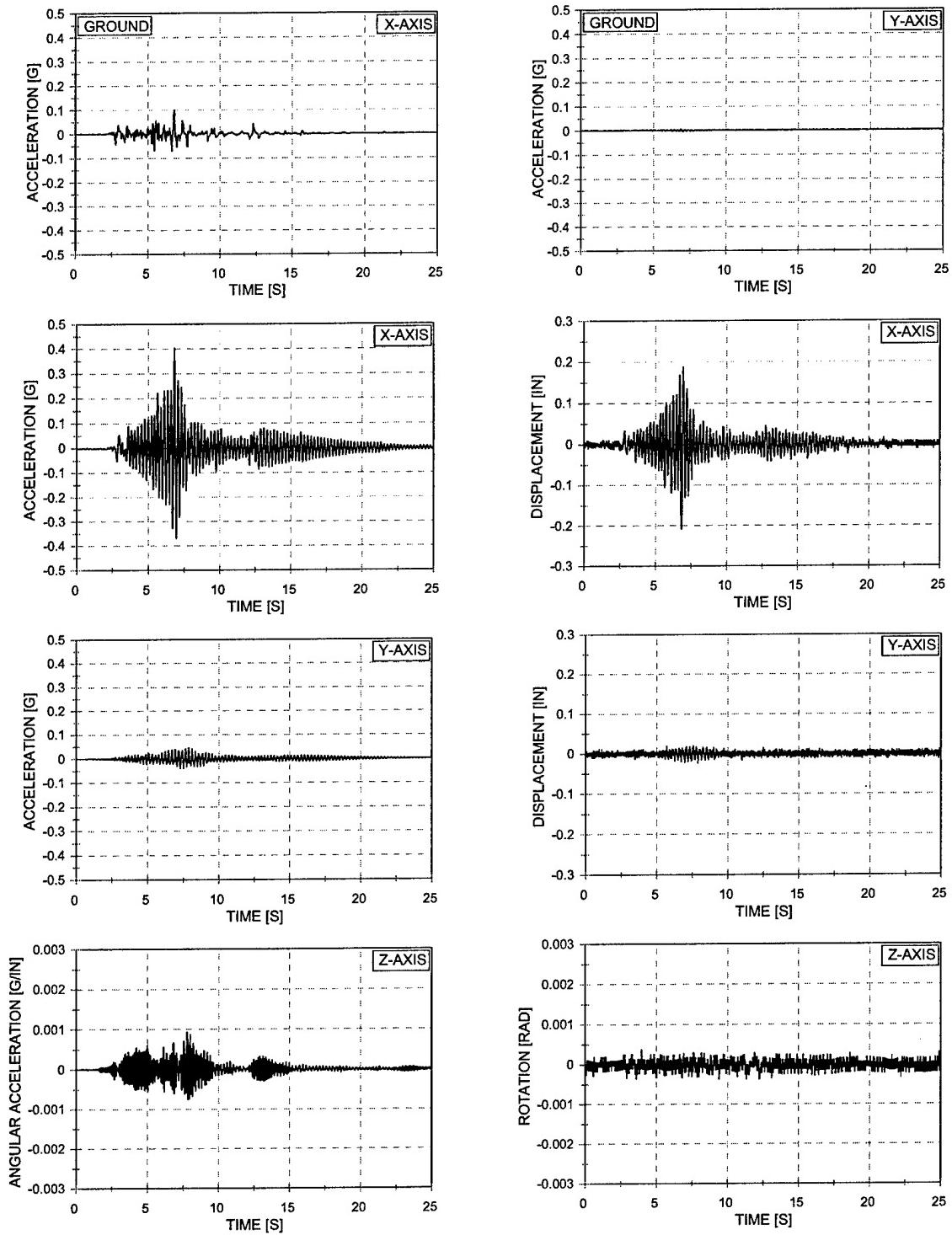


Figure 9.2. Acceleration and Displacement vs. Time – EQ 30
 10% X-Axis Imperial Valley – 1/2 Asymmetric Mass
 Two 5" Standard Columns and Two 4" Double Extra-Strong Columns

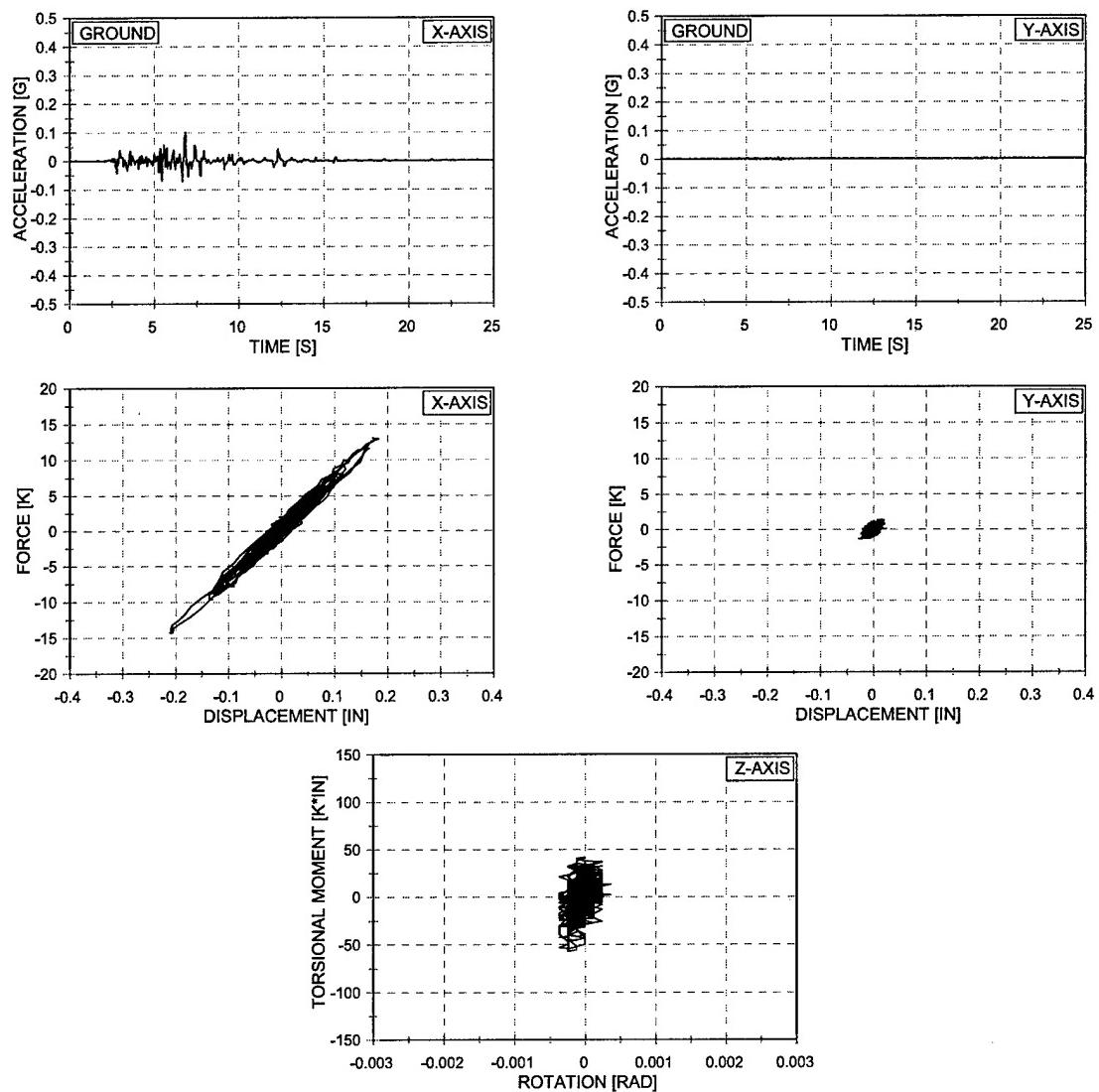


Figure 9.3. Force vs. Displacement and Torsional Moment vs. Rotation – EQ 30
 10% X-Axis Imperial Valley – 1/2 Asymmetric Mass
 Two 5" Standard Columns and Two 4" Double Extra-Strong Columns

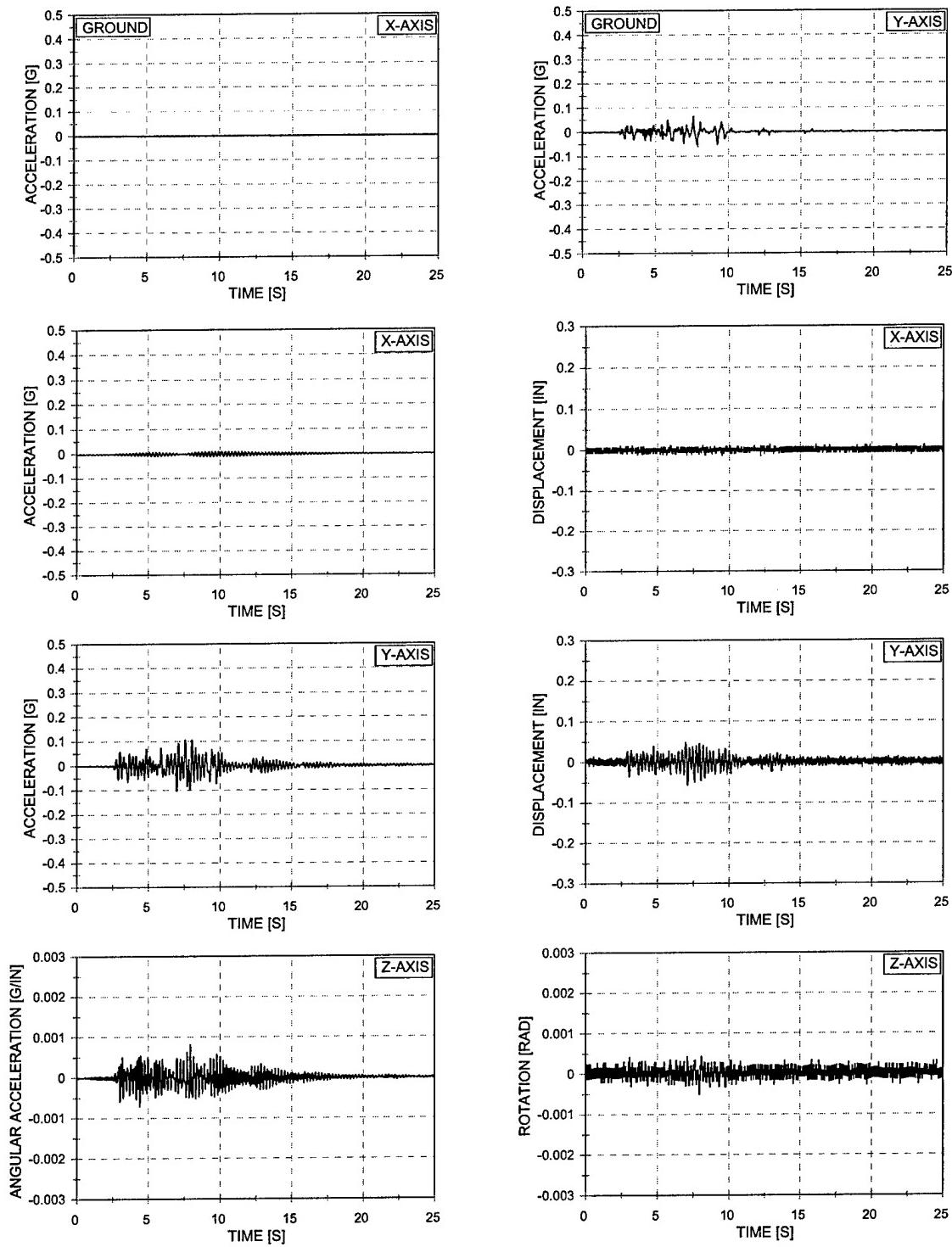


Figure 9.4. Acceleration and Displacement vs. Time – EQ 31
 10% Y-Axis Imperial Valley – 1/2 Asymmetric Mass
 Two 5" Standard Columns and Two 4" Double Extra-Strong Columns

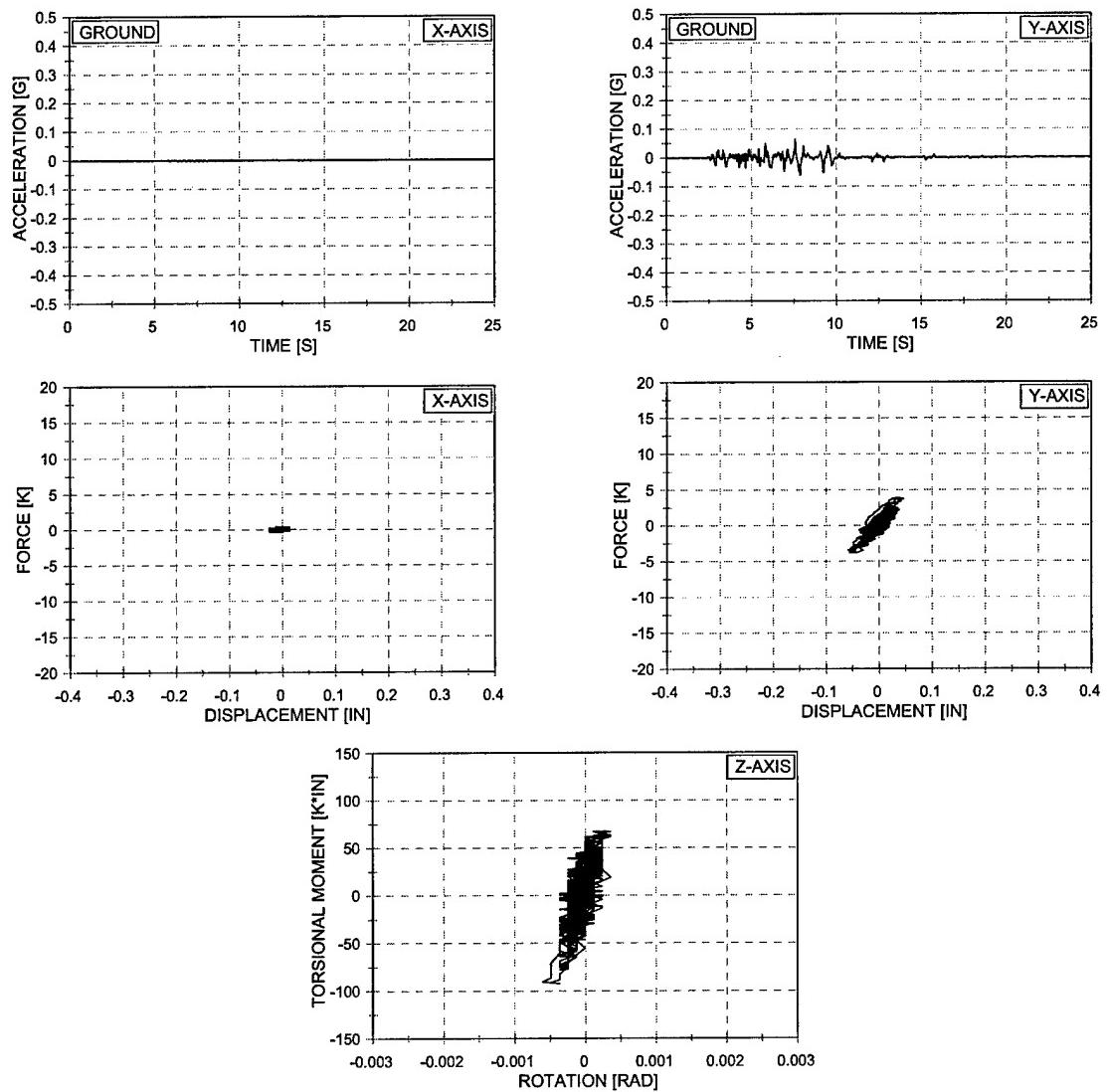


Figure 9.5. Force vs. Displacement and Torsional Moment vs. Rotation - EQ 31
 10% Y-Axis Imperial Valley – 1/2 Asymmetric Mass
 Two 5" Standard Columns and Two 4" Double Extra-Strong Columns

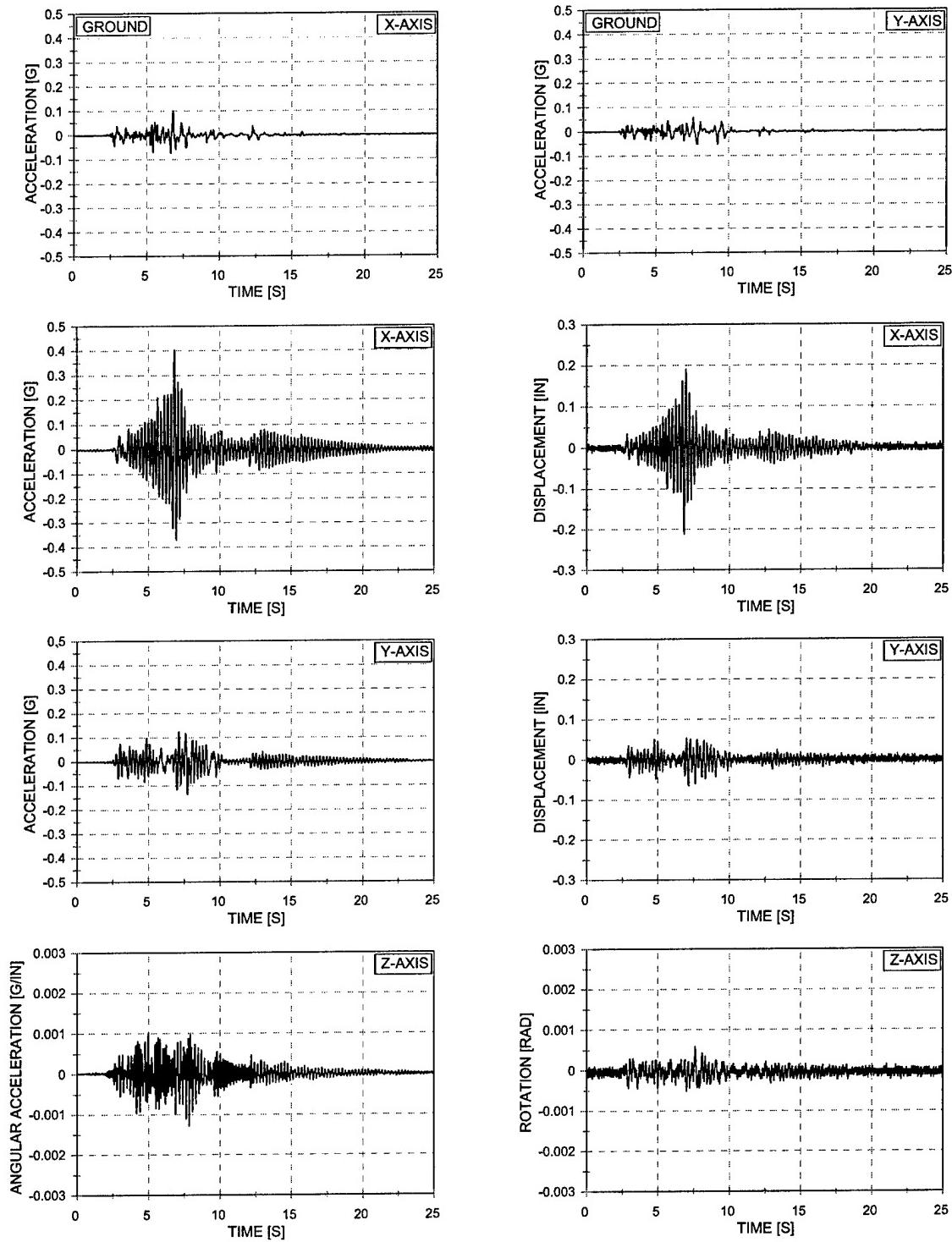


Figure 9.6. Acceleration and Displacement vs. Time – EQ 32
 10% Biaxial Imperial Valley – 1/2 Asymmetric Mass
 Two 5" Standard Columns and Two 4" Double Extra-Strong Columns

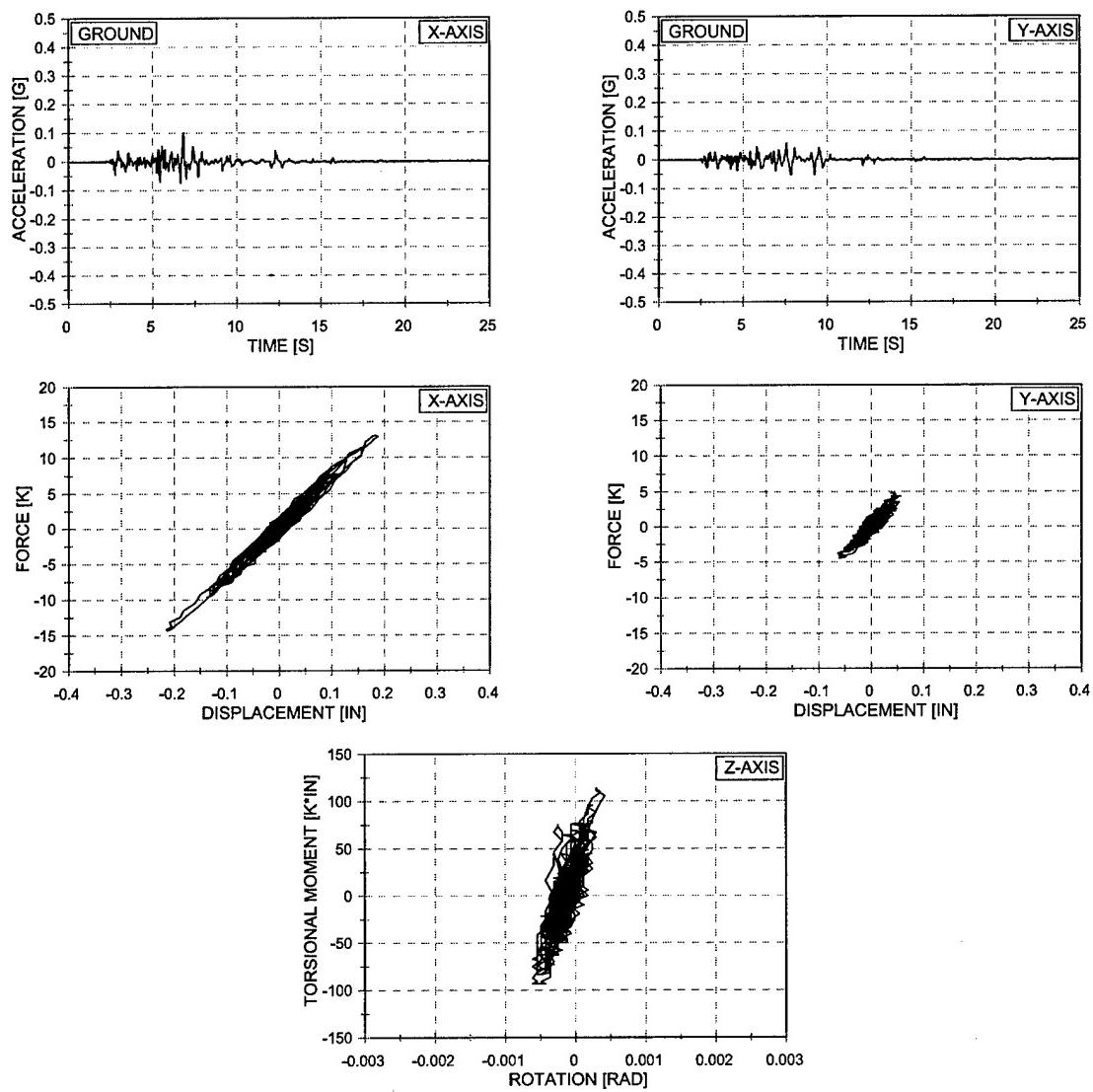


Figure 9.7. Force vs. Displacement and Torsional Moment vs. Rotation – EQ 32
 10% Biaxial Imperial Valley – 1/2 Asymmetric Mass
 Two 5" Standard Columns and Two 4" Double Extra-Strong Columns

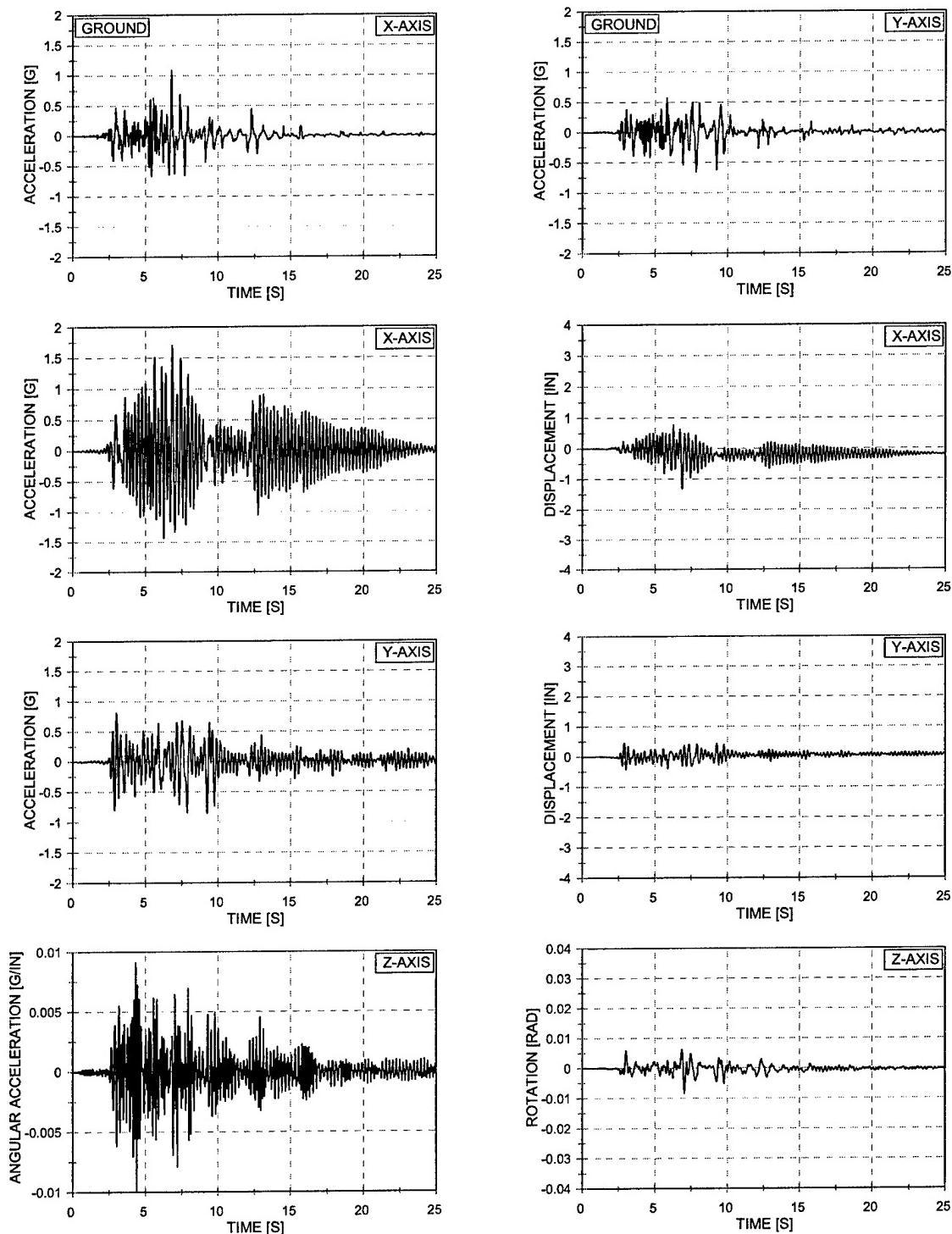


Figure 9.8. Acceleration and Displacement vs. Time – EQ 34
 100% Biaxial Imperial Valley – 1/2 Asymmetric Mass
 Two 5" Standard Columns and Two 4" Double Extra-Strong Columns

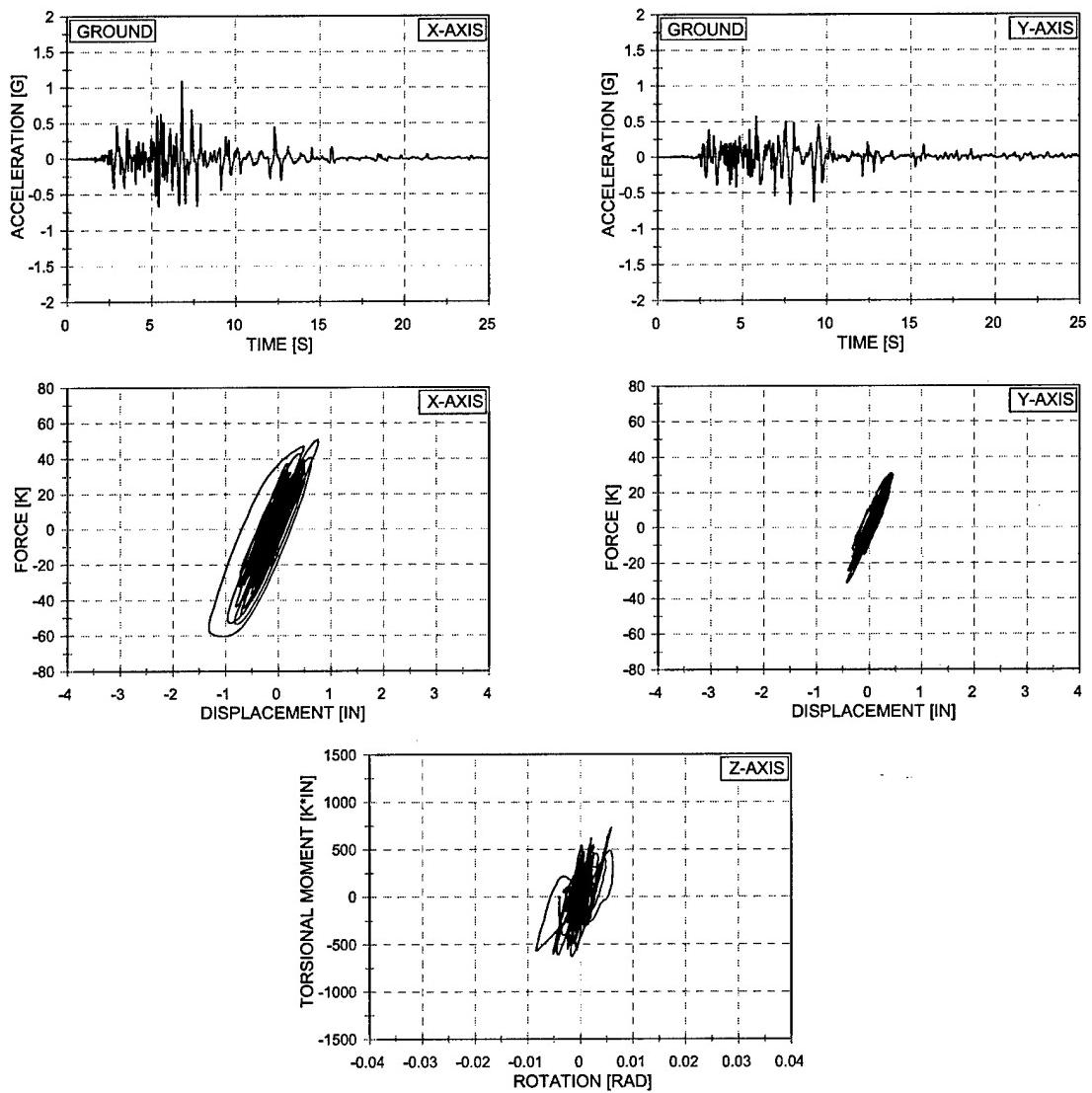


Figure 9.9. Force vs. Displacement and Torsional Moment vs. Rotation – EQ 34
 100% Biaxial Imperial Valley – 1/2 Asymmetric Mass
 Two 5" Standard Columns and Two 4" Double Extra-Strong Columns

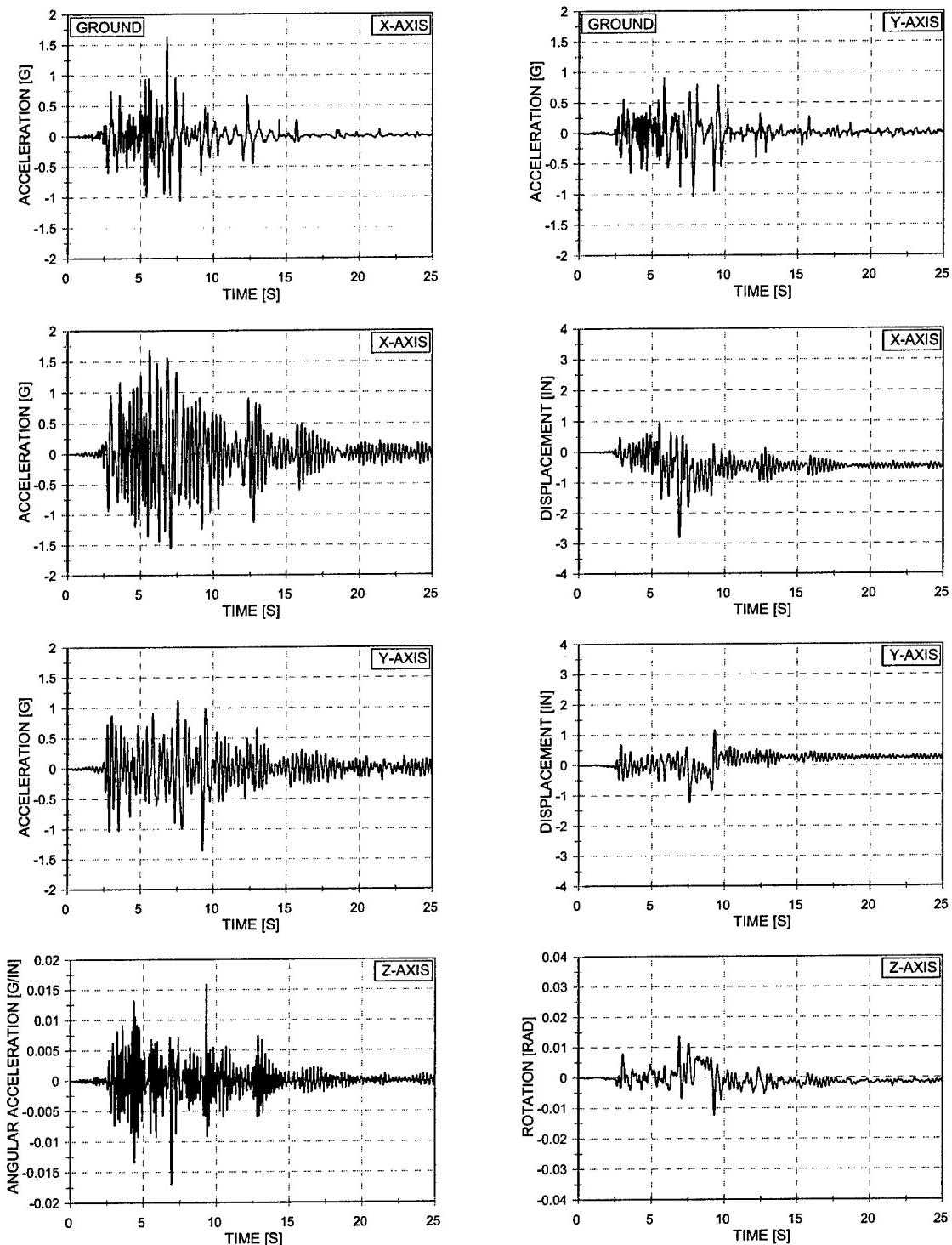


Figure 9.10. Acceleration and Displacement vs. Time – EQ 35
 150% Biaxial Imperial Valley – 1/2 Asymmetric Mass
 Two 5" Standard Columns and Two 4" Double Extra-Strong Columns

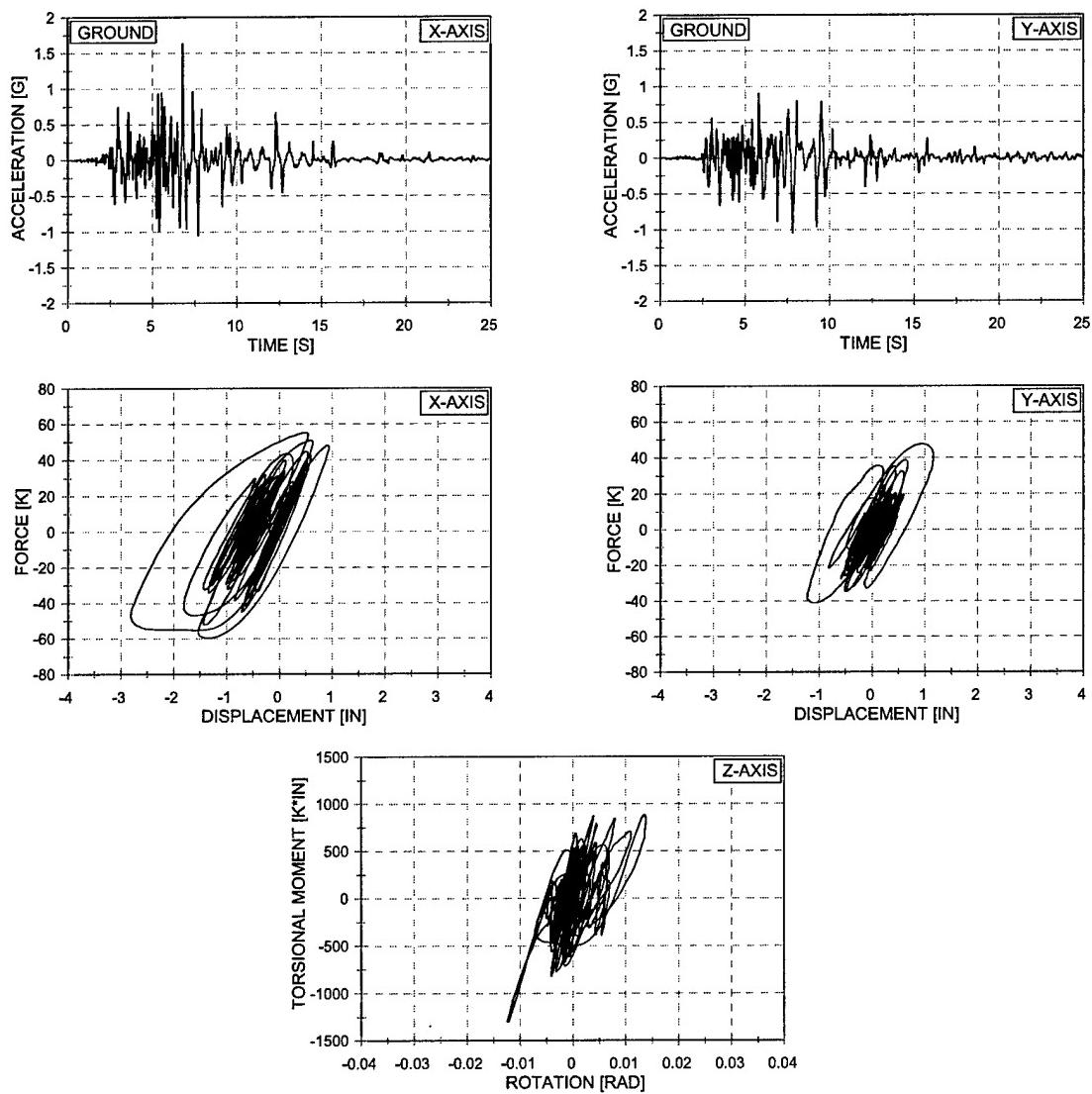


Figure 9.11. Force vs. Displacement and Torsional Moment vs. Rotation – EQ 35
 150% Biaxial Imperial Valley – 1/2 Asymmetric Mass
 Two 5" Standard Columns and Two 4" Double Extra-Strong Columns

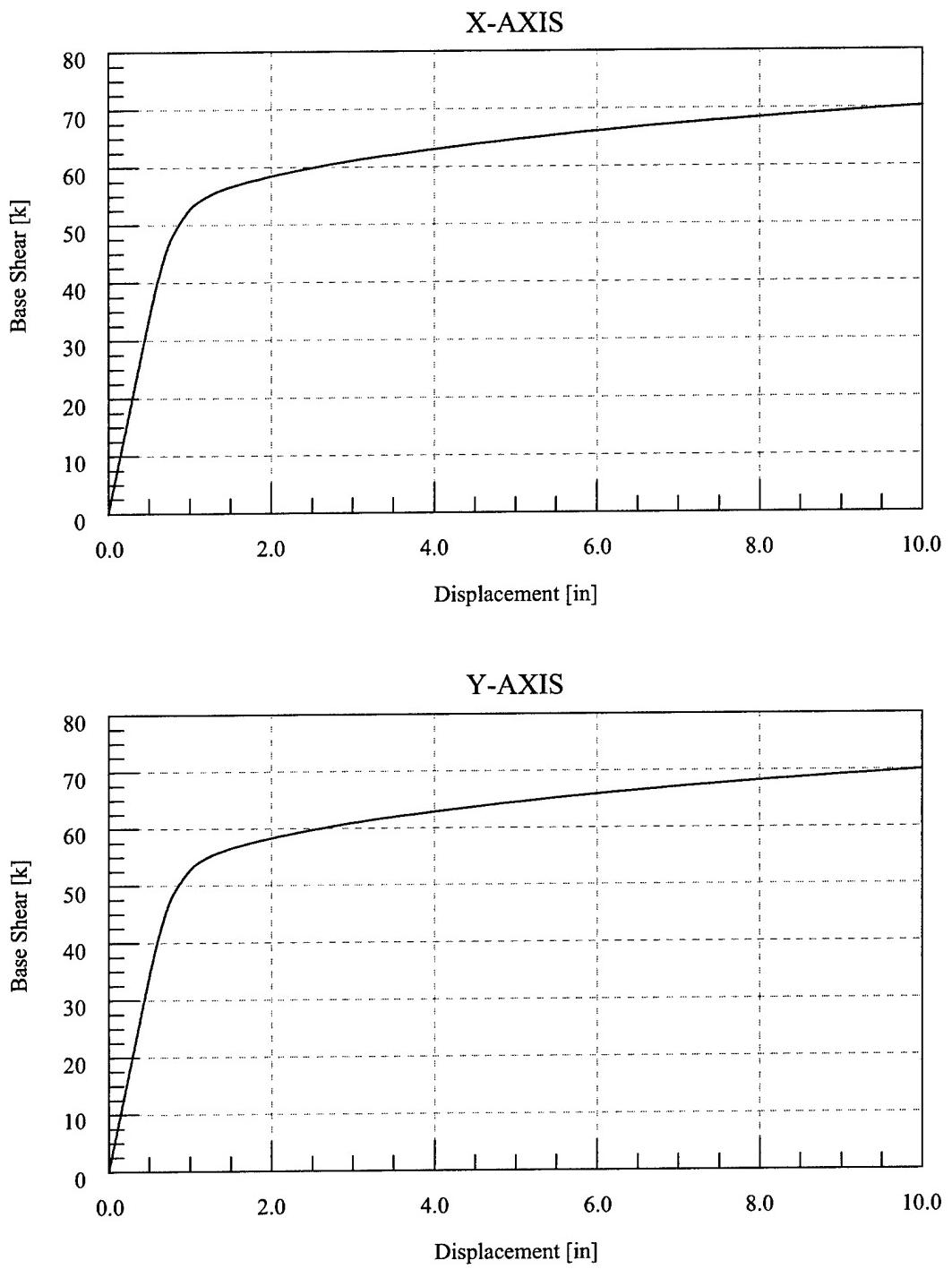


Figure 9.12 Force-Deformation Response – Test Configuration 5

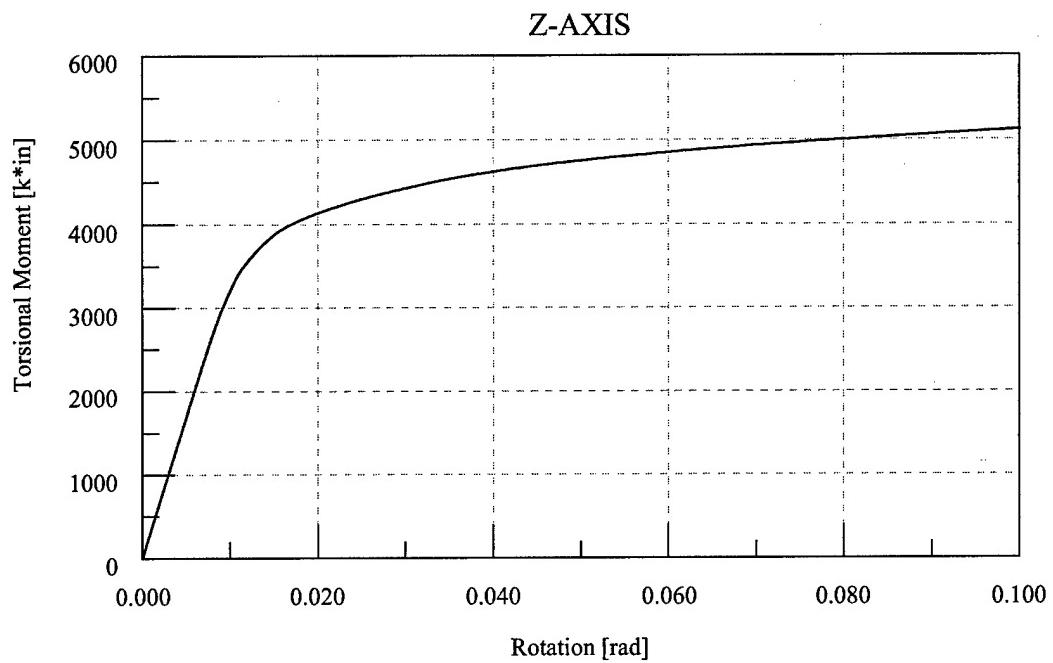


Figure 9.13 Torsional Moment-Rotation Response – Test Configuration 5

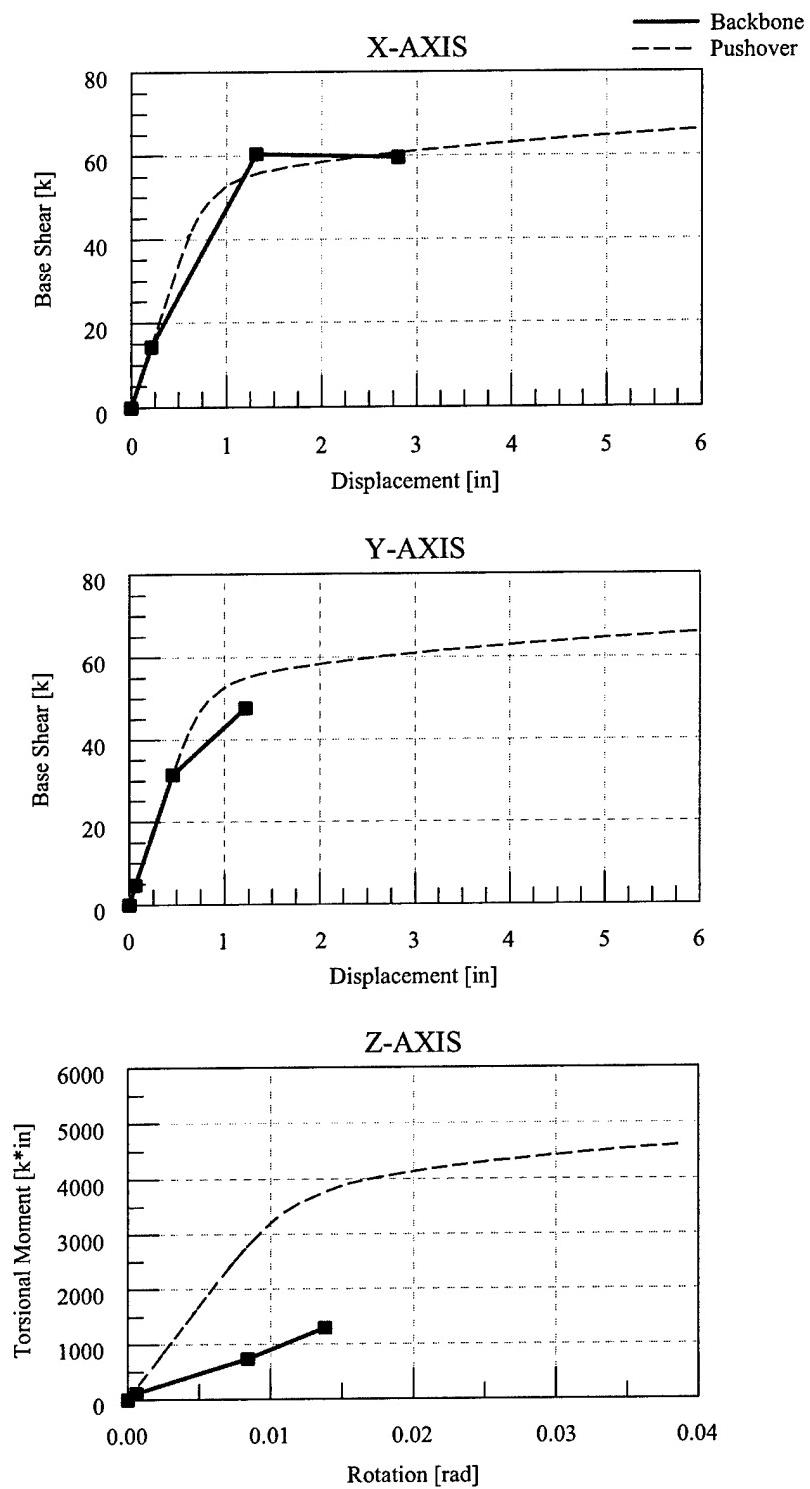


Figure 9.14 Maximum Force vs. Displacement and Maximum Torsional Moment vs. Rotation
 10% - 150% Biaxial Imperial Valley – 1/2 Asymmetric Mass
 Two 5" Standard Columns and Two 4" Double Extra-Strong Columns

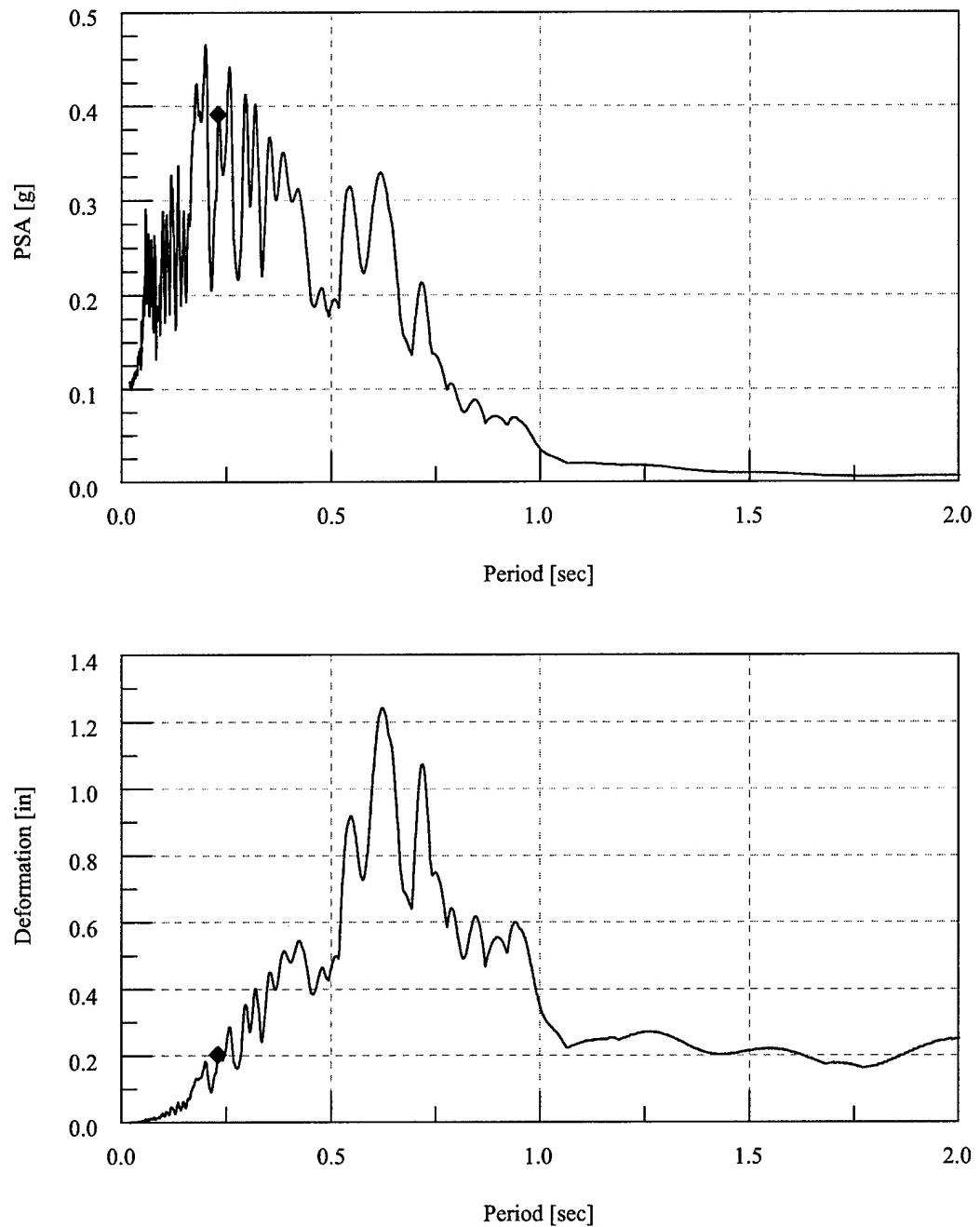


Figure 9.15 Elastic Response Spectra – EQ 30 – 10% X-Axis Imperial Valley Ground Motion

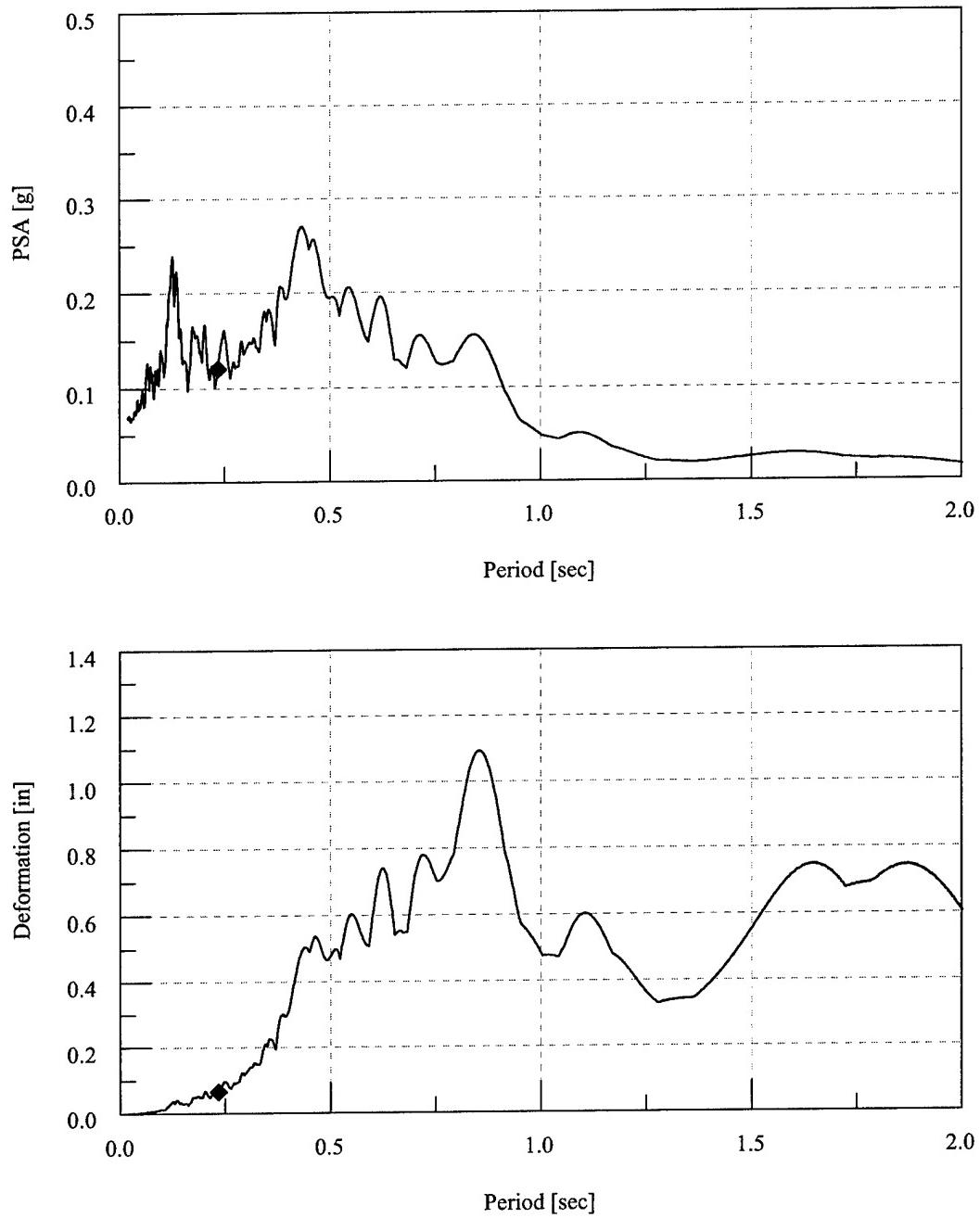


Figure 9.16 Elastic Response Spectra – EQ 31 – 10% Y-Axis Imperial Valley Ground Motion

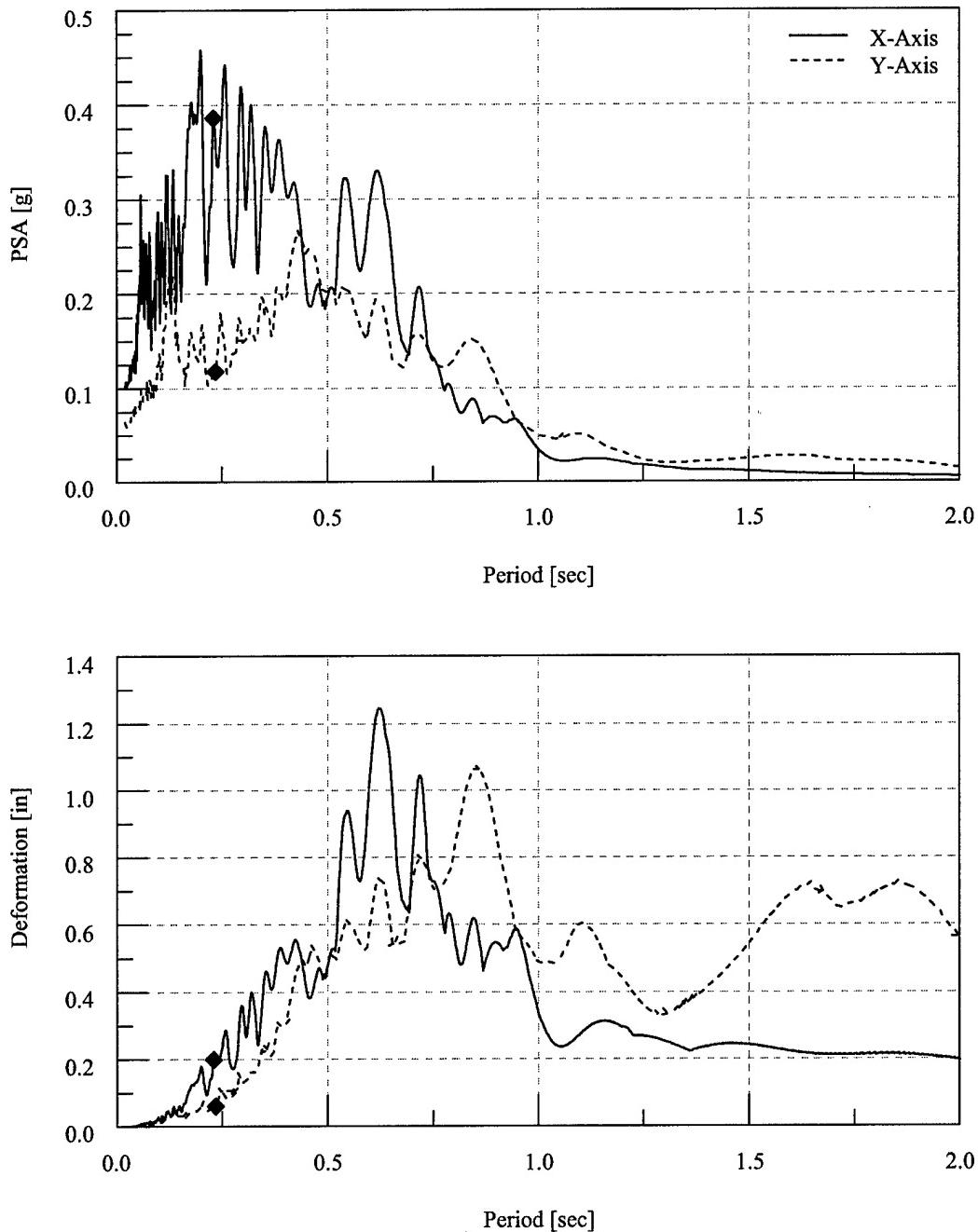


Figure 9.17 Elastic Response Spectra – EQ 32 – 10% Biaxial Imperial Valley Ground Motion

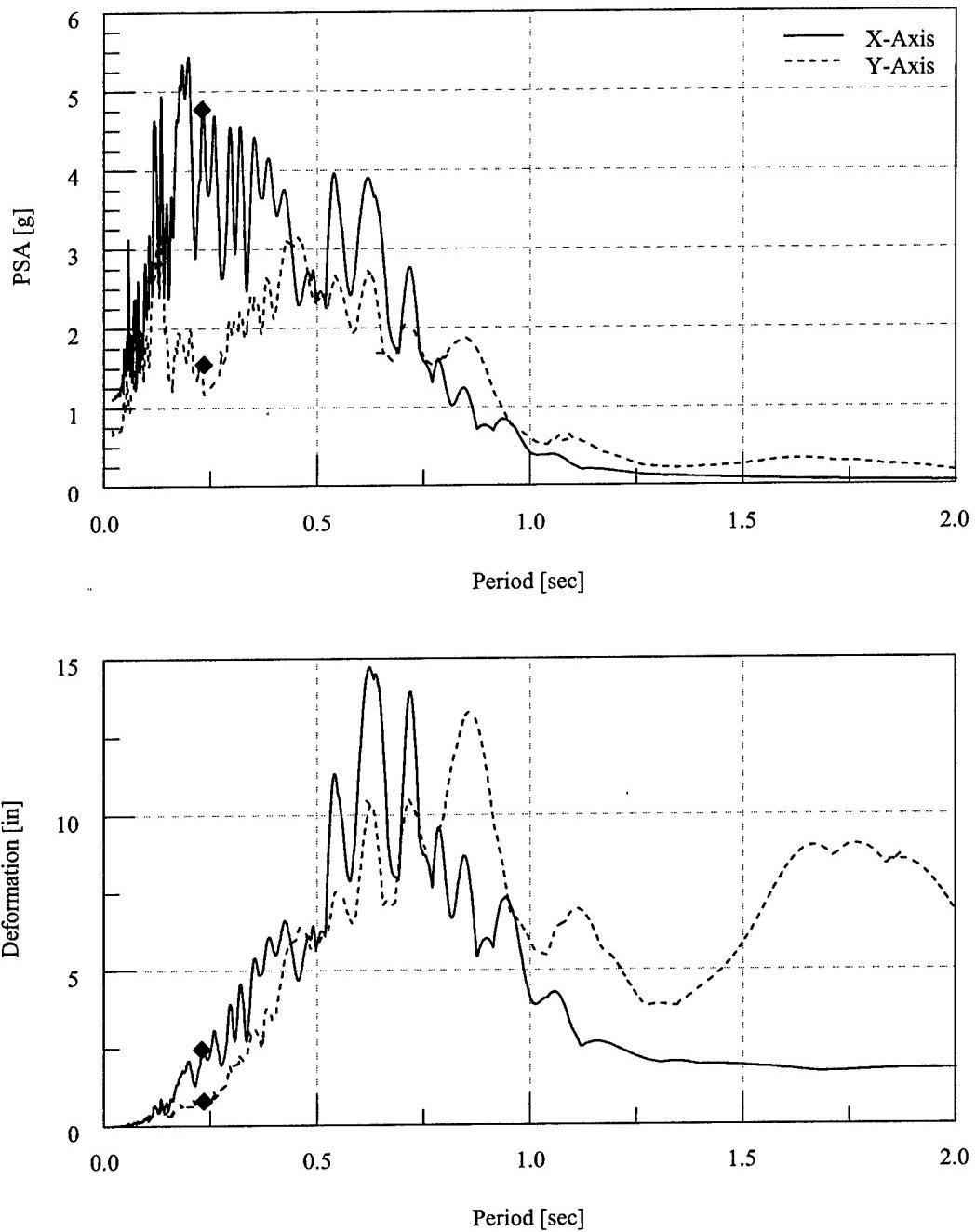


Figure 9.18 Elastic Response Spectra – EQ 34 – 100% Biaxial Imperial Valley Ground Motion

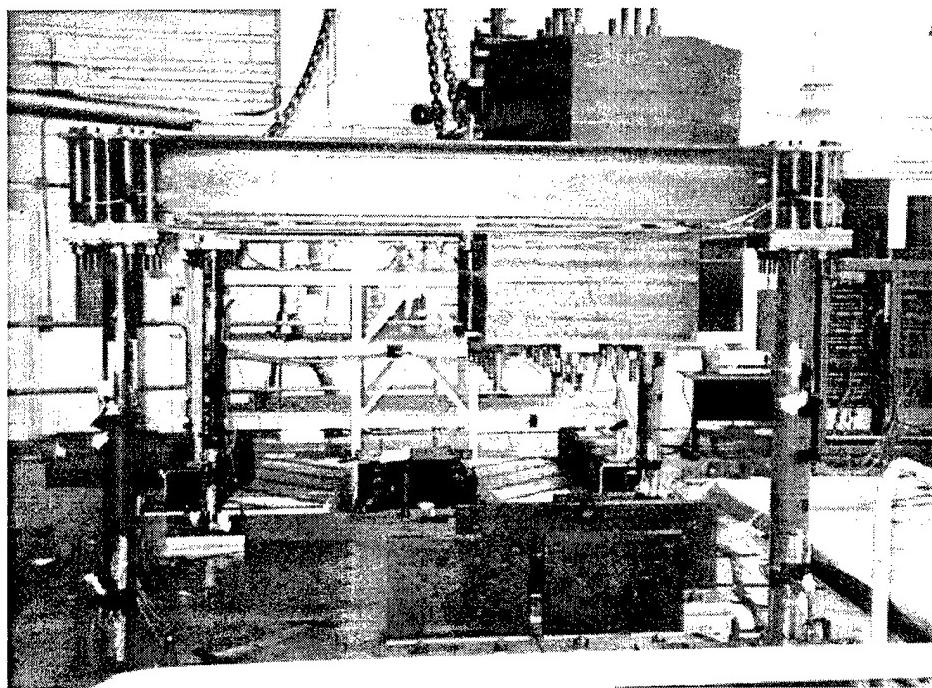


Figure 9.19 Test Structure prior to Earthquake Simulations

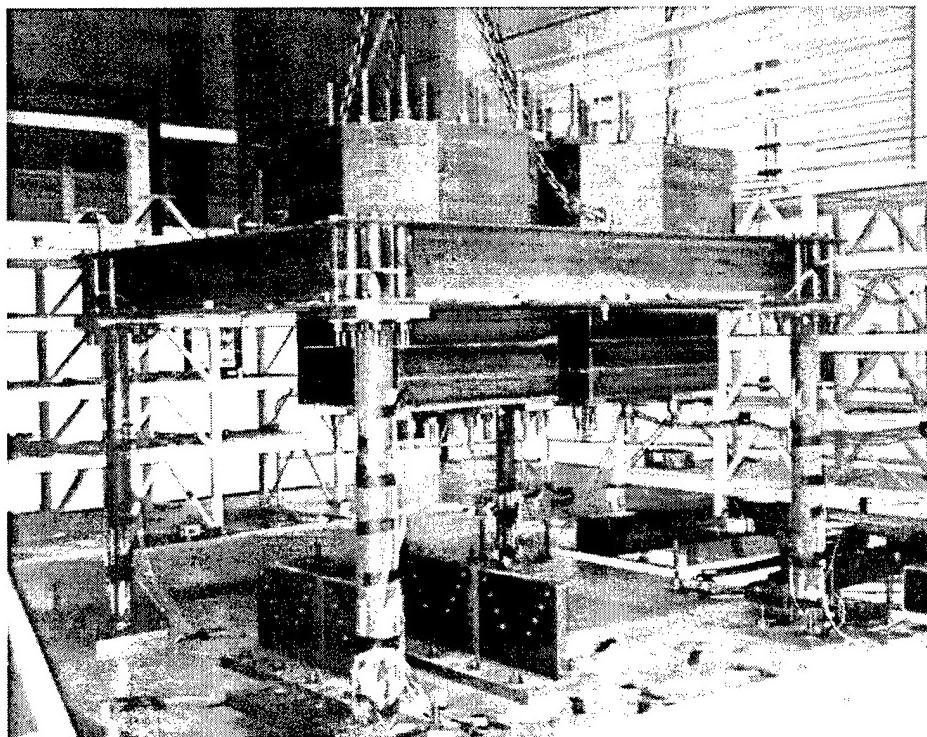


Figure 9.20 Test Structure prior to Earthquake Simulations

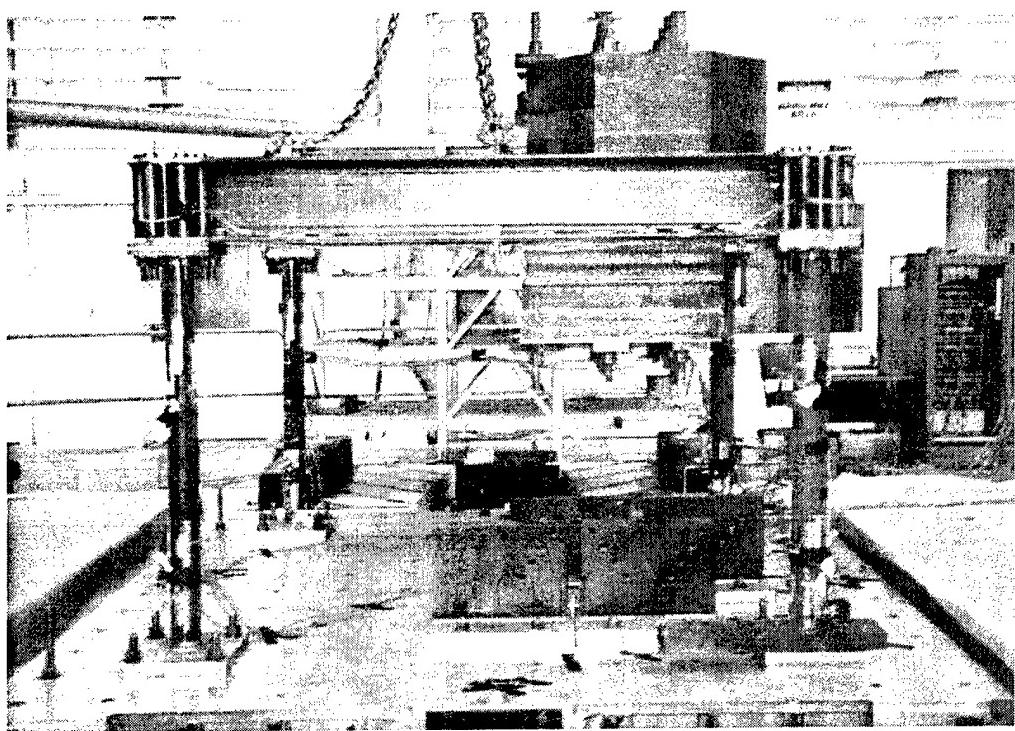


Figure 9.21 Test Structure prior to Earthquake Simulations

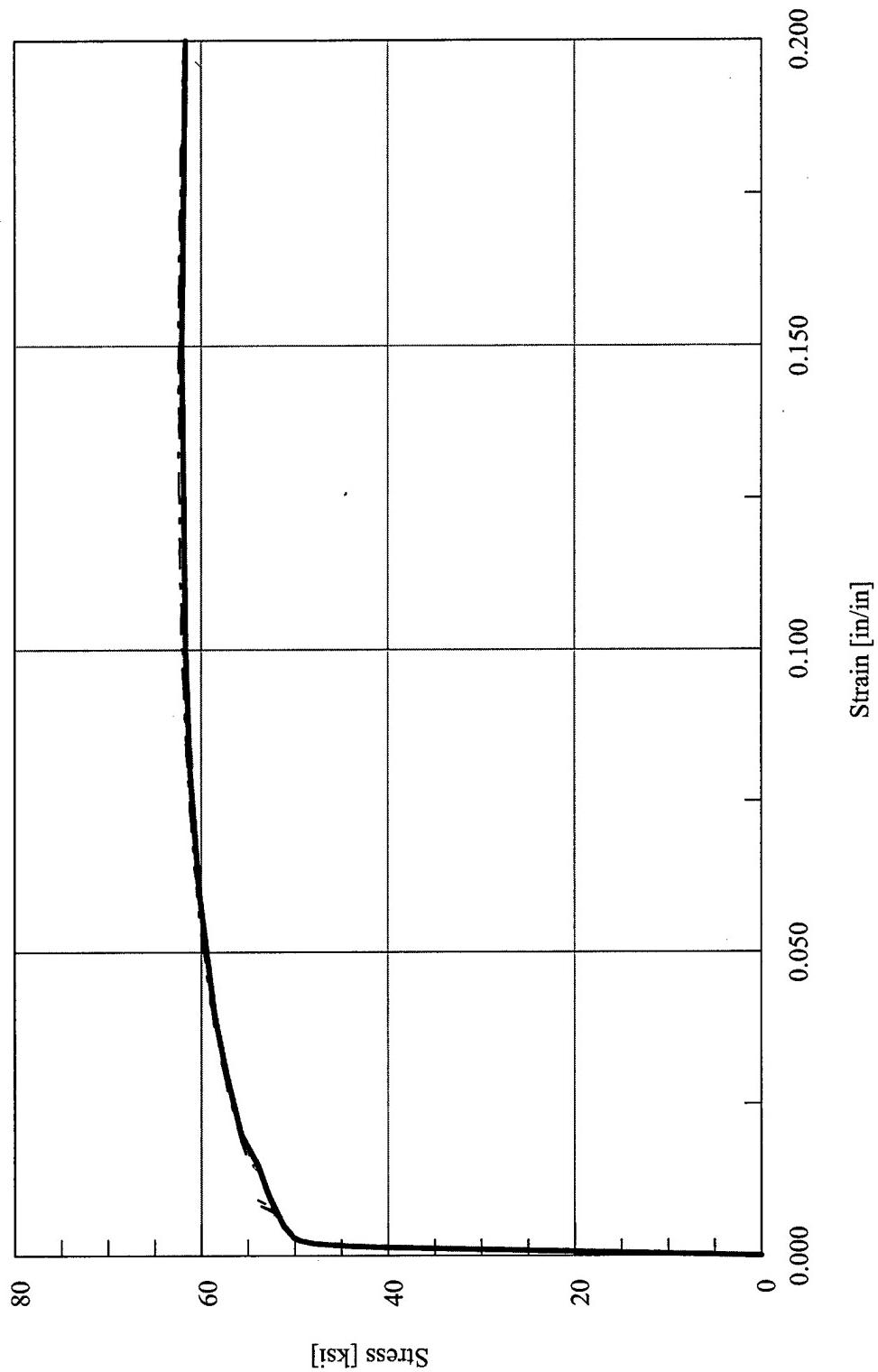


Figure 9.22 Abaqus Stress vs. Strain Finite Element Material Model Definition – 5" Standard Columns – Test Configuration 5

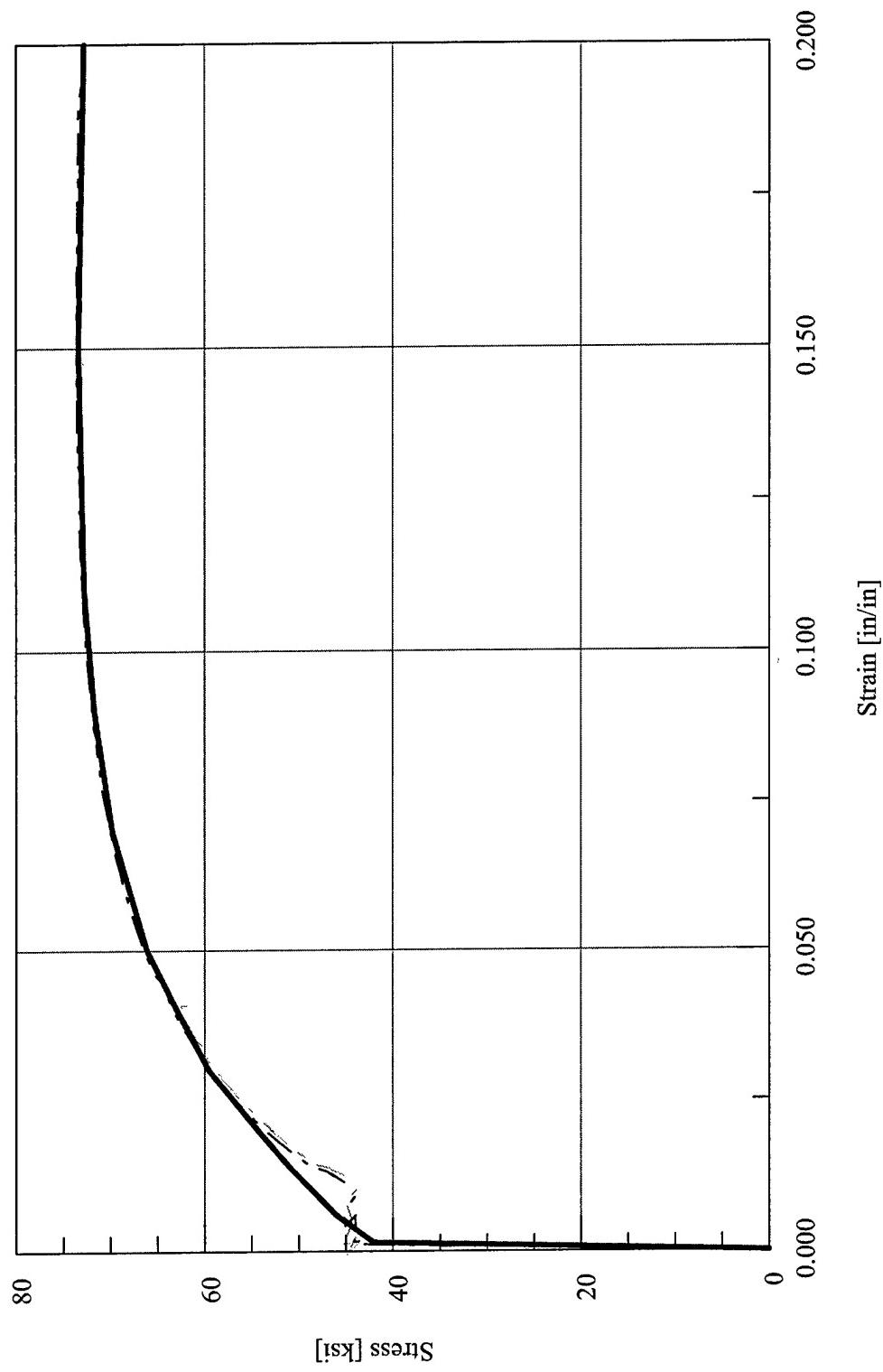


Figure 9.23 Abaqus Stress vs. Strain Finite Element Material Model Definition – 4" Double Extra-Strong Columns – Test Configuration 5

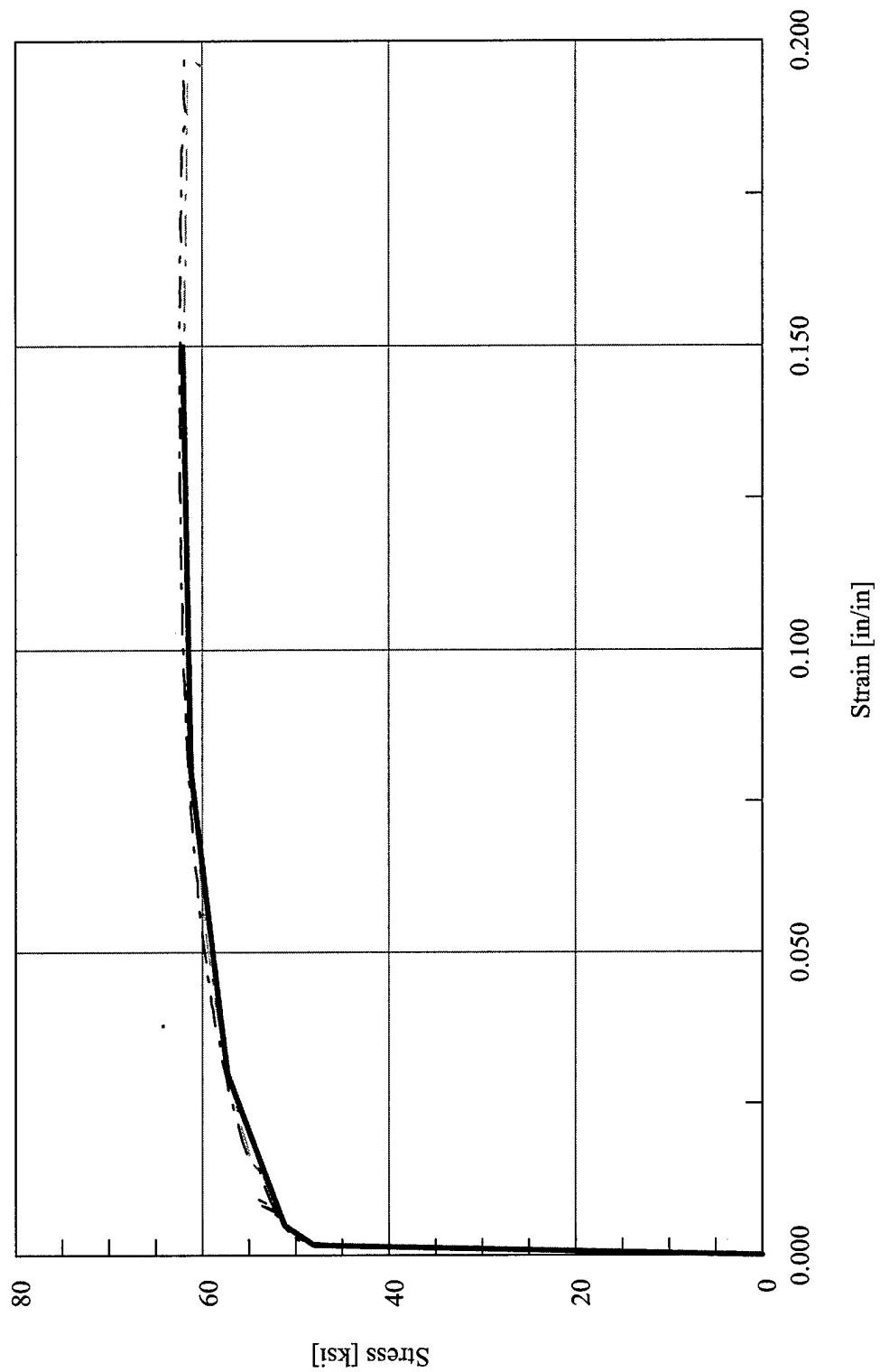


Figure 9.24 Drain-3DX Stress vs. Strain Finite Element Material Model Definition – 5" Standard Columns – Test Configuration 5

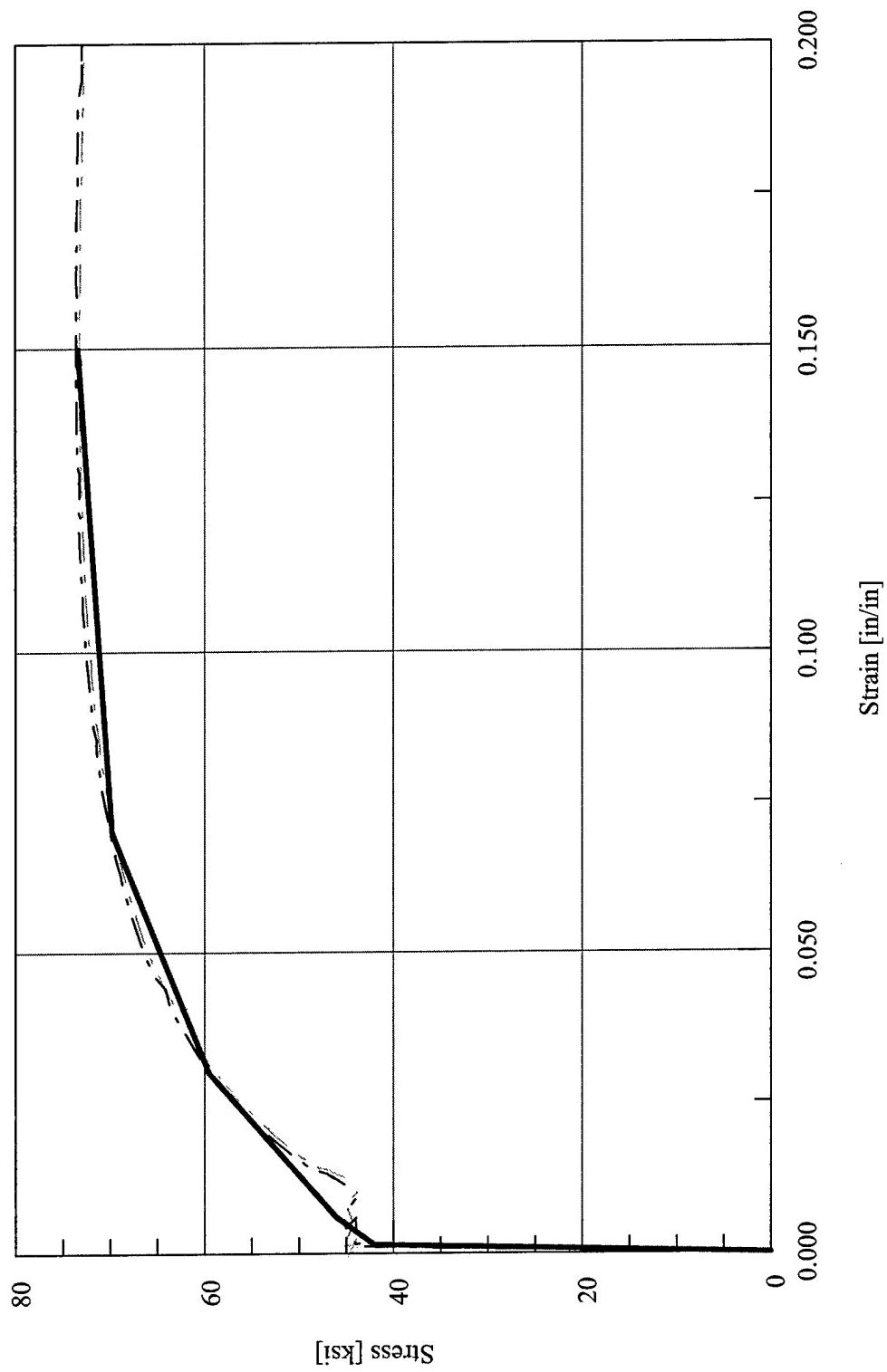


Figure 9.25 Drain-3DX Stress vs. Strain Finite Element Material Model Definition – 4" Double Extra-Strong Columns – Test Configuration 5

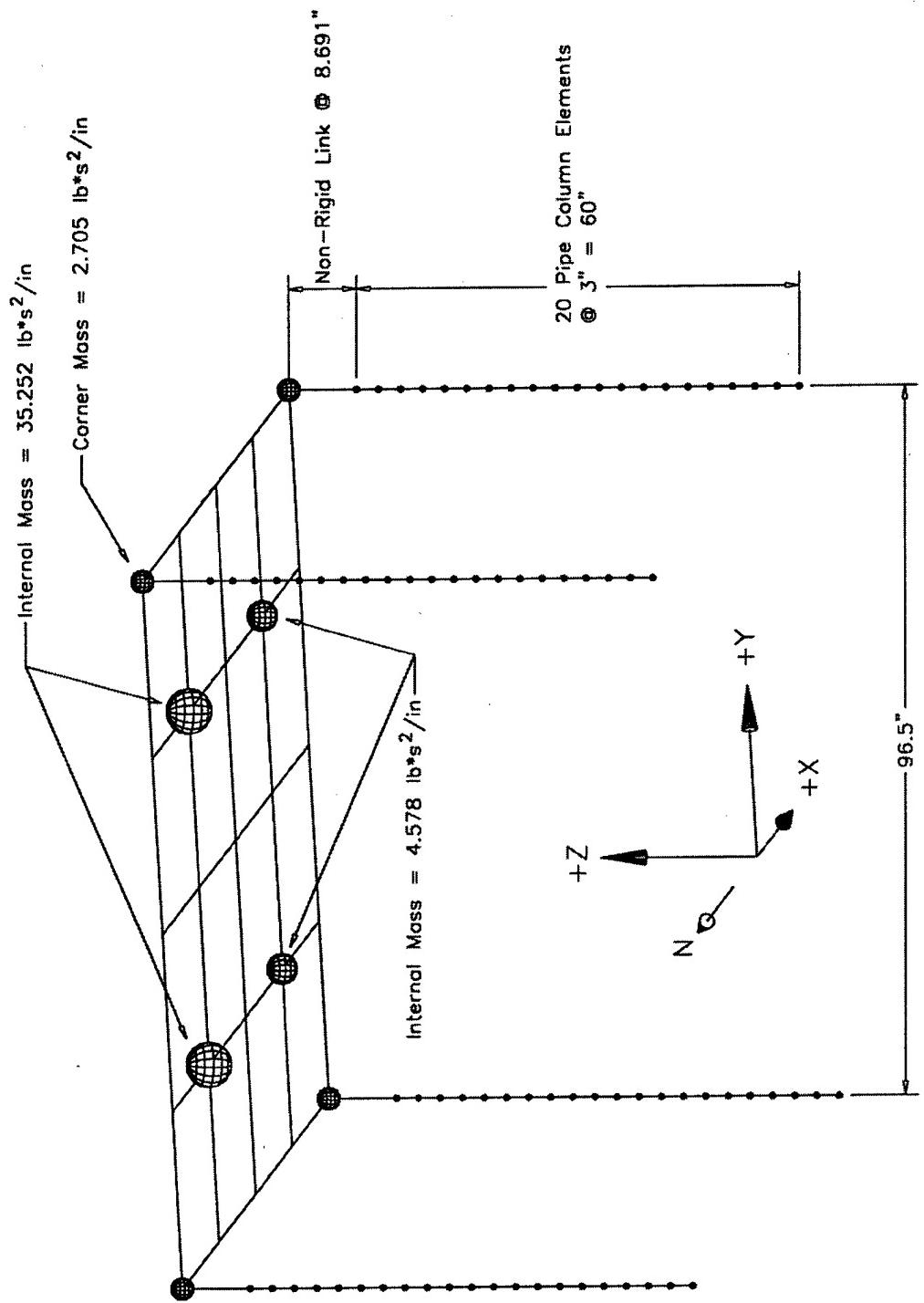


Figure 9.26 Abaqus Finite Element Model for Test Configuration 5

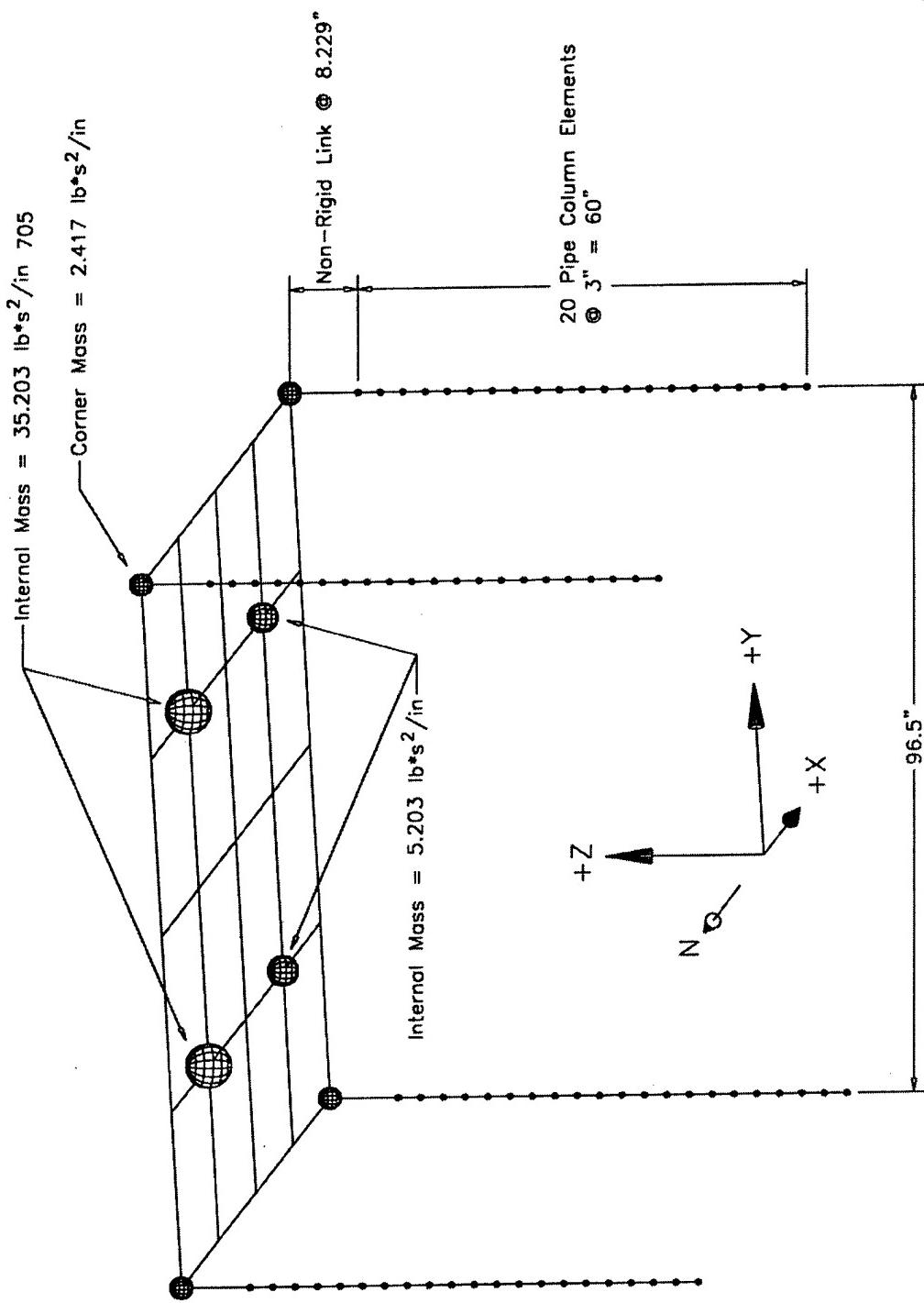


Figure 9.27 Drain-3DX Finite Element Model for Test Configuration 5

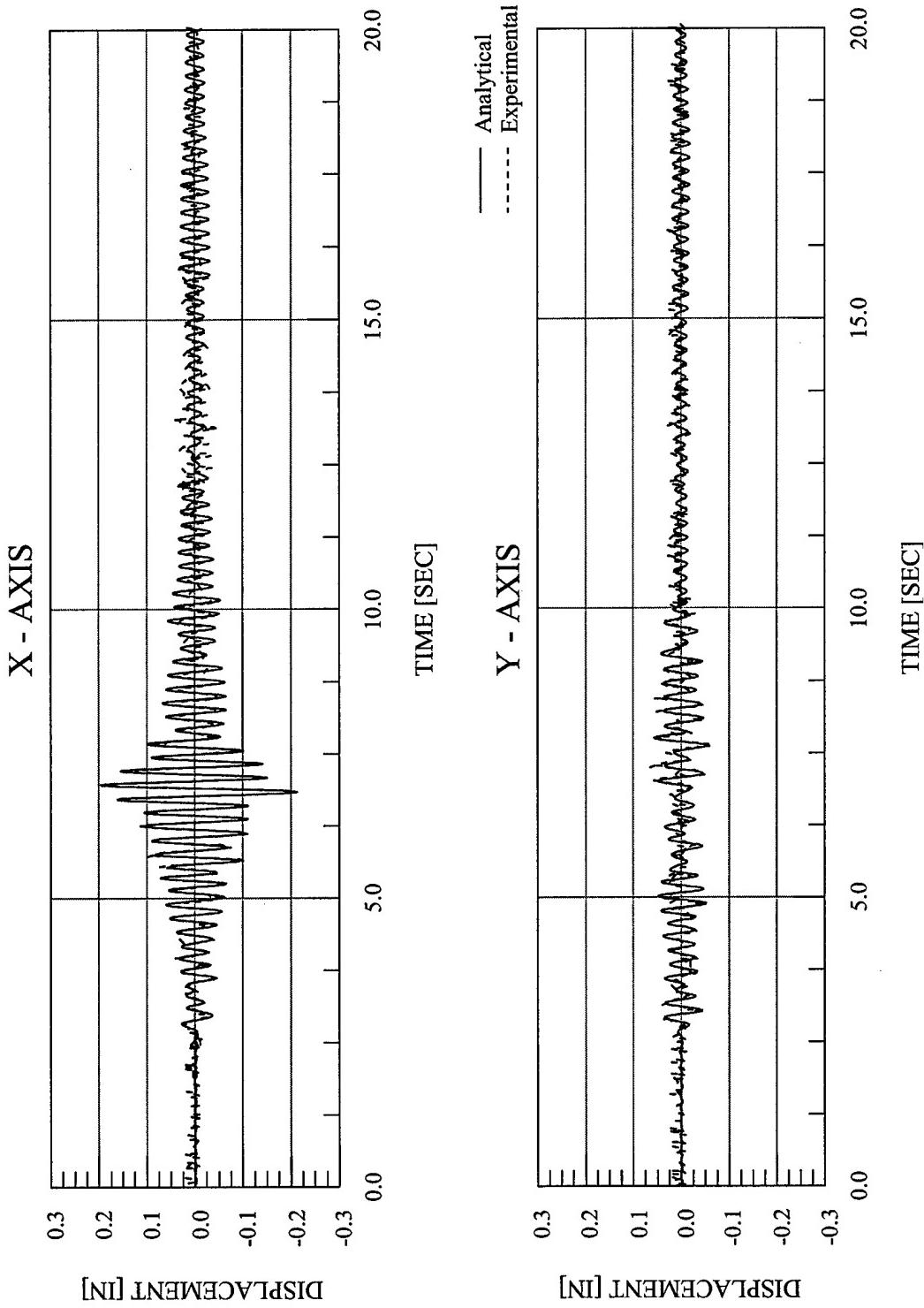


Figure 9.28 Abaqus Displacement vs. Time – EQ 32 – 10% Biaxial Imperial Valley

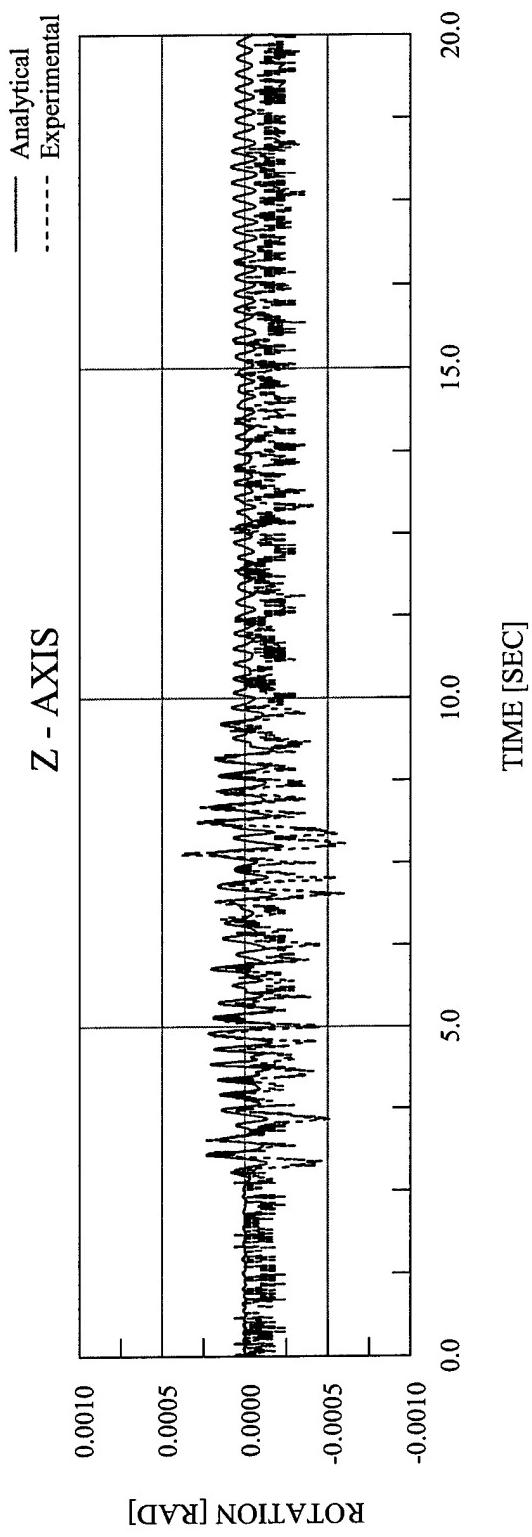


Figure 9.29 Abaqus Rotation vs. Time – EQ 32 – 10% Biaxial Imperial Valley

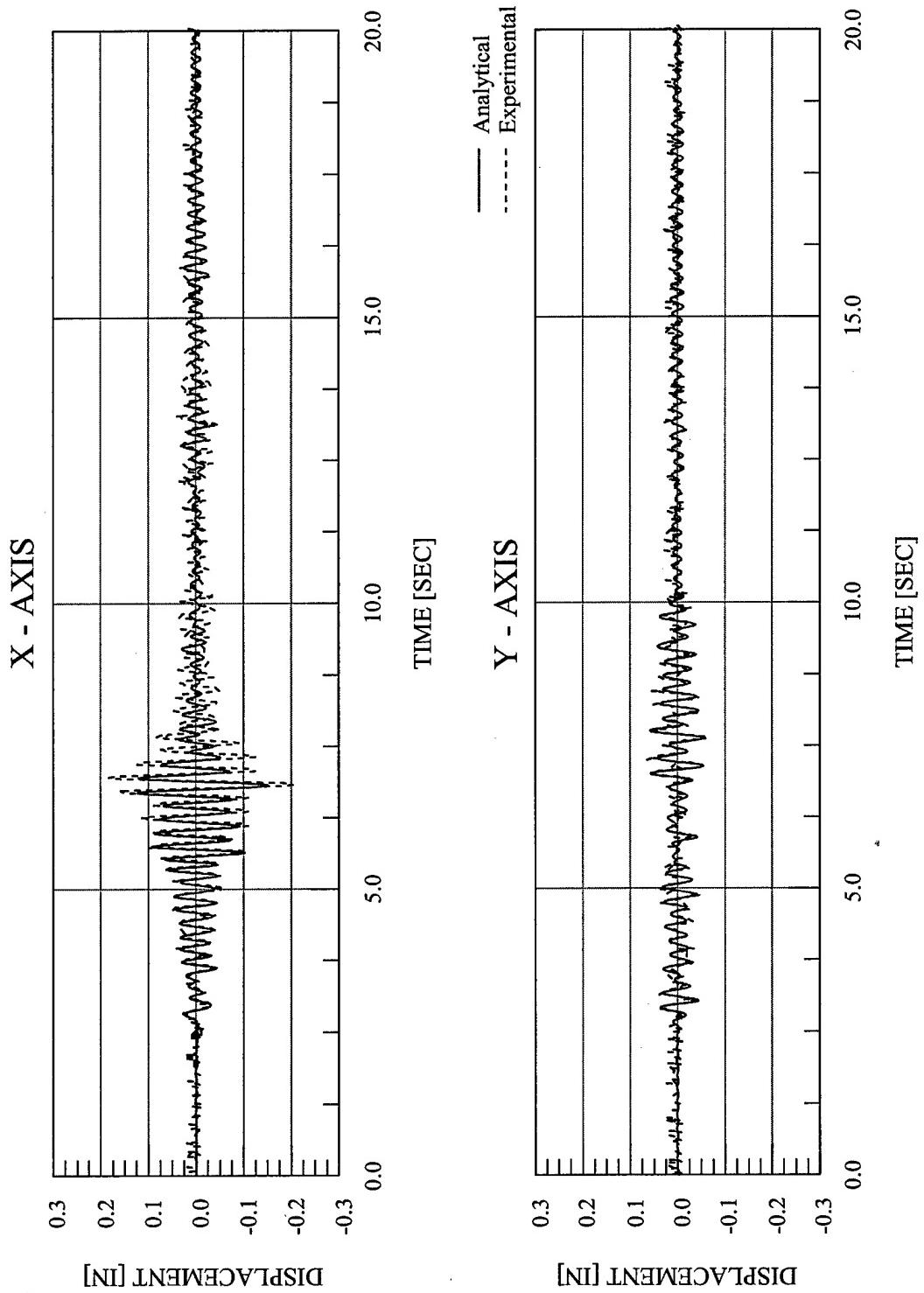


Figure 9.30 Drain-3DX Displacement vs. Time – EQ 32 – 10% Biaxial Imperial Valley

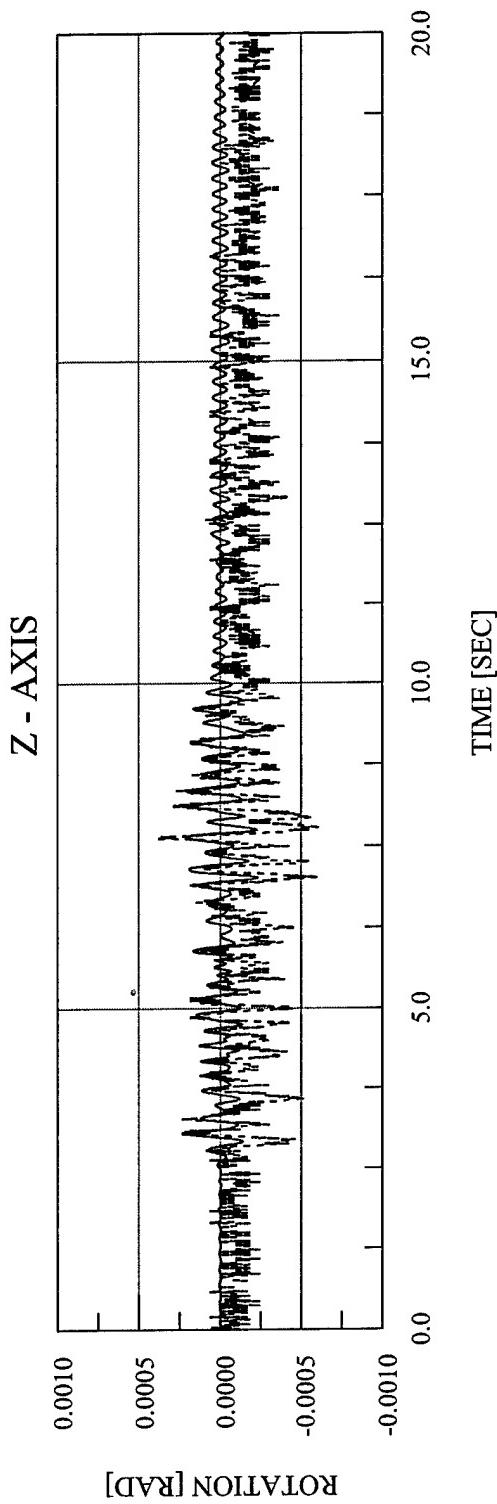


Figure 9.31 Drain-3DX Rotation vs. Time – EQ 32 – 10% Biaxial Imperial Valley

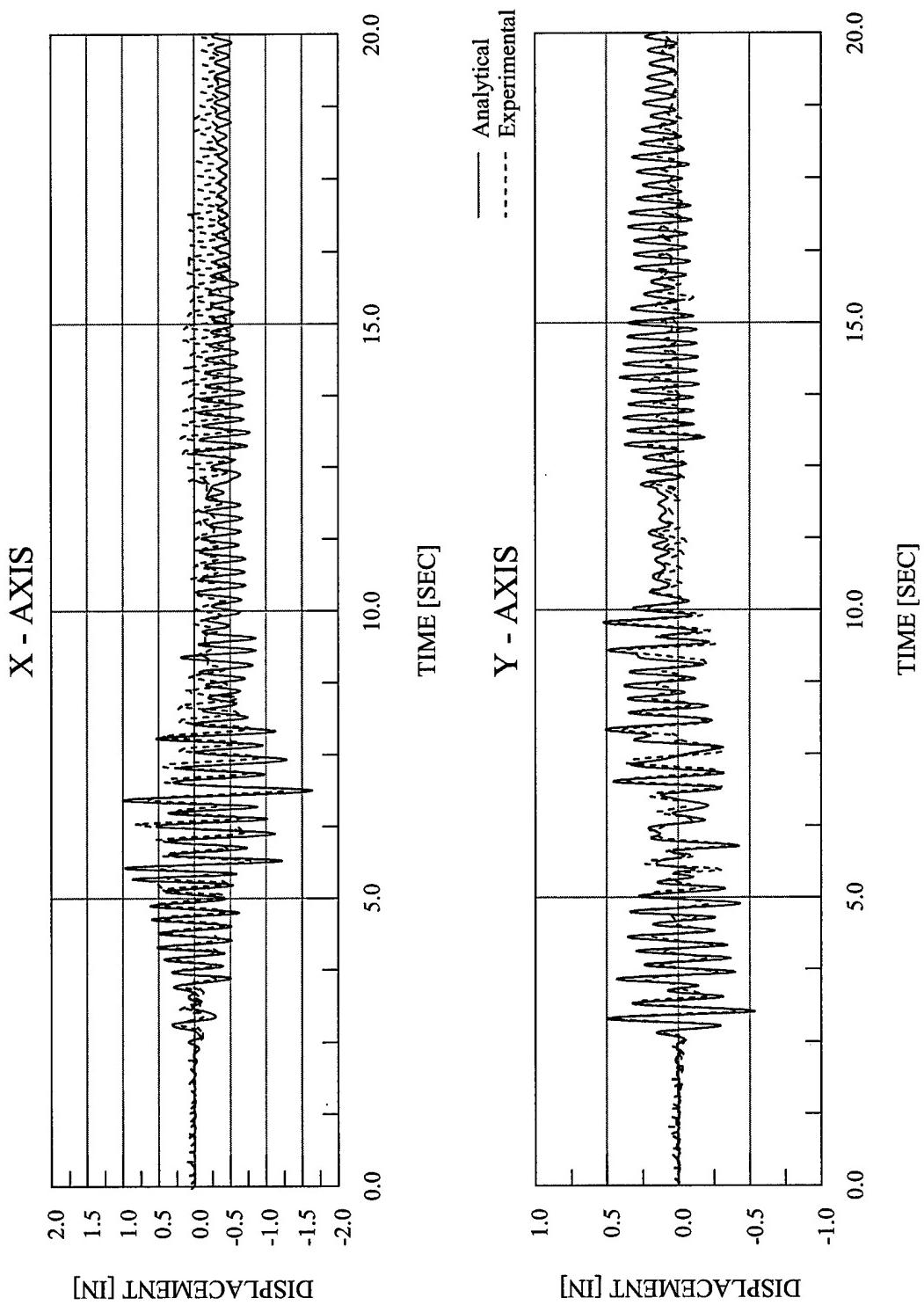


Figure 9.32 Abaqus Displacement vs. Time – EQ 34 – 100% Biaxial Imperial Valley

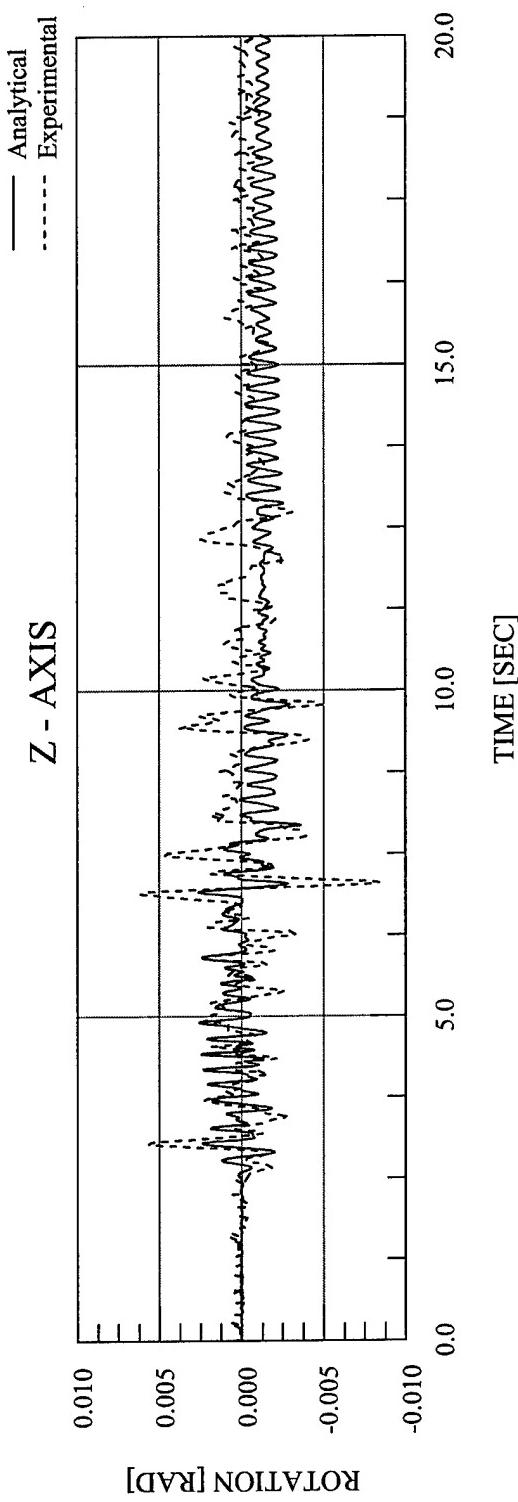


Figure 9.33 Abaqus Rotation vs. Time – EQ 34 – 100% Biaxial Imperial Valley

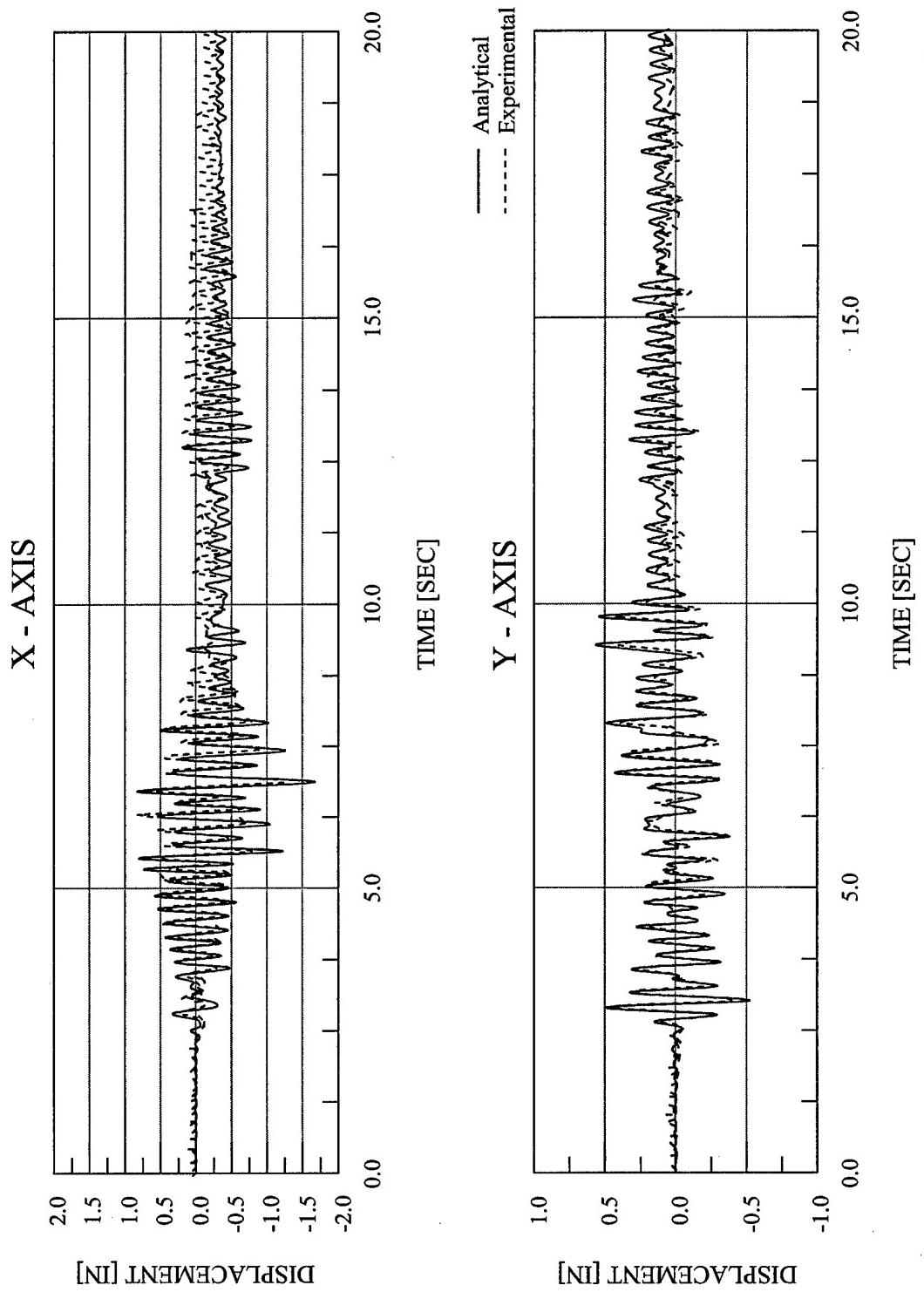


Figure 9.34 Drain-3DX Displacement vs. Time – EQ 34 – 100% Biaxial Imperial Valley

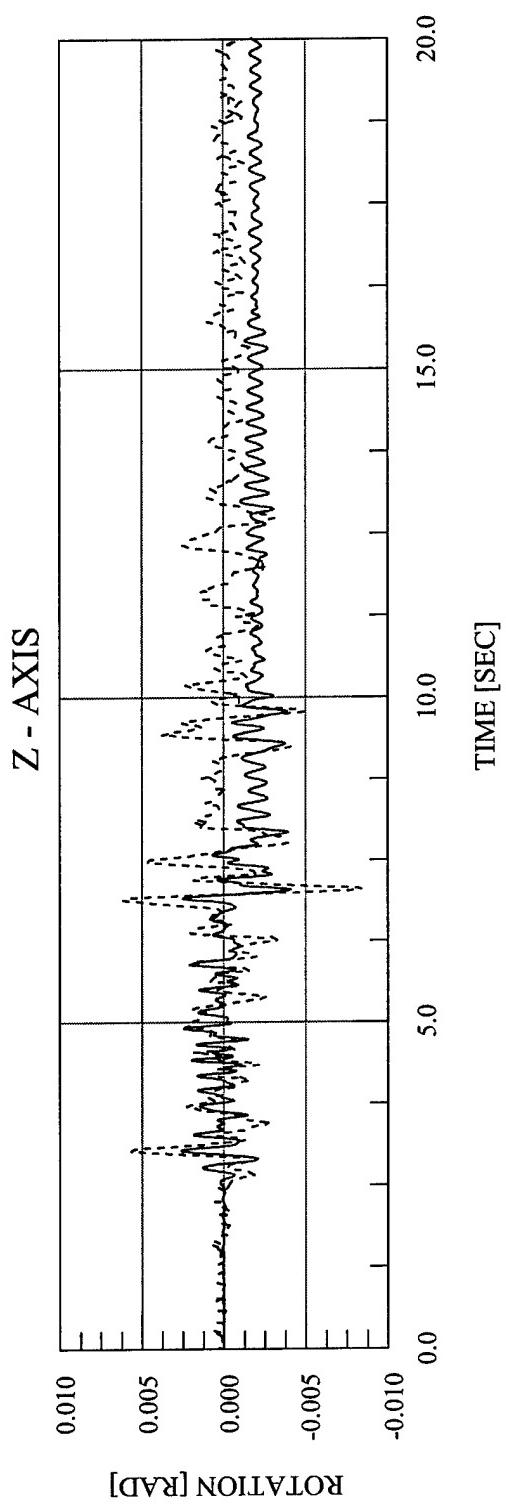


Figure 9.35 Drain-3DX Rotation vs. Time – EQ 34 – 100% Biaxial Imperial Valley

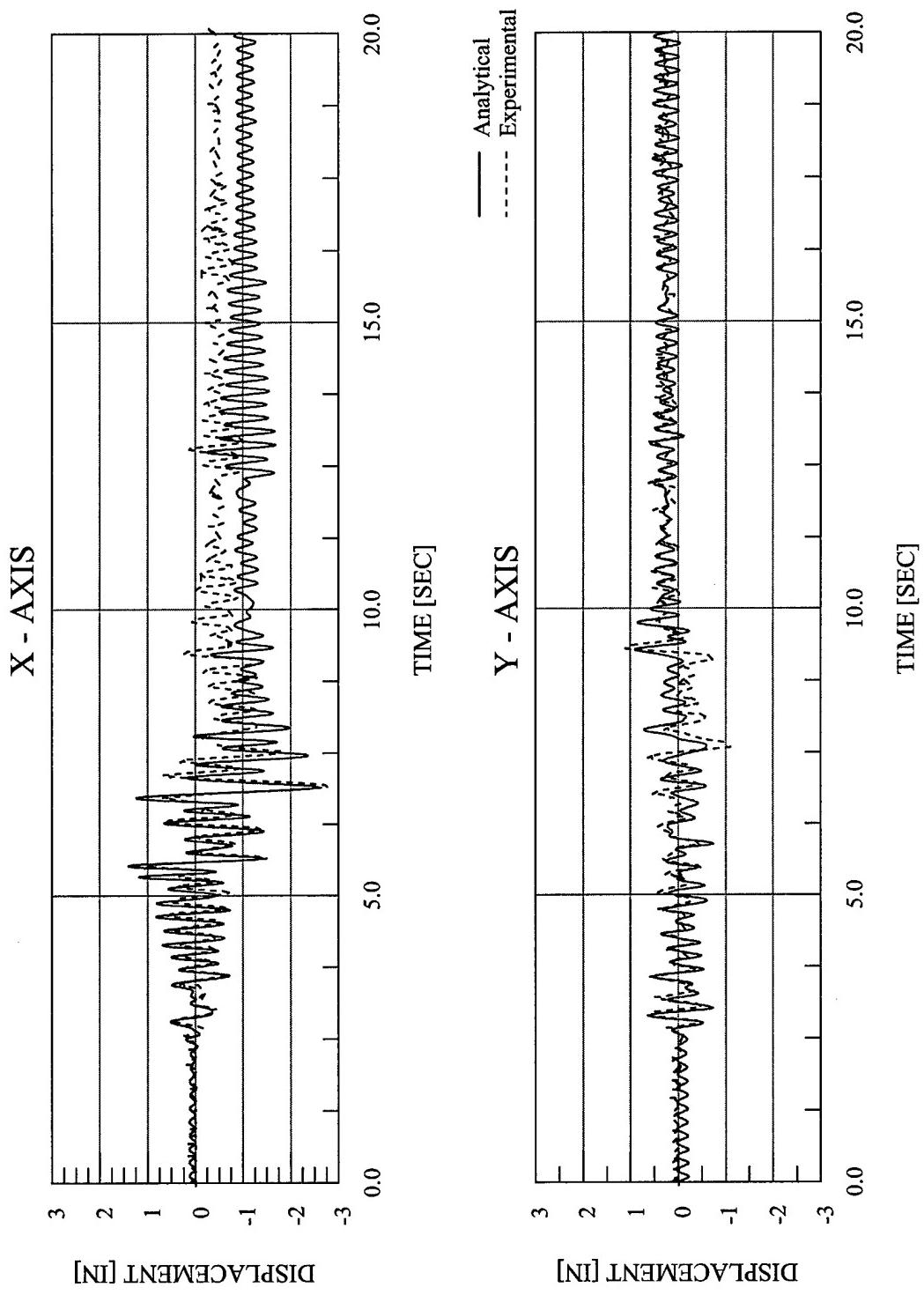


Figure 9.36 Abaqus Displacement vs. Time – EQ 35 – 150% Biaxial Imperial Valley

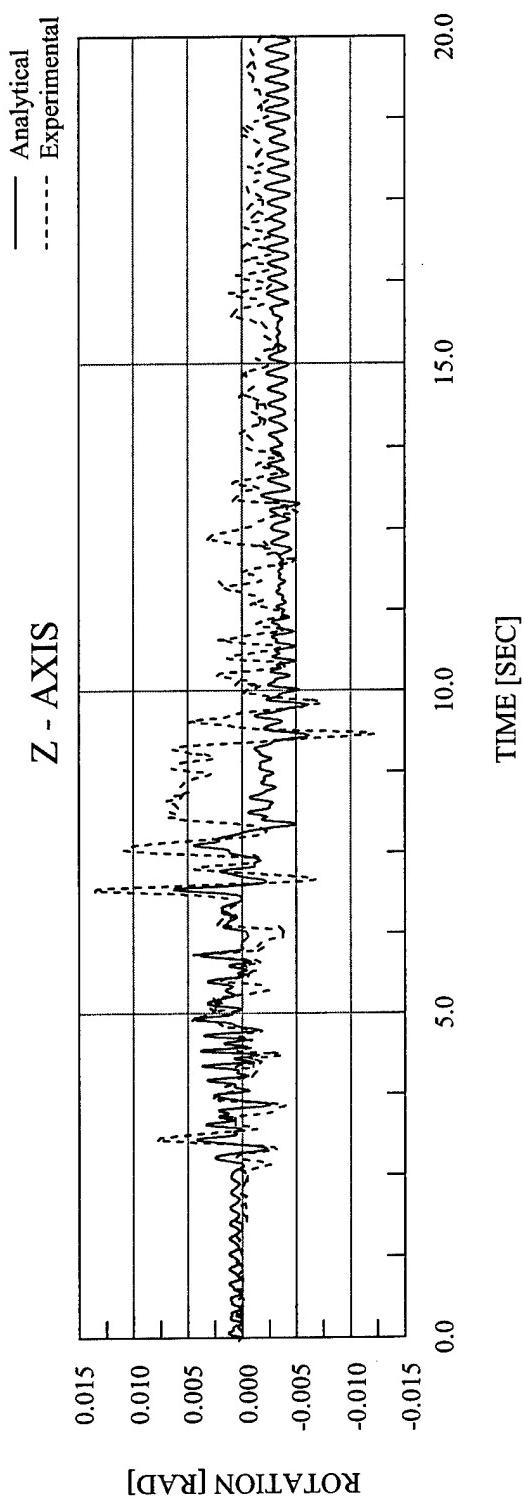


Figure 9.37 Abaqus Rotation vs. Time – EQ 35 – 150% Biaxial Imperial Valley

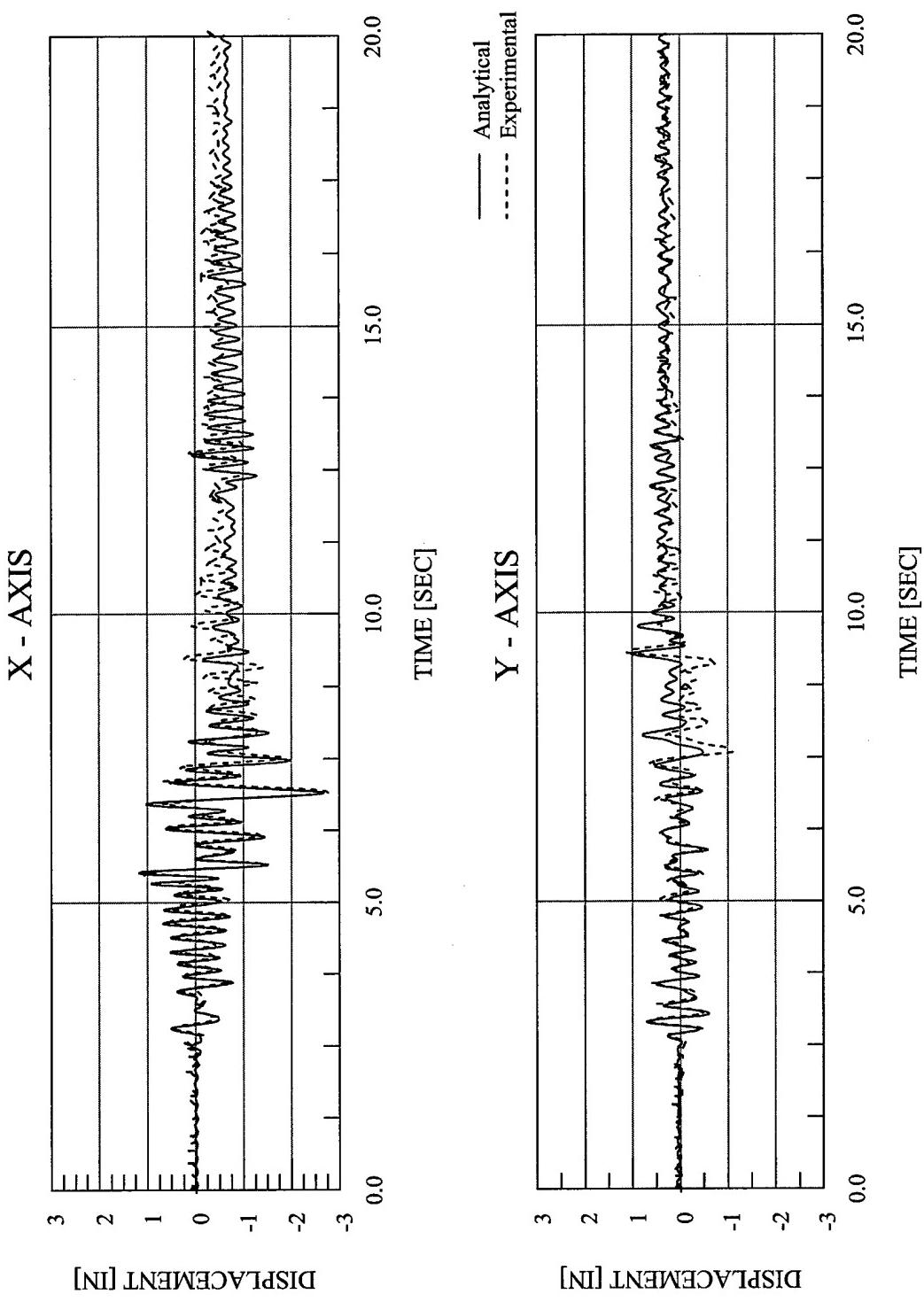


Figure 9.38 Drain-3DX Displacement vs. Time – EQ 35 – 150% Biaxial Imperial Valley

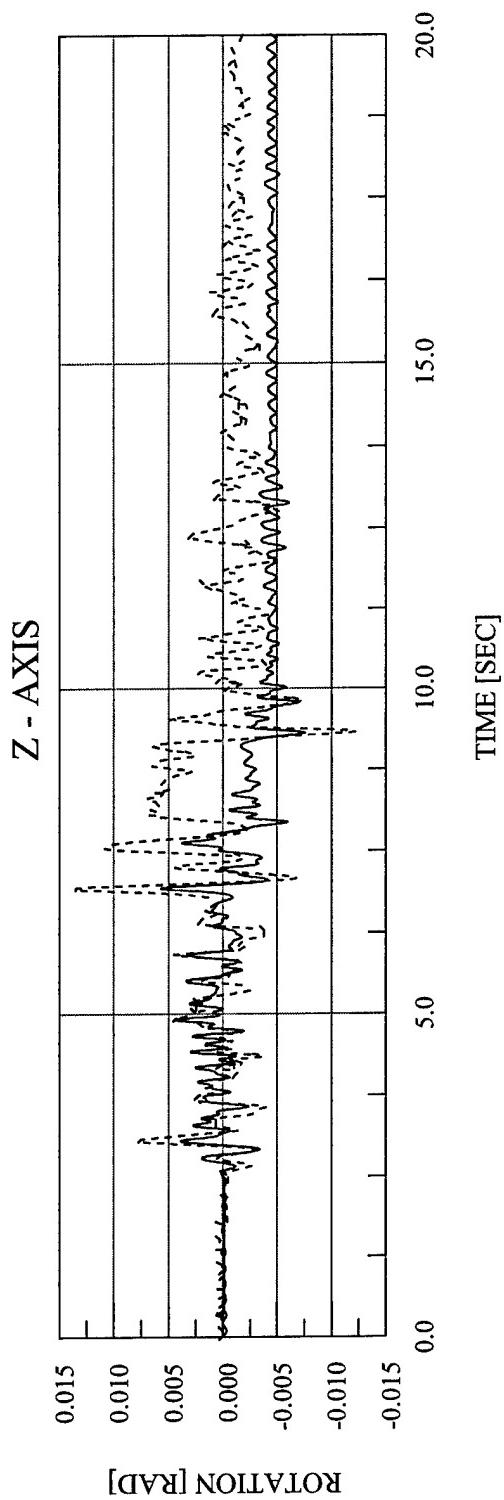


Figure 9.39 Drain-3DX Rotation vs. Time – EQ 35 – 150% Biaxial Imperial Valley

CHAPTER 10

EXPERIMENTAL AND FINITE ELEMENT RESPONSE OF TEST CONFIGURATION 6

This chapter provides a summary of the experimental test data and the finite element analysis results of Test Configuration 6. The sixth configuration, as seen in Figure 10.1, featured all of the masses loaded on the south side of the diaphragm, resulting in a $\frac{1}{2}$ mass asymmetry, and four 4" Extra-Strong Columns. In addition, concentric lateral bracing was located on the north and south sides of the structure. The bracing on the north side of the structure was 1-3/8" x 1/4", while on the south side the bracing used was 1-7/8" x 1/4". The dynamic properties of the test structure in Test Configuration 6 are shown in Table 10.1.

Due to increase in strength and stiffness with the addition of the concentric bracing, it was determined that the current set of ground motions would be insufficient to produce the desired Y-Axis displacement ductility. As a result, the Y-Axis Imperial Valley ground motion used in each of the previous configurations was modified. The ground motion was subjected to a high-pass filter at 1 Hz, followed by scaling the result by a factor of 4. The result of this modification can be readily seen as the Y-Axis PGA of EQ 39, the first 100% Biaxial simulation, is 1.926 g. In comparison, the Y-Axis PGA of EQ 28, the first 100% Biaxial simulation in Test Configuration 4, was 0.711 g. The X-Axis ground motion remained unchanged from that used in previous configurations. This new set of reference ground motions was also used in Test Configuration 7, which also featured concentric bracing in the north and south frames of the structure.

Five earthquake simulations were performed with this test configuration: 10% X-Axis only [$\text{PGA}_X = 0.119 \text{ g}$], 10% Y-Axis only [$\text{PGA}_Y = 0.189 \text{ g}$], 10% Biaxial [$\text{PGA}_X = 0.117 \text{ g}$ and $\text{PGA}_Y = 0.191 \text{ g}$], 100% Biaxial [$\text{PGA}_X = 0.846 \text{ g}$ and $\text{PGA}_Y = 1.926 \text{ g}$], and a final set with 100% X-Axis 90% Y-Axis motions [$\text{PGA}_X = 1.318 \text{ g}$ and $\text{PGA}_Y = 1.951 \text{ g}$]. Characterization tests were performed to determine the dynamic properties of the model. The complete test sequence for Test Configuration 6 is shown in Table 10.2.

The first three earthquake simulations, EQ 37 with 10% X-Axis, EQ 38 with 10% Y-Axis, and EQ 36 with 10% Biaxial input motions, featured elastic behavior only. The fourth simulation, EQ 39 using 100% Biaxial input motions, was the initial inelastic test for this configuration. During the fourth simulation, EQ 39, the test aborted less than halfway through due to the shake table reaching its velocity limit along the Y-Axis. Subsequently, an additional test was performed, EQ 40, in which Y-Axis input motion was reduced to 90% while the X-Axis input motion remained at 100%. This final test therefore featured not only inelastic behavior, but also pre-existing damage in the model columns; however, the final test again aborted less than halfway through the record.

This chapter summarizes response data of the test structure during the earthquake simulations and the dynamic characterization tests. Summaries of test model accelerations, displacements, torsional moments, overturning moments, column end moments, and base shears are provided.

10.1 OBSERVED STRUCTURAL RESPONSE

The diaphragm acceleration and displacement time history responses for the 10% X-Axis simulation are shown in Figure 10.2. The base shear vs. displacement and torque vs. rotation are shown in Figure 10.3. Similar responses for the 10% Y-Axis simulation are shown in Figures 10.4 and 10.5. Results for the 10% Biaxial simulation are shown in Figures 10.6 and 10.7. The responses for the 100% Biaxial simulation are shown in Figures 10.8 and 10.9. Results for the 100% X-Axis 90% Y-Axis simulation are shown in Figures 10.10 and 10.11.

Tables 10.3 – 10.7 list the peak recorded diaphragm relative displacements and peak diaphragm accelerations, and corresponding PGA for each of the five earthquake simulations performed in this test configuration. Also listed are the maximum base shears, maximum torsional moments, maximum overturning moments, maximum column end moments for each column, and maximum column end shears for each column.

10.2 OBSERVED RESPONSE DISCUSSION

The analytical force-deformation behavior of the structure in the X and Y directions and about the Z-Axis is shown in Figures 10.12 and 10.13. In the X direction, the model has a yield displacement of 0.79 inches at a yield force of 38.0 kips. In the Y direction, the model has a yield displacement of 0.27 inches at a yield force of 71.0 kips. The model has a yield rotation of 0.0055 radians at a yield moment of 4160 kip*inches. Elastic response spectra of the recorded table motions for EQ 36 – EQ 39 are shown, along with the modal frequencies for this configuration, in Figures 10.14 – 10.17, respectively.

The first earthquake simulation for this configuration, EQ 37, features 10% Imperial Valley input motion in the X-Axis only [$\text{PGA}_X = 0.119 \text{ g}$]. Time history plots of the structural response are shown in Figure 10.2. The peak displacements of the structure in the X and Y directions were 0.185 inches and 0.014 inches, respectively, while static analysis predicts 0.202 inches along the X-Axis and no Y-Axis displacement. The peak rotation of the structure was 0.16×10^{-3} radians, with no rotation predicted by static analysis. This simulation features no eccentricity, thus a torsional effect is not expected. The angular acceleration response shown in Figure 10.2 is in-phase with the X-Axis acceleration response and is relatively small in magnitude, which would indicate that the torsional response is due to the lack of perfect symmetry of the structure in the X direction. The peak base shears and peak torsional moment are 10.02 kips in the X direction, 0.60 kips in the Y direction, and 46.14 kip*inches about the vertical axis. Figure 10.3 shows the base shear vs. displacement plots and torsional moment vs. rotation plots. The shear vs. displacement plot for the X direction is tight and linear, indicating no yielding.

In EQ 38 the model is subjected to a 10% Y-Axis input motion [$\text{PGA}_Y = 0.189 \text{ g}$]. Time history plots of the structural response are shown in Figure 10.4. The peak displacements of the structure were 0.055 inches in the Y direction and 0.019 inches in the X direction, with a peak rotation of 0.58×10^{-3} radians. Static analysis predicts a displacement of 0.053 inches in the Y direction and a rotation of 0.15×10^{-3} radians, with no displacements predicted along the X-Axis. The peak base shear in the Y direction is 14.92 kips. Figure 10.5 shows the base shear vs. displacement plots and torsional moment vs. rotation plot. The shear vs. displacement plot for the Y direction and the torsional moment vs. rotation plot are both tight and linear.

The third earthquake simulation for this configuration, EQ 36, features 10% Biaxial Imperial Valley input motion [PGA_X = 0.117 g and PGA_Y = 0.191 g]. Time history plots of the structural response are shown in Figure 10.6. The peak displacements of the structure were 0.177 inches in the X direction, 0.053 inches in the Y direction, and 0.76×10^{-3} radians about the Z-Axis. The peak displacements predicted by static analysis are 0.209 inches along the X-Axis, 0.055 inches along the Y-Axis, and 0.15×10^{-3} radians about the Z-Axis. The displacement time histories indicate no residual displacement or permanent deformation. The peak base shears and peak torsional moment are 9.74 kips in the X direction, 15.29 kips in the Y direction, and 349.15 kip*inches about the vertical axis. The Y-Axis peak base shear is roughly 50% larger than the X-Axis base shear, while the Y-Axis peak displacement is about $\frac{1}{4}$ of the peak X-Axis displacement. This follows from the fact that, with the addition of the lateral bracing along the Y-Axis, the stiffness of the structure in the Y direction is now much larger than in the X direction. The noticeably larger frequency of the Y-Axis acceleration response and angular acceleration response than the X-Axis acceleration response also confirms the increased Y-Axis stiffness due to the bracing. Also due to the large stiffness of the braced frames, the peak rotational response is roughly one-third that observed for Test Configuration 4 in Chapter 6, in which the structure had similar columns and mass eccentricity but no lateral bracing. Figure 10.7 shows the base shear vs. displacement plots and torsional moment vs. rotation plot. The base shear vs. displacement plots in the X and Y directions are both tight and linear. The torsional moment vs. rotation plot is also linear, but not as tight as the shear vs. displacement plots.

Thus, for this test configuration, the static analysis is consistently conservative in predicting the elastic peak displacements in the unbraced X direction by about 20%. In the braced Y direction, the static analysis predicted the elastic peak displacements fairly accurately. However, the static analysis is consistently unconservative in predicting the elastic peak rotations by roughly a factor of 4. Note that the structural response does not qualify the model as torsionally irregular in any of the elastic simulations.

In comparing EQ 36 with EQ 38, the addition of the 10% X-Axis input motion results in little change in the Y-Axis response of the diaphragm, as the peak displacement and base shear are 0.055 inches and 14.92 kips for EQ 38 and 0.053 inches and 15.29 kips for EQ 36. Because this configuration has an eccentricity in the X direction only, the addition of an input motion and thus response in the X direction should not add to the torsional effect. This is verified by the fact that the torsional moment is virtually unchanged between EQ 38, 329.74 kip*inches, and EQ 36,

349.15 kip*inches. In comparing EQ 36 to EQ 37, the addition of the 10% Y-Axis input motion results in a change in the Y-Axis response, as well as the torsional response, but very little change in the X-Axis response. The peak displacement in the X-Axis decreases from 0.185 inches in EQ 37 to 0.177 inches in EQ 36. However, the peak ground acceleration in the X-Axis also decreases from 0.119 g in EQ 37 to 0.117 g in EQ 36. The peak rotation increases from 0.16×10^{-3} radians in EQ 37 to 0.76×10^{-3} radians. This rotation response in EQ 37 was previously observed to be due to the lack of perfect symmetry in the X direction, which is consistent with the fact that the peak rotation in EQ 36, the elastic biaxial simulation, is roughly equal to the sum of the peak rotations in EQ 37 and EQ 38, the two elastic uniaxial simulations. Some portion of the torsional response in these simulations might also be a result of the shaketable cross-coupling problem discussed in Chapter 3.

In EQ 39, the first test in this configuration that features inelastic response, the model structure is subjected to 100% Imperial Valley input motion along both the X-Axis and Y-Axis [PGA_X = 0.846 g and PGA_Y = 1.926 g]. Time history plots of the structural response are shown in Figure 10.8. The peak displacements of the structure were 1.64 inches in the X direction and 1.96 inches in the Y direction, with a peak rotation of 18.49×10^{-3} radians. Thus, all of the displacements exceed the yield displacements. The peak base shears, which are 39.48 kips in the X direction and 67.93 kips in the Y direction, are slightly less than the yield shears, 38.00 kips in the X direction and 70.98 kips in the Y direction. Although the peak base shear in the Y direction is slightly less than the observed yield shear, the structure achieves a Y-Axis displacement ductility of more than 7. In addition, in the X direction, the peak base shear is only slightly larger than the yield shear while the displacement ductility is greater than 2. This behavior, in which the peak shears are elastic or nearly elastic while the ductility is much larger than unity, has been observed in previous configurations for the torsional response of the structure. It was observed that the peak torsional moment was smaller than, or nearly equal to, the yield moment, while the peak rotation was much greater than the yield rotation. One possible factor in this behavior is the lateral and torsional response interaction. Each column participates in the seismic resistance of the structure in all three directions of motion, and as a result of the phase of the response in each direction the effective instantaneous stiffness of each columns may frequently be less than their elastic stiffnesses. However, a more likely factor in this behavior is the effect of the tension-only bracing. Once the displacement response of the structure becomes large enough that the braces yield, upon load reversal the braces provide no stiffness. The braces do not provide stiffness until the previous maximum displacement is reached and the braces become taut again. Because the

braces provide a significant fraction of the lateral, and thus rotational stiffness, the rotational stiffness of the structure is significantly reduced for a period of time during each load reversal. This behavior can be observed in the torsional moment vs. rotation plot in Figure 10.9. Verifying the yielding in the X and Y directions and torsionally is a noticeable degree of permanent offset in all three directions of motion. Figure 10.9 shows the base shear vs. displacement plots and torsional moment vs. rotation plot, which are no longer tight and linear, but now are taking on a fuller shape. The hysteresis plot for the Y-Axis response is beginning to take on a different characteristic shape than that observed for all previous hysteresis diagrams, and is consistent with that expected of a concentrically brace frame. This shape is also somewhat apparent in the torsional moment vs. rotation plot, which would be expected as the concentrically braced frames provide roughly 80% of the torsional stiffness for this configuration. From the X-Axis hysteresis plot, the structure does not appear to lose any stiffness during the inelastic response in the X direction. However, the Y-Axis hysteresis plot appears to indicate that the structure does lose a small amount of stiffness during the hysteretic motion. Although the resisting system in the Y direction is composed of both a moment resisting frame and concentric lateral bracing, more than 80% of the stiffness is provided by the tension-only bracing. The degree of overstrength of a lateral brace yielding in tension is significantly less than a pipe-column yielding in flexure. Thus, the lateral bracing, and consequently the Y-Axis force resisting system, experiences significantly more inelastic straining and permanent damage, resulting in the loss of stiffness observed.

The final earthquake simulation for this configuration, EQ 40, features 100% X-Axis and 90% Y-Axis Imperial Valley input motion [PGA_X = 1.318 g and PGA_Y = 1.951 g]. Time history plots of the structural response are shown in Figure 10.10. The peak displacements of the structure were 3.90 inches in the X direction and 2.94 inches in the Y direction, with a peak rotation of 27.80 x 10⁻³ radians. The peak base shears are 46.83 kips in the X direction and 63.49 kips in the Y direction. The peak Y-Axis base shear is slightly less than the yield shear, while the displacement ductility is more than 13. This behavior was also observed in EQ 39, and is a more extreme example of the interaction between the X-Axis, Y-Axis and torsional response. Also, the torsional ductility is roughly 5, while the peak torsional moment is about half the yield moment. Figure 10.11 shows the base shear vs. displacement and torsional moment vs. rotation hysteresis loops, which exhibit more full, smooth shapes than for EQ 39. The characteristic hysteresis shape of a concentrically braced frame is even more apparent in the torsional hysteresis plot for EQ 40 than it was for EQ 39. As mentioned above, this is not unexpected as the concentrically braced frames provide roughly 80% of the torsional stiffness. The loss of stiffness in the Y-Axis force-

resisting system during the hysteretic motion observed in EQ 39 is even more apparent in EQ 40. This loss of stiffness also can be seen in the torsional hysteresis plot. In addition, although the X-Axis response featured the largest inelastic excursion, the Y-Axis braced frame response featured a greater number of large inelastic excursions than the X-Axis response. This indicates a greater degree of inelastic straining and energy dissipation, as mentioned above for EQ 39. Although the braced frame, oriented along the Y-Axis, is roughly 4 times stiffer elastically than the moment-resisting frame oriented along the X-Axis, after a number of load cycles, the stiffness of the braced frame does not appear to be any greater than the moment-resisting frame.

10.3 DYNAMIC CHARACTERIZATIONS OF THE MODEL

Prior to performing any shake table simulations using the earthquake input motions, white noise, sine sweep, and sine decay tests were performed, as discussed in Chapter 3. This general pattern was followed for Test Configuration 6, as can be seen in Table 10.2. In addition, white noise tests were performed immediately after the final earthquake simulation exhibiting inelastic behavior, EQ 40.

The dynamic properties of the test structure, as measured before EQ 36, and then after EQ 40, are shown in Table 10.1. The results indicate that despite the inelastic behavior in EQ 39 and EQ 40 permanent softening of the structure occurred in the Y direction but not in the X direction. The structure softened torsionally as well. These measurements confirm the observations made above regarding the loss of stiffness apparent in the Y-Axis force vs. displacement plot and torsional moment vs. rotation plot. The large change in the modal frequency in the Y and Z directions correlates with the permanent damage experienced by the diagonal bracing. Following EQ 40, the bracing was no longer a significant contributor to the stiffness or damping at small displacements. This is verified by observing that the dynamic properties following EQ 40 correspond fairly well to the dynamic properties of the structure during Test Configuration 4, in which bracing was not present but a $\frac{1}{2}$ mass asymmetry was present. Thus, in comparing the damping and modal frequencies in the Y and Z directions prior to and following the simulations, the contribution of the bracing to the dynamic properties can be seen.

The damping ratio of the test structure for all degrees-of-freedom following the simulations is at or below one percent, which is consistent with the damping ratios of the first four test

configurations, in which 4" Extra-Strong Columns alone were used. The damping ratio of the structure in the Y and Z directions prior to EQ 36 were significantly greater than one percent, indicating that the diagonal bracing provided some additional measure of damping. The damping ratio in the X direction, which was not affected by the lateral bracing, prior to EQ 36 was also below one percent.

10.4 OBSERVED CONDITION OF THE STRUCTURE

Following each of the major earthquake simulations, the model structure was physically inspected. Historically, the most problematic location on the model was column-to-bottom plate welded joint on each column. For Test Configuration 6, no fracture occurred at these or any other locations. In observing the structure condition after EQ 39, the formation of plastic hinges near the tops and bottoms of the columns was becoming discernable. Following the completion of EQ 40, permanent plastic damage in the columns was evident, with the locations of the plastic hinges in the columns becoming very clear. This could also be seen through the final resting displacement of the diaphragm, being permanently offset from the original location, and with respect to the ground. Permanent plastic damage was also very evident in the concentric lateral bracing, beginning with the first inelastic simulation, EQ 39. Figure 10.18 is a photograph of the test structure taken before the earthquake simulations were performed. Figures 10.19 – 10.21 are photographs of the test structure taken after the final earthquake simulation in this configuration, EQ 40, illustrating the inelastic behavior and permanent damage of the structure. Figure 10.21 clearly shows the damage experienced by the lateral bracing. Figure 10.22 also shows the formation of plastic hinges near the top and bottom of the column.

10.5 FINITE ELEMENT ANALYSIS

In modeling the behavior of the test structure, the nonlinear finite element analysis programs Abaqus and Drain-3DX were employed. A more complete discussion of the applicable features of Abaqus and Drain-3DX is presented in Chapter 3. Also, some aspects of the finite element model, such as the modeling of the diaphragm as a rigid component, are common throughout each test configuration, and are discussed more completely in Chapter 3.

(A) PIPE COLUMN AND LATERAL BRACE MATERIAL MODELS

Two coupons were taken from the overall batch of pipe columns used in Test Configuration 6. The material model of the pipe columns in this test configuration was based on stress-strain data produced during the tension tests performed on each coupon. Figure 10.23 shows both the original stress-strain data recorded during the coupon tension tests, and the best-fit material model used in the Abaqus finite element analyses. Figure 10.25 shows the best-fit material model used in the Drain-3DX finite element analyses. Shown in Tables 10.8 and 10.10 are the numerical stress-strain best-fit model data used in the Abaqus and Drain-3DX finite element analyses, respectively. Coupons were also taken from the material used for the diagonal braces in Test Configuration 6. Figures 10.24 and 10.26 respectively show both the original stress-strain data recorded during the coupon tension tests, and the best-fit material model used in the Abaqus and Drain-3DX finite element analyses. Shown in Tables 10.9 and 10.11 are the numerical stress-strain best-fit model data for the diagonal braces used in the Abaqus and Drain-3DX finite element analyses, respectively.

(B) FINITE ELEMENT MODEL

The Abaqus and Drain-3DX finite element models employed to analyze the behavior of Test Configuration 6 are shown in Figures 10.27 and 10.28. Beyond the features of the finite element models common throughout each test configuration, Figures 10.27 and 10.28 illustrate the location and magnitudes of the interior and corner nodal masses, the height of the Non-Rigid Links, and the configuration of the diagonal braces. Rigid links are used to connect the diagonal braces to the rest of the model and to the ground, and both can be seen in the figures. For clarity only the braces and rigid links on the south side of the model are shown, although they are also present on the north side of the model as well. The diagonal braces on the south side of the model have cross-sectional dimensions of 1-7/8" x 1/4", while on the north side the braces have cross-sectional dimensions of 1-3/8" x 1/4".

Two steps were taken in calibrating the model frequencies of the finite element model. First, the modal frequencies of the test structure measured after the final simulation were used to calibrate the finite element model without the diagonal braces in place. Next, the diagonal braces were added to the model, and the model was calibrated using the test structure modal frequencies

measured before the first simulation. This allows a means of accounting for the relative contributions of both the braces and the columns to the dynamic properties of the structure.

(C) OBSERVED RESPONSE

Displacement histories along the X- and Y-Axis and about the Z-Axis are provided for the 10% Biaxial simulation [$\text{PGA}_X = 0.117 \text{ g}$ and $\text{PGA}_Y = 0.191 \text{ g}$] in Figures 10.29 – 10.32, the 100% Biaxial simulation [$\text{PGA}_X = 0.846 \text{ g}$ and $\text{PGA}_Y = 1.926 \text{ g}$] in Figures 10.33 – 10.36, and the 100% X-Axis 90% Y-Axis simulation [$\text{PGA}_X = 1.318 \text{ g}$ and $\text{PGA}_Y = 1.951 \text{ g}$] in Figures 10.37 – 10.40. Table 10.12 lists the maximum peak relative displacements in the X and Y directions and the peak rotation for the three earthquake simulations featuring biaxial input motions performed in this test configuration.

(D) OBSERVED RESPONSE DISCUSSION

In Figures 10.29 – 10.32, the Abaqus and Drain-3DX displacement and rotation response histories for EQ 36 [$\text{PGA}_X = 0.117 \text{ g}$ and $\text{PGA}_Y = 0.191 \text{ g}$] can be seen for both the test structure and the analytical model. For both displacements and the rotation, the frequency contents of the response histories in the Abaqus and Drain-3DX simulations match the test data very well. As seen in Table 10.12, the peak displacements in both directions of the Abaqus model match the test data fairly well, agreeing to within 12% and 4% in the X and Y directions, respectively. The Drain-3DX displacements also match well, agreeing to within 2% in the X direction and 20% in the Y direction. As has commonly been observed in previous configurations, the peak rotation in the analytical models does not agree nearly as well. The experimental peak rotation was found to be roughly four times as large as the peak rotations predicted by both the Abaqus and Drain-3DX models.

In Figures 10.33 and 10.34, the displacement and rotation response histories for EQ 39 can be seen for both the test structure and the Abaqus finite element model. For both displacements and the rotation, the frequency contents of the response histories in the Abaqus simulations match the test data fairly well. However, in both the X and Y directions, the magnitudes of the displacements do not match very well. For the rotation response history, the Abaqus simulation

predicts larger peak displacements at a number of points in the time history and a greater degree of permanent deformation, the opposite of that observed for EQ 36. As seen in Table 10.12, the peak displacements in the X direction are different by 50%, while the peak displacements in the Y direction disagree by more than 100%. The analytical rotation also differs from the experimental value by approximately 50%. This lack of conformity continues in the response histories for EQ 40, shown in Figures 10.37 and 10.38. The peak displacement in the X direction is actually in better agreement for EQ 40, with a difference of about 20%. The Y-Axis peak displacements disagree by nearly 200% and the peak rotations disagree by nearly 150%. For the Y-Axis response in both EQ 39 and EQ 40, a very large inelastic excursion occurs which appears to be the primary cause of the lack of accuracy in the Abaqus predictions. Similar excursions occur in the rotational response of EQ 39 and EQ 40, which is expected as the torsional response is primarily a result of the Y-Axis response and the mass eccentricity about the Y-Axis.

In Figures 10.35 and 10.36, the EQ 39 displacement and rotation response can be seen for the Drain-3DX finite element model. For EQ 39, the Drain-3DX analyses predict the frequency content, peak displacements and rotations, and permanent offset very accurately. The peak displacements agree to within 5% and 13% in the X and Y directions, respectively. The Drain-3DX peak rotation, which has proved to be the most difficult response quantity to predict, is accurate to within 7%. In EQ 40, shown in Figures 10.39 and 10.40, the response histories do not match as well as for EQ 39, but are still somewhat accurate nonetheless. The X-Axis peak displacement agrees to within 15%, while the Y-Axis peak displacement predicted by Drain-3DX is roughly half the experimental value. The peak rotation agrees to within 35%. Although the Drain-3DX Y-Axis and rotational peak responses are not as accurate for EQ 40, they are nevertheless significantly more accurate than the Abaqus predictions. Drain-3DX is also fairly accurate in predicting the permanent displacements and rotations in both EQ 39 and EQ 40. It appears that with the addition of the concentric lateral bracing in the Y direction of the structure, the Y-Axis response has become nearly as difficult to predict as the rotational response, especially for the Abaqus analyses.

10.6 SUMMARY AND CONCLUSIONS

In the previous three chapters, the *Modified μ/R Ratio* was introduced and discussed. This ratio gives a measure of the amount of ductility the 2000 NEHRP Seismic Provisions expects a

particular structure to experience and thus for which it must be designed. The *Modified μ/R Ratio* was computed as the normalized displacement in an inelastic test divided by the normalized displacement during an elastic test and also as the ratio of the normalized rotation during an inelastic simulation to the normalized rotation during an elastic simulation. In previous configurations, the *Modified μ/R Ratios* were compared with values in the range of 0.86 to 0.69, which are the values corresponding to an Ordinary Moment Resisting Frame (OMRF) and a Special Moment Resisting Frame (SMRF). For this configuration, the X-Axis force-resisting system remains a moment-resisting frame, while in the Y direction is a concentrically braced frame.

Configuration	EQ	μ/R Ratio		
		X-Axis	Y-Axis	Z-Axis
Symmetric Mass 100% Uniaxial	7	N/A	0.77	N/A
Symmetric Mass 100% Biaxial	15	1.37	0.86	0.84
Symmetric Mass 150% Biaxial	16	1.77	1.83	1.08
$\frac{1}{2}$ Asymmetric Mass 100% Biaxial	28	0.90	0.51	1.07
$\frac{1}{2}$ Asymmetric Mass 150% Biaxial	29	1.17	1.03	1.39
$\frac{1}{4}$ Asymmetric Mass 100% Biaxial	23	1.60	0.61	1.90
$\frac{1}{2}$ Asymmetric Mass Strength Asymmetry 100% Biaxial	34	0.56	0.67	1.28
$\frac{1}{2}$ Asymmetric Mass Strength Asymmetry 150% Biaxial	35	0.80	1.19	1.39
$\frac{1}{2}$ Asymmetric Mass Stiffness Asymmetry Concentric Bracing 100% Biaxial	39	1.28	3.66	2.42
$\frac{1}{2}$ Asymmetric Mass Strength Asymmetry Concentric Bracing 100% X-Axis 90% Y-Axis	40	1.96	5.44	3.59

The Y-Axis force-resisting system does not qualify as a Dual System in the *NEHRP Provisions*, which require that the moment-resisting frame portion of the system resist at least 25% of the seismic lateral loading. The *Provisions* specifies a *Modified μ/R Ratio* of 0.83 for a Special Steel Concentrically Braced Frame and 0.9 for an Ordinary Steel Concentrically Braced Frame.

As seen above, in the X direction the *Modified μ/R Ratio* is 1.28 for EQ 39 and 1.96 for EQ 40. Although larger than the specified range of 0.86 to 0.69 for a moment-resisting frame, they are similar to values observed in previous configurations. As discussed previously, although this would appear to suggest that the *Provisions* should specify a greater degree of ductility in design, overstrength in actual structures is assumed to be a mitigating factor. In the Y direction, the *Modified μ/R Ratio* is 3.66 for EQ 39 and 5.44 for EQ 40. These values are significantly greater than the range specified in the *Provisions*, and the system overstrength for a concentrically braced frame is not as great as for a moment-resisting frame. In addition, because the design of concentrically braced frames is not typically controlled by drift or deflection, unlike moment-resisting frames, there is a lesser degree of design overstrength for these types of force-resisting systems as well. Because the concentrically braced frames provide roughly 80% of the torsional stiffness for this configuration, it is not surprising that the *Modified μ/R Ratio* rotationally are also large and appear to be changing with the Y-Axis *Modified μ/R Ratios*. The *Modified μ/R Ratio* rotationally for EQ 40 is roughly 75% larger than the largest *Ratio* observed in all previous configurations. These factors in total lead to a concern about the specified ductility in design for concentrically braced frames.

The methodology used in the *Seismic Provisions* of using an elastic analysis as the basis for determining inelastic response of structures implies that the ratio of the peak rotation to the peak lateral displacement and the ratio of the two peak lateral displacements remain constant for elastic and inelastic response. For previous configurations, not only were the u_y/u_x ratio and u_θ/u_x ratio for the elastic and inelastic simulations in one particular configuration compared, but these ratios were also compared with those from other configurations. These comparisons between different configurations were meaningful because the ground motions used for each configuration were very similar. With this configuration, the addition of the concentric bracing necessitated a significant change in the Y-Axis input ground motions, as discussed previously in this chapter. Thus, making comparisons in the u_y/u_x ratio and the u_θ/u_x ratio with previous configurations would be difficult. In addition, in this configuration the peak rotation will be compared with the

peak Y-Axis displacement, instead of the X-Axis displacement as before, since the mass asymmetry is now about the Y-Axis.

As shown below, the u_y/u_x ratio is 0.30 for EQ 36. The ratio for EQ 39, the first inelastic simulation, increases by a factor of 4 to 1.20. This would indicate that the Y-Axis displacement response increases to a much greater degree than the X-Axis response. The largest increase in the u_y/u_x ratio from an elastic test to an inelastic test observed in any of the previous configurations was 50% in Test Configuration 5. The likely cause of this behavior is the presence of two different force-resisting systems: a moment-resisting frame along the X-Axis, and a concentrically brace frame along the Y-Axis. As mentioned previously, although the resisting system in the Y direction is composed of both a moment resisting frame and concentric lateral bracing, more than 80% of the stiffness is provided by the tension-only bracing. As the structure begins to yield in both the X and Y directions, the degree of overstrength of the braces yielding in tension is significantly less than the pipe-columns yielding in flexure. This translates into the concentrically braced frame in the Y direction losing stiffness at a more rapid rate than the moment-resisting frame in the X direction. This would result in the peak Y-Axis displacement increasing to a greater degree than the X-Axis peak displacement. The u_y/u_x ratio for EQ 40 has decreased slightly to 0.75, which still remains over twice the value for the elastic simulation.

This decrease corresponds to a change in the input ground motions from EQ 39 to EQ 40.

Although it appears that the X-Axis ground motion remained the same and the Y-Axis ground motion decreased by 10%, in actuality the X-Axis PGA increased from 0.846 g to 1.318 g, while the Y-Axis PGA remained virtually unchanged. It would appear that the increased X-Axis ground motion has caused the moment-resisting frame to travel further along the yield path than for EQ 39. Extending this situation, it would be reasonable to assume that with a larger X-Axis ground motion, or a reduction in the strength of the force-resisting system in the X direction, the u_y/u_x ratio would decrease even further, as the degree of stiffness loss in the X direction would “catch up” to that in the Y direction. This also would likely happen if the X-Axis and Y-Axis ground motions were scaled to the same level, but to 150% or 200%, a level where the X-Axis stiffness loss would catch up to the Y-Axis loss. However, from the results presented here, it is impossible to know if the u_y/u_x ratio would decrease to the point of being equal to the value for the elastic simulation. One mitigating factor in the impact of the results shown here is that a moment-resisting frame is typically designed using a large strength-reduction factor, with the intention of the frame achieving significant ductility. The degree of ductility achieved in the X direction here, 2.1, is likely less than would be experienced in a properly designed moment-

resisting frame under large ground motions. Although these factors might mitigate the large change in the u_Y/u_X ratio, the impact of two different types of force-resisting systems on the inelastic behavior of the system is important to consider in design.

Configuration	EQ	u_Y/u_X	u_θ/u_Y
10% Biaxial ½ Asymmetric Mass [Y-Axis] Concentric Bracing [Y-Axis] Stiffness Asymmetry [Y-Axis]	36	0.30	0.69
100% Biaxial ½ Asymmetric Mass [Y-Axis] Concentric Bracing [Y-Axis] Stiffness Asymmetry [Y-Axis]	39	1.20	0.46
100% X-Axis 90% Y-Axis ½ Asymmetric Mass [Y-Axis] Concentric Bracing [Y-Axis] Stiffness Asymmetry [Y-Axis]	40	0.75	0.46

The general trend observed in previous configurations for the u_θ/u_X ratio was that the ratio increased noticeably for inelastic response as compared with elastic response. For EQ 36, the u_θ/u_Y ratio is 0.69. The value decreases to 0.46 for EQ 39, the first inelastic simulation, and remains at 0.46 for EQ 40, the second inelastic simulation. The u_θ/u_Y ratio clearly does not remain constant from the elastic simulation to the inelastic simulation, as the drop is roughly 35%. Although the change is significant, the decrease would prove to be conservative from a design standpoint.

The performances of the time history analyses using Abaqus and Drain-3DX for this configuration were mixed in their response predictions. In past test configurations, the Abaqus analyses generally proved to be more accurate in predicting displacement response while the Drain-3DX typically proved to be more accurate in predicting rotational response. In this configuration, the first with concentric bracing comprising a portion of the force-resisting system, the Drain-3DX proved to be significantly more accurate in predicting all of the response quantities. For the low-level elastic simulations, the Drain-3DX and Abaqus analyses performed equally well in predicting the displacement response, showing accuracy within 2 - 20%. Both analysis programs were equally inaccurate in predicting the elastic rotational response, underestimating the actual peak response by a factor of roughly 4. The finite element analyses

underestimating the rotational response is a trend observed a number of times in previous configurations. For the inelastic simulations, the Drain-3DX analyses proved to be surprisingly accurate, while the Abaqus analyses proved to be surprisingly inaccurate. The Abaqus analyses predicted the X-Axis displacement response fairly well, differing by 20 - 40%. However, the Y-Axis response, in which the concentrically braced frames are the dominant force-resisting system, overestimate the peak displacement by 200 - 300%. The rotational response was also overestimated in the two inelastic simulations by 50 – 250%. The Drain-3DX analyses predicted every response quantitiy for EQ 39 and EQ 40 more accurately than Abaqus by a significant margin. The greatest degree of inaccuracy was 51%, which occurred in predicting the Y-Axis displacement for EQ 40, when the Abaqus analysis was off by over 300%. The Drain-3DX predicted the peak rotations fairly well, agreeing with the experimental values to within 7% and 37%, again significantly better than the Abaqus analyses. In addition, the Drain-3DX analyses even predicted the permanent offset, when present, reasonably well, which had proved to be a weakness in previous configurations. The previous configuration, which featured two different types of columns with noticeably different strengths, proved to be a more difficult configuration to accurately predict with Abaqus and Drain-3DX than the earlier configurations. This most likely was a result of the presence of two different types of columns with different material properties. With the additional complexity added by the presence of the concentric bracing, which possessed different material properties than the columns, it would not have been unexpected if the finite element analyses were noticeably less accurate than previous configurations. This proved to be the case when analyzing the response using Abaqus, but the opposite was true when using Drain-3DX.

Mass [lb*s ² /in]	Mass Centers [in]			Stiffness Centers [in]	
	X ₀	Y ₀	Z ₀	X ₀	Y ₀
95.943	13.429	0.0	69.810	5.833	2.217

	Modal Frequencies [Hz]			Modal Damping [%]		
	X	Y	θ	X	Y	θ
Before EQ 36	3.636	8.333	13.333	0.653	4.617	2.217
After EQ 40	3.704	3.509	7.143	0.659	1.000	0.737

Table 10.1 Test Structure Dynamic Properties - Test Configuration 6

Test Designation	Input Motions
WNT40	White Noise X-Axis
WNT41	White Noise Y-Axis
WNT42	White Noise Yaw-Axis
SIN22	Sine Decay X-Axis
SIN23	Sine Decay Y-Axis
SIN24	Sine Decay Yaw-Axis
SWP22	Sine Sweep X-Axis
SWP23	Sine Sweep Y-Axis
SWP24	Sine Sweep Yaw-Axis
EQ36	10% Biaxial Imperial Valley
EQ37	10% X-Axis Imperial Valley
EQ38	10% Y-Axis Imperial Valley
EQ39	100% Biaxial Imperial Valley
EQ40	100% X-Axis 90% Y-Axis Imperial Valley
WNT43	White Noise X-Axis
WNT44	White Noise Y-Axis
WNT45	White Noise Yaw-Axis
SIN25	Sine Decay X-Axis
SIN26	Sine Decay Y-Axis
SIN27	Sine Decay Yaw-Axis
SWP25	Sine Sweep X-Axis
SWP26	Sine Sweep Y-Axis
SWP27	Sine Sweep Yaw-Axis

Table 10.2 Earthquake Simulations and Dynamic Characterization Tests - Test Configuration 6

Earthquake Test No.	Input Motions	PGA [g]			Relative Displacement [in]			Rotation [10^{-3} rad]			Normalized Displacement [in/g]			Ductility
		X-Axis	Y-Axis	Z-Axis	X-Axis	Y-Axis	Z-Axis	X-Axis	Y-Axis	Z-Axis	X-Axis	Y-Axis	Z-Axis	
37	10% X-Axis	0.119	N/A	0.185	0.014	0.16	1.55	N/A	0.23	0.05	0.03			
38	10% Y-Axis	N/A	0.189	0.019	0.055	0.58	N/A	0.29	0.02	0.20	0.11			
36	10% Biaxial	0.117	0.191	0.177	0.053	0.76	1.51	0.28	0.22	0.19	0.14			
39	100% Biaxial	0.846	1.926	1.635	1.955	18.49	1.93	1.02	2.07	7.14	3.37			
40	100% X-Axis 90% Y-Axis	1.318	1.951	3.904	2.944	27.80	2.96	1.51	4.95	10.74	5.07			

Table 10.3 Maximum Diaphragm Relative Displacement and Rotation - Test Configuration 6

Earthquake Test No.	Input Motions	PGA [g]			Diaphragm Acceleration [g]	Diaphragm Angular Acceleration [10^{-3} g/in]	Normalized Acceleration
		X-Axis	Y-Axis	Z-Axis			
37	10% X-Axis	0.119	N/A	0.270	0.016	0.85	2.27
38	10% Y-Axis	N/A	0.189	0.028	0.388	3.43	N/A
36	10% Biaxial	0.117	0.191	0.263	0.398	3.54	2.05
39	100% Biaxial	0.846	1.926	1.065	1.980	32.06	2.25
40	100% X-Axis 90% Y-Axis	1.318	1.951	1.263	1.973	30.00	2.08
						0.96	1.03
						1.26	1.01

Table 10.4 Maximum Diaphragm Acceleration and Angular Acceleration Response - Test Configuration 6

Earthquake Test No.	Input Motions	PGA [g]			Base Shear [k]	Torsional Moment [k*in]	Diagonal Brace Force [k]	Overturning Moment [k*in]	
		X-Axis	Y-Axis	Z-Axis				X-Axis	Y-Axis
37	10% X-Axis	0.119	N/A	10.02	0.60	46.04	0.28	0.42	702.8
38	10% Y-Axis	N/A	0.189	1.04	14.92	330.48	4.74	7.55	73.3
36	10% Biaxial	0.117	0.191	9.74	15.29	349.15	4.87	7.70	682.9
39	100% Biaxial	0.846	1.926	39.48	67.93	2117.60	28.65	35.76	2768.8
40	100% X-Axis 90% Y-Axis	1.318	1.951	46.83	63.49	2318.05	28.74	39.67	3284.1
									4452.6

Table 10.5 Maximum Base Shear, Torsional Moment, Brace Force, and Overturning Moment - Test Configuration 6

Earthquake Test No.	Input Motions	PGA [g]				Column End Moments [k*in]					
		X-Axis	Y-Axis	SE Column	SW Column	X-Axis	Y-Axis	NW Column	X-Axis	Y-Axis	NE Column
37	10% X-Axis	0.119	N/A	1.26	75.90	1.27	74.31	1.16	74.31	1.16	75.90
38	10% Y-Axis	N/A	0.189	23.03	7.09	23.03	11.39	19.69	11.39	19.69	7.09
36	10% Biaxial	0.117	0.191	23.48	72.35	23.48	73.79	20.26	73.79	20.26	72.35
39	100% Biaxial	0.846	1.926	109.09	291.08	109.09	304.09	119.11	304.09	119.11	291.08
40	100% X-Axis 90% Y-Axis	1.318	1.951	121.00	353.72	121.00	349.73	119.47	349.73	119.47	353.72

Table 10.6 Maximum Column End Moments - Test Configuration 6

Earthquake Test No.	Input Motions	PGA [g]		Column End Shears [k]							
				SE Column		SW Column		NW Column		NE Column	
		X-Axis	Y-Axis	X-Axis	Y-Axis	X-Axis	Y-Axis	X-Axis	Y-Axis	X-Axis	Y-Axis
37	10% X-Axis	0.119	N/A	2.53	0.04	2.48	0.04	2.48	0.04	2.53	0.04
38	10% Y-Axis	N/A	0.189	0.24	0.77	0.38	0.77	0.38	0.66	0.24	0.66
36	10% Biaxial	0.117	0.191	2.41	0.78	2.46	0.78	2.46	0.68	2.41	0.68
39	100% Biaxial	0.846	1.926	9.70	3.64	10.14	3.64	10.14	3.97	9.70	3.97
40	100% X-Axis 90% Y-Axis	1.318	1.951	11.79	4.03	11.66	4.03	11.66	3.98	11.79	3.98

Table 10.7 Maximum Column End Shears - Test Configuration 6

E [ksi] = 29000

Stress [ksi]	Strain [in/in]	Plastic Strain [in/in]
0.000000	0.000000	
48.050000	0.001481	0.000000
49.250000	0.004000	0.002482
50.200000	0.010000	0.008453
50.800000	0.015000	0.013434
52.300000	0.020000	0.018388
53.400000	0.030000	0.028354
54.200000	0.040000	0.038329
55.400000	0.060000	0.058292
56.000000	0.080000	0.078274
56.400000	0.100000	0.098261
56.600000	0.150000	0.148255
55.900000	0.200000	0.198277

Table 10.8 Abaqus Stress-Strain Best-Fit Material Model - 4" Extra-Strong Columns
Test Configuration 6

E [ksi] = 29000

Stress [ksi]	Strain [in/in]	Plastic Strain [in/in]
0.000000	0.000000	
58.000000	0.002000	0.000000
63.500000	0.002500	0.000310
67.800000	0.003000	0.000662
70.800000	0.004000	0.001559
72.800000	0.006000	0.003490
73.800000	0.008000	0.005455
74.400000	0.010000	0.007434
76.950000	0.020000	0.017347
78.500000	0.030000	0.027293
79.400000	0.040000	0.037262
79.900000	0.050000	0.047245
79.900000	0.060000	0.057245
77.700000	0.070000	0.067321

Table 10.9 Abaqus Stress-Strain Best-Fit Material Model - Diagonal Braces
Test Configuration 6

E [ksi] = 29000.0

Stress [ksi]	Strain [in/in]
0.00000	0.00000
48.05000	0.001700
50.20000	0.010000
53.40000	0.030000
56.00000	0.080000
56.60000	0.150000

Table 10.10 Drain-3DX Stress-Strain Best-Fit Material Model – 4" Extra-Strong Columns
Test Configuration 6

E [ksi] = 29000.0

Stress [ksi]	Strain [in/in]
0.00000	0.00000
63.50000	0.002190
70.80000	0.004000
73.80000	0.008000
78.50000	0.030000
79.90000	0.060000

Table 10.11 Drain-3DX Stress-Strain Best-Fit Material Model – Diagonal Braces
Test Configuration 6

Earthquake Test No.	Input Motions	PGA [g]				Relative Displacement [in]				Rotation [10^{-3} rad]		
		X-Axis		Y-Axis		X-Axis		Y-Axis		Z-Axis		
		Abaqus	Drain	Test	Abaqus	Drain	Test	Abaqus	Drain	Test	Abaqus	Drain
36	10% Biaxial	0.117	0.191	0.199	0.175	0.177	0.051	0.040	0.053	0.20	0.14	0.76
39	100% Biaxial	0.846	1.926	2.29	1.57	1.64	4.56	1.70	1.96	28.14	19.84	18.49
40	100% X-Axis 90% Y-Axis	1.318	1.951	3.08	3.31	3.90	9.11	1.51	2.94	68.01	17.63	27.80

Table 10.12 Analytical vs. Experimental Displacement and Rotation Response Comparison - Test Configuration 6

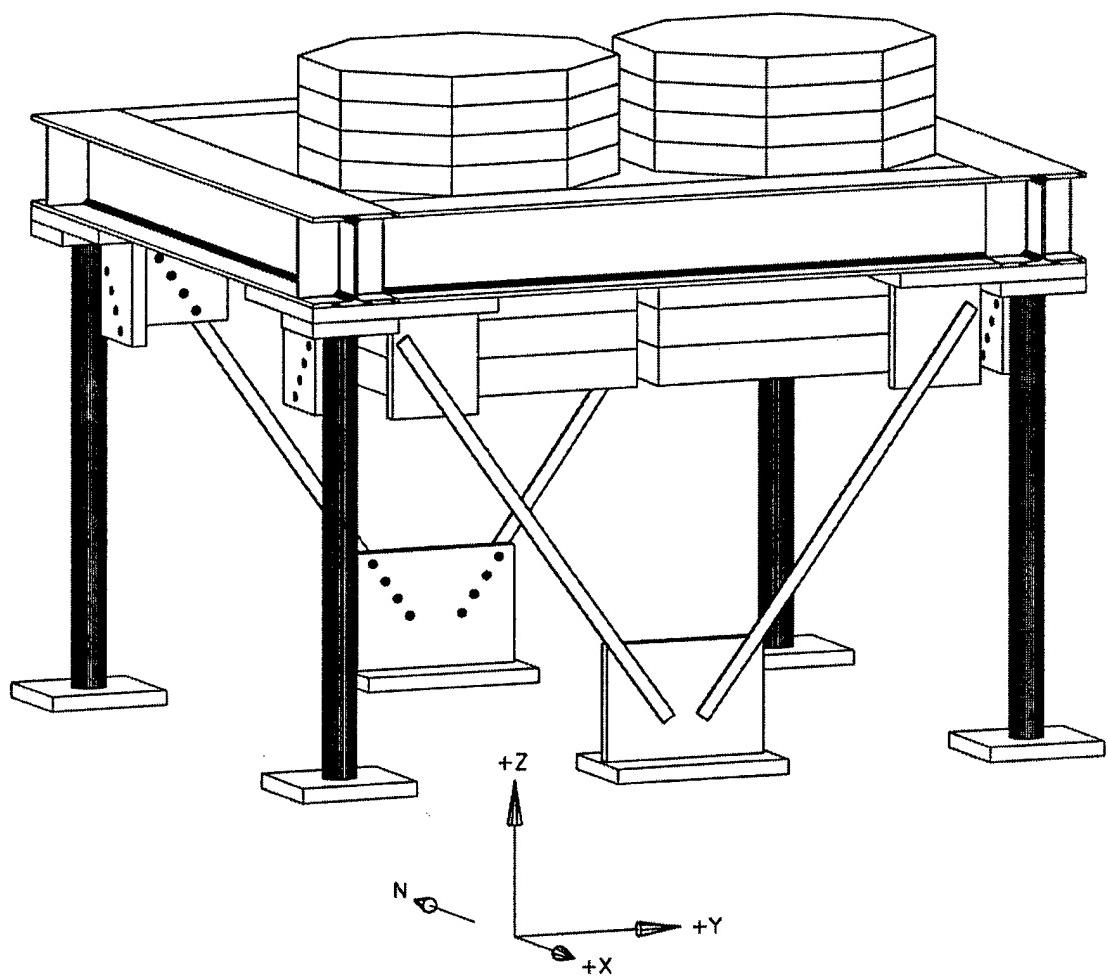


Figure 10.1 Perspective View of Test Configuration Model 6
4 - 4" Extra-Strong Columns

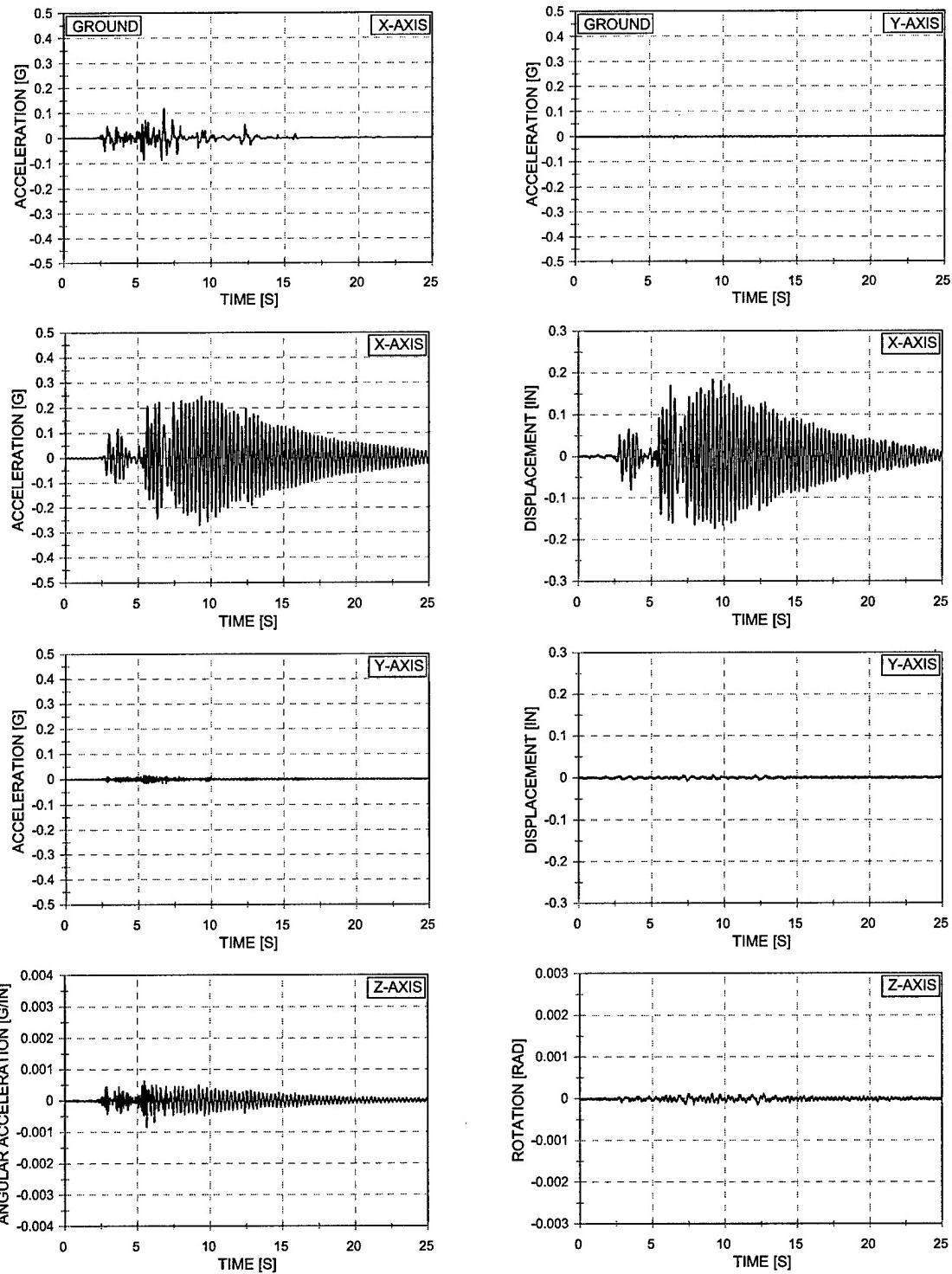


Figure 10.2 Acceleration and Displacement vs. Time – EQ 37
 10% X-Axis Imperial Valley – 1/2 Asymmetric Mass – Concentric Bracing
 Four 4" Extra-Strong Columns

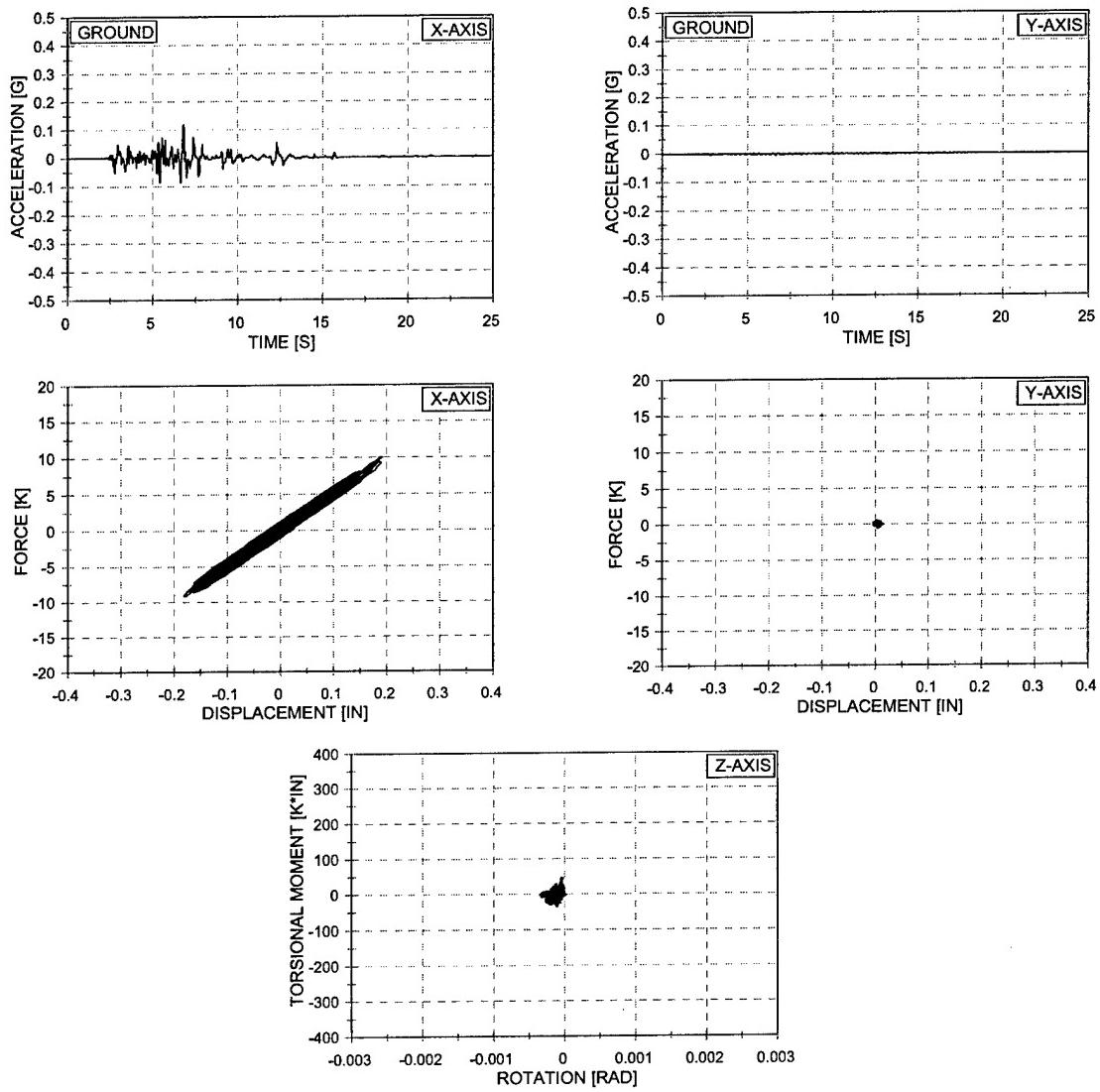


Figure 10.3 Force vs. Displacement and Torsional Moment vs. Rotation – EQ 37
 10% X-Axis Imperial Valley – 1/2 Asymmetric Mass – Concentric Bracing
 Four 4" Extra-Strong Columns

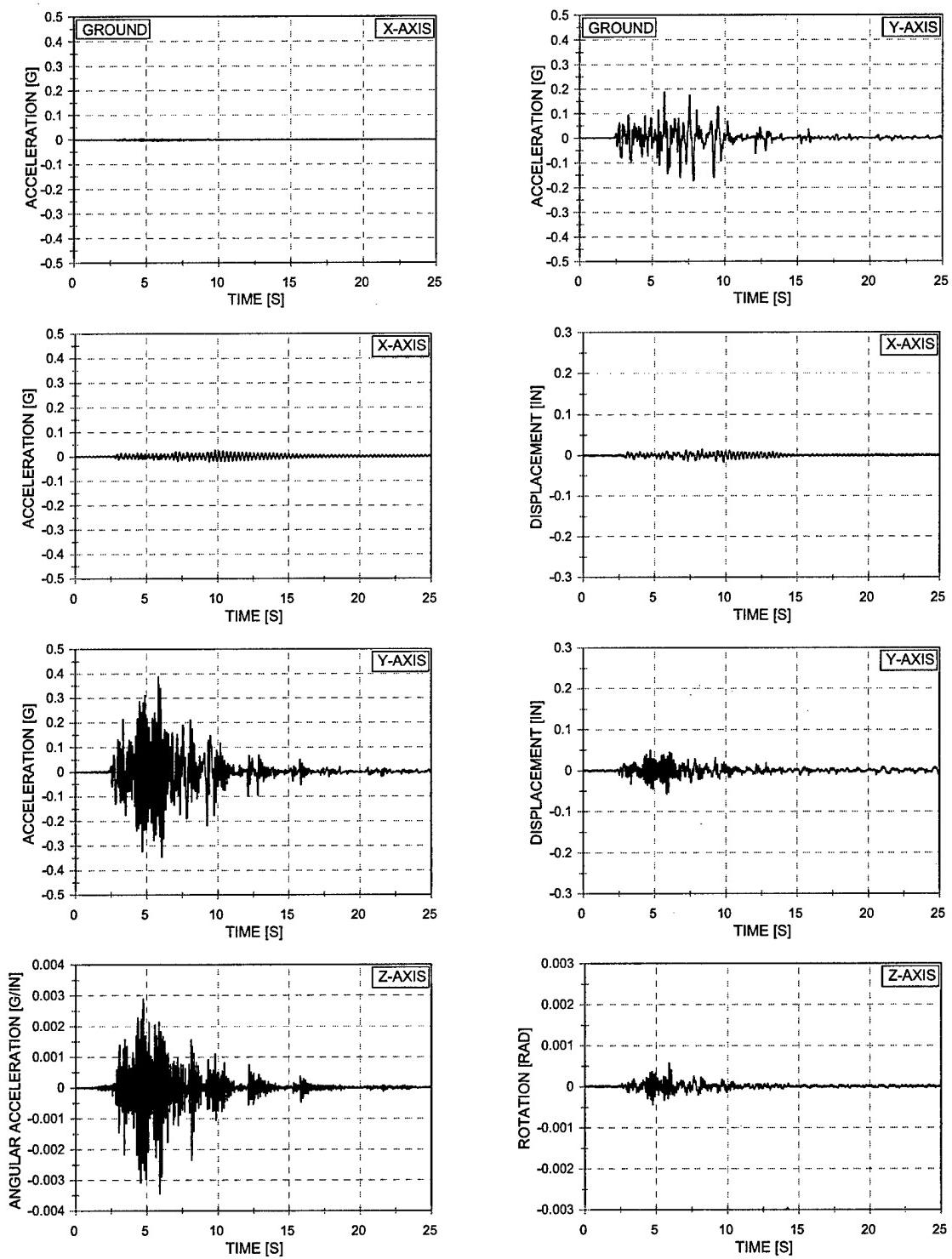


Figure 10.4 Acceleration and Displacement vs. Time – EQ 38
 10% Y-Axis Imperial Valley – 1/2 Asymmetric Mass – Concentric Bracing
 Four 4" Extra-Strong Columns

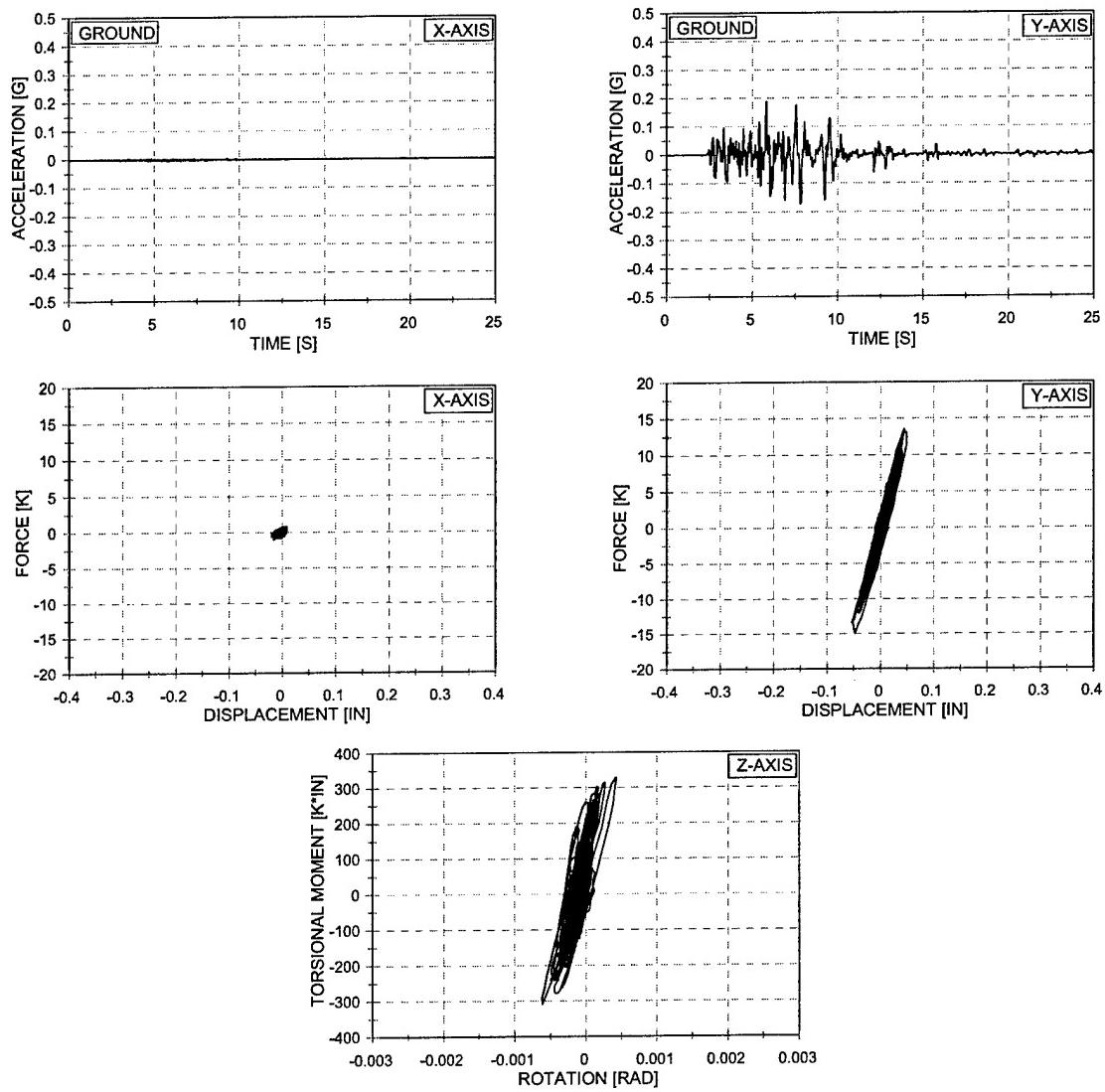


Figure 10.5 Force vs. Displacement and Torsional Moment vs. Rotation – EQ 38
 10% Y-Axis Imperial Valley – 1/2 Asymmetric Mass – Concentric Bracing
 Four 4" Extra-Strong Column

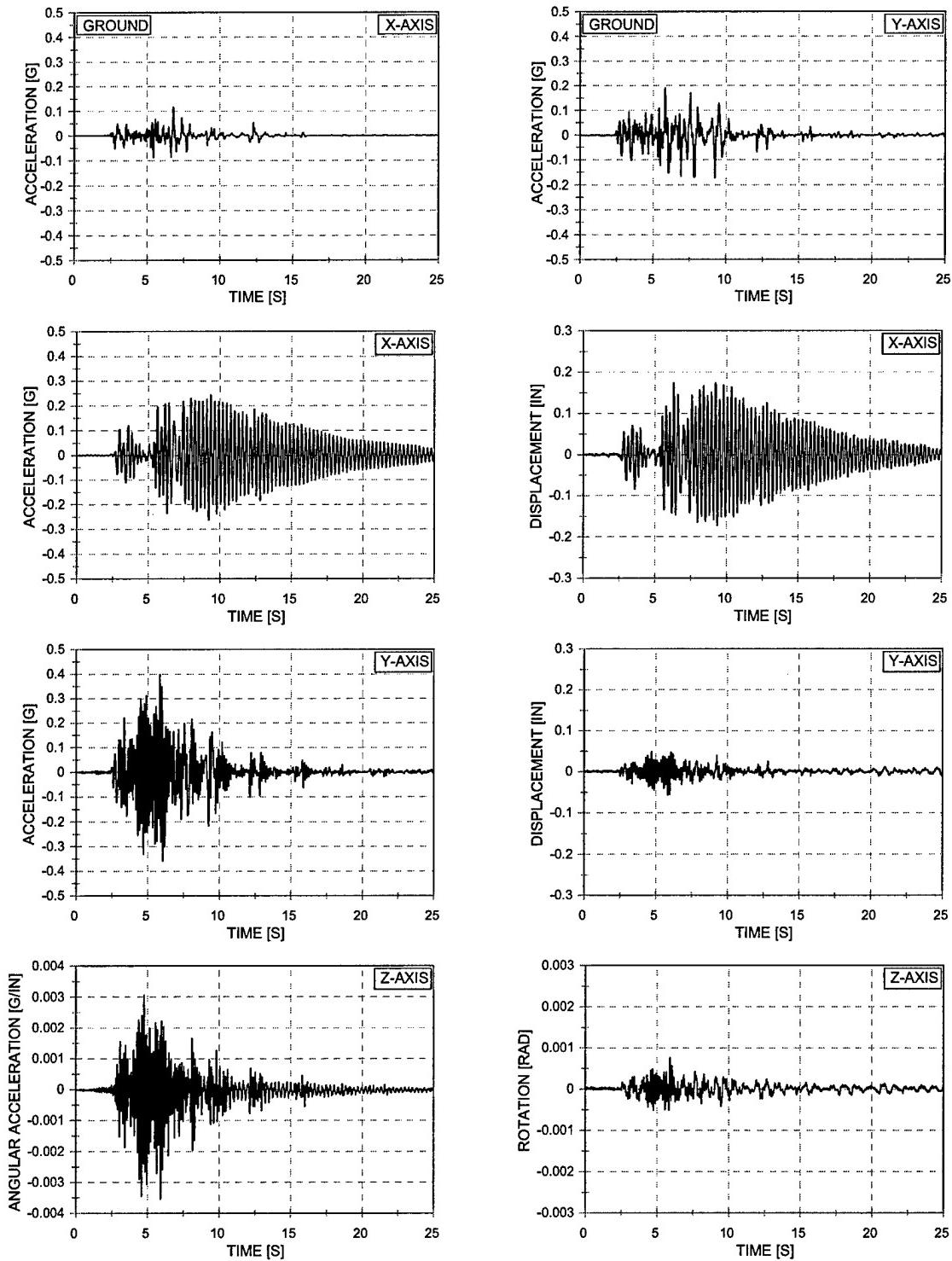


Figure 10.6 Acceleration and Displacement vs. Time – EQ 36
 10% Biaxial Imperial Valley – 1/2 Asymmetric Mass – Concentric Bracing
 Four 4" Extra-Strong Columns

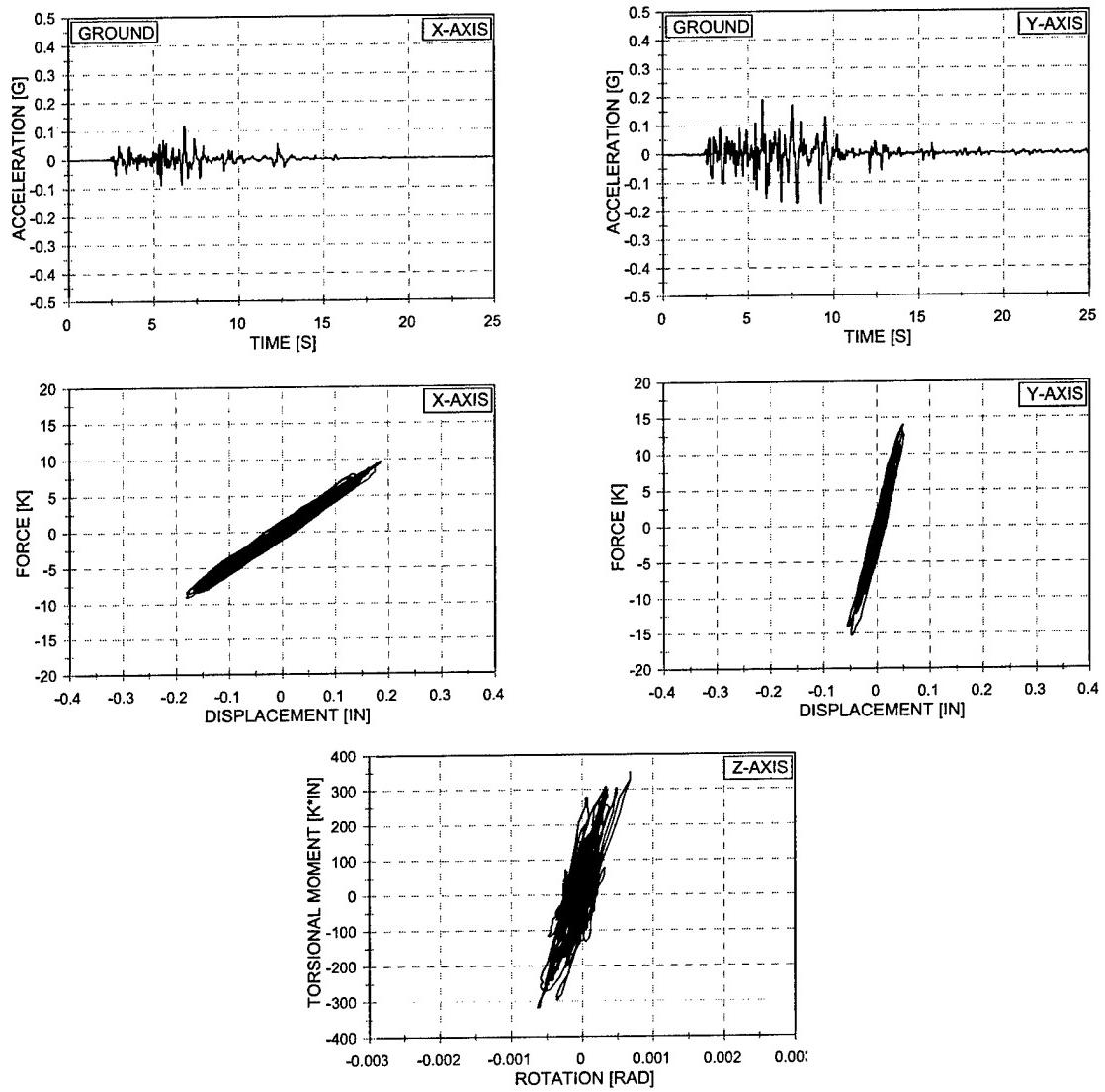


Figure 10.7 Force vs. Displacement and Torsional Moment vs. Rotation – EQ 36
 10% Biaxial Imperial Valley – 1/2 Asymmetric Mass – Concentric Bracing
 Four 4" Extra-Strong Columns

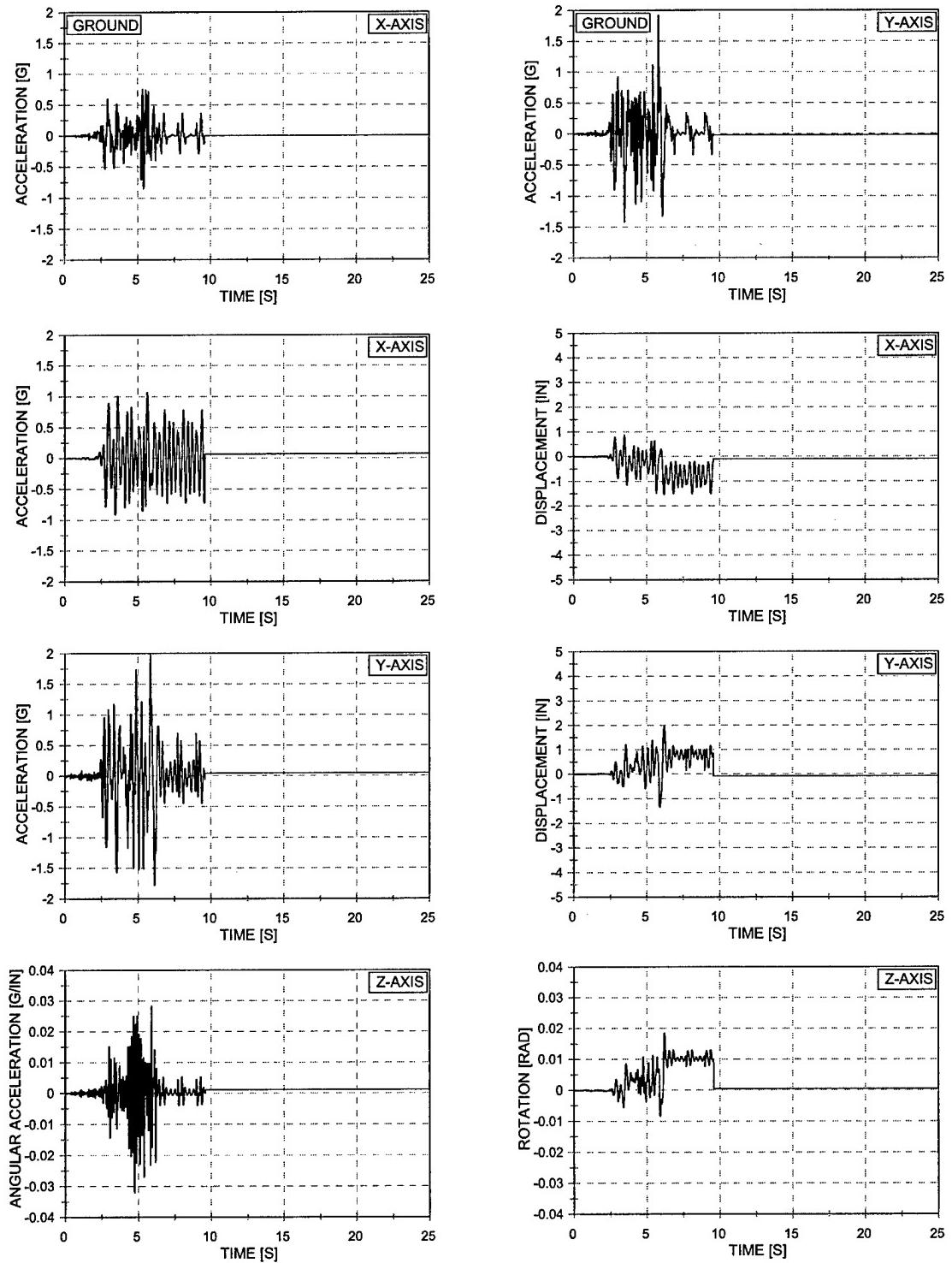


Figure 10.8 Acceleration and Displacement vs. Time – EQ 39
 100% Biaxial Imperial Valley – 1/2 Asymmetric Mass – Concentric Bracing
 Four 4" Extra-Strong Columns

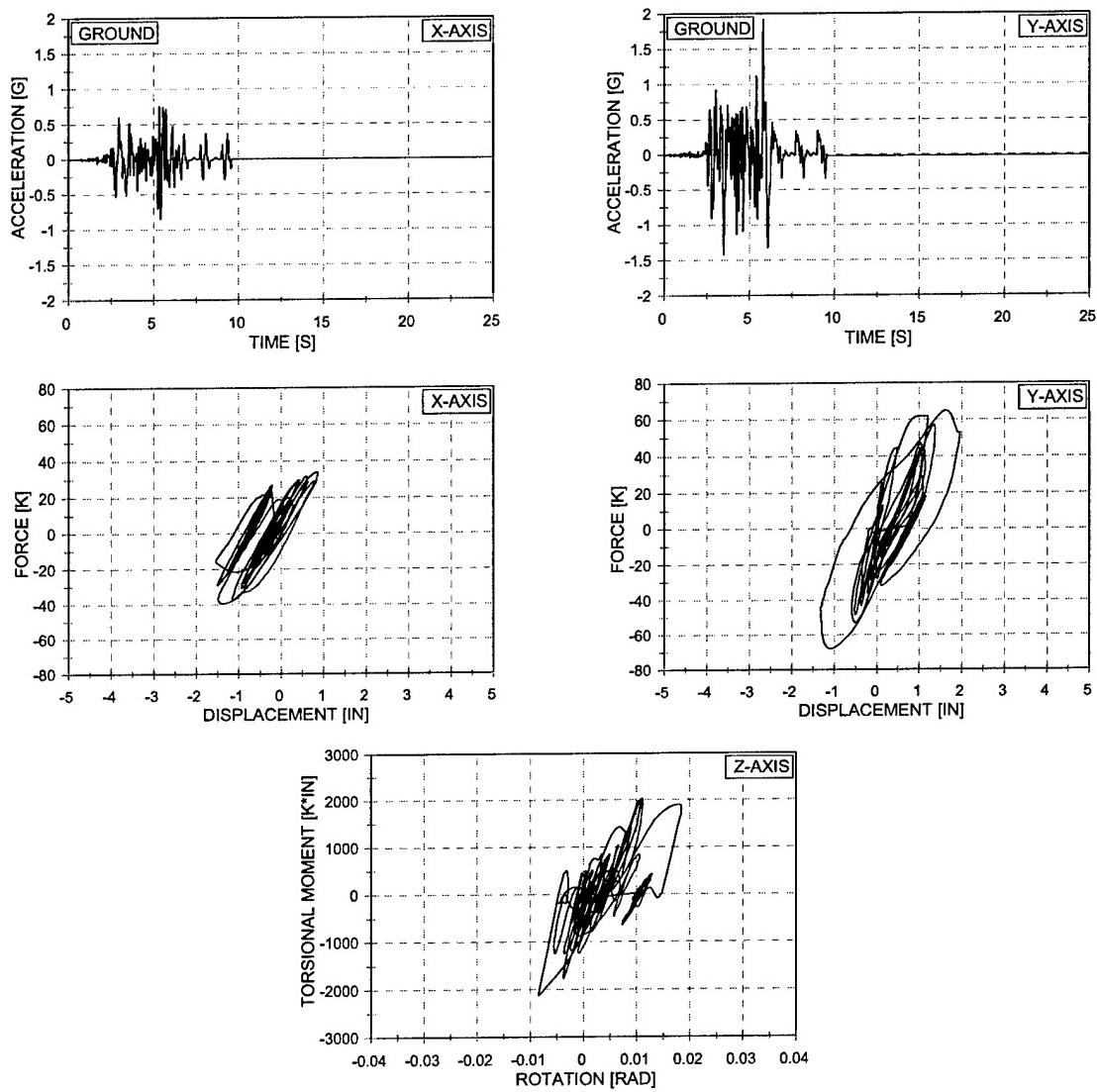


Figure 10.9 Force vs. Displacement and Torsional Moment vs. Rotation – EQ 39
 100% Biaxial Imperial Valley – 1/2 Asymmetric Mass – Concentric Bracing
 Four 4" Extra-Strong Columns

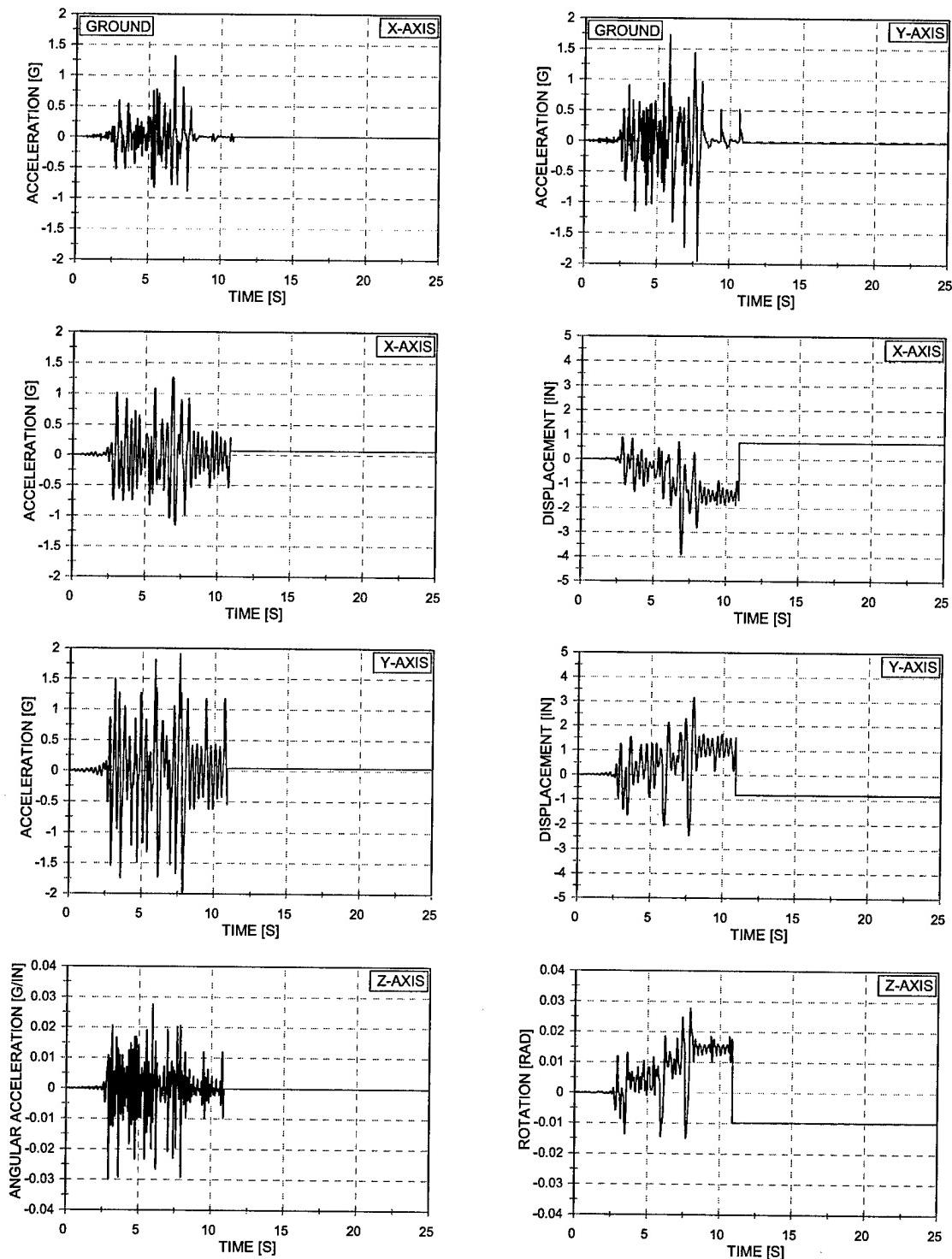


Figure 10.10 Acceleration and Displacement vs. Time – EQ 40
 100% X-Axis 90% Y-Axis Imperial Valley – 1/2 Asymmetric Mass – Concentric Bracing
 Four 4" Extra-Strong Columns

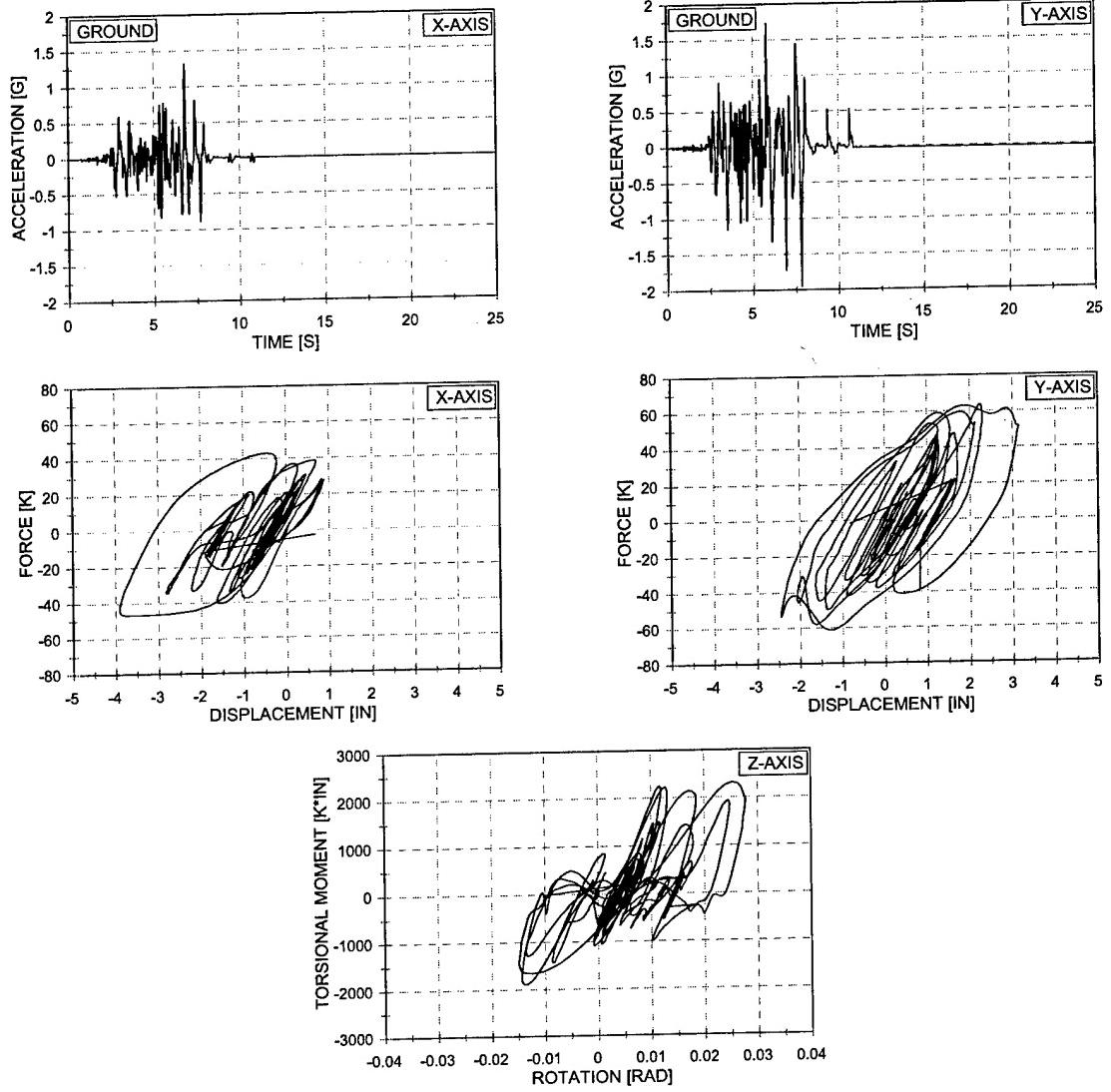


Figure 10.11 Force vs. Displacement and Torsional Moment vs. Rotation – EQ 40
 100% X-Axis 90% Y-Axis Imperial Valley – 1/2 Asymmetric Mass – Concentric Bracing
 Four 4" Extra-Strong Columns

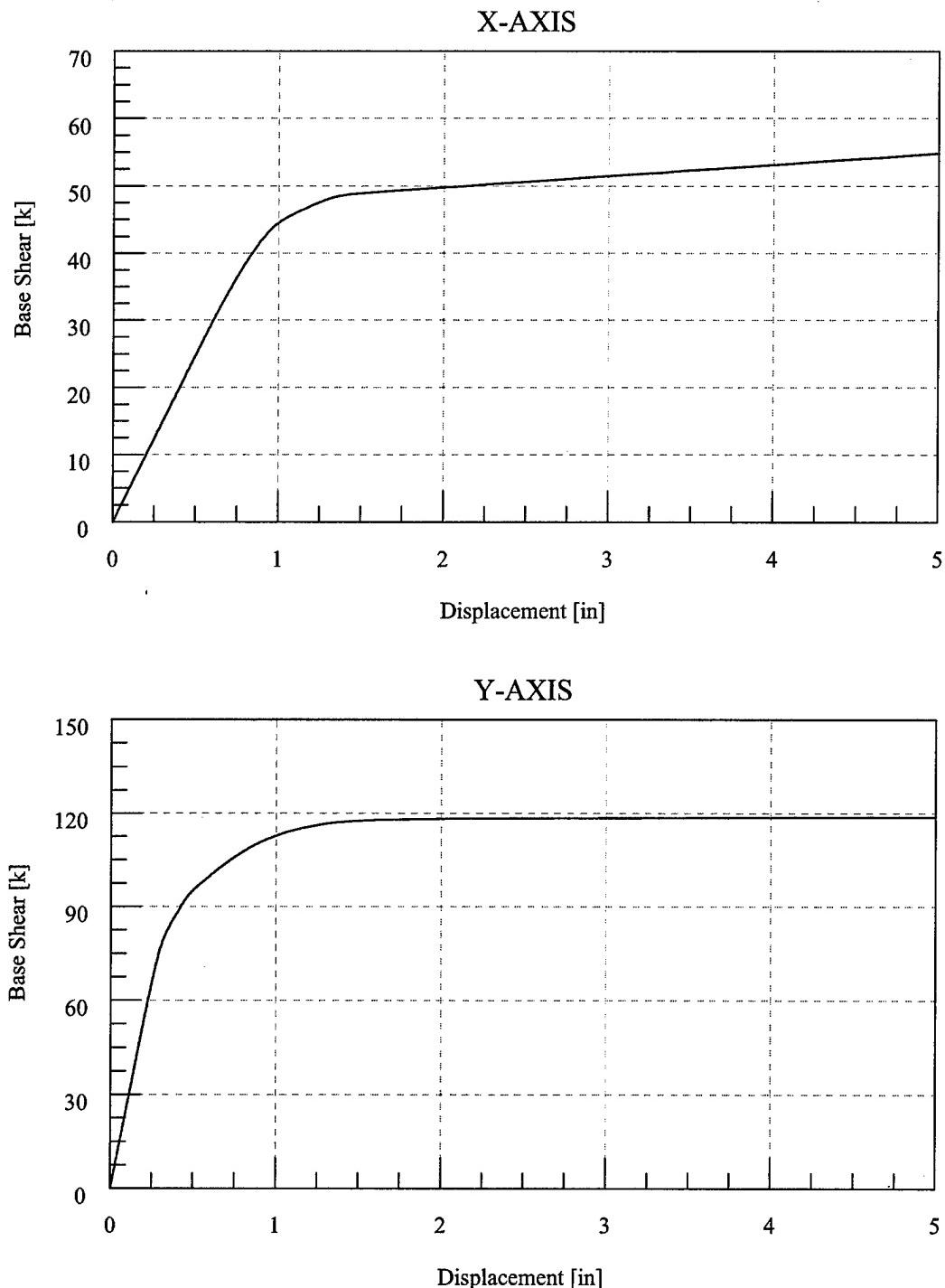


Figure 10.12 Force-Deformation Response – Test Configuration 6

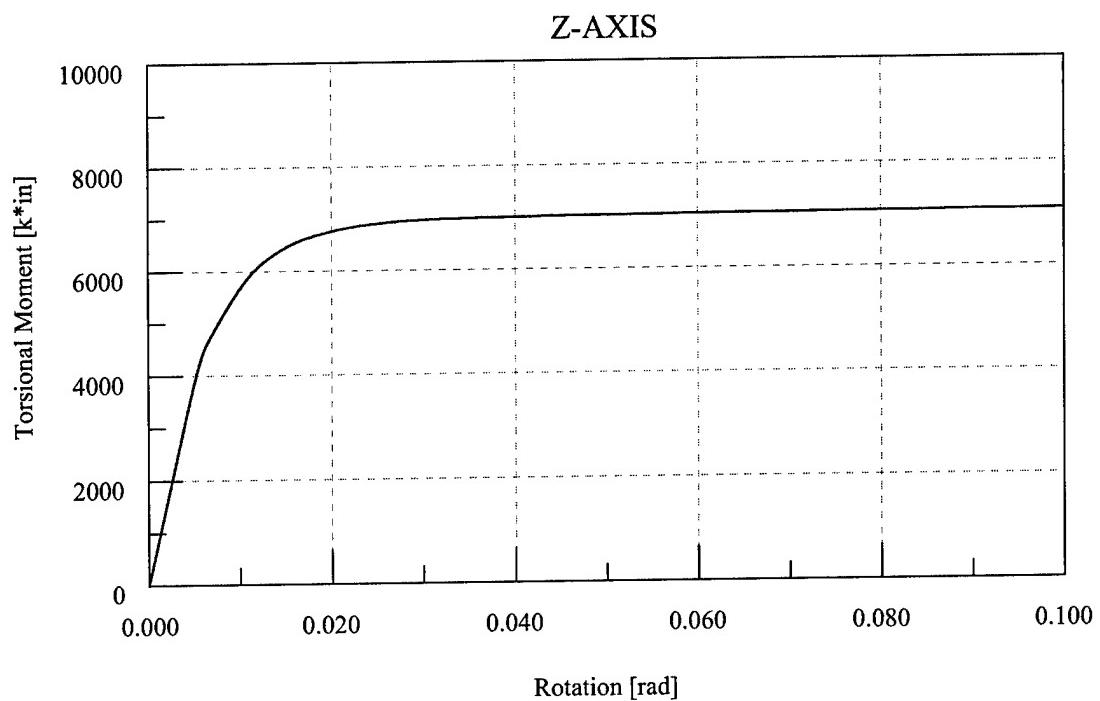


Figure 10.13 Torsional Moment-Rotation Response – Test Configuration 6

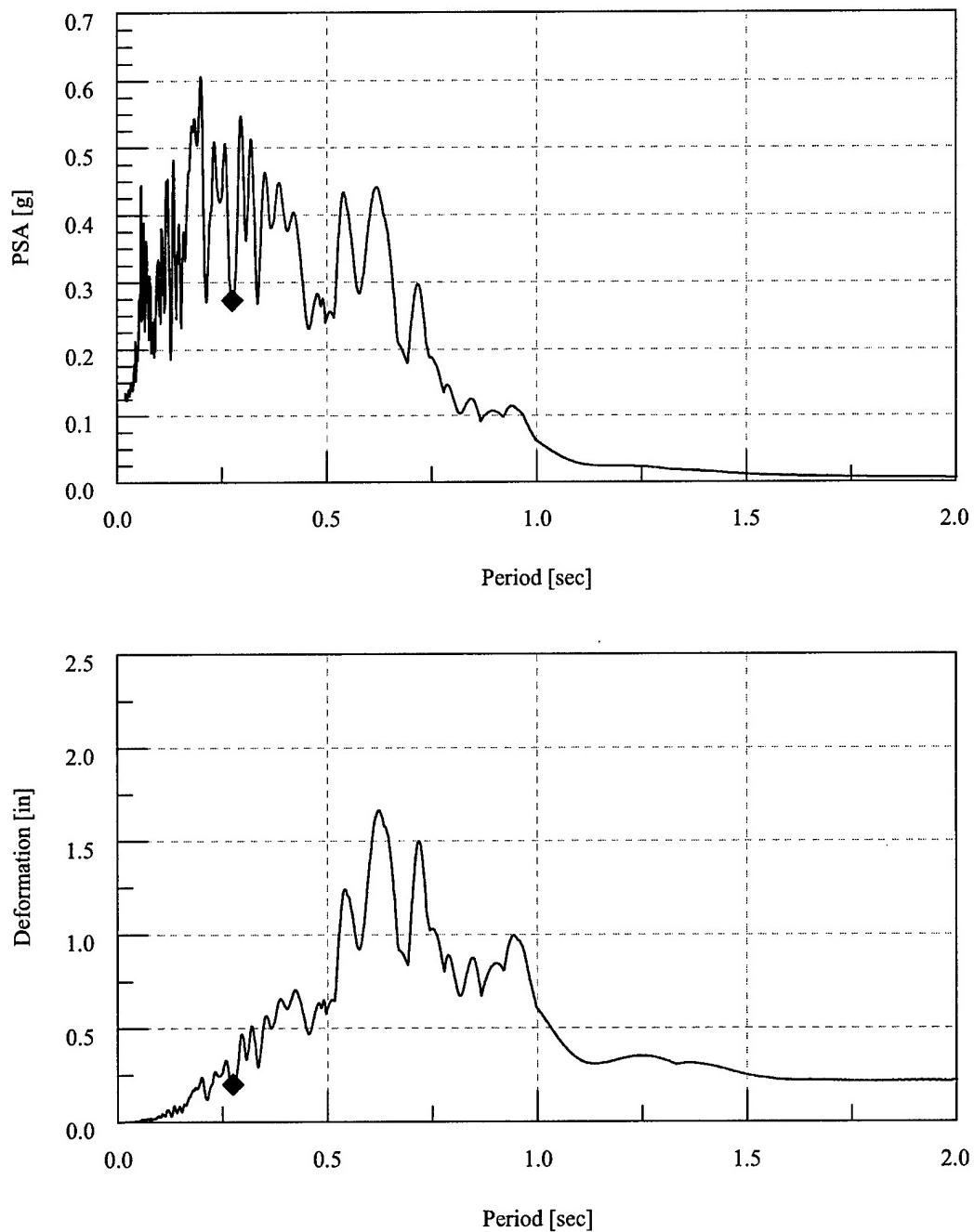


Figure 10.14 Elastic Response Spectra – EQ 37 – 10% X-Axis Imperial Valley Ground Motion

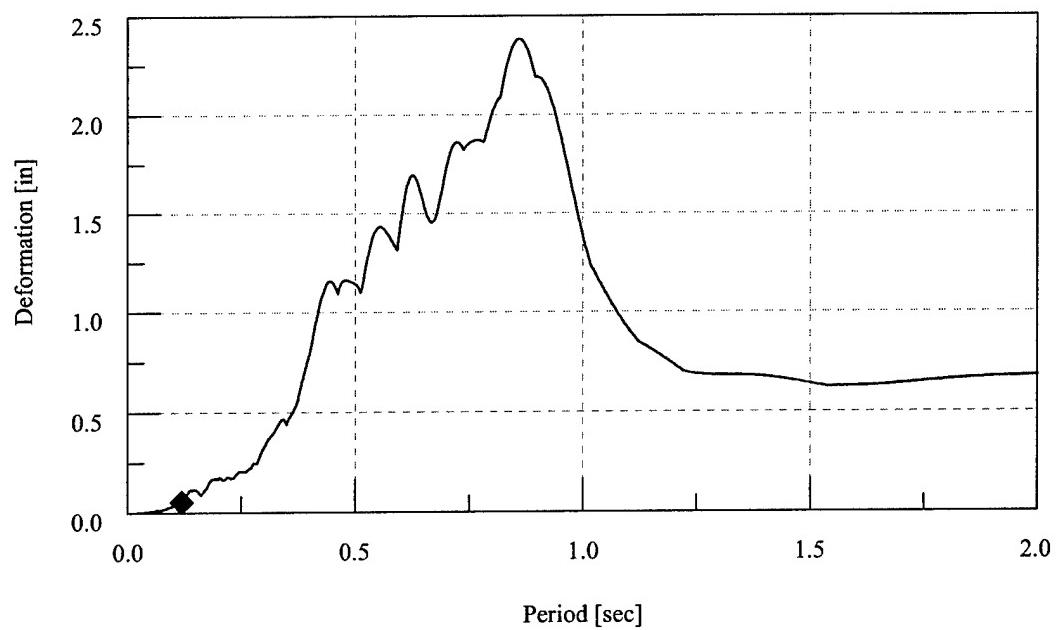
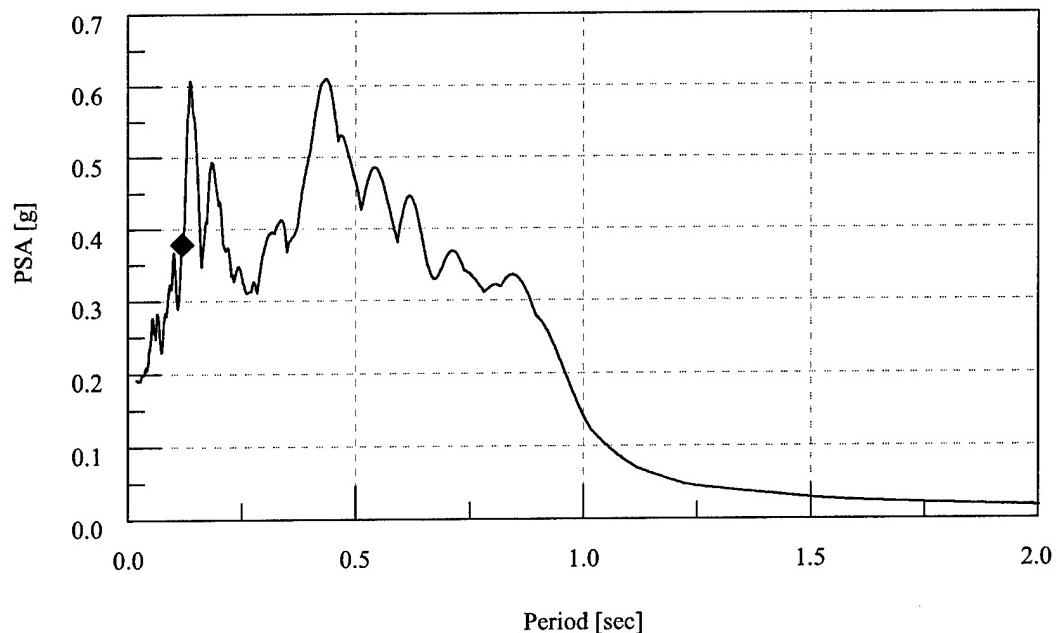


Figure 10.15 Elastic Response Spectra – EQ 38 – 10% Y-Axis Imperial Valley Ground Motion

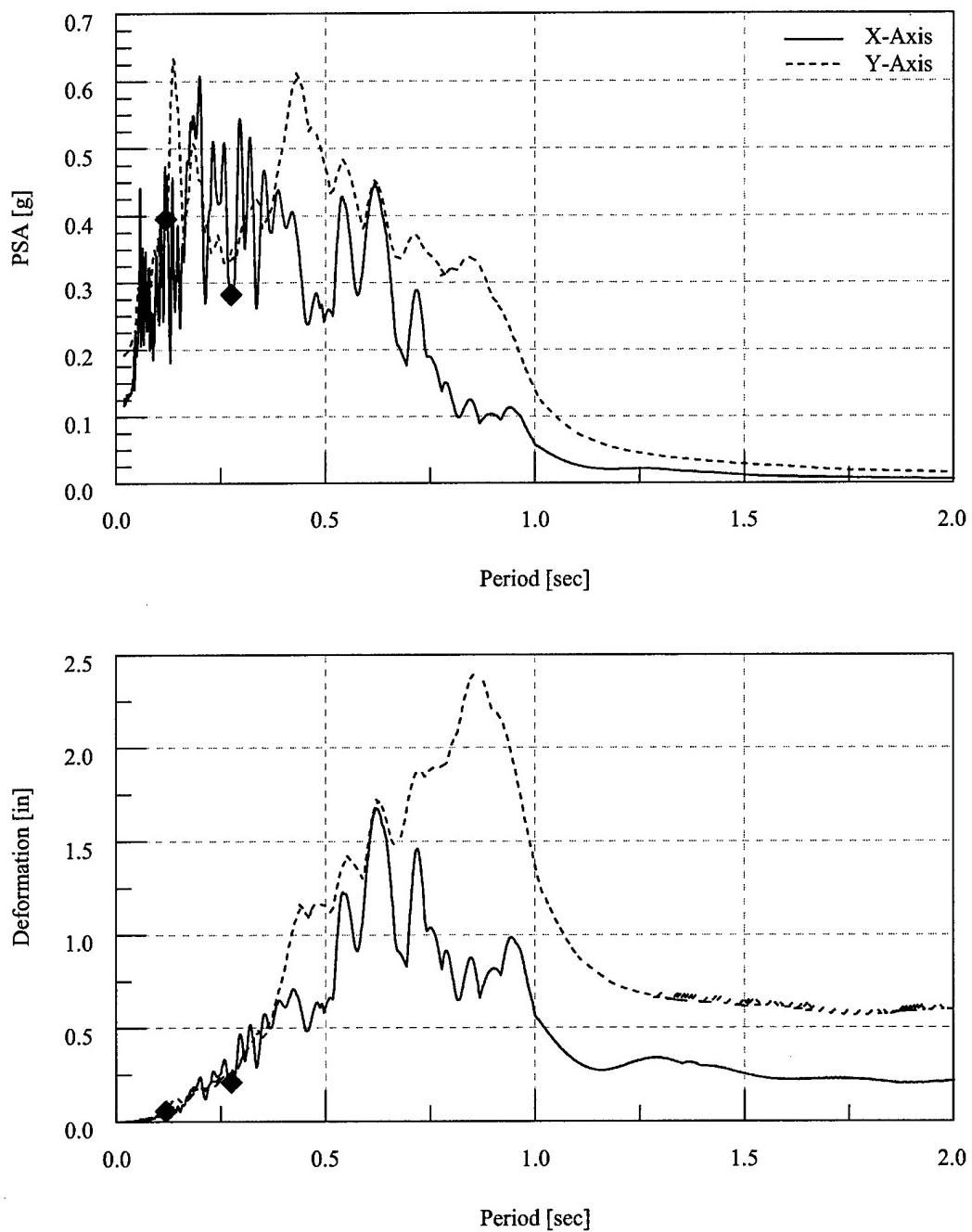


Figure 10.16 Elastic Response Spectra – EQ 36 – 10% Biaxial Imperial Valley Ground Motion

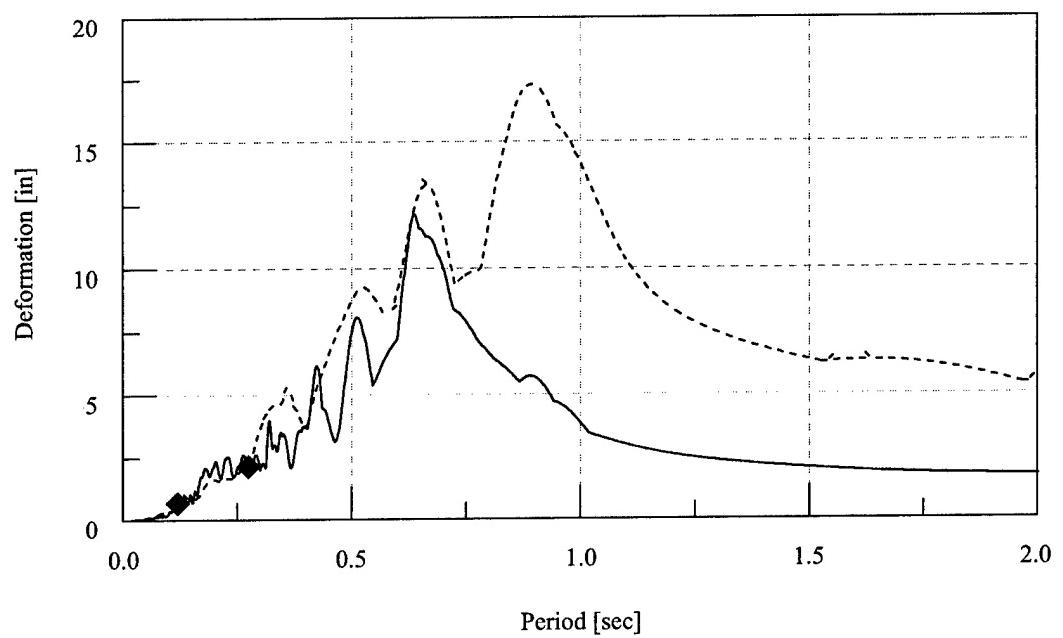
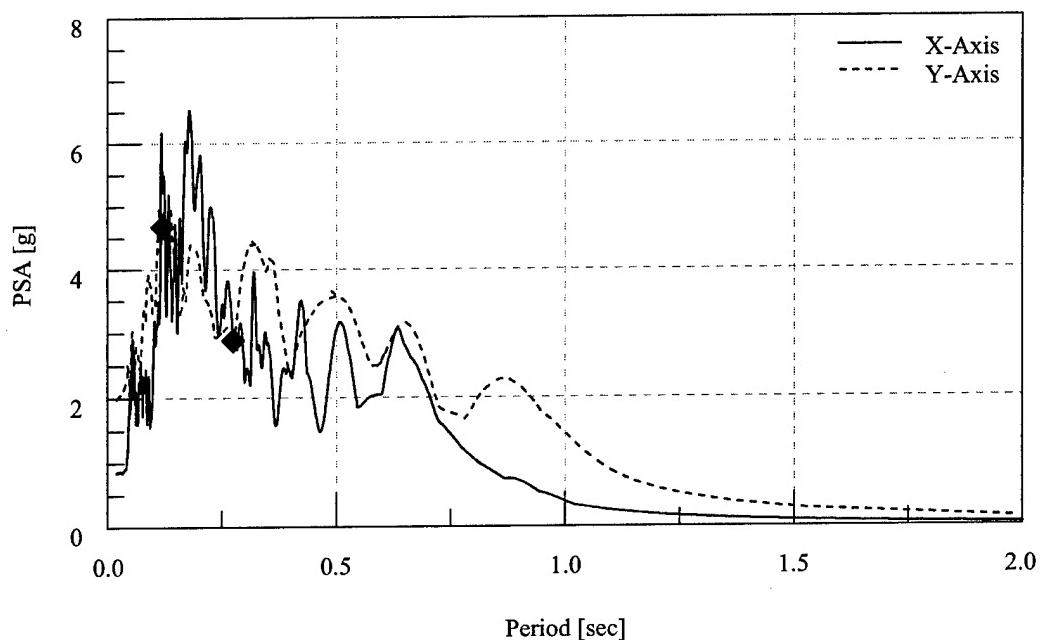


Figure 10.17 Elastic Response Spectra – EQ 39 – 100% Biaxial Imperial Valley Ground Motion

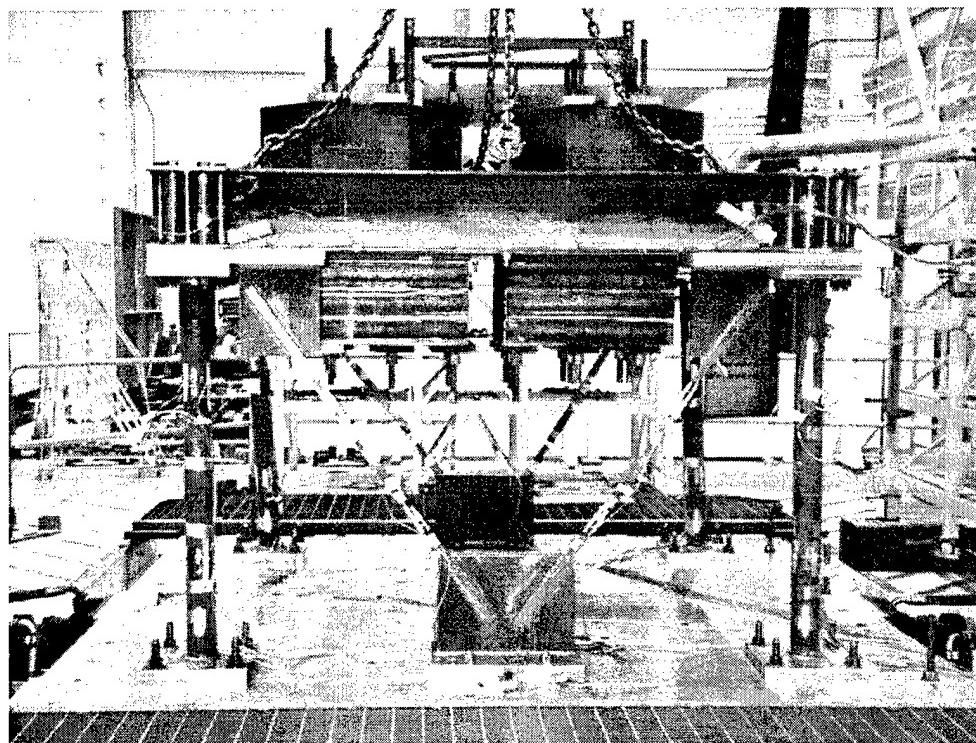


Figure 10.18 Test Structure prior to Earthquake Simulations

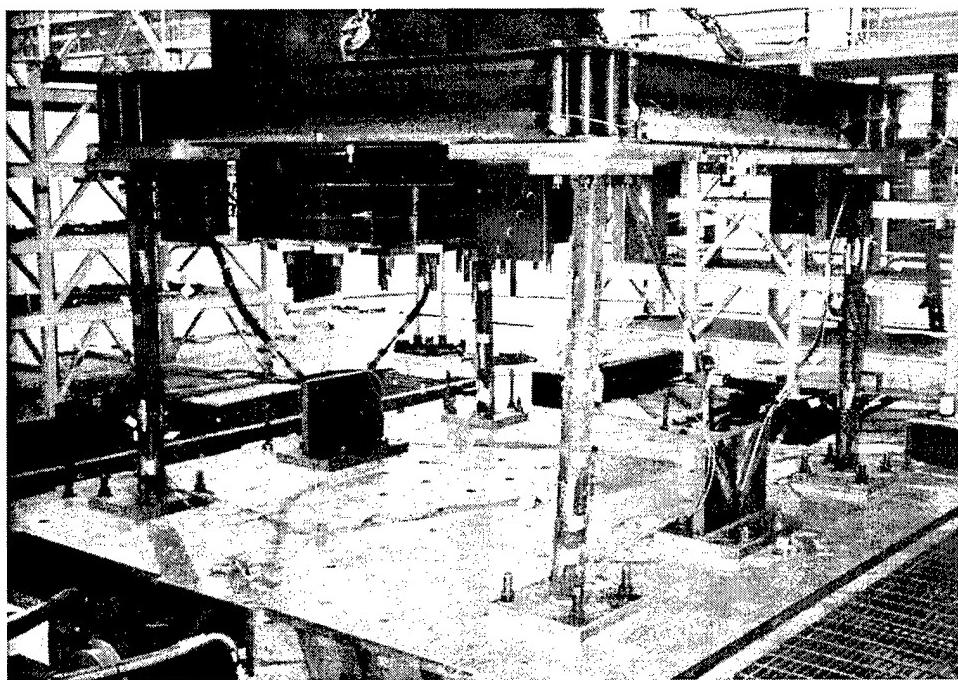


Figure 10.19 Test Structure after Earthquake Simulations

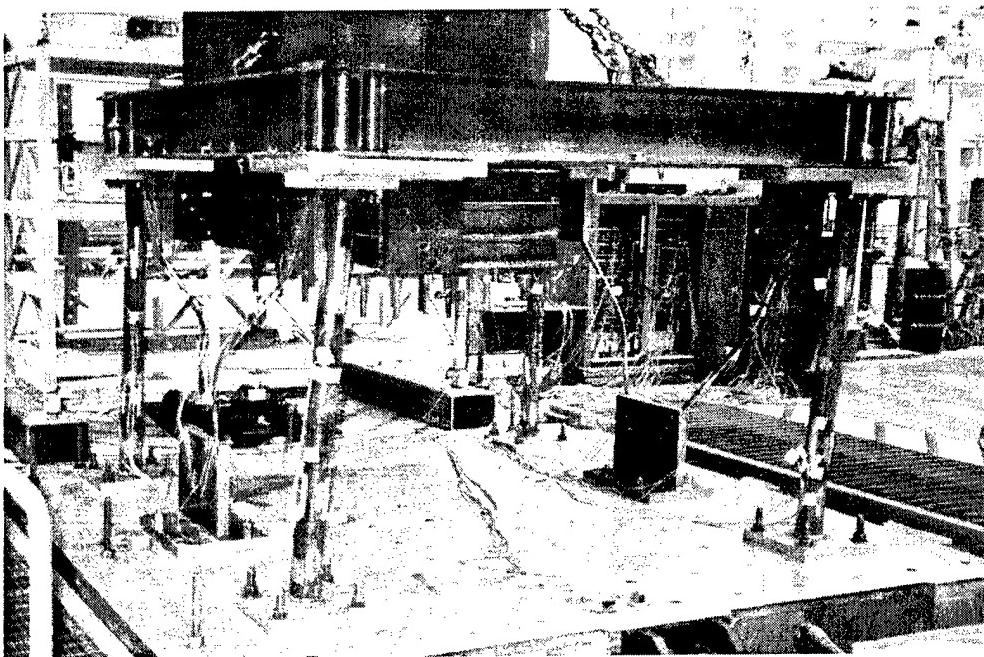


Figure 10.20 Test Structure after Earthquake Simulations

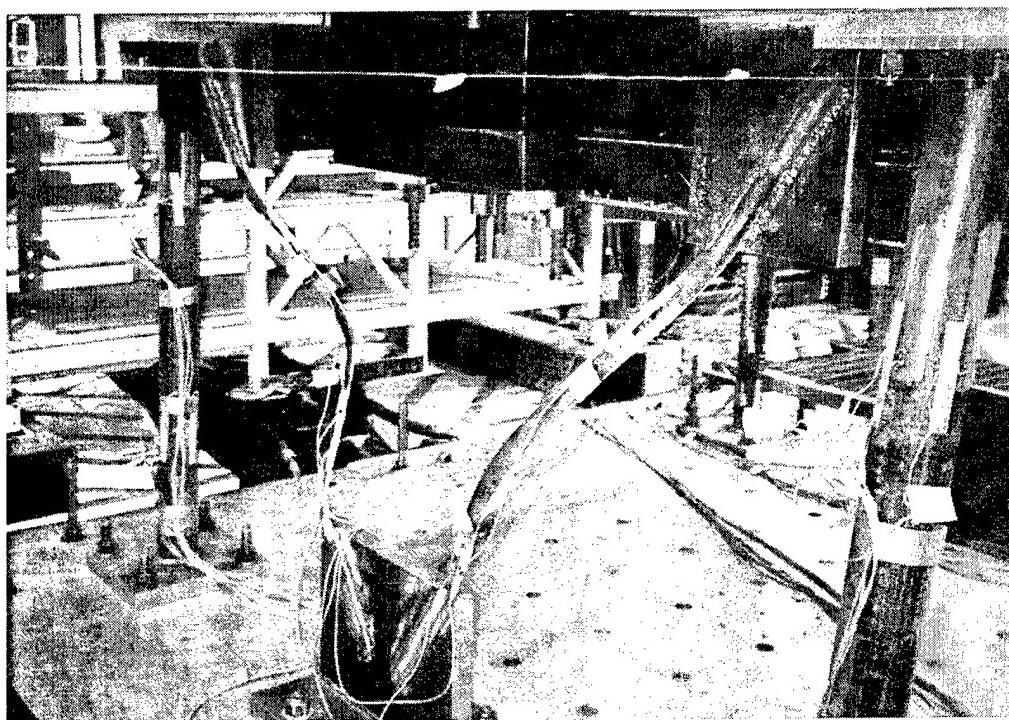


Figure 10.21 Test Structure after Earthquake Simulations

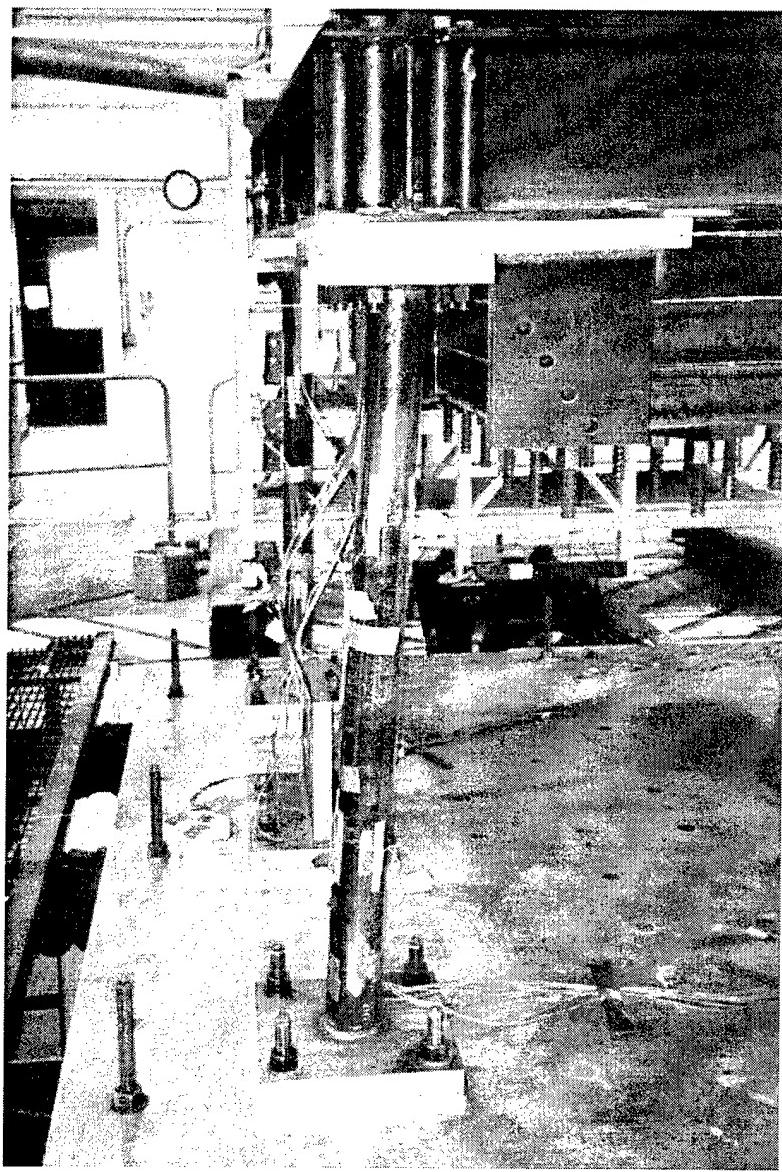


Figure 10.22 Test Structure Southeast Column After Earthquake Simulation

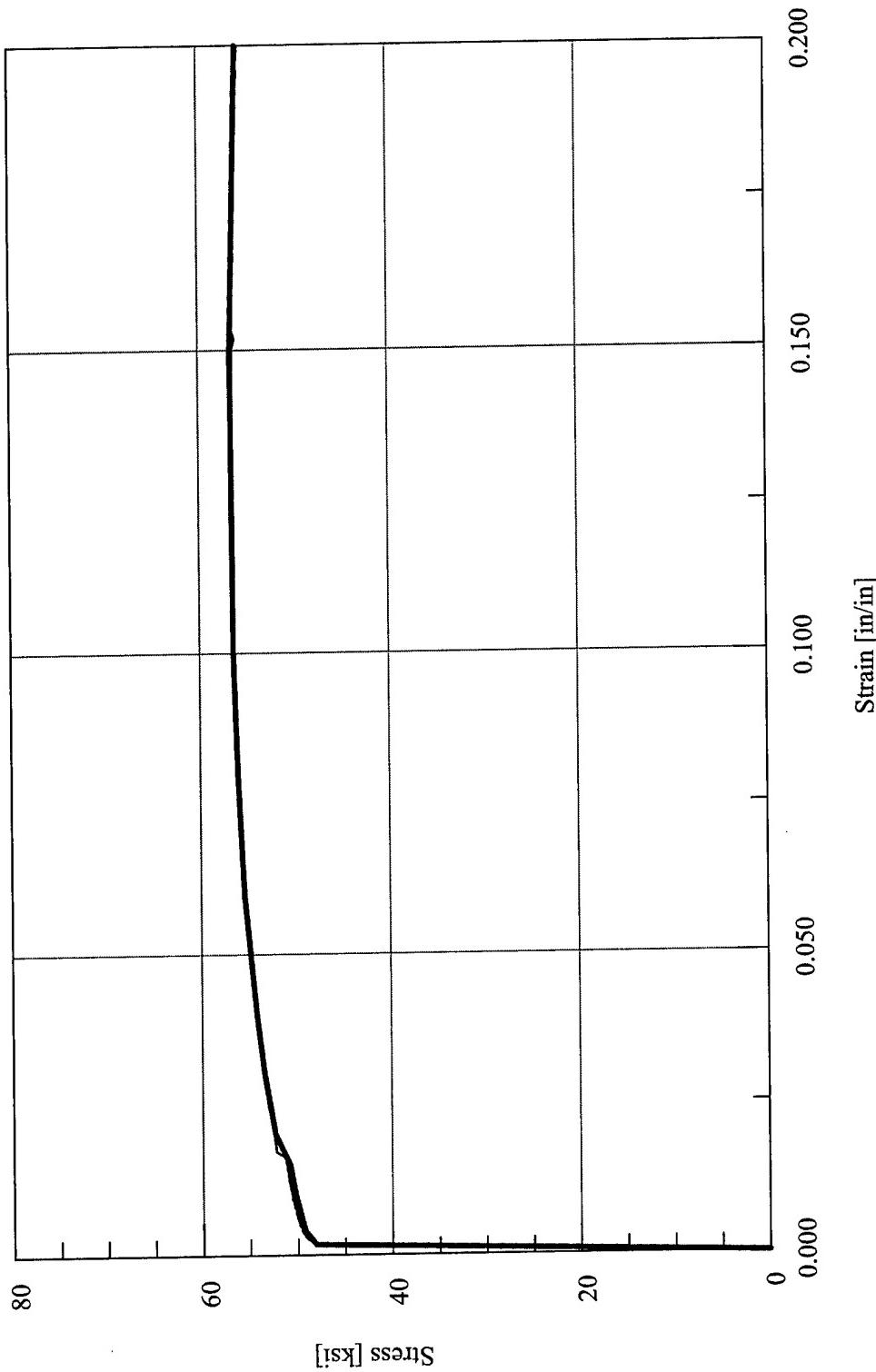


Figure 10.23 Abaqus Stress vs. Strain Analytical Material Model Definition – 4" Extra-Strong Columns – Test Configuration 6

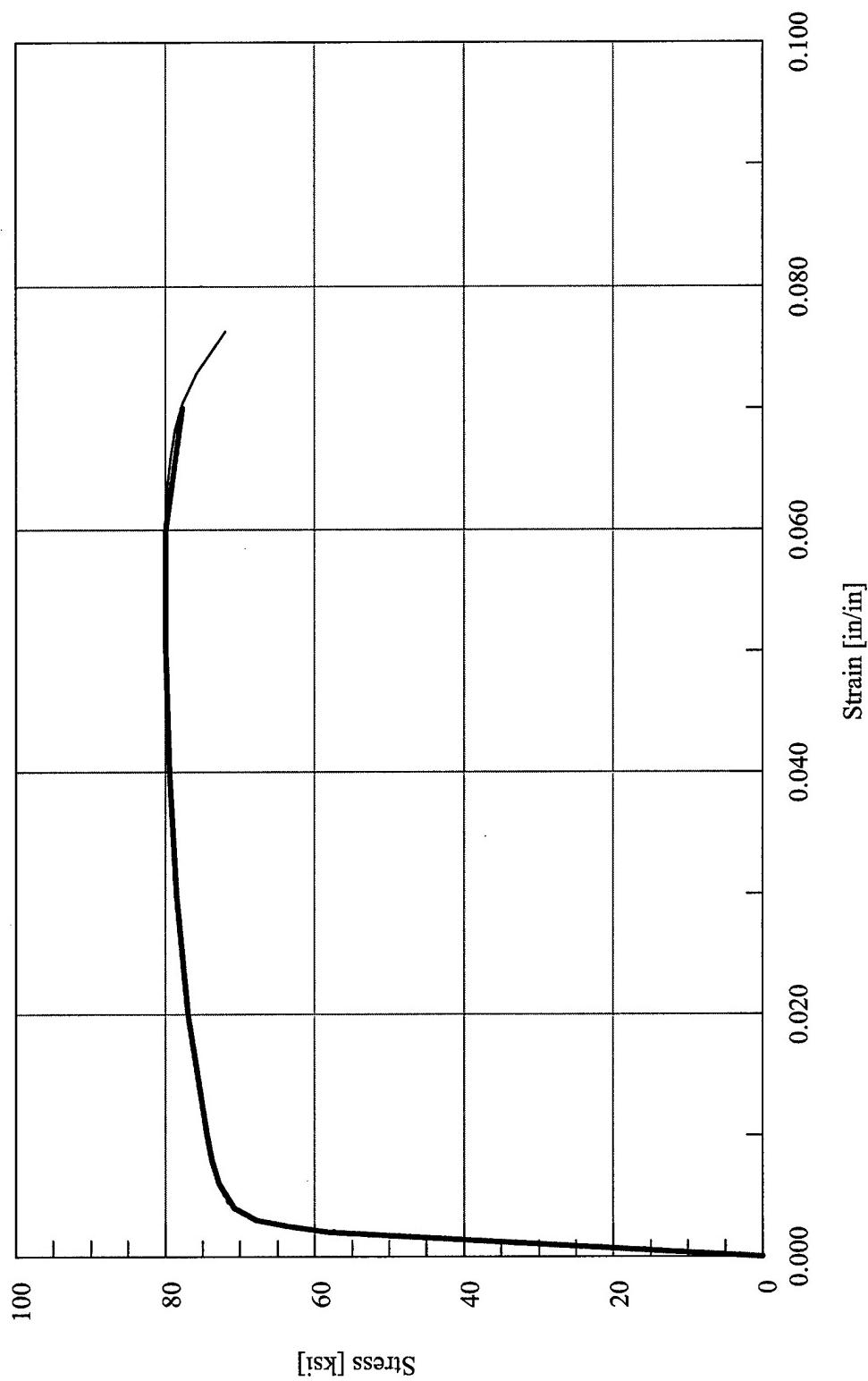


Figure 10.24 Abaqus Stress vs. Strain Analytical Material Model Definition – Diagonal Bracing – Test Configuration 6

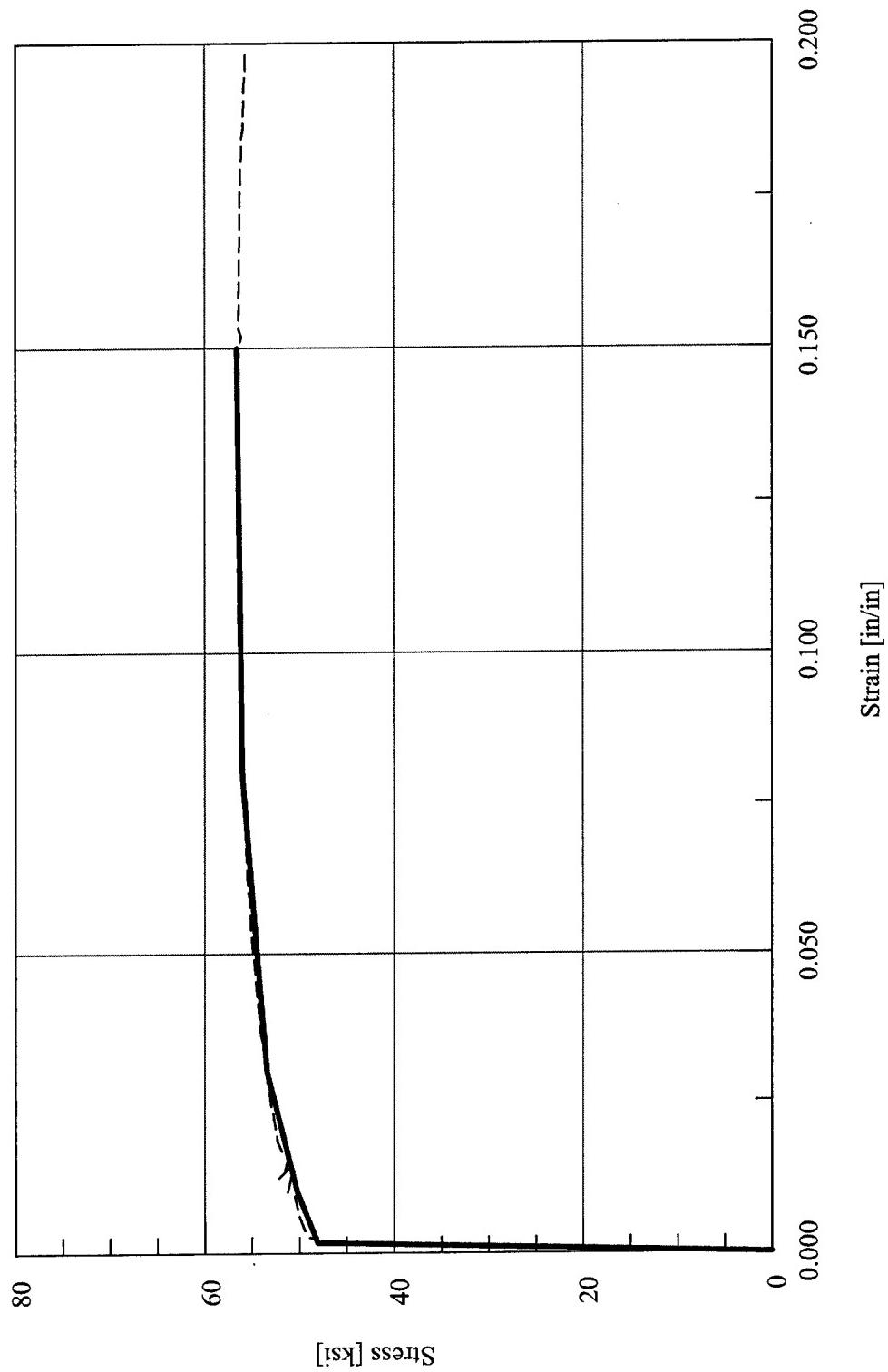


Figure 10.25 Drain-3DX Stress vs. Strain Analytical Material Model Definition – 4” Extra-Strong Columns – Test Configuration 6

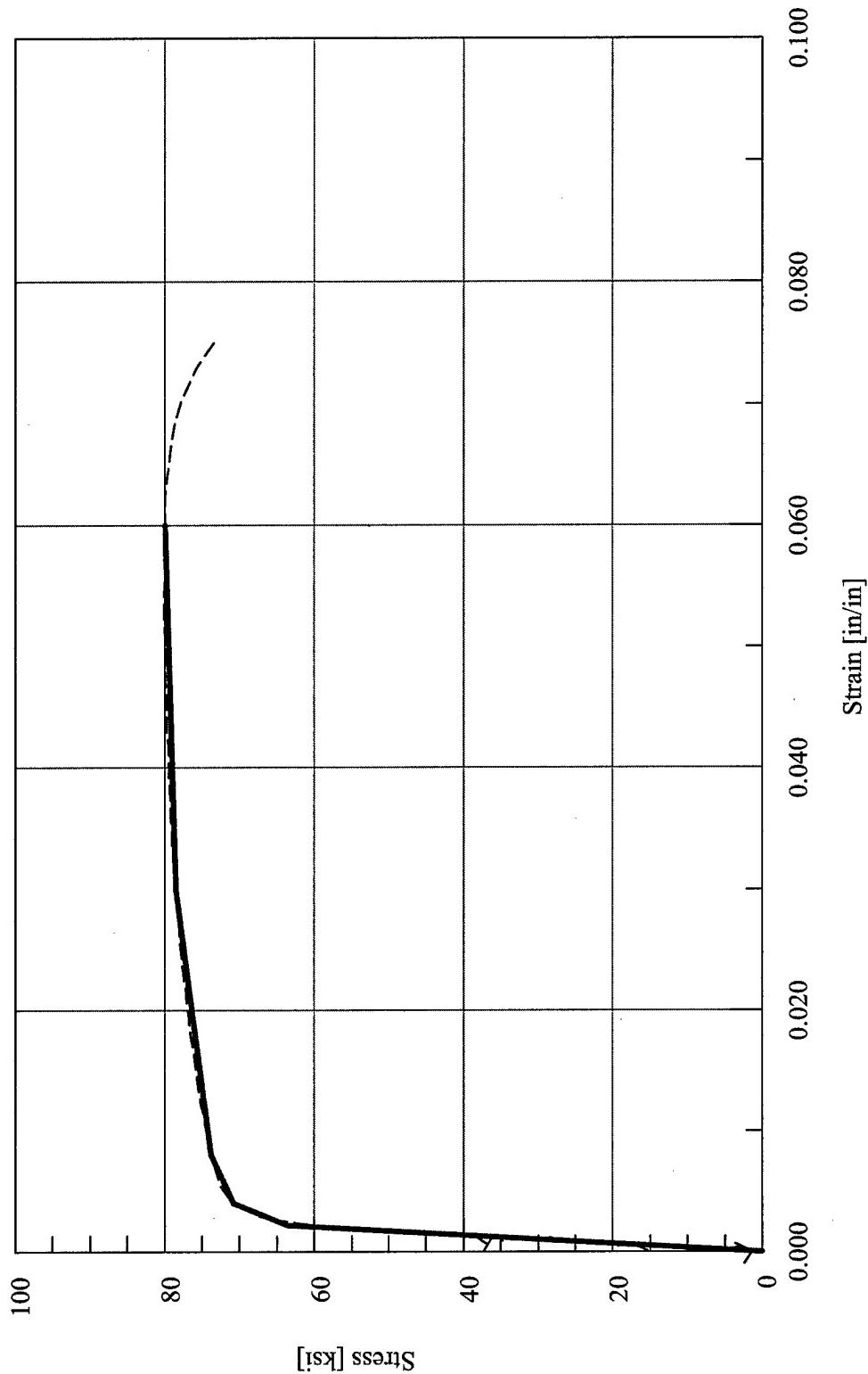


Figure 10.26 Drain-3DX Stress vs. Strain Analytical Material Model Definition – Diagonal Bracing – Test Configuration 6

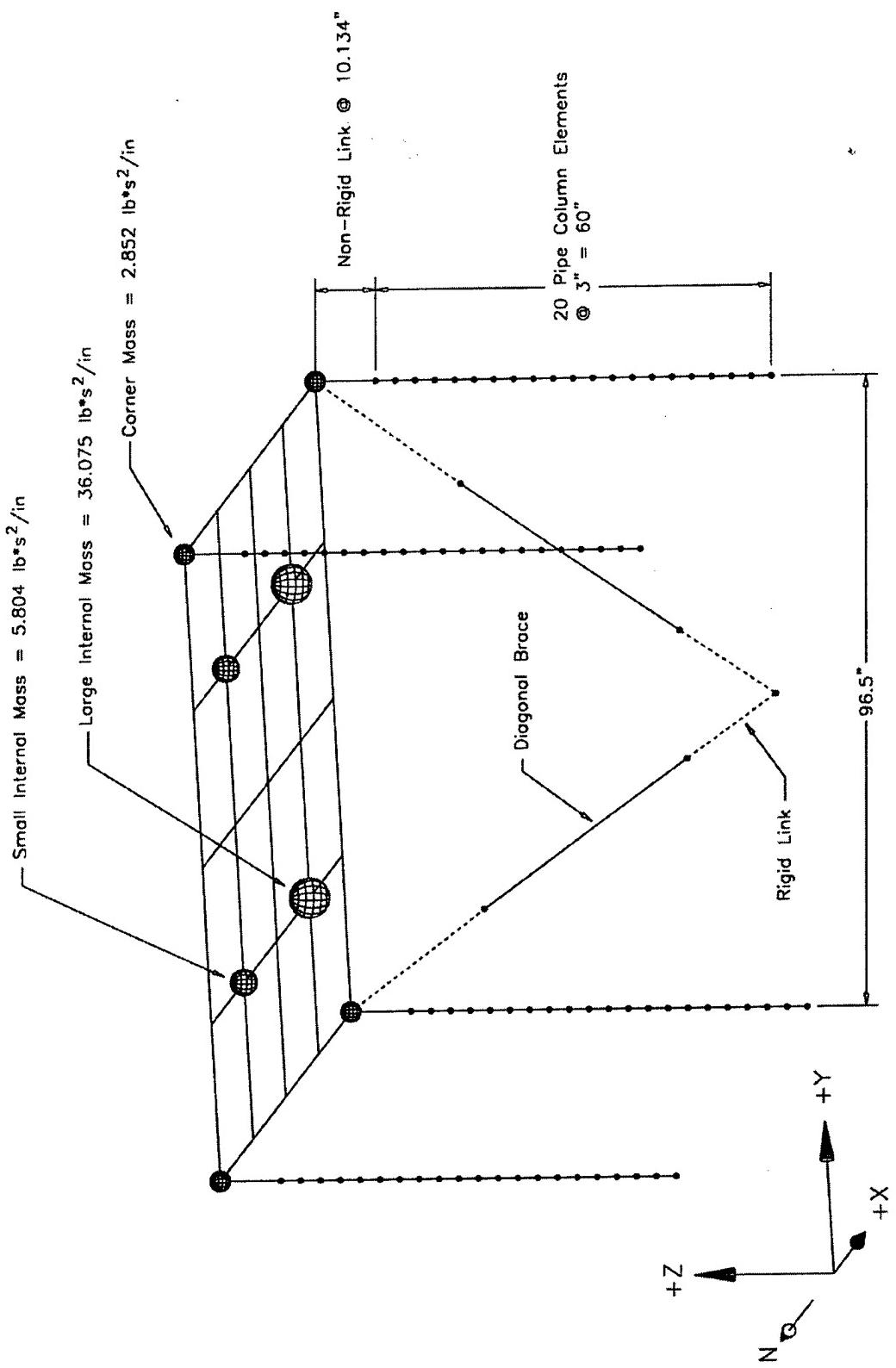


Figure 10.27 Abaqus Finite Element Model for Test Configuration 6

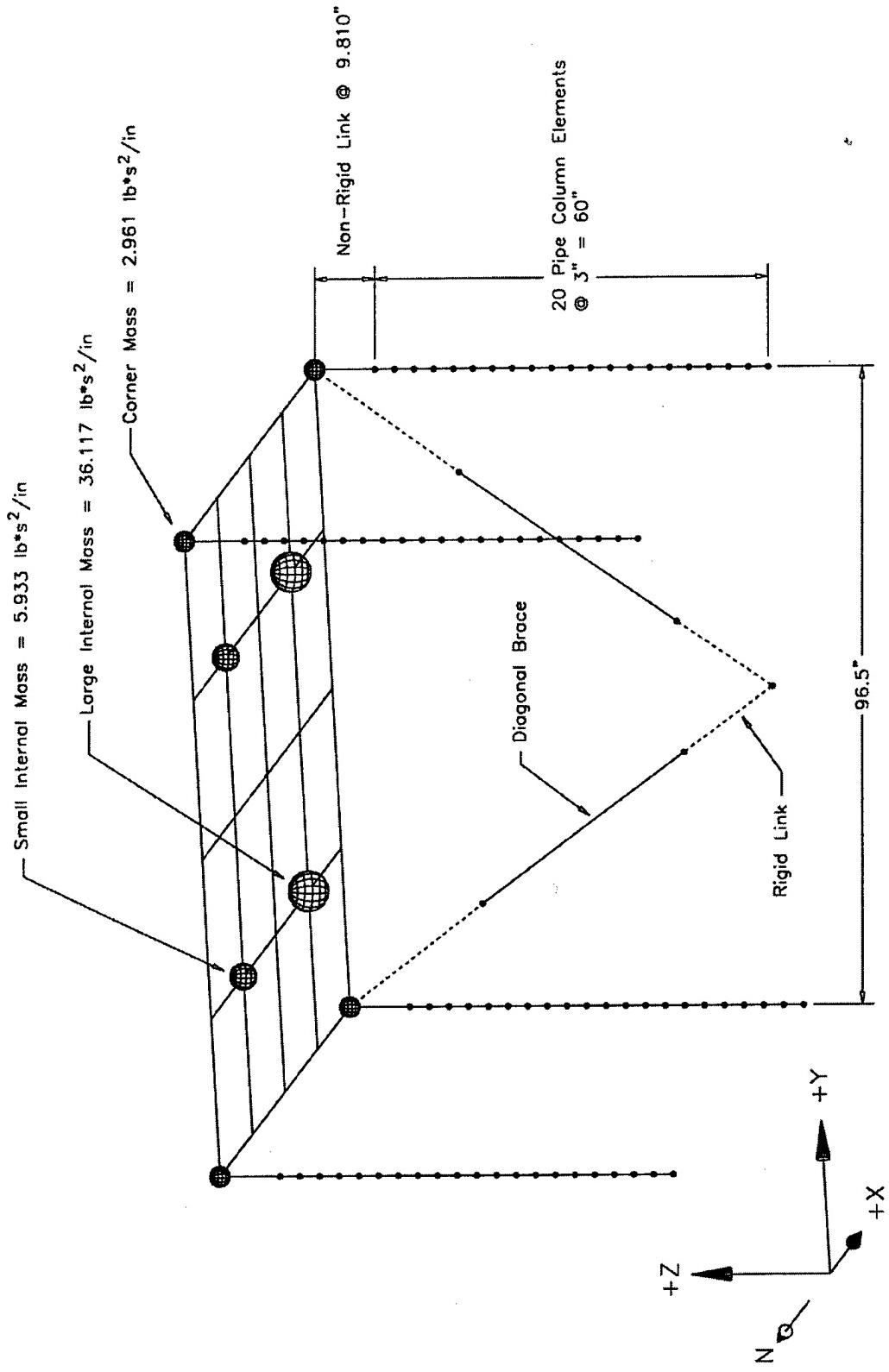


Figure 10.28 Drain-3DX Finite Element Model for Test Configuration 6

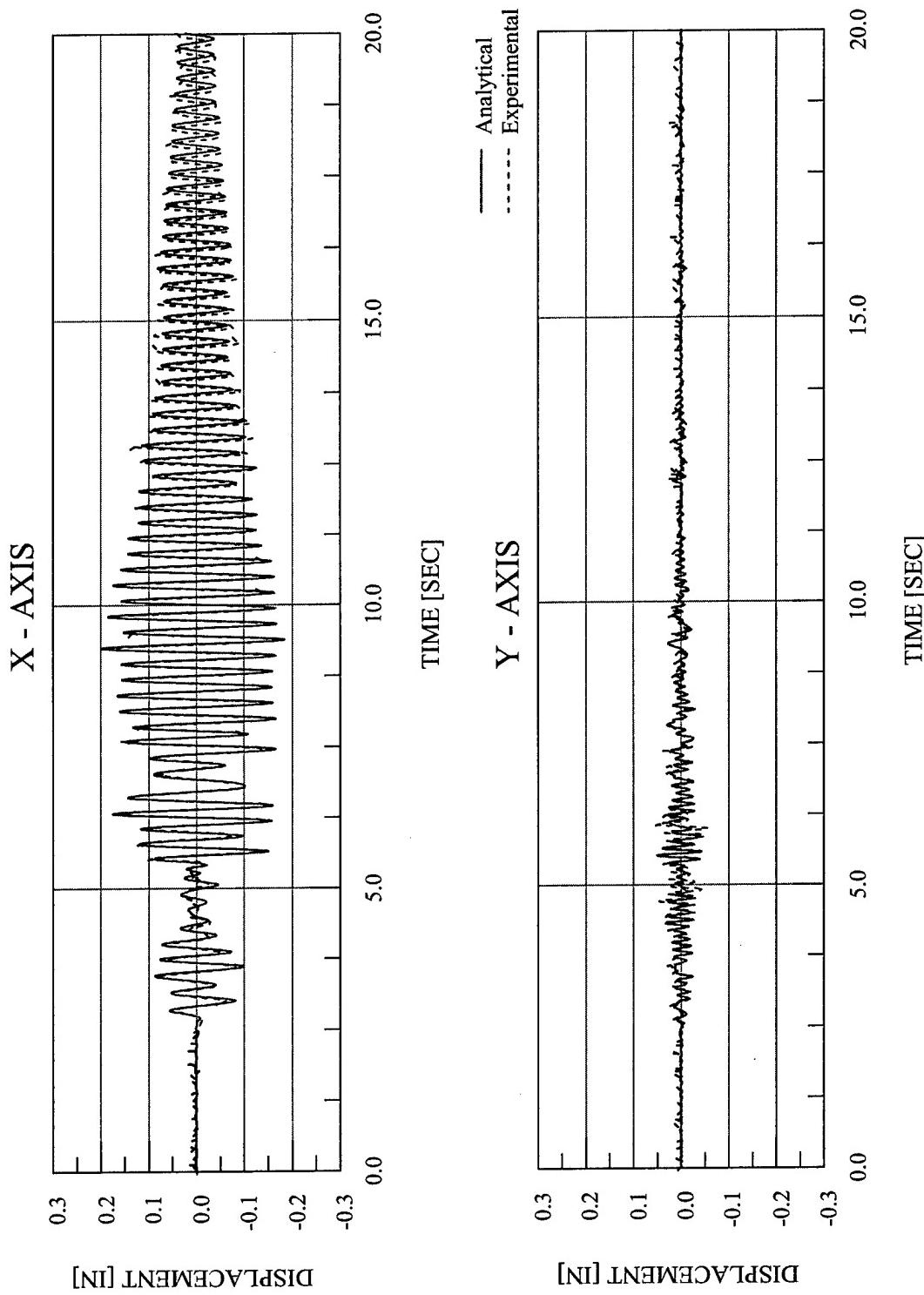


Figure 10.29 Abaqus Analytical Displacement vs. Time – EQ 36 – 10% Biaxial Imperial Valley

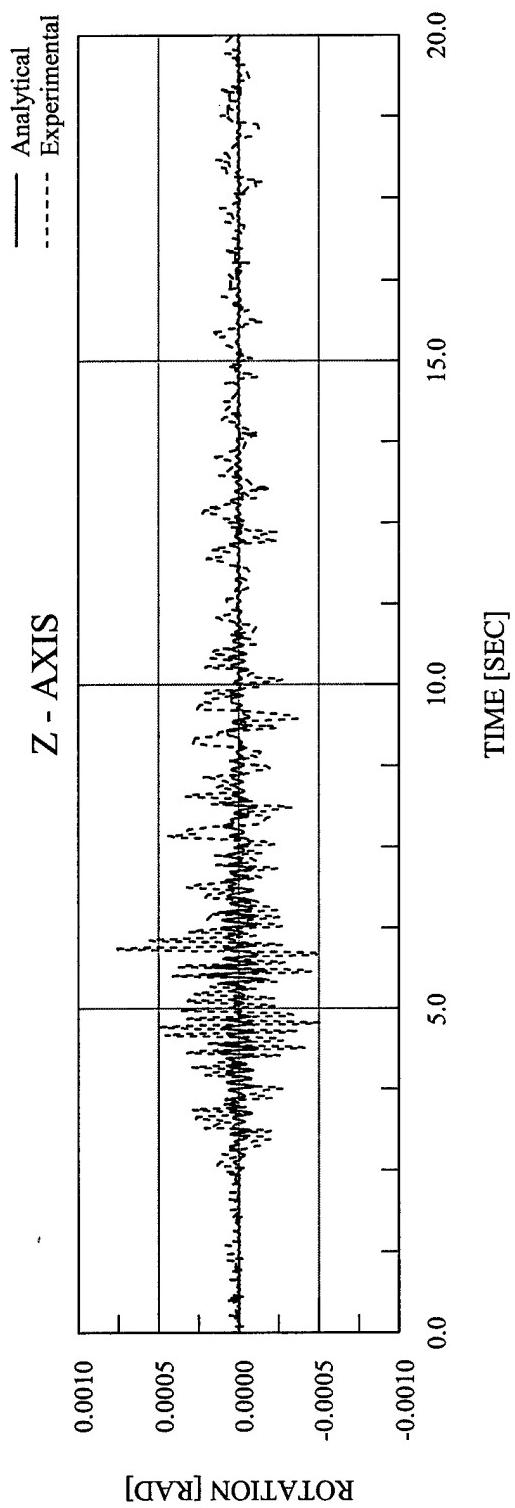


Figure 10.30 Abaqus Analytical Rotation vs. Time – EQ 36 – 10% Biaxial Imperial Valley

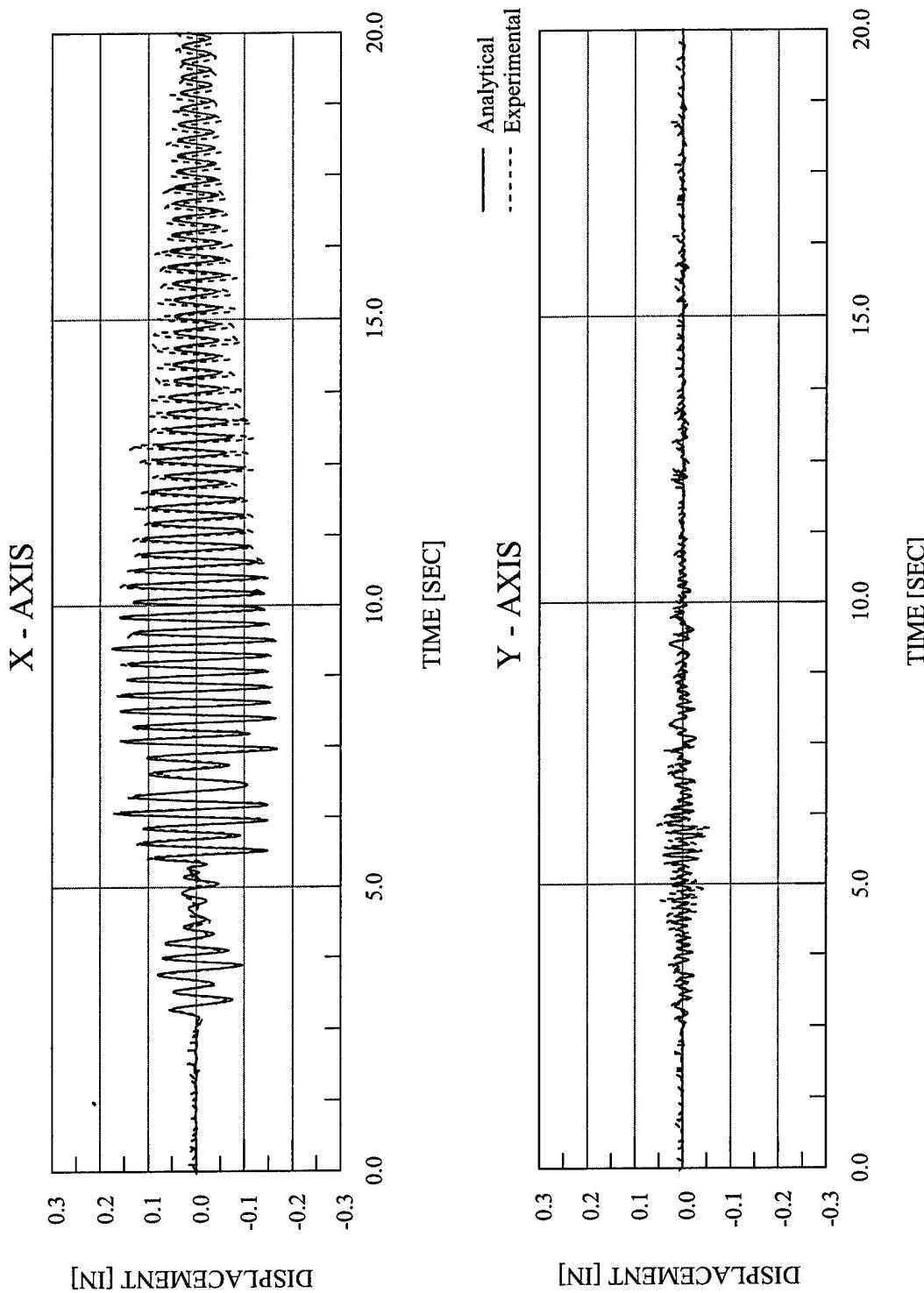


Figure 10.31 Drain-3DX Analytical Displacement vs. Time – EQ 36 – 10% Biaxial Imperial Valley

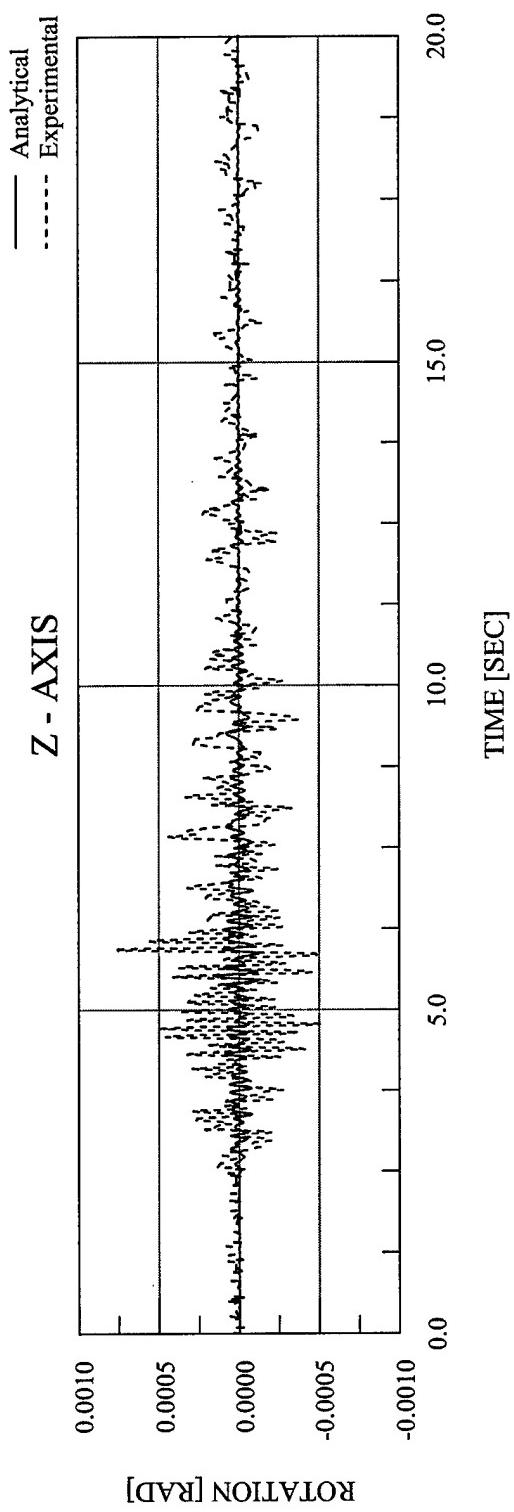


Figure 10.32 Drain-3DX Analytical Rotation vs. Time – EQ 36 – 10% Biaxial Imperial Valley

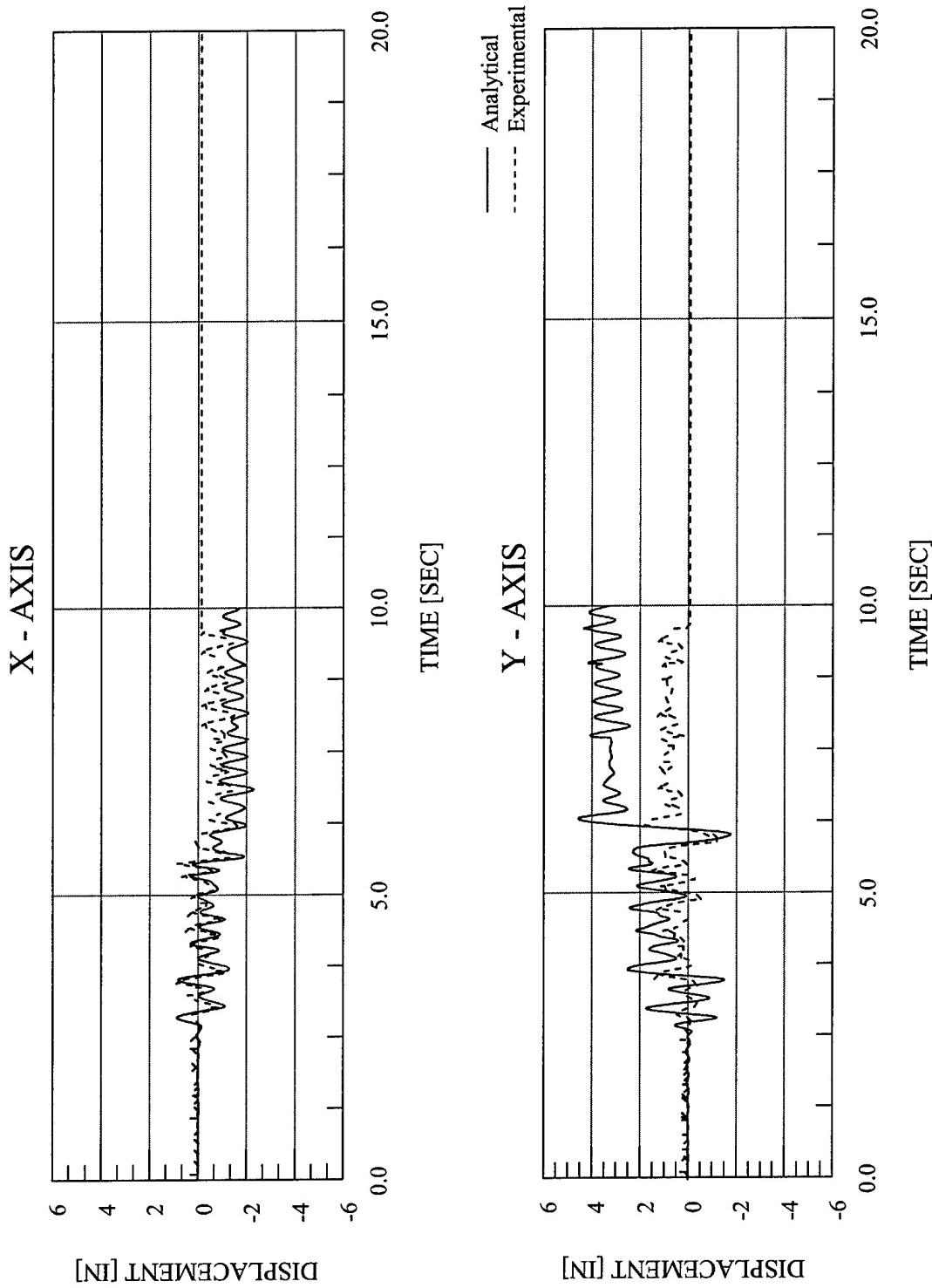


Figure 10.33 Abaqus Analytical Displacement vs. Time – EQ 39 – 100% Biaxial Imperial Valley

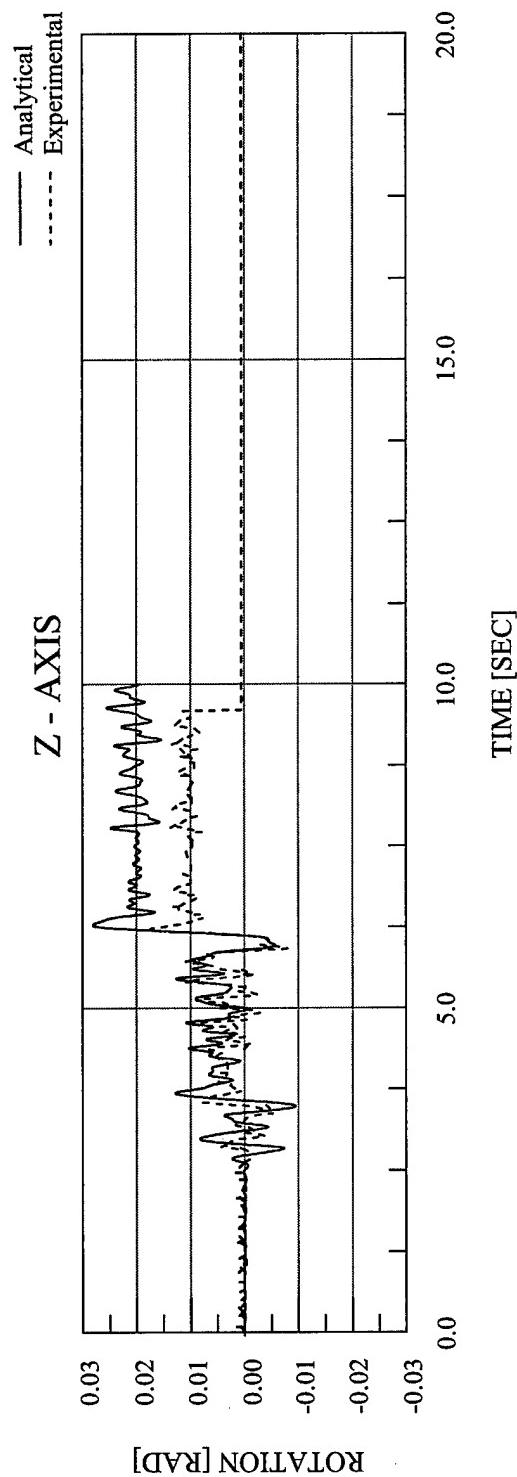


Figure 10.34 Abaqus Analytical Rotation vs. Time – EQ 39 – 100% Biaxial Imperial Valley

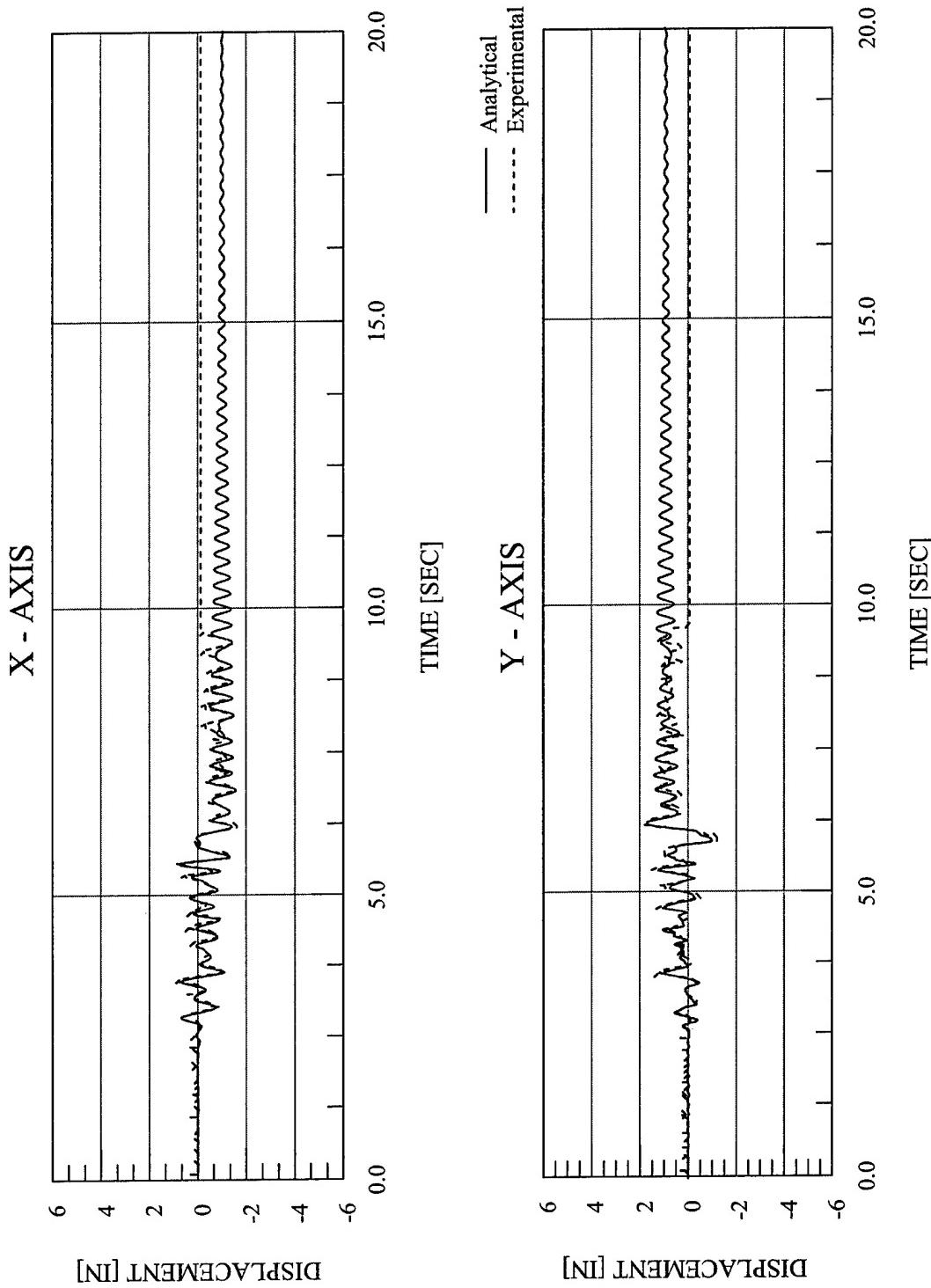
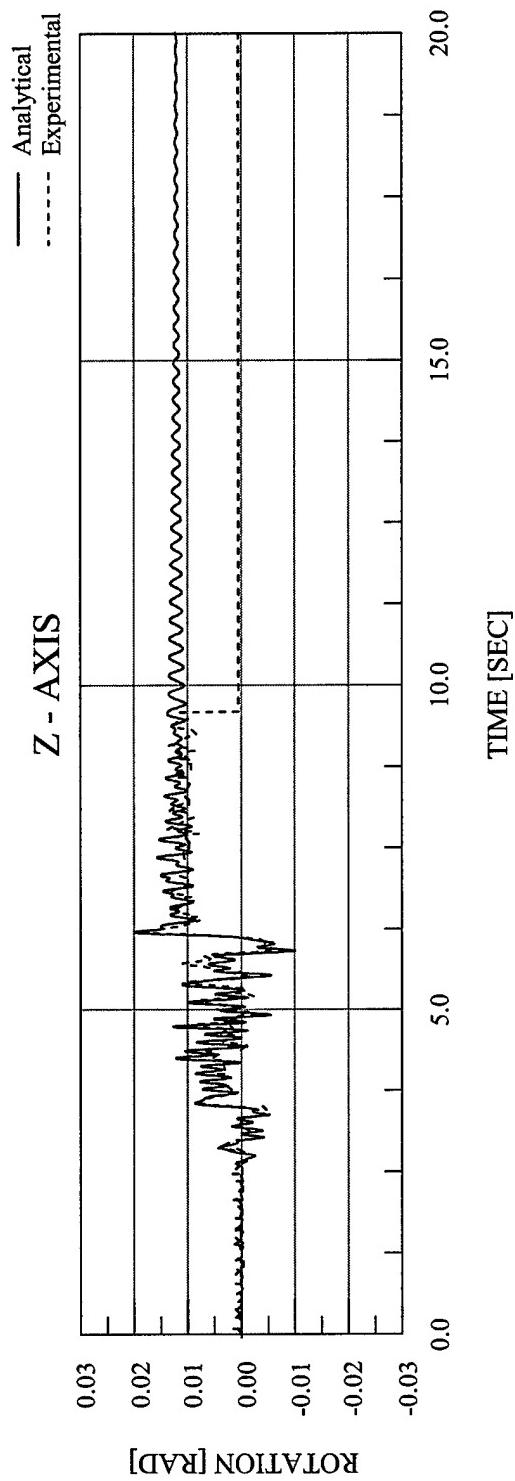


Figure 10.35 Drain-3DX Analytical Displacement vs. Time – EQ 39 – 100% Biaxial Imperial Valley



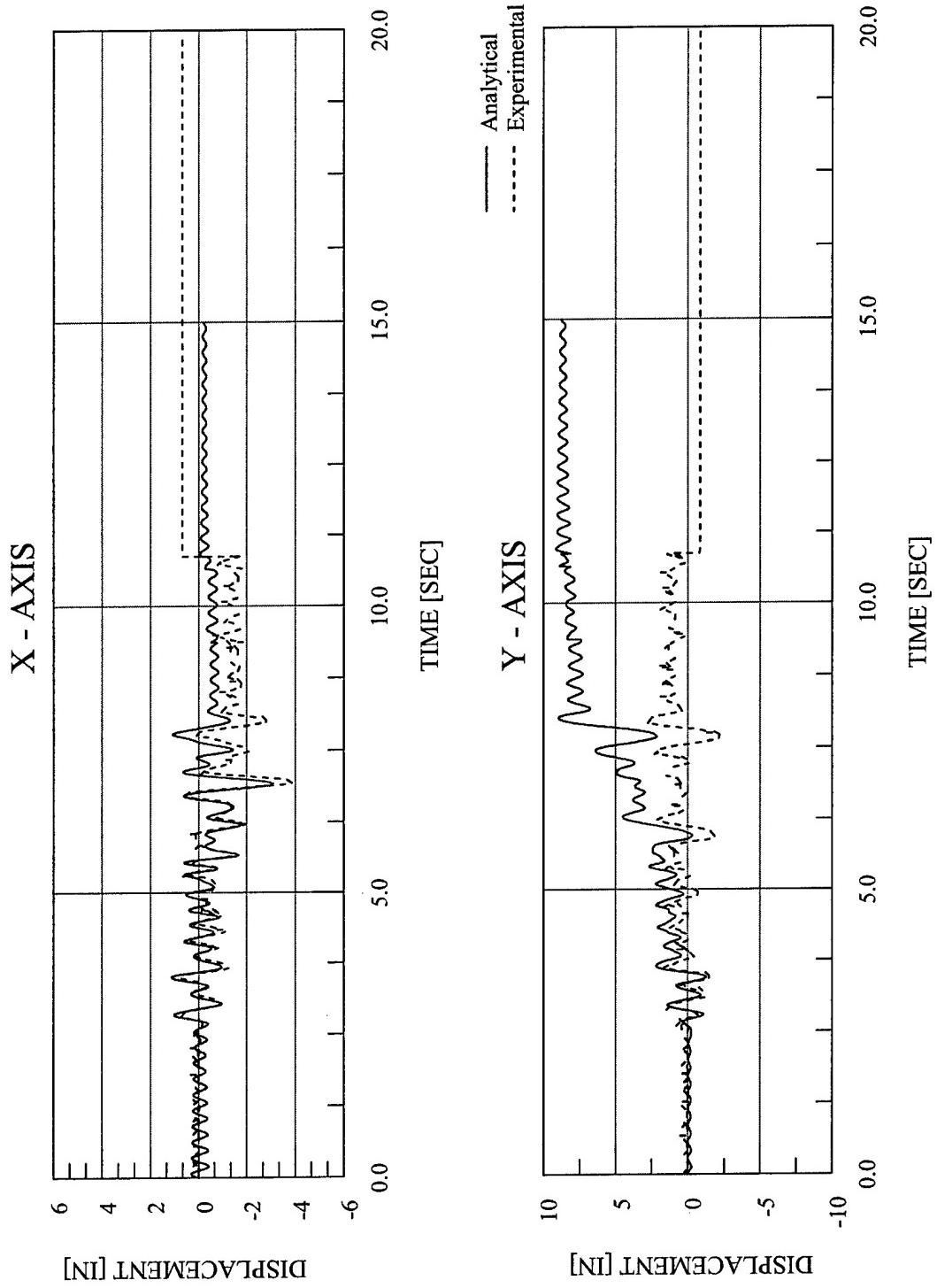


Figure 10.37 Abaqus Analytical Displacement vs. Time – EQ 40 – 100% X-Axis 90% Y-Axis Imperial Valley

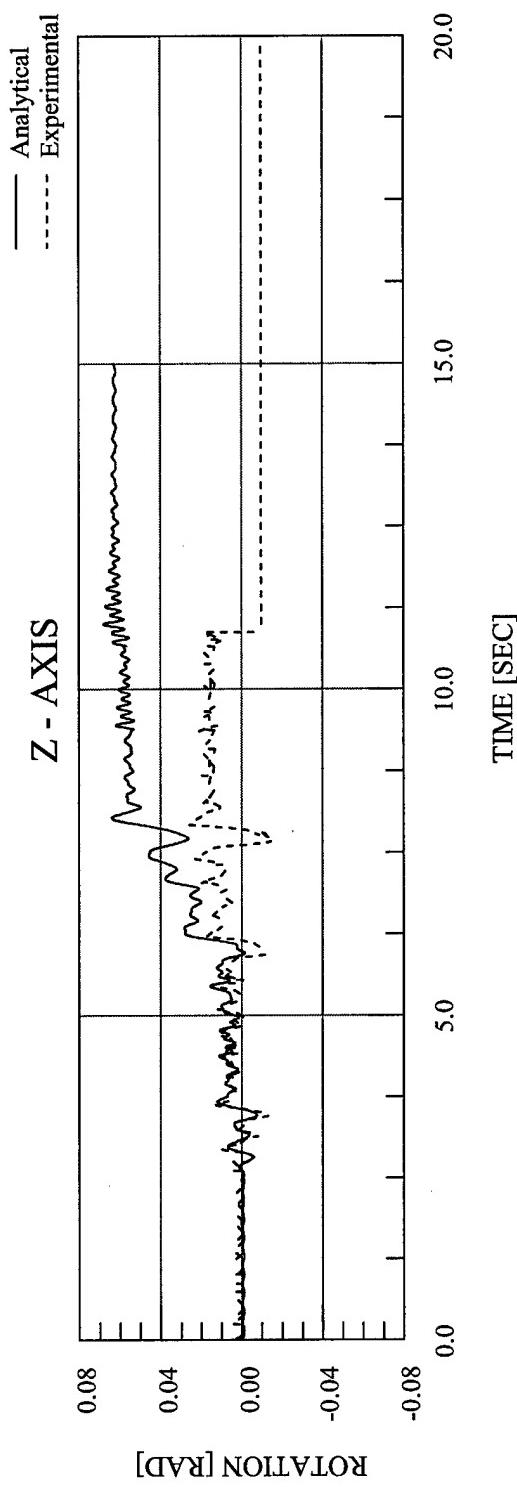


Figure 10.38 Abaqus Analytical Rotation vs. Time – EQ 40 – 100% X-Axis 90% Y-Axis Imperial Valley

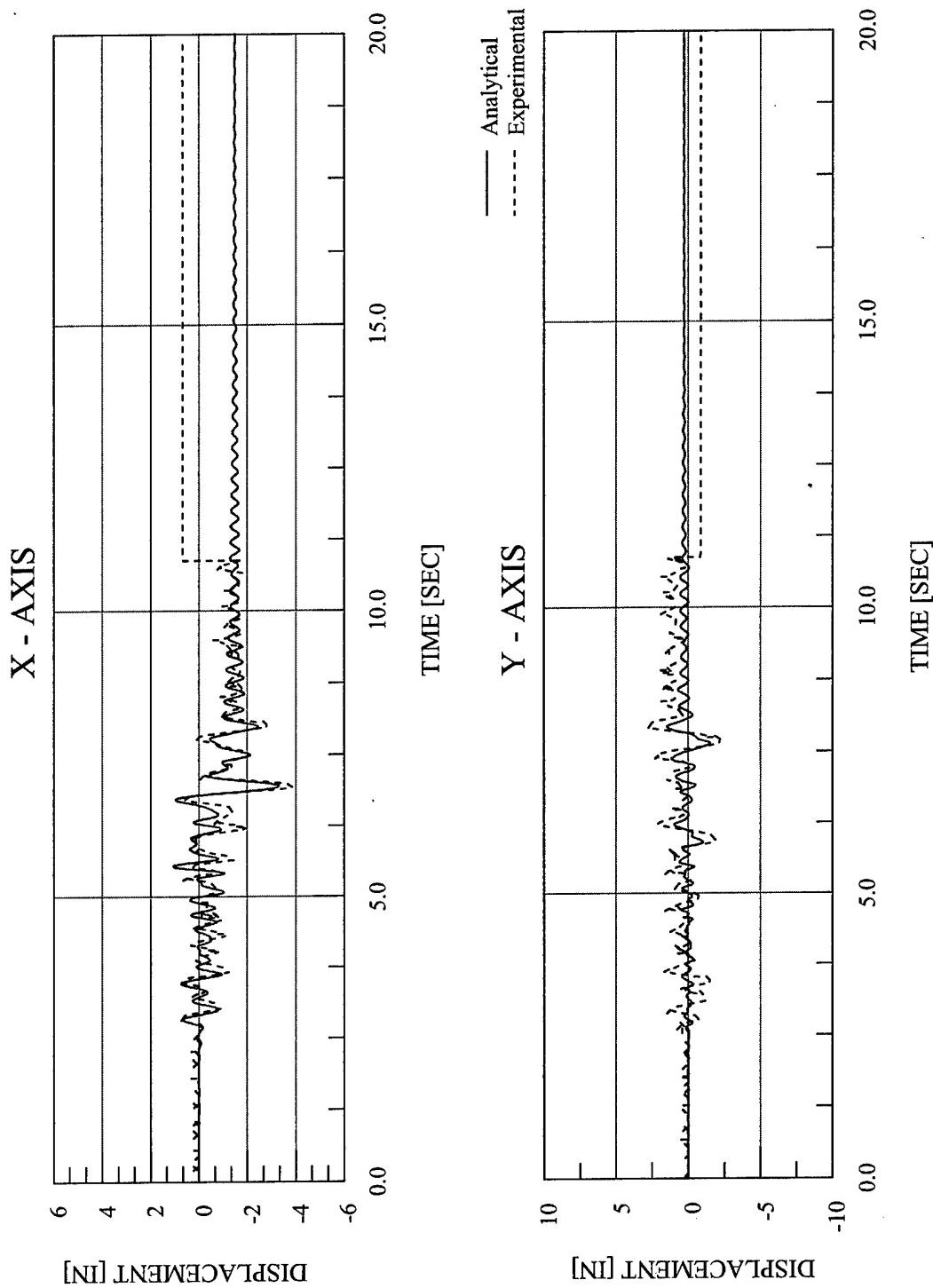


Figure 10.39 Drain-3DX Analytical Displacement vs. Time – EQ 40 – 100% X-Axis 90% Y-Axis Imperial Valley

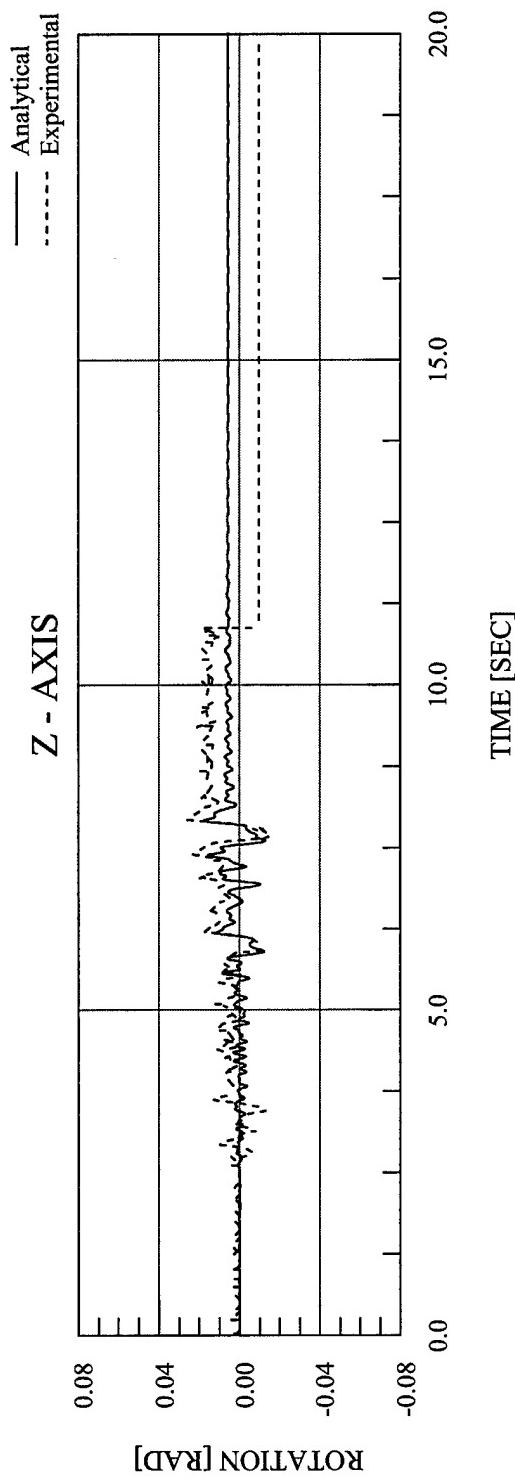


Figure 10.40 Abaqus Analytical Rotation vs. Time – EQ 40 – 100% X-Axis 90% Y-Axis Imperial Valley

CHAPTER 11

EXPERIMENTAL AND FINITE ELEMENT RESPONSE OF TEST CONFIGURATION 7

This chapter provides a summary of the experimental test data and the finite element analysis results of Test Configuration 7. The seventh configuration, as seen in Figure 11.1, featured all of the masses loaded on the south side of the diaphragm, resulting in a $\frac{1}{2}$ mass asymmetry. Two 4" Double Extra-Strong Columns and two 5" Standard Columns were used. The use of these columns resulted in a strength asymmetry, as the yield bending moment and yield axial load for the 4" Double Extra-Strong Columns are both roughly 100% larger, respectively, than those of the 5" Standard Columns. In addition, concentric lateral bracing is located on the north and south sides of the structure. The bracing on the north side of the structure was 1-1/4" x 1/4" and on the south side was 1-3/4" x 1/4", which produced both stiffness and strength eccentricities. The dynamic properties of the test structure in Test Configuration 7 are shown in Table 11.1.

Four earthquake simulations were performed with this test configuration: EQ 41 with 100% X-Axis 75% Y-Axis [$\text{PGA}_X = 1.318 \text{ g}$ and $\text{PGA}_Y = 1.951 \text{ g}$], EQ 42 with 100% X-Axis 85% Y-Axis [$\text{PGA}_X = 1.318 \text{ g}$ and $\text{PGA}_Y = 1.951 \text{ g}$], EQ 43 with 100% Biaxial, and EQ 44 with 100% X-Axis 90% Y-Axis. All four simulations featured inelastic behavior. During the third simulation, EQ 43, the test aborted less than halfway through due to the shake table reaching its velocity limit along the Y-Axis. Subsequently, an additional test was performed, EQ 44, in which Y-Axis input motion was reduced to 90% while the X-Axis input motion remained at 100%, however, the final test again aborted less than halfway through the record. Only the results from the first two simulations will be presented in this chapter. Characterization tests were performed to determine the dynamic properties of the model as described in Chapter 2. The complete test sequence for Test Configuration 7 is shown in Table 11.2.

This chapter summarizes response data of the test structure during the earthquake simulations and the dynamic characterization tests. Summaries of test model accelerations, displacements, torsional moments, overturning moments, column end moments, and base shears are provided.

11.1 OBSERVED STRUCTURAL RESPONSE

The diaphragm acceleration and displacement motion, and base shear vs. displacement and torsional moment vs. rotation are provided for respectively by the following representative time histories: 100% X-Axis 75% Y-Axis simulation in Figures 11.2 and 11.3 and 100% X-Axis 85% Y-Axis simulation in Figures 11.4 and 11.5.

Tables 11.3 – 11.7 list the peak recorded diaphragm relative displacements and peak diaphragm accelerations, and corresponding PGA for each of the five earthquake simulations performed in this test configuration. Also listed are the maximum base shears, maximum torsional moments, maximum overturning moments, maximum column end moments for each column, and maximum column end shears for each column.

11.2 OBSERVED RESPONSE DISCUSSION

The computed force-deformation behavior of the structure in the X and Y directions and about the Z-Axis is shown in Figures 11.6 and 11.7. In the X direction, the model has a yield displacement of 0.52 inches at a yield force of 38.0 kips. In the Y direction, the model has a yield displacement of 0.29 inches at a yield force of 67.0 kips. The model has a yield rotation of 0.0058 radians at a yield moment of 4270 kip*inches. Elastic response spectra of the recorded table motions for EQ 41 are shown, along with the modal frequencies for this configuration, in Figure 11.8.

The first earthquake simulation for this configuration, EQ 41, features 100% X-Axis and 75% Y-Axis Imperial Valley input motion [PGA_X = 1.367 g and PGA_Y = 1.582 g]. Time history plots of the structural response are shown in Figure 11.2. The peak displacements of the structure were 2.17 inches in the X direction and 1.02 inches in the Y direction, with a peak rotation of 11.52 x 10³ radians. All are larger than the yield displacements. Also verifying the inelastic response are the peak base shears and peak torsional moment, which are 61.99 kips in the X direction, 75.08 kips in the Y direction, and 1913 kip*inches about the vertical axis. Although the peak base shear in the Y direction is only slightly greater than the yield shear, the structure achieves a Y-Axis displacement ductility of roughly 3.5. This behavior was also observed and discussed in the

previous test configuration, which also features concentric lateral bracing. This behavior, in which the peak shears are elastic or nearly elastic while the ductility is much larger than unity, has been observed in previous configurations for the torsional response of the structure. It was observed that the peak torsional moment was smaller than, or nearly equal to, the yield moment, while the peak rotation was much greater than the yield rotation. As discussed in the previous chapter, the effect of the tension-only braces on the hysteretic behavior of the structure is such that upon load reversal the stiffness provided by the braces is lost until the previous maximum deflection is reached again. Thus, for a period of time after each load reversal, both the lateral and torsional stiffnesses of the structure are significantly reduced, allowing the rotational response of the structure to increase accordingly. Figure 11.3 shows the base shear vs. displacement plots and torsional moment vs. rotation plot, which are not tight and linear but have a somewhat full shape, indicating inelastic behavior. Both the X-Axis shear vs. displacement loop and the moment vs. rotation loop exhibit a very large inelastic excursion. As compared with the Y-Axis hysteresis plots for the inelastic simulations in the previous test configuration, the Y-Axis hysteresis response for EQ 41 does not appear to take on the characteristic shape of a concentrically braced frame. Nor does there appear to be the loss of stiffness observed in the Y-Axis force-resisting system in the previous configuration, which was also attributed to the behavior of the concentric lateral bracing. In this configuration, the braces used are slightly smaller in size as compared with the previous configuration. In addition, the columns used in this configuration possess a bending stiffness roughly 50% larger than those used in Test Configuration 6. Both of these factors result in the moment-resisting frame influencing the Y-Axis force-deformation behavior to a greater degree as compared with the concentric bracing. The Y-Axis force-resisting system still provides 70% of the torsional stiffness in this configuration, and therefore the differences observed in the Y-Axis behavior between this and the previous configuration can also be observed in the torsional hysteretic behavior.

The second earthquake simulation for this configuration, EQ 42, features 100% X-Axis and 85% Y-Axis Imperial Valley input motion [$\text{PGA}_X = 1.357 \text{ g}$ and $\text{PGA}_Y = 1.881 \text{ g}$]. Time history plots of the structural response are shown in Figure 11.4. The peak displacements of the structure were 2.31 inches in the X direction, 1.45 inches in the Y direction, and 13.66×10^{-3} radians about the Z-Axis. The peak base shears are 60.75 kips in the X direction, 85.29 kips in the Y direction, and 2028 kip*inches about the Z-Axis. The peak base shear in the Y direction is the only shear that has increased noticeably from EQ 41. Accordingly, the peak displacement in the Y direction is the only displacement that has increased noticeably from EQ 41. This is also seen in the base

shear vs. displacement and torsional moment vs. rotation hysteresis plots shown in Figure 11.5, as they appear to be very similar to those for EQ 41. This indicates that the inelastic behavior experienced by the structure in EQ 41 did not produce permanent softening of the structure. Had a significant degree of softening taken place, the hysteresis loops for EQ 42 would be expected to be more full than those for EQ 41. The observations made for EQ 41 regarding the shape of the Y-Axis and torsional hysteresis plots appear to hold for EQ 42 as well.

11.3 DYNAMIC CHARACTERIZATIONS OF THE MODEL

Prior to performing any shake table simulations using the earthquake input motions, white noise, sine sweep, and sine decay tests were performed, as discussed in Chapter 3. This general pattern was followed for Test Configuration 7, as can be seen in Table 11.2. In addition, white noise tests were performed immediately after the final earthquake simulation exhibiting inelastic behavior, EQ 44.

The dynamic properties of the test structure, as measured before EQ 41, and then again after EQ 44, are shown in Table 11.1. The results indicate that due to the inelastic behavior in this configuration permanent softening of the structure occurred in the Y direction but not in the X direction. Also, the structure softened torsionally as well. The large change in the modal frequency in the Y and Z directions correlates with the permanent damage experienced by the diagonal bracing. Once the structure began to respond inelastically, the bracing was no longer a significant contributor to the stiffness or damping at small displacements. This is verified by observing that the dynamic properties following EQ 44 correspond fairly well to the dynamic properties of the structure during Test Configuration 5, in which bracing was not present but a $\frac{1}{2}$ mass asymmetry and a strength asymmetry due to two 4" Double Extra-Strong Columns and two 5" Standard Columns were both present. Thus, in comparing the damping and modal frequencies in the Y and Z directions prior to and following the simulations, the contribution of the bracing to the dynamic properties can be seen. These observations are consistent with those made for the previous test configuration, also with concentric lateral bracing.

11.4 OBSERVED CONDITION OF THE STRUCTURE

Following each of the major earthquake simulations, the model structure was physically inspected. Typically photographs were taken as well, predominantly after the final earthquake simulation of the test configuration. Historically, the most problematic location on the model was column-to-bottom plate welded joint on each column. These areas were inspected carefully in order to document any fracture in the weld or in the base material. For Test Configuration 7, no fracture occurred at these or any other locations. No photographs were taken of this configuration.

11.5 FINITE ELEMENT ANALYSIS

In modeling the behavior of the test structure, the nonlinear finite element analysis programs Abaqus and Drain-3DX were employed. A more complete discussion of the applicable features of Abaqus and Drain-3DX is presented in Chapter 3. Also, some aspects of the finite element model, such as the modeling of the diaphragm as a rigid component, are common throughout each test configuration, and are discussed more completely in Chapter 3.

(A) PIPE COLUMN AND LATERAL BRACE MATERIAL MODELS

The pipe columns used in Test Configuration 7 and those used in Test Configuration 5 were produced from the same batch of raw pipe column lengths. As a result of this, two coupons were taken from each of the two types of pipe used in Test Configurations 5 and 7, 4" Double Extra-Strong and 5" Standard. The material models of the pipe columns in these two test configurations were based on stress-strain data produced during coupon tension tests. Coupons were also taken from the material used for the diagonal braces in Test Configuration 7. Figures 11.9 and 11.10 show both the original stress-strain data recorded during the coupon tension tests, and the best-fit material model used in the Abaqus finite element analyses for the 5" Standard and 4" Double Extra-Strong pipe material, respectively. Figure 11.11 shows both the original stress-strain data recorded during the coupon tension tests, and the best-fit material model used in the Abaqus analyses for the braces. Figures 11.12 and 11.13 show the original material data and the best-fit material model used in the Drain-3DX finite element analyses for the 5" Standard and 4" Double

Extra-Strong pipe material, respectively. Figure 11.14 shows the best-fit material model used for the braces in the Drain-3DX analyses. Shown in Tables 11.8 and 11.9 are the Abaqus numerical stress-strain best-fit model data for the 5" Standard and 4" Double Extra-Strong pipe material, respectively. Shown in Tables 11.11 and 11.12 are the Drain-3DX best-fit material model data for the two types of pipe material. Shown in Tables 11.10 and 11.13 are the numerical stress-strain best-fit model data for the diagonal braces used in the Abaqus and Drain-3DX finite element analyses, respectively.

(B) FINITE ELEMENT MODEL

The Abaqus and Drain-3DX finite element models used to analyze the behavior of Test Configuration 7 is shown in Figures 11.15 and 11.16, respectively. Beyond the features of the finite element models common throughout each test configuration, Figures 11.15 and 11.16 illustrate the location and magnitudes of the interior and corner nodal masses, the height of the Non-Rigid Links, and the configuration of the diagonal braces. Rigid links are used to connect the diagonal braces to the rest of the model and to the ground, and both can be seen in the figures. For clarity only the braces and rigid links on the south side of the model are shown, although they are also present on the north side of the model as well. The diagonal braces on the south side of the model have cross-sectional dimensions of 1-3/4" x 1/4", while on the north side the braces have cross-sectional dimensions of 1-1/4" x 1/4".

In calibrating the model frequencies of the finite element model, two steps were taken. First, the modal frequencies of the test structure measured after the final simulation were used to calibrate the finite element model without the diagonal braces in place. Next, the diagonal braces were added to the model, and the model was calibrated using the test structure modal frequencies measured before the first simulation. This allows a means of accounting for the relative contributions of both the braces and the columns to the dynamic properties of the structure.

(C) OBSERVED RESPONSE

Displacement histories along the X- and Y-Axis and rotation histories about the Z-Axis are provided for the 100% X-Axis 75% Y-Axis simulation [$\text{PGA}_X = 1.367 \text{ g}$ and $\text{PGA}_Y = 1.582 \text{ g}$] in

Figures 11.17 – 11.20 and the 100% X-Axis 85% Y-Axis simulation [PGA_X = 1.357 g and PGA_Y = 1.881 g] in Figures 11.21 – 11.24. Table 11.14 lists the maximum peak relative displacements in the X and Y directions and the peak rotation for the two earthquake simulations performed in this test configuration.

(d) OBSERVED RESPONSE DISCUSSION

Shown in Figures 11.17 – 11.21 are the displacement and rotation response histories for EQ 41 [PGA_X = 1.367 g and PGA_Y = 1.582 g]. For both displacements and the rotation, the frequency contents of the response histories in the Abaqus and Drain-3DX simulations match the test data fairly well. Also, as seen in Table 11.12, the maximum relative displacement of the Abaqus model in the X direction matches the experimental value well, to within 10%. This is a significant improvement over EQ 39, the first inelastic simulation in Chapter 10, which also featured diagonal bracing. In the Y direction, the peak displacement only agrees to within 50%, but overall the time histories appear to match fairly well. Although the Y-Axis peak displacement only agrees to within 50%, this is also a significant improvement over EQ 39 in which the Abaqus predictions were off by 200-300% in the braced direction. The peak displacements in the Drain-3DX simulations agree to within 18% and 2% in the X and Y directions, respectively. The Drain-3DX analyses proved to be fairly accurate in the previous configuration in predicting response, and that trend appears to continue for this configuration. About the Z-Axis, the peak rotations for both the Abaqus and Drain-3DX analyses agree with the experimental value to within roughly 30%.

The analytical and experimental response time histories for EQ 42 [PGA_X = 1.357 g and PGA_Y = 1.881 g] are shown in Figures 11.22 – 11.25. As with EQ 41, the frequency content of the analytical responses matches the experimental results very well for both the X-Axis and Y-Axis motion. In addition, as seen in Table 11.14, the peak displacements in both the X and Y directions match the experimental data to within 20% for both the Drain-3DX and Abaqus analyses. Again, for the Abaqus simulations in the braced direction a significant improvement in performance over the previous configuration is evident. The overall analytical response in the rotational direction does not match quite as well as the translational directions, as has been consistently observed in previous simulations, but the Abaqus and Drain-3DX models predicts the peak rotation to within 14% and 20%, respectively, of the peak experimental rotation. Thus,

despite the pre-existing damage, both analytical models predict the structural response fairly accurately. The Abaqus results for EQ 42 again represent a significant improvement over the results seen in EQ 40, the second inelastic simulation for the previous test configuration, in which diagonal bracing was used. Although the Y and Z direction peak displacements do not match as well as the X direction, they overall are a significant improvement over the results obtained in the previous configuration with diagonal bracing. Typically in previous configurations, the greater the degree of inelastic behavior, the more difficult it becomes to accurately model the structural response analytically. The improvement in agreement between analytical and experimental peak responses for this configuration as compared to Test Configuration 6 is most likely a result of a lesser degree of inelastic behavior occurring during the simulations. The peak displacements and rotations for this inelastic simulation are roughly half of those for EQ 39 and EQ 40, the two inelastic simulations performed in Test Configuration 6. This is not unexpected, as the columns used in this configuration are significantly stronger and stiffer than those used in the previous configuration.

11.6 SUMMARY AND CONCLUSIONS

The methodology used in the *Seismic Provisions* of using an elastic analysis as the basis for determining inelastic response of structures implies that the ratio of the peak rotation to the peak lateral displacement and the ratio of the two peak lateral displacements remain constant for elastic and inelastic response. The only two simulations performed for this configuration featured inelastic response, which makes it impossible to evaluate the u_Y/u_X ratio and u_θ/u_Y ratio for elastic and inelastic response. Test Configuration 8 also was performed with only inelastic simulations, but that configuration was identical to Test Configuration 3 and thus results could be inferred. This configuration is similar to the previous configuration, Test Configuration 6, with the exception of a different set of columns. The 4" Double Extra-Strong and 5" Standard columns used in this configuration produced a strength eccentricity along the X-Axis which was not present in Test Configuration 6. The u_Y/u_X ratio for EQ 41 was 0.41, while for EQ 42 the value increases to 0.63. The increase corresponds to a change in the Y-Axis ground motion, increasing from a PGA of 1.582 g to 1.881 g. In the previous chapter, it was stated that if the X-Axis ground motion were increased, or a reduction in the strength of the X-Axis force-resisting system, the u_Y/u_X ratio would decrease even further than 0.75, the value for EQ 40. The decrease in the Y-Axis ground motion would produce the same overall effect as increasing the X-

Axis ground motion, and therefore the u_Y/u_X ratio values seem to support this idea. Although a direct comparison cannot be made with the elastic u_Y/u_X ratio as none of the sets of ground motions in this configuration have the same proportions as in EQ 36, it does appear that the u_Y/u_X ratio changes with the relative changes in the X-Axis and Y-Axis ground motions used in each simulation. This behavior is expected in elastic systems, and appears to extend to inelastic systems.

Configuration	EQ	u_Y/u_X	u_θ/u_Y
10% Biaxial ½ Asymmetric Mass [Y-Axis] Concentric Bracing [Y-Axis] Stiffness Asymmetry [Y-Axis]	36	0.30	0.69
100% Biaxial ½ Asymmetric Mass [Y-Axis] Concentric Bracing [Y-Axis] Stiffness Asymmetry [Y-Axis]	39	1.20	0.46
100% X-Axis 90% Y-Axis ½ Asymmetric Mass [Y-Axis] Concentric Bracing [Y-Axis] Stiffness Asymmetry [Y-Axis]	40	0.75	0.46
½ Asymmetric Mass 100% X-Axis 75% Y-Axis Concentric Bracing [Y-Axis] Stiffness Asymmetry [Y-Axis] Strength Asymmetry [X-Axis]	41	0.47	0.55
½ Asymmetric Mass 100% X-Axis 85% Y-Axis Concentric Bracing [Y-Axis] Stiffness Asymmetry [Y-Axis] Strength Asymmetry [X-Axis]	42	0.63	0.45

It appears from the u_θ/u_Y ratio values shown above for EQ 41 and EQ 42 that the ratios for inelastic response extend from the previous configuration to this one, as the values are similar. This would appear to somewhat validate the decrease in u_θ/u_Y ratio for inelastic response from elastic response. However, as shown in Test Configuration 5, the presence of a strength eccentricity can have a significant impact on the inelastic torsional response, as the strength eccentricity can produce a stiffness eccentricity that is not present during elastic response. It is difficult to quantify the impact of the strength eccentricity on the torsional response in this configuration because there is also a stiffness eccentricity present from the concentric bracing,

and the two asymmetries are about different axes. The influence of each eccentricity, along with the mass eccentricity, would depend on the relative responses of the system along the X-Axis and Y-Axis at any instant.

The performances of the time history analyses using Abaqus and Drain-3DX for this configuration were overall very good in their response predictions, especially considering the complexity of the force-resisting system. In the first simulation, EQ 41, the Abaqus analysis overestimated the peak Y-Axis displacement by 50%. However, with that exception, both analysis programs predicted the remaining peak displacements for both simulations with an accuracy of within roughly 15 – 20%. In the first simulation, both the Drain-3DX and Abaqus analyses underestimated the peak rotation by roughly 30%; and in the second simulation, they underestimated the peak rotation by 14% and 20%, respectively. As with the displacement response, overall these are a noticeable improvement over Test Configuration 6.

Although the Y and Z direction peak displacements do not match as well as the X direction, they overall are a significant improvement over the results obtained in the previous configuration with diagonal bracing, especially for the Abaqus analyses. Typically in previous configurations, the greater the degree of inelastic behavior, the more difficult it has become to accurately model the structural response analytically. The improvement in agreement between analytical and experimental peak responses for this configuration as compared to Test Configuration 6 is most likely a result of a lesser degree of inelastic behavior occurring during these simulations. The peak displacements and rotations for these inelastic simulation are roughly half of those for EQ 39 and EQ 40, the two inelastic simulations performed in Test Configuration 6. In addition, for both simulations in this configuration, there is very little permanent offset in either translational direction or rotationally. This is not unexpected, as the columns used in this configuration are significantly stronger and stiffer than those used in the previous configuration.

Mass [lb*s ² /in]	Mass Centers [in]			Stiffness Centers [in]	
	X ₀	Y ₀	Z ₀	X ₀	Y ₀
96.259	13.552	0.0	69.679	5.574	0.0

	Modal Frequencies [Hz]			Modal Damping [%]		
	X	Y	θ	X	Y	θ
Before EQ 41	4.444	7.692	11.765	0.818	5.237	1.271
After EQ 44	4.444	4.255	8.696	0.909	1.609	0.580

Table 11.1 Test Structure Dynamic Properties - Test Configuration 7

Test Designation	Input Motions
WNT46	White Noise X-Axis
WNT47	White Noise Y-Axis
WNT48	White Noise Yaw-Axis
SIN28	Sine Decay X-Axis
SIN29	Sine Decay Y-Axis
SIN30	Sine Decay Yaw-Axis
SWP28	Sine Sweep X-Axis
SWP29	Sine Sweep Y-Axis
SWP30	Sine Sweep Yaw-Axis
EQ41	100% X-Axis 75% Y-Axis Imperial Valley
EQ42	100% X-Axis 85% Y-Axis Imperial Valley
EQ43	100% Biaxial Imperial Valley
EQ44	100% X-Axis 90% Y-Axis Imperial Valley
WNT49	White Noise X-Axis
WNT50	White Noise Y-Axis
WNT51	White Noise Yaw-Axis
SIN31	Sine Decay X-Axis
SIN32	Sine Decay Y-Axis
SIN33	Sine Decay Yaw-Axis
SWP31	Sine Sweep X-Axis
SWP32	Sine Sweep Y-Axis
SWP33	Sine Sweep Yaw-Axis

Table 11.2 Earthquake Simulations and Dynamic Characterization Tests - Test Configuration 7

Earthquake Test No.	Input Motions	PGA [g]		Relative Displacement [in]		Rotation [10^{-3} rad]	Normalized Displacement [in/g]	Ductility		
		X-Axis	Y-Axis	X-Axis	Y-Axis			X-Axis	Y-Axis	Z-Axis
41	100% X-Axis 75% Y-Axis	1.367	1.582	2.173	1.015	11.52	1.59	0.64	4.21	3.45
42	100% X-Axis 85% Y-Axis	1.357	1.881	2.312	1.451	13.66	1.70	0.77	4.48	4.94

Table 11.3 Maximum Diaphragm Relative Displacement and Rotation - Test Configuration 7

Earthquake Test No.	Input Motions	PGA [g]			Diaphragm Acceleration [g]			Diaphragm Angular Acceleration [10^{-3} g/in]			Normalized Acceleration
		X-Axis	Y-Axis	Z-Axis	X-Axis	Y-Axis	Z-Axis	X-Axis	Y-Axis	Z-Axis	
41	100% X-Axis	1.367	1.582	1.667	1.909			20.08			1.22
	75% Y-Axis										1.21
42	100% X-Axis	1.357	1.881	1.633	2.214			25.08			1.20
	85% Y-Axis										1.18

Table 11.4 Maximum Diaphragm Acceleration and Angular Acceleration Response - Test Configuration 7

Earthquake Test No.	Input Motions	PGA [g]			Base Shear [k]	Torsional Moment [k*in]	Diagonal Brace Force [k]	Overturning Moment [k*in]		
		X-Axis	Y-Axis	Z-Axis					X-Axis	Y-Axis
41	100% X-Axis 75% Y-Axis	1.367	1.582	61.99	75.08	1913.27	19.04	33.60	4347.5	5265.6
42	100% X-Axis 85% Y-Axis	1.357	1.881	60.75	85.29	2028.28	22.33	36.79	4260.3	5981.6

Table 11.5 Maximum Base Shear, Torsional Moment, Brace Force, and Overturning Moment - Test Configuration 7

Earthquake Test No.	Input Motions	PGA [g]				Column End Moments [k*in]					
		SE Column		SW Column		NW Column		NE Column			
		X-Axis	Y-Axis	X-Axis	Y-Axis	X-Axis	Y-Axis	X-Axis	Y-Axis	X-Axis	Y-Axis
41	100% X-Axis 75% Y-Axis	1.367	1.582	213.94	485.79	213.94	447.39	174.33	447.39	174.33	485.79
42	100% X-Axis 85% Y-Axis	1.357	1.881	234.27	475.80	234.27	436.02	204.38	436.02	204.38	475.80

Table 11.6 Maximum Column End Moments - Test Configuration 7

Earthquake Test No.	Input Motions	PGA [g]				Column End Shears [k]					
		X-Axis	Y-Axis	SE Column X-Axis	SE Column Y-Axis	SW Column X-Axis	SW Column Y-Axis	NW Column X-Axis	NW Column Y-Axis	NE Column X-Axis	NE Column Y-Axis
41	100% X-Axis 75% Y-Axis	1.367	1.582	16.19	7.13	14.91	7.13	14.91	5.81	16.19	5.81
42	100% X-Axis 85% Y-Axis	1.357	1.881	15.86	7.81	14.53	7.81	14.53	6.81	15.86	6.81

Table 11.7 Maximum Column End Shears - Test Configuration 7

E [ksi] = 29000.0

Stress [ksi]	Strain [in/in]	Plastic Strain [in/in]
0.000000	0.000000	
41.000000	0.001414	0.000000
44.000000	0.001600	0.000083
46.200000	0.001800	0.000207
47.820000	0.002000	0.000351
49.400000	0.002500	0.000797
50.080000	0.003000	0.001273
51.200000	0.005000	0.003234
52.800000	0.010000	0.008179
53.920000	0.015000	0.013141
55.700000	0.020000	0.018079
57.300000	0.030000	0.028024
58.600000	0.040000	0.037979
60.200000	0.060000	0.057924
61.200000	0.080000	0.077890
61.700000	0.100000	0.097872
62.100000	0.150000	0.147859
61.700000	0.200000	0.197872

Table 11.8 Abaqus Stress-Strain Best-Fit Material Model - 5" Standard Columns
Test Configuration 7

E [ksi] = 29000.0

Stress [ksi]	Strain [in/in]	Plastic Strain [in/in]
0.000000	0.000000	
42.000000	0.001448	0.000000
46.000000	0.006000	0.004414
51.000000	0.014000	0.012241
54.300000	0.020000	0.018128
59.500000	0.030000	0.027948
62.900000	0.040000	0.037831
66.100000	0.050000	0.047721
69.800000	0.070000	0.067593
71.700000	0.090000	0.087528
72.800000	0.110000	0.107490
73.400000	0.150000	0.147469
72.800000	0.200000	0.197490

Table 11.9 Abaqus Stress-Strain Best-Fit Material Model - 4" Double Extra-Strong Columns
Test Configuration 7

E [ksi] = 29000.0

Stress [ksi]	Strain [in/in]	Plastic Strain [in/in]
0.000000	0.000000	
48.050000	0.001481	0.000000
49.250000	0.004000	0.002482
50.200000	0.010000	0.008453
50.800000	0.015000	0.013434
52.300000	0.020000	0.018388
53.400000	0.030000	0.028354
54.200000	0.040000	0.038329
55.400000	0.060000	0.058292
56.000000	0.080000	0.078274
56.400000	0.100000	0.098261
56.600000	0.150000	0.148255
55.900000	0.200000	0.198277

Table 11.10 Abaqus Stress-Strain Best-Fit Material Model - Diagonal Braces
Test Configuration 7

E [ksi] = 29000.0

Stress [ksi]	Strain [in/in]
0.00000	0.00000
48.00000	0.001666
51.20000	0.005000
57.30000	0.030000
61.20000	0.080000
62.10000	0.150000

Table 11.11 Drain-3DX Stress-Strain Best-Fit Material Model – 5" Standard Columns
Test Configuration 7

E [ksi] = 29000.0

Stress [ksi]	Strain [in/in]
0.00000	0.00000
42.00000	0.001448
46.00000	0.006000
59.50000	0.030000
69.80000	0.070000
73.40000	0.150000

Table 11.12 Drain-3DX Stress-Strain Best-Fit Material Model – 4" Double Extra-Strong Columns
Test Configuration 7

E [ksi] = 29000.0

Stress [ksi]	Strain [in/in]
0.00000	0.00000
63.50000	0.002190
70.80000	0.004000
73.80000	0.008000
78.50000	0.030000
79.90000	0.060000

Table 11.13 Drain-3DX Stress-Strain Best-Fit Material Model – Diagonal Braces
Test Configuration 7

Earthquake Test No.	Input Motions	PGA [g]						Relative Displacement [in]						Rotation [10^{-3} rad]		
		X-Axis		Y-Axis		X-Axis		Abaqus		Y-Axis		Abaqus		Drain		Z-Axis
		Abaqus	Test	Drain	Test	Abaqus	Drain	Test	Abaqus	Drain	Test	Abaqus	Drain	Test	Drain	Test
41	100% X-Axis 75% Y-Axis	1.367	1.582	1.97	1.77	2.17	1.53	0.99	1.01	7.84	7.77	11.52				
42	100% X-Axis 85% Y-Axis	1.357	1.881	1.92	1.89	2.32	1.68	1.10	1.42	10.98	11.81	13.66				

Table 11.14 Analytical vs. Experimental Displacement and Rotation Response Comparison - Test Configuration 7

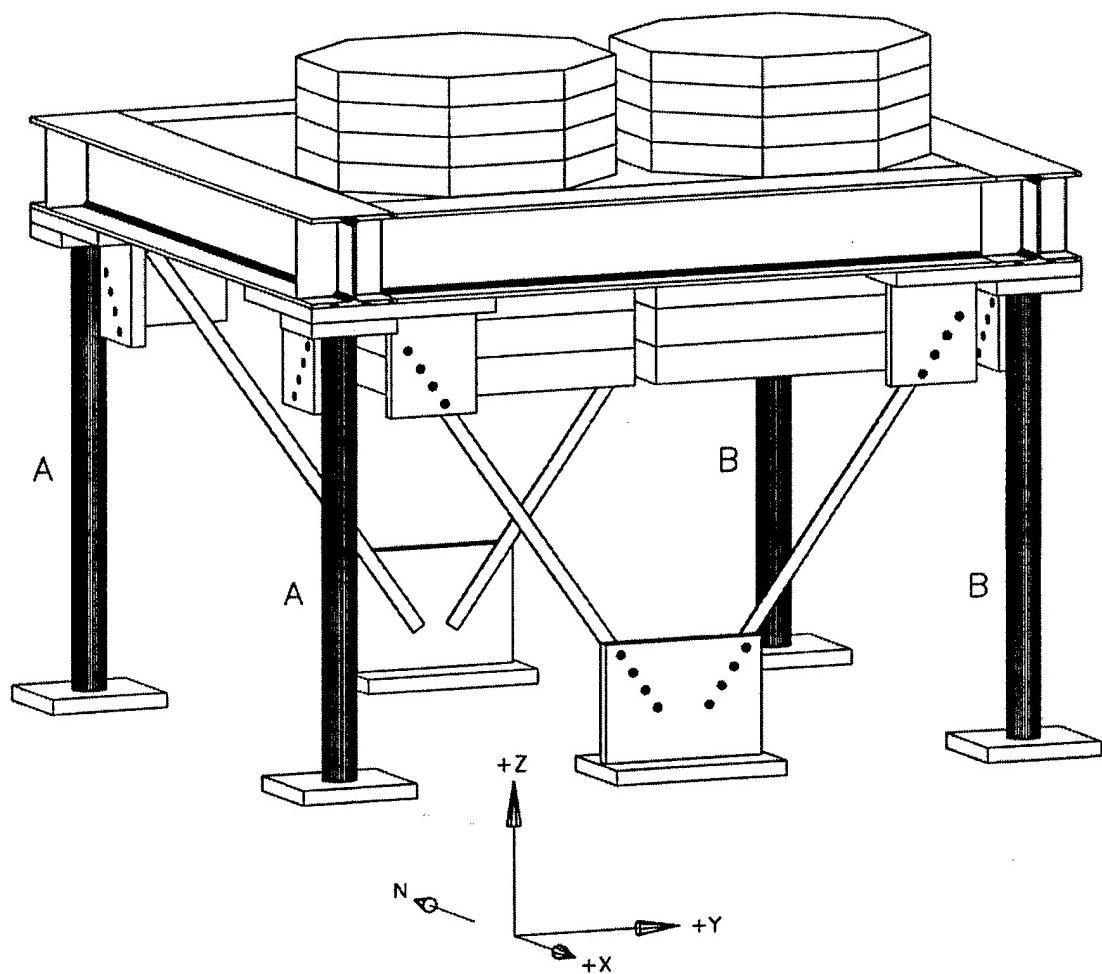


Figure 11.1 Perspective View of Test Configuration Model 7
[A] 2 – 5" Standard Columns and [B] 2 – 4" Double Extra-Strong Columns

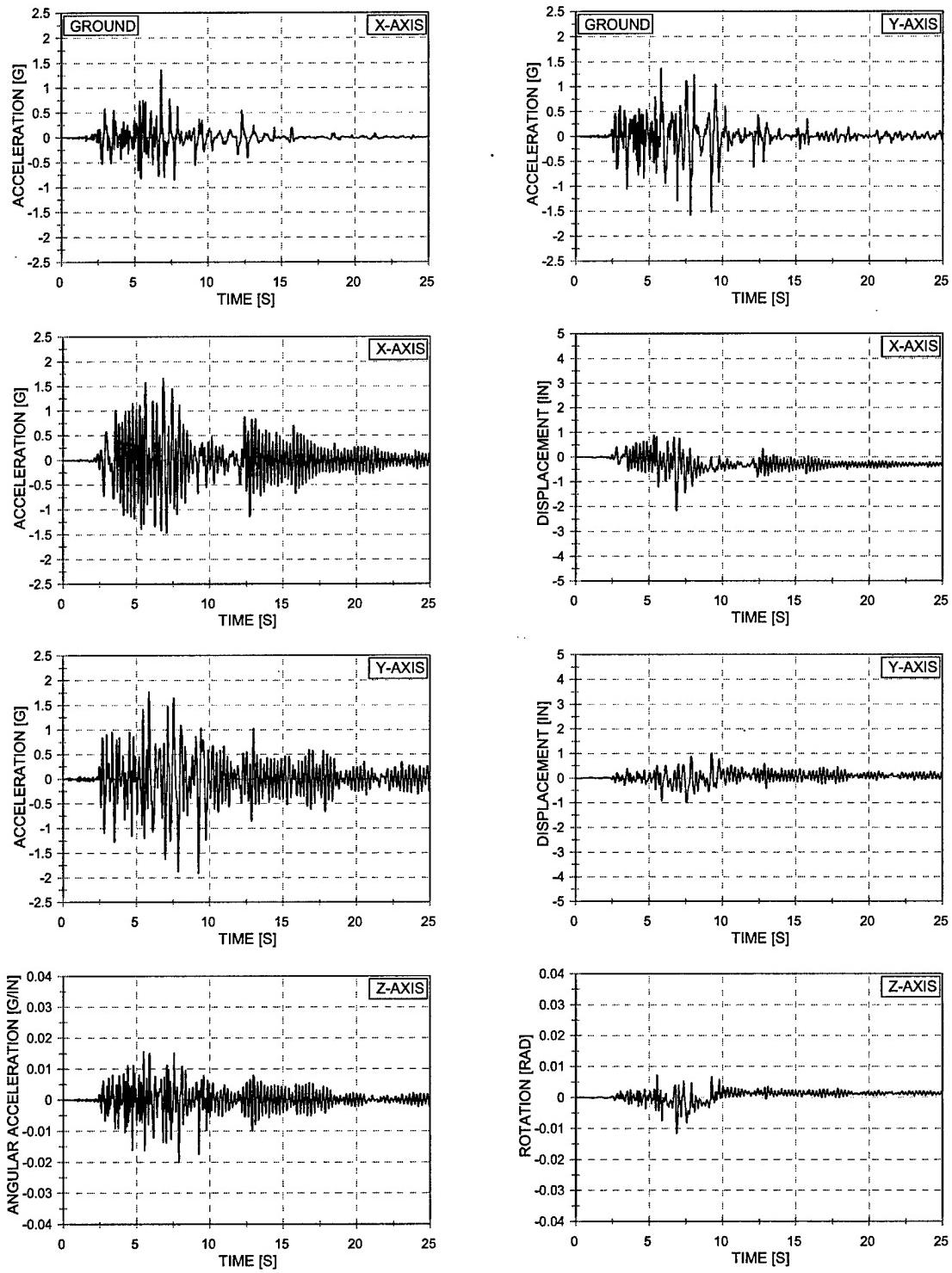


Figure 11.2 Acceleration and Displacement vs. Time – EQ 41
 100% X-Axis 75% Y-Axis Imperial Valley – 1/2 Asymmetric Mass – Concentric Bracing
 Two 5" Standard Columns and Two 4" Double Extra-Strong Columns

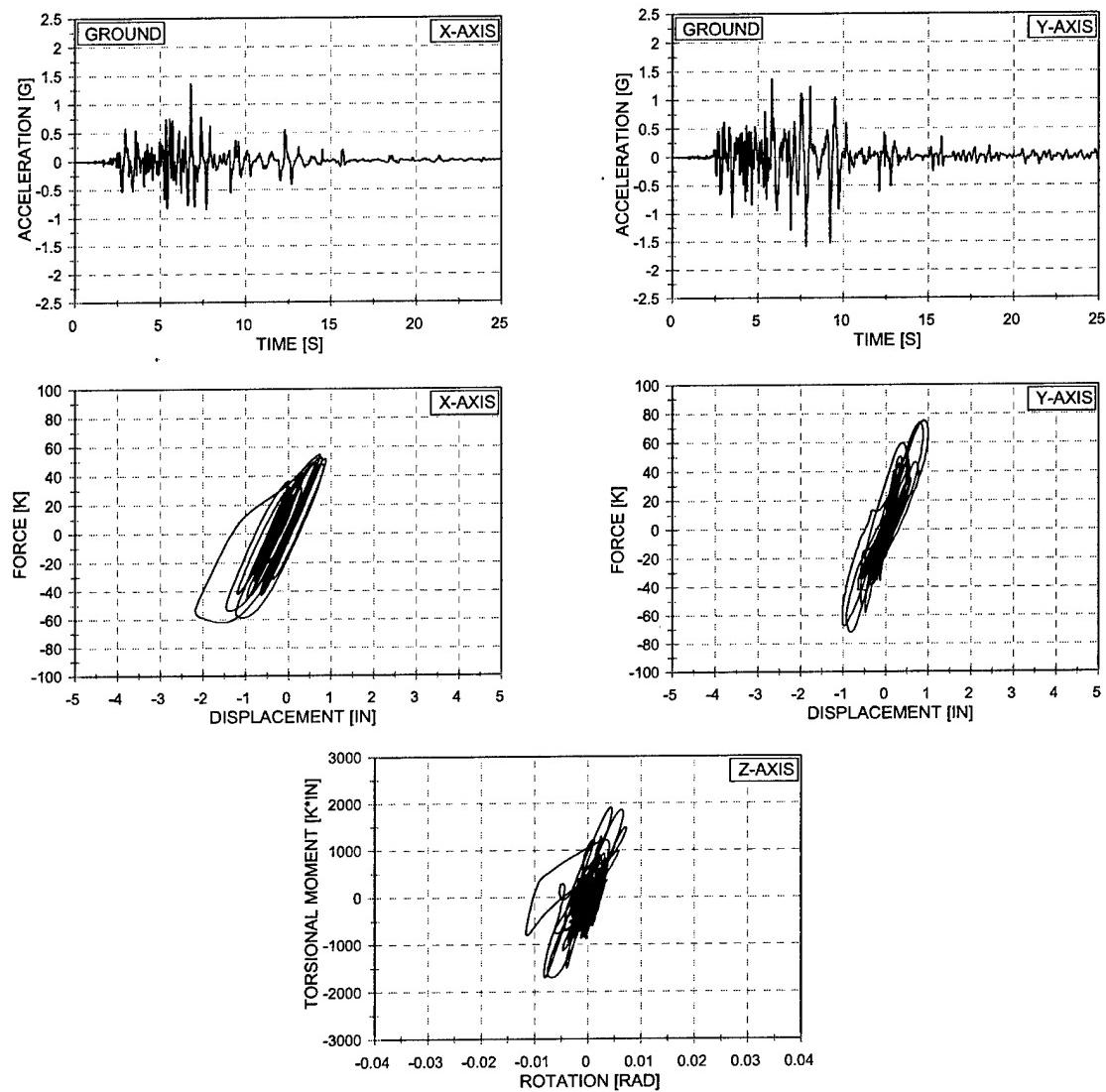


Figure 11.3 Force vs. Displacement and Torsional Moment vs. Rotation – EQ 41
 100% X-Axis 75% Y-Axis Imperial Valley – 1/2 Asymmetric Mass – Concentric Bracing
 Two 5" Standard Columns and Two 4" Double Extra-Strong Columns

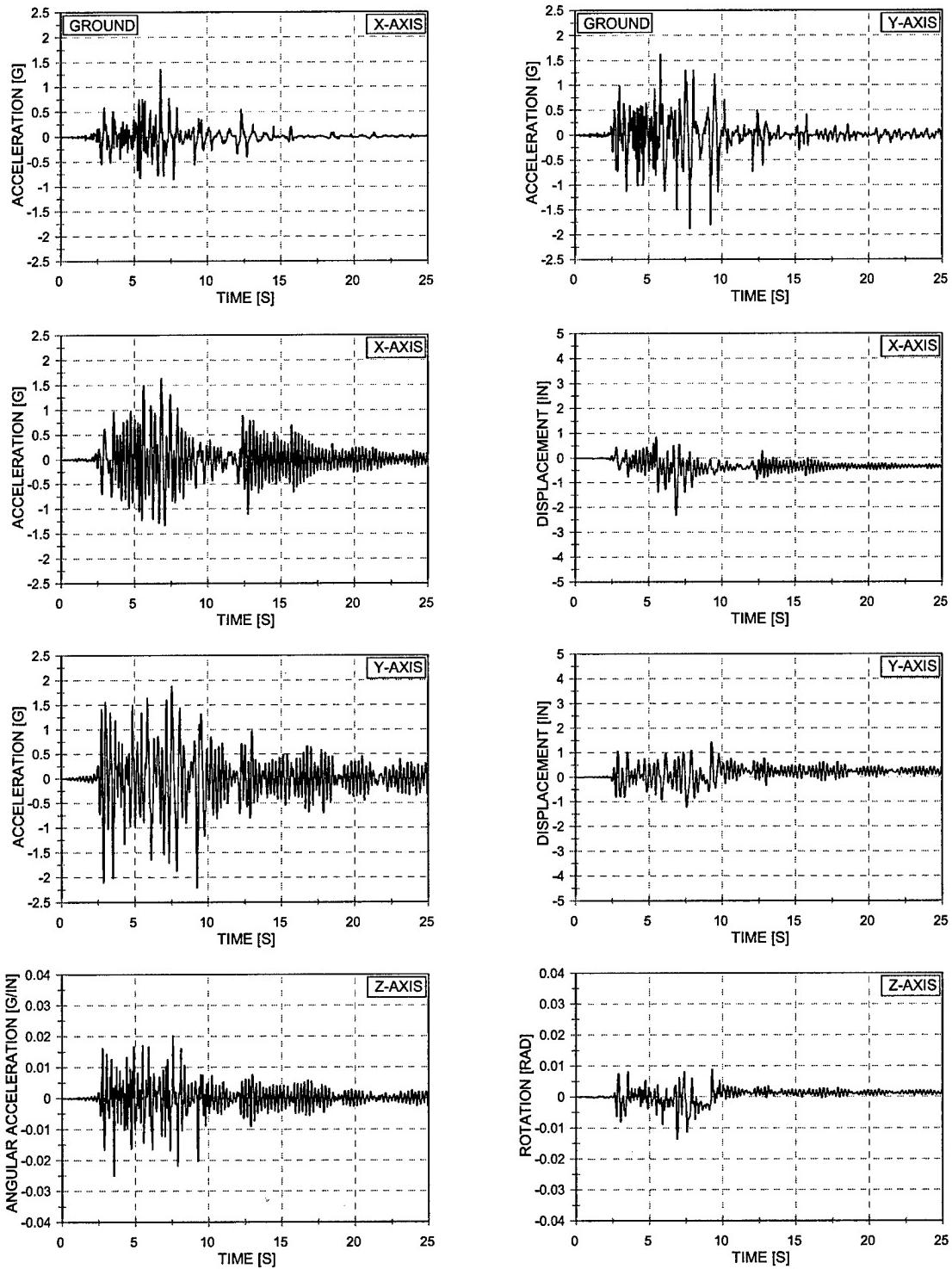


Figure 11.4 Acceleration and Displacement vs. Time – EQ 42
 100% X-Axis 85% Y-Axis Imperial Valley – 1/2 Asymmetric Mass – Concentric Bracing
 Two 5" Standard Columns and Two 4" Double Extra-Strong Columns

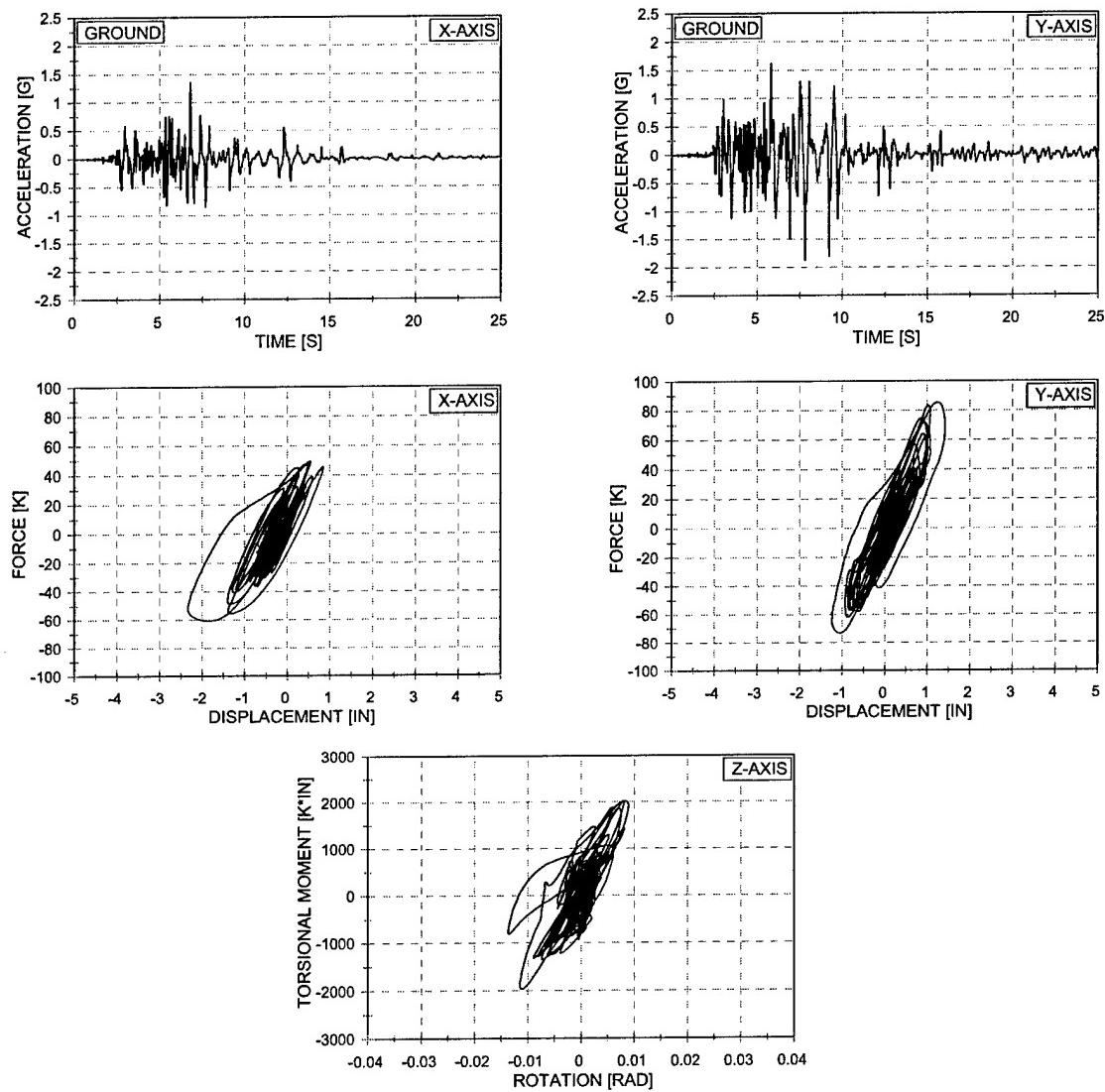


Figure 11.5 Force vs. Displacement and Torsional Moment vs. Rotation - EQ 42
 100% X-Axis 85% Y-Axis Imperial Valley – 1/2 Asymmetric Mass – Concentric Bracing
 Two 5" Standard Columns and Two 4" Double Extra-Strong Columns

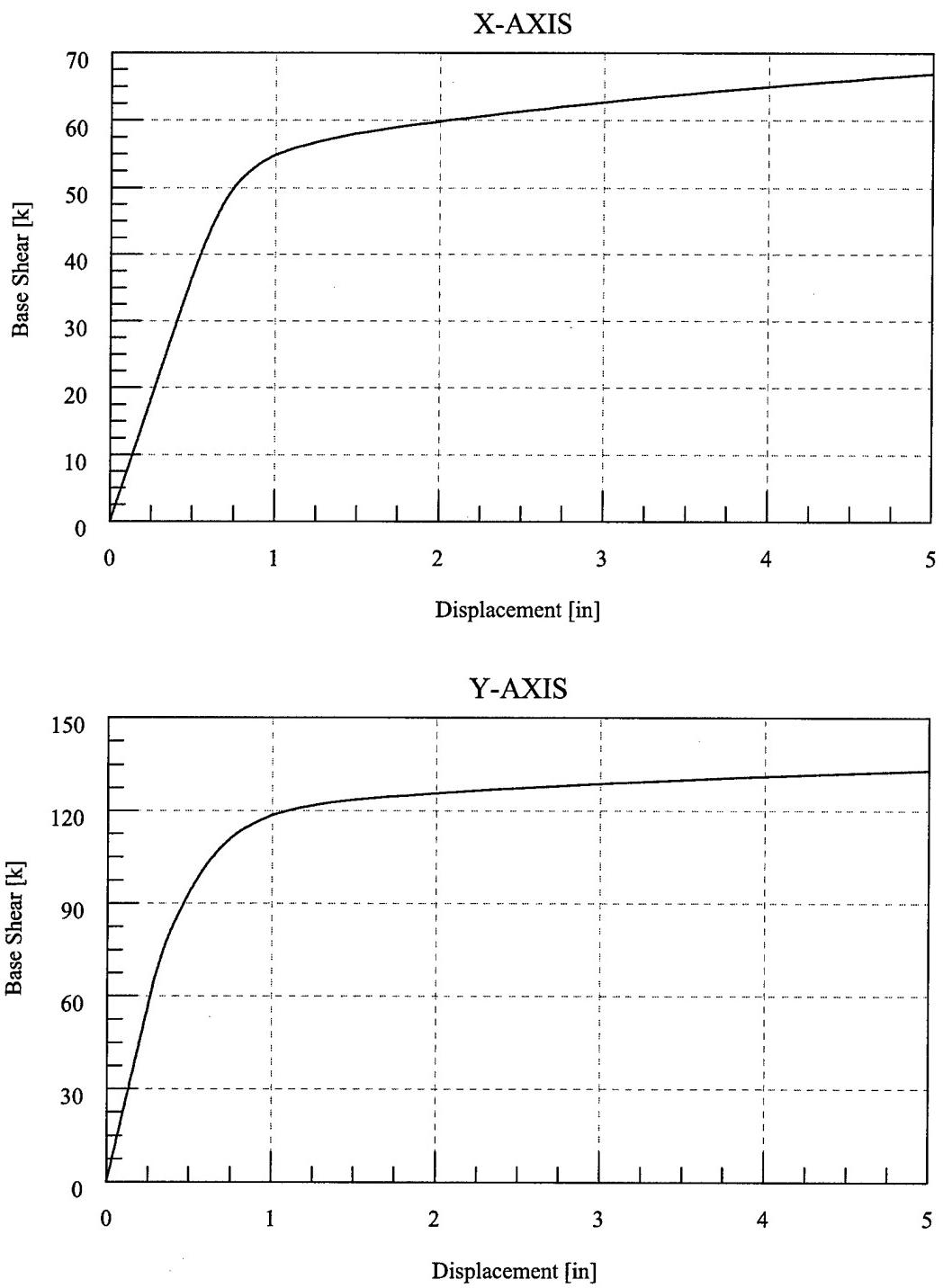


Figure 11.6 Force-Deformation Response – Test Configuration 7

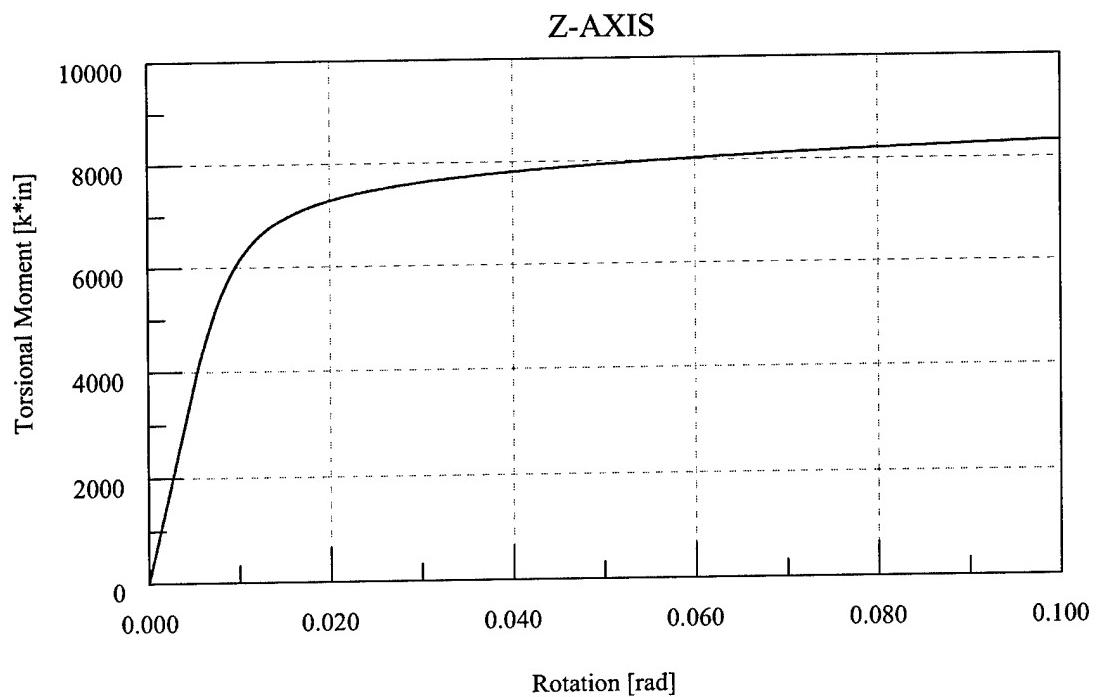


Figure 11.7 Torsional Moment-Rotation Response – Test Configuration 7

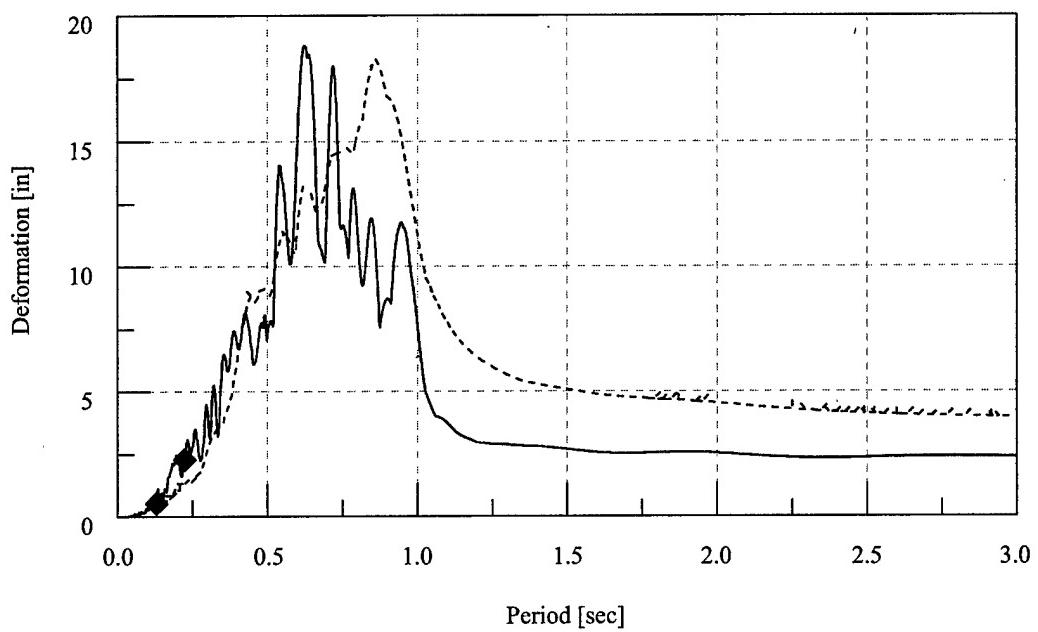
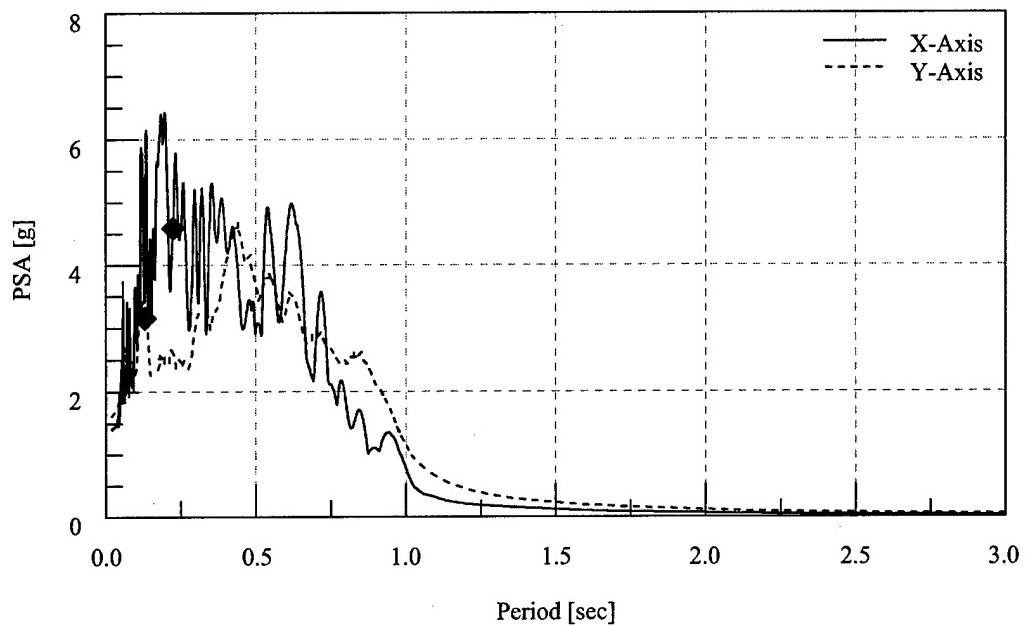


Figure 11.8 Elastic Response Spectra – EQ 41 – 100% X-Axis 75% Y-Axis Imperial Valley Ground Motion

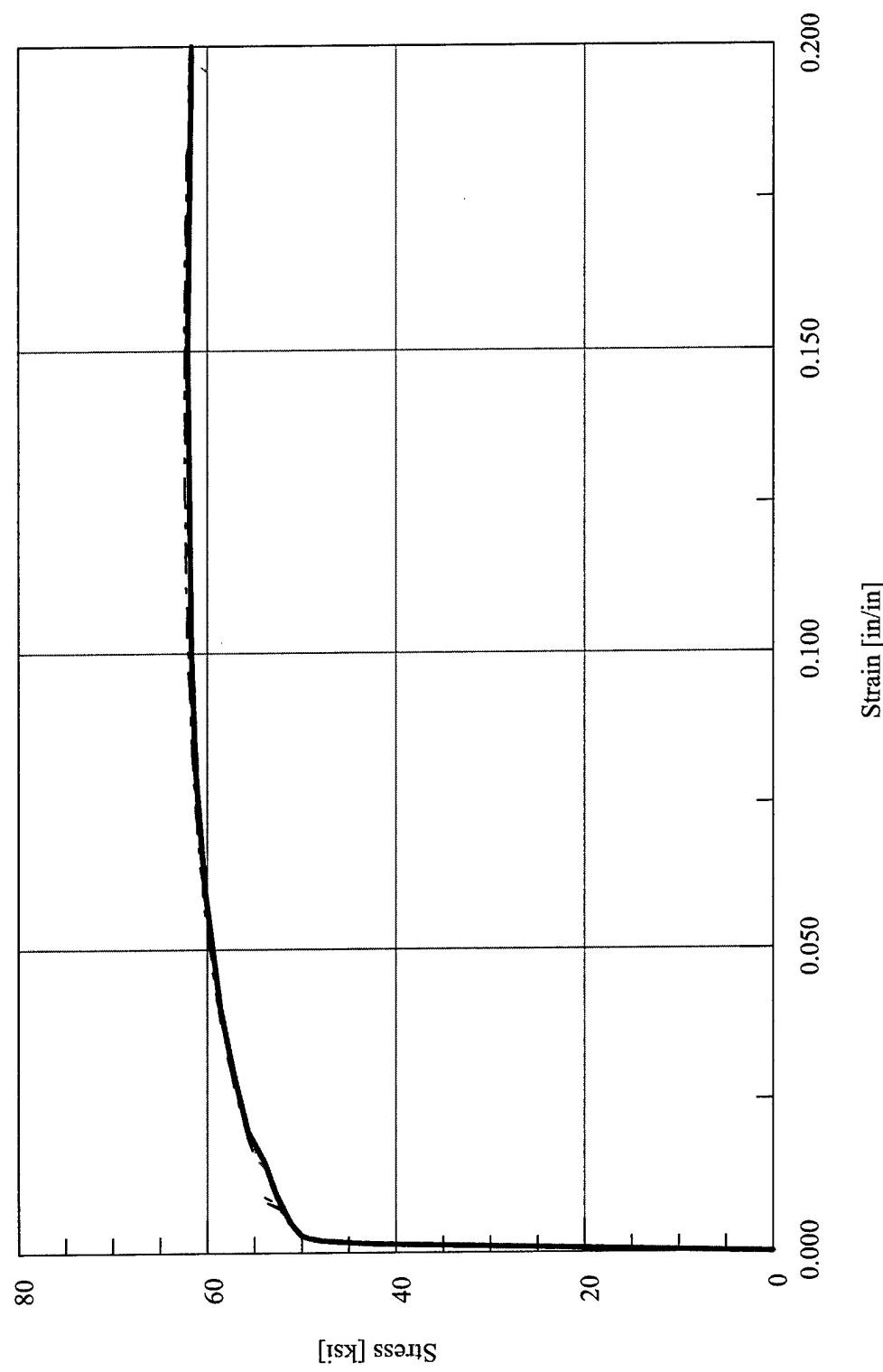


Figure 11.9 Abaqus Stress vs. Strain Finite Element Material Model Definition – S" Standard Columns – Test Configuration 7

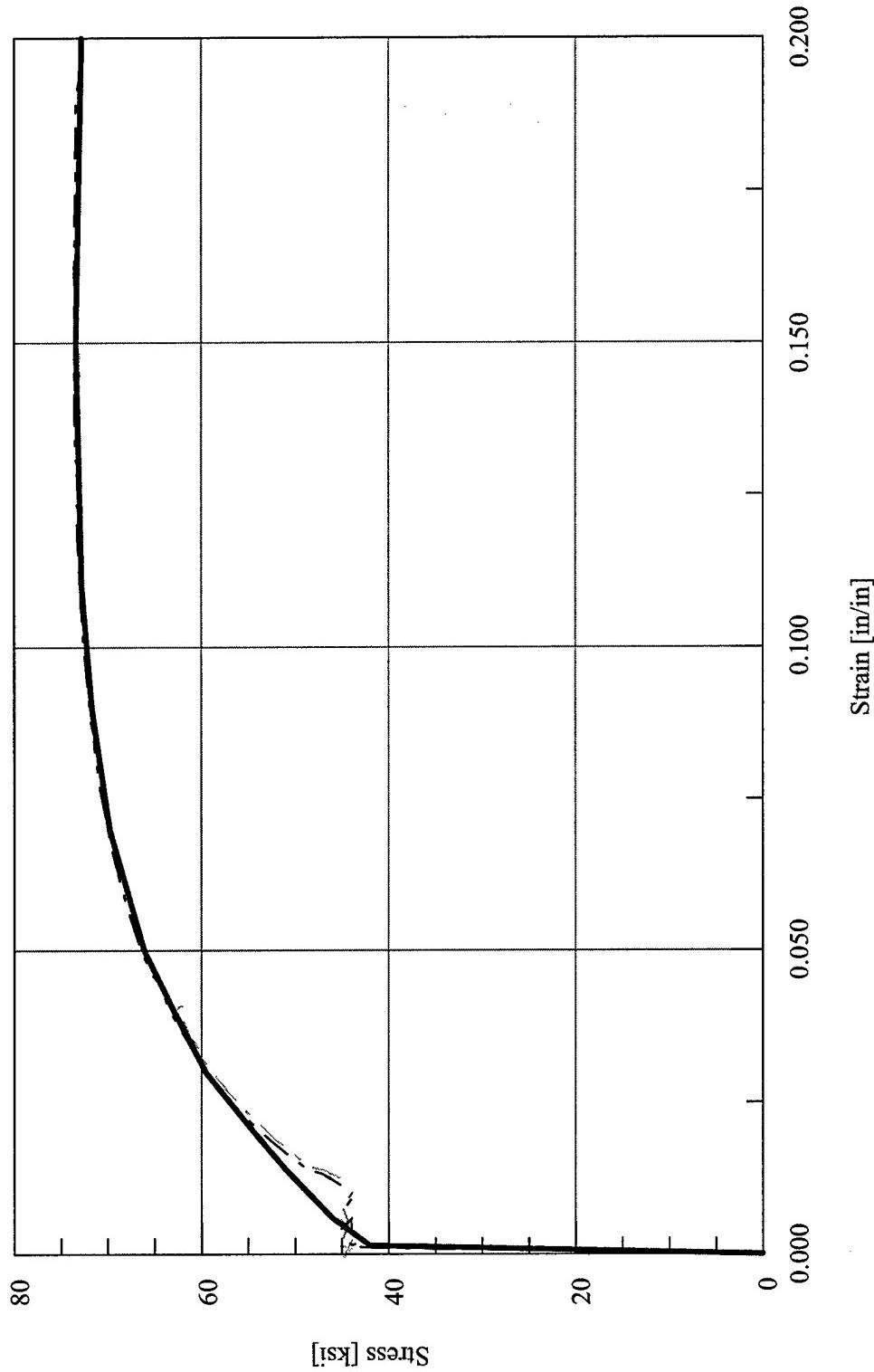


Figure 11.10 Abaqus Stress vs. Strain Finite Element Material Model Definition – 4" Double Extra-Strong Columns – Test Configuration 7

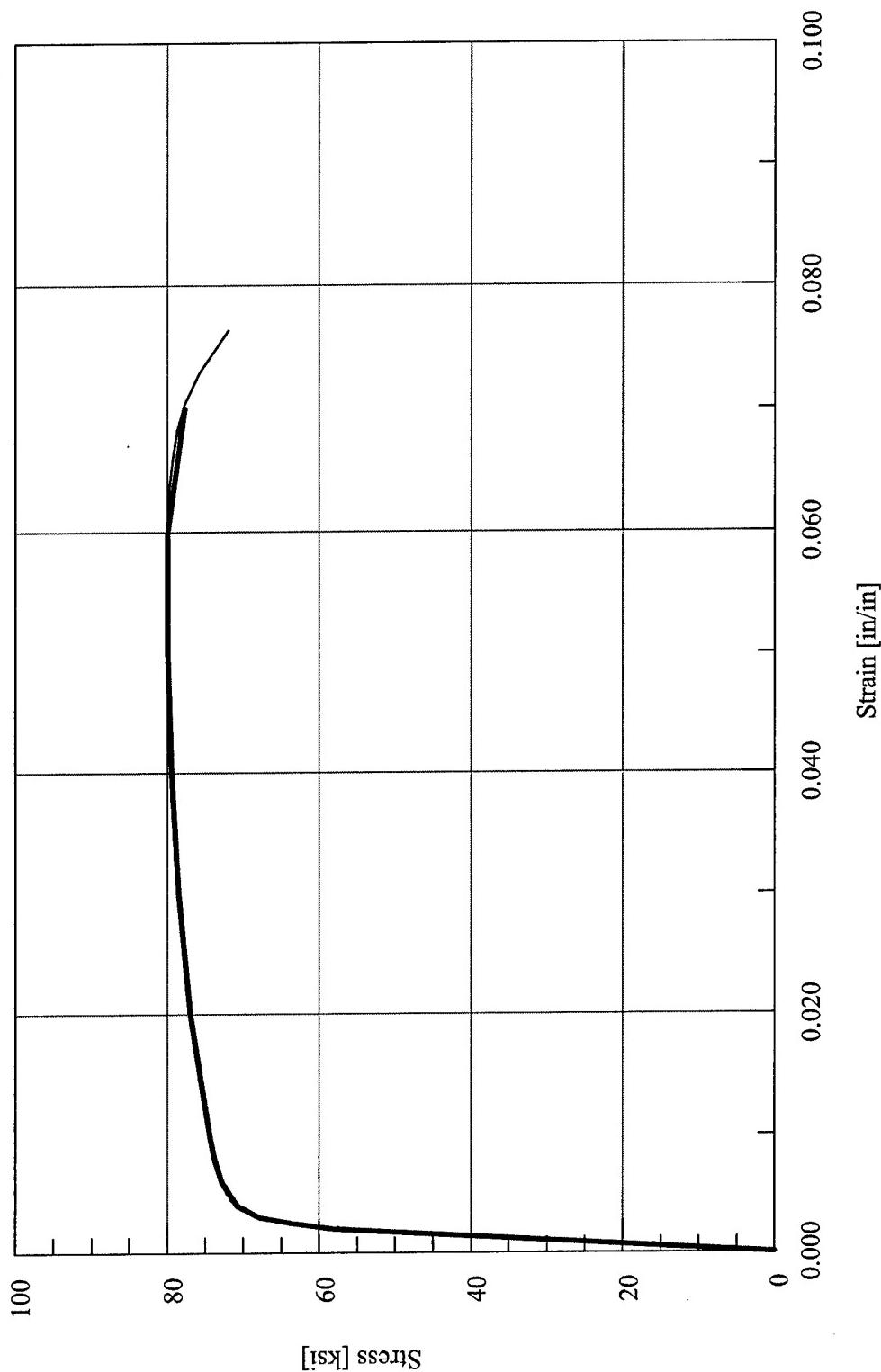


Figure 11.11 Abaqus Stress vs. Strain Analytical Material Model Definition – Diagonal Bracing – Test Configuration 7

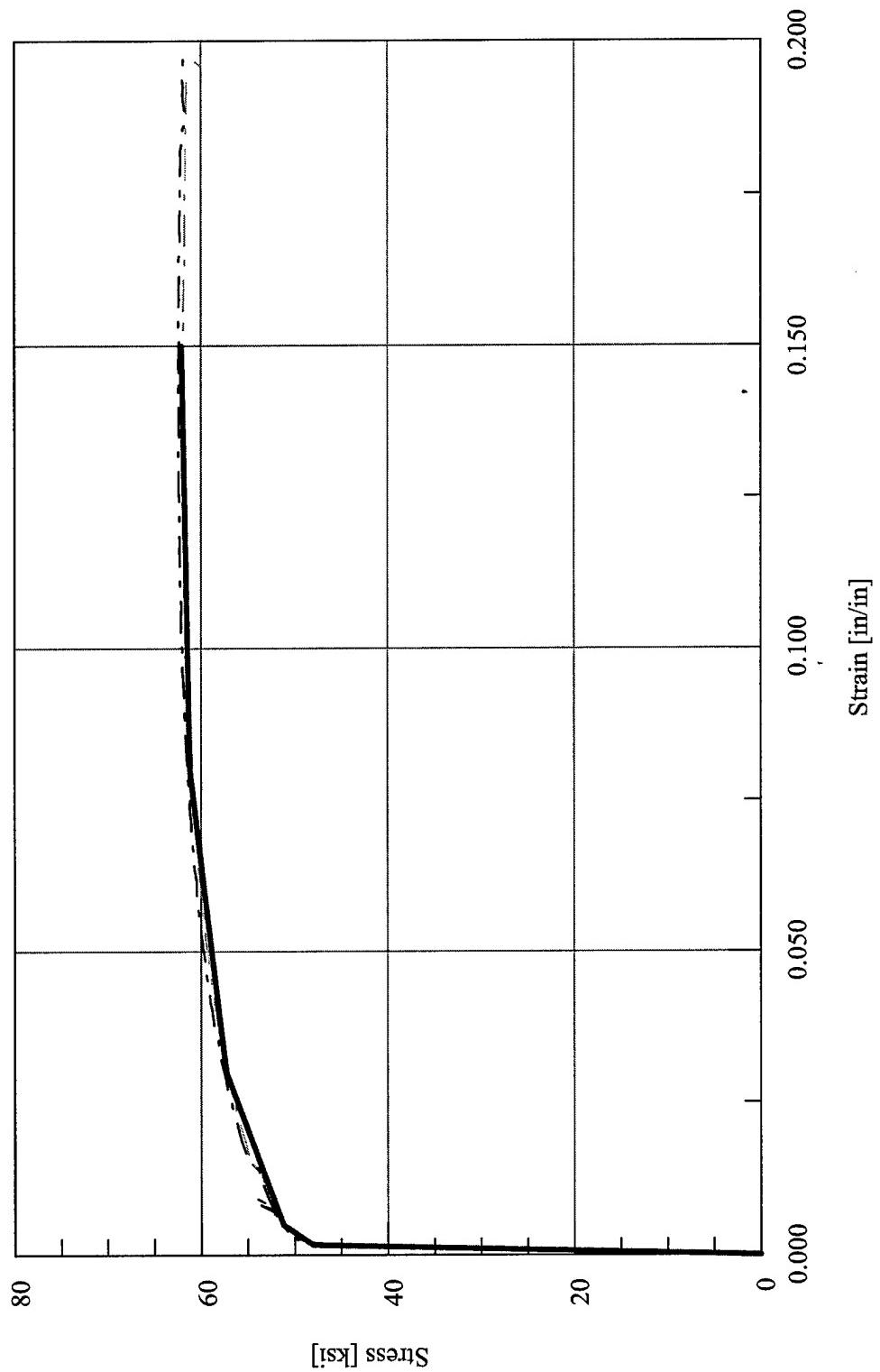


Figure 11.12 Drain-3DX Stress vs. Strain Finite Element Material Model Definition – 5" Standard Columns – Test Configuration 7

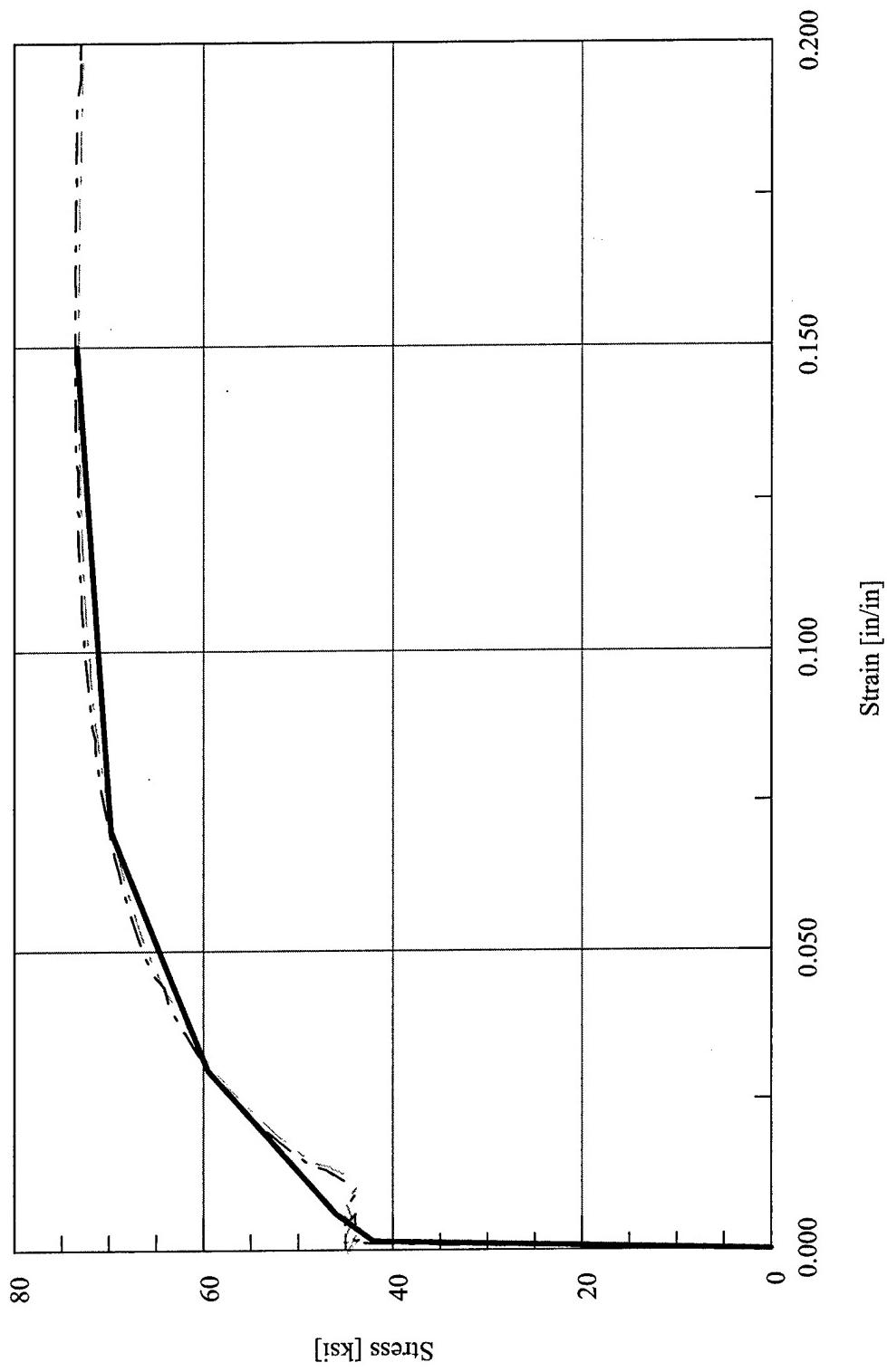


Figure 11.13 Drain-3DX Stress vs. Strain Finite Element Material Model Definition – 4" Double Extra-Strong Columns – Test Configuration 7

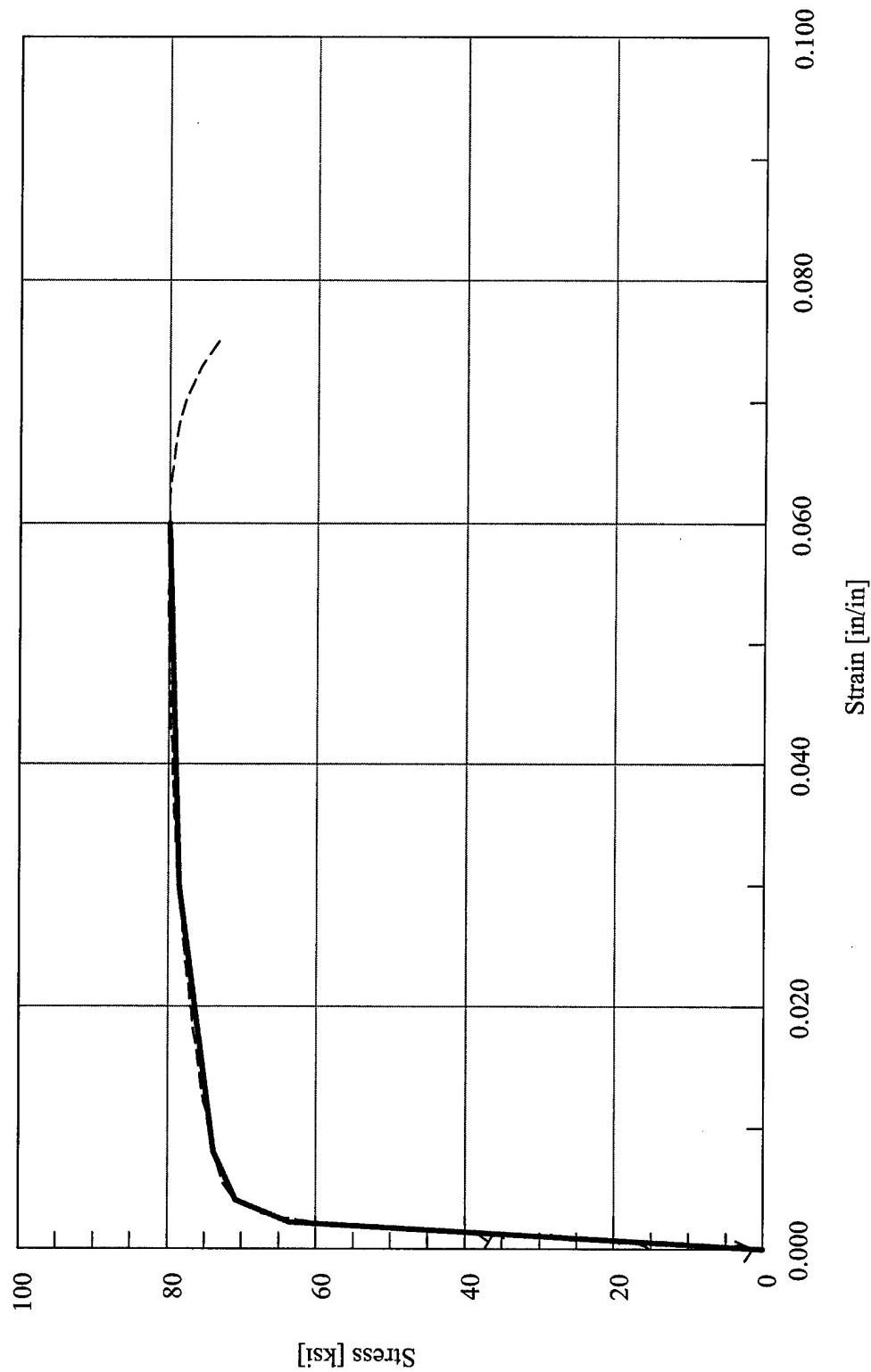


Figure 11.14 Drain-3DX Stress vs. Strain Analytical Material Model Definition – Diagonal Bracing – Test Configuration 7

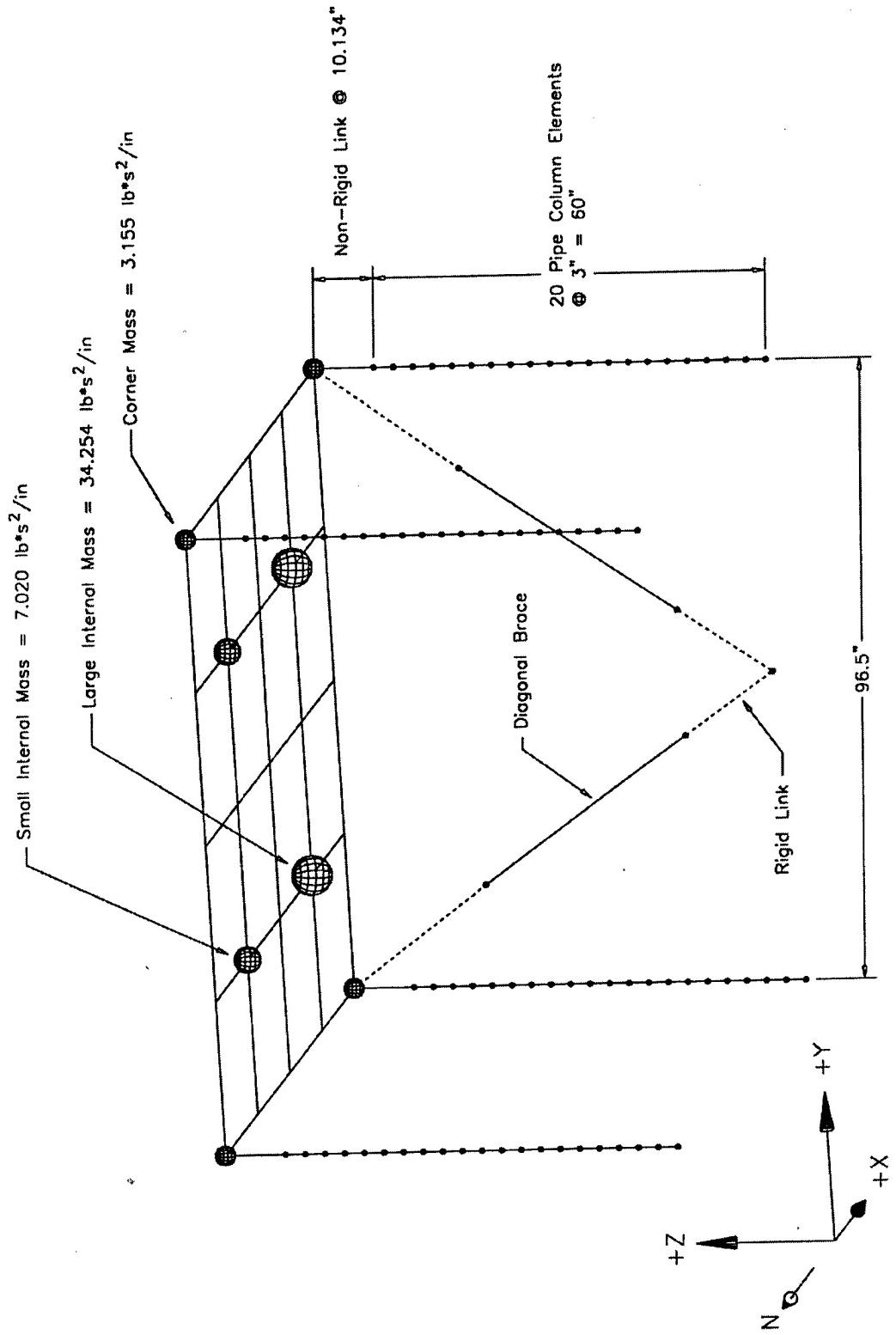


Figure 11.15 Abaqus Finite Element Model for Test Configuration 7

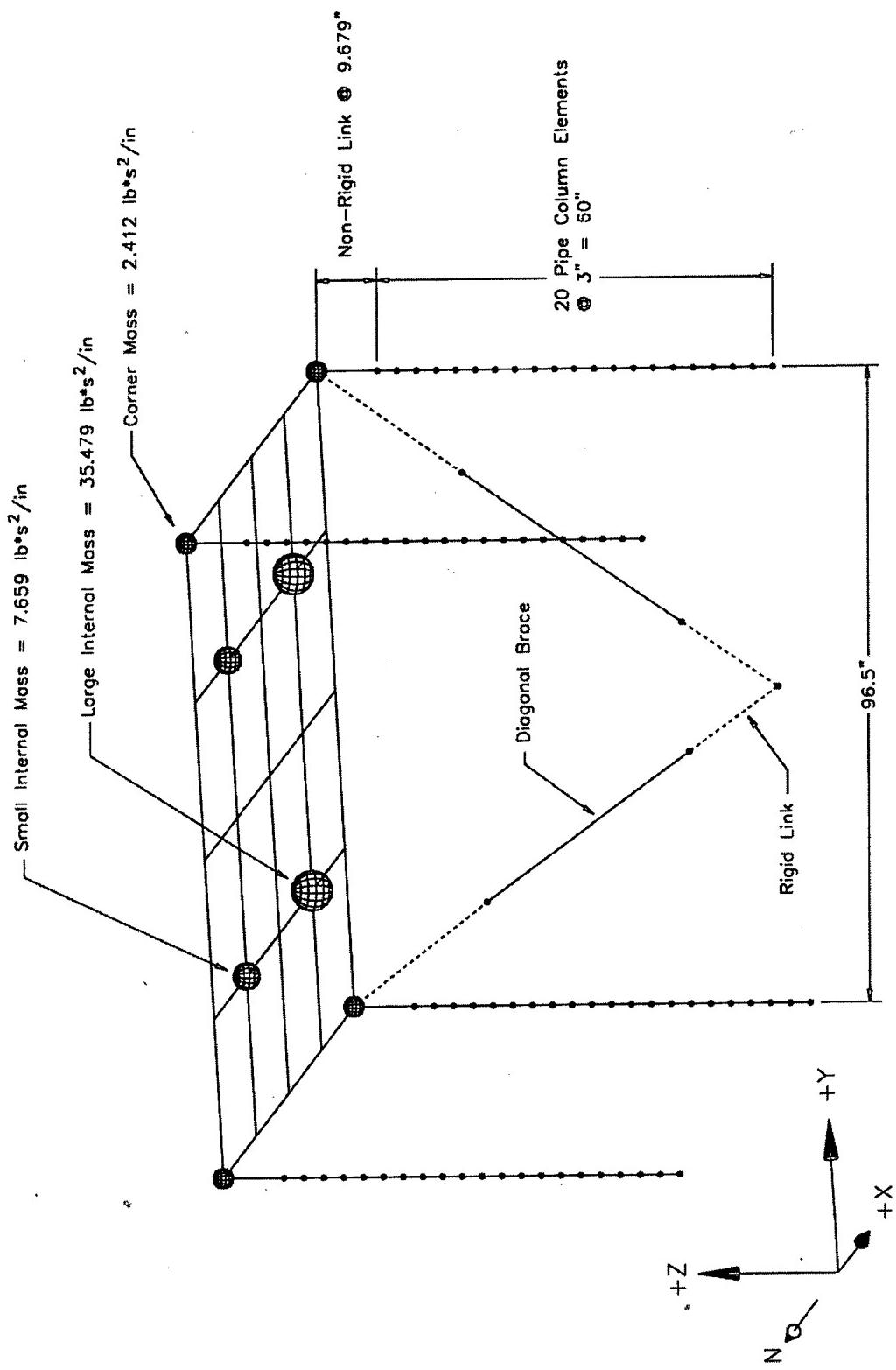


Figure 11.16 Drain-3DX Finite Element Model for Test Configuration

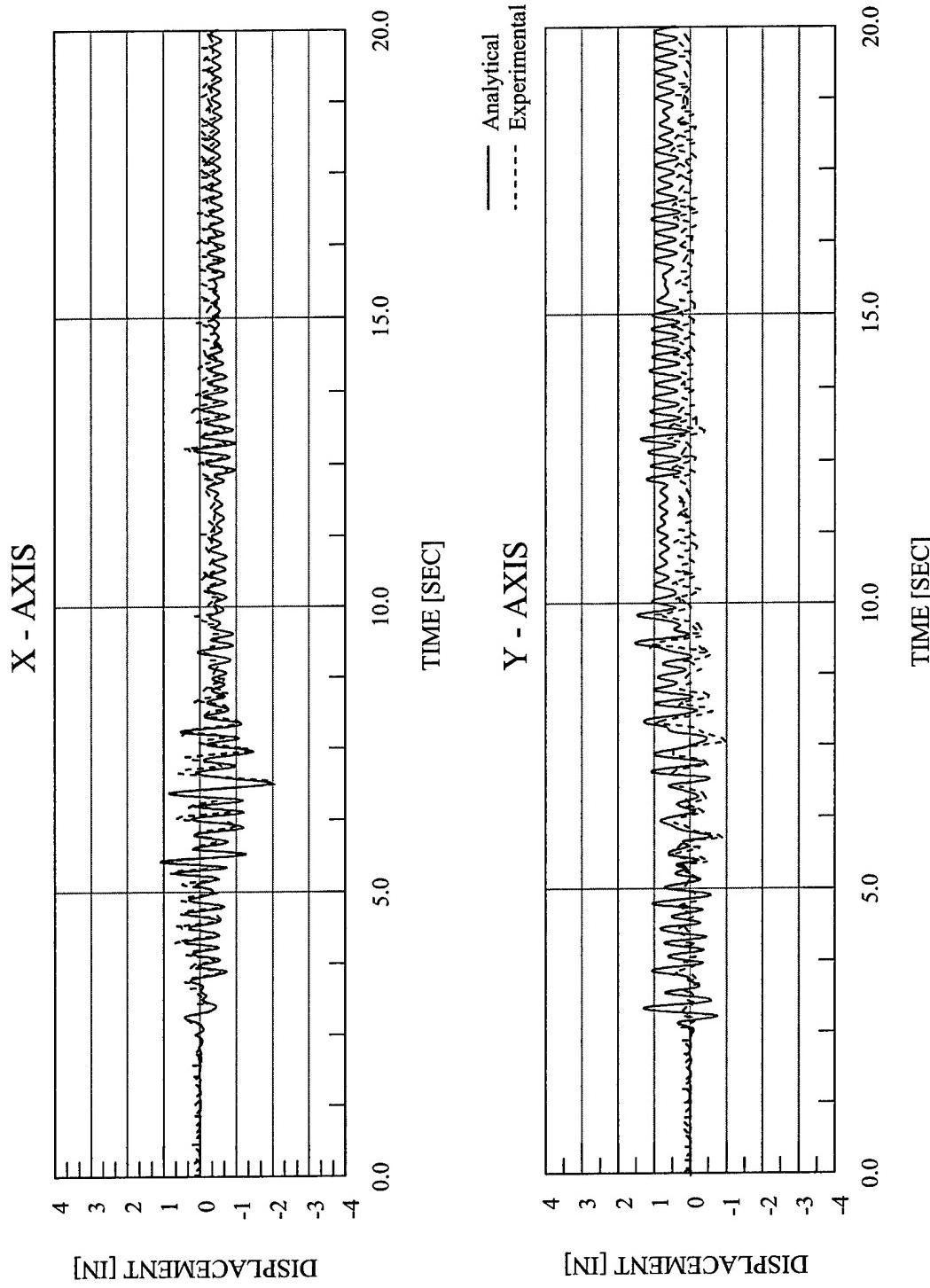


Figure 11.17 Abacus Analytical Displacement vs. Time – EQ 41 – 100% X-Axis 75% Y-Axis Imperial Valley

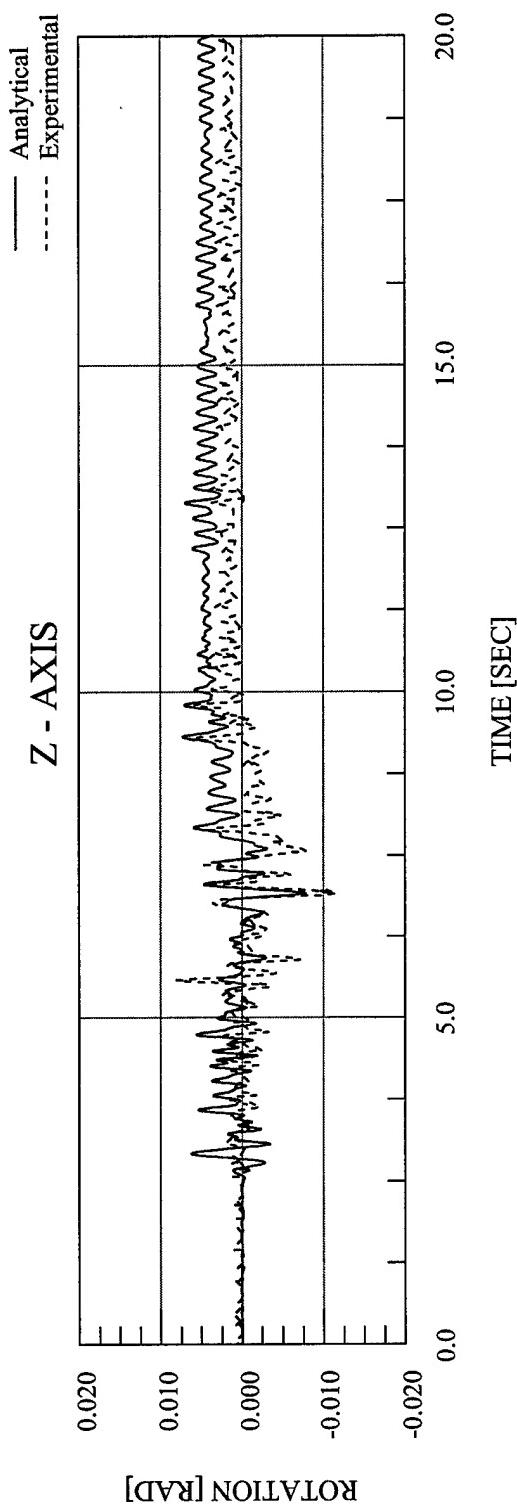


Figure 11.18 Abaqus Analytical Rotation vs. Time – EQ 41 – 100% X-Axis 75% Y-Axis Imperial Valley

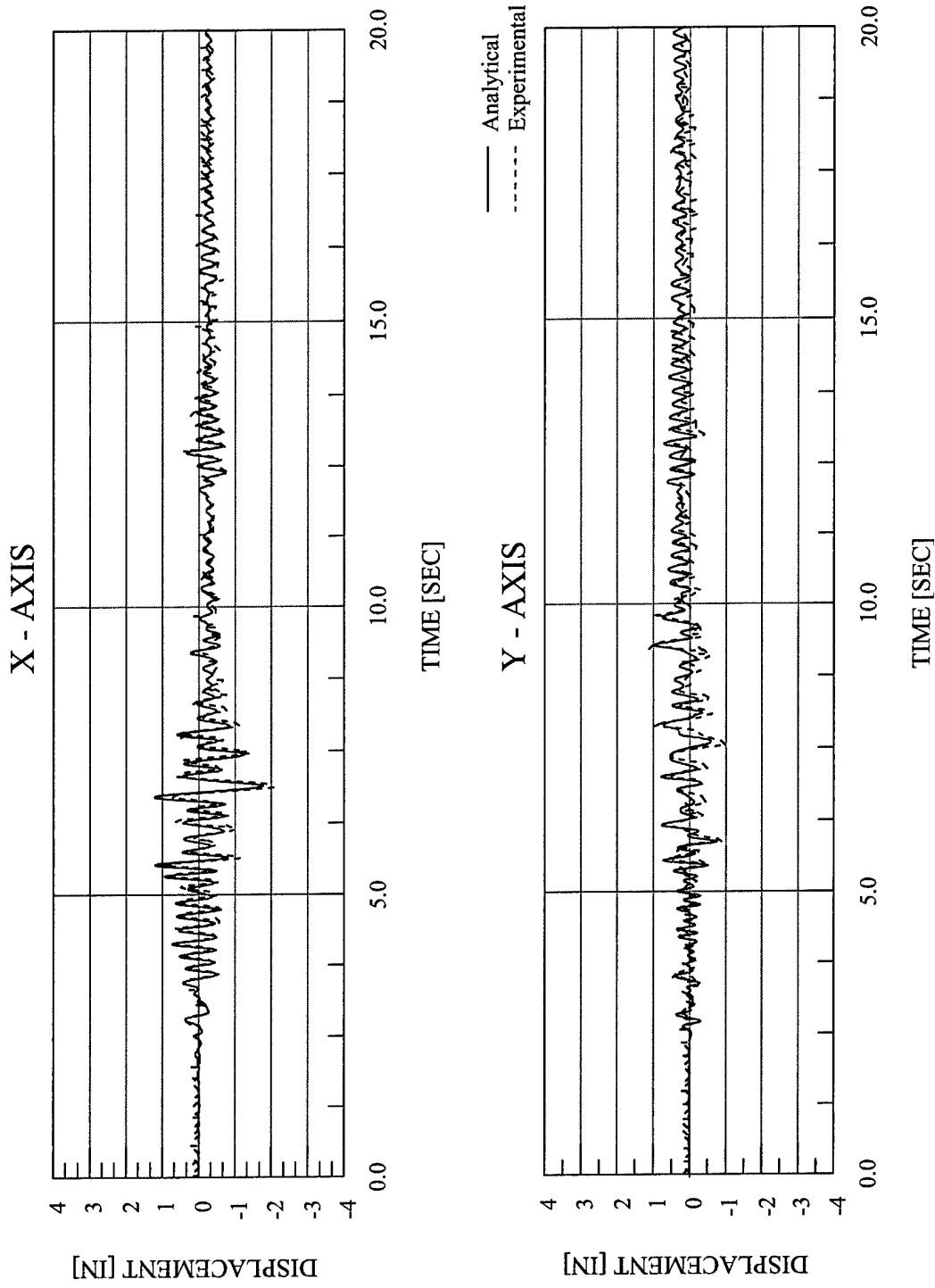


Figure 11.19 Drain-3DX Analytical Displacement vs. Time – EQ 41 – 100% X-Axis 75% Y-Axis Imperial Valley

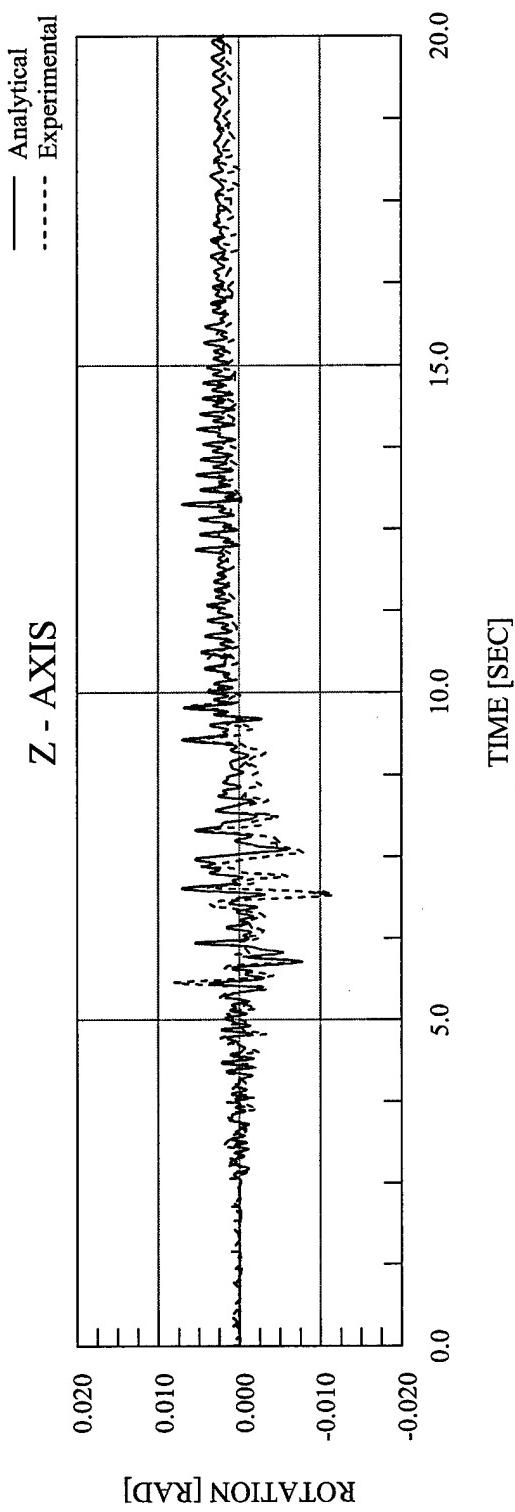


Figure 11.20 Drain-3DX Analytical Rotation vs. Time – EQ 41 – 100% X-Axis 75% Y-Axis Imperial Valley

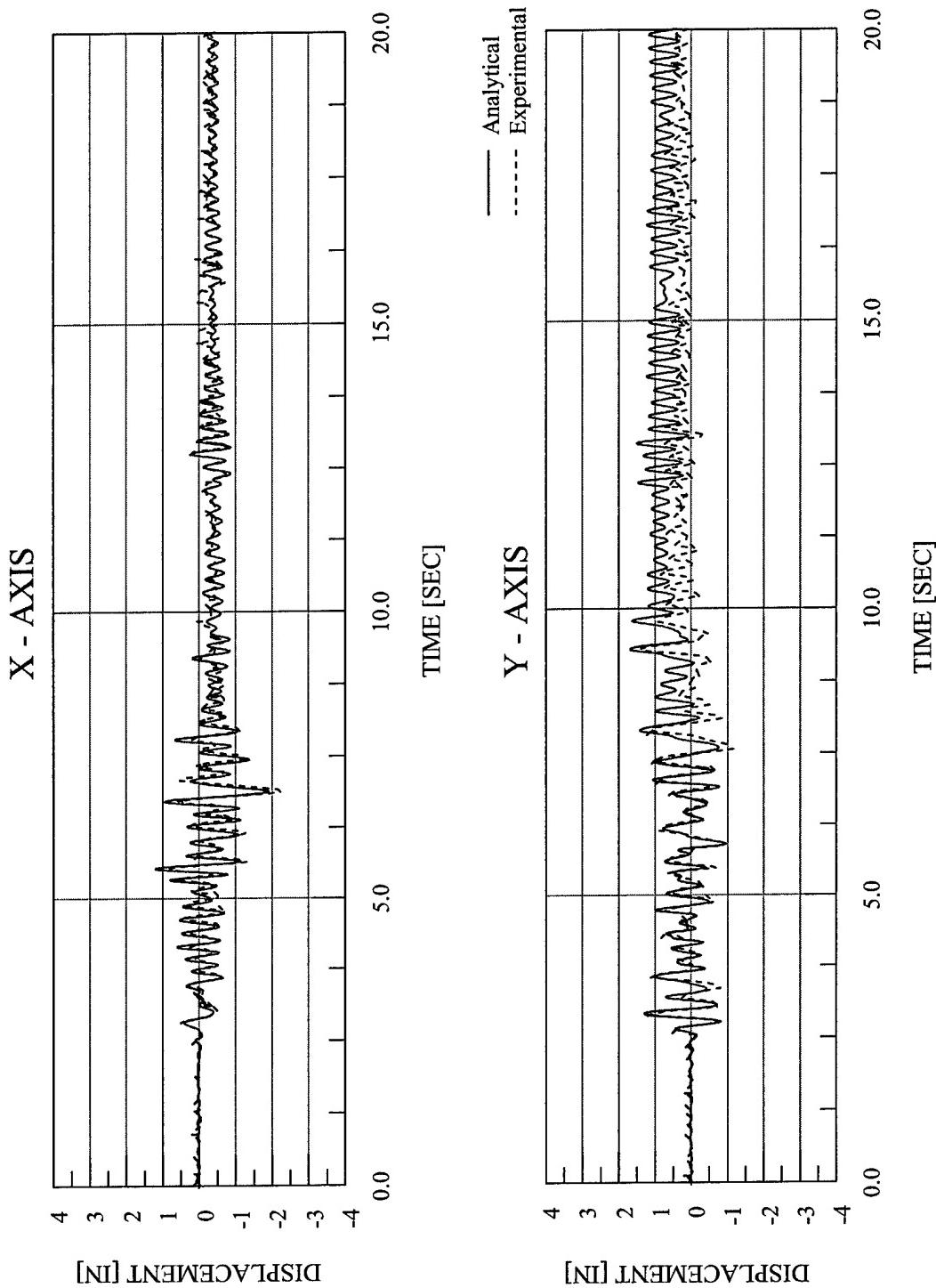


Figure 11.21 Abaqus Analytical Displacement vs. Time – EQ 42 – 100% X-Axis 85% Y-Axis Imperial Valley

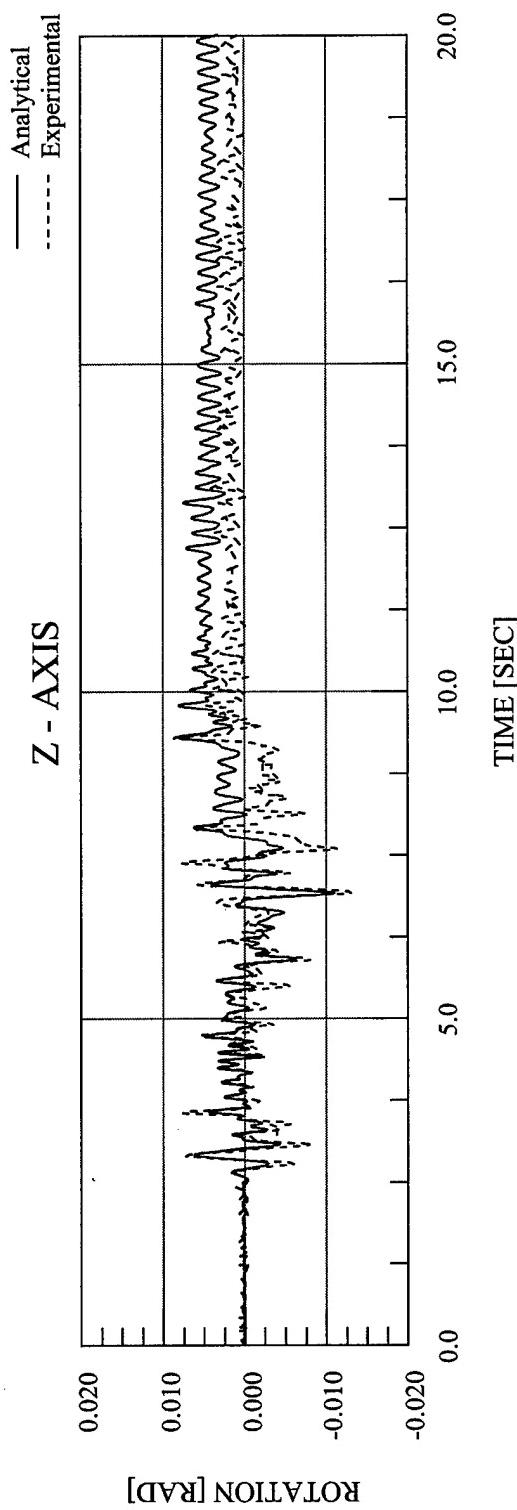


Figure 11.22 Abaqus Analytical Rotation vs. Time – EQ 42 – 100% X-Axis 85% Y-Axis Imperial Valley

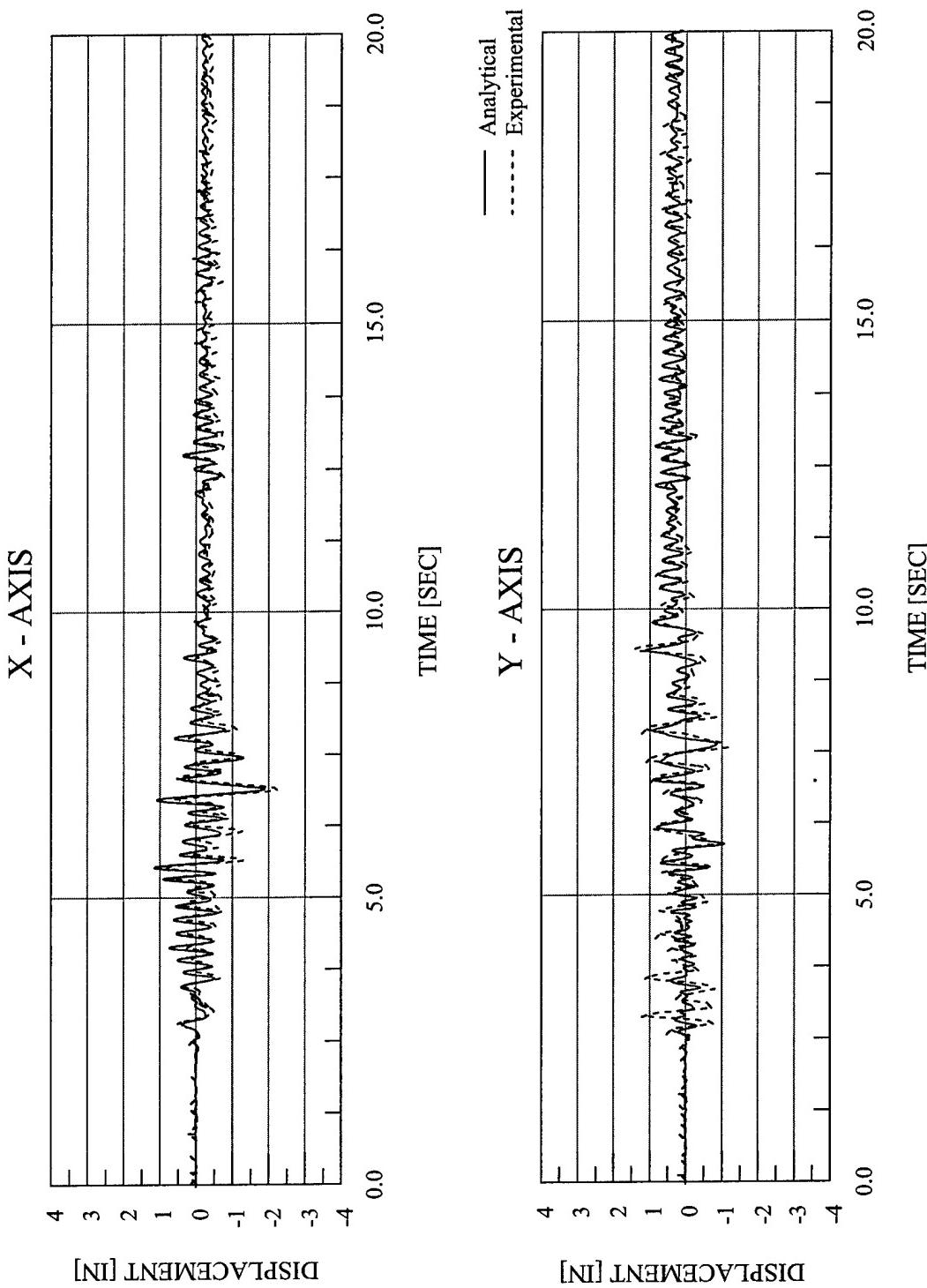


Figure 11.23 Drain-3DX Analytical Displacement vs. Time – EQ 42 – 100% X-Axis 85% Y-Axis Imperial Valley

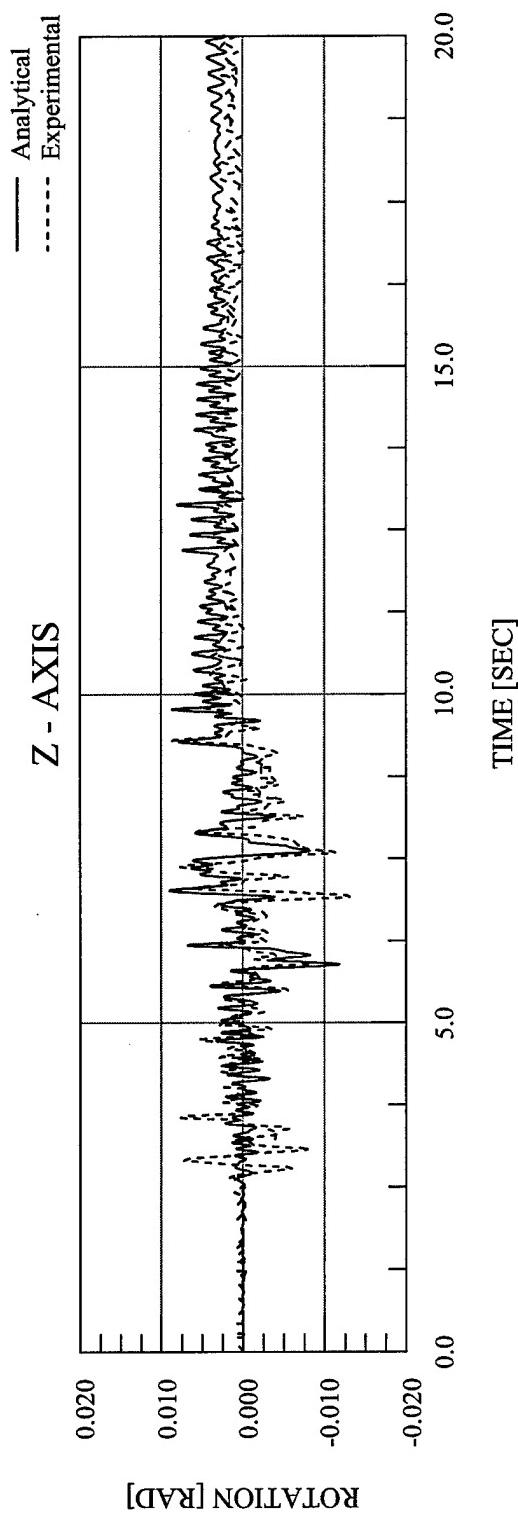


Figure 11.24 Drain-3DX Analytical Rotation vs. Time – EQ 42 – 100% X-Axis 85% Y-Axis Imperial Valley

CHAPTER 12

APPLICABILITY OF ANALYTICAL RESULTS

Despite the good agreement, in most cases, between the analytical response and the experimental response, the finite element models used in these analyses must be examined for their degree of applicability to models that would typically be used during design. Four specific elements of the finite element models used are examined: the Non-Rigid Links, the column and concentric bracing material behavior, the material damping, the exclusion of accidental eccentricity, and the length of the concentric bracing. In an effort to quantify the impact, if any, of these elements on the predicted response in a design situation, a series of finite element analyses using Drain-3DX was performed as discussed below.

In creating the finite element models used in both the Abaqus and Drain-3DX analyses, Non-Rigid Links were incorporated into the model to connect the top of the 60-inch column sections to the corners of the diaphragm. As explained in Chapter 3, the Non-Rigid Links were used to allow the columns in the finite element model to have a length of 60 inches while allowing the diaphragm to be placed at the height of the actual center of mass in the structure. Further, the cross-sectional dimensions of the Non-Rigid Links were chosen for each Test Configuration such that the translational modal frequencies of the finite element models matched the measured modal frequencies of the actual structure. The rotational modal frequency was also “tuned” by altering the rotational mass moment of inertia of the model, in conjunction with the modification of the Non-Rigid Links’ properties. In a design situation, the actual modal frequencies of the structure would not be known in advance when the response predictions were being made. The rotational moment of inertia would be based on the known geometry of the structure, and two likely design alternatives to the “tuned” Non-Rigid Links in the finite element model would be: first, extending the columns to the height of the diaphragm, and second, incorporating elastic Non-Rigid Links with some pre-determined cross section. Both options are investigated here. For the first case, whichever type of column is used in a particular Configuration, the columns will be extended to reach the height of the diaphragm. This has the effect of changing the column length, and subsequently the amount of material able to deform inelastically, from 60 inches in each Configuration to between 67.5 inches and 70.1 inches, depending on the particular Configuration. For the second case, elastic Non-Rigid Links were used with twice the stiffness of the respective columns in each Configuration. It was felt that using Rigid Links was not appropriate to model this structure, and would result in an analytical model that was too stiff. Choosing Links with stiffnesses equal to twice the column stiffnesses, as opposed to three or

four times the column stiffnesses, was an arbitrary decision. However, it was important to be consistent throughout all of the Configurations once a choice was made.

In defining the material properties of the columns, tension tests were performed with steel coupons to determine the actual stress-strain behavior of each of the column types. In all, five different batches of columns were used for Configurations 1 – 8: the 4" Extra-Strong Columns used in Configurations 1 – 4; the 5" Standard Columns used in Configurations 5 and 7; the 4" Double Extra-Strong Columns used in Configurations 5 and 7; the 4" Extra-Strong Columns used in Configuration 6; and the 4" Extra-Strong Columns used in Configuration 8. Despite the fact that steel in each of these column groups was specified to the manufacturer as A36 steel, each batch had noticeably different stress-strain properties. As can be seen in Figures 12.1 – 12.5, the yield stress, ultimate stress, and general post-yield behavior varied significantly between the five batches of columns. The steel for the diagonal bracing used in Configurations 6 & 7 was specified to the manufacturer as Grade 50 steel, with a yield stress of 50 ksi and an ultimate stress of 65 ksi. As can be seen in Figure 12.6, the actual yield stress and ultimate stress were significantly greater. In a design situation, the actual material properties would not be known in advance to the designer, and most likely idealized properties would be assumed. Two likely design assumptions for the stress-strain behavior would be an elastic-perfectly plastic material model, with no material hardening, or an elastic-plastic model in which material hardening was designated. These two material models are also shown in Figures 12.1 – 12.6, and are the two material models investigated here. The columns with A36 steel are assumed to have a yield stress of 36 ksi and an ultimate stress of 58 ksi. The material model that includes hardening is assumed to have linear post-yield behavior, with the ultimate stress being achieved at a strain of 20%. The diagonal bracing with Grade 50 steel are assumed to have a yield stress of 50 ksi and an ultimate stress of 65 ksi, with the ultimate stress again being achieved at a strain of 20%.

In defining the material or modal damping in the finite element models, the amount of damping provided to each model was chosen to try to best match the analytical elastic responses for each Configuration to the experimental elastic responses. The limitations of both Abaqus and Drain-3DX in defining the damping for a structure in the X and Y directions independently have been discussed previously. As such, even with an effort to “optimize” the damping, the analytical elastic responses rarely matched the experimental responses along both axes. Regardless, in a design situation, the measured structural damping properties would not be known during the design process, and some amount of damping would be designated. For the Drain-3DX models used in this “design applicability” investigation, the damping is assumed to be 0.5%, which would be a representative value for a steel structure’s framework, absent

any walls and floors, etc. As discussed previously, this relatively small amount of damping should have virtually no impact on the inelastic response of the model.

In Configurations 6 and 7, diagonal bracing was added to the structure in the Y direction. As outlined previously, each brace was welded to a bottom gusset plate and a top gusset plate. The bottom gusset plate was rigidly attached to the shaketable, and effectively moved with the “ground”, and the top gusset plate was rigidly attached to the structure. The dimensions of the gusset plates were very large relative to the cross-sectional dimensions of the braces, and thus were assumed to be rigid elements in the analytical models. The clear-span length of each of the braces was roughly 43 inches. However, in creating the analytical models for Abaqus and Drain-3DX, the length of each diagonal brace was modified in order to “tune” the analytical model to match the Y-Axis modal frequency of the test structure. The “effective lengths” of the braces in Configurations 6 and 7 were noticeably larger than the actual clear-span length of 43 inches. As was discussed with the Non-Rigid Links, the actual modal frequencies of the structure would not be known during design. Noting that the diagonal bracing was welded to the gusset plates, and that the welds were continuous to the edge of each gusset plate, a typical design assumption would take the “effective length” of each brace as the clear-span length plus one width on each brace end. The brace widths vary, with the largest being 1-7/8”. For this investigation, the “effective length” was taken to be roughly 47 inches.

Thus, the primary factors being investigated here are the impact of the material model, the links connecting the column tops to the diaphragm, and the “effective length” of the diagonal bracing. With regard to the modal frequencies of the analytical models, the Non-Rigid Links and the diagonal bracing are the two factors that would have an influence. As stated above, with regard to the Non-Rigid Links, Case 1 is taken with the columns extending up to the diaphragm and Case 2 is taken with the Non-Rigid Links having twice the stiffness of the columns and responding elastically. Shown in Table 12.1 are the experimentally measured modal frequencies, along with the modal frequencies for Cases 1 and 2. It appears that the frequencies for Case 2, with Non-Rigid Links having twice the stiffness of the columns, are somewhat closer to the actual modal frequencies. However, this is not consistently true, as in a number of Configurations, the frequencies for the Case 1 analytical model are closer to the actual frequencies. Overall, the modal frequencies for the Case 1 models are, on average, 7.4% different from the measured frequencies, while the Case 2 models are 5.0% different. This result is not surprising, as on the actual test structure, the region between the column tops and the vertical center-of-mass of the diaphragm clearly is more stiff than the columns. The height of this region, in proportion to the column height, is greater for the test structure than would be for an actual building. Thus, for an actual building,

an analytical model using columns extended to the mass center of each floor would likely result in modal frequencies somewhat more accurate than found here. Both Case 1 and Case 2 analytical models have Y-Axis modal frequencies significantly larger than the actual frequencies for Configurations 6 and 7, roughly 12% and 22% different, respectively, in which lateral bracing is an element of the structure in the Y direction.

The first set of analytical simulations performed to evaluate the impact of the aforementioned design assumptions on the ability to accurately predict the structural response are shown in Table 12.2. This set consists of two elastic biaxial simulations, one with the Case 1 model and one with the Case 2 model, from five unique Configurations. The Configuration descriptions, along with the peak displacements and rotations for the experimental test structure, the Case 1 model, and the Case 2 model, are shown in Table 12.2. For the Case 1 model, the mean error for the displacement predictions was 33.0%, with a median error of 32.7%. The Case 2 model had a mean displacement error of 28.1% and a median error of 28.0%. The results for the Case 2 model were slightly more accurate, which parallels the modal frequencies for the Case 2 model being slightly closer to the actual frequencies. The Drain-3DX displacement predictions for the “tuned” model, reported previously, were in error by an average of 13.1%. In comparison to the “tuned” model, the displacement predictions using the Case 1 model and Case 2 model are equally inaccurate. For the Case 1 model, the mean error for the rotational predictions was 43.1%, with a median error of 43.1%. The Case 2 models had a mean rotational error of 58.8%, with a median error of 60.7%. The average error for the “tuned” model was 44.1%. The Case 1 model was equally accurate to the “tuned” model in predicting the peak rotations, while the Case 2 model was somewhat less accurate. Thus, the results here indicate that, overall, small differences between the design and actual modal frequencies of a structure result in larger differences between the predicted and actual response. Consistent with the elastic displacement predictions using the “tuned” model, no particular Configuration proved more difficult to predict accurately. Also consistent with the “tuned” model, predicting the peak elastic rotations for Configurations 5 and 6 proved more difficult than for Configurations 3 and 4, and the peak rotations for Configurations 5 and 6 were consistently underestimated. Overall, using the Case 1 or Case 2 analytical model, a “design” model, resulted in peak elastic response predictions that were roughly 17% less accurate, with an overall mean error of 36%, than using the “tuned” elastic analytical model, with an overall error of 19%.

The second set of analytical simulations performed to assess the applicability of the “tuned” analytical model results are shown in Table 12.3. This set consists of two inelastic biaxial simulations, one with the Case 1 model and one with the Case 2 model, from seven of the eight Configurations. Each of these

models in this set of simulations features a material model determined experimentally by coupon tension tests. The Configuration descriptions, along with the peak inelastic displacements and rotations for the test structure, the Case 1 model, and the Case 2 model, are shown in Table 12.3. For the Case 1 model, the mean error for the inelastic displacement predictions was 42.8%, with a median error of 39.0%. The Case 2 model had a mean displacement error of 19.6%, with a median error of 11.1%. As reported previously, the mean error for the Drain-3DX “tuned” model was 15.2%. Thus, the Case 2 model is, on average, significantly more accurate than the Case 1 model in predicting the peak inelastic displacements, and is also nearly as accurate as the “tuned” model. For the Case 1 model, the mean error for the inelastic rotational predictions was 32.2%, with a median error of 16.0%. The Case 2 models had a mean rotational error of 33.3%, with a median error of 29.8%. The average error for the “tuned” model was 28.1%. Thus, it appears that there is little difference in the ability of the Case 1 model, Case 2 model, or “tuned” model to predict peak inelastic rotations. Consistent with the results for the “tuned” model, the peak inelastic rotations for Configurations 5, 6, and 7 proved to be more difficult to predict overall for both the Case 1 and Case 2 models. Overall, the Case 2 analytical model proved to be only 5% less accurate, with an overall mean error of 24%, than the “tuned” model, with an overall error of 19%, while the Case 1 model was 20% less accurate, with an overall error of 39%. This is a significantly different result than when analyzing elastic response. The primary difference between these two models for inelastic response is that the Case 2 models have 60 inches of material at each column that can deform inelastically, while the Case 1 models have between 67.5 and 70.1 inches of material, depending on the configuration, that can deform inelastically. The impact of the extra inelastic material is also apparent by the fact that the Case 1 models generally overestimated the peak displacements. This appears to indicate that using an analytical model which accurately models the length of each column that can behave inelastically is more critical than accurately modeling the modal frequencies when predicting inelastic response.

Also briefly examined in this set of simulations was the impact of the “effective length” of the concentric bracing used in Configurations 6 and 7. It was reported previously that for both Case 1 and Case 2 analytical models, the Y-Axis modal frequency was significantly larger than the actual Y-Axis modal frequency for the test structure. In order to lower the Y-Axis frequency in the Case 2 analytical model, the length of each of the diagonal braces in the analytical model was increased beyond the design length of 47 inches to approximately 65 inches. This brought the Y-Axis modal frequency to within less than 1% of the actual measured value. The effect on the elastic Y-Axis peak displacement was significant, decreasing the error in the prediction from 45% to 24%. However, the effect on the inelastic peak response quantities was insignificant.

The third set of analytical simulations performed in this sequence are shown in Table 12.4. This set consists of two inelastic biaxial simulations using the Case 2 model, one with a material model that is elastic – plastic with linear strain hardening, and one with a material model that is elastic – perfectly plastic. The specifics of these two material models were discussed previously in this section. The Configuration descriptions, along with the peak inelastic displacements and rotations for the test structure, the Case 2 model with Elastic – Plastic Hardening material model, and the Case 2 model with Elastic – Perfectly Plastic material model, are shown in Table 12.4. The two aforementioned design material models, along with the material models based on experimental coupon tension tests, are again shown in Figures 12.1 – 12.6 for the five batches of columns and the diagonal bracing. From these figures, it is evident that these simplified “design” models not only behave differently during strain hardening than the actual material, but in almost every case the assumed yield stress and ultimate stress, 36 ksi and 58 ksi in this case, are noticeably different than the actual yield and ultimate stress. For the Elastic – Plastic Hardening model, the mean error for the inelastic peak displacement predictions was 29.0%, with a median error of 16.6%. For the Elastic – Perfectly Plastic model, the mean error for the displacement predictions was 43.0%, with a median error of 30.2%. Thus, the addition of even a simple strain-hardening model to an analytical model yields significant additional accuracy in predicting the displacement response. The mean rotational error with the Elastic – Plastic Hardening model is 22.8%, with a median error of 19.0%. For the Elastic – Perfectly Plastic model, the mean error for the rotational predictions was 23.8%, with a median error of 8.7%. Thus, the predicted rotational response appears to be equally accurate with either material model. The overall mean error in the inelastic response predictions using the Elastic – Plastic Hardening material model with the Case 2 model was 26.9%, while the overall error using the Elastic – Perfectly Plastic material model was 36.6%. In comparison, the mean error for the original “tuned” model was 19.4%, and the mean error for the Case 2 model with the experimental tension test material model was 24.1%. Thus, using an analytical model with the design assumptions of elastic Non-Rigid Links having twice the column stiffness and a simple material model with some degree of post-yield hardening, the inelastic response can be predicted with only an additional 7.5% error as compared with an analytical model “tuned” to the experimentally determined structural properties.

Overall, the rotations proved consistently more difficult to predict than the displacements. The rotations became more difficult to predict for configurations with more complicated force-resisting systems, for both elastic and inelastic response. The displacement response did not prove to be more difficult to predict for the more complicated configurations. Overall, the degree of eccentricity of the structure had

less of an impact on the accuracy of response predictions than did the complexity of the force-resisting system. The results found by using a “tuned” analytical model proved to be consistent with results using a more simplified analytical model with “design” assumptions. When analyzing elastic response, any differences in the modal frequencies of the analytical model and actual structure can produce larger errors in the predicted response. When analyzing inelastic response, differences in the modal frequencies become less important, while the amount of the structure able to deform plastically becomes more important to model accurately. Changing the “effective length” of the diagonal bracing altered the modal frequency in the direction of the bracing, and as a result had a noticeable impact on the elastic peak response. However, changing the length of the bracing had no significant impact on the inelastic response. Using an analytical model with some degree of strain hardening results in response predictions that are significantly more accurate than an analytical model with an elastic – perfectly plastic material model. When performing inelastic analysis, it is recommended that a simple elastic-plastic material model with a linear strain hardening segment is satisfactory to give reasonably accurate response predictions. In addition, it is recommended that the regions of the actual structure that are able to deform inelastically be the only parts in the analytical model that are capable of deforming inelastically.

Configuration No.	Configuration Description	Experimental Modal Frequencies [Hz]			Case 1 Modal Frequencies [Hz]			Case 2 Modal Frequencies [Hz]		
		X	Y	θ	X	Y	θ	X	Y	θ
2	Symmetric Mass	3.589	3.454	6.450	3.280	3.280	5.840	3.566	3.566	6.352
4	$\frac{1}{2}$ Asymmetric Mass [X]	3.468	3.415	7.255	3.246	3.353	6.675	3.519	3.635	7.237
3	$\frac{1}{4}$ Asymmetric Mass	3.546	3.283	8.287	3.439	3.245	7.747	3.702	3.494	8.342
8	$\frac{1}{4}$ Asymmetric Mass	3.704	3.333	8.696	3.439	3.245	7.747	3.702	3.494	8.342
5	$\frac{1}{2}$ Asymmetric Mass [Y] Strength Asymmetry	4.348	4.255	9.091	4.201	4.068	8.470	4.551	4.405	9.182
6	$\frac{1}{2}$ Asymmetric Mass [Y] Concentric Bracing [Y] Stiffness Asymmetry [Y]	3.636	8.333	13.333	3.185	9.310	13.295	3.492	9.428	13.549
7	$\frac{1}{2}$ Asymmetric Mass [Y] Concentric Bracing [Y] Stiffness Asymmetry [Y] Strength Asymmetry [X]	4.444	7.692	11.765	3.960	9.319	13.383	4.339	9.492	13.799

Table 12.1 Modal Frequencies – Test Structure and Case 1 & 2 Analytical Models

EQ Test No.	Configuration	Model	Relative Displacement [in]			Rotation [10^{-3} rad]
			X-Axis	Y-Axis	Z-Axis	
14	25% Biaxial Symmetric Mass	Test Structure	0.482	0.354	0.703	
		Case 1 [Columns Extended to Diaphragm]	0.758	0.525	0.000	
		Case 2 [Links with Twice Column Stiffness]	0.428	0.294	0.000	
27	10% Biaxial $\frac{1}{2}$ Asymmetric Mass [X]	Test Structure	0.256	0.219	1.546	
		Case 1 [Columns Extended to Diaphragm]	0.260	0.212	1.077	
		Case 2 [Links with Twice Column Stiffness]	0.163	0.094	0.717	
22	10% Biaxial $\frac{1}{2}$ Asymmetric Mass	Test Structure	0.165	0.152	1.062	
		Case 1 [Columns Extended to Diaphragm]	0.234	0.150	1.110	
		Case 2 [Links with Twice Column Stiffness]	0.172	0.155	0.787	
32	10% Biaxial $\frac{1}{2}$ Asymmetric Mass [Y] Strength Asymmetry	Test Structure	0.212	0.065	0.588	
		Case 1 [Columns Extended to Diaphragm]	0.162	0.074	0.292	
		Case 2 [Links with Twice Column Stiffness]	0.102	0.047	0.189	
36	10% Biaxial $\frac{1}{2}$ Asymmetric Mass [Y] Concentric Bracing Stiffness Asymmetry	Test Structure	0.177	0.053	0.759	
		Case 1 [Columns Extended to Diaphragm]	0.347	0.030	0.096	
		Case 2 [Links with Twice Column Stiffness]	0.227	0.029	0.094	

Table 12.2 Analytical vs. Experimental Displacement and Rotation Response Comparison – Elastic Simulations
Analytical Models with Design Assumptions

EQ Test No.	Configuration	Non-Rigid Link Model	Relative Displacement [in]			Rotation [10^{-3} rad]
			X-Axis	Y-Axis	Z-Axis	
15	100% Biaxial Symmetric Mass	Test Structure	2.859	1.239	2.850	
		Case 1 [Columns Extended to Diaphragm]	3.203	2.275	0.794	
		Case 2 [Links with Twice Column Stiffness]	2.718	0.984	0.916	
28	100% Biaxial $\frac{1}{4}$ Asymmetric Mass [X]	Test Structure	2.529	1.292	18.260	
		Case 1 [Columns Extended to Diaphragm]	2.560	1.795	21.820	
		Case 2 [Links with Twice Column Stiffness]	2.452	1.155	17.238	
23	100% Biaxial $\frac{1}{4}$ Asymmetric Mass	Test Structure	3.171	1.177	21.938	
		Case 1 [Columns Extended to Diaphragm]	3.059	1.459	19.489	
		Case 2 [Links with Twice Column Stiffness]	2.817	1.537	17.951	
45	100% Biaxial $\frac{1}{4}$ Asymmetric Mass	Test Structure	2.463	1.566	16.462	
		Case 1 [Columns Extended to Diaphragm]	2.572	1.251	18.545	
		Case 2 [Links with Twice Column Stiffness]	2.192	1.547	13.896	
34	100% Biaxial $\frac{1}{4}$ Asymmetric Mass [Y] Strength Asymmetry	Test Structure	1.313	0.458	8.394	
		Case 1 [Columns Extended to Diaphragm]	2.059	0.763	7.880	
		Case 2 [Links with Twice Column Stiffness]	1.123	0.704	5.262	
39	100% Biaxial $\frac{1}{4}$ Asymmetric Mass [Y] Concentric Bracing [Y] Stiffness Asymmetry [Y]	Test Structure	1.635	1.955	18.490	
		Case 1 [Columns Extended to Diaphragm]	2.707	4.018	34.710	
		Case 2 [Links with Twice Column Stiffness]	2.333	3.218	29.295	
41	100% X-Axis 75% Y-Axis $\frac{1}{4}$ Asymmetric Mass [Y] Concentric Bracing [Y] Stiffness Asymmetry [Y] Strength Asymmetry [X]	Test Structure	2.173	1.015	11.520	
		Case 1 [Columns Extended to Diaphragm]	3.022	1.805	13.360	
		Case 2 [Links with Twice Column Stiffness]	2.170	1.068	8.089	

Table 12.3 Analytical vs. Experimental Displacement and Rotation Response Comparison – Inelastic Simulations
Non-Rigid Link Models Case 1 and Case 2 – Experimental Material Model

EQ Test No.	Configuration	Material Model	Relative Displacement [in]			Rotation [10^{-3} rad]
			X-Axis	Y-Axis	Z-Axis	
15	100% Biaxial Symmetric Mass	Test Structure	2.859	1.239	2.850	
		Elastic – Plastic with Hardening	3.320	1.225	1.998	
		Elastic – Perfectly Plastic	3.894	1.381	3.047	
28	100% Biaxial $\frac{1}{2}$ Asymmetric Mass [X]	Test Structure	2.529	1.292	18.260	
		Elastic – Plastic with Hardening	2.721	1.131	18.430	
		Elastic – Perfectly Plastic	3.088	1.253	22.410	
23	100% Biaxial $\frac{1}{4}$ Asymmetric Mass	Test Structure	3.171	1.177	21.938	
		Elastic – Plastic with Hardening	3.308	1.859	17.773	
		Elastic – Perfectly Plastic	3.687	2.296	18.353	
45	100% Biaxial $\frac{1}{4}$ Asymmetric Mass	Test Structure	2.463	1.566	16.462	
		Elastic – Plastic with Hardening	2.601	1.834	14.376	
		Elastic – Perfectly Plastic	2.960	2.096	15.026	
34	100% Biaxial $\frac{1}{2}$ Asymmetric Mass [Y] Strength Asymmetry	Test Structure	1.313	0.458	8.394	
		Elastic – Plastic with Hardening	1.417	0.765	7.480	
		Elastic – Perfectly Plastic	1.410	0.825	8.532	
39	100% Biaxial $\frac{1}{2}$ Asymmetric Mass [Y] Concentric Bracing [Y] Stiffness Asymmetry [Y]	Test Structure	1.635	1.955	18.490	
		Elastic – Plastic with Hardening	2.475	3.601	30.017	
		Elastic – Perfectly Plastic	2.457	4.218	37.441	
41	100% X-Axis 75% Y-Axis	Test Structure	2.173	1.015	11.520	
		$\frac{1}{2}$ Asymmetric Mass [Y]				
		Concentric Bracing [Y]	2.581	1.562	8.786	
	Stiffness Asymmetry [Y] Strength Asymmetry [X]					
		Elastic – Perfectly Plastic	2.750	1.865	12.440	

Table 12.4 Analytical vs. Experimental Displacement and Rotation Response Comparison – Inelastic Simulations Elastic-Plastic with Hardening and Elastic-Perfectly Plastic Material Models – Non-Rigid Link Model Case 2

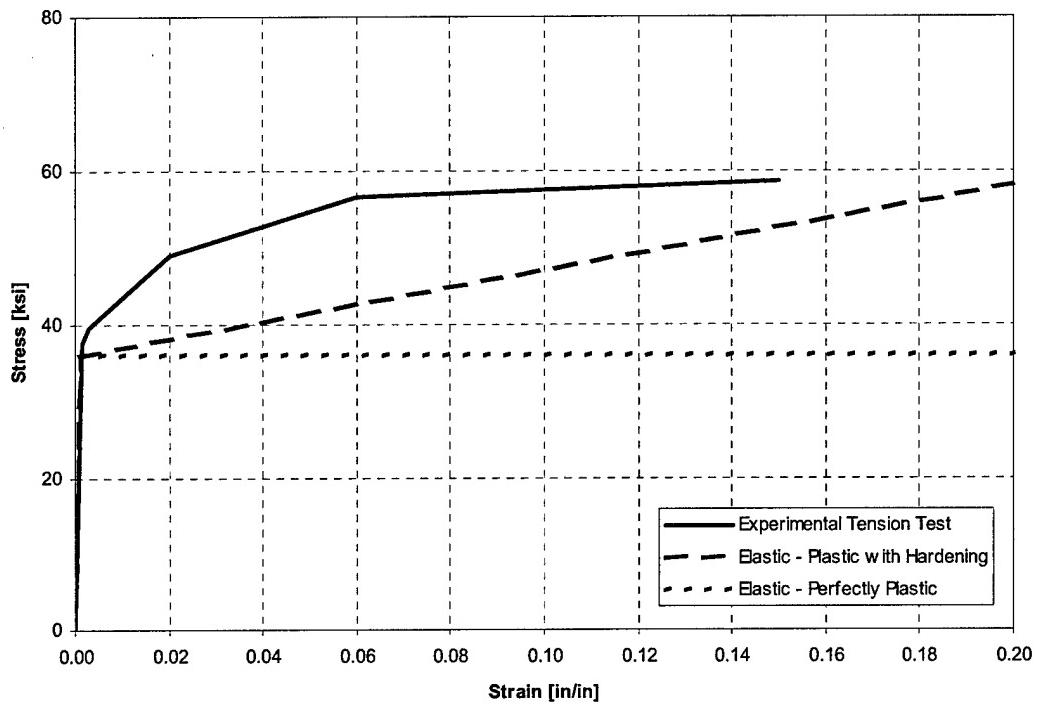


Figure 12.1 Material Models – 4” Extra-Strong Columns – Test Configurations 1 – 4

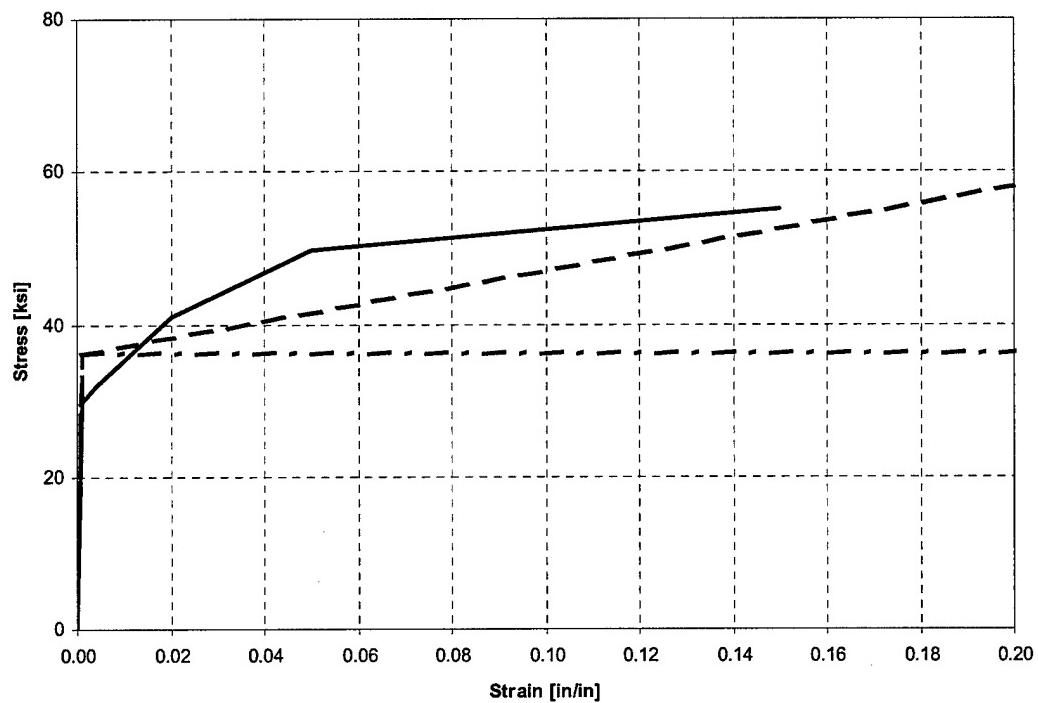


Figure 12.2 Material Models – 4” Extra-Strong Columns – Test Configuration 8

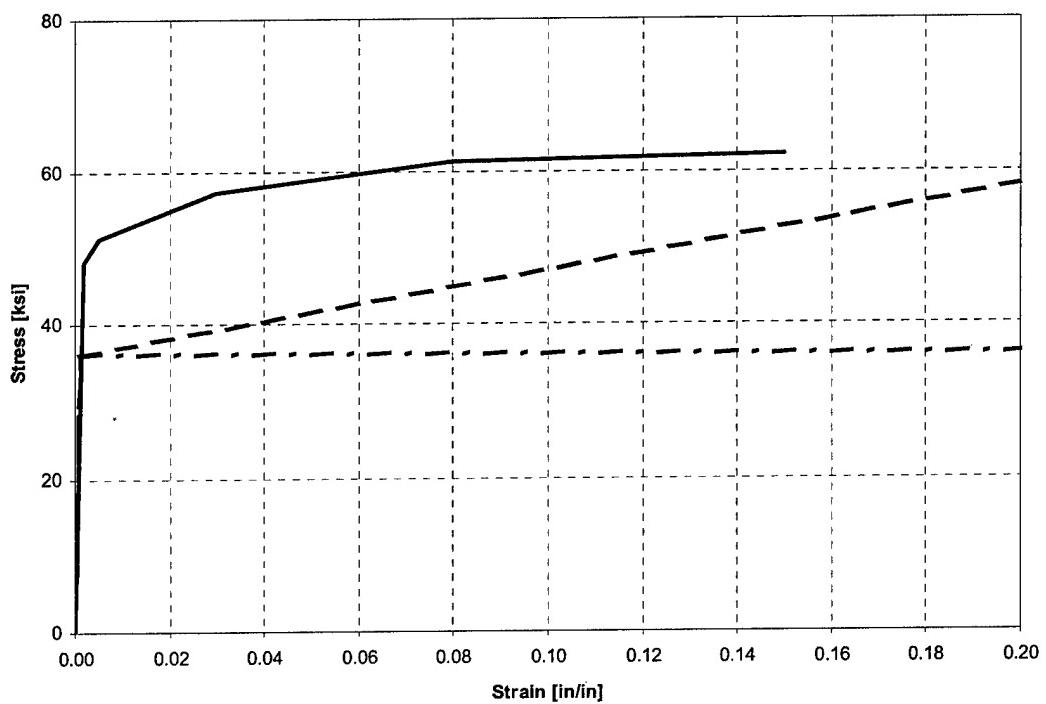


Figure 12.3 Material Models – 5" Standard Columns – Test Configurations 5 & 7

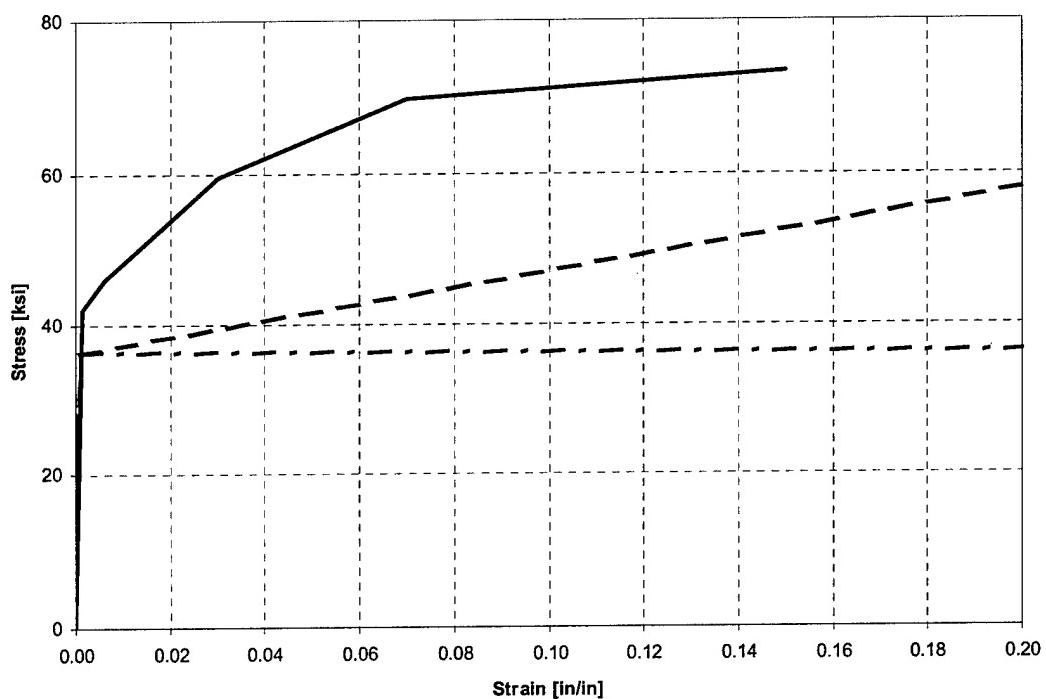


Figure 12.4 Material Models – 4" Double Extra-Strong Columns – Test Configurations 5 & 7

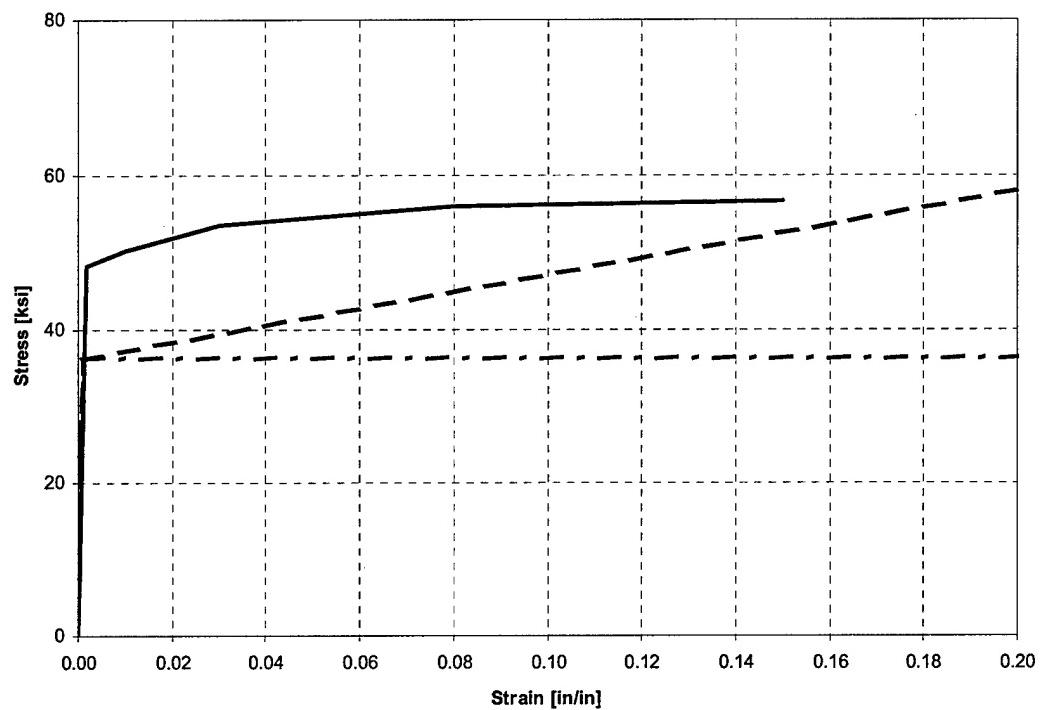


Figure 12.5 Material Models – 4" Extra-Strong Columns – Test Configuration 6

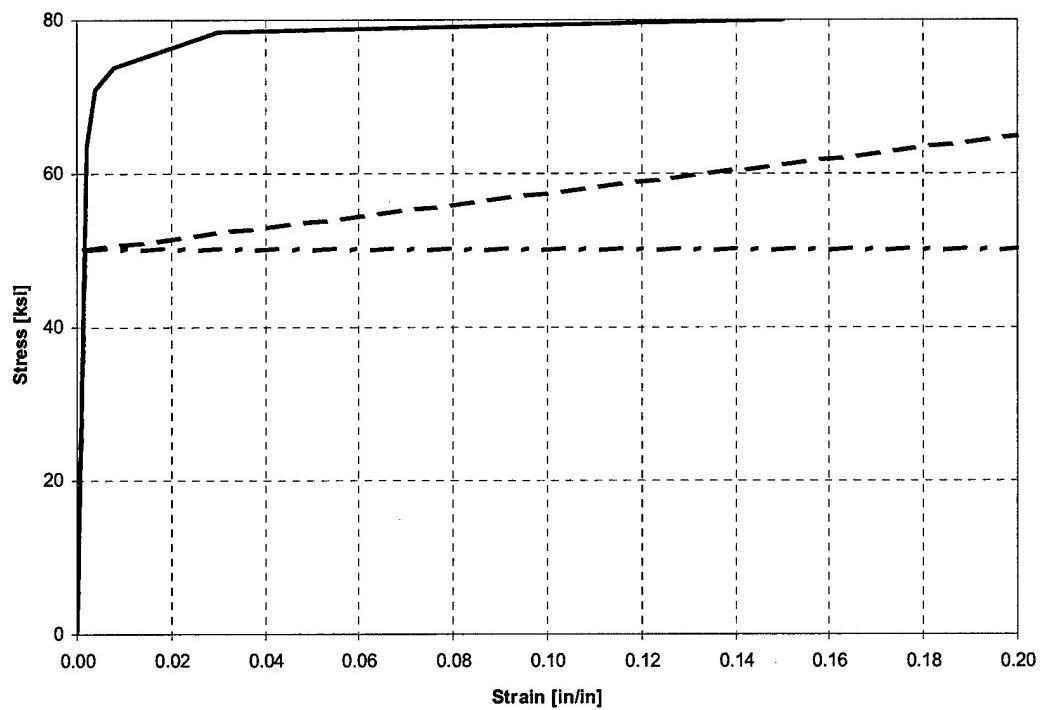


Figure 12.6 Material Models – Diagonal Concentric Bracing – Test Configurations 5 & 7

CHAPTER 13

SUMMARY AND CONCLUSIONS

13.1 OBJECTIVE AND SCOPE

The purpose of this study is to investigate the nonlinear, inelastic response of one-story, symmetric- and asymmetric-plan structures to uniaxial and biaxial lateral earthquake ground motions. The investigation is a combined experimental and analytical program. The experimental part of the investigation involved subjecting a single-story steel moment-frame to a series of earthquake ground motions on the CERL shaketable. The subsequent analytical part of the investigation involved the nonlinear finite element programs Abaqus and Drain-3DX to analyze the response of the model during the earthquake simulations. Through the study, the lateral-torsional response of the system will be studied for a range of system parameters with the goals of examining the adequacy of current building code torsional design provisions and the ability of analytical software to predict inelastic response.

13.2 EXPERIMENTAL PROGRAM

(A) MODEL STRUCTURE

Since this is one of the first experimental studies of this kind, a simple one-story system is appropriate to lay the groundwork for further experimental studies of more complex structures. The structure used in this study was a rigid diaphragm, approximately eight feet on a side, supported by four circular steel pipe columns, five feet in length, as seen in Figures 2.1 – 2.4. Eight octagonal and eight rectangular steel masses, as seen in Figures 2.16 and 2.17, were available to be attached to the slab in various configurations in order to provide dead load and mass asymmetry. The pipe columns had base- and top- plates welded to the columns to provide attachment points to the shaketable and to the diaphragm, as seen in Figures 2.12 – 2.14. The diaphragm was designed to be used throughout the entire sequence of tests, while the columns, having plastically deformed, were replaced after each model configuration sequence was completed. Circular pipe columns were chosen because of their complete plan symmetry and their reduced sensitivity to torsional buckling and, thus, greater stability. The focus of this study is the lateral-

torsional behavior of the system as a whole, not the local behavior of the columns; non-circular columns would only add unnecessary complexity to the analysis of the system.

Eight different model configurations were studied, as seen in Table 2.1. The configurations consisted of different combinations of varying parameters: one-quarter asymmetric mass, one-half asymmetric mass, symmetric mass, asymmetric and symmetric column strength, and concentric lateral bracing. The mass asymmetries were achieved simply by placing the masses all on one-quarter or one-half of the diaphragm. In both the asymmetrical and symmetrical cases, half of the masses were attached above and half below the diaphragm to keep the vertical mass center reasonably near the center of the diaphragm. Three different types of pipe columns were used: 4" Extra-Strong, 5" Standard, and 4" Double Extra-Strong. The strength asymmetry in the structure was achieved by pairing two sets of columns which had similar stiffnesses, but different yield strengths. The stiffness asymmetry was achieved through the use of asymmetrical lateral bracing, as seen in Figure 2.19.

Overall, the structure tested and analyzed in this study was a low-period, acceleration-sensitive system. This fact increases the importance of using biaxial ground motions as Riddell and Santa-Maria (68) and Correnza and Hutchinson (15) both indicate that accurate assessment of the response of short-period systems can be achieved only by using bi-directional analyses. They show that bi-directional ground motions have the largest impact on low-period systems, and the impact increases as the eccentricity increases. The eccentricity typically found in the configurations in this study is roughly 0.4 times the radius of gyration, which is considered a moderate degree of eccentricity. Riddell and Santa-Maria also indicate that low-period systems can achieve inelastic response significantly greater than elastic response. For intermediate- and long-period systems, lateral deformations are not as affected by yielding so that elastic and inelastic systems experience, on average, essentially the same lateral deformation.

The structures in this study had an uncoupled torsional-to-lateral frequency ratio, Ω , of about 1.8, which is relatively large. With a large Ω such as this, the dynamic torsional amplification is not nearly as great as would be the case if Ω was closer to 1.0. Future experimental testing to increase the generality of results would benefit from a structure with an uncoupled torsional-to-lateral frequency ratio closer to 1.0, different sets of recorded ground motions, and a structure with stiffness eccentricity rather than mass eccentricity.

(B) TESTING PROCEDURES

Following construction, the model was placed on the shaketable for the experimental simulations. Response quantities measured included accelerations and displacements of the table and diaphragm in both planar directions, and strains in the columns. The test sequence for each model configuration was essentially the same. Preliminary tests were performed before the earthquake simulations in order to determine the natural frequencies and damping characteristics of the structure, as discussed in Chapter 2.

Following the preliminary tests, the structure was subjected to earthquake simulations. The 230 [X] and 140 [Y] degree acceleration components from the 1979 Imperial Valley earthquake recorded at Bonds Corner were chosen as the base earthquake motions. The motions were modified using a combination of scaling and filtering, as detailed in Chapter 2, in order to produce ductility responses of roughly 4 – 5.

The structure was first subjected to low-level uniaxial and biaxial earthquake tests, typically at 10 – 25% of the reference. Next, the structure was subjected to the full-scale reference accelerograms, followed by white noise tests to analyze any changes in the natural frequencies of the structure. Typically, the shaketable displacement limits were such that the earthquake reference accelerograms could be scaled up by 50%, in order to perform a subsequent simulation. This general sequence of preliminary tests and earthquake simulations was followed for each of the eight different model configurations.

13.3 PRIMARY OBSERVATIONS FROM THE EXPERIMENTAL PROGRAM

The applicability of the experimental results to the behavior of code-designed structures is important to establish before detailing the experimental results. Overall, the peak accelerations of the ground motions used in the inelastic simulations were larger than those specified by the *Seismic Provisions* for design. However, this is a product of the “backwards” approach that was taken in designing the test matrix. Typically, during most analytical studies, the ground motions are chosen first and the overall layout of the force-resisting elements is chosen. The yield strength of the elements is then defined based on the desired Strength Reduction Factor. For this study, the structure was designed first and the ground motions were then selected and modified in order to achieve the desired displacement ductilities. Thus, making a direct comparison between the ground motions used during this study and design ground motions specified by the *Seismic Provisions* is not a good measure of the applicability to code-designed structures, as the test structure was not designed according to the *Provisions*. A better indicator of the similarity to code

designed structures is the ductility experienced by the test structure or the effective Strength Reduction Factor. An effective Strength Reduction Factor for a particular simulation is computed as the ratio of the base shear force for the ground motion if the structure remained elastic to the yield base shear. The Seismic Provisions specifies a Strength Reduction Factor (R) of 8 for Special Steel Moment Frames and 3.5 for Ordinary Steel Moment Frames. The Strength Reduction Factors for the inelastic simulations performed in this study generally fall within this range. Only two simulations, EQ 16 and EQ 46, possessed an effective Strength Reduction Factor larger than 8, and in both cases the values are roughly 9. This attribute of EQ 16 and EQ 46 must be considered when assessing the applicability of the results found.

(A) μ/R RATIO

Two of the primary parameters in the seismic design of structures are the Strength Reduction Factor, or the Response Modification Coefficient R as termed in the *Seismic Provisions*, and the Ductility Factor μ , or the Deflection Amplification Factor C_d in the *Provisions*. These parameters are utilized with the Equivalent Lateral Force Procedure and the Modal Response Spectrum Analysis Procedure. The ratio μ/R is studied to determine the impact of different magnitude ground motions and plan asymmetries. This ratio gives a measure of the amount of ductility the *Seismic Provisions* expects a particular structure to experience and thus for which it must be designed. It also indicates how the peak inelastic displacements and rotations compare with the peak displacements and rotations of the equivalent elastic system. The Strength Reduction Factor and the Ductility Factor are coefficients that are chosen independently of any torsional irregularities or plan asymmetries, and are also independent of the presence of uniaxial or biaxial design ground motions and their magnitudes. The aforementioned ratio, μ/R , is numerically equal to u_m/u_e , or the ratio of the actual peak displacement in an elastoplastic system to the peak displacement in the corresponding linear system. This relationship is presented in Chapter 4, is referred to as the *Modified μ/R Ratio*, and is computed as the ratio of the normalized displacement during an inelastic simulation to the normalized displacement during an elastic simulation. The *Modified μ/R Ratio* can also be defined as the ratio of the normalized rotation during an inelastic simulation to the normalized rotation during an elastic simulation. As discussed previously, the *Seismic Provisions* provides a range for the *Modified μ/R Ratio* of 0.86 to 0.69 for an Ordinary Moment Resisting Frame (OMRF) and a Special Moment Resisting Frame (SMRF), respectively. For Configurations 6, or EQ 39 and EQ 40 , the X-Axis force-resisting system was a moment-resisting frame, while a concentrically braced frame was present in the Y direction. The *Provisions* specifies a *Modified μ/R Ratio* of 0.83 for a Special Steel Concentrically Braced Frame

and 0.90 for an Ordinary Steel Concentrically Braced Frame. One factor to consider when interpreting the μ/R Ratio with respect to those specified in the *Seismic Provisions* is that pipe columns were used in this test structure, not the wide-flange shapes typically found in earthquake-resistant buildings. The pipe columns possess a shape factor of about 1.37, as compared to the typical shape factor for wide-flange shapes of about 1.1. The effect of the larger shape factor is that the pipe columns possess a greater amount of reserve strength after initial yield, which also reduces the rate of stiffness degradation after initial yield. This would imply that the peak displacements observed here during the inelastic simulations, and consequently the μ/R Ratio, would be smaller than those expected for a structure with wide-flange shape columns. As the ductility factor increases, and hence the amount of inelastic behavior increases, the discrepancy in response due to the column shape factor increases. The *Modified μ/R Ratios* for all Configurations are shown below.

Configuration	μ/R Ratio			
	EQ	X-Axis	Y-Axis	Z-Axis
Symmetric Mass 100% Uniaxial	7	N/A	0.77	N/A
Symmetric Mass 100% Biaxial	15	1.37	0.86	0.84
Symmetric Mass 150% Biaxial	16	1.77	1.83	1.08
$\frac{1}{2}$ Asymmetric Mass [X-Axis] 100% Biaxial	28	0.90	0.51	1.07
$\frac{1}{2}$ Asymmetric Mass [X-Axis] 150% Biaxial	29	1.17	1.03	1.39
$\frac{1}{4}$ Asymmetric Mass 100% Biaxial	23	1.60	0.61	1.90
$\frac{1}{2}$ Asymmetric Mass [Y-Axis] Strength Asymmetry 100% Biaxial	34	0.56	0.67	1.28
$\frac{1}{2}$ Asymmetric Mass [Y-Axis] Strength Asymmetry 150% Biaxial	35	0.80	1.19	1.39
$\frac{1}{2}$ Asymmetric Mass [Y-Axis] Stiffness Asymmetry Concentric Bracing 100% Biaxial	39	1.28	3.66	2.42
$\frac{1}{2}$ Asymmetric Mass [Y-Axis] Strength Asymmetry Concentric Bracing 100% X-Axis 90% Y-Axis	40	1.96	5.44	3.59

Overall, the μ/R Ratios for the X-Axis response and Y-Axis response of the unbraced configurations, are quite varied in their values, ranging from 0.51 to 1.83. In some cases the Ratios are less than the Provisions range of 0.69 to 0.86, but in a number of cases the μ/R Ratios are significantly larger. In comparing EQ 07 and EQ 15, it appears that the addition of a perpendicular ground motion component does not significantly affect the Ratio for systems that ostensibly have no eccentricity. There does not appear to be any correlation between degree of eccentricity and the μ/R Ratio, as the X-Axis Ratio for EQ 15, the symmetric system, is greater than that of EQ 28, with one-way eccentricity, but less than that of EQ 23, with two-way eccentricity. Further, the Y-Axis Ratio for the symmetric system is greater than the Ratios for both the one-way and two-way asymmetric systems. In comparing EQ 15 and EQ 16, and also EQ 28 and EQ 29, in both cases the Ratios for the simulations with 150% ground motions are greater than those with 100% ground motions, as would be expected. Also in both cases, the Y-Axis μ/R Ratios nearly double when the ground motions are increased by 50%, while the X-Axis ground motions increase to a lesser degree. The structure has yielded to a greater degree during the 100% simulations, as the X-Axis ground motion PGA is significantly larger than the Y-Axis motion. When the ground motions are increased to 150%, the additional degree of yielding and loss of stiffness is greater in the Y direction than in the X direction, causing the larger increase in the μ/R Ratio. The systems in both Configuration 4, EQ 28 and EQ 29, and those in Configuration 5, EQ 34 and EQ 35, possess one-way asymmetry, about the X-Axis in the former and Y-Axis in the latter. In all four simulations, the μ/R Ratio in the direction of asymmetry is larger than in the symmetric direction, from 14% to 76%, with an average of roughly 40%, greater. It appears that the coupling of the lateral and torsional responses amplifies the responses in the direction of the asymmetry. This trend appears to not be a function of the differences in ground motions, because with Configuration 4 the larger motion is along the direction of asymmetry, and with Configuration 5 the opposite is true. In most cases when the Ratio exceeds the range specified by the provisions, the value is near 1.0. This would indicate that the peak inelastic displacement is equal to the peak elastic displacement, which a conservative designer might assume. However, there are three values much larger than 1.0, but two of them occur for a simulation which achieved displacement ductilities in the X and Y directions of roughly 12 and 9, respectively. The response of this particular simulation is such that it might not be representative of code-designed structures.

More consistent than the μ/R Ratios for the displacement responses were the Ratios for the rotational responses. Every rotational μ/R Ratio but one was larger than 1.0. In comparing EQ 15, EQ 16, EQ 28,

EQ 29, and EQ 23, the clear trend is that the rotational *Ratio* increases with increasing eccentricity and with increasing ground motion magnitude. The largest value of the μ/R *Ratio* rotationally is 1.90 and occurs for EQ 23, the only simulation discussed here that features eccentricity about both the X-Axis and Y-Axis. In assessing the μ/R *Ratio* for EQ 23, it must be noted that this configuration is classified as *Torsionally Irregular* according to the *Seismic Provisions*. The dynamic amplification of torsion prescribed in the *Provisions* for a structure possessing a *Torsional Irregularity* or *Extreme Torsional Irregularity* could potentially mitigate the disparity between the Z-Axis μ/R *Ratio* for EQ 23 and those values prescribed by the *Provisions*. However, for the degree of torsional irregularity present in this structural configuration, the dynamic amplification is roughly 5%, and therefore not a significant mitigating factor in the comparison.

For EQ 39 and EQ 40, a system possessing lateral bracing in the Y direction, in the X direction the *Modified μ/R Ratio* is larger than the specified range of 0.86 to 0.69 for a moment-resisting frame, they are similar to values observed in previous configurations. In the Y direction, the *Modified μ/R Ratio* is 3.66 for EQ 39 and 5.44 for EQ 40. These values are significantly greater than the range specified in the *Provisions*, and the system overstrength for a concentrically braced frame with tension-only bracing is not as great as for a moment-resisting frame. In addition, because the design of concentrically braced frames is not typically controlled by drift or deflection, unlike moment-resisting frames, there is a lesser degree of design overstrength for these types of force-resisting systems as well. Because the concentrically braced frames provide roughly 80% of the torsional stiffness for this configuration, it is not surprising that the *Modified μ/R Ratio* rotationally are also large and appear to be changing with the Y-Axis *Modified μ/R Ratios*. The *Modified μ/R Ratio* rotationally for EQ 40 is roughly 75% larger than the largest *Ratio* observed in all previous configurations. These factors in total lead to a concern that the ductility in design required in the *Provisions* for concentrically braced frames may be inadequate.

(B) U_Y/U_X RATIO

A constant μ/R *Ratio* implies that the ratio of the two peak lateral displacements remains constant regardless of whether the structure responds elastically or inelastically, and also regardless of the amount of structural asymmetry. In addition, these design assumptions also imply that the ratio of the peak rotation to the peak lateral displacement remains constant. The u_Y/u_X ratios and u_θ/u_X ratios are shown below.

Configuration	EQ	u_Y/u_X	u_θ/u_X
Symmetric Mass 25% Biaxial	14	0.73	N/A
Symmetric Mass 100% Biaxial	15	0.43	N/A
Symmetric Mass 150% Biaxial	16	0.80	N/A
$\frac{1}{2}$ Asymmetric Mass 10% Biaxial	27	0.86	0.29
$\frac{1}{2}$ Asymmetric Mass 100% Biaxial	28	0.51	0.35
$\frac{1}{2}$ Asymmetric Mass 150% Biaxial	29	0.85	0.35
$\frac{1}{4}$ Asymmetric Mass 10% Biaxial	22	0.96	0.28
$\frac{1}{4}$ Asymmetric Mass 100% Biaxial	23	0.37	0.33
$\frac{1}{4}$ Asymmetric Mass 100% Biaxial	45	0.64	0.32
$\frac{1}{4}$ Asymmetric Mass 135% Biaxial	46	1.04	0.30
$\frac{1}{2}$ Asymmetric Mass Strength Asymmetry 10% Biaxial	32	0.29	0.14
$\frac{1}{2}$ Asymmetric Mass Strength Asymmetry 100% Biaxial	34	0.35	0.31
$\frac{1}{2}$ Asymmetric Mass Strength Asymmetry 150% Biaxial	35	0.44	0.24

The first four Configurations listed here, including the simulations EQ 14 – 16, EQ 27 – 29, EQ 22 – 23, and EQ 45 – 46, are all similar with the exception of the degree of eccentricity. One phenomenon that is present throughout each of these four Configurations involves the change in the u_Y/u_X ratio. For EQ 14, the u_Y/u_X ratio is equal to 0.73. For EQ 15, an inelastic simulation, the ratio drops to 0.43, a decrease of over 40%. For EQ 16, the second inelastic simulation, the ratio of u_Y/u_X increases to 0.80. This trend is seen for both the system with one-way asymmetry and two-way asymmetry. As discussed in Chapter 5, it appears that due to the differences in the X- and Y-Axis ground motions, the structure in EQ 15 has

yielded to a greater degree in the X direction than in the Y direction. In the Y direction, the structure is still in the region of the pushover curve, Figure 5.12, where the lateral stiffness has not yet decreased significantly. In the X direction, the lateral stiffness has decreased to a much greater degree, resulting in a much larger peak displacement proportionally to the Y-Axis peak displacement. In EQ 16, the stiffness appears to have decreased to a similar degree in the Y direction as in the X direction, as the structure has traveled further along the pushover curve. This phenomenon, yielding at different rates in the two lateral directions, would be expected to occur regularly in actual structures, as orthogonal ground motion components are typically different and structures lose stiffness during yielding in a very gradual manner. The result of this is that the ratio u_Y/u_X may not remain constant as the structure proceeds along its yield path, indicated by the pushover curves. But it also appears that if there is sufficient yielding in each lateral direction, the u_Y/u_X ratio during inelastic response is nearly equal to that for elastic response, irrespective of whether the system is symmetric, one-way asymmetric, or two-way asymmetric.

Configuration	EQ	u_Y/u_X	u_θ/u_Y
10% Biaxial ½ Asymmetric Mass [Y-Axis] Concentric Bracing [Y-Axis] Stiffness Asymmetry [Y-Axis]	36	0.30	0.69
100% Biaxial ½ Asymmetric Mass [Y-Axis] Concentric Bracing [Y-Axis] Stiffness Asymmetry [Y-Axis]	39	1.20	0.46
100% X-Axis 90% Y-Axis ½ Asymmetric Mass [Y-Axis] Concentric Bracing [Y-Axis] Stiffness Asymmetry [Y-Axis]	40	0.75	0.46
½ Asymmetric Mass 100% X-Axis 75% Y-Axis Concentric Bracing [Y-Axis] Stiffness Asymmetry [Y-Axis] Strength Asymmetry [X-Axis]	41	0.47	0.55
½ Asymmetric Mass 100% X-Axis 85% Y-Axis Concentric Bracing [Y-Axis] Stiffness Asymmetry [Y-Axis] Strength Asymmetry [X-Axis]	42	0.63	0.45

For Configuration 5, EQ 32 – 35, the u_Y/u_X ratios are significantly smaller than those of the previously discussed simulations. The differences are due to the modal frequencies being larger for this configuration than for the previous configurations, as the columns have greater stiffnesses. For EQ 27,

the X-Axis PSA was 0.36 while the Y-Axis PSA was 0.30. For EQ 32, the X-Axis PSA was 0.39 while the Y-Axis PSA was only 0.12. Also different from previous configurations, the u_y/u_x ratio does not exhibit a large drop when comparing the first inelastic test to the elastic test. The different degrees of yielding between the X and Y directions seen in the previous configurations is not present here because there is an overall lesser degree of yielding for this configuration. As the ground motions are increased for this configuration, the u_y/u_x ratio gradually increases, meaning that the peak Y-Axis displacement is increasing relative to the X-Axis displacement. One explanation for this lies in the presence of the strength eccentricity, which is about the Y-Axis. When the columns on the north side of the structure are yielding, the center of stiffness would move significantly to the south, or further away from the Y-Axis. The instantaneous stiffness eccentricity that would be present, and the rotation of the structure about a point noticeably different from the geometric center, would increase the displacement of the geometric center due to the torsion. As the ground motions increased, and the degree of yielding of the columns on the north side of the structure increased, the peak Y-Axis displacement and the u_y/u_x ratio would also increase. Having the u_y/u_x ratio remain constant during the move from elastic to inelastic response requires a system that yields similarly in both directions, as evidenced by the previous configurations. However, for a more complicated configuration in which the system doesn't yield similarly in both directions, or doesn't even yield uniformly in each direction, as is the case here with a strength eccentricity, it would be unlikely that the u_y/u_x ratio would remain constant.

With Configurations 6 and 7, EQ 36 – 42, the addition of the concentric bracing necessitated a significant change in the Y-Axis input ground motions, as discussed in Chapter 10. Thus, making comparisons in the u_y/u_x ratio and the u_θ/u_x ratio with previous configurations is difficult. In comparing EQ 36 to EQ 39, the u_y/u_x ratio increases by roughly a factor of 4. The largest increase in the u_y/u_x ratio from an elastic test to any inelastic test observed in any of the previous configurations was 50% in Test Configuration 5. The likely cause of this behavior is the presence of two different force-resisting systems: a moment-resisting frame along the X-Axis, and a concentrically braced frame along the Y-Axis. More than 80% of the stiffness is provided by the tension-only bracing in the Y direction, and the degree of overstrength of the braces yielding in tension is significantly less than the pipe-columns yielding in flexure. The result of this is the concentrically braced frame in the Y direction loses stiffness at a more rapid rate than the moment-resisting frame in the X direction. With EQ 40, the u_y/u_x ratio decreases, corresponding to the X-Axis PGA increasing 55%, while the Y-Axis PGA was virtually unchanged. Extending this scenario, with a larger X-Axis ground motion or a reduction in the strength of the force-resisting system in the X direction, the u_y/u_x ratio would decrease even further, since the degree of stiffness-loss in the X direction would “catch up” to that in the Y direction. This also would likely

happen if the X-Axis and Y-Axis ground motions were both scaled up to a greater level, a level where the X-Axis stiffness loss would catch up to the Y-Axis loss. From the results of this study, it is impossible to know if the u_Y/u_X ratio would decrease to the point of being equal to the value for the elastic simulation. One mitigating factor in the impact of the results shown here is that a moment-resisting frame is typically designed using a large strength-reduction factor, with the intention of the frame achieving significant ductility. The degree of ductility of 2.1 achieved in the X direction for Configuration 6 is likely less than would be experienced in a properly designed moment-resisting frame under large ground motions. The results from Configuration 7 appear to follow the trends observed for Configuration 6. The u_Y/u_X ratio for the initial inelastic simulation is smaller than those observed in Configuration 6, however this can be attributed to the reduction of the Y-Axis ground motion. The u_Y/u_X ratio increases slightly for EQ 42, which is most likely the result of the increase in the Y-Axis ground motion. But as this configuration possesses a strength eccentricity similar to Configuration 5, the increase in the u_Y/u_X ratio might also be the result of the differential yielding of the columns on the north and south sides of the structure, as discussed previously. Although a direct comparison cannot be made with the elastic u_Y/u_X ratio as none of the sets of ground motions in this configuration have the same proportions as in EQ 36, it does appear that the u_Y/u_X ratio changes with the relative changes in the X-Axis and Y-Axis ground motions used in each simulation.

(C) U_θ/U_X RATIO

One limitation in using elastic design occurs when rotational response is a product of inelastic behavior. When yielding occurs in one or both of the transverse directions, the torsional stiffness decreases and the torsional response of the structure increases. However, it is important to know if the elastic rotational response can be correlated to the inelastic rotational response. Three of the first four Configurations discussed with the u_Y/u_X ratio, encompassing EQ 27 – 29, EQ 22 – 23, and EQ 45 – 46, also exhibit consistency with regard to the u_θ/u_X ratio. For the system with one-way mass eccentricity, the u_θ/u_X ratio increases roughly 20% in moving from elastic response to inelastic response. Further, the u_θ/u_X ratio remains constant for the second inelastic simulation, EQ 29. This trend appears to continue for the system with two-way mass eccentricity, as the u_θ/u_X ratio increases roughly 18% in moving to inelastic response and remains fairly constant during further inelastic simulations with increased ground motions. The large “dip” observed previously in the u_Y/u_X ratio for these configurations does not appear to be present for the u_θ/u_X ratio. The u_θ and u_X displacements are much more tightly coupled than the u_Y and u_X displacements are. Due to the fact that this behavior is consistent for not just the one-way but also the

two-way mass eccentric systems, it appears that the coupling between the u_θ and u_X displacements is primarily due to the difference in the X-Axis and Y-Axis ground motions. For these configurations, the X-Axis input ground motion has a peak acceleration and elastic spectral acceleration over 50% larger than for the Y-Axis. Thus, it appears that the X-Axis motion impacts the torsional displacement to a greater degree than the Y-Axis motion here.

For Configuration 5, the u_θ/u_X ratio more than doubles when moving from elastic response to inelastic response. It then decreases somewhat for the second inelastic simulation, instead of remaining constant as with the configurations discussed above. As the response increases to the point where yielding begins, the two weaker columns, located on the north side of the structure, will yield before the stronger columns and to a much greater degree. In fact, it is possible that the two stronger columns may remain elastic throughout the entire response. During these instances or periods of differential yielding between the stronger and weaker columns, an instantaneous stiffness eccentricity appears which may significantly increase the torsional response of the structure. In previous configurations it is likely that all four columns did not yield simultaneously. Therefore this phenomenon may have occurred to some degree, however the presence and degree of the strength eccentricity increased the effect substantially, as demonstrated by the u_θ/u_X ratios in this configuration. This type of eccentricity may present a significant problem in design, as the stiffness eccentricity that may appear will do so only in inelastic simulations. Thus, the assumption that the u_θ/u_X ratio remains the same for elastic and inelastic response clearly does not hold for this case. The degree to which this parameter will increase for inelastic response will depend on the specific configuration and material properties of the structure. With the previous configurations, comparing u_θ with u_X was most useful because of the greater dependence of u_θ on u_X as opposed to u_Y . With this configuration, the correlation is not as clear. The X-Axis ground motion remains significantly larger than the Y-Axis ground motion, however the mass eccentricity for this configuration is about the Y-Axis only. Therefore, it is useful to also compute the u_θ/u_Y ratio, in which case the value is 0.44 for the elastic simulation and increases to 0.88 for the first inelastic simulation. This appears to be a similar increase as observed for the u_θ/u_X ratio. The u_θ/u_Y ratio decreases to 0.55 for the second inelastic simulation, which is roughly 25% larger than the ratio observed for the elastic simulation. The decrease in the u_θ/u_Y ratio could be the result of u_Y increasing due to a larger degree of yielding along the Y-Axis. The system would be expected to respond inelastically to a greater degree rotationally than translationally along the Y-Axis, at least initially. As noted earlier, the system will begin to rotate significantly as the weaker columns yield, however, the system will not begin to translate significantly until both the weaker and stronger columns yield. Thus, it appears that the trend observed

for the earlier configurations, of the ratio of rotational to lateral response increasing by roughly 20% for the inelastic simulations, might also follow for this configuration, although it is more difficult to tell with a more complicated configuration. If true, it would indicate that the rotational response is correlated to a greater degree to the lateral response in the direction of eccentricity, as opposed to the direction of larger ground motion. In addition, this configuration illustrates the importance of uniform yielding of the system when trying to correlate the rotational response to lateral response, as also seen in correlating the two lateral responses.

With Configurations 6 and 7, which incorporate lateral bracing, the peak rotation was compared with the peak Y-Axis displacement, as both the mass eccentricity and stronger ground motion component were along the Y-Axis. For Configuration 6, the u_θ/u_y ratio decreases roughly 35% in moving from elastic to inelastic response. The ratio remains constant for the second inelastic simulation, although the ground motions did not significantly change for EQ 40. Although the change is significant, the decrease would prove to be conservative from a design standpoint. The displacement ductility in the Y-Axis is significantly greater than in the X-Axis, which might indicate that the lack of yielding in the X direction is preventing the rotational stiffness from decreasing to the same degree as the Y-Axis translational stiffness. As stated above for the displacement ratio, the degree of ductility achieved in the X direction for Configuration 6 is likely less than would be experienced in a properly designed moment-resisting frame under large ground motions. It appears that the u_θ/u_y ratios for Configuration 7 that the ratios for inelastic response extend from the previous configuration, as the values are similar. This would appear to validate the decrease in u_θ/u_y ratio for inelastic response from elastic response. However, as shown in Test Configuration 5, the presence of a strength eccentricity can have a significant impact on the inelastic torsional response, as the strength eccentricity can produce a stiffness eccentricity that is not present during elastic response. It is difficult to quantify the impact of the strength eccentricity on the torsional response in this configuration because there is also a stiffness eccentricity present from the concentric bracing, and the two asymmetries are about different axes. The influence of each eccentricity, along with the mass eccentricity, would depend on the relative responses of the system along the X-Axis and Y-Axis at any instant.

13.4 PRIMARY OBSERVATIONS FROM THE ANALYTICAL PROGRAM

The primary focus of seismic design is to resist large-scale earthquakes, in which the structure will respond well into the inelastic region, and thus it is important to be able to accurately predict inelastic

structural response. However, it is also important in designing or assessing a building to consider the response to lower level earthquakes, which would be more likely to occur during the lifetime of the building but might not produce significant yielding, if any at all.

Finite element analyses were performed for a selected group of earthquake simulations in an effort to accurately predict the structural response of the system for each test configuration. Initially, the nonlinear analysis program Abaqus was chosen to carry out the analyses. However, due to the considerable amount of computing time required in some cases, a second program was chosen, Drain-3DX, to provide, in addition to response predictions, a comparison with Abaqus regarding prediction accuracy and the overall features and limitations of each program and their potential impact on the analysis solutions.

A summary of the analytical peak displacement and rotational responses as compared to the recorded experimental responses is shown for the elastic simulations in Table 13.1. Overall, both Abaqus and Drain-3DX predicted the peak translational displacements very well for the selected elastic simulations, with the Abaqus predictions proving to be slightly more accurate than the Drain-3DX predictions. In order to quantitatively compare the two, the percent difference, or percent error, was computed between each of the predicted response quantities and the corresponding measured experimental response quantities. The mean percent error for the X-Axis and Y-Axis peak displacements using Abaqus was 7.8%, with a coefficient of variation of 0.72. The median Abaqus percent error for the same response quantities was 7.3%, which being similar in magnitude to the mean, indicates that mean was not overly influenced by extreme values. This is verified by the range of percent error, being from 0.4% to 19.1%. In comparison, the mean percent error using Drain-3DX to predict the peak elastic displacements was 13.2%, with a standard deviation of 0.79. The median Drain-3DX error for the elastic displacements was 10.0%. While not significantly different from the mean, this indicates a few larger error values. The percent error range was 0.9% to 39.4%. Thus in predicting the elastic displacements, the Abaqus analyses proved to be slightly more accurate and more consistent than the Drain-3DX analyses, although both were satisfactory.

The ability to predict the elastic rotational response and peak rotations proved to be significantly more difficult than the elastic displacement response. The mean percent error in predicting the peak elastic rotations using Abaqus was 40.5%, with a coefficient of variation of 0.78. The median Abaqus percent error for the same response quantity was 38.4%, with a range of values of 11.5% to 73.7%. In comparison, the mean error using Drain-3DX to predict the elastic rotations was 44.1%, with a coefficient of variation of 0.74. The median Drain-3DX error was 42.3%, again very close to the mean. The range of errors for the rotational predictions was 10.2% to 81.6%.

In analyzing the test structure with eight different test configurations, it became apparent that some response quantities were more difficult to predict accurately depending on the particular test configuration and whether the response was elastic or inelastic. With regard to the elastic X-Axis and Y-Axis displacements, no particular configuration proved to be more difficult to model than the others. However, this was not the case with the elastic rotational response. Peak rotations were predicted for elastic simulations in four test configurations: Configuration 4, with one-way mass asymmetry; Configuration 3, with two-way asymmetry; Configuration 5, with one-way mass asymmetry and a strength asymmetry; and Configuration 6, with a one-way mass asymmetry and concentric bracing. In both the Abaqus and Drain-3DX analyses, the predicted elastic peak rotations in Configurations 5 and 6 were significantly less accurate than those in Configurations 3 and 4. The average error for Configurations 3 and 4 was 15.5%, while the experimental peak rotations in Configurations 5 and 6 were roughly 2.5 and 4 times larger than the predicted values. The elastic peak rotations for Test Configurations 5 and 6 predicted by static analysis are 0.20×10^{-3} radians and 0.15×10^{-3} radians, respectively. Even considering the dynamic amplification, the peak rotation predicted for Configuration 6 by static analysis is in much better agreement with that predicted by Abaqus and Drain-3DX, as opposed to the experimental peak rotation. It is not clear why the analytical models so severely underestimate the rotational response for these two configurations.

Overall, the rotations proved to be significantly more difficult to predict than the displacements. A number of factors could have played a role in this. Imprecise placement of the structure on the shaketable, imprecise placement of the masses on the diaphragm, nonuniformity of the diaphragm, etc. Each of these possible factors could have contributed to an additional effective eccentricity, or accidental eccentricity. In creating the analytical models, the model structures were “tuned” to the experimentally measured modal frequencies by altering the stiffnesses of the Non-Rigid Links, in an effort to replicate the dynamic properties of the actual test structure in each configuration. However, no accidental eccentricity was added to the finite element model despite the fact that it was most likely present in the actual test structure. The first difficulty in adding any accidental eccentricity is the impossibility of measuring its magnitude. One solution would be to take some arbitrary fraction of the plan dimension, most likely less than the standard 5% as the physical specifications and geometry of this test structure are more precisely known than that of an actual building. The second difficulty in adding any accidental eccentricity is the positioning. It is possible to add to or subtract from, in both the X and Y directions, the actual eccentricity, allowing for four possibilities, each of which would have differing impacts on the

rotational response of the structure. Thus, any accidental eccentricity present in the test structure was neglected.

Although the absence of any additional “accidental” eccentricity in the analytical models may have contributed to the consistent underestimation of the torsional response, the translational response does not appear to be affected, as the peak elastic displacements are predicted fairly accurately. The test structure in Configurations 1 – 4 possessed an eccentricity roughly 40% of the radius of gyration and an uncoupled torsional-to-lateral frequency ratio $\Omega = 1.8$. For a structure with this moderate degree of eccentricity and large degree of torsional stiffness, the impact of any torsional response on the elastic translational response is small. Thus, the inaccuracy of the rotational response in the analytical models would not have a significant effect on the accuracy of the translational response.

A summary of the analytical peak displacement and rotational responses as compared to the recorded experimental responses is shown for the inelastic simulations in Table 13.2. Overall, both Abaqus and Drain-3DX predicted the peak inelastic translational displacements less accurately than the elastic displacements. The mean error in predicting the peak inelastic displacements using Abaqus was 25.2%, with a coefficient of variation of 1.80. The median inelastic displacement error was 13.6%. For Test Configuration 6, the first configuration with concentric lateral bracing along the Y-Axis, the Abaqus analyses overestimated the peak Y-Axis displacement by 133.2% and 209.4%, respectively, in the two inelastic simulations. If those two values are removed from consideration, the mean error and median error are in much better agreement at 13.5% and 9.3%, respectively. Although these two aberrant predictions were for the first configuration with concentric bracing, the following test configuration did also feature concentric bracing. The Abaqus displacement predictions for Test Configuration 7 were much more accurate than those for Test Configuration 6, suggesting that the results from Configuration 6 were not an indicator of a general difficulty with Abaqus analyses of a braced structure. As stated in Chapter 10, a very large inelastic excursion occurs during the Y-Axis displacement response which is the primary cause of the lack of accuracy in the Abaqus predictions for Configuration 6.

In comparison, the mean peak inelastic displacement error using Drain-3DX was 15.2%, with a coefficient of variation of 0.76. The median peak displacement error is also 15.2%, indicating that the mean is a very good overall measure of the response of the entire selection of inelastic simulations. Thus, in removing the two Abaqus predictions for Test Configuration 6, both Abaqus and Drain-3DX predicted the peak inelastic displacements fairly accurately. The Abaqus analyses proved to be slightly more accurate than the Drain-3DX analyses, the two Configuration 6 predictions notwithstanding, although the

differences were small. Both the Abaqus analyses and Drain-3DX analyses were less accurate in predicting the peak inelastic displacements than in predicting the peak elastic displacements, but again, the differences were not significant.

As with the elastic rotational response, the inelastic rotational response proved to be more difficult to accurately predict than the inelastic translational response. The mean error in the peak inelastic rotations predicted by Abaqus analyses was 49.8%, with a coefficient of variation of 0.69. The median peak rotation error was 31.9%, while the error spanned a wide range of values from 11.5% to 144.6%. The two inelastic simulations in Configuration 6 discussed above, for which Abaqus significantly overestimated the Y-Axis peak displacement, also had their peak rotations significantly overestimated by the Abaqus analyses. In fact, these were the only two inelastic simulations in which the Abaqus analyses overestimated the peak rotational response. That fact, coupled with the observation that the peak rotational error appears to increase as the peak Y-Axis displacement error increases for the two Configuration 6 simulations, and the fact that the torsional response for Configuration 6 is primarily a product of the Y-Axis response and the eccentricity, appears to indicate that the large errors in predicting the peak rotation are due to the errors in predicting the peak Y-Axis displacements. In addition to the inaccuracies in Configuration 6, the peak rotations for the two inelastic simulations in Configuration 2, with no mass eccentricity, were underestimated by roughly 75% each. This was primarily attributed in earlier chapters to the lack of inclusion of any amount of accidental eccentricity in the finite element models, despite the fact that some small amount would most likely be present. The mean Abaqus peak rotation error becomes 33.5% if all of the configurations with the exception of Configurations 2 and 6 are considered.

The mean error in the peak inelastic rotations predicted by the Drain-3DX analyses was 28.1%, with a coefficient of variation of 0.82 and a median error of 17.0%. As with the Abaqus predictions discussed above, the Drain-3DX predictions underestimate the inelastic peak rotations in Configuration 2 by roughly 65% and the inaccuracies are again attributable to the lack of any accidental eccentricity. Without incorporating the results from Configuration 2, the mean error, at 21.3%, is in much better agreement with the median error. Overall, the Drain-3DX analyses prove to be significantly more accurate in predicting the inelastic rotational response than the Abaqus analyses. Both the Abaqus analyses and the Drain-3DX analyses are more accurate in predicting the peak inelastic rotations than the peak elastic rotations, with the Drain-3DX inelastic predictions being roughly twice as accurate as the elastic predictions.

13.5 CONCLUSIONS

1. The μ/R Ratio is not constant for differing test configurations, earthquake magnitudes, and component directions. The addition of a perpendicular ground motion component appears to have little affect on the μ/R Ratio for symmetric systems, and there does not appear to be any correlation between degree of mass asymmetry and the μ/R Ratio. In addition, it appears to be consistently larger than the range of μ/R Ratios prescribed by the *Seismic Provisions*, especially for the system with concentric lateral bracing. The rotational μ/R Ratio is consistently larger than 1.0, and increases with increasing eccentricity and ground motion magnitude. The expected level of overstrength that structures are assumed during design to possess, roughly on the order of 2 – 4, would be a significant mitigating factor in comparing the μ/R Ratios prescribed by the *Provisions* with those determined experimentally here. When considering the effect of structural overstrength, the μ/R Ratios would generally not exceed those prescribed by the *Seismic Provisions*. However, even considering the system overstrength which is less for a concentrically braced frame than a moment-resisting frame, the μ/R Ratios for the laterally braced configuration were significantly larger than those specified in the *Provisions*, indicating that the specified design ductilities for concentrically braced frames may be inadequate.
2. The u_y/u_x ratio remains constant, or somewhat close to constant, during the change from elastic to inelastic response. However, this result does depend significantly on the system achieving a significant degree of yielding in both directions. This appears to hold true for systems with no mass eccentricity, one-way mass eccentricity, two-way mass eccentricity, and lateral bracing. The small, but non-trivial, differences in the ground motions used for the various configurations also lend additional validation to the results. However, the configuration with a strength eccentricity and no bracing clearly did not exhibit similar response results. This type of eccentricity tends to produce non-uniform yielding, which is critical for the u_y/u_x ratio to remain constant.
3. The u_θ/u_y ratio increases roughly 20% in moving from elastic response to inelastic response. Results indicate that the increase is applicable for both one-way and two-way mass eccentric structures. The increase also appears to be independent of the magnitude of the inelastic ground motions, as long as the ground motions are sufficient to produce relatively uniform yielding in both translational directions. The results for the systems featuring lateral bracing do not directly support these conclusions, but it is not felt that enough data exists for braced systems to contradict the conclusions either. For the system with a strength eccentricity, however, the u_θ/u_y ratio roughly doubles in moving from elastic response to

inelastic response. The non-uniform column yielding due to the strength eccentricity likely produced significant instantaneous stiffness eccentricities, resulting in noticeable increases in torsional response. This type of eccentricity presents particular difficulties for design because the resulting instantaneous stiffness eccentricities are not present during elastic response.

4. In the finite element analysis of elastic displacement response, no one configuration proved more difficult to predict than the others. With one exception, the predictions for the inelastic responses of each of the configurations using were equally accurate. Overall, the analytical predictions of the elastic displacement response were accurate to within about 7.5%, while the predictions of the inelastic response were accurate to within about 14.5%. A number of the configurations featured two inelastic simulations, with the structure possessing pre-existing inelastic damage and typically amplified ground motions during the second simulation, and the peak displacement predictions proved to be equally accurate as those predicted for the initial inelastic simulation.
5. The elastic torsional response for the more complicated force-resisting systems, including those systems with lateral bracing and with two different types of columns, is more difficult to predict. This trend appears to continue for the inelastic response, as Configurations 5 – 7, which each feature either concentric lateral bracing or two different types of columns, or both, appear on average to be more difficult to predict rotationally than Configurations 3, 4, and 8, having only mass eccentricity. Overall, the analytical predictions of the elastic rotational response were accurate to within about 42%, while the predictions of the inelastic response were accurate to within about 31%. The peak rotations, for both elastic and inelastic simulations, were consistently underestimated by the analytical analyses.
6. Overall, the Abaqus and Drain-3DX analyses predicted equally well the measured peak displacements for both elastic and inelastic response and for a variety of structural configurations. Drain-3DX is slightly more accurate in predicting the peak inelastic rotations than Abaqus, although both were reasonably accurate. Despite the increased modeling capabilities of Abaqus, including a much more general and detailed post-yield material hardening model, Drain-3DX proved to be equally capable, and in some instances more capable, in its analytical performance. In addition, the Abaqus analyses required significantly more computing time and power to complete.
7. The results found by using a “tuned” analytical model proved to be consistent with results using a more simplified analytical model with “design” assumptions, as discussed in Chapter 12. When analyzing elastic response, any differences in the modal frequencies of the analytical model and actual

structure can produce larger errors in the predicted response. When analyzing inelastic response, differences in the modal frequencies become less important, while the amount of the structure able to deform plastically becomes more important to model accurately. Changing the "effective length" of the diagonal bracing altered the modal frequency in the direction of the bracing, and as a result had a noticeable impact on the elastic peak response. However, altering this parameter had no significant impact on the inelastic response. Using an analytical model with some degree of strain hardening results in response predictions that are significantly more accurate than an analytical model with an elastic – perfectly plastic material model.

EQ Test No.	Configuration	PGA [g]				Relative Displacement [in]				Rotation [10^{-3} rad]		
		X-Axis	Y-Axis	Abaqus	Test	X-Axis	Y-Axis	Abaqus	Test	Z-Axis	Drain	Drain
01	25% X-Axis Symmetric Mass	0.238	N/A	0.539	0.475	0.515	0.0	0.0	0.076	N/A	N/A	N/A
02	25% Y-Axis Symmetric Mass	N/A	0.162	0.0	0.0	0.037	0.430	0.368	0.387	N/A	N/A	N/A
03	25% Biaxial Symmetric Mass	0.232	0.160	0.508	0.468	0.472	0.424	0.360	0.408	N/A	N/A	N/A
12	25% X-Axis Symmetric Mass	0.250	N/A	0.470	0.444	0.492	0.0	0.0	0.059	N/A	N/A	0.32
13	25% Y-Axis Symmetric Mass	N/A	0.168	0.0	0.0	0.020	0.342	0.306	0.339	N/A	N/A	0.37
14	25% Biaxial Symmetric Mass	0.248	0.170	0.480	0.437	0.482	0.329	0.318	0.354	N/A	N/A	0.70
27	10% Biaxial $\frac{1}{2}$ Asymmetric Mass [X]	0.102	0.062	0.305	0.282	0.256	0.244	0.201	0.219	1.30	1.17	1.55
22	10% Biaxial $\frac{1}{4}$ Asymmetric Mass	0.109	0.066	0.179	0.230	0.165	0.174	0.186	0.152	0.94	1.17	1.06
32	10% Biaxial $\frac{1}{2}$ Asymmetric Mass [Y] Strength Asymmetry	0.100	0.059	0.213	0.152	0.212	0.056	0.057	0.065	0.230	0.234	0.588
36	10% Biaxial $\frac{1}{2}$ Asymmetric Mass [Y] Concentric Bracing Stiffness Asymmetry	0.117	0.191	0.199	0.175	0.177	0.051	0.040	0.053	0.20	0.14	0.76

Table 13.1 Analytical vs. Experimental Displacement and Rotation Response Comparison – Elastic Simulations

EQ Test No.	Configuration	PGA [g]				Relative Displacement [in.]				Rotation [10 ⁻³ rad]			
		X-Axis	Y-Axis	Abaqus	Drain	X-Axis	Test	Abaqus	Drain	Y-Axis	Test	Abaqus	Drain
07	100% Y-Axis Symmetric Mass	N/A	0.678	0.0	0.0	0.06	1.23	1.27	1.22	N/A	N/A	N/A	N/A
15	100% Biaxial Symmetric Mass	1.080	0.699	2.70	2.76	2.86	1.07	1.12	1.24	0.75	0.84	2.85	
16	150% Biaxial Symmetric Mass	1.582	1.141	5.53	4.61	5.41	4.14	4.63	4.31	1.28	2.14	5.35	
28	100% Biaxial $\frac{1}{2}$ Asymmetric Mass [X]	1.115	0.711	2.53	2.54	2.53	1.18	1.36	1.29	12.94	18.31	18.26	
29	150% Biaxial $\frac{1}{2}$ Asymmetric Mass [X]	1.629	1.121	4.79	3.75	4.78	4.03	5.05	4.08	24.94	30.12	34.58	
23	100% Biaxial $\frac{1}{4}$ Asymmetric Mass	1.299	0.797	3.07	3.21	3.17	1.20	1.43	1.18	14.94	18.40	21.94	
45	100% Biaxial $\frac{1}{4}$ Asymmetric Mass	1.187	0.699	2.84	2.35	2.46	1.96	2.03	1.57	12.85	16.79	16.46	
46	135% Biaxial $\frac{1}{4}$ Asymmetric Mass	1.559	0.990	4.47	2.60	3.72	3.74	3.25	3.87	16.93	19.33	23.28	
34	100% Biaxial $\frac{1}{2}$ Asymmetric Mass [Y] Strength Asymmetry	1.086	0.658	1.65	1.68	1.31	0.54	0.56	0.46	3.60	4.12	8.39	
35	150% Biaxial $\frac{1}{2}$ Asymmetric Mass [Y] Strength Asymmetry	1.637	1.045	2.59	2.68	2.81	0.91	1.02	1.22	6.28	7.56	13.82	

Table 13.2a Analytical vs. Experimental Displacement and Rotation Response Comparison – Inelastic Simulations

EQ Test No.	Configuration	PGA [g]				Relative Displacement [in]				Rotation [10^{-3} rad]				
		X-Axis	Y-Axis	Abaqus	Drain	X-Axis	Test	Abaqus	Drain	Y-Axis	Test	Abaqus	Drain	Z-Axis
39	100% Biaxial $\frac{1}{2}$ Asymmetric Mass [Y] Concentric Bracing [Y] Stiffness Asymmetry [Y]	0.846	1.926	2.29	1.57	1.64	4.56	1.70	1.96	28.14	19.84	18.49		
40	100% X-Axis 90% Y-Axis $\frac{1}{2}$ Asymmetric Mass [Y] Concentric Bracing [Y] Stiffness Asymmetry [Y]	1.318	1.951	3.08	3.31	3.90	9.11	1.51	2.94	68.01	17.63	27.80		
41	100% X-Axis 75% Y-Axis $\frac{1}{2}$ Asymmetric Mass [Y] Concentric Bracing [Y] Stiffness Asymmetry [Y] Strength Asymmetry [X]	1.367	1.582	1.97	1.77	2.17	1.53	0.99	1.01	7.84	7.77	7.77	11.52	
42	100% X-Axis 85% Y-Axis $\frac{1}{2}$ Asymmetric Mass [Y] Concentric Bracing [Y] Stiffness Asymmetry [Y] Strength Asymmetry [X]	1.357	1.881	1.92	1.89	2.32	1.68	1.10	1.42	10.98	11.81	13.66		

Table 13.2b Analytical vs. Experimental Displacement and Rotation Response Comparison – Inelastic Simulation

LIST OF REFERENCES

1. Annigeri, Satish., and A K. Mittal, and Ashok K. Jain. "Uncoupled Frequency Ratio in Asymmetric Buildings." Earthquake Engineering & Structural Dynamics, volume 25, number 8, August 1996, pages 871-881.
2. Bozorgnia, Y., and W. K. Tso. "Inelastic Earthquake Response of Asymmetric Structures." Journal of Structural Engineering, volume 112, number 2, February 1986, pages 383-400.
3. Bruneau, Michel, and Niandi Wang. "Some Aspects of Energy Methods for the Inelastic Seismic Response of Ductile SDOF Structures." Engineering Structures, volume 18, number 1, January 1996, pages 1-12.
4. Bugeja, M. N., and D. P. Thambiratnam, and G. H. Brameld. "The Influence of Stiffness and Strength Eccentricities on the Inelastic Earthquake Response of Asymmetric Structures." Engineering Structures, volume 21, 1999, pages 856-863.
5. Chandler, A. M., and G. L. Hutchinson. "Evaluation of Code Torsional Provisions by a Time History Approach." Earthquake Engineering and Structural Dynamics, volume 15, number 4, May 1987, pages 491-516.
6. Chandler, A. M., and X. N. Duan. "Evaluation of Factors Influencing the Inelastic Seismic Performance of Torsionally Asymmetric Buildings." Earthquake Engineering and Structural Dynamics, volume 20, number 1, January 1991, pages 87-95.
7. Chandler, A. M., and J. C. Correnza, and G. L. Hutchinson. "Inelastic Response of Code-Designed Eccentric Structures Subject to Bi-directional Loading." Structural Engineering and Mechanics, volume 5, number 1, January 1997, pages 51-58.
8. Chandler, A. M., and J. C. Correnza, and G. L. Hutchinson. "Influence of Accidental Eccentricity on Inelastic Seismic Torsional Effects in Buildings." Engineering Structures, volume 17, number 3, April 1995, pages 167-178.
9. Chandler, A. M., and X. N. Duan. "Performance of Asymmetric Code-Designed Buildings for Serviceability and Ultimate Limit States." Earthquake Engineering and Structural Dynamics, volume 26, number 7, July 1997, pages 717-735.
10. Chandler, A. M., and J. C. Correnza, and G. L. Hutchinson. "Period-Dependent Effects in Seismic Torsional Response of Code Systems." Journal of Structural Engineering, volume 120, 1994, pages 3418-3434.
11. Chandler, A. M., and X. N. Duan, and A. Rutenberg. "Seismic Torsional Response: Assumptions, Controversies and Research Progress." European Earthquake Engineering, volume 10, 1996, pages 37-51.

12. Chandler, A. M., and G. L. Hutchinson. "Torsional Coupling Effects in the Earthquake Response of Asymmetric Buildings." Engineering Structures, volume 8, number 4, October 1986, pages 222-236.
13. Chen, G. and J. Wu. "Seismic Performance of Multiple Tuned Mass Dampers in Suppressing Multi-mode Responses of Building Structures." Proceedings of The International Society for Optical Engineering, volume 4330, 2001, pages 460-470.
14. Chopra, Anil K., and Rakesh K Goel. "Evaluation of Torsional Provisions in Seismic Codes." Journal of Structural Engineering, volume 117, number 12, December 1991, pages 3762-3782.
15. Correnza, J. C., and G. L. Hutchinson. "Effect of Transverse Load-Resisting Elements on Inelastic Earthquake Response of Eccentric-Plan Buildings." Earthquake Engineering and Structural Dynamics, volume 23, number 1, January 1994, pages 75-89.
16. Correnza, J. C., and G. L. Hutchinson, and A. M. Chandler. "A Review of Reference Models for Assessing Inelastic Seismic Torsional Effects in Buildings." Soil Dynamics and Earthquake Engineering, volume 11, number 8, 1992, pages 465-484.
17. Correnza, J. C., and A. M. Chandler, and G. L. Hutchinson. "Seismic Response of Flexible-Edge Elements in Code-Designed Torsionally Unbalanced Structures." Engineering Structures, volume 17, number 3, April 1995, pages 158-166.
18. Cruz, E. F. and A. K. Chopra. "Elastic Earthquake Response of Building Frames". Journal of Structural Engineering, volume 112, number 3, March 1986, pages 443-459.
19. Cruz, E. F. and A. K. Chopra. "Simplified Procedures for Earthquake Analysis of Buildings". Journal of Structural Engineering, volume 112, number 3, March 1986, pages 461-480.
20. De-La-Colina, J. "Effects of Torsion Factors on Simple Non-Linear Systems Using Fully-Bidirectional Analyses." Earthquake Engineering and Structural Dynamics, volume 28, 1999, pages 691-706.
21. De La Llera, Juan C., and Anil K. Chopra. "Estimation of Accidental Torsion Effects for Seismic Design of Buildings." Journal of Structural Engineering, volume 121, number 1, January 1995, pages 102-114.
22. De La Llera, Juan C., and Anil K. Chopra. "Evaluation of Code Accidental-Torsion Provisions from Building Records." Journal of Structural Engineering, volume 120, number 2, February 1994, pages 597-616.
23. De La Llera, Juan C., and Anil K. Chopra. "Inelastic Behavior of Asymmetric Multistory Buildings." Journal of Structural Engineering, volume 122, number 6, June 1996, pages 597-606.
24. De La Llera, Juan C., and Anil K. Chopra. "A Simplified Model for Analysis and Design of Asymmetric-Plan Buildings." Earthquake Engineering and Structural Dynamics, volume 24, number 4, April 1995, pages 573-594.

25. De La Llera, Juan C., and Anil K. Chopra. "Understanding the Inelastic Seismic Behavior of Asymmetric-Plan Buildings." Earthquake Engineering and Structural Dynamics, volume 24, number 4, April 1995, pages 549-572.
26. DeStefano, M., and A. Rutenberg. "Comparison of the Present SEAOC/UBC Torsional Provisions with the Old Ones." Engineering Structures, volume 19, number 8, August 1997, pages 655-664.
27. DeStefano, Mario, and Giuseppe Faella, and Roberto Ramasco. "Inelastic Response and Design Criteria of Plan-Wise Asymmetric Systems." Earthquake Engineering and Structural Dynamics, volume 22, number 3, March 1993, pages 245-259.
28. DeStefano, Mario, and Giuseppe Faella, and Roberto Ramasco. "Inelastic Seismic Response of One-Way Plan-Asymmetric Systems Under Bi-Directional Ground Motions." Earthquake Engineering and Structural Dynamics, volume 27, number 4, April 1998, pages 363-376.
29. Duan, X. N., and A. M. Chandler. "An Optimized Procedure for Seismic Design of Torsionally Unbalanced Structures." Earthquake Engineering and Structural Dynamics, volume 26, 1997, pages 737-757.
30. Ferhi, A., and K. Z. Truman. "Behavior of Asymmetric Building Systems Under a Monotonic Load - I." Engineering Structures, volume 18, number 2, February 1996, pages 133-141.
31. Ferhi, A., and K. Z. Truman. "Behavior of Asymmetric Building Systems Under a Monotonic Load - II." Engineering Structures, volume 18, number 2, February 1996, pages 142-153.
32. Filiatrault, André, and Pierre Leger, and Rene Tinawi. "Computation of Seismic Energy in Inelastic Structures." Engineering Structures, volume 16, number 6, August 1994, pages 425-436.
33. Ghersi, Aurelio, and Pier Paolo Rossi. "Influence of Bi-Directional Ground Motions on the Inelastic Response of One-Storey In-Plan Irregular Systems." Engineering Structures, volume 23, 2001, pages 579-591.
34. Goel, Rakesh K., and Anil K. Chopra. "Dual-Level Approach for Seismic Design of Asymmetric-Plan Buildings." Journal of Structural Engineering, volume 120, number 1, January 1994, pages 161-179.
35. Goel, Rakesh K., and Anil K. Chopra. "Effects of Plan Asymmetry in Inelastic Seismic Response of One-Story Systems." Journal of Structural Engineering, volume 117, number 5, May 1991, pages 1492-1513.
36. Goel, Rakesh K., and Anil K. Chopra. "Inelastic Seismic Response of One-Story, Asymmetric-Plan Systems - Effects of Stiffness and Strength Distribution." Earthquake Engineering and Structural Dynamics, volume 19, number 7, October 1990, pages 949-970.

37. Goel, Rakesh K., and Anil K. Chopra. "Inelastic Seismic Response of One-Story, Asymmetric-Plan Systems - Effects of System Parameters and Yielding." Earthquake Engineering and Structural Dynamics, volume 20, number 3, March 1991, pages 201-222.
38. Goel, Rakesh K. "Seismic Response of Asymmetric Systems: Energy-Based Approach." Journal of Structural Engineering, volume 123, number 11, November 1997, pages 1444-1453.
39. Gupta, R. K., and G. L. Hutchinson. "Horizontal and Vertical Seismic Response of Torsionally Coupled Buildings." Engineering Structures, volume 16, number 1, January 1994, pages 11-24.
40. Hahn, G. D., and X. Liu. "Torsional Response of Unsymmetric Buildings to Incoherent Ground Motions." Journal of Structural Engineering, volume 120, number 4, April 1994, pages 1158-1181.
41. Hao, H., and X. N. Duan. "Seismic Response of Asymmetric Structures to Multiple Ground Motions." Journal of Structural Engineering, volume 121, number 11, November 1995, pages 1557-1564.
42. Hao, Hong. "Torsional Response of Building Structures to Spatial Random Ground Excitations." Engineering Structures, volume 19, number 2, February 1997, pages 105-112.
43. Hejal, Reem, and Anil K. Chopra. "Earthquake Response of Torsionally Coupled Frame Buildings." Journal of Structural Engineering, volume 115, number 4, April 1989, pages 834-851.
44. Humar, J. L. and A. M. Awad. "Design for Seismic Torsional Forces." Canadian Journal of Civil Engineering, volume 11, 1984, pages 150-163.
45. Humar, J. L. and P. Kumar. "Effect of Orthogonal Inplane Structural Elements on Inelastic Torsional Response." Earthquake Engineering and Structural Dynamics, volume 28, 1999, pages 1071-1097.
46. Humar, J. L. and P. Kumar. "Torsional Motion of Buildings During Earthquakes. I. Elastic Response." Canadian Journal of Civil Engineering, volume 25, 1998, pages 898-916.
47. Humar, J. L. and P. Kumar. "Torsional Motion of Buildings During Earthquakes. II. Inelastic Response." Canadian Journal of Civil Engineering, volume 25, 1998, pages 917-934.
48. Jiang, W., and G. L. Hutchinson, and J.L. Wilson. "Definitions of Static Eccentricity for Design of Asymmetric Shear Buildings." Engineering Structures, volume 15, number 3, 1993, pages 167-178.
49. Jiang, W., and G. L. Hutchinson, and J.L. Wilson. "Inelastic Torsional Coupling of Building Models." Engineering Structures, volume 18, number 4, 1996, pages 288-300.

50. Kan, Christopher L., and Anil K. Chopra. "Effects of Torsional Coupling on Earthquake Forces in Buildings." Journal of Structural Engineering, volume 103, number ST4, April 1977, pages 805-819.
51. Kan, Christopher L., and Anil K. Chopra. "Elastic Earthquake Analysis of a Class of Torsionally Coupled Buildings." Journal of Structural Engineering, volume 103, number ST4, April 1977, pages 821-838.
52. Kan, Christopher L., and Anil K. Chopra. "Simple Model for Earthquake Response Studies of Torsionally Coupled Buildings." Journal of the Engineering Mechanics Division, volume 107, number EM5, October, 1981, pages 935-951.
53. Kan, Christopher L., and Anil K. Chopra. "Torsional Coupling and Earthquake Response of Simple Elastic and Inelastic Systems." Journal of Structural Engineering, volume 104, number ST8, April 1981, pages 1569-1587.
54. Lam, Nelson, and John L. Wilson, and Graham L. Hutchinson. "Review of the Torsional Coupling of Asymmetrical Wall-Frame Buildings." Engineering Structures, volume 19, number 3, March 1997, pages 233-246.
55. Lamaitre, J. and J. L. Chaboche. Mechanics of Solid Materials, Cambridge University Press, 1990.
56. Lin, Wen-Hsiung, and Anil K. Chopra, and Juan Carlos De la Llera. "Accidental Torsion in Buildings: Analysis Versus Earthquake Motions." Journal of Structural Engineering, volume 127, number 5, May 2001, pages 475-481.
57. Maher, M. R., and A. M. Chandler, and R. H. Bassett. "Coupled Lateral-Torsional Behaviour of Frame Structures Under Earthquake Loading." Earthquake Engineering and Structural Dynamics, volume 20, number 1, January 1991, pages 61-85.
58. Mittal, A. K. and A. K. Jain. "Effective Strength Eccentricity Concept for Inelastic Analysis of Asymmetric Structures." Earthquake Engineering and Structural Dynamics, volume 24, number 1, January 1995, pages 69-84.
59. Nader, M. N. and A. Astaneh-Asl. "Shaking Table Tests of Rigid, Semirigid, and Flexible Steel Frames." Journal of Structural Engineering, volume 122, number 6, June 1996, pages 589-596.
60. Palazzo, B. and F. Fraternali. "Seismic Ductility Demand in Buildings Irregular in Plan: A New Single Story Nonlinear Model." Proceedings of the 9th World Conference on Earthquake Engineering, Tokyo - Kyoto, Japan, volume V, V-43 - V-48, 1988.
61. Park, Chang-Ho, and Dong-Guen Lee, and Jin-Keun Kim. "Effect of Gravity Load on Seismic Response of Steel Framed Structures." Engineering Structures, volume 19, number 6, June 1997, pages 439-451.
62. Paulay, Thomas. "Are Existing Seismic Torsion Provisions Achieving the Design Aims?." Earthquake Spectra, volume 13, number 2, May 1997, pages 259-279.

63. Paulay, T. "Displacement-Based Design Approach to Earthquake-Induced Torsion in Ductile Buildings." Engineering Structures, volume 19, number 9, September 1997, pages 699-707.
64. Pecknold, D. A. "Inelastic Structural Response to 2D Ground Motion." Journal of The Engineering Mechanics Division, volume 100, number EM5, October 1974, pages 949-963.
65. Pekau, O. A. and A. Rutenberg. "Evaluation of the Torsional Provisions in the 1985 NBCC." Proceedings from the 5th Canadian Conference for Earthquake Engineering, Ottawa, 1987.
66. Plummer, Frederick Boyd. "Cyclic Plasticity and Structural Energy Dissipation." Dissertation, University of Illinois at Urbana-Champaign, Urbana, Illinois, 1975.
67. Prasad, B. K., and K. S. Jagadish. "Inelastic Torsional Response of a Single-Story Framed Structure." Journal of Engineering Mechanics, volume 115, number 8, August 1989, pages 1782-1797.
68. Riddell, Rafael, and Hernan Santa-Maria. "Inelastic Response of One-Storey Asymmetric-Plan Systems Subjected to Bi-Directional Earthquake Motions." Earthquake Engineering and Structural Dynamics, volume 28, 1992, pages 273-285.
69. Rutenberg, A. "Nonlinear Response of Asymmetric Building Structures and Seismic Codes: A State of the Art Review." European Earthquake Engineering, volume 2, 1992, pages 3-19.
70. Rutenberg, A., and O. A. Pekau. "Seismic Code Provisions for Asymmetric Structures: A Re-evaluation." Engineering Structures, volume 9, number 4, October 1987, pages 255-264.
71. Rutenberg, A., and O. A. Pekau. "Seismic Code Provisions for Asymmetric Structures: Low Period Systems." Engineering Structures, volume 11, April 1989, pages 92-97.
72. Sadek, A. W., and W. K. Tso. "Strength Eccentricity Concept for Inelastic Analysis of Asymmetric Structures." Engineering Structures, volume 11, number 3, July 1989, pages 189-194.
73. Thewalt, Christopher R., and Stephen A. Mahin. "Non-planar Pseudodynamic Testing." Earthquake Engineering and Structural Dynamics, volume 24, number 5, May 1995, pages 733-746.
74. Tso, W. K. and H. Ying. "Additional Seismic Inelastic Deformation Caused by Structural Asymmetry." Earthquake Engineering and Structural Dynamics, volume 19, number 2, February 1990, pages 243-258.
75. Tso, W. K. and T. J. Zhu. "Design of Torsionally Unbalanced Structural Systems Based on Code Provisions I: Ductility Demand." Earthquake Engineering and Structural Dynamics, volume 21, 1992, pages 609-627.
76. Tso, W. K. "Discussion on a Paper by X. N. Duan and A. M. Chandler." Earthquake Engineering and Structural Dynamics, volume 23, number 11, November 1994, pages 1275-1278.

77. Tso, W. K. and A. W. Sadek. "Inelastic Seismic Response of Simple Eccentric Structures." Earthquake Engineering and Structural Dynamics, volume 13, number 2, March-April 1985, pages 255-269.
78. Tso, W. K. and H. Ying. "Lateral Strength Distribution Specification to Limit Additional Inelastic Deformation of Torsionally Unbalanced Structures." Engineering Structures, volume 14, number 4, 1992, pages 263-277.
79. Tso, W. K. Discussion on a Paper by J. C. Correnza, and G. L. Hutchinson, and A. M. Chandler, "A Review of Reference Models for Assessing Inelastic Seismic Torsional Effects in Buildings," and Authors' reply. Soil Dynamics Earthquake Engineering, volume 12, 1993, pages 445-447.
80. Tso, W. K., and C. M. Wong. "Seismic Displacements of Torsionally Unbalanced Buildings." Earthquake Engineering and Structural Dynamics, volume 24, number 10, October 1995, pages 1371-1387.
81. Tso, W. K. and K. M. Dempsey. "Seismic Torsional Provisions for Dynamic Eccentricity." Journal of Earthquake Engineering and Structural Dynamics, volume 8, number 3, May-June 1980, pages 275-289.
82. Tso, W. K. "Static Eccentricity Concept for Torsional Moment Estimation." Journal of Structural Engineering, volume 116, number 5, May 1990, pages 1199-1212.
83. Tso, W. K. and V. Meng. "Torsional Provisions in Building Codes." Canadian Journal of Civil Engineering, volume 9, 1982, pages 38-46.
84. Wong, C. M., and W. K. Tso. "Evaluation of Seismic Torsional Provisions in Uniform Building Code." Journal of Structural Engineering, volume 121, number 10, October 1995, pages 1436-1442.
85. Wong, C. M., and W. K. Tso. "Inelastic Seismic Response of Torsionally Unbalanced Systems Designed Using Elastic Dynamic Analysis." Earthquake Engineering and Structural Dynamics, volume 23, number 7, July 1994, pages 777-798.
86. Zhu, T. J. and W. K. Tso. "Design of Torsionally Unbalanced Structural Systems Based on Code Provisions II: Strength Distribution." Earthquake Engineering and Structural Dynamics, volume 21, 1992, pages 629-644.

APPENDIX A

SHAKING TABLE CHARACTERISTICS, INSTRUMENTATION, AND DATA DESCRIPTIONS

This appendix describes the physical characteristics of the Construction Engineering Research Laboratory (CERL) shaking table and data acquisition system, and describes the instrumentation systems and their application in the earthquake simulations. Section A.1 describes the shake table's physical characteristics, performance specifications, and control system. Section A.2 provides an overview of the instrumentation used in this project. Each type of transducer utilized in this experimental research is described, and its location on the model structure is described.

A.1 CERL SHAKETABLE

(A) GENERAL DESCRIPTION

The CERL shake table, or Biaxial Shock Test Machine (BSTM), was constructed by the U.S. Army in 1971 to support research for the SAFEGUARD antiballistic missile system development. This research required the unique operating characteristics of high frequency and high acceleration for payloads weighing up to 12,000 lbs. In 1996, a complete "triaxial" upgrade of the BSTM was completed, and was hence renamed the Triaxial Earthquake and Shock Simulator (TESS). This project was conducted after the triaxial upgrade was completed, thus this description summarizes the capabilities of the new TESS configuration.

A plan view of the TESS is shown in Figure A.1. The TESS has controlled motion capability for its vertical axis and both horizontal axes. Prior to the "triaxial" upgrade, the shake table had controlled motion capability for only its vertical axis and one horizontal axis. The triaxial motion control requires that six degrees of freedom (DOFs) be controlled: translations for each of the three axes of motion, roll, pitch, and yaw. The roll DOF corresponds to rotation about the north-south horizontal axis, the pitch DOF corresponds to rotation about the east-west horizontal axis, and the yaw DOF corresponds to rotation about the vertical axis. For the testing in this project, no vertical motions were input. Earthquake simulations were either uniaxial, utilizing one horizontal axis, or biaxial, utilizing both horizontal axes.

The TESS, operating in the earthquake simulation mode, can test payload as heavy as 120,000 lb. TESS can produce displacements of up to ± 6 in. to simulate any recorded or theoretical earthquake event. In this mode, the TESS can test larger specimens over larger displacement ranges more typical of seismic vibrations. The table below lists the performance parameters for the two test modes. The TESS combines a high payload capability with a broad frequency range, high acceleration performance, a wide displacement range, and simultaneous, independent control of up to three axes of vibration. Biaxial performance is rated with a 12 kip payload, and the triaxial performance with a 120 kip payload. Larger payloads can be tested at lower acceleration levels, while smaller payloads can be tested at up to twice the rated accelerations.

The shake table platform is a welded cellular aluminum structure measuring 12-ft x 12-ft in plan. This construction results in a table that is rigid and lightweight. The system is powered by 17 electro-hydraulic actuators, as described in Table A.1. Separate reinforced concrete vertical and horizontal foundations accommodate all reactions. Their combined weight is approximately 4,000 kips. The separate foundations minimize cross-coupling between vertical and horizontal reaction forces. Seismic test control is provided in the three primary degrees of freedom (x-horizontal, y-horizontal and z-vertical axes), and also provides active control of the remaining three degrees of freedom (yaw, pitch and roll axes) to minimize undesirable out of plane vibrations during a test. The Seismic Test Execution (STEX) computer software/hardware system provides the operator interface to the TESS system. The STEX system provides the capability to completely define uniaxial, biaxial, or triaxial shake table tests, execute the tests, and record all test response data. The system also provides extensive data analysis and plotting capabilities. A 128-channel transducer signal conditioning and data acquisition system is used to record test response data from a wide variety of transducers such as accelerometers, displacement sensors, strain gauges, etc. Shake table input and response parameters are recorded along with the response data from the test item mounted on the shake table platform, which documents the input and the response of each test.

A.2 INSTRUMENTATION

Instrumentation was provided to measure displacements and accelerations of the shake table platform and model structure diaphragm, and strains in the columns. For certain model configurations, instrumentation was provided to measure strains in diagonal bracing, accelerations at the top of the mass stack, and relative displacements of the column bottom plates. Table A.2 lists all of the data channels, including for

which model configuration(s) each data channel was utilized. Figures A.2 – A.10 show the locations of all transducers, and where appropriate, the directions of measured displacement or acceleration.

(A) ACCELEROMETERS

Endevco model 7290-10 and 7290-30 accelerometers were used to measure accelerations. These accelerometers employ variable capacitance microsensors with a frequency response of 0-500 Hz. The accelerometers were connected to Endevco model 4476.2 and 4476.2A signal conditioners, which provided power, balancing, and signal amplification. Acceleration measurement ranges for the various sensors differed, but checks of all data recorded indicated the ranges were satisfactory. All accelerometers were mounted on aluminum blocks that had been epoxied to the model, the shake table, or the top of the mass stack.

As shown in Figure A.2, two accelerometers measured the north-south accelerations of the shake table surface, and two accelerometers measured the east-west accelerations of the shake table surface. In addition, four accelerometers measured the vertical accelerations of the shake table surface. This configuration was the minimum required to not only measure the accelerations of the shake table surface along each of the three axes, but to also measure any angular accelerations which might be present about each of the three axes. In addition, three accelerometers located within the shake table itself measure the accelerations along the vertical axis and both horizontal axes.

As shown in Figure A.3, the diaphragm accelerations were measured by five accelerometers along the north-south horizontal axis, and five accelerometers along the east-west horizontal axis. Based on the assumption that the diaphragm was completely rigid, this configuration surpassed the minimum required to completely measure the acceleration and angular acceleration motion of the diaphragm, as discussed above. However, the additional accelerometers provided a means to check the assumption of diaphragm rigidity, providing valuable redundancy in the acceleration data acquisition.

For one test configuration, accelerometers were mounted on the top of the mass stack to measure accelerations along both horizontal axes as shown in Figure A.6. These accelerometers provided a means of verifying that the masses were rigidly attached to the diaphragm, and that the entire stack was accelerating in concert with the diaphragm. One of the test configurations in which the masses were

stacked in one corner only, Test Configuration 8, was chosen to measure the mass stack accelerations, as this configuration would be the most severe case for the aforementioned phenomenon.

(B) ABSOLUTE DISPLACEMENT TRANDUCERS

Celesco model PT101-10 and PT101-60A variable resistance displacement transducers were used to measure the absolute displacement of the shaking table. The Celesco unit employs a spring-loaded precision rotary potentiometer with flexible steel wire cable wrapped around the potentiometer shaft. The other end of the cable is attached to the point where displacement is to be measured. When displacement occurs, the cable motion rotates the shaft of the potentiometer, causing a change in electrical resistance that is proportional to displacement. Transducers were connected to Endevco model 4471.3 signal conditioners, which provided DC power and electrical balancing, but no signal amplification.

The transducers were mounted on large steel reference frames that were placed on the shake table foundation; transducer mounts were bolted to the reaction frame members. Transducer sensing elements were attached to the model and the shake table using stranded steel extension wires. In measuring the displacements of the shaking table surface, the wires were typically connected to shake table mounting bolts that were secured in the shake table platform. In measuring the displacements of the diaphragm, the wires were typically connected below the diaphragm to the ends of the bolts that secure the column assemblies to the diaphragm. Measurement locations are shown in Figures A.4 and A.5.

As shown in Figures A.4 and A.5, three displacements were measured along both the north-south and east-west horizontal axis of both the shake table surface and the diaphragm. Three displacements along one axis allows the measurement of both the translational and rotational motion. In actuality, displacements at only two locations are required to measure both of these motions along one axis. Thus, the third displacement measurement provides a measure of redundancy. Utilizing the displacements along the other horizontal axis to measure the rotation provides, in the case of the shake table surface, redundancy for the rotation measurement. The aforementioned displacements also provide, in the case of the diaphragm, another means of verifying the rigidity of the diaphragm, and if true, provides further redundancy in the displacement data acquisition.

(C) LINEAR VARIABLE DISPLACEMENT TRANSDUCERS (LVDTs)

Schaevitz model HR200 AC LVDTs with a measurement range of +/- 0.2 inches were used to measure vertical uplift displacement between the base of a column and the shake table surface. These measurements were performed at the base of two of the four columns. The LVDTs were connected to Endevco model 4478.1A signal conditioners, which provide AC power, demodulation, signal amplification and electrical balancing.

The LVDTs were used to measure the displacement of the column bottom plates near the pipe relative to the displacement of the shake table surface in an effort to check on the possibility of bending in the column bottom plate. As seen in Figures A.7 and A.8, a 28" x 10" x 2" steel plate was mounted to the shake table mounting bolts that secure the column base plate. A smaller 10" x 2" x 1/4" steel plate was then clamped to the larger steel plate. The LVDT transducer was then clamped to the smaller steel plate. Note that in Figures A.7 and A.8, the clamps and the shake table mounting bolts have been omitted from the diagrams to provide clarity.

(D) STRAIN GAGES

Electrical resistance strain gages were installed on all of the pipe columns used in the first seven test configurations and on the steel straps used as diagonal bracing in test configurations six and seven. Each of the pipe columns was instrumented with Measurements Group type EA-06-125TF-120 strain gages, which contain two constantan alloy sensing grids located in a 90° rosette pattern that are temperature compensated for steel. These gages are of open-faced construction with a 1.0 mil polyimide film backing. Each gage sensing grid is 0.125 inches long by 0.150 inches wide. Each gage was connected to a Vishay model 2120 signal conditioner to provide power, balancing, and signal amplification. In this configuration, the strain gage formed two arms of a Wheatstone bridge, with the remaining two arms consisting of precision resistors in the signal conditioner equipment.

For each pipe column, as shown in Figure A.9, four gages were equally spaced about the perimeter at each end, for a total of eight gages. In placing the four gages around the pipe perimeter, two were lined up along the north-south axis, and two along the east-west axis, in order to measure each of the two bending moment components in the pipe at the location of the strain gages. Prior to attaching each gage

to the column, the column surface in the vicinity of the proposed gage location was ground to remove the rough surface treatment on the pipe columns.

In order to facilitate the computation of the bending moments from the strain measurements, strain gages should be placed at a location that does not experience plastic strain. The closer the gages are to the ends of the pipe, the larger the measured strains will be. In the first four test configurations, the gages were placed approximately 10 inches from each end of the pipe column. However, the data indicated that the strain gages were experiencing plastic strain. In the following three test configurations, the gages were moved to approximately 15 inches from each end of the pipe. For the last test configuration, strain gages were not mounted on the pipe columns. Prior to being placed in the model, each column assembly was subjected to a proof test in a 650-kip load frame. The aforementioned 650-kip load frame is located at Newmark Civil Engineering Laboratory at the University of Illinois at Urbana-Champaign. The purpose of these proof tests was to check the integrity of the pipe column to base plate welds, and also to calibrate the strain gages. The calibration check of the strain gages was performed by comparing the output of the strain gages to the strain calculated using another strain measuring device, a clip-on deflection gage with a known gage length.

The diagonal bracing, as seen in Figure A.10, used in test configurations six and seven was instrumented with Measurements Group type EA-06-125TF-120 strain gages, which contain two constantan alloy sensing grids located in a 90° rosette pattern that are temperature compensated for steel. These gages are of open-faced construction with a 1.0 mil polyimide film backing. Each gage sensing grid is 0.125 inches long by 0.150 inches wide. Each gage was connected to a Vishay model 2120 signal conditioner to provide power, balancing, and signal amplification. In this configuration, the strain gage formed two arms of a Wheatstone bridge, with the remaining two arms consisting of precision resistors in the signal conditioner equipment.

The design of each strap was to act as a tension-only brace. Thus, using only two strain gages each brace would be satisfactory to characterize the brace behavior. The braces were expected to buckle in compression, therefore, the strain gages were placed as far away from the center of the strap as possible, in a location where the out-of-plane bending of the strap during buckling would not damage the strain gage. However, the strain gages needed to be placed far enough away from the locations where the braces were welded to the gusset plates to ensure that strains would be uniform throughout the strap cross section, or to minimize St. Venant's effects. The gages were ultimately placed approximately 19-1/2 inches from the strap ends, which corresponds to approximately 5 inches from the locations where the

braces were welded to the gusset plates. Prior to being placed on the model, each diagonal brace strap was subjected to a proof test in a 850-kip load frame in order to calibrate the strain gages. The 850-kip load frame previously mentioned is located at the Construction Engineering Research Laboratory (CERL).

In Figure A.10, two strain gage channels are shown at each strain gage location on the diagonal braces. The first channels listed correspond to the strain gages located on the braces on the north side of the model structure, which is the side shown in the figure. The second channels listed correspond to the strain gages located in the same position on the braces on the south side of the model structure. Thus, SD4T is the channel corresponding to the strain gage on the top of the northeast brace, while SD1T is the channel corresponding to the strain gage on the top of the southeast brace.

(E) DATA ACQUISITION AND SHAKING TABLE CONTROL

Figure A.11 is a schematic block diagram of the instrumentation, data acquisition, and test control systems. The transducer channels were recorded using a digital data acquisition system. Transducer output signals were connected to the STEX data acquisition system, which has a 128-channel capability. All data was sampled at 200 Hz. The STEX data acquisition system provides a sample-and-hold and antialias filter on each channel to prevent time-skewing and eliminate high-frequency noise and aliasing effects. The Seismic Test Execution (STEX) computer program includes setup and execution of the seismic test, data acquisition of experimental test data, data analysis, and data management information. All of this information is incorporated into a common database for each test performed.

	Z Axis [Vertical] (Triaxial / Biaxial)	X Axis [N-S] (Triaxial / Biaxial)	Y AXIS [E-W] (Triaxial Only)
Actuators	9 @ 90 kips	6 @ 75 kips	2 @ 75 kips
Maximum Stoke	+/- 1.38 in	+/- 2.75 in	+/- 6.0 in
Peak Velocity	30 in/sec	50 in/sec	50 in/sec
Peak Acceleration	1.0 g / 30 g	2.0 g / 20 g	2.0 g
Frequency Range	100 Hz / 200 Hz	100 Hz / 200 Hz	100 Hz
Test Specimen Weight	120 kips / 12 kips		

Table A.1 TESS Performance Parameters

Transducer	Quantity	Direction	Gage Location	Configuration
AT2Y	Acceleration	E-W Axis	Table Surface, South Side	1,2,3,4,5,6,7,8
AT2Z	Acceleration	Vertical	Table Surface, South Side	1,2,3,4,5,6,7,8
AT4X	Acceleration	N-S Axis	Table Surface, West Side	1,2,3,4,5,6,7,8
AT4Z	Acceleration	Vertical	Table Surface, West Side	1,2,3,4,5,6,7,8
AT6Y	Acceleration	E-W Axis	Table Surface, North Side	1,2,3,4,5,6,7,8
AT6Z	Acceleration	Vertical	Table Surface, North Side	1,2,3,4,5,6,7,8
AT8X	Acceleration	N-S Axis	Table Surface, East Side	1,2,3,4,5,6,7,8
AT8Z	Acceleration	Vertical	Table Surface, East Side	1,2,3,4,5,6,7,8
AS1X	Acceleration	N-S Axis	Diaphragm, Southeast Corner	1,2,3,4,5,6,7,8
AS1Y	Acceleration	E-W Axis	Diaphragm, Southeast Corner	1,2,3,4,5,6,7,8
AS2Y	Acceleration	E-W Axis	Diaphragm, South Side	1,2,3,4,5,6,7,8
AS3X	Acceleration	N-S Axis	Diaphragm, Southwest Corner	1,2,3,4,5,6,7,8
AS3Y	Acceleration	E-W Axis	Diaphragm, Southwest Corner	1,2,3,4,5,6,7,8
AS4X	Acceleration	N-S Axis	Diaphragm, West Side	1,2,3,4,5,6,7,8
AS5X	Acceleration	N-S Axis	Diaphragm, Northwest Corner	1,2,3,4,5,6,7,8
AS5Y	Acceleration	E-W Axis	Diaphragm, Northwest Corner	1,2,3,4,5,6,7,8
AS6Y	Acceleration	E-W Axis	Diaphragm, Midpoint of North Side	1,2,3,4,5,6,7,8
AS7X	Acceleration	N-S Axis	Diaphragm, Northeast Corner	1,2,3,4,5,6,7,8
AS7Y	Acceleration	E-W Axis	Diaphragm, Northeast Corner	1,2,3,4,5,6,7,8
AS8X	Acceleration	N-S Axis	Diaphragm, East Side	1,2,3,4,5,6,7,8
AS9X	Acceleration	N-S Axis	Diaphragm, Center	1,2,3,4,5,6,7,8
AS9Y	Acceleration	E-W Axis	Diaphragm, Center	1,2,3,4,5,6,7,8
ATX	Acceleration	N-S Axis	Internal to Table, Center	1,2,3,4,5,6,7,8
ATY	Acceleration	E-W Axis	Internal to Table, Center	1,2,3,4,5,6,7,8
ATZ	Acceleration	Vertical	Internal to Table, Center	1,2,3,4,5,6
AM7X	Acceleration	N-S Axis	Top of Mass Stack	8
AM7Y	Acceleration	E-W Axis	Top of Mass Stack	8

Table A.2.a Instrumentation List for Model

Transducer	Quantity	Direction	Gage Location	Configuration
DTX	Displacement	N-S Axis	Internal to Table, Center	1,2,3,4,5,6,7,8
DTY	Displacement	E-W Axis	Internal to Table, Center	1,2,3,4,5,6,7,8
DTZ	Displacement	Vertical	Internal to Table, Center	1,2,3,4,5,6,7,8
DT3Z	Displacement	Vertical	Southwest Corner Column Base Plate	1,2,3,4,5,6
DT5Z	Displacement	Vertical	Northwest Corner Column Base Plate	1,2,3,4,5,6
DT1X	Displacement	N-S Axis	Table Surface, Southeast Corner	1,2,3,4,5,6,7,8
DT2X	Displacement	N-S Axis	Table Surface, Midpoint of South Side	1,2,3,4,5,6,7,8
DT3X	Displacement	N-S Axis	Table Surface, Southwest Corner	1,2,3,4,5,6,7,8
DT3Y	Displacement	E-W Axis	Table Surface, Southwest Corner	1,2,3,4,5,6,7,8
DT4Y	Displacement	E-W Axis	Table Surface, Midpoint of West Side	1,2,3,4,5,6,7,8
DT5Y	Displacement	E-W Axis	Table Surface, Northwest Corner	1,2,3,4,5,6,7,8
DTPIT	Displacement	Pitch Axis	Internal to Table, Center	7
DTROL	Displacement	Roll Axis	Internal to Table, Center	7
DTYAW	Displacement	Yaw Axis	Internal to Table, Center	7
DS1X	Displacement	N-S Axis	Diaphragm, Southeast Corner	1,2,3,4,5,6,7,8
DS2X	Displacement	N-S Axis	Diaphragm, Midpoint of South Side	1,2,3,4,5,6,7,8
DS3X	Displacement	N-S Axis	Diaphragm, Southwest Corner	1,2,3,4,5,6,7,8
DS3Y	Displacement	E-W Axis	Diaphragm, Southwest Corner	1,2,3,4,5,6,7,8
DS4Y	Displacement	E-W Axis	Diaphragm, Midpoint of West Side	1,2,3,4,5,6,7,8
DS5Y	Displacement	E-W Axis	Diaphragm, Northwest Corner	1,2,3,4,5,6,7,8
VTX	Velocity	N-S Axis	Internal to Table, Center	7
VTY	Velocity	E-W Axis	Internal to Table, Center	7
VTZ	Velocity	Vertical	Internal to Table, Center	7

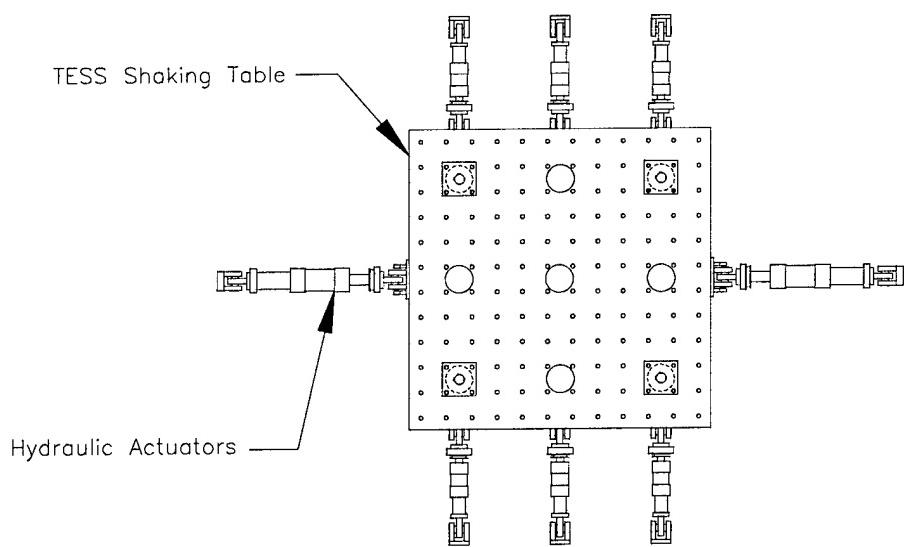
Table A.2.b Instrumentation List for Model

Transducer	Quantity	Direction	Gage Location	Configuration
S1TS	Strain	Column	Southeast Column, Top, South Side	1,2,3,4,5,6,7
S1TW	Strain	Column	Southeast Column, Top, West Side	1,2,3,4,5,6,7
S1TN	Strain	Column	Southeast Column, Top, North Side	1,2,3,4,5,6,7
S1TE	Strain	Column	Southeast Column, Top, East Side	1,2,3,4,5,6,7
S1BS	Strain	Column	Southeast Column, Bottom, South Side	1,2,3,4,5,6,7
S1BW	Strain	Column	Southeast Column, Bottom, West Side	1,2,3,4,5,6,7
S1BN	Strain	Column	Southeast Column, Bottom, North Side	1,2,3,4,5,6,7
S1BE	Strain	Column	Southeast Column, Bottom, East Side	1,2,3,4,5,6,7
S2TS	Strain	Column	Southwest Column, Top, South Side	1,2,3,4,5,6,7
S2TW	Strain	Column	Southwest Column, Top, West Side	1,2,3,4,5,6,7
S2TN	Strain	Column	Southwest Column, Top, North Side	1,2,3,4,5,6,7
S2TE	Strain	Column	Southwest Column, Top, East Side	1,2,3,4,5,6,7
S2BS	Strain	Column	Southwest Column, Bottom, South Side	1,2,3,4,5,6,7
S2BW	Strain	Column	Southwest Column, Bottom, West Side	1,2,3,4,5,6,7
S2BN	Strain	Column	Southwest Column, Bottom, North Side	1,2,3,4,5,6,7
S2BE	Strain	Column	Southwest Column, Bottom, East Side	1,2,3,4,5,6,7
S3TS	Strain	Column	Northwest Column, Top, South Side	1,2,3,4,5,6,7
S3TW	Strain	Column	Northwest Column, Top, West Side	1,2,3,4,5,6,7
S3TN	Strain	Column	Northwest Column, Top, North Side	1,2,3,4,5,6,7
S3TE	Strain	Column	Northwest Column, Top, East Side	1,2,3,4,5,6,7
S3BS	Strain	Column	Northwest Column, Bottom, South Side	1,2,3,4,5,6,7
S3BW	Strain	Column	Northwest Column, Bottom, West Side	1,2,3,4,5,6,7
S3BN	Strain	Column	Northwest Column, Bottom, North Side	1,2,3,4,5,6,7
S3BE	Strain	Column	Northwest Column, Bottom, East Side	1,2,3,4,5,6,7
S4TS	Strain	Column	Northeast Column, Top, South Side	1,2,3,4,5,6,7
S4TW	Strain	Column	Northeast Column, Top, West Side	1,2,3,4,5,6,7
S4TN	Strain	Column	Northeast Column, Top, North Side	1,2,3,4,5,6,7
S4TE	Strain	Column	Northeast Column, Top, East Side	1,2,3,4,5,6,7
S4BS	Strain	Column	Northeast Column, Bottom, South Side	1,2,3,4,5,6,7
S4BW	Strain	Column	Northeast Column, Bottom, West Side	1,2,3,4,5,6,7
S4BN	Strain	Column	Northeast Column, Bottom, North Side	1,2,3,4,5,6,7
S4BE	Strain	Column	Northeast Column, Bottom, East Side	1,2,3,4,5,6,7

Table A.2.c Instrumentation List for Model

Transducer	Quantity	Direction	Gage Location	Configuration
SD1B	Strain	Diagonal Brace	Southeast Diagonal Brace, Bottom	6,7
SD1T	Strain	Diagonal Brace	Southeast Diagonal Brace, Top	6,7
SD2B	Strain	Diagonal Brace	Southwest Diagonal Brace, Bottom	6,7
SD2T	Strain	Diagonal Brace	Southwest Diagonal Brace, Top	6,7
SD3B	Strain	Diagonal Brace	Northwest Diagonal Brace, Bottom	6,7
SD3T	Strain	Diagonal Brace	Northwest Diagonal Brace, Top	6,7
SD4B	Strain	Diagonal Brace	Northeast Diagonal Brace, Bottom	6,7
SD4T	Strain	Diagonal Brace	Northeast Diagonal Brace, Top	6,7

Table A.2.d Instrumentation List for Model



Up = + Vertical Z-Axis
East = + Lateral Y-Axis
South = + Longitudinal X-Axis

Figure A.1 Plan View of USACERL Shake Table

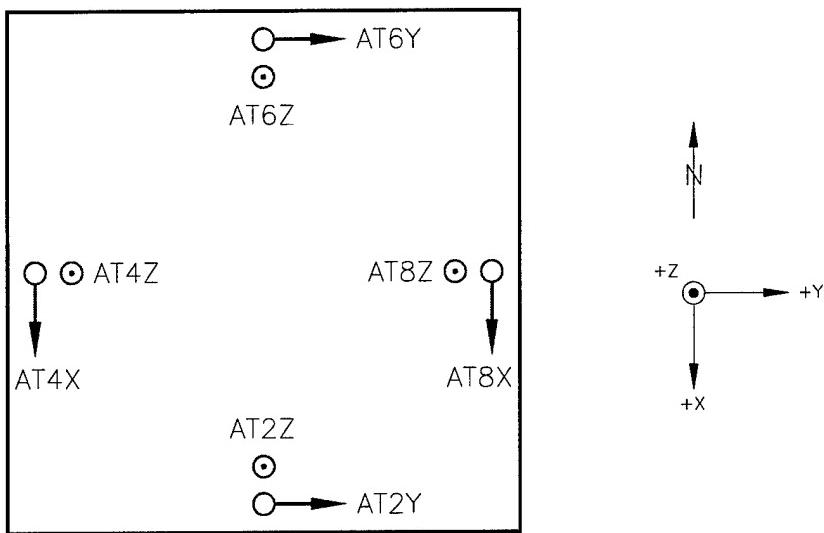


Figure A.2 Shaketable Acceleration Transducers

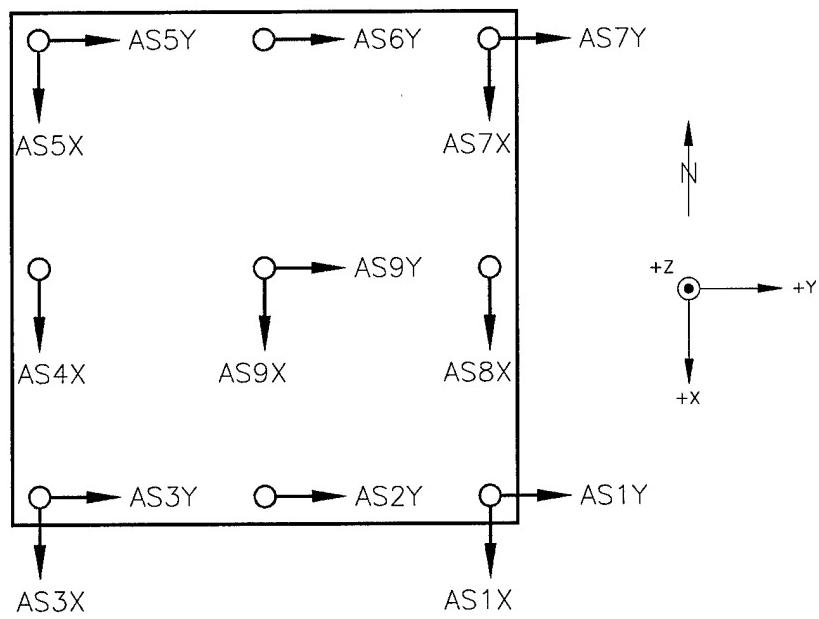


Figure A.3 Diaphragm Acceleration Transducers

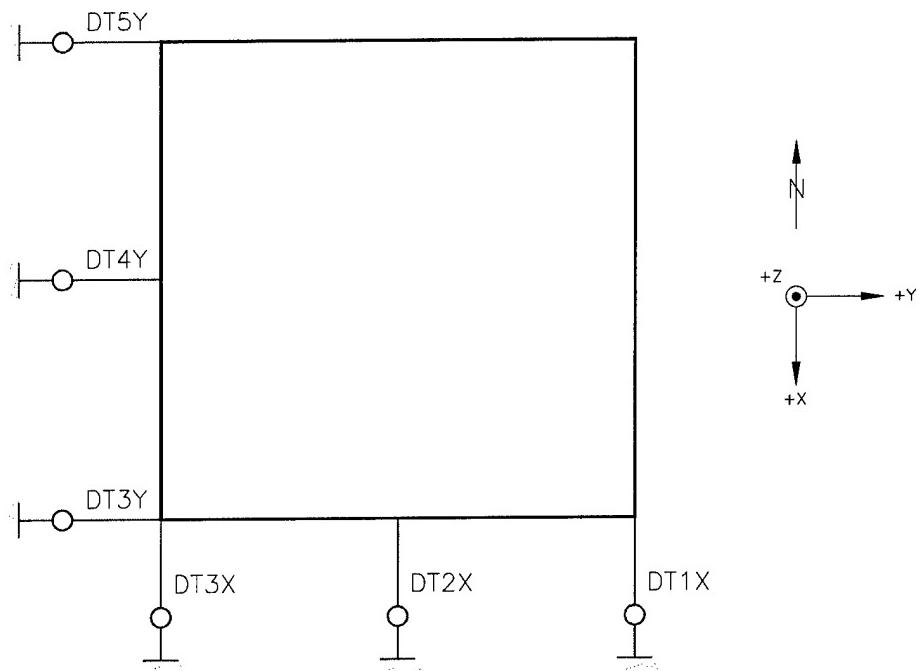


Figure A.4 Shaketable Displacement Transducers

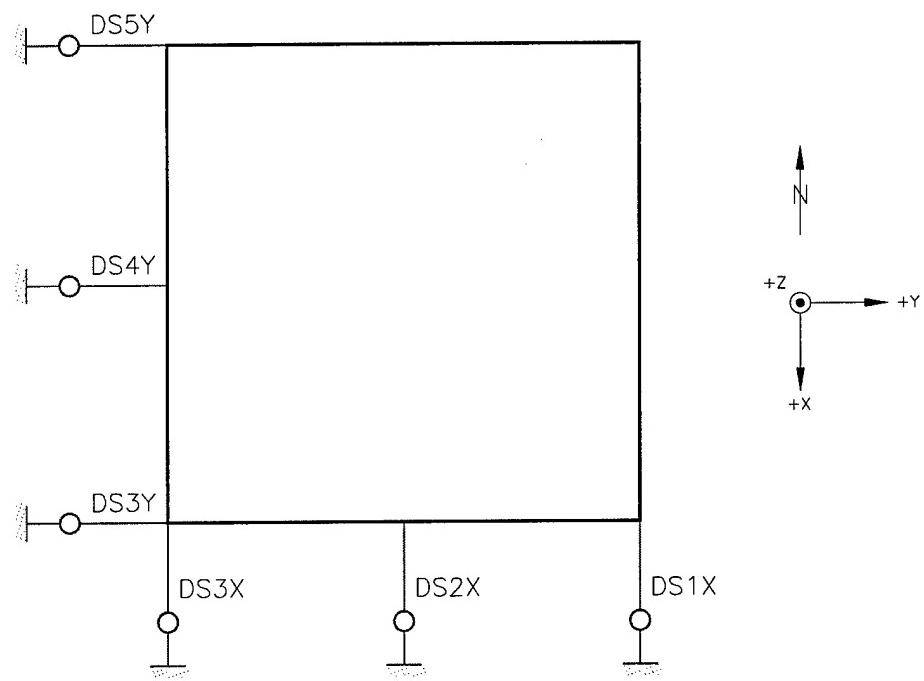


Figure A.5 Diaphragm Displacement Transducers

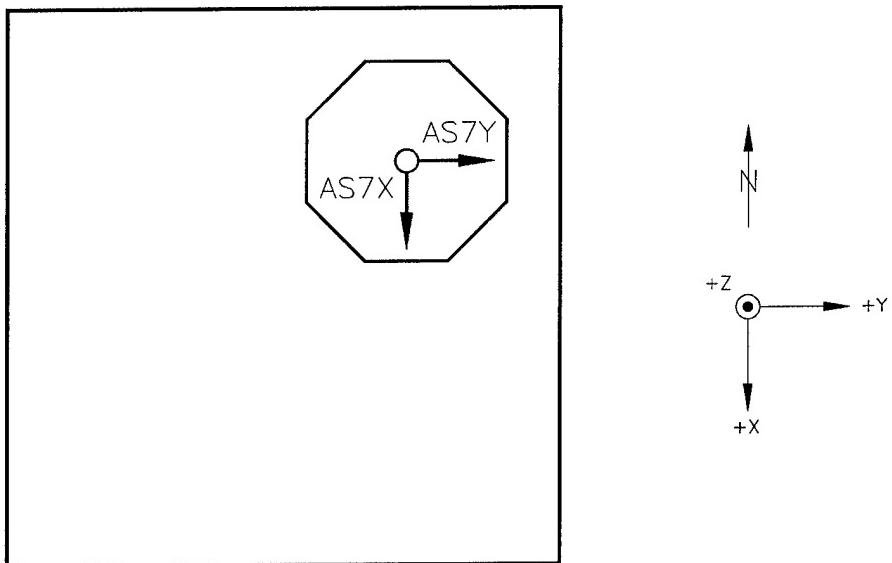


Figure A.6 Mass Stack Acceleration Transducers

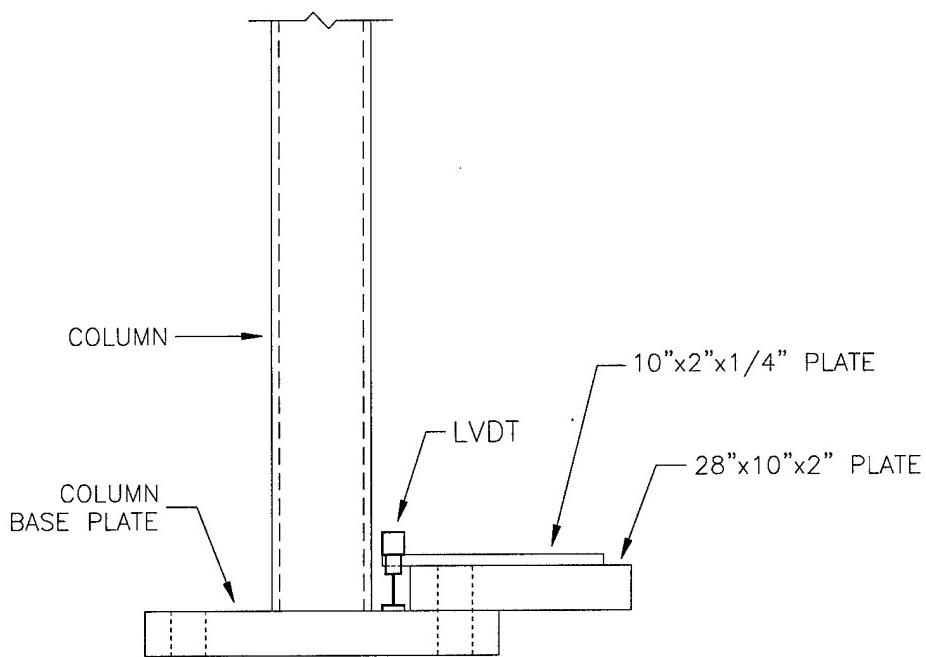


Figure A.7 Elevation View of Column Base Plate LVDT Transducer

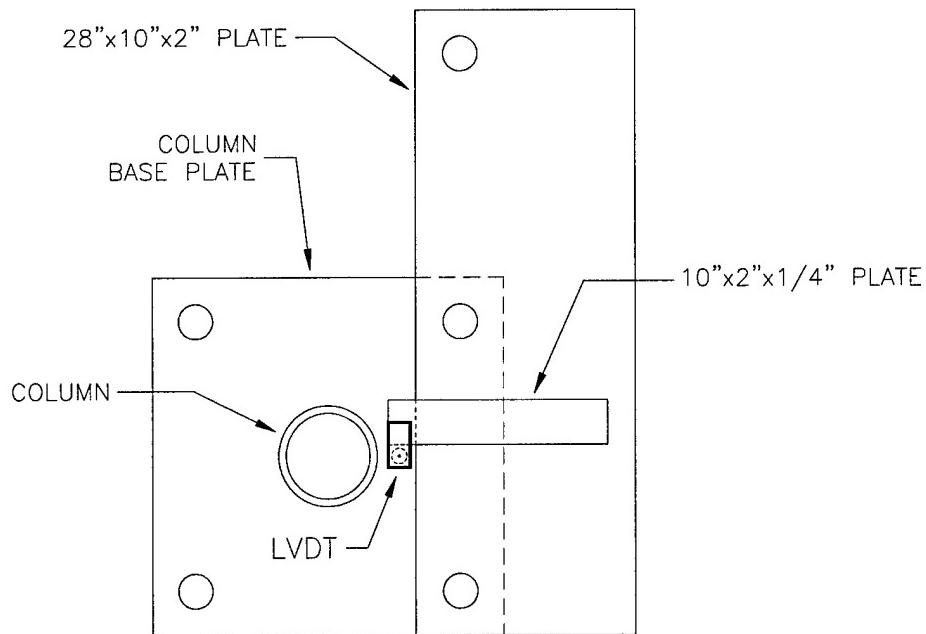


Figure A.8 Plan View of Column Base Plate LVDT Transducer

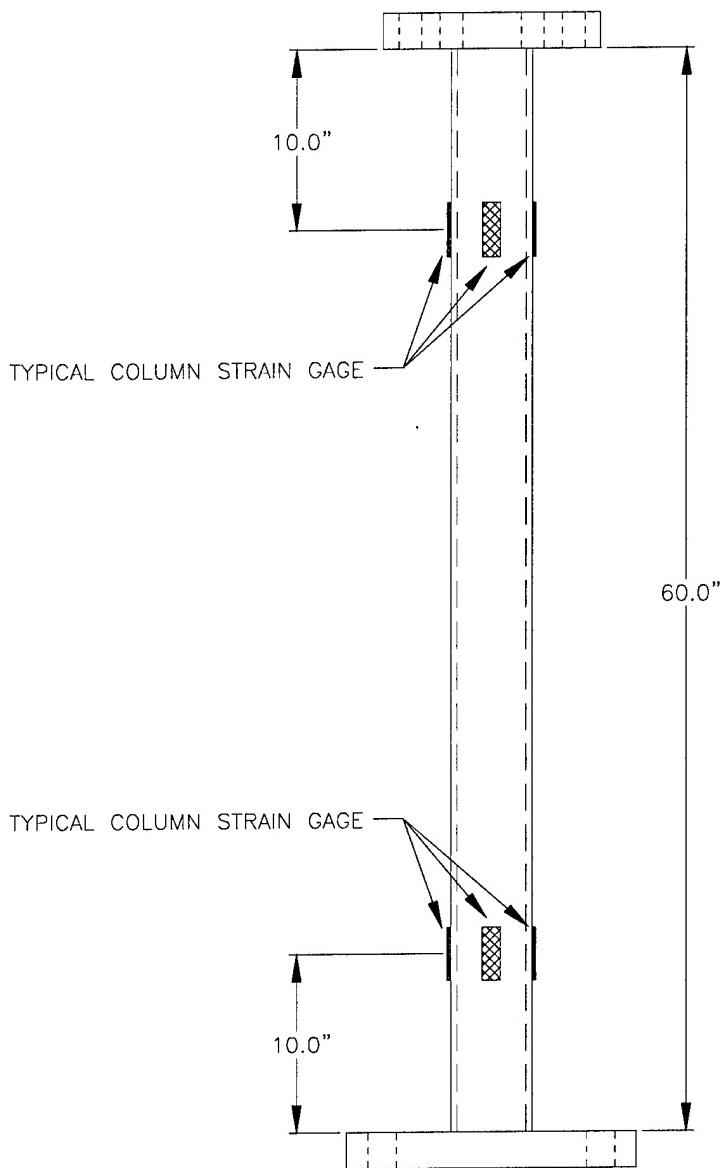


Figure A.9 Column Strain Gage Locations

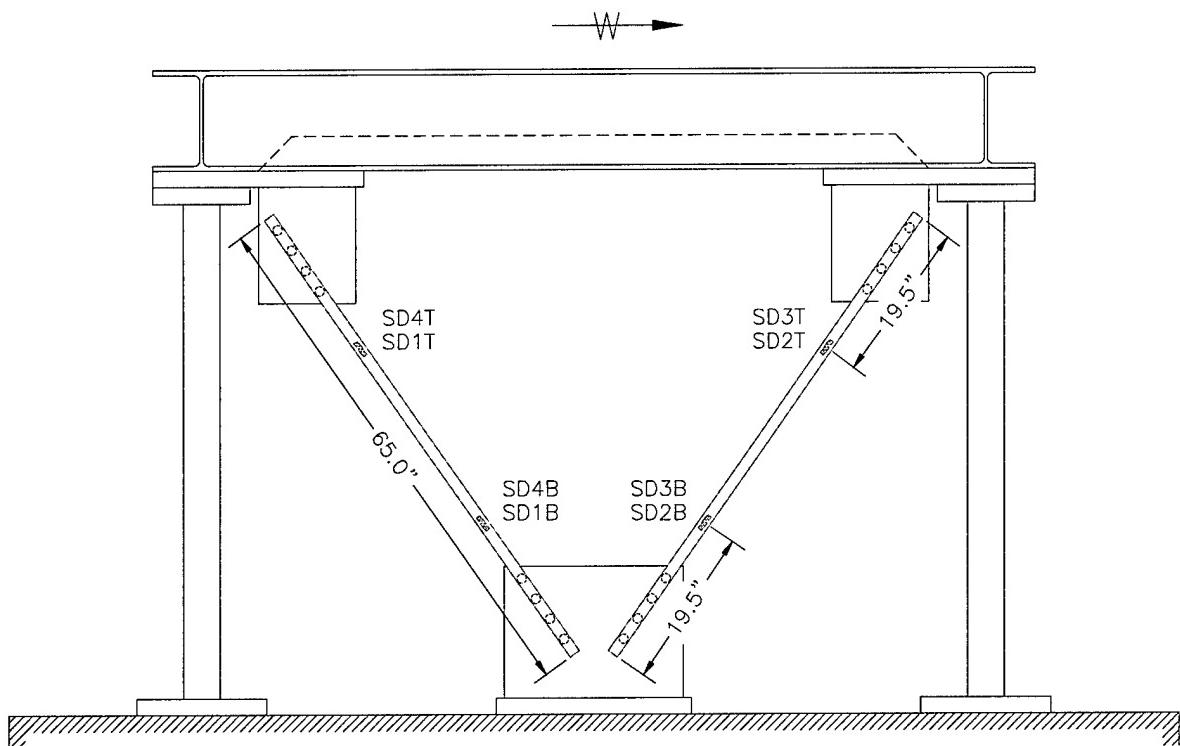


Figure A.10 Diagonal Brace Strain Gage Locations

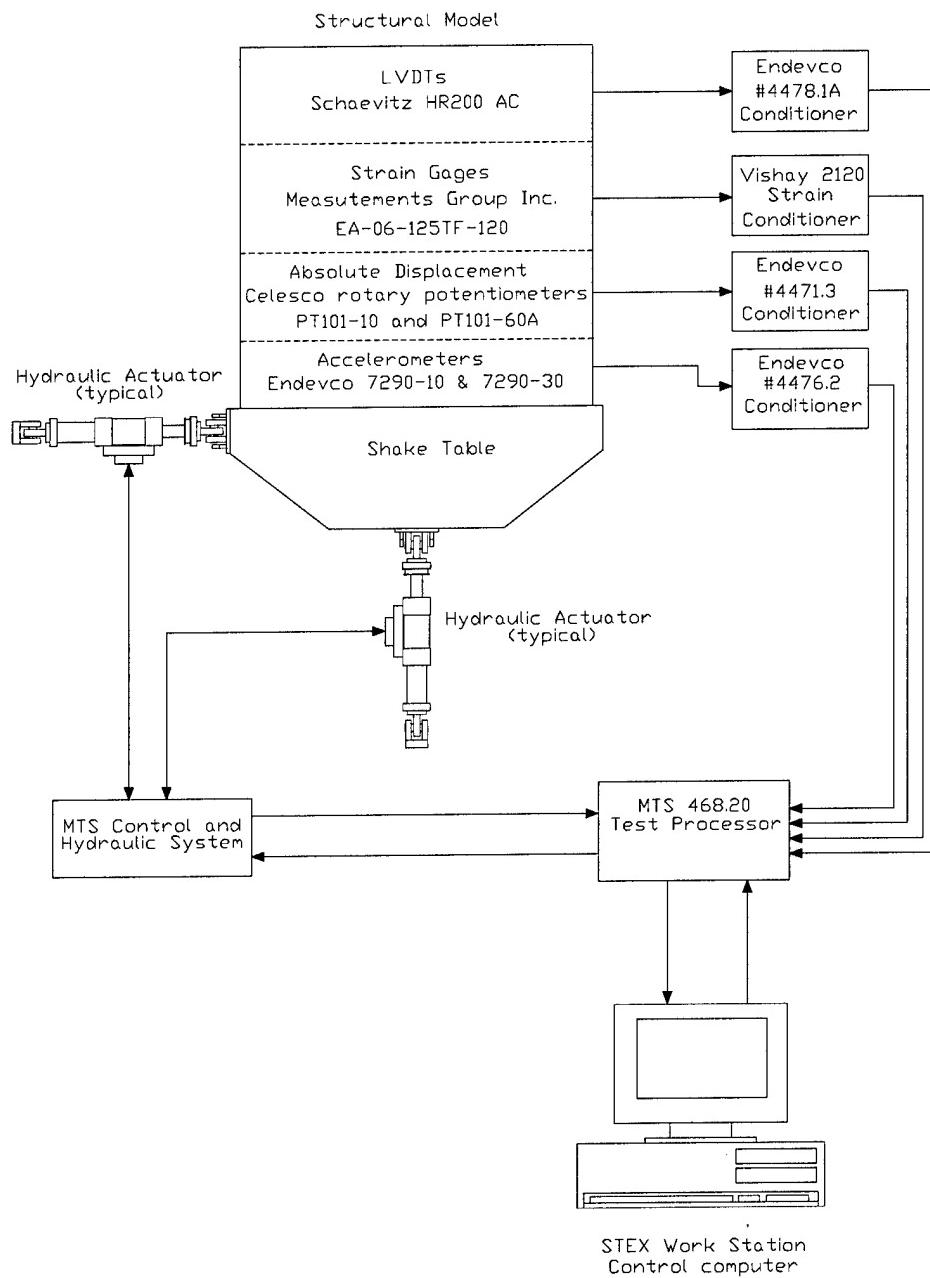


Figure A.11 Block Diagram Showing Shake Table Controls and Data Acquisition Systems

REPORT DOCUMENTATION PAGE

*Form Approved
OMB No. 0704-0188*

Public reporting burden for this collection of information is estimated to average 1 hour per response, including the time for reviewing instructions, searching existing data sources, gathering and maintaining the data needed, and completing and reviewing this collection of information. Send comments regarding this burden estimate or any other aspect of this collection of information, including suggestions for reducing this burden to Department of Defense, Washington Headquarters Services, Directorate for Information Operations and Reports (0704-0188), 1215 Jefferson Davis Highway, Suite 1204, Arlington, VA 22202-4302. Respondents should be aware that notwithstanding any other provision of law, no person shall be subject to any penalty for failing to comply with a collection of information if it does not display a currently valid OMB control number. PLEASE DO NOT RETURN YOUR FORM TO THE ABOVE ADDRESS.

1. REPORT DATE (DD-MM-YYYY) 07-2003		2. REPORT TYPE Final		3. DATES COVERED (From - To)	
4. TITLE AND SUBTITLE Nonlinear Seismic Response of Asymmetric Structures		5a. CONTRACT NUMBER			
		5b. GRANT NUMBER			
		5c. PROGRAM ELEMENT NUMBER			
6. AUTHOR(S) John F. Sfura		5d. PROJECT NUMBER 4A161102AT23			
		5e. TASK NUMBER			
		5f. WORK UNIT NUMBER EJ0			
7. PERFORMING ORGANIZATION NAME(S) AND ADDRESS(ES) U.S. Army Engineer Research and Development Center (ERDC) Construction Engineering Research Laboratory (CERL) PO Box 9005 Champaign, IL 61826-9005		8. PERFORMING ORGANIZATION REPORT NUMBER ERDC/CERL MP-03-2			
9. SPONSORING / MONITORING AGENCY NAME(S) AND ADDRESS(ES)		10. SPONSOR/MONITOR'S ACRONYM(S)			
		11. SPONSOR/MONITOR'S REPORT NUMBER(S)			
12. DISTRIBUTION / AVAILABILITY STATEMENT Approved for public release; distribution is unlimited.					
13. SUPPLEMENTARY NOTES Copies are available from the National Technical Information Service, 5285 Port Royal Road, Springfield, VA 22161.					
14. ABSTRACT The purpose of this study was to investigate the nonlinear, inelastic response of one-story, symmetric- and asymmetric-plan structures to uniaxial and biaxial lateral earthquake ground motions. The investigation is a combined experimental and analytical program. Through the study, the lateral-torsional response of the system was studied for a range of system parameters with the goals of examining the adequacy of current building code torsional design assumptions and the ability of analytical software to predict inelastic response. The experimental part of the investigation involved subjecting a single-story steel moment-frame to a series of uniaxial and biaxial earthquake ground motions on the U.S. Army CERL shaketable. The analytical part of the investigation involved the nonlinear finite element programs Abaqus and Drain-3DX to analyze the response of the model during the earthquake simulations. Implications of the experimental results on the adequacy of seismic design provisions are discussed. In addition, the ability of analytical software to predict inelastic torsional response is discussed for both a model tuned to the measured dynamic properties of the actual structure and a model based on common modeling assumptions. Further, the effects on prediction accuracy of different analytical modeling parameters and assumptions is discussed.					
15. SUBJECT TERMS seismic testing, earthquake ground motion, shake table, structural engineering, simulation and modeling, thesis					
16. SECURITY CLASSIFICATION OF: a. REPORT Unclassified			17. LIMITATION OF ABSTRACT SAR	18. NUMBER OF PAGES 683	19a. NAME OF RESPONSIBLE PERSON John F. Sfura
b. ABSTRACT Unclassified					19b. TELEPHONE NUMBER (include area code)
c. THIS PAGE Unclassified					